Effects of Hydrogen on Materials

Proceedings of the 2008 International Hydrogen Conference

September 7–10, 2008
Jackson Lake Lodge
Grand Teton National Park, Wyoming, USA

Edited by
Brian Somerday
Petros Sofronis
Russell Jones





Published by
ASM International
Materials Park, Ohio 44073-0002
www.asminternational.org

Copyright © 2009
by
ASM International®
All rights reserved

No part of this book may be reproduced, stored in a retrieval system, or transmitted, in any form or by any means, electronic, mechanical, photocopying, recording, or otherwise, without the written permission of the copyright owner.

First printing, July 2009

Great care is taken in the compilation and production of this Volume, but it should be made clear that NO WARRANTIES, EXPRESS OR IMPLIED, INCLUDING, WITHOUT LIMITATION, WARRANTIES OF MERCHANTABILITY OR FITNESS FOR A PARTICULAR PURPOSE, ARE GIVEN IN CONNECTION WITH THIS PUBLICATION. Although this information is believed to be accurate by ASM, ASM cannot guarantee that favorable results will be obtained from the use of this publication alone. This publication is intended for use by persons having technical skill, at their sole discretion and risk. Since the conditions of product or material use are outside of ASM's control, ASM assumes no liability or obligation in connection with any use of this information. No claim of any kind, whether as to products or information in this publication, and whether or not based on negligence, shall be greater in amount than the purchase price of this product or publication in respect of which damages are claimed. THE REMEDY HEREBY PROVIDED SHALL BE THE EXCLUSIVE AND SOLE REMEDY OF BUYER, AND IN NO EVENT SHALL EITHER PARTY BE LIABLE FOR SPECIAL, INDIRECT OR CONSEQUENTIAL DAMAGES WHETHER OR NOT CAUSED BY OR RESULTING FROM THE NEGLIGENCE OF SUCH PARTY. As with any material, evaluation of the material under end-use conditions prior to specification is essential. Therefore, specific testing under actual conditions is recommended.

Nothing contained in this book shall be construed as a grant of any right of manufacture, sale, use, or reproduction, in connection with any method, process, apparatus, product, composition, or system, whether or not covered by letters patent, copyright, or trademark, and nothing contained in this book shall be construed as a defense against any alleged infringement of letters patent, copyright, or trademark, or as a defense against liability for such infringement.

Comments, criticisms, and suggestions are invited, and should be forwarded to ASM International.

ISBN-13: 978-1-61503-003-3
ISBN-10: 1-61503-003-4
SAN: 204-7586

ASM International®
Materials Park, OH 44073-0002
www.asminternational.org

Printed in the United States of America

Preface

The co-organizer of three previous international hydrogen conferences, Neville Moody, had informed us prior to the last conference in 2002 that he and Tony Thompson planned to cede responsibility for organizing the conference series to two other willing colleagues. We must admit that perhaps Neville did mention that he identified us as these candidate conference co-organizers. But either Neville was too oblique or we were simply in denial because when he announced at the 2002 conference banquet that we were indeed the honored successors, we were both somewhat stunned. Prodded by the pressure of such a public pronouncement, we did not protest but rather instinctively arose to acknowledge our nominations. We must give a sincere nod to Neville for such an effective tactic in conscripting the next two conference organizers.

Once we accepted the reality of our commitment, we realized that a unique opportunity awaited us. Shortly after the 2002 conference, it was evident that a renewed interest in developing hydrogen fuel cells was intensifying in places such as the U.S., Japan, and Europe. Indeed, during this time we both added projects funded by the U.S. Department of Energy to our research portfolios, where the objective of these projects was to enable the safe design of components for transporting and storing hydrogen fuel. We anticipated that in the ensuing few years, there would be keen interest in convening another international conference on effects of hydrogen on materials. We judged that many new research efforts dedicated to developing hydrogen fuel infrastructure would be mature enough to present results by 2008—so this was the year we chose for the seventh international conference in this series. Despite our novice stature as conference organizers, we had enough sense to return to Jackson Lake Lodge in Grand Teton National Park and to follow as closely as possible the successful format of previous conferences.

We structured the conference sessions and proceedings volume to highlight several themes: the technological importance of hydrogen effects on structural materials; the impact of bridging science and engineering; and the opportunity to apply new research tools, including simulation techniques as well as experimental methods. We intended to communicate these themes in the opening session of the conference through five invited speakers: Ian Robertson, Rick Gangloff, Yukitaka Murakami, Gjalt Tiekstra, and Monterey Gardiner. The themes were also threaded through many of the other 115 presentations in the oral and poster sessions. The presentations also reflected the international interest in the topics, as authors from 24 different countries were represented.

Now that we are no longer distracted by the many tasks associated with organizing a conference, we can recognize the conference as a success. But this success depended on contributions from many individuals and institutions, and we want to acknowledge them here. We wanted to create a solid technical foundation in the conference sessions, and we are grateful to the 19 speakers we invited to establish this foundation. The technical foundation was also enabled by input from the four other members of the conference program committee: David Delafosse,

Russ Jones, Yukitaka Murakami, and Rick Ricker. We want to express particular thanks to Russ Jones, who not only provided wise counsel as a veteran conference organizer but also served as a co-editor of the proceedings volume. We were able to upgrade some of the conference amenities, maintain affordable conference fees, and provide some modest financial support to the invited speakers largely due to generous financial contributions from several sponsors: American Society of Mechanical Engineers (ASME), ArcelorMittal, ASM International, General Motors, and Toyota. Our time and effort devoted to organizing the conference was explicitly supported by our employers, Sandia National Laboratories and the University of Illinois, and we appreciate that our institutions recognize the importance of the conference series. Two students from the University of Virginia, Yongwon Lee and Michael Francis, provided invaluable support of audio/visual needs in the oral presentation sessions. Lastly, our most profound gratitude is directed to Theresa Beckett at the University of Illinois. Theresa provided tireless administrative support in more ways than we can enumerate here. Her participation was particularly impressive because she was intimately involved during every phase of the project: preparing for the event at Jackson Lake Lodge, helping with tasks on location at the conference, and facilitating creation of the conference proceedings.

As with many new experiences, we encountered some unexpected discoveries during our maiden voyage as co-organizers of the international hydrogen conference. And perhaps the most rewarding discoveries were the many traditions that have been established in this conference series, ranging from the dedication to technical excellence to the choices of conference format and venue. We learned that this conference series belongs to a broad technical community and not to a particular institution or set of conference organizers. Our role has been to merely serve as the current stewards of traditions that we hope will endure.

Brian Somerday
Sandia National Laboratories
Livermore, CA, USA

Petros Sofronis
University of Illinois
Urbana, IL, USA

Contents

Preface iii

Keynote Speaker Session

Science-Based Prognosis to Manage Structural Alloy Performance in Hydrogen 1
R.P. Gangloff, University of Virginia, Charlottesville, VA, USA

Revealing the Fundamental Processes Controlling Hydrogen Embrittlement 22
I.M. Robertson[1], D. Lillig[2], and P.J. Ferreira[3];
1) University of Illinois at Urbana-Champaign, Urbana, IL, USA,
2) ExxonMobil Development Company, Houston, TX, USA,
3) University of Texas at Austin, Austin, TX, USA

Hydrogen Effects on Mechanical Properties

A Coexistent View of Hydrogen Effects on Mechanical Behavior of Crystals: HELP and HEDE 38
W.W. Gerberich[1], D.D. Stauffer[1], and P. Sofronis[2];
1) University of Minnesota, USA,
2) University of Illinois, Urbana-Champaign, IL, USA

Recent Observation of Hydrogen-Induced Cracking of High-Strength Steels 46
C.J. McMahon, Jr.[1], X. Liu[1], J. Kameda[1], and M.J. Morgan[2];
1) University of Pennsylvania, Philadelphia, PA, USA,
2) Savannah River National Laboratory, Aiken SC, USA

Hydrogen Embrittlement of High Strength Steels and Environmental Hydrogen Entry 54
E. Akiyama[1], S. Li[1], Z. Zhang[1], M. Wang[1], K. Matsukado[1], K. Tsuzaki[1], and B. Zhang[2];
1) National Institute for Materials Science, Tsukuba, Ibaraki, Japan,
2) University of Science and Technology Beijing, Beijing, China

Effect of Hydrogen on the Mechanical Properties of Multiphase High Strength Steels 62
L. Duprez[1], K. Verbeken[2], and M. Verhaege[2];
1) ArcelorMittal Research Industry Gent, Zelzate, Belgium,
2) Ghent University, Ghent, Belgium

Mixed-Mode Hydrogen Assisted Cracking in Progressively Drawn Pearlitic Steels 70
J. Toribio and E. Ovejero; University of Salamanca, Zamora, Spain

Hydrogen Effects on the Plasticity of FCC Nickel and Austenitic Alloys 78
D. Delafosse[1], X. Feaugas[2], I. Aubert[3], N. Saintier[4], and J.M. Olive[5];
1) Ecole des Mines de Saint-Etienne, Saint-Etienne, France,
2)Université de La Rochelle, La Rochelle, France,
3) CNRS/Université Bordeaux, Talence, France,
4) Université Bordeaux, Talence, France,
5) Kyushu University-AIST, Fukuoka, Japan

Hydrogen-Assisted Fracture of Austenitic Stainless Steels 88
C. San Marchi[1], K.A. Nibur[1], D.K. Balch[1], B.P. Somerday[1],
X. Tang[2], G.H. Schiroky[2], and T. Michler[3];
1) Sandia National Laboratories, Livermore, CA, USA,
2) Swagelok Company, Solon, OH, USA,
3) Adam-Opel GmbH, Ruesselsheim, Germany

Effect of Hydrogen on Plastic Strain Localization in Single Crystals of Nickel and Austenitic Stainless Steel 97
Y. Yagodzinskyy[1], T. Saukkonen[1], H. Hänninen[1], F. Tuomisto[1],
S. Barannikova[2], and L. Zuev[2];
1) Helsinki University of Technology, Espoo, Finland,
2) Institute of Strength Physics and Materials Science, Tomsk, Russia

Influence of Hydrogen and Prestrain on Tensile Properties of Type 316L Austenitic Stainless Steel 105
T. Matsuo, J. Yamabe, S. Matsuoka, and Y. Murakami;
Kyushu University, Fukuoka-city, Fukuoka, Japan

Effect of Crack-Tip Hydrogen Profiles on the Embrittled Fracture Toughness of a Stainless Steel 113
R.J. Melcher and P.E. Schembri;
Los Alamos National Laboratory, Los Alamos, NM, USA

Hydrogen-Induced Cracking of Metastable Austenitic Stainless and High-Strength Carbon Steels 123
Y. Yagodzinskyy, T. Saukkonen, E. Andronova, L. Rissanen, and H. Hänninen;
Helsinki University of Technology, Espoo, Finland

Hydrogen-Induced Fatigue Crack Growth Acceleration and Martensitic Transformation of an Austenitic Stainless Steel 131
T. Kanezaki, Y. Mine, S. Matsuoka, and Y. Murakami;
Kyushu University, Fukuoka, Japan

Effect of Internal Hydrogen on Fatigue Strength of Type 316 Stainless Steel 139
C. Skipper[1], G. Leisk[1], A. Saigal[1], D. Matson[1], and C. San Marchi[2];
1) Tufts University, Medford, MA, USA,
2) Sandia National Laboratories, Livermore, CA, USA

Hydrogen-Assisted Fracture of Welded AISI 316 Austenitic Stainless Steel 147
X. Tang[1], G.H. Schiroky[1], C. San Marchi[2], and B.P. Somerday[2];
1) Swagelok Company, Solon, OH, USA,
2) Sandia National Laboratories, Livermore, CA, USA

The Role of Hydrogen Induced Microstructural Changes in the Embrittlement of Austenitic-Ferritic Steel 155
W. Świątnicki; Warsaw University of Technology, Warsaw, Poland

Hydrogen-Induced ε-Martensite and Hydrogen Embrittlement of Austenitic Steels 163
V.N. Shyvanyuk, S.M. Teus, and V.G. Gavriljuk;
G.V. Kurdyumov Institute for Metal Physics, Kiev, Ukraine

Hydrogen Effects on Strain-Induced Martensite Formation in Type 304L Stainless Steel 171
M.J. Morgan[1], P.-S. Lam[1], and D.A. Wheeler[2];
1) Savannah River National Laboratory, Aiken, SC, USA,
2) PCC Airfoils, Minerva, OH, USA

Orientation Specific Mechanical Assessment of Hydrogen Precharged Stainless Steels Using Nanoindentation 179
D.F. Bahr[1], N.R. Overman[1], C.W. San Marchi[2], and K.A. Nibur[2];
1) Washington State University, WA, USA,
2) Sandia National Laboratories, Livermore, CA, USA

In situ Electrochemical Nanoindentation: A Nanomechanical Approach to Rank Hydrogen Embrittlement in Extremely Small Volumes 187
A. Barnoush and H. Vehoff; Saarland University, Saarbruecken, Germany

Lattice Defect Formation and Degradation Enhanced by Hydrogen and Strain of Metals 195
K. Takai, and H. Shoda; Sophia University, Tokyo, Japan

Effect of Hydrogen on Microscopic Deformation Process Near Stage II Fatigue Crack Tip 203
Y. Takahashi[1], M. Tanaka[2], K. Higashida[2], and H. Noguchi[2];
1) National Institute of Advanced Industrial Science and Technology, Fukuoka, Japan,
2) Kyushu University, Fukuoka, Japan

Characterization of Hydrogen-Assisted Fracture Mechanism by Fracture Surface Topography Analysis (FRASTA) 211
T. Kobayashi[1], B. Somerday[2], C. San Marchi[2], and K.A. Nibur[2];
1) SRI International, Menlo Park, CA, USA,
2) Sandia National Laboratories, Livermore, CA, USA

The Influence of Hydrogen on the Elastic Modulus and Anelastic Response of Cold Worked Pure Iron 219
R.E. Ricker and D.J. Pitchure;
National Institute of Standards and Technology, Gaithersburg, MD

Improving the Fatigue Properties of Metastable Beta Titanium Alloys by Thermohydrogen Processing 227
P. Schmidt and H.-J. Christ; Universität Siegen, Siegen, Germany

Study of Hydrogen Treatment for Improving Strength and Plasticity of Ti-6Al-4V Alloy 235
Q. Wang and D.L. Sun;
Harbin Institute of Technology, Harbin, Heilongjiang, China

Hydrogen from Aqueous Environments

Stress-Corrosion Cracking of Al-Zn-Mg-Cu Alloys Effects of Composition and Heat-Treatment 243
S.P. Lynch, S.P. Knight, N. Birbilis, and B.C. Muddle;
Monash University, Melbourne, Australia

Stress Corrosion Cracking Behaviour of Alloy 7050-T7451 Plate in an Aqueous Chloride-Nitrate Solution 251
R. Braun; DLR – German Aerospace Center, Köln, Germany

The Role of Hydrogen in the Stress Corrosion Cracking of Mg-Al Alloys 259
N. Winzer[1], A. Atrens[2], W. Dietzel[3], and K.U. Kainer[3];
1) Bundesanstalt für Materialforschung und -prüfung, Berlin, Germany,
2) The University of Queensland, Brisbane, Australia,
3) GKSS-Forschungszentrum Geesthacht GmbH, Geesthacht, Germany

Microstructural Effects on the Stress Corrosion Cracking Response of an Alloy 600 267
A. Aguilar[1], O. Flores[1], J.M. Zagal[1], L. Martinez[1], B. Campillo[2], and H.F. López[3];
1) Universidad Nacional Autónoma de México. Cuernavaca, Morelos, México,
2) Ciudad Universitaria Del Coyoacan, México,
3) University of Wisconsin-Milwaukee, Milwaukee, WI, USA

Hydrogen Sour Environments Conditions for Microalloyed Pipeline Steels Cracking 275
S. Serna[1], F. Cruz-Hernández[1], J. Colín[1], A. Torres-Islas[1], B. Campillo[2], and A. Fragiel[3];
1) CIICAp-FCQeI-UAEM, Cuernavaca, Morelos, México,
2) ICF-FQ-UNAM, Cuernavaca, Morelos, México,
3) PDVSA, Gran Caracas, Venezuela

Analytical Methods for Studying Cathodic Hydrogen Charging into Metals under Competitive Adsorption Conditions 284
F.M. Al-Faqeer[1] and H.W. Pickering[2];
1) Saudi Aramco, Saudi Arabia,
2) The Pennsylvania State University, University Park, PA, USA

The Impact of Dislocation Distribution on Hydrogen Evolution Reaction on Nickel Metal in Sulphuric Acid 292
J. Creus, H. El Alami, and X. Feaugas;
L.E.M.M.A., Université de La Rochelle, France

**Cathodic Hydrogenation of Very High Strength Steels –
Influence of Arsenic as a Hydrogenation Promoter 300**
C. Ly[1], M. Jérome[1], J. Sojka[2], N. Ruscassier[1], and J.-B. Guillot[1];
1) Chemical and Material Engineering Laboratory,
Châtenay-Malabry, France,
2) Technical University of Ostrava, Ostrava, Czech Republic

Structural Design and Materials for Hydrogen Service

**Structural Materials Issues in the Development of the
Hydrogen Energy Infrastructure in Japan 308**
Y. Murakami; Kyushu University, Fukuoka, Japan

Hydrogen Delivery: Infrastructure, Challenges, and Materials Needs 316
S.J. Pawel[1] and M.R. Gardiner[2];
1) Oak Ridge National Laboratory, Oak Ridge, TN, USA
2) U.S. Department of Energy, Washington, DC, USA

**Recent Progress of Research and Development for
Fuel Cell Vehicle Application 324**
K. Kojima; Toyota Motor Corporation, Aichi, Japan

**Metallurgical Considerations for Commercial Steels Used for
Hydrogen Service 332**
D. Stalheim[1] and L. Hayden[2];
1) DGS Metallurgical Solutions, Inc.,Vancouver, WA, USA,
2) Louis Hayden Consultants, Bethlehem, PA, USA

Sustained Load Cracking of Steels for Hydrogen Storage and Delivery 341
K.A. Nibur, B.P. Somerday, D.K. Balch, and C. San Marchi;
Sandia National Laboratories, Livermore, CA, USA

**Tensile and Fracture Properties of Carbon and Low Alloy Steels in
High Pressure Hydrogen 349**
K. Xu and M. Rana; Praxair, Tonawanda, NY, USA

**Damage under High-Pressure Hydrogen Environment of a
High Strength Pipeline Steel X80 ..... 357**
*I. Moro[1], L. Briottet[1] P. Lemoine[1], E. Andrieu[2], C. Blanc[2], G. Odemer[2],
J. Chêne[3], and F. Jambon[3];*
1) CEA, LITEN, DTH, Grenoble, France,
2) CIRIMAT/ENSIACET, Toulouse, France,
3) CEA, DEN, Saclay, France

**Effects of Hydrogen and Prestrain on Tensile Properties of
Low-Carbon Steel Used in Hydrogen Pipelines 365**
H. Nishiguchi, Y. Fukushima, and S. Matsuoka;
Kyushu University, Fukuoka, Japan

The Effect of Residual Hydrogen on High-Cycle Fatigue Property of Welded Joints for Gas Pipeline Steel 373
T. Yamaoka, S.M. Stepanyuk, and S. Matsuoka;
Kyushu University,Fukuoka, Japan

Hydrogen Effects on Fatigue Crack Growth Rate in High Strength Pipeline Steel 381
Ph.P. Darcis, J.D. McColskey, A.N. Lasseigne, and T.A. Siewert;
NIST, Boulder, CO, USA

Blister Fracture of Rubbers for O-Ring Exposed to High Pressure Hydrogen Gas 389
J. Yamabe[1], S. Nishimura[1], M. Nakao[1], and H. Fujiwara[2];
1) Kyushu University, Fukuoka, Japan
2) Research Center for Hydrogen Industrial Use and Storage, (Hydrogenius), Fukuoka, Japan

A Study on Blister Damages of Rubber O-Ring by High Pressure Hydrogen Durability Tester 397
A. Koga[1], J. Nakayama[1], H. Tokumitsu[1], M. Otsuka[2], J. Yamabe[3], and S. Nishimura[3];
1) NOK Corporation, Kanagawa, Japan
2) NOK Corporation, Kumamoto, Japan
3) Kyushu University, Fukuoka, Japan

Friction and Wear of Metals and Coatings Used in Hydrogen 405
R. Erck, G. Fenske, and O. Eryilmaz;
Argonne National Laboratory, Argonne, IL, USA

Residual Stress Relaxation in Shot-Peened High Strength Low Alloy Steel and Its Implications for Hydrogen Assisted Cracking 413
A. Turnbull; National Physical Laboratory, Teddington, Middlesex, UK

Determination of Stainless Steels Mechanical Properties in High-Pressure Hydrogen 421
A.I. Balitskii and V.I. Vitvitskii;
Karpenko Physico-Mechanical Institute National Academy of Sciences of Ukraine, Lviv, Ukraine

Hydrogen Uptake, Transport, and Trapping

Quantitative Analysis of Hydrogen Isotopes in the Near Surface Region of Solids 429
P. Trocellier; CEA – DEN/DANS/DMN, Yvette, France

Hydrogen Trapping Mechanisms in Structural Materials 438
D. Eliezer[1] and T. Boellinghaus[2];
1) Ben-Gurion University of the Negev, Israel
2) Federal Institute for Materials Research and Testing, Berlin, Germany

Nano-Precipitates Design with Hydrogen Trapping Character in High Strength Steels 448
F.-G. Wei, T. Hara, and K. Tsuzaki;
National Institute for Materials Science,Tsukuba, Ibaraki, Japan

Hydrogen Trapping Character of Nano-Sized NBC Precipitates in Tempered Martensite 456
F.-G. Wei and K. Tsuzaki;
National Institute for Materials Science, Tsukuba, Ibaraki, Japan

Hydrogen Trapping at Dislocations in Palladium at Low Temperature: Results from Inelastic Neutron Scattering and Advanced Computations 464
B.J. Heuser[1], H. Ju[1], D.R. Trinkle[1], and T.J. Udovic[2];
1) University of Illinois, Urbana, IL, USA
2) National Institute of Standards and Technology, Gaithersburg, MD, USA

Comparing Thermal Desorption Spectroscopy with Electrochemical Permeation in Order to Reveal the Hydrogen Management in High Strength Steels 469
K. Verbeken[1], L. Duprez[2], M. Verhaege[1];
1) Ghent University, Ghent, Belgium,
2) ArcelorMittal Research Industry Gent, Zelzate, Belgium

Experimental Evaluation of the Hydrogen Distribution in Steel by Thermal Desorption Spectroscopy 477
D.P. Escobar[1], K. Verbeken[1], L. Duprez[2], M. Verhaege[1];
1) Ghent University, Ghent, Belgium
2) ArcelorMittal Research Industry Gent, Zelzate, Belgium

Identification of the Hydrogen Trap Sites in a High Strength TRIP Steel by Means of Thermal Desorption Spectroscopy 485
D.P. Escobar[1], L. Duprez[2], K. Verbeken[1], M. Verhaege[1];
1) Ghent University, Ghent, Belgium
2) ArcelorMittal Research Industry Gent, Zelzate, Belgium

Determination of Diffusible Hydrogen Content in Coated High-Strength Steel 493
C. Georges[1] and T. Sturel[2];
1) Centre for Research in Metallurgy, Liege, Belgium,
2) ArcelorMittal Research, Maizières-les-Metz, France

Hydrogen Distribution in Stressed Super Alloys – A Tritium Autoradiography Investigation 501
M. Au; Savannah River National Laboratory, Aiken, SC, USA

Hydrogen Diffusion in 9Cr Steel: Effect of Microstructure 508
C.H. Noreña[1] and P. Bruzzoni[2];
1) Universidad de San Martín, Provincia de Buenos Aires, Argentina,
2) Comisión Nacional de Energía Atómica, Buenos Aires, Argentina

Surface Effects during Hydrogen Permeation in Pd-Plated and Ni-Plated Iron Membranes 516
P. Bruzzoni, J.R. Collet Lacoste and R.M. Carranza;
Comisión Nacional de Energía Atómica, Buenos Aires, Argentina

Non-Destructive Determination of the Diffusion Coefficient of Hydrogen in Steel 524
A.N. Lasseigne[1], J.D. McColskey[1], T.A. Siewert[1], K. Koenig[2], J.E. Jackson[2], D.L. Olson[2], and B. Mishra[2];
1) National Institute of Standards and Technology, Boulder, CO, USA,
2) Colorado School of Mines, Golden, CO, USA

Hydrogen Penetration Behavior of High Strength Low Alloy Steel with Plastic Deformation in Gaseous Hydrogen 532
K. Takasawa, Y. Wada, R. Ishigaki, and Y. Tanaka;
The Japan Steel Works, Ltd., Muroran, Hokkaido, Japan

Magnetocorrosion of Pipeline Steel 540
J.E. Jackson[1], D.L. Olson[1], B. Mishra[1], A.J. Roubidoux[1], and A.N. Lasseigne[2];
1) Colorado School of Mines, Golden, CO, USA,
2) National Institute of Standards and Technology, Boulder, CO, USA

Hydrogen Interactions with Titanium Thin Films 548
E. Tal-Gutelmacher, R. Gemma, A. Pundt, and R. Kirchheim;
Georg-August University of Goettingen, Goettingen, Germany

Corrosion of Uranium by Hydrogen at Low Hydrogen Pressures 556
G.L. Powell[1], R.K. Schulze[2], W.J. Siekhaus[3];
1) Y-12 National Security Complex, Oak Ridge, TN, USA,
2) Los Alamos National Laboratory, Los Alamos, NM, USA,
3) Lawrence Livermore National Laboratory, Livermore, CA, USA

Continuum Modeling and Simulation

Crack-Tip Hydrogen Accumulation in Metals under Transient Loading 562
J. Toribio and V. Kharin; University of Salamanca, Zamora, Spain

Sensitivity to Temperature and Material Properties of Hydrogen Concentration at a Crack Tip in Austenitic Stainless Steel 570
P. Schembri; Los Alamos National Laboratory, Los Alamos, NM, USA

Finite Element Analysis of Hydrogen Diffusion in Materials 580
H. Kanayama, S. Ndong-Mefane, M. Ogino;
Kyushu University, Fukuoka, Japan

Modeling of Hydrogen Assisted Cold Cracking in High Strength Steel Welds 588
Th. Boellinghaus[1] and P. Wongpanya[2];
1) Federal Institute for Materials Research and Testing, Berlin, Germany,
2) Suranaree University of Technology, Nakhon Ratchasima, Thailand

Influence of Drawing-Induced Residual Stresses and Strains on Hydrogen Embrittlement of Cold Drawn Wires 596
J. Toribio, M. Lorenzo, and V. Kharin; University of Salamanca, Zamora, Spain

Cohesive Zone Model for Hydrogen Embrittlement of Grain Boundaries in Al 5xxx Alloys 604
F. El-Houdaigui[1], N. Benal[1], R. Estevez[1], D. Tanguy[2];
1) Université de Lyon, Villeurbanne, France,
2) Ecole Nationale Supérieure de Mines de St Etienne, St Etienne, France

Modeling Issues on Hydrogen-Induced Intergranular Cracking under Sustained Load 613
M. Dadfarnia[1], P. Sofronis[1], B.P. Somerday[2], J.B. Liu[1], D.D. Johnson[1], and I.M. Robertson[1];
1) University of Illinois at Urbana-Champaign, Urbana, IL, USA,
2) Sandia National Laboratories, Livermore, CA, USA

Hydrogen Induced Stress Cracking in 25% Cr Duplex Stainless Steel Simulated by Cohesive Zone Modelling 622
V. Olden[1], E. Østby[1], C. Thaulow[2], and R. Johnsen[2];
1) SINTEF, Trondheim, Norway,
2) NTNU, Trondheim, Norway

Atomistic Modeling and Simulation

First-Principles Prediction of Hydride Phase Stability and the Thermodynamics of Decohesion 632
A. Van der Ven, Q. Xu, and J. Bhattacharya;
The University of Michigan, Ann Arbor, MI, USA

Modeling the Plastic Zone Ahead of a Crack by Two Dimensional Discrete Dislocation Dynamics 640
D. Tanguy, D. Delafosse, and M. Razafindrazaka;
CNRS, Saint-Etienne, France

Multi-Scale Simulation of Crack Tip Shielding: Constrained Molecular Dynamics and Elastic Calculations 647
D. Tanguy; CNRS, Saint-Etienne, France

Atomistic Study of Hydrogen Diffusion around Dislocations in Alpha Iron 655
S. Taketomi, R. Matsumoto, and N. Miyazaki;
Kyoto University, Sakyo-ku, Kyoto, Japan

Estimation of Hydrogen Distribution around Dislocations Based on First Principles Calculations 663
R. Matsumoto, S. Taketomi, N. Miyazaki, and Y. Inoue;
Kyoto University, Sakyo-ku, Kyoto, Japan

Monte Carlo Simulation of Vacancies at Al-Σ=33(554)[1-10]: Towards Intergranular Superabundant Vacancies 671
E. Vamvakopoulos[1] and D. Tanguy[2];
1) Centre Européen de Calcul Atomique et Moléculaire, Lyon, France,
2) CNRS, Saint-Etienne, France

Effects of the Density of States on the Stacking Fault Energy and Hydrogen Embrittlement of Transition Metals and Alloys 678
J.A. Lee; NASA-Marshall Space Flight Center, Huntsville, AL, USA

Hydrogen Isotopes and Helium in Materials

Physics of He Platelets in Metal Tritides 686
D.F. Cowgill; Sandia National Laboratories, Livermore, CA, USA

Transmission Electron Microscopy Study of Helium-Bearing Fusion Welds 694
M.H. Tosten and M.J. Morgan;
Savannah River National Laboratory, Aiken, SC, USA

Synergistic Effects between Hydrogen and/or Helium Accumulation and Ion Irradiation Damage in Nuclear Related Materials 702
P. Trocellier; CEA – DEN/DANS/DMN, Yvette, France

Adhesion and Fracture of Scandium Deuteride Films 710
M.S. Kennedy[1], N.R. Moody[2], M. Clift[2], D.P. Adams[3], L. Espada[3], D.R. Kammler[3], E.D. Reedy, Jr.[3], and D.F. Bahr[4];
1) Clemson University, Clemson, SC, USA,
2) Sandia National Laboratories, Livermore, CA, USA,
3) Sandia National Laboratories, Albuquerque, NM, USA,
4) Washington State University, Pullman, WA, USA

D Loss as a Function of Temperature in ErD_2 Films on Kovar with and without an Intermediate Mo Diffusion Barrier 718
D.R. Kammler, W.R. Wampler, S.B. Van Deusen, S.H. King, R.G. Tissot, L.N. Brewer, L.I. Espada, and R.S. Goeke;
Sandia National Laboratories, Albuquerque, NM, USA

Tritium Effects on Dynamic Mechanical Properties of Polymeric Materials 726
E.A. Clark; Savannah River National Laboratory, Aiken, SC, USA

Studies of Hydrogen Isotopes Superpermeation through Membranes of Group V Metals on "Prometheus" Setup 735
R.K. Musyaev[1], A.A. Yukhimchuk[1], B.S. Lebedev[1], A.O. Busnyuk[2], M.E. Notkin[2], A.A. Samartsev[2], A.I. Livshits[2];
1) Russian Federal Nuclear Center-All–Russian Research Institute of Experimental Physics, Nizhny Novgorod Region, Russia,
2) St. Peterburg State University of Telecommunications, St. Peterburg, Russia

Author Index 743

Subject Index 747

Effects of Hydrogen on Materials
Proceedings of the 2008 International Hydrogen Conference
Brian Somerday, Petros Sofronis, Russell Jones, editors, p 1-21
Copyright © 2009 ASM International®
All rights reserved.
www.asminternational.org

SCIENCE-BASED PROGNOSIS TO MANAGE STRUCTURAL ALLOY PERFORMANCE IN HYDROGEN

Richard P. Gangloff
Center for Electrochemical Science and Engineering
Department of Materials Science and Engineering
University of Virginia
Charlottesville, VA 22904-4745
USA

ABSTRACT

Safe, durable, and economic containment of hydrogen in energy systems is challenging because H_2 promotes a variety of cracking modes in metals. The opportunity exists to implement advanced prognosis methods in parallel with new H_2 infrastructure. The challenge is to transform debate on mechanisms of H damage into quantitative models of material cracking properties and laboratory test methods.

Extensive fracture mechanics data enable prognosis to resist hydrogen environment assisted cracking (HEAC). The severity of HEAC is proportional to crack tip H uptake; governed by H_2 pressure or electrochemical overpotential, hydrostatic stress, and H trapping; and exacerbated by active loading. Fatigue-H_2 interaction is particularly deleterious, and the time-cycle dependence of crack growth is challenging to characterize experimentally and theoretically.

Only the decohesion mechanism has been developed to predict HEAC thresholds and rates, providing a scientific foundation for prognosis. In this view cracking is dominated by the high concentration of H in the crack tip fracture process zone. Experimental calibration of models of K_{TH}, da/dt and da/dN is required to define uncertain parameters; however, this approach effectively quantifies hydrogen pressure, temperature and loading frequency effects on these material properties.

PROGNOSIS OF HYDROGEN ENVIRONMENT CRACKING

Gaseous H_2 promotes significant hydrogen environment assisted cracking (HEAC), as well as internal hydrogen assisted cracking (IHAC), in most metals. Time and load-cycle dependent cracking occurs subcritically across a spectrum of alloy composition and strength; and is affected by interacting metallurgical, loading format, and environment chemistry variables [1-3], as captured in an emerging data base [4]. This paper is limited to HEAC near ambient temperature, relevant to hydrogen storage and transport for energy technologies. IHAC, and combined IHAC plus HEAC are relevant when components are exposed to elevated temperature H_2 followed by loading in a benign environment or H_2 at near-ambient temperature [5].

Figure 1 illustrates the elements of HEAC. The H_2 molecule dissociates chemically to H adsorbed on the clean-straining crack tip surface, dissolves in the metal lattice and trap sites, and diffuses over a distance of order 0.1 to 5 μm to sites of damage formation in the crack tip fracture process zone (FPZ) [6]. The mechanism of H damage is controversial [1,2]: (a) Hydrogen Enhanced Decohesion after Troiano and Oriani, (b) Hydrogen Enhanced Localized Plasticity after Beachem and Birnbaum, or (c) Adsorption Induced Dislocation Emission after Lynch. Each can be described by a cohesive-zone law in cracking models of material properties [7,8]. HEAC produces characteristic microscopic features, including: (a) intergranular cracking with a strong role of segregated impurities, (b) transgranular cracking with a strong role of martensite or slip band-matrix interfaces, (c) microvoid cracking with H enhanced nucleation, growth, and/or linkup, and (d) slip band cracking with H enhanced heterogeneous-planar slip. HEAC is manifest by degradation of mechanical properties that are relevant to component performance, including the threshold stress intensity for the onset of subcritical crack propagation (K_{TH}) and rate of crack growth with regard to loading time (da/dt) or reversed-loading cycles (da/dN). HEAC is time-cycle dependent, governed by the kinetics of the reaction and mass transport steps in Fig. 1 [9]. These issues are detailed in the six-prior proceedings from *Hydrogen in Metals* conferences [e.g., 10].

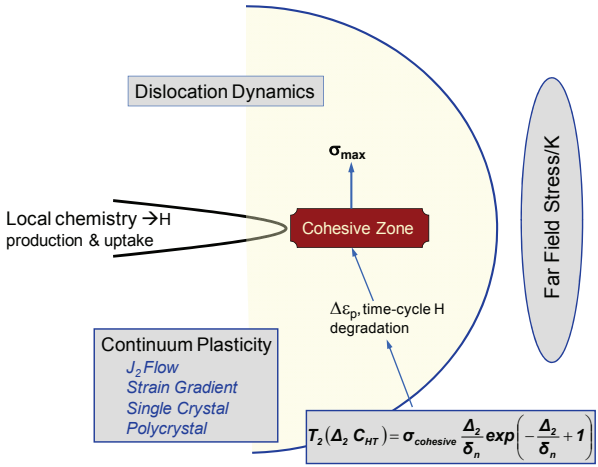


***Figure 1**: Elements of HEAC focused on the dominance of crack tip chemical, mechanical, and microstructure processes necessary for damage [2].*

The unique opportunity exists to implement advanced component-performance prognosis methods in parallel with developments of infrastructure for H_2 energy systems. The approach should follow from well-known fitness-for-service methods used in the petro-chemical industry and guided by prognosis capabilities emerging in aerospace systems, as summarized in Fig. 2 [11]. Sensor based evaluations of the current damage state of a component, as well as measurements of load and environment history, are the starting point for damage evolution modeling. This is accomplished with a mechanics description of global loading/stress intensity, perhaps including microstructure-level stress/strain, and integrated with mechanism-based modeling of hydrogen damage processes and material properties. The output is near-term prediction of fitness for a defined mission. Aircraft prognosis has

centered on fatigue and not considered environmental effects [12]. The vision is that future capability of a component in H_2 service will be predicted from a known-current state using a material property data base that is leveraged by models derived from fundamental understanding of HEAC. This prognosis approach is a challenging multi-scale problem requiring close coupling of science and engineering.

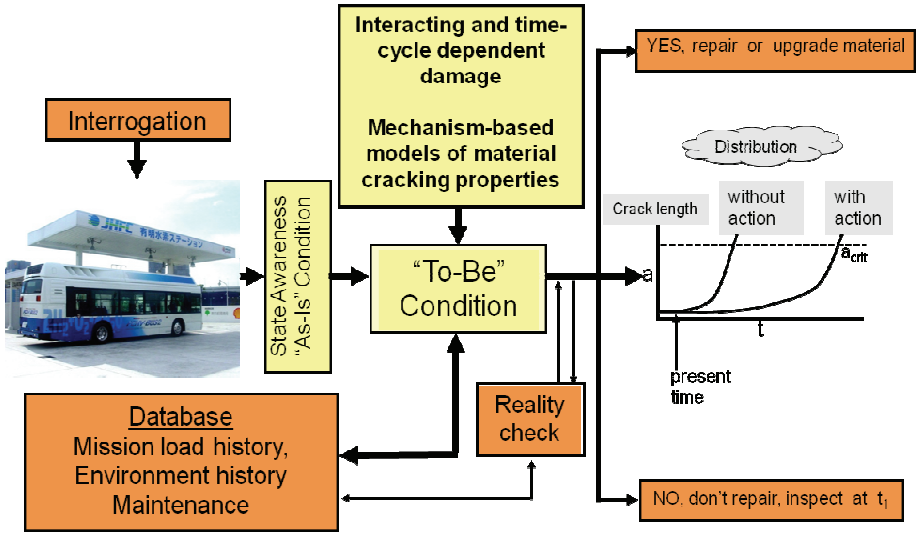


Figure 2: Prognosis of H_2 damage evolution in a complex structure; modified from [11].

Quantitative prognosis for components in H_2 service is challenging. First, "Safe Life" and "Damage Tolerant" methods must be coupled to correctly reflect the flaw or defect state of a component at the microstructure or surface-finish/corrosion topography size scales [13]. Second, interacting variables plus the complex laboratory requirement to simulate long-time loading in high pressure H_2 confound data base development particularly when prognosis is probabilistic-risk based [14]. Finally, debates on fundamental physics-based descriptions of H damage mechanisms have been qualitative and not resulted in quantitative models of the HEAC properties (K_{TH}, da/dt, and da/dN) necessary to implement prognosis (Fig. 2). The substantial-required investment is justified from a historical perspective. For example in the area of nuclear reactor structure, stress corrosion cracking of austenitic stainless steels was neither sufficiently understood nor incorporated in emerging alloy selection and structural designs [15]. As a result, the technology was forced to react to major problems that hindered economic plant operations for several decades. Science based prognosis will contribute to reducing the likelihood that HEAC adversely impacts the infrastructure for H_2-energy technologies [16].

Each of the past Jackson Lake conferences had an overriding theme. It is hoped that this current meeting will advance the prognosis capability and build on past accomplishments to: (a) *transform* rich phenomenology and qualitative understanding of HEAC into quantitative laboratory characterization methods and

data bases, and (b) *transform* important debate on H damage mechanisms into material property prediction models that are connected across multiple length and time scales, probabilistically capable, and validated.

HEAC DATA BASE AND CHARACTERIZATION OF VARIABLE EFFECTS

This review focuses on phenomenological characterization and damage mechanism modeling of HEAC for structural alloys stressed in H_2. Discussion is limited to crack propagation, with cracking resistance based on the elastic crack tip stress intensity factor (K). This approach is justified because components likely contain microstructural, manufacturing, or corrosion defects that reduce the importance of crack initiation and early growth. The fracture mechanics foundation is being applied quantitatively to predict performance in H_2 service, as embodied in ASME rules for Section VIII, Division 3 pressure vessel design [17]. Consideration of testing to measure K_{TH} and da/dN in H_2 (*Article KD-10*) suggests issues that must be resolved. Uncertainties are associated with: (a) crack growth incubation and rising crack mouth opening displacement effects not considered in ASTM standard E1681 focused on quasi-static loading, (b) low loading frequency (f), crack closure, near-threshold (ΔK_{TH}), and load-history effects on da/dN not considered in ASTM standard E647 on fatigue, (c) probabilistic fracture mechanics, and (d) modeling to leverage complex and long-time experiments involving interacting variables.

Extensive materials property data exist to guide prognosis [2,4,10]. Results establish the variables (alloy strength, H mobility/solubility, rising or cyclic loading, temperature, H_2 pressure, segregated impurities, and microstructural heterogeneity) that affect the threshold and kinetics of H_2 cracking. Management of HEAC requires understanding of the interactive windows of these variables where cracking occurs.

HEAC cracking is sensitive to two primary variables, trap-modified H diffusivity (D_H) and alloy yield strength (σ_{YS}). Figures 3 and 4 summarize the effects of these variables on the transport/reaction rate limited maximum speed of subcritical crack growth (da/dt_{II}) and a threshold property (K_{TH}), respectively. The trend in Fig. 3 shows that for a wide range of alloys; from bcc Ti alloys ("Ti") to bcc steels ("Fe"), fcc aluminum alloys ("Al"), and high strength austenitic stainless steels or nickel-based superalloys ("Ni"); da/dt_{II} decreases in direct proportion to D_H [6]. The growth rates plotted are upper bounds measured for severe hydrogen environment conditions such as high pressure H_2 or H_2S, as well as aqueous electrolytes with cathodic polarization. (The difference in behavior for the solutions compared to H_2 is speculatively attributed to dissolution-stimulated vacancy trapping of H that reduces D_H for electrolytes below the bulk values plotted in Fig. 4 [6]). Lower growth rates are produced when HEAC is governed by surface reaction control [9]. While Al alloys are susceptible to HEAC in electrolytes and water vapor, such alloys have not been reported to crack in dry H_2 presumably because clean Al does not catalyze H_2 dissociation to H. The alloys represented in Fig. 4 are among the highest strength for each class. For example, the Fe-based superalloy (IN903) is represented, but lower strength stainless steels such as Type 316 are not.

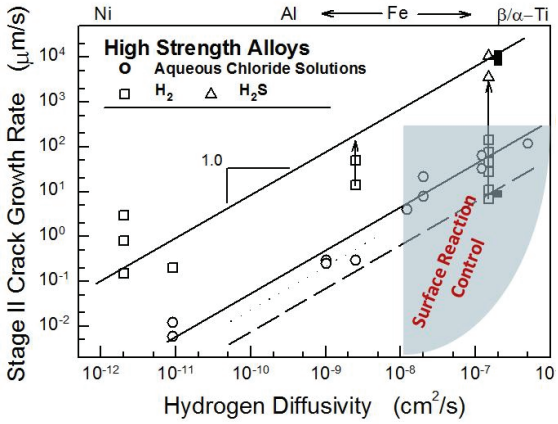


***Figure 3**: Dependence of upper bound da/dt_{II} on D_H for high strength alloys stressed in H producing gases and electrolytes at 25^{0}C. Austenitic Fe and Ni superalloys ("Ni") were cracked in high pressure (100–200 MPa) H_2. Martensitic alloy steels ("Fe") were cracked in low pressure (~100 kPa) H_2. Open squares with arrows represent increasing H_2 pressure and filled squares show a transition from H_2 to thermally dissociated H [6].*

The lower bound trends in Fig. 4 show that susceptibility to both IHAC and HEAC increases with increasing steel strength for a range of environments as well as prior H charging in high pressure H_2 at elevated temperature [5,18]. This inverse yield strength dependence is broadly observed [2], including the notion that hydrogen cracking does not occur below a critical strength as suggested by the steeply rising K_{TH} trends for strengths below about 550 MPa in Fig. 4a. The line noted "K_{IH}" is counter to this trend and could be important behavior for prognosis.

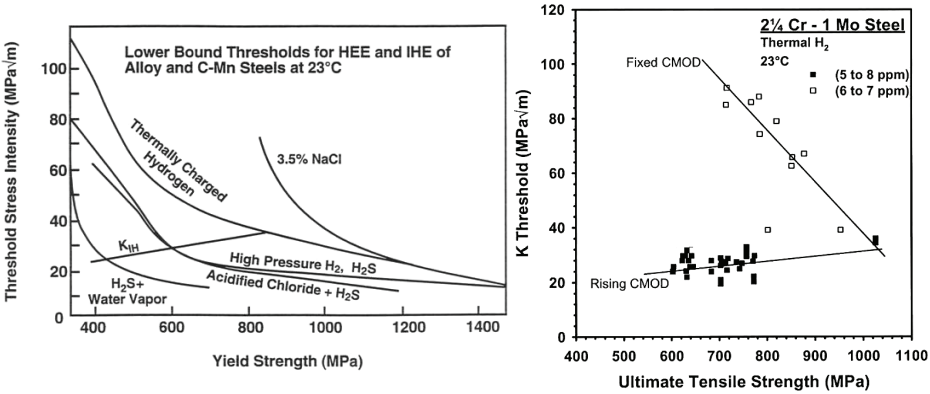


***Figure 4**: (Left-a) Lower bounds for 400 measurements of the threshold stress intensity for C-Mn and alloy steels exposed to IHAC and HEAC at 25°C [18]. All thresholds (K_{TH}) were measured for constant load or constant crack mouth opening, except for "K_{IH}" measured under rising CMOD [5]. These IHAC data are amplified on the right (b) where "Rising CMOD" refers to K_{IH} while "Fixed CMOD" refers to K_{TH} for the "Thermally Charged Hydrogen" trend line in (a). Plane strain fracture toughness is 250 to 400 MPa√m for low strength steels (σ_{YS} ~400 MPa) and 75 to 140 MPa√m for high strength steels (1500 MPa).*

Rising crack mouth opening displacement (CMOD) and cyclic loading may exacerbate HEAC relative to quasi-static loading, particularly for low strength

alloys. This effect is clearly established for IHAC of low strength Cr-Mo pressure vessel steel that was precharged in high pressure-hot H_2 then cracked at ambient temperature in moist air, Fig. 4b. The threshold stress intensity for the onset of subcritical cracking under slow-rising CMOD (K_{IH}) is substantially lower than K_{TH} for IHAC of the same precharged steel loaded at fixed CMOD. Moreover, K_{IH} decreases with decreasing steel strength; the effect of rising *vs.* fixed CMOD loading is accentuated at lower strength and unimportant for high to ultra-high strength steels. When rising-CMOD is fixed during crack growth at K levels above K_{IH}, the da/dt falls rapidly 0; that is, IHAC appears to cease during fixed CMOD then restart if CMOD is again increased. These results were confirmed to be an intrinsic crack tip loading or strain rate effect, rather than an artifact due to H loss during long-time fixed-CMOD exposure [5]. The implications of this effect to prognosis are important, however, data are not adequate to confirm this behavior for HEAC, and particularly for stressing in H_2; research is required.

The potential for significant H_2 cracking in low strength steels, enhanced by active loading, is indicated by the data shown in Figs. 5 through 7. Figure 5 suggests such behavior for low strength C-Mn steel stressed in high pressure H_2 at 23°C, with data presented in the crack growth resistance (R-curve) format [19-21]. The K_{IH} values at the initiation of crack extension on the R-curve are 130 MPa√m to 90 MPa√m, and the slope of the R-curve is reduced, as H_2 pressure increases from 3.5 to 34.5 MPa. Clearly, HEAC is produced in this very low strength steel during rising CMOD. While the high pressure H_2 trend in Fig. 4a shows a lower bound K_{TH} of 85 MPa√m for 300 MPa yield strength, this is a significant extrapolation beyond the limited high pressure H_2 data base. Moreover, only moderate H_2 pressures are represented in Fig. 5 compared to the very high pressures in Fig. 4a. The comparison in Fig. 6 affirms the deleterious effect of rising CMOD; the K_{IH} values from Fig. 5 are compared to

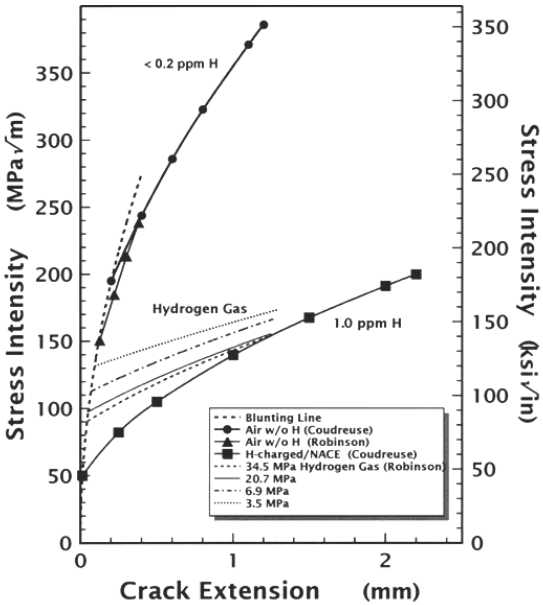


***Figure 5**: Crack extension vs applied K for low strength ferrite-pearlite A516(70) steel (σ_{YS} = 300 MPa) stressed at fixed CMOD rate and 25°C in high pressure H_2 [19,20]. R-curves for as-received (<0.2 ppm H) and H-precharged (1.0 ppm H) conditions stressed in moist air are shown for comparison [21].*

classic fixed-CMOD K_{TH} results for significantly higher strength steels, measured over a very wide H_2 pressure range. In the low pressure regime, the rising-CMOD threshold for the low strength A516 steel equals the static CMOD values for the higher strength steels. This is circumstantial evidence for enhanced HEAC due to rising CMOD, particularly for low strength ferritic steels and analogous to the IHAC results shown in Fig. 4b. It remains to be proven that the benefit of lower strength for static loading (Fig. 3a), is nonconservative for active loading [22].

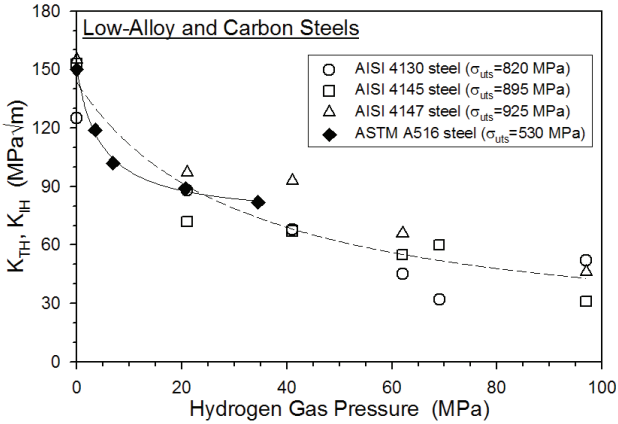


***Figure 6**: Laboratory data by Loginow and Phelps [31] showing the effect of P_{H2} on K_{TH} for crack arrest in 3 alloy steels stressed at fixed CMOD, compared to results for rising-CMOD K_{IH} from crack growth initiation points (♦) in Fig. 5. Tensile yield strengths are 634, 669, 724, and 300 MPa for the steels from top to bottom in the legend. Reproduced from [32].*

The sensitivity of lower strength steels to HEAC under rising CMOD suggests that fatigue crack propagation rate, da/dN, is increased significantly by stressing in H_2 relative to an inert environment. This degradation is observed for most structural alloys [3]. Typical data are presented in Fig. 7 for low strength bcc C-Mn [23] and fcc austenitic stainless [24-26] steels stressed in moderate pressure H_2 at 25°C. These data show that H_2 enhances da/dN as a function of stress intensity range ($\Delta K = K_{MAX} - K_{MIN}$ and $R = K_{MIN}/K_{MAX}$); critically, the effect increases with decreasing *f*. These, along with results for Cr-Mo pressure vessel steels [27,28], demonstrate that fatigue-H_2 interaction may limit metallic components in actively loaded H_2 systems. Limited results suggest that Al alloys may be prone to mild HEAC under cyclic loading in H_2 [29], but this finding is contradicted by an earlier report of no enhancement [30]. Prognosis of H_2 fatigue is complicated by the likely increase of da/dN at slow loading frequencies, particularly in the lower ΔK regime where data do not exist and experiments are prohibitively long. Mechanism-based modeling to define such behavior is proposed in an ensuing section.

Environmental variables affect HEAC for quasi static and cyclic loading. K_{TH} decreases and da/dt (and probably da/dN) increase as H_2 pressure (P_{H2}) increases. Examples are shown in Figs. 5 and 6. The fundamental variable controlling HEAC is the concentration of reversibly trapped-diffusible H (C_H) produced on the crack tip surface in equilibrium with the surrounding pressure of H_2; given by Sievert's law with C_H proportional to $P_{H2}^{1/2}$ and a material-temperature dependent proportionality constant [18,33,34]. The data in Fig. 6 were analyzed using estimated Sievert's law

coefficients [18] and the results plotted in Figures 8. (With C_H as wppm and P_{H2} as kPa, these coefficients are 0.0027, 0.0027, 0.0016 and 0.050 with increasing σ_{YS} for the steels in Fig. 6.) A similar analysis was carried out for two superalloys stressed in H_2 of varying P_{H2} as well as in sulfuric acid electrolyte of varying pH; the results are plotted in Figure 8 [35,36]. This analysis employed known Sievert's law coefficients for each superalloy, plus an electrochemical approximation of crack tip pH and overpotential for H production [35].

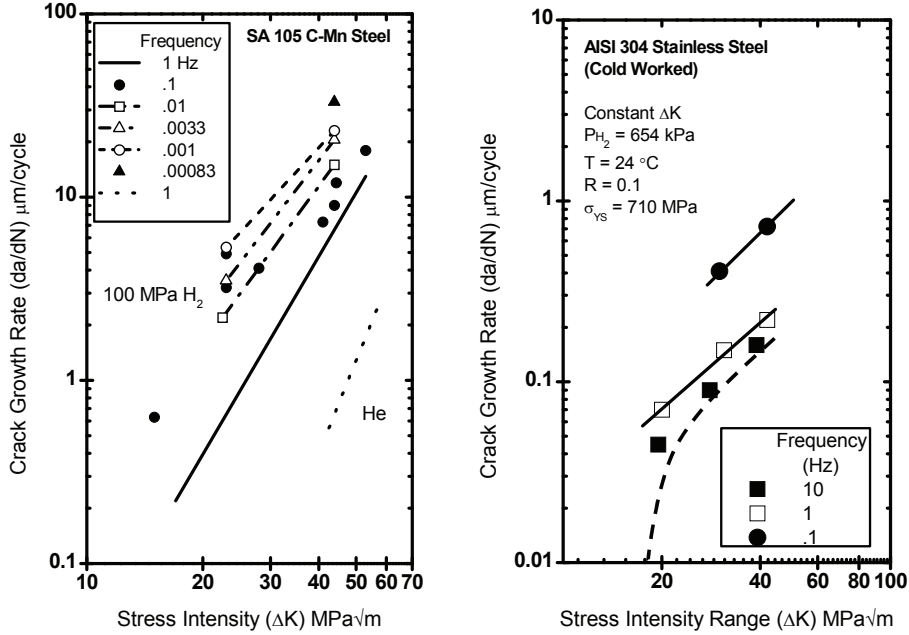


***Figure** 7: Deleterious effect of H_2 on fatigue crack propagation rate in low strength (left-a) SA-105 C-Mn steel in 100 MPa H_2, reproduced from [23]; and (right-b) cold worked 304 austenitic stainless steel at 700 MPa H_2 pressure, reproduced from [24]. Experiments were conducted at constant ΔK and frequency varied for each data set. A wide-range decreasing ΔK result is indicated by the dashed line for stainless steel [24].*

Two points are notable for prognosis. First, K_{TH} depends on a material-specific power law function of C_H. Second, the data in Fig. 8 support a single K_{TH} *vs* C_H correlation for high pressure H_2 and the H-producing electrolyte. Understanding of occluded crack electrochemistry, and dependencies of C_H on pH and electrode potential, is substantial. As such, an electrochemical environment can provide a simplified surrogate for laboratory experiments in high pressure H_2. As a caution, convection effects unique to fatigue loading complicate this approach [37].

Temperature and H_2 composition affect alloy susceptibility to HEAC, providing approaches to mitigate cracking and reduce the complexity of prognosis. Seminal work by Johnson showed that O_2 addition to H_2 eliminated HEAC due to adsorption

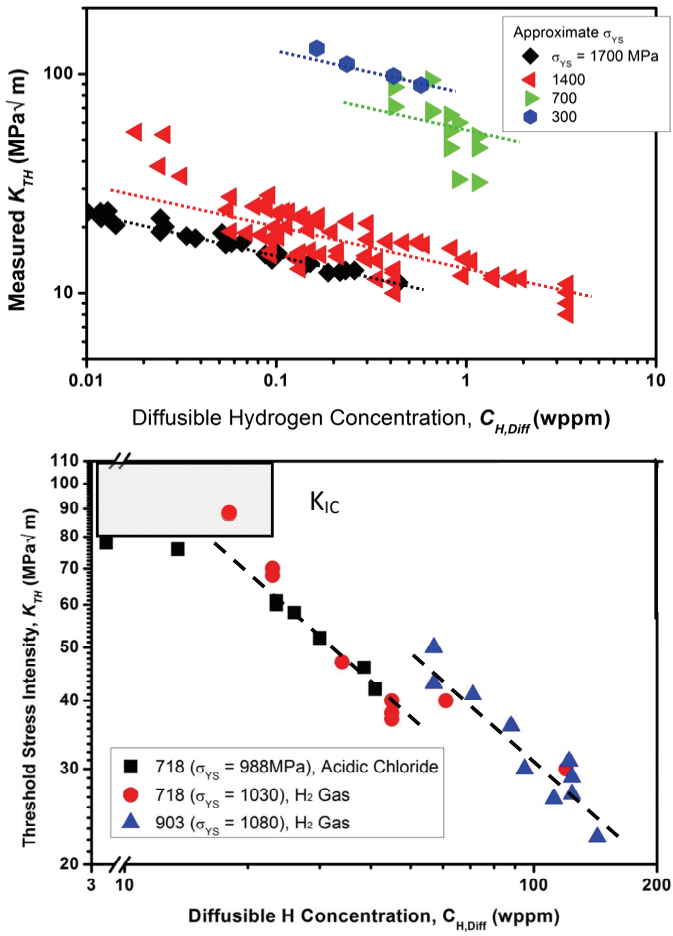


***Figure 8**: The H concentration dependence of threshold stress intensity for: (top) steels from Fig. 6; and (bottom) Ni and Fe- superalloys subjected to static CMOD loading in H_2 of varying P_{H2} at 23°C [36], and rising-CMOD loading for IN718 in sulfuric acid of varying pH [35]. Curve-fits are: (top) K_{TH} (MPa√m) = $13.2C_H^{-0.18}$ (wppm) and (bottom) $K_{TH} = 350C_H^{-0.53}$ based on H_2 data only.*

of oxygen atoms on the crack surface to block H uptake [38]. The data in Fig. 9 show a similar beneficial effect of hydrocarbon additions to H_2 [39]. Molecules with multiple carbon-carbon bonds such as ethylene (C_2H_4) react with H dissociated on the crack surface to form inert methane (CH_4), and thus reduce H coverage and da/dN. Considering the effect of temperature for pure H_2, HEAC is typically most severe near 25°C [2], but da/dt [40] and da/dN [41] fall with increasing and decreasing temperature. Figure 10 shows K_{TH} for high strength steels stressed in low pressure H_2 [40,42]. (K_{TH} does not increase at low temperatures provided that the threshold measurement allows sufficient time for H diffusion into the FPZ.) Precise temperature and gas composition dependencies of HEAC depend on steel strength

and P_{H2} [40]; the benefits of temperature and inhibiting molecules have not been demonstrated for high pressure H_2.

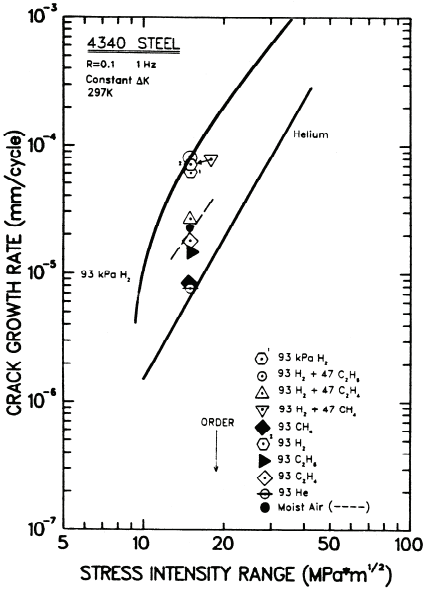


***Figure 9**: Hydrocarbon inhibition of low P_{H2} environment enhanced fatigue propagation in a high strength steel (R_C 36) stressed at 1 Hz and 23°C [39].*

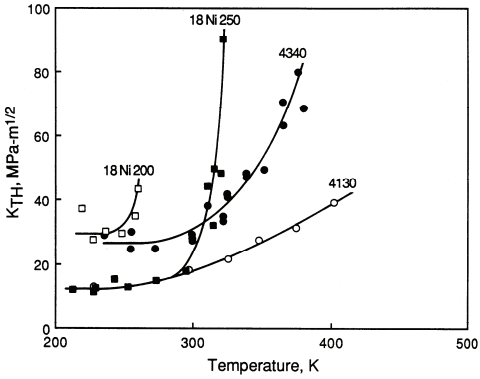


***Figure 10**: Temperature dependence of K_{TH} for HEAC in high strength martensitic steels stressed in H_2 at constant or rising load. σ_{YS}: 18Ni(200) = 1270 MPa, 18Ni(250) = 1650 MPa, 4340 = 1235 MPa, 4130 = 1330 MPa. Reproduced from [40,42].*

HEAC MECHANISM-BASED MODELING

Damage-mechanism based modeling to predict HEAC properties of the type shown in Figs. 3 through 10 is a key part of prognosis (Fig. 2) and enables reduced experimentation. Significant progress has been reported in predicting K_{TH} and da/dt [1,2,9], but less effort has been directed at modeling hydrogen environment assisted fatigue crack propagation [3]. The state-of-the-art is captured in recent works [7,8,43-45], based on the hypothesis that H reduces cohesive strength of microstructural interfaces where H accumulates to provide a path for HEAC [46]. Quantitative models of K_{TH}, da/dt, and da/dN have not been developed based on HELP or AIDE. The HEAC sequence in Fig. 1 provides the framework for modeling, including [2]: (a) production of C_H on the crack surface, (b) crack tip stress and strain distributions well within the crack tip plastic zone, (c) C_H enhancement due to stress and trapping, and (d) a local failure criterion given by a H-sensitive cohesive law. Examples demonstrate modeling capabilities and needs for future research to enhance prognosis. A common theme is that each model contains one or more adjustable parameters due to incomplete understanding. However, such parameters can be calibrated by fits to limited experimental data,

enabling the models to be reasonably validated and useful in prognosis pending more rigorous models.

Hydrogen Localization in the Crack Tip Facture Process Zone

A first step is to model H localization by hydrostatic tension dilation and microstructural trapping in the crack tip FPZ. This concentration, $C_{H\sigma}$, is given by [2,33,34]:

$$C_{H\sigma} = \frac{C_L exp\left(\frac{E_{B-Crack}}{RT}\right) \cdot exp\left(\frac{\sigma_H V_H}{RT}\right)}{\left[1 + C_L exp\left(\frac{E_{B-Crack}}{RT}\right) \cdot exp\left(\frac{\sigma_H V_H}{RT}\right)\right]} \quad (1)$$

where C_L is lattice H concentration in equilibrium with crack tip P_{H2} or electrochemical overpotential, $E_{B\text{-}Crack}$ is the binding energy of H to trap sites that define the crack path, σ_H is crack tip hydrostatic stress proximate to fracture sites, V_H is partial molar volume of H in Fe, and RT has the usual meaning. An example calculation using Eq. 1 is shown in Table 1 for moderate and ultrahigh yield strengths of steel, four bounding levels of crack tip σ_H, and E_B values typical of H trapping along transgranular and intergranular crack paths. Values of $C_{H\sigma}$ are listed for moderate strength Cr-Mo-V and the lined boundary shows all cells to the right where localized H concentration is ~10^6 wppm for ultra-high strength steel (UHSS). The predicted large enhancement of H should govern steel susceptibility to HEAC; $C_{H\sigma}$ exceeds C_L by 10^4 to 10^{16}, approaching 10-100 atomic pct even for low pressure (100 kPa) H_2 or an overpotential of 0 mV. Substantial literature shows that intergranular HEAC in steel is exacerbated by S and P impurities segregated to prior austenite grain boundaries, and Mn and Si play a deleterious role in such cracking [47]. However, since H can localize to very high levels at grain boundaries and other interfaces (Table 1), impurity segregation is not a prerequisite for HEAC. While impurity segregation reasonably contributes to boundary decohesion at any H concentration and strength level [47], the high-H enhancements predicted in Table 1 (even for low hydrogen fugacity) suggest that impurity control will not broadly mitigate hydrogen cracking. For example, recent research shows severe HEAC and IHAC in very high purity UHSSs [45,48,49], even at zero overpotential for concurrent or precharging H production. In this case prior austenite boundary cracking was not observed, likely due to reduced impurity segregation; however, severe H cracking occurred along interfaces associated with the martensitic microstructure. While the impurity contribution may be more important for low strengths and static loading, rising or cyclic CMOD loading coupled with strong H localization according to Eq. 1 should reduce the benefit of impurity control in HEAC and IHAC [5]. This analysis affirms the importance of stress and trapping dominated H localization in the decohesion mechanism, as proposed by Oriani four decades earlier [46]. None-the-less, fundamental research is required to better define the relative contributions of H localization and interface composition, interacting with interface atomic structure and the potential for highly localized dislocation-scale stresses.

***Table 1**: Crack tip localization of H in steel governed by hydrostatic stress and H-trap binding energy*

Cr-Mo-V Steel σ_{YS} = 700 MPa

		Localized H Concentration (wppm)			
C_L = 0.0003 wppm 0.1 MPa H_2 or 0 V T = 300 K	$\sigma_H V_H$ kJ/mol	E_B = 0 kJ/mol	E_B = 10 kJ/mol Dislocations; Coherent precipitates	E_B = 40 kJ/mol Martensite interfaces	E_B = 60 kJ/mol Austenite grain boundaries
$\sigma_H = \sigma_{YS}$	2.1	.0007	.04	6,600	10^6
$\sigma_H = 5\sigma_{YS}$ HRR	6.3	.004	.2	36,000	10^6
$\sigma_H = 10\sigma_{YS}$ SGP 2 x HRR	12.6	.05	3	450,000	10^6
$\sigma_H = 20\sigma_{YS}$ SGP 4 x HRR	25.2	7	400	10^6	10^6

UHSS σ_{YS} = 1800 MPa

Threshold Stress Intensity for HEAC under Quasi-Static Loading

Assuming H-decohesion reduction of intrinsic fracture resistance, Gerberich and coworkers coupled H localization (Eq. 1) with a dislocation model of crack tip stresses to predict the threshold for HEAC [44].

$$K_{TH} = \frac{1}{\beta'} exp\left[\frac{(k_{IG} - \alpha C_{H\sigma})^2}{\alpha'' \sigma_{YS}}\right] \qquad (2)$$

where $C_{H\sigma}$ (Eq. 1) applies to the H-trap binding energy that establishes diffusible H concentration adjacent to (but not along) the crack path, k_{IG} is intrinsic Griffith toughness, α is a parameter related to the effectiveness of H decohesion, and β' and α'' are constants from computer simulation of dislocation structure about the crack tip. Equation 2 was validated experimentally for IHAC and HEAC of a UHSS [44,45,49], with resulting curve fit parameters in agreement with those reported by Gerberich et al. (α = 0.5 MPa$\sqrt{m}$(at frac H)$^{-1}$, β' = 0.2 (MPa$\sqrt{m}$)$^{-1}$, α''= 0.0002 MPa·m and k_{IG} = 0.85 MPa$\sqrt{m}$). As further validation, data in Fig. 8 were analyzed using this model; results in Fig. 11 show good agreement between measured and predicted K_{TH} for steels and superalloys. The parameters used to obtain the fits in Fig. 11 are summarized in Table 2 and agree with those reported by Gerberich and coworkers for high strength steel [44], but vary with material. The decohesion weighting factor (α) and crack tip σ_H are not known *apriori* and were selected for best fits in Fig. 11 using α'', β, and k_{IG} reported by Gerberich et al. For the steels, α is in the range of 0.2 to 0.5 MPa$\sqrt{m}$(at frac H)$^{-1}$ for the ultra-high to moderate strengths, but is higher for the lowest strength steel (excluding the outlying case for the 669 MPa strength). For the superalloys, two separate values of α correlate with the observation that HEAC is intergranular (α = 0.4 to 0.5 MPa$\sqrt{m}$(at frac H)$^{-1}$) at high C_H, above the shaded bar in Fig. 11 (left), but associated with slip band intersections and higher α (0.9 MPa$\sqrt{m}$(at frac H)$^{-1}$) at low C_H [35,36].

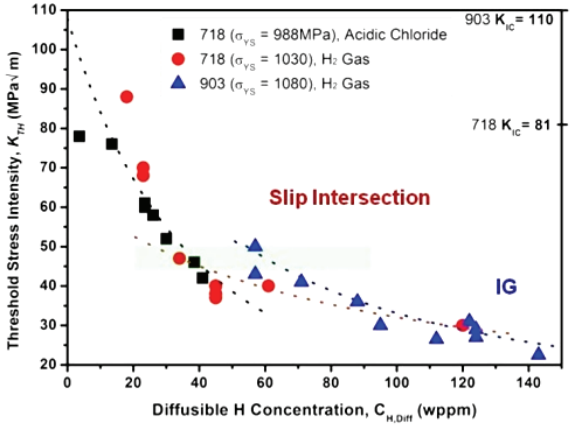
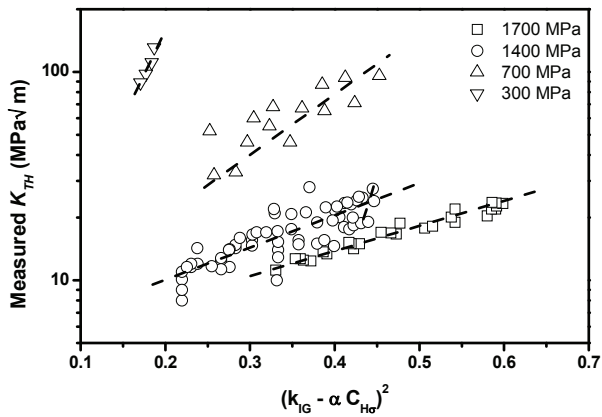


***Figure 11**: Comparisons of measured and model predicted K_{TH} vs H concentration using Eq. 2 and best-fit parameters in Table 2. Left: Eq. 2 (dotted lines) is compared to measured K_{TH} vs diffusible C_H data (filled ■, ●, ▲) from Fig. 8 for Ni and Fe-based superalloys using $C_{H,Diff} = C_H = C_L exp(E_B/RT)$ for reversibly trapped H in equilibrium with crack P_{H2} or H overpotential and stress enhanced according to Eq. 1. Right: K_{TH} from Fig. 8 for four steels are plotted logarithmically vs H-reduced Griffith toughness calculated using stress enhanced C_H, α, and k_{IG} (Table 2) to show linearity validating Eq. 2. Each slope scales with $(\alpha''\sigma_{YS})^{-1}$ and intercepts the ordinate at log 1/β' (K_{TH} = 5 MPa√m) according to Eq. 2. (A plot similar to the superalloy format (top) showed excellent agreement between measurements and Eq. 2.)*



The α parameter describes the interaction of intergranular and transgranular crack path structure, strength, and composition characteristics with decohesion, but must be calibrated experimentally due to limited fundamental understanding. Crack tip stress enhancement is uncertain in the range from that characteristic of a blunted crack tip (σ_H = 3 to 6 times σ_{YS}) to much higher levels (~10 to 25σ_{YS}) characteristic of mechanisms for shielded crack tip plasticity [44,50]. Crack tip hardening due to strain gradient plasticity provides a speculative justification as to why crack tip stresses should be enhanced increasingly as steel strength decreases, as suggested by the σ_H/σ_{YS} required (Table 2) to achieve good agreement between Eq. 2 and measured K_{TH} vs C_H in Fig. 11. Other reasons can be developed and these uncertainties indicate a path for research. None-the-less, the model represented in Eq. 2 predicts the effects of temperature and P_{H2} (or H overpotential for an electrochemical environment) on K_{TH} for use in prognosis, provided that limited experiments are conducted to calibrate α and crack tip σ_H for a given material.

***Table 2**: Adjustable parameters used in the decohesion-based model of K_{TH} (Eq. 2)*

	Alloy Steels						Superalloys		
σ_{YS} (MPa)	1725	1400	724	669	634	300	988 ■	1080 ▲	1030 ●
σ_H/σ_{YS}	9	10	15	15	19	25	6		
α (MPa$\sqrt{m}$) (atom frac H)$^{-1}$	0.27	0.24	0.52	1.4	0.50	2.0	0.88	0.49	0.38
α'' (MPa m)	0.0002						0.00018		
β' (MPa$\sqrt{m}$)$^{-1}$	0.2						0.26		
k_{IG} (MPa$\sqrt{m}$)	0.81	0.70	0.74	0.75	0.76	0.44	0.77	0.79	0.69

HEAC Growth Rate under Quasi-Static Loading

Stage II crack growth rate, da/dt_{II}, is modeled as rate limited by the slow step among environmental mass transport, crack surface reaction, and crack tip process zone H diffusion (Fig. 1) [2,9]. The experimental results in Fig. 3 suggest that the upper bound of such cracking is rate limited by H diffusion with analysis yielding [6]:

$$\frac{da}{dt_{II}} = \frac{4D_H}{X_C}\left[erf^{-1}\left(1 - \frac{C_C}{C_L exp\left(\frac{\sigma_H V_H + E_B}{RT}\right)}\right)\right]^2 \qquad (3)$$

X_C is the distance ahead of the crack tip where H damage occurs and C_C is the stress-dependent critical concentration of H for damage. The trends in Fig. 3 represent upper bound HEAC ($C_C << C_{H\sigma}$) in H_2 and electrolytes; da/dt_{II} is proportional to D_H/X_C, affirming Eq. 3. The predictive power of Eq. 3 is limited by uncertainties in alloy-dependent X_C and C_C. Sievert's law estimates C_L vs. P_{H2} and temperature, enabling Eq. 3 to predict the effects of these environmental variables on da/dt_{II} provided that: (a) crack growth is not rate limited by surface reaction kinetics [6,51], (b) an accurate D_H is known for the highly strained crack tip [45], and (c) limited crack growth rate measurements are performed in H_2 to calibrate C_C. It is important to understand the temperature above which da/dt_{II} for HEAC in H_2 tends to 0 due to intervention of surface reaction limitation [40,51,52].

Meaningful but circumstantial evidence suggests that X_C is small ($\leq$ 1 μm) for HEAC in high strength alloys; for example, an upper bound estimate of X_C equaling 700 nm or less follows by fitting Eq. 3 to the data in Fig. 3 [6]. This short distance and steep gradients necessitate reevaluation of crack tip stress and strain. The importance of accurate stresses for HEAC modeling is apparent considering the exponential hydrostatic stress effect on $C_{H\sigma}$ (Eq. 1), as well as the implicit stress dependence of C_C in Eq. 3. Crack tip stress analysis must be refined to consider shielding of plasticity and such small length scale. Gerberich and coworkers

approached this problem with a super-dislocation model of crack tip stresses to formulate the K_{TH} model in Eq. 2 [44]. The assumed dislocation arrangement is speculative. An alternate approach is to augment the Hutchinson, Rice, Rosengren (HRR) continuum solution by a hardening term in the flow rule due to strain gradient plasticity (SGP) [50]. A result of a high resolution finite element analysis following this approach is shown in Fig. 12. Crack tip normal and hydrostatic stresses are elevated substantially above the HRR prediction due to geometrically necessary dislocations to accommodate the strain gradient, with the magnitude depending on the SGP description employed; that is, either a single or multiple microstructure-dependent length, l_i [50].

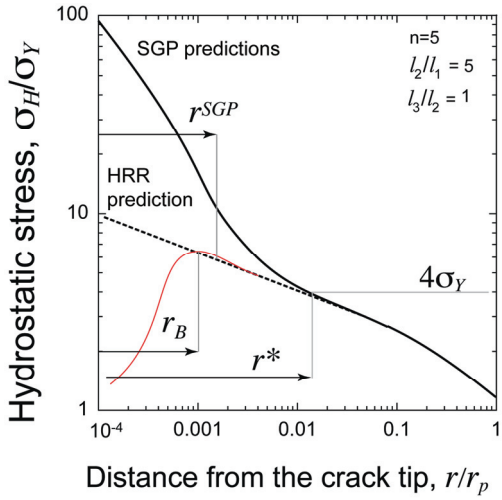


***Figure 12**: HRR and SGP hydrostatic stress distributions ahead of a stationary crack tip, illustrating the key length-scales associated with blunting (r_B), strain gradient effects (r^{SGP} and r^*), and remote loading (r_p).*

Uncertainties are associated with SGP modeling of crack tip stresses. First, stress elevation is confined to a very small fraction of the plastic zone, of order 1% of the plane strain plastic zone diameter (r_p) or ~ $0.001(K/\sigma_{YS})^2$. For K levels typical of subcritical HEAC, the distance over which σ_H from SGP exceeds twice the value from the HRR formulation, r^{SGP}, is physically small in the range of 100 nm where a continuum model may not be accurate. Moreover, the results in Fig. 12 were calculated with a sharp-crack finite element model. If r^{SGP} is smaller than the blunted crack tip radius ($r_B \sim K^2/\sigma_{YS}E$), then this model must be improved with large deformation theory. Finally, experimental description of material length scales, l_i, often from the size dependence of nano-indentation, is in an infant state [50,53].

Time Dependence of HEAC under Cyclic Loading

While fatigue modeling has centered on cyclic plasticity [54], it is important to recognize interaction of cyclic plastic strain accumulation with stress controlled H cracking. Particularly at lower growth rates where fatigue cracking is discontinuous, the role of cyclic deformation over multiple cycles may be to develop a dislocation structure and associated concentration of H trapped at these locations. Once a critical level of H concentrates after a number of load cycles, damage occurs just

ahead of the crack tip governed by tensile stress, and the process repeats. As suggested in Fig. 1, the cohesive zone relationship is reduced as a function of time and cycles as H accumulates. This scenario is speculative, but there is increasing recognition that fatigue crack growth in environments that produce H involves both cyclic plasticity (ΔK) and normal stress (K_{Max}) [55,56].

Cyclic loading frequency affects H_2 enhanced fatigue crack propagation rate, as illustrated in Fig. 7 and elsewhere [23,24]. The challenge in prognosis is to generate da/dN data over a wide range of ΔK, R, and f [17]. The combination of low f and low da/dN cracking relevant to long-life structures in H_2 service is difficult to probe experimentally. Modeling can leverage such experiments for input to prognosis. While only limited work in this regard has been reported for alloys in H_2, substantial results are available for steels and aluminum alloys stressed cyclically in environments that produce H electrochemically [3,57]. Here, the f dependence of da/dN is modeled as rate limited by H diffusion in the crack tip process zone:

$$\frac{da}{dN_{Crit}} = \frac{2}{N}\sqrt{\frac{D_H}{f_{Crit}}}\ erf^{-1}\left[1 - \frac{C_C}{C_L \exp\left(\frac{\sigma_H V_H + E_B}{RT}\right)}\right] \qquad (4)$$

where da/dN_{Crit} is the (plateau) crack growth rate independent of loading frequency for all $f < f_{Crit}$ because of sufficient time for H diffusion to crack tip damage sites in the FPZ, and N is the number of load cycles for an increment of crack advance at this rate. The f_{Crit} is the frequency above which da/dN declines with increasing f due to insufficient time for H diffusion during N cycles. The da/dN_{Crit} increases with increasing applied ΔK raised to the ~2 to 6 power, governed by the crack tip stress field, and the associated f_{Crit} decreases according to Eq. 4. This relationship, particularly da/dN_{Crit} proportional to $f^{-1/2}$, was confirmed experimentally for precipitation hardened aluminum alloys stressed in chloride solution [58].

The C_C in Eq. 4 is unknown but can be calibrated by limited experiments to predict da/dN over a range of ΔK and f. This framework has important potential to model the frequency dependence of fatigue crack propagation in H_2 service. This idea is validated by the data in Fig. 13. The f dependence of da/dN is established based on data for C-Mn steels in NaCl with cathodic polarization at constant ΔK of 23 MPa√m [59,60]. Since these corrosion fatigue results are explained based on the HEAC mechanism [3,60], it is reasonable to represent the limited-scattered data for fatigue in H_2 from Fig. 7a using a parallel format. The resulting curve fit in Fig. 13 is reasonably similar to the NaCl data. A constant value of f_{Crit} ~ 0.1Hz is indicated, however, the da/dN_{Crit} values are not equal perhaps due to yield strength or metallurgical effects [58-60]. If additional experiments establish that Eq. 4 and the form of the dependence shown in Fig. 13 accurately describe the frequency dependence of da/dN for HEAC in H_2, then the following procedure can be employed to leverage experiments for a given alloy, P_{H2}, and temperature.

- For a single-applied ΔK and R, measure da/dN *vs* f, and establish a specific-single set of da/dN_{Crit} and f_{Crit} from a relationship of the form shown in Fig. 13.
- Scale $da/dN_{Crit} \sim f_{Crit}^{-1//2}$ according to Eq. 4; a material-environment property.
- For a second (and perhaps more) applied ΔK and the same R, determine f_{Crit} and da/dN_{Crit} to confirm the square root relationship of Eq. 4, and estimate the power-law dependence of da/dN_{Crit} on ΔK^m.
- Use the slopes of the 2 or 3 measured da/dN *vs* f relationships, for $f > f_{Crit}$, to estimate the fall-off in crack growth rate from da/dN_{Crit} (or plateau level), to the value characteristic of fatigue in an inert environment.

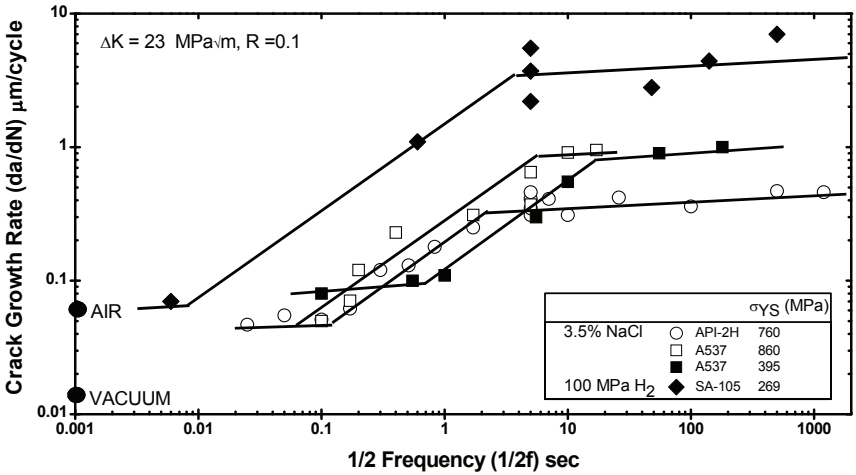


***Figure 13**: Effect of frequency on da/dN for C-Mn steels stressed in NaCl solution with applied-cathodic potential (○, □, ■) [59], and in high pressure H_2 from Fig. 7a [23]. The result from Fig. 7 for inert-He is plotted arbitrarily at 1/2f = 0.006 s. Note that the abscissa represents time-to-maximum load for a sinusoidal or triangle load-waveform, and is thus proportional to reciprocal* frequency.

This experimental information is sufficient, within the limitations of the assumptions, to extrapolate da/dN *vs* ΔK and f data of the sort shown in Fig. 7. For example, since da/dN_{Crit} falls with decreasing ΔK, Eq. 4 predicts that increasingly high f can be used to accelerate laboratory measurements of near-threshold H_2 enhanced da/dN while yielding da/dN_{Crit} relevant to lower frequency component service. Uncertainties in the diffusion model of da/dN; including precise values of N, D_H, C_C, and C_L vs. P_{H2} and temperature from Sievert's Law; are not limiting since absolute values of da/dN are calibrated by experiment and not predicted using a damage-based model. Equation 4 only scales this measured material-environment property using the square root dependence suggested based on H diffusion control. This framework provides an engineering application of a semi-quantitative mechanism-based model of HEAC in fatigue. This approach can be used until more

detailed models of da/dN emerge, using a cohesive zone approach of the sort illustrated in Fig. 1 [54].

CONCLUSIONS

- Safe, durable, and economic containment of H_2 in energy systems is challenging because H_2 promotes multiple stable (subcritical) cracking modes in structural alloys.
- The opportunity exists to implement advanced prognosis methods in parallel with developments of H_2 production, storage, and transmission infrastructure.
- The challenge is to transform persisting debate on basic mechanisms of H damage into quantitative models of material cracking behavior and prognosis-capable properties, as well as relevant-quantitative laboratory test methods.
- Extensive fracture mechanics based data exist, but must be leveraged by mechanism-based models of crack growth to enable prognosis.
- The loading time and cycle dependencies of crack growth are particularly challenging to characterize and model.
- Simple electrochemical environments can provide a quantitative surrogate for complex laboratory experiments in high pressure H_2.
- The severity of HEAC is proportionate to hydrogen uptake; governed by H_2 pressure or electrochemical overpotential, crack tip stress, and H trapping; and is exacerbated by active-rising or cyclic loading.
- Fatigue-H_2 interaction may limit metallic components in energy systems because HEAC is substantial. Prognosis is complicated for low frequency-low ΔK loading typical of long-life components.
- Temperature and H_2 composition affect alloy susceptibility to HEAC, and provide an approach to mitigate cracking.
- Hydrogen cracking is dominated by the extra-ordinary concentration of H localized in the crack tip fracture process zone due to hydrostatic tension and H-trapping at interconnected interfaces that provide a crack path.
- Only the decohesion mechanism of HEAC has been developed to quantitatively predict crack growth thresholds and rates, necessary to provide a scientific foundation for prognosis.
- Experimental calibration of K_{TH}, da/dt and da/dN models is required to define uncertain-adjustable parameters; however, this approach effectively predicts hydrogen pressure, temperature, and load frequency effects on HEAC.

ACKNOWLEDGMENTS

This research was sponsored by the Office of Naval Research, Grant N00014-06-1-0366 with Dr. Airan Perez as Scientific Officer, and Air Force Office of Scientific Research, Grant F49620-03-0155 with Dr. Brett Conner as Scientific Officer.

REFERENCES

1. R.P. Gangloff, in Environment Induced Cracking of Materials, Sergei Shipilov et al., eds., Elsevier Science, Oxford, UK, pp. 141-166 (2007).
2. R.P. Gangloff, in Comprehensive Structural Integrity, I. Milne, R.O. Ritchie and B. Karihaloo, eds., Vol. 6, Elsevier Science, New York, NY, pp. 31-101 (2003).
3. R.P. Gangloff, in Environment Induced Cracking of Metals, R.P. Gangloff and M.B. Ives, eds., NACE, Houston, TX, pp. 55-109 (1990).
4. Technical Reference on Hydrogen Compatibility of Materials, C. San Machi and B.P. Somerday, eds., Sandia National Laboratory, Livermore, CA (2007).
5. A.M. Al-Rumaih, *Measurement and Modeling of Temperature Dependent Hydrogen Embrittlement of Cr-Mo Steel to Enable Fitness-for-Service Modeling*, PhD Dissertation, University of Virginia, Charlottesville, VA (2004).
6. R.P. Gangloff, in Hydrogen Effects on Material Behavior and Corrosion Deformation Interactions, N.R. Moody et al. eds., TMS, Warrendale, PA, pp. 477-497 (2003).
7. S. Serebrinsky et al., Mech. Phys. Sol., Vol. 52, pp. 2403-2430 (2004).
8. I. Scheider et al., Engr. Frac. Mech., Vol. 75, pp. 4283-4291 (2008).
9. R.P. Wei and R.P. Gangloff, in Fracture Mechanics: Perspectives and Directions, ASTM STP 1020, R.P. Wei and R.P. Gangloff, eds., ASTM International, West Conshohocken, PA, pp. 233-264 (1989).
10. Hydrogen Effects on Material Behavior and Corrosion Deformation Interactions, N.R. Moody et al. eds., TMS, Warrendale, PA (2003).
11. Materials Damage Prognosis, J.M. Larsen et al., eds., Materials Science and Technology, Vol. 04, TMS, Warrendale, PA (2004).
12. J.M. Papazian et al., "Structural Integrity Prognosis", in Proceedings, 24th ICAF Symposium, Naples, Italy (2007).
13. M. Kresten and K.-F Windgassen, in Hydrogen Effects in Metals, I.M. Bernstein and A.W. Thompson, eds., TMS, Warrendale, PA, pp. 987-995 (1981).
14. E.J. Veseley et al., in Hydrogen Effects on Material Behavior and Corrosion Deformation Interactions, N.R. Moody et al. eds., TMS, Warrendale, PA, pp. 424-441 (2003).
15. R.W. Staehle, in Uhlig's Corrosion Handbook, 2nd edition, R.W. Revie, ed., John Wiley and Sons, NY, NY, pp. 27-84 (2000).
16. *Basic Research Needs for the Hydrogen Economy*, Report of the Basic Energy Sciences Workshop, US DOE, Washington, DC (2004).
17. M.D. Rana et al., "Technical Basis and Application of New Rules on Fracture Control of High Pressure Hydrogen Vessel in ASME Section VIII, Division 3 Code", PVP2007-26023, ASME, NY, NY (2007).

18. R.P. Gangloff, in Corrosion Prevention and Control, 33rd Sagamore Army Materials Research Conference, M. Levy and S. Isserow, eds., US Army Laboratory Command, Watertown, MA, pp. 64-111 (1986).
19. S.L. Robinson and R.E. Stoltz, in Hydrogen Effects in Metals, I.M. Bernstein and A.W. Thompson, eds., TMS, Warrendale, PA, pp. 987-995 (1981).
20. W.R. Hoover et al., "Hydrogen Compatibility of Structural Materials for Energy Storage and Transmission", Final Report SAND81-8006, Sandia National Laboratories, Livermore, CA (1981).
21. L. Coudreuse et al., in Interaction of Steels with Hydrogen in Petroleum Industry Pressure Vessel and Pipeline Service, MPC, NY, NY, pp. 759-767 (1994).
22. W. Dietzel and M. Pluff, in Hydrogen Transport and Cracking in Metals, A. Turnbull, ed., Institute of Materials, London, UK, pp. 77-86 (1995).
23. R.J. Walter and W.T. Chandler, in Effect of Hydrogen on Behavior of Materials, A.W. Thompson and I.M. Bernstein, eds., TMS, Warrendale, PA, pp. 273-286 (1976).
24. T.R. Fabis et al., in Environment-Sensitive Fracture: Evaluation and Comparison of Test Methods, ASTM STP 821, S.W. Dean et al., eds., ASTM International, West Conshohocken, PA, pp. 470-483 (1984).
25. L.W. Tsay et al., Corrosion Science, Vol. 50, pp. 2973-2980 (2008).
26. G. Schuster and C. Altstetter, Metall. Trans. A, Vol. 14A, pp. 2085-2090 (1983).
27. S. Suresh and R.O. Ritchie, Metal Science, Vol. 16, pp. 529-538 (1982).
28. C.A. Hippsley, "Hydrogen and Temper Embrittlement Interactions in Fatigue of 2¼Cr-1Mo Steel", Harwell Laboratory Report AERE R 12322, Oxon, UK (1986).
29. A. Hagihara et al., Key Engineering Materials, Vols. 353-358, pp. 174-177 (2007).
30. S. Suresh et al., Fatg. Frac. Engr. Matls. Struc., Vol. 5, pp. 133-150 (1982).
31. A.W. Loginow and E.H. Phelps, Corrosion, Vol 31, pp. 404-412 (1975).
32. B.P. Somerday and C. San Marchi, in Materials for the Hydrogen Economy, R.H. Jones and G.J. Thomas, eds., Taylor and Francis Group, Boca Raton, FL, pp. 157-179 (2008).
33. J.P. Hirth, Metall. Trans. A, Vol. 11A, pp. 861-890 (1980).
34. R.A. Oriani, Acta Metall., Vol. 18, pp. 147-157 (1970).
35. J.A. Lillard, *Environment Assisted Cracking of a Nickel-Based Superalloy in Hydrogen-Producing Solutions*, PhD Dissertation, University of Virginia, Charlottesville, VA (1998).
36. N.R. Moody et al., Engr. Frac. Mech., Vol. 68, pp. 731-750 (2001).
37. A. Turnbull, Corrosion, Vol. 57, pp. 175-189 (2001).
38. H.H. Johnson and A.M. Willner, App. Matls. Res., Vol. 4, pp. 34-43 (1965).

39. R.P. Gangloff, in Basic Questions in Fatigue, Vol. 2, ASTM STP 924, R.P. Wei and R.P. Gangloff, eds., ASTM International, West Conshohocken, PA, pp. 230-251 (1988).
40. R.P. Gangloff and R.P. Wei, Metall. Trans. A, Vol. 8A, pp. 1043-1053 (1977).
41. J.D. Frandsen and H.L. Marcus, Metall. Trans. A, Vol. 8A, pp. 265-272 (1977).
42. N.R. Moody et al., Res. Mech., Vol. 30, pp. 143-206 (1990).
43. A. Taha and P. Sofronis, Engr. Frac. Mech., Vol. 68, pp. 803-837 (2001).
44. N. Katz et al. Engr. Frac. Mech., Vol. 68, pp. 619-646 (2001).
45. Y. Lee and R.P. Gangloff, Metall. Mater. Trans. A, Vol. 38A, pp. 2174-2190 (2007).
46. R.A. Oriani and P.H. Josephic, Acta Metall., Vol. 25, pp. 979-988 (1977).
47. C.J. McMahon, Jr., Engr. Frac. Mech., Vol. 68, pp. 773-788 (2001).
48. X.-Y Liu et al., Matls. Sci. Engr. A, Vol. 492, pp. 218-220 (2008).
49. R.L.S. Thomas et al., Metall. Mater. Trans. A, Vol. 34A, pp. 327-344 (2003).
50. Uday Komaragiri et al., J. Mech. Phys. Sol., Vol. 56, pp. 3527-3540 (2008).
51. M. Lu et al., Metall. Trans. A, Vol. 12A, pp. 805-811 (1981).
52. X. Chen and W.W. Gerberich, Metall. Trans. A, Vol. 22A, pp. 59-70 (1991).
53. Y.J. Ro et al., Matls. Sci. and Engr. A, Vol. 435-436, pp. 333-334 (2006).
54. V.S. Despande et al., Acta Mater., Vol. 51, pp. 1-15 (2003).
55. R. Sunder, Fatg. Frac. Engr. Mater. Struct., Vol. 28, pp. 289-300 (2005).
56. K. Sadananda and A.K. Vasudevan, Intl. J. Fatg., Vol. 26, pp. 39-47 (2004).
57. R.P. Gangloff, in Fatigue '02, Anders Blom, ed., Engineering Materials Advisory Services, West Midlands, UK, pp. 3401-3433 (2002).
58. Z. Gasem and R.P. Gangloff, in Chemistry and Electrochemistry of Corrosion and Stress Corrosion Cracking, R.H. Jones, ed., TMS, Warrendale, PA, pp. 501-521 (2001).
59. R. Krishnamurthy et al., in Hydrogen Effects on Material Behavior, N.R. Moody and A.W. Thompson, eds., TMS, Warrendale, PA, pp. 891-908 (1990).
60. R. Krishnamurthy, *Microstructure and Yield Strength Effects on Hydrogen Environment Fatigue of Steels,* PhD Dissertation, University of Virginia, Charlottesville, VA (1991).

Effects of Hydrogen on Materials
Proceedings of the 2008 International Hydrogen Conference
Brian Somerday, Petros Sofronis, Russell Jones, editors, p 22-37
Copyright © 2009 ASM International®
All rights reserved.
www.asminternational.org

REVEALING THE FUNDAMENTAL PROCESSES CONTROLLING HYDROGEN EMBRITTLMENT

I. M. Robertson
Department of Materials Science and Engineering,
University of Illinois at Urbana-Champaign, Urbana, IL 61801 USA

D. Lillig
ExxonMobil Development Company, PO Box 4876, Houston, TX 77210-4876

P. J. Ferreira
Materials Science and Engineering Program,
University of Texas at Austin, Austin, TX 78712

ABSTRACT

To discover the fundamental mechanism governing the macroscopic property response requires the ability to "see" the processes as they occur. One tool that has been instrumental in advancing our understanding of the mechanisms of hydrogen embrittlement is the controlled environment transmission electron microscope coupled with straining stages as these transform the microscope from a static to a dynamic system in which the full functionality and resolution of the instrument can be used to observe and characterize in real time the changes induced by internal hydrogen. This paper reviews the work that provided the first direct support for hydrogen enhancing the mobility of dislocations, which served as the foundation for the now accepted Hydrogen Enhanced Localized Plasticity model. With the understanding of how hydrogen interacted with dislocations and how this changed dislocation behavior it became possible to explain effects such as slip localization and to explain how hydrogen caused the fracture mode to change from ductile transgranular to intergranular. It will be shown how this transition depends on the composition and misorientation of the grain boundaries.

INTRODUCTION

Johnson [1] in 1875 reported that hydrogen reduced the ductility and the fracture stress of iron and some steels. Since that time, it has been shown that the deleterious effects of hydrogen on the mechanical properties is pervasive, occurring in all but a few metals. The notable exceptions are copper, gold, silver and tungsten, although conditions may exist in which they too are susceptible. The fracture mode in the presence of hydrogen can change from ductile transgranular to either transgranular cleavage or intergranular fracture. Furthermore, the nature of the slip can change and become more localized and planar when hydrogen is present. Since the work of Johnson, many microscopic mechanisms have been put forth to explain the macroscopic effects of hydrogen but predominantly without direct support. The ones

that remain include the internal pressure mechanism, in which the pressure of hydrogen in voids generates sufficient stress to nucleate and propagate a crack [2-4]; hydrogen adsorption at crack tips and surface imperfections, which results in a reduction in the surface energy [5, 6]; hydrogen reduction of the cohesive strength of the lattice – the decohesion model [7-9]; film-induced cleavage [10, 11]; hydrogen accumulation at precipitates and second phases, which results in dislocation generation or crack nucleation and propagation [12, 13]; hydrogen reduction in the stacking-fault energy [14-18], which increases slip planarity [16, 19, 20]; hydrogen-induced increase in the density of strain-induced vacancies, which leads to the formation of microcracks or microvoids [21-25]; hydrogen adsorption induced dislocation injection from surfaces [26, 27]; and hydrogen-enhanced localized plasticity – the HELP mechanism [28-32]. In Nb, V, Zr, Ti and alloys based on them, a hydride phase can form and grow; embrittlement is then attributed to cleavage of the brittle hydride phase [33, 34]. Several reviews of the experimental evidence and the arguments for and against these mechanisms exist in the literature [9, 30, 35] and for brevity are not repeated here. From a review of the extensive body of literature that has been amassed on hydrogen embrittlement of metals, it appears unlikely that a single mechanism can account for all the observations. It is more feasible that several mechanisms operate simultaneously, but that one dominates under specific conditions. It is also possible that one mechanism can dominate initially but as conditions change so does the mechanism. For example, in α-Ti the embrittlement process changes from cleavage of the brittle hydride phase to the HELP mechanism when the crack propagation rate exceeds that of hydride nucleation and growth [34]. In this paper, a brief review of the TEM evidence for hydrogen enhancing dislocation motion is presented; a more extensive review can be found in Robertson [29].

From the literature, it is evident that there is abundant evidence, in macroscopic test data [36-39] and on fracture surfaces [40-43], for plasticity occurring during hydrogen embrittlement. What has been the subject of debate is when the dislocation activity occurs and its role in hydrogen embrittlement. Advocates of the decohesion mechanism proposed that the plasticity was an after effect of the embrittlement process and not intrinsic to the failure or the influence of hydrogen. For example, Oriani and Josephic[36] attributed
the observed hydrogen-enhanced relaxation rate to a decrease in the internal stress caused by a hydrogen-assisted decohesive nucleation and growth of microvoids, which caused the generation of dislocations. That is, the generation of the dislocations was a by-product of the embrittlement process. Beachem [42] in 1972 proposed that hydrogen enhanced the motion of dislocations and this was an integral component of the embrittlement process.

Identifying the atomistic processes responsible for hydrogen embrittlement remains challenging and the microscopic mechanisms and processes are generally inferred from macroscopic property changes or measurements. One approach that does enable the effect of hydrogen on the deformation and fracture behavior to be visualized is to conduct deformation experiments in a transmission electron

microscope equipped with an environmental cell. Such an approach requires modification of the sample holder or the objective pole-piece of the microscope such that the sample can be exposed to the gas environment without degrading the resolution or performance of the microscope; see Butler and Hale [44] for details. In addition, to deform a sample a straining stage is needed that is compatible with the selected gas confinement system. The approach adopted at the University of Illinois was to incorporate the environmental cell within the objective pole-piece [45, 46] and to use a displacement-controlled, single-axis tilt straining stage to deform an electron transparent specimen in a gaseous environment. An important feature of this microscope was the operating pressure range, which was up to 200 torr of H_2 gas for a few minutes at room temperature. This pressure was significantly higher than achievable in other environmental cell TEM designs, but it came with a concomitant reduction in the spatial resolution; the spatial resolution was approximately 0.9 nm which was sufficient for diffraction contrast studies. A noteworthy point is that the fugacity is significantly higher than the externally measured pressure as the H_2 molecules are dissociated and ionized by the electron beam. Bond *et al.*[47] indirectly determined the pressure through measurement of the critical radius of a blister formed on the surface of an Al sample during exposure to hydrogen and the electron beam. They reported the fugacity to be several orders of magnitude greater than the measured pressure. This approach, although enabling visualization of the effect of the environment on the deformation and failure modes, suffers from the drawback that the observations could not be correlated with the macroscopic stress-strain curve and the location and concentration of the hydrogen could not be determined. Nevertheless, with this capability new insights to the atomistic processes responsible for hydrogen embrittlement were visualized directly for the first time. In the following some examples are presented to highlight what is possible with such an instrument and how these observations contributed to the hydrogen enhanced localized plasticity mechanism.

RESULTS AND DISCUSSION.

Using the environmental cell transmission electron microscope, the hydrogen embrittlement of numerous FCC [28, 48-51], BCC [52, 53], and HCP[34] systems were investigated. In all systems studied, it was observed that the introduction of hydrogen to the metal increased the dislocation velocity of moving dislocations (the stage displacement rate was constant during the test) or caused stationary dislocations under load to move (the stage displacement was held constant during the test). The dislocation velocity was dependent on the pressure of gas introduced and increased with increasing pressure. Removal of the gas from the environmental cell, and, hence the sample, reduced the dislocation velocity to zero unless the external force was being increased. Re-introduction of the gas caused the dislocation velocity to increase again. This observation was independent of the dislocation character and nature; the mobility of screw and edge dislocations and of partial and perfect dislocations was affected similarly. Furthermore, it was observed to occur for isolated dislocations, and dislocations in cell walls and in grain boundaries. An example of hydrogen causing motion of stationary partial dislocations in 310S

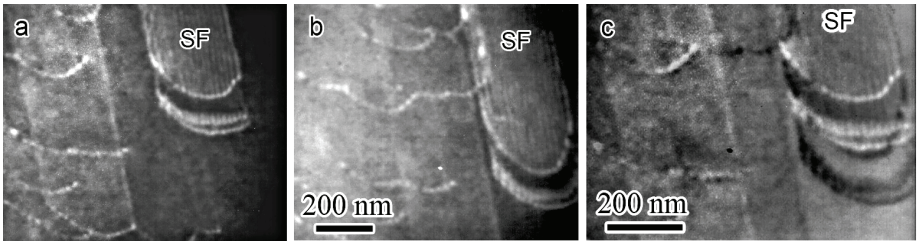


Figure 1. Motion of partial dislocations in 310S stainless steel due to the introduction of hydrogen. a. initial position, b. position with hydrogen introduced. c. composite image to show magnitude of the movement of the partial dislocations [54].

stainless steel is shown in the weak-beam dark-field images shown in Figure 1. The initial positions of the partial dislocations with the trailing ribbons of stacking fault are shown in Figure 1a. These were produced by deforming the sample in vacuum and then holding the stage displacement constant until the dislocation motion stopped. Introducing hydrogen causes the partial dislocations to move as shown in Figure 1b. The hydrogen-induced motion is easier to visualize in the difference image presented in Figure 1c. This image was formed by superimposing a negative image of Figure 1b (white features become black and vice versa) on a positive image of Figure 1a. As can be seen in Figure 1c, the leading partial dislocation has moved approximately 130 nm. Interestingly, the perfect dislocations do not show the same response and move only slightly due to the addition of hydrogen. Hydrogen also affected the emission of dislocation from cell walls and from dislocation sources. An example of hydrogen-induced emission from a dislocation cell wall in Ni is shown in the series of time resolved images presented in Figure 2. As in the

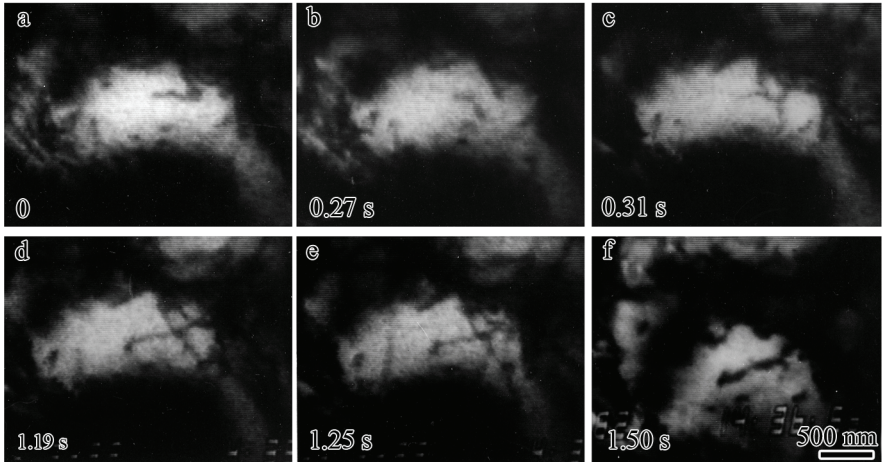


Figure 2. Hydrogen-induced release of dislocations from cell walls and the motion of those dislocations across the cell interior. Material: Ni. Adapted from [28].

previous case, the sample was held under constant load such that no dislocations were being released from the cell walls or moving in the cell interior and then the gas was introduced. On the introduction of the gas, dislocations were ejected from one wall, moved across the interior and were accommodated in the wall on the other side of the cell; some examples of released and mobile dislocations are indicated in the figure. The mobility of grain boundary dislocations was also enhanced by hydrogen, see Figure 3. The difference image presented in Figure 3d shows the initial positions of dislocations (white dislocations) on the grain boundary in the absence of hydrogen and the position of the same dislocations (black) after hydrogen has been introduced; the material in this case was 310S stainless steel. These observations along with those presented by Robertson, Birnbaum and co-workers show the generality of the effect of internal hydrogen on the mobility of all dislocation types in a wide range of materials with different crystal structures.

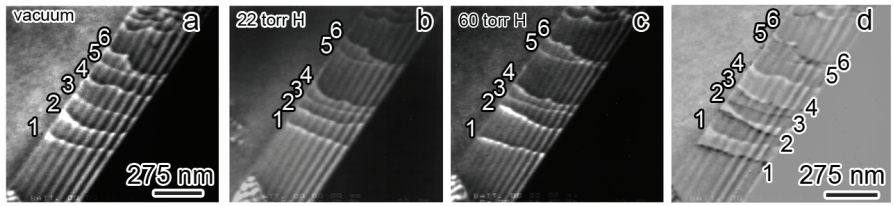


Figure 3. Dislocation motion induced along a grain boundary by the addition of hydrogen. The progress of the dislocations is arrested by a step in the grain boundary. d. shows a comparison image of the initial and final positions [54].

In addition to increasing the mobility of dislocations for a constant stress, the introduction of hydrogen can cause an arrested crack to propagate [28, 52]. Prior to crack advance extensive thinning occurred ahead of the crack. The series of images presented in Figure 4 shows the advancement of an arrested crack in IN 903 due to the addition of hydrogen gas. The extensive thinning that occurs ahead of the crack and the formation of a void or microcrack is seen in Figure 4g. Crack advance occurs by the linkage of these microcracks with the primary crack. Similar to dislocations, the progress of the crack could be halted by removing the hydrogen and restarted by

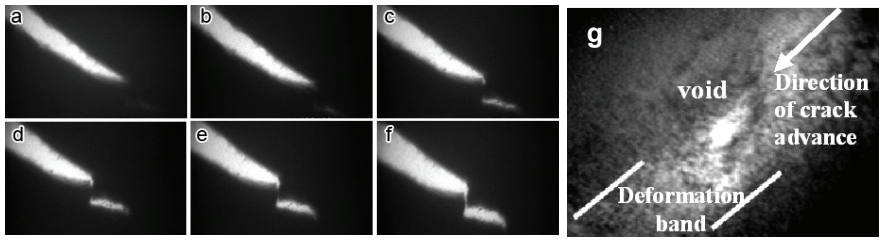


Figure 4. Crack advance in IN903 due to the introduction of hydrogen gas. The time between each image is: a. 0 sec, b. 17s, c.21s, d. 29s, e. 32s and f.39s. Hydrogen was introduced at t = 17 sec. g. Void formation within the intense deformation band ahead of the propagating crack.

reintroducing it. Observations within the thinned region revealed extensive dislocation activity, which was also accelerated by the presence of hydrogen.

The electron microscopy experiments demonstrated that hydrogen can enhance the velocity of dislocations and crack propagation rate. The effect on the dislocations was attributed to the change in the stress field associated with the hydrogen-dislocation complex that results from hydrogen segregation to and accumulation at the dislocations. A result of this modification is that the dislocation-hydrogen complex has a lower interaction energy with other elastic obstacles in specific directions than just the dislocation. Consequently, the introduction of hydrogen to a dislocation pile-up should result in the separation distance between the dislocations decreasing as the hydrogen concentration is increased. Conversely, the separation distance between the dislocations in the pile-up should increase when hydrogen is removed. This reversibility in separation distance on hydrogen removal has been demonstrated in aluminum [54]. An example of this effect is shown in Figure 5, in which the dislocation positions against an obstacle in hydrogen is shown in Figure 5a and the position after hydrogen is removed in Figure 5b. To illustrate the change in position, a composite image formed by superimposing a negative image of the final positions on a positive image of the initial positions was formed and the resultant image is shown in Figure 5c. A small but measureable shift in the dislocation positions is seen; the direction of motion is indicated by the arrow. Observations of this type support the predictions of the elastic shielding model of hydrogen enhanced localized plasticity.

It has been proposed that hydrogen reduces the stacking-fault energy and that this in turn is responsible for the observed increase in the degree of slip planarity [14-20, 55, 56]. Atomistic simulations of the effect of hydrogen on the stacking-fault energy have been made. Wen *et al.* [17] found that with hydrogen homogeneously distributed along the slip plane, the separation distance between partial dislocations in Ni increases, which would be indicative of a decrease in the stacking-fault energy *Ab initio* calculations based on density functional theory predict that the stacking-fault energy of Al will decrease from 134 mJ m^{-2} to 77 mJ m^{-2} in the presence of

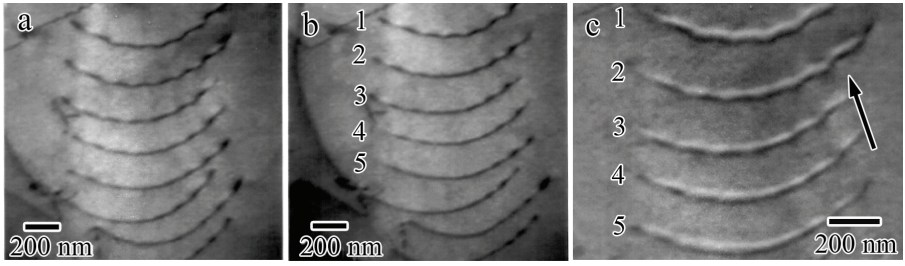


Figure 5. Increasing the separation distance between dislocations in a pile-up due to the removal of hydrogen. The hydrogen pressure was 72 torr in a, and essentially zero in b. c. is a composite image produced by superimposing a negative image of b on a positive image of a. The shift in the dislocation positions is then evident [54].

hydrogen [57]. It is not known if such a decrease is sufficient to change the deformation behavior in Al. Only a few direct measurements of the effect of hydrogen on the stacking-fault energy have been made [14, 58, 59]. From these limited studies, the decrease in stacking-fault energy due to hydrogen is between 47 and 20%, but all measurements have been in low stacking-fault energy materials. It is worth noting that a low stacking-fault energy material does not deform solely by movement of partial dislocations, perfect dislocations also participate in the deformation so a decrease in stacking-fault energy will not affect all dislocations responsible for the plasticity.

A hydrogen-induced reduction in the stacking-fault energy explanation has been invoked to explain the observed increase in slip planarity. However, the hydrogen-shielding concept provides an alternate explanation that is simply related to the atmosphere of hydrogen attached to the dislocations and the physical process of cross-slip. Hydrogen will be attracted to both edge and screw dislocations, although to a lesser extent to screw dislocations. Assuming the dislocations are of mixed character, the distribution of hydrogen will vary depending on the ratio of the edge to screw components. Only the screw dislocation component can cross slip, the remainder of the line dislocation would have to reorient to cross-slip and to do so it must expel hydrogen from the atmosphere and return it to the lattice. As there is no driving force for this to occur, the presence of the hydrogen environment attached to the dislocation prohibits the dislocation from cross-slipping. This effect has been demonstrated for mixed character dislocations in high purity Al [48]. Figure 6 shows a time series of bright-field images of dislocations in the process of cross-slipping and the process being halted by the introduction of hydrogen. The primary slip direction is indicated by the arrow marked 1 and the cross-slip direction by arrow 2. As the hydrogen concentration is increased, the cross-slip process is arrested and the dislocations remain locked in this configuration until the hydrogen is removed from the system. That no change in the dislocation configuration occurs at the higher hydrogen concentration is apparent from the difference image, Figure 6f, which is a comparison of the dislocation positions at times 1.51s and 2.26s in 85 torr

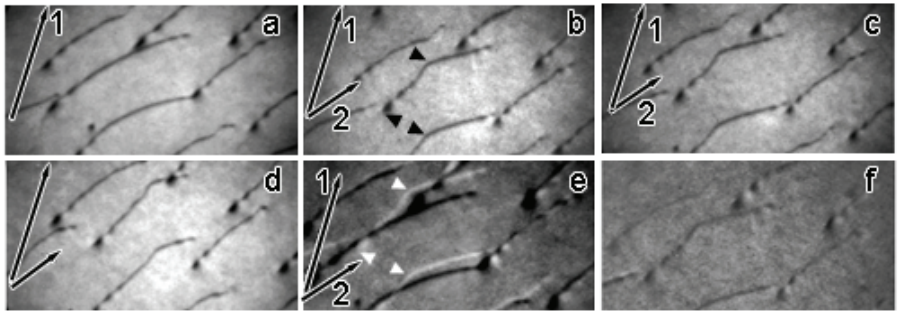


Figure 6. Effect of hydrogen on the process of cross-slip in Al. a. vacuum; b. 85 torr H2 gas; c. 85 torr H2 gas; d.25 torr H2 gas The comparison images, e and f show the change in dislocation position between a and b, and b and c, respectively. Note the lack of contrast and change in h, which indicated no change in position. Adapted from [48].

of H_2 gas. Removal of the hydrogen allows the dislocations to continue to cross-slip as can be seen in Figure 6d through the change in line length of the segments on each slip plane. Extending this result to operation of sources would suggest that dislocations generated with a hydrogen environment and capable of dragging it along would never be able to cross-slip and planar slip would dominate.

An important effect to consider is the composition of the material being tested. For example, it is known, and was demonstrated during *in situ* TEM straining experiments, that changing the composition of the grain boundary in conjunction with hydrogen in a Ni-S alloy could cause the fracture mode to transition from ductile transgranular to intergranular [51, 60, 61]. It is important to note that without hydrogen the material with low levels of sulfur at the grain boundary failed in ductile transgranular manner and without the segregation of sulfur to the grain boundary the failure mode in low concentrations of hydrogen was also ductile transgranular. It was the synergistic effect of the presence of low levels of both hydrogen and sulfur at the grain boundary that was responsible for the transition in failure mode. This change in response mode is illustrated in Figure 7. The starting condition with sulfur at the grain boundary was for slip transmission across the grain boundary, as is shown in Figure 7a. Adding hydrogen to the system concentrates hydrogen at the grain boundary where it acts synergistically with the sulfur to cause a change in the faillure mode from transgranular to intergranular, Figure 7b. In this situation, the crack travels along the grain boundary with significant dislocation activity occurring

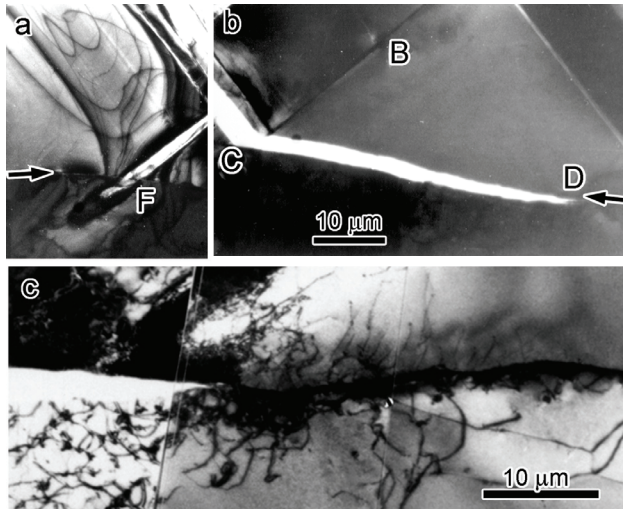


Figure 7. Hydrogen-induced transition from transgranular to intergranular failure in a Ni-S alloy. a. slip transmission through a grain boundary (arrowed) on deforming in vacuum; b. transition to grain boundary failure on the introduction of hydrogen, and c. dislocation activity ahead of and at the grain boundary crack tip. The boundary is the same with the transmission and crack nucleation points separated by 22 x 10^{-6} m . Adapted from [51].

at and in advance of the propagating crack, Figure 7c. This result is supported by the macroscopic observations of the changes in fracture mode in Ni-S alloys [61].

Understanding these synergistic effects is important in determining the failure mechanisms. However, the composition of the grain boundaries is only one contributing factor, the distribution of grain boundary misorientations is also important. For example, consider the environmental sensitivity of drop–cast and forged Ni_3Al with and without boron compared to rolled and recrystallized single crystals of boron-free Ni_3Al. In the drop-cast and forged condition, this alloy was found to have low ductility and to fail in an intergranular manner unless boron was added and segregated to the grain boundaries [62]. Initially, this effect was attributed to an inherent weakness of the grain boundaries. However boron-free polycrystalline material produced by rolling and recrystallizing a single crystal exhibited 3-4% ductility in air and failed in transgranular manner [63]. Later, the intergranular failure of the boron-free Ni_3Al was attributed to hydrogen embrittlement, with the hydrogen source being the environment [64-67]. The polycrystalline boron-free Ni_3Al produced from a single crystal showed less susceptibility to hydrogen embrittlement than the conventionally produced alloy [64]. One aspect that was not investigated in detail was the composition of the grain boundary in the boron-free material. Lillig [68] demonstrated by using Secondary Ion Mass Spectrometry, SIMS, that sulfur was present in boron-free drop-cast and forged Ni_3Al and that depending on the heat treatment it could be segregated and removed from the grain boundary; see Figure 8. The ^{32}S and ^{34}S signals show

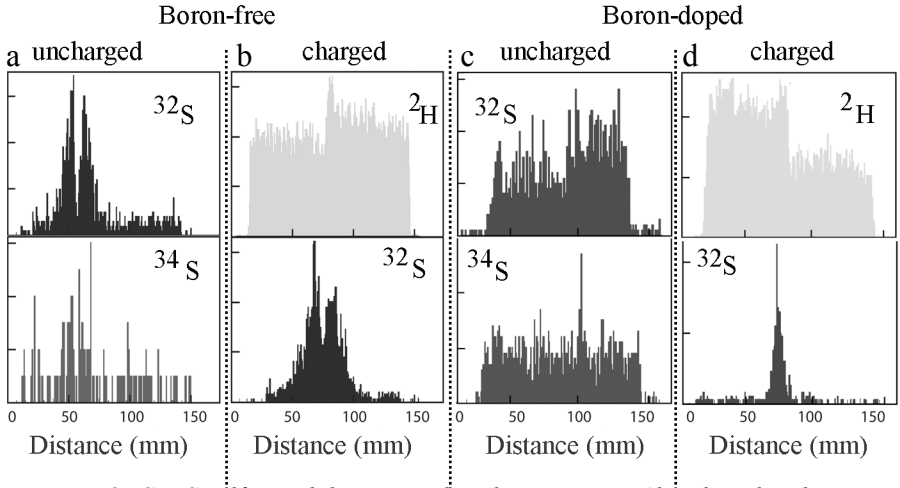


Figure 8. SIMS sulfur and deuterium distributions in Ni_3Al with and without boron. a. sulfur distribution across a grain boundary in uncharged boron-free material; b. sulfur and deuterium distribution across a grain boundary in charged boron-free material; c. sulfur distribution across a grain boundary in uncharged boron-doped material; d. sulfur and deuterium distribution across a grain boundary in charged boron-doped material [68].

peaks in the distribution in association with the grain boundary. To investigate the effect of sulfur on the grain boundary strength, electron energy loss spectroscopy can be used to assess the changes in the bonding strength. This can be achieved by determining the shape and area under the Ni L_3-edge in an electron energy loss spectrum can be used [69]. Figure 9 shows the comparison of the Ni L_3-peaks in various Ni_3Al alloys as well as Ni. Based on this assessment, a ranking of the strength would be grain boundaries with boron, bulk Ni_3Al, grain boundary with no boron, grain boundary with sulfur but no boron, and bulk nickel. This has two consequences, the grain boundaries in boron-free Ni_3Al will be weaker when sulfur is present and the lower density of states at the grain boundary will increase the solubility of hydrogen. Both effects favor weakening of the grain boundaries. Lillig [68] examined the propensity for deuterium to segregate to grain boundaries in boron-free material with and without sulfur segregated to the grain boundary. The results of this analysis are shown in Figures 8b, c and d. In the drop-cast and forged

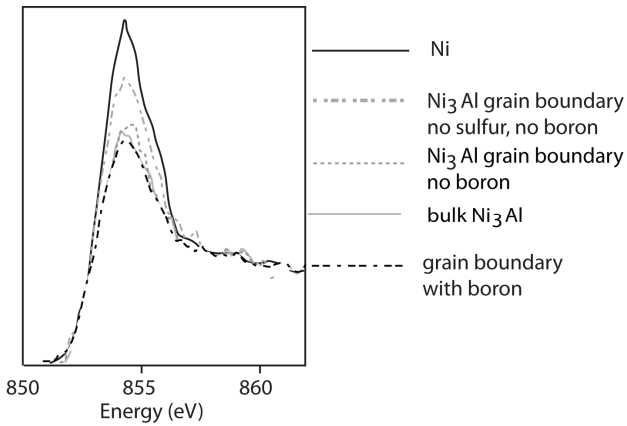


Figure 9. The Ni L_3 peak in different materials [68]. The results for nickel and for a grain boundary with boron segregated to it are from Muller et al [69].

boron-free material, the deuterium distribution follows that of sulfur, see Figure 8b. In contrast in the boron doped alloy, although some boundaries show the presence of sulfur there is no co-segregation of both sulfur and deuterium. The difference in the signal heights in the boron-doped alloy containing deuterium reflects the different sputtering rates for different grain orientations. These results suggest that the environmental sensitivity of Ni_3Al is attributed to the synergistic effects of sulfur and hydrogen on the cohesive strength of the grain boundary.

Lastly, the effect of tailoring the distribution of grain boundary misorientations on the susceptibility of a material to hydrogen embrittlement is demonstrated in a polycrystalline alloy that was produced by rolling and recrystallizing a single crystal of boron-free Ni_3Al. An orientation distribution map along with an analysis of the fraction of grain boundaries as a function of misorientation is presented as Figure 10. Notable is the percentage of special grain boundaries. Deformation of this material

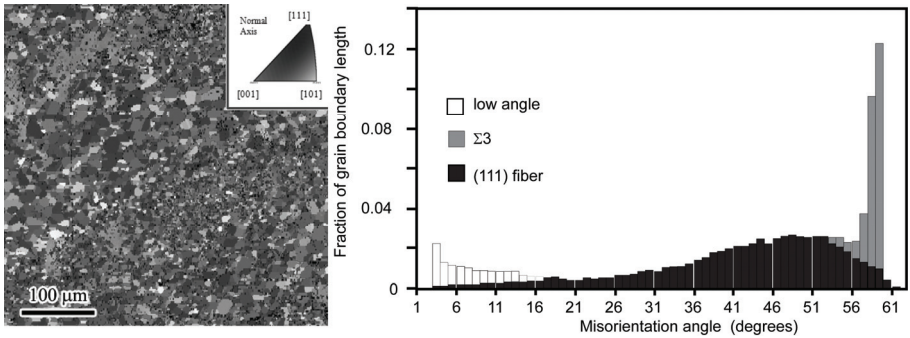


Figure 10. Misorientation map and distribution of misorientation angles for a rolled and recrystallized single crystal of boron free Ni_3Al [68].

in the presence and absence of hydrogen demonstrated that this alloy was less susceptible to hydrogen embrittlement and that the failure mode was no longer predominantly intergranular but rather was mixed mode. The difference in how the grain boundaries respond to deformation in hydrogen for the boron-free materials produced by the different processing strategies is shown in Figure 11. In the boron-free alloy produced by drop-casting and forging shows an intergranular fracture whereas in the alloy containing the high volume fraction of special grain boundaries, slip is transferred through the boundaries and the crack follows.

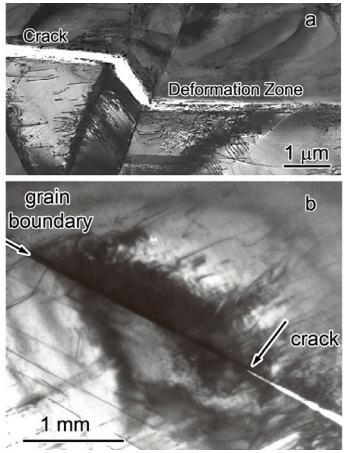


Figure 11. Comparison of the deformation and cracking modes in Ni_3Al in hydrogen. Materials produced by: a. rolling and recrystallizing a boron-free crystal [68] and b. drop-cast and forged boron-free material [49].

SUMMARY

The studies performed in the transmission electron microscope that initiated the formulation of the hydrogen enhanced localized plasticity mechanism were briefly described along with some of the examples that verified at least qualitatively the

predictions of the hydrogen shielding concept. The effect of hydrogen shielding is independent of the type of dislocation and of the crystal structure. It has been shown that the transition from transgranular to intergranular failure is sensitive to the composition of the grain boundary and segregated elements in conjunction with hydrogen may be more detrimental than either the segregant or hydrogen alone. Lastly, it has shown that by controlling the volume fraction of special grain boundaries the susceptibility to hydrogen can be reduced.

ACKNOWLEDGEMENTS

The work described in this paper is drawn from work performed by DL and PJF during their graduate studies at the University of Illinois. It also includes work from many other graduate students and post-doctoral fellows at the University of Illinois and their contribution to this work, even if not highlighted, was significant and immeasurable. I would like to acknowledge all of their efforts for without them this paper would not have been possible. Special mention should be made for my friend and colleague, Howard Birnbaum, without whom this would not have been possible. The microscopy presented in this work was performed in the Center for Microanalysis of Materials at the University of Illinois which is supported by the University of Illinois.

REFERENCES.

[1] Johnson W.H. "On some remarkable changes produced in iron and steel by the action of hydrogen and acids". Proceedings of the Royal Society of London 1875;23:reproduced in "Hydrogen damage" : Ed. Cedric D. Beachem.

[2] Zapffe C. "Discussion of Metal Arc Welding of Steels by S. A Herres". Transactions, American Society for Metals 1947;39:191.

[3] Tien J.K., Thompson A.W., Bernstein I.M., Richards R.J. "Hydrogen transport by dislocations". Metall. Trans. A 1976;7A:821.

[4] Bernstein I.M. "The role of hydrogen in the embrittlement of iron and steel". Mater. Sci. Engng. 1970;6:1.

[5] Tromans D. "On surface energy and the hydrogen embrittlement of iron and steels". Acta Metall. Mater. 1994;42:2043.

[6] Petch N.J. "Lowering of the fracture stress due to surface adsorption". Phil. Mag. 1956;1:331

[7] Troiano A.R. "The role of hydrogen and other interstitials in the mechanical behavior of metals". Trans. ASM 1960;52:54

[8] Morlet J.G., Johnson H.H., Troiano A.R. "A new concept of hydrogen embrittlement in steel". J. Iron and Steel Inst. 1958;189:37.

[9] Oriani R.A. "Hydrogen-the versatile embrittler". Corrosion 1987;43:390.

[10] Sieradzki K. "Kinetic aspects of slow crack growth in the gaseous hydrogen embrittlement of steels". J. Mater. Sci. 1979;14:2703.

[11] Pasco R.W., Sieradzki K., Ficalora P.J. "A surface chemistry kinetic model of gaseous hydrogen embrittlement". Scripta Metall. 1982;16:881.

[12] Pressouyre G.M. "Trap theory of hydrogen embrittlement". Acta Metall. 1980;28:895.
[13] Pressouyre G.M., Bernstein I.M. "A kinetic trapping model for hydrogen-induced cracking.". Acta Metall. 1979;27:89
[14] Whiteman M.B., Troiano A.R. "The influence of hydrogen on the stacking fault energy of an austenitic stainless steel". Phys. Stat. Sol. 1964;7:K109.
[15] Windle A.H., Smith G.C. "Effect of hydrogen on plastic deformation of nickel single crystals". Metal Science Journal 1968;2:187.
[16] Bernstein I.M. Role of microstructure and the environment on dislocation behavior. In: Chu S. N. G., Liaw P. K., Arsenault R. J., Sadananda K., Chan K. S., Gerberich W. W., Chau C. C., Kung T. M., editors. Micromechanics of Advanced Materials. Symposium in Honor of Professors James C.M.Li`s 70th Birthday. Proceedings., 1995. p.401.
[17] Wen M., Fukuyama S., Yokogawa K. "Atomistic simulations of hydrogen effect on dissociation of screw dislocations in nickel". Scripta Mater. 2005;52:959.
[18] Hermida J.D., Roviglione A. "Stacking fault energy decrease in austenitic stainless steels induced by hydrogen pairs formation". Scripta Mater. 1998;39:1145.
[19] Ulmer D.G., Altstetter C.J. "Hydrogen-induced strain localization and failure of austenitic stainless steels at high hydrogen concentrations". Acta Metall. Mater. 1991;39:1237.
[20] Tang X., Thompson A. "Hydrogen effects on slip character and ductility in Ni-Co alloys". Mater. Sci. Eng. A 1994;A186:113.
[21] Nagumo M., Ishikawa T., Endoh T., Inoue Y. "Amorphization associated with crack propagation in hydrogen-charged steel". Scripta Mater. 2003;49:837.
[22] Nagumo M. "Hydrogen related failure of steels - a new aspect ". Mater. Sci. and Tech. 2004;20:940
[23] Nagumo M., Matsuda H. "Function of hydrogen in intergranular fracture of martensitic steels". Phil. Mag. A 2002;82:3415.
[24] Sakaki K., Kawase T., Hirato M., Mizuno M., Araki H., Shirai Y., Nagumo M. "The effect of hydrogen on vacancy generation in iron by plastic deformation". Scripta Mater. 2006;55:1031.
[25] Geng W.-T., Freeman A.J., Olson G.B., Tateyama Y., Ohno T. "Hydrogen-promoted grain boundary embrittlement and vacancy activity in metals: Insights from ab initio total energy calculatons". Materials Transactions 2005;46:756.
[26] Lynch S.P. "Environmentally assisted cracking: overview of evidence for an adsorption-induced localised-slip process". Acta Metall. 1988;36:2639.
[27] Lynch S.P. "Mechanisms of hydrogen-assisted cracking". Met. Forum 1979;2:189.
[28] Robertson I.M., Birnbaum H.K. "HVEM study of hydrogen effects on the deformation of nickel". Acta Metall. 1986;34:353.
[29] Robertson I.M. "The effect of hydrogen on dislocation dynamics". Eng. Frac. Mech, 2001;68:671.

[30] Birnbaum H.K. Mechanisms of hydrogen related fracture of metals. In: Moody N. R., Thompson A. W., editors. Hydrogen Effects on Material Behavior: The Minerals, Metals and Materials Society, 1990. p.639
[31] Birnbaum H.K., Sofronis P. "Hydrogen-enhanced localized plasticity-a mechanism for hydrogen-related fracture". Mater. Sci. Eng. A, Struct. Mater., Prop. Microstruct. Process. 1993; A176:191.
[32] Bahr D.F., Nibur K.A., Somerday B.P. "Hydrogen effects on dislocation activity in austenitic stainless steel". Acta Mater. 2006;54:2677.
[33] Westlake D.G. "Habit planes of zirconium hydride in zirconium and zircaloy". J. Nucl.Mater. 1968;26:208.
[34] Shih D.S., Robertson I.M., Birnbaum H.K. "Hydrogen embrittlement of alpha titanium: in situ TEM studies". Acta Metall. 1988;36:111.
[35] Hirth J.P. "Effects of hydrogen on the properties of iron and steel". Metall. Trans. A 1980;11A:861.
[36] Oriani R.A., Josephic P.H. "Hydrogen-enhanced load relaxation in a deformed medium-carbon steel.". Acta Metall. 1979;27:997.
[37] Abraham D.P., Altstetter C.J. "The effect of hydrogen on the yield and flow stress of an austenitic stainless steel". Metall. Mater. Trans. A, 1995;26A:2849.
[38] Sirois E., Birnbaum H.K. "Effects of hydrogen and carbon on thermally activated deformation of nickel". Acta metall. mater 1992;40:1377.
[39] Lunarska E. "Effect of hydrogen on relaxation phenomena in pure iron.". Scripta Metall. 1977;11:283.
[40] Beachem C.D. "Orientation of cleavage facets in tempered martensite (quasi-cleavage) by single surface trace analysis". Metall. Trans. 1973;4:1999.
[41] Beachem C.D. Microscopic versus macroscopic aspects of hydrogen-assisted cracking ('hydrogen-embrittlement'). 5th Spring Meeting of the Metallurgical Society of AIME (abstracts only received). Philadelphia, Pa., USA. 29 May - 1 June 1973. 1973.
[42] Beachem C.D. "A new model for hydrogen -assisted cracking (hydrogen embrittlement)". Metall. Trans. A 1972;3:437
[43] Yeh M.S., Huang J.H. "Internal hydrogen-induced subcritical crack growth in Ti-6Al-4V". Scr. Mater. 1997;36:1415.
[44] Butler E.P., Hale K.F. In-situ studies of gas-solid interactions. In: Glauert A. M., editor. Practical Methods in Electron Microscopy, vol. 9. Amsterdam: North-Holland, 1981. p.239
[45] Lee T.C., Dewald D.K., Eades J.A., Robertson I.M., Birnbaum H.K. "An environmental cell transmission electron microscope.". Rev. Sci. Instr. 1991;62:1438
[46] Robertson I.M., Teter D. "Controlled Environment Transmission Electron Microscopy". J. Micros. Res. and Tech. 1998;42:260
[47] Bond G.M., Robertson I.M., Birnbaum H.K. "On the Determination of the Hydrogen Fugacity in an Cell TEM Facility". Scripta Metall. 1986;20:653.
[48] Ferreira P.J., Robertson I.M., Birnbaum H.K. "Hydrogen effects on the interaction between dislocations". Acta Mater. 1998;46:1749.

[49] Bond G.M., Robertson I.M., Birnbaum H.K. "On the mechanisms of hydrogen embrittlement of Ni_3Al alloys". Acta Metall. 1989;37:1407.
[50] Bond G.M., Robertson I.M., Birnbaum H.K. "Effects of hydrogen on deformation and fracture processes in high-purity aluminum". Acta Metall. 1988;36:2193.
[51] Lee T.C., Robertson I.M., Birnbaum H.K. "HVEM in situ deformation study of nickel doped with sulfur". Acta Metall. 1989;37:407.
[52] Tabata T., Birnbaum H.K. "Direct observations of hydrogen enhanced crack propagation in iron". Scr. Metall. 1984;18:231.
[53] Robertson I.M., Tabata T., Wei W., Heubaum F., Birnbaum H.K. "*Hydrogen Embrittlement and Grain Boundary Fracture.*". Scripta Metall. 1984;18:841
[54] Ferreira P.J. Hydrogen effects on crystal dislocations and stacking-fault energy. Mater. Sci. Eng, Ph.D. Thesis. University of Illinois at Urbana-Champaign, 1996.
[55] Domain C., Besson R., Legris A. "Atomic-scale ab initio study of the Zr-H system: II. Interaction of H with plane defects and mechanical properties". Acta Mater. 2004;52:1495.
[56] Gao K.W., Nakamura M. "Hydrogen embrittlement of Ti-49Al at various strain rates". Intermetallics 2002;10:233.
[57] Gang L., Orlikowski D., Park I., Politano O., Kaxiras E. "Energetics of hydrogen impurities in aluminum and their effect on mechanical properties". Phys. Rev. B 2002;65:064102.
[58] Pontini A.E., Hermida J.D. "X-ray diffraction measurement of the stacking fault reduction induced by hydrogen in an AISI 304 steel". Scripta Mater. 1997;37:1831
[59] Ferreira P.J., Robertson I.M., Birnbaum H.K. "Influence of hydrogen on the stacking-fault energy of an austenitic stainless steel". Mater. Sci. Forum 1996;207-209:93.
[60] Lassila D.H., K. B.H. "The effect of diffusive segregation on the fracture of hydrogen charged nickel". Acta Metall. 1988;36:2821.
[61] Lassila D.H., Birnbaum H.K. "Intergranular fracture of nickel: the effect of hydrogen-sulphur co-segregation". Acta Metall. 1987;35:1815.
[62] Liu C.T., White C.L., Horton J.A. "Effect of boron on grain-boundaries in Ni_3Al ". Acta Metall. 1985;33:213.
[63] George E.P., Liu C.T., Pope D.P. "Intrinsic ductility and environmental embrittlement of binary Ni_3Al". Scripta Metall. 1993;28:857
[64] George E.P., Liu C.T., Pope D.P. Reexamination of grain boundary fracture in Ni_3Al Environmental and alloying effects. International symposium on structural intermetallics, Champion, PA (United States). United States, 1993. p.26.
[65] George E.P., Liu C.T., Pope D.P. "Intrinsic ductility and environmental embrittlement of binary Ni_3Al ". Scripta Metall. et Mater. 1993;28:857.
[66] George E.P., Liu C.T., Pope D.P. "Environmental embrittlement: the major cause of room-temperature brittleness in polycrystalline Ni_3Al ". Scripta Metall. et Mater. 1992;27:365.

[67] George E.P., Liu C.T., Pope D.P. "Mechanical behavior of Ni_3Al: effects of environment, strain rate, temperature and boron doping". Acta Mater. 1996;44:1757.
[68] Lillig D. Understanding the environmental sensitivity of Ni_3Al. Mater. Sci. Eng., Ph.D. Thesis, University of Illinois at Champaign-Urbana, 1998.
[69] Muller D.A., Subramanian S., Batson P.E., Sass S.L., Silcox J. "Near atomic scale studies of electronic structure at grain boundaries in Ni_3Al". Phys.Rev. Lett. 1995;75:4744.

Effects of Hydrogen on Materials
Proceedings of the 2008 International Hydrogen Conference
Brian Somerday, Petros Sofronis, Russell Jones, editors, p 38-45
Copyright © 2009 ASM International®
All rights reserved.
www.asminternational.org

A Coexistent View of Hydrogen Effects on Mechanical Behavior of Crystals: HELP and HEDE

W.W. Gerberich, D.D. Stauffer
Dept. of Chemical Engineering and Materials Science,
University of Minnesota

P. Sofronis
Mechanical Science and Engineering,
University of Illinois, Urbana-Champaign

ABSTRACT

The literature is now replete with publications extolling the virtues of hydrogen-enhanced localized plasticity (HELP) versus hydrogen-enhanced decohesion (HEDE). What this contribution desires to accomplish is separating the various stages of dislocation plasticity and fracture. To that end it is proposed that HELP almost always occurs but may have very different ramifications on the interpretation of dislocation nucleation and dislocation velocities. Similarly, whether or not decohesion or ductile rupture occurs in a given system cannot be divorced from the combinative effects of hydrogen on plasticity, except perhaps in rare cases. From a fracture mechanics viewpoint, a couple of plausible interactions of HELP and/or HEDE are described for hydrogen-enhanced cleavage, microvoid growth, or shear instability.

Introduction

A coexistent view of hydrogen effects is something many researchers have struggled with due to inconsistent results often obtained due to the type of testing conditions. What is known for sure is that HELP occurs in most metals, alloys, and intermetallic compounds [1-9]. This is both from direct transmission electron microscopy (TEM) [4] and mechanical tests exhibiting slip line traces [5] and nanoindentation [2,3,5,10]. There is some controversy regarding whether hydrogen increases or decreases the activation volume for dislocation plasticity in view of some recent results from nanoindentation tests. This will be addressed first. Following that there is the more complex issue of fracture [5,12-16]. What is known for sure is that HELP contributes to reducing the ductile fracture resistance of 21-6-9 [6] and 316 stainless steel [12] and HEDE is accepted as producing brittle fracture of BCC Ti30Mo [14,15] and BCC titanium [15,16] at high hydrogen concentrations. One might also make the case in Fe-3%Si and some semi-brittle intermetallics that cleavage is the dominant mode of fracture [2,9,13].

The flow chart in Fig. 1, best describes what will be addressed here. Stage I considers incipient plasticity whether it is in a region of sparsely or densely populated dislocations of a whole volume or a local volume at a singularity. Stage II will then consider how the incipient and later stages of plasticity interact with the crack process.

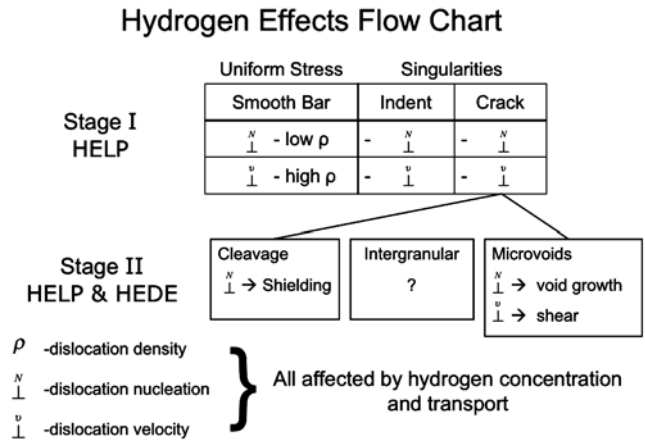


Figure 1: Effect of low density and high density dislocation populations, relative to smooth bars or singularities, on HELP and HEDE.

I. Stage I, HELP

Hydrogen enhances localized plasticity with many ramifications including its effect on dislocation nucleation, interaction energies, arrangements, propensity of heterogeneous deformation, and velocities. Here, the discussion points will be twofold, first with respect to large volume, smooth bars where under uniform stress states (e.g. smooth bars in tension) large density dislocation velocities control plasticity. Secondly, consider small volumes. One example is within localized shear bands in which dislocation activity is concentrated while the rest of the body experiences no further plasticity. Additionally this would be the case at an indenter tip or crack singularities. For these, it is proposed that with sparse or nonexistent densities dislocation nucleation is dominant.

I.1 Dislocation velocity effects

Using a series of stress relaxation and differential temperature tests, Sirois and Birnbaum [1] demonstrated that in thin sheet (0.4 mm) specimens of well-annealed Ni that activation volumes could be measured. With applied stresses in the 25 to 150 MPa regimes, it was found that activation volumes, V^*, ranged from 350 to 2500 b^3. These were interpreted with standard thermal activation analysis based on dislocation velocity effects. Specifically, regarding hydrogen at the 600 appm level, the V^* values were about 60 percent of those without hydrogen. The activation enthalpies, ΔH^*, were also reduced from 1.9 eV to 1.4 eV by hydrogen. It is considered then that smooth bar tests of large volumes are controlled by the motion of many available dislocations. As such, this is a dislocation velocity-controlled process.

I.2 Dislocation nucleation effects (singularities)

At nanoindenter or crack tips, the stresses become rather large, in the 1 to 10 GPa range, implying that the plasticity mechanism may change. A number of recent investigations [2,10] theoretical and experimental, have clearly shown in single crystals or coarse grain polycrystals that dislocation nucleation is the dominant process. It is proposed then that at singularities there is a strong tendency for dislocation nucleation to be controlling plasticity. This would particularly be the case in relatively low dislocation density single crystals or well-annealed polycrystals. In previous work [10], it was demonstrated that for relatively small activation volumes in the range of 50 b^3, that the normalized activation volume, could be given by

$$V^* / b^3 \simeq \mu / \sigma_{ys} \quad . \qquad (1)$$

This inverse relationship between activation volume and yield stress is clearly shown in a large number of single crystals evaluated under tension, compression, or bending in conjunction with TEM or by nanoindentation [10]. The experimental and theoretical basis is described elsewhere [10]. Subsequently, the simple homogeneous nucleation theory of Christian [11] was modified with surface nucleation at a stress concentration, k_T, near the edge of the indenter, giving [17]

$$V^* / b^3 \simeq \frac{\mu}{4 k_T \tau_{ys}} \left[\ln\left(\frac{\alpha V^*}{\pi b^3} \right) + 1 \right] \quad . \qquad (2)$$

It can be shown that this athermal analysis approaches the same inverse relationship of Eq. (1) for activation volumes greater than about 300 b^3. With this confirmation, it was decided to use this nucleation model at the very high stresses associated with singularities. Using the dislocation wall concept [10] and stress relaxation as well, activation volumes were calculated. For nanoindentation, the shear stress was determined at the first displacement instability for both hydrogen–free and gas-phase charged crystals. Stress relaxation was also conducted using a nanoindenter with a 175 nm tip radius. Examples of the normal load-displacement curves for 21-6-9 stainless steel [5] and Ti-30Mo [7] are shown in Fig. 2.

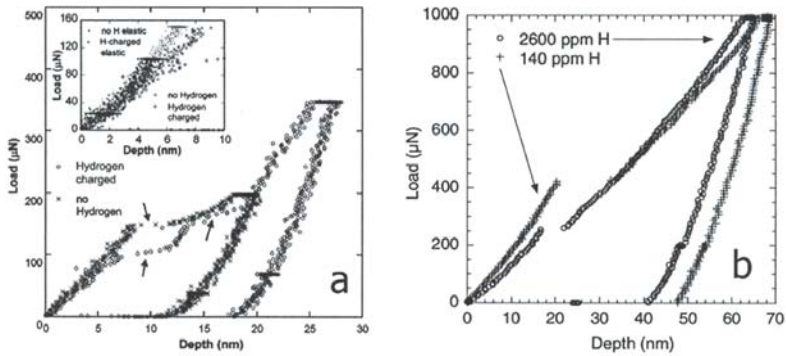


Figure 2: Load-displacement curves for (a) hydrogen-charged and uncharged 21-6-9 stainless steel showing displacement excursions (arrows) from Ref.(5); (b) nanoindentation into Ti-30Mo from Ref.(7).

From these and stress relaxation evaluations, normalized activation volume, V^*/b^3, was calculated using Eq. (2) with constant values of a surface stress concentration factor, k_T = 1.6 and the core parameter, α = 3.6.

First consider the difference between dislocation velocity and dislocation nucleation control of activation volumes. Three sets of data are shown in Fig. 3. Here, the nanoindentation data from FeAl [2] and NiAl [13] are shown where the indentation yield stresses, taken as one-third the hardness, ranged from about 1-6 GPa. Calculation details are shown elsewhere [18].

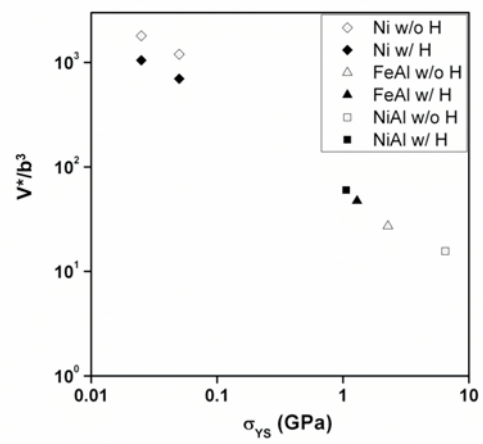


Figure 3: Normalized activation volumes for aluminides are shown with and without gas-phase charging.

These are compared to the smooth bar stress results of Sirois and Birnbaum [1] determined from thermally activated rate theory for dislocation velocities. Their data, in Fig. 3, represent applied stresses of 0.025-0.05 GPa, about two orders of magnitude smaller in stress. The dislocation velocity controlled results at these low stresses can be determined at the same stress by stress relaxation for both samples with and without hydrogen. The data clearly demonstrate that hydrogen decreases the activation volume. In addition, Sirois and Birnbaum observed that the hydrogen effects tend to diminish as the stress increased toward 150 MPa. For instance, whereas the activation enthalpy reduction for pure Ni with 600 appm hydrogen at 50 MPa was 0.32 eV, it was only 0.05 eV at 150 MPa. This indicates that at moderate stresses, the hydrogen effect is associated with the hydrogen/defect interactions through their long range stress fields [19].

In contrast, the data for the single crystal aluminides in Fig. 3 both show the activation volume increasing with hydrogen. One could argue this is at least partially due to the very different stress levels at which dislocations were nucleated under the indenter tip. To illustrate the effect of hydrogen independence of the stress level, five single crystal or well-annealed polycrystals were assessed as described elsewhere [18]. The result in Fig. 4 is that there is a nearly 50 percent increase in activation volumes due to hydrogen, independent of stress level. This does not appear to be a modulus effect since if this were

normalized on shear modulus, the spread would be even greater due to the possible reduction of the moduli by hydrogen.

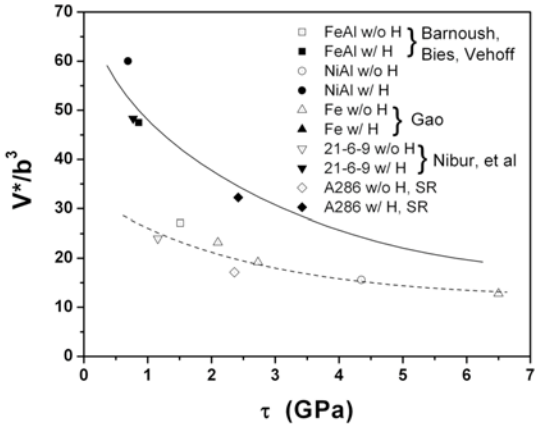


Figure 4: Effect of hydrogen on increasing the activation volume as a function of applied shear stress in aluminides and steels.

To summarize Stage I, hydrogen-enhanced localized plasticity (HELP) is found to reduce local stresses required for homogenous plasticity, e.g. smooth tensile bars. The dominant mechanism at low stresses in large volumes appears to be dislocation velocity controlled. At the small volumes and high stresses with high strain rates associated with singularities, it appears to be dislocation nucleation controlled. These two different processes, yet to be clearly understood, appear to have opposite effects on the activation volume for dislocation plasticity. The next section examines how the slip localization process at singularities might affect the fracture mechanism.

II. Stage II, HELP and HEDE

One concludes from the literature [6,9] that there is more than one type of localized fracture process that requires different aspects of hydrogen/defect interactions. As indicated in Fig. 1, it is proposed that hydrogen can promote cleavage, grain boundary failure, and two types of plastic instabilities, one associated with void growth and one, for want of a better terminology, designated as a shear instability.

II.1 Hydrogen enhanced cleavage

This terminology is chosen rather than HEDE since, except for Ti-30Mo where large amounts of hydrogen are known to reduce moduli substantially, the cleavage process may be affected by HEDE or HELP or both. Iron is chosen since this does fail by cleavage on the {100} planes and intergranular fracture will not be addressed. Some recent work on how dislocation shielding processes affect fracture may be used to model the most brittle materials, e.g., ceramics, semiconductors and intermetallics [8]. The simple dislocation

shielding analysis is based on a crack extension force criterion and dislocation shielding which gives [8]

$$K_{IC} = \frac{4}{3}\left[\frac{N\mu\sigma_{ys}b}{1-\upsilon}\right]^{1/2} \qquad (3)$$

where N is the number of dislocations in the pile-up, σ_{ys} the yield strength, μ the shear modulus, and υ the Poisson's ratio. Elsewhere, [8] for sharp point contacts inducing cleavage, the number of shielding dislocations for the fit to 22 semiconductor, oxide, carbide, silicide and nitride data used 12 dislocations. The slightly tougher intermetallics required 808 shielding dislocations. What is proposed here is that even in these brittle materials, dislocation emission precedes brittle fracture at singularities. This is well researched in silicon [20] silicon carbide [21], and magnesium oxide [22].

Given the above behavior, the mechanism of dislocation shielding is proposed for metals, alloys and intermetallics, with and without hydrogen. For cleavage of Fe, there is evidence that dislocation shielding is an appropriate model [9]. There is ample evidence of gas-phase charging at 100°C under high-pressure hydrogen giving clean cleavage fracture surfaces. There is also evidence [9] that discontinuous crack growth on {100} cleavage planes occurs by step-wise growth steps of about 1 μm. The fracture toughness of Fe-3%Si is about 60 MPa • $m^{1/2}$ and gas-phase charging or atmosphere hydrogen reduces this to a threshold of 17 MPa • $m^{1/2}$. One can hypothesize how a group of dislocations on inclined slip planes, as in Fig. 5(a), shield the crack tip. A TEM section shows that the dislocation slip band spacing in Fig. 5(b) is of the same size as the crack arrest markings in Fig. 5(c). The previous hypothesis was associated with hydrogen-induced decohesion.

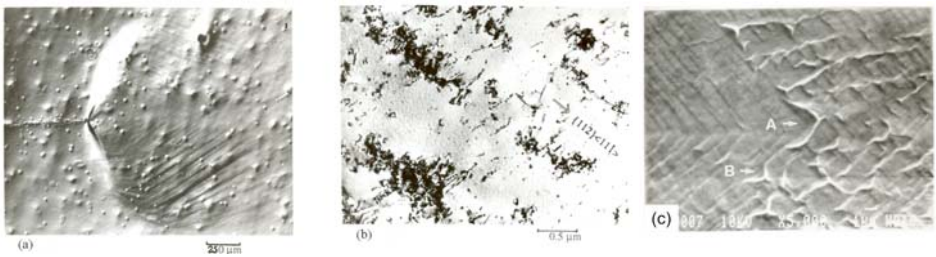


Figure 5: Hydrogen-induced slow crack growth in Fe-3% Si showing (a) slip bands, optically; (b) dislocation slip bands from TEM cross-section; (c) fracture surface.

One could argue that the dislocations in the presence of hydrogen did not shield the crack tip as effectively as dislocations without hydrogen. *The result would be that the action of highly localized slip, which reduced shielding effectiveness, could precipitate cleavage even without the decohesion stress being lowered by hydrogen.*

Turning to the other extreme of materials with very high fracture toughness levels, consider a stainless steel of many current investigations, 21-6-9, which has a nominal composition of 21Cr-6Ni-9Mn but is often nitrogen strengthened. Nibur and Somerday, et al. [5] have shown that a very high toughness, low ferrite (or non-existent) heat having

a yield strength of 656 MPa has values of J-integral toughness, J_Q = 1164K J/m^2, the baseline toughness, reduced by a factor of five when exposed to hydrogen J_Q^H = 233 k J/m^2. This amounts to reducing K_{IC} = 480 MPa • m$^{1/2}$ to 216 MPa • m$^{1/2}$ for the shielded toughness threshold, K_{Ith}^S. The plasticity is such that the strain energy release rate for discontinuous crack growth is two orders of magnitude greater than that for Fe-3% silicon, about 200,000 J/m^2 vs. 2000 J/m^2. Nevertheless, the fracture instabilities for discontinuous crack growth and arrest could be taken from fractography to be about the same, e.g., 1 μm. With multiple, parallel slip bands shielding, the enhanced localized plasticity with degraded shielding capacity could lead to shear instabilities and slow crack growth. This is discussed in detail elsewhere [18]. If proven, this would be a clear case of HELP-induced fracture without decohesion.

Conclusions

There is no question that hydrogen reduces the stress required for dislocation nucleation at singularities. It is proposed that this results in a different effect on the activation volume for plasticity wherein large stresses at singularities control plasticity through dislocation nucleation as opposed to thermally-activated dislocation velocities controlling plasticity at smaller stresses. With dislocation nucleation controlling plasticity in many instances, one operational mechanism that can rationalize both HELP and HEDE is dislocation shielding at crack tips. It is proposed that the localized plasticity mechanism, with hydrogen screening, could enhance cleavage with or without reduced decohesion.

ACKNOWLEDGMENTS

This research was funded through NSF grant number CMS-0322436, an NSF IGERT program through DGE-0114372, and an Air Force cooperative grant AOARD-08-04131. Parts of this work were carried out in the University of Minnesota I.T. Characterization Facility, which receives partial support from NSF through the NNIN program. We also appreciate support for one of us (DDS) from Hysitron, Inc. We would like to acknowledge Prof. Dave Bahr for providing the A286 samples. P. Sofronis was supported by U.S. Department of Energy Grant GO15045 and the NSF Grant DMR 0302470.

REFERENCES

1. E. Sirois and H.K. Birnbaum, “Effect of hydrogen and carbon on thermally activated deformation in nickel,” *Acta Metall. Mater.* **40** (1992) 1377-1385.
2. A. Barnoush, C. Bies, and H. Vehoff, “In-situ electrochemical nanoindentation of FeAl(100) single crystal: Hydrogen effect on dislocation nucleation,” *J. Mat’ls Res*. (2008) submitted.
3. X. Gao, “Displacement burst and hydrogen effect during loading and holding in nanoindentation of an iron single crystal,” *Scripta Mater.* **53** (2005) 1315-1320.

4. I.M. Robertson and H.K. Birnbaum, "HVEM study of hydrogen effects on the deformation of nickel," *Acta Metall.* **34** (1986) 353.
5. K.A. Nibur, D.F. Bahr, and B.P. Somerday, "Hydrogen effects on dislocation activity in austenitic stainless steel," *Acta Mater.* **54** (2006) 2677-2684.
6. K.A. Nibur, B.P. Somerday, D.K. Balch, and C. San Marchi, "The role of localized deformation in hydrogen-assisted crack propagation in 21Cr-6N-9Mn stainless steel," *Acta Mater.* (submitted 2009).
7. K.R. Morasch and D.F. Bahr, "The effects of hydrogen on deformation and cross-slip in a BCC titanium alloy," *Scripta Mater.*, **45** (2001) 839.
8. W.W. Gerberich, W.M. Mook, C.B. Carter, and R. Ballarini, "A crack extension force correlation for hard materials," *Int. J. Fracture* **148** (2007) 109-114.
9. M.J. Lii, X.F. Chen, Y. Katz, and W.W. Gerberich, "Dislocation modeling and acoustic emission observation of alternating ductile/brittle events in Fe-3wt%Si crystals," *Acta Metall*. **38** (1990) 2435-2453
10. M.J. Cordill, N.R. Moody, and W.W. Gerberich, "The role of dislocation walls for nanoindentation to shallow depths," *Inter. J. Plasticity*, 2008,
11. J.N. Christian, *Transformations in Metals and Alloys, Part I,* Pergamon Press, Oxford, 1975, 279.
12. C. San Marchi, B.P. Somerday, X. Tang, G.H. Schiroky, Inter. J. of Hydrogen Energy, **33**, 889-904, 2008
13. J.W. Hoehn, "Nanoindentation of NiAl," University of Minnesota, (1999) unpublished.
14. W.W. Gerberich, K. Jatavallibhula, K.A. Peterson, and C.L. Jensen, "Hydrogen-induced fracture phenomena in a BCC titanium alloy," 5th Inter. Conf. Fract. *Adv. In Fract. Res., 2,* ICF 5, D. Francois, ed., Pergamon Press, Oxford (1981), 989
15. K.A. Peterson, "Electron channeling studies of hydrogen embrittlement and cleavage fractures in BCC metals," Ph.D. thesis, University of Minnesota, August 1983.
16. D.F. Teter, I.M. Robertson, H.K. Birnbaum, "The effects of hydrogen on the deformation and fracture of β-titanium," *Acta Mater*, v 49, Dec. (2001), 4313-23.
17. W.W. Gerberich, D.D. Stauffer, A.R. Beaber, and W.M. Mook, "Connectivity between plasticity and brittle fracture: An overview from nanoindentation studies," *J. of Nanoengineering and Nanosystems,* (2008) accepted.
18. W.W. Gerberich, D.D. Stauffer, P. Sofronis, "A Coexistent View of Hydrogen Effects on Mechanical Behavior of Crystals: Ductile or Brittle", (2008) in submission
19. P. Sofronis and H. K. Birnbaum, "Mechanics of the Hydrogen-Dislocation-Impurity Interactions: Part I-Increasing Shear Modulus," *J. of Mechs. and Phys. of Solids,* 43 (1995) 49-90.
20. W.M. Mook, J.D. Nowak, C.R. Perrey, C.B. Carter, R. Mukherjee, S.L. Girshick, P.H. McMurry, and W.W. Gerberich, "Compressive stress effect on nanoparticle modulus and fracture," *Phys. Rev. B* **75** (2007) 214112/1-10.
21. T.F. Page, L. Riester, and S.V. Hainsworth, "The plasticity response of 6H-SiC and related isostructural materials to nanoindentation," *MRS Symp.* **522** (1998) 113-118.
22. Y. Gaillard, C. Tromas, and J. Woirgard, "Quantitative analysis of dislocation pile-ups nucleated during nanoindentation in MgO," *Acta Mater*, **54**, (2006) 1409-17.

Effects of Hydrogen on Materials
Proceedings of the 2008 International Hydrogen Conference
Brian Somerday, Petros Sofronis, Russell Jones, editors, p 46-53
Copyright © 2009 ASM International®
All rights reserved.
www.asminternational.org

RECENT OBSERVATION OF HYDROGEN-INDUCED CRACKING OF HIGH-STRENGTH STEELS

C. J. McMahon, Jr,
Department of Materials Science, University of Pennsylvania, Philadelphia, PA

Xinyu Liu
Department of Materials Science, University of Pennsylvania, Philadelphia, PA
now at Materials & Engineering Physics Program, Ames Laboratory, USDoE, Ames, IA

Jun Kameda
Department of Materials Science, University of Pennsylvania, Philadelphia, PA
now at Structural Integrity Associates, Annapolis MD

Michael J. Morgan
Savannah River National Laboratory, Aiken SC

ABSTRACT

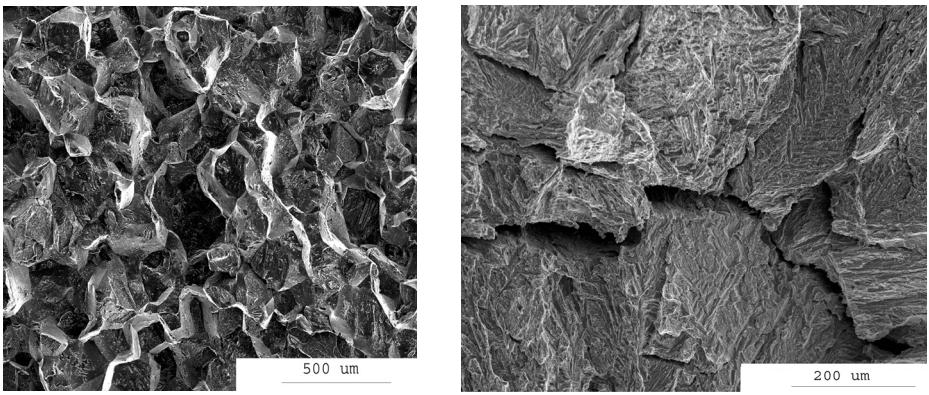
Recent efforts to understand the reasons why hydrogen-induced cracking (HIC) of high-strength steels occurs along the prior austenite grain boundaries and to devise ways to convert this cracking to plasticity-related transgranular cracking at higher stress intensities are reported.

INTRODUCTION

It was discovered in the past that there are two modes of hydrogen-induced cracking in quenched-and-tempered ferritic steels [1,2]. One is a brittle mode that occurs by intergranular decohesion at rather low stress intensities. It involves cracking along prior-austenite grain boundaries, Fig. 1(a), and is the mode that one associates with the term “hydrogen embrittlement.” The brittle mode is, of course, enhanced by a high yield strength, because that increases the local hydrogen concentration at the tip of a stressed crack or notch, as well as allowing the local cohesive stress to be reached.

The other mode is transgranular with respect to the prior austenite microstructure, Fig. 1(b), and because of its appearance it has been called “quasi cleavage.” There is no generally accepted explanation for what constitutes the crack path in this case, but it has been suggested [3] that glide-plane decohesion is involved, the glide plane being assumed to lie along the lathes of the tempered martensite microstructure. This mode

occurs at fairly high stress intensities and has been called plasticity-related hydrogen-induced cracking (PRHIC), because it tends to occur on planes of maximum shear stress [1]. One fairly obvious hypothesis would be that hydrogen is gathered up in the cores of gliding dislocations and enhances their mobility by lowering the Peierls stress. The increased local hydrogen concentration in the glide plane would be expected to lower the cohesion across that plane. So far, it does not appear that this hypothesis has received the necessary test of atomistic modeling.



(a) (b)

Figure 1: (a) IG fracture in 4340-type steel in 10 psi hydrogen; (b) TG fracture in modified HY130-type steel in 0.1N NaOH+As2O3 at 9.0A/m2.

Results on An Ultra-High-Strength Steel

Also discovered in the past is the fact that segregated impurities at grain boundaries can play a major role in determining which mode of HIC is found [4,5]. A good illustration of this is given in Fig. 2, which shows that a vacuum-melted lab heat of 4340-type steel without Mn or Si had a higher resistance to intergranular HIC than a commercial heat that contained these elements, along with other impurities like phosphorus and sulfur [2].

The question raised at the time of this result was what would happen if all impurities were eliminated from the steel. Recently, it became possible to address this question, because of the availability of very-high-purity iron and steel made in the laboratory of Professor Kenji Abiko at Sendai University in Japan. The Abiko group produced a heat of 4340-type steel using special high-purity electrolytic iron and the purest available alloy elements. Auger electron spectroscopy was carried out on a sample of this steel that was heated in UHV at a succession of elevated temperatures to determine what elements could segregate to a clean surface. It was found that the only detectible segregation was that of carbon and a small amount of sulfur. Sulfur is extremely surface active and can be found to segregate to a free

surface in iron at very low bulk concentrations, and we have never found sulfur to be present on intergranular fracture surfaces in steels containing manganese or chromium, both of which lower the sulfur potential in the matrix. Therefore, it was concluded that for the purposes of the experiment, this steel was as nearly ideally pure as we could get. The rather disappointing result [6], illustrated in Fig. 3, was that at a hardness level of Rc 55 brittle intergranular fracture occurred even in the presumed absence of segregated impurities.

This result raises the question of why supposedly pure prior-austenitic grain boundaries in such a steel would be cracked by hydrogen, aside from the fact that they comprise a continuous three-dimensional surface along which fracture could occur. The obvious hypothesis would be that the dislocations left over from the martensite transformation that lie along what is actually a set of interfaces between colonies of martensite lathes would be highly attractive to hydrogen, which could collect there and reduce the local cohesion. Unfortunately, this hypothesis cannot be checked in this type of steel, because it is not possible to anneal out the defects without substantially lowering the hardness. Therefore, it was necessary to turn to a type of steel that is lower in strength, but on which extensive work had been done on the effects of hydrogen.

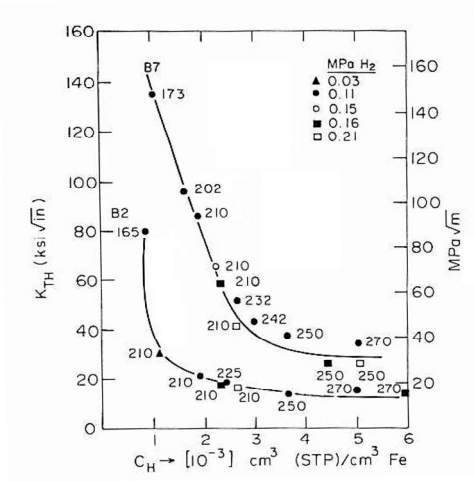
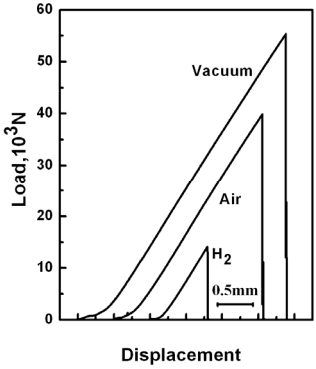


Figure 2: Dependence of threshold stress intensity for cracking in hydrogen gas for two heats of 4340 steel: a commercial heat, B2, and a high-purity lab heat without manganese or silicon, B7, on the calculated hydrogen concentration in the steel. The values of the yield strength of the specimens are given for each data point in kpsi. Ref. 2.

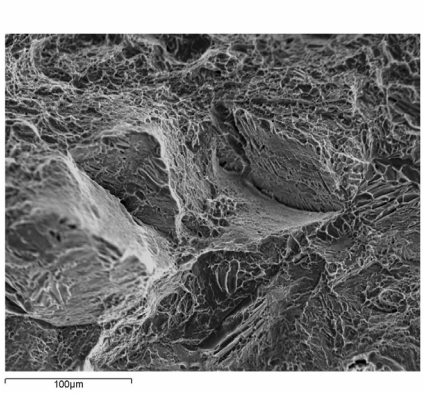
Results on A 5% Nickel Steel

In contrast to the lower-nickel, higher-carbon 4340-type steel in which toughness is sacrificed in favor of strength, a 5%-nickel steel containing around 0.1% carbon and that featured toughness at the expense of strength was developed for the U.S. Navy several decades ago and was the steel studied in refs. 1, 4, and 5. This steel was found to be highly susceptible to

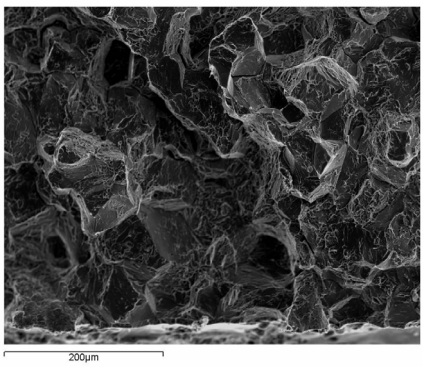
temper embrittlement, but the problem was greatly reduced when the manganese and silicon were omitted in lab heats [1]. Furthermore, when these elements were omitted, the intergranular brittle fracture at low stress intensities in hydrogen environments was replaced by PRHIC that occurred at high stress intensities, as indicated by Fig. 4.



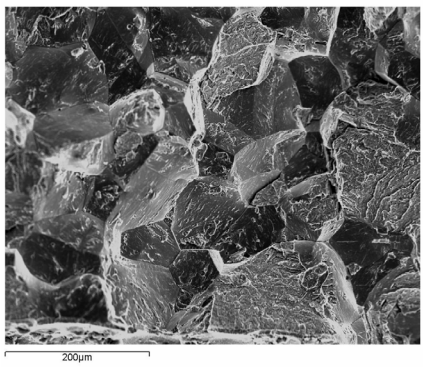
(a)



(b) vacuum



(c) air



(d) hydrogen

Figure 3: Test results for an "ideally pure" 4340-type steel. (a) the load-displacement curves in vacuum (10-3 Pa), lab air, and 0.1 MPa hydrogen. (b-c) the corresponding fracture modes.

When the opportunity to make lab heats of improved purity became available, the hydrogen behavior of this steel was revisited. Based on past experience, the working hypothesis was that we could think of three major variables that control whether such a steel would undergo PRHIC or

intergranular HIC in hydrogen: the yield strength of the steel, the hydrogen fugacity, and the impurity content of the steel. At a particular level of purity, we would postulate a diagram of yield strength vs. hydrogen fugacity, analogous to Fig. 2, showing the boundary along which the cracking mode would shift to intergranular as either yield strength or hydrogen fugacity is increased, as shown schematically in Fig. 5.

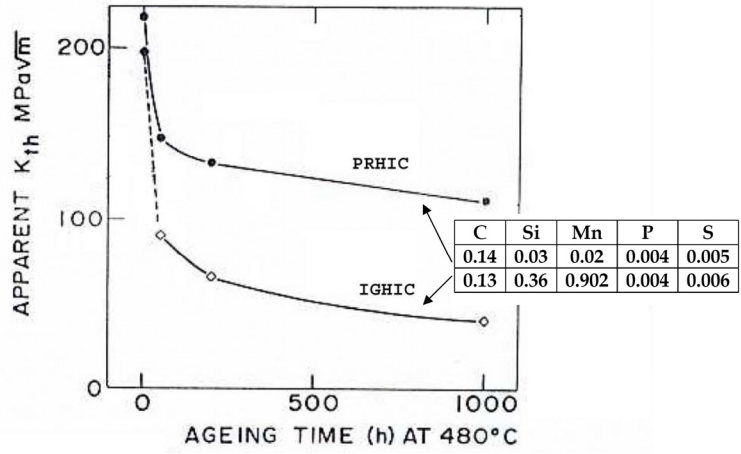


Figure 4: Effect of aging time to promote impurity segregation on the threshold stress intensity for cracking in 0.21 MPa hydrogen in a 5%NiCrMoV steel (HY130-type) for lab heats with and without manganese and silicon. Ref. 1.

Using the Japanese high-purity electrolytic iron, a heat of the 5%-nickel steel was prepared at the Ames Lab and had the composition shown in Table 1. This steel, which was heat treated by austenitizing at 850˚C (1123K) and tempering at 200˚C (473K) to a hardness of Rc 36 and a yield strength of 1054 MPa, was remarkably resistant to HIC. When tested in an NaOH solution at a high cathodic potential, calculated to be equivalent to a hydrogen fugacity of 3000 atm [7], the steel cracked by PRHIC at a K level of 119 MPa√m, as shown in Fig. 6. Unfortunately, the calculated hydrogen fugacity in the solution does not give the actual value inside the pre-crack, so it was considered necessary to shift to an environment of hydrogen gas. The maximum pressure that could be used at Penn was 20 psi (0.14 MPa), but again the failure in hydrogen occurred by PRHIC at a K level of 124 MPa√m, as shown in Fig, 7.

Table 1: Composition of high-purity modified HY130-type steel

	C	Cr	Mn	Mo	Ni	P	S	Si	V
HY130	0.10	0.47	<0.01	0.50	5.12	0.004	<0.001	<0.01	0.077

In order to explore higher pressures, subsize arc tension specimens were fabricated and tested in a special chamber at 1500 psi (10.3 MPa) hydrogen at the Savannah River National Lab. The results are summarized in Table 2. It can be seen that the behavior in hydrogen at this pressure is very sensitive to the loading rate. The maximum K level decreased and the percent intergranular fracture increased when the loading rate was decreased by a factor of ten. In addition, the beneficial effect of a higher tempering temperature, aimed at decreasing the defect concentration at prior austenite grain boundaries, was quite small; however, there was some increase in the maximum K level, corresponding to a small decrease in the amount of intergranular fracture.

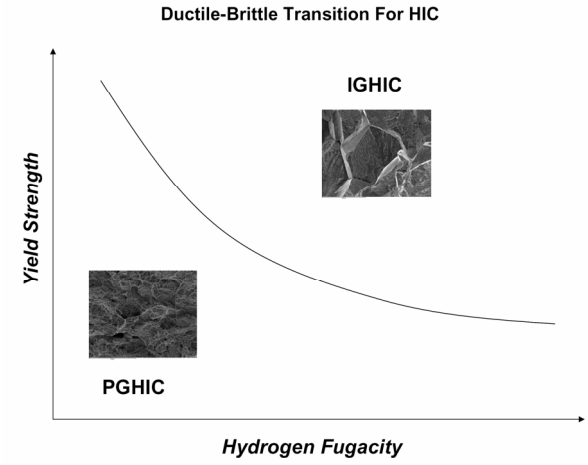
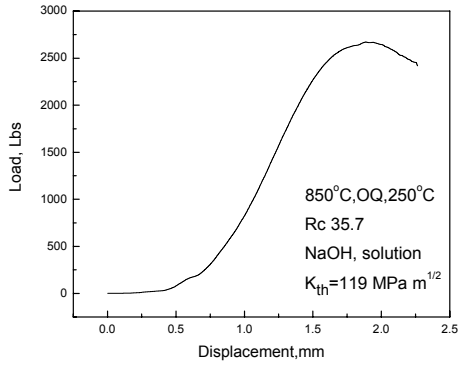


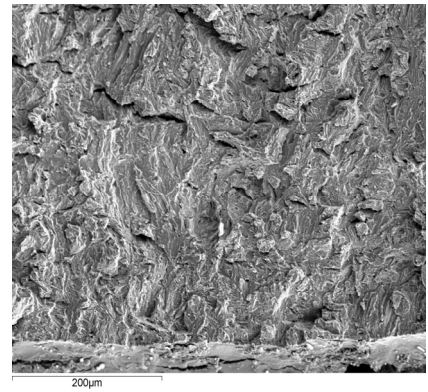
Figure 5: Schematic diagram illustrating the envisioned transition from "ductile" to brittle behavior in hydrogen for an ideally pure high-strength steel. (cf. Fig. 2)

To assess whether residual impurities could have played a role in this steel, a specimen was heated in UHV and Auger-analyzed to determine what elements would segregate to the free surface. This would identify the mobile impurities that could possible segregate to grain boundaries. Sulfur was found upon heating to 350˚C (623K). After ion sputtering to return to a clean surface and heating to 550˚C (823K), a possible presence of phosphorus was found. It may be that these elements played a role in the susceptibility of this steel to HIC.

Table 2: Results for 5% NiCrMoV Steel in 1500 psi hydrogen

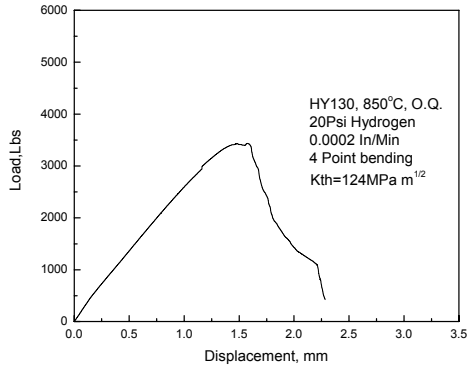
Temperature, °C	Hardness, Rc	C.H. Speed in/min	K_{Max}, MPa $m^{1/2}$	I.G.
0.002	69.2	0.002	76.0	<5%
200	35.5	0.0002	35.6	~35%
400	35.1	0.0002	44.7	~30%

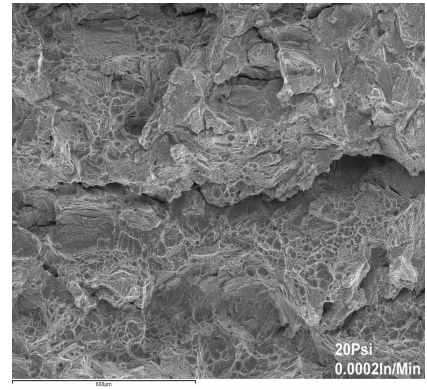




(a) (b)

Figure 6: For the high-purity 5% Ni steel, (a) the load-displacement curve in 0.1N NaOH solution at 9.0A/m2 current density, giving a calculated hydrogen fugacity of 3000 atm (304 MPa). (Ref. 7), and (b) the corresponding fracture mode.





(a) (b)

Figure 7: For the high-purity 5% Ni steel, (a) the load-displacement curve for 0.14 MPa hydrogen, and (b) the corresponding fracture mode.

These results indicate that this particular heat of steel is probably not pure enough to give a baseline behavior for an ideally pure steel. What is needed for future efforts along this line is a heat of steel made using a melting practice that would eliminate this kind of contamination. At this point, it appears that this is available only at the lab of Professor Abiko in Japan

CONCLUSIONS

The present progress report shows that the ultra-high-strength 4340-type steel, even if ideally pure, cannot safely be used for service in a hydrogen environment. Some of the strength must be given up in favor of more toughness, which can be achieved by reducing the carbon content and increasing the nickel content. The 5%NiCrMoV steel with about 0.1% carbon shows promise in this regard, especially in an aqueous environment and in hydrogen at around atmospheric pressure. However, we have not yet achieved a purity level high enough to establish the baseline behavior of an ideally pure version of this steel in high-pressure hydrogen.

ACKNOWLEDGMENTS

This research was carried out with the support of the U.S. Department of Energy, Office of Basic Energy Sciences, under grant no. DE-FG02-01ER45924; the interest and support of Dr. Yok Chen is gratefully acknowledged.

REFERENCES

1. Y. Takeda and C. J. McMahon, Jr., "Strain Controlled vs. Stress Controlled Hydrogen Induced Fracture in a Quenched and Tempered Steel," *Met. Trans. A*, 1981, **12A**, 1255.
2. N. Bandyopadhyay, J. Kameda, abd C. J. McMahon, Jr., "Hydrogen-Induced Cracking in 4340-Type Steel: Effects of Composition, Yield Strength, and H_2 Pressure," *Met. Trans. A,* 1983, **14A**, 881.
3. C. J. McMahon, Jr., "Effects of Hydrogen on Plastic Flow and Fracture in Iron and Steel", in *Hydrogen Effects in Metals*, ed. I.M. Bernstein and A.W. Thompson, TMS AIME, 1981, p. 219.
4. K. Yoshino and C. J. McMahon, Jr., "The Cooperative Relation Between Temper Embrittlement and Hydrogen Embrittlement in a High Strength Steel," *Metallurgical Transactions*, **5**, (1974) 363.
5. C.L. Briant, H.C. Feng, and C. J. McMahon, Jr.,, "Embrittlement of a 5 pct Nickel High Strength Steel by Impurities and Their Effects on Hydrogen-Induced Cracking," *Metallurgical Transactions A*, **9A** (1978) 625.
6. X-Y. Liu, J. Kameda, J.W. Anderegg, S. Takaki, K. Abiko, and C.J. McMahon, Jr., "Hydrogen-Induced Cracking in a Very-High-Purity High-Strength Steel," *Matls Sci & Eng A* 492, 2008, 218.
7. R. A. Oriani and P. H. Josephic, "Effects of Hydrogen on the Plastic Properties of Medium-Carbon Steels," *Metallurgical Transactions a-Physical Metallurgy and Materials Science*, vol. 11, pp. 1809-1820, 1980.
8. C. J. McMahon, Jr. and Xinyu Liu, "Quench Cracking in Steel as a Case of Hydrogen Embrittlement" *Matls Sci & Eng A*, in press.

Effects of Hydrogen on Materials
Proceedings of the 2008 International Hydrogen Conference
Brian Somerday, Petros Sofronis, Russell Jones, editors, p 54-61
Copyright © 2009 ASM International®
All rights reserved.
www.asminternational.org

HYDROGEN EMBRITTLEMENT OF HIGH STRENGTH STEELS AND ENVIRONMENTAL HYDROGEN ENTRY

Eiji Akiyama, Songjie Li[*], Zuogui Zhang[†1], Maoqiu Wang[†2], Katsuhiro Matsukado[†3], Kaneaki Tsuzaki
National Institute for Materials Science, Tsukuba, Ibaraki, Japan

Boping Zhang
University of Science and Technology Beijing, Beijing, China

ABSTRACT

Delayed fracture properties of martensitic high strength steels have been evaluated by measuring the change in fracture stress of circumferentially notched bar specimens pre-charged with hydrogen by means of slow strain rate test (SSRT). The fracture stress of a steel with higher strength level showed sharper decrease indicating higher susceptibility to delayed fracture. It has been found that the decrease of fracture stress with hydrogen concentration follows a power law relationship when intergranular fracture mode is observed. Another finding is that the local stress and the local hydrogen concentration estimated by finite element analysis are determining delayed fracture. Hydrogen entry into steels caused by atmospheric corrosion has been evaluated as well by using cyclic corrosion test (CCT) simulating atmospheric corrosion. The circumferentially notched bar specimens were exposed to the CCT condition and SSRT was performed at humid environment to investigate both hydrogen entry and its influence on the decrease of fracture stress in the environment. The relation between fracture stress and the content of hydrogen in corrosive environment was compared with the relation of hydrogen pre-charged specimens. The SSRT combined with CCT was proposed as evaluation method considering both the effect of hydrogen in metals and hydrogen entry into metals.

INTRODUCTION

Establishing an evaluation method for susceptibility of high strength steels to delayed fracture is quite important for the safe and reliable use of currently used and newly developed high strength steels. Delayed fracture is known as a typical example of hydrogen embrittlement. Although its mechanism has not been fully understood yet [1, 2], quantitative analysis of hydrogen concentration is being

---

[*] *On leave from University of Science and Technology Beijing, Beijing, China*
[†1] *Now at Baoshan Iron & Steel Co., LTD., Shanghai, China*
[†2] *Now at Central Iron and Steel Research Institute, Beijing, China*
[†3] *Now at Kobe Steel, LTD., Moka, Tochigi, Japan*

adopted for the evaluation of susceptibility to delayed fracture. This is because diffusible hydrogen which can evolve out from specimens during exposure at room temperature is considered to be responsible for hydrogen embrittlement of high strength steels [3]. The progress of the measurement techniques for hydrogen content in materials in a couple of decades is also conducive to more accurate hydrogen analyses and it has been promoting the hydrogen content-based evaluation. Critical diffusible hydrogen content for delayed fracture, H_c, has been proposed as a parameter determining delayed fracture property of high strength steels, and H_c is measured by means of either constant load test [4-8], stepwise test [9, 10] and slow strain rate test (SSRT) [11-14]. Among these techniques, SSRT seems more convenient to obtain H_c because it requires a shorter test time and fewer specimens. In this paper, our attempt of evaluation of delayed fracture properties of high strength steels by means of slow strain rate test is portrayed.

Another essential factor determining the susceptibility to delayed fracture is the content of diffusible hydrogen entering to steels in the environment where the steels are used, H_e. Even if a material has a high H_c it suffers from delayed fracture when it absorbs hydrogen exceeding H_c. The balance between H_c and H_e is considered to be determining the occurrence of delayed fracture and both of these parameters have to be evaluated [6]. For high strength steels used as high strength fasteners, for instance, the cause of hydrogen entry to steels is atmospheric corrosion. In the present study hydrogen content of specimens corroded by simulated atmospheric corrosion has been measured. However, quantitative measurement of diffusible hydrogen caused by corrosion is not easy because the hydrogen is released from specimens and the content is changing with the change of the atmosphere. Furthermore, hydrogen may distribute heterogeneously in a specimen though we can measure only the average hydrogen concentration by means of thermal desorption spectrometry (TDS). In order to investigate hydrogen entry and its influence on delayed fracture, SSRT of rusted specimen was performed in conjunction with the measurement of hydrogen content in this study. If we know the relation between fracture stress and hydrogen content, we can estimate the hydrogen content of fractured specimen by measuring fracture stress.

EXPERIMENTAL

Materials and Specimens

Commercially pure AISI 4135 steel and boron-bearing JIS F10T steels commonly used for high strength fasteners are used in this study. The chemical compositions of these steels are Fe-0.35C-0.19Si-0.79Mn-0.019P-0.014S-1.16Cr-0.16Mo-0.17Cu and Fe-0.20C-0.06Si-1.00Mn-0.018P-0.008S-0.0020B (mass%), respectively. The steels were austenitized and quenched, and then tempered with the heat treatment condition summarized in Table 1. Circumferentially notched round bar specimens with a notch section diameter of 6 mm and with a notch root radius of ρ=0.1, 0.25 and 0.8 mm were machined from heat treated bars and were used for slow strain rate tests

(SSRT). The calculated elastic stress concentration factors, K_t, for the specimens with notch root radii of 0.1, 0.25 and 0.8 mm were 4.9, 3.3 and 2.1, respectively [9].

Table 1: Heat treatment conditions of the steels used and obtained tensile strengths.

	Austenitization	Tempering	Tensile strength / MPa	Sign
Boron-baring steel	1153 K, 1 h, water quench	678 K, 1.5 h	1050	A11
		563 K, 1.5 h	1305	A13
AISI 4135	1133K, 1 h, oil quench	733 K, 1.5 h	1320	B13
		633 K, 1.5 h	1450	B15

Hydrogen Charging and Slow Strain Rate Test (SSRT)

Hydrogen was introduced into the circumferentially notched round bars by electrochemical charging in either 3% NaCl+0.3% NH_4SCN or 0.1 M NaOH aqueous solutions for 48 or 72 h at room temperature (RT). Solution and current density were changed to control the hydrogen content. After the hydrogen charging, the specimens were plated with cadmium to prevent hydrogen release from the specimens. In case of 48 h hydrogen charging, the specimens were kept at RT for a day before SSRT to homogenize hydrogen distribution. SSRT was carried out on a Shimadzu AG-250kNI tensile testing apparatus with a constant crosshead speed of 0.005 mm min^{-1}. The crosshead speed chosen was slow enough to allow hydrogen to diffuse to stress concentrated region near the notch root according to stress induced diffusion [11]. The fracture stress of the notched specimens was defined as the nominal maximum fracture stress calculated from the maximum tensile load divided by the initial cross section net area of the notch. The time for SSRT varies from about 1 to 6 h depending on the test sample and hydrogen content. After fracture the specimens were immediately dipped into liquid nitrogen to avoid hydrogen release. Before TDS measurements, the cadmium plating on the specimens was dissolved out by anodic polarization.

Cyclic Corrosion Test and Slow Strain Rate Test (SSRT)

Cyclic corrosion tests were conducted on the circumferentially notched round bars with the same shape as used SSRT of hydrogen charged specimens with the calculated elastic stress concentration factors, K_t, of 4.9. A corrosion cycle consists of dry term at 30°C and 50%RH for 5.75 h, wet term at 30°C, 98%RH for 1.75 h and salt spray term of 0.5% NaCl at 30°C for 0.5 h, and the cycle is repeated. After CCT the fracture stress was measured by means of SSRT with a constant crosshead speed of 0.005 mm min^{-1} in order to measure the decrease of fracture stress caused by hydrogen introduced by corrosion. During SSRT the specimen was covered with a cell. In the cell the relative humidity was controlled at about 98%RH by using saturated K_2SO_4 aqueous solution in order to keep hydrogen entry caused by corrosion. After SSRT the specimen was kept frozen in liquid nitrogen and the surface rust layer was removed by means of sand blast before TDS.

Thermal Desorption Analysis

The hydrogen content in a specimen was measured by means of a thermal desorption spectrometer (R-Dec Co., Ltd.) equipped with a quadru-pole mass (Q-mass) spectrometer. The TDS analyses were conducted from ambient temperature to 800°C at a heating rate of 100°C h^{-1} to obtain hydrogen desorption profiles. The total hydrogen content desorbed at the first peak desorbed below about 300°C was defined as diffusible hydrogen content.

RESULTS AND DISCUSSION

Slow Strain Rate Test of Hydrogen-Charged Specimens

The fracture stresses of hydrogen pre-charged specimens as a function of diffusible hydrogen content for the steels of A11, A13, B13 and B15 are compared in Fig. 1 on normal axes (a) and double logarithmic axes (b). Apparently, the fracture stress decreases with increase in diffusible hydrogen content. The A11 specimen shows slight decrease at low hydrogen content region and it shows sharper drop at relatively high hydrogen content region over about 0.5 weight-ppm (wtppm). The decrease of fracture stresses of A13 and B13 specimens is more obvious than that of A11, and the fracture stress of B15 which has the highest strength level dropped most sharply among the steels. Thus, the order of susceptibility to delayed fracture is B15>>B13>A13>>A11.

In the low hydrogen content region where A11 shows slight decrease of fracture stress, around the crack initiation site of A11 showed quasi-cleavage, and in the higher hydrogen region it showed intergranular fracture which is typical for hydrogen embrittlement [12]. Intergranular fracture was observed also around crack

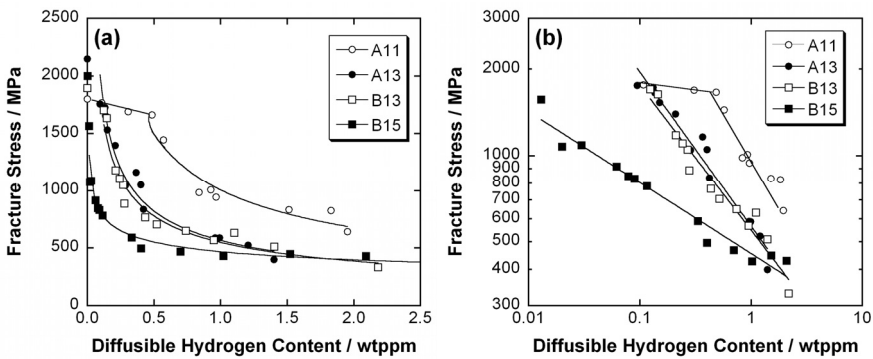


Figure 1: The fracture stresses of circumferentially notched round bar specimens as a function of hydrogen content measured by means of TDS plotted on normal scale (a) and double logarithmic scale (b) [12-14].

initiation site for all of the A13, B13 and B15 specimens [12-14]. As shown in the log-log plot of Fig. 1(b), the decrease of fracture stress shows almost a straight line when intergranular fracture takes place. Therefore, the relation between fracture stress and diffusible hydrogen content can be expressed by a power law relationship expressed by Eq.1,

$$\sigma_f = a\, H_D^{-b} \qquad (1)$$

where σ_f is the fracture stress, H_D diffusible hydrogen content, a and b material constants corresponding to susceptibility to delayed fracture [13]. From this power law relationship, critical hydrogen content for delayed fracture, H_c, can be calculated for any applied stress.

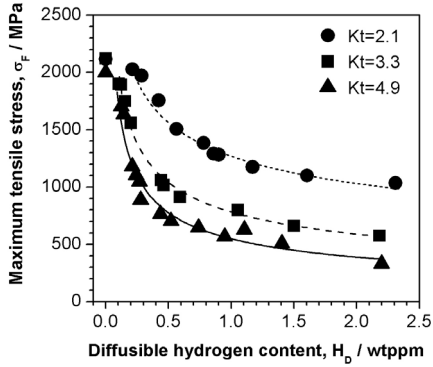


Fig. 2: Influence of stress concentration factor on the relation between fracture stress and hydrogen content of B13 steel. [13].

The dependence of the fracture stress of B13 steel on stress concentration factor, K_t, is shown in Fig. 2. Clearly, the increase of K_t enhances the susceptibility of the specimen to delayed fracture. In order to know the influence of K_t on fracture stress in detail, the peak value of the maximum principal stress was calculated by means of finite element analysis (FEA). Peak value of locally accumulated hydrogen concentration was also obtained from hydrostatic stress calculated by means of FEA and by assuming that the local hydrogen concentration is determined by the following equation [15];

$$H = H_D \exp\left[\frac{-V_H\left(\sigma_h - \sigma_{h,\min}\right)}{RT}\right] \qquad (2)$$

where σ_h is the hydrostatic stress at the stress concentration region, $\sigma_{h,min}$ the hydrostatic stress in the region far from the notched section, V_H the partial molar volume of hydrogen in bcc-Fe (V_H=2.1×10^{-6}m^3/mol) [16], R the gas constant, T the testing temperature (T=300 K) and H_D is the diffusible hydrogen content. The

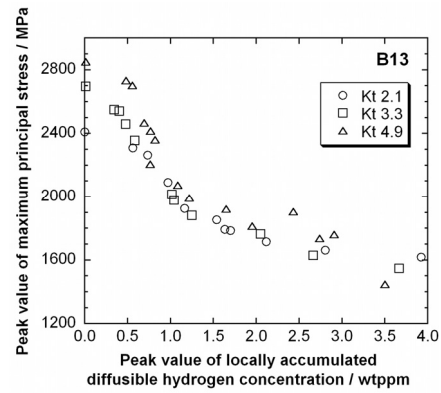


Fig. 3: The peak value of maximum principal stress as a function of the peak value of locally accumulated diffusible hydrogen concentration for the B13 specimens with different stress concentration factors [13].

relation between fracture stress and hydrogen content shown in Fig. 2 is converted to the relation between the peak value of the maximum principal stress and peak value of locally accumulated hydrogen concentration as shown in Fig. 3. Despite the difference in K_t, all the data points were almost on one curve showing good agreement with a power law relationship. Therefore, it can be considered that local stress and local hydrogen are controlling the occurrence of delayed fracture. The relation is useful because it is expected that H_c for any applied stress and notch geometry can be estimated by using the relation and by applying FEA.

In a recent study, conventional strain rate test (CSRT) method was applied to evaluate delayed fracture property of high strength steels [17]. In this method the crosshead speed is 1 mm/min which is 200 times as high as that of the SSRT in this paper, and it does not allow stress induced hydrogen diffusion. Although the CSRT and SSRT methods are different to each other, the relation between local stress and average hydrogen concentration (=local hydrogen content) obtained by means of CSRT is in good agreement with the relation between local stress and local hydrogen concentration obtained by SSRT in this study. This supports the idea that local stress and local hydrogen concentration are the controlling factors of delayed fracture.

Slow Strain Rate Test of Specimens after Cyclic Corrosion Test

The change in fracture stress of B15 and B13 specimens with corrosion cycle number was measured by means of SSRT in a humid cell (Fig. 4). The humid condition was applied to keep corrosion and hydrogen entry going. This is based on an assumption that the property of rust layer with incorporated chloride ion and hydrolysis of dissolved iron ions are influencing the hydrogen entry and high humidity reproduces active hydrogen entry into rusted specimens. The fracture stress of both steels decreases with CCT cycle number up to about 120 cycles and then recovers slightly. The hydrogen content increases with increase in CCT cycle. This can be responsible for the decrease of the fracture stress. The decrease in fracture

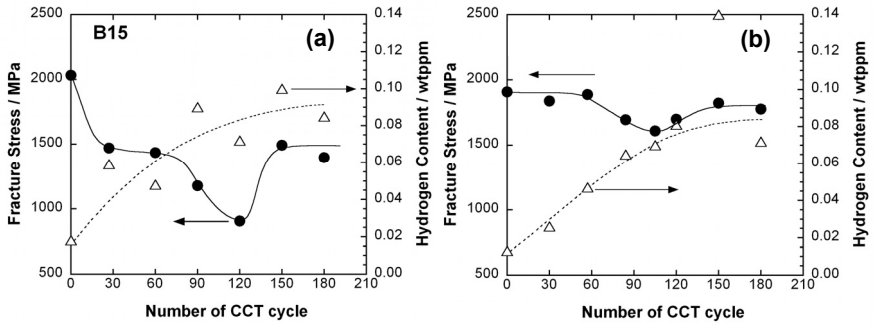


Fig. 4: The change in fracture stress and diffusible hydrogen concentration of specimens corroded in cyclic corrosion test chamber. The left figure is ofB15 (a) and the right is of B13 (b).

stress of B15 is more significant than that of B13. Since the hydrogen entries into both steels are similar, B15 which showed sharper decrease of fracture stress with hydrogen content for hydrogen pre-charged specimen also represented higher susceptibility to delayed fracture with CCT. The slight recovery of fracture stress can be interpreted by the change of K_t caused by corrosion of the notch root. From a measurement of the corrosion loss of the same material in the CCT condition, the corrosion thickness after 150 cycles is about 0.11 mm. This is thick enough to change K_t value.

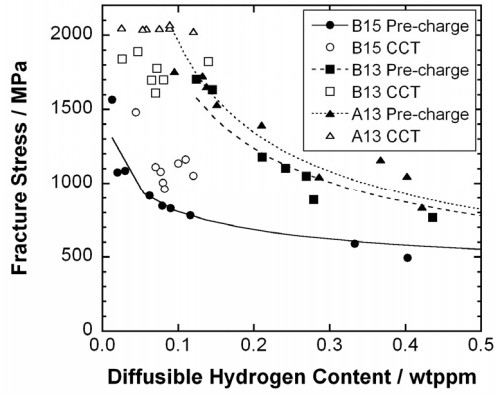


Fig. 5: The relation between fracture stress and diffusible hydrogen concentration of B15, B13 and A13 specimens corroded by cyclic corrosion test is shown with open marks and that of hydrogen pre-charged specimen is also plotted in solid marks for comparison.

Fig. 5 summarizes the relation between fracture stress and hydrogen content of B15, B13 and A13 steels corroded by CCT. A13 showed no obvious change in fracture stress. In contrast, B15 and B13 steels exhibited obvious decrease in fracture stress with hydrogen content which is similar to that of hydrogen pre-charged specimens. From the results, the order of delayed fracture susceptibility with consideration of hydrogen entry under atmospheric corrosion is B15>B13>A13.

CONCLUSIONS

The following conclusions can be drawn from the results in this study.

1. Power law relationship between fracture stress and hydrogen content is applicable when intergranular fracture takes place.
2. Local stress and local hydrogen concentration are controlling the initiation of the intergranular fracture.
3. The proposed evaluation method of SSRT after atmospheric corrosion test is relatively convenient evaluation method which can allow for both influences of H_c and H_e.

REFERENCES

1. Hirth, JP., Carnahan, B., “Hydrogen Adsorption at Dislocations and Cracks in Fe,” *Acta Metallurgica*, Vol. 26, No. 12 (1978), pp. 1795-1803.
2. Nagumo, M., “Hydrogen Related Failure of Steels – a new aspect,” *Mater. Sci. Tech.*, Vol. 20, No. 8 (2004), pp. 940-950.

3. Takai, K., Watanuki, R., "Hydrogen Trapping States Innocuous to Environmental Degradation of High-strength Steels," *ISIJ International*, Vol. 43, No. 4 (2003), pp. 520-526.
4. Suzuki, N., Ishii, N., Miyagawa, T., Harada, H., "Estimation of Delayed Fracture of Steels ," *Tetsu-to-Hagané*, Vol. 79 (1993), pp. 227-232.
5. Hirai, K., Wakiyama, K., Uno, N., "Experimental Study on Delayed Fracture of High Strength Bolt (Part 1 A Proposal for the Critical Diffusible Hydrogen Method)," *J. Struct. Constr. Eng., AIJ*, Vol. 490, No. 12 (1996), pp. 215-222.
6. Yamasaki, S., Takahashi, T., "Evaluation Method of Delayed Fracture Property of High Strength Steels," *Tetsu-to-Hagané*, Vol. 83, No. 7 (1997), pp. 454-459.
7. Takagi, S., Inoue, T., Hara, T., Hayakawa, M., Tsuzaki, K., Takahashi, T., "Parameters for the Evaluation of Hydrogen Embrittlement of High Strength Steel," *Tetsu-to-Hagané*, Vol. 86, No. 10 (2000), pp. 689-696.
8. Wang, M.Q., Akiyama, E., Tsuzaki, K., "Determination of the Critical Hydrogen Concentration for Delayed Fracture of High Strength Steel by Constant Load Test and Numerical Calculation," *Corrosion Science*, Vol. 48, No. 8 (2006) 2189–2202.
9. Takagi, S., Inoue, T., Tsuzaki, K., Minami, F., "Determination Method of Weibull Shape Parameter for Evaluation of the Hydrogen Embrittlement Susceptibility of High Strength Steels," J. Japan Inst. Metals, Vol. 65, No. 12 (2001), pp. 1082-1090.
10. Takagi, S., Terasaki, S., Tsuzaki, K., Inoue, T., Minami, F., "A New Evaluation Method of Hydrogen Embrittlement Fracture for High Strength Steel by Local Approach," *ISIJ International*, Vol. 45 (2005), pp. 263-271.
11. Wang, M.Q., Akiyama, E., Tsuzaki, K., "Crosshead Speed Dependence of the Notch Tensile Strength of a High Strength Steel in the Presence of Hydrogen," *Scripta Materialia*, Vol. 53, No. 6 (2005), pp. 713–718.
12. Wang, M.Q., Akiyama, E., Tsuzaki, K., "Hydrogen Degradation of a Boron-Bearing Steel with 1050 and 1300MPa Strength Levels," *Scripta Mater.*, vol. 52 (2005), pp. 403-408.
13. Wang, M.Q., Akiyama, E., Tsuzaki, K., "Effect of Hydrogen and Stress Concentration on the Notch Tensile Strength of AISI 4135 Steel," *Mater. Sc. & Eng. A*, vol. A398, No. 1-2 (2005), pp. 37-46.
14. Wang, M.Q., Akiyama, E., Tsuzaki, K., "Effect of Hydrogen on the Fracture Behavior of High Strength Steel during Slow Strain Rate Test," Corrosion Science, Vol. 49, No. 11 (2007), pp. 4081–4097.
15. Li, J.C.M., Oriani, R.A., Darken, L.W., "The Thermodynamics of Stressed Solids," *Z. Phys. Chem*., Vol. 49 (1966), pp. 271–290.
16. H. Wagenblast, H.A. Wriedt, "Dilation of Alpha Iron by Dissolved Hydrogen at 450 to 800°C," *Metall. Trans.*, Vol. 2 (1971) 1393–1397.
17. Hagihara, Y., Ito, C., Hisamori, N., Suzuki, H., Takai, K., E. Akiyama, "Evaluation of Delayed Fracture Characteristics of High Strength Steel Based on CSRT Method," Tetsu-to-Hagané, Vol. 94, No. 6 (2008), pp. 215-221.

Effects of Hydrogen on Materials
Proceedings of the 2008 International Hydrogen Conference
Brian Somerday, Petros Sofronis, Russell Jones, editors, p 62-69
Copyright © 2009 ASM International®
All rights reserved.
www.asminternational.org

Effect of Hydrogen on the Mechanical Properties of Multiphase High Strength Steels

Lode Duprez
ArcelorMittal Research Industry Gent, J.F.Kennedylaan 3, B-9060 Zelzate, Belgium

Kim Verbeken
Department of Metallurgy and Materials Science, Faculty of Engineering, Ghent University (UGent), Technologiepark 903, B-9052 Ghent, Belgium
Microstructure Physics, Max-Planck-Institut für Eisenforschung, Max-Planck-Strasse 1, 40237 Düsseldorf, Germany
Postdoctoral fellow with the Fund for Scientific Research-Flanders (Belgium) (F.W.O. Vlaanderen)

Marc Verhaege
Department of Metallurgy and Materials Science, Faculty of Engineering, Ghent University, Ghent, Belgium

INTRODUCTION

The research interest for H in steel has many causes and originates from a wide range of application conditions where H related defects may occur [1-5]: hydrogen induced cracking (HIC) and sulphide stress corrosion cracking (SSCC) in steel pipes, fish scale formation in enamelling grades, hydrogen embrittlement of welds, delayed fracture in high strength steel grades. In particular the latter, together with the prospects of hydrogen as a potential future energy carrier, causes hydrogen to be in the spotlight these days.
To investigate the behaviour and effect of hydrogen experimentally on laboratory scale, hydrogen is in most cases introduced into the steel in an artificial way, *i.e.* by means of chemical or electrochemical charging techniques [6]. The laboratory charging conditions described in literature show a huge scatter: current densities are varying from 0.02 mA/cm² to 100 mA/cm², charging times are varying from 5 minutes to 300 hours, up to 25 different electrolytes are used. This huge scatter makes the interpretation and correlation of the various literature data very difficult as the H-charging procedure has a major influence on the results obtained afterwards. Indeed, when applying a specific H-charging procedure, several uncertainties arise:

- First, when determining the H-content of a steel sample (*e.g.* by melt extraction), charged chemically or electrochemically, the result will be influenced by
    - the microstructure of the steel, *i.e.* grain size, precipitates, second phases such as bainite, martensite, retained austenite, etc.
    - the prepared surface state, *i.e.* chemical composition, roughness, etc..
- Second, in each experiment consisting of H-charging and subsequent mechanical testing, the results of the mechanical tests will be influenced by 3 different “H-contributions”:

- Hydrogen in interstitial solution, *i.e.* mobile, diffusible hydrogen
- Hydrogen tied to H-traps (precipitates, phase boundaries, etc.)
- Irreversible damage induced during the hydrogen charging procedure (blisters, microcracks, voids, corrosion)

The aim of this work was to get a better understanding of these issues. First, it was the authors' idea that comparing the results of tensile tests performed immediately and 1 week after the H-charging would allow to evaluate if significant irreversible damage was induced by the H-charging. Second, by selecting 4 multiphase steel grades with clearly different microstructures and similar strength levels (in the range 450-700MPa), the effect of the presence of second phases could be studied.

EXPERIMENTAL

Materials

4 materials with 4 distinctively different microstructures were investigated in this study: a ferrite-bainite-retained austenite TRIP700 grade, a ferrite-martensite DP600 grade, a Ti-Nb precipitation strengthened ferrite-cementite S550MC grade, ferrite-bainite FB450 grade. The optical microstructures and their chemical compositions are shown in the table and figure below.

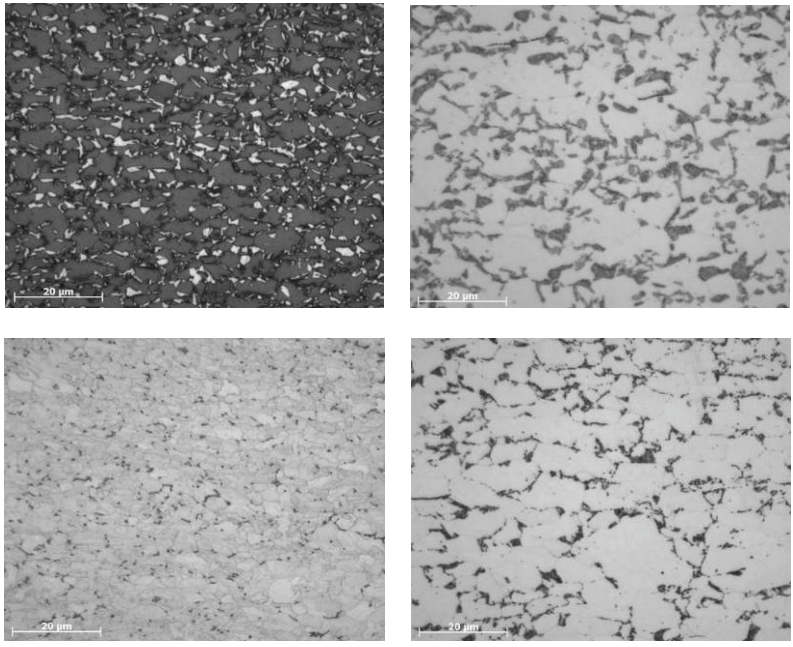


Figure 1: Optical microstructures of the TRIP700 (upper left), DP600 (upper right), S550MC (down left) and FB450 grade (down right).

H-charging

The samples for Thermal Desorption Analysis (TDA), *i.e.* discs of 1mm thick and 20mm diameter, were charged electrochemically with H by cathodic charging at room temperature. The electrolyte used in the tests is an arsenic aqueous solution (0.5g As_2O_3 – 0.25g $HgCl_2$ – 60ml H_2SO_4 / 1l H_2O). Initially, charging tests were performed at various current densities to evaluate the blister formation at the surface of the charged sample, Figure 2. Visual inspection revealed that for current densities of 0.8mA/cm², no blister formation occurred during several hours. Although this wasn't a guarantee that no irreversible damage was caused at all by charging, this current density was taken as charging condition for further tests.

Table 1: Chemical composition in wt% of the investigated steel grades.

	C	Mn	Si	Other
FB450	0.07	1.00	0.10	0.5%-1.0% Cr
TRIP700	0.17	1.60	0.40	1%-2% Al 0.04%-0.1% P
DP600	0.07	1.50	0.25	0.4%-0.8% Cr+Mo
S550MC	0.07	0.95	0.00	0.08%-0.12% Ti+Nb

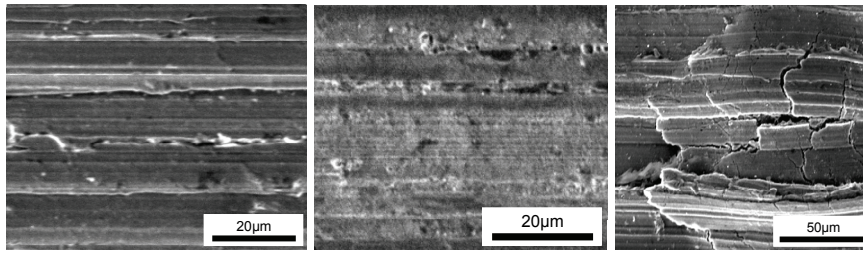


Figure 2: Steel surface before cathodic hydrogen charging (left), after "correct" hydrogen charging (middle) and after charging in too severe conditions (right)

Next, for each material, the H-content was determined by melt extraction immediately after H-charging, for a series of charging times varying from 5 to 240 minutes, using the selected 0.8 mA/cm² as charging current density. Each measurement was started exactly 60s after the end of the charging operation. The results for the DP600 grade are shown in Figure 3. Whereas the DP600, FB450 and S550MC grade had steady state values around 6.5 ppm, the TRIP700 grade had steady state values around 9 ppm.

Tensile testing of H-charged samples

Tensile test samples (A80 geometry) were prepared by spark erosion, the tensile axis being parallel to the rolling direction. To minimise the electrochemical effect of the surface segregation of alloying elements, *e.g.* the presence of Mn-, Si-, Al-oxides on the surface, the tensile samples were ground to a thickness of 1.0mm. This also allowed to minimise thickness effects (causing different absorption and effusion kinetics). Only the TRIP samples were grinded to 0.7mm, as the initial thickness was already below 1.0mm.

The tensile samples were then cathodically charged at 0.8 mA/cm², the charging time varying from 5 minutes to 3 days. For each charging time, one sample was tested immediately, *i.e.* exactly 90s after the charging, and one sample was tested 1 week after the charging.

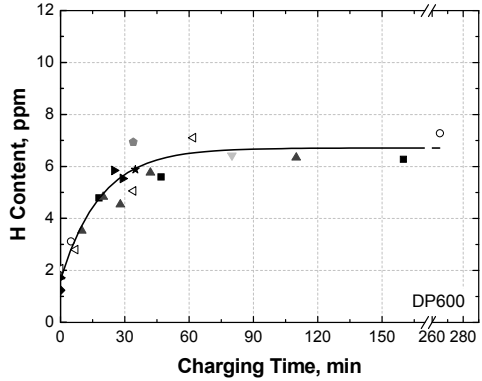


Figure 3: H-charging curve for the DP600. The measurements were performed after several recalibrations (cfr. different symbols). The H-content is expressed in wppm.

Thermal Desorption Analysis

For the Thermal Desorption Analysis (TDA), a similar set-up was used as for the tensile tests. Here, the samples were grinded discs with a thickness of 1mm and a diameter of 20mm. The samples were charged during 1h at 0.8 mA/cm². The TDA results in this work were done on hydrogen charged samples of the DP600 grade immediately after the charging and on charged samples that were stored at room temperature during 1 week.

RESULTS & DISCUSSION

Figure 4 shows the evolution of the tensile curves for the TRIP700 grade. The bold grey curve is the reference result of a standard tensile test on a non-charged sample. The black curves are the results of the tensile tests that were performed "immediately" after the hydrogen charging, *i.e.* start of the test 90 seconds after the charging. For very long charging times (~days), the ductility decreased to extremely low values. When the tensile samples are tested 1 week after the hydrogen charging (grey curves), the ductility comes almost completely back to the level of the reference curve. The shape of the tensile curves didn't really differ between the immediate testing and the 1 week testing.

The evolution of the A80 values is shown more in detail for all grades in Figure 5. As said, when the TRIP700 samples are tested immediately after the H-charging (black data points), the ductility drops very rapidly down to 10% and lower, *i.e.* for charging times longer than 15 minutes. For the TRIP samples tested after 1 week (white data points), the ductility is recovered to the range of the reference sample. Only for very long hydrogen charging times, it seemed that the ductility did not return to the original levels, which could indicate that irreversible damage is induced for very long charging times.

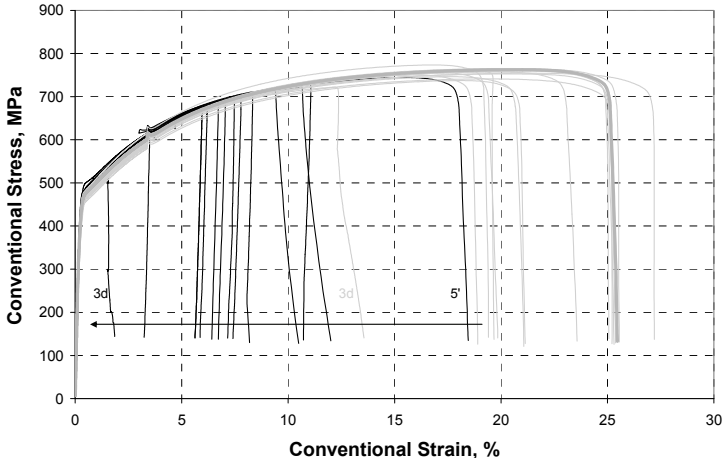


Figure 4: Tensile curves for the TRIP700 grade.

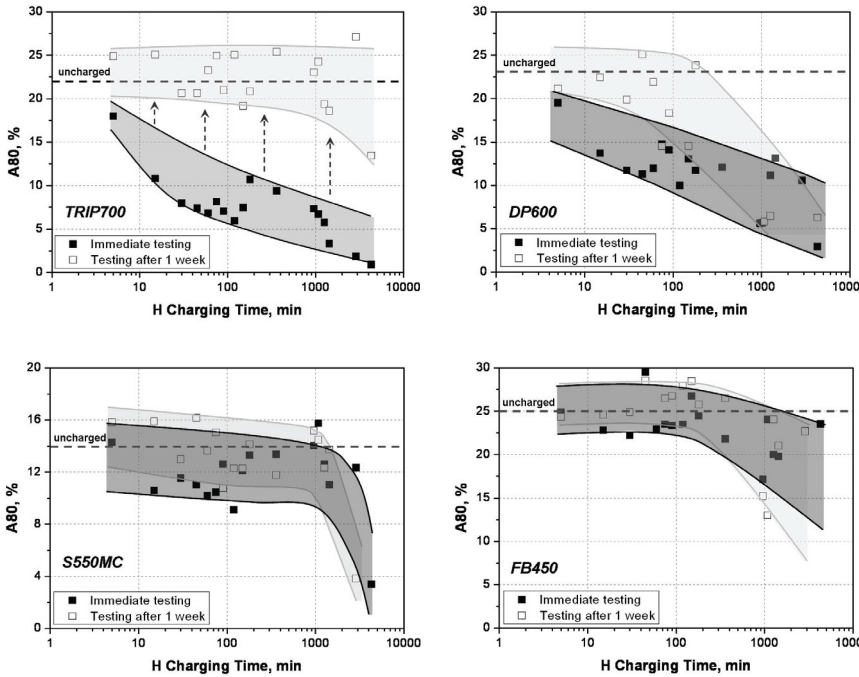


Figure 5: Evolution of the A80 value as a function of H-charging time, for immediate testing and tensile testing after 1 week.

The fact that a large part of the ductility is regained when testing the charged samples after 1 week instead of immediately indicates that the ductility loss during immediate

testing is not due to an irreversible damage caused by hydrogen charging, but due to the intrinsic presence of hydrogen in the steel. Indeed, if irreversible damage had occurred during charging (formation of microscopic defects such as voids and/or blisters), the ductility would remain low, independent of the time between charging and mechanical testing. Hence, it may be concluded that for the charging times used in this study, a current density of 0.8mA/cm² allows to introduce hydrogen in the steel in a rather correct way, *i.e.* without causing irreversible internal damage. Only for very long charging times (~days), some irreversible damage seems to occur during the charging, as the ductility is not regained completely when samples are tested after one week.

Although less than for the TRIP700, a rather fast and significant loss of ductility was also observed during immediate tensile testing for the DP600 grade. The FB450 and S550MC were found to be less sensitive. A large difference was found for the TRIP700 and DP600 material between the "immediate" tests and the "1 week" tests. For the FB450 and S550MC, the difference between immediate and 1 week testing was very limited.

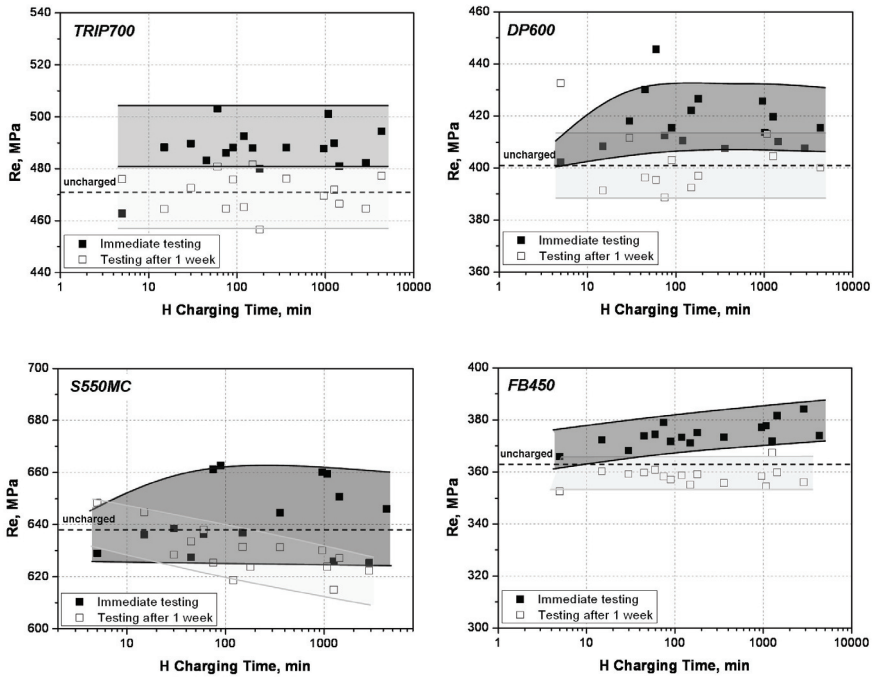


Figure 6: Evolution of the Re as a function of H-charging time, for immediate testing and tensile testing after 1 week.

Figure 6 shows the yield strength evolution. As mentioned before, no significant changes were observed in the shape of the tensile curves of the various materials, *i.e.* no yield point, no change in n-value evolution by introducing H in the steel. However, the

samples tested immediately after hydrogen charging, which thus contain more hydrogen, have a slightly higher yield strength than the samples tested after 1 week. For all materials, the increase is situated around 20MPa, although it takes longer charging times for the FB450 and S550MC grades to observe this difference. More, for the S500MC a decrease was observed with increasing charging time for the values after 1 week. The explanation for this phenomenon is not clear today. The reason for the increased yield strength immediately after H-charging is not clear, but might be a solid solution strengthening effect of the interstitial hydrogen. Considering the H content as determined by melt extraction, a strengthening effect was found to be in the range of 25000MPa/mass%H.

Except for an increased Re value, the shape of the tensile curves of the "immediate samples" does not differ much from the original shape. n-value calculations (strain hardening exponent) showed no clear changes and are therefore not reported here.

To elucidate the different ductilities obtained in immediate testing and testing after one week, thermal desorption measurements were done on the DP600 grade that was charged during 1h at 0.8 mA/cm². The results that were obtained immediately and one week after the charging are shown in Figure 7. When measured immediately after charging, 2 peaks were observed up to 250°C: a large peak around 80°C, and a smaller peak around 170°C. The first peak disappeared completely after 1 week. The physical meaning for this peak is not clear, but TDA research on generic alloys, such as pure iron, indicated that this peak is not related to grain boundaries, nor to dislocations [7]. Similarly, more detailed measurements have been done on the other grades. The results are reported elsewhere [8]. Further research is ongoing to understand the results, but the figure below illustrates how TDA can be a very helpful tool for the understanding of H-effects in steel.

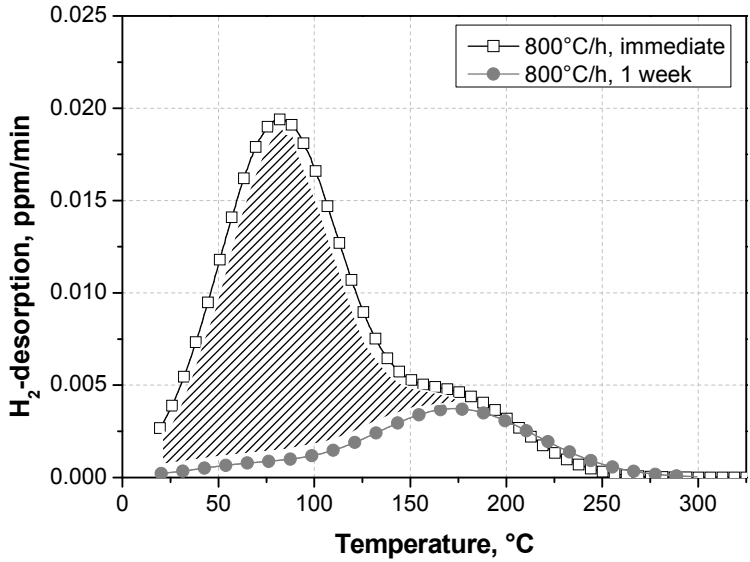


Figure 7: Hydrogen Thermal Desorption curve for the DP600 grade recorded at 800°C/h; 1h after charging and 1 week after charging.

CONCLUSIONS

Four high strength steel grades, with varying multiphase microstructures were tested extensively on their response to dissolved hydrogen: TRIP700, DP600, FB450 and S550MC. The microstructure of the various materials was characterised by means of optical microscopy. The effect of H on the mechanical properties was tested by means of tensile tests immediately after and 1 week after cathodic H-charging. The H dissolved in the steel caused an increase in yield strength in the range around 25000MPa/mass%H. For the TRIP700 and DP600 grades, a fast and significant loss of ductility was observed during immediate tensile testing. The FB450 and S550MC were found to be less sensitive to loss of ductility. A large difference was found for the TRIP700 and DP600 material between the "immediate" tests and the "1 week" tests, which indicated a strong effect of the diffusible or more weakly trapped hydrogen. For the FB450 and S550MC, the difference between immediate and 1 week testing was limited. For very long charging times, *i.e.* in the order of days, some irreversible damage is induced by the hydrogen charging in all materials. This effect was most pronounced for the DP600 grade, which is possibly related to a central segregation effect.

REFERENCES

1. Oriani R. A., *et al*, Hydrogen Degradation of Ferrous Alloys, Noyes Publications (New Jersey, 1985)
2. Fang B., Han E.-H., Wang J., "Hydrogen in Stress Corrosion Cracking of X70 Pipeline Steels in near-neutral pH solutions", *Journal of Materials Science*, Vol. 41, No. 6 (2006), pp. 1797-1803.
3. Ćwiek J., Nikiforov K., "Hydrogen Degradation of High-Strength Weldable Steels in Seawater", *Materials Science*, Vol. 40, No. 6 (2004), pp. 831-835.
4. Radkevych O.I., Chumalo H.V., "Damage to the Metal of Industrial Pipelines in a H_2S Environment", *Materials Science*, Vol. 39, No. 4 (2003), pp. 596-600.
5. Tang J.-Q., Gong J.-M., Zhang X.-C., Tu S.-T., "Comparison on the Cracking Susceptibility of Different Low Alloy Steel Weldments Exposed to the Environment Containing Wet H_2S", *Engineering Failure Analysis*, Vol. 13, No. 7 (2006), pp. 1057-1064
6. Mertens G., Duprez L., De Cooman B.C., Verhaege M., "Hydrogen Absorption and Desorption in Steel by Electrolytic Charging", *Advanced Materials Research*, Vols. 15-17 (2007), pp. 816-821
7. Escobar D.P., Duprez L., Verbeken K., Verhaege M., "Identification of the Hydrogen Trap Sites in Multiphase High Strength Steels", submitted for Hydrogen 2008
8. Van Lierop K., Verbeken K., Duprez L., Verhaege M., "Experimental Evaluation of the Hydrogen Distribution in Steel by Thermal Desorption Spectroscopy", submitted for Hydrogen 2008

Effects of Hydrogen on Materials
Proceedings of the 2008 International Hydrogen Conference
Brian Somerday, Petros Sofronis, Russell Jones, editors, p 70-77
Copyright © 2009 ASM International®
All rights reserved.
www.asminternational.org

MIXED-MODE HYDROGEN ASSISTED CRACKING IN PROGRESSIVELY DRAWN PEARLITIC STEELS

J. Toribio and E. Ovejero
Department of Materials Engineering, University of Salamanca
Campus Viriato, Avda. Requejo 33, 49022 Zamora, Spain

ABSTRACT

This paper analyses the hydrogen assisted cracking (HAC) behaviour of cold drawn prestressing steels with different degrees of cold drawing. The experimental results showed a progressively anisotropic behaviour as the degree of cold drawing increases, with an evolution in the fracture behaviour from mode I (isotropic behaviour in slightly drawn steels) to mixed mode propagation (strongly anisotropic behaviour in heavily drawn steels). The fractographic analysis revealed changes in the microscopic topography depending on the fracture propagation mode, with evolution from pure tearing topography surface (TTS) in slightly drawn steels to a kind of very deformed TTS in heavily drawn steels

INTRODUCTION

Cold drawn eutectoid steels are high-strength materials used as constituents of prestressed concrete structures in civil engineering. In these steels, cold drawing produces a marked orientation of the pearlitic microstructure of the steel at the size scales of pearlitic colonies and lamellae [1–6], inducing strength anisotropy. Thus, although this manufacturing technique improves the mechanical properties of the steel, the microstructural changes may affect dramatically its stress corrosion cracking (SCC) performance and this is potentially dangerous when the engineering structures work in aggressive environments [7-9]. This paper analyzes the hydrogen assisted cracking (HAC) behaviour of cold drawn wires with different degrees of cold drawing, to elucidate the influence of the strain hardening level on the HAC phenomenon.

EXPERIMENTAL PROGRAMME

The materials used in this work were high-strength steels taken from a real manufacturing process. Wires with different degree of drawing were obtained by

stopping the manufacturing chain and taking samples from the intermediate stages. The steels were named with digits 0 to 6 which indicate the number of drawing steps undergone, so steel 0 is the original hot rolled material (not cold drawn at all) and steel 6 is the prestressing steel wire (final commercial product). The chemical composition (common to all steels) was eutectoid, i.e., 0.80% C, the yield strength ranged from 700 MPa (steel 0) to 1500 MPa (steel 6) and the fracture toughness (evaluated as the critical stress intensity factor in the wires using the expression given in [10]) ranged from 60 $MPam^{1/2}$ (steel 0) to 108 $MPam^{1/2}$ (steel 6).

To analyse the HAC behaviour of the different steels, slow strain rate tests were performed on precracked steel wires. Samples were precracked by axial fatigue in the normal laboratory air environment to produce a transverse precrack, so that the maximum stress intensity factor during the last stage of fatigue precracking was only 30% of the respective fracture toughness, and the crack depth was a = 0.30D in all cases, with D as the wire diameter. After precracking, the samples were placed in a corrosion cell containing an aqueous solution of 1g/l $Ca(OH)_2$ plus 0.1g/l NaCl (pH=12.5) The experimental device consisted of a potentiostat and a three-electrode assembly. All tests were conducted under potentiostatic control at –1200 mV vs. SCE at which the SCC mechanism is HAC [9]. The applied displacement rate in axial direction was constant during each test and proportional to each wire diameter: 1.7×10^{-3} mm/min for steel 6 and 3.0×10^{-3} mm/min for steel 0.

EXPERIMENTAL RESULTS

Fig. 1 shows the evolution of the fracture profile in HAC as the degree of cold drawing increases. In the first steps of cold drawing (specimens 0 and 1) the crack growth develops in mode I in both fatigue precracking and HAC. In steels 2 and 3 there is a slight deflection in the hydrogen-assisted crack. For the most heavily drawn specimens (4 to 6) the crack deflection takes place suddenly after the fatigue precrack and the deviation angle is even higher. In these last stages of cold drawing, not only crack deflection but also crack branching is observed just after the fatigue precrack tip, i.e., there are two pre-damage directions (crack *embryos*), only one of which becomes the final fracture path. A mode I propagation distance associated with subcritical crack growth by HAC appears only in the first stages of cold drawing, since in heavily drawn steels crack deflection takes place just at the fatigue precrack and thus the mode I propagation distance is zero.

Fractographic Analysis

A fractographic analysis by scanning electron microscopy (SEM) was carried out on the fracture surfaces to elucidate the microscopic modes of fracture. Figs. 2 and 3 offer the microscopic topographies for the progressively drawn pearlitic steels. In the hot rolled material which is not cold drawn at all (steel 0; Fig. 2), after the fatigue

precrack, there is a subcritical crack growth in mode I by *tearing topography surface* (TTS, cf. [11-15]) before the unstable cleavage-like propagation associated with mechanical final fracture. This special microscopic fracture mode is undoubtedly associated with hydrogen-assisted micro-damage in steels with pearlitic microstructure [13-15].

In heavily drawn steel 6 (Fig. 3) the microscopic fracture mode is a kind of *very deformed* TTS, the deformation axis coincident with the cold drawing direction. This topography is produced as a consequence of the macroscopic crack deflection with mode II propagation, i.e., as if a previous TTS mode had been strained by shear in its own fracture plane (quasi-parallel to the drawing axis).

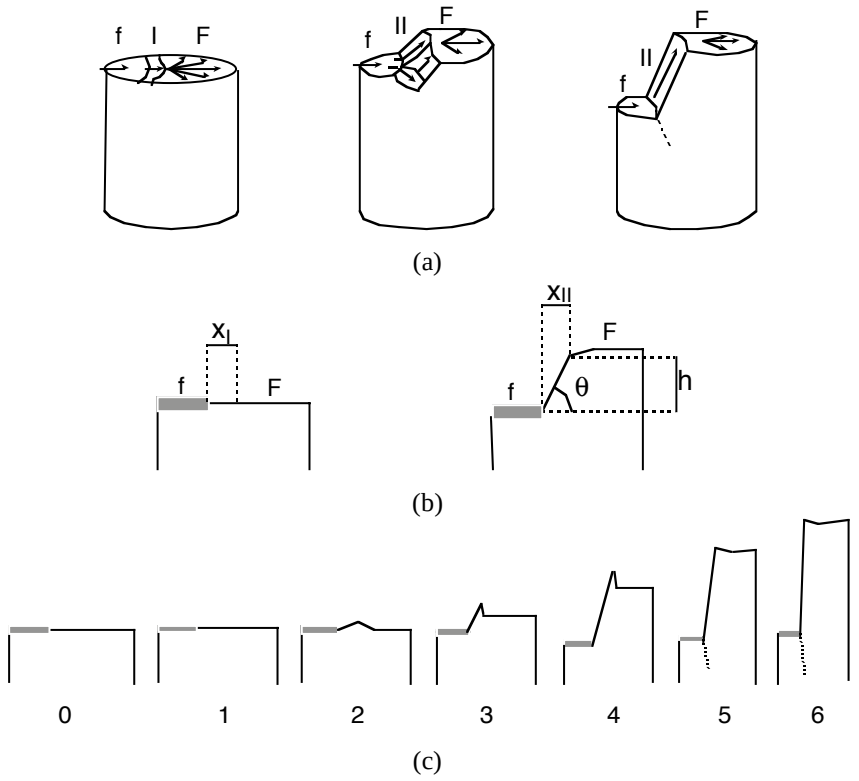


Figure 1: Evolution of fracture surfaces with cold drawing: (a) general appearance; (b) geometric parameters describing the fracture path; (c) evolution of fracture profiles; f: fatigue crack growth; I: mode I propagation; II: mixed mode propagation; F: final fracture.

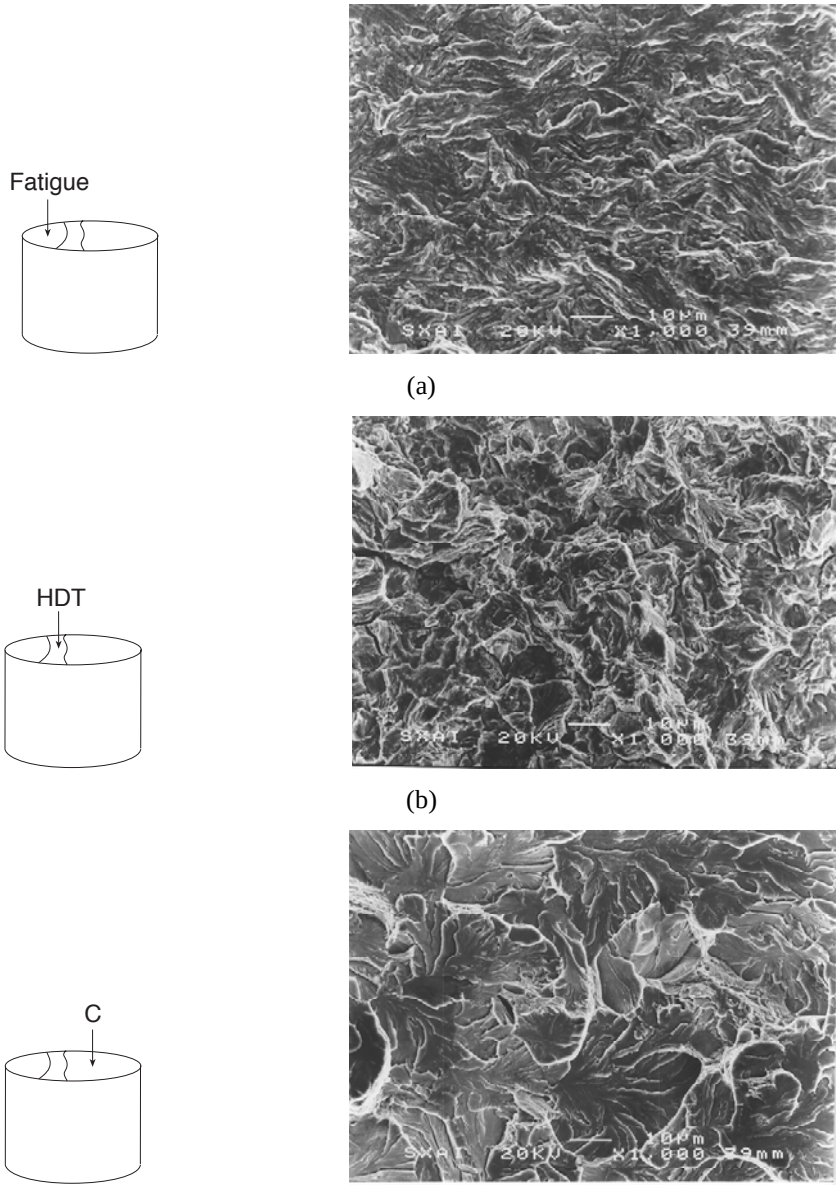
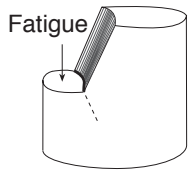
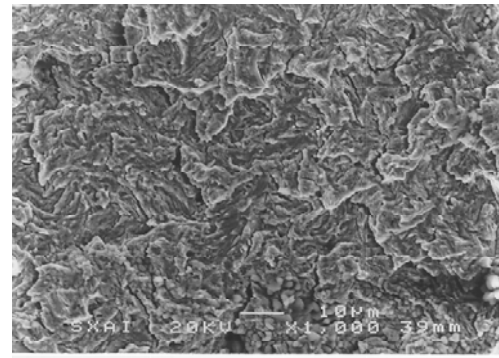
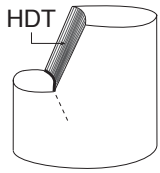


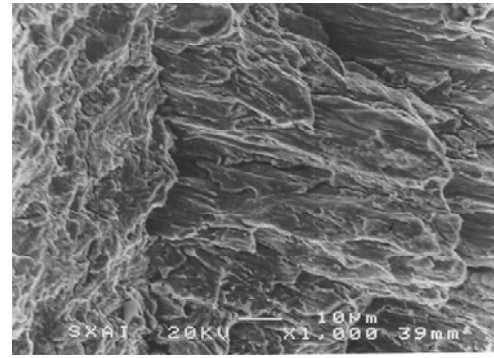
Figure 2: Microscopic modes of fracture in steel 0: (a) fatigue precrack; (b) hydrogen damage topography; (c) cleavage.



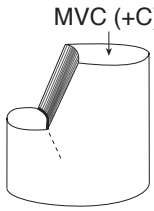


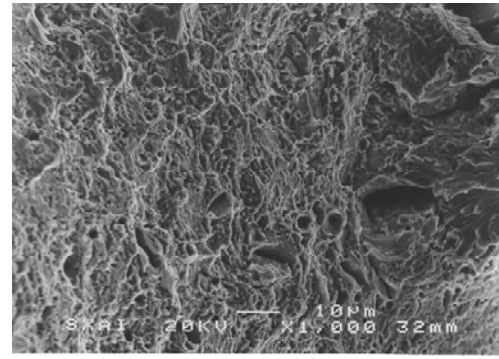
(a)





(b)





(c)

Figure 3: Microscopic modes of fracture in steel 6: (a) fatigue precrack; (b) hydrogen damage topography; (c) micro-void coalescence and some cleavage facets.

Materials Science Approach

In this section a material science approach to the phenomenon of HAC in progressively drawn eutectoid steel is provided in the form of relationship between the pearlitic microstructure and the macroscopic behaviour, in order to provide insight into the micromechanisms of HAC in these materials.

Fig 4 plots the orientation angles of the two basic microstructural size scales, namely the pearlitic colonies [4] and the pearlite lamellae [6], showing a progressive orientation of both microstructural units with cold drawing, as reflected by the evolution of their respective angles in Fig. 4: angle α between the transverse axis of the wire and the major axis of the pearlite colony modelled as an ellipsoid; angle α' between the transverse axis of the wire and the direction marked by the pearlite lamellae in the longitudinal metallographic section. Fig. 4 also shows the variation of the macroscopic crack parameters, the deflection angle θ and the step height h, cf. Fig. 1. It is seen that the progressive microstructural orientation (at the two levels of colonies and lamellae) clearly influences the angle and height of the fracture step (increasing with the degree of cold drawing). This suggests that the macroscopic HAC behaviour of the different steels —progressively anisotropic with cold drawing— is a direct consequence of the microstructural evolution towards an oriented arrangement.

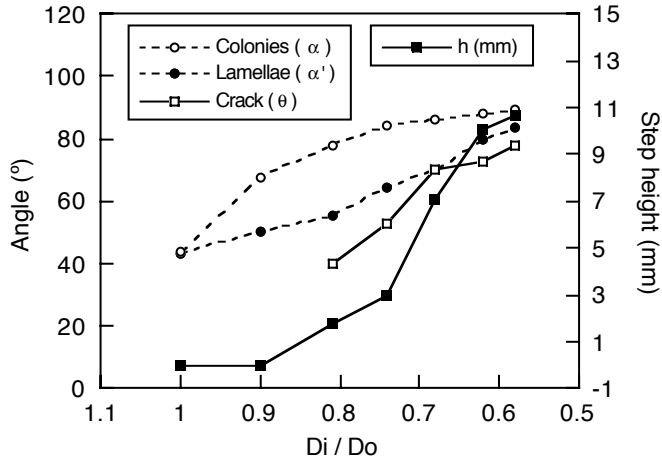


Figure 4: Relationship between the microstructural orientation angles α and α' (pearlite colonies and lamellae) and the macroscopic crack parameters (deflection angle θ and step height h) associated with HAC.

CONCLUSIONS

Environmentally assisted cracking of cold drawn eutectoid steel for civil engineering structures was studied in the cathodic regime of hydrogen assisted cracking. The degree of cold drawing (or strain hardening level) was treated as a fundamental variable to analyse the phenomenon.

The fractographic analysis demonstrated that the steels exhibit a progressively anisotropic behaviour as the degree of cold drawing increases, with crack deflection and mixed mode propagation in heavily drawn steels as a consequence of the very markedly oriented pearlitic microstructure.

In slightly drawn steels, the microscopic fracture mode resembles tearing topography surface in the subcritical fractured area related to environmentally assisted cracking. This microscopic fracture mode is associated with hydrogen-assisted micro-damage in pearlitic microstructures.

In heavily drawn steels, the microscopic fracture mode is a kind of very deformed tearing topography surface, the deformation axis coincident with the cold drawing direction. This topography is produced as a consequence of the macroscopic crack deflection with mode II propagation.

There is a material science relationship between microstructure and macroscopic fracture behaviour of the steel in conditions of hydrogen assisted cracking, since the progressive microstructural orientation with cold drawing causes the increasingly anisotropic behaviour.

ACKNOWLEDGMENTS

The authors gratefully acknowledge the financial support received from different institutions: MCYT (Grant MAT2002-01831), MEC (Grant BIA2005-08965), JCyL (Grants SA078/04, SA067A05 and SA111A07) and Spanish Foundation "*Memoria D. Samuel Solórzano Barruso*" (Grants for scientific and technological research). In addition, the authors wish to thank EMESA TREFILERÍA (La Coruña, Spain) for providing the steel used in the experimental programme.

REFERENCES

1. J. D. Embury, R.M. Fisher, The structure and properties of drawn pearlite, Acta Metall. 14 (1966) 147-159.
2. G. Langford, A Study of the deformation of patented steel wire, Metall. Trans. 1 (1970) 465-477.
3. J. Toribio, E. Ovejero, Microstructure evolution in a pearlitic steel subjected to progressive plastic deformation, Mater. Sci. Eng. A234-236 (1997) 579-582.
4. J. Toribio, E. Ovejero, Microstructure orientation in a pearlitic steel subjected to progressive plastic deformation, J. Mater. Sci. Lett. 17 (1998) 1037-1040.
5. J. Toribio, E. Ovejero, Effect of cumulative cold drawing on the pearlite interlamellar spacing in eutectoid steel, Scripta Mater. 39 (1998) 323-328.
6. J. Toribio, E. Ovejero, Effect of cold drawing on microstructure and corrosion performance of high-strength steel, Mech. Time-Dependent Mater. 1 (1998) 307-319.
7. B.W. Cherry, S.M. Price, Pitting, crevice and stress corrosion cracking studies of cold drawn eutectoid steels, Corros. Sci. 20 (1980) 1163-1184.
8. D.C. Langstaff, G. Meyrick, J.P. Hirth, Hydrogen induced delayed failure of high strength alloy steel wires, Corrosion 37 (1981) 429-437.
9. R.N. Parkins, M. Elices, V. Sánchez-Gálvez, L. Caballero, Environment sensitive cracking of pre-stressing steels, Corros. Sci. 22 (1982) 379-405.
10. A. Valiente, Criterios de fractura para alambres. Ph. D Thesis, Polytechnic University of Madrid, Spain, 1980.
11. A.W. Thompson , J.C. Chesnutt, Identification of a fracture mode: the tearing topography surface, Metall. Trans. 10A (1979) 1193-1196.
12. J.E. Costa, A.W. Thompson , Hydrogen cracking in nominally pearlitic 1045 steel, Metall. Trans. 13A (1982) 1315-1318.
13. J. Toribio, A.M. Lancha , M. Elices, Characteristics of the new tearing topography surface, Scripta Metall. Mater. 25 (1991) 2239-2244.
14. J. Toribio, A.M. Lancha , M. Elices, The tearing topography surface as the zone associated with hydrogen embrittlement processes in pearlitic steel, Metall. Trans. 23A (1992) 1573-1584.
15. J. Toribio, Fracture mechanics approach to hydrogen assisted microdamage in eutectoid steel, Metall. Mater. Trans. 28A (1997) 191-197.

Effects of Hydrogen on Materials
Proceedings of the 2008 International Hydrogen Conference
Brian Somerday, Petros Sofronis, Russell Jones, editors, p 78-87
Copyright © 2009 ASM International®
All rights reserved.
www.asminternational.org

Hydrogen Effects on the Plasticity of FCC Nickel and Austenitic Alloys

D. Delafosse[a], X. Feaugas[b], I.Aubert[c], N.Saintier[d], JM.Olive[c,e]
[a]Ecole des Mines de Saint-Etienne, 158 Cours Fauriel, 42023 Saint-Etienne, France
[b] LEMMA, EA 3167, Université de La Rochelle, Bat. Marie Curie, 25 rue Enrico Fermi, 17000 La Rochelle, France
[c]Laboratoire de Mécanique Physique - CNRS/Université Bordeaux 1 - 351, cours de la Libération- 33405 Talence cedex, France.
[d]LA.M.E.F.I.P - Equipe d'Accueil 2727 - Université Bordeaux 1 - ENSAM - Esplanade des Arts et Métiers - 33405 Talence cedex, France.
[e]Department of Mechanical Engineering Science, HYDROGENIUS Center, Kyushu University-AIST, Moto-oka, Nishi-ku, Fukuoka, 819-0395, Japan

ABSTRACT

The principles of the "hydrogen-elasticity" theory are used to model the effects of solid solution hydrogen on elementary dislocation properties and plasticity mechanisms that derive from the classical line tension model. Tensile experiments are conducted on nickel single crystals and the TEM observation of dislocation microstructures shows that cross-slip is the elementary plasticity process which is the most affected by solute hydrogen. Quantitative measurements of slip band localization in 316L polycrystals also show a strong effect of hydrogen on slip planarity and localization. Consequences for H-induced fracture are discussed

INTRODUCTION

The popularity of the "Hydrogen Enhanced Localized Plasticity" (HELP) model is the result of the combination between a consistent theoretical framework and unique *in-situ* observations in the Environmental TEM, both developed at the University of Illinois. The screening of the interactions between elastic stress centres by mobile solid solution hydrogen is indeed widely accepted today as an important ingredient in any attempt to model H-induced damage in austenitic alloys. However, quantifying these effects to derive H-modified "macroscopic" stress-strain relationships remains a challenging task, because in f.c.c. crystals, the dislocation behaviour is essentially collective. Furthermore, only in very specific cases, such as the monotonic or cyclic deformation of single crystals in single glide, do the pair interactions between dislocations have a direct influence on the flow stress and/or deformation microstructure. In more general cases, e.g.: stage II / III deformation in polycrystals, the rate of dislocation storage by the formation of junctions and organized microstructures (wall, cells) play a more important role. An elementary process that controls the transition between these stages is the cross-slip probability of screw dislocations.

In this communication, we recall modelling results on the effect of hydrogen on elementary properties of dislocations and we present recent experimental results obtained in Saint-Etienne, La Rochelle and Bordeaux, which illustrate the effects of solid-solution hydrogen on the plasticity of nickel single crystals on the one hand and polycrystalline austenitic stainless steels on the other.

H-EFFECTS ON ELEMENTARY PLASTICITY MECHANISMS

Implementing the "hydrogen-elasticity" formalism of Sofronis [1] with an alternative numerical scheme for the first-order coupling level, Chateau [2] showed that the screening of the resolved shear stress between the edge components of two dislocations, which is a function of the temperature T, the hydrogen atomic concentration c and material parameters contained in the β coefficient, can be expressed in a simple form, provided dislocations are aged to saturation by their hydrogen atmospheres:

$$S(T,c) = \frac{S_0}{1+\beta\frac{T}{c}} \text{ with } S_0 = 0.75 \text{ , and } \beta = 2.33\ 10^{-4}\ K^{-1} \text{ for nickel} \qquad (1)$$

This dimensionless coefficient represents the relative amount by which edge dislocation pair interactions are decreased in the presence of a uniform atomic concentration c at temperature T. We make use of this "screening index" to evaluate the influence of solute hydrogen on the properties of individual dislocations, by considering H effects on the orientation dependence of the line energy. The line energy and line tension are first examined.

Considering an initially straight dislocation with a "bow-out" along its line, we evaluated the energy increase caused by this incremental bend. Following the classical model of de Wit and Koehler [3], the self energy per unit length of a dislocation line depends on the orientation through the angle θ between the Burgers vector and the original straight line. Integrating the elastic interactions between incremental segments along a dislocation line, its energy per unit length is given by:

$$E(\theta) = \frac{\mu b^2}{4\pi K(\theta)} \ln\left(\frac{R}{r_0}\right), \text{ with } \frac{1}{K(\theta)} = \cos^2\theta + \frac{\sin^2\theta}{1-\nu} \qquad (2)$$

where b is the Burgers vector magnitude, μ the shear modulus, ν the Poisson ratio, R and r_0 are, respectively, the outer and inner cut-off radii. Introducing the screening index S(*T,c*) defined by the expression (1) to account for hydrogen effects on the edge components, the K(θ) factor becomes:

$$\frac{1}{K_S(\theta)} = \cos^2\theta + \frac{(1-S(T,c))\sin^2\theta}{1-\nu} \qquad (3)$$

In the presence of hydrogen, the self-energy E(θ) is as a function of the dislocation character and the screening index S(T,c). The variation of the self-energy per unit length is plotted Fig. 1.a for three different levels of shielding: 0.11, 0.22 and 0.33 respectively, corresponding to H concentrations of 0.012, 0.029 and 0.055 respectively in nickel at room temperature. Predictably, by relaxing the hydrostatic component of the dislocations' stress tensor, hydrogen lowers the line energy of edge dislocations ($\theta = 90°$), while screw segments ($\theta = 0° / 180°$) remain unaffected to the first order by hydrogen dilatation strains. After de Wit and Koehler, the line tension is defined by the first derivative of the self-energy with respect to the incremental increase in length caused by a small bow-out. The screening effect due to hydrogen gives the following expression for the line tension:

$$\zeta_S(\theta) = \frac{\mu b}{4\pi(1-\nu)}\left[1 + \boldsymbol{S}(T,c) - 2\nu + 3(\nu - \boldsymbol{S}(T,c))\cos^2\theta\right]\ln\left(\frac{R}{r_0}\right) \qquad (4)$$

Fig. 1.b shows the line tension dependence for different levels of S(T,c). The line tension of screw segments decreases with the increase of the screening index, as edge segments become more rigid. Consequently, a dislocation loop, which is elongated in the screw direction in an isotropic crystal without hydrogen tends toward isotropy as the screening effect increases.

Based on the previous calculation, we evaluated the critical stress for the expansion of a dislocation loop. Following Hirth and Lothe [4], the shape of a circular dislocation loop was approximated by a hexagonal loop. In the presence of hydrogen, the expression for the total energy of a hexagonal loop of side L reads:

$$W^H = \frac{3\mu b^2 L}{4\pi(1-\nu)}\left[(2 - \nu - S(T,c))(0.16 + \ln\left(\frac{L}{r}\right)\right] \qquad (5)$$

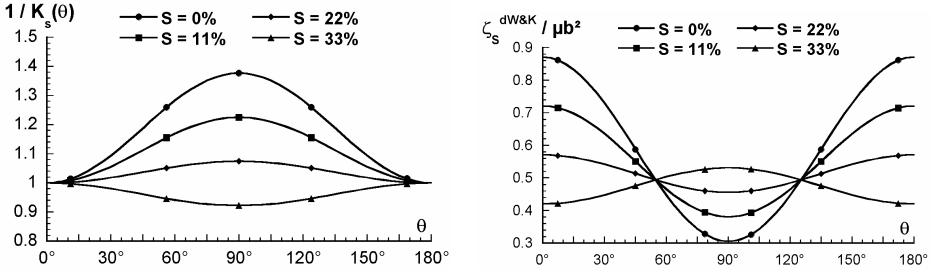


Figure 1: Evolution of (left) the self-energy per unit length and (right) the line tension of a dislocation with the screening index S(T,C), both normalised by μb², as a function of the dislocation character (with θ=90° for edge dislocations and S in units of percentage).

The force for the isotropic expansion of such a loop is the first derivative of the energy W with respect to the loop radius L. Expressing the ratio of this force in the presence of hydrogen F^H to that of the force without hydrogen F gives the following simple expression as a function of S(T,c):

$$\frac{F^H}{F} \approx 1 - 0.58S(T,c) \tag{6}$$

Finally, applying the above results to more complex configurations we showed [5]:

- By evaluating the equilibrium of line tensions at a node between secant slip systems, that dislocation junctions were weakened by solute hydrogen, with the collinear and Hirth types of junctions being significantly more affected than Lomer junctions. Collinear junctions are responsible for the self-hardening of primary slip systems in stage I deformation of single crystals and ultimately responsible for the exhaustion of stage I [6].
- By computing the equilibrium shape of a triple node taking into account the screening effect on partial dislocations, that both the reduction in Stacking Fault Energy (SFE) and alteration of pair interactions between partials were implicated in the reduction of cross-slip probability in the presence of hydrogen.

While being more difficult to model quantitatively, this effect on the cross-slip probability is arguably the one that has the most important practical consequences on the plasticity of hydrogenated samples, as shown in the following two experimental studies.

PLASTICITY OF NICKEL SINGLE CRYSTALS

In this section, we present experimental results in tension of non-charged and hydrogen-charged nickel single crystals oriented for single slip, which illustrate the above results. Smooth specimens with a 4-mm wide square section and a 10-mm gauge length were cut in a pure Ni single crystal along the [153] direction, corresponding to a "single slip" orientation. Samples were hydrogenated and stored in the conditions described in [7], giving a 1600 at. ppm hydrogen concentration. Stress strain curves for nickel and nickel-hydrogen at a plastic strain rate of 10^{-2} s^{-1} are shown in Fig. 2. Comparing the stress-strain curves of Ni and Ni-H crystals, one can identify the following features related to hydrogen charging, along with our current interpretation of such features:

- Hydrogen causes a noticeable increase of the magnitude of τ_I (~ 0.05 10^{-3} μ). At room temperature, mobile dislocations are continuously aged during straining by mobile hydrogen atoms [7]. This hardening effect induced by hydrogen is attributed to the viscous drag of solute atmospheres.
- Hydrogen delays the emergence of stage II. In stage I ("easy glide"), a unique slip system is active. Plastic deformation during this stage is accommodated by the activation of Frank-Read sources. Few obstacles impede the glide of emitted dislocation loops, resulting in a very low work hardening rate. According to the

results presented in the previous section, both multiplication and planar glide are expected to be favoured by solute hydrogen, whereas the weakening of collinear junctions limits the self-hardening of the primary slip system, thus delaying the transition to stage II.

– In stage II, the introduction of hydrogen in nickel results in a significant increase of the work hardening. This stage of rapid linear hardening is characterised by the activation of secondary slip systems and the work hardening is governed by the interaction between dislocations from the first activated system and those from secondary slip systems. The flow stress is essentially controlled by the dislocation mean free path, which will be investigated by transmission electron microscopy.

These results provide experimental evidences of hydrogen effects on elementary plasticity mechanisms. The observed hydrogen effects on stage I (increase of τ_I due to solute drag and extension of the planar glide stage) are consistent with Yagodzinskyy *et al*. [8] on 18Cr-16Ni-10Mn austenitic stainless steel single crystals with a much higher H content.

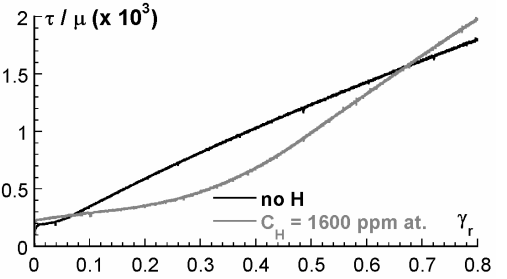


Figure 2: True stress-strain curves of non-charged and hydrogen-charged nickel single crystals oriented for single slip. Shear stress normalised by μ the shear modulus

The dislocation structures were compared between Ni and Ni-H by Transmission Electron Microscopy (TEM). TEM foils were sampled in deformed Ni and Ni-H single crystals after 0.2 and 0.7 of plastic shear strain. Fig. 3 displays the dislocation microstructure at 0.2 plastic shear. The hydrogenated sample still is in stage I. It exhibits a microstructure of parallel elongated screw dislocations with a density $\rho=1.3\ 10^{13}m^{-2}$ and numerous double kinks related to cross-slip events. The fact that the stored dislocation lines are of screw character seems to be at variance with what could be predicted qualitatively from equation (3). However, it can be seen in Fig. 1 that it is only for the highest values of solute hydrogen concentrations that the line energy of edge segments drops below that of screw lines. At 0.7, both curves intersect. Both crystals have the same flow stress, but different strain hardening rates. Fig. 4 shows that the increased strain hardening rate in Ni-H stems from the higher dislocation density in this specimen. Moreover, the dislocation structures themselves display very different features. The nickel single crystal is well in the stage III regime, with equiaxed dislocation cells already formed. On the contrary, the hydrogenated sample displays a planar structure of dislocation walls, typical of alloys with a low Stacking Fault Energy (SFE), where the low probability of cross-slip prevents the onset of dynamic recovery

and the formation of dislocation cells. This demonstrates the effects of solute hydrogen on the cross-slip mechanism, and its indirect consequences on the strain hardening rate, *via* a decrease of the dislocation mean free path.

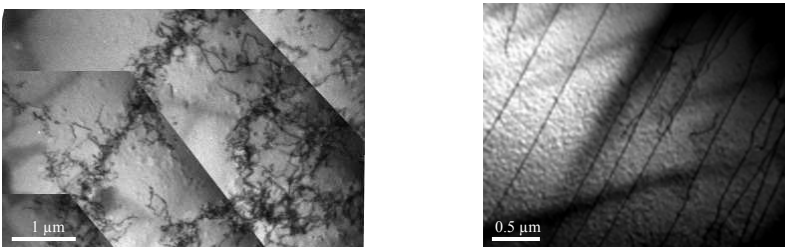


Figure 3: TEM observation of the dislocation structures in the [153] "single glide" plane of (left) Ni and (right) Ni-H single crystals, after 0.2 plastic shear strain. The Ni single crystal is in stage II, with the formation of clusters and cell precursors, whereas in Ni-H, a low density of parallel elongated screws is observed, typical of stage I deformation.

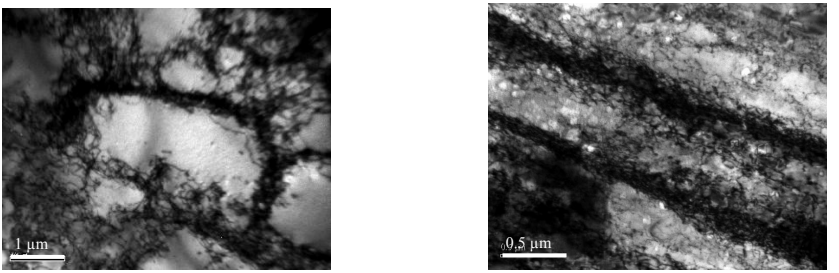
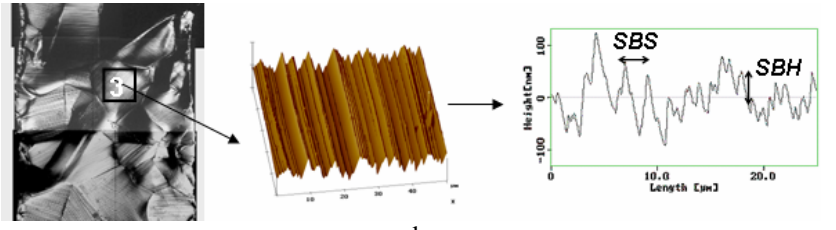


Figure 4: TEM observation of the dislocation structures in the [153] "single glide" plane of (left) Ni and (right) Ni-H single crystals, after 0.75 plastic shear strain. The Ni single crystal has well entered the stage III regime with the formation of equiaxed dislocation cells, whereas in Ni-H, a high density of planar dislocation walls is observed, typical of stage II deformation.

SLIP LOCALIZATION IN POLYCRYSTALLINE 316L

Experimental conditions were described in detail in [9] and correspond also to the conditions used in [10]. Flat tensile samples of high nickel content 316L stainless steel (gauge length 8mm, width 2mm) were heat treated to obtain a homogeneous coarse microstructure with an average equiaxed grain size of 300 µm. The specimen thickness was reduced to 500µm to allow for hydrogen diffusion to the bulk. After electropolishing, the hydrogen charging conditions were selected to avoid hydrogen-induced phase transformations. Hydrogen was introduced into the steel samples by cathodic charging from 0.1 M NaOH at 95°C at 100 mA/cm^2 for 6 days. The total hydrogen content was quantified with the nitrogen-carrier fusion thermal conductivity

method (JUWE H-Mat 2500 analyzer). The average hydrogen concentration in the uncharged samples was equal to 27.7 +/- 2.4 appm and in the hydrogenated samples to 1067 +/- 40 appm (labeled as135 wt.ppm on Fig. 8) Tensile tests were performed in air at room temperature at a constant strain rate of 10^{-3} s^{-1} up to a strain of 4%. The characterization of the strained specimen surfaces was carried out by Atomic Force Microscopy (AFM - VEECO type Dimension 3100) in contact mode. AFM scans were performed in the centre of each chosen grain to observe only primary slip and avoid multiple slip system activation usually encountered at grain boundaries. Measurements of all slip-band heights (SBH) and slip-band spacings (SBS) of each analyzed grain were performed perpendicularly to the slip lines extracted from the topographical AFM images (Figs. 5b, 5c). 12 grains, representing about 500 slip lines per polycrystal were observed to ensure statistical data representativeness. In each grain, average values of the SBS and SBH were computed and projected in the direction of the 3 slip systems emerging at the surface, taking the grain orientation into account (Fig. 6). These values are denoted SBS^g and SBH^g. Evaluating the number of emerging dislocations per slip step requires the computation of the plastic shear in each of the 12 slip systems.



a b c

Figure 5: a) Optical images of a large grain sample (d=300 µm), b) Topographical AFM image of grain surface, c) Cross-section of slip steps (z-scale magnified x100)

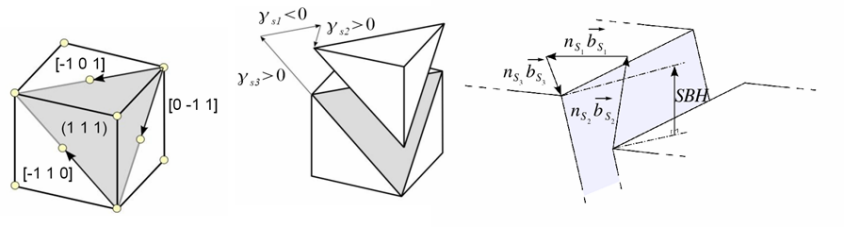


Figure 6: Sum of slip shears on the three slip systems and number of emerging dislocations

Crystal plasticity modeling

The plastic strain in each grain was obtained from finite element computations using the ZéBuLoN code, developed at Ecole des Mines de Paris. Electron Back-Scattered Diffraction (EBSD) was used to obtain the grain geometry and orientations at the specimen surface, from which a 2D mesh was built. Crystal orientation (Euler's angles) and material properties were attributed to each Gauss point. The elastic behaviour was

described as linear isotropic, and strain rate dependent phenomenological formulation was used for the crystal plasticity model [11,12]. Homogeneous strain boundary conditions were applied to the 2D mesh in uniaxial tension (Fig. 7).

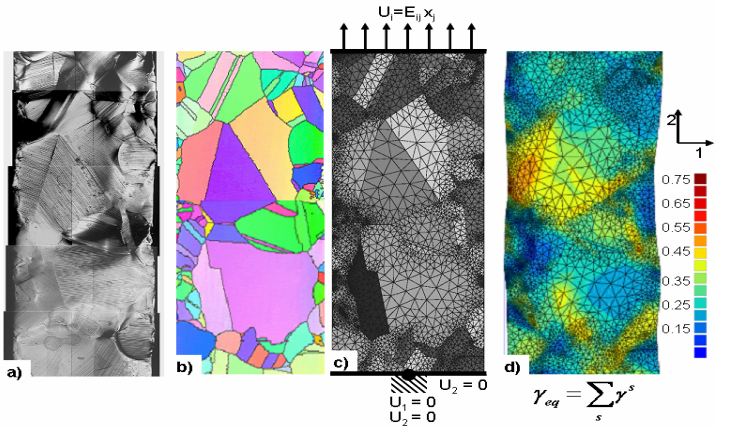


Figure 7: Steps of the numerical calculation: a) Optical image, b) crystallographic orientation (EBSD), c) 2D mesh and boundary conditions, d) FE results: cumulative plastic strain on the 12 slip systems.

In any given grain, FE calculations provided the amount of shear γ_{si} in each of the 12 slip systems, only 3 of which actually participate in the formation of a given slip step (Fig. 6). We can then obtain the total number N of emerging dislocations having built the observed slip band (the details of the calculation can be found in [11]):

$$N = \frac{SBH^g}{\left(\frac{\gamma_{s1}}{\gamma_{\max}} \vec{b}_{s1} + \frac{\gamma_{s2}}{\gamma_{\max}} \vec{b}_{s2} + \frac{\gamma_{s3}}{\gamma_{\max}} \vec{b}_{s3} \right)} \qquad (7)$$

Where : SBH^g is the slip band height observed by AFM
b_{si} is the Burgers vector of the slip system s_i
γ_{si} is the computed plastic shear of the slip system s_i
γ_{max} is the max computed value among the 12 slip systems

Results

The projected SBS^g is plotted in Fig. 8.a as a function of the plastic shear sum on the three slip systems emerging at the surface. It shows that at the same plastic strain, the projected SBS^g of hydrogenated grains are 2.2 times higher in the hydrogen containing samples than the hydrogen-free ones. Similarly, the number of dislocations per slip step (Fig. 8b) is 2.3 times higher in the hydrogen charged sample. In the plastic shear range 3.5% to 6%, the same level of plastic strain results from twice more dislocations emerging on half the number of slip planes. In 316L austenitic stainless steel, cathodic hydrogen charging up to 1067 appm results in a twice higher level of slip localization,

which is qualitatively in agreement with the effects of hydrogen on the cross-slip probability demonstrated above in nickel single crystals.

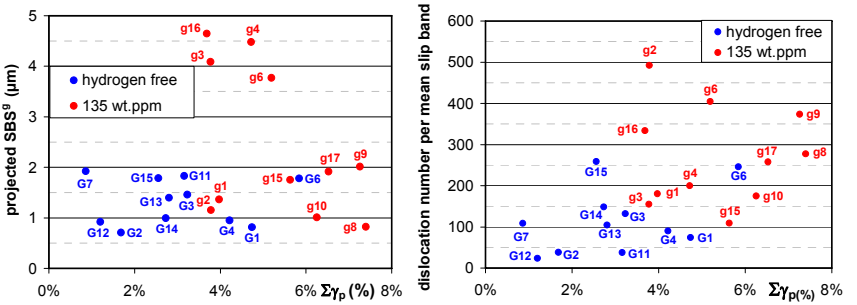


Figure 8: a) Projected SBS^g of the mean slip band as a function of the computed plastic shear sum on the three active co-planar slip systems b) Dislocation number per band as a function of the computed plastic shear sum on the three active co-planar slip systems

DISCUSSION AND CONCLUSIONS

The formalism of "hydrogen-elasticity" can be introduced in classical expressions of dislocation properties, provided they pertain to the linear elastic theory of discrete dislocation. Those properties which derive from the core structure of crystal defects such as, e.g.: the saddle point configuration of constricted partials during cross-slip or the trapping of hydrogen solutes in complex grain boundary structures or at heterogeneous interfaces have to be handled by atomistic approaches before one can derive simple models to be used at the scale of discrete defects. The linear elastic approach enables quantitative estimates of the effects of hydrogen on plasticity mechanisms that basically depend on the line energy, line tension, as well as long distance interactions, such as dislocation multiplication, junction formation and destruction. However, experiments in nickel single crystals show that the major influence of solid solution hydrogen on the plasticity of f.c.c. crystals derives from a large decrease of the cross-slip ability in the presence of hydrogen. This process is indeed a mixture of elastic properties (the equilibrium separation distance between dissociated partials) and atomistic ones (the Stacking Fault Energy and the saddle point configuration during thermally activated constriction). Both scales are equally important and a comprehensive quantitative model for H-effects on cross-slip remains to be proposed.

The experiments on 316L polycrystals show that even in a material with a low SFE and a "natural" tendency to planar glide, the slip planarity and slip band localization is significantly enhanced by hydrogen charging. In environments with an intermediate hydrogen activity, austenitic stainless steels experience a reduced toughness but their fracture remains ductile. The measured H-effects on slip localization provide a straightforward explanation, which can be modeled and quantified [13,14]. The cases of brittle intergranular (case of many nickel-based alloys) and transgranular fracture (austenitic stainless steel in the presence of a high hydrogen activity) are more complex. Hydrogen effects on the surface energy and Griffith criterion have to be estimated

together with those on the plastic shielding and/or blunting of cracks. Discrete dislocation dynamics simulations are being developed to evaluate these effects [15].

REFERENCES

[1] Sofronis, P., 1995, "The Influence of Mobility of Dissolved Hydrogen on the Elastic Response of a Metal," Journal of the Mechanics and Physics of Solids, 43(9) pp. 1385-1407.

[2] Chateau, J. P., Delafosse, D., Magnin, T., 2002, "Numerical Simulations of Hydrogen - Dislocations Interactions in Fcc Stainless Steels - Part I : Hydrogen - Dislocations Interactions in Bulk Crystals," Acta Materialia, 50(6) pp. 1507-1522.

[3] De Wit, G., and Koehler, J. S., 1959, "Interaction of Dislocations with an Applied Stress in Anisotropic Crystals," Physical Review, 116(5) pp. 1113-1120.

[4] Hirth, J.P., and Lothe, J., 1992, "Theory of dislocations," Reprint Edition, Krieger Publishing Co., Malabar, FL;

[5] Girardin, G., 2004, "Interactions Hydrogène - Plasticité Dans Le Nickel Et Ses Alliages," PhD dissertation, Ecole des Mines de Saint-Etienne.

[6] Madec, R., Devincre, B., Kubin, L. P., 2003, "The Role of Collinear Interaction in Dislocation-Induced Hardening," Science, 301, pp. 1879-1882.

[7] Girardin, G. and Delafosse, D., 2004, "Measurement of the Saturated Dislocation Pinning Force in Hydrogenated Nickel and Nickel Base Alloys," Scripta Materialia, 51(12) pp. 1177-1181.

[8] Yagodzinskyy, Y., Tarasenko, O., Hänninen, H., 2002, "Effect of hydrogen on plastic deformation of stable 18Cr-16Ni-10Mn austenitic stainless steel single crystals," International Conference on Hydrogen Effects on Material Behavior and Corrosion Deformation Interactions H-CDI 2002, pp. 201-210.

[9] Aubert, I., Plessier, F., Saintier, N., Olive, J.M., 2008, Modification of plastic strain localization induced by hydrogen absorption, Advances in Materials Science, Vol 8, issue 1, in press

[10] Brass , A.-M., Chene, J., 2006, Hydrogen uptake in 316L stainless steel: Consequences on the tensile properties, Corrosion Science 48, pp. 3222–3242

[11] Barbe F., Decker L., Jeulin D., Cailletaud G., 2001, intergranular and intragranular behavior of polycrystalline aggregates. Part 1: FE model. International Journal of Plasticity, 17, pp. 513-536.

[12] Cailletaud, G., Forest, S., Jeulin, D., Feyel, F., Galliet, I., Mounoury, V., Quilici, S., 2003, Some elements of microstructural mechanics, Computational Materials Science 27, pp. 351–374

[13] Liang, Y., Sofronis, P., and Dodds, R. H., 2004, "Interaction of Hydrogen with Crack-Tip Plasticity: Effects of Constraint on Void Growth", Materials Science and Engineering A, 366(2) pp. 397-411.

[14] Liang, Y., Ahn, D. C., Sofronis, P., 2008, "Effect of Hydrogen Trapping on Void Growth and Coalescence in Metals and Alloys", Mechanics of Materials, 40 pp. 115-132.

[15] Tanguy, D., Delafosse, D., Razafindrazaka, M., 2008, this conference

Effects of Hydrogen on Materials
Proceedings of the 2008 International Hydrogen Conference
Brian Somerday, Petros Sofronis, Russell Jones, editors, p 88-96
Copyright © 2009 ASM International®
All rights reserved.
www.asminternational.org

HYDROGEN-ASSISTED FRACTURE OF AUSTENITIC STAINLESS STEELS

C. San Marchi, K.A. Nibur, D.K. Balch, B.P. Somerday
Sandia National Laboratories, Livermore CA
X. Tang and G.H. Schiroky
Swagelok Company, Solon OH
T. Michler
Adam-Opel GmbH, GM Europe R&D, Ruesselsheim, Germany

ABSTRACT

Although austenitic stainless steels are often categorized as negligibly embrittled in hydrogen, resistance to hydrogen-assisted fracture in this broad class of materials is realized only within certain windows of variables. In reality, hydrogen-assisted fracture is strongly influenced by environmental and material variables such as temperature, hydrogen environment, alloy composition, ferrite content, and microstructure. Under particular intersections of variables, hydrogen-assisted fracture can actually be quite severe. For example, in the 300-series austenitic stainless steels, specimens with low nickel content tested at sub-ambient temperature can suffer substantial reduction in ductility when exposed to hydrogen. The variation in resistance to hydrogen-assisted fracture over a range of environmental and material variables is reflected in the fracture mechanisms, which can feature microvoid nucleation at inclusions, microvoid nucleation at the intersection of deformation bands, fracture along interfaces, and fracture in ferritic phases (when present). In many cases, the fracture mechanism is strongly linked to the effects of hydrogen on deformation. In this brief report, we provide an overview of work performed primarily at Sandia National Laboratories on hydrogen-assisted fracture in austenitic stainless steels, emphasizing the environmental and material variables that dominate the observed deformation and fracture mechanisms.

INTRODUCTION

In the absence of internal hydrogen, common Fe-Cr-Ni austenitic stainless steels generally deform uniformly, resulting in fracture surfaces that are characterized by equiaxed dimples and typical of microvoid coalescence. Low nickel content and sub-ambient temperature are two variables that promote the localization of deformation in austenitic stainless steels, which is apparent as deformation concentrated in bands [1]. Higher local stresses are associated with the localization of deformation into bands, although this generally does not affect the equiaxed dimple morphology on tensile fracture surfaces of common Fe-Cr-Ni austenitic stainless steels. Non-equiaxed dimple morphologies, on the other hand, can develop in some metals under conditions that sufficiently localize deformation [2, 3], and facetted fracture surfaces may result from boundary separation when deformation becomes exceptionally localized.

There is significant evidence that hydrogen enhances the localization of deformation in austenitic stainless steels [4-6]. Internal hydrogen inhibits cross slip in austenitic stainless steels [5, 6] (thus promoting localized deformation), because the edge component of dislocations is stabilized by hydrogen [7-10]. Internal hydrogen also screens stress centers such as dislocations [10-12], which enhances dislocation mobility and contributes to deformation instabilities [13]. Additionally, internal hydrogen increases the density of dislocations in pile-ups, which increases the stress concentration at the microstructural obstacles that create these pile-ups [14]. In short, hydrogen has a strong effect on deformation in austenitic stainless steels, and this knowledge provides a phenomenological framework for explaining the observed fracture modes in a variety of austenitic stainless steels and their associated microstructures. In the following sections, we combine this phenomenological understanding of deformation with the physical and mechanical metallurgy of austenitic stainless steels to describe hydrogen-assisted fracture in these alloys with specific examples from studies in our laboratory.

For the purposes of this discussion, we focus on results from tests with a single reproducible environmental condition, namely thermal precharging of tensile specimens in 138 MPa hydrogen gas at 300˚C to achieve uniform hydrogen concentration across the diameter of the specimens [15]. With this environmental condition, we obviate the need for long-range hydrogen transport on the time scale of the test [16], which, in this case, are relatively short-term tensile tests. Fracture surfaces and cross section profiles from tensile tests of hydrogen-precharged type 316 austenitic stainless steels and a duplex stainless steel are used to inform our understanding of deformation and fracture in these alloys and by extension in other austenitic stainless steels. Our discussion here concentrates on the observed fracture modes, including microvoid coalescence (MVC), twin-boundary fracture, and cleavage; quantitative assessment of ductility and resistance to hydrogen-assisted fracture in austenitic stainless steels can be found in companion references [15-21].

DISCUSSION

Microvoid Coalescence

Hydrogen-precharged austenitic stainless steels that fracture by MVC exhibit a spectrum of dimple morphologies from equiaxed to elongated depending on the cross section of environmental conditions (e.g., temperature) and material variables (e.g., nickel content). The equiaxed dimple morphology that is characteristic of uniform deformation during tensile fracture in the absence of hydrogen is shown in Figure 1a, Figure 2a, and Figure 3a for type 316 austenitic stainless steels. Localized deformation in austenitic stainless steels is enhanced by low nickel content and/or deforming at low temperature in the absence of hydrogen, while the addition of hydrogen exacerbates this localized deformation leading to changes in fracture mechanisms [4-6].

Alloys and microstructures that deform uniformly generally show resistance to hydrogen-assisted fracture [5] and feature equiaxed dimples on tensile fracture

surfaces. Type 316 austenitic stainless steels with greater than ~12 wt% Ni, for example, show a relatively modest change in fracture mode at room temperature (Figure 1), although, in this case, the size of the dimples is reduced and their morphology is somewhat less equiaxed. These differences in size and morphology of dimples are related to the role of hydrogen on the process of MVC [22]. Since hydrogen enhances localized deformation, hydrogen also likely activates different void nucleation sites and impacts their growth [22, 23]. Additionally, hydrogen may affect interface cohesion at inclusions and other void nucleation sites.

Nickel content in austenitic stainless steels strongly correlates with deformation mode; localized deformation increases for austenitic stainless steels with lower nickel content [1], particularly in alloys with less than about 12 wt% Ni. The role of nickel content on hydrogen-assisted fracture is clearly demonstrated in Figure 2, which shows tensile fracture surfaces of a type 316 stainless steel with ~10 wt% nickel. In this case, ductile dimples still form, however, in the hydrogen-precharged material these dimples are non-equiaxed (e.g., elongated). Similar dimple structures have been observed in alloys (such as in titanium) that deform non-uniformly due to limited number of available slip systems, causing void nucleation at the intersection of deformation bands [2, 3]. In the austenitic stainless steels, hydrogen enhances localization of deformation in bands, facilitating nucleation of voids at the intersection of these deformation bands. Since the deformation bands tend to be nominally planar, have regular spacing and intersect along lines, voids that nucleate at these intersections appear as parallel, elongated dimples as shown in Figure 2b. Additional evidence that hydrogen promotes this deformation and fracture mode is described in ref. [19] for the stable austenitic stainless steel 21Cr-6Ni-9Mn.

Environmental variables (other than hydrogen content) can also influence the uniformity of deformation: for example, decreasing the temperature promotes non-uniform deformation in austenitic stainless steels as distinguished by the formation of deformation bands [1]. When localized deformation is sufficiently enhanced by the combination of low temperature and internal hydrogen, non-equiaxed dimple morphologies can be observed, as shown in Figure 3b and Figure 3c (for the same alloy as in Figure 1). While the localization of deformation in bands at sub-ambient temperature in the absence of hydrogen was not sufficient to change the fracture mode (compare Figure 1a and Figure 3a), the addition of hydrogen resulted in localized areas of non-equiaxed dimples (Figure 3c); although much of the fracture surface still featured equiaxed dimples (Figure 3d). The regions with equiaxed and non-equiaxed dimples in this alloy can be correlated with local compositional variations (compositional banding is not uncommon in high-alloy steels). Energy dispersive spectroscopy (EDS) on the fracture surface of this alloy reveals lower nickel content in the localized areas featuring non-equiaxed dimples (Figure 3c) than the areas that feature predominantly equiaxed dimples (Figure 3d). Such analysis is semi-quantitative, however, the trends are unequivocal and demonstrate the importance of nickel content and temperature on hydrogen-assisted fracture in austenitic stainless steels.

Microstructural Boundaries

Fracture mode changes due to hydrogen can be much more substantial than modifications of dimple morphology. For example, hydrogen can induce fracture along grain boundaries in some alloys [24], although intergranular fracture is not commonly observed in austenitic stainless steels. In some materials, however, flat facet-like features are apparent on the fracture surface as shown in Figure 4a for a hydrogen-precharged type 316 stainless steel fractured in tension at 223 K, which is also shown in cross section in Figure 4b. This type of fracture surface has been observed previously in hydrogen-precharged Fe-Cr-Ni austenitic stainless steels when fractured at sub-ambient temperature [25, 26]. There is also evidence of facetted fracture in hydrogen-precharged 21Cr-6Ni-9Mn austenitic stainless steel at room temperature [19]. This facetted fracture is typical of hydrogen-precharged type 300-series austenitic stainless steels with nickel content around 10 wt% or lower when tested at sub-ambient temperature.

Caskey determined that the facets in hydrogen-precharged type 304L stainless steel represent annealing twin boundaries [25]. Our own analysis using electron-backscattered diffraction (EBSD) on type 316 austenitic stainless steel also shows these boundaries to be consistent with annealing twin boundaries. As mentioned above, hydrogen enhances localized deformation resulting in high stresses at obstacles such as boundaries. These stresses likely scale with the degree of localized deformation in the material, as dislocations become increasingly confined to deformation bands, larger pile-ups are created at obstacles, which produce higher local stresses. Thus, hydrogen is more likely to induce boundary separation in austenitic alloys as deformation becomes exceptionally localized, as observed, for example, in the lower nickel-containing alloys deformed at sub-ambient temperature.

Two-Phase Microstructures

Although austenitic stainless steels are generally designed to be single phase, in some cases, ferrite is present either intentionally or unintentionally. Duplex stainless steels, for instance, are designed to contain nearly equal parts austenite and ferrite, while ferrite is also desirable in austenitic stainless steel welds to prevent solidification cracking. The two-phase microstructure of duplex alloys, being relatively uniform, can also be used as a model microstructure for the more complex two-phase microstructures of austenite and ferrite in austenitic stainless steel welds. MVC characterizes the fracture mode of super duplex stainless steel 2507 (Fe-25Cr-7Ni) in the annealed and strain-hardened conditions (Figure 5a), while the addition of high concentrations of internal hydrogen results in a significant change in fracture mode (Figure 5b) [17].

The fracture mode in hydrogen-precharged 2507 consists of cleavage fracture of the ferrite phase. Linkage of cleavage facets subsequently occurs by MVC in the austenite [17]. Hydrogen-enhanced localized plasticity in the austenite promotes stress concentration at the ferrite-austenite boundary resulting in cleavage of the

ferrite; however, the fracture of the ferrite is preceded by substantial deformation as indicated by the slip lines on the facets. Similar fracture processes have been observed in welded austenitic stainless steels [21] and wrought stainless steel containing residual ferrite stringers [19].

The microstructure developed due to the formation of martensite during deformation of austenitic stainless steels can also be considered a two-phase microstructure. In the literature, reduction of ductility due to hydrogen in the metastable austenitic stainless steels is often attributed to strain-induced martensite [25, 26]; however, there is no direct evidence relating hydrogen-assisted fracture to the strain-induced martensite. The EBSD results, as mentioned above, are particularly enlightening in this regard: these results show that the cracks (as shown in Figure 4b) occur along twin boundaries. In addition, the strain-induced martensite is clearly identified in the EBSD patterns, usually forming along planes inclined with respect to the observed boundary separation. Moreover, the stable austenitic stainless steel 21Cr-6Ni-9Mn [19] shows essentially the same hydrogen-assisted fracture modes as the metastable alloys, implying strain-induced martensite is neither necessary nor sufficient for hydrogen-assisted fracture in austenitic stainless steels.

More work is necessary to definitively elucidate whether the strain-induced martensite or the martensite-austenite boundary exacerbates hydrogen-assisted fracture. It may ultimately be difficult to distinguish the importance of strain-induced martensite from the importance of enhanced localized deformation since the same microstructural variables (e.g. nickel content) and environmental variables (e.g., temperature) that affect the formation of strain-induced martensite, also have a similar effect on the localization of deformation [1]. A particularly clever study in this regard used nickel and nitrogen contents to produce a series of alloys with equivalent resistance to strain-induced martensite but differing alloy content [27], showing that the alloys with higher nickel content had greater resistance to hydrogen-assisted fracture than the higher nitrogen containing alloys. The character of deformation was not assessed directly in that study; however, the influence of these alloying elements on hydrogen-assisted fracture can be inferred from their effect on localization of deformation in the absence of hydrogen: nickel content in austenitic stainless steels has a strong effect on localization of deformation [1, 28], while nitrogen has a limited effect on localizing deformation for nitrogen contents typical of type 316 austenitic stainless steels [16] (nitrogen content does appear to promote localization of deformation at higher contents typical of nitrogen-strengthened alloys, such as 21Cr-6Ni-9Mn [29]). In other words, it appears that explanations invoking the role of strain-induced martensite are not sufficient to account for the observed trends of hydrogen-assisted fracture in austenitic stainless steels.

SUMMARY

Internal hydrogen induces a variety of fracture modes in austenitic stainless steels. Moreover, these variations in fracture mode are a strong function of test temperature

and alloy content (within a given alloy type). In general, the observed fracture modes for hydrogen-precharged specimens correlate with the uniformity of plastic deformation, which is influenced by temperature and alloy content. Microvoid coalescence is the dominant fracture mode for austenitic stainless steels with high nickel content. The morphology of dimples becomes increasingly non-equaixed for alloys with lower nickel content or as the temperature is reduced. Twin boundary fracture is observed for the combination of sub-ambient temperature and low nickel content as deformation becomes sufficiently localized. Hydrogen-enhanced localized plasticity also produces local stress concentrations that induce cleavage fracture in the ferritic phase of duplex stainless steels and austenitic stainless steel welds.

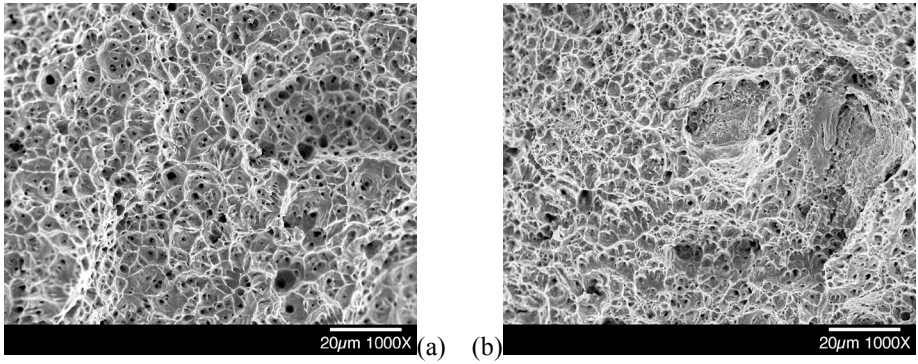
ACKNOWLEDGMENTS

Sandia is a multiprogram laboratory operated by Sandia Corporation, a Lockheed Martin Company, for the United States Department of Energy under contract DE-AC04-94AL85000.

REFERENCES

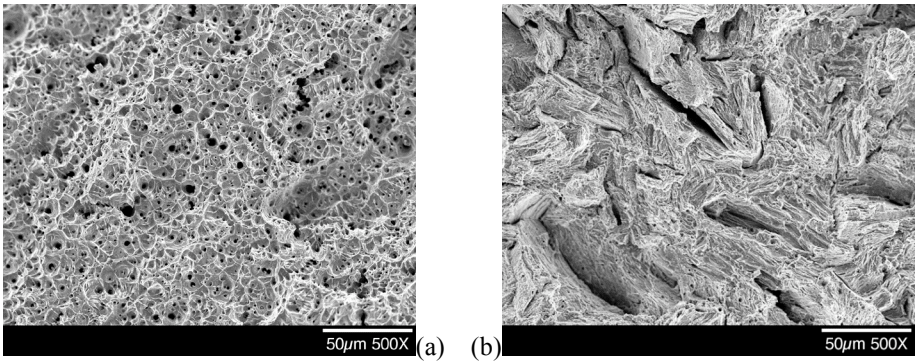
1. J. Talonen and H. Hanninen, *Acta Mater* **55,** 6108 (2007).
2. A. Gysler, G. Luetjering and V. Gerold, *Acta Metall* **22,** 901 (1974).
3. R. H. Van Stone, T. B. Cox, J. R. Low and J. A. Psoida, *International Metals Review* **30,** 157 (1985).
4. D. P. Abraham and C. J. Altstetter, *Metall Mater Trans* **26A,** 2859 (1995).
5. C. J. Altstetter and D. Abraham, *Hydrogen Effects in Materials*. Proceedings of the Fifth International Conference on the Effect of Hydrogen on the Behavior of Materials (Moran WY, 1994), volume AW Thompson and NR Moody, editors. Warrendale PA: TMS (1996) p. 599.
6. K. A. Nibur, D. F. Bahr and B. P. Somerday, *Acta Mater* **54,** 2677 (2006).
7. P. Sofronis, *J Mech Phys Solids* **43,** 1385 (1995).
8. P. J. Ferreira, I. M. Robertson and H. K. Birnbaum, *Acta Mater* **47,** 2991 (1999).
9. I. M. Robertson, *Eng Fract Mech* **68,** 671 (2001).
10. J. P. Chateau, D. Delafosse and T. Magnin, *Acta Mater* **50,** 1507 (2002).
11. H. K. Birnbaum and P. Sofronis, *Mater Sci Eng* **A176,** 191 (1994).
12. P. Sofronis and H. K. Birnbaum, *J Mech Phys Solids* **43,** 49 (1995).
13. Y. Liang, P. Sofronis and N. Aravas, *Acta Mater* **51,** 2717 (2003).
14. J. P. Chateau, D. Delafosse and T. Magnin, *Acta Mater* **50,** 1523 (2002).
15. C. San Marchi, D. K. Balch, K. Nibur and B. P. Somerday, *J Pressure Vessel Technol* **130,** 041401 (2008).
16. C. San Marchi, B. P. Somerday, X. Tang and G. H. Schiroky, *Int J Hydrogen Energy* **33,** 889 (2007).
17. C. San Marchi, B. P. Somerday, J. Zelinski, X. Tang and G. H. Schiroky, *Metall Mater Trans* **38A,** 2763 (2007).

18. C. San Marchi, B. P. Somerday, X. Tang and G. H. Schiroky, Proceedings of PVP-2008: ASME Pressure Vessels and Piping Division Conference, 2008, Chicago IL. ASME.
19. K. A. Nibur, B. P. Somerday, D. K. Balch and C. San Marchi, *Acta Mater* (submitted), (2009).
20. T. Michler, A. A. Yukhimchuk and J. Naumann, *Corros Sci* **60,** 3519 (2008).
21. B. P. Somerday, D. K. Balch, M. Dadfarnia, K. A. Nibur, C. H. Cadden and P. Sofronis, *Metall Mater Trans* (in publication), (2008).
22. A. W. Thompson, *Metall Trans* **10A,** 727 (1979).
23. D. C. Ahn, P. Sofronis and R. H. Dodds, *Int J Hydrogen Energy* **32,** 3734 (2007).
24. B. C. Odegard and A. J. West, *Hydrogen Effects in Metals*. Proceedings of the Third International Conference on Effect of Hydrogen on Behavior of Materials (Moran WY, 1980), volume IM Bernstein and AW Thompson, editors. New York: The Metallurgical Society of AIME (1981) p. 597.
25. G. R. Caskey, *Fractography and Materials Science, ASTM STP733*. LN Gilbertson and RD Zipp, editors. Philadelphia PA: American Society of Testing and Materials (1981) p. 86.
26. L. Zhang, M. Wen, M. Imade, S. Fukuyama and K. Yokogawa, *Acta Mater* **56,** 3414 (2008).
27. L. Zhang, M. Wen, M. Imade, S. Fukuyama and K. Yokogawa, Fracture of Nano and Engineering Materials and Structures. Proceedings of the 16th European Conference of Fracture, 2006, Alexandroupolis, Greece. EE Gdoutos, editor. Dorecht: Springer.
28. L. Vitos, J.-O. Nilsson and B. Johansson, *Acta Mater* **54,** 3821 (2006).
29. R. E. Stoltz and J. B. VanderSande, *Metall Trans* **11A,** 1033 (1980).



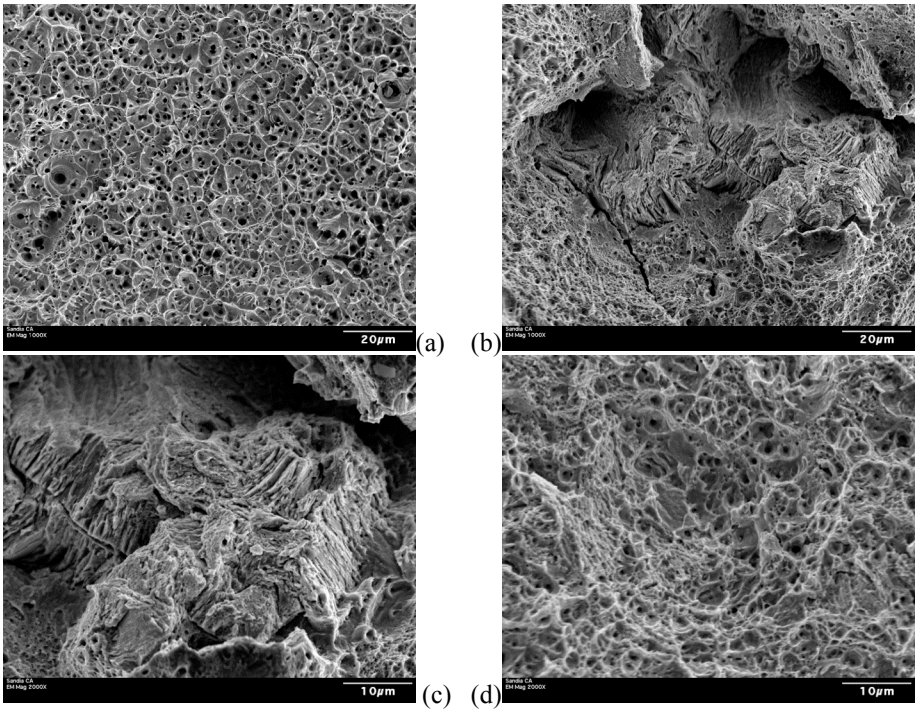
(a) (b)

Figure 1. Tensile fracture surfaces of type 316 austenitic stainless steel (12.3 wt% Ni) tested at room temperature: (a) non-charged, and (b) hydrogen-precharged.



(a) (b)

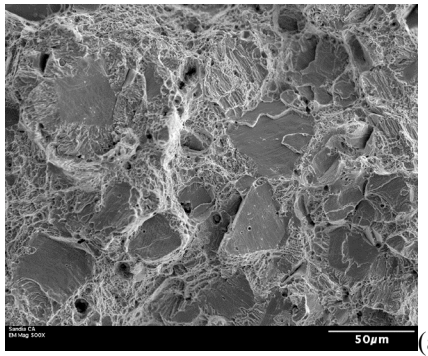
Figure 2. Tensile fracture surface of type 316 austenitic stainless steel (10.2 wt% Ni) tested at room temperature: (a) non-charged, and (b) hydrogen-precharged.



(a) (b)

(c) (d)

Figure 3. Tensile fracture surfaces of type 316 austenitic stainless steel (12.3 wt% Ni) tested at temperature of 223 K: (a) non-charged, (b) hydrogen-precharged. Higher resolution images from (b) show regions of (c) non-equiaxed dimples, and (d) equiaxed dimples.



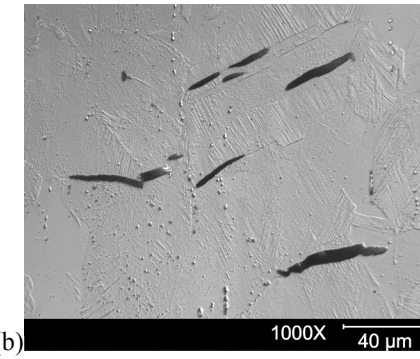
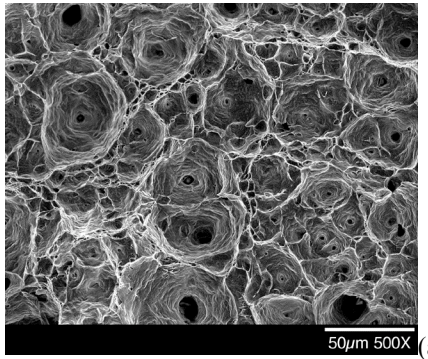
(a) (b)


Figure 4. (a) Fracture surface of hydrogen-precharged type 316 austenitic stainless steel (10 wt% Ni) tested at temperature of 223 K, showing facetted fracture surface. (b) Profile near fracture surface showing formation of facets (tensile axis is vertical).



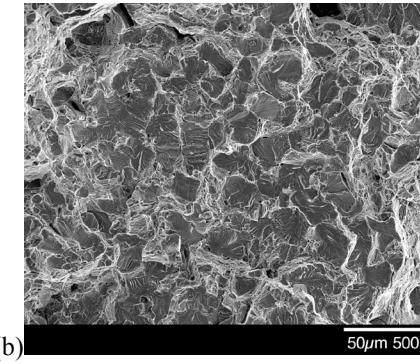
(a) (b)


Figure 5. Fracture surface of super duplex 2507 stainless steel tested at room temperature: (a) non-charged and (b) hydrogen-precharged.

Effects of Hydrogen on Materials
Proceedings of the 2008 International Hydrogen Conference
Brian Somerday, Petros Sofronis, Russell Jones, editors, p 97-104
Copyright © 2009 ASM International®
All rights reserved.
www.asminternational.org

EFFECT OF HYDROGEN ON PLASTIC STRAIN LOCALIZATION IN SINGLE CRYSTALS OF NICKEL AND AUSTENITIC STAINLESS STEEL

Y. Yagodzinskyy, T. Saukkonen, H. Hänninen
Laboratory of Engineering Materials, Helsinki University of Technology, P.O. Box 4200, FIN-02015 HUT, Espoo, Finland

F. Tuomisto
Laboratory of Physics, Helsinki University of Technology, P.O. Box 1100, FIN-02015 HUT, Espoo, Finland

S. Barannikova, L. Zuev
Institute of Strength Physics and Materials Science, SB RAS, Akademichesky blvd., 2/1, Tomsk, Russia.

ABSTRACT

Tensile tests accompanied with on-line *in situ* FEG-SEM observations are performed to study hydrogen effects on plastic strain localization in the form of slip lines in single crystals of nickel and AISI 316L austenitic stainless steel. Flat tensile test specimens are pre-charged potentiostatically with hydrogen at conditions not forming hydride or other hydrogen-induced phases. It is found that slip lines on the hydrogen-charged AISI 316L stainless steel specimens are markedly shorter in length than those on the hydrogen-free surfaces. Positron annihilation spectroscopy is applied to study the mutual effect of hydrogen and plastic deformation on excessive generation of vacancies and vacancy complexes in the studied single crystals. In hydrogen-charged AISI 316L stainless steel pre-strain to about 15 % in tension results in vacancy clusters and probably hydrogen filled microvoids. No vacancy complexes were detected in hydrogen-charged nickel deformed to about 7 %. The obtained results are analyzed and discussed in terms of the hydrogen enhanced localized plasticity (HELP) mechanism with special attention to the effect of hydrogen on the non-conservative dislocation-dislocation interactions.

INTRODUCTION

Hydrogen effects on the dislocation mobility and interactions have become a key element of the recent progress in understanding of the hydrogen embrittlement and other hydrogen-induced phenomena of engineering materials. Many experimental evidences on the plastic strain localization induced by hydrogen together with *in situ* transmission electron microscopy (TEM) observations of the hydrogen-enhanced dislocation mobility have been generalized in HELP mechanism [1, 2], which has

promoted further experimental studies and theoretical modelling of hydrogen-induced plastic strain localization and damage in metals. Analysis of the hydrogen effects on the plastic instabilities in metals based on the continuum constitutive models needs, as it was emphasized in [3], more detailed knowledge about the hydrogen-dislocation interactions including possible diffusion re-distribution of hydrogen caused by inhomogeneous dislocation generation and flow. It was shown that hydrogen has a remakable effect on dislocation behavior at the very beginning stages of plastic strain, which correspond to easy glide of dislocations, increasing the yield stress of austenitic stainless steels [4, 5] and markedly extending the Stage I of the stainless steel single crystals oriented to easy glide [5].

The present study is focused on the initial stages of the plastic strain of hydrogen-charged single crystals of pure nickel and AISI 316L stainless steel. The aim is to answer the questions: are there any evidences of hydrogen effects on the slip line morphology and does hydrogen affect the dislocation-dislocation reactions at the beginning of the region of linear hardening (Stage II) of the single crystals resulting in the excessive vacancy generation? The first question is important in the sense of hydrogen effects on dislocation source operation and slip development. The second one deals with the role of hydrogen in non-conservative dislocation activity, which can markedly modify the plastic strain behavior resulting in the local dynamical softening of the metal and nucleation of the vacancy clusters and microvoids filled with molecular hydrogen.

EXPERIMENTAL

Materials and specimens. Pure nickel of 99.99 % and austenitic stainless steel AISI 316L (18Cr-12Ni-2Mo with about 0.02 wt.% C+N) were used in the study. The materials are stable single-phase FCC crystals in the range of plastic deformation applied in the study. Single crystal ingots were obtained by using Bridgeman technique in the Institute of Strength and Plasticity SB RAS (Tomsk, Russia). Two sets of specimen billets were cut by spark erosion method from the ingots after their homogenization at 1200 ^{o}C for 70 h. The first set of dog-bone shape specimens for mechanical tensile testing with gauge length dimensions of 0.5 × 3 × 8 mm was thinned to about 0.3 mm mechanically with emery paper and final polishing with 1 μm diamond paste. The second set of specimens was prepared for positron annihilation spectroscopy (PAS). The single crystal specimens with typical dimensions of 0.3 × 3 × 18 mm and the same crystallographic orientation as for the first set were prepared using the above-mentioned procedures. Two identical pieces, which were cut from the specimen plate in as-supplied state and after hydrogen charging or from the gauge length of the dog-bone specimen after tensile test, were used for PAS measurements.

Hydrogen charging procedures. Hydrogen was introduced in the studied specimens electrochemically under controlled cathodic overpotential of 100 mV from 1N H_2SO_4 solution with addition of 20 mg/l of thiourea as a hydrogen poison. Electrochemical cell with calomel reference and platinum counter electrodes was de-aerated and kept under N_2-gas bubbling and 50 ^{o}C during the whole charging process of 70 h for all specimens. Current density at the applied potential was less than a few

mA/cm^2 during the whole charging process for both materials. No hydride or any other phases were detected with X-ray diffraction method in the specimens after applied hydrogen charging.

Experimental methods and techniques. Mechanical tensile tests were performed by using 2 kN load device (Deben, UK) *in situ* with Zeiss Ultra 55 Field Emission Gun (FEG)-SEM. All tests were done with an initial strain rate of 9×10^{-5} s^{-1} at room temperature. Some tests were interrupted at strain of about 7 % for nickel and about 15 % for stainless steel just after the transition from Stage I to Stage II of the stress-strain curves.

PAS measurements were carried out with the positron lifetime method using a conventional fast-fast spectrometer in collinear geometry [6] with time resolution of 250 ps. In this scheme the positron source ^{22}Na deposited on 1.5 mm Al foil is sandwiched between two identical specimen pieces. The lifetime spectrum was analyzed as the sum of the exponential decay components convoluted with the Gaussian resolution function of the spectrometer, after subtracting the constant background and annihilations in the source material.

RESULTS AND DISCUSSION

Parts of the tensile engineering stress-strain curves obtained for pure nickel and AISI 316L austenitic stainless steel single crystals are shown in Figs 1 and 2, respectively. They correspond to the tests which were interrupted for further investigation of the obtained pre-strained single crystals with PAS. For the whole strain range both tested materials manifest similar, multistage curves, which are characteristic for single crystals oriented to easy glide.

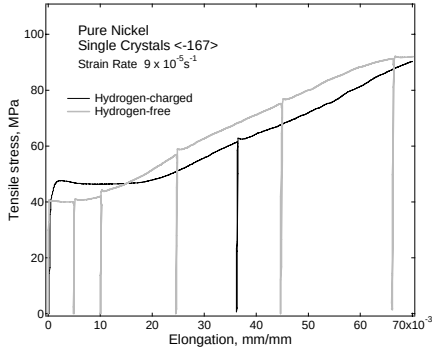


Figure 1. Initial parts of the stress-strain curves for hydrogen-free (in grey) and hydrogen-charged nickel single crystals.

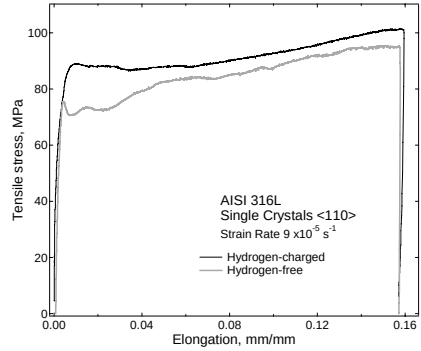


Figure 2. Initial parts of the stress-strain curves for hydrogen-free (in grey) and hydrogen-charged AISI 316L steel single crystals.

Similarly to the results obtained earlier in [5], hydrogen affects the flow stress of both materials starting from the very early stage of the plastic strain. It was seen that the yield strength increases about 20 % for pure nickel as well as for the austenitic stainless steel after their hydrogen charging. At the same time the plateaus behind the yeld point, which correspond to the Lüders front propagation and represent Stage I of

the single crystal hardening, become about two times more extended for both studied materials after their charging with hydrogen. At least two Lüders fronts from opposite sides of the specimen start to develop simultaneously in the single crystals with hydrogen, while only one front nucleates in the hydrogen-free specimens.
Micrographs of slip lines arising behind the Lüders front in the hydrogen-free and hydrogen-charged nickel are shown in Figs 3 a and 3 b, respectively. Slip lines are long and straight, and homogeneously distributed in pure nickel, while they look shorter and more dense in the hydrogen-charged specimens with a space variation of the slip magnitude, which results in a more coars surface relief. Such a relief was already observed with atomic force microscopy (AFM) method in hydrogen-charged austenitic stainless steel single crystals [5] in the form of a bi-modal distribution of the slip magnitude. It is seen from Fig. 3 b that the characteristic scale of the additional surface relief or hydrogen-induced mesoscopic strain localization in nickel can be estimated to be about 15 μm. Similar features of the slip distribution were observed in AISI 316L steel single crystals.
Only a few slip lines are visible on the micrographs obtained from the specimen areas ahead of the Lüders fronts. Such micrographs are interesting because they reflect the operation of the individual dislocation sources or mutual operation of a few of them. Typical examples of the slip line features of AISI 316L austenitic stainless steel single crystal are shown in Figs 4 a and 4 b. In the case of hydrogen-free specimen (Fig. 4 a) slip lines are long and straight and one can assume that dislocation sources operate mainly independently, except some of them which form coupled slip lines. Rather different slip pattern (see Fig. 4 b) develops in the presence of hydrogen: slip lines become markedly shorter (ends of the slip lines are shown by arrows) forming apparent slip lines with a fine substructure.
The apparent slip line consists of a sequence of a number of overlapping short slip lines arising on the adjacent slip planes with a scale of sub-micron spacing as shown in Fig. 5 a. In turn, the apparent slip lines form groups with scale of spacing of about 10 μm (see Fig. 4 b) and with a layered fine structure shown in Fig. 5 b.
The result evidences that in the presence of hydrogen the austenitic stainless steel exhibits plastic strain localization in form of the apparent slip lines at the micro-meter scale and by grouping of the apparent slip lines at meso-scale, at about 10 μm. The last localization feature may result in a further development of the above-mentioned surface relief. The overlapping of the short slip lines within the apparent slip line seems to provide more shear deformation in comparison to that in the case of the single slip line in hydrogen-free austenite.
One can assume also that the fine structure of the apparent slip line originates from a strong hydrogen-induced coupling of the dislocation sources in the adjacent slip planes. Hydrogen atmospheres forming around dislocations emitted from the sources can modify the dislocation-dislocation interactions forming dislocation pile-ups and pile-up dipole and multipole configurations. It seems that hydrogen-induced interaction between dislocation sources resulting in their coupling restricts further development of the single slip lines and forms the observed fine structure of the apparent slip lines. The interaction between dislocation pile-ups of adjacent slip planes can result in dislocation-dislocation reactions, which progress probably by

cross-slip of screw and climb of edge components of the dislocation loops and results in linking of the dislocation sources.

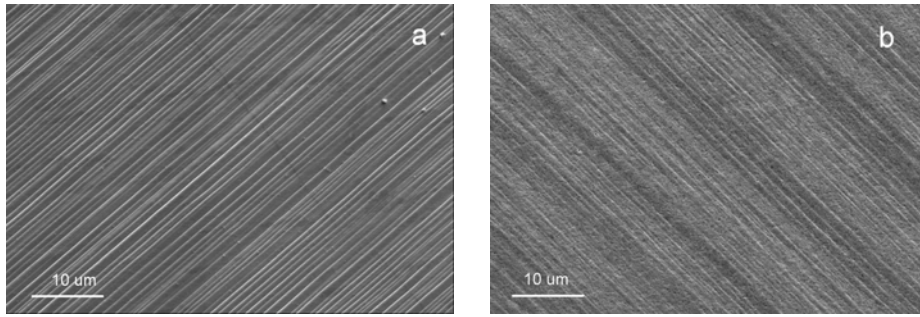


Figure 3. Micrographs of slip lines arising behind the Lüders front in the hydrogen-free (a) and hydrogen-charged (b) nickel single crystals loaded in $< \bar{1}67 >$ *direction.*

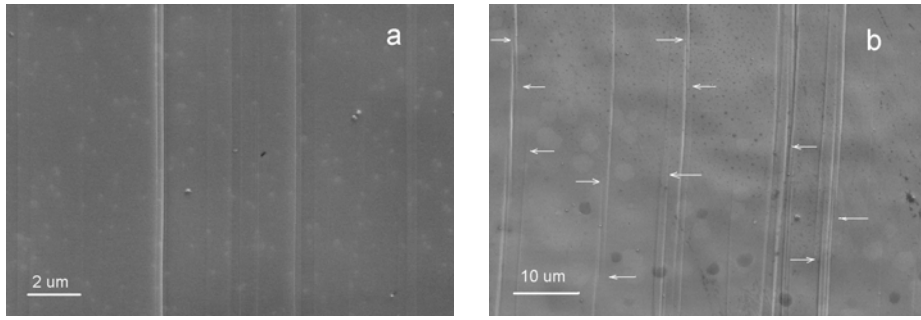


Figure 4. Micrographs of the slip line structure obtained from the area just ahead the Lüders front of hydrogen-free (a) and hydrogen-charged AISI 316L steel single crystals. Specimen oriented for tension in <110> *direction. Arrows mark the ends of the short slip lines.*

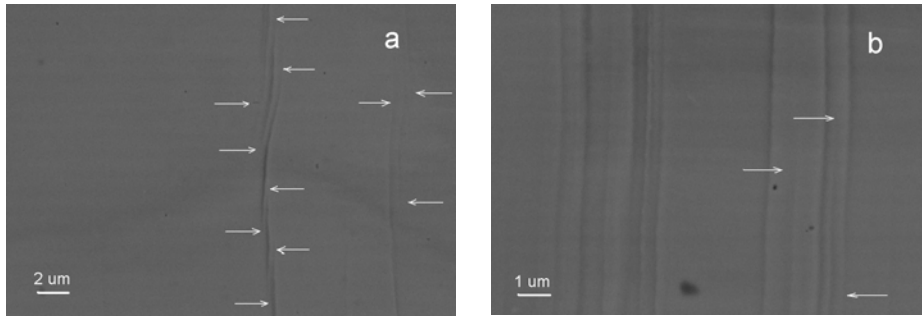


Figure 5. Typical electron backscatter diffraction (EBSD) images of the slip line structure (a) and the slip line grouping (b) in hydrogen-charged AISI 316L steel single crystal obtained from the area just ahead the Lüders front. Specimen oriented for tension in <110> *direction. Arrows mark the ends of the short slip lines.*

Since hydrogen markedly modifies the character of the plastic strain already at the region of easy glide and promotes the dislocation-dislocation reactions, a remarkable enhancement in the point defect generation can be expected, which attributes always the dislocation reactions, especially at the stages of well-developed plasic deformation [7].
PAS measurements were performed in order to identify the type of defects induced by mutual effects of hydrogen and plastic deformation. Lifetime spectroscopy used in the study is a powerful technique in defect studies, which allows to determine the number of positron states, their annihilation rates (lifetimes) and relative intensities. Two-component analysis of the positron annihilation spectra obtained in the present study for single crystal nickel in as-supplied state, after pre-srain to about 7 %, after hydrogen charging without strain and with plastic pre-strain to about 7 % gives approximately the same lifetime values for all studied states of nickel, which are about 79 ps and 178 ps for short and long lifetime components, respectively. The last, long lifetime corresponds to annihilation of positrons captured by monovacancies.
Hydrogen effects on the vacancy generation and evolution in polycrystalline nickel and AISI 316L stainless steel were studied with PAS methods [9]. It was found that the long positron annihilation lifetime in nickel measured just after electrochemical hydrogen charging is about 150 ps, but it increased with natural annealing up to 350 ps. It is necessary to notice here that the hydrogen charging conditions applied in [9] were markedly stronger (cathodic current density was, at least, 10 times higher) than that used in the present study. The evolution of the long lifetime with annealing at room and elevated temperatures observed in [9] was obviously caused by hydride and other hydrogen-induced phases formed in the strong charging conditions. No hydrogen-induced phases were observed in the present study.
Parameters of the two-component analysis of the positron annihilation spectra for different states of AISI 316L steel single crystal specimens are shown in Fig. 6. The short and long lifetime components were obtained to be close to 70 ps and 170 ps, respectively, for as-supplied, pre-strained to about 15 % in tension and hydrogen-charged specimen without pre-strain. Similarly to the nickel specimen the long lifetime component corresponds to trapping of positrons by monovacancies. Deformation of the hydrogen-charged AISI 316L steel single crystal to about 15 % in tension results in changes of the PAS behavior. In addition to the component of 137 ps, which corresponds probably to positron annihilation in monovacancies filled with hydrogen atoms, a new, longer lifetime component of 245 ps appears in the spectrum. It was shown by numerical modelling of the positron states in solids [10] that the positron lifetimes comparable or longer than the above-mentioned value correspond to vacancy clusters. The modelling was performed for pure metals and the lifetme of 245 ps represents the clusters consisting of four vacancies in the case of pure nickel. There are no calculations of the lifetimes for positron captured by vacancy clusters in multiconponent FCC alloys such as austenitic stainless steel, yet. One can only assume that in the case of hydrogen-filled vacancy clusters the lifetime of 245 ps may correspond to markedly increased number of vacancies in the agglomerations.

The obtained results evidence that hydrogen, at least in AISI 316L stainless steel, affects considerably the character of the plastic strain even at the stage of the easy glide of dislocations. It seems that hydrogen enhances non-conservative modes of dislocation motion resulting in excessive generation of vacancies and vacancy clusters.

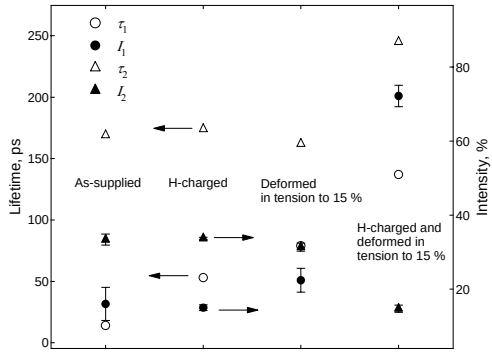


Figure 6. Comparison of the PAS parameters for different states of studied AISI 316L steel single crystal. τ_1 and τ_2 are lifetimes and I_1 and I_2 are relative intensities ($I_1 + I_2 = 100$ %) of short- and longtime component of the positron annihilation spectra, respectively.

Finally, the differences observed in PAS results for nickel and AISI 316L steel single crystals can originate from the different amount of the pre-strain applied. Higher vacancy mobility in nickel in comparison to that in austenitic stainless steel can also result in rather different vacancy cluster kinetics with their nucleation at higher pre-strain values.

CONCLUSIONS

The obtained results evidence that hydrogen has a remarkable effect on the generation, motion and interaction of dislocations even at the very early stage of plastic deformation of FCC single crystals oriented to easy glide. The plastic flow stress increases in hydrogen-charged nickel and AISI 316L steel single crystals to about 20 % in comparison to the flow stress of the hydrogen-free material. Amount of plastic strain, which corresponds to the transition from the easy glide of dislocations to the linear hardening stage, becomes about two times higher in the presence of hydrogen in both studied materials. The last result together with *in situ* observations of the slip line fine structure and distribution evidence clearly the hydrogen-induced enhancement of plastic strain localization.

Slip lines observed in hydrogen-charged AISI 316L stainless steel single crystals at the easy glide stage manifest a fine deformation structure consisting of overlapping sequences of short slip lines with sub-micrometer spacing. The overlapping short slip lines reflect the operation of the dislocation sources, which become restricted and coupled due to the presence of hydrogen.

It seems that hydrogen promotes dislocation-dislocation reactions, which result in the dislocation source coupling and in generation of excessive vacancies and vacancy

complexes. The vacancy complexes can be indicated by a new component of 245 ps in the positron annihilation lifetime spectra of the hydrogen-charged AISI 316L steel single crystal after its pre-strain to about 15 % in tension. Annealing of the hydrogen-charged and pre-strained specimen at room temperature for about 100 h results in the development of hydrogen-filled microvoids.

ACKNOWLEDGEMENTS

This study has been partly supported by the Research Programme of the Research Fund for Coal and Steel of EC.

REFERENCES

1. Birnbaum H. K., "Mechanism of Hydrogen Related Fracture of Metals", Environment-induced Cracking of Metals, R. P. Gangloff and M. B. Ives, eds., NACE, (Houston, 1988), pp. 21-30.
2. Birnbaum H. K. *et al*, "Mechanisms of Hydrogen Related Fracture – A Review", Hydrogen Effects on Material Behavior, N. R. Moody and A. W. Thompson, eds., The Mineral, Metals and Material Society, (New York, 1990), pp. 639-660.
3. Liang Y. *et al*, "On the Effect of Hydrogen on Plastic Instabilities in Metals", *Acta Mater*, Vol. 51 (2003), pp. 2717-2730.
4. Abraham D. P. *et al*, "The Effect of Hydrogen on the Yield and Flow Stress of an Austenitic Stainless Steel", *Met. Mater. Trans.* A, Vol. 26A (1995), pp. 2849-2858.
5. Yagodzinskyy Y. *et al*, "Effect of Hydrogen on Plastic Deformation of Stable 18Cr-16Ni-10Mn Austenitic Stainless Steel Single Crystals", Hydrogen Effects on Material Behavior and Corrosion Deformation Interactions, N. R. Moody, A. W. Thompson, R. E. Ricker, G.W. Was and R.H. Jones, eds., The Mineral, Metals and Material Society, (New York, 2002), pp. 201-210.
6. Saarinen K. *et al*, Identification of Defects in Semiconductors, M. Stavola, ed. Academic, (Boston, 1998), 209 p.
7. J. Friedel, Dislocations, Pergamon Press, (Oxford, 1964), 491 p.
8. Onyewuenyi O. A., "Plastic Instability and Hydrogen in Iron-Based Alloys", Hydrogen Degradation of Ferrous Alloys, R. A. Oriani, J. P. Hirth and M. Smialowski eds., Noyes Publications, (New Jersey, 1995), pp. 414-450.
9. Ohkubo H. *et al*, "Positron-Lifetime Study of Electrically Hydrogen Charged Ni, Austenitic Stainless Steel and Fe", *J. Nucl. Mater.*, Vol. 283-287 (2000), pp. 858-862.
10. Puska M.J. and Nieminen R.M., "Defect Spectroscopy with Positrons: a General Calculation Method", J. *Phys. F: Met. Phys.*, Vol. 13 (1983), pp. 333-346.

Effects of Hydrogen on Materials
Proceedings of the 2008 International Hydrogen Conference
Brian Somerday, Petros Sofronis, Russell Jones, editors, p 105-112
Copyright © 2009 ASM International®
All rights reserved.
www.asminternational.org

INFLUENCE OF HYDROGEN AND PRESTRAIN ON TENSILE PROPERTIES OF TYPE 316L AUSTENITIC STAINLESS STEEL

Takashi MATSUO
Department of Mechanical Engineering Science, Graduate School of Engineering, Kyushu University, Fukuoka-city, Fukuoka, Japan

Junichiro YAMABE, Saburo MATSUOKA, Yukitaka MURAKAMI
Department of Mechanical Engineering Science, Kyushu University, Research Center for Hydrogen Industrial Use and Storage (HYDROGENIUS) and National Institute of Advanced Industrial Science and Technology (AIST), Fukuoka-city, Fukuoka, Japan

INTRODUCTION

Type 316L austenitic stainless steel JIS-SUS316L is used in parts of fuel-cell vehicles, such as pipes, valves, and springs. According to the NASA standard [1], SUS316L is classified in the least-susceptible group, "Negligibly Embrittled," on the basis of the results of tensile tests in 69 MPa hydrogen gas and 69 MPa helium gas at room temperature. Fukuyama et al. [2] conducted tensile tests in hydrogen gas at 10–70 MPa at room temperature, and they reported that the tensile properties of SUS316L are little affected by hydrogen. However, in the case of tensile tests in hydrogen gas at room temperature for SUS316L, hydrogen enters only into a thin layer of the specimen's surface, and the distribution of hydrogen content in the specimen is not uniform. Kanezaki et al. [3] measured the distribution of hydrogen content in SUS316L cathodically-charged in a pH = 3.5 aqueous solution of H_2SO_4 at a current density of 27 A/m^2 at 50 °C for 672 h, and identified that in this condition hydrogen diffused only into a very thin surface layer (approximately 100 μm) in SUS316L. To understand the effect of hydrogen on the bulk tensile properties of the material, tensile tests need to be carried out by using specimens in which hydrogen is uniformly distributed [4]. In addition, when SUS316L is used as a material for pipes, springs, etc., its strength is increased by cold working. Consequently, it is necessary to investigate the effects of hydrogen on the tensile properties of prestrained SUS316L.

In this study, two types of specimen for tensile tests and hydrogen-content measurements were machined from solution heat-treated plate and prestrained plates of SUS316L. The specimens were exposed to 10 MPa hydrogen gas at 250 °C to give a uniform distribution of hydrogen content. The influences of prestrain on the hydrogen-absorption property and the influences of hydrogen and prestrain on the tensile properties were investigated by using specimens containing a uniform distribution of hydrogen content. In addition, the influence of hydrogen on the

formation of dimples on the tensile-fracture surface was investigated by scanning electron microscopy (SEM).

MATERIAL AND EXPERIMENTAL METHOD

The material used is a solution heat-treated plate of SUS316L with a thickness of 30 mm. The solution heat treatment was conducted at 1100 °C. Table 1 shows the chemical composition and the Vickers hardness values averaged from 20 measurements. Vickers hardness tests were conducted at a load of 9.8 N and a hold time of 30 s. The tensile tests were conducted by using virgin specimens and prestrained specimens. Virgin specimens were machined from the solution heat-treated plate. Prestrained specimens were machined from cold-rolled plates with true strains of 0.16, 0.36, 0.60, and 0.92 with the tensile axis parallel to the rolling direction. Assuming that the width of the plate was kept constant during cold-rolling, the true prestrain in the axial direction of the tensile specimen, ε_{pre}, was calculated by the equation, $\varepsilon_{pre}=-\ln(t/t_0)$, where t is the thickness of the plate after cold-rolling, t_0 is the initial thickness of the plate. The tensile specimen was a cylindrical-shaped test specimen measuring 5 mm in diameter and 30 mm long. The surface of the specimen was polished with #600 emery paper. Cylindrical specimens for hydrogen-content determination, measuring 5 mm in diameter and 40 mm long, were also machined from solution heat-treated plate and prestrained plates. All testing was performed at room temperature in air. The crosshead speed was 1 mm/min. An extensometer with a 25-mm gage length was attached to the parallel part (i.e. the gauge section) of the tensile specimen. The tensile-fracture surface was examined by SEM.

The tensile specimens were exposed to hydrogen gas at 10 MPa and 250 °C for 192 h so that they became charged with hydrogen. These specimens are referred to as "hydrogen-exposed specimens." The hydrogen content was measured by means of thermal desorption spectrometry (TDS): the rate of temperature increase was 0.33 °C/s, and the temperature was raised to 600 °C. The residual hydrogen content of tensile-fracture specimens was measured on 1-mm-thick disks machined from the tested part approximately 8 mm from the fracture surface.

Tensile specimens exposed to argon gas at 0.1 MPa and 300 °C for 192 h were also prepared to permit the estimation of the effects on the tensile properties of microstructural changes that occurred on exposure to 10-MPa hydrogen gas at 250 °C for 192 h. The specimens exposed to 0.1-MPa argon gas are referred to as "argon-exposed specimens."

Table 1: Chemical composition (mass %) and Vickers hardness HV for SUS316L.

C	Si	Mn	P	S	Ni	Cr	Mo	*HV*
0.010	0.53	0.77	0.023	0.001	12.13	17.16	2.86	144

RESULTS AND DISCUSSION

Hydrogen Absorption Properties

Two disk-shaped specimens with thicknesses of 0.15 and 0.25 mm, respectively, were machined from the hydrogen-analysis specimen with a prestrain of 0.60, and these were then exposed to hydrogen gas at 10 MPa and 250 °C for 192 h. Figure 1 shows the relationship between the hydrogen content, C_H, and thickness for the hydrogen-exposed disk-shaped specimens. The hydrogen contents of the two disk-shaped specimens were almost the same (approximately 22 wppm). The residual hydrogen content, $C_{H,R}$, of the tensile-fracture specimen with ε_{pre} = 0.60 is also plotted in Fig. 1. The hydrogen content was 21.7 wppm, a value that is almost equal to those for the disk-shaped specimens. These results show that when the 5-mm-diameter bar with ε_{pre} = 0.60 was exposed to 10-MPa hydrogen gas at 250 °C for 192 h, the hydrogen content became saturated at around 22 wppm. In other words, the distribution of hydrogen content in 5-mm-diameter tensile specimens becomes almost uniform on exposure to hydrogen at 10 MPa and 250 °C for 192 h.

Figure 2 shows the residual hydrogen content against the prestrain. The residual hydrogen content increases with increasing prestrain: this is because dislocations introduced by the prestrain act as sites for trapping of hydrogen.

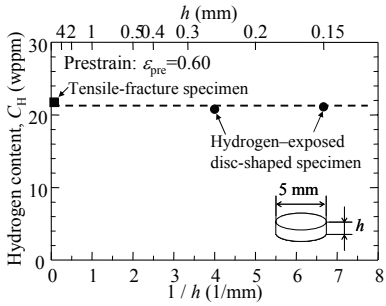


Figure 1: Relationship between the hydrogen content and the thickness of hydrogen exposed disc-shaped specimens with a prestrain ε_{pre} = 0.60.

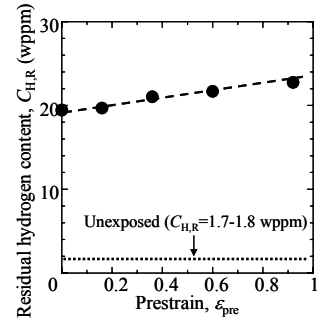


Figure 2: Relationship between the residual hydrogen content and prestrain for tensile- fracture specimens

Tensile Properties

Figure 3 shows the true stress – true strain (σ–ε) curves of hydrogen-exposed specimens (solid lines) and argon-exposed specimens (broken lines). In this figure, the true prestrains induced by cold working are added to the true strains induced by tensile testing. The σ–ε curve for an unexposed virgin specimen (ε_{pre} = 0) in the true-strain range from 0.04 to 0.45 is approximated by the equation, $\sigma = \varepsilon_p^n$ (where

σ is the true stress, ε_p is the plastic true strain, and n is the hardening exponent): the curve obtained by this approximation is shown as the dashed–dotted line. The σ–ε curves of argon- and hydrogen-exposed specimens with ε_{pre} = 0, 0.16, 0.36, and 0.60 are coincident with the approximated curve for the unexposed virgin specimen, but the flow stresses of hydrogen- and argon-exposed specimen with ε_{pre} = 0.92 are below the values for the approximated curve.

Figure 4 shows a plot of the reduction of area (RA) against the prestrain. RA decreases slightly with increasing prestrain for unexposed, argon-exposed, and hydrogen-exposed specimens. RAs of unexposed and argon-exposed specimens are coincident with each other at a given prestrain. This means that no microstructural changes in SUS316L, such as a decrease in dislocation density, occur during exposure to argon at 300 °C for 192 h or during exposure to hydrogen at 250 °C for 192 h. However, RA is lower in hydrogen-exposed specimens than in unexposed and argon-exposed specimens. That is, the ductility is degraded by hydrogen in SUS316L when the hydrogen-content distribution in the specimen is uniform. Therefore, it should be noted that when SUS316L is used in components of fuel-cell systems, a loss of ductility resulting from hydrogen exposure (i.e. so-called hydrogen embrittlement) occurs depending on exposure conditions, even with this alloy.

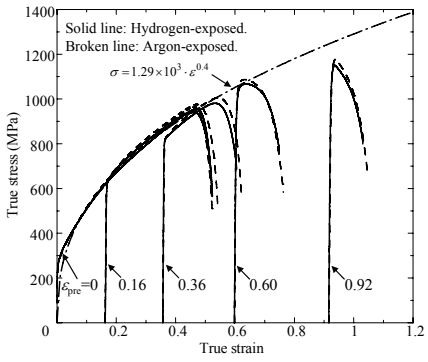


Figure 3: True stress-strain curves of argon- and hydrogen-exposed specimens.

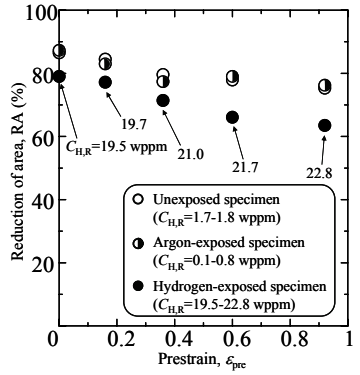


Figure 4: Reduction of area against prestrain. Numbers such as 19.5 wppm in the figure indicate the residual hydrogen content, $C_{H,R}$.

Influence of Hydrogen on Dimple Formation

Figures 5 and 6 show the appearance of representative fractures of tensile specimens exposed to argon and hydrogen. As shown in Figs. 5(a)–5(c), cup–cone fracture consisting of a normal stress-fracture region and shear stress-fracture region occurs in all the specimens.

Figures 5(d)–5(f) show the dimples observed in the normal stress-fracture regions in Figs. 5(a)–5(c). The normal stress-fracture regions are covered by two types of dimple: the first type corresponds to large dimples with diameters of approximately 20 μm, and the second type corresponds to small dimples with diameters of approximately 2 μm. In both argon- and hydrogen-exposed specimens, the area of the small dimples increases with increasing prestrain. A comparison of the fracture surfaces of the argon- and hydrogen-exposed specimens at a given prestrain level shows that the area covered by the small dimples in the hydrogen-exposed specimen is greater than that in the argon-exposed specimen. As the area covered by small dimples increases, the diameter of the large dimples decreases. Figure 6(a) shows the dimples in the shear stress-fracture region of the virgin ($\varepsilon_{pre} = 0$) specimen exposed to argon. There are also large- and small-type dimples in the shear stress-fracture region. The large dimples are typical elongated dimples. From the point of view of a typical elongated dimple, the large dimples formed in the normal stress-fracture region [Figs. 5(d)–5(f)] appear to be equiaxial dimples. The small dimples are similar in size and appearance in both the normal and shear stress-fracture regions.

To further elucidate the mechanism of dimple formation, the three-dimensional profiles of dimples were constructed by using a pair of stereographic SEM images. Figures 5(g)–5(i) show the profiles of dimples in the normal stress-fracture regions at the cross sections indicated by AA' in Figs. 5(d)–5(f). “L” and “S” in Figs. 5(g)–5(i) indicate large and small dimples, respectively. The large dimples are deep, whereas the small dimples are formed at planes oriented at the angles of about 45° to the tensile axis. Figure 6(b) shows the profile of dimples in the shear stress-fracture region at the cross sections BB' in Fig. 6(a). The large (L) and small (S) dimples in the shear stress-fracture regions are formed on planes oriented at the angles of about 45° to the tensile axis. It is apparent from the three-dimensional dimple profiles that the large dimple in the normal stress-fracture region is an equiaxial dimple, and the large dimple in the shear stress-fracture region is an elongated dimple.

Roger [5] conducted tensile tests on oxygen-free high-conductivity copper and investigated the initiation, growth, and coalescence of voids. He reported that the shear strain was concentrated on the planes at angles of 30° through 40° to the tensile axis around the large grown void, and a large number of small voids, called the “void sheet”, were nucleated in the region of very heavy local shear deformation. Based on the results of tensile tests on AISI 4340 alloys, Cox et al. [6] also reported that adjacent large voids coalesce by means of a void sheet oriented at approximately 45° to the tensile axis. On the basis of these results, it can be concluded that the regions of small dimples in Figs. 5(d)–5(f) and 6(a) are the void sheets.

There are two main theories regarding the mechanism of hydrogen embrittlement: the lattice decohesion theory [7] and the hydrogen-enhanced localized plasticity (HELP) theory [8,9]. The dimple formation of hydrogen-exposed specimens of SUS316L is very different from that of argon-exposed specimens and the major

process of dimple formation observed in this study is the local shear fracture enhanced by hydrogen. In hydrogen-exposed specimen, hydrogen enhances the localization of shear deformation (i.e. slip deformation). As a result, the area of small dimples in the normal stress-fracture region, i.e. the void sheet, becomes wider in hydrogen-exposed specimens at a given prestrain level, as shown in Figs. 5(d)–5(f). Furthermore, most of the shear stress-fracture region is covered by the small dimples, as shown in Figs. 6(a) and 6(b). Therefore, the shear stress-fracture region is wider in the hydrogen-exposed specimen than in the argon-exposed specimen, as shown in Figs. 5(a)–5(c), because the localization of shear deformation is enhanced by hydrogen.

The ratio of A_S to A_0 (A_S/A_0) is used as a measure of the enhancement of the formation of void sheet by hydrogen in both the normal and shear stress-fracture regions. A_S indicates the area of the shear stress-fracture region projected on a plane perpendicular to the tensile axis. A_0 indicates the initial cross section area of tested part of specimen. Figure 7 shows the relationship between RA and A_S/A_0. RA is correlated very closely to the area of the shear stress-fracture region. As the area of the shear stress-fracture region increases, the RA decreases. Accordingly, we conclude that the degradation of RA, i.e. so-called the hydrogen embrittlement in SUS316L, is caused by the local shear fracture enhanced by hydrogen.

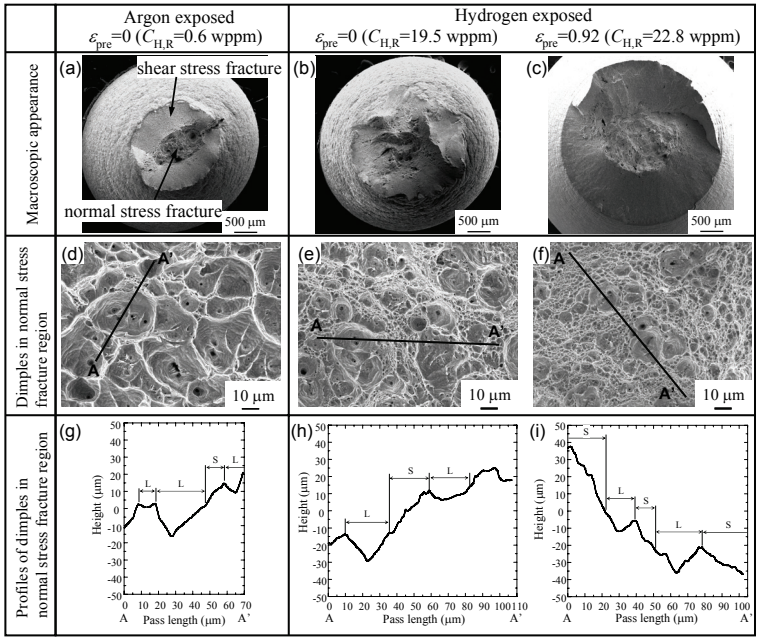


Figure 5: SEM images of tensile-fracture surfaces, dimples in the normal stress-fracture region and profiles of dimples in this region.

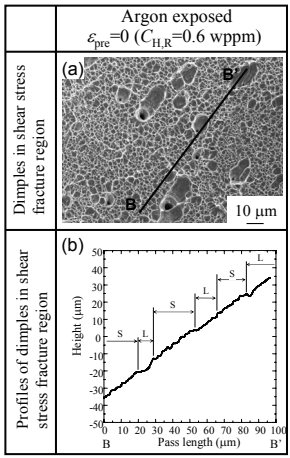


Figure 6: SEM images of dimples and profile of dimples in shear stress-fracture region.

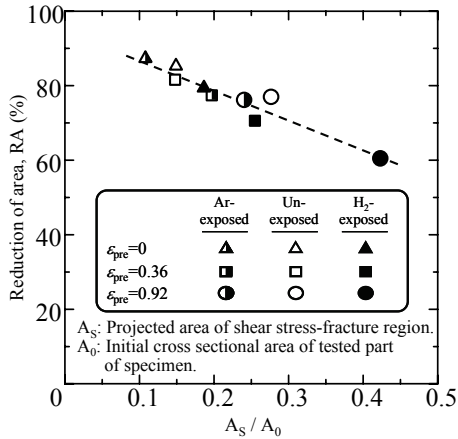


Figure 7: Relationship between the reduction of area and the ratio of the projected area of shear stress fracture region to the initial cross section area of tested part of specimen.

CONCLUSIONS

The influence of prestrain on hydrogen absorption and the influence of hydrogen and prestrain on the tensile properties of SUS316L were investigated by using specimens containing a uniform distribution of hydrogen content. The uniform distribution of hydrogen content was achieved by exposing specimens to hydrogen gas at 10 MPa and 250 °C for 192 h. The conclusions can be summarized as follows.

1. The hydrogen content increases with increasing prestrain.
2. When the hydrogen is evenly distributed in the specimen, the reduction of area is decreased by the presence of hydrogen even in the case of SUS316L.
3. Cup–cone fracture occurs in all the specimens. The fracture surfaces are covered by two types of dimple: large dimples and small dimples. The area of small dimples is greater in hydrogen-exposed specimens than in argon-exposed specimens. As the area coverage by small dimples increases, the diameter of the large dimples decreases.
4. According to a three-dimensional analysis of the dimples, the large dimples formed in the normal stress-fracture region are equiaxial dimples, and the regions of small dimples are the void sheet produced by local shear strain.
5. Because hydrogen enhances the localization of shear deformation, the area of void sheet increases in hydrogen-exposed specimen, resulting in a degradation in the reduction of area.

ACKNOWLEDGMENTS

This research has been supported by the NEDO Fundamental Research Project on Advanced Hydrogen Science (2006 to 2012).

REFERENCES

1. NASA, *Safety Standard for Hydrogen and Hydrogen Systems*, NSS 1740.16, Office of Safety and Mission Assurance (Washington, DC, 2005).
2. Fukuyama, S., *et al*, "Development of Materials Testing Equipment in High Pressure Hydrogen and Hydrogen Environment Embrittlement of Austenitic Stainless Steels," *J. Japan Inst. Metals*, Vol. 68 (2004), pp. 62–65.
3. Kanezaki, T., *et al*, "Effects of Hydrogen on Fatigue Crack Growth Behavior of Austenitic Stainless Steels," *Int. J. Hydrogen Energy*, Vol. 33, No. 10 (2008), pp. 2604–2619.
4. San Marchi, C., et al, "Effects Of Alloy Composition and Strain Hardening on Tensile Fracture of Hydrogen-Precharged Type 316 Stainless Steels," *Int. J. Hydrogen Energy*, Vol. 33, No. 2 (2008), pp. 889–904.
5. Roger, H. C., "The Tensile Fracture of Ductile Metals," *Trans. Metall. Soc. AIME*, Vol. 218 (1960), pp. 498–506.
6. Cox, T. B. and Low, J. R., Jr., "An Investigation of the Plastic Fracture of AISI 44340 and 18 Nickel-200 Grade Maraging Steels," *Metall. Trans.*, Vol. 5 (1974), pp. 1457–1470.
7. Troiano, A. R., "The Role of Hydrogen and Other Interstitials in the Mechanical Behavior of Metals," *Trans. ASM*, Vol. 52 (1960), pp. 54–81.
8. Beachem, C. D., "A New Model for Hydrogen-Assisted Cracking (Hydrogen "Embrittlement")," *Metall. Trans.*, Vol. 3 (1972), pp. 437–451.
9. Birnbaum, H. K. and Sofronis, P., "Hydrogen-Enhanced Localized Plasticity: A Mechanism for Hydrogen-Related Fracture," *Mater. Sci. Eng.*, Vol. A176 (1994), pp. 191–202.

Effects of Hydrogen on Materials
Proceedings of the 2008 International Hydrogen Conference
Brian Somerday, Petros Sofronis, Russell Jones, editors, p 113-122
Copyright © 2009 ASM International®
All rights reserved.
www.asminternational.org

EFFECT OF CRACK-TIP HYDROGEN PROFILES ON THE EMBRITTLED FRACTURE TOUGHNESS OF A STAINLESS STEEL

Ryan J. Melcher and Philip E. Schembri
Los Alamos National Laboratory, Los Alamos, NM, USA

ABSTRACT

As part of ongoing work to determine the bounds of transferability of hydrogen embrittled fracture toughness test data, this paper investigates the sensitivity of hydrogen embrittled fracture toughness to modification of the crack tip hydrogen field. Compact tension fracture specimens manufactured from 21Cr-6Ni-9Mn stainless steel are preconditioned in 63 MPa hydrogen at 300˚C to achieve a uniform internal hydrogen concentration. Once uniformly preconditioned, the pressure and temperature are controlled to partially remove hydrogen from the crack tip subsurface, creating a hydrogen profile in the region in which the plastic strains are expected to be highest during the fracture test. Standard *J*-R curve fracture toughness tests are then performed on each specimen in ambient air. Differing fracture toughness between specimens with different hydrogen profiles would be evidence that the hydrogen affected fracture mechanism is active mainly within the large plastic strain region ahead of the crack tip and is sensitive to these concentration perturbations. This knowledge would then provide insight into whether toughness data obtained using hydrogen preconditioned specimens is transferable to components in hydrogen service.

INTRODUCTION

For applications that do not involve environmental effects such as hydrogen assisted cracking, the conditions necessary to ensure the appropriateness of a fracture toughness test in evaluating the integrity of a defect-containing component – that is, the data's *transferability* - have been studied extensively and are well documented, e.g. [1-3], and standardized [4]. While linear-elastic fracture toughness testing standards exist for hydrogen embrittlement [5], such extensive analytical and experimental studies on the transferability of hydrogen embrittled fracture toughness data have not been conducted and are an identifiable need within the scientific community [6]. The assurance of specimen-to-component transferability in the

assessment of hydrogen gas containment structures is the motivation behind the work presented here.

Although hydrogen embrittled fracture toughness data for austenitic stainless steels has been obtained, (e.g., the review compiled by San Marchi and Somerday [7]), assuring transferability of the data is particularly challenging due to inherently low diffusivities (requiring long times to reach equilibrium concentrations) and relatively high retained toughness (eliminating the possibility of size-valid *K*-testing for specimens of a practical size, e.g., as was the case in [8]). Since standardized, hydrogen embrittled linear-elastic fracture toughness results [5] may not be obtainable for this class of materials, it would be of great value to determine whether elastic-plastic *J*-R curve tests on hydrogen pre-conditioned specimens could be shown to give equivalent results to structures or specimens loaded and exposed to hydrogen gas for long times, i.e. in the spirit of the study performed by Moody et al. [9]. Although this rather grand objective is beyond the scope of the present study, it is hoped that the results presented here will inform and motivate such a study.

To gain a rudimentary understanding of the effect of differing crack tip conditions between specimen and component (i.e., to build a knowledge base that will eventually allow assessment of whether transferability has been achieved), the hydrogen field in a fracture toughness specimen was intentionally varied by controlled off-gassing at the crack tip after uniform hydrogen preconditioning. The applied *J*-integral was then recorded at both the provisional fracture toughness J_Q and the onset of visible tearing, as observed through in-situ optical microscopy, for the three conditions of 1) as-received, 2) "uniformly" hydrogen saturated and 3) hydrogen saturated and partially off-gassed.

EXPERIMENT DESCRIPTION

Material and Specimen Definitions

An axisymmetric, cylindrically shaped 21Cr-6-Ni-9Mn stainless steel forging was investigated in this study due to its current use in hydrogen containment vessels. The material chemistry and engineering tensile properties of the forging, in both as-received and hydrogen exposed conditions, are provided in Table 1. It is noted that the tensile properties exhibited a seemingly unique trend of being slightly improved with hydrogen exposure. Delta ferrite content and ASTM standard grain size of the forging was found to be < 0.5% and 8.5, respectively. Variability in room temperature fracture toughness behavior of the forging due to inhomogeneity and anisotropy were examined in an internal, unpublished study and found to be minimal, thereby not confounding the results of the current study.

Table 1: Chemistry and room temperature tensile properties of the selected 21Cr-6Ni-9Mn forging, in both as-received and uniformly hydrogen charged conditions.

Al	C	Cr	Mn	N	Ni	O	P	S	Si
.02	.027	20.84	8.75	0.28	6.86	.005	.016	.0002	0.54

Condition	0.2% YS (MPa)	Ultimate TS (MPa)	Unif. Elong. (%)	Fract. Strain (%)
As-Received	725	910	22.5	41.5
7900 appm H	745	950	26.5	44.9

Standard compact tension (C[T]) fracture toughness specimens were selected for study, having a width (W) dimension of 12.7 mm and a specimen width to thickness ratio of 2:1 due to forging geometry constraints. Integral knife-edges with a gage spacing of 1.9mm were machined into the specimen to facilitate load-line displacement measurement. After fatigue pre-cracking to a nominal a/W ratio of 1:2, 0.6mm deep specimen side-grooves with an included angle of 75° and root radius of 0.3mm were cut, providing an overall specimen thickness reduction of 20%.

Hydrogen Exposure

To examine the effect of hydrogen exposure, the specimens were pre-conditioned by immersing them in a pressure vessel at 63 MPa of 99.999% hydrogen at 300°C for 53 days, a procedure often referred to as hydrogen "charging". No mechanical load was applied to the specimens during exposure. The parameters and duration of exposure were selected so as to provide a uniformly distributed internal hydrogen concentration of 7900 appm in the specimen using the hydrogen solubility relationships and constants summarized by San Marchi et al [10].

After the predetermined duration of charging at elevated temperature was completed, the charging pressure vessel was slowly cooled down for 2 hrs to near 125°C while simultaneously raising the hydrogen pressure (up to a maximum of 125 MPa) to maintain a constant specimen surface solubility of 7900 appm during the period of high hydrogen diffusivity during initial cool-down. After the maximum pressure had been reached, the vessel was then rapidly cooled to room temperature (in ~20 min.), after which the hydrogen pressure was vented and the specimens extracted and placed in a freezer at -54°C. This detailed cool-down procedure was executed to ensure that the internal hydrogen distribution near the crack-tip surface remained near uniform with a sharp step-function gradient at the surface (to the 0 appm H air boundary condition present during the subsequent tests).

After charging, some of the hydrogen charged specimens were removed from the freezer and plated with a ~1μm thick, low hydrogen solubility gold plating on all specimen machined surfaces (not including the pre-crack fracture surface). This process was performed within 24 - 48 hrs at room temperature. Subsequently, these

specimens were exposed to 240°C for 72 hrs under vacuum. The purpose for this procedure was to remove ("off-gas"), via the pre-cracked surface, some of the internal hydrogen from the region very near the crack tip, uniformly along the length of the crack front. However, this technique of blocking the hydrogen off-gassing from all surfaces except the crack mouth with the plating proved unsuccessful, as subsequent hydrogen determination analysis on fully gold-plated test discs showed full off-gassing after exposure to the high temperature vacuum treatment. As a result, this off-gassing step on the fracture specimens, while creating a near tip hydrogen concentration gradient along the crack advance direction, also likely created a gradient in concentration at the crack edges (specimen faces). Nonetheless, the off-gassing treatment still enables study of the effect of the hydrogen profile along the crack advance direction (depth).

Fracture Toughness Testing

Fracture toughness tests were performed in accordance with the requirements of ASTM E1820-06 [4] in room temperature ambient air on all of the three specimens conditions. Loading was applied through E1820-style 0.24(W) pin clevis grips with universal joints on a 10kN load cell equipped 100kN servohydraulic load frame. Crack extension was measured throughout the tests using the elastic compliance method. A load-line displacement rate of .025 mm/min was used in the tests. A full test was therefore completed in approximately 45 min., a time insufficient to allow significant internal hydrogen redistribution (by diffusion) at room temperature. Standard J-R curves and J_Q (provisional toughness) values were calculated per ASTM E1820-06. Multiple replicates were tested for each material condition to provide a qualitative measure of repeatability.

During fracture toughness test execution, the specimen crack tip was monitored with a horizontally mounted zoom system optical microscope equipped with a charge-coupled device (CCD) camera for digital image acquisition. This arrangement allowed monitoring of the crack tip blunting and tearing process to more closely examine the onset of tearing during the standard fracture test, a technique documented more thoroughly in [11].

Mechanics and Diffusion Modeling

A finite element model was used to estimate the distribution of the hydrogen concentration around the crack tip relative to the fracture process zone (i.e. the region of elevated plastic strain and hydrostatic stress in which material damage occurs). The model (including the mesh) was similar to that described in [12], except that since the hydrogen charging did not occur under load, a coupled stress/diffusion model was not necessary; therefore, the deformation and diffusion calculations were performed independently for the present study. Hydrogen trapping was neglected, a hardening curve was used that yields the tensile properties given in Table 1, and the diffusivity and solubility recommended by [10] were used in the calculations. Material damage is not explicitly calculated in this model.

RESULTS AND DISCUSSION

J-R Curve and J_{IC}

The resulting *J*-R curves for the three conditions are shown in Fig. 1. The average J_Q fracture toughness values obtained from these curves for the as-received, uniform H and partially off-gassed conditions were 490, 170 and 290 kJ/m^2 respectively. Given the small specimen size and relatively high retained ductility, only the uniform H concentration condition produced size-independent (transferable stress state) J_{IC} toughness values per E1820-06.

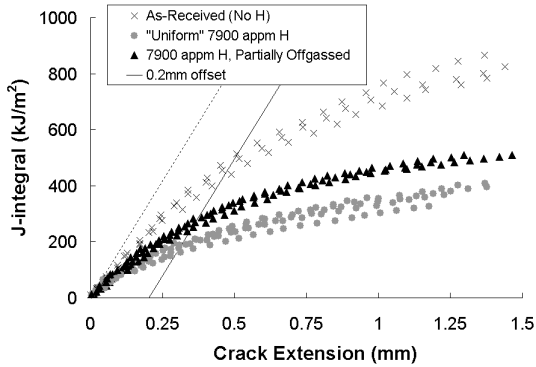


Figure 1: Effect of specimen crack-tip hydrogen concentration profiles on the J-R curves for the as-received, uniformly charged and partially off-gassed conditions.

It is readily apparent from the *J*-R curves of Fig. 1 that hydrogen affects both the initiation and tearing behavior of this forged stainless steel. However, it is more noteworthy that the resulting J_Q averages for the uniform and partially off-gassed conditions differed significantly, with the J_Q value for the partially off-gassed condition being higher, yet not as elevated as that of the as-received condition. A simple conclusion is that the partially off-gassed J_Q results are not transferable in the analysis of components exposed to hydrogen, as one might have expected at the outset. However, in comparing the R-curve behavior for the uniform and partially off-gassed conditions, it is noted that the tearing modulus (slope of the R-curve) of the two conditions appear to become similar at a crack extension of ~1mm. This similarity will be explored further in the analysis of the internal hydrogen distribution.

Optical Microscopy

Digital images of the blunting and initial tearing process for one of the "uniformly" charged specimens, as viewed from the root of the specimen side-groove, are shown in Fig. 2. The first image in Fig. 2, taken at an applied *J*-integral of 85 kJ/m^2, is just prior to the onset of visible tearing from the blunted crack tip. The second image, taken at an applied *J*-integral of 180 kJ/m^2, is approximately at the value of J_{IC} for the specimen. In comparing the two photographs, it is evident that at a value of J_{IC}, appreciable tearing has occurred, as is expected in the use of a *J*-R curve toughness determination method [13]. Consideration of this behavior is critical in the potential comparison of any *J*-R curve derived toughness data with that from other embrittlement test methods (e.g. [5]) - equivalence or transferability in the test specimen hydrogen concentration distributions notwithstanding.

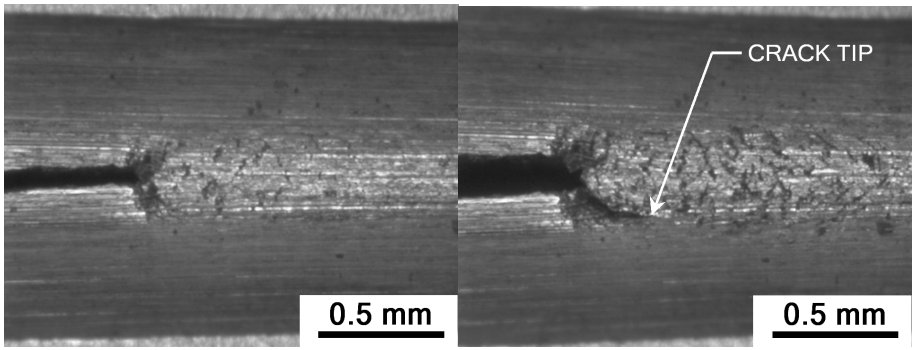


Figure 2: Optical microscopy images from a "uniformly" charged specimen near visible tearing onset, 85 kJ/m^2 (L), and at J_{IC}, 180 kJ/m^2 (R).

Also evident in Fig. 2 are the apparent damage processes occurring at and ahead of the crack tip. Crack propagation appears to initiate from the blunted pre-crack tip, growing into the void-filled (i.e. damaged) region ahead of the tip. Direct conclusions from this and the previous observation of visible tearing onset "toughness" are limited by the fact that they are surface observations (i.e. through-thickness inconsistency of the stress state and hydrogen concentration is possible). However, previous analyses [14] have shown the side-groove root to represent the mid-thickness stress state relatively well at these specimen loading levels. In addition, the constant-solubility cooling of the specimens at the conclusion of charging provided a uniform hydrogen concentration in the lattice up to the subsurface as close as practicably possible.

Figure 3 presents the effect of the hydrogen exposure and subsequent partial off-gassing on both the visible onset of tearing from microscopy and the *J*-R derived provisional fracture toughness. It is evident in the comparisons of Fig. 3 that while the off-gassing of the uniformly charged specimens appeared to cause an increase in the *J*-R derived toughness measures (J_Q or J_{IC}), the onset of visible tearing is even more so affected, increasing to the same average as that of the as-received

specimens. This observation is consistent with the observation that crack initiation occurs at the root of the blunted notch, where the hydrogen concentration of the partially off-gassed specimens is most depleted.

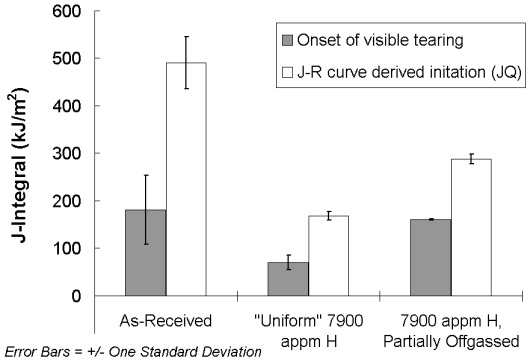


Figure 3: Comparison of crack-tip hydrogen concentration profile effects on both the visual tearing onset and J-R curve derived tearing onset.

Calculated Crack-Tip Hydrogen Profile

The finite element results shown in Fig. 4 provide insight into the conditions about the crack-tip during the fracture test. In the figure, normalized plastic strain and hydrostatic stress values at an applied *J*-integral loading of ~165 kJ/m^2 (near visible tearing onset) are presented along with the calculated lattice hydrogen concentration profiles for both the "uniformly" charged and partially off-gassed conditions.

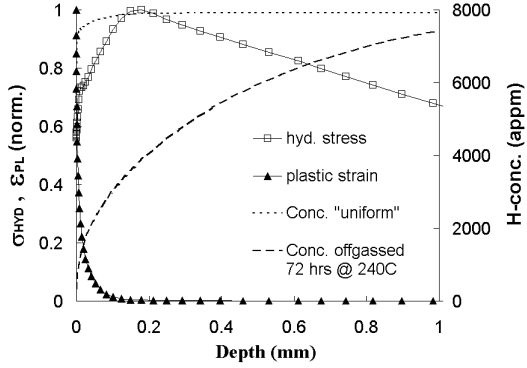


Figure 4: Comparison of calculated crack-tip hydrogen concentration profiles, hydrostatic stress and plastic strain in a specimen near the onset of visible tearing.

In evaluating the typical near-tip stress and strain results and comparing them with the "uniform" concentration condition microscopy images of Fig. 2, it can be deduced that the onset of tearing (as observed in the microscopy) appears to most likely proceed from the region of high strain rather than the region of maximum

hydrostatic stress. This, coupled with the stable tearing *J*-R curve specimen behavior witnessed in the tests, supports the inference that the mechanism of crack extension in this material system (i.e. forging) in hydrogen is strain-driven. This enables the use of the ductile crack extension specimen-size requirement (J_{IC}) conditions for assuring transferability of the stress state / fracture-process zone rather than stress-based requirements (e.g. J_C) of E1820-06.

In viewing the concentration profile results, it can be seen that the partially off-gassed concentration reaches ~90% of the uniform concentration at a depth of ~1mm – the same point at which the *J*-R curve tearing modulus results of the two conditions appeared to become similar. Hence, from the standpoint of "environmental transferability", the tearing modulus results of both conditions after ~1mm of tearing appear to be transferable, e.g., to the analysis of structural tearing through a truly uniform internal H concentration. (Note, however, that mechanically loaded cracks in hydrogen will *not* have a uniform near-tip *equilibrium* concentration, e.g., [12]). In a similar fashion, since the "uniform" concentration condition reaches ~90% of true uniformity at a much shallower depth of only microns, one might postulate that the shape of the entire *J*-R curve for the "uniform" concentration condition is fully transferable (both concentration and stress-state). However, due to the high initial slope of the *J*-R curve and the possible differences in crack tip blunting and visible tearing behavior, assertions of the transferability of either J_{IC} or visible tearing onset cannot be made without further investigations. Namely, comparison of these or similar hydrogen charged tests with those performed with a truly uniform internal hydrogen concentration – that only achieved in a pressurized hydrogen gas environment – must be made in order to establish the transferability of either measures of tearing onset. It is noted that such a comparison may be logistically difficult, as very high pressures are needed to achieve the same solubility in a room temperature test as that in the elevated charging conditions (e.g. >200 MPa at room temperature to create surface concentrations equivalent to the internal concentrations at charging in these tests). Many other hydrogen-material interactions may also be of influence in the high plastic strain region of the crack tip, which are not captured here, providing further necessity for in-gas testing to ensure equivalence.

CONCLUSIONS AND RECOMMENDATIONS

In this study, the effect of a modification to the crack tip hydrogen field of pre-charged 21Cr-6Ni-9Mn austenitic stainless steel C[T] specimens was studied. The *J*-R curve derived provisional toughness J_Q was compared to visible tearing onset from microscopy, and the material damage was observed in relation to the hydrogen concentration, the hydrostatic stress, and plastic strain fields. It was observed that:

1. The onset of tearing occurs at a *J*-integral level significantly lower than J_Q for all conditions tested (including the as-received condition)

2. The tearing modulus is the same for the "uniformly" charged and partially off-gassed specimens once the crack has grown into the region of a 90% equivalent hydrogen concentration
3. Significant material damage is visible in the region of high hydrostatic stress, while crack initiation appears to occur in the region of highest plastic strain.

Although uncertainties exist in the interpretation of the results due to the possible loss of hydrogen at the side faces of the specimens, there is evidence to suggest that both J_Q and visible tearing onset do indeed vary when hydrogen is not uniform near the crack tip. A possible explanation for the observed tearing modulus behavior may be that the tearing modulus is a function of the amount of damage induced by the hydrostatic stress field, which is likely a function of the hydrogen concentration. But if the effect of this damage on the *J*-integral required to *initiate* tearing is negligible (which has not been proven here), then the initiation depends mostly on the hydrogen concentration present in only the plastic strain region. While the present results are certainly consistent with such an explanation, they also do not provide enough information to prove it. Nevertheless, these results do provide strong motivation to investigate these relationships more closely. Indeed, it must be emphasized that without a more thorough understanding of the conditions necessary for transferability (such as we have with non-embrittled fracture toughness) the wealth of hydrogen embrittled toughness data that has been (and is being) generated is at risk of being inappropriately utilized.

ACKNOWLEDGMENTS

The authors would like to thank Brian Somerday, Petros Sofronis and Dorian Balch for the many collaborative discussions regarding this subject. Los Alamos National Laboratory is operated by Los Alamos National Security, LLC for the National Nuclear Security Administration of the U.S. Department of Energy under contract DE-AC52-06NA25396.

REFERENCES

1. Brown, W. F. and Strawley, J. E., Plane Strain Crack Toughness Testing of High Strength Metallic Materials, ASTM STP 410, ASTM International (West Conshohocken, PA, 1966), pp. 16-27.
2. McMeeking, R. M. and Parks, D. M., "On Criteria for *J*-Dominance of Crack-Tip Fields in Large-Scale Yielding," *Elastic-Plastic Fracture, ASTM STP 668,* ASTM International (West Conshohocken, PA, 1979), pp. 175-194.
3. Landes, J. D. and Begley, J. A., "Test Results from *J*-Integral Studies: An Attempt to Establish a J_{IC} Testing Procedure," *Fracture Analysis, ASTM STP 560,* ASTM International (West Conshohocken, PA, 1974), pp. 170-186.
4. ASTM Standard E1820-06e1, "Standard Test Method for Measurement of Fracture Toughness," *Annual Book of ASTM Standards, Vol. 03.01*, ASTM International (West Conshohocken, PA, 2006).

5. ASTM Standard E1681-03, "Standard Test Method for Determining a Threshold Stress Intensity Factor for Environment-Assisted Cracking of Metallic Materials," *Annual Book of ASTM Standards, Vol. 03.01*, ASTM International, (West Conshohocken, PA, 2003).
6. Gangloff, R. P., in Comprehensive Structural Integrity, Elsevier Ltd. (Oxford, 2003), pp. 31-101.
7. San Marchi, C. and Somerday, B. P., Technical Reference on Hydrogen Compatibility of Materials, Sandia Report SAND2008-1163, Sandia National Laboratories (Livermore, CA, 2008). http://www.ca.sandia.gov/matlsTechRef/
8. Perra, M. W., "Sustained-Load Cracking of Austenitic Steels in Gaseous Hydrogen" *Environmental Degradation of Engineering Materials in Hydrogen*, Blacksburg, VA, 1981, pp. 321-333.
9. Moody, N. R., Perra, M. W. and Robinson, S. L., "Hydrogen-Induced Cracking in an Iron-Based Superalloy IN903," in *Hydrogen Effects in Material Behavior,* Moody, N.R. and Thompson, A.W., Eds., (1990), pp.625-634.
10. San Marchi, C., Somerday, B. P. and Robinson, S. L., "Permeability, Solubility and Diffusivity of Hydrogen Isotopes in Stainless Steels at High Gas Pressures," *International Journal of Hydrogen Energy*, Vol. 32 (2007), pp. 100-116.
11. Melcher, R. J., "Evaluating the Onset of Tearing in Elastic-Plastic Fracture Toughness Testing Using In Situ Optical Microscopy", *Journal of Testing and Evaluation*, (2009), in press.
12. Schembri, P. E., "Sensitivity to Temperature and Material Properties of Hydrogen Concentration at a Crack Tip in Austenitic Stainless Steel", To be published in these proceedings.
13. Roos, E. and Eisele, E., "Determination of Material Characteristic Values in Elastic-Plastic Fracture Mechanics by Means of *J*-Integral Crack Resistance Curves," *Journal of Testing and Evaluation*, Vol. 16, No. 1 (1988), pp. 1-11.
14. Shih, C. F., deLorenzi, H. G. and Andrews, W. R., "Elastic Compliances and Stress-Intensity Factors for Side-Grooved Compact Specimens", *International Journal of Fracture*, Vol. 13 (1977), pp. 544-548.

Effects of Hydrogen on Materials
Proceedings of the 2008 International Hydrogen Conference
Brian Somerday, Petros Sofronis, Russell Jones, editors, p 123-130
Copyright © 2009 ASM International®
All rights reserved.
www.asminternational.org

HYDROGEN-INDUCED CRACKING OF METASTABLE AUSTENITIC STAINLESS AND HIGH-STRENGTH CARBON STEELS

Y. Yagodzinskyy, T. Saukkonen, E. Andronova, L. Rissanen and H. Hänninen
Laboratory of Engineering Materials, Helsinki University of Technology, P.O. Box 4200, FIN-02015 HUT, Espoo, Finland

ABSTRACT

Hydrogen effects on mechanical properties of austenitic stainless steels AISI 301, AISI 301LN, AISI 201, duplex stainless steel LDX 2101 and some carbon steels with ultimate tensile stress (UTS) in the range of 600 to 1200 MPa were studied and compared. Slow strain rate and constant load tests were performed with potentiostatic electrochemical hydrogen charging of flat specimens in electrochemical cell. It was shown that austenitic stainless steels strengthened with deformation-induced α'-martensite exhibit a remarkable sensitivity to hydrogen embrittlement. Mn-alloyed AISI 201 austenitic and LDX 2101 duplex stainless steels strengthened by nitrogen alloying were found to be very sensitive to hydrogen-induced failure. Fractography and hydrogen thermal desorption of hydrogen-free and hydrogen-charged steels after slow strain rate tensile (SSRT) test were performed to clarify the differences of hydrogen effects on high-strength austenitic and carbon steels.

INTRODUCTION

Interest in high-strength steels for a variety of industrial applications has markedly increased during last decades, due to the efforts in reduction of energy consumption and environmental problems. It has been found that increase of the strength level of steels can result in deleterious effects on the material properties, particularly, on the increased sensitivity to hydrogen embrittlement. Intensive studies of hydrogen-induced failure phenomena and mechanism have been performed mainly for different microstructural states of high-strength carbon steels [1, 2]. In the same time, high-strength austenitic stainless steels have become the focus of many applications, especially in automotive industry. Providing many beneficial properties for the transport applications, such as high damping capacity and high crash-worthiness, the austenitic stainless steels in high-strength states similarly to high-strength carbon steels can exhibit enhanced sensitivity to hydrogen embrittlement. Austenitic stainless steels, which are traditionally considered as more resistant to hydrogen effects in comparison to carbon steels, in their strengthened states consist

of a variety of microstructural factors, such as strain-induced ε- and α′-martensite [3, 4], fine grain size and hardening precipitates, which can markedly change the sensitivity of the steels to hydrogen-induced failure.
Aim of the present study consists of a comparison of some industrial high-strength carbon and austenitic stainless steels including LDX 2101 duplex stainless steel, in terms of their sensitivity to hydrogen embrittlement. Additional interest of the study belongs to the effects of Mn-alloying on the sensitivity of stainless steels to hydrogen-induced failure. Tendency to substitution of the expensive Ni by Mn with additional austenite stabilizing by nitrogen has become of great importance during the last years.

EXPERIMENTAL

Materials and specimens. A set of nine steels with UTS in the range from 600 to 1200 MPa chosen to study is shown in Table 1.

Table 1. Mechanical properties, phase structure and average grain size of the studied steels.

Material	$R_{p0.2}$, MPa	R_m, MPa	Microstructure Chemical composition	Grain size, μm
HCT800C	715	892	ferrite + martensite 0.1C0.14Si0.013Cr2.17Mn0.01Ni0.02Mo0.024Nb	4.3
TRIP700	479	705	ferrite + austenite (12 %) + martensite + bainite 0.2C0.35Si1.75Mn0.03Cr0.02Ni1.0Al0.019Cu	6.2
DP600CR	402	648	ferrite + martensite (23 %) 0.074C0.13Si1.44Mn0.8Cr0.022Ni0.014Cu	6.1
S700MC	782	819	ferrite + martensite + bainite 0.046C0.19Si1.68Mn0.24Ni0.13Mo0.094Ti0.064Nb	5.0
AISI 301LN 2H/C1000	675	1015	austenite + martensite (7 %), pre-strained 0.026C0.52Si1.18Mn17.9Cr6.59Ni0.09Mo0.223N	4.2
AISI 201	389	732	austenite, annealed 0.055C0.3Si7.1Mn16.9Cr¤.38Ni0.1Mo0.222N	14.1
LDX 2101	583	792	ferrite + austenite, annealed 0.025C0.73Si4.95Mn21.36Cr1.63Ni0.28Mo0.243N	3.7 (aust.) 4.9 (ferr.)
AISI 301 2H/C1000	668	1044	austenite + martensite (4 %), pre-strained 0.11C0.88Si1.18Mn16.9Cr7.1Ni0.29Mo	21.0
AISI 310	316	603	austenite, annealed 0.049C0.56Si0.88Mn25.54Cr19.09Ni0.24Mo0.011Ti	15.5

The carbon steels have ferrite-martensite structure in the case of HCT800C and DP600CR steels, and a fine ferrite-martensite-bainite structure is characteristic for S700MC steel. TRIP700 steel in addition to ferrite-martensite-bainite structure contains also about 12 % of retained austenite.Austenitic stainless steels used in the study consist in as-supplied state of austenite (AISI 201 and AISI 310 steels) or austenite with minor amount of strain-induced α′-martensite in pre-strained

metastable AISI 301 and AISI 301LN steels. Duplex stainless steel LDX 2101 consists of about fifty-fifty ferrite-austenite banded structure, with a characteristic spacing of the bands of about 50 μm. All the steels were supplied in sheet form with thickness from 1.2 to 2.0 mm. Tensile test specimens of 10 × 200 mm plates with gauge length of 5 × 25 mm in the middle of the plate were cut by an industrial laser cutting machine from the as-supplied sheets. The thickness of the gauge length part of the austenitic and duplex stainless steel specimens was reduced to 0.5 mm by machining. The gauge length part of all specimens was mechanically polished with emery paper finishing with No. 2500.

Hydrogen charging procedure. Hydrogen was introduced electrochemically under controlled cathodic overpotential of 100 mV from 1N H_2SO_4 solution with addition of 20 mg/l of thiourea as a hydrogen poison. Electrochemical cell with calomel reference and platinum counter electrodes was de-aerated and kept under N_2-gas bubbling and 50 ^oC or RT for austenitic and carbon steel specimens, respectively. Current density at the applied potential was less than a few mA/cm^2 during the whole charging process for austenitic stainless steels. No hydride or any other new phases were detected with X-ray diffraction method in the specimens after applied hydrogen charging. All specimens were pre-charged with hydrogen before testing for 18 h of austenitic grades and for 2 h of carbon steels.

Experimental methods and techniques. Slow Strain Rate (SSRT) and Constant Load (CLT) mechanical tensile tests were performed by using a 20 kN MTS 858 Desktop Test System equipped with an environmental cell. All SSRT tests were performed with an initial strain rate of 10^{-4} s^{-1}. Time to fracture at applied stress ratio $R = \sigma / \sigma_m$, where σ_m is the ultimate tensile stress of the steel, was used as the main parameter in CLT tests for hydrogen-charged specimens. Except the SSRT tests for stainless steels all the tests were performed with continuous hydrogen charging.

Fractography of the specimens after SSRT or CLT was obtained using FEG-SEM Zeiss Ultra 55. Hydrogen thermal desorption spectra were obtained at constant heating rate of 6 ^oC/min in the temperature range from 50 to 650 ^oC by measuring the hydrogen partial pressure in the UHV chamber of a TDS apparatus. The basic vacuum in the apparatus was kept better than 10^{-7} mbar.

RESULTS AND DISCUSSION

SSRT tensile tests. SSRT tensile test stress-strain curves for carbon and austenitic stainless steels are shown in Figs 1 a and b. Except AISI 310 austenitic stainless steel all the tested materials exhibit a remarkable sensitivity to hydrogen embrittlement, especially the carbon steels, the elongation of which drops to less than 10 % after hydrogen pre-charging for 2 h. Metastable austenitic stainless steels AISI 301 and AISI 301LN, which were strain-hardened resulting in small amounts of strain-induced α´-martensite, exhibit also reduction of elongation to fracture after hydrogen pre-charging for 18 h at 50 ^oC. Yield strength values were only slightly affected by hydrogen in metastable austenitic and in AISI 201 stainless steels, while more pronounced effects take place in stable AISI 310 and duplex LDX 2101 steels. Similarly to results obtained in [5], $R_{p0.2}$ value of AISI 310 steel increases about 10

% after hydrogen charging (Fig. 1a, curve 1). The opposite effect of hydrogen pre-charging (see Fig. 1a, curve 5) takes place for LDX 2101 steel. The origin of the yield stress reduction for duplex stainless steel caused by hydrogen is still unclear. Mn-alloyed stable austenitic stainless steel AISI 201 and duplex stainless steel LDX 2101 show high sensitivity to hydrogen embrittlement with about 50 % reduction of elongation to fracture relative to that for hydrogen-free specimens. Reduction of elongation to fracture of the ferrite-martensite carbon steels (see Fig. 1b, curves 1, 3) increases with the yield strength. TRIP700 carbon steel containing about 12 % of retained austenite shows highest sensitivity to hydrogen (Fig. 1b, curve 2), while the ferrite-martensite-bainite S700MC steel with markedly higher yield and tensile strength exhibits the best resistance to hydrogen-induced failure among the carbon steels. Origin of the favorable effect of the ferrite-martensite-bainite microstructure is still under study.

Constant Load Tests. All the studied steels were tested at constant applied stress ratio $R = 0.8$. Time to fracture in CLT is shown for the tested steels in Fig. 2. It was found for high-strength carbon steels that the time to fracture in CLT decreases with the increasing ultimate tensile strength, except for the ferrite-martensite-bainite S700MC steel. The times to fracture for austenitic stainless steels, however, do not show any correlation with corresponding R_m values. Duplex stainless steel LDX 2101 has a medium value of the time to fracture as compared to that for the austenitic stainless steels. Short times to fracture at $R = 0.8$ were found for Mn-alloyed stable AISI 201 austenitic stainless steel and ferrite-martensite HCT800C carbon steel. These steels were also tested at different applied stress ratios in order to estimate the threshold of the applied stress, at which the material becomes resistant to hydrogen-induced fracture. No threshold stress value was found for both steels down to applied stress ratio of $R = 0.35$ (see Fig. 3). It has also to be noticed that the linear approximation of the experimental data R *vs* log t_f evidences that AISI 201 austenitic stainless steel is more sensitive to hydrogen-induced fracture than HCT800C carbon steel.

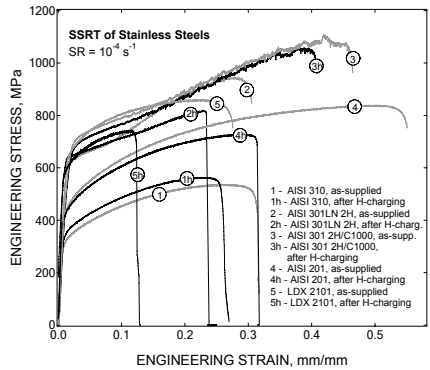


Figure 1a. SSRT stress-strain curves of studied austenitic (1 – 4), and duplex (5) stainless steels. Strain rate is 10^{-4} s^{-1}.

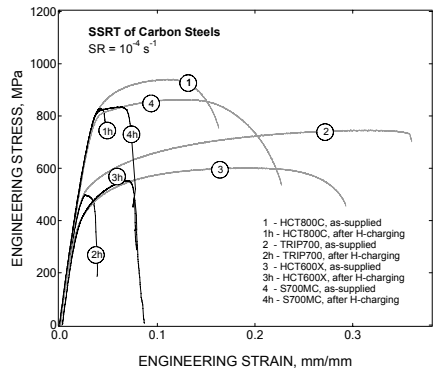


Figure 1b. SSRT stress-strain curves of studied carbon steels. Strain rate is 10^{-4} s^{-1}.

Fractography. After hydrogen charging SSRT tests were made also in air for stainless steels to produce clean fracture surfaces of all the test materials for

fractography. For carbon steels SSRT was performed under hydrogen charging in the cell to guarantee the presence of hydrogen. In the following only the fractography of the hydrogen charged specimens is shown. SSRT testing was also performed in air for non-charged specimens and all samples showed relatively high reduction of area, necking and ductile fracture surface.

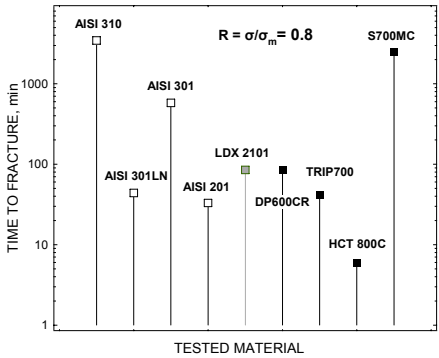


Figure 2. Time to fracture in CLT of the studied steels with applied stress ratio R = 0.8.

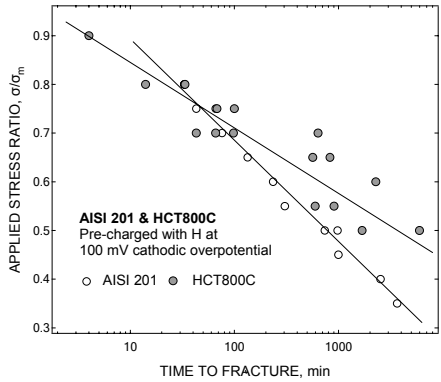


Figure 3. Time to fracture in CLT of AISI 201 and HCT800C steels as a function of applied stress ratio.

Stainless steels showed marked hydrogen embrittlement in the surface layers, because of nonhomogeneous distribution of hydrogen in the samples. The brittle fracture surface is mainly transgranular, but cracking takes place also along twin boundaries of the steels [6]. In duplex LDX 2101 stainless steel cracking is transgranular brittle fracture in both phases, austenite and ferrite. C-steels showed mainly ductile fracture surface even though the elongation to fracture was always markedly reduced by hydrogen. Ductile dimpled fracture surface of hydrogen charged specimens shows different dimple size and shape as compared to the fracture surface produced in air. If brittle quasi-cleavage fracture was observed it always initiated from the corners of the sample or from the edge (see Figs 4 f and h). Brittle fracture surface was mainly transgranular with varying features of ductility – in higher strength materials the fracture surface was more brittle.

Measurements of hydrogen thermal desorption. Studied steels exhibit rather different hydrogen desorption spectra. Thermal desorption spectrometry (TDS) curves of metastable AISI 301LN austenitic stainless steel are shown in Fig. 5 a. In contrast to the only one peak of the hydrogen desorption from the hydrogen pre-charged, as-supplied steel located around 260 ^{o}C, two peaks appear at about 230 and 470 ^{o}C for the TDS-sample which was cut from the gauge length of the CLT specimen after testing. The shift of the main peak to lower temperature is probably caused by an enhancement of the apparent diffusion of hydrogen in the presence of strain-induced α'-martensite. The detailed origin of the second, high-temperature peak is still unclear. One can assume that it results from hydrogen leaving the hydrogen-filled voids, which form in the steel during plastic strain instabilities before fracture. The similar, but markedly pronounced high-temperature peak of hydrogen desorption was observed in stable AISI 201 austenitic stainless steel after

fracture in CLT, which exhibits highest sensitivity to hydrogen embrittlement (see Fig. 5 b). TDS-curves of duplex stainless steel LDX 2101 shown in Fig. 5 c manifest complex behaviour.

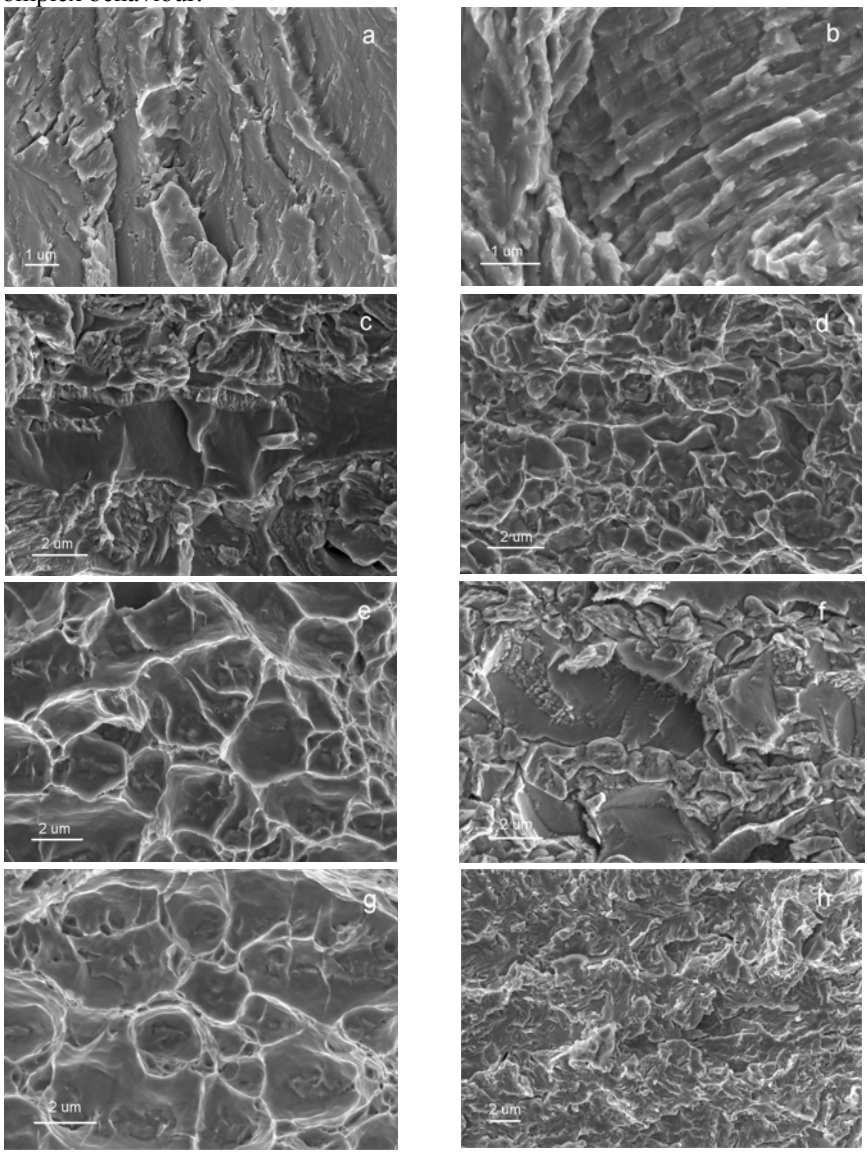


Figure 4. Fractography of the studied steels after H-charging and SSRT with strain rate of 10^{-4} s^{-1}. a, b: AISI 301LN and AISI 201 austenitic stainless steels, respectively; c: LDX 2101 duplex stainless steel; d: HCT800C carbon steel; e, f: TRIP700 carbon steel from middle and corner part of the SSRT specimen, respectively; g,h: S700MC carbon steel, as the previous case.

The hydrogen pre-charged LDX 2101 steel in as-supplied state shows hydrogen desorption from austenite phase (peak at about 260 °C) only, while LDX 2101 steel after fracture in CLT exhibits hydrogen evolution mainly from the ferrite phase or from the interfaces (peak below 200 °C), where the diffusion of hydrogen is higher than in the austenite phase. The second peak of hydrogen desorption from the fractured duplex stainless steel (about 330 °C) may originate from the residual hydrogen in the austenite phase or it may correspond to hydrogen release from vacancy-type trapping sites induced in the ferrite by plastic strain [7].
Only one broad peak of hydrogen desorption was observed in ferrite-martensite HCT800C carbon steel (see Fig. 5 d) after its fracture in CLT. The peak may consist of several components and its more detailed study will be performed.

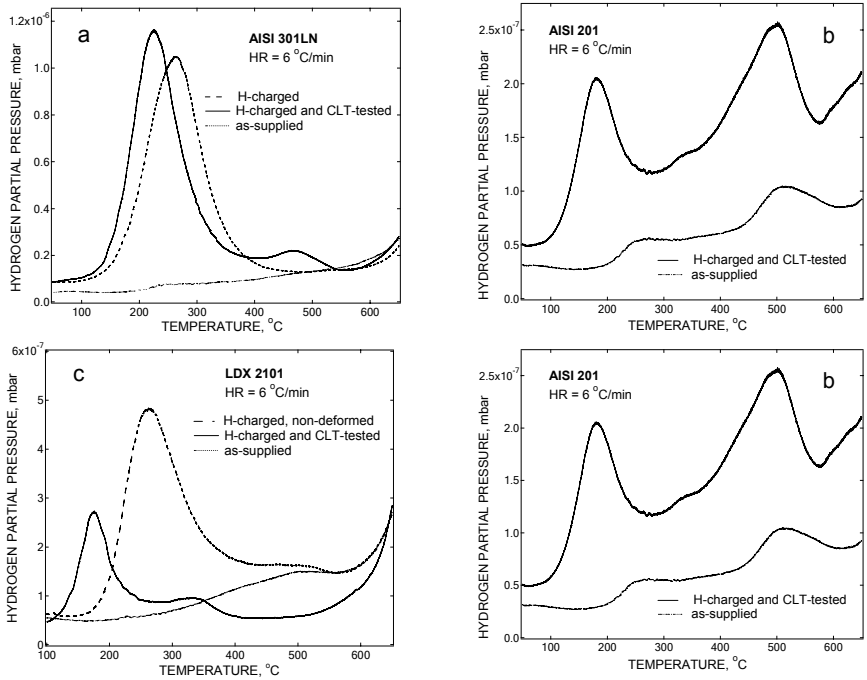


Figure 5. Temperature dependencies of hydrogen partial pressure in TDS apparatus for some of the studied steels. Heating rate is 6 °C/min.

CONCLUSIONS

Austenitic stainless steels strengthened by strain-induced α'-martensite exhibit a remarkable, while less than carbon steels, sensitivity to hydrogen embrittlement in SSRT. Mn-alloyed stainless steels, namely stable austenitic AISI 201 and duplex LDX 2101 stainless steel, are more sensitive to hydrogen than metastable AISI 301 and AISI 301LN steels.
In contrast to high-strength carbon steels, the strengthened austenitic stainless steels do not exhibit a reduction of the time to fracture with increasing tensile strength in CLT. Mn-alloyed AISI 201 austenitic stainless steel shows in CLT markedly higher

sensitivity to hydrogen embrittlement in comparison to highest strength ferrite-martensite HCT800C carbon steel.
Fractography of the austenitic stainless steels shows mainly a brittle, cleavage-like fracture morphology, while the studied carbon steels exhibit both quasi-cleavage and dimpled fracture with larger dimple size as compared to hydrogen-free ductile fracture. Fractography together with obtained TDS data indicates on rather different mechanisms of hydrogen embrittlement in high-strength austenitic and carbon steels.

ACKNOWLEDGEMENTS

This study has been supported by the Research Programme of the Research Fund for Coal and Steel of European Community.

REFERENCES

1. McIntyre P., "Hydrogen Effects in High Strength Steels", Hydrogen Degradation of Ferrous Alloys, R. A. Oriani, J. P. Hirth and M. Smialowski, eds., Noyes Publications, New Jersey, (1995), pp. 763-798.

2. Nagumo M., "Hydrogen Related Failure of Steels – a New Aspect", *Mater. Sci. Tech.,* Vol. 20 (2004), pp. 940-950.

3. Talonen J., Hänninen H., "Formation of shear bands and strain-induced martensite during plastic deformation of metastable austenitic stainless steels", *Acta Mater.* , Vol. 55 (2007), pp. 6108-6118.

4. Narita N., Altstetter C. J., and Birnbaum H. K., "Hydrogen-Related Phase Transformations in Austenitic Stainless Steels", *Metall. Mater. Trans. A*, Vol. 13A (1982), pp. 1355-1365.

5. Abraham D. P., Altstetter C.J., "The Effect of Hydrogen on the Yield and Flow Stress of an Austenitic Stainless Steel", *Metall. Mater. Trans. A*, Vol. 26A (1995), pp. 2849-2858.

6. Caskey G. R., "Hydrogen Effects in Stainless Steels", Hydrogen Degradation of Ferrous Alloys, R. A. Oriani, J. P. Hirth and M. Smialowski, eds., Noyes Publications, New Jersey, (1995), pp. 822-862.

7. Nagumo M., Tamaoki T., Sugawara T., "Functions of Microstructures in Delayed Fracture of Martensitic Steels", Hydrogen Effects on Material Behavior and Corrosion Deformation Interactions, N. R. Moody, A. W. Thompson, R. E. Ricker, G. W. Was and R. H. Jones, eds., The Mineral, Metals and Material Society, New York, (2002), pp. 999-1008.

Effects of Hydrogen on Materials
Proceedings of the 2008 International Hydrogen Conference
Brian Somerday, Petros Sofronis, Russell Jones, editors, p 131-138
Copyright © 2009 ASM International®
All rights reserved.
www.asminternational.org

HYDROGEN-INDUCED FATIGUE CRACK GROWTH ACCELERATION AND MARTENSITIC TRANSFORMATION OF AN AUSTENITIC STAINLESS STEEL

T. Kanezaki, Y. Mine, S. Matsuoka and Y. Murakami
Research Center for Hydrogen Industrial Use and Storage, National Institute of Advanced Industrial Science and Technology, and Department of Mechanical Engineering Science, Kyushu University, Fukuoka, Japan

INTRODUCTION

Research and development on the industrial use and storage of hydrogen are being accelerated in order to achieve the "Low-Carbon Society" with using hydrogen. Significant resources are being expended for the development and commercialization of fuel cell vehicles (FCV) and stationary fuel cell (FC) systems. Austenitic stainless steels are used for various components in FC systems. However, hydrogen embrittlement in austenitic stainless steels has been reported in many studies [1-2]. In order to ensure the long term safety and reliability of FC systems, it is essential to quantify the effects of hydrogen on the mechanical properties of the structural materials. The influence of hydrogen on fatigue strength is of particular importance from the view point of the service loading of FC and the related infrastructure. In this study, the effect of hydrogen and test frequency on the fatigue crack growth of a type 304 austenitic stainless steel was investigated in terms of hydrogen migration in the vicinity of the fatigue crack tip. It is presumed that a martensitic transformation in the vicinity of the fatigue crack tip enhances hydrogen diffusion. Therefore, the electron back scatter diffraction (EBSD) method was applied to investigate the martensitic transformation in the vicinity of the fatigue crack tip.

MATERIAL, SPECIMEN AND EXPERIMENTAL METHODS

Material and Specimen

A 304 type austenitic stainless steel (JIS SUS304) was used. Table 1 shows the chemical composition of the material. The Vickers hardness (Load: 9.8 N) of specimen was HV = 176. The observed scatter in 20 hardness measurements was ±3% or less. The 0.2% proof stress is 309 MPa and the tensile strength is 713 MPa. Round bars of SUS304 were solution heat-treated and subsequently machined to fatigue specimens. Specimen surfaces were polished using #2000 emery paper followed by final buffing with a colloidal SiO_2 (0.04 μm) solution. After polishing, a small hole with a diameter of 100 μm and a depth of 100 μm was drilled into the

specimen surface to serve as a point of crack initiation. Figures 1 (a) and (b) show the dimensions of the fatigue specimen and the small hole.

*Table 1: Chemical composition of SUS304 (wt. %, * wt. ppm).*

C	Si	Mn	P	S	Ni	Cr	H*
0.06	0.36	1.09	0.030	0.023	8.19	18.66	2.2

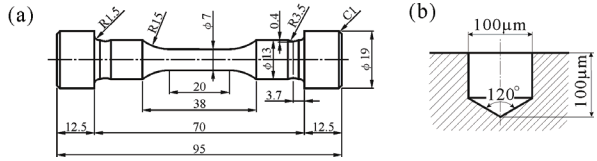


Figure 1: Dimensions of (a) the fatigue test specimen and (b) drilled hole.

Fatigue Tests

Before the fatigue test, 200 μm pre-crack was introduced by fatigue test in air at 1.0 Hz at a stress ratio $R = -1$. Fatigue tests of specimens with a 200 μm pre-crack were carried out at room temperature in laboratory air and a 0.68 MPa (in absolute pressure) H_2 gas at testing frequencies 0.0015 to 1.0 Hz at a stress ratio $R = -1$. The purity of the H_2 gas is 99.999 vol. %. Following the fatigue tests, in order to measure the hydrogen contents remaining in specimens, 0.8 mm thick disks were immediately cut from each specimen, under water-cooling. Then, hydrogen contents of disks were measured by thermal desorption spectrometry (TDS) using a quadruple mass spectrometer. The measurement accuracy of the TDS is 0.01 wt.ppm. Measurements were carried out up to 800 °C at a heating rate of 0.5 °C/s. The volume fractions of martensite on the specimen surfaces and on the fracture surfaces were measured by X-ray diffraction (XRD) using monochromatic Cr-Kα radiation. The martensite content was evaluated by the ratio of the integrated intensity of the {220} austenite and the {211} martensite peaks. The martensite contents of the solution-treated SUS304 were ≤ 3 vol. % before fatigue testing. It should be noted that the amount of martensite measured by the XRD method also includes the amount of δ-ferrite because both δ-ferrite and martensite are BCC structure. The electron back scatter diffraction (EBSD) method was used to investigate martensitic transformation near fatigue crack tip.

RESULTS AND DISCUSSION

Effect of Hydrogen on Fatigue Crack Growth

Figure 2 (a) shows the fatigue crack growth curves starting from a 200 μm pre-crack in the specimens of SUS304. Figure 2 (b) shows the relationship between fatigue crack growth rate and stress intensity factor range, ΔK. The hydrogen contents of the

specimens, which were measured immediately after fatigue tests, are also marked in the figure. The fatigue crack growth rates of the specimen tested in the H_2 gas were higher than those tested in air. Furthermore, the effect of hydrogen on fatigue crack growth rate is definitely dependent on the test frequency. In the test at 0.01 Hz in the H_2 gas, the acceleration rate in fatigue crack growth due to hydrogen was approximately 5 in all the range of ΔK and was almost equal to that in the test at 0.0015 Hz in the H_2 gas. Thus, the acceleration rate, approximately 5, is considered to be the upper limiting value in the 0.68 MPa H_2 gas at room temperature. On the other hand, in the test at 1.0 Hz in the H_2 gas, the fatigue crack growth rate was reduced to the level for the test in air at 1.0 Hz as ΔK increased until 11 MPa·m$^{1/2}$. Over the $\Delta K \approx 11$ MPa·m$^{1/2}$, the fatigue crack growth rate in the test at 1.0 Hz in the H_2 gas was accelerated again.

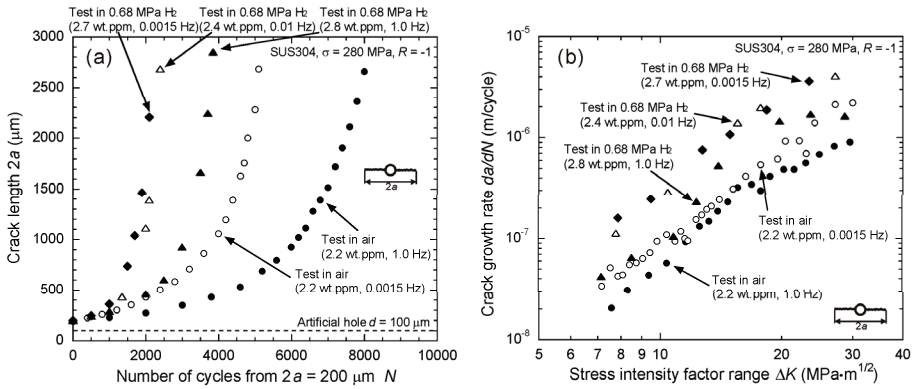


Figure 2: Influence of hydrogen on crack growth from 200 μm pre-crack for SUS304. (a) fatigue crack growth curves and (b) relationship between fatigue crack growth rate and stress intensity factor range.

The fatigue crack growth rates of specimen tested in air at 0.0015 Hz, were approximately twice higher in the ΔK range from 7 to 12 MPa·m$^{1/2}$ than those at 1.0 Hz in air. On the other hand, in the ΔK range from 12 to 17 MPa·m$^{1/2}$, the fatigue crack growth rates in the test in air at 0.0015 Hz are equal to those at 1.0 Hz. Over the $\Delta K = 17$ MPa·m$^{1/2}$, the fatigue crack growth for the test in air at 0.0015 Hz is accelerated again. It has been found in the authors' previous study of SUS316L [2] that the hydrogen at a level of 2 ~ 3 wt.ppm, which is originally introduced into materials by steel making process, definitely increases fatigue crack growth rates when the loading frequency is reduced to 0.0015 Hz.

Martensitic Transformation

Strain-induced martensitic transformation enhances hydrogen diffusion and concentration to the fatigue crack tip. Therefore, the investigation of martensitic

transformation in the vicinity of crack tip is very important for discussing hydrogen effect on fatigue crack growth. Figure 3 shows the volume fraction of transformed martensite measured on the fracture surfaces as a function of the maximum stress intensity at the point of measurement that was present during fatigue test. The degree of martensitic transformation for the SUS304, tested in the H_2 gas at 0.0015 Hz, was definitely lower compared with the specimen tested in air at 0.0015 Hz.

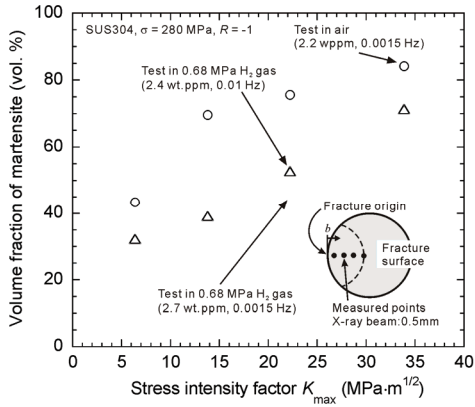


Figure 3: The amount of transformed martensite on fatigue fracture surface.

Micro structural analysis near fatigue crack tip was performed by EBSD to investigate the difference in martensite fraction between test in the H_2 gas and test in air. The EBSD analysis was applied to the section at the vicinity of fatigue crack tip on the plane which is parallel to the specimen axis and passes through the small hole (See Fig. 4(c)). Figure 4 shows crystal-structural map of the vicinity of the fatigue crack tip. A large α' martensite region was observed in the vicinity of fatigue crack tested in air. A ε martensite was not observed. The martensitic-transformed region spreads more widely above and below the fatigue crack than ahead of the fatigue crack. A martensitic-transformed region was also observed in the vicinity of fatigue crack tested in the H_2 gas. However, the width of the martensitic-transformed region around the fatigue crack tested in the H_2 gas was 1/10 times smaller than that in air. The martensitic transformation is not necessarily continuous along crack growth line at least on two dimensional observation. The intermittent martensitic transformation at the fatigue crack tip may be caused by the difference in the difficulty of martensitic transformation, which depends on the orientations of each crystal.

Figure 5 shows the microscopic morphology of slip bands near the fatigue crack tip of SUS304. From these figures, we can observe that slip bands near the fatigue crack tip of the specimen tested in the H_2 gas are more planar and discrete than those in air. The specimen tested in air has more complicated and dense slip bands, whereas more localized slip bands are activated in the specimen tested in the H_2 gas. The difference in slip bands morphology in air and in the H_2 gas is schematically illustrated in Fig.

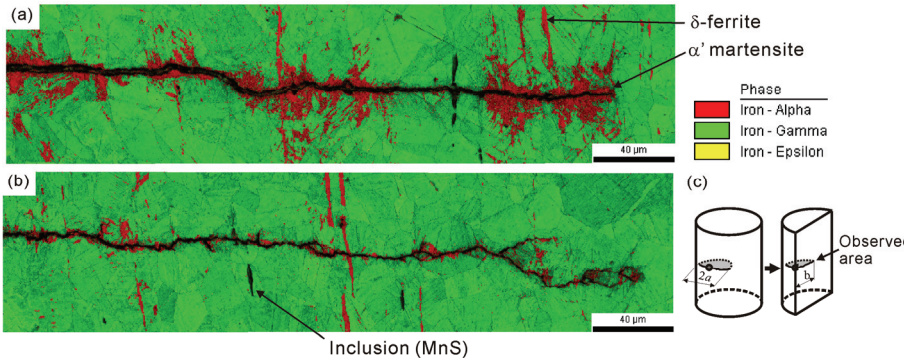


Figure 4: Martensitic transformation near fatigue crack of SUS304 (a) tested in air at 1.0 Hz (σ = 280 MPa, ΔK = 25.9 MPa·m$^{1/2}$, 2a = 3019 μm, b/a = 0.84, N = 8200) and (b) tested in 0.68 MPa H_2 at 0.01 Hz (σ = 280 MPa, ΔK = 25.5 MPa·m$^{1/2}$, 2a = 3093 μm, b/a = 0.84, N = 2450). (c) Schematic image of observed area.

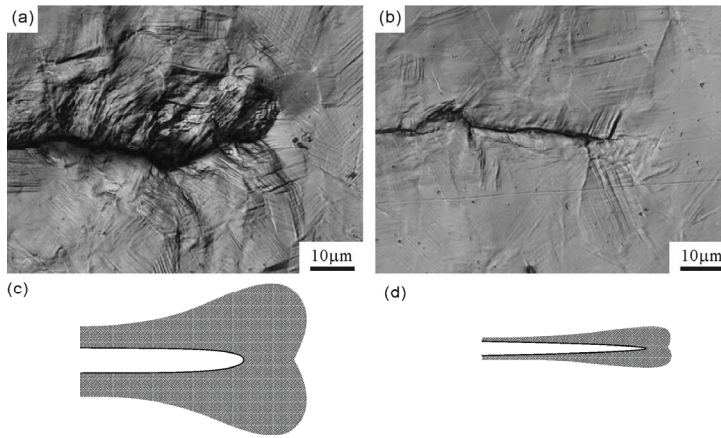


Figure 5: Microscopic morphology of slip bands near the crack tip of SUS304 (a) tested in air at 1.0 Hz (σ = 280 MPa, ΔK = 29.5 MPa·m$^{1/2}$, 2a = 3019 μm, N = 8200), (b) tested in 0.68 MPa H_2 at 0.01 Hz (σ = 280 MPa, ΔK = 27.2 MPa·m$^{1/2}$, 2a = 2685 μm, N = 2400), (c) Schematic image of thick plastic zone produced at a crack under no hydrogen, and (d) Schematic image of shallow plastic zone produced at a crack under hydrogen effect.

5 (c) and (d). The authors [2] have proposed the hydrogen-induced crack growth mechanism as follows. The slip deformation at crack tip causes both crack tip blunting and crack growth at the initial stage of loading. In absence of hydrogen, under a given load level, crack tip blunting occurs as a crack grows and, finally, at the maximum load, the crack growth is ceased. On the other hand, in presence of hydrogen, a large amount of hydrogen concentrates near fatigue crack tips, and a fatigue crack continues to grow before the crack tip becomes fully blunt. Since the

corresponding plastic zone at the crack tip does not become large, the plastic zone wake observed on the specimen surface is slim.

The strain-induced martensitic transformation depends on the amount of plastic strain and temperature [3]. It has been reported that hydrogen decreases stacking fault energy [4]. The decrease in stacking-fault energy promotes martensitic transformation. In this study, the martensitic transformation is considered to depend only on the amount of plastic strain, because all of the fatigue tests in this study were carried out at room temperature (16 ~ 25 °C). It is presumed that hydrogen easily enters into material at fatigue crack tip tested in the H_2 gas. Therefore, the hydrogen content at fatigue crack tip tested in the H_2 gas is thought to be larger than that tested in air. Martensitic transformation at fatigue crack tip tested in H_2 gas is considered to be enhanced by hydrogen which causes the decrease in stacking-fault energy. On the other hand, hydrogen promotes local plastic deformation in the vicinity of fatigue crack tip as is clear from Fig. 5. As a result, in the fatigue test in H_2 gas, martensitic transformation occurs in only a narrow area in the vicinity of fatigue crack. In XRD analysis using monochromatic Cr-Kα radiation, an atomic arrangement information of approximately 10 μm surface layer is reflected in XRD. In the measurement of the amount of martensite by XRD, the measured volume fraction of martensite denotes average of thin surface layer. As shown in Fig. 4, the martensitic transformation in presence of hydrogen occurs only in the narrow area in the vicinity of fatigue crack. Accordingly the smaller amount of martensite was detected by the XRD method in fatigue test in H_2.

Hydrogen-induced Fatigue Crack Growth Acceleration and Hydrogen Migration in the Vicinity of Fatigue Crack Tip

As has been mentioned, hydrogen-induced fatigue crack growth acceleration depends on ΔK (fatigue crack growth rate) and test frequency. The dependence is considered to be attributed to the hydrogen diffusion and concentration to the region which contributes to fatigue crack growth. The relationship between hydrogen-induced fatigue crack growth acceleration and hydrogen migration in the vicinity of fatigue crack tip is discussed in this section.

Figure 6 shows the relationship between fatigue crack growth acceleration rate and ΔK. The acceleration rate in the fatigue test at 0.01 and 0.0015 Hz in the H_2 gas was approximately 5 in all the range of ΔK. On the other hand, the acceleration rate in the fatigue test at 1.0 Hz in the H_2 gas depends on the value of ΔK. Similar phenomenon was observed also in the fatigue test at 0.0015 Hz in air. The relationship between acceleration rate and ΔK for the test in the H_2 gas at 1.0 Hz is almost equal to that for the test in air at 0.0015 Hz, although the test frequency for the test in the H_2 gas is approximately 3 orders of magnitude more than that in air. These phenomena are attributed to the difference in hydrogen migration in the vicinity of fatigue crack tip. However, the hydrogen migration behavior in the

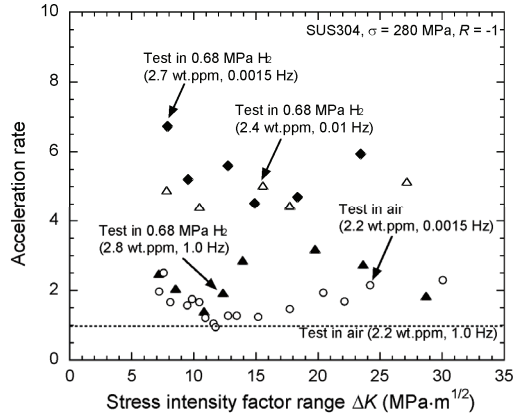


Figure 6: *Acceleration rate of hydrogen-induced fatigue crack growth rate.*

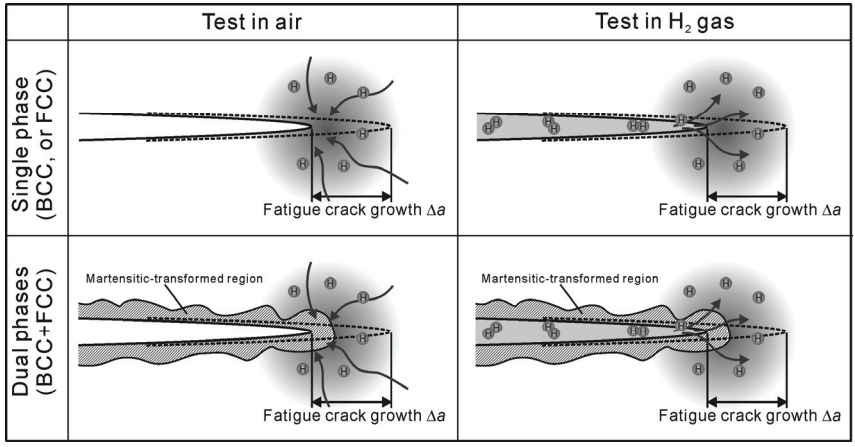


Figure 7: Schematic image of difference in hydrogen migration in the vicinity of fatigue crack tip.

vicinity of fatigue crack tip of SUS304 is complicated because of a large plastic deformation and a martensitic transformation at fatigue crack tip. We can classify the hydrogen migration behavior into four models as shown in Fig. 7. Two factors must be noted as the cause for the different acceleration rate: (1) Influence of test frequency on the acceleration rate, and (2) Influence of gas environment, air or H_2 on the acceleration rate. In the case of the single phase, the acceleration rate is based on the relationship between hydrogen diffusion distance (test frequency) and fatigue crack growth rate *da/dN*. Namely, if there is sufficient time for hydrogen to diffuse to fatigue crack tip, fatigue crack growth is accelerated by hydrogen. In the test in H_2 gas, hydrogen is considered to diffuse and concentrate in the vicinity of fatigue crack tip more easily than that in air because hydrogen can enter into material directly from the crack surface. In the case of the dual phases (BCC + FCC), BCC phase

enhances hydrogen diffusion. In the fatigue test of SUS304 at higher ΔK, hydrogen diffusion is enhanced by the transformed martensite and plastic deformation, and consequently, the acceleration rate is increased.

CONCLUSIONS

The effect of hydrogen and test frequency on the fatigue crack growth of a type 304 austenitic stainless steel was investigated in terms of hydrogen migration in the vicinity of the fatigue crack tip. The conclusions can be summarized as follows.

(1) The fatigue crack growth rates of the specimen tested in H_2 gas were higher than those tested in air. The effect of hydrogen on fatigue crack growth rate is strongly dependent on the test frequency. The hydrogen-induced acceleration rate in 0.68 MPa H_2 gas at room temperature reaches approximately 5 which is considered to be the upper bound of the acceleration.

(2) A large strain-induced α' martensite region was observed by EBSD in the vicinity of fatigue crack tested in air. A martensitic-transformed region was observed in the vicinity of fatigue crack tested in H_2 gas. However, the width of the martensitic-transformed region around the fatigue crack tested in the H_2 gas was 1/10 times smaller than that in air. This is because only a narrow area in the vicinity of fatigue crack tip is extensively plastic-deformed by the presence of hydrogen.

(3) The hydrogen-induced fatigue crack growth acceleration is strongly influenced by hydrogen migration behavior in the vicinity of fatigue crack tip.

ACKNOWLEDGEMENT

This research has been supported by the NEDO project "Fundamental Research Project on Advanced Hydrogen Science (2006-2012)".

REFERENCES

1. Vennett, R. M. and Ansell, G. S., “The effect of high-pressure hydrogen upon the tensile properties and fracture behavior of 304L stainless steel”, *Trans-ASM*, Vol. 60 (1967), pp. 242-251.
2. Murakami, Y., Kanezaki, T., Mine, Y. and Matsuoka, S., “Hydrogen embrittlement mechanism in fatigue of austenitic stainless steels”, *Metall-Mater-Trans-A*, Vol. 39 (2008), pp. 1327-1339.
3. Fiedler, H. C., Averbach, B. L. and Cohen, M., “The effect of deformation on the martensitic transformation in austenitic stainless steels”, *Trans-ASM*, Vol. 47 (1955), pp. 267-290.
4. Pontini, A. E. and Hermida, J. D., “X-Ray diffraction measurement of the stacking fault energy reduction induced by hydrogen in an AISI 304 steel”, *Script-Mater*, Vol. 37 (1997), pp. 1831-1837.

Effects of Hydrogen on Materials
Proceedings of the 2008 International Hydrogen Conference
Brian Somerday, Petros Sofronis, Russell Jones, editors, p 139-146
Copyright © 2009 ASM International®
All rights reserved.
www.asminternational.org

EFFECT OF INTERNAL HYDROGEN ON FATIGUE STRENGTH OF TYPE 316 STAINLESS STEEL

C. Skipper, G. Leisk, A. Saigal, D. Matson
Dept. of Mech. Engineering, Tufts University, Medford, MA, USA

C. San Marchi
Sandia National Laboratories, Livermore, CA, USA

ABSTRACT

The effects of hydrogen embrittlement has been extensively researched, however, relatively little research has been devoted to the effects of internal hydrogen on the fatigue strength of structural metals. This paper examines the effect of internal hydrogen on the fatigue strength of strain-hardened type 316 stainless steel in rotating beam fatigue tests. The tensile properties and high cycle fatigue life of two type 316 stainless steel alloys were studied using thermal precharging to approximate high-pressure hydrogen exposure for long times. Tensile testing was found to be consistent with previous studies using the identical environmental condition. Hydrogen precharging increased the number of cycles to failure by 5 to 10 times compared to non-charged specimens. The basic shape of the S-N curve and the apparent fatigue limit were essentially unchanged by thermal precharging with hydrogen.

INTRODUCTION

Environmental similitude is an important concept when interpreting the effects of hydrogen on mechanical properties, particularly with regard to design for gaseous hydrogen environments. In metals, degradation of mechanical properties generally occurs due to atomic hydrogen that has diffused into the metal lattice. Hydrogen can be taken up by metals in many environments, including when exposed to electrochemical environments or to gaseous hydrogen. Electrochemical environments often produce very high fugacity hydrogen on the surface, which can be many orders of magnitude greater than can be achieved in gaseous environments. Under these conditions, hydrogen can distort the metal lattice causing phase changes or physical damage; therefore, electrochemical methods generally do not provide an adequate model for high-pressure gaseous hydrogen environments. In addition, hydrogen must be given time to diffuse into the metal in order to affect properties. For austenitic stainless steels, diffusion of hydrogen is extremely slow and testing in

gas may not always be sufficient to allow sufficient time for hydrogen uptake. Hydrogen precharging metals by exposing them to gaseous hydrogen at elevated temperature is one method of facilitating hydrogen uptake into the metal lattice over length scales comparable to the dimensions of standard mechanical specimens. Thermal precharging has been shown to be effective for measuring hydrogen-assisted fracture in austenitic stainless steels.

Tensile properties of austenitic stainless steel have been extensively studied and the literature reveals that internal hydrogen leads to a loss of ductility and an increase in tensile flow stress [1-3]. Studies on the effects of hydrogen on fatigue using standardized methodologies are substantially less common than tensile studies [4-11]. Several studies on austenitic stainless steels show decreases in the number of cycles to failure in fatigue life tests due to internal hydrogen produced by electrochemical methods [7-11]. Studies in gaseous hydrogen environments, on the other hand, have shown in an increase in fatigue life [12]. These studies and others with internal hydrogen generated in low-fugacity environments [7] have also shown delayed crack initiation and accelerated crack propagation in austenitic stainless steels due to hydrogen. The majority of studies on type 316 austenitic stainless steels have considered annealed material. The aim of this study is to measure the fatigue life of strain-hardened type 316 stainless steels that have been thermally precharged with hydrogen to simulate long-term exposure to high-pressure hydrogen gas. In addition, the trends established from tensile testing under identical environmental conditions are compared to these fatigue results.

EXPERIMENTAL METHODS

Materials and Hydrogen Precharging

This paper examines the tensile and fatigue-life properties of two type 316 austenitic stainless steels with high concentrations of internal hydrogen. Table 1 lists the compositions of these two alloys. Alloy H (type 316) has a relatively high alloy content compared to alloy I; while the latter is a low-carbon variety of type 316 austenitic stainless steel (type 316L). Alloys H and I were supplied as 9.5 mm and 12.7 mm round bar stock, respectively, in the strain-hardened condition. The tensile test procedures were identical to a previous study [1], thus the alloys are given designations consistent with that study, i.e. H and I.

High concentrations of internal hydrogen was achieved by thermal precharging at 573K in 138 MPa hydrogen gas for a period of more than 30 days. After hydrogen-precharging, specimens were stored in a freezer to minimize hydrogen loss prior to and after completion of testing. Each sample was warmed to room temperature over a period of approximately one hour just prior to testing. The hydrogen concentration of selected specimens was measured after testing by inert gas fusion at a commercial vendor. In addition, fractured fatigue specimens were sectioned and analyzed to determine the effect of deformation and temperature rise on hydrogen content. This sectioning included removing radial surface layers near the fracture surface to

estimate the hydrogen concentration profile through the diameter of the fractured specimens.

Tensile Testing

Tensile specimens were machined according to ASTM E8-04 with a 4 mm gauge diameter from the center of the bar stock. Four specimens were produced for each alloy: two for testing in the as-machined condition and two for testing in the hydrogen-precharged condition. Testing was performed at a constant displacement rate of 0.02 mm/s in air at room temperature. Reduction of area (RA) is reported based on measurements of nominal diameter using a scanning electron microscope (SEM). Yield strength (S_y) and tensile strength (S_u, engineering stress at maximum load) are reported along with uniform elongation (El_u, strain at maximum load) and total elongation (El_t, strain at failure).

Fatigue Testing

Fatigue specimens were machined according to ASTM E466-96 from the center of the bar stock. Twenty-four samples of each of the two alloys were machined for a total of 48 samples. Each specimen was electropolished to achieve a surface finish of 1 Ra. Twelve samples of each alloy were precharged with hydrogen gas along with the tensile specimens. Fatigue testing was performed at room temperature on a R.R. Moore rotating beam fatigue testing machine at a frequency of 50 Hz. The stress amplitude (S) in rotating beam fatigue tests is constant throughout the test. The number of cycles to failure (N) is determined by fracture of the specimen or when sufficient deformation precluded rotation (i.e., deflection at the end of the specimen of about two degrees from the centerline).

Table 1: Compositions (wt%) of the type 316 stainless steels used in this study.

ID	alloy	Fe	Cr	Ni	Mn	Mo	N	C	Si	S	P
H	316	Bal	17.8	12.1	1.2	2.1	0.02	0.046	0.59	0.025	0.025
I	316L	Bal	16.8	11.2	1.6	2.0	0.02	0.020	0.61	0.026	0.027

RESULTS

Tensile Properties

Tensile properties measured for alloys H and I are displayed in Table 2. Figure 1 shows representative engineering stress-strain curves for alloys with and without internal hydrogen. High concentrations of internal hydrogen increased the yield strength in these tests by as much as 17%, while also increasing ultimate strength by 10%. The reduction of area is similar for the two alloys, about 80% when not precharged with hydrogen; however, internal hydrogen lowers RA to 66 and 62% for alloys H and I respectively. Elongation is only moderately affected by internal hydrogen.

Microvoid coalescence dominates the fracture surface of both alloys in the non-charged and hydrogen-precharged conditions as shown in Figure 2. The size of the ductile dimples appears to be smaller for the hydrogen-precharged materials compared to the non-charged materials. The average diameter of dimples from the fracture surface of hydrogen-precharged alloy H is 2.6 μm while for the non-charged alloy the dimple size is 4.0 μm. For alloy I, the dimple sizes are 3.0 μm and 3.1 μm for hydrogen-precharged and non-charged material respectively.

Table 2: Mechanical properties observed in tensile testing of alloys H and I.

Alloy	Condition	S_y (MPa)	S_u (MPa)	RA (%)	El_u (%)	El_t (%)
H	Non-	608	720	81	32	52
	Precharged	680	789	66	35	53
I	Non-	599	734	80	28	49
	Precharged	701	805	62	26	46

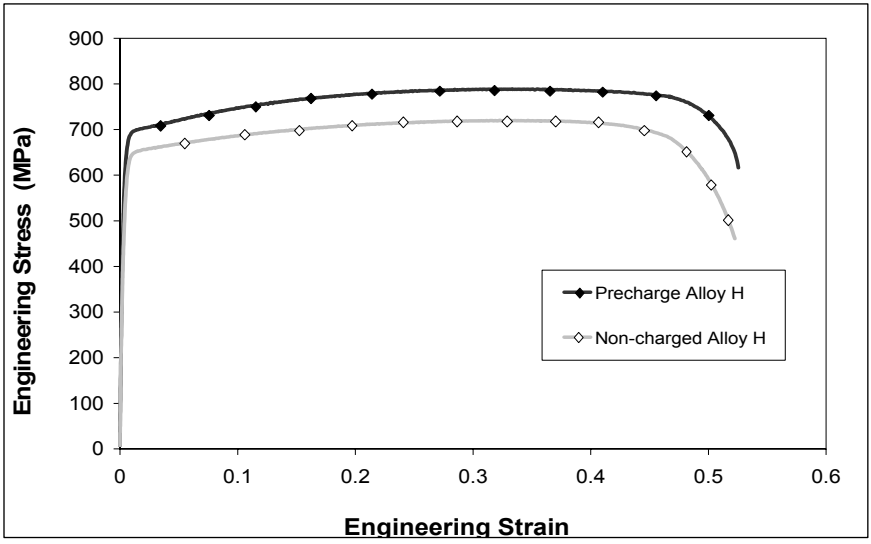


Figure 1: Representative tensile flow curves for alloy H in the hydrogen-precharged and non-charged conditions.

Fatigue Life

Figure 3 shows the results from fatigue testing for both the hydrogen-precharged and non-charged conditions for both alloys H and I. There is essentially no difference between the S-N curves for the two alloys. Hydrogen precharging, however, increased the number of cycles to failure of these materials by a factor of 5 to 10 for the same stress amplitude. The apparent fatigue limit is approximately the same for

both non-charged and hydrogen-precharged specimens and for both alloys. The repeatability of the measured fatigue life was examined for alloy H by testing three samples at stress amplitude of nominally 500 MPa (72 ksi) for both precharged and non-charged conditions. At this stress level the non-charged samples failed at an average of 10,000 ± 500 cycles, while the hydrogen-precharged samples failed at 92,000 ± 14,000 cycles.

Hydrogen Content

The measured hydrogen content in the grip section of the hydrogen-precharged specimens was 109 ± 11 ppm (by weight). The hydrogen content near the fracture surface was essentially the same: 108 ± 10 ppm. Sectioning combined with hydrogen analysis revealed that there was no measurable concentration gradient across the diameter of the specimen, implying that there was no significant hydrogen loss during fatigue testing.

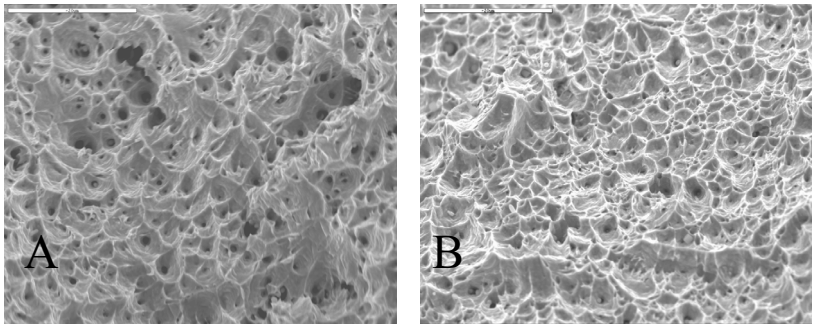


Figure 2: Fractography for alloy H in the non-charged condition (A) and the hydrogen-precharged condition (B). The white bar at the top of the images is approximately 20 μm in length.

DISCUSSION

The results from tensile testing are consistent with previous work using the same conditions for hydrogen precharging [1]: measures of strength are increased by 10 to 15% when type 316 austenitic stainless steels are hydrogen-precharged, while the elongation is only modestly affected by internal hydrogen. The effect of hydrogen on tensile properties is most often quantified by changes in the reduction of area (RA). The reductions of RA observed in this study are consistent with previous work and follow a basic trend of lower RA for lower nickel content in the alloy [1, 13]. This explains the slightly lower RA for alloy I, which has a lower nickel content that alloy H. Nickel content in austenitic stainless steels is an important parameter, since nickel has a strong effect on slip mode: low nickel content enhances planar slip. Austenitic stainless steels that display predominantly planar slip are more susceptible to hydrogen-assisted fracture than materials that are characterized by cross slip (or uniform slip behavior) [1,14,15]. The fracture morphology is also consistent with previous studies: despite 20% reduction of ductility when hydrogen-precharged, the fracture surface of both alloys H and I are characterized by microvoid coalescence.

The average size of the dimples is slightly reduced by internal hydrogen, indicating that hydrogen affects deformation, likely increasing the density of void nucleation events.

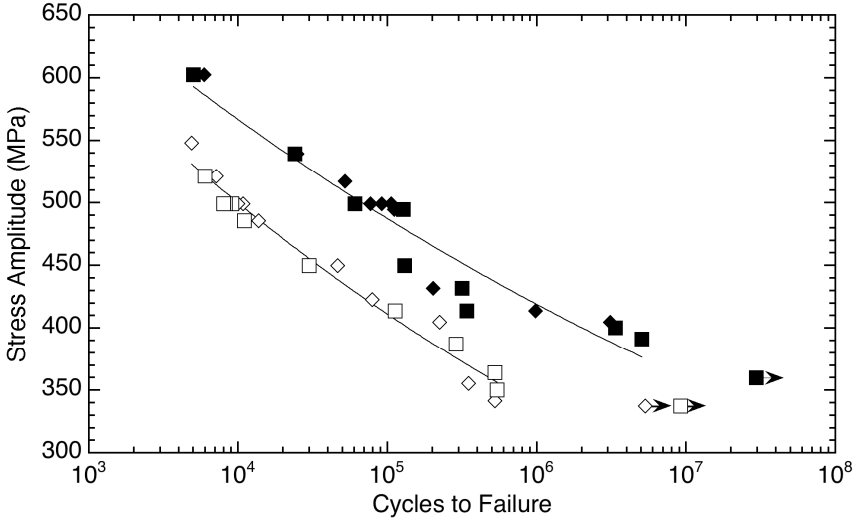


Figure 3: S-N curve generated from fatigue testing. (Diamonds indicate alloy H; squares indicate alloy I; filled in shapes indicate hydrogen-precharged specimens; empty shapes indicate non-charged specimens; arrows indicate specimens that did not fail at the given number of cycles.)

The fatigue results for the two alloys are similar, which is consistent with the general similarity that was found for the tensile properties. While lower tensile ductility was observed for alloy I compared to alloy H when hydrogen-precharged, the S-N curves are essentially the same for the two hydrogen-precharged alloys (Figure 3). The difference in tensile tests is attributed to nickel content, however, the similarity in fatigue results for the two alloys implies that nickel content may not be important in rotating beam fatigue of type 316 austenitic stainless steels with internal hydrogen at room temperature. As mentioned above, nickel content affects the slip mode in tensile tests, and one might expect that a propensity for planar slip would enhance persistent slip bands, which often nucleate fatigue cracks in metals [16]. On the other hand, macroscopic slip mode in austenitic stainless steels may be less important than surface finish and other characteristics that directly influence the nucleation of a surface crack, or the intrinsic scatter in fatigue data may simply make it difficult to resolve variations due to relatively small differences in nickel content. More work is necessary to inform our understanding of compositional parameters on fatigue in hydrogen environments; nevertheless, the results presented here imply that nickel content in austenitic stainless steels is less important in fatigue life measurements than in tensile tests.

Figure 3 shows that the cycles to failure are increased with internal hydrogen at a given stress amplitude, similar results are reported in the literature for type 304 austenitic stainless steel [12]. However, the tests from the literature were performed in hydrogen gas, and this result was interpreted to be a consequence of the low oxygen and low moisture environment, since gaseous hydrogen and nitrogen environments similarly delayed crack nucleation compared to air [12]. All tests in this study were performed in air, thus the greater fatigue life must have a different origin. In addition, the increase in cycles to failure is greater in this study, than tests performed in hydrogen gas. One explanation is the higher strength of the hydrogen-precharged material, which would result in less strain per cycle for the same stress amplitude and presumably longer lifetimes. Post-mortem measurements of surface cracks, on the other hand, show that the hydrogen-precharged specimens have fewer and larger cracks, suggesting that internal hydrogen delays crack nucleation and enhances crack propagation similar to interpretations in the literature. Hydrogen in austenitic stainless steels tends to promote planar slip, while decreasing the number active slip bands [1,17]; this may delay the nucleation of cracks since it will widen fatigue intrusions and make them less effective at initiating a crack. In summary, the shift in cycles to failure to higher values when hydrogen-precharged is not well understood and may be related to a combination of factors including higher strength due to high concentrations of hydrogen and delayed crack nucleation due to hydrogen-induced changes in slip behavior.

CONCLUSION

Tensile tests and rotating beam fatigue tests were performed on strain-hardened type 316 stainless steels. The tensile tests revealed properties consistent with previous studies: 10 to 15% increase of strength and reduction of ductility. The reduction of ductility (RA) depends on the nickel content of the alloy, but is about 20% for nickel content of 12 wt%. At a given stress amplitude the cycles to failure of the hydrogen-precharged samples were 5 to 10 times greater than the non-charged samples; this results in a shift of the S-N curve to higher values of N. The fatigue limit appears to be nominally unchanged by internal hydrogen. A mechanistic understanding of the effects of hydrogen on the S-N curve have not been elaborated, but it is speculated that crack nucleation may be delayed due to hydrogen-enhanced localized plasticity (which increases slip band spacing and increases strength).

ACKNOWLEDGEMENTS

This research was funded by DOE contract No. 711187. Sandia is a multiprogram laboratory operated by Sandia Corporation, a Lockheed Martin Company, for the United States Department of Energy under contract DE-AC04-94AL85000.

REFERENCES

1. San Marchi, C., et al., “Effects of alloy composition and strain hardening on tensile fracture of hydrogen-precharged type 316 stainless steels,” *Int J Hydrogen Energy,* Vol. 33, No. 2 (2008), pp. 889-904.

2. San Marchi, C., et al., "Mechanical properties of super duplex stainless steel 2507 after gas phase thermal precharging with hydrogen," *Metallurgical and Materials Transactions A,* Vol. 38A, No. 11 (2007), pp. 2763-2775.
3. Herms, E., et al., "Hydrogen embrittlement of 316L stainless steel." *Materials Science and Engineering A,* Vol. 272A, No. 2 (1999), pp. 279-283.
4. Doig, P., "A model for the initiation of hydrogen embrittlement cracks at blunt notches during elastic fatigue loading," *Materials Science and Engineering,* Vol. 28, No. 2 (1981), pp. 181-188.
5. Uyama, H., et al., "Effects of hydrogen charge on microscopic fatigue behaviour of annealed carbon steels," *Fatigue and Fracture of Engineering Material and Structures*, Vol. 29, No. 12 (2006), pp. 1066-1074.
6. Kanezaki, T., et al., "Effects of hydrogen on fatigue crack growth behaviour and ductility loss of austenitic stainless steels," *Transactions of the Japan Society of Mechanical Engineers, Part A,* Vol. 72, No. 5 (2006), pp. 653-660.
7. Murakami, Y., "The effect of hydrogen on fatigue properties of metals used for fuel cell system," *International Journal of Fracture,* Vol. 138, No. 1-4 (2006), pp. 167-195.
8. Kuromoto, N., et al., "Superficial and internal hydrogenation effects on the fatigue life of austenitic steels," *Materials Science and Engineering A*, Vol. 381, No. 1-2 (2004), pp. 216-222.
9. Fukuyama, S., et al. "Fatigue properties of type 304 stainless steel in high pressure hydrogen at room temperature," *Transactions of the Japan Institute of Metals,* Vol. 26, No. 5 (1985), pp. 325-331.
10. Nagumo, M., et al., "Fatigue damage and its interaction with hydrogen in martensitic steels," *Materials Science and Engineering A,* Vol. 348, No. 1-2 (2003), pp. 192-200.
11. Nagata, J., et al., "Effect of hydrogen charge on fatigue strength of martensitic stainless steel," *Journal of the Society of Materials Science, Japan,* Vol. 54, No. 12 (2005), pp. 1217-1224.
12. Aoki, Y., et al., "Fatigue characteristics of a type 304 austenitic stainless steel in hydrogen gas environment," *International Journal of Fracture,* Vol. 133, No. 3 (2005), pp. 277-288.
13. Zhang, L., et al., "Effect of nickel equivalent on hydrogen gas embrittlement of austenitic stainless steels based on type 316 at low temperatures," *Acta Metallurgica,* Vol. 56, No. 14 (2008), pp. 3414-3421.
14. Odegard, B., et al., "The effect of hydrogen on mechanical behavior of nitrogen-strengthened stainless steel," *Proc of an international conf on effect of hydrogen on behavior of materials,* Moran, WY, Sept. 1975, pp. 116–125.
15. Perng, T., et al., "Comparison of hydrogen gas embrittlement of austenitic and ferritic stainless steels," *Metallurgical Transactions A,* Vol. 18A, No. 1 (1987), pp. 123-134.
16. Lin, M., et al., "Fatigue crack initiation on slip bands: theory and experiment," *Acta Metallurgica,* Vol. 34, No. 4 (1986), pp. 619-628.
17. Nibur, K., et al., "Hydrogen effects on dislocation activity in austenitic stainless steel," *Acta Metallurgica,* Vol. 54, No. 10 (2006), pp. 2677-2684.

Effects of Hydrogen on Materials
Proceedings of the 2008 International Hydrogen Conference
Brian Somerday, Petros Sofronis, Russell Jones, editors, p 147-154
Copyright © 2009 ASM International®
All rights reserved.
www.asminternational.org

HYDROGEN-ASSISTED FRACTURE OF WELDED AISI 316 AUSTENITIC STAINLESS STEEL

X. Tang and G.H. Schiroky,
Swagelok Company, Solon, OH, USA

C. San Marchi and B.P. Somerday,
Sandia National Laboratories, Livermore, CA, USA

ABSTRACT

AISI 316 austenitic stainless steel is a preferred material of construction for valves, fittings, and other fluid system components for high-pressure gaseous hydrogen service. The interaction of hydrogen with stainless steel depends on the prevailing stress-state and the microstructural characteristics of a component's material of construction, among other variables. To evaluate the effects of geometrical stress-risers and two-phase microstructures on hydrogen-assisted fracture of AISI 316 stainless steel, smooth and notched tensile properties were measured for annealed material as well as for autogenously welded specimens after thermal precharging with hydrogen. The tensile ductility of welded microstructures is significantly reduced by hydrogen precharging, and the addition of a notch further degrades ductility. These observations are rationalized in terms of hydrogen-enhanced localized plasticity.

INTRODUCTION

Hydrogen gas is increasingly being considered as an energy storage medium for stationary and mobile power generation. Fluid system components for hydrogen delivery, containment and refueling, such as filling nozzles, receptacles, tubing, fittings and valves must retain satisfactory mechanical properties when they are in contact with high pressure hydrogen over an anticipated operating temperature range of -50˚C to 100˚C.

The mechanical properties of many metallic materials can be affected by hydrogen gas, especially when gas pressure is high. Hydrogen-induced property degradation of materials has been studied for many decades [1-7]. Austenitic stainless steels in general are more resistant to hydrogen-assisted fracture than ferritic steels [7]. Among the austenitic stainless steels, the AISI 316 family of alloys represents particularly attractive candidates for components in hydrogen service. Recently

published results show that the composition of AISI 316 stainless steel has a rather significant effect on the material's resistance to hydrogen-assisted fracture [8] and that the effect of hydrogen on property degradation becomes even more evident at sub-ambient temperatures [9, 10]. In particular, these studies show that AISI 316 alloys with the minimally required content of 10% nickel are much more affected by hydrogen than the properties of alloys with more than 12% nickel [8-10].

The objective of this study was to evaluate additional effects of hydrogen-induced property degradation that may be observed in components with stress risers such as sharp corners and notches, and with welds. Weld zones tend to have two-phase dendritic microstructures (similar to casting microstructures) because ferrite is desirable during solidification of austenitic stainless steels in fusion welding processes to prevent weld cracking. Consequently, since ferritic stainless steels are typically not as resistant to degradation by hydrogen as austenitic stainless steels [7], ferrite-containing welds in AISI 316 may be more susceptible to hydrogen-assisted fracture. In this study, hydrogen effects on both smooth and notched tensile properties of non-welded and welded specimens were determined and compared.

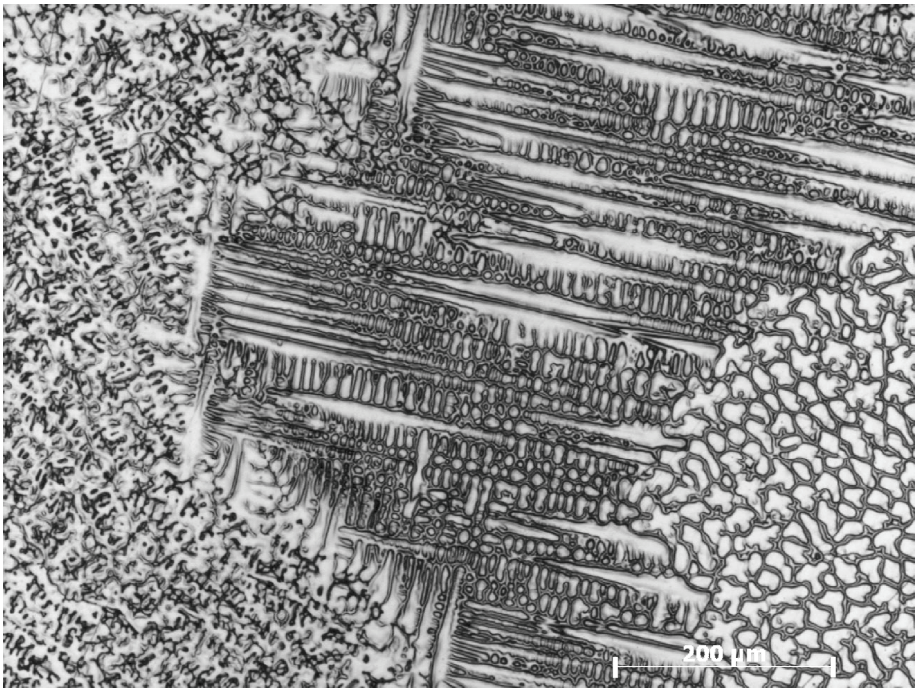


Figure 1: Micrograph of the fusion zone in the welds produced in this study, showing the two-phase austenite-ferrite microstructure.

EXPERIMENTAL

The AISI 316L stainless steel used in this study (Table 1) is the same heat of material as alloy E in Refs. [8, 9]. This material was produced by electric arc furnace (EAF) melting, argon oxygen decarburization (AOD) and vacuum arc remelting (VAR). Materials refined by VAR have low levels of residual elements and improved compositional homogeneity. The welded tensile bars were produced by orbital autogenous gas tungsten arc welding of cylindrical butt joints; since filler was not used, the average chemical compositions of welds and base metal are identical. The welded specimens were produced from material in the strain-hardened condition; however, welding yields nominally annealed microstructures in the heat-affected zone (HAZ) adjacent to the fusion zone. The full-penetration welds were centered in the gauge length of the test specimens. Figure 1 shows an example of the significant microstructural variation found in the fusion zone of the welds. The two-phase microstructure is estimated to have 5-7% ferrite in the austenitic matrix.

Table 1: Alloy composition (weight percent).

C	Cr	Ni	Mo	Mn	Si	P	S	N
0.022	17.55	13.25	2.70	1.16	0.63	0.015	0.006	0.04

Two types of tensile specimens were used in this study: smooth and notched. The ASTM E8 subsized smooth tensile specimens had a gauge diameter of 4 mm. The gauge length consists of the fusion zone, HAZ, and strain-hardened material. The notched tensile specimens were proportionally scaled from the standard specimen that is suggested in ASTM G142. The V-notch has an included angle of 60˚, the major and minor diameters are 8 and 4 mm respectively, and the notch root radius is nominally 0.05 mm. For the welded specimens, notches were located either in the fusion zone or in the heat-affected zone (HAZ) approximately 1.5 mm from the edge of the fusion zone; specimens with notches in these two locations are referred to as the weld and HAZ respectively.

All tensile testing was conducted at constant displacement rate: smooth specimens at 0.02 mm/s and notched specimens at 0.002 mm/s. The measured strain rate for the smooth tensile specimens was approximately 1.5×10^{-3} /s (in the plastic regime). Yield strength (S_y, 0.2% offset), tensile strength (S_u), and reduction of area (RA) are reported for the smooth tensile tests. Notched tensile strength (σ_S) and RA are reported for the notched tensile tests. Reported values are an average of at least two measurements.

Thermal precharging of the final machined specimens was achieved in 138 MPa H_2 gas at 300˚C for at least 20 days. This length of time is sufficient to ensure that the hydrogen concentration was essentially uniform across the largest diameter of the specimens based on predictions for hydrogen diffusion. Details of this thermal precharging process can be found elsewhere [6]. The hydrogen concentration in the tested specimens was measured to be approximately 140 ppm by weight, consistent with other work [11].

RESULTS AND DISCUSSIONS

Smooth Tensile Properties

The tensile strength of the welded smooth specimens is approximately the same as the annealed base material. The yield strength, however, is slightly higher for the welded specimens, probably due to constraint provided by the strain-hardened base material adjacent to the HAZ. In contrast to the strength, the RA of the welded specimens (69%) is clearly lower than the base material (83%). This difference is likely related to the higher defect population intrinsic to weld (cast) microstructures.

Internal hydrogen leads to a significant increase of strength for both the annealed and welded specimens (Table 2), similar to previous reports on wrought austenitic stainless steels [6-9]. Tensile elongation is generally not used to evaluate hydrogen-assisted fracture in austenitic stainless steels and previous work has shown that elongation is relatively insensitive to high concentrations of internal hydrogen [6-9]. Reduction of area (RA), on the other hand, is particularly sensitive to hydrogen and commonly used for evaluation of hydrogen-assisted fracture. As previously reported [8], wrought AISI 316 stainless steels experience moderate reduction of RA when thermally precharged with hydrogen. Welded material, however, experiences significantly greater loss of ductility due to internal hydrogen than the annealed material (Table 2). Austenite-ferrite microstructures tend to be more sensitive to hydrogen-assisted fracture than single-phase austenite [12, 13], which may explain the lower RA for the welded specimens. Similar values of RA have been reported elsewhere for both non-charged and hydrogen-precharged austenitic stainless steel welds [14].

Table 2: Smooth tensile properties of AISI type 316L austenitc stainless steel

Specimen	Condition	Sy (MPa)	Su (MPa)	RA (%)
Annealed (Non-welded)	non-charged	242	585	83
	H-precharged	301	631	72
Welded	non-charged	272	572	69
	H-precharged	323	623	43

Notched Tensile Properties

The notched tensile strength of the welded specimens is nominally the same as the annealed base material (Table 3). The notched tensile strength of the HAZ specimens is slightly higher, probably due to incomplete annealing of the strain-hardened microstructure during welding. The ductility (as measured by RA) is significantly lower in the weld and HAZ specimens (22 and 26% respectively) compared to the annealed base material (43%).

Hydrogen precharging increases the notched tensile strength of the annealed base material (Table 3), similar to smooth specimens. The strength of the hydrogen-precharged weld and HAZ appears to decrease slightly compared to the non-charged weld and HAZ respectively; however, these differences are essentially within the variation of these measurements. Hydrogen-precharging reduces RA of the annealed, welded and HAZ specimens to greater extent in notched specimens than in smooth specimens (Table 3). The RA of hydrogen-precharged, notched specimens is greatest for the HAZ (23%) and lowest for the welded specimens (13%).

AISI 316 stainless steel is generally considered to be notch insensitive, since the notched tensile strength (σ_S) is significantly greater than the unnotched tensile strength. The high RA of the annealed base material (43%) also demonstrates the inherent ductility of this microstructure, which also implies notch insensitive behavior. Lower RA for notched specimens compared to smooth specimens (83%) is expected due to the triaxial state of stress generated by the presence of the notch. The notched tensile strength is relatively unaffected by internal hydrogen, while the RA is significantly degraded by internal hydrogen for all the tested conditions. These observations show that while hydrogen affects the deformation in these microstructures, fracture is associated with macroscopic plasticity. This is explored in more detail in the following section.

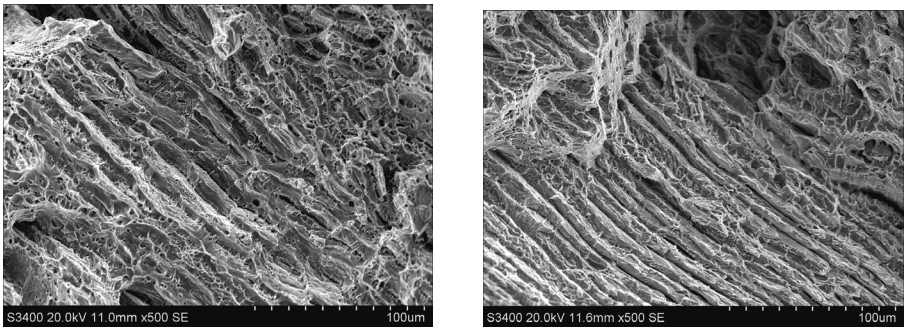
Table 3: Notched tensile properties of AISI type 316L austenitic stainless steel.

Specimen	Condition	σ_S (MPa)	RA (%)
Annealed (Non-welded)	non-charged	850	43
	H-precharged	904	18
Weld	non-charged	854	22
	H-precharged	843	13
HAZ	non-charged	936	26
	H-precharged	926	23

Fracture Mode

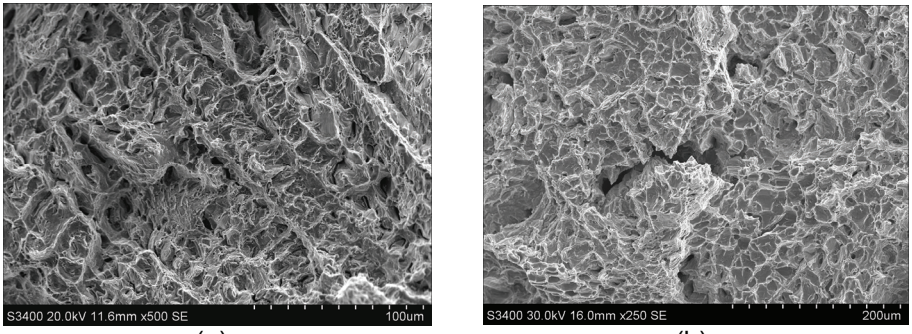
AISI type 316 austenitic stainless steels are very ductile materials that typically display dimpled fracture surfaces that are indicative of microvoid coalescence (MVC). The characteristics of MVC are observed for both the annealed and welded tensile specimens fractured in this study. The welded specimens also display localized areas that appear to reflect the solidified microstructure inherent in fusion welds (Figure 2). Although no evidence of weld cracking was observed, the Cr-Ni ratio (Hammar-Svensson equivalents) for this material is 1.5, which corresponds to the empirical compositional boundary for susceptibility to weld cracking in austenitic stainless steel [15]. Despite fracture features associated with the welded microstructure and the potential for weld cracking in these welds, the measured tensile ductility is consistent with quality welds that feature only MVC [14].

The observed fracture modes for the welded specimens are essentially unchanged by hydrogen-precharging. The majority of the fracture surface shows evidence of microvoid coalescence (Figure 3). The underlying solidification microstructure, however, is more apparent on the fracture surfaces of hydrogen-precharged, smooth specimens than the non-charged specimens (Figure 2), covering about one-third of the fracture surface of the hydrogen-precharged specimens. Ductile dimples characterize the fracture appearance near the center of the notched specimens for all the tested materials and conditions. The prevalence of MVC underscores the inherently ductile nature of these materials and microstructures despite high concentrations of hydrogen. The data (Tables 2 and 3), however, clearly show an effect of hydrogen on the measured RA.



(a) (b)

Figure 2: Fracture features of welded smooth tensile specimens that appear to be associated with the solidified microstructure; (a) non-charged; (b) hydrogen-precharged.



(a) (b)

Figure 3: Fracture surfaces of hydrogen-precharged welds; (a) smooth tensile specimen; (b) notched tensile specimen.

Previous studies on austenitic stainless steel welds have shown that the ferrite in the weld plays an important role in hydrogen-assisted fracture [13, 14]. Interpretation of the fractographic evidence, however, is complicated by the inhomogeneity of the

weld microstructures (Figure 1), which is reflected in a range of fracture features (Figures 2 and 3). The austenite-ferrite boundaries, nevertheless, appear to be an important attribute for hydrogen-assisted fracture in welded materials. The furrows that are observed on the fracture surfaces of the smooth tensile specimens, for example, are significantly sharper in the hydrogen-precharged condition (Figure 2b) compared to the non-charged condition (Figure 2a). This observation implies that hydrogen enhances fracture associated with the two-phase microstructure, in particular with the austenite-ferrite boundaries. Since cross slip is inhibited by hydrogen [16], the effectiveness of boundaries as obstacles to dislocation motion is enhanced, facilitating the pile-up of dislocations and contributing to the development of stress concentration at boundaries [14]. Local stress concentration at the austenite-ferrite boundaries can cause failure along these boundaries [14], or can induce cleavage fracture in the ferritic phase as observed for duplex stainless [12] and welds [13]. In either case, hydrogen-enhanced localized plasticity [16] is an important element for inducing fracture associated with these boundaries.

SUMMARY

The effect of internal hydrogen was evaluated on the tensile properties of welded AISI 316 stainless steel. Although internal hydrogen significantly reduces RA, fracture is associated with plastic deformation in both annealed and welded microstructures. As compared to wrought annealed material, welded metal was found to be more susceptible to hydrogen-assisted fracture. Other studies have attributed hydrogen-assisted fracture in two-phase microstructures to hydrogen-enhanced stress concentration at austenite-ferrite boundaries. The results and observations of fracture surfaces in this study are consistent with this interpretation. Notches increase stress in the specimens, which contributes to further reduction of tensile ductility compared to smooth tensile specimens. Notches are particularly effective at reducing tensile ductility in two-phase microstructures (welds) exposed to hydrogen, since local stress concentrations at the boundaries due to hydrogen are further enhanced by the higher far-field stresses.

ACKNOWLEDGMENTS

We would like to express our gratitude to Mr. Jacob Barnes of Swagelok for his service on specimen welding for this research. Sandia is a multiprogram laboratory operated by Sandia Corporation, a Lockheed Martin Company, for the United States Department of Energy under contract DE-AC04-94AL85000.

REFERENCES

1. RJ Walter and WT Chandler. Effects of High-Pressure Hydrogen on Metals at Ambient Temperature: Final Report. Rocketdyne (report no. R-7780-1) for the National Aeronautics and Space Administration, Canoga Park CA (February 1969).
2. AW Thompson. Ductility Losses in Austenitic Stainless Steels Caused by Hydrogen. in: IM Bernstein and AW Thompson, editors. Hydrogen in Metals. Proceedings of the International Conference on the Effects of Hydrogen on

Materials Properties and Selection and Structural Design (Champion PA, 1973), Metals Park OH: American Society of Metals (1974) p. 91-105.
3. GR Caskey. Hydrogen Compatibility Handbook for Stainless Steels (DP-1643). EI du Pont Nemours, Savannah River Laboratory, Aiken SC (June 1983).
4. JA Harris and MCV Wanderham. Properties of Materials in High Pressure Hydrogen at Cryogenic, Room, and Elevated Temperatures. Pratt and Whitney Aircraft (report no. FR-5768) for the National Aeronautics and Space Administration (Marshall Space Flight Center), West Palm Beach FL (Jul 1973).
5. MR Louthan, GR Caskey, JA Donovan and DE Rawl. Hydrogen Embrittlement of Metals. Mater Sci Eng 10 (1972) 357-368.
6. C San Marchi, DK Balch, K Nibur and BP Somerday. Effect of high-pressure hydrogen gas on fracture of austenitic steels. J Pressure Vessel Technol 130 (2008) 041401.
7. C San Marchi and BP Somerday. Technical Reference on Hydrogen Compatibility of Materials (SAND2008-1163). Sandia National Laboratories, Livermore CA (2008).
8. C San Marchi, BP Somerday, X Tang and GH Schiroky. Effects of alloy composition and strain hardening on tensile fracture of hydrogen-precharged type 316 stainless steels. Int J Hydrogen Energy 33 (2007) 889-904.
9. C San Marchi, BP Somerday, X Tang and GH Schiroky. Hydrogen-assisted fracture of type 316 stainless steel at subambient temperature (PVP2008-61240). in: Proceedings of PVP-2008: ASME Pressure Vessels and Piping Division Conference, 2008, Chicago IL. ASME
10. L Zhang, M Wen, M Imade, S Fukuyama and K Yokogawa. Effect of nickel equivalent on hydrogen gas embrittlement of austenitic stainless steels based on type 316 at low temperatures. Acta Mater 56 (2008) 3414-3421.
11. C San Marchi, BP Somerday and SL Robinson. Permeability, Solubility and Diffusivity of Hydrogen Isotopes in Stainless Steels at High Gas Pressure. Int J Hydrogen Energy 32 (2007) 100-116.
12. C San Marchi, BP Somerday, J Zelinski, X Tang and GH Schiroky. Mechanical properties of super duplex stainless steel 2507 after gas phase thermal precharging with hydrogen. Metall Mater Trans 38A (2007) 2763-2775.
13. BP Somerday, DK Balch, M Dadfarnia, KA Nibur, CH Cadden and P Sofronis. Hydrogen-assisted crack propagation in austenitic stainless steel fusion welds. Metall Mater Trans (submitted) (2008).
14. JA Brooks and AJ West. Hydrogen Induced Ductility Losses in Austenitic Stainless Steel Welds. Metall Trans 12A (1981) 213-223.
15. JA Brooks and AW Thompson. Microstructural development and solidification cracking susceptibility of austenitic stainless steel welds. International Materials Review 36 (1991) 16-44.
16. HK Birnbaum and P Sofronis. Hydrogen-enhanced localized plasticity–a mechanism for hydrogen-related fracture. Mater Sci Eng A176 (1994) 191-202.

Effects of Hydrogen on Materials
Proceedings of the 2008 International Hydrogen Conference
Brian Somerday, Petros Sofronis, Russell Jones, editors, p 155-162
Copyright © 2009 ASM International®
All rights reserved.
www.asminternational.org

THE ROLE OF HYDROGEN INDUCED MICROSTRUCTURAL CHANGES IN THE EMBRITTLEMENT OF AUSTENITIC-FERRITIC STEEL

Wiesław Świątnicki
Warsaw University of Technology, Faculty of Materials Science and Engineering, Warsaw, Poland

INTRODUCTION

Hydrogen embrittlement is a phenomenon that considerably reduces the life of structures and industrial installations subjected to the environment containing or producing hydrogen. Although this phenomenon has been known for a long time, its mechanism has not been definitely explained, in spite of the fact that numerous theoretical and experimental investigations have been conducted e.g. [1-3]. Thus, the problem is still vital both scientifically and for the present industrial applications as well as for the future development of hydrogen economy, which requires hydrogen resistant materials. In this respect one may consider the use of austenitic-ferritic duplex stainless steels which have very high resistance to corrosion and to stress corrosion cracking. The question arises to what extent are these steels resistant to hydrogen corrosion? Some works have been already published presenting the results of investigations on hydrogen behaviour in the structure of duplex steels e.g. [4, 5] and their mechanical properties in hydrogen charging environment, e.g. [6, 7]. The aim of the present study is to summarize the results of the author's investigations on the hydrogen induced structural changes and mechanical properties of duplex steel in hydrogen generating environment. On the basis of the results obtained, factors responsible for hydrogen embrittlement of duplex steel have been discussed.

MATERIAL AND EXPERIMENTAL TECHNIQUES

The material used in this study was X2CrNiMN23-5-3 (EN) austenitic-ferritic steel. Specimens in as-received state were in the form of bars of 8 mm in diameter, or 6 mm thick plates with the following chemical composition (Table 1). The bars in as-received state were previously cold-drawn. Then, the specimens were annealed at 1000°C for 1 hour and quenched in water. The plates were hot-rolled, then annealed at 1100°C for 1 hour and cooled in air. The resultant microstructure in both types of

specimens was recrystallised and contained similar volume fractions of austenite and ferrite. A detailed description of the steel microstructure is presented in [8, 9].

Table 1: Chemical composition of investigated steel samples under study [wt. %]

	C	Cr	Ni	Mo	Si	Mn	S	P	N
bar	0.026	22.94	5.43	2.75	0.39	1.57	0.001	0.021	0.164
plate	0.017	22.41	5.68	3.18	0.41	1.52	0.001	0.022	0.181

Susceptibility to hydrogen embrittlement was examined by *slow strain rate tests* (SSRT) and fatigue crack propagation tests performed in hydrogen charging solutions with cathodic polarisation of steel samples. The character of fracture surfaces was examined using Scanning Electron Microscopy (SEM). The influence of hydrogen charging on the steel microstructure was investigated with the use of Transmission Electron Microscopy. (TEM), Atomic Force Microscopy in the magnetic force imaging mode (MFM) and Electron Backscatter Diffraction (EBSD).

RESULTS AND DISCUSSION

Investigation of hydrogen embrittlement in slow strain rate tests

The first stage of investigations was aimed at determining the influence of hydrogen charging on the plasticity of steel by uniaxial tensile tests carried out at slow strain rate. The tensile test specimens machined from bars were initially hydrogen pre-charged for 14 days with cathodic polarization in different solutions: 0.1 M H_2SO_4 or 0.1 M NaOH with the addition of 10 mg/l of As_2O_3 used as a hydrogen entry promoter or without the promoter. The specimens were subsequently tensile tested in the same conditions, at the strain rate of $2.6\times10^{-7}s^{-1}$. For comparison, SSRTs were also performed in air. Details of SSRT experiments can be found in [10]. The results of tensile tests, presented in Fig. 1, show that elongation is significantly less in tests performed during hydrogen charging, as compared to those performed in air; at the same time the reduction in elongation depends on the solution used [10]. The greatest reduction in the ductility of the samples was observed for the test conducted in the H_2SO_4 with the addition of As_2O_3. More conspicuous is the influence of testing environment on the reduction in area at fracture (RA_f), the value of which was determined on the basis of the following formula:

$$RA_f = (A_0 - A_f) / A_0 \quad (1)$$

where A_0 is the initial cross-section area of the sample, A_f is the cross-section area of the sample at fracture.

The question arises why is the loss in ductility different for samples tested in different environments? The examination of hydrogen concentration in specimens tensile tested in different solutions has revealed that the amount of hydrogen absorbed varies depending on the hydrogen charging solution [10]. In this study hydrogen content

was determined using electrochemical desorption method, by anodic polarization in 0.1 M NaOH at the same potential of 0.15 VHg/HgO [11]. Changes in the area at fracture as the function of hydrogen content are presented in Fig. 2.

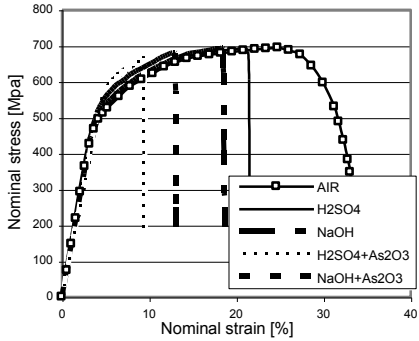


Fig. 1: Stress-strain curves of duplex steel in air and during hydrogen charging in different solutions [10]

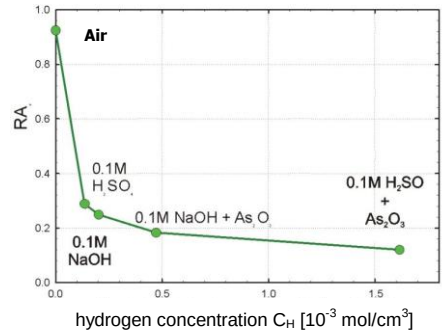


Fig. 2: Reduction in the area at fracture RA_f [%] as a function of hydrogen concentration in a sample [10]

The graph shows that ductility decreases with the increasing amount of hydrogen absorbed by the steel during cathodic charging [10]. Further investigations have revealed that in the case of samples that were initially pre-charged for 14 days and subsequently remained in air for 30 days for hydrogen desorption, the ductility measured during SSRT in air was not completely restored to the value of non precharged samples [12]. This means that during precharging hydrogen induces irreversible changes in the steel structure which leads to loss of ductility.
SEM observations of fracture surfaces after tensile tests have shown that the decrease in ductility is accompanied by the change in the fracture character - from ductile after tensile tests in air (Fig. 3) to brittle or brittle-ductile after tests performed in hydrogen charging environment (Fig. 4).

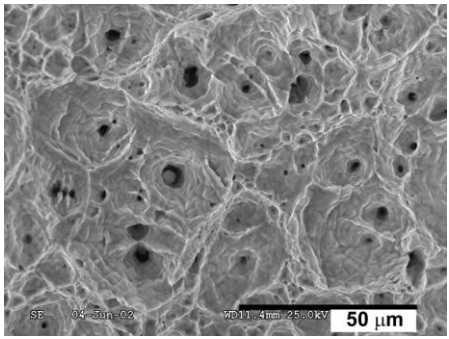


Fig. 3:. Steel fracture surface after tensile test in air (SEM)

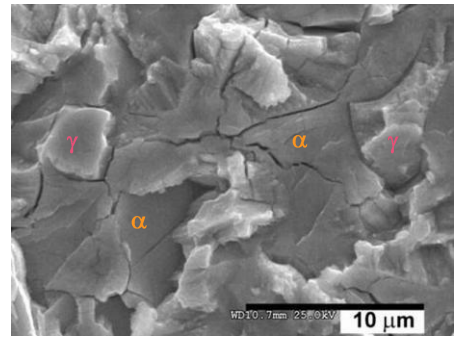


Fig. 4: Steel fracture surface after tensile test in H_2SO_4 + As_2O_3 (SEM)

In the latter case the observations have revealed cracks on the lateral surface of the sample (Fig. 5) as well as intercrystalline micro-cracks on ferrite/austenite interphase boundaries and transcrystalline cracks, mainly in the ferrite grains (Fig. 4). The analysis of the above results allows us to advance a thesis that the initiation and propagation of cracks during steel deformation may play a significant role in ductility loss and thus in hydrogen embrittlement.

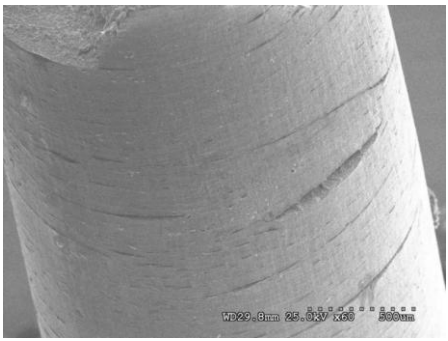


Fig. 5: Secondary cracks on the lateral surface of the sample after tensile test in 0.1 M H_2SO_4 + 10 mg/l As_2O_3 (SEM)

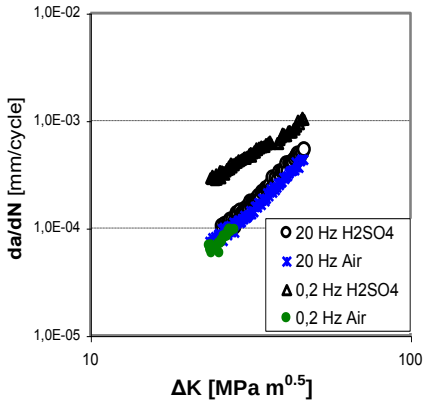


Fig. 6: Fatigue crack propagation rate for different loading frequencies in air and in 0.1 M H_2SO_4 + 10 mg/l As_2O_3

Investigations of fatigue crack propagation

In order to check if hydrogen favours crack propagation in duplex steel and to what extent, the fatigue crack propagation (FCP) rate was investigated in air and in hydrogen charging solution (0.1 M H_2SO_4 with the addition of 10 mg/l As_2O_3) with cathodic polarization. Compact tension specimens containing elecro-machined starting notch and pre-cracking by fatigue in air, were used for the fatigue tests. The tests were carried out with the use of horizontal dynamic testing machine, at constant force amplitude ΔP = 2970 N and load ratio R=0.1, at two frequencies of 0.2 Hz and 20 Hz. The values of rate da/dN as a function of stress intensity factor range ΔK are shown in Fig. 6. The experimental procedure is described in detail in [9]. The FCP rate da/dN in air is similar for both loading frequencies applied and does not differ significantly from the FCP rate in hydrogen charging solution at the frequency of 20 Hz. However, at the frequency of 0.2 Hz, FCP rate is considerably higher for the tests performed in hydrogen charging solution [9]. SEM studies revealed brittle character of crack surfaces during tests performed at low frequency in hydrogen charging solution, whereas EBSD studies revealed that in samples tested in air fatigue crack propagation is accompanied by plastic deformation [13].

The fact that hydrogen charging favours the initiation of cracks during tensile tests and accelerates crack propagation during fatigue tests suggests that hydrogen induces microstructural changes which increase the susceptibility of duplex steel to cracking.

Microstructural changes induced by hydrogen charging

Various microscopic and diffraction techniques of investigation were used to reveal hydrogen induced microstructural changes. It was proved on the basis of TEM observations [14, 15] that hydrogen charging leads to irreversible changes in steel microstructure: an increase of dislocation density and grain refinement in ferrite as well as a formation of stacking faults and martensite laths in austenite (Fig. 7). The occurrence of martensitic transformation after hydrogen charging was confirmed by the MFM (Fig. 8) [8] and EBSD technique [16].

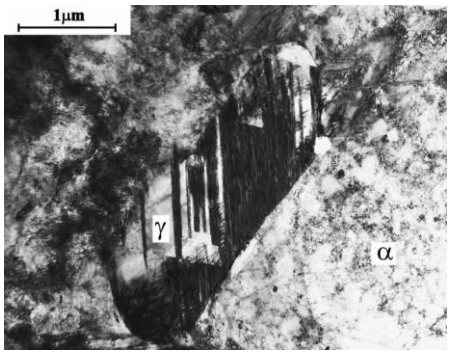


Fig. 7: Steel microstructure after hydrogen charging in 0.1M H2SO4 + 10mg/l As2O3. Stacking faults in austenite and high density of dislocations in ferrite.



Fig. 8: AFM image in a magnetic mode of steel after hydrogen charging. Dark (magnetic) laths of martensite in the light (paramagnetic) grains of austenite [8]

Similar microstructural changes were observed near crack tips in specimens submitted to corrosion fatigue tests at the frequency of 0.2Hz in hydrogen generating solution [17]. Apart from the microstructural transformations, the electron microscopy observations of samples after hydrogen charging also revealed transcrystalline microcracks in ferrite grains, located along stacking faults in austenite and on the ferrite/austenite and ferrite/martensite interphase boundaries [14-16]. It was shown that hydrogen charging for 14 days induced microstructural changes in external layer of the steel up to 0.2 mm from the surface. These microstructural transformations limit the possibility of plastic accommodation of stresses, and thus favour the formation of microcracks in the surface layer of steel (Fig. 5).

Factors inducing hydrogen embrittlement

The observed microstructural changes resulting from hydrogen charging allow us to explain the observed effects of hydrogen embrittlement by various factors:
- reduced ability of plastic accommodation of stresses due to hydrogen induced transformations in steel microstructure,
- formation of transcrystalline cracks, mainly in ferrite, the phenomenon that may be attributed to the presence of diffusive hydrogen, which reduces cohesion energy of ferrite [3],
- formation of intercrystalline cracks, the phenomenon that may be attributed to hydrogen trapping on interphase boundaries [4].

To determine the influence of each factor on the decrease of steel ductility tensile test with the strain rate of $2.6\times10^{-7}s^{-1}$ in various conditions were conducted. The testing conditions are presented in Table 2.

Table 2: Changes in ductility of DSS samples submitted to SSRT carried out in various conditions

No	Tensile test conditions	RA_f [%]	ΔRA [%] = $RA_{air} - RA_f$
1	Tensile test in air [RA_{air}]	93	0
2	hydrogen pre-charging in H_2SO_4 + As_2O_3 (14 days) followed by tensile test during hydrogen charging in the same environment	12	81.0
3	hydrogen pre-charging in H_2SO_4 + As_2O_3 (14 days) followed by hydrogen desorption for 30 days in air and tensile test in air	40	53
4	hydrogen pre-charging in H_2SO_4 + As_2O_3 (14 days), followed by removing of external layer (0.2 mm), hydrogen desorption for 30 days and tensile test in air	67	26

The table shows values for the reduction in area at fracture RA_f and ductility decrease ΔRA expressed as the difference between the reduction in area at fracture in air RA_{air} and reduction RA_f obtained in a given test. Tests 1 and 2 are described in first Section. In Test 3 the specimen was initially pre-charged for 14 days and then remained for 30 days in air for hydrogen desorption. One may notice a considerable decrease of ductility in Test 3 performed in air, compared to the sample that had not been pre-charged with hydrogen (see Test 1). This decrease may be related to hydrogen induced microstructural changes which are of irreversible nature.

During Test 4 the surface layer, where microstructural changes occurred, was removed, nevertheless the ductility was lower, compared to the non-charged sample. Reduced ductility in this case (ΔRA=26%) may be attributed to the hydrogen trapped on defects, mainly intercrystalline boundaries. It follows that all the factors

mentioned above have a similar contribution to the decrease of ductility in duplex steel.

SUMMARY AND CONCLUSIONS

In the light of the mechanical and microstructural results one may explain the phenomenon of hydrogen embrittlement of two-phase steel. Microstructural transformations occurring in ferrite and austenite under the influence of hydrogen limit the possibility of plastic stress accommodation during tensile tests. Reduced ability to plastic accommodation of stresses applies especially to ferrite where a considerable and uniform increase in dislocations density and grain refinement occur. In these conditions a possible mechanism of stress relaxation in ferrite is cracking which is additionally favoured by the presence of diffusive hydrogen reducing decohesion energy of ferrite. Consequently, fractures in this phase are brittle. In austenite microstructural changes consisting in stacking faults and martensite laths formation are more localised. As a result the surface of cracks in austenite has more ductile character.

Another factor contributing to steel embrittlement is the absorption and trapping of hydrogen at interphase boundaries, which phenomenon reduces intercrystalline cohesion. As a result of hydrogen induced microstructural changes, cracks are formed on the surface of the hydrogen charged steel. Hydrogen penetrates the cracks causing microstructural transformations in deeper areas of steel sample. This phenomenon favours the propagation of cracks and explains their brittle character.

To summarize, one may draw a conclusion that hydrogen embrittlement of duplex stainless steel results from synergistic effect of hydrogen induced microstructural transformations on the one side, and on the other, from the presence of diffusive hydrogen in grains and trapped hydrogen at intercrystalline boundaries.

ACKNOWLEDGMENTS

This work was supported by the Warsaw University of Technology and the Ministry of Science and Higher Education of Poland under the contract No. 3 T08A 032 27.

REFERENCES

1. Śmiałowski, M., Hydrogen in Steel, Pergamon Press (Oxford 1962)
2. Oriani, R.A. *et al*, Hydrogen degradation of ferrous alloys, Noyes Publications, Park Ridge, (New Jersey 1985)
3. Gavriljuk, V.G., Shivanyuk, V.N. and Foct, J., "Diagnostic experimental results on the hydrogen embrittlement of austenitic steels", *Acta Materialia*, Vol. 51 No. 5 (2003), pp. 1293-1305

4. Turnbull, A. and Hutchings R.B., "Analysis of hydrogen atom transport in two-phase alloy" *Mater. Sci. & Eng*., Vol. A177, (1994), pp. 161-171
5. Zakroczymski, T. and Owczarek E., "Electrochemical investigation of hydrogen absorption in a duplex stainless steel", *Acta Materialia*, Vol. 50, No. 10 (2002), pp. 2701-2713
6. El-Yazgi, A.A. and Hardie, D., "Stress corrosion cracking of duplex and super duplex stainless steels in sour environments", *Corrosion Science*, Vol. 40, No. (1998), pp. 909-930
7. Makhlouf, K. Sidhom, H., Triguia, I. and Braham C., "Corrosion fatigue crack propagation of a duplex stainless steel X6Cr Ni Mo Cu 25-6 in air and in artificial sea water", *Int. Journal of Fatigue*, Vol. 25, No. 2 (2003), pp. 167-179
8. Głowacka, A., Woźniak, M.J. and Świątnicki, W.A., "AFM study of austeno-ferritic stainless steel microstructure after cathodic hydrogen charging" *J. of Alloys & Compounds*, Vol. 404-406 (2005), pp. 595-598
9. Głowacka, A., Wysocka, O., Miśkiewicz, M., Pakieła, Z. and Świątnicki, W.A., "Fatigue–corrosion of austenitic-ferritic steel during hydrogen charging" (in polish) *Mechanika, Z. Nauk. Polit. Opolska*, Vol. 82, No. 304 (2005), pp. 305-314.
10. Zakroczymski, T., Głowacka, A. and Świątnicki, W.A., „Effect of hydrogen concentration on the embrittlement of a duplex stainless steel", *Corrosion Science*, Vol. 47, No. 6 (2005), pp. 1403-1414
11. Zakroczymski, T., "Electrochemical determination of hydrogen in metals" *J. of Electroanal. Chemistry*, Vol. 475, No 1 (1999), pp. 82-88
12. Głowacka, A., Gołaszewski, A. and Świątnicki, W.A., **"**Hydrogen Embrittlement of Austenitic-Ferritic Steel" *Inżynieria Materiałowa*, Vol. XXVIII, No 3-4 (2007), pp. 768-773
13. Głowacka A., Nolze G. and Świątnicki W.A., "EBSD study of corrosion fatigue of austenitic-ferritic steel", *Archives of Metallurgy and Materials Quarterly*, Vol. 50, No 1 (2006), pp. 7-11
14. Głowacka, A. and Świątnicki, W.A., "Effect of Hydrogen on the Microstructure Evolution of Duplex Stainless Steel" *J. of Alloys & Compounds*, Vol. 356-357 (2003), 701-704
15. Głowacka, A., Jezierska, E. and Świątnicki, W.A., "Hydrogen induced defects in austenite and ferrite of a duplex steel", *Journal of Microscopy*, Vol. 223, No. 3, (2006), pp. 282-284
16. Głowacka, A., Woźniak, M.J., Nolze, G. and Świątnicki, W.A., "Hydrogen induced phase transformations in austenitic-ferritic steel" *Solid State Phenomena*, Vol. 112 (2006), pp. 133-140
17. Golebiowski, B., Świątnicki, W.A. and Gasperini, M. "Microstructural changes induced near crack tip during corrosion fatigue tests in austenitic - ferritic steel" paper submitted to *J. of Microscopy* (2008)

Effects of Hydrogen on Materials
Proceedings of the 2008 International Hydrogen Conference
Brian Somerday, Petros Sofronis, Russell Jones, editors, p 163-170
Copyright © 2009 ASM International®
All rights reserved.
www.asminternational.org

HYDROGEN-INDUCED ε-MARTENSITE AND HYDROGEN EMBRITTLEMENT OF AUSTENITIC STEELS

V.N. Shyvanyuk*, S.M. Teus, V.G. Gavriljuk
G.V. Kurdyumov Institute for Metal Physics, Vernadsky Blvd. 36, 03142 Kiev, Ukraine
** e-mail: shyva@imp.kiev.ua, tel/fax: 380 44 4246427*

ABSTRACT

The effect of alloying elements (Cr, Mn, Ni, Cu, Al, Si) on the fraction of hydrogen-induced ε-martensite has been studied. It is shown that Cr, Mn, Si assist the hydrogen-induced γ→ε transformation, whereas Ni, Cu, Al retard it. The fraction of hydrogen-induced ε-martensite decreases or increases in accordance with the corresponding change of stacking fault energy due to alloying. Mechanical properties of austenitic steels do not deteriorate with increasing fraction of ε-martensite and, moreover, the resistance to hydrogen brittleness increases at high ε-martensite contents. This result is at variance with the generally accepted opinion about the ε-martensite as a reason for hydrogen brittleness.

***Keywords*:** Austenitic steel, Hydrogen brittleness, Epsilon-Martensite.

INTRODUCTION

Stable austenitic steels are known as materials which don't reveal martensitic transformations under any cold work or cooling down to low temperatures. Nevertheless, the hydrogen charging of these steels (gaseous or electrolytic) leads to the splitting of fcc reflections in the X-ray diffraction patterns, which is attributed to formation of so-called γ* phase, and to appearance of new reflections from the hcp ε_H-phase (e.g. [1,2]). The hydrogen-induced ε-phase is considered to be responsible for hydrogen brittleness (e.g., [1-3]). However, as shown in the recent study [4], the increase in the fraction of the ε-phase caused by the alloying of the austenitic steel with Si decreases hydrogen brittleness. This interesting effect merits to be studied in more detail.

Usually the hydrogen-induced γ→ε transformation is discussed in terms of mechanical stresses like it occurs due to cold work (see e.g. [5,6]). Nevertheless, it was obtained in the *ab initio* calculations of the electronic structure [7] that, in absence of any stresses, hydrogen transforms the fcc structure into the hcp one because it decreases the total electron energy of crystal lattice.

Correspondingly, as reliably shown in [3] using TEM and in [8] by means of X-ray diffraction, hydrogen decreases stacking fault energy (SFE) in austenitic steels, which should decrease their stability to the γ→ε transformation. Therefore, one can vary the hydrogen-caused fraction of ε-martensite due to alloying steel with elements which affect the SFE of austenite.

The aim of this paper is to clarify the effect of alloying elements on the amount of hydrogen-induced ε-martensite and compare it with mechanical properties of studied alloys.

EXPERIMENTAL

A set of steels based on the Cr15Ni25 composition was additionally alloyed with Mn, Si, Cu, Al (see Table 1). The alloying elements were chosen in accordance with their effect on SFE. Ni, Cu, Al are known to increase SFE in austenitic steels, whereas Cr, Mn, Si decrease it [9-11].

Table 1. Chemical compositions of studied alloys*

Alloy	Cr	Ni	Mn	Si	Al	Cu
C15Ni20	15.3	19.8	0.2	<0.01	<0.1	<0.1
Cr15Ni25	14,7	25,8	—	—	—	—
Cr15Ni40	14,7	40,5	—	—	—	—
Cr15Ni25Cu2	14,7	25,6	—	—	—	2,01
Cr15Ni25Si2	15	25,5	—	1,85	—	—
Cr15Ni25Al2	15,1	26	—	—	1,98	—
Cr15Ni25Mn15	15,3	25,6	14,77	—	—	—
Cr25Ni25	24,6	25,9	—	—	—	—

*Elements not purposefully induced were not determined.

The ingots of 200 g in the mass were melted in an induction furnace under argon atmosphere followed by the homogenization at 1150 °C for 24 h. For all specimens, the final solid solution treatment was performed at 1050 °C for 30 min.

Some details of experiments are given in Table 2.

Table 2. Methods, experimental and charging conditions

Method	Specimen shape and size [mm^3]	Conditions of hydrogen charging			Experimental conditions
		T, [K]	J, [mA/cm^2]	t, [hours]	
X-ray diffraction	Plate, 15×15×1	295	50	72	CoK_α radiation, measured at 295 K
Mechanical tests	Foil, 120×8×0.08	295	50	72	Strain rate: 1.7×10^{-3} s^{-1}, tested at 295 K

The specimens were charged with hydrogen at room temperature in 1N H_2SO_4 solution containing 0.01 g/l $NaAsO_2$. A platinum foil was used as anode. After charging, the specimens were put into liquid nitrogen to prevent the hydrogen degassing. The installation of specimens into the holder of X-ray diffractometer or the machine for mechanical tests took less than 120 s.

A single crystal of Cr18Ni10N0.2 steel obtained using the Bridgeman technique (Institute of Physical Engineering, Tomsk, Russia) was used for the studies of the role of dislocation splitting on the $\gamma\rightarrow\varepsilon_H$ transformation. The 1 mm thick single

crystal plates were cut on the {110} plane. Thereafter, the specimens of nearly 1×1 mm^2 cross section were cut in this plane on <100> and <111> directions.

The machine H5K-T produced by Hounsfield company, UK, was used for mechanical tests. The strain rate was $1.7 \cdot 10^{-3}$ s^{-1}. All measurements were carried out at room temperature. The hydrogen embrittlement was estimated using the formula $HE = (\delta_0 - \delta_H)/\delta_0$, where δ_0 and δ_H are the relative elongations of hydrogen-free and hydrogen-charged samples, respectively.

RESULTS AND DISCUSSION

1. Stress-induced splitting of dislocations and hydrogen-induced ε-martensite.

We used the orientation dependence of dislocation splitting in order to demonstrate its role in the hydrogen-caused γ→ε transformation. It is known [12-14] that the splitting of dislocations under applied stress depends on actual stresses on the leading and trailing dislocations. The crystals with "hard" orientation <100> along the tension axis are characterized by the narrowing of dislocations and, correspondingly, reveal the largest yield strength and cold work hardening. The "soft" orientation <111> provides the additional dislocation splitting, which leads to decreasing the strength. The hydrogen charging changes this relation (see Table 3).

Table 3. Yield strength, ultimate strength and relative elongation of single crystals of steel Cr18Ni10N0.2 with orientations [100](110) and [111](110) before (numerator) and after (denominator) hydrogen charging.

Orientation	$R_{p0.2}$, MPa	R_m, MPa	δ, %
<100>	485/150	1150/395	35/32
<111>	240/291	635/560	45/35

It transforms the <100> direction to "hard" and the <111> direction to "soft" orientations. A reason for this phenomenon was found due to the X-ray diffraction study of samples deformed by 15% tension before or after H-charging (Fig. 1).

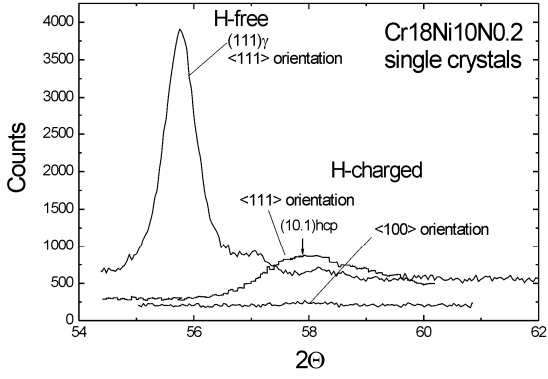


Fig. 1. X-ray diffraction of hydrogen-free and hydrogen-charged single crystals

The X-ray diffraction of samples which were not hydrogen-charged does not depend on the crystallographic orientation. Hydrogen dissolution causes the following effect: reflection [10.1] of ε-martensite appears in the X-ray diffraction pattern of <111> single crystal and it is absent in case of <100> orientation.

Thus, the stress-induced splitting or narrowing of dislocations assists or excludes the hydrogen-caused γ→ε transformation and, for this reason, changes the orientation dependence of mechanical properties.

2. Effect of alloying elements on the hydrogen-induced γ→ε transformation and brittleness.

As example, a fragment of X-ray diffraction pattern for hydrogen-charged steel Cr25Ni25 is presented in Fig. 2. The fraction of ε-martensite was estimated using the comparative intensities of (γ^*+γ_e)- and ε-phases, where $\gamma^*$and γ_e denote the hydrogen-rich and hydrogen-exhausted fcc phases (see Table 4).

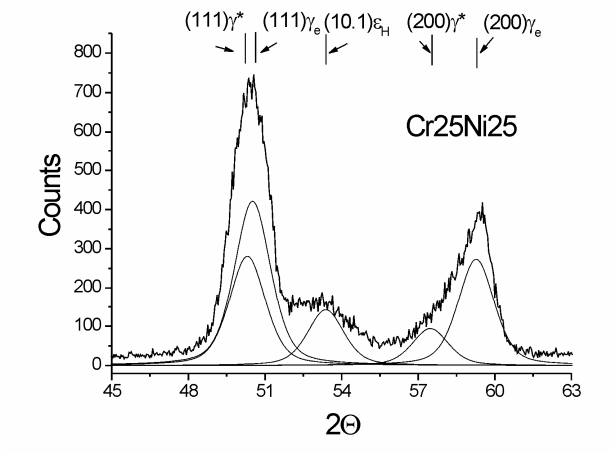


Fig. 2. Fragment of X-ray diffraction pattern for hydrogen-charged steel Cr25Ni25. Fitting is carried out in terms of hydrogen-caused miscibility gap in the fcc solid solution (see, e.g. [1,2]) and γ→ε transformation.

Table 4. Fraction of ε_H-martensite as estimated from X-ray diffraction patterns.

Steel	Area under peak $(111)\gamma_H$	Area under peak, $(10.1)\varepsilon_H$	Ratio, ε_H/γ_H
Cr15Ni25	23082	3811	0,1651
Cr15Ni40	717001	—	0
Cr25Ni25	23299	7976	0,3423
Cr15Ni25Cu2	10218	1420	0,1390
Cr15Ni25Si2	5743	1202	0,2093
Cr15Ni25Al2	21184	—	0
Cr15Ni25Mn15	23127	5528	0,2390

The addition of nickel, aluminum, and copper reduces the γ→ε transformation, whereas alloying with chromium, silicon and manganese intensifies it.

Thus, the effect of alloying elements on the hydrogen-induced fraction of ε-martensite is consistent with their effect on the SFE.

The results of tension tests for hydrogen-free and hydrogen-charged Cr15Ni25-based steels are presented in Figures 3 and 4, respectively. Mechanical properties are given in Table 5.

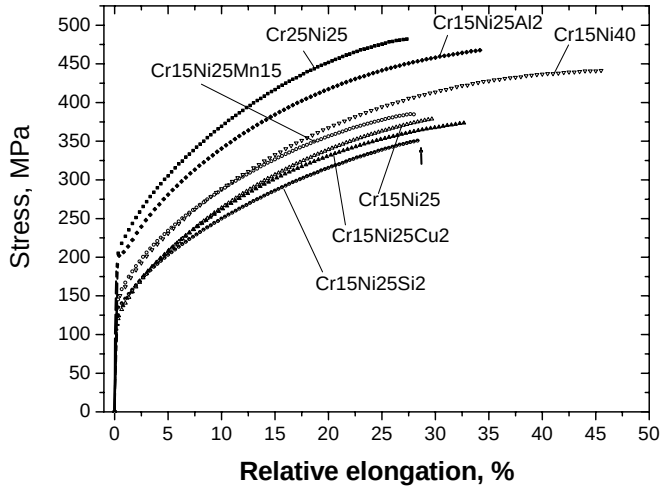


Fig. 3. Stress-elongation curves of hydrogen-free steels.

It is seen that alloying with Ni, Al and Cu improves plasticity of hydrogen-free steels, whereas Mn, Si, and Cr impair it. After hydrogen charging the steels which had a higher plasticity become more brittle in comparison with those having lower plasticity in the hydrogen-free state.

Table 5. Mechanical properties of hydrogen-free (numerator) and hydrogen-charged (denominator) steels.

Steel	$R_{p0.2} \pm 5$, MPa	$R_m \pm 5$, MPa	δ, %	HE, %
Cr15Ni25	125 210	378 228	29 1.6	94
Cr15Ni40	147 192	442 195	45.2 0.35	99
Cr25Ni25	205 276	480 380	27.3 10.1	63
Cr15Ni25Cu2	131 199	374 212	32 1.0	97
Cr15Ni25Al2	205 295	470 350	34 1.7	95

Cr15Ni25Si2	135 260	350 290	28 4.4	84
Cr15Ni25Mn15	155 275	385 315	27.3 5.5	80

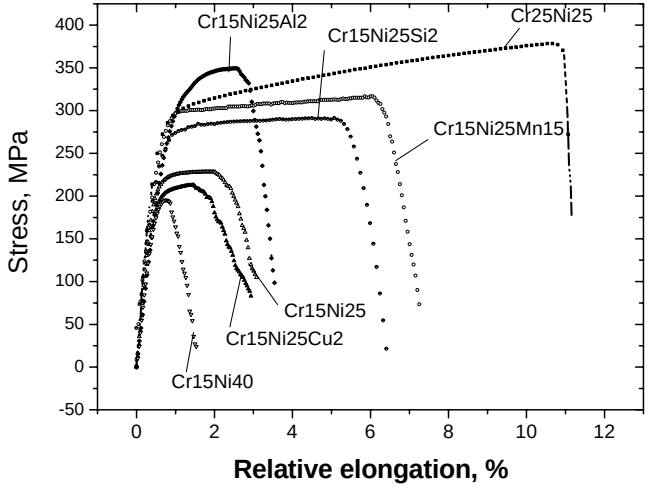


Fig. 4. Stress-elongation curves of hydrogen-charged steels.

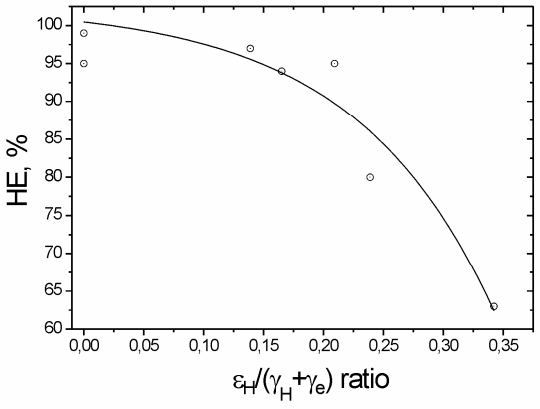


Fig. 5. Effect of ε-martensite fraction on hydrogen embrittlement of studied alloys.

It is seen from Fig. 5 that plasticity of hydrogen-charged steels does not deteriorate due to the ε-martensite. Moreover, at its high contents, the steel becomes more stable to hydrogen brittleness.

A reason for this effect can be understood while analyzing the stress-elongation curves in Fig.4. Steels with no or small fraction of ε-martensite

(Cr15Ni40, Cr15Ni25Cu2, Cr15Ni25 and Cr15Ni25Al2) are characterized by a rapid localization of plastic deformation. The applied stress decreases after rather small tension strain, which is the evidence for the locally reduced cross section of the samples under deformation. The increase in the fraction of the hydrogen-induced ε-martensite (steels Cr15Ni25Si2, Cr15Ni25Mn15, and Cr25Ni25) leads to higher values of elongation before the localization of plastic flow starts.

Therefore, one can suppose that, at sufficiently large fractions of the ε-matensite, it prevents the hydrogen-caused localization of plastic flow and, for this reason, can increase the resistance to hydrogen embrittlement.

CONCLUSIONS

1. Alloying of Fe–Cr–Ni-based solid solutions with Ni, Al and Cu decreases the effect hydrogen-induced $\gamma \rightarrow \varepsilon$ transformation, whereas Mn, Cr, and Si intensify it. It can be attributed to the influence of these elements on the SFE in the iron austenite.
2. The intensity of hydrogen-caused $\gamma \rightarrow \varepsilon_H$ transformation in austenitic steels correlates with the effect of alloying elements on stacking fault energy: the smaller the SFE the higher the ε_H fraction in the hydrogen-charged steel is.
3. Hydrogen embrittlement of austenitic steels is not concerned with the hydrogen-caused $\gamma \rightarrow \varepsilon_H$ transformation. Moreover, at its large fraction, the ε_H martensite increases the resistance of austenitic steels to hydrogen embrittlement.

AKNOWLEGEMENTS

The present work was carried out within the frame of Science and Technology Center in Ukraine, project 3145.

REFERENCES

1. Narita N., Alstetter C.J., Birnbaum H.K., “Hydrogen-related phase transformations in austenitic stainless steels”, Metal. Trans. A, Vol. 13 (1982), pp. 1355-1365.
2. Ulmer D.G., Altstetter C.S., „Phase Relations in the Hydrogen-Austenite System“, Acta Metal et Mater, Vol. 41 (1993) pp. 2235-2241.
3. Inoue A., Hosoya Y., Masumoto T., “The effect of Hydrogen on Crack Propagation Behavior amd Microstructures around Cracks in Austenitic Stainless Steels”, Transactions ISIJ, Vol. 19 (1979), pp. 170-178.
4. Gavriljuk V.G. , . Shivanyuk V.N, Foct J., “Diagnostic experimental results on the hydrogen embrittlement of austenitic steels”, Acta materialia, Vol.51 (2003), pp. 1293-1305
5. Rigsbee J. M., “TEM observations on hydrogen-induced ε-HCP martensite”, Metallography, Vol. 11 (1978), pp. 493-498.

6. Mathias H., Katz Y., Nadiv S., “Hydrogenation effects in austenitic steels with different stability characteristics”, Metal. Science, Vol. 12 (1978), pp.129-137.
7. Vakhney A.G., Yaresko A.N., Antonov V.N., Nemoshkalenko V.V., Gavriljuk V.G., Tarasenko A.V., Smurov I., “The effect of hydrogen on the electronic structure and phase stability of iron-based alloys doped with chromium and nickel”, J. Phys.: Condensed Matter, Vol. 10 (1998), pp. 6987-6994.
8. Pontini A., Hermida J., “X-ray diffraction measurement of the stacking fault energiy reduction induced by hydrogen in an AISI 304 steel”, Scripta Mater., Vol. 39 (1998), pp. 1831-1837.
9. Schramm R.E., Reed R.P., “Stacking fault energies of seven commercial austenitic stainless steels”, Metall. Trans. A, Vol. 6 (1975), pp. 1345-1351.
10. Dulieu D., Nutting J., Metallurgical developments in high-alloy steels (Special report №86) The Iron and Steel Institute (London, 1964), pp. 140-145.
11. Vitos L., Nilsson J-O., Johansson B. , ”Alloying effects on the stacking fault energy in austenitic stainless steels from first-principles theory”, Acta Mater., Vol.54 (2006), pp. 3821-3826.
12. Copley S.M., Kear B.H., “The dependence of the width of a dissociated dislocation on dislocation velocity”, Acta Metall., Vol. 16 (1968), pp. 227.
13. Kestenbach H.J., “Effect of applied stress on partial dislocation. separation and dislocation substructure in austenitic stainless-. Steel ”, Phil Mag., Vol.36 (1977), pp. 1509-1515.
14. Vergnol J.F.M., Grilhe J.R., “Relationship between extrinsic stacking faults and mechanical twinning in F.C.C. solid solutions with low stacking fault energy”, J. Physique, Vol. 45 (1984), pp.1479-1490.

Effects of Hydrogen on Materials
Proceedings of the 2008 International Hydrogen Conference
Brian Somerday, Petros Sofronis, Russell Jones, editors, p 171-178
Copyright © 2009 ASM International®
All rights reserved.
www.asminternational.org

HYDROGEN EFFECTS ON STRAIN-INDUCED MARTENSITE FORMATION IN TYPE 304L STAINLESS STEEL

Michael J. Morgan, Poh-Sang Lam
Savannah River National Laboratory, Aiken, SC, USA

Dean A. Wheeler
PCC Airfoils, Minerva, OH, USA

INTRODUCTION

Unstable austenitic stainless steels undergo a strain-induced martensite transformation. The effect of hydrogen on this transformation is not well understood. Some researchers believe that hydrogen makes the transformation to martensite more difficult because hydrogen is an austenite stabilizer. Others believe that hydrogen has little or no effect at all on the transformation and claim that the transformation is simply a function of strain and temperature [1-4]. Still other researchers believe that hydrogen should increase the ability of the metal to transform due to hydrogen-enhanced dislocation mobility and slip planarity [5, 6]. While the role of hydrogen on the martensite transformation is still debated, it has been experimentally verified that this transformation does occur in hydrogen-charged materials [1-7].

What is the effect of strain-induced martensite on hydrogen embrittlement? Martensite near crack-tips or other highly strained regions could provide much higher hydrogen diffusivity and allow for quicker hydrogen concentration [8-10]. Martensite may be more intrinsically brittle than austenite and has been shown to be severely embrittled by hydrogen [1]. However, it does not appear to be a necessary condition for embrittlement since Type 21-6-9 stainless steel is more stable than Type 304L stainless steel but susceptible to hydrogen embrittlement [1].

In this study, the effect of hydrogen on strain-induced martensite formation in Type 304L stainless steel was investigated by monitoring the formation of martensite during tensile tests of as-received and hydrogen-charged samples and metallographically examining specimens from interrupted tensile tests after increasing levels of strain. The effect of hydrogen on the fracture mechanisms was also studied by examining the fracture features of as-received and hydrogen-charged specimens and relating them to the stress-strain behavior.

EXPERIMENTAL PROCEDURE

Tensile specimens were machined from the plate grade Type 304L stainless steel having the composition shown in Table 1. The specimen axis was aligned parallel to the rolling direction. Samples were exposed to 69 MPa of hydrogen gas at 350 C for three weeks. The treatment was designed to saturate the samples with hydrogen and the hydrogen concentration was estimated to be 5500 atomic parts per million by using the solubility values of San Marchi, et al. [11]. As-received and hydrogen-charged samples were tested at room temperature in air at an initial strain rate of 1 x 10^{-4} / sec. The formation of strain-induced α' (alpha-prime) martensite during the tensile test was monitored by recording the change in the magnetic phase of the sample by using a ferrite meter mounted to the center of the tensile specimen. The meter was calibrated by using a mild steel sample (100% bcc phase) with a maximum ferrite # of 30.0. In addition, the amount of martensite transformed was qualitatively determined by metallography after interrupted tensile tests.

TABLE 1: COMPOSITIONS OF STAINLESS STEEL FORGINGS (WEIGHT %)

	Cr	Ni	Mn	Mo	C	Si	P	S	N	Co	O	Cu
Type 304L Heat V73204	18.24	8.19	1.85	.33	.018	.36	.028	.004	.073	.14	.002	.21

RESULTS

Figure 1 shows a comparison of the stress-strain behavior for the as-received and hydrogen charged specimens. Internal hydrogen increased the yield strength of the steel by about 10% and decreased the elongation by 66%. The hydrogen-charged sample failed suddenly prior to necking at a stress value that was lower than the ultimate strength of the uncharged sample which necked down prior to failure. This suggests a fracture mode controlled by a critical stress. The uncharged samples showed a large reduction in area and a prominent necked region. The hydrogen-charged specimens showed much smaller reduction-in-area, almost no necking, and numerous secondary cracks on the specimen surface (Fig. 2).

Figure 3 shows the fracture modes of the uncharged and hydrogen-charged samples. Uncharged samples failed by dimpled rupture (Fig. 3a) while charged samples had two distinct fracture features. Twin-boundary parting characterized by large, flat facets, extending over one grain only, was interspersed within larger regions of quasi-cleavage (Fig. 3b). Traces of deformation bands in the underlying grain could be seen on many of the large flat facets, another characteristic of twin-boundary parting [1-3]. The quasi-cleavage fracture appearance was most likely due to hydrogen-induced separation along austenite-martensite interfaces [3] or deformation bands [8].

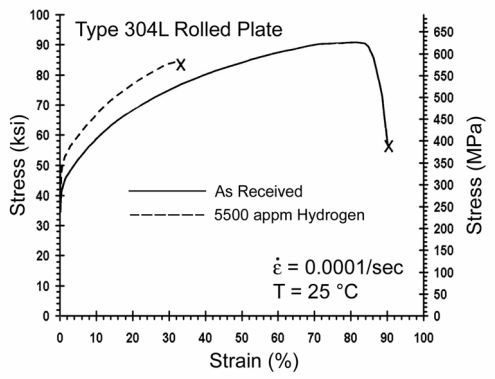
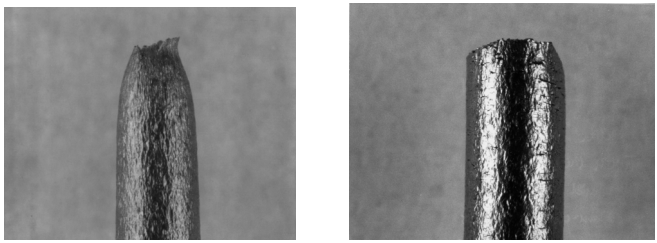
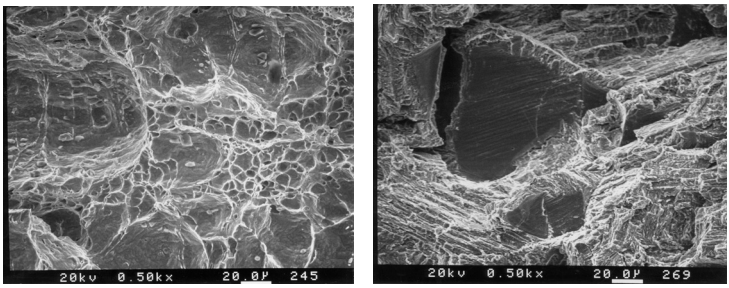


Figure 1: Comparison of Tensile Behavior for the Type 304L Stainless Steel Specimens in the As-Received and Hydrogen-Charged Conditions. Uncharged Samples Necked Down before Failure; Charged Samples Failed before Necking as Indicated by the "x".



(a) **(b)**

Figure 2: Comparison of Fractured Tensile Specimens in the (a) As-Received and (b) Hydrogen-Charged Conditions.



(a) **(b)**

Figure 3: Comparison of Fracture Appearance of Tensile Specimens in the (a) As-Received and (b) Hydrogen-Charged Conditions.

Figure 4 shows the results of the in-situ measurement of transformed martensite during the tensile tests. The results suggest that hydrogen charged samples had slightly less transformed martensite than the uncharged samples. The results are different than those of Caskey at ambient temperature, which indicated that hydrogen caused a slight increase in strain-induced martensite in Type 304L stainless steel [3]. However, the results of Fig. 4 are misleading because the samples did not always fail in the center of the gage section, where the ferrite probe was mounted. Measurements after the tensile test indicated that ferrite was higher at the point of fracture than it was at the center of the gage.

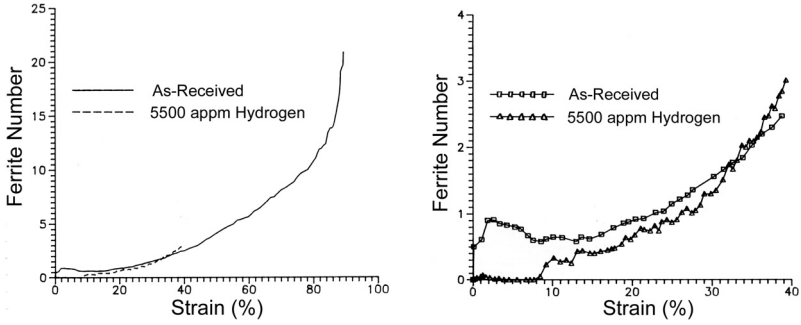
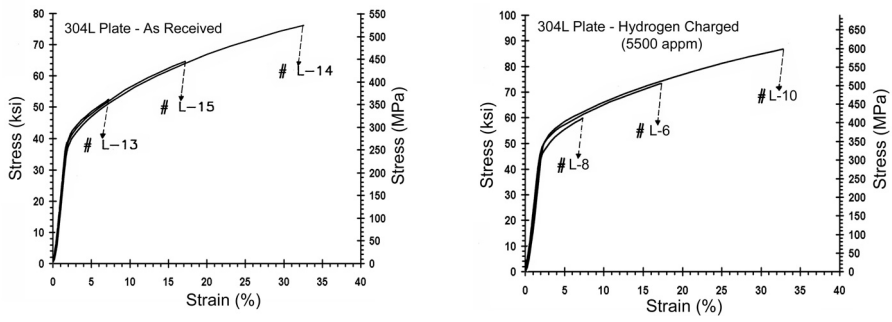


Figure 4: Increase in Ferrite Number with Increasing Strain during Tensile Test for As-Received and Hydrogen-Charged Samples. Low Strain Region on Right.



(a) **(b)**

Figure 5: Tensile Specimens were interrupted at Plastic Strain Values of 5, 15, and 30% and Metallographically Examined: (a) As-Received and (b) Hydrogen-Charged

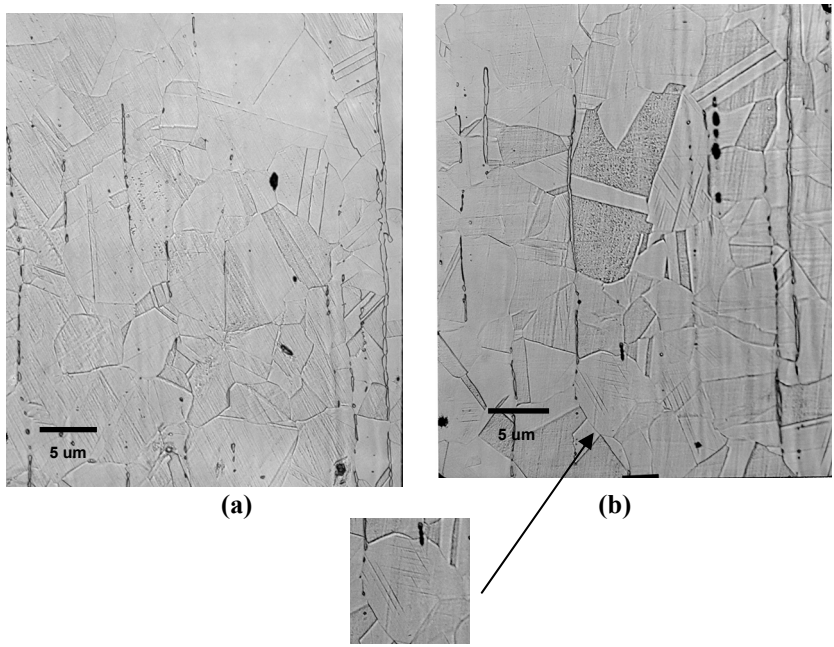


Figure 6: Tensile Specimens Interrupted after 5% Plastic Strain: (a) As-Received and (b) Hydrogen-Charged. Inset Shows Transformed Martensite.

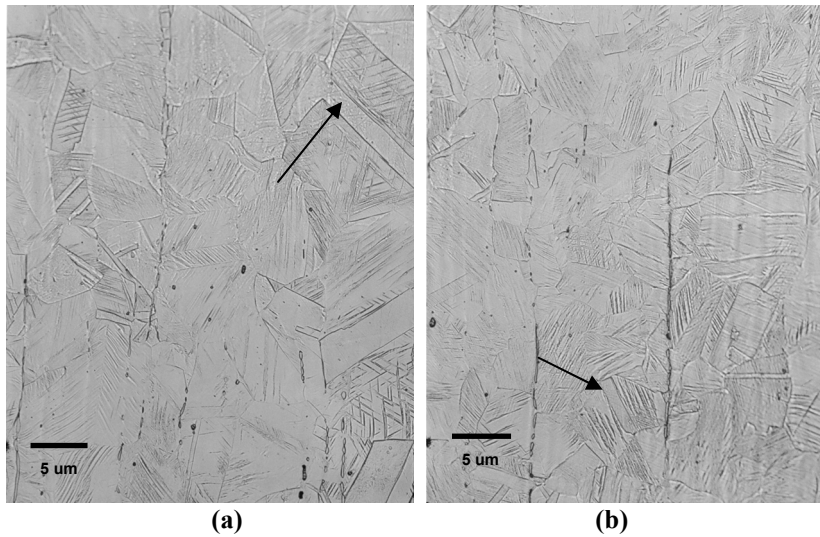


Figure 7: Tensile Specimens Interrupted after 30 % Plastic Strain: (a) As-Received and (b) Hydrogen-Charged. Arrows Indicate Feathery Appearance of Transformed Martensite.

Metallographic examination of interrupted tensile tests (Figures 5-7) indicates that hydrogen slightly increases the amount of transformed martensite at equivalent levels of plastic strain. Little or no martensite was seen in the elastically strained samples. At low levels of plastic strain ($\varepsilon_p < 5\%$), a very small amount of martensite could be seen in the center of few grains for the hydrogen-exposed samples (Fig. 6). No martensite was seen in the unexposed sample at this level of plastic strain (Fig. 6). For higher levels of plastic strain (up to 30% ε_p), the hydrogen-exposed samples had slightly more transformed martensite than the unexposed samples (Fig. 7). In total, the metallographic observations did not indicate a very strong effect of hydrogen on the amount of strain-induced martensite in this steel.

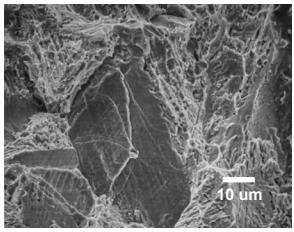


Figure 8: Hydrogen-Charged Sample Fracture Features. A Particle in the Center of the Twin Boundary Facet Apparently Acted as a Crack Nucleus.

DISCUSSION

The stress-strain tests did not indicate a very strong effect of hydrogen on the amount of strain-induced martensite. However, they did indicate a rather dramatic effect of hydrogen on the fracture behavior. The fracture surfaces of the hydrogen-charged specimens revealed two distinctly different fracture features (Fig. 3b). Isolated, flat twin-boundary facets were separated by more ductile features like dimpled rupture and quasi-cleavage fracture. The microvoids in the dimpled rupture areas were much smaller and more closely spaced than the microvoids on the as-received sample fracture surfaces. The quasi-cleavage fracture modes were only seen in the hydrogen-charged samples. Figure 8 shows that at least some of the twin boundary facets contained particles that apparently act as crack nuclei.

The stress-strain behavior of the hydrogen-charged samples was different than the as-received sample behavior as well. Hydrogen-charged samples tended to fail well after yield and just at or after maximum load. The maximum load point was very sharp, unlike the as-received samples which tended to show a much more smooth and rounded-off stress strain curve at maximum load and beyond. Caskey reports numerous twin boundary microcracks oriented transverse to the tensile axis in longitudinal sections of tensile specimens [3].

Together, these observations suggest that, in hydrogen-charged samples, the twin-boundaries are weakened by hydrogen and separate after some amount of plastic strain. High local stresses from deformation bands intersecting the twin boundaries

may be needed to separate the weakened twin-boundary interface. After nucleation of numerous microcracks in the gage section of the tensile sample, the effective cross-sectional area would be substantially reduced, which would lead to the fast, overload fracture of the remaining ligaments as shown schematically in Fig. 9. The fast overload fracture regions of the hydrogen-charged samples were dominated by a quasi-cleavage fracture appearance.

What is the role of martensite formation on this fracture mode? Hydrogen may have slightly increased the amount of strain-induced martensite at any given level of strain. The formation of flat facets has been related to the cracking of twin boundaries [12-14]. Strain-induced martensite was not evident on the fracture surfaces of the uncharged samples (Fig. 3a). On the other hand, a significant increase in the extent of quasi-cleavage fracture was observed on the fracture surfaces of hydrogen-charged samples (Fig. 3b). Apparently, the ligaments between the areas of cracked twin boundaries separate along the austenite-martensite interfaces or deformation bands when hydrogen is present in the steel, resulting in the quasi-cleavage appearance. Thus, cracking of hydrogen weakened twin boundary interfaces and hydrogen-induced quasi-cleavage of the ligaments between the fractured twin boundaries results in the marked reduction in elongation (Fig. 1).

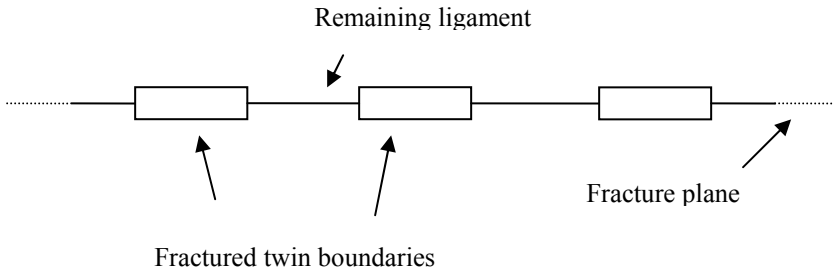


Figure 9: Schematic showing the apparent fracture mechanism of hydrogen-charged samples.

SUMMARY

Tensile tests showed that hydrogen-charged samples had higher yield strengths, lower elongations and different fracture modes than uncharged samples. Metallographic observations indicate that hydrogen-charged samples had slightly more material transformed to martensite than uncharged samples at equivalent levels of strain. Uncharged samples failed by the microvoid nucleation and growth process. Hydrogen-charged samples failed by isolated twin-boundary cracking near maximum load followed by quasi-cleavage of transformed martensite of the ligaments between the twin-boundary facets.

ACKNOWLEDGMENTS

This document was prepared in conjunction with work accomplished under Contract No. DE-AC09-08SR22470 with the U. S. Department of Energy.

REFERENCES

1. G. R. Caskey, Jr., "Hydrogen Effects in Stainless Steels", Hydrogen Degradation of Ferrous Alloys, ed. J. P. Hirth, R. W. Oriani, and M. Smialowski, eds., (Park Ridge, NJ: Noyes Publication, 1985), p. 822.
2. G. R. Caskey, Jr., "The Role of Twinning and Transformation in Hydrogen Embrittlement of Austenitic Stainless Steels", Environmental Degradation of Engineering Materials, (M. R. Louthan and R. P. McNitt, eds.), pp. 437-450, Virginia Polytechnic Institute, Blacksburg, VA (1977).
3. G. R. Caskey, Jr., "Hydrogen Compatibility Handbook for Stainless Steels", E. I. du Pont de Nemours & Co., Savannah River Laboratory, Aiken, SC 29808, DP-1643, June, 1983.
4. A. W. Thompson and O. Buck, *Metall. Trans.,* Vol. 7A (1976), pp. 329-331.
5. M. R. Louthan, G. R. Caskey, J. A. Donovan, and D. E. Rawl, *Materials Science and Engineering,* Vol. 10 (1972), pp. 357-68.
6. A. W. Thompson, *Metall. Trans*, Vol. 4 (1973), pp. 2819-25.
7. C. Pan, W. Y. Chu, Z. B. Li, D. T. Liang, Y. J. Su, K. W. Gao, L. J. Qiao, *Materials Science and Engineering,* Vol. A351 (2003), pp. 293-298.
8. D. G. Ulmer and C. J. Altstetter, "Mechanism For Hydrogen Embrittlement of Austenitic Stainless Steels", Proc. Fourth Int. Conf. on Hydrogen Effects on Material Behavior, ed. A. W. Thompson and N. R. Moody, (Warrendale, PA: The Minerals, Metals & Materials Society, 1989), p. 421.
9. T. P. Perng and C. J. Alstetter, "Effects of Deformation on Hydrogen Permeation in Austenitic Stainless Steels", *Acta Met*, Vol. 34 (1986), p. 1771.
10. T. P. Perng, C. J. Altstetter, *Metall. Trans.,* Vol. 19A (1988), p. 145.
11. C. San Marchi, B. P. Somerday and S. L. Robinson, "Permeability, Solubility and Diffusivity of Hydrogen Isotopes in Stainless Steels at High Gas Pressures", *International Journal of Hydrogen Energy*, Vol. 32, Issue 1 (2007), pp. 100-116.
12. W. Y. Chu, J. Yao, C.M. Hsiao, *Metall. Trans. A,* Vol. 15 (1980), p. 729.
13. H. Hanninen and T. Hakarainer, *Corrosion*, Vol. 36 (1980), p. 47.
14. G. H. Yu, Y. H. Cheng, L. J. Chen, W.Y. Chu, *Corrosion*, Vol. 53 (1997), p. 762.

Effects of Hydrogen on Materials
Proceedings of the 2008 International Hydrogen Conference
Brian Somerday, Petros Sofronis, Russell Jones, editors, p 179-186
Copyright © 2009 ASM International®
All rights reserved.
www.asminternational.org

ORIENTATION SPECIFIC MECHANICAL ASSESSMENT OF HYDROGEN PRECHARGED STAINLESS STEELS USING NANOINDENTATION

D.F. Bahr, N.R. Overman
Washington State University, WA USA

C.W. San Marchi and K.A. Nibur
Sandia National Laboratories, Livermore, CA USA

ABSTRACT

In this paper we present measurements of the localized mechanical response in two commercial stainless steels and a nickel-based alloy using a combination of nanoindentation, orientation imaging microscopy, and atomic force microscopy. Individual grains of the material were identified using OIM both before and after gas phase hydrogen precharging. The effective elastic response of these various grains was measured using nanoindentation, and, once corrected for orientation effects, was shown to be sensitive to hydrogen precharging. In most cases the measured unloading modulus decreased with hydrogen precharging, while the hardness generally increased after hydrogen charging.

INTRODUCTION

While extensive studies of hydrogen embrittlement mechanisms have been documented over many years, it is only more recently that studies, which can locally probe the effects of hydrogen in bulk materials, have become experimentally viable. Observations of hydrogen interactions on a very localized scale, such as *in situ* observations in the transmission electron microscopy [1] have different stress states than studies of the effects of cathodic hydrogen charging on the behavior of stainless steel foils during tension testing [2,3]. In these cases hydrogen increased the yield stress and decreased ductility. Examination of foil surfaces after testing revealed a coarsening of slip steps, which suggests increased slip planarity. Examination of the fracture surfaces revealed signs of plasticity. These results lead to the belief that hydrogen retards the rapid motion of dislocations, but enhances slow movement. Decreases in dislocation velocity in the presence of hydrogen have also been noted in Ni_3Al using a dislocation etch pit technique and bend tests [4].

Indentation testing provides a mechanism to study localized effects of hydrogen on engineering alloys [5]. Studies using nanoindentation and subsequent scanning probe microscopy have shown in Ti that hydrogen decreases dislocation pile up (analogous to increasing strain hardening behavior) and the hardness [6]. More complete studies in stainless steels [7] have demonstrated that yield points corresponding to the onset of plastic deformation in engineering alloys, when

normalized by the measured elastic modulus, are relatively independent of hydrogen content. However, that study also noted an effect of hydrogen on the measured elastic properties, and as such merits further study. The purpose of this research is to both improve the understanding of the mechanisms of hydrogen embrittlement and determine the effects of hydrogen concentration on the elastic modulus and hardness in a set of commercial alloys; Nitronic 40 (stainless 21-6-9), an iron-based superalloy A286 and a nickel-based superalloy, Hastelloy C22.

EXPERIMENT DESIGN

The alloys and their nominal compositions before and after hydrogen charging can be found in Table 1. Hydrogenated samples were precharged in 138MPa (20ksi) H_2 at 300˚C to saturation and were stored in a freezer after receipt to prevent degassing of hydrogen until they were tested. Tensile testing data from previous internal Sandia National Laboratory studies for the tested alloys are shown in Table 2.

Table 1: Composition of alloys in this study in wt. %

Alloy	Fe	Cr	Ni	Mn	Mo	W	Ti
21-6-9	Bal	21	6	9	—	—	—
Hastelloy C-22	3	22	Bal	<1	13	3	—
A-286	Bal	15	30	—	1	—	2

Table 2: Tensile testing data of alloys in this study

Alloy		YS (MPa)	TS (MPa)	RA (%)
A286	As Machined	817	1079	47
	Hydrogen Charged	814	1071	21
Hastelloy	As Machined	383	810	71
	Hydrogen Charged	426	793	41
21-6-9	As Machined	425	735	74
	Hydrogen Charged	536	800	59

To measure the mechanical properties of these samples using nanoindentation, each was ground and polished to a 0.05µm finish. After polishing, Vickers indents were made and used as fiduciary markers to clearly identify the area in which nanoindentation was performed. Nanoindentation data was recorded with the use of a Hysitron Triboscope. Indentations were made using a Berkovich indenter tip and were repeated four to six times at each applied load. Loads ranged from 1000µN to 7000µN, which corresponded to depths ranging from 60nm to 220nm. The loading

sequence used included a hold at the max depth, showing creep of the material and a second hold during the unloading curve to account for drift in the system. Analysis of the unloading curve hold was performed on all indentations, which were then corrected for drift if needed. Precharged samples were prepared in the same way, however considerable effort was spent minimizing prep time to limit the amount of hydrogen that might de-gas from the sample before testing. Each nanoindentation pattern was comprised of 30 to 40 indentations and was performed within a 15µm by 15µm area on the sample surface to hopefully be placed in a single grain. In general, this means that the indentations may be slightly closer together than would be ideal (where usually the indentations are separated by 3-5 times the diameter of the indentation impression), but the close spacing would only impact hardness and should not impact the elastic properties measured via nanoindentation.

After indentation data was recorded, Orientation Imaging Microscopy (OIM) was then performed with the use of an FEI Sirion 200 Scanning Electron Microscope in order to determine the grain orientation in the region of the nanoindentation pattern in a manner similar to that in previous studies using electron backscattered diffraction (EBSD) [8]. The orientation was then used to calculate a theoretical elastic modulus for each indentation pattern. In this way, the effect of grain orientation masking or exaggerating changes due to hydrogen precharging is eliminated.

RESULTS

Figure 1 shows a nanoindentation pattern and the subsequent EBSD method used to determine the orientation of a given grain.

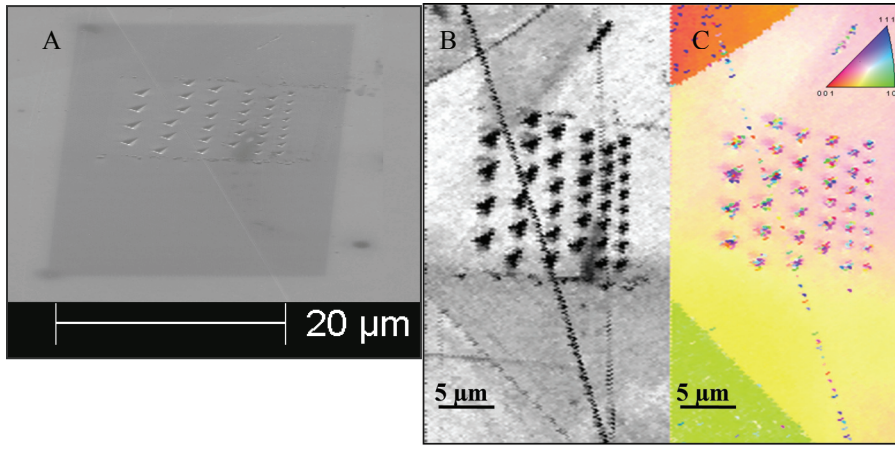


Figure 1 shows progression of analysis a) SEM image of indentation pattern, sample tilted to highlight indentations (b) and (c) show EBSD results before and after overlay of grain map.

Typical load – displacement graphs of uncharged and hydrogen-precharged A286 are shown in Figure 2. As noted in the figure, it is clear that the indentation technique is sufficient to distinguish between the two conditions. The hydrogen precharging is typically harder than the as-machined condition.

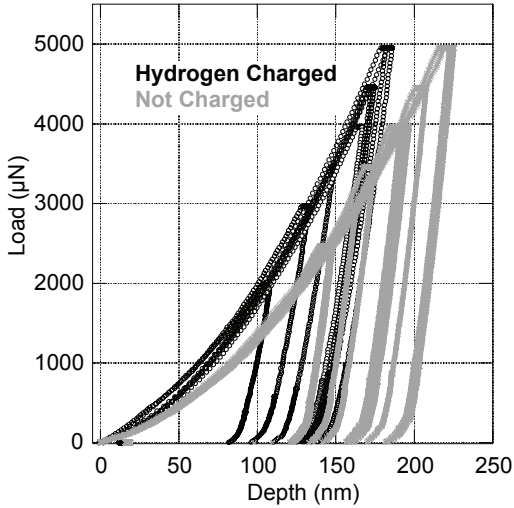


Figure 2. Typical load – displacement curves for indentations into hydrogen charged and as machined specimens, showing an increased hardness for the hydrogen charged samples.

The challenges in using nanoindentation to assess the properties of a polycrystalline alloy are that both elastic modulus and hardness may indeed be altered by the orientation of the indentation. Therefore, for each set of nanoindentation experiments, the normal orientation of the grain was determined via EBSD. Vlassak and Nix [9] have demonstrated how to calculate the effective indentation modulus (which is not equivalent to the modulus normal to the indented grain due to the general hemispherical nature of the deformation zone surrounding an indenter impression). In short, the expected indentation modulus (M_{hkl}) of a given orientation

$$M_{hkl} = \beta_{hkl}\left(\frac{E}{1-\nu^2}\right)_{isotropic} \qquad (1)$$

can be determined, where E is the Young's Modulus of the material, ν is Poisson's ratio and β_{hkl} is the correction factor from [9], determined by

$$\beta_{hkl} = a + c(A - A_0)^B \qquad (2)$$

where the constants A, A_0, B, a, and c are found in [9]. Table 3 shows the values used for the materials in this study. Compliance factors for fcc iron [10] were used

in determining the anisotropy factor (A) for all alloys. In all cases, the unloading slope analysis method was used to determine the modulus from the indentation [11].

Table 3 Constants used for calculations of indentation modulus

		(100)	(110)	(111)
21-6-9	v	0.285	0.285	0.285
	a	1.301	0.731	0.735
	c	-0.301	0.237	0.266
	Ao	0.000	-1.194	0.024
	B	0.275	0.155	0.190
	A	2.362	2.362	2.362
	E(GPa)	200.0	200.0	200.0
Hastelloy 22	v	0.250	0.250	0.250
	a	1.338	0.730	0.725
	c	-0.338	0.245	0.278
	Ao	0.000	-0.858	0.062
	B	0.260	0.151	0.191
	A	2.362	2.362	2.362
	E(GPa)	206.0	206.0	206.0
A-286	v	0.300	0.300	0.300
	a	1.227	0.732	0.741
	c	-0.276	0.234	0.258
	Ao	0.000	-1.338	-0.002
	B	0.285	0.157	0.190
	A	2.362	2.362	2.362
	E(GPa)	201.0	201.0	201.0

Using this methodology the elastic modulus and hardness was measured (E_m and H) for samples before and after hydrogen precharging, and compared to the theoretical modulus, E_{th}. The results are shown in table 4.

For all samples, the hardness consistently increased with hydrogen precharging. In the case of the Hastelloy, this difference was minor and statistically insignificant, but in both the other samples a Wilcoxan Mann Whitney ranked sum analysis showed the samples did come from different populations. While there is not a clear relationship between the orientation and hardness (as there is for the modulus), the 21-6-9 sample, where the as received and hydrogen-precharged samples were of similar orientations (close to {112} types), showed similar behavior as previously seen in this alloy [7]. It should be noted that these hardness values are larger than conventionally measured for these alloys because of the small scale of the sample (i.e. the indentation size effect) and the possible increased work hardening due to the

indentation spacing being such that the plastic zones around each indentation may overlap. The trends in hardness (though not the values) are similar to the tensile data on these alloys; 21-6-9 shows the highest change in hardness and showed the largest change in tensile stress in the tensile testing data. The differences may well be due to both the surface sensitive nature of the nanoindentation testing and the fact that hardness relates to a flow stress, rather than strictly yield or tensile strength.

Table 4. Elastic modulus of samples before and after hydrogen charging

	E_m (GPa)	Orientation	E_{th}(GPa)	H (GPa)	ΔE relative to E_{th}
21-6-9 As received	206±6.6	(-9 10 5)	225.0	7.2±0.6	-19
H-precharged	220.7±10.9	(-10 12,17)	225.1	8.6±0.7	-4.4
A-286 As received	200.2±9.6	(-1 5 1)	216.0	7.3±0.4	-16
H-precharged	200.2±10.0	(-1 26 –19)	220.8	8.6±0.9	-18.8
Hastelloy As received	214.6±9.1	(-2 9 4)	218.8	8.4±0.6	-4.2
H-precharged	165.7±9.6	(15 16 –22)	226.8	8.5±0.8	-61.1

The effect of hydrogen precharging on the elastic modulus, as determined from measured unloading stiffness, was small for the 21-6-9 and A-286, but a large decrease was observed for the Hastelloy. Due to variations in crystal orientation of the grains tested, the relevant comparison was between the measured values and the theoretical value calculated for each orientation. Table 4 shows the measured values, theoretical values and the difference between the two for each material and condition. The measured values of modulus were less than the theoretical values in all cases. Hydrogen precharging caused no significant change for the 21-6-9 and A-286, but caused a 25% reduction for the Hastelloy.

The changes observed in the modulus are related to the stiffness of the unloading slope, and are not due to calibration issues in the area function of the nanoindenter tip or testing methodology. If the area function was, by some method, inaccurate and was producing an erroneous measurement of hardness (as the values here were large due most likely to the indentation size effect), the smaller area would lead to a larger measured modulus. Similarly, if there was time dependent deformation and creep occurring during the unloading segment (as might be expected if the dislocation velocity were decreased due to hydrogen), the unloading stiffness would be inaccurately high, and the calculated modulus would be greater than expected. Neither of these cases seems appropriate for the experiments presented in this study. The most likely cause of the observations would be the result of additional point defects on the near surface region, which may result from outgassing of the samples during sample preparation for indentation, and could harden (and yet increase the compliance of) the near surface region. Future work will be needed to further

quantify both the testing method and the effects of grain orientation on the mechanical properties of these engineering alloys as functions of hydrogen content.

CONCLUSIONS

Nanoindentation has been used to measure the elastic modulus and hardness in three engineering alloys in their as machined state and after hydrogen precharging. By coupling the effect of grain orientation to the measurement it is possible to eliminate orientation effects from the localized testing method and compare "before" and "after" samples without requiring the indentation to occur in the same grain. In general, hydrogen precharging increased the hardness of 21-6-9 and A-286, and had only a limited effect on the hardness of Hastelloy. The elastic modulus measured using indentation did not change significantly in 21-6-9 subjected to hydrogen precharging (when compared to the theoretical indentation modulus expected from the grain orientation), while hydrogen-precharing decreased the measured modulus by approximately 9% in the A-286 alloy (although a similar difference was noted between the measured and theoretical values for the as-received A-286). A clear reduction of modulus was discerned for the Hastelloy in the hydrogen-precharged condition, decreasing by almost 25%. In no case did the measured modulus increase due to hydrogen precharging.

ACKNOWLEDGMENTS

This work was supported by Sandia National Laboratories, a Lockheed Martin Company for the United States Department of Energy's National Nuclear Security Administration under Contract DE-AC04 94AL85000. DFB wishes to acknowledge helpful discussions with Prof. J.P. Hirth regarding the impact of hydrogen on deformation mechanisms in these alloys.

REFERENCES

1. P.J. Ferreira, I.M. Robertson, and H.K. Birnbaum, "Hydrogen Effects on the Interactions Between Dislocations" Acta Mater. 1998;46:1749
2. G. Ulmer and C. J. Alstetter, "Mechanism for Hydrogen Embrittlement of Austenitic Stainless Steels, Hydrogen Effects on Material Behavior Ed. Neville R. Moody and Anthony W. Thompson TMS (1990) pp. 421-430
3. D.P. Abraham and Carl J. Alstetter, "Hydrogen- Enhanced Localization of Plasticity in an Austenitic Stainless Steel" Metall. Mater. Trans. 1995;26A:1995
4. C.B. Jiang, Hong Li, J. Tan, S. D. Wu, L. J. Rong and S. Patu, "A Dramatic Decrease of the Dislocation Velocity in Ni3Al Single Crystals Under the Influence of Hydrogen" Intermetallics, 2001;9:355
5 . Y. Katz, N. Tymiak, and W.W. Gerberich, "Nanomechanical probes as new approaches to hydrogen/deformation interaction studies", Eng. Fract. Mech., 2001;68:619

6. K.R. Morasch, D. F. Bahr “The Effects of Hydrogen on Deformation and Cross Slip in a BCC Titanium Alloy” Scripta Mater., 2001;45:839
7. K.A. Nibur, D.F. Bahr, and B.P. Somerday “Hydrogen effects on dislocation activity in austenitic stainless steel” Acta Mater., 2006;54:2677
8. K.A. Nibur, D.F. Bahr, “Identifying slip systems around indentations in FCC metals” Scripta Mater., 2003; 49:1055
9. J.J. Vlassak, WD. Nix “Measuring the elastic properties of anisotropic materials by means of nanoindentation experiments” J. Mech. Phys. Solids, 1994; 42: 1223
10. H. Ogi, H. Niho, M. Hirao, “Elastic Stiffness Distribution on Dual Phase Stainless Steel Studied by Resonance Ultrasound Microscopy” Acta Mater., 2006; 54:4143
11 . W.C. Oliver, G.M. Pharr, “An improved technique for determining hardness and elastic modulus using load and displacement sensing indentation experiments” J. Mater. Res., 1992;7:1564

Effects of Hydrogen on Materials
Proceedings of the 2008 International Hydrogen Conference
Brian Somerday, Petros Sofronis, Russell Jones, editors, p 187-194
Copyright © 2009 ASM International®
All rights reserved.
www.asminternational.org

IN SITU ELECTROCHEMICAL NANOINDENTATION: A NANOMECHANICAL APPROACH TO RANK HYDROGEN EMBRITTLEMENT IN EXTREMELY SMALL VOLUMES

Afrooz Barnoush, Horst Vehoff

Saarland University, Department of Materials Science, Bldg. D22. P.O. Box 151150, D-66041 Saarbruecken, Germany

INTRODUCTION

The usual approach taken in hydrogen embrittlement (HE) studies is conventional mechanical testing in combination with different in situ or ex situ H charging techniques. However such tests usually result in contradictory observations, like reduction of the ductility and increase in the yield and tensile stresses [1,2], or softening [3,4]. Considering HE as a phenomenon on the atomic scale, reveals the shortcomings of the macro scale mechanical tests. In contrast, environmental TEM has been used to study in detail the effect of H on dislocations [5]. From these tests it is concluded that solute H reduces the flow stress and enhances dislocation activity. These in situ TEM experiments on thin films are difficult to interpret, since the electron beam produces high H fugacities and local heating [6].

Mainly based on these two different experimental approaches (Conventional mechanical testing and in situ environmental TEM), H enhanced decohesion (HEDE) and/or H enhanced local plasticity (HELP) are discussed as the possible causes of HE. In the HEDE model, H accumulates at trapping sites such as cracks or interfaces, and reduces the bond strength there [7]. Two important mechanisms have been established for HELP: (1) H facilitates dislocation motion by shielding dislocation stress fields, and (2) H promotes planar slip by stabilizing the edge component of dislocations [5].

The instrumented nanoindentation technique combined with atomic force microscopy, NI-AFM, offers several advantages over conventional deformation experiments for investigating the effects of H on deformation [8-10]. NI-AFM, unlike other mechanical testing methods, also allows dislocation nucleation events to be detected on well-prepared surfaces [11]. The indenter produces shear stresses underneath the tip contact region that approach the theoretical shear strength. A pop-in occurs in the load displacement (L-D) curves at the onset of plasticity, which correlate to the homogeneous dislocation nucleation (HDN). It should be noted, however, that the probing depth of this technique is limited to a few tens of nanometers below the surface. Interpretation of ex situ experiments are therefore complicated, since H out-gassing during the experiment produces a concentration

gradient between the surface and the bulk [10]. In situ experiments are therefore necessary. In the present study, the effect of in situ electrochemically charged H on the HDN in small volumes has been studied. The aims were to determine the mechanism by which HE occurs and introduce a new method for ranking the susceptibility of different metals to HE.

EXPERIMENTAL PROCEDURE

The materials used in this study and the electropolishing parameters and electrochemical H-charging solutions for each of them are summarized in Tab. 1. After careful annealing special attention was paid to surface preparation, since, as mentioned before, a defect free and low roughness surface is necessary in order to observe the dislocation nucleation by means of NI-AFM. Therefore specimens were mechanically polished to 1 μm and then electropolished according to the parameters given in Tab. 1. When examined with an AFM, the sample surface had an rms roughness of less than 1 nm, and asperities or steps appeared only infrequently on the surface.

Tab. 1: Summary of the samples studied and their preparations and testing conditions.

Material	Micro-structure	Electropolishing condition				Test solution	pH
		Solution	Pot.	Temp.	Time		
Nickel	(111)	H_2SO_4/CH_3OH	30 V	15 °C	60 s	0.05M Na_2SO_4	6
Copper	(111)	H_3PO_4/Ethanol	20 V	20 °C	30 s	Borate buffer	9
Aluminum	1 mm grain[1]	$HClO_4$/Ethanol	40 V	0 °C	30 s	Borate buffer	9
Fe3wt.%Si	1 mm grain[1]	H_2SO_4/CH_3OH	12 V	10 °C	60 s	Borate buffer	9
FeAl	(100)	H_2SO_4/CH_3OH	35 V	10 °C	90 s	0.05M Na_2SO_4	6

The experiments were performed with a Hysitron Triboscope® in conjunction with a Digital Instruments (DI) Nanoscope II®. The indenter, designed specially for tests in liquid, was a Berkovich or conical diamond tip. For the NI-AFM system, a three-electrode electrochemical setup with a platinum counter electrode and an Ag/AgCl reference electrode was developed. All samples were in situ electrochemically charged at −1000 mV versus Ag/AgCl reference electrode. Detailed descriptions of the instrumentation and procedures we use to perform indentations under electrochemical control in solution are provided elsewhere [12-14] and the details are omitted here for brevity.

RESULTS

Figure 1 shows the typical L-D curves and statistical distribution of pop-in load for Fe-3wt.%Si in H-charged and H-free conditions. Other samples show a similar

[1] Indentations were carried out in a single grain of the mm size grains

distribution and reduction in pop-in load under H-charged conditions [12-14] as summarized in table.2. The initial portion of the loading curves in Fig. 1 can be well fitted with the Hertzian elastic response

$$P = \frac{4}{3} E_r \sqrt{Rh^3} \quad (1)$$

where P is the applied load, h is the indentation depth, R is the radius of the tip curvature, and E_r is the reduced modulus, given by

$$\frac{1}{E_r} = \frac{1-\nu_1^2}{E_1} + \frac{1-\nu_2^2}{E_2} \quad (2)$$

where E is the elastic modulus of the material, ν is the Poisson's ratio, and the subscripts 1 and 2 refer to the tip and the sample respectively. The predictions of Eq. 1 is shown in Fig. 1, where the deviation of the experiments from the theory can be associated with a "pop-in," as is typical in load controlled nanoindentation experiments. Furthermore, when indentations were performed below the critical burst load, the response was purely elastic (recoverable) and there was no residual impression left at the site of the indentation.

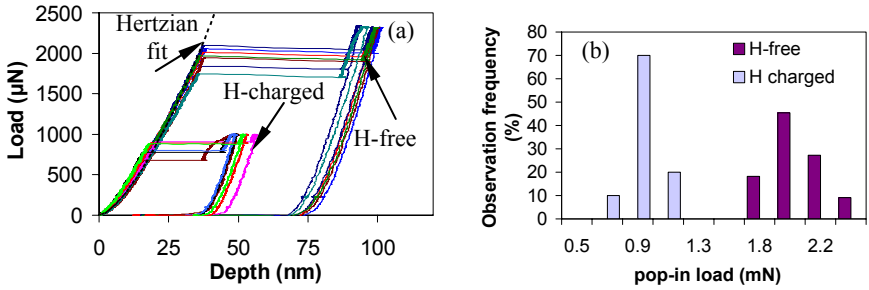


Fig. 1: Some representative L-D curves (a) and statistical distribution of pop-in load (b) of Fe 3wt.%Si for H-charged and H-free conditions.

Tab. 2: Summary of the mean pop-in load for H-charged and H-free condition and comparison between theoretical strength, μ/20, and measured shear stress at the onset of the pop-in.

Material	Mean $F_{pop\text{-}in}$ (μN)		τ_{max} (GPa)		$z_{\tau(max)}$ (nm)		μ/20 in GPa	R in μm
	H free	H charged	H free	H charged	H free	H charged		
Nickel	185	95	3.3	2.7	37	27	4	1
Copper	380	360	1.23	1.21	93	95	2	3.8
Aluminum	280	80	0.93	0.6	100	65	1.1	3
Fe3wt.%Si	2000	840	4.9	3.6	122	82	4.2	2
FeAl	1300	280	5.4	3.2	77	46	4.7	1.5

DISCUSSION

The above results clearly indicate that the pop in load in the H-charged condition of the samples is distinctively different from the H-free condition. This change can not be attributed to the surface topography since it has been imaged and revealed no surface roughening [12,13]. For an indentation test, the applied shear stress that nucleates a dislocation can be assumed to be the maximum shear stress beneath the indenter at the onset of a pop-in. According to continuum mechanics the maximum shear stress is reached at a point below the sample surface of approximately 0.48 times the contact radius. Computer simulations support this approximation [15]. The position and value of the maximum shear stress $z_{\tau(max)}$, and τ_{max}, are given by [13].

$$z_{\tau(\max)} = 0.48\left(\frac{3PR}{4E_r}\right)^{\frac{1}{3}} \qquad (3); \qquad \tau_{\max} = 0.31\left(\frac{6E_r^2}{\pi^3 R^2}P\right)^{\frac{1}{3}} \qquad (4)$$

The tip radius was obtained during indentation of each sample by fitting a Hertzian model to the elastic loading part of the L-D curves [16,17] (Tab. 2). If we insert this tip radius into Eq. 4, we obtain a maximum shear stress for each pop-in load (Tab. 2). This maximum shear stress is responsible for the HDN at $z_{\tau(max)}$ below the tip. Classic dislocation theory predicts the free energy required for HDN during nanoindentation as follow [13,16]

$$\Delta G = \frac{2-\upsilon}{1-\upsilon}\frac{\mu b^2 r}{4}\left(\ln\frac{4r}{\rho}-2\right)+\pi r^2\gamma-\pi r^2 b\tau \qquad (5)$$

where r is the dislocation loop radius, b is the Burgers vector, τ is the external shear stress acting on the loop, μ is the shear modulus, γ is the stacking fault energy (SFE) and ρ is the dislocation core radius. Fig. 3 shows the plots of ΔG as a function of loop radius calculated for observed mean values of τ_{max} in H-charged and H-free condition given in Tab. 2 and material constants given in Tab. 3. The free energy curves for HDN pass through a maximum which defines the activation energy for HDN (ΔG^*). The ΔG^* at a loop size r^* could be found by setting $\partial\Delta G/\partial r = 0$. In H-free condition the free energy curve for each sample has a maximum about 0 eV. It means that the process of HDN for H-free condition happens spontaneously and without thermal contribution from surrounding. Calculated value of pop-in load when ΔG=0 and ΔG^*=0 is given in Tab. 3 for comparison. In contrast the free energy curves for H-charged condition showing relatively high activation energy which should be overcome in order to nucleate a dislocation. Since the tests were performed in the same condition there is no possible external contribution for overcoming the activation energy of HDN. The only possible explanation is a reduction of the activation energy for HDN by H. To include the effect of H in the proposed model, Eq. 5 can be rewritten by introducing the effect of H as follows

$$\Delta G = \frac{2-\upsilon}{1-\upsilon}\frac{\mu_H b^2 r}{4}\left(\ln\frac{4r}{\rho_H}-2\right)+\pi r^2\gamma\ -\pi r^2 b\tau \qquad (6)$$

where μ_H is the shear modulus under the effect of H, ρ_H is the H affected dislocation core radius. Hydrogen effects on the other parameters involved in the Eq. 6 are either negligible or inapplicable.

Tab. 3: Material constants used to calculate free energy curves of HDN

Material	E_r (GPa)	μ (GPa)	ν	γ (J/m^2)	b (nm)	ρ (nm)	$F_{pop\text{-}in}$ (μN) (ΔG and ΔG^* = 0 eV)
Nickel	191	79	0.31	0.24	0.14	0.24	210
Copper	111	42	0.32	0.06	0.15	0.29	377
Aluminum	67	23	0.35	0	0.29	0.29	274
Fe3wt.%Si	202	85	0.32	0	0.25	0.17	2042
FeAl	217	94	0.3	0	0.25	0.17	1314

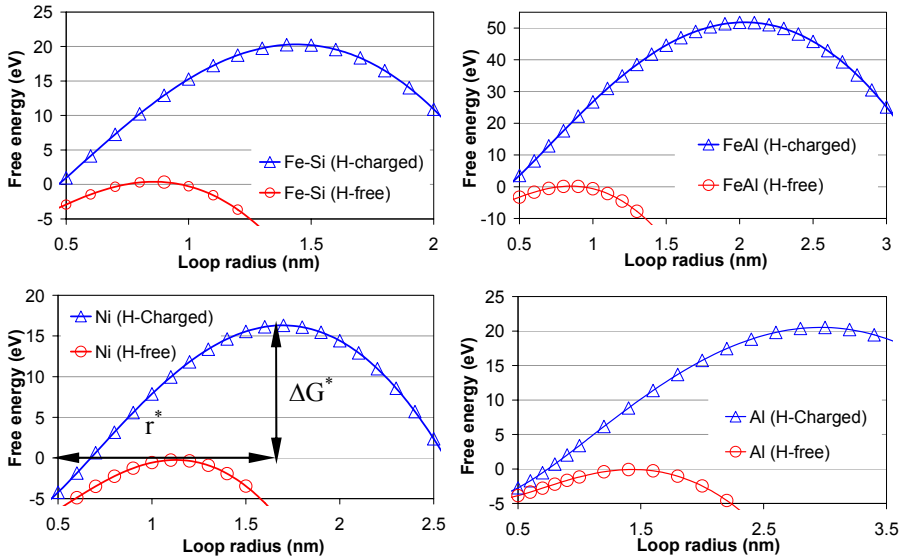


Fig. 2: Free energy curves

The experimental data now can be used to calculate the effect of H on μ and ρ. To do this, the rule of spontaneous HDN shall be applied to Eq. 6, i.e. $\Delta G^* = 0$ and $\Delta G = 0$. This results in the following equations:

$$\tau_H = \frac{2-\upsilon}{1-\upsilon}\frac{\mu_H b}{4r^*\pi}\left(\ln\frac{4r^*}{\rho_H} - 2\right) + \frac{\gamma}{b} \qquad (7)$$

where τ_H is the shear stress required for the HDN in H charged condition. Eq. 7 shows the reduction of shear stress required for HDN in H-charged sample can be attributed to decrease in μ_H and/or increase in the ρ_H. Table. 4 summarize the effect

of H on μ or ρ for the tested samples when assuming that the H will only affect one of these parameters. The resulted changes in these parameters normalized to the initial values can be use to rank the materials susceptibility to HE.

Tab. 4: summary of the H effect on μ or ρ in samples studied.

Material	Nickel	Copper	Aluminum	Fe3wt.%Si	FeAl
$\delta\Delta G_H^*$(eV)	17	2	23	21	51
μ_H (GPa)	50	41	15	62	56
$\Delta\mu/\mu$ (%)	36	2.5	35	27	41
ρ_H (nm)	0.29	0.3	0.41	0.22	0.24
$\Delta\rho/\rho$ (%)	23	2.4	43	37	45

Rose et al. [18] have shown that metallic binding-energy distance curves can be approximately scaled into a single universal relation. Therefore for uniform dilation of a bulk metal

$$\frac{U}{l^2}\left[\frac{\partial^2 U_C^*\left(d^*\right)}{\partial d^{*2}}\right]_{d^*=0} = \mu\frac{8\pi\left(1+\upsilon\right)}{\left(1-2\upsilon\right)}r_{ws} \quad (8)$$

where U is the cohesive energy, $U_c^*(d^*)$ is an approximately universal function which describes the shape of the binding-energy curve for metals. The d^* is a scaled length, l is a scaling length and r_{ws} is Wigner-Seitz radius [18]. Because of the universality, the ratio of the second derivative in the large parentheses is independent of the metal considered. Eq. 8 has a simple physical meaning: the reduction in the shear modulus is equal to the reduction of the strength of the interatomic bonds, as assumed in the HEDE model.

According to classic dislocation theory an increase in the dislocation core radius means reduction of dislocation line energy [14]. On the other hand the solute excess definition for dislocation [19], Γ^D, can be used to derive the change in the Helmholtz free energy per unit length of a dislocation, γ_D, due to segregation of a solute on the dislocation

$$\left.\frac{\partial\gamma_D}{\partial c_A}\right|_{n_B,T,V,l_D} = -\Gamma_A^D \quad (9)$$

where c_A is the chemical potential of solute atom A dissolved in a material of B atoms with a constant number n_B. The dislocation length l_D, temperature T and volume V are maintained constant. According to Eq. 9 the line energy of a dislocation decreases with increasing solute chemical potential if the excess is positive, i.e. solute atoms segregate at the dislocation core. Hence, the increase in the core radius is a direct evidence for decrease in dislocation line energy due to H segregation on the dislocation line [20].

CONCLUSIONS

The fine scale mechanical probing capability of NI-AFM was used to examine H effect on HDN. It was shown that H reduces the pop-in load which can be interpreted as the HELP mechanism. Classical dislocation theory was used to model the HDN and it was shown that H reduces the activation energy for HDN. The activation energy for HDN is related to the material specific parameters; μ and ρ. These material properties can be influenced by H resulting in reduced activation energy for dislocation nucleation.

The normalized change in μ and ρ can be used to rank the sensitivity to HE. In the tested materials copper shows a very low sensitivity to HE and FeAl intermetallic alloy shows the highest.

The universality of cohesion in bulk metals relates the reduction of the shear modulus to the reduction of the cohesion, meaning HEDE mechanism. The increase in the core radius of a dislocation due to H is a direct evidence of decrease in dislocation line energy and H segregation on the dislocation line.

Thus, HELP and HEDE are the two sides of a coin resulting in HE. However depending on the experimental approach utilized to probe the H effect, either HELP or HEDE can be observed. In this study, however, by utilizing a proper experimental approach, it was possible to resolve the interconnected nature of the HE.

ACKNOWLEDGMENTS

The authors would like to thank Prof. E. P. Goerge from Oak Ridge national Lab for providing FeAl single crystals. Financial support from the German Research Foundation (DFG) is gratefully acknowledged.

REFERENCES

1. Borchers, C, Michler, T, and Pundt, A, "Effect of hydrogen on the mechanical properties of stainless steels," *Adv. Eng. Mater.*, vol. 10, (2008), pp. 11–23.
2. Olden, V *et al.*, "Application of hydrogen influenced cohesive laws in the prediction of hydrogen induced stress cracking in 25%cr duplex stainless steel," *Eng. Frac. Mec.*, vol. 75, no. 8, (2008), pp. 2333–2351.
3. Dadfarnia, M *et al.*, "On the small scale character of the stress and hydrogen concentration fields at the tip of an axial crack in steel pipeline: Effect of hydrogen-induced softening on void growth," *Int. J. Mater. Res.*, vol. 99, no. 5, (2008), pp. 557–570.
4. Jagodzinski, Y *et al.*, "Interaction of hydrogen with dislocation pile-ups and hydrogen induced softening of pure iron," *Scr. Mater.*, vol. 43, (2000), pp. 245–251.
5. Robertson, I. M, "The effect of hydrogen on dislocation dynamics," *Eng. Frac. Mec.*, vol. 68, (2001), pp. 671–692.

6. Bond, G. M, Robertson, I. M, and Birnbaum, H. K, “On the determination of the hydrogen fugacity in an environmental cell tem facility.” *Scr. Met*, vol. 20, no. 5, (1986), pp. 653–658.
7. Olden, V *et al.*, “Cohesive zone modeling of hydrogen-induced stress cracking in 25% cr duplex stainless steel,” *Scr. Mater.*, vol. 57, (2007), pp. 615–618.
8. Katz, Y, Tymiak, N, and Gerberich, W. W, “Nanomechanical probes as new approach to hydrogen/deformation interaction studies,” *Eng. Frac. Mec.*, vol. 68, (2001), pp. 619–646.
9. Barnoush, A and Vehoff, H, “In situ electrochemical nanoindentation of a nickel (111) single crystal: Hydrogen effect on pop-in behaviour,” *Int. J. Mater. Res.*, vol. 97, (2006), pp. 1224–1229.
10. Nibur, K, Bahr, D, and Somerday, B, “Hydrogen effects on dislocation activity in austenitic stainless steel,” *Acta Mater.*, vol. 54, (2006), pp. 2677–2684.
11. Vehoff, H *et al.*, “Mechanical properties of nanomaterials examined with a NI-AFM,” *Z. Phys. Chemie*, vol. 222, (2008), pp. 499–525.
12. Barnoush, A, Bies, C, and Vehoff, H, “In situ electrochemical nanoindentation of FeAl (100) single crystal: Hydrogen effect on dislocation nucleation,” *J. Mater. Res.*,” (submitted).
13. Barnoush, A and Vehoff, H, “In situ electrochemical nanoindentation: A technique for local examination of hydrogen embrittlement,” *Corros. Sci.*, vol. 50, (2008), pp. 259–267.
14. Barnoush, A and Vehoff, H, “Hydrogen embrittlement of aluminum in aqueous environments examined by in situ electrochemical nanoindentation,” *Scr. Mater.*, vol. 58, (2008), pp. 747–750.
15. Vehoff, H, “From in situ crack growth tests to nanoindentation in UFG materials,” *Model. Simul. Mater. Sci. Eng.*, vol. 15, no. 1, (2007), pp. S313–S323.
16. Bahr, D. F, Kramer, D. E, and Gerberich, W. W, “Non-linear deformation mechanisms during nanoindentation,” *Acta Mater.*, vol. 46, (1998), pp. 3605–3617.
17. Gerberich, W. W *et al.*, “Indentation induced dislocation nucleation: The initial yield point,” *Acta Mater.*, vol. 44, (1996), pp. 3585–3598.
18. Rose, J *et al.*, “Universal features of the equation of state of metals,” *Physical Review B*, vol. 29, no. 6, (1984), pp. 2963–2969.
19. Kirchheim, R, “Reducing grain boundary, dislocation line and vacancy formation energies by solute segregation. i. theoretical background,” *Acta Mater.*, vol. 55, no. 15, (2007), pp. 5129–5138.
20. Pundt, A and Kirchheim, R, “Hydrogen in metals: Microstructural aspects,” *Annu. Rev. Mater. Res.*, vol. 36, no. 1, (2006), pp. 555–608.

Effects of Hydrogen on Materials
Proceedings of the 2008 International Hydrogen Conference
Brian Somerday, Petros Sofronis, Russell Jones, editors, p 195-202
Copyright © 2009 ASM International®
All rights reserved.
www.asminternational.org

Lattice Defect Formation and Degradation Enhanced by Hydrogen and Strain of Metals

K. Takai, Sophia University
Tokyo 102-8554, JAPAN

H. Shoda, Graduate Student, Sophia University
Tokyo 102-8554, JAPAN

ABSTRACT

Hydrogen absorbed during corrosion causes the environmental degradation of mechanical properties. The principal factor causing the degradation was investigated using Inconel 625 as an face-centered-cubic (fcc) metal and pure iron as a body-centered-cubic (bcc) metal to clarify the role of hydrogen. The hydrogen content of Inconel 625 was 20 mass ppm, when Inconel 625 with zero hydrogen content was loaded up to a strain of 0.02, and after unloading the specimen was then charged by hydrogen. Whereas, the hydrogen content of Inconel 625 was 29 mass ppm, when the Inconel 625 containing hydrogen was loaded up to a strain of 0.02, and after unloading the specimen was then charged by hydrogen,. A similar tendency was observed for pure iron. These results suggest that both hydrogen and strain induce the hydrogen trapping sites, or the formation of lattice defects in metals. To identify the type of lattice defect causing hydrogen degradation, various mechanical tests were conducted by the slow strain rate technique (SSRT). The ductility did not recover, when the Inconel 625 containing hydrogen was loaded up to a strain of 0.02, after unloading the specimen was maintained at 30 °C for 2160 h to release all the hydrogen, and the specimen was reloaded until failure. In contrast, the ductility completely recovered, when the Inconel 625 containing hydrogen was loaded up to a strain of 0.02, after unloading the specimen was maintained at 200 °C to release all the hydrogen, and the specimen was reloaded. A similar tendency was observed for pure iron. These results suggest that the principal factor causing hydrogen degradation is the formation of vacancies and vacancy clusters induced by hydrogen and strain, since maintaining the specimens at 200°C results in the annihilation of vacancies and vacancy clusters.

INTRODUCTION

Developing high-strength steels to reduce the weight of cars results in the saving of energy. However, the susceptibility to hydrogen degradation increases with the tensile strength of to be used steels. Hydrogen fuel-cell systems are expected to be used as a next-generation source of clean energy. The pressure of hydrogen in more

recent fuel-cell vehicles has tended to increase from 35 MPa to 70 MPa, so that the vehicle can be driven for long distances. In addition, the pressure of hydrogen at refuelling stations is as high as 100 MPa. Therefore, the development of fcc and bcc metals that are highly resistant to hydrogen degradation is required, since many materials are deteriorated by hydrogen.

Although a large number of studies have been carried out on hydrogen degradation over many years, there is little agreement as to its mechanism, for example, lattice decohesion theory [1], hydrogen enhanced local plasticity theory [2], absorption-induced dislocation emission theory [3], and vacancy contribution theory [4,5] have all been suggested as mechanism.

The thermal desorption analysis (TDA) of hydrogen in high-strength steels representing bcc metals [6,7] and stainless steels representing fcc metals [8] has been performed extensively over the past few years to measure the hydrogen content and analyze the trapping states of metals. This method of hydrogen analysis can be applied to clarify the mechanism by combining with the result of slow strain rate technique (SSRT).

With this background, to clarify the role of hydrogen in mechanical degradation during deformation, Inconel 625 as an fcc metal and pure iron as a bcc metal were prepared. The two principal features of this study are (1) the acceleration of lattice defect formation induced by hydrogen and strain, and (2) the identification of the factor causing hydrogen degradation by TDA and SSRT. On the basis of our results, the mechanism of hydrogen degradation is discussed.

Experimental

Materials

The Ni-based alloy, Inconel 625 (Ni:60.8%, Cr:21.5%, Mo:9.0%, Fe:3.9%, Nb:3.5%) as an fcc metal and 99.98% (20 mass ppm C) pure iron as a bcc metal were employed in the present study. Inconel 625 was solution-treated at 1150 °C and the pure iron was annealed at 900 °C.

Hydrogen Charging

Hydrogen was introduced into the specimens by cathodic charging, which was performed at constant current density under galvanostatic control. The charging was carried out in an aqueous solution of pH 2.5 H_2SO_4 adding 0.09 mass% NH_4SCN at a current density of 50A/m^2, and at a temperature of 90 °C for Inconel 625 and 30 °C for pure iron.

TDA

The TDA apparatus consists of a gas chromatograph, a thermal conductivity detector, a heating unit, and a recorder. The gas chromatograph was calibrated using standard gas mixture (Ar + 50 vol ppm H_2) to quantify the hydrogen content in the specimens. TDA was conducted in the temperature range from 25°C to 800°C. The sensitivity limit for the detection of hydrogen is 0.01 mass ppm in this method.

Hydrogen Degradation Evaluation

Hydrogen degradation of the mechanical properties was evaluated as the decrease in fracture strain during the application of tensile stress by SSRT. SSRT was conducted at a strain rate of 8.3×10^{-6} /s for Inconel 625 in air because of the low diffusion coefficient of hydrogen, whereas SSRT was conducted at a strain rate of 1.6×10^{-5} /s for pure iron while performing cathodic charging to prevent the release of hydrogen because of the high diffusion coefficient of hydrogen in pure iron.

RESULTS AND DISCUSSION

Acceleration of Lattice Defect Formation Induced by Hydrogen and Strain

Lattice defects formed by interactions between hydrogen and plastic straining were examined by TDA. Since hydrogen is trapped at lattice defects, the amount of hydrogen absorbed in a strained specimen is a measure of the defect density. The procedures for detecting lattice defects introduced by straining with/without hydrogen are schematically shown in Fig. 1. These three specimens [no strain] ,[strain] and [H+strain] were charged by hydrogen until saturation under a constant condition of 50A/m^2, then the hydrogen content was measured using TDA.

Figure 2 shows the TDA profiles and hydrogen content of Inconel 625. The hydrogen content of the [strain] specimen for which tensile stress is applied up to a strain of 0.02 is greater than that of the [no strain] specimen. This increase in hydrogen content corresponds to that of the density of lattice defects formed by plastic deformation. Furthermore, the hydrogen content of the [H+strain] specimen is greater than that of

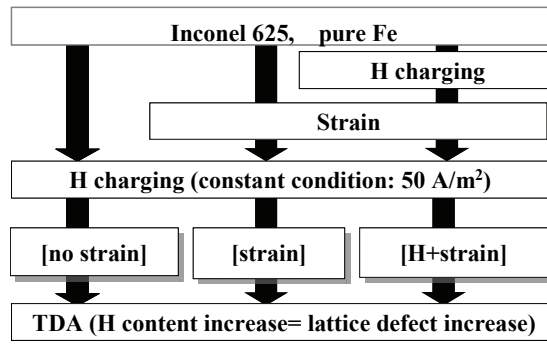


Fig.1 Procedure to clarify interaction between hydrogen and strain.

the [strain] specimen. This increase in hydrogen content in spite of the same strain of 0.02 means that the hydrogen accelerates the formation of lattice defects, such as dislocations and vacancies, in Inconel 625.

Figure 3 shows the TDA profiles and hydrogen content of pure iron. The hydrogen content of the [strain] specimen for which tensile stress is applied up to a strain of 0.20 is also greater than that of the [no strain] specimen. Furthermore, the hydrogen content of the [H+strain] specimen is greater than that of the [strain] specimen. For not only the fcc metal but also the bcc metal, hydrogen accelerates the formation of lattice defects such as dislocations and vacancies during deformation.

From these results, the role of hydrogen is to accelerate the formation of lattice defects such as dislocations and vacancies during deformation under constant strain.

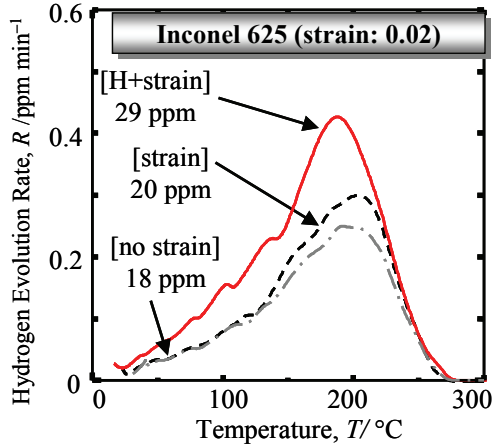


Fig.2 TDA profiles and hydrogen content of Inconel 625.

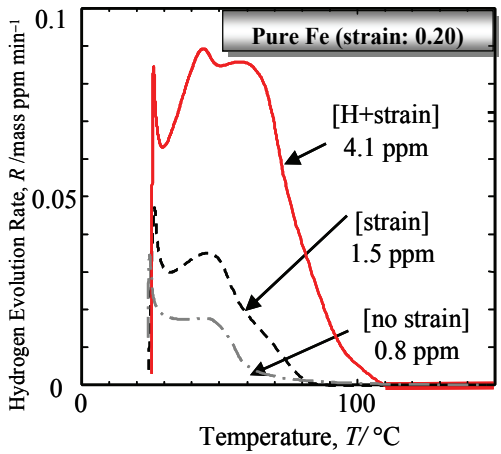


Fig.3 TDA profiles and hydrogen content of pure iron.

Identification of Factor Causing Hydrogen Degradation

In order to discriminate the contribution of strain-induced defects from that of hydrogen itself to degradation, four types of loading cycles were given prior to the final fracture. The procedures are shown schematically in Fig. 4. The first one (a) was the reference without hydrogen charging, given interposed unloading and immediate reloading during the tensile test. The second one (b) was the same cycle as (a) using hydrogen-charged specimens. The third one (c) was to remove hydrogen in (b) at the unloaded stage by aging at 30˚C for 2160 h for Inconel 625 and 168 h for iron. In this case, hydrogen was not present in the later stage of reloading, *i.e.*, at the time of

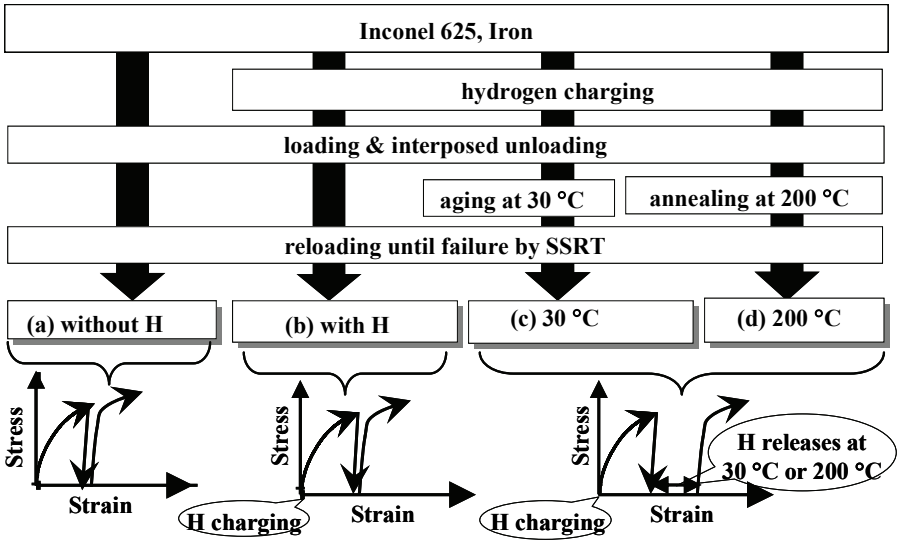


Fig.4 Procedure to identify the lattice defect causing hydrogen degradation of Inconel 625 and pure iron.

fracture, but enhanced lattice defects were assumed to be introduced by the initial straining in the presence of hydrogen. The fourth one (d) was to remove hydrogen and also some of the defects introduced during the initial straining by annealing at 200˚C for 0.5 h for Inconel 625 and 2 h for iron at the unloaded stage.

Figure 5 shows that TDA profiles of Inconel 625 after hydrogen charging, after aging at 30 ˚C for 2160 h, and after annealing at 200 ˚C for 0.5 h. It is confirmed that hydrogen is not presence in specimen (c) and specimen (d).

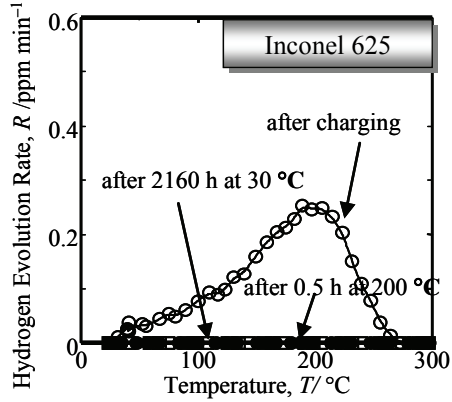


Fig.5 TDA profiles of Inconel 625; the open circle (○) is after H-charging, the solid circle (●) is after aging at 30 °C for 2160 h, and the open square (□) is after annealing at 200 °C for 0.5 h.

Figure 6 shows the stress-strain curves, hydrogen content, and degradation susceptibility (*DS*) of Inconel 625 specimens. Inconel 625 was loaded up to a strain of 0.02, and after unloading the specimen is reloaded until failure. The fracture strain of specimen (a) is about 0.5, which is determined as standard value for comparison. The degradation

susceptibility of specimens is defined as fracture strain after hydrogen charging divided by fracture strain without hydrogen charging. When the *DS* value is one, this means no decrease in ductility. When the *DS* value is lower than one, there is a decrease in ductility. The *DS* value of specimen (b) is 0.05, since it absorbs hydrogen to a concentration of 18 ppm. The *DS* value of the specimen (c) is 0.36 even though all the hydrogen is released by maintaining the specimen at 30°C. The *DS* value of specimen (d) is 1.02.

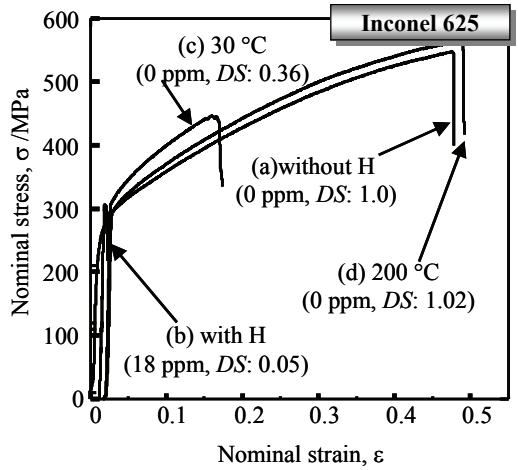


Fig.6 Stress-strain curves, hydrogen content, and degradation susceptibility (*DS*) of Inconel 625 specimens.

The result for specimen (c) which includes vacancies and dislocations accelerated by interaction between strain and hydrogen, indicates that it is not necessary for hydrogen to be present in metals for fracture to occur due to the degradation of ductility. The specimen (c) retains its decrease in ductility regardless of there being no hydrogen present. This suggests that hydrogen does not reduce the lattice strength and break the lattice bonding directly, but hydrogen enhances lattice defect formation during applying strain as shown in Fig.2, and the accumulation of the lattice defects in the metal causes the decrease in ductility.

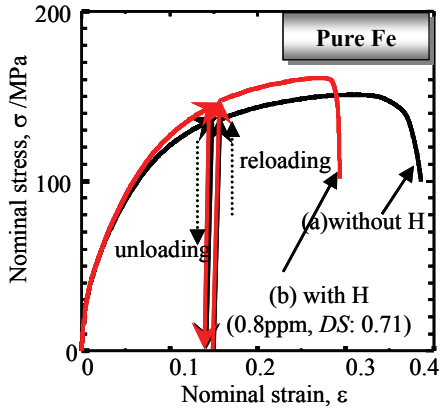


Fig.7 Stress-strain curves, hydrogen content, and *DS* values of pure iron.

The result for specimen (d) indicates that the ductility recovers completely after the specimen is maintained at 200°C to that of the specimen (a). Maintaining the specimen at 200°C results in hydrogen desorption and the annihilation of vacancies and their clusters [9]. Therefore, the complete recovery of ductility indicates that the vacancies and their clusters induced during applying strain with hydrogen are the most important factors causing the hydrogen degradation of the fcc metal.

Figure 7 shows the stress-strain curves, hydrogen content, and *DS* values of pure iron, which is a bcc metal. The pure iron is loaded up to a strain of 0.15, and after

unloading the specimen is reloaded until failure. The fracture strain of the specimen (a) is about 0.4, which is determined as the standard value for comparison. The *DS* value of the specimen (b) is 0.71, since it absorbs hydrogen to a concentration of 0.8 ppm.

Figure 8 shows the stress-strain curves, hydrogen content, and *DS* values of pure iron maintained at 30°C for 168 h to release all the hydrogen. The standard stress-strain curve of pure iron changes upon maintaining the specimen at 30°C after prestrain, as shown in Fig.8, due to the Cottrell effect. The *DS* value of the specimen (c) is 0.81 although all the hydrogen is released by maintaining the specimen at 30°C.

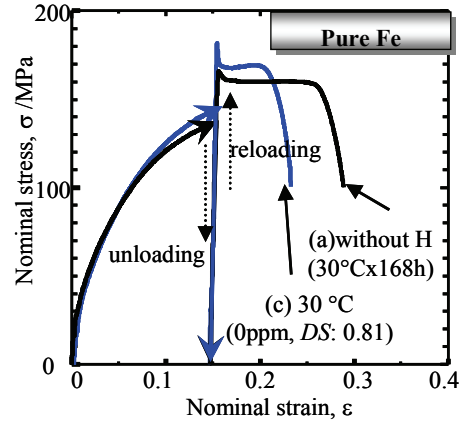


Fig.8 Stress-strain curves, hydrogen content, and *DS* values of pure iron maintained at 30°C for 168 h to release all the hydrogen.

Figure 9 shows the stress-strain curves, hydrogen content, and *DS* values of pure iron maintained at 200°C for 2h to release all the hydrogen. The *DS* value of specimen (d) is 0.97.

The increases in the densities of vacancies and clusters enhanced by the interaction between the strain and the hydrogen play a common important role in the hydrogen degradation of both fcc and bcc metals [10].

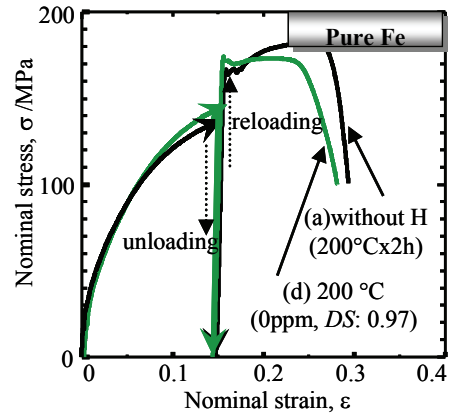


Fig.9 Stress-strain curves, hydrogen content, and *DS* values of pure iron maintained at 200°C for 2 h to release all the hydrogen.

CONCLUSIONS

The role of hydrogen and the identification of the factor causing the hydrogen degradation of Inconel 625, an fcc metal, and pure iron, a bcc metal, have were investigated using TDA and SSRT. The results obtained in the present study can be summarized as follows:

(1) The role of hydrogen is to accelerate the formation of lattice defects during deformation under constant strain.

(2) The vacancies and their clusters formed during applying strain with hydrogen are the most important factors causing the hydrogen degradation.

ACKNOWLEDGMENTS

This study was supported by Industrial Technology Research Grant Program in 2007 from New Energy and Industrial Technology Development Organization (NEDO) of Japan.

REFERENCES

1. Oriani, R.A. and Josephic, P.H., "Equilibrium Aspects of Hydrogen-Induced Cracking of Steels", *Acta Metall.* , 22 (1974), pp.1065-1074.
2. Birnbaum, H.K. and Sofronis, P., "Hydrogen-Enhanced Localized Plasticity – A Mechanism for Hydrogen Related Fracture", *Materials Science and Engineering*, A176 (1994), pp.191-202.
3. Lynch, S.P., "Environmentally Assisted Cracking: Overview of Evidence for An Adsorption- Induced Localised-Slip Process", *Acta Metall.*, 36 (1988), pp.2639-2661.
4. Nagumo, N., "Hydrogen Related Failure of Steels – A New Aspect", *Materials Science and Technology*, 20 (2004), pp.940-950.
5. Takai, K., Shoda, H., Suzuki, H., and Nagumo, M., "Lattice Defects Dominating Hydrogen-Related Failure of Metals", *Acta Materialia*,(2008) in press.
6. Takai, K. and Watanuki, R., "Hydrogen in Trapping States Innocuous to Environmental Degradation of High-Strength Steels", *ISIJ International*, 43 (2003), pp.520-526.
7. Takai, K., Chiba, Y., Noguchi, K., and Nozue, A., "Visualization of Hydrogen Desorption Process from Ferrite, Pearlite and Graphite by Secondary Ion Mass Spectrometry", *Metall. Mater. Trans. A*, 33A (2002), pp.2659-2665.
8. Takai, K., "Hydrogen Degradation and its Mechanism in Fcc Metals for High-Pressure Hydrogen Storage Tank", *Advances in Materials Science*, 7 (2007), pp.205-210.
9. Okubo, H, Sugiyama, S., Fukuzato, K., Takenaka, M., Tsukuda, N., and Kuramoto, E., "Positron-lifetime study of electrically hydrogen charged Ni, austenitic steel and Fe", *J. Nuclear Materials*, 283-287 (2000), pp.858-862.
10. Takai, K., Shoda, H, Suzuki, H. and Nagumo, M. : "Lattice defects dominating hydrogen degradation of metals", *Acta Mater.*, 56 (2008), pp.5158-5167.

Effects of Hydrogen on Materials
Proceedings of the 2008 International Hydrogen Conference
Brian Somerday, Petros Sofronis, Russell Jones, editors, p 203-210
Copyright © 2009 ASM International®
All rights reserved.
www.asminternational.org

Effect of hydrogen on microscopic deformation process near Stage II fatigue crack tip

Yoshimasa TAKAHASHI
National Institute of Advanced Industrial Science and Technology (AIST), Fukuoka, Japan

Masaki TANAKA, Kenji HIGASHIDA, Hiroshi NOGUCHI
Kyushu University, Fukuoka, Japan

INTRODUCTION

In order to establish the safe use of hydrogen as an energy carrier, it is urgent to clarify the effect of a hydrogen environment on the mechanical properties, particularly on fatigue crack propagation property of metallic materials. As fatigue crack propagation property is strongly dependent on the cyclic slip behavior near the crack tip region [1], it is important to elucidate the effect of hydrogen on cyclic slip deformation at the near-tip region.

A number of studies have employed polycrystalline metals to investigate the effect of hydrogen on fatigue crack propagation. The crack tip slip behavior in a polycrystalline metal is, however, sensitive to the grain boundary or the crystallographic orientation of the grain [2]. In addition, the grain boundary itself could be damaged by hydrogen and become the primary crack path [3]. Hence a single-crystalline metal can be favorably used for the purpose of evaluating the hydrogen effect solely on the crack tip slip behavior. There have been experimental reports on the hydrogen effects on the crack propagation using single-crystalline metal with body-centered cubic (BCC) structure (silicon ferrite alloy) [2,4-6]. These studies focus on the crack propagation under static load condition. On the other hand, there have been few attempts to use single-crystalline metal for studying the hydrogen effects on the crack tip slip under cyclic loading.

In this study, a fatigue crack propagation test using single-crystalline Fe-3.2%Si is implemented both in hydrogen and non-hydrogen (helium) atmosphere. The effect of hydrogen on the crack tip slip behavior is investigated in detail not only by the fractographic approach but also by the cross-sectional observation of the crack tip region by transmission electron microscopy (TEM).

EXPERIMENTAL METHOD

The material tested is a single-crystalline Fe-3.2%Si alloy plate which is rolled in the [001] direction and has a (110) surface. Figure 1 shows the geometry and the crystallographic orientation of the specimen. A rectangular-shaped specimen is cut from the mother plate, and a through-notch is machined at the center position. The

specimen is uniaxially loaded in the $[1\bar{1}0]$ direction and the macroscopic crack face is expected to be parallel to $(1\bar{1}0)$. From the calculation of the crack tip resolved shear stress ($\tau_{rss|tip}$), the following slip systems are predicted to be operative during crack propagation; $(1\bar{1}\bar{2})[1\bar{1}1]$ and $(1\bar{1}2)[\bar{1}11]$ with largest $\tau_{rss|tip}$ and $(011)[1\bar{1}1]$, $(\bar{1}01)[1\bar{1}1]$, $(101)[\bar{1}11]$ and $(0\bar{1}1)[\bar{1}11]$ with second largest $\tau_{rss|tip}$.

The fatigue crack propagation tests are conducted using a servo-controlled electro-hydraulic testing machine equipped with an environmental chamber. The fatigue crack is observed through a window of the chamber by a CCD camera. The test conditions are summarized in Table 1. The tests are conducted as follows. First, the relationship between applied stress intensity factor range (ΔK) and crack propagation rate ($\mathrm{d}a/\mathrm{d}N$) is evaluated both in helium and in hydrogen atmospheres. On the basis of these results, the crack propagation is next interrupted at a certain ΔK value (in this study 20 $\mathrm{MPam}^{1/2}$) that yields different $\mathrm{d}a/\mathrm{d}N$ in helium and in hydrogen atmospheres. This allows a direct comparison of the different crack tip deformation at the same mechanical condition.

After the fatigue crack propagation test, the fracture surface and the crack tip region are observed in detail by scanning electron microscopy (SEM) and TEM, respectively. For TEM observation, the interrupted crack tip region is carefully cut from the specimen and thinned by focused ion beam (FIB) machining. The TEM observation is conducted using JEM-1300NEF at an acceleration voltage of 1250 kV, which enables fairly stable observation of magnetic materials and yields enough electron transparency for FIBed specimens with relatively large thickness. The radiation damage introduced by the high acceleration voltage presumably has little effect on the image interpretation associated with the slip behavior.

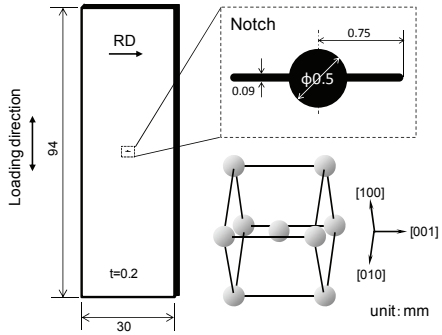


Figure 1: Geometry and crystallographic orientation of specimen.

Table 1: Test conditions

Nominal maximum stress	Stress ratio	Wave form	Frequency	Atmosphere	
280 MPa	0.05	Sinusoidal	1 Hz	Helium Hydrogen	0.58 MPa 0.58 MPa

RESULTS AND DISCUSSION

Figure 2 shows the da/dN-ΔK relationships in helium and hydrogen atmosphere. The ΔK value was evaluated using:

$$\Delta K = \frac{\Delta P}{\mathrm{B}} \sqrt{\frac{\pi a}{\mathrm{W}^2}} \sec \frac{\pi a}{\mathrm{W}} \qquad (1)$$

Here, ΔP is the applied load range, a the crack half-length projected along the [001] axis, B the specimen thickness and W the specimen width. It is clear from the figure that crack propagation is accelerated by the hydrogen atmosphere and is approximately four times larger for Specimen C than for Specimen A at ΔK = 20 (MPam$^{1/2}$). The magnitude of acceleration is more enhanced at elevated ΔK region. These curves are fitted to the following equation (Paris' law) by the least square method.

$$\frac{\mathrm{d}a}{\mathrm{d}N} = \mathrm{C}(\Delta K)^{\mathrm{m}} \qquad (2)$$

The m value of Specimen A is 3.9, which is close to the value reported for polycrystalline ductile metals (2 - 4). In contrast, the value of Specimen C is 6.4, which suggests that the crack propagation process of this specimen is rather brittle in nature.

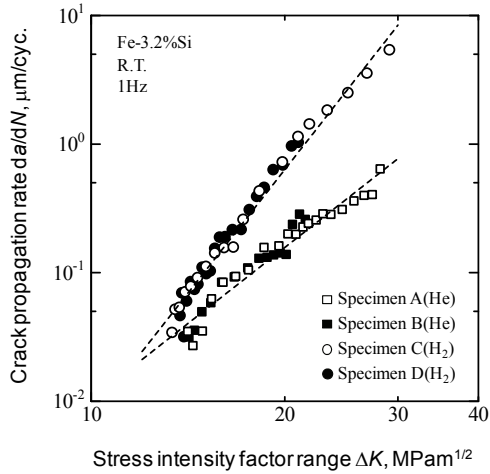
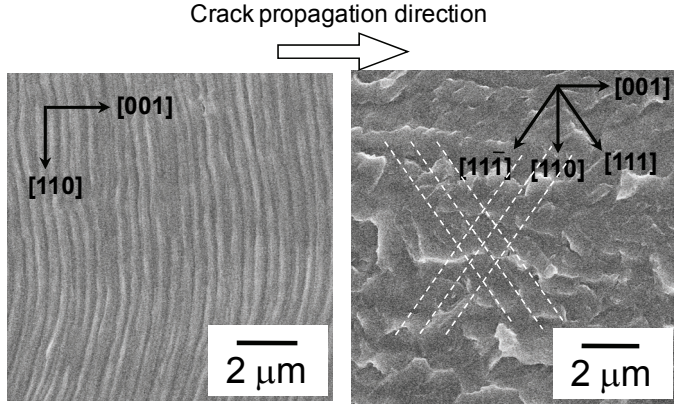


Figure 2: Relationship between stress intensity factor range and crack propagation rate.

Figure 3 shows the fracture surfaces of Specimen A and C observed by SEM. Fig.3(a) and (b) are taken at almost the same $\Delta K \approx$ 20 MPam$^{1/2}$. In Fig.3(a), a striation pattern almost parallel to the [110] direction is clearly seen. The striation spacing is 0.2 - 0.3 μm, which is close to the measured da/dN value in Fig.2. The

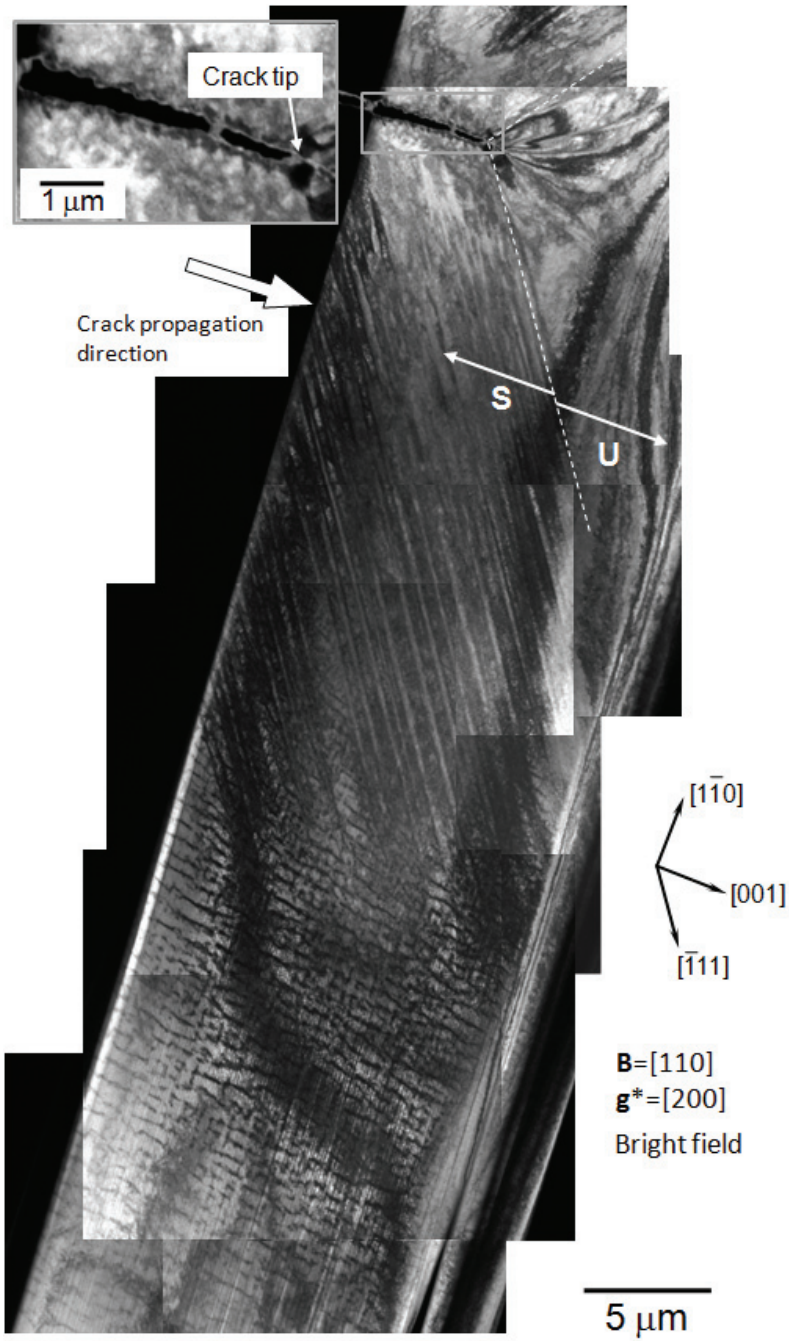
striation pattern is formed by the activation of $(1\bar{1}\bar{2})[1\bar{1}1]$ / $(1\bar{1}2)[\bar{1}11]$ slip systems as discussed later. In Fig.3(b), on the other hand, the [110] striation can hardly be recognized. Instead, the striation is nearly parallel to the [111] and the $[11\bar{1}]$ directions outlined by tear-ridges. These directions suggest the activation of $(011)[1\bar{1}1]$ / $(101)[\bar{1}11]$ slip systems and $(\bar{1}01)[1\bar{1}1]$ / $(0\bar{1}1)[\bar{1}11]$ slip systems, respectively. The spacing of each pattern is approximately the same (0.8 - 0.9 μm) and close to the measured da/dN value in Fig.2.



(a) Specimen A (in He) *(b) Specimen C (in H_2)*

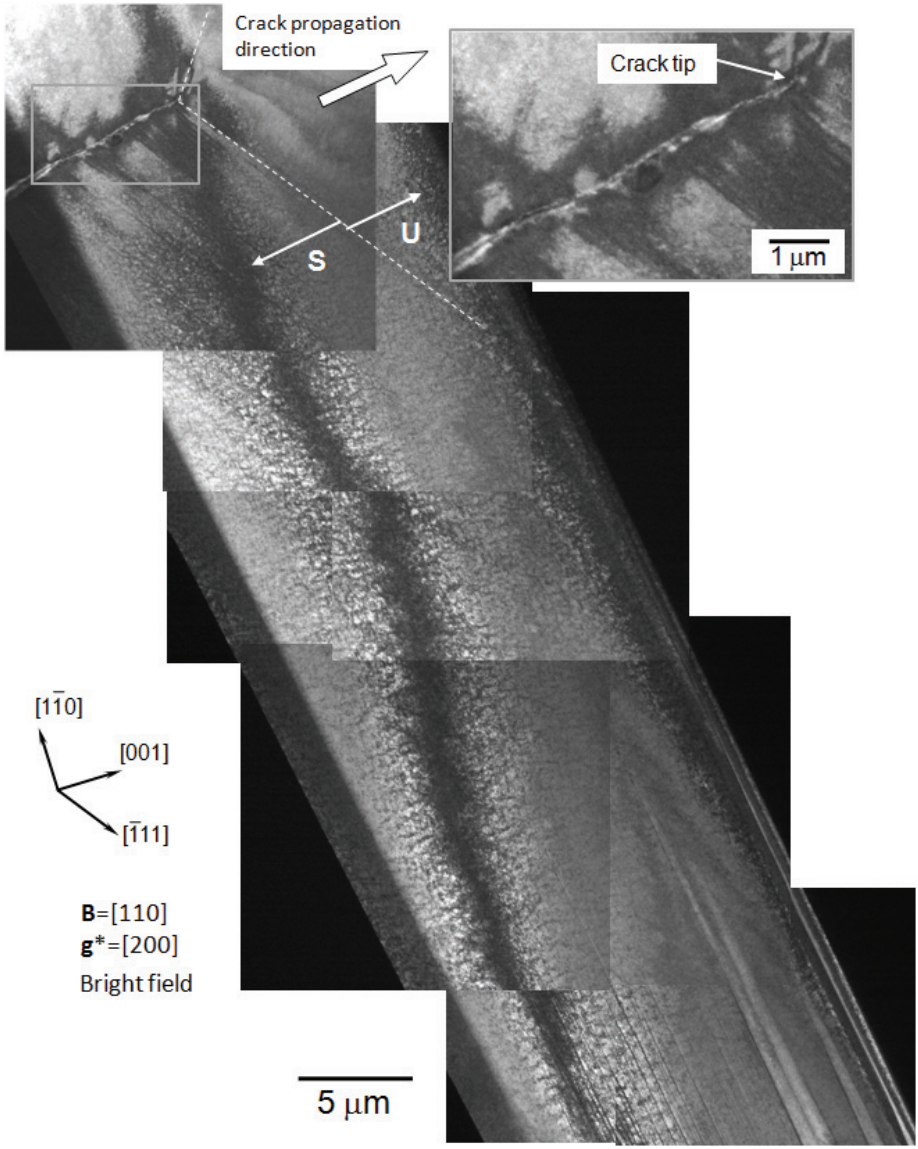
Figure 3: SEM images of fracture surface at $\Delta K \approx 20$ MPam$^{1/2}$.

Figure 4 shows the cross-sectional images of the crack tip region in Specimen B and D observed by TEM. In Fig.4(a), the slip bands formed along $(1\bar{1}2)[\bar{1}11]$ system are very clearly seen. The distinct boundary between slipped area (S) and unslipped area (U) indicates that the slip band is emitted from the crack tip. The dense slip bands reach about 30 μm from the crack. In addition, regular arrays of dislocation cell walls can be seen below the densely slipped region. The cell structure is aligned almost perpendicular to the loading direction, indicating that the structure is formed under a uniaxial stress field that precedes the crack tip stress field. The fatigue crack advances by emitting dense slip bands into the matrix filled with the cell structure. The crack wake has a wavy shape which corresponds to the striation pattern on the fracture surface shown in Fig.3(a). This suggests that crack blunting and re-sharpening due to the 'slip-off' process of the two symmetrical slip systems about the crack face (i.e. $(1\bar{1}\bar{2})[1\bar{1}1]$ / $(1\bar{1}2)[\bar{1}11]$ pair) results in the formation of such a cyclic pattern in non-hydrogen atmosphere [1]. In the hydrogen atmosphere, on the other hand, the slip behavior is quite different from that in the helium atmosphere. In Fig.4(b), the slip trace of $(1\bar{1}\bar{2})[1\bar{1}1]$ / $(1\bar{1}2)[\bar{1}11]$ systems can be seen in Specimen



(a) Specimen B (in He)

Figure 4: Cross-sectional TEM image of near-tip region at $\Delta K \approx 20$ MPam$^{1/2}$.



(b) Specimen D (in H_2)

Figure 4: Continued.

D although it is not as intense as that in Specimen B. The slip bands reach as far as about 30 μm from the crack, which is not much different from Specimen B. However, the cellular structure is not as distinct as that in Specimen B. Since the fractography in Fig.3(b) shows the different slip trace ((011)[1$\bar{1}$1] / (101)[$\bar{1}$11] pair and ($\bar{1}$01)[1$\bar{1}$1] / (0$\bar{1}$1)[$\bar{1}$11] pair), it seems that three pairs of slip system are simultaneously active in the hydrogen atmosphere.

Figure 5 shows the magnified view of the crack wake ($\Delta K \approx 20$ (MPam$^{1/2}$)) in Specimen D. The heavily dislocated region is concentrated close to the crack wake, and the overall appearance of the crack propagation is quite brittle. It can be postulated from Figs.3(b) and 5 that hydrogen atmosphere strongly localizes the cyclic slip near the propagating crack with the simultaneous activation of different pairs of slip systems. The two-dimensional slip-off model, in which a single pair of symmetrical slip about the crack is considered, is therefore too simple to explain the observed crack propagation behavior in a hydrogen atmosphere. A more detailed observation of the dislocation structure near the crack would reveal the effect of hydrogen on the slip localization and the apparent brittle cracking behavior; this work is now in progress.

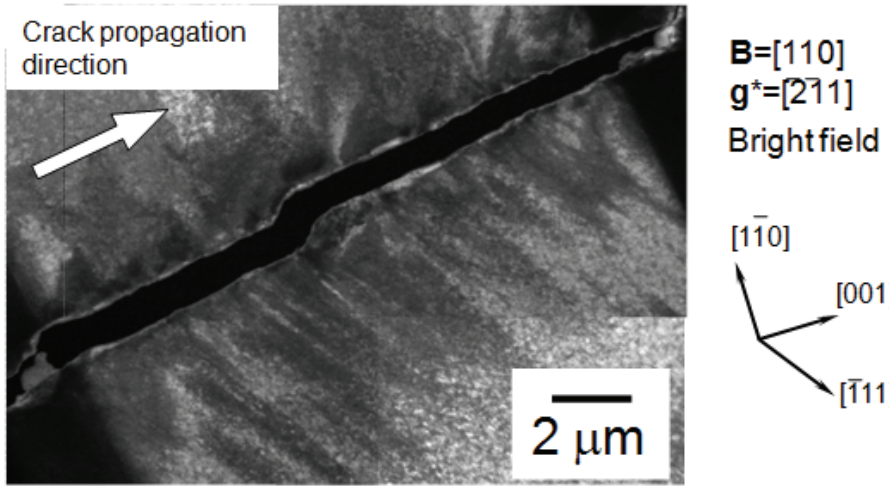


Figure 5: Cross-sectional TEM image of crack wake at $\Delta K \approx 20$ MPam$^{1/2}$.

SUMMARY

The effect of hydrogen on the crack tip cyclic slip deformation is investigated using a single-crystalline Fe-3.2%Si alloy. The fracture surface and the near-tip cross-

section are observed in detail by SEM and TEM respectively. The cyclic slip-off process by a pair of symmetrical slip system about the crack ($(1\bar{1}\bar{2})[1\bar{1}1]$ / $(1\bar{1}2)[\bar{1}11]$ pair) is operative in the non-hydrogen atmosphere. On the other hand, other pairs of slip system ($(011)[1\bar{1}1]$ / $(101)[\bar{1}11]$ pair and $(\bar{1}01)[1\bar{1}1]$ / $(0\bar{1}1)[\bar{1}11]$ pair) are also found to be operative and slip is localized around the vicinity of the crack in the hydrogen atmosphere.

ACKNOWLEDGEMENTS

This study has been conducted as a part of "Fundamental Research Project on Advanced Hydrogen Science" funded by New Energy and Industrial Technology Development Organization (NEDO). The authors are greatly indebted to the support by HVEM Laboratory in Kyushu University for the specimen preparation and observation.

REFERENCES

1. Laird, C., "The Influence of Metallurgical Structure on the Mechanism of Fatigue Crack Propagation," ASTM STP No. 415 (1967), pp. 131-180.
2. Tanaka, K., Hojo, M., Nakai, Y., "Plastic Deformation around a Fatigue Crack near Threshold in 3%Si-Fe," Mater. Sci. Eng., Vol. 55, No. 1(1982), pp. 85-96.
3. Shewmon, P. G., "The 1997 Edward DeMille Campbell Memorial Lecture ASM International – Grain Boundary Cracking," Metall. Mater. Trans. B, Vol. 29, No. 3(1998), pp. 509-518.
4. Marrow, T. J., Aindow, M., Prangnell, P., Strangwood, M., Knott, J. F., "Hydrogen-Assisted Stable Crack Growth in Iron-3wt% Silicon Steel," Acta. Mater. Vol. 44, No. 8(1996), pp. 3125-3140.
5. Chen, X., Kozubowski, J. A., Gerberich, W. W., "Hydrogen-induced Sustained Load Cracking in Single Crystal Fe-3wt.%Si," Scr. Metall., Vol. 22, No. 2(1988), pp. 245-248.
6. Narita, N., Shiga, T., Higashida, K., "Crack-impurity Interactions and Their Role in the Embrittlement of Fe Alloy Crystals Charged with Light Elements," Mater. Sci. Eng. A, Vol. 176, No. 1-2(1994), pp. 203-209.

Effects of Hydrogen on Materials
Proceedings of the 2008 International Hydrogen Conference
Brian Somerday, Petros Sofronis, Russell Jones, editors, p 211-218
Copyright © 2009 ASM International®
All rights reserved.
www.asminternational.org

CHARACTERIZATION OF HYDROGEN-ASSISTED FRACTURE MECHANISM BY FRACTURE SURFACE TOPOGRAPHY ANALYSIS (FRASTA)

Takao Kobayashi
Center for Fracture Physics
SRI International,
Menlo Park, CA, U.S.A. 94025

Brian Somerday, Chris San Marchi, and Kevin A. Nibur
Sandia National Laboratories,
Livermore, CA, U.S.A. 94550

ABSTRACT

The fracture surface topography analysis (FRASTA) technique was applied to the crack arrest threshold region in a wedge-opening-load (WOL) ASME SA 372 Grade J sample tested in hydrogen gas at 100 MPa. FRASTA juxtaposed and incrementally displaced conjugate fracture surface topographs to reconstruct microfracture processes, and displayed the results graphically. Although qualitative fracture surface examination revealed little evidence of intergranular cracking and did not show the precise fracture path with respect to the microstructure, FRASTA established the sequence of local microcrack formation, growth, and coalescence at the crack front. In addition, FRASTA was successful in determining the local crack opening displacement and assessing local fracture resistance.

INTRODUCTION

Efficient and economical hydrogen use will require its transportation and storage at high pressure. Effects of hydrogen on the degradation of materials have been studied; however, the available data on effects of high-pressure gaseous hydrogen on fracture processes in structural materials are relatively limited.

A team of researchers at the Sandia National Laboratories, Livermore, CA (SNL/CA) is conducting programs funded by the US Department of Energy (DOE) to (1) prepare a resource for engineering data relevant to gaseous hydrogen embrittlement [1], and (2) to perform material testing in a high-pressure hydrogen gas environment [1, 2]. Their material testing is focused on generating fracture mechanics data for engineering materials that can be used in design of structures for hydrogen gas service. The Sandia team is using the standardized wedge-opening load (WOL) geometry to measure the time–dependent crack growth response of many structural metals in hydrogen gas (ASTM E1681). The detail of the test

procedures and the results of several low alloy pressure vessel steels and C-Mn line pipe steel are summarized and presented elsewhere [3, 4].

Among the pressure vessel steels the Sandia team tested, the behavior of the ASME SA 372 Grade J steel is of particular interest; this steel is a Cr-Mo low-alloy steel similar to AISI 4137. Qualitative fracture surface examination revealed little evidence of intergranular cracking, and the precise fracture path with respect to the microstructure was not readily evident.

In order to establish a more detailed understanding of hydrogen-assisted fracture mechanisms, FRASTA (fracture surface topography analysis), an SRI International-developed technology, was applied. A detailed explanation of the concept and implication of FRASTA can be found elsewhere [5, 6]. In this paper, a brief explanation of FRASTA procedures and the anticipated results are presented, followed by the results obtained from a SA372 Grade J WOL sample that had been tested at SNL in high-pressure hydrogen.

FRASTA PROCEDURE

The basic principle of FRASTA is to assess the degree of local plastic deformation during the fracture process through matching conjugate topographs and to reconstruct the fracture process using the information on the local differences of the amount of plastic deformation. The basic assumption is that the material exhibits plastic deformation up to the point of fracture; however, when the fracture occurs the stresses are relieved at the newly formed fracture surfaces and the plastic deformation that existed at the moment of fracture is "frozen" in the material immediately below the fracture surfaces. The applied load is re-distributed to unfractured material in front of the crack tip, which continues to deform plastically until it also fractures. This sequential process produces different amounts of local plastic deformation in the material as a function of distance from the crack nucleation site.

The assessment of plastic deformation that occurred during the fracture process requires juxtaposing conjugate topographs because plastic deformation at the crack tip is not distributed equally on the surfaces.

Figure 1 shows the juxtaposed topographs and two views of the operation. Looking through two surfaces from the top, a binary plot of the overlapped area (black) and the gapped area (white) can be constructed. Overlapped areas represent material still intact, and gapped areas already fractured. The plane-view plot is called a fractured-area-projection plot (FAPP). The FAPP is equivalent to an X-ray radiograph and shows the cracked area, crack front position and shape, and, if it occurs, microcrack formation ahead of the crack front. A cross-sectional plot (XSP) is obtained by virtual sectioning on any planes normal to the fracture surface. The XSP shows crack opening profiles and also the amount of plastic deformation ahead of the crack

front; thus, the XSP allows crack opening displacements and crack opening angles to be determined.

By adjusting the spacing between the conjugate topographs, a series of FAPPs and XSPs can be produced. Measuring the fractured area in each FAPP and plotting the

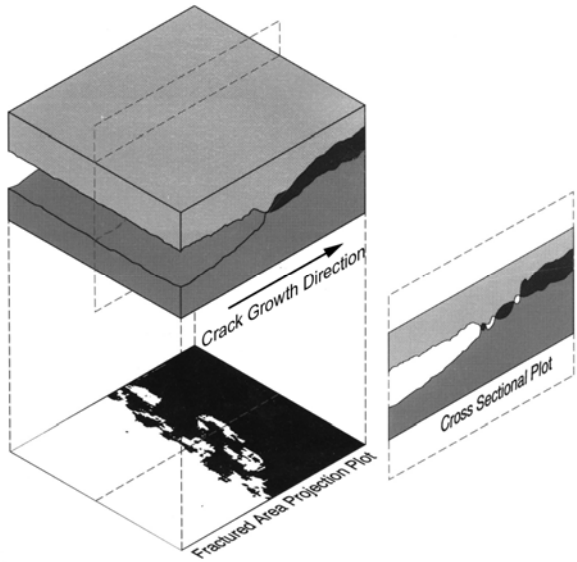


Figure 1. A graphic presentation of the FRASTA operation; Fractured Area Projection Plot (FAPP) and Cross Sectional Plot (XSP).

area as a function of the spacing between the conjugate topographs, a fracture progression curve (FPC) can be obtained. The slope of the FPC is related to the crack growth rate, and is sensitive to the changes in loading conditions and environmental factors. We can also determine the spacing that corresponds to the onset of a rapid crack extension.

In the present work precision surface topography characterization was achieved with a confocal-optics scanning laser microscope. The matching of the conjugate surface areas was also accomplished by a computer-assisted microscope system.

SPECIMEN ANALYZED

Sustained-load cracking measurements were performed on SA 372 Grade J steel using WOL specimens in high-pressure gaseous hydrogen. Detailed information on testing method, specimen geometry, and the results can be found elsewhere [3, 4]. Figure 2 shows a macro photograph of the fracture surface on one side of the specimen. The fracture surface shows that the area of fatigue pre-cracking was smooth and flat; however, as the crack extended, the surface became rougher. An

area where the crack arrested (marked by an arrow in Fig. 2) was selected since the fracture process near the crack arrest threshold is of interest.

FRASTA RESULTS

Figure 3 shows a series of FAPPs superimposed on a SEM image of the same area. In these plots the red area represents still intact material, and gray areas represent fractured material. The number shown at each figure represent a relative spacing between conjugate surfaces (0 represents complete overlap of the conjugate materials, and 1 represents no contact anywhere).

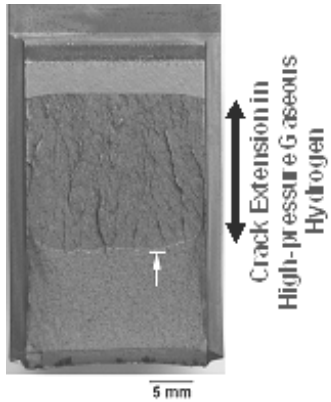


Figure 2. Macro photograph of fracture surface of the SA372 Grade J specimen

The FAPPs clearly delineate the sequential failure of the specimen and a relationship between the fracture surface features to microcrack formation and growth. Figures 3c and 3d show the formation of microcracks ahead of the main crack front and their subsequent growth parallel and in the direction of the overall crack front.

Figure 4 shows a series of XSPs along the lines A-A and B-B in Fig. 3d. Figures 4(a) and 4(e) show the onset of microcracks at these cross sections. Significant variation in the amount of overlap along the line indicates the variation in the amount of plastic deformation (parallel to the average crack front). The subsequent plots indicate the crack opening displacement measured from the state shown in Figs. 4(a) and 4(e). Figures 4(d) and 4(h) show the state where the crack is about to expand rapidly parallel to the crack front because the overlap is about to disappear. The crack opening displacements at this stage were 9.9 μm along A-A and 11.4 μm along B-B.

Examination of the area in the vicinity of these isolated microcrack shown particularly in Fig. 3(d) and 3(e) reveals that the initial expansion of the fractured area was circular and gradual; however, after Fig. 3(e) the rate of increase of the fractured area around these microcracks was higher. The inflection in the FPC curve (Fig. 5) at a spacing of 0.405 indicates that the opening displacement shown in Figs. 4(d) and 4(e) represents the critical state in crack extension.

Local fracture toughness can be estimated by using the following equation which relates stress intensity, K, to the crack tip opening displacement (CTOD):

$$K^2 = mE \sigma_{ys} \delta / (1 - \nu^2) \qquad (1)$$

where E is elastic modulus, σ_{ys} is yield stress, δ is CTOD, ν is Poisson's ratio, and m is a dimensionless constant [7]*.

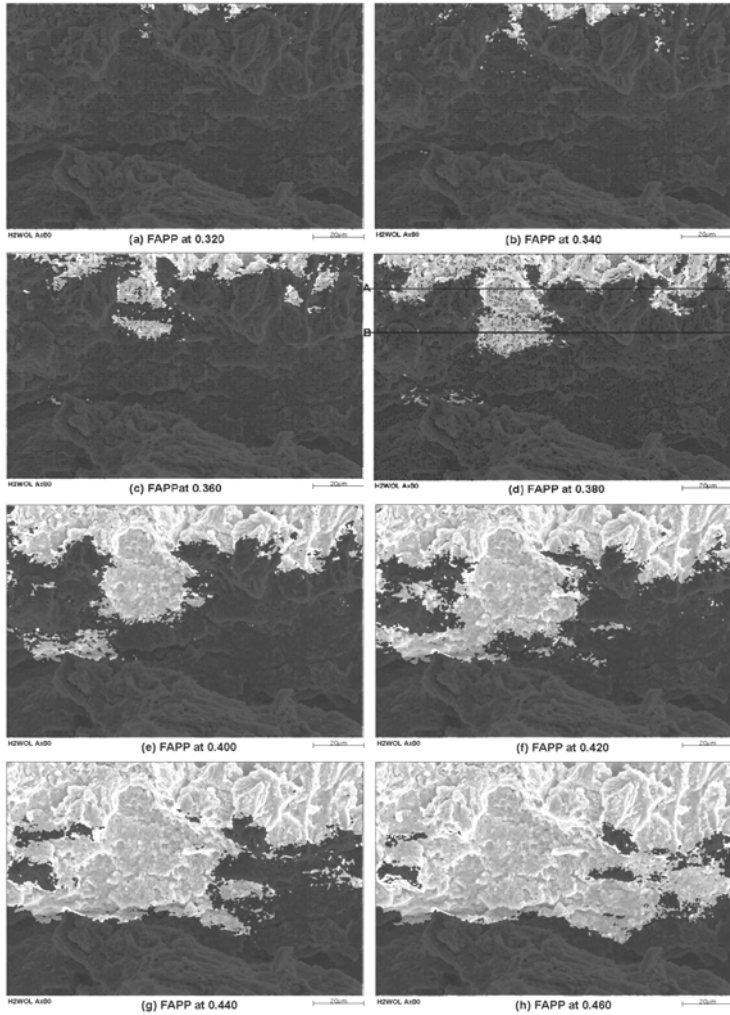


Figure 3. Selected FAPPs superimposed over SEM image

* Various values of m have been reported, and they depend upon the exact place where the CTOD is determined and the assumptions made for the analysis [7]. The values range from m=1 for plane stress condition to m=1.48 for non-strain hardening material in plane strain [8], m=2 for plane strain [9], and to m=2.14 by finite element analysis [10]. McMeeking suggests values between 2 and 3 for strain hardening materials [11].
The direct experimental measurement of m was also made by Bowles who found m=1 at the mid-section CTOD using metallographic sectioning of the crack tip region [7]. Similarly, Robinson and Tetelman who also found m=1 by infiltrating hardening rubber into the crack [7].

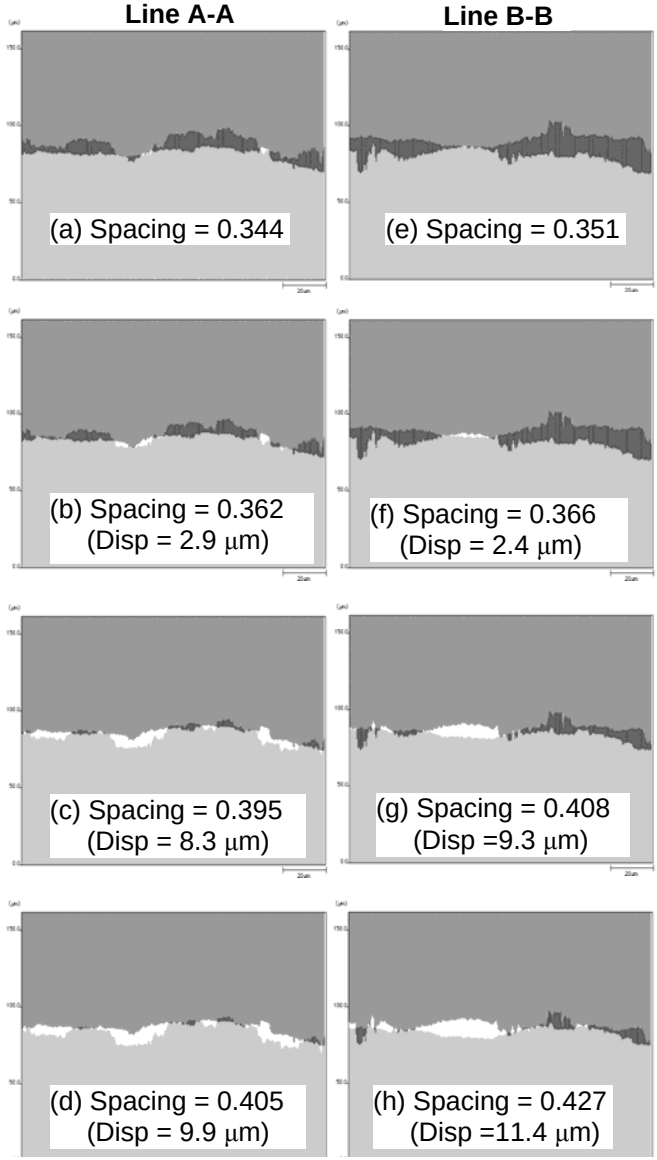


Figure 4. Cross-sectional plots along the lines A-A and B-B.

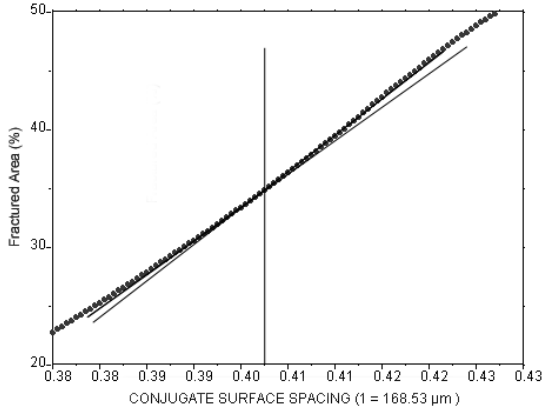


Figure 5. Inflection in the fractured area increase as a function of conjugate surface spacing

Choosing m=1 and m=3 and substituting the following values of SA 372 Grade J steel properties: E = 207 GPa, σ_y = 715 MPa [3, 4], δ = 10 µm as determined above, and ν = 0.3, stress intensity factors (K) of K = 41 MPa √m and 70 MPa √m were obtained, respectively. These values were lower than the threshold value of 90 MPa √m measured by Sandia [3, 4]. Considering that an area with microcracks ahead of the nominal crack front was characterized, these values are plausible. More measurements along the arrested crack front may provide additional statistics about the range of values that can be determined for the local resistance to fracture.

More work is also needed to determine a suitable value of m for this local analysis. Most of the analyses of CTOD-K relation assume an engineering size crack and it is not clear whether these formulas apply to microscopic cracks. Nevertheless, FRASTA can be used to probe susceptible features (such as microcracked features in Fig 3d), which can then be isolated and evaluated by complementary microscopy techniques.

SUMMARY AND CONCLUSIONS

Insight into the hydrogen-assisted fracture modes was obtained by analyzing the fracture surface topography of SA 372 Grade J steel WOL specimen that had been tested in high-pressure hydrogen gas. FRASTA delineated the sequence of microcracking ahead of the main crack front resulting in an irregular crack front. Measurements of local crack tip opening displacement (δ) indicated a local fracture toughness (K) of between 41 MPa√m and 70 MPa√m depending on the choice of the coefficient value of dimensionless parameter m. More work is needed to evaluate the appropriate value for m in determining the local K values from local

δ measurements; however, the measurement of local crack tip opening displacement can contribute to the evaluation of the role of microstructural constituents.

ACKNOWLEDGEMENTS

Sandia is a multiprogram laboratory operated by Sandia Corporation, a Lockheed Martin Company, for the United States Department of Energy under contract DE-AC04-94AL85000. Funding for the work described here was provided by contract No. 690380.

REFERENCES

1. San Marchi, C, and Somerday, B.P., "Technical Reference on Hydrogen Compatibility of Materials (SAND2008-1163)". Sandia National Laboratories, Livermore CA, 2008.
2. San Marchi, C., and Somerday, B.P., "Effects of High-Pressure Gaseous Hydrogen on Structural Metals," *SAE 2007 Transactions, Journal of Materials and Manufacturing, Section 5,* Vol. 116, Paper No. 2007-01-0433, 2007, pp 35-50.
3. Nibur, K.A. et al., "Sustained Load Cracking of Steels for Hydrogen Storage and Delivery, " A paper presented at 2008 International Hydrogen Conference, September 7-10, 2008.
4. Nibur, K. A., et al., "Measurement of Sustained-Load Cracking Thresholds fro Steels in Hydrogen Delivery and Storage," Proceedings of PVP2008, 2008ASME Pressure Vesels and Piping Division Conference, July 27-31, 2008, Chicago, Illinois, PVP2008-61298.
5. Kobayashi, T. and Shockey, D.A.," "FRASTA: A New Way to Analyze Fracture Surfaces, Part 1: Reconstructing Crack Histories," *Advanced Materials & Processes*, Vol. 140, No. 5, (1991), pp 28-34.
6. Kobayashi, T. and Shockey, D.S., "Fracture Analysis via FRASTA, Part 2: Determining Fracture Mechanisms and Parameters," *Advanced Materials & Processes*, Vol. 140, No. 6, (1991), pp. 24-32.
7. Broek, D., Elementary Engineering Fracture Mechanics, 4th ed., Martinus Nijhoff Publishers, 1986.
8. Rice, J.R., "A path independent integral and the approximate analysis of strain concentrations by notches and cracks," J Appl Mech, Vol. 35, pp 379-386, 1968.
9. Anderson, T.L. "Fracture Mechanics: Fundamentals and Applications, " CRC Press, 1991
10. Levy, N. et al., "Small scale yielding near a crack in plane strain: a finite element analysis," Int J Fract Mech, Vol. 7, pp. 143-146, 1971.
11. McMeeking, R. M., "Finite deformation analysis of crack tip opening in elastic-plastic materials and implications for fracture," *J Mech Phys Solids,* Vol. 25 pp. 357-381, 1977

Effects of Hydrogen on Materials
Proceedings of the 2008 International Hydrogen Conference
Brian Somerday, Petros Sofronis, Russell Jones, editors, p 219-226
Copyright © 2009 ASM International®
All rights reserved.
www.asminternational.org

THE INFLUENCE OF HYDROGEN ON THE ELASTIC MODULUS AND ANELASTIC RESPONSE OF COLD WORKED PURE IRON

R. E. Ricker and D. J. Pitchure
Metallurgy Division, National Institute of Standards and Technology,
U.S. Dept. of Commerce, Gaithersburg, MD 20899-8553

ABSTRACT

Understanding the influence of hydrogen on elastic deformation and anelastic response should contribute to our understanding of the influence of hydrogen on deformation and fracture. To accomplish this objective, samples of pure iron were cold-worked, charged with hydrogen, and examined in a dynamic mechanical analyzer. For these measurements, square wave loads were applied at different frequencies and the response of the sample quantified into time-independent and time-dependent components. These measurements were then analyzed to determine the influence of hydrogen on the time-independent, elastic, modulus and time-dependent, anelastic, relaxation. Hydrogen lowered the measured elastic modulus by a small, but statistically significant, amount.

INTRODUCTION

The mechanisms responsible for hydrogen-induced sub-critical crack propagation ("hydrogen embrittlement") have been the subject of considerable study, and there are a number of excellent reviews available in the scientific literature [1-5]. Many mechanisms have been proposed to explain hydrogen embrittlement in different materials and alloys including nucleation of gas filled voids and blisters [6-10], brittle hydride nucleation [5,11], reduced plasticity (dislocation pinning) [12,13], lattice decohesion [14,15], enhanced localized plasticity [16-20], and surface energy modification [21-23].

Whatever the mechanism or mechanisms of embrittlement may be, it is clear that hydrogen can influence fracture morphology by either: (i) modifying normal ductile fracture (e.g. enlarging dimples), (ii) inducing transgranular "cleavage-like" fracture features, (iii) inducing intergranular or interphase interface fractures, or (iv) nucleation of second phases (blisters or hydrides). Also, two or more of these fracture modes may be observed in the same alloy system depending on hydrogen

fugacity, strain rate, stress state, microstructure, and crack tip orientation with respect to susceptible interfaces. Hydrogen supersaturation by cooling or cathodic charging can result in interfacial cracking, blistering, or hydride cracking. Recent research has focused on hydrogen levels more representative of service conditions expected for a hydrogen fuel based economy and newer alloys. Typically, newer alloys are less susceptible to hydrogen induced intergranular fracture due to improvements in alloy chemistry and metallurgical practices. For these alloys and conditions, transgranular "cleavage-like" fractures are more common, and crack propagation is usually attributed to either decohesion [14,15] or enhanced localized plasticity [16-20].

Decohesion and enhanced plasticity mechanisms differ in the basic phenomena believed to be responsible for crack propagation. The decohesion mechanism attributes fracture to a lowering of the bond energy holding the lattice together resulting in a reduced cleavage stress. The enhanced plasticity mechanism assumes that increased dislocation activity localized to the crack tip plastic zone is responsible. While in real solids it may not be possible to alter one of these factors without influencing the other, understanding the contribution of each to embrittlement requires measuring the extent that hydrogen actually alters one or both of these factors. An experimental technique for accomplishing this objective would be to apply a cyclic square wave load to hydrogen charged and uncharged samples and compare the time-independent and time-dependent elastic and anelastic response of the solid. Since lowering the cohesive forces binding the lattice together will alter the curvature of the interatomic potential energy (Fig. 1), the underlying hypothesis of the decohesion mechanism means that a lower elastic modulus should be observed when hydrogen is present. On the other hand, if hydrogen increases dislocation activity, then an increase in the anelastic strains should be observed similar to that found in steels with increasing cold work [24].

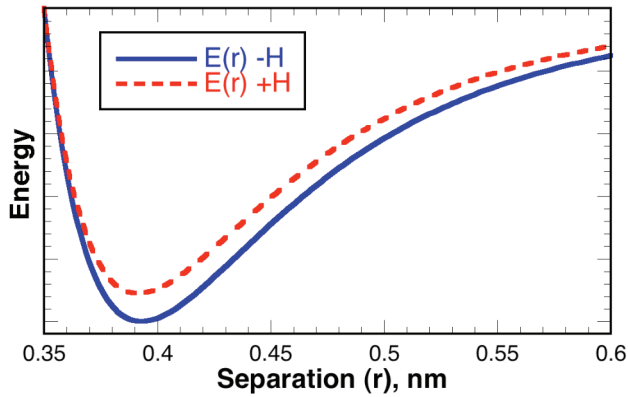


Figure 1: Diatomic potential energy vs. separation curves illustrating the change that hydrogen would have on curvature and modulus if it lowers attractive forces.

EXPERIMENTAL

Samples of pure iron (composition in Table 1) were cold rolled 47 % to a thickness of 0.83 mm. Pieces cut from the cold rolled strip were stacked and machined simultaneously to produce samples of nearly identical width (12.42 mm) and length (60 mm). The samples were tested in a commercially manufactured dynamic mechanical analyzer (DMA). This equipment consists of a furnace with a cryogenic (liquid nitrogen) cooling system capable of testing at temperatures from -150 °C to 600 °C and an electromagnetic driver capable of testing at frequencies from 0 Hz to 200 Hz and at applied loads up to 18 N. The closed-loop temperature control system uses a feedback thermocouple placed ≈ 3 mm from the test sample and is capable of controlling the temperature to ± 0.5 °C of the testing temperature (-100 °C). The force from the linear drive motor is applied with a frictionless air bearing and a three-point bending grip with a 50 mm span. An optical encoder with a resolution of 1.0 nm is used to measure displacement. The system is calibrated with the three-point bend grip in place to minimize errors from grip geometry and compliance.

Table 1: Chemical analysis of the Ferrovac E iron alloy. The identification of any commercial product or trade name does not imply endorsement or recommendation by the authors or NIST.

Element	Mass Fraction, %	Element	Mass Fraction, %	Element	Mass Fraction, %
Fe	Bal	Ni	0.03	Cu	0.001
C	0.006	Cr	0.01	Al	0.01
Mn	0.001	V	0.004	Sn	0.001
P	0.003	W	0.01	Pb	0.0006
S	0.007	Mo	0.001	O	0.026
Si	0.008	Co	0.003	N	0.0004

The samples were tested in three conditions: (1) uncharged, (2) hydrogen charged, and (3) hydrogen desorbed (desorbed). The samples were charged with hydrogen by polarizing them cathodically at room temperature in a solution of 0.1 mol/L NaOH for one hour using a closed-loop controller to hold the potential of the sample at -1.3 V with respect to a saturated calomel electrode. Diffusion calculations indicate that samples of this size will reach over 90 % of saturation at these conditions for hydrogen diffusion coefficients great than 4.0 E-11 m^2/s [25,26]. Following charging, the samples were immediately rinsed in water and alcohol, dried, and stored in liquid nitrogen until tested. The samples were tested in three point bending at -100 °C using a square wave load with a minimum force of 0.050 ± 2.0 E-7 N and a maximum force of 4.61327 ± 2.0 E-6 N, corresponding to a change in the bending stress in the sample of 40 MPa, at wavelengths of 6, 60, and 600 seconds. When the hydrogen charged tests were completed the samples were left in the grips untouched for a period of time sufficient to allow hydrogen desorption (overnight at ambient temperature). As with most elastic modulus measurements, the greatest source of uncertainty comes from sample dimensions, grips, and alignment. Re-testing the

same sample without repositioning it in the grips removes these sources of uncertainty [24]. No attempt has been made to correct for the influence of hydrogen content on sample dimensions. This correction requires additional measurements (i.e. hydrogen content) beyond the scope of the present work. However, it is well known that the iron lattice expands as the hydrogen content increases, which would reduce the displacements measured in three point bending for the same applied force if the elastic modulus were constant. Therefore, assuming that the sample dimensions are constant is a conservative test of the hypothesis that hydrogen lowers the elastic modulus.

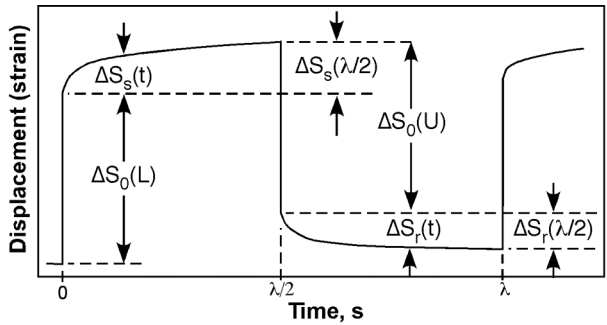


Figure 2: Schematic of the displacements produced by a square wave load with the magnitude of the time-dependent strains greatly exaggerated for illustration.

RESULTS AND DISCUSSION

When a square wave cyclic force is applied to a sample, the resulting displacements should consist of nearly instantaneous displacements when the load is applied and removed ($\Delta S_0(L)$ and $\Delta S_0(U)$ in Fig. 2) followed by a period of time equal to half the wavelength where the displacement is essentially constant. Small time-dependent microstructural relaxations, $\Delta S_s(t)$ and $\Delta S_r(t)$, occur during these periods of static stress as shown in Fig. 2. These strains are several orders of magnitude smaller than the time-independent strains, and they are due to relaxation of microstructural defects in the applied stress. The magnitude of this relaxation depends on the population of microstructural defects and the ability of these defects to respond to the applied stress and produce an increment of strain [27,28]. Since cold work increases the magnitude of these time-dependent strains [24], dislocations are one of the types of microstructural defects that contribute to these strains. The goal of the present study is not to evaluate these mechanisms, but to determine if these strains are modified by the presence of hydrogen in a manner consistent with the decohesion or enhanced localized plasticity mechanisms for hydrogen embrittlement. For this purpose, the time-independent strains will be quantified by the displacements measured on load application or removal, $\Delta S_0(L)$ and $\Delta S_0(U)$ respectively, and the time-dependent strains will be quantified by the relaxation over the half cycle at maximum load, $\Delta S_s(\lambda/2)$, and the recovery during the half cycle at the minimum load, $\Delta S_r(\lambda/2)$. Since the sample dimensions and the applied forces are constant,

changes in the measured displacements will be inversely proportional to the changes in the modulus.

The time-independent strains were examined by first comparing response during loading and unloading, $\Delta S_0(L)$ and $\Delta S_0(U)$, and no statistically significant difference could be determined. Also, no significant trend could be discerned with increasing cycle count. A slightly greater range was observed for the first load application and attributed to seating of the sample in the grips. Therefore, these measurements, minus the first loading transient, were grouped together for the evaluation of the effects of hydrogen desorption. To minimize experimental uncertainties, the samples were left mounted in the grips with the chamber closed during desorption (overnight at ambient temperature). Table 2 summarizes the results of this comparison and shows that displacements were slightly smaller for the same loading conditions after hydrogen desorption. However, a t-test for the statistical significance of this difference found essentially zero probability that this difference could be due to measurement uncertainty. Therefore, it is concluded that removal of the hydrogen cathodically charged into the samples resulted in a small increase in the observed elastic modulus. While this difference may not actually be due to a change in the interatomic bonding forces and other hydrogen microstructure interactions could be responsible, one cannot rule out decohesion as a potential mechanism for hydrogen embrittlement, as this observation is consistent with the fundamental hypothesis of this mechanism.

Table 2: Analysis of the influence of hydrogen on the elastic displacement measured when the applied force is stepped between the minimum and maximum.

		Sample A	Sample B
After H Charging $\Delta S_0(+H)$	Mean, µm	87.528	95.030
	Std Dev, µm	0.061	0.099
	n (meas.)	15	15
After H Desorption $\Delta S_0(-H)$	Mean, µm	87.090	93.998
	Std Dev, µm	0.032	0.069
	n (meas.)	15	15
Statistical Test of Significance	ΔMean, µm	0.439	1.031
	t-Test Statistic	26.399	35.143
	DOF	28	28
	t-Test Prob	1.35E-20	5.79E-24

To evaluate the effect of hydrogen on the magnitude of anelastic relaxations, the total relaxations over the half wavelength ($\lambda/2$) at the maximum and minimum loads of each load cycle were compared with and without hydrogen over a sequence of 3 cycles. These results are shown in Fig. 3 with error bars determined from the standard deviations of the measurements. This figure shows that the anelastic relaxations determined for the static period at the maximum load (ΔS_s) were greater with hydrogen in the lattice for all cycles for $\lambda/2$ of 3 s and 30 s and for the first cycle at 300 s. The anelastic strain recovered over the static period after the load was

reduced from the maximum (ΔS_r) was not significantly different with hydrogen content for any of the loading cycles and periods except for the first cycle with $\lambda/2$=3 seconds. Since there is greater error in these measurements and the error bars frequently overlap, these conclusions are not as strong as those for the time-independent response, but Fig. 3 shows that greater relaxations were observed at the maximum stress when hydrogen was present in the lattice. Since the measurements include all mechanisms of microstructural relaxations one cannot conclude that dislocation activity was increased when hydrogen was present [29]. However, one can conclude that removal of hydrogen from the samples reduced the magnitude of the observed relaxations consistent with the hypothesis that hydrogen increases dislocation activity.

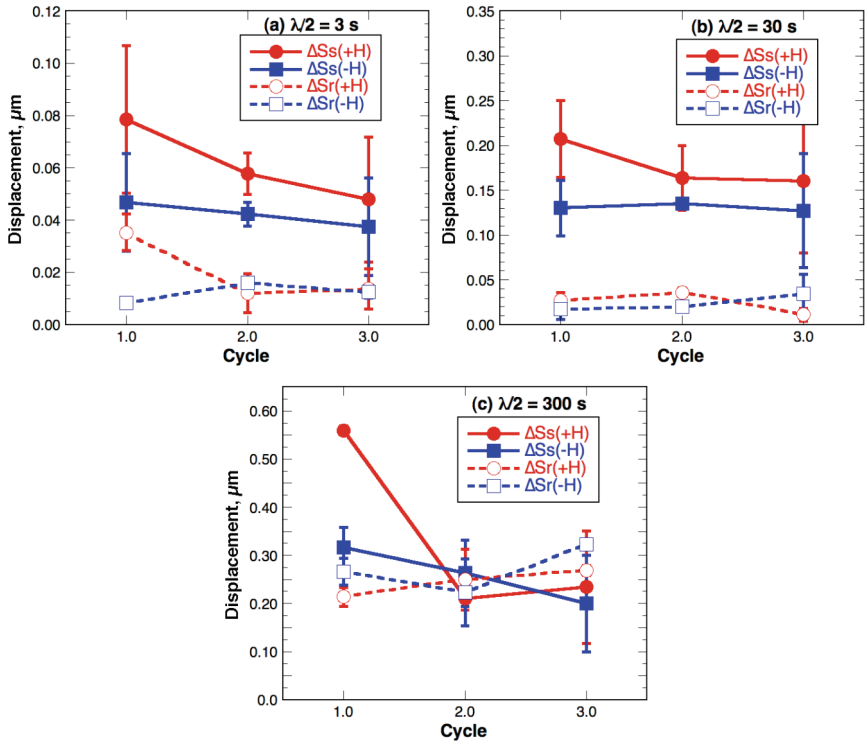


Figure 3: Comparison of the anelastic relaxations at maximum load with hydrogen present and after desorption (ΔS_s(+H) and ΔS_s(-H)) and after release of the maximum load with hydrogen present and after desorption (ΔS_r(+H) and ΔS_r(-H)) as a function of the cycle count for three cycles with a half wavelength ($\lambda/2$) of (a) 3 s, (b) 30 s, and (c) 300 s.

CONCLUSIONS

There were three objectives to these experiments: (i) test the hypothesis that hydrogen lowers the elastic modulus, (ii) test the hypothesis that hydrogen increases anelastic relaxations, and (iii) evaluate dynamic mechanical analysis as a measurement tool for investigation of fundamental interactions contributing to hydrogen embrittlement. These experiments accomplished all three objectives although the change in the anelastic response was not definitive. While the changes in the time-independent and time-dependent responses were consistent with these mechanistic hypotheses, it is premature to conclude these mechanisms are the only mechanisms that could be responsible for the observations. Additional testing and analysis will be required to evaluate and eliminate other mechanistic possibilities before this can be concluded unequivocally. In any event, dynamic mechanical analysis has proven to be an effective tool for investigating the influence of hydrogen on mechanical properties.

REFERENCES

1. A. S. Tetelman, "Recent Developments In Classical (Internal) H Embr.," Hydrogen in Metals, A. W. Thompson and I. M. Bernstein ed., ASM, (Metals Park, OH, 1974), pp. 17-34.
2. H. H. Johnson, "H_2 Gas Embr.," Hydrogen in Metals, I. M. Bernstein and A. W. Thompson ed., ASM, (Metals Park, OH, 1974), pp. 35-49.
3. M. R. Louthan, Jr., "Effects of H on the Mech. Props. of Low-C and Austenitic Steels," Hydrogen in Metals, I. M. Bernstein and A. W. Thompson ed., ASM, (Metals Park, OH, 1974), pp. 53-77.
4. I. M. Bernstein *et al.*, "Effect of Dissolved H on Mech. Behavior of Metals," Effect of Hydrogen on Behavior of Materials, A. W. Thompson and I. M. Bernstein ed., TMS/AIME, (New York, 1976), pp. 37-58.
5. H. K. Birnbaum, "H Related Failure Mechanisms in Metals," Environment-Sensitive Fracture of Engineering Materials, Z. A. Foroulis ed., TMS/AIME, (Warrendale PA, 1979), pp. 326-60.
6. C. Zapffe and C. Sims, "H Embr. Internal Stress and Defects in Steel," *Trans AlME,* Vol. 145, (1941), pp. 225-61.
7. P. G. Bastien, "Cracking of Steel in the Presence of H and H2S," Physical Metallurgy of Stress Corrosion Fracture, T. N. Rhodin ed., Interscience Publ., (New York, 1959), pp. 311.
8. A. S. Tetelman and W. D. Robertson, "Direct Observation and Analysis of Crack Propagation in Fe-3% Si Single Crystals," *Acta Metall.,* Vol. 11, No. 5 (1963), pp. 415.
9. J. K. Tien *et al.*, "H Transport by Dislocations," *Metall. Trans.,* Vol. 7A, No. 6 (1976), pp. 821.
10. J. K. Tien, "Diffusion and the Dislocation Sweeping Mechanism for H Transport," Effect of Hydrogen on Behavior of Materials, A. W. Thompson and I. M. Bernstein ed., TMS/AIME, (New York, 1976), pp. 309-26.

11. D. G. Westlake, "A Generalized Model for H Embr.," *Trans ASM,* Vol. 62, No. 4 (1969), pp. 1000-06.
12. A. H. Windle and G. C. Smith, "The Effect of H on the Deform. and Fracture of Polycrystalline Ni," *Met. Sci.,* Vol. 4, (1970), pp. 136-44.
13. C. C. Chen and R. J. Arsenault, "Low Temp. Strengthening of Group VA Metal Single Crystals by H," Hydrogen in Metals, I. M. Bernstein and A. W. Thompson ed., ASM, (Metals Park, OH, 1974), pp. 393-406.
14. E. A. Steigerwald *et al.*, "The Role of Stress in H Induced Delayed Failure," *Trans AIME,* Vol. 218, No. 1960 (1960), pp. 832.
15. R. A. Oriani and P. H. Josephic, "Equilibrium and Kinetic Studies of the H-Assisted Cracking of Steel," *Acta Metall.,* Vol. 25, No. 9 (1977), pp. 979.
16. C. D. Beachem, "A New Model for H-Assisted Cracking," *Metall. Trans.,* Vol. 3, No. 2 (1972), pp. 437.
17. S. P. Lynch, "Mechanisms of H-Assisted Cracking," *Metals Forum,* Vol. 2, No. 3 (1979), pp. 189-200.
18. C. J. McMahon, Jr., "Effects of H on Plastic Flow and Fracture in Fe and Steel," Hydrogen Effects in Metals, A. W. Thompson and I. M. Bernstein ed., TMS/AIME, (Warrendale, PA 15086, USA, 1981), pp. 219-34.
19. J. Eastman *et al.*, "H Effects in Ni-Embr. or Enhanced Ductility?," Hydrogen Effects in Metals, A. W. Thompson and I. M. Bernstein ed., TMS/AIME, (Warrendale, PA, 1981), pp. 397-409.
20. H. K. Birnbaum and P. Sofronis, "H-enhanced localized plasticity-a mechanism for H related fracture," *Mater. Sci. Engg.,* Vol. A176, (1994), pp. 191-202.
21. N. J. Petch and P. Stables, "Delayed Fracture of Metals Under Static Load," *Nature,* Vol. 169, No. 5 (1952), pp. 842.
22. N. J. Petch, "The Lowering of Fracture-Stress Due to Surface Adsorption," *Phil. Mag.,* Vol. I, No. 4 (1956), pp. 331.
23. S. P. Lynch, "A Comparative Study of Stress-Corrosion Cracking, Hydrogen-Assisted Cracking and Liquid-Metal Embr.," Hydrogen Effects in Metals, A. W. Thompson and I. M. Bernstein ed., TMS/AIME, (Warrendale, PA, 1981), pp. 863-71.
24. D. J. Pitchure and R. E. Ricker, "The Recovery of Elastic Props. in Deformed TRIP 700," *J. Mater. Eng. Perf.,* Vol. 16, No. 3 (2007), pp. 349-53.
25. J. Crank, The Mathematics of Diffusion, Clarendon Press, (Oxford, 1975).
26. J. Volkl and G. Alefeld, "H Diffusion in Metals," Diffusion in Solids, A. S. Nowick and J. J. Burton ed., Academic Press, (New York, 1975), pp. 231-302.
27. C. Zener, Elasticity and Anelasticity, Univ of Chicago, (Chicago, IL, 1965).
28. A. S. Nowick and B. S. Berry, Anelastic Relaxation in Crystalline Solids, Academic Press, (New York, 1972).
29. M. S. Blanter *et al.*, Internal Friction in Metallic Materials - A Handbook, Springer, (New York, 2007).

Effects of Hydrogen on Materials
Proceedings of the 2008 International Hydrogen Conference
Brian Somerday, Petros Sofronis, Russell Jones, editors, p 227-234
Copyright © 2009 ASM International®
All rights reserved.
www.asminternational.org

IMPROVING THE FATIGUE PROPERTIES OF METASTABLE BETA TITANIUM ALLOYS BY THERMOHYDROGEN PROCESSING

Peter Schmidt, Hans-Jürgen Christ
Institut für Werkstofftechnik, Universität Siegen, 57068 Siegen, Germany

Keywords: Ti 10-2-3®, Beta-C™, thermohydrogen processing (THP), fatigue limit

Abstract

The use of hydrogen as a temporary alloying element is a promising approach to improve the fatigue properties of metastable beta titanium alloys due to modifying effects of hydrogen on prevailing microstructures. The idea is to take advantage of the beta-stabilizing hydrogen effect on the morphology and composition of the body-centered cubic beta phase and the hexagonal alpha phase. In this study Ti 10V-2Fe-3Al (Ti 10-2-3) and Ti 3Al-8V-6Cr-4Mo-4Zr (Beta-C) served as beta titanium alloys for research into THP. Both alloys are metastable but differ with respect to beta stability. In the case of Ti 10-2-3 solution treatment is usually carried out sub-transus, whereas Beta-C is solutionized in the single-phase beta regime. First, a quantification of hydrogen diffusion and solubility was performed, followed by systematic hydrogenation in hydrogen containing gas atmospheres. The analysis of modified microstructures by microscopic methods revealed the dependence of the beta transition temperature on hydrogen content. An increase in the ultimate tensile strength of 200MPa was achieved compared to the ordinary heat treated alloy. The results clearly demonstrated that keys to success for the simultaneous improvement of both tensile strength and fatigue limit is a feasible technique, which allows the use of the beneficial effects of hydrogen during the heat treatment homogeneously throughout the cross sections of the samples and a sophisticated method for fast and complete dehydrogenation.

Introduction

Beta titanium alloys are the most versatile of all commercial titanium alloys because they offer a broad range of strength to ductility ratios. Applying the correct heat treatment beta titanium alloys can be hardened to high strength levels and they allow tailoring the combination of strength and fracture thoughness properties desired. As a consequence, beta titanium alloys are used primarily in applications requiring a high specific strength such as structural components in modern aircraft. Additionally, beta titanium alloys are found in products used in petroleum downhole piping systems due to a reasonable combination of mechanical and corrosive properties. Recent developments of so-called “low-cost beta” titanium alloys are aiming at first mass production applications in the automotive and the surgical device industry [1].

Hydrogen interaction with metals and alloys often leads to severe degradation of fracture-related mechanical properties, but in the case of titanium hydrogen can basically be removed easily by vacuum degassing [2]. According to the Ti–H binary phase diagram, hydrogen solubility of the body-centered cubic (bcc) beta phase is much higher compared to the hexagonal alpha phase and hydrogen diffusion takes place much faster in the high temperature phase at a corresponding temperature [3,4]. Previous studies [5] have shown, that the value of the hydrogen diffusion coefficient increases strongly with increasing beta stability of the titanium alloy and may also be influenced sensitively by special microstructure features such as dense layers of precipitated hexagonal alpha phase along the beta grain boundaries.

In summary, these facts make beta titanium alloys perfect candidates for the strategic use of hydrogen as a temporary alloying element because the bcc beta phase can be retained completely either as a metastable phase or as the thermodynamic equilibrium phase after quenching from solution annealing temperature down to room temperature. Therefore, beta titanium alloys are assumed to be almost insensitive to effects such as hydride formation when hydrogen is used as a temporary alloying element. The literature postulates this often termed “ThermoHydrogen Process” (THP) as an auspicious approach to control microstructures due to utilization of the beta-stabilizing hydrogen effect on present phases, phase compositions and kinetics of phase reactions, thereby improving final mechanical properties of even complete parts made of titanium [2]. However, in the case of beta titanium alloys, systematic research into THP is still rare. This might be attributed to the lack of thermodynamic and kinetic data available for the quantitative description of the required hydrogenation – dehydrogenation processes and to the advanced microstructures of beta titanium alloys, which are known to require a very careful processing.

The key to success for the improvement of fatigue and fracture related properties of beta titanium alloys will be a feasible technique allowing the use of the beneficial effects of hydrogen during the heat treatment homogeneously throughout the cross sections of the samples and a sophisticated method for fast and complete dehydrogenation at low temperature.

The present study introduces the first attempts to develop concepts of a THP for the two metastable beta titanium alloys Ti 10V-2Fe-3Al and Ti 3Al-8V-6Cr-4Mo-4Zr aiming at an improvement of cyclic strength with emphasis on the fatigue limit and fatigue crack growth threshold. As shown in Fig. 1, the basic idea of THP is to decrease the (alpha + beta) / beta transition temperature (beta transus) due to hydrogenation in the 1st step. This enables solution treating in the 2nd step at a much lower temperature in the beta regime without taking the risk of distinct grain coarsening. The initial single-phase beta condition provides an enhanced driving force for the precipitation of strengthening secondary alpha particles during final aging and simultaneous dehydrogenation.

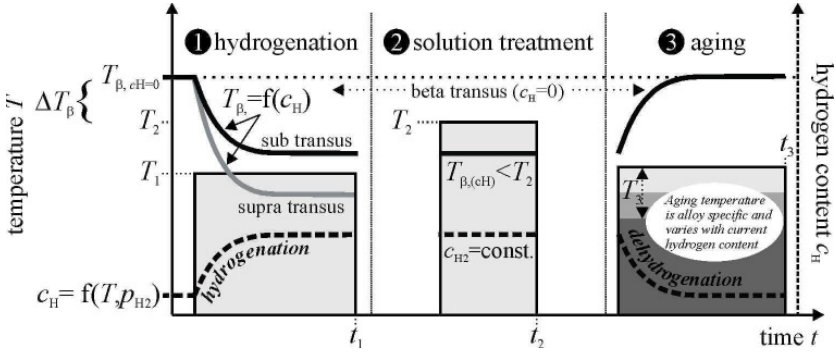


Figure 1: ThermoHydrogen Processing (THP) of beta titanium alloys

Experimental

Two metastable beta titanium alloys were choosen for this study differing considerably in terms of beta stability. Ti 10V-2Fe-3Al (Ti 10-2-3) is marginal in terms of beta stability but Ti 3Al-8V-6Cr-4Mo-4Zr (Beta-C) is highly beta-stabilized. Table 1 provides information on alloy composition and beta stability of both materials, which is expressed in terms of the molybdenum equivalent (ME) and the beta transus T_β. Both alloys were heat treated according to the requirements to achieve high strength [6]. This condition is referred to as the reference condition.

Table 1: Compositions (wt.%) and beta stability of beta titanium alloys studied

	Al	V	Cr	Mo	Zr	Fe	Ti	ME	T_β [°C]
Ti 10-2-3	3.0	9.85				1.79	bal.	9.5	792
Beta-C	3.11	8.11	5.77	3.89	4.05		bal.	16	730

A successful application of THP requires reliable data on the kinetics and thermodynamics of hydrogen uptake and release. In order to determine the hydrogen diffusion coefficient D_H the following procedure was applied. Electrodischarge machined titanium rods with a diameter of 3mm and a length of 100mm were insulated along the half of their length. A hydrogen concentration step profile was established in each sample by cathodic hydrogenation according to the charging conditions inserted in Fig. 2a. The concentration step profile obtained served as an initial condition for the subsequent diffusion annealing carried out at temperatures between 200°C–800°C. The resulting hydrogen concentration profiles were determined after the serial sectioning of each rod into small discs with a thickness of 3mm to analyze the hydrogen concentration of each disc in a commercial Leco® system. D_H-values were calculated by applying the finite-difference and the Matano techniques [5,7]. By means of volumetric measurements the rate of hydrogen uptake from a sorrounding gas atmosphere containing high purity hydrogen and the final hydrogen concentration (equilibrium solubility $c_{H,eq}$) were determined for hydrogen partial pressures p_{H2} up to 100mbar and temperatures T between 500°C and 800°C.

Optical (OM) and electron microscopy (SEM, TEM) were used in order to determine T_β as a function of hydrogen content. For this purpose, samples were hydrogenated to identical hydrogen concentrations. Subsequent heat treatment at temperatures near the expected beta transus defined the accurate value of T_β as the maximum temperature where the hexagonal alpha phase was detected. TEM analyses were found to be most convenient for the detection of very small amounts of alpha phase.

Besides morphology and volume fraction of the alpha precipitates the beta grain size is the 2nd important factor determining the fatigue endurance of beta titanium alloys [1]. Therefore, samples were hydrogenated to predefined hydrogen concentrations and subsequently annealed in the beta phase regime. Kinetics of beta grain growth was monitored using Electron BackScattered Diffraction (EBSD).

Microstructural changes due to THP were evaluated by performing tensile tests and HCF tests under stress control at a frequency of 12Hz in a MTS servo-hydraulic closed-loop system. The fatigue limit $\sigma_{50\%}$ corresponding to a maximum number of loading cycles of $N = 2 \cdot 10^6$ and the standard deviation s were determined according to the modified staircase method [8]. Single edge notch bend (SENB) samples were used to measure long crack growth behavior under 4-point bending in a resonance system. According to the load shedding method [9] the fatigue crack growth threshold ΔK_{th} was determined at a stress ratio R of 0.1.

Results and Discussion

The Matano evaluation of the hydrogen concentration profiles resulting from diffusion annealing of electrochemically hydrogenated samples (see Fig. 2a) proved that the D_H-values can be treated as being dependent on temperature only at the applied hydrogen concentrations up to 2000 mass-ppm. The results of the finite-difference calculations and the Matano evaluations agree reasonably and show Arrhenius-type behavior at the temperatures considered (see Fig. 2b), so that an effective hydrogen diffusion coefficient was quantified in terms of activation energies Q and pre-exponentials D_0 according to Eqs. 1 and 2. In agreement with previous results obtained for Ti–Mo and Ti–V binary alloys [5] the D_H-values increase with increasing beta stability of the respective titanium alloy at the corresponding temperature. The results indicate that hydrogen diffusion is primarily determined by the beta phase if a continuous bcc beta phase diffusion path is established in the particular alloy. Microstructure features such as continuous dense layers of fine precipitated alpha phase along the beta grain boundaries were shown to impede hydrogen diffusion to a considerable extent [5].

$$D_{\mathrm{H,Ti\,10-2-3}} = 3.1 \cdot 10^{-8} \cdot \mathrm{e}^{-27.6\mathrm{kJ/mol}\cdot(RT)^{-1}} \quad (1)$$

$$D_{\mathrm{H,Beta-C}} = 10^{-7} \cdot \mathrm{e}^{-21.0\mathrm{kJ/mol}\cdot(RT)^{-1}} \quad (2)$$

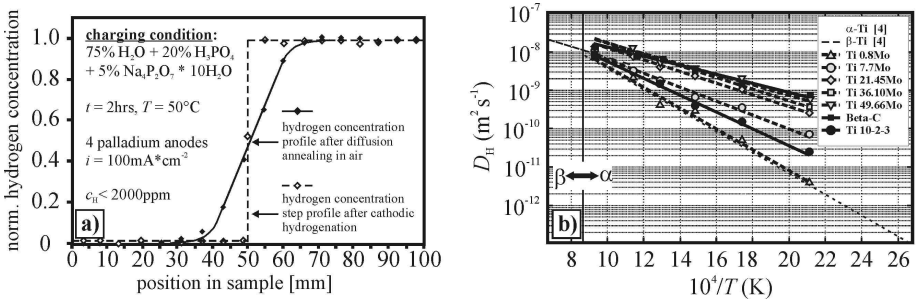


Figure 2: a) Normalized hydrogen concentration profiles after cathodic charging and after subsequent aging of titanium rod samples, b) Arrhenius plots of hydrogen diffusion coefficients D_H in Ti 10-2-3 and Beta-C, results were supplemented by data obtained on Ti–Mo binary alloys [5]

Figure 3a represents typical volumetric test results showing fast hydrogen pickup of both alloys at 800°C and two different hydrogen partial pressures. The curves approach asymptotically a constant value showing the amount of dissolved hydrogen being in equilibrium with the corresponding gas phase. These equilibrium concentrations are summarized in Fig. 3b for Ti 10-2-3. The hydrogen solubility increases with decreasing temperature. Hydride formation was not indicated at hydrogen partial pressures up to 100mbar and Sievert's law is fulfilled only for low p_{H2}-values. The hydrogen solubility increases with increasing hydrogen partial pressure and decreasing beta stability of the alloy.

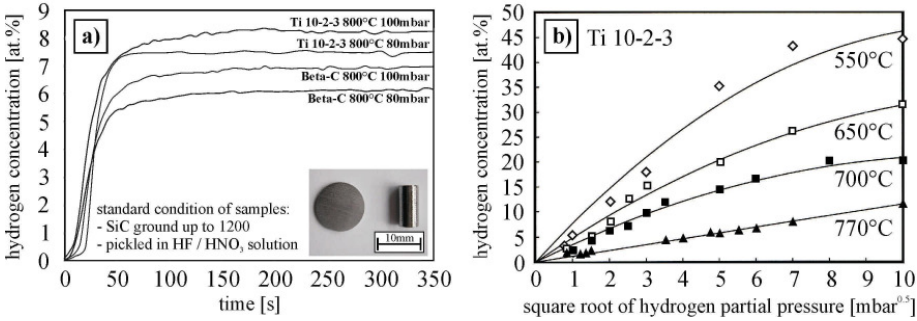


Figure 3: a) Kinetics of hydrogen uptake from pure hydrogen gas atmosphere in Beta-C and Ti 10-2-3, b) hydrogen equilibrium solubility in Ti 10-2-3

Data on hydrogen solubility and diffusion were used to determine the stabilizing effect of hydrogen on the bcc beta phase by means of microstructural studies. Figure 4a shows some results obtained on Ti 10-2-3. Each datapoint results from TEM studies of a single sample. The symbols document, whether alpha phase was detected or not and the results were complemented by literature data [1,6]. Results in Fig. 4b

show clearly reduced beta grain growth during solution annealing at 660°C in the hydrogenated condition as compared to 830°C for the reference condition.

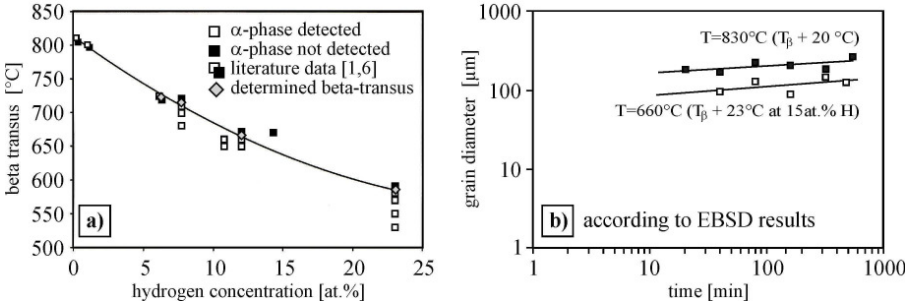


Figure 4: Beta-stabilizing hydrogen effect in the near-beta titanium alloy Ti 10-2-3

A short THP (sTHP) consisting of two heat treatment steps was applied to Ti 10-2-3 as an initial attempt to use hydrogen as a temporary alloying element. As shown in Fig. 5 the sTHP was complemented by two further heat treatment steps. This 4-step strategy differs from the THP shown in Fig. 1 with respect to dehydrogenation, which was shown to be not feasible at the aging temperature because of a strong inhibiting effect of dense TiO_2 scales on hydrogen permeability. Therefore, dehydrogenation was combined with solution annealing at 660°C, but unfortunately this led to the formation of a continuous alpha phase along the beta grain boundaries deteriorating the fatigue properties of Ti 10-2-3. Hydrogenation was done at 10°C below the final beta transus in the *1st* step. The accompanying TEM micrograph shows some globular primary alpha phase retaining, while secondary alpha precipitates were dissolved completely. A short solution annealing about 20°C above the hydrogen-reduced beta transus in the *2nd* step and simultaneous dehydrogenation led back into the (alpha + beta) regime causing the formation of the grain boundary alpha phase. Therefore, the THP was complemented by a solution treatment at 770°C as a *3rd* step transforming the fringe-shaped alpha phase into a nearly spherical shape. A fine dispersive secondary alpha phase was established by final aging for 4hrs at 460°C in the *4th* step.

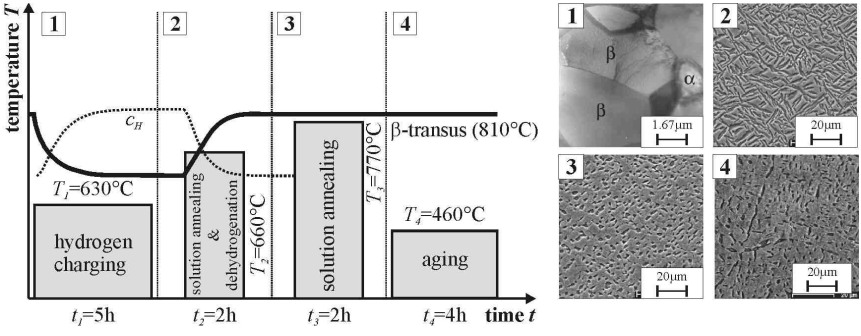


Figure 5: 4-step-sTHP concept for the near-beta titanium alloy Ti 10-2-3

The effects of hydrogen on microstructure and the mechanical properties of the alloy Ti 10-2-3 were evaluated by mechanical tests. Samples heat treated entirely along the THP route offered an ultimate tensile strength (UTS) being 200MPa higher compared to the reference condition due to an increased volume fraction of secondary alpha precipitates. As opposed to the UTS-increase the fatigue limit ($\sigma_{50\%}$ = 572MPa, s = 22.5MPa) was reduced by about 100MPa. Comparative fatigue crack growth tests did not show significant changes in the (da/dN vs. ΔK) behavior and ΔK_{th} remained almost unaffected at about 3.3MPam$^{0.5}$ at a stress ratio R = 0.1.

As shown in Fig. 6, this inconsistent behavior can be attributed to an inhomogeneous microstructure resulting from the application of the 4-step-THP. Figure 6a shows equiaxed alpha grains surrounded by homogeneously distributed fine secondary alpha precipitates. This morphology is considered to be ideal concerning the fatigue strength of Ti 10-2-3. The microstructure in Fig. 6b contains disadvantageous alpha lamellae. These microstructure differences are probably the result of hydrogen concentration gradients existing during dehydrogenation. The locally different beta stabilities result in different corresponding phase transformation processes.

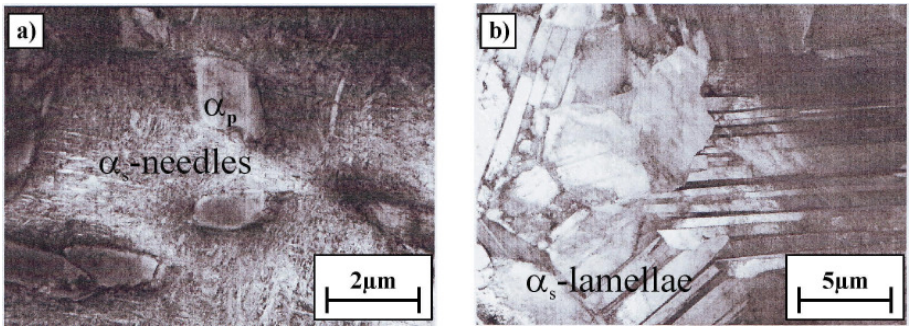


Figure 6: Kinetics of dehydrogenation determines the microstructure of Ti 10-2-3

Despite the fact that a first attempt of applying a THP to improve fatigue properties of Ti 10-2-3 was not successful, the results showed that the use of hydrogen as a temporary alloying element is a promising approach in order to improve the mechanical properties of beta titanium alloys, since optimization of microstructures by THP was found to be basically possible. Key to success for future concepts is a feasible technique utilizing the beta stabilizing hydrogen effect homogeneously throughout the cross sections and a sophisticated method for fast and complete dehydrogenation at low temperatures.

Conclusions

The main results of this study on the applicability of THP on beta titanium alloys Ti 10-2-3 and Beta-C in order to improve fatigue properties are summarized as follows:

1) The hydrogen solubility was determined quantitatively by means of volumetric and gravimetric experiments. Higher beta stability of the alloy and an increase in temperature was found to reduce the hydrogen solubility.
2) No hydrides were formed in the alloys under the conditions applied.
3) The hydrogen diffusion coefficient D_H was measured as a function of temperature. A Matano analysis revealed that D_H is independent of hydrogen concentration. The D_H-values increase with increasing beta stability and obey an Arrhenius-type temperature dependence.
4) The beta transus temperatures of the two alloys studied were determined experimentally and were found to depend strongly on the hydrogen concentration.
5) On the basis of the thermodynamic and kinetic data obtained, hydrogenation and dehydrogenation heat treatment steps were developed for THP.
6) A 4-step THP was applied to Ti 10-2-3 as an initial strategy leading to an increase of UTS by about 200MPa up to 1380MPa while sufficient ductility remained.
7) Microstructure inhomogenities in form of coarse alpha lamellae resulting from dehydrogenation in the 2nd step of this THP reduced the fatigue limit by 100MPa.

Acknowledgements

The authors wish to thank the Deutsche Forschungsgemeinschaft (DFG) for financial support of this research work under Grant No. Ch92/21-1 and -2.

References

1. Lütjering G., Williams J.C., Titanium, Springer (Berlin, 2003).
2. Senkov O.N., Froes F.H., Progress in hydrogen treatment of materials, Kassiopeya Ltd (Donetsk, 2001), pp. 255-279.
3. Massalski T.B., Murray J.L., Bennet L.H., Baker H., Binary Alloy Phase Diagrams, ASM International (Materials Park Ohio, 1986), p. 1283.
4. Wasilewski R.J., Kehl G.L., "Diffusion of Hydrogen in Titanium", *Metallurgica*, Vol. 50, (1954), pp. 225-230.
5. Schmidt P., Christ H.-J., "Effect of Beta Stability on Diffusion of Hydrogen in Beta Titanium Alloys", *Proc. 11th World Titanium Conf. (Ti-2007)*, Kyoto, Japan, June. 2007, pp. 765-768.
6. Boyer R., Welsch G., Collings E.W., Materials Properties Handbook: Titanium Alloys, ASM International (Materials Park Ohio, 1994).
7. Matano C., "On the Relation between the Diffusion-Coefficients and Concentrations of Solid Metals", *Jap. J. Phys.*, Vol. 8, (1933), pp. 109-113.
8. Deubelbeiss E., "Dauerfestigkeitsversuche mit einem modifizierten Treppenstufenverfahren", *Materialprüfung*, Vol. 16, (1974), pp. 240-244.
9. Saxena A., Hudak S.J., Donald J.K., Schmidt D.W., "Computer Controlled Decreasing Stress Intensity Technique for Low Rate Fatigue Crack Growth Testing", *Journal of Testing and Evolution*, Vol. 6, (1978), pp. 167-174.

Effects of Hydrogen on Materials
Proceedings of the 2008 International Hydrogen Conference
Brian Somerday, Petros Sofronis, Russell Jones, editors, p 235-242
Copyright © 2009 ASM International®
All rights reserved.
www.asminternational.org

STUDY OF HYDROGEN TREATMENT FOR IMPROVING STRENGTH AND PLASTICITY OF TI-6AL-4V ALLOY

Q.Wang，D.L.Sun

Harbin Institute of Technology, Harbin，Heilongjiang , China

ABSTRACT: Two novel hydrogen treatment processes of improving strength and plasticity of Ti-6Al-4V alloy have been developed. The procedures are that specimens were hydrogenised at 600℃ for one hour and at 0.1MPa hydrogen partial pressure, compressed 60% at 700℃, and then treated separately by two procedures which are dehydrogenating at 750℃ for 8 hours directly and/or dehydrogenating at 750℃ for 8 hours after solution at 850℃ for 0.5 hours, quenching into water and aging at 590℃ for 8 hours. The results showed that compared with original specimens, the yield strength and the elongation of specimens, treated by dehydrogenating directly, were increased by 19.3% and 41.8% separately, and treated by solution, quenching and dehydrogenizing, were increased by 8.4% and 100% separately. The microstructures of each treatment step were examined by optical microscope and transmission electron microscope, and the fracture surfaces were observed by scanning electron microscope. The evolution of microstructures during hydrogen treatment processes was studied and the mechanism of improvement of properties for Ti-6Al-4V alloy was discussed.

KEYWORDS: Ti-6Al-4V alloy, microstructures, hydrogenising treatment, tensile property.

1. INTRODUCTION

Titanium alloys have wide application prospect in many industrial fields due to their high strength-to-density ratio, good elevated temperature properties and good corrosion resistance [1]. One of the most important mechanical properties of titanium alloys is high yield strength/ultimate strength radio, which is normally between 0.7-0.9 and more closer to the upper limit, as well as low Young's modulus which is only half as high as that of steel. Therefore, titanium alloys, because of their high resistance to deformation and high spring back, belong to

difficult forming materials. Abundant studies have been done to overcome this problem and hydrogen treatment of titanium alloys, unitizing temporary element hydrogen to improve mechanical properties, has been developed [2~4]. As is known that it can cause hydrogen embrittlement and delayed hydride cracking [5,6], hydrogen's reversibility in titanium and titanium alloys has been noticed and hydrogen is used as a temporary element to refine microstructure and improve the properties of the alloys. In this paper, based on the strong diffusivity and hydrogen-induced thermal plasticity of hydrogen in titanium, hydrogen treatment process has been used to refine the microstructure of Ti-6Al-4V alloy, enhance strength and plasticity, decrease hot deformation resistance, improve hot workability of alloys and, thus, extend the application range of Ti-6Al-4V alloy.

2. EXPERIMENTAL

Ti-6Al-4V alloy forged bar was used in the test. Hydrogenated treatment was performed in a tube-type furnace. Hydrogenating temperature was 600℃, 700℃, and 800℃, soaking time was from 1 hour to 7 hours respectively and the flow velocity of hydrogen gas in the tube was kept stable all long. The specimens had been cooled in the hydrogen atmosphere until they reached 300℃ and then taken out from the tube and cooled to room temperature. The weight of specimens before and after hydrogenating was measured by Satrorius BP211D, electron balance, with a sensitivity of 10^{-5} g, and the hydrogen content was calculated for the hydrogenated specimens. The calculated error of hydrogen content was less than 2.5×10^{-3}wt%. Different hydrogen content could be attained through changing hydrogenating temperature, time, and flow velocity of hydrogen gas in the tube or changing specific surface area of specimens. Metallographic samples were corroded by mixed solution, including HF, HNO_3 and H_2O, whose proportion was 1:1:6. Metallographic microstructure was observed through Zeiss microscope. Tensile test was conducted on Instron1186 electric tension machine at room temperature.

3. RESULTS AND DISCUSSION

3.1 Evolution of microstructure after hydrogen treatment

The hydrogen contents reached 0.4wt% after hydrogenating for 1 h at 600℃. Subsequently, specimens were compressed 60% at 700℃, with deformation

rate of $8.3\times10^{-3}s^{-1}$. Compressed specimens were carried out solid solution treatment at 850℃ for 0.5 h, water quenched, heated to 590℃ with the heat preservation time of 8 h and then air cooled. At last they were dehydrogenated in vacuum at 750℃ for 8 h and furnace cooled to room temperature, during which vacuum degree is controlled at 10^{-2}Pa.

Fig.1 shows microstructure and morphology before and after hydrogenation. The original structure was similar to (α+β) basket microstructure. Transmission electron microscope images showed band shaped α phase. The microstructure of alloys with 0.4wt% hydrogen content is refined and the size of α lathe decreased. The equiaxed microstructure of transformed β phase with fine α phase lath was founded and a small amount of primary α grain distributed in the grains of transformed β phase. The microstructure after hydrogenation is consist of (α_H+β_H).

Fig.2 shows microstructure of the specimen with 0.4wt% hydrogen, which was compressed with the rate of $8.3\times10^{-3}s^{-1}$ at 700℃. When the specimen was deforming at 700℃, δ hydride dissolved back and part of α_H transformed to β_H. Because hydrogen made the phase transition temperature of β lower, the amount of β_H in hydrogenated specimens was more than that β in specimens which had not been hydrogenated, resulting in higher thermal plasticity, lower deformation resistance and distortion of basket microstructure after thermal deformation. When cooled to room temperature, （α_H +β_H）changed to α_H and （α_H +β_H）.

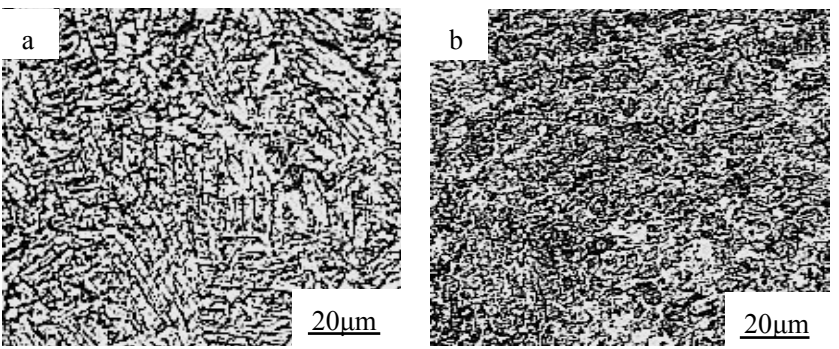


Fig.1 Microstructure of Ti-6Al-4V alloy before and after hydrogenating at 600℃ for 1 hour

a)original specimen；b) specimen with 0.4wt% hydrogen；

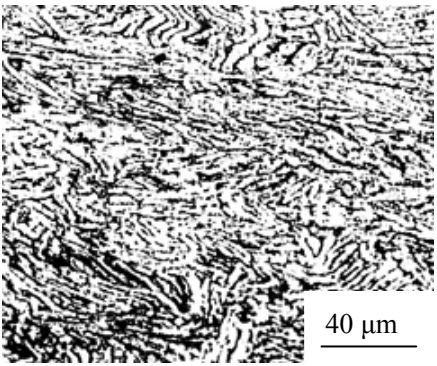


Fig.2 Microstructure of the specimen with 0.4wt% hydrogen after deformation at 700℃

Fig.3 shows microstructure of Ti-6Al-4V alloy which undergone thermal deformation and dehydrogenation. Hydrogen escaped during vacuum heating process and hydrogen content fell below the safe concentration; meanwhile, microstructure of thermal deformation occurred recrystallization, leading to the microstructure refinement and a change from lath shape structure to nearly equiaxed one.

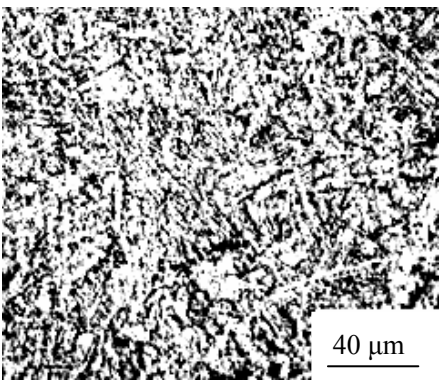


Fig.3 Microstructure of specimen hydrogenated at 600℃ for 1 hour, deformed at 700℃/ $8.3\times10^{-3}s^{-1}$ and vacuum dehydrogenated at 700℃ for 8 hours

The microstructure of Ti-6Al-4V alloy by compression at 700℃ and solid solution and eutectoid treatment was showed in Fig.4. Since hydrogen lowed the phase transition temperature of β, during solid solution treatment at 850℃,

α_H+（α_H+β_H）all changed to β_H and formed needle martensite, namely $\beta_H \rightarrow \alpha_H'$ (Fig.3(a)).Then apply eutectoid treatment to alloys at 590℃ and martensite decomposed during the soaking period. A short time eutectoid treatment resulted in incomplete martensite decomposition, leaving some needle martensite (Fig.4 (a)) and if prolonged the time of eutectoid treatment, the amount of martensite kept decreasing till it disappeared (Fig.4 (b)), that is $\alpha_H' \rightarrow \alpha_H+\beta_H+\delta$. During the subsequent period of furnace cooling, $\beta_H \rightarrow \alpha+\delta$、$\alpha_H \rightarrow \alpha+\delta$. Changing from β-Ti(H) to δ hydride caused volume expansion of 18.3% and high density dislocation stress field was formed around δ hydride.

Vacuum dehydrogenation was applied to the specimens after solid solution and eutectoid treatment. δ hydride first dissolved back to the matrix, hydrogen atoms synthesized hydrogen molecules and escaped and α+β was formed after

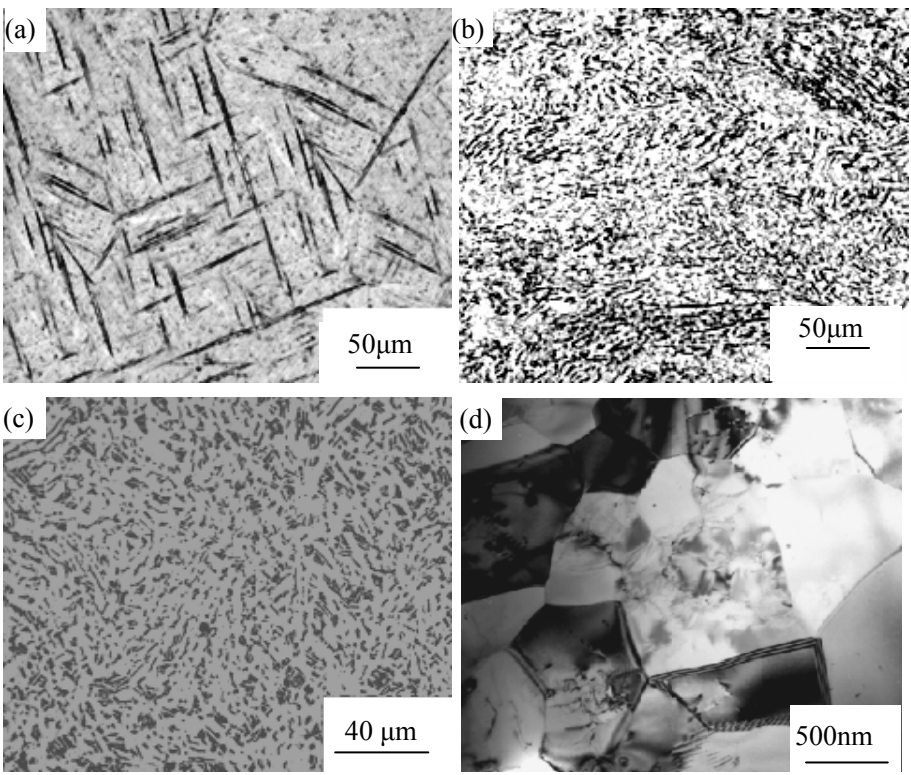


Figure 4 Microstructure of Ti-6Al-4V alloy after solid solution and aging at 590℃

(a) solid solution; (b) solid solution + aging;

(c)(d) solid solution + aging + dehydrogenation

furnace cooling (Fig.4 (c)). The equiaxed subgrains were observed by a transmission electron microscope (Fig.4 (d)).

3.2 Mechanical properties of alloy by hydrogenation

Tensile properties of Ti-6Al-4V alloy by hydrogenation had been shown in Table 1. Through hydrogenation-thermal deformation-dehydrogenation, the strength and plasticity have been improved. The ultimate strength and yield strength were increased by 22% and 19% respectively and elongation by 42%; Solid solution and eutectoid treatment before dehydrogenation could make further improvement on plasticity, the ultimate strength and yield strength were only increased by 10.5% and 8.5% respectively but the elongation by 100%. Dehydrogenation of alloys after solid solution and eutectoid treatment could obtain equiaxed α+β microstructure whose strength was slightly lower than former process; however, plasticity was greatly improved.

The fracture morphology of the tensile specimens was observed by scanning electron microscope. Fig.5 showed images of tensile fracture surfaces of alloy. The morphology of fracture surface in crack nucleating zone of specimens which were not hydrogenated (Fig.5(a)) is typical dimple like. The fracture

Table 1 Mechanical properties of Ti-6Al-4V alloy

Procedure Number	Technological Procedure	Tensile Strength σ_b/ MPa	Yield Strength $\sigma_{0.2}$/ MPa	Elongation δ / %
1#	Original Specimen	936	915	11.0
2#	600℃/1h hydrogenation+700℃ deformation+750℃/8h dehydrogenation	1141	1092	15.6
3#	600℃/1h hydrogenation +700℃deformation +850℃/0.5h water quenched+590℃/8h aging+750℃/8h dehydrogenation	1034	992	22.0

surface morphology of hydrogenated specimens was also dimple like, and the specimens had obvious necking phenomenon. There were a lot of dimples, whose dimension increased, in the surface of tensile instantaneous fracture (Fig.5(b) and (c)). After hydrogenation, the microstructure was refined and the resistance of crack nucleation and propagation increased, resulting in a great improvement of strength and plasticity.

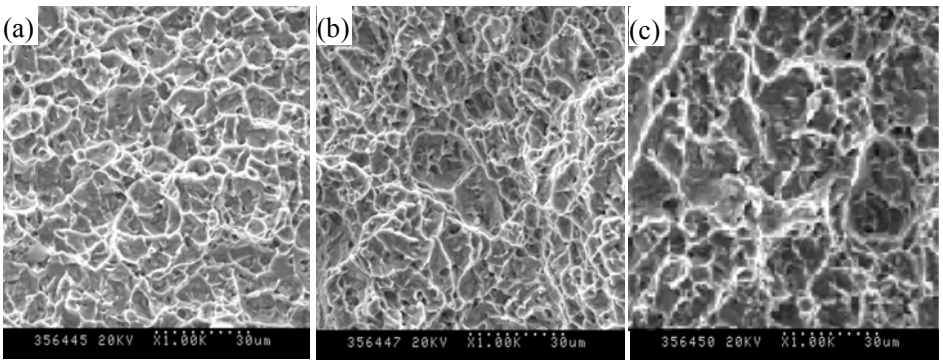


Fig.5 Fracture morphologies of Ti-6Al-4V alloy

(a)original； (b) thermal deformation + dehydrogenation；

(c) thermal deformation + aging + dehydrogenation

surface morphology of hydrogenated specimens was also dimple like, and the specimens had obvious necking phenomenon. There were a lot of dimples, whose dimension increased, in the surface of tensile instantaneous fracture (Fig.5(b) and (c)). After hydrogenation, the microstructure was refined and the resistance of crack nucleation and propagation increased, resulting in a great improvement of strength and plasticity.

4. CONCLUSIONS

(1) Hydrogen treatment processes improved greatly the strength and plasticity of Ti-6Al-4V alloy. Hydrogenation-deformation-dehydrogenation could increase the yield strength and elongation by 19% and 42% respectively; hydrogenation -deformation-solid solution and eutectoid treatment-dehydrogenation could increase the yield strength and elongation by 8.5% and 100% respectively.

(2) Hydrogen treatment processes changed original basket microstructure to nearly equiaxed one and caused grain refinement. Whereas part of the deformation microstructure was persevered in alloys by direct dehydrogenation

after thermal deformation and the increase of strength was greater than that of plasticity deformation, the deformation microstructure of specimens, applied solid solution and eutectoid treatment before dehydrogenation, totally disappeared and the increase of strength is smaller, while the increase of plasticity was greater.

(3) Hydrogenation improved thermal plasticity of alloy and is beneficial to their thermal forming; the subsequent dehydrogenation or solid solution and eutectoid treatment lowed the concentration of hydrogen to a safe level, avoiding hydrogen embrittlement and improving plasticity of alloy. Hydrogen treatment is an effectual technical method to improve hot workability and service performance.

ACKNOWLEDGEMENT

This work has been supported by the National Science Foundation of China (Grant Number 50671028).

REFERENCES

1 Y.Liu, Z.Qu, B.X.Wang, “Research Development and Application of Ti6A14V Alloy,” Materials Science and Engineering. Vol. 28, No. 3 (2005), pp. 47-50

2 O.N.Senkov, F.H.Froes, “Thermohydrogen Processing of Titanium Alloys, ” International Journal of Hydrogen Energy, Vol. 24, Issue 6 (1999), pp. 565-567

3 D.L. Sun, Q. Wang, X. Han, et al, “Influence of hydrogen on tensile property of Ti-6Al-4V, ” Key Engineering Materials, Vol. 297-300, (2005)， pp. 1133-1138

4 Q. Wang, X. Han, et al, “Hydrogenation and its effect on behavior of hot deformation for Ti-6Al-4V alloy,” Materials Forum, Vol. 29, (2005), pp 318-322

5 J.L. Cao，B.L. Shen，S.J.Gao，Y.R.Jiang，X.He, “Hydrogen induced delayed fracture behavior of Ti-Al-Zr alloy，The Chinese Journal of Nonferrous Metals，Vol. 12, Special 1, (2002), pp. 74-77

6 C.L. Briant, Z.F. Wang, N.Chollocoop, “Hydrogen Embrittlement of Commercial Purity Titanium,” Corrosion Science, Vol. 44, Issue 8, (2002), pp. 1875-1888

Effects of Hydrogen on Materials
Proceedings of the 2008 International Hydrogen Conference
Brian Somerday, Petros Sofronis, Russell Jones, editors, p 243-250
Copyright © 2009 ASM International®
All rights reserved.
www.asminternational.org

STRESS-CORROSION CRACKING OF Al-Zn-Mg-Cu ALLOYS EFFECTS OF COMPOSITION AND HEAT-TREATMENT

S.P. Lynch, S.P. Knight, N. Birbilis and B.C. Muddle
ARC Centre of Excellence for Design in Light Metals,
Monash University, Melbourne, Australia

INTRODUCTION

Intergranular stress-corrosion cracking (SCC) has been a long standing problem in precipitation-hardened Al-Zn-Mg-Cu alloys, although SCC-resistant alloy compositions and heat-treatments have now been developed. Initially, overageing (OA) was used to give good resistance to SCC at the expense of strength. More recently, retrogression and re-ageing (RRA) treatments have been used, which provide high resistance to SCC with only a small loss in strength.

The increased SCC resistance of OA and RRA material has been variously attributed to: (i) increased grain-boundary precipitate (GBP) size, spacing, or volume fraction, (ii) changes in grain-boundary segregation of Zn, Mg, and Cu, (iii) changes in solute concentration profiles across grain boundaries, (iv) changes in precipitate-free zone (PFZ) widths, and (v) coarser, incoherent matrix precipitates that decrease slip planarity, so that stress concentrations at grain-boundaries are reduced. There is no consensus regarding which factors are important, partly because it is not possible to vary one microstructural parameter without affecting others, so that interpretation of results is difficult [1]. The mechanism of SCC in Al alloys is also controversial, although most workers consider that 'hydrogen-embrittlement' is involved [1].

The aim of the present work was to obtain a better understanding of the effects of microstructure, microchemistry, slip-mode, and alloy composition (especially Cu content) on SCC of 7xxx Al alloys [2]. Detailed comparisons have been made for low-Cu 7079 and 7022 alloys and the relatively high Cu 7075 alloy, in the form of thick plate tested in the short-transverse (S-L) crack-plane orientation. In the present paper, the focus is on SCC at high stress-intensity factors (K) for heat-treatment conditions where it transpired that there were orders of magnitude differences in crack growth rates for (i) different alloys, and (ii) different positions with respect to plate thickness. A reversal of the relative SCC susceptibilities of the alloys with high and low Cu levels in low relative humidity (RH) air compared with aqueous environments is also highlighted.

EXPERIMENTAL

SCC velocities were measured optically on the side surfaces of bolt-loaded, double-cantilever beam (DCB) specimens immersed in saturated NaCl solution under open-circuit conditions or exposed to moist air at 20°C. Specimens with a 25 mm height were cut from 7079, 7022, and 7075 plates (76 mm thick) at the mid-thickness (T/2) and near-surface (T/6) centerline positions. Alloy compositions are shown in Table 1. Specimens were tested in the as-received peak-aged (T651) condition, and after overageing the T651 condition for various times at 160°C. Some specimens were also re-solution-treated, quenched in cold water or cooled in air, and then aged.

Table 1: Alloy compositions (wt%)

	Zn	Mg	Cu	Cr	Mn	Fe	Si	Ti
7079 (T/6)	4.40	3.36	0.62	0.16	0.19	0.22	0.12	0.05
7079 (T/2)	4.18	3.08	0.56	0.17	0.19	0.19	0.10	0.07
7022	4.78	3.07	0.90	0.15	0.26	0.17	0.16	0.04
7075	5.35	2.29	1.37	0.20	0.02	0.26	0.06	0.03

RESULTS AND DISCUSSION

SCC Velocity Data

For tests in NaCl at high K levels, the crack velocity was not dependent on K, as observed in previous studies of SCC in Al alloys and many other materials [1-3]. Plots of the plateau velocity (V_{II}) for 7079, 7022, and 7075 alloys, for T/2 and T/6 positions, as a function of ageing time at 160°C showed that:

(i) The 7079 (T/6) peak-aged material had the highest V_{II} (~2×10^{-6} m/s), which did not change significantly with ageing time (up to 100 h),

(ii) The 7079 (T/2) peak-aged material had a ten times lower V_{II} than the 7079 (T/6) peak-aged material, with V_{II} decreasing with increasing overageing time (>5 h) such that it was about 100 times lower than the T/6 material after ageing for 16 h,

(iii) The 7022 and 7075 peak-aged materials (T/6 and T/2 positions) had the lowest V_{II}, which were about 100 times lower than the 7079 (T/6) peak-aged material, with V_{II} decreasing with increasing ageing time such that it was over 1000 times lower than the 7079 (T/6) material after ageing for 16 h (Fig. 1).

The V_{II} values for 7075-T651 and 7079-T651 (T/6) material and the effects of overageing observed in the present work are similar to those reported by Speidel [3]. However, the present V_{II} measurements for the 7022-T651 alloy were about 100 times lower than that observed previously [4]. After re-heat-treating DCB specimens, V_{II} for the rapidly quenched peak-aged 7079 (T/2) material was similar to that for the as-received peak-aged 7079 (T/6) material. Conversely, the slowly cooled peak-aged 7079 T/6 material behaved similarly to the as-received 7079 peak-aged T/2 material. These results strongly suggest that the as-received 7079 material from the

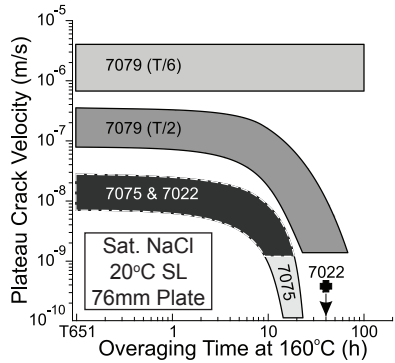


Figure 1: Plot of SCC plateau velocity vs ageing time for 7079 (near-surface T/6 and mid-thickness T/2 positions in 76 mm plate), 7022 and 7075 alloys in sat. NaCl.

near-surface position had experienced a more rapid quench than material from the mid-thickness position, as would be expected unless special techniques were used to minimise differences in quench rates through the 76 mm thick plates. For the 7022 (T/6) material, re-heat-treatment of DCB specimens, using a rapid quench, resulted in similar SCC behaviour as for the rapidly quenched 7079 material, viz. V_{II} ~$2x10^{-6}$ m/s, in both the peak-aged and overaged conditions. Thus, it was presumed (since heat-treatment details were proprietary) that the as-received 7022 plate had been subjected to a controlled quench, such that both T/6 and T/2 positions were slowly cooled from the solution-treatment temperature.

In moist air, SCC velocities for the peak-aged alloys decreased with decreasing K, unlike SCC in NaCl where there was a plateau velocity. Moreover, SCC (at high K) in moist air (43%RH) was about 100 times faster for the 7075 alloy than for the 7079 and 7022 alloys, which were essentially immune. A 'cross-over' in the SCC rankings of the 7079/7022 and 7075 alloys occurs around 75%relative humidity (Fig.2).

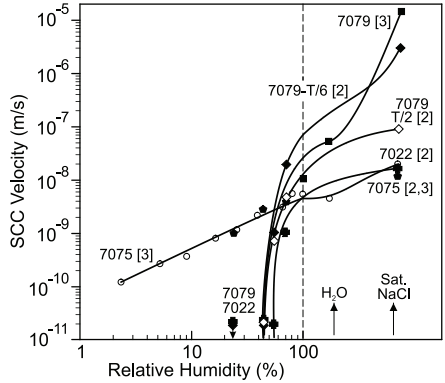


Figure 2: Plot of SCC velocity at high K for 7079 (T/2 and T/6), 7022 and 7075 alloys in moist air of varying RH, distilled water, and saturated NaCl solution.

Microstructural Comparisons of PA and OA 7079 (T/6 Position)

There were, not surprisingly, large differences in matrix and grain-boundary precipitation, PFZ width, and hardness for peak-aged (PA), overaged (OA), and very overaged (VOA) conditions for the 7079 (T/6) alloy (Table 2) (Fig.3). In addition, optical microscopy and atomic force microscopy showed that the slip mode became much less planar with increasing ageing time [2], as would be expected due to coarsening and loss of coherency of matrix precipitates. The fact that there was little difference in V_{II} in saturated NaCl for all these ageing conditions is, therefore, somewhat surprising in view of the suggestions that there are correlations between these features and SCC resistance. Speidel also found that V_{II} for 7079 was unaffected by overageing time. However, Speidel did not report on the variation of microstructure, and this result has not been widely discussed in the literature. The results do, in fact, suggest that the microstructural features listed in Table 2 (and slip mode) do not markedly affect SCC resistance, contrary to previous proposals [1].

Table 2: SCC plateau velocity (V_{II}), hardness, matrix precipitate size (M ppt), GBP length (GBP l) and area-fraction (GBP A_f), and PFZ width (PFZW) for 7079 (T/6 position). PA – T651; OA – T651 + 16h at 160°C; VOA – T651 + 100h at 160°C.

7079	V_{II} (m/s)	Vickers (VHN)	M ppt (nm)	GBP *l* (nm)	GBP A_f (%)	PFZW (nm)
PA (T/6)	2×10^{-6}	180	3-10	39±12	17±6	62±8
OA (T/6)	2×10^{-6}	149	10-15	68±17	31±4	72±10
VOA (T/6)	2×10^{-6}	134	15-50	69±30	36±4	94±12

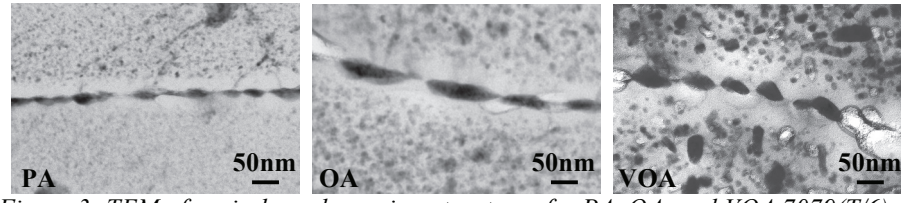


Figure 3: TEM of grain-boundary microstructures for PA, OA, and VOA 7079(T/6).

Microstructural Comparisons of Overaged 7079 (T/6 and T/2) and 7075

Comparisons of the microstructures of OA 7079 (T/6), 7079 (T/2) and 7075 alloys showed that there were no obvious differences that could account for such large differences in V_{II} values (Table 3) (Fig.4). For the 7079 alloy, there were only slight differences in bulk composition through the thickness of the plate (Table 1), and only small differences in grain size and shape through the thickness for all these alloys [2], so that these factors can be ruled out as causes of the SCC differences. There were marked differences in crystallographic texture through the thickness [2], but the re-heat-treatments (which do not affect texture) showed that texture differences are also not important. There was, however, an apparent correlation between V_{II} values

and the microchemistry of GBP, determined by analytical TEM, with the lowest Cu content in GBP resulting in the highest V_{II} (Table 3).

Table 3: SCC plateau velocity (V_{II}), Vickers hardness, matrix precipitate size (M ppt), GBP length (GBP l) and area-fraction (GBP A_f), PFZ width (PFZW), and GBP copper content for T651 alloys overaged at 160°C for 16 h.

Overaged Alloys	V_{II} (m/s)	VHN	M ppt (nm)	GBP *l* (nm)	GBP A_f (%)	PFZW (nm)	GBP Cu (at.%)
7079 (T/6)	2×10^{-6}	149	10-15	68±17	31±4	72±10	1±1
7079 (T/2)	8×10^{-9}	146	10-15	70±23	26±7	84±12	9±3
7075 (T/6)	2×10^{-10}	162	10-15	62±22	16±3	60±12	10±1

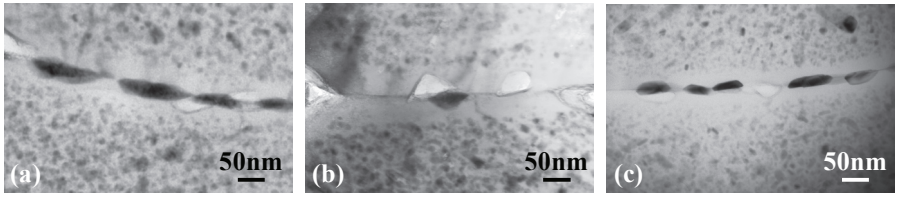


Figure 4: TEM of grain-boundary microstructures for (a) 7079 (T/6), (b) 7079 (T/2), and (c) 7075 alloys overaged 16h at 160 °C.

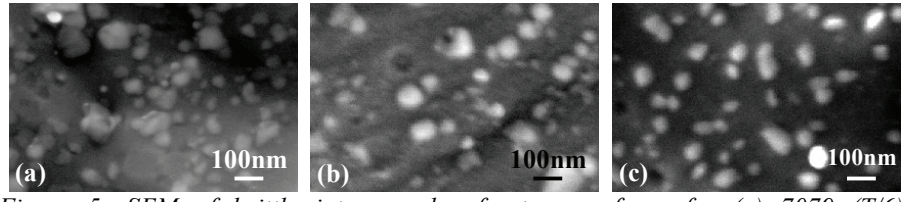


Figure 5: SEM of brittle intergranular fracture surfaces for (a) 7079 (T/6), (b) 7079 (T/2), and (c) 7075 overaged alloys showing grain-boundary precipitates.

Electrochemical Measurements

Open-circuit potential (OCP) measurements on initially uncorroded, brittle intergranular fracture (BIF) surfaces (produced by fast fracture at -196°C) were made for the overaged 7079 (T/6), 7079 (T/2), and 7075 alloys immersed in a NaCl solution. The fracture surfaces exhibited large area-fractions of GBP (Fig.5) and, hence, the mixed potential is probably dominated by the GBP. The initial OCP values (versus the saturated calomel electrode) were lowest (most negative) for the 7079 (T/6) material and highest for the 7075 material. Plots of the OCP versus time of immersion showed that there was generally a small decrease in potential during the first 10 seconds, and then a gradual increase, attaining about the same OCP as that for polished bulk specimens (where there was no significant change in OCP with time of immersion) after about 5 minutes (Fig. 6(a)). The initial decrease in OCP is possibly related to dissolution of oxide films on GBP, while the gradual increase is almost certainly due to the progressive dissolution or de-alloying (of Zn and Mg) of

GBP. Plotting the V_{II} values (on a log scale) versus the 'initial' (10 s) OCP values (or the difference between these values and the bulk OCP) for OA alloys (16h at 160°C) showed that there was an approximately linear relationship (Fig. 6(b)).

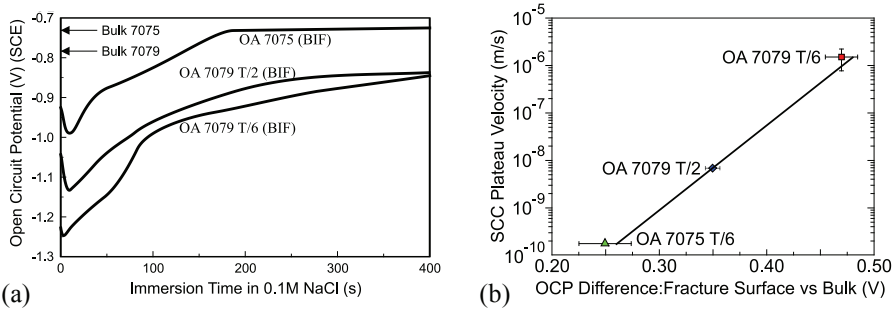


Figure 6: (a) Variation of OCP of initially uncorroded brittle intergranular fracture surfaces with time of immersion in dilute (0.1M) NaCl solution for overaged 7079 (T/6), 7079 (T/2) and 7075 alloys compared with steady OCP values for bulk polished specimens (Average of three runs shown for clarity), (b) Plot of V_{II} (in saturated NaCl) versus the OCP difference between fracture surfaces and the bulk.

Electrochemical measurements on bulk intermetallic $MgZn_{(2-x)}Cu_x$ compounds (with compositions similar to those for GBP) show that they become 'less anodic' with increasing Cu levels [1]. Thus, the initial OCP of fracture surfaces for OA 7079 (T/6) (most negative), 7079 (T/2), and 7075 (least negative) are consistent with the analytical TEM data showing that Cu contents of GBP were lowest for 7079 (T/6) and highest for 7075. Comparisons of the OCP of OA and PA fracture surfaces, taking into account differences in area fraction of GBP, suggested that Cu levels in GBP were increased by overageing [2].

Rate-Controlling Processes

The results suggest that the rate-determining step for SCC at high K in aqueous environments is the rate of anodic dissolution/de-alloying of GBP (with higher rates for GBP with less Cu), which determines the rate of cathodic hydrogen generation. This would be consistent with:

(i) The lack of an effect of K on crack-growth rates,

(ii) The correlation between the V_{II} and the OCP of fracture surfaces, and the lack of an effect of GBP size/spacing/area-fraction, etc., on the rate of SCC in the 7079 T/6 material (assuming Cu contents of GBP did not change), and

(iii) The much greater SCC susceptibility of the 7079-T651 T/6 material compared with the 7075-T651 material for tests in saturated NaCl solution, with less difference in susceptibilities for tests in distilled water (where electrochemical reactions are inhibited by low ionic conductivities), and a reversal of the susceptibilities of the two alloys for tests in low-humidity air (where electrochemical reactions cannot occur).

For SCC in moist air, the steep dependence of crack velocity on relative humidity for the low-Cu 7079/7022-T651 alloys, and the lesser dependence for the 7075-T651 alloy, suggest that the rate-controlling step may be associated with oxide-film characteristics. The structure of oxide films is known to be affected by relative humidity [5] and by alloy composition, and there could be a phase change at particular relative humidities, compositions, and temperatures [4]. The structure of oxide films could affect the diffusion of species through the film or rates of film rupture which, in turn, could affect the hydrogen concentration at crack-tips.

Mechanism of SCC

For SCC in moist air, dissolution can probably be discounted since a bulk water phase is unlikely to be present. High-resolution SEM fractography after SCC in 75% RH air also showed that there were no signs of significant dissolution of 'anodic' grain-boundary precipitates and that crack-arrest markings (CAMs) were present (Fig.7), matching on opposite fracture surfaces, as observed by others [6].

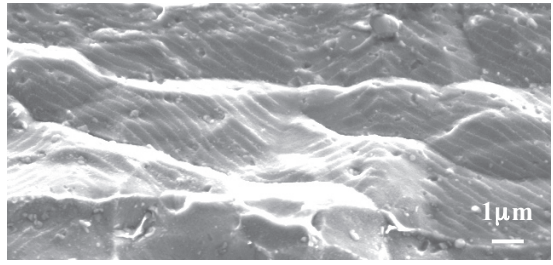


Figure 7: SEM of intergranular fracture surface produced by SCC of OA 7079 in moist air (75%RH), showing crack-arrest markings and GBPs.

The above observations suggest that SCC in moist air occurs entirely by a 'hydrogen embrittlement' mechanism involving:

(i) Hydrogen generation, probably by dissociation of water molecules incorporated in hydrated oxide films at crack-tips, during crack arrest periods,
(ii) Diffusion of hydrogen along boundaries ahead of crack-tips for ~100-250nm,
(iii) Rapid crack-growth increments owing to hydrogen-induced weakening of interatomic bonds across grain-boundaries, when film rupture occurs and/or the hydrogen concentration reaches a critical level, and
(iv) Crack-arrest and blunting when hydrogen levels are insufficient to promote further crack growth.

CAMs were not observed after SCC in the saturated NaCl solution in the present work. However, they have been observed after SCC in aqueous environments by others [6,7], and intermittent acoustic emission indicative of discontinuous cracking on the scale of CAMs has also been observed during SCC in 3.5% NaCl solution [7]. Thus, these observations suggest that the mechanism of SCC in aqueous environments is probably the same as that in moist air, and that corrosion after cracking in aqueous environments often obliterates CAMs.

GENERAL COMMENTS AND CONCLUSIONS

1. The SCC resistance of 7xxx Al alloys in NaCl solutions at high K depends mainly on the Cu content of grain-boundary precipitates (GBP), not precipitate size, etc.
2. The Cu content of GBP, for a given ageing time, depends not only on bulk Cu levels, but also on quench-rate after solution treatment for low-Cu 7xxx alloys.
3. Overageing decreases the SCC plateau velocity for high-Cu 7xxx alloys, and for slowly quenched low-Cu 7xxx alloys, probably because it increases Cu levels in GBP. Further analytical TEM is required to check this hypothesis.
4. The reasons for the effect of quench-rate and ageing times on the Cu contents of GBP are not well understood, and further analytical TEM and other techniques are required to substantiate and understand the effects. The effects of quench rate and ageing on GBP composition could possibly be related to precipitation during quenching and/or vacancy concentrations after quenching, which affect the composition of matrix precipitates near grain boundaries. Dissolution of these precipitates during ageing provides solute to GBP and, hence, the compositions of matrix precipitates near grain boundaries and GBP may be linked.
5. The relative SCC susceptibilities of low and high Cu 7xxx alloys can depend on the environment, e.g. SCC of peak-aged 7079 can be one to two orders of magnitude faster than peak-aged 7075 in salt solutions, but several orders of magnitude slower in low-humidity air environments.
6. The rate of SCC in NaCl solutions is determined by the rate of anodic dissolution/de-alloying of GBP, which controls the rate of cathodic hydrogen charging of grain-boundary regions just ahead of crack tips.
7. The rate of SCC in low humidity air is probably controlled by oxide-film characteristics that depend, for example, on the solute concentrations of grain-boundary regions between GBP. Easier film rupture or more porous oxides could promote SCC due to greater amounts of hydrogen production.
8. SCC occurs discontinuously, producing crack-arrest markings on fracture surfaces, with bursts of crack growth probably occurring when critical hydrogen concentrations are achieved ahead of cracks. Whether crack growth occurs by decohesion or dislocation-emission/nano-void coalescence is still debatable [1,2].

REFERENCES

1. N.J.H. Holroyd, Environment-Induced Cracking of Metals, Eds. R.P. Gangloff and H.B. Ives, (NACE, Houston, 1990), pp. 311-345, and references therein.
2. S.P. Knight, PhD Thesis, Monash University, 2008.
3. M.O. Speidel, M.V. Hyatt, Advances in Corrosion Science and Technology, Vol. 2, Plenum Press, (New York, 1972), pp. 115-335.
4. H. Vogt, M.O. Speidel, *Corrosion Sci*., Vol.40, No.2-3, 1998, pp.251-270.
5. H.A. Al-Abadleh, V.H. Grassian, *Langmuir*, Vol.19, (2003), pp. 341-347.
6. G.M. Scamans, *Metall. Trans*., Vol.11A, (1980), pp. 846-850.
7. P. Martin, J.L. Dickson, J.-P. Baïlon, *Mater. Sci. and Eng*, Vol..69, no.1, (1985), pp. L9-L13.

Effects of Hydrogen on Materials
Proceedings of the 2008 International Hydrogen Conference
Brian Somerday, Petros Sofronis, Russell Jones, editors, p 251-258
Copyright © 2009 ASM International®
All rights reserved.
www.asminternational.org

STRESS CORROSION CRACKING BEHAVIOUR OF ALLOY 7050-T7451 PLATE IN AN AQUEOUS CHLORIDE-NITRATE SOLUTION

Reinhold Braun
DLR – German Aerospace Center, Institute of Materials Research,
D-51170 Köln, Germany

INTRODUCTION

Al-Zn-Mg-Cu alloys providing the highest strength among heat treatable aluminium alloys are sensitive to stress corrosion cracking (SCC) in underaged and peak-aged tempers [1]. Using duplex heat treatment practices, the exfoliation corrosion and SCC behaviour can be improved by overaging. Most recent developments in high strength aluminium alloys are products of the alloys 7X50 and 7055 [2]. Various overaged tempers were developed providing a range of combination of strength and corrosion properties. These thermal treatments improve the resistance to stress corrosion cracking being characteristically intergranuar by transforming the grain boundary precipitation to a less susceptible microstructure. However, transgranular environment-induced cracking was also observed, primarily with 7XXX series aluminium alloys, when severe loading conditions were applied [3]. Fractographic examinations revealed crystallographic facets with fan-like pattern and crack arrest markings indicating discontinuous crack propagation [4]. Under static loading conditions, the occurrence was often associated with pitting corrosion causing notch effects. Transgranular SCC failure of notched specimens was promoted by cyclic loading [4,5]. Sensitivity to transgranular environment-induced cracking did not depend on heat treatment.

Stress corrosion cracking in aluminium alloys is induced by humid environments containing chloride which is ubiquitously found in marine and rural atmosphere [1]. In addition, industrial environments can contain further pollutants, such as sulfate and nitrate ions. For 7XXX series alloys, synergistic effects of chloride and nonhalide anions on the SCC behaviour were observed [6,7]. When exposed to an aqueous chloride-nitrate solution, alloy 7075-T7351 being immune to intergranular stress corrosion cracking failed at an applied short transverse stress of 300 MPa due to pitting and transgranular environment-induced cracking. The aim of this work was to study the SCC behaviour of the alloy 7050-T7451 under different loading conditions, in particular with regard to transgranular environmentally assisted cracking.

EXPERIMENTAL

The material used was a 45 mm thick plate of the alloy 7050 in the temper T7451. From this plate smooth and notched, round tension specimens were machined in short transverse orientation. The smooth samples had a gauge length of 15.7 mm and a cross section of 10 mm^2. In the centre of the gauge length of notched specimens, a 60° circumferential V-notch was machined with a depth of 0.61 mm and a notch tip radius of 0.14 mm. The root diameter was 3.50 mm. Short transverse tensile properties of the 7050-T7451 plate were: 0.2% yield strength = 446 ± 5 MPa, ultimate tensile strength = 532 ± 1 MPa, and fracture elongation = 8.1 ± 0.7 %. The notch strength related to the specified sample geometry was determined to 677 ± 14 MPa.

The SCC behaviour was investigated under constant load and cyclic loading conditions. The synthetic environment used was an aerated aqueous solution of 0.6 M NaCl + 0.06 M $NaNO_3$. The specimens were permanently immersed at free corrosion potential. Constant load tests were carried out using dead weight loaded tensile testing machines. Failure criterion for smooth and notched samples was fracture. Performing cyclic loading tests, stress applied to notched specimens exhibited a sawtooth shaped waveform. Using a slow strain rate testing machine, the load was increased from a lower to an upper limit at constant cross-head speed. The displacement rates were in the range from 2×10^{-6} to 2×10^{-4} mms^{-1}. The stress ratio $R = \sigma_{min}/\sigma_{max}$ was 0.2, and the maximum stresses ranged from 200 to 400 MPa with regard to original cross-sectional area at the notch. Fracture surfaces were examined by scanning electron microscopy (SEM) after cleaning in an aqueous solution of chromic and phosphoric acids, as recommended in ASTM Standard Practice G1 for aluminium alloys.

RESULTS AND DISCUSSION

Figure 1 shows time-to-failure data of 7050-T7451 plate obtained from constant load tests using an aqueous solution of 0.6 M NaCl + 0.06 M $NaNO_3$. When stressed in short transverse direction, both smooth and notched tensile specimens failed at applied stresses down to 200 MPa. On the fracture surfaces pronounced transgranular SCC was observed exhibiting crystallographic facets with fan-like pattern (Fig. 2).

Results of the cyclic loading tests for alloy 7050-T7451 are presented in Table 1. Applying various stress ranges $\Delta\sigma = \sigma_{max} - \sigma_{min}$ with σ_{max} between 200 and 400 MPa, the notched specimens were cyclically loaded at different displacements rates. All tests were carried out at an R-ratio of 0.2. The loading frequency depended upon the stress range and displacement rate. Time-to-failure data vs. displacement rate and number of cycles-to-failure vs. frequency are plotted in Figure 3. The time-to-failure decreased with increasing displacement rate. Failure occurred at shorter time with higher maximum stress. The number of cycles-to-failure decreased with decreasing frequency. At a given frequency, the number of cycles-to-failure increased with decreasing stress range $\Delta\sigma$, e.g. decreasing σ_{max}. A linear dependence was found

between the log values (Fig. 3b). For all three curves a slope of about 0.5 was obtained. The following constants of the curves log Y (number of cycles-to-failure) = A log X (frequency) + B were determined: σ_{max} = 200 MPa: A = 0.547, B = 5.048; σ_{max} = 300 MPa: A = 0.533, B = 4.575; σ_{max} = 400 MPa: A = 0.548, B = 4.346.

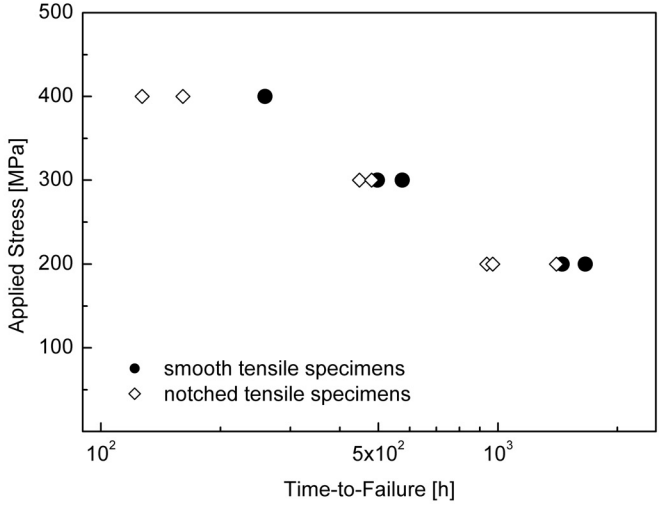


Figure 1: Time-to-failure data of 7050-T7451 alloy plate obtained from constant load tests. Smooth and notched short transverse tensile specimens were permanently immersed in an aqueous solution of 0.6 M NaCl + 0.06 M $NaNO_3$.

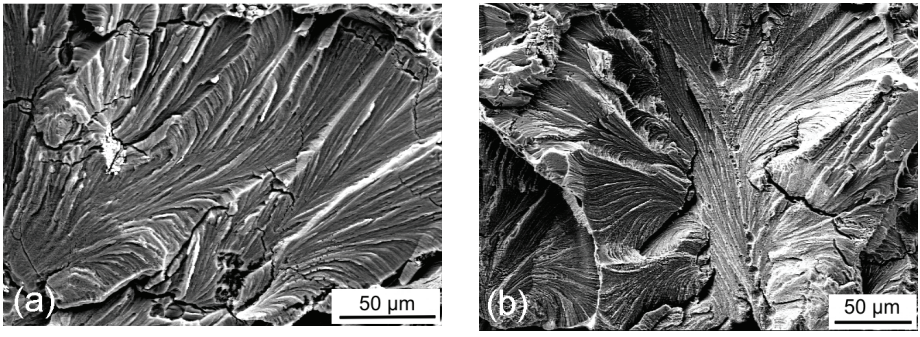
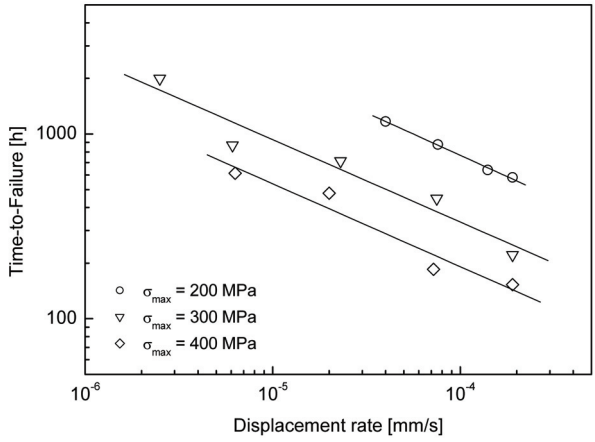


Figure 2: Scanning electron fractographs of (a) smooth and (b) notched 7050-T7451 tensile specimens showing transgranular stress corrosion cracking. The samples were permanently immersed in an aqueous solution of 0.6 M NaCl + 0.06 M $NaNO_3$ at an applied stress of 300 MPa in short transverse direction and failed after (a) 574 and (b) 481 h of exposure, respectively.

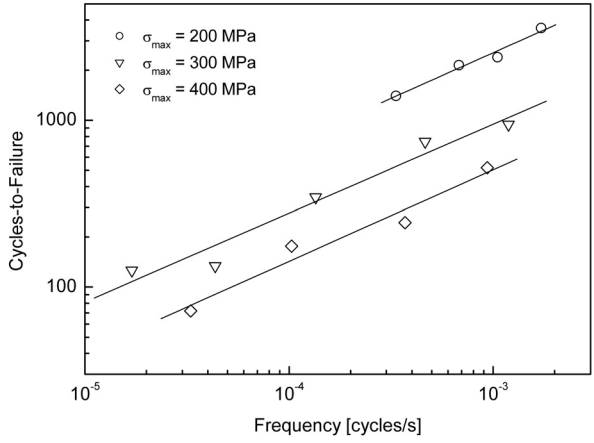
Table 1: Time-to-failure data of 7050-T7451 plate obtained from cyclic loading tests. Notched short transverse tensile specimens were tested in an aqueous solution of 0.6 M NaCl + 0.06 M $NaNO_3$ at different stress ranges $\Delta\sigma = \sigma_{max} - \sigma_{min}$ and displacement rates.

Displacement Rate [mms^{-1}]	Loading Frequency [s^{-1}]	Cycles-to-Failure	Time-to-Failure [h]
$\Delta\sigma$ = 320 MPa with σ_{max} = 400 MPa			
6.3×10^{-6}	3.26×10^{-5}	72	613
2.0×10^{-5}	1.02×10^{-4}	176	478
7.2×10^{-5}	3.67×10^{-4}	244	185
1.9×10^{-4}	9.42×10^{-4}	519	153
$\Delta\sigma$ = 240 MPa with σ_{max} = 300 MPa			
2.5×10^{-6}	1.75×10^{-5}	126	1995
6.1×10^{-6}	4.28×10^{-5}	134	870
2.3×10^{-5}	1.35×10^{-4}	346	714
7.5×10^{-5}	4.62×10^{-4}	744	448
1.9×10^{-4}	1.18×10^{-3}	943	222
$\Delta\sigma$ = 160 MPa with σ_{max} = 200 MPa			
4.0×10^{-5}	3.33×10^{-4}	1403	1169
7.6×10^{-5}	6.78×10^{-4}	2142	878
1.4×10^{-4}	1.04×10^{-3}	2389	639
1.9×10^{-4}	1.71×10^{-3}	3585	581

Fractographic examinations of the cyclically loaded specimens revealed a brittle transgranular fracture (Fig. 4). On the flat facets striations were observed, indicating discontinuous crack propagation. Different types of markings were found: fine regularly spaced striations related to crack advance during a cycle and probably created by dissolution of the exposed bare fracture surface at crack arrest as well as coarse brittle striations consisting of deep slots. With propagating crack striation spacing increased due to the higher stress resulting from reduced cross-section of the samples (Fig. 4c). Generally, the distance between the markings became larger with decreasing loading frequency. Similarly to transgranular SCC cracking, cleavage-like fracture with feathery pattern and river lines was observed (Fig. 5), suggesting that an akin mechanism caused failure under cyclic loading conditions at low frequencies. At an applied maximum stress of 200 MPa, the samples exhibited distinct flat fracture surfaces with featureless appearance (Fig. 6). At higher magnifications, secondary cracks and, sometimes, fine striations were observed (Figs. 6c and d).



(a)



(b)

Figure 3: Curves of (a) time-to-failure vs. displacement rate and (b) number of cycles-to-failure vs. frequency for alloy 7050-T7451. Notched specimens were cyclically loaded in an aqueous solution of 0.6 M NaCl + 0.06 M $NaNO_3$ at an R-ratio of 0.2 applying different maximum stresses.

Alloy 7050-T7451 was found to be sensitive to transgranular environment-induced cracking under static and cyclic loading conditions at applied stresses down to 200 MPa. Fitting the logarithmic plots of the results of cyclic loading tests, a slope of 0.5 was obtained. The number of cycles-to-failure was dependent on the square root of frequency, i.e. proportional to $1/\sqrt{\tau}$ with τ being the cycle period. This square root dependence indicated an embrittlement mechanism controlled by diffusion. The crack growth in the aqueous chloride-nitrate solution was probably related to hydrogen diffusion ahead of the crack tip, as suggested by Holroyd and Hardie [8].

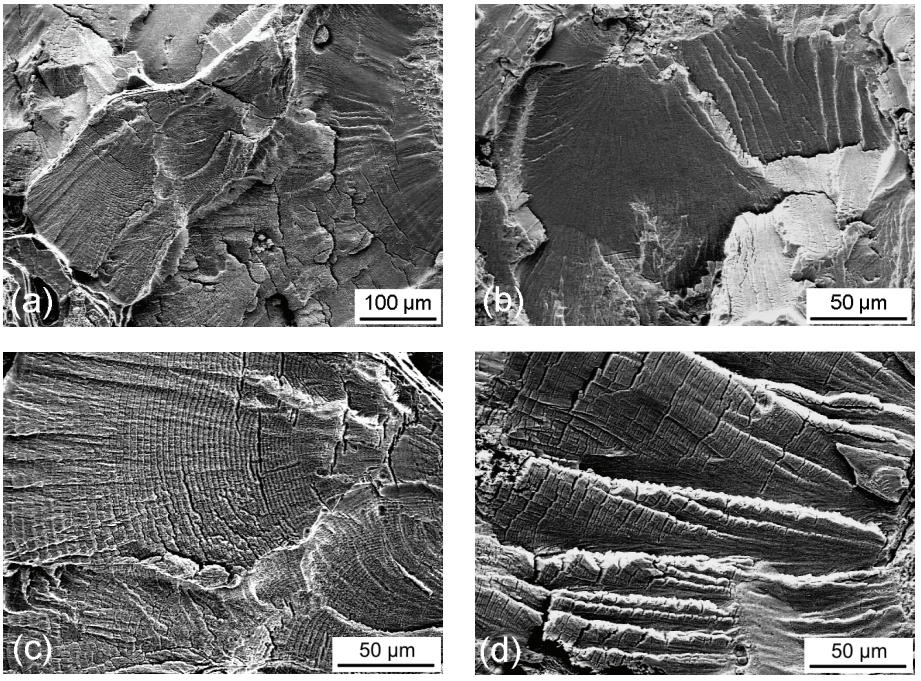


Figure 4: Scanning electron fractographs of alloy 7050-T7451 showing (a,b) brittle transgranular fracture and (c,d) striations on cleavage-like facets. The notched specimens were cyclically loaded in an aqueous solution of 0.6 M NaCl + 0.06 M $NaNO_3$ at frequencies of (a,c) 1.02×10^{-4}, (b) 9.42×10^{-4} and (d) $3.67\times10^{-4}s^{-1}$, applying a stress range $\Delta\sigma$ = 320 MPa with σ_{max} = 400 MPa.

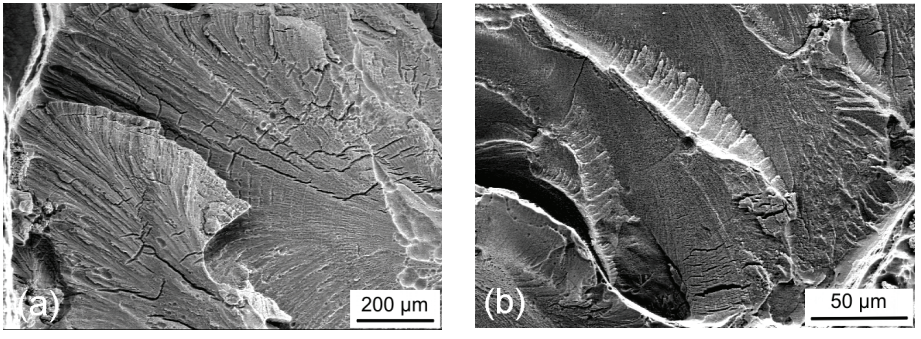


Figure 5: Scanning electron fractographs of alloy 7050-T7451 showing cleavage-like fracture. The notched specimens were cyclically loaded in an aqueous solution of 0.6 M NaCl + 0.06 M $NaNO_3$ at frequencies of (a) 1.75×10^{-5} and (b) $4.62\times10^{-4}s^{-1}$, applying a stress range $\Delta\sigma$ = 240 MPa with σ_{max} = 300 MPa.

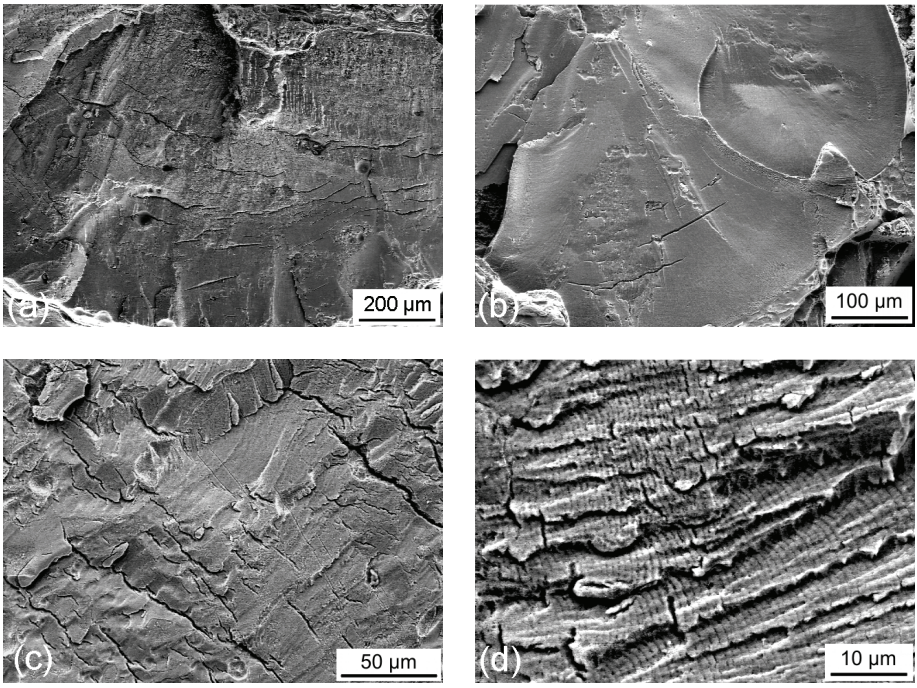


Figure 6: Scanning electron fractographs of alloy 7050-T7451 showing (a,b) transgranular stress corrosion cracking with (c) secondary cracks and (d) crack arrest markings. The notched sample was cyclically loaded in an aqueous solution of 0.6 M NaCl + 0.06 M $NaNO_3$ at a frequency of $3.33\times10^{-4}s^{-1}$, applying a stress range $\Delta\sigma$ = 160 MPa with σ_{max} = 200 MPa.

Hydrogen assisted cracking models and corrosion enhanced plasticity models have been adopted to explain transgranular cleavage-like cracking in aluminium alloys. An adsorption-induced localised-slip mechanism was proposed by Lynch [9]. Adsorbed hydrogen weakens interatomic bonds at the crack tip, resulting in injection of dislocations. The crack grows by alternate slip and coalesces with voids formed by dislocation activity ahead of the crack. The corrosion enhanced plasticity model developed by Magnin can also be applied to transgranular environment-induced cracking in aluminium alloys [10]. It is based on the corrosion-deformation interactions at the stress corrosion crack tip. Localised anodic dissolution on {111} slip planes and hydrogen entry result in an enhanced plasticity at the crack tip. Mobile dislocations can be injected owing to stress concentration, vacancy production, adsorption and absorption of hydrogen. These dislocations emitted by the crack tip will then interact with obstacles, and zig-zag microcracking assisted by hydrogen absorption can occur on {111} and/or {100} facets.

CONCLUSIONS

1. An aqueous 3.5% NaCl solution containing nitrate promoted environment-induced cracking with alloy 7050-T7451. Failure observed under constant load conditions was mainly associated with transgranular stress corrosion cracking.
2. When cyclically loaded at displacement rates ranging from $2 \cdot 10^{-6}$ to $2 \cdot 10^{-4}$ mms^{-1}, notched specimens failed by transgranular environment-induced cracking.
3. The number of cycles-to-failure deceased with decreasing frequency. At an R-ratio of 0.2, the time-to-failure decreased with increasing maximum stress.
4. On the cleavage-like facets, striations were observed related to discontinuous crack propagation.
5. Fitting the number of cycles-to-failure vs. frequency curves on a log-log basis, a linear dependence was obtained with a slope of about 0.5, indicating a diffusion controlled degradation mechanism being probably hydrogen embrittlement.

REFERENCES

1. Summerson, T.J., Sprowls D.O., "Corrosion behavior of aluminum alloys", *Aluminum Alloys – Their Physical and Mechanical Properties*, Charlottesville, VA, June 1996, pp. 1576-1662.
2. Hunt, W.H., Staley, J.T., "High strength aluminum alloys for aerospace application", *Light-Weight Alloys for Aerospace Applications*, Las Vegas, NV, March 1989, pp. 111-120.
3. Holroyd, N.J.H., "Environment-induced cracking of high-strength aluminum alloys", *Environment-Induced Cracking of Metals*, Kohler, WI, October 1988, pp. 311-345.
4. Braun, R., "Environmentally assisted cracking of aluminum alloys", *Materialwiss. Werkstofftech.*, Vol. 38, No. 9 (2007), pp. 674-689.
5. Braun, R., "Transgranular environment-induced cracking of 7050 aluminium alloy under cyclic loading conditions at low frequencies" *Int. J. Fatigue*, Vol. 30, No. 10-11 (2008), pp. 1827-1837.
6. Braun, R., "Effects of nonhalide anions on the stress corrosion cracking behaviour of alloy 7475 in the tempers T651 and T7351", *Mater. Corros.*, Vol. 51, No. 9 (2000), pp. 607-615.
7. Braun, R., "Anion effects on the stress corrosion cracking behaviour of aluminium alloys", *Mater. Corros.*, Vol. 54, No. 3 (2003), pp. 157-162.
8. Holroyd, N.J.H., Hardie, D., "Factors controlling crack velocity in 7000 series aluminium alloys during fatigue in an aggressive environment", *Corros. Sci.*, Vol. 23, No. 6 (1983), pp. 527-546.
9. Lynch, S.P., "Metallographic contributions to understanding mechanisms of environmentally assisted cracking", *Metallography*, Vol. 23, No. 2 (1989), pp. 147-171.
10. Magnin, T., Chambreuil, A., Chateau, J.P., "Stress corrosion cracking mechanisms in ductile FCC materials", *Int. J. Fracture*, Vol. 79, No. 2 (1996), pp. 147-163.

Effects of Hydrogen on Materials
Proceedings of the 2008 International Hydrogen Conference
Brian Somerday, Petros Sofronis, Russell Jones, editors, p 259-266
Copyright © 2009 ASM International®
All rights reserved.
www.asminternational.org

The Role of Hydrogen in the Stress Corrosion Cracking of Mg-Al Alloys

N. Winzer
Bundesanstalt für Materialforschung und -prüfung, Berlin, Germany

A. Atrens
The University of Queensland, Brisbane, Australia

W. Dietzel, K.U. Kainer
GKSS-Forschungszentrum Geesthacht GmbH, Geesthacht, Germany

INTRODUCTION

The increasing demand for lighter, more fuel-efficient automobiles has spurred renewed interest in the use of Mg alloys for automobile components. A major barrier to the increased use of Mg alloys for automobile components is their high susceptibility to Stress Corrosion Cracking (SCC) in common service environments [1]. While there exists a considerable body of research outlining the phenomenology of SCC of Mg alloys, there is little consensus in the literature regarding the underlying mechanisms [1]. The development of durable Mg alloys for automobile components requires a profound understanding of these mechanisms. SCC of Mg alloys can be intergranular (IGSCC) or transgranular (TGSCC), with TGSCC being the inherent mode [1]. It is generally known that Hydrogen Embrittlement (HE) plays an important role in TGSCC of Mg alloys; however, the specific nature of this role is unknown. HE mechanisms that may be involved in TGSCC of Mg alloys include: Hydrogen Enhanced Decohesion (HEDE) [2, 3]; Hydrogen Enhanced Localised Plasticity (HELP) [2, 3]; Adsorption Induced Dislocation Emission (AIDE) [2, 3, 4]; and Delayed Hydride Cracking (DHC) [2, 3, 5, 6, 7, 8, 9]. It is likely that combinations of these mechanisms occur, with the predominant mechanism being dependent on microstructure, environment and mechanical loading. This paper summarises the key outcomes and open issues resulting from our recent work, which was aimed at developing a mechanistic understanding of the influences of microstructure, environment and mechanical loading on the SCC susceptibility of Mg alloys [1, 2, 3, 5, 10, 11,]. The work focused primarily on Mg-Al alloys, which are the most commonly used in industry and are particularly susceptible to SCC [1].

EXPERIMENTAL METHOD

The test materials were the Mg alloys AZ91 (8.9%Al-0.8%Zn-0.2%Mn), AZ31 (2.6%Al-0.8%Zn-0.6%Mn) and AM30 (2.9%Al-0.4%Mn). AZ91 specimens were machined from cast ingots (from Hydro Magnesium), whereas AZ31 and AM30 specimens were machined from large extrusions (supplied by GM) with their tensile

axis parallel with the extrusion direction. The grain sizes were 50-100μm for AZ91 and 1-2μm for AZ31 and AM30 (equiaxed in all cases). All alloys were machined into cylindrical tensile specimens with a 5mm diameter waisted gauge section. AZ91 contained: (i) an extensive Mg-Al interdendritic β phase; (ii) fine Mg-Al-Mn plate-like crystals within the β particles; and (iii) small Al-Mn intragranular precipitates. AZ31 and AM30 contained a sparse dispersion of: (i) ~10μm Al-Mn quadrilateral plate-like crystals; (ii) ~3-4μm Mg-Si interdendritic particles; and (iii) elongated ~3-6μm Al-Mn plate-like crystals that were aligned collinearly in the extrusion direction. The quadrilateral plate-like crystals were larger and more numerous for AZ31 than for AM30. The test environment was double-distilled H_20 at room temperature and open circuit conditions with control tests carried out in air. The mechanical load was applied under Constant Extension Rate Test (CERT) conditions. SCC was detected using the DC Potential Drop (DCPD) method. The average stress corrosion crack velocity, V_c, was calculated from $\Delta a/\Delta t_{SCC}$, where Δa is the maximum size of the SCC fracture surface zone and Δt_{SCC} is the time between crack initiation (furnished by the DCPD measurements) and the end of the test.

RESULTS

Figures 1-3 show the stress vs. apparent strain curves for AZ91, AZ31 and AM30, in distilled water and laboratory air, under CERT conditions. For specimens in distilled water, the apparent plastic deformation is largely attributed to SCC. All alloys suffered a reduction in UTS and apparent ductility in distilled water relative to tests in laboratory air, with the UTS and apparent ductility decreasing with decreasing strain rate. The apparent ductility of AZ31 was considerably more sensitive to changes in strain rate than those of AZ91 and AM30. For strain rates in the range 10^{-7}-$5x10^{-7}s^{-1}$, the V_c for AZ91 and AZ31 were in the range 10^{-9}-10^{-8}m/s, whereas the V_c for AM30 were in the range $4x10^{-10}$-$9x10^{-10}$m/s.

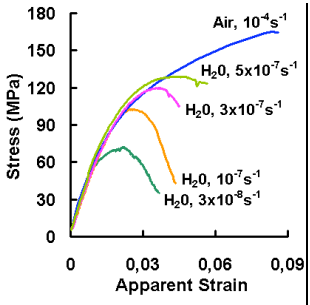


Figure 1: Stress vs apparent strain curves for AZ91 [2].

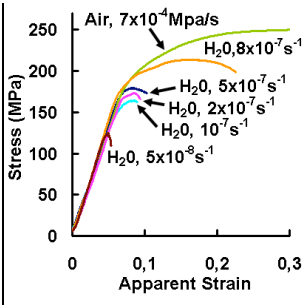


Figure 2: Stress vs apparent strain curves for AZ31 [2].

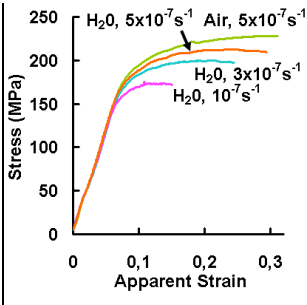


Figure 3: Stress vs apparent strain curves for AM30 [2].

Secondary cracks were apparent on the gauge surfaces of all specimens fractured in distilled water, although the density of secondary cracks in AZ91 specimens was lower than in AZ31 and AM30 specimens. Secondary cracks in AZ91 specimens were macroscopically sharp, with cracks nucleating within β-particles ahead of the principle crack tip (Fig. 4). The cracks nucleated within β-particles propagated

transgranularly in a relatively constant direction, with perpendicular cliffs forming between converging consecutive cracks. Secondary cracks in AZ31 and AM30 appeared to be due to localised dissolution at sites of surface film rupture [2, 3].

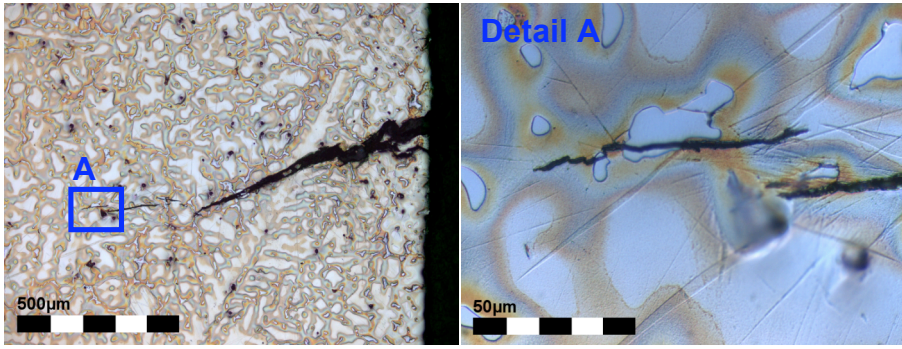


Figure 4: Secondary crack in AZ91 specimen [2].

The SCC fracture surfaces for AZ91 specimens tested at 10^{-7}-$5x10^{-7}s^{-1}$ in distilled water contained multiple thumbnail-shaped SCC zones, characterised by: (i) parallel facets ~5µm wide; (ii) jogging at the edges of each facet; (iii) extensive crack branching; and (iv) cleavage through β-particles (Fig. 5). Examination at high magnification revealed that the parallel facets contained fine parallel markings (<0.5 µm apart) or ellipsoidal micro-dimples. The orientation of the parallel facets and fine parallel markings was influenced by β-particles (Fig. 5B and Fig. 6). For specimens tested at 10^{-7}-$5x10^{-7}s^{-1}$, the non-SCC fracture surface regions were comprised of broken, jagged features consistent with fracture in laboratory air. In contrast, for specimens tested at $3x10^{-8}s^{-1}$, the non-SCC fracture surface regions were comprised of smooth, rounded features somewhat comparable to shrinkage porosity [12], interspersed with small (<50µm across) regions of broken, jagged facets consistent with fracture in laboratory air (Fig. 7). These "quasi-porous" features were similar to those found on fracture surfaces for AZ91 specimens tested in laboratory air after pre-charging in H_2 gas at 300°C and 30bar for 15h, and attributed to precipitation, fracture and decomposition of metastable MgH_2 particles [3].

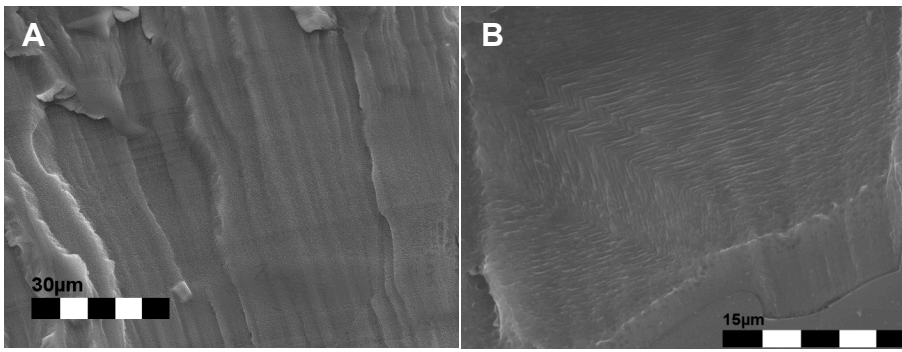


Figure 5: SCC fracture surface for AZ91 showing (A) parallel facets and (B) fine parallel markings [3].

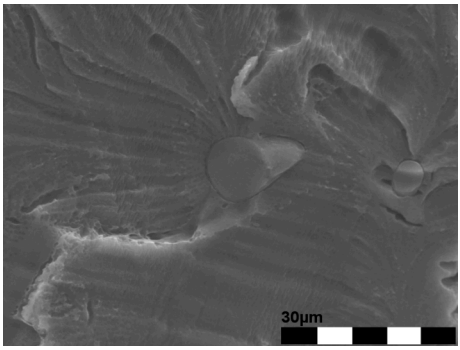


Figure 6: SCC fracture surface for AZ91 showing the influence of β-particles on the orientation of parallel markings [3].

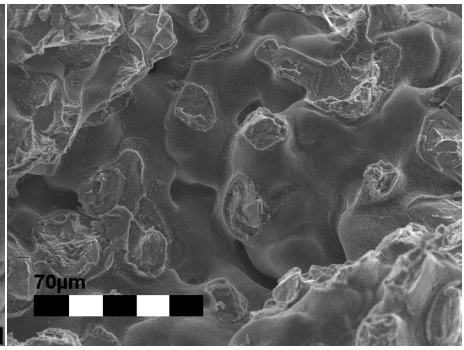


Figure 7: Fracture surface morphology for AZ91 in distilled water at $3x10^{-8}$ s^{-1} showing quasi-porous features [3].

The SCC fracture surfaces for AZ31 and AM30 specimens consisted of three separate morphologies: (i) a 100-200µm wide region at the gauge surface consistent with severe localised dissolution; (ii) a macroscopically-flat SCC "band"; and (iii) a final overload fracture region consistent with fracture in an inert environment (Fig. 8). The SCC band for AZ31 was characterised by quasi-crystallographic markings containing small (<0.5µm across) specifically oriented ellipsoidal dimples (Fig. 9A), similar to those observed within parallel facets on SCC fracture surfaces for AZ91 (Fig. 5B). In contrast with that for AZ31, the SCC band for AM30 was characterised by distinctly cleavage-like markings (Fig. 9B).

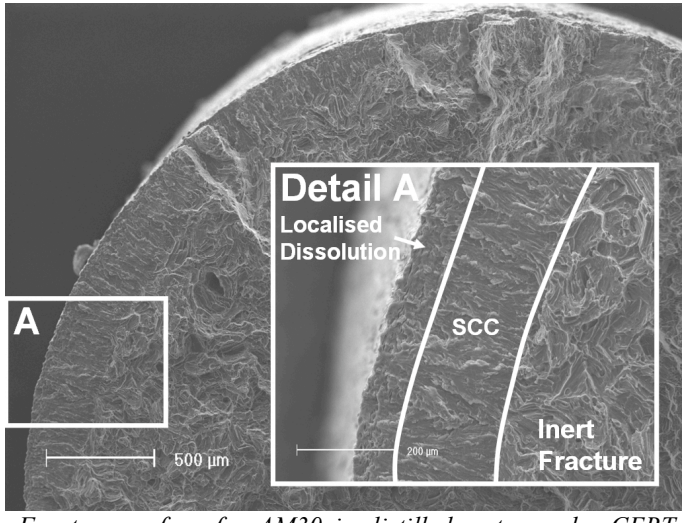


Figure 8: Fracture surface for AM30 in distilled water under CERT conditions showing zones corresponding to localised dissolution, SCC and inert fracture. Fracture surfaces for AZ31 in distilled water were similarly composed [3].

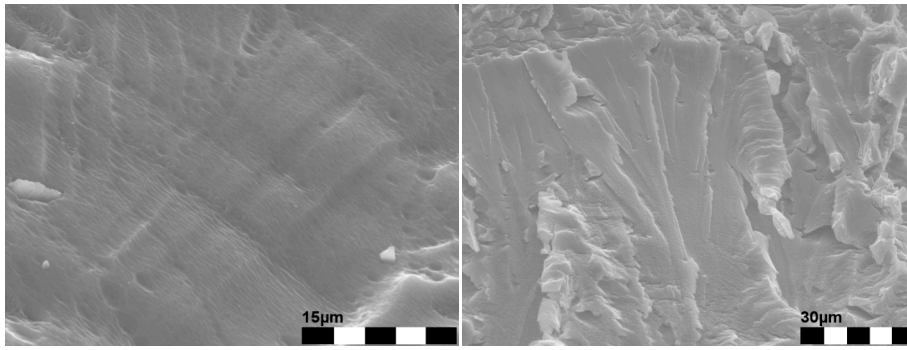


Figure 9: Morphology of SCC fracture surface for AZ31 (A) and AM30 (B) [3].

DISCUSSION

For AZ31 and AM30, SCC initiation occurs by localised dissolution (tunneling), with a transition in SCC mechanism occurring at a crack length of 100-200µm (Fig. 8). The fractography corresponding to propagation beyond this critical crack length is indicative of a mechanism involving HE. Some difference in the mechanism or critical (rate limiting) process for HE in AZ31 and AM30 is indicated by: (i) the lower V_c for AM30 relative to AZ31; and (ii) the contrast in the fracture surface morphologies for AZ31 and AM30 (Fig. 9). These differences may be related to the influences of Zn and second phase particles (which were more concentrated in AZ31) on the diffusivity of H in the α-matrix. The difference in H diffusivity for AZ31 and AM30 could be such that: (i) different HE mechanisms occur in each alloy; or (ii) that the same HE mechanism occurs, with the difference in H diffusivity affecting V_c and the fracture surface morphology (the crystallographic orientation of the cleavage-like facets and the size of the micro-dimples).

The mechanism for SCC initiation in AZ91 does not involve localised dissolution as per AZ31 and AM30. The specific nature of the mechanism for SCC initiation in AZ91 is unclear; however, it is likely that it somehow involves HE. It is clear that β-particles play an important role in the mechanism for SCC propagation in AZ91. This is evidenced by: (i) the nucleation of stress corrosion cracks within β-particles ahead of the principal crack tip (Fig. 4); and (ii) the influence of β-particles on the orientation of SCC fracture surface markings (Fig. 5B and Fig. 6). The nucleation of stress corrosion cracks within β-particles ahead of the principal crack tip could be attributed to: (i) the inherently low fracture toughness of the β-particles; (ii) a reduction in the fracture toughness of β-particles by internal H (by HEDE or transformation to MgH_2); or (iii) the synergistic effects of dislocation pile-ups at the α-β interface (as observed by Wang et al [13]) and H-enhanced dislocation mobility. Recently, Chen et al [14] showed that immersion of AZ91 in Na_2SO_4 solution (cathodically polarised and at the free corrosion potential) in the absence of external stress resulted in fracture of β-particles at the surface, indicating that it is indeed due to H and not their inherently low fracture toughness (i.e. ii or iii). Thus, the increase in SCC susceptibility of Mg-Al alloys with increasing Al concentration [1] may be related to the propensity for crack nucleation within β-particles. Moreover, if the

mechanism for SCC propagation involves H transport with mobile dislocations (as per HELP), then the influence of strain rate may be mitigated by the presence of H at multiple internal sources [15]. Thus, if β-particles behave as reversible H traps (i.e. as sinks and sources), this may explain why the elongation-to-failure for AZ31 (which consists of an α-matrix only) is more dependent on strain rate than that for AZ91 (which contains β-particles).

It was previously proposed that SCC of Mg alloys at very slow crack velocities (strain rates) involves precipitation, fracture and decomposition of metastable MgH_2 particles ahead of the stress corrosion crack [3]. This was based on the observation of quasi-porous fracture surface features (Fig. 7) for AZ91 specimens: (i) tested in distilled water at $3x10^{-8}s^{-1}$; and (ii) tested in air after pre-charging in H_2 at 300°C and 30bar for 15h. Numerical analysis of the H concentration imparted by pre-charging under these conditions, and the reduction in the H solvus concentration upon cooling to room temperature, indicated that MgH_2 precipitation was likely to result. Schober [16] also reported MgH_2 precipitation in pure Mg after charging in H_2 gas under similar conditions, with the precipitates taking the form of large agglomerates. These MgH_2 precipitates dissolved when exposed to aqueous environments, resulting in the formation of large cavities in their place. This is consistent with the quasi-porous fracture morphology for specimens tested in distilled water at $3x10^{-8}s^{-1}$ (Fig. 7).

The specific mechanisms for SCC propagation in AZ91, AZ31 and AM30 remain uncertain. The occurrence of micro-dimples on AZ91 and AZ31 SCC fracture surfaces is consistent with a mechanism involving microvoid nucleation (HELP and/or AIDE). In the case of AZ31, the micro-dimples occurred within macroscopically flat, quasi-crystallographic facets (Fig. 9A). Observations of dimples within cleavage-like facets on SCC fracture surfaces have been ascribed to AIDE by other workers [4, 17]; however, in the present case it has not been determined whether the dimpled facets correspond to a specific crystallographic plane. Cleavage-like fracture surfaces, such as those observed in the present work for AM30 (Fig. 9B), are typically associated with HEDE [18, 19]; however, it is also possible that micro-dimples do occur on the SCC fracture surfaces for AM30, albeit on a smaller scale than for AZ31.

CONCLUSIONS

- For AZ31 and AM30, SCC initiation occurs by transgranular localised dissolution, with a transition in mechanism to HE at a crack length of 100-200μm. There were differences in the mechanisms or critical processes for HE in AZ31 and AM30, manifested in: (i) V_c; (ii) the crystallography of cleavage-like fracture surface markings; and (iii) the appearance of micro-dimples within the cleavage-like facets. These differences may be due to the influences of Zn and second phase particles (more concentrated in AZ31) on H diffusivity in the α-matrix. The influences of Zn and second phase particles could be such that: (i) different HE mechanisms occur for AZ31 and AM30; or (ii) the same HE mechanism occurs in AZ31 and AM30, with the difference in H diffusivity affecting V_c and the fracture surface morphology.
- The mechanism for SCC initiation in AZ91 does not occur by localised

dissolution as per AZ31 and AM30, implying that it somehow involves H.

- β-particles play an important role in SCC of AZ91, as evidenced primarily by the nucleation of stress corrosion cracks within β-particles ahead of the principal crack tip. Crack nucleation within β-particles could be due to: (i) a reduction in the fracture toughness of β-particles by internal H; or (ii) the synergistic effects of dislocation pile-ups at the α-β interface and H-enhanced dislocation mobility. The role of β-particles implies that the increasing SCC susceptibility of Mg alloys with increasing Al concentration is related to the distribution of, and propensity for crack nucleation within, β-particles.
- The fracture surfaces for AZ91 specimens tested in distilled water at very slow strain rates were similar to those resulting from pre-charging in gaseous H_2 to induce hydride precipitation, implying that the quantity of H transported ahead of the crack tip during SCC of AZ91 at very slow crack velocities is sufficient for hydride precipitation.

REFERENCES

1. Winzer, N. *et al*, "A Critical Review of the Stress Corrosion Cracking (SCC) of Magnesium Alloys," *Adv. Eng. Mater.*, Vol. 8 (2005), pp. 659-693.
2. Winzer, N. *et al*, "Characterisation of Stress Corrosion Cracking (SCC) of Mg–Al alloys," *Mat. Sci. Eng.*, Vol. 488A (2008), pp. 339-351.
3. Winzer, N. *et al*, "Fractography of Stress Corrosion Cracking of Mg-Al Alloys," *Metall. Mater. Trans.*, Vol. 39A (2008), pp. 1157-1173.
4. Lynch, S.P. and Trevena, P., "Stress Corrosion Cracking and Liquid Metal Embrittlement in Pure Magnesium," *Corrosion*, Vol. 44 (1988), pp. 113-124.
5. Winzer, N. *et al*, "Evaluation of the Delayed Hydride Cracking Mechanism for Transgranular Stress Corrosion Cracking of Magnesium Alloys," *Mat. Sci. Eng.*, Vol. 466A (2007), pp. 18-31.
6. Meletis, E.I. and Hochman, R.F., "Crystallography of Stress Corrosion Cracking in Pure Magnesium," *Corrosion*, Vol. 40 (1984), pp. 39-45.
7. Chakrapani, D.G. and Pugh, E.N., "Hydrogen Embrittlement in a Mg-Al Alloy," *Metall. Trans.*, Vol. 7A (1976), pp. 173-178.
8. Bursle, A.J. and Pugh, E.N., Mechanisms of Environment Sensitive Cracking of Materials, Materials Society (London, 1977), pp. 471-481.
9. Makar G.L. *et al*, "Stress Corrosion Cracking of Rapidly Solidified Magnesium-Aluminium Alloys," *Corros. Sci.*, Vol. 34 (1993), pp. 1311-1342.
10. Winzer, N. *et al*, "Comparison of the Linearly Increasing Stress Test and the Constant Extension Rate Test in the Evaluation of Transgranular Stress Corrosion Cracking of Magnesium," *Mat. Sci. Eng.*, Vol. 472A (2008), pp. 97-106.
11. Winzer, N. *et al*, "Stress Corrosion Cracking (SCC) in Mg-Al Alloys Studied using Compact Specimens," *Adv. Eng. Mater.*, Vol. 10 (2008), pp. 453-458.
12. Munitz A. *et al*, "Mechanical Properties and Microstructure of Gas Tungsten Arc Welded Magnesium AZ91D plates," *Mat. Sci. Eng.*, Vol. 302A (2001), pp. 68-73.
13. Wang R.M. *et al*, "An Investigation on the Microstructure of an AM50 Magnesium Alloy," *Mat. Sci. Eng.*, Vol. 355A (2003), pp. 201-207.

14. Chen J. *et al*, "States and Transport of Hydrogen in the Corrosion Process of an AZ91 Magnesium Alloy in Aqueous Solution," *Corros. Sci.*, Vol. 50 (2008), pp. 1292-1305.
15. Pressouyre G.M., "Trap Theory of Hydrogen Embrittlement," *Acta. Metall.*, Vol. 28 (1980), pp. 895-911.
16. Schober T., "The Magnesium-Hydrogen System: Transmission Electron Microscopy," *Metall. Mater. Trans.*, Vol. 12A (1981), pp. 951-957.
17. Lynch S.P., "Mechanisms of Hydrogen Assisted Cracking – A Review," Acta. Metall., Vol. 34 (1988), pp. 2639-2661.
18. Birnbaum H.K., Hydrogen Effects on Material Behavior, TMS (Warrendale, 1990), pp. 639-660.
19. Gangloff R.P., Comprehensive Structural Integrity, Vol. 6.02, Elsevier, (Oxford, 2003), pp. 31-101.

Effects of Hydrogen on Materials
Proceedings of the 2008 International Hydrogen Conference
Brian Somerday, Petros Sofronis, Russell Jones, editors, p 267-274
Copyright © 2009 ASM International®
All rights reserved.
www.asminternational.org

MICROSTRUCTURAL EFFECTS ON THE STRESS CORROSION CRACKING RESPONSE OF AN ALLOY 600

A. Aguilar*. O. Flores J. M. Zagal, L. Martinez*
Universidad Nacional Autónoma de México. Instituto de Ciencias Físicas, A. P. 48-3, C. P. 62251, Cuernavaca, Morelos, México.

B. Campillo
**Facultad de Química, UNAM. Ciudad Universitaria. Del. Coyoacan. México, D. F. C. P. 04510*

H. F. López
Materials Department, University of Wisconsin-Milwaukee. P. O. Box 784, Milwaukee, Wisconsin 53201, USA.

ABSTRACT

There have been numerous works aimed to elucidate the active mechanisms involved in the intergranular stress corrosion cracking (IGSCC) of Ni-based alloys. In particular, it has been found that hydrogen might play a dominant role in either crack initiation and/or crack growth during the IGSCC of Inconel 600 when exposed to pressurized water reactor (PWR) environments. In the present work, pre-cracked compact self-loaded modified WOL specimens were employed in order to investigate the IGSCC resistance of a heat-treated Inconel alloy 600. Various heat treatments were performed in order to obtain several microstructural initial conditions. Moreover, the potential drop technique was used to monitor crack propagation in a simulated PWR environment under constant temperature. It was found that the IGSCC susceptibility can be linked to the exhibited microstructures, specifically the grain boundary carbide precipitation reactions (carbide free, low-decorated or semi-continuous grain boundaries). In particular, the microstructures which induce relatively low crack growth rates were associated with the development of significant plastic deformation at the crack tip. In addition, some common features were found between the IGSCC performance and the pre-fatigue cracking conditions. For this purpose, the fatigue crack growth properties of this alloy were also evaluated using the ASTM E 606-92 Standard.

KEYWORDS: IGSCC, Alloy 600, Heat treatment, Hydrogen

INTRODUCTION

Inconel alloy 600 is currently employed in steam generator tubing components for pressurized water reactor (PWR) environments [2]. The PWR environment consists of hydrogen-supersaturated steam. Hydrogen can also

be generated or involved during intergranular stress corrosion cracking (IGSCC) [3]. Hence, it is important to establish the role of hydrogen in these environments and its interaction with the grain boundaries (gbs) and grain boundary (gb) precipitates. According to the literature, Inconel alloy 600 exhibits IGSCC under PWR operating conditions, particularly in the solid solution condition [4-10]. It has been reported that elevated hydrogen concentrations are build up in Ni-based alloys which easily exceeds Sievert's law predictions (up to 20 to 80 ppm atomic hydrogen [8,9]). In turn, this indicates that there are effective hydrogen trapping sites, which can influence the potential alloy susceptibility to IGSSC.

The type and density of hydrogen trapping sites can be modified by heat treating [11]. Hence, hydrogen permeation in Inconel alloys is expected to be strongly influenced by the microstructure and the type and distribution of carbide phases. Accordingly, it is important to establish the possible interactions between any absorbed atomic hydrogen and the exhibited alloy microstructure.

In Ni-base alloys, it has been recognized that the grain boundary chemistry and its microstructural heterogeneities are key factors in the inherent potential for environmental degradation [12]. However, clear answers for the possible relationships between the grain boundary chemistry and the IGSSC susceptibility are still not available [13]. In this work, the role of heat treating on the exhibited IGSSC susceptibility of alloy 600 in simulated PWR environments. In particular, the resultant IGSCC is discussed in terms of the grain boundary carbide coverage induced by the implemented heat treatments.

EXPERIMENTAL

The Inconel alloy 600 used in this work was supplied in a 1 inch plate thick from Inco Alloys Int. Table 1 shows the chemical composition of the Inconel 600 alloy in the as received (AR) condition.

Table 1. Chemical composition of the Inconel 600 (wt %).

C	Cr	Fe	Mn	Si	Cu	Ni
0.08	15.7	6.9	0.2	0.007	0.05	Balance

Inconel alloy samples of 1cm x 1cm x 1 cm were cut and then heat treated at 600°C and 800°C for 30 minutes followed by water cooling. In addition, a mill annealing (MA) treatment was implemented that consisted of heating at 930°C for 1 hour and then air cooling. Table 2 shows the mechanical properties performed for the Inconel alloy in the AR and heat treated (HT) conditions.

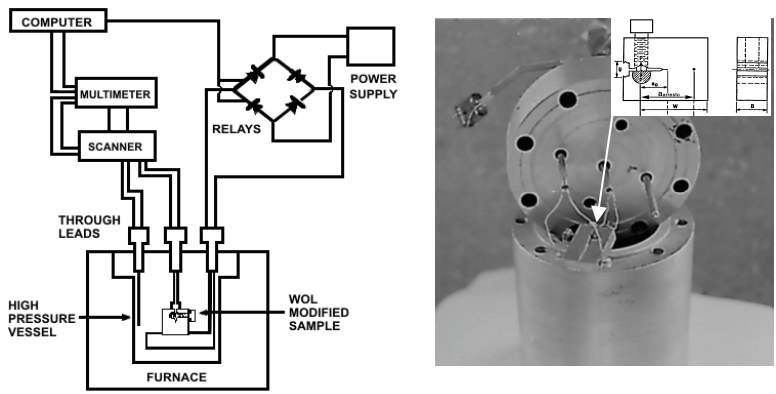
Crack growth tests in simulating PWR environments were carried out by introducing modified wedge opening load (M-WOL) specimens in a high

pressure autoclave. The testing parameters were (a) a temperature of 300°C,(b) a pressure of 5 kg/ cm^2 and (c) an applied load of 95% of the yield strength (σ_y). Figure 1 shows schematically the experimental setup. Crack growth was monitored using the potential drop technique [14]. Microstructural characterization was performed using scanning and transmission electron microscopy (SEM-EDS JEOL-6400 and a JEOL 2010 TEM microscopes).

Fatigue testing was performed in a rotating beam machine under similar stress conditions to the ones employed in the IGSCC tests.

Table 2. Mechanical properties of AR and HT Inconel 600

Material	Temperature ºC	Time min	Cooling media	σ_y MPa	E GPa
AR	---	--	---	407	255
MA	930	60	Air	384	120
HT	600	30	Water	285	198
HT	800	30	Water	267	159



(a) (b)

Figure 1. (a) Experimental setup and (b) exposed M-WOL sample.

RESULTS

It was found that heat treating had a strong effect on the exhibited Inconel 600 microstructures. In the MA condition, it was found that the grain boundary carbide precipitation was maximum. In this condition, the grain structure was equiaxial with some grains developing annealing twins. Heat treating at 930 ºC (MA) resulted in grain boundaries with very few carbide coverage. Figure 2 shows the exhibited microstructures in the AR and HT conditions.

The experimental outcome on crack growth in simulated PWR environments indicated that the alloy resistance to crack propagation is significantly improved in the MA and the 800°C HT. These samples were found to exhibit the longest incubation and testing times, and hence the lowest crack growth rates. Moreover, the most susceptible condition was found in the 600°C HT specimen. Table 3 gives the results of crack propagation rates for the various implemented HTs. Figure 3 shows the exhibited crack paths. In the case of the AR (3a) and MA (3b) conditions, the cracks exhibit an almost lineal trend. However, there is a slightly change in the total crack length which can be attributed to strain hardening as a result of the initially high stress (95% σ_y). Apparently, hydrogen diffusion alone is not enough to induce an intergranular crack path. In addition, stepwise crack growth was observed that can be related to the presence of relatively high precipitate densities in the matrix of the alloy in the MA condition (3b).

In the 600°C HT condition (3c), the initial crack path seemed to be induced by a combination of high mechanical stressing coupled with crack branching from the he main crack path, all of intergranular nature. Alternatively, it was found that in the 800°C HT condition, crack initiation and growth start at the base of the wedge, with multiple crack paths interconnected to the main crack (3d).

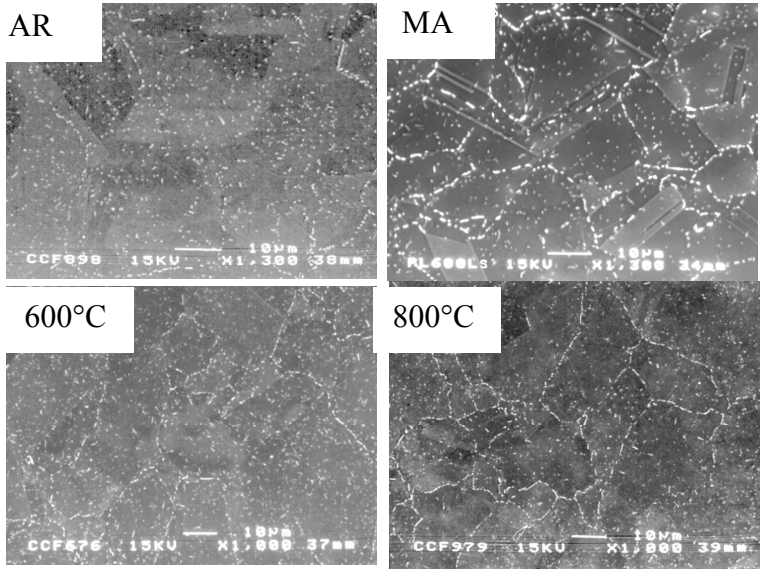


Figure 2. Exhibited microstructures in (a) AR, (b) MA, (c) 600°C HT and (d) 800°C HT specimens.

Table 3. Crack growth rates in AR and HT specimens exposed to PWR environments

Condition	K_I MPa $\sqrt{m}$	K_{ISCC} MPa $\sqrt{m}$	a_o mm	a_{arrest} mm	Crack size, mm	t_{inc} hrs	t_{arrest} hrs	t_{tot} hrs	COD m	da/dt m/s
AR	49.49	39.10	11.28	11.35	0.07	72	384	456	1.59*E-4	1.72*E-11
Mill annealed	46.51	36.36	11.25	11.26	0.014	720	720	720	3.31*E-4	1.86*E-12
600°C	35.18	34.01	11.45	12.60	1.15	168	240	408	1.48*E-4	7.01*E-10
800°C	34.78	33.81	11.12	11.19	0.075	720	720	720	9.98*E-4	2.27*E-11

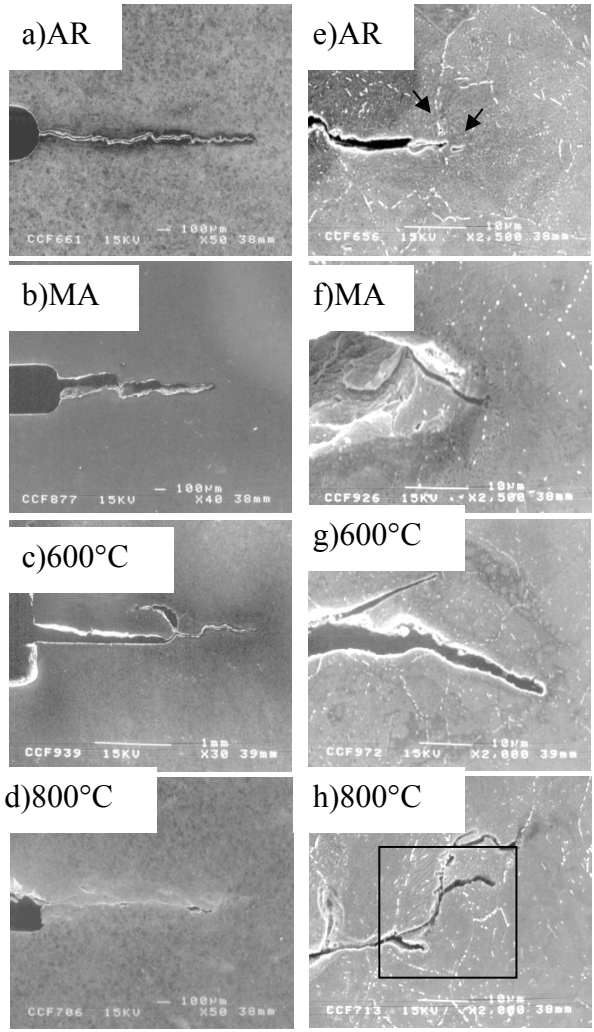


Figure 3. (a to d) Exhibited crack paths for the AR and HT specimens and (e to h) detail of corresponding crack tips.

In the AR condition, SEM observations indicated that the crack was intergranular and that crack arrest is likely in the vicinity of intersecting grain boundaries (3e). In addition, the development of fine grain boundary cavities was found to occur probably due to the interaction between plastic deformation bands (arrows) and the grain boundaries. In the MA condition (3f) accelerated material dissolution bounding the crack tip was observed. Alternatively, the 600°C HT exposed specimen (3g) shows a bounded crack tip and the presence of crack ramification. In the 800°C HT condition (3h), evidence significant plastic deformation was found as a result of the interaction of slip bands with the crack tip front. In addition, crack branching and grain boundary cavitations were observed along the crack path (see Fig. 3h).

From TEM observations on the AR specimens (Fig. 4a) it was found that the matrix consists of a structure with highly disperse precipitates of the $Cr_{23}C_6$ and Cr_3C_2 types. In addition, discontinuous grain boundary precipitation with Cr_7C_3 type and CrS particles was observed in the AR condition. Similar precipitates were found in the 600°C HT condition (Fig. 4b) and in the 800°C HT condition (Fig. 4c). In all the cases, grain boundary carbides were present in the matrix structure but the main difference is the extent of grain boundary precipitate coverage.

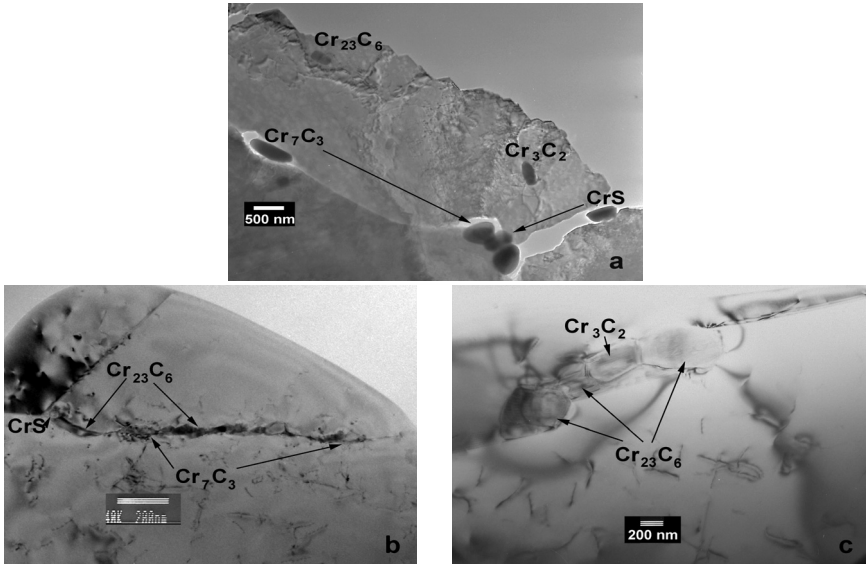


Figure 4. Exhibited Inconel alloy precipitates, type and location in (a) AR, (b) 600°C HT and 800°C HT conditions.

Preliminary fatigue testing results on the AR and HT specimens are summarized in Table 4. From these results it is evident that the 800°C HT

condition (>10^7 cycles) exhibits the highest fatigue resistance, which is consistent with the highest IGSCC resistance found for the same heat treatment. Based on these observations, it is likely that some of the active mechanisms in either fatigue or SCC might have some very close similarities. Accordingly, the active fatigue mechanisms are being investigated in an attempt to elucidate possible contributions to the proposed mechanisms for crack propagation.

Table 4. Fatigue testing results.

Condition	Applied Stress $\%\sigma_y$	Load Kg-m	Cycles	rpm	Ø Minimum (cm)
AR	95	1.03*E-1	7.3*E5	485	0.3
Mill Annealed	95	1.15*E-1	6.6*E5	485	0.31
600°C	95	5.76*E-2	3.4*E6	485	0.28
† 800°C	95	6.91*E-2	1.0*E7	485	0.3

† This test was suspended because there is not fatigue fracture.

CONCLUSIONS

- An Inconel alloy in the as-received (AR) condition was heat treated and the resultant microstructures indicated an increase in the relative volume fractions of inter-trans precipitates in comparison with the AR condition.
- The precipitates found were of the type: Cr_7C_3, $Cr_{23}C_6$, Cr_3C_2 and CrS.
- The 600°C HT sample condition was more susceptible to crack growth when compared with the other HT conditions.
- The 800°C HT sample condition was less susceptible and had a better performance in stress corrosion cracking PWR environments.
- Apparently, relatively high work hardening at the crack tip regions was closely related to the time for crack initiation. In turn, this lead to increasing crack growth rates in the more susceptible microstructures
- The present work provides evidence for a strong correlation between the fatigue strength properties and the SCC behavior for similar microstructures obtained by heat treatment.

ACKNOWLEDGMENTS

The authors want to acknowledge the technical assistance of Mr. Anselmo Gonzalez and to Mr. Abraham Verdiguel for the fatigue testing. Also we acknowledge the grants 42454-A1 and 44568-Y from Conacyt.

REFERENCES

1. S. R. Novak and S. T. Rolfe. Journal of Materials Vol. 4, No. 3, September 1969, p. 701-728.
2. Krystyna Stiller. Intergranular precipitation in Ni-Cr-Fe alloys. Surface science 266 (1992), p. 402.

3. Xing-Hong Luo, Mahmoud Habashi. Effect of environmental hydrogen on tensile behavior of inconel 690. Hydrogen effects on material behavior and corrosion deformation interactions, TMS (2003), p. 409-410.
4. G. P. Airey, Corrosion, 35, (1979), pp. 129-135.
5. S. Matshumima, Y. Shimizu, Transactions of the Japan Institute of Metals, 24, (1983), pp. 149-153.
6. N. Totuska, E. Lunarska, G. Grangnolino, and Z. Szklarska-Smialowska, Corrosion, 43, (1987), pp. 505-14.
7. C, Shen and P. G. Shewmon, Metall. Trans. A, 21A (1990), pp. 1261-1271.
8. P.G. Shewmon and Y. Shen, Metall. Trans. A. 22A, (1991), pp. 1857-1864.
9. T. Magnin, N. Renaudot, F. Foct, Materials Transactions, JIM, (2000), pp. 210-218.
10. H. F. Lopez, A. Mehboob, J. L. Albarran and L. Martinez, Conf . Proceedings, Hydrogen Effects on Materials behavior and Corrosion deformation Interactions, Eds: N. R. Moody, A. W. Thompson, R. E. Ricker, G. W. Was and R. H. Jones, TMS, Moran Wyoming, 2002, pp. 989-998.
11. D.F. Taylor, Corrosion, Vol.35.p. 550 (1999).
12. G.S. Was. Grain-Boundary Chemistry and Intergranular Fracture in Austenitic Nickel – Base Alloys. Corrosion. Vol. 46, No. 4. April 1990., 319-320.
13. G.P. Airey, A.R. Vaia, and R.G. Aspden, Nucl. Technol. 55(1981), pp. 436-448.
14. W. F. Deans and C. E. Richards. Journal of Testing and Evaluation, 7, p. 147.

Effects of Hydrogen on Materials
Proceedings of the 2008 International Hydrogen Conference
Brian Somerday, Petros Sofronis, Russell Jones, editors, p 275-283
Copyright © 2009 ASM International®
All rights reserved.
www.asminternational.org

HYDROGEN SOUR ENVIRONMENTS CONDITIONS FOR MICROALLOYED PIPELINE STEELS CRACKING

S. Serna, F. Cruz-Hernández, J. Colín, A. Torres-Islas
CIICAp-FCQeI-UAEM, Av. Univ. 1001 Col Chamilpa CP 62209, Cuernavaca, Morelos México

B. Campillo
ICF-FQ-UNAM, Av. Univ. 1001 s/n Col Chamilpa CP 62209, Cuernavaca, Morelos México

A. Fragiel
PDVSA, Av. Libertador Caracas Edif. Petróleos de Venezuela Torre Este, La Campiña, Caracas, Gran Caracas Venezuela

ABSTRACT

Microalloyed pipeline steels were evaluated varying the concentration of H_2S by means of hydrogen embrittlement tests at room temperature and 50 ºC, using Linear Elastic Fracture Mechanics MWOL (Modified Wedge Open Loading) specimens to measure its cracking susceptibility and propagation. H_2S concentration was found to be an important factor that controlled the extent of hydrogen uptake and embrittlement at crack tips. Threshold stress intensities (K_{Ith}) were obtained for each condition, and the optimal H_2S concentration for minimizing the risk of hydrogen embrittlement as a by-product of corrosion was established. The different steels microstructural features such as, grain boundaries shape, dislocations, and precipitation distribution proved to play an important role for the cracking susceptibility of these microalloyed steels, being more remarkable at room temperature.

KEYWORDS: crack growth, sour environment conditions, microalloyed steel, hydrogen evolved, NaCl-H_2S concentrations

INTRODUCTION

For transportation of oil and gas which contain hydrogen sulfide (H_2S), the application of pipeline steels are limited due to mechanical and corrosion problems induced by hydrogen. Some requirements for transmission of oil and sour gas through pipelines include good weldability and fracture toughness [1]. In order to fulfill API grades specifications pipeline steels have to achieve the best possible combination of strength and toughness through optimization of alloy design in combination with thermomechanical

processing. In recent investigations [2-4], it has been shown that the demanding properties necessary for pipeline steels can be obtained by low-C, low-Mn and Nb containing steels that are characterized by fine-grained polygonal ferrite, acicular ferrite, and ferrite with lower bainite microstructures.

On the other hand NACE solution is widely used to evaluate materials that would be installed as pipelines and storage tanks that had to work under sour environments. NACE solution was designed to yield worst conditions in which materials could be placed [5]. However, field conditions could be less severe than NACE solution but can also cause the failure of steel components over time. Is has been a major concern regarding the set-up conditions or the extent of stress level in which materials safely work without developing a crack of a suitable length that give rise to a failure in a particular environment. Although is known that H_2S concentration increases the hydrogen content in steels [6], there is no information that considers the role of H_2S and NaCl in different concentrations in order to induce cracking by means of corrosion or hydrogen embrittlement mechanisms. By increasing pH and working temperature conditions [7, 8] are known to control the deleterious hydrogen effects in steel under sour environments; here the microstructure and hydrogen permeability rate behavior of the steel may play a key role in order to resist hydrogen induced cracking [9]. H_2S and NaCl concentrations within pipelines could be different from one location to another, conferring the conditions to increase or lower the generation and absorption of atomic hydrogen, which may cause cracking in susceptible steels by hydrogen embrittlement.

Hence, it is important to elucidate the limiting conditions (i.e. H_2S-NaCl concentration) to lower corrosion levels and achieve an acceptable risk for hydrogen embrittlement. The aim of the present work is to investigate the extent of cracking by corrosion and hydrogen embrittlement mechanisms of two API X52 microalloyed pipeline steels with classical microstructures in different sour environments, ranging from high H_2S-NaCl concentrations to low H_2S-NaCl concentrations under room temperature and real steel operation temperature condition of 50 ^{0}C.

EXPERIMENTAL

Two API X52 microalloyed pipeline steels used in sour gas transport in Mexico were evaluated in the as received condition, having yield strengths of 350 MPa. The composition of steels designated as X52E and X52T are shown in Table 1 in wt-%.

Steels microstructures were reported elsewhere [9], for steel X52E ferritic-pearlitic and for steel X52T an acicular ferrite with carbide and bainite patches preferentially at grain boundaries.

Table 1, steels chemical composition in wt %

Steels	C	Si	Mn	P	S	Mo	V	Nb	Ti	Al
X52E	0.06	0.30	1.05	0.013	0.002	0.008	0.05	0.05	0.02	-
X52T	0.075	0.334	0.823	0.013	0.003	-	0.031	-	0.02	0.021

Different test solutions were used for 30 days for assessing steels crack growth by hydrogen embrittlement at 50 ^{0}C: 1) 1500 ppm (parts per million in wt%) of H_2S dissolved in distilled water and 2) 500 ppm of H_2S dissolved in distilled water varying the NaCl concentration in 50,000, 300 and 3 ppm. The pH was between 3 and 4. These solutions resulted from a sampling carried out in different zones of installed API X52 microalloyed pipelines in Mexico. The NACE solution consists of 1500 ppm of H_2S dissolved in distilled water and 50,000 ppm of NaCl at room temperature was also reported for comparison [9]. All solutions were purged with argon.

Crack growth tests were carried out using MWOL specimens [10] in the T-L orientation of the pipelines at free corrosion potential to measure the threshold stress intensity for hydrogen embrittlement (K_{Ith}) in both steels. Each specimen was pre-fatigued to give a short microscopically sharp pre-crack. The initial crack tip stress intensity $K_{I,}$ was calculated from the following relationship [11], $K_I = (YP)/(B\sqrt{a})$. Where Y is potential series as a function of the crack length, P is the applied load, E is Young's modulus of the material, and B is the specimen thickness. The specimen thickness B (12.5 mm) was designed to minimize the time taken for a uniform hydrogen concentration to be established, while satisfying the plane strain criterion [11]. The specimens were loaded to give initial stress intensities close to 45 and 41 MPa.m $^{-1/2}$ for X52E and X52T steels respectively. This K_I values corresponds to 95% of the steels K_{Ic} values determined by ASTM E399 Standard. The specimens were loaded just before exposure to the tests solutions for 30 days, as already mentioned, in the laboratory.

Optical measurements of the crack lengths were made after the MWOL specimens were removed at the end of the tests. The notch region was cleaned of corrosion products using 60 up to 1200 grid silicon carbide paper. The final crack length was measured on both sides of the specimen and the mean length was calculated and used to determine steels K_{Ith} values. The K_{Ith} value was established from the following equation [11]: $K_{Ith} = VE\ [B/(B_n \times a_{arrest})]^{1/2}[C_3/C_6]$. Where E is the Young´s Modulus, V is the distance displaced at the mouth of the specimen, a_{arrest} is the maximum propagation distance of the crack, C_3 and C_6 are potential series as a function of the crack length a measured from the line load.

RESULTS AND DISCUSSION

The SSC (Stress Sulfide Cracking) of pipeline steels can be explained by the following mechanism, when H_2S is in contact with water it can dissociates into HS^-, H^+, $2H^+$ and S^{2-}then a corrosion reaction takes place with steel forming iron ions in anodic sites and hydrogen reduction in cathodic sites over the steel surface, in accordance to the following overall reaction [12]:

$$_xFe^{2+} + _yHS^-(aq) \rightarrow Fe_xS_y + _yH^+ \qquad (1)$$

Ought to the presence of HS^- ions, the recombination of atomic hydrogen to produce molecular hydrogen is inhibited. So, hydrogen can diffuse in an easier form into the steel, intensifying any embrittlement effect. The confirmation of permeated hydrogen was evidenced from the presence of blisters, second micro-cracks, and quasi-cleavage fracture [13].

Figure 1a shows corrosion potentials vs Ag/AgCl reference electrode obtained by means of linear polarization resistance (LPR) tests. From the figure, it is observed that for both steels in NACE solution under room temperature their corrosion potentials were less negative, suggesting that raising temperature to 50 °C more hydrogen can be evolved. However, this tendency disappears when 100 ppm H_2S concentration exist. At this concentration steels could have the lowest hydrogen cracking susceptibility due to their lower negative potentials. Also, it is noticeable that in all environments, excluding the 100 ppm of H_2S condition, steel X52E had more negative potentials. So, it was expected that more hydrogen could evolve, possibly increasing the hydrogen cracking susceptibility of this steel. The corrosion potential tendency over the variation of H_2S concentration is clear as seen before, but when the NaCl concentration varies while keeping steady H_2S concentration, the tendency in the corrosion potential is not clear.

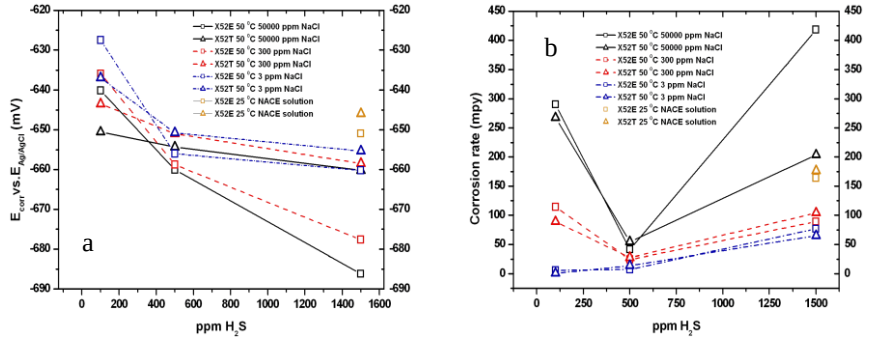


Figure 1. a) Free corrosion potentials and b) Corrosion rates for steels under several sour environments conditions

Corrosion rates illustrated on Fig 1b in NACE solution at room temperature for both steels are lower than at 50 ^{0}C. However, when H_2S concentration decreases this tendency disappears, being the corrosion rates lower until 100 ppm H_2S concentration is reached. Then the corrosion rates increases as the NaCl concentration is incremented. This behavior indicates that S^{2-} ions are more reactive to iron than Cl^- ions and that these ions depend on S^{2-}ions behavior to participate in the steel corrosion and upon NaCl concentration. Thus, the H_2S concentration controls the steel corrosion rates and the hydrogen generation behavior. Under these environments and in relation to lower corrosion rates values, the protective corrosion products could be evolved in steels surfaces. Its width and evolution time depends on the steel-environment interaction. As a result of the formation of these corrosion products it can be distinguished two stages over the general corrosion process. On the first stage a charge transfer process with possible generation of surface protecting corrosion products, that in these environments it could be made of FeS, plus the evolution and diffusion of embrittlement species toward the metal-environment interphase. On the second stage the diffusion of embrittlement species has to be through these corrosion products. The general corrosion process is limited due to the transport of embrittlement species which may induce the formation or not of a protective film (corrosion products). For example, limiting the transport of hydrogen cations to steels surfaces by a protective corrosion products film prevent a cathodic charge transfer to evolve atomic hydrogen. Then, any further corrosion and embrittlement processes are inhibited, unless the film is broken by mechanical, chemical factors or poor adhesion to steel surface. From these results it can pointed out, that even in environments with less H_2S concentration could exists hydrogen evolution. This hydrogen can be transported towards steels crack tip regions, contributing for its growth. On the other hand, a strong competition is expected between steel dissolution and hydrogen diffusion during the cracking process in the condition of highest corrosion rates.

Crack growth rates are shown in Fig 2a, it is observed that the fastest crack growth for both steels take place in NACE solution at room temperature and crack propagation present the same behavior for both steels. This is in agreement to the general acceptance that the worst working condition for cracking is at room temperature.

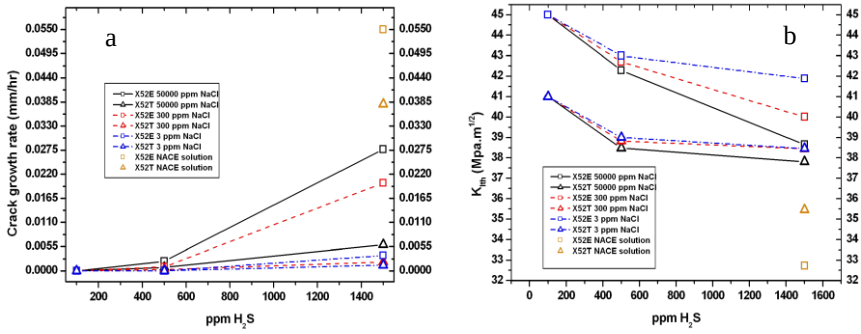


Figure 2. a) Crack growth rates and b) K_{Ith} values for steels under test solutions at 50 ºC, only tests at NACE solution were carried out at room temperature.

The crack tip for X52T steel presented a blunted morphology showed elsewhere [14]. This morphology can be attributed to its bigger corrosion rate as seen in Fig 1b with respect to steel X52E.On the other hand from the same Figs, the following tendency is fulfilled at 50 ^{0}C for both steels: at a steady H_2S concentration increasing the content of NaCl the crack length increases too, these could be explained ought to the corrosion potential that can be increased related to the (H^+), (H_2S), and (Cl^-) amounts as well to the raise in temperature, more over either S^{2-} or Cl^- ions can encourage steel dissolution [15]. The H_2S action can be attributed to its acidification contribution accelerating corrosion rates, even though a small concentration is present [16].

Related to corrosion rates H_2S concentration dictates the cracking behavior, and as seen from Table 2, by reducing H_2S concentration to 500 ppm, the crack growth is reduced for the two steels upon NaCl concentration. Therefore, the crack growth is consistent with the increment on H_2S concentration in all the environments no matter if X52E or X52T is being tested. Furthermore the increment of hydrogen concentration respect H_2S concentration is a consequence of the increase of corrosion rate that is in direct proportion to H_2S concentration. From these results it could be concluded that at 500 ppm of H_2S and 50,000 ppm of NaCl, steels crack growth becomes insignificant indicating that is irrelevant to carry out tests at lower H_2S and NaCl concentrations. Besides, under these conditions, if any crack growth rate takes place, their propagation is gone be principally by dissolution being imperceptible at least in a very long time period.

Table 2, steels crack growths under the different sour environments conditions

Environment		Work conditions	X52E steel crack growth (mm)	X52T steel crack growth (mm)
H_2S (ppm)	NaCl (ppm)			
NACE Solution		Room temperature	7.930	2.281
1500	50,000	50 ^{0}C	2.585	0.705
	300	50 ^{0}C	1.710	0.330
	3	50 ^{0}C	0.580	0.300
500	50,000	50 ^{0}C	0.370	0.285
	300	50 ^{0}C	0.155	0.110
	3	50 ^{0}C	0.000	0.000

For a chemical specie, like hydrogen, can produce embrittlement, their atoms have to be adsorbed, dissolved in the steels lattice and permeate into crack tip regions or at incipient crack sites. However, crack growth can be repressed by limiting the contact of the solution with the crack tip. Steels crack growth rates (Fig 2a) in environments with 1500 ppm of H_2S at 50 ^{0}C are greater by one and two orders of magnitude in the extreme case, that in any other working environments. This could be the result of having a major concentration of hydrogen ions, which can be more frequently in contact with crack tip zones. As a result, the severity of hydrogen effects depends on the skill of these atoms to be adsorbed on the steel surface. When long quantities of hydrogen could be present these can absorb easily on steel surfaces and be transported to plastic crack tip zones where can contribute to the steels cracking. Consequently, if hydrogen concentration in the crack tip is augmented or if hydrogen is directly adsorbed like atomic hydrogen then the crack growth rate is gone be incremented in a remarkable way [17]. Besides, in these environments, the presence of ions like HS^- in solution tends to retard the H_2 molecule formation incrementing hydrogen availability towards the crack tip. So, sour environments composition and concentration are key factors that affect the harshness of cracking at least in accordance with these results.

The parameter K_{Ith}, give a quantitative reference of the stress needed for both steels to be susceptible to hydrogen cracking under the several sour environments and working conditions tested as shown in Fig 2b. Here is clearly seen that NaCl do not have a appreciable contribution to the cracking susceptibility in both steels. And as already seen H_2S plays the leading roll again. Here, X52E steel which has the major yield strength present the lowers values of K_{Ith} that means a greater cracking susceptibility in relation to steel

X52T, in accordance with the increment on the corrosion aggressively of the environments (Fig 1). This becomes particularly significant at NACE solution at pressure and room temperature. As mentioned elsewhere [14] these major cracking susceptibility of steel X52E can be related to its manufacturing process and its microstructure.

CONCLUSIONS

For the two steels and in all environments and working conditions hydrogen evolution is possible. Corrosion rates are greater for X52E steel favoring hydrogen reduction than in steel X52T, so a major embrittlement could occur in this steel. In general at room temperature steel X52T have comparable crack growth rate, but can arrest crack propagation faster than steel X52E. Under working conditions of 50 ^{0}C the major crack growth rates switches to steel X52E and at lower H_2S concentrations crack growth rates tend to zero in both steels. Steel X52E proved to be more susceptible to cracking as shown by its lower K_{Ith} values in relation to steel X52T. These results indicate that NACE solution induce and make more susceptible to cracking both steels. Also showed that at lower concentrations mainly of H_2S and different temperature working conditions, with less severity, can induce cracking until 500 ppm of H_2S is reached at 50 ^{0}C, leading these to safer working conditions.

REFERENCES

1. I. De S. Bott, L.F.G. De Souza, J.C.G. Teixeira, P.R. Rios, Metall. Trans. A 36A (2005) 443
2. Ming-Chun Zhaoa, Ming Liu, Andrej Atrens, Yi-Yin Shan, Ke Yang Materials Science and Engineering A 478 (2008) 43–47,
3. Gyu Tae Park, Sung Ung Koh, Hwan Gyo Jung, Kyoo Young Kim Corrosion Science 50 (2008) 1865–1871
4. S.S. Nayak, R.D.K. Misra, J. Hartmann, F. Siciliano, J.M. Gray Materials Science and Engineering A in press
5. R. S. Tesseder, Petroleum Production and Refining, in: Corrosion Tests and Standards: Application and Interpretation, ed. R. Baboian, ASTM Manual Series, Philadelphia, (1995), p. 683
6. J. B. Geer. Factors Affecting the Sulfide Stress Cracking Performance of High Strength Steels, *Materials Performance* (1985) 11
7. B. Gu, J. Luo and X. Mao, *Corrosion* (1999) 96
8. L. M. Dvoraceck *Corrosion* **26** (1970) 177
9. S. Serna, H. Martínez, S. Y. López, J. G. Gonzalo-Gonzalez, J. L. Albarran, *International Journal of Hydrogen Energy*, 30 (2005) 1333 – 1338
10. S.R. Novak and S.T. Rolfe, Modified WOL Specimen for K_{Iscc} Environmental Testing, *J. of Materials,* Vol 4 (No. 3), 1969, p 701-728

11. A. J. Sedriks, Stress Corrosion Cracking, Test Methods, Corrosion Testing Made Easy Vol 1, (1990) p. 50
12. A. A. El-Yazgi, D. Hardie, *Corrosion Science* (1998) **40** 909
13. M.C. Zhao, B. Tang, Y.Y. Shan, K. Yang, Metall. Mater. Trans. A 34 (2003) 1089
14. S. Serna, B. Campillo, J. L. Albarrán, *Journal of Materials Engineering and Performance*, (2005) **14** 224
15. P. R. Rhodes, G.A. Weich, L. Abrego, "SCC Susceptibility of DSS in Sour Gas Environments", in: Duplex Stainless Steels, ed. R.A. Lula (Materials Park, OH: ASM), (1983) p.757,
16. H. Amaya, M. Ueda, "Effect of Test Solution Compositions in Corrosion Resistant of 13Cr Materials in a Little Amount of H_2S Environment" CORROSION/99, (Houston, TX: NACE), (1999) paper no. 585
17. H.G. Nelson, D.P. Williams, A.S. Tetelman, *Met. Trans.* (1971) **2** 953

Effects of Hydrogen on Materials
Proceedings of the 2008 International Hydrogen Conference
Brian Somerday, Petros Sofronis, Russell Jones, editors, p 284-291
Copyright © 2009 ASM International®
All rights reserved.
www.asminternational.org

ANALYTICAL METHODS FOR STUDYING CATHODIC HYDROGEN CHARGING INTO METALS UNDER COMPETITIVE ADSORPTION CONDITIONS

Faisal M. Al-Faqeer
Consulting Services Department, Saudi Aramco, Dhahran 31311, Saudi Arabia

Howard W. Pickering
Department of Materials Science and Engineering, The Pennsylvania State University, University Park, PA 16802, U.S.A

ABSTRACT
This paper describes the IPZ (Iyer, Pickering, Zamanzadeh) and IPZA (Iyer, Pickering, Zamanzadeh, Al-Faqeer) methods for analyzing the steady state hydrogen permeation data obtained by the well known electrochemical hydrogen permeation technique. They yield the (i) individual rate constants of the hydrogen evolution reaction (HER), k_1 and k_2, the hydrogen surface coverage, θ_H, and the hydrogen concentration in the metal at the charging side of the membrane, C_H^o, and (ii) the kinetic-diffusion rate constant, k, the absorption rate constant, k_{abs}, and the desorption rate constant, k_{des}, of the hydrogen absorption reaction (HAR). The IPZA also yields the surface coverage of a second adsorbent, θ_A. Data for iodide ion adsorption is presented in this paper. The IPZA-iodide coverage values, θ_I, were in reasonable agreement with θ_I- values determined by two other independent methods: electrochemical quartz crystal microbalance (EQCM) and the estimated corrosion current density (i_{corr}). This agreement is a powerful documentation of the validity of the underlying framework of the IPZ and IPZA analysis methods.

THE NEW IPZA ANALYSIS
An analysis was developed in 1989 to evaluate steady state hydrogen permeation data and describe the kinetics of the hydrogen evolution reaction (HER) and hydrogen absorption reaction (HAR), including the hydrogen surface coverage,[1] following the progress of earlier workers, e.g., Devanathan and Stachurski[2] and the Bockris group.[3] See two reviews for the details.[4,5] It was called the IPZ analysis, and assumes that only hydrogen atoms are adsorbed on the metal and that there is no interaction between them (Langmuir-type adsorption).[4] Its equations relate the charging, recombination and steady state hydrogen permeation current densities, i_c, i_r and i_∞, respectively, and the overpotential, η, of the HER. This analysis and another covering Frumkin-type adsorption were presented in this forum in 2002.[6]

The IPZ analysis has been used in cases where a species in the solution competes with hydrogen for the available adsorption sites on the metal surface. In these cases, use of the IPZ analysis brought into question the assumption that hydrogen atoms were the only adsorbed species on the surface. This led to a further modification of the IPZ which includes a second adsorbent that competes with hydrogen for surface sites called the IPZA analysis.[7,8] It was used to evaluate all the relevant parameters

including the coverage of the second adsorbent, which was hexamethyltetramine (HMTA)[7] or iodide ions[8] in these experiments. This paper will cover the iodide case and compare the results from the IPZA analysis with those from the earlier IPZ analysis given by Abd Elhamid, et.al.[9]

The IPZA analysis, like the IPZ analyses, assumes that the HER proceeds according to a coupled discharge-recombination (Volmer-Tafel) mechanism, Langmuir-type adsorption and the charging current density is the sum of the recombination and steady state permeation current densities ($i_c = i_r + i_\infty$). The IPZA analysis, unlike the IPZ analyses, recognizes that a portion of the surface may be covered by solution species other than hydrogen atoms as a result of a competitive adsorption.[7,8]

The Volmer–Tafel mechanism describes the HER in two steps: the discharge of the hydrogen ion on the metal surface to form an adsorbed hydrogen atom and the recombination of two adsorbed hydrogen atoms to form a hydrogen molecule that accumulates with other hydrogen molecules and bubbles off the surface,

$$H^+ + e^- + Fe \xrightarrow{k_1} Fe\text{-}H_{ads} \quad (1)$$

$$Fe\text{-}H_{ads} + Fe\text{-}H_{ads} \xrightarrow{k_2} 2Fe + H_2 \quad (2)$$

where $Fe\text{-}H_{ads}$ is an adsorbed hydrogen atom on the metal surface and k_1 and k_2 are the forward rate constants of reactions 1 and 2 of the HER. The HAR will take place as a side reaction of the HER where some of the adsorbed hydrogen atoms will absorb (H_{abs}) into the metal lattice and quickly establish the back equilibria,

$$Fe - H_{ads} \underset{k_{des}}{\overset{k_{abs}}{\Longleftrightarrow}} Fe + H_{abs} \quad (3)$$

where k_{abs} and k_{des} are the rate constants of the forward and backward directions of reaction 3.

Including the surface coverage of the second adsorbent on the membrane surface, θ_A, and assuming Langmuir-type adsorption, one has for the discharge and recombination steps of the HER[7,8],

$$i_c = Fk_1C_{H^+}(1 - \theta_H - \theta_A)\exp(-a\alpha\eta) \quad (4)$$

$$i_r = Fk_2\theta_H^2 \quad (5)$$

where C_H^+ is the hydrogen ion concentration in the electrolyte, a = F/RT, and α is the transfer coefficient. Rearranging equation 4, one has

$$i_c\exp(a\alpha\eta) = i_o'(1-\theta_H - \theta_A) \quad (6)$$

where $i_c\exp(a\alpha\eta)$ is referred to as the charging function[1,4] and is solely determined by conditions at the charging side of the membrane, and i_o' is given by[1,4]

$$i_o' = Fk_1C_{H^+} = i_o/(1-\theta_H^e) = i_o \text{ for } \theta_H^e << 1 \quad (7)$$

where i_o is the exchange current density of the HER and θ_H^e is the equilibrium hydrogen surface coverage.

For Langmuir-type adsorption, equation 5 is not affected by the coverage of the other adsorbents since it is the recombination of two hydrogen atoms which results in this current. Equation 5 is the same as in the original IPZ analysis. The i_∞ is given by Fick's first law

$$i_\infty = \mathrm{F} D \frac{C_H^o}{L} \quad (8)$$

Also, writing the rate expression for the HAR as given in the earlier literature,[2] and used in the original IPZ analysis,[1] i_∞ is given by

$$i_\infty = \mathrm{F} k_{abs} \theta_H - \mathrm{F} k_{des} C_H^o \quad (9)$$

where the absorption and desorption rate constants, k_{abs} and k_{des}, can be determined from permeation data.[5] Substituting C_H^o from equation 8 into equation 9 and rearranging gives[1,4]

$$i_\infty = \mathrm{F}\, k\, \theta_H \quad (10)$$

where k is the kinetic-diffusion constant and is given by[1,4,10]

$$k = \frac{k_{abs}}{1 + k_{des} \frac{L}{D}} \quad (11)$$

Equation 10 relates i_∞ to θ_H. Equations 5 and 10 are two major relations in the original IPZ analysis[1,4] that are not affected by the surface coverage of a second adsorbent under Langmuir conditions. Substituting θ_H from equation 10 into equation 5 and rearranging gives[1,4]

$$i_\infty = k \sqrt{\frac{\mathrm{F}}{k_2}} \sqrt{i_r} \quad (12)$$

Equation 12 shows the relation between the i_∞ and $\sqrt{i_r}$. The relation should be a straight line passing through the origin with a slope of $k\sqrt{\frac{\mathrm{F}}{k_2}}$ for the application of the IPZA analysis. This relation is exactly the same as derived in the original IPZ analysis[1,4] and previously experimentally observed,[11] and is not affected by the surface coverage of a second adsorbent.

Similarly, substituting θ_H from equation 10 and inserting i_o from equation 7 into equation 4 and rearranging gives

$$i_c \exp(a\alpha\eta) = i_o (1 - \theta_A) - \frac{i_o}{\mathrm{F}k} i_\infty \quad (13)$$

Equation 13 shows the relation between $i_c \exp(a\alpha\eta)$ and i_∞. This relation should be a straight line with a slope of $-\frac{i_o}{\mathrm{F}k}$ and an intercept of $i_o (1-\theta_A)$. It is similar to the relation in the original IPZ but also is different in that it includes the surface coverage of a second adsorbent. This added another parameter to the usual ones evaluated by the original IPZ analysis. There are two parameters in the intercept of equation 13. These are i_o and θ_A. De-convolution of these two parameters is a complication. However, if one of these parameters can be estimated or determined using another relation or another technique, all other kinetic and thermodynamic parameters of the HER and HAR can be evaluated using equation 12 and the modified relation, equation 13.

One of these parameters is i_o of the HER which is usually evaluated using the Tafel part of the polarization curve. This information is part of the electrochemical hydrogen permeation technique. The cathodic charging current and η are measured

at the charging side of the iron sample. Therefore, the construction of the Tafel plot to evaluate i_o can be done with data collected from the hydrogen permeation experiment with no additional work. The cathodic Tafel relation is,

$$\eta = \frac{2.303}{a\alpha}\log i_o - \frac{2.303}{a\alpha}\log i_c \qquad (14)$$

Plotting η vs. $\log(i_c)$ will give a straight line with a slope of $-\frac{2.303}{a\alpha}$, and an intercept of $\frac{2.303}{a\alpha}\log i_o$. From the slope, one can determine the transfer coefficient, α. Then, using the determined value of α as obtained previously in the IPZ analysis and the intercept of equation 14, i_o can be determined.

This shows that the kinetic and thermodynamic parameters of the HER and HAR, including θ_A can be determined using the IPZA analysis. In this paper θ_A will be the iodide ion, θ_I-.

The procedure to evaluate the different parameters is summarized as follows:[7]

1. From the slope of equation 14, α can be determined. From the intercept of equation 14 and knowing α, i_o can be determined.
2. Knowing i_o and the solution pH, k_1 can be determined using equation 7.
3. From the slope of equation 13 and knowing i_o, k can be determined.
4. From the intercept of equation 13 and knowing i_o, θ_A can be determined.
5. From the slope of equation 12 and knowing k, the k_2 can be determined.
6. From equation 10 and knowing k, θ_H at different i_∞ can be determined.

RESULTS AND DISCUSSIONS

Abd Elhamid, et.al.,[9] studied the effect of iodide ions on the kinetics of the HER and HAR on iron. It was found that the iodide ions inhibit the HER while enhancing the HAR, in agreement with earlier findings.[3,11] The IPZ analysis yielded values for the parameters: k_1, k_2, k, i_o, and θ_H. In using the IPZ analysis, any surface coverage of the iodide ions, θ_{I^-}, or other solution species, needed to be small in order for the results to closely approximate the actual situation. The new IPZA analysis was then applied to these same steady state hydrogen permeation data of Abd Elhamid, et.al.,[9] in order to obtain new values for these same parameters, as well as for θ_I-.

The k_1 and i_o values obtained using the IPZA analysis for increasing iodide ion concentrations in the electrolyte are shown in Figure 1, along with the corresponding values obtained from the original IPZ analysis in the Abd Elhamid paper.[9] The IPZA yields higher values for k_1 and i_o, in accord with equation 4 for which the $(1-\theta_{I^-}-\theta_H)$ term for competitive adsorption between the hydrogen and iodide ions in the IPZA analysis is smaller than the $(1-\theta_H)$ term in the original IPZ analysis at the same i_c and iodide ion concentration.

In Figure 1 both analyses (IPZA and IPZ) also show that k_1 and i_o decrease with increasing concentration of iodide ions in the charging solution. This is in accord with a lower fraction of available adsorption sites on the surface as θ_{I^-} (θ_A in equation

4) increases. It follows from equation 4 that in order to maintain the impressed current, i_c, the exponential term has to increase as the iodide ion concentration increases. That the exponential term increases is shown in the earlier experiments of Abd Elhamid, et.al.,[9] who report an increasing η of the HER with increasing iodide ion concentration.

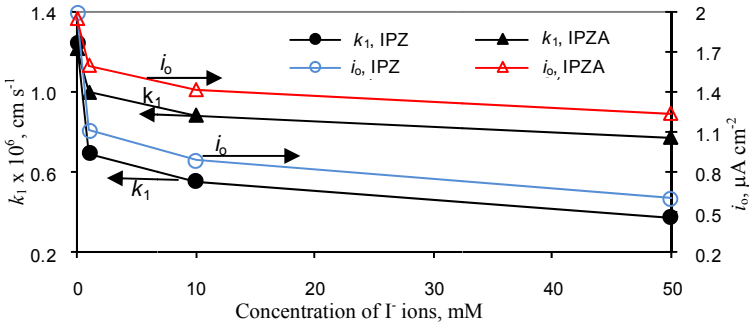


Figure 1: The k_1 and i_o values from the Abd Elhamid paper[9] using the original IPZ analysis, and these same parameters using the IPZA analysis in this paper.

A plot $i_c\exp(a\alpha\eta)$ and i_∞ yields straight lines with negative slopes and positive intercepts,[9] in accord with the IPZA analysis (equation 14). From the intercepts of these lines and the determined values of i_o, θ_{I^-} values were determined and are shown in Figure 2. These values of θ_{I^-} can be compared with those obtained using other independent experimental techniques: EQCM and the estimated corrosion current densities (potentiodynamic technique) which are also shown in Figure 2.

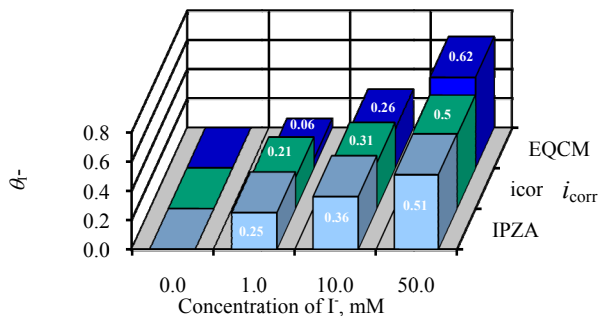


Figure 2: Comparison of θ_{I^-} determined by the different techniques.

The corrosion current densities in the absence and in the presence of the iodide ions, i^o_{corr} and i^{inh}_{corr}, respectively, were estimated from the polarization curves and θ_{I^-} was estimated from these current densities using equation 16,[12]

$$\theta_{I^-} = \frac{i^o_{corr} - i^{inh}_{corr}}{i^o_{corr}} \qquad (16)$$

Figure 2 shows a reasonable agreement which supports the possibility of using the new IPZA analysis when competitive adsorption occurs between hydrogen and

another solution species. A similar agreement of the surface coverage of the second adsorbent, iodide in this case, θ_{I^-}, obtained by the three different methods was also found for HMTA.[7]

The kinetic-diffusion constant, *k,* at different iodide ion concentrations was also determined using the slopes of the charging function plot[9] and the determined i_o values. The *k* values from the IPZA analysis in this paper are larger and show a stronger dependence on the concentration of iodide ions than in the case of the original IPZ analysis[9] as shown in Figure 3.

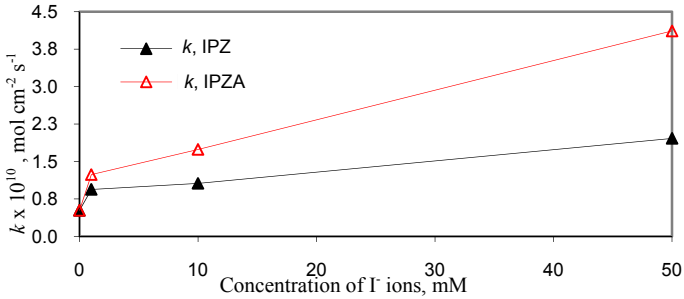


Figure 3: The k values from the original IPZ analysis[9], and the new IPZA analysis.

Both the IPZA and IPZ analyses show that *k* increases as the concentration of iodide ions increases in the charging solution, corresponding to an increasing tendency for hydrogen absorption to occur, i.e., partitioning of the recombination and absorption reactions (reactions 2 and 3, respectively) is in the direction of the latter (reaction 3) with increasing iodide ion concentration in the charging solution. Thus, *k* given in terms of k_{abs} and k_{des} in equation 11 increases with increasing iodide ion concentration, as shown in Figure 3.

Figure 4 shows the surface coverage of hydrogen, θ_H, at different iodide ion concentrations and η as determined using the calculated *k* from the IPZA analysis. These are compared in Figure 4 with the θ_H values obtained by Abd Elhamid, et.al.,[9] using the original IPZ analysis. Figure 4 shows that θ_H is smaller when θ_{I^-} is considered. Figure 4 also reveals that with both analyses the θ_H value decreases with increasing iodide ion concentration in the charging solution at the same i_c. It is also known from the data of Abd Elhamid, et.al.,[9] that i_∞ increases with increasing iodide ion concentration at a given i_c value. Thus, from equation 10 the increase in *k* dominates over the decrease in θ_H as i_∞ increases with increasing iodide ion concentration. One also sees in equation 8 that the increasing i_∞ means that C_H^o increases with increasing iodide ion concentration in the charging solution. Inserting an increasing i_∞ and C_H^o and decreasing θ_H into equation 9 reveals that k_{abs} increases and/or k_{des} decreases with increasing iodide ion concentration in the charging solution.

The relation between i_∞ and $\sqrt{i_r}$ shows straight lines passing by the origin in accordance with equation 12, as reported elsewhere.[7,8] Values of k_2 at different iodide ion concentrations were determined from the slopes of equation 12 and the determined k. These values and those calculated using the original IPZ analysis in the Abd Elhamid paper[9] are shown in Figure 5.

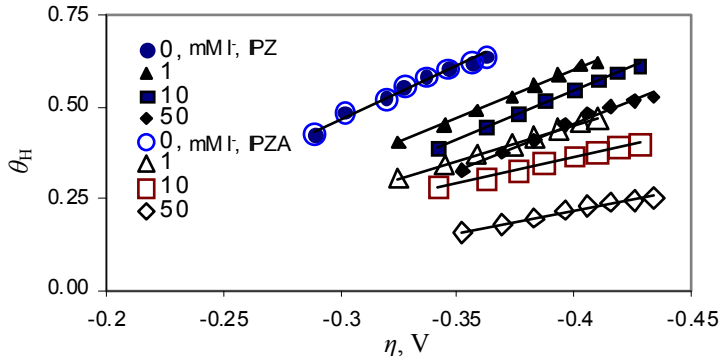


Figure 4: Values of θ_H for different iodide ion concentrations using the original IPZ analysis in the Abd Elhamid paper[9] and the new IPZA analysis[8].

The new IPZA analysis yields higher k_2 values than does the original IPZ analysis. This is in accord with the lower θ_H when iodide is also adsorbed on the input surface. The IPZA, but not the IPZ, recognizes the presence of another adsorbent on the input surface. This interdependence of k_2 and θ_H is illustrated in equation 5 which shows that k_2 is larger when θ_H is smaller for the same i_r (corresponding approximately to the same applied i_c value). Thus, the IPZA analysis is closer to the actual experimental conditions when a second adsorbent competes with hydrogen for surface sites than is the IPZ analysis.

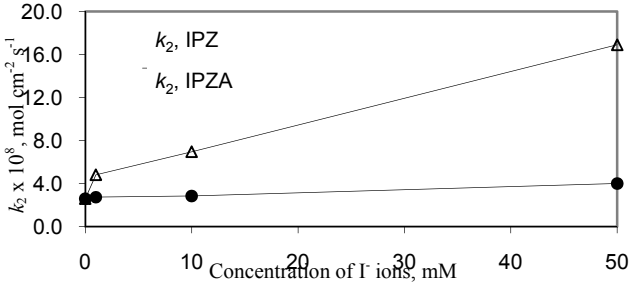


Figure 5: The recombination rate constants, k_2, from the original IPZ analysis in the Abd Elhamid paper[9] and from the new IPZA analysis in this paper.

Both the IPZ and IPZA analyses show that k_2 increases with increasing concentration of iodide ion but the IPZA indicates a stronger dependence on the iodide ion concentration than does the IPZ. That k_2 increases in spite of a decreasing θ_H on the input surface with increasing iodide ion concentration, is a consequence of the increasing η of the HER.[9]

CONCLUSIONS

Different analyses have been developed to study the kinetics of hydrogen entry into metals. The original IPZ analysis has been applied to steady state hydrogen permeation data to yield the individual rate constants, k_1, k_2, θ_H, C_H^o and k.[5] Values of k_{abs} and k_{des} of the HAR can also be determined from permeation data or in the case of metal/electrolyte systems of low hydrogen absorption into the metal from the measured HER polarization curve.[5]

The new IPZA analysis considers competitive adsorption between hydrogen and a second adsorbent, and has been applied to steady state hydrogen permeation data for iron in aqueous solutions containing either HMTA or iodide ions as adsorbents. The surface coverages of HMTA[7] and iodide ions[8] were obtained along with the other above mentioned parameters of the HER and HAR, and were in approximate agreement with θ_A values obtained using two other independent methods: EQCM and i_{corr} (polarization technique). Values of θ_H determined using the IPZA analysis which recognizes the presence of a second adsorbent on the input surface are lower than those determined by the original IPZ analysis which ignores the second adsorbent in the analysis, i.e., of the two analysis procedures the IPZA is expected to be closer to the actual conditions when competitive adsorption occurs.

REFERENCES

1. R. N. Iyer, H. W. Pickering, and M. Zamanzadeh, Journal of the Electrochemical Society 136:2463 (1989).
2. M. A. V. Devanathan and Z. Stachurski, Journal of the Electrochemical Society 111:619 (1964).
3. J. O. M. Bockris, J. McBreen, and L. Nanis, Journal of the Electrochemical Society 112:1025 (1965) and J. O. M. Bockris, J. L. Carbajal, B. R. Scharifker, and Chandrasekaran, Journal of the Electrochemical Society 134:1957 (1987).
4. R. N. Iyer and H. W. Pickering, Annual Review of Materials Science 20:299 (1990).
5. F. M. Al-Faqeer and H. W. Pickering, "Kinetics of Electrochemical Hydrogen Entry into Metals and Alloys", Modern Aspects of Electrochemistry, No. 37, R. E. White, B. E. Conway and C. G. Vayenas, Editors, pp. 1-54, Kluwer Academic/Plenum Publishers, New York 2004.
6. F. M. Al-Faqeer and H. W. Pickering, in International Conference on Hydrogen Effects on Materials Behavior and Corrosion Deformation Interactions (Hydrogen Meeting, Jackson Hole, WY) (N. R. Moody, ed.), TMS, Warrensville, PA, 2002.
7. F. M. Al-Faqeer, K. G. Weil, and H. W. Pickering, Journal of Electrochemical Society 150:B221 (2003).
8. F. M. Al-Faqeer, K. G. Weil, and H. W. Pickering, Electrochimica Acta 48:1331 (2003).
9. M. H. Abd Elhamid, B. G. Ateya, and H. W. Pickering, Journal of the Electrochemical Society 147:2258 (2000).
10. M. Ramasubramanian, B. N. Popov, and R. E. White, Journal of the Electrochemical Society 145:1907 (1998).
11. E. G. Dafft, K. Bohnenkamp, and H. J. Engell, Corrosion Science 19:591 (1979).
12. R. H. Hausler, in Corrosion Chemistry (R. F. Gould, ed.), American Chemical Society, Washington, D.C., 1979, p. 262 and R. H. Hausler, Corrosion 33:117 (1977).

Effects of Hydrogen on Materials
Proceedings of the 2008 International Hydrogen Conference
Brian Somerday, Petros Sofronis, Russell Jones, editors, p 292-299
Copyright © 2009 ASM International®
All rights reserved.
www.asminternational.org

THE IMPACT OF DISLOCATION DISTRIBUTION ON HYDROGEN EVOLUTION REACTION ON NICKEL METAL IN SULPHURIC ACID

J. Creus, H. El Alami, X. Feaugas
Laboratoire d'Etude des Matériaux en Milieux Agressifs, Université de La Rochelle, Av. Michel Crépeau, 17042 La Rochelle, France

ABSTRACT

The dependence of hydrogen adsorption on plastic strain has been studied on single and polycrystalline pres-stained nickel electrodes in H_2SO_4, 1M using linear voltametry. Dislocation emergence at atomic scale promotes the adsorption process in large range of plastic strain and strength path. The importance to consider dislocation distributions on the description of dislocation density effect on adsorption step has been illustrated.

INTRODUCTION

The damaging effect of aqueous media on the mechanical properties of face-centered cubic (fcc) metals has been well known for a long time. However, the rate-controlling steps that assist damage in media causing environment degradation remain a subject of much controversy. Particularly, hydrogen adsorption causes mechanical and structural degradation. In hydrogen embrittlement process, structural defects (dislocations, vacancies, grain-boundaries …) are known to interact with hydrogen atoms that lead to the modification or the loss of mechanical properties [1]. The first step of these interactions occurs at the interface of metallic structure and electrolytic medium during hydrogen adsorption step. The rate of hydrogen entry is determined by the surface coverage of adsorption atomic hydrogen as intermediate of the HER (Hydrogen Evolution Reaction) *via* the discharge-Tafel recombination and/or the discharge–Heyrovsky desorption. The most part of the adsorbed hydrogen reacts to give dihydrogen molecules evolving to medium and a fraction of the adsorbed hydrogen may diffuse into the metal. Thus knowledge of surface defects implication on absorption step seems to be of first importance to better understand atomic hydrogen entry in metallic structure. The earlier investigations on this subject conduce at 300 K on nickel samples seem demonstrate that dislocation emergence modifies the proportions of already existing sites: the number of low symmetry sites increases when plastic strain increases [2-4]. More recently, a particular attention has been devoted to kinetic and thermodynamic parameters (which characterize hydrogen adsorption and desorption [3,4]. The most relevant result of this last study is that dislocation density affects not only the number of actives sites but also energetic aspects of adsorption and desorption processes. Guided by the results

obtained in Ref. 4, the scope of the current study is to continue that work and to contribute in understanding the coupling between the mechanical state and the adsorption step. A thermo-kinetic approach is proposed to determine the influence of dislocation density and distribution on HER characteristic parameters as symmetry coefficients, activation enthalpies, and number of active sites associated with adsorption and desorption steps [3]. Different kinds of dislocation densities and distributions has been developed on single crystal and non-textured polycrystals nickel using tensile and cyclic loadings at different levels of plastic strain [5-6]. Surface roughness associated with slip emergence has been suppressed to study only dislocation emergence at atomic scale.

EXPERIMENTAL AND SIMULATIONS DETAILS

Experimental setup

The cathodic electrochemical behaviour of polycrystalline and monocrystalline nickel electrodes, plastically pre-strained under tensile and cyclic loadings is investigated in H_2SO_4 1M desaerated by argon. The different samples only considered to differ by their density and distribution of dislocation. Thus we consider polycrystal only as an average behaviour of each grain and discuss mainly the heterogeneous dislocation distribution at intra-granular scale than grain-boundaries effect. Some comment on this simple approach can be finding in precious work [4]. Consequently, the influence of tensile plastic strain and plastic strain amplitude is studied in term of density and distribution of reaction sites. The mechanical [5-6] and the electrochemical pre-treatment of nickel electrode performed after pre-strained sequence are described in detail in ref. [2-4, 7-9]. Particular attention was paid to the surface state before electrochemical investigation. Surface roughness associated with slip emergence is suppressed to study only dislocations emergence at atomic scale. Experimental polarization curves have been obtained using Solartron 1280 potentiostat on a potential range between 150 mV and -500 mV/SHE and on a temperature range between 288 K and 305 K. A set of current density-potential curves for different temperature is presented in figure 1a for unstrained polycrystalline nickel. The activity increases clearly with the temperature. Moreover, as revealed in the inset of figure 1b, two regimes are allowed which correspond respectively to a predominance of Volmer process (adsorption) and Heyrovsky process (desorption): from low potentials, the first linear domain hydrogen coverage rate slowly increases and in second domain observed in higher potential regime, the hydrogen coverage approach the value one. These two regimes have been observed on the all set of experiments performed in present issue. To determine the effect of plastic strain, non-textured poly-crystal (grain size equal to 168 μm), [135] and [001] single crystals pres-strained at different tensile plastic strain are considered (table 1). Moreover to complete this set of data, we have strengthened under cyclic loading polycrystalline sample (grain size equal to 18 μm) with a constant plastic strain amplitude of 3×10^{-4} which correspond

to a hardening stage II_0 [5, 10], a constant strain rate of 3×10^{-4} s^{-1} and a cyclic number equal to 5×10^3. As previously, extensive illustrate, the different levels of plastic strain are characterized by hardening stages (I-III and II_0 in present work) where dislocations features differ [5-8]. Stage I correspond mainly to planar/single slip activity with a quite homogenous dislocation distribution [8]. Multiple slip and cross slip generalization occur in stage II, which induce the formation of heterogeneous dislocation structures (tangles, dipolar walls polarized walls, and cells). In stage III, a recovery processes (cross-slip and/or climb) reduce the dislocation density and the thickness of the dislocation walls. Cyclic hardening stage II_0 corresponds to the formation of veins constituted by a large density of edge dislocation dipoles [6]. Despite this fact, on the basis to the high diversity of dislocation distributions, it seems reasonable, in first approach, to consider an equivalent structure as 2D pattern in each slip planes with a fraction of "hard phase" f_w [5, 12]. Consistent with the mean field approach adopted earlier [12-13], the dislocation patterns are represented by corresponding averaged properties of two-phase periodic composite: walls (w) and channel (c). The distribution of the dislocation associated with this microstructure is characterized by the thickness of the walls e, the inter-walls spacing λ, the fraction of walls f_W and the dislocation densities of respectively the wall and the channel: ρ_w and ρ_c (table 1).

Table 1: Different parameters which characterize the dislocation patterns issues to different kinds of strength paths. e is the thickness, λ inter-walls spacing, ρ_c and ρ_w the dislocation density in channel and wall respectivelly, fw the fraction of walls. (ρ =3.5±-0.5 10^{14} m^{-2} and f_w=23±3%)

Type	strain	e (nm)	λ (nm)	$\rho_c\,10^{14}$ (m^{-2})	$\rho_w\,10^{14}$ (m^{-2})	f_W (%)
[135]	γ_p=0.22	235	824	0.86	9.3	22
[001]	γ_p=0.25	200	600	0.44	9.5	25
Poly.tension	ε_p=0.05	220	930	0.85	10	19
Poly.tension	ε_p=0.34	104	419	0.88	12	24
Poly.cyclic	$\varepsilon_{pa}=3.10^{-4}$	500	1428	0.012	14	26

Thermo-kinetic analyze

Hydrogen Evolution Reaction (HER) is commonly described in acid media [2,3,14-15] by mechanism of hydrogen adsorption (Volmer step), H_2 electrochemical desorption (Heyrovsky step) and/or chemical desorption (Tafel step) and absorption of a part of the adsorbed hydrogen. In acid media, the HER on nickel can reasonably be described by a Volmer-Heyrovsky mechanism [2,3]:

$M + H^+ + e^- \Leftrightarrow MH_{ads}$ Volmer (V)

$MH_{ads} + H^+ + e^- \Leftrightarrow H_2 + M$ Heyrovsky (H)

$2MH_{ads} \Leftrightarrow H_2 + 2M$ Tafel (T)

$MH_{ads} + M_{subsurface} \Leftrightarrow M_{surface} + MH_{abs}$ Absorption (Abs)

According to modern aspects of electrochemistry [16,17] the HER step rates (v_i) will be expressed as a function of kinetic and thermodynamic parameters:

$v_i = \bar{k}_i f_i(a_{H^+}, \theta_i, \Gamma_i)$ with $\bar{k}_i = \kappa \frac{k_B T}{h} \exp\left(-\frac{\Delta G_i^* - \beta_i EF}{RT}\right)$

and $\Delta G_i^* = \Delta H_i^* - T\Delta S_i^*$, $\beta_i = \beta_i^H + T\beta_i^S$.

For each step i, the rate v_i can be described by f_i a function of a_{H^+} H^+ activity, θ hydrogen coverage rate, and Γ_i the number of active sites, and by a rate constant $\bar{k}_i$ in which k_B is Bolzman constant, h Plank constant, κ is a transmission coefficient generally taken as one, ΔG_i^* is the free energy of activation, β_i the symmetry factor and F is the Faraday constant. The Faradaic current density which crosses the solution/metal interface is then equal to: $j = -F(v_V + v_H)$ and the rate of coverage of adsorbed intermediate H_{ads} on metal surface is described by: $\frac{q}{F}\frac{d\theta}{dt} = v_V - v_H - 2v_T - v_{abs}$ with q the charge of a monolayer of H_{ads}. At steady state $\frac{d\theta}{dt}$ is equal to zero. The distinction between v_T and v_{abs} can not be accessible without permeation test. The only motivation of this work is to discuss the Volmer step (adsorption step) in relation with emergence of dislocations. The detail on the identification procedure and the evolution of the other HER steps, are provided in previous work [3]. Kinetic constants are rationalized to separate respectively potential E and temperature effects:

$\frac{k_V}{T} = \kappa \frac{k_B}{h} \Gamma_V \exp\left(\frac{\Delta S_v^*}{R}\right) \exp\left(-\frac{\Delta H_v^*}{RT}\right)$ with $\upsilon_V = k_V a_{H^+}(1-\theta) \exp\left(\frac{\beta_V EF}{RT}\right)$

By drawing $\ln(k_V/T)$ as a function of 1/T for each conditions (plastic strain, single crystal and polycrystal), the Γ_V the number of active sites, and the activation chemical enthalpy ΔH_V^* can be calculated with ΔS_V^* =-542 J $mol^{-1}K^{-1}$ [3] (figure 1c). In the following we posed V=ad.

RESULTS AND DISCUSSION

The figure 1b illustrates the fact that the adsorption regime occurs for lower potential than 250 mV/SHE. The strengthening conditions explored in this work (table 1), allow to an increase of electrochemical activity (current density) with defects at 200 mV/SHE: the ratio between pre-strained j and un-strained j(0%) current densities is

higher than one (figure 1d). This point has been extensively related in dissolution regime [7-9] and HER regime [2-4]. However the physical bases of this behavior stays unclear mainly in raison to the occurrence of a variety of concurrencies events. In recent years the work of our team has been focus on a direct correlation between crystallographic defects associated with dislocations density and electrochemical processes associated with HER [2-4]. An interesting thing we should notice from the set of curves in figures 2f and 2g is that we see clearly the increase of the number of active sites Γ_{ad}, and of the activation chemical enthalpy ΔH_{ad} as total dislocation density ρ is increased indicates a large sensitivity to mechanical state. If plastic strain leads globally to a promoting effect on adsorption efficiency [2,8], the activation effect is partially balanced by an increase of adsorption energy (figure 2g).

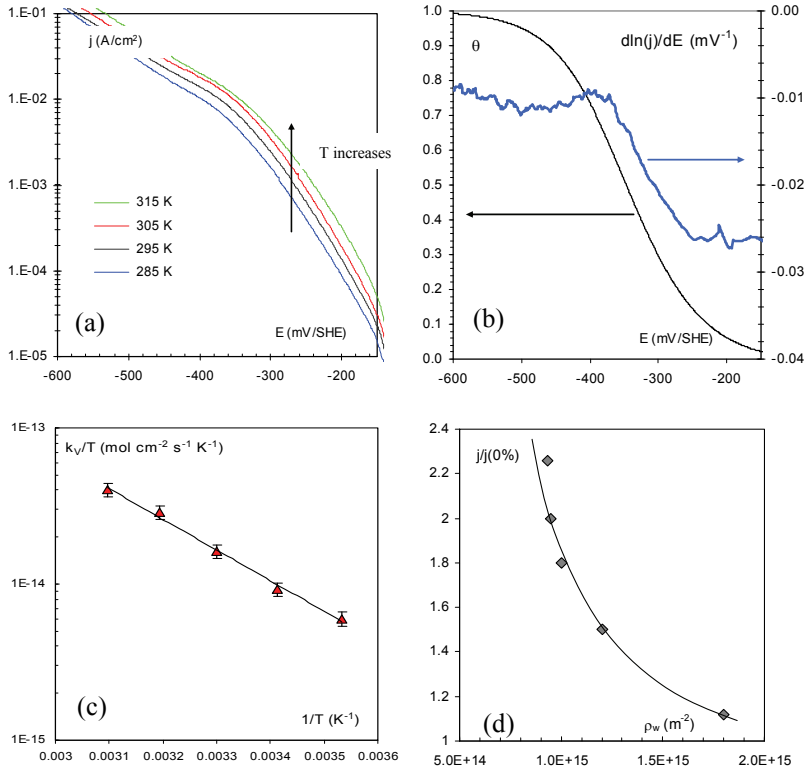


Figure 1: (a) Experimental temperature dependence of cathodic polarization curves. (b) Evolution of $d\ln(j)/dE$ *and hydrogen coverage* θ *as a function of potential E at 295 K for pre-strained polycrystal (*ε_p*=14%). (c) Dependence of Volmer kinetic constant* k_V *normalized by the temperature as a function of the ratio 1/T. (d) Evolution of ratio j/j(0%) as a function of dislocation density of the dislocation walls* ρ_w.

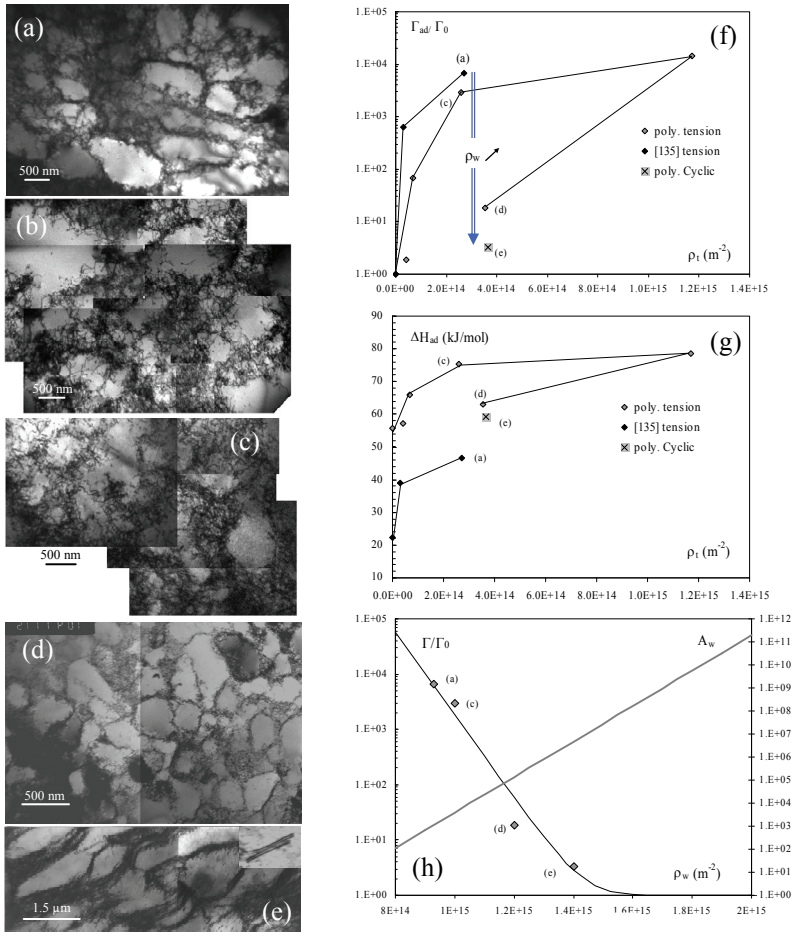


Figure 2: (a-e) Dislocations distributions for the different strength paths reported on table 1. (f) Dependence of the ratio between the number of adsorption sites for pre-strained Γ_{ad} and un-strained Γ_0 nickel as a function of total dislocation density. (g) Dependence of activation energy of the adsorption as a function of total dislocation density. (h) Evolution of Γ_{ad}/Γ_0 and A_w versus ρ_w.

Moreover, the complex evolutions of Γ_{ad} as a function of ρ for different conditions (single crystal and poly-crystal) can not allow to a direct correlation between the number of active sites and the number of dislocations. The number of active adsorption sites and the activation enthalpy increases with the increase of dislocation density for a homogeneous dislocation distribution ($\rho < 6.\ 10^{13}$ m^{-2}). This last point (the increase of activation enthalpy) is a de-activating effect which is hidden by the large increase of the number of adsorption sites. For large plastic strain, additional

insight into the relationship between plastic strain and adsorption process can be gained by considering the distribution of dislocations. This one depends classically to the plastic strain but also to the strength path. Figures 2a-e illustrated the fact that for a same total dislocation density ρ (3.5±0.5 10^{14} m^{-2}) and a same fraction of walls f_w (23±3%), different kinds of dislocation distribution can be find. In these conditions, the main part of dislocation density is concentrated in the walls. Thus it is obviously interesting to correlate the electrochemical activity with dislocation density in the walls (ρ_w). The figure 1d illustrates the decrease of current density with the increase of ρ_w. This result has significant implication, as it indicates an occurrence of a de-activation process when the dislocation density increases in the walls. More advanced thermo-kinetic treatment of electrochemical data offers the opportunity to discuss this point in term of number of active sites Γ_{ad} for hydrogen adsorption. Figures 2e and 2h show that the number of active sites decreases with the increase of the dislocation density concentrated in the walls. Consequently the fact that plastic strain promotes adsorption process is partially suppressed for high dislocation densities in relation to the idea that geometric and/or energetic disorder developed by concentration of dislocations in walls lead to the spacing of adsorption sites and so to a decrease in the number of active adsorption sites. Present results confirm our earlier approach performed without thermo-kinetic considerations [2]. To complete this analysis we use a simple model, recently developed to represent the number of adsorption sites created by emergence of dislocations [2,8]. We supposed that adsorptions sites associated with dislocations in channel are negligible comparatively to the ones associated with dislocations in the walls. Thus the ratio between the number of adsorption sites for pre-strained Γ_{ad} and un-strained Γ_0 can be expressed as a function of dislocation in the wall ρ_w: $\frac{\Gamma_{ad}}{\Gamma_0} = 1 + \frac{f_w}{A_w}\sqrt{\rho_w}$. A_w is a screening parameter which depends on the distance between two adjacent sites. A_w is an increase function of the dislocation density in the walls ρ_w (figure 1h) and follows a simple law: $A_w = 8.10^{-5}\exp(1.7710^{-14}\rho_w)$. Moreover, the activation process associated with dislocation density seems disappear for higher dislocation density than 1.6 10^{15} m^{-2}. The formation of polarized walls (figure 2d) and dipolar walls (figure 2e) offers the opportunity to storage a large dislocations density and to reduce adsorption step.

CONCLUSIONS

The importance to study the influence of dislocation patterning on adsorption step efficiency associated with Hydrogen Evolution Reaction has been demonstrated. The fact, to storage a large density of dislocations in walls induces geometric and/or energetic disorder which partially screens the activation process associated with dislocation emergence at atomic scale. The impact of dislocation density and distribution on absorption step is in progress.

ACKNOWLEDGMENTS

The authors thank the Centre Commun d'Analyse, Université de La Rochelle for electron microscopy facilities.

REFERENCES

1. Magnin, T., Advances in Corrosion-Deformation interactions, Material Science Forum, Trans. Tech Publications (1995), p. 202.
2. El Alami, H., Creus, J., Feaugas, X., *Electrochem. Acta*, vol. 51 (2006) pp. 4716-4727.
3. El Alami, H., Creus, J., Feaugas, X., *Electrochem. Acta,* Vol. 52 (2007) pp. 4004-4014.
4. El Alami, H. Creus, J., Sabot, R., Feaugas, X., *Proc. EDEM Conf.*, Pologne 2007.
5. Haddou, H., Risbet, M. , Marichal, G.and Feaugas, X., *Mater. Sci; and Eng. A*, vol. A379 (2004) pp. 102-111.
6. Feaugas, X., Haddou, H., *Phil. Mag*., Vol. 87 (2007) p. 989-1018.
7. Sahal, M., Creus, J., Sabot, R., Feaugas, X., *Scripta Met.,* Vol. 51 (2004) pp. 869-873.
8. Sahal, M., Creus, J., Sabot, R., Feaugas, X., *Acta Mater.*, Vol. 54 (2006) pp. 2157-2167.
9. Large, D., Sabot, R., Feaugas, X., *Electrochem. Acta,* Vol. 52 (2007) pp. 7746-7753.
10. Pedersen, O.B., *Acta Metall.*, Vol. 38 (1990) p. 1221.
11. Haddou, H., Ph. D., University of Technology de Compiègne (2003) p. 162.
12. Feaugas, X, *Acta Mater.* Vol. 47 (1999) pp. 3617-3632.
13. Feaugas, X., Tensile and cyclic hardening : back and effective stresses concepts and their applications, Recent Research Developments in Materials Science, Research Signpost , Vol. 4 (2003) pp. 35-64.
14. Gao L., Conway B.E., *Electrochim. Acta*., Vol. 39 (1994) p. 1681.
15. Popic, J.P., Drazic, D.M., *Electrochim. Acta*., Vol. 49 (2004) p. 4877.
16. Damjanovic, A., Electroanal. Chem., Vol. 355 (1993) p. 57.
17. Brian, E., Conway, B.E., in Interfacial Electrochemistry Theory Experiment and Applications. Marcel Dekker Inc. New York (1999) p. 131.

Effects of Hydrogen on Materials
Proceedings of the 2008 International Hydrogen Conference
Brian Somerday, Petros Sofronis, Russell Jones, editors, p 300-307
Copyright © 2009 ASM International®
All rights reserved.
www.asminternational.org

CATHODIC HYDROGENATION OF VERY HIGH STRENGTH STEELS – INFLUENCE OF ARSENIC AS A HYDROGENATION PROMOTER

LY Céline[1], JÉROME Michel[1], SOJKA Jaroslav[2]
RUSCASSIER Nathalie[1], GUILLOT Jean-Bernard[1]

1 Chemical and Material Engineering Laboratory
École Centrale Paris, 92295 Châtenay-Malabry - France
2 Faculty of Metallurgy and Material Engineering
Technical University of Ostrava, 708-33 Ostrava – Czech Republic

ABSTRACT

Hydrogen embrittlement mechanisms of two very high strength steels (VHSS) with ultimate tensile strength reaching 1000 MPa were studied in severe hydrogen charging conditions. These VHSS are a TRIP steel (A) and a Cr-V enriched high strength steel (B). They were submitted to cathodic charging in a sulfuric acid 0.1 N solution with an addition of 5 mg L^{-1} of As_2O_3, as a promoter of hydrogen absorption. Electrochemical permeation technique and subsequent hydrogen dosage by thermal desorption tests provided values for hydrogen diffusion characteristics. A and B present diffusivity of respectively 2.6 10^{-11} m^2 s^{-1} and 2.2 10^{-10} m^2 s^{-1}. Blistering occurred at high charging currents, but residual hydrogen content appeared to be very low for both steels. The results are attributed to the fine homogeneous microstructures with very few lattice defects like inclusions, precipitations, impurities or microcracks that are the most potential sites for H trapping.
Otherwise, ordinary tensile tests performed on hydrogenated steel show higher loss of ductility in the presence of arsenic. Fracture surface observations suggest brittle fractures: transgranular for A and intergranular for B. Diffusible hydrogen is to be incriminated in the loss of plasticity since diffusion to crack tips is easy in these steels. All the results highlight As_2O_3 role in enhancing the steels susceptibility to hydrogen embrittlement.

Keywords: hydrogen embrittlement, high strength steel, electrochemical permeation, trapping, tensile tests

INTRODUCTION

In the automotive industry, increasing demand for the reduction of car weight and improvement of the security led to the developpment of new high strength steels that must be able to whithstand higher working stress. These materials present good combination of high hardenability and plasticity. These outstanding properties are attributed to a fine multi-phase microstructure resulting from specifical metallurgical treatments. However, it is generally admitted that increasing yield strength make steel more susceptible to hydrogen embrittlement. That means a low hydrogen content in very high strength steel can be sufficient to embrittle the material. Hydrogen absorption can result in considerable loss of mechanical properties such as plasticity and strength. Some authors think that ferrite-martensite interfaces may be responsible for hydrogen embrittlement of the material [1] while Tomohiko and all [2] propose that hydrogen is mainly trapped in the metastable austenite and that the fine microstructure would be favorable for hydrogen embrittlement. In fact, susceptibilty to hydrogen embrittlement strongly depends on metallurgical parameters such as microstruture and external factors like hydrogen absorption conditions and residual stresses or external loading. Previous work [3] show low susceptibility for those steels in industrial conditions as hydrogen absorption by the material is limited by adding proper organic inhibitors to the pickling solution. As the aim of the study is to compare and understand mechanisms of degradation due to HE, steels were submitted to very severe electrochemical hydrogen charging in the presence of arsenic as a hydrogenation promoter.

MATERIALS

The materials selected for the study are two very high strength steels noted A steel and B steel. The chemical compositions in weight percent are shown on Table 1.
Samples for traction tests and lozenges for permeation tests were took off from as received sheets metal.

Table 1: Chemical composition of steels (wt %)

Steel	C	Si	Mn	P	S	Al	Nb
A	0.226	1.707	1.654	0.020	0.004	0.043	-
B	0.120	0.21	1.5	0.010	0.004	0.029	0.003
	Ni	Cr	Ti	Mo	V	Cu	Sn
A	0.020	0.026	0.004	0.009	0.06	0.021	0.006
B	0.090	1.290	0.002	0.405	0.135	0.12	0.009

The A steel elaboration is composed of different heat treatments that lead to four different phases: first an intercritical annealing at around 850 °C creates a diphase microstructure that consists of about equal volume fractions of ferrite and austenite. Then the steel is quenched into the temperature regime of bainite formation. It is kept

at this temperature in order to transform intercritical austenite into bainitic ferrite. The ultimate step consists in a straining that will allow the metastable austenite at room temperature to transform into martensite. A steel microstructure presents a ferritic matrix and a dispersion of multiphase grains of bainite, martensite needles and metastable retained austenite stabilized thanks to the addition of elements such as Si, AL, Nb, Ti and P [4].
Additional X-Ray diffraction (XRD) tests provided an austenite proportion of 8 % in A steel.
B steel treatment consists in an air quenching followed by an ageing that generates an essentially bainitic microstructure with important molybdenum and chromium carbides that enhance the steel strength.

EXPERIMENTAL PROCEDURES

Electrochemical permeation tests

The principle of this technique originally developed by Devanathan and Stachursky is described in [3] and [5]. It is employed in order to determine hydrogen diffusion characteristics through a steel membrane of about 1 x 10^{-3} m thickness.
Both sides of permeation samples are mechanically polished up to 1200 grinding paper, then ethanol rinsing and ultrasonically cleaning in ethanol are done before deposit of a palladium coating on the exit [6].
Both solutions (entry and exit sides) are deaerated by N_2 bubbling. An ion-exchange membrane is used to avoid charging solution contamination by O_2 evolving at the auxiliary electrode.
For tests without arsenic, after residual current stabilisation, a first permeation transient is performed using a charging current density i_c = -100 A m^{-2}. When the permeation current reaches a steady-state level, the entry side is polarised anodically at a current density of + 350 A m^{-2} in order to refresh the membrane surface by an anodic dissolution and extract diffusive hydrogen (decay transient). At the end of this period (few minutes), H_2SO_4 charging solution is continuously renewed to eliminate metallic ions and two successive build-up transients at i_c = -100 and -200 A m^{-2} are recorded. This procedure avoids the deposition of iron from metallic ions, and the H^+ reduction only occurs on a clean metallic surface. These operations are repeated a second time. All permeation experiments were achieved at room temperature.
For tests in the presence of arsenic, successive build up transients are performed by increasing successively cathodic current i_c applied to the entry side from -100 A m^{-2} to – 500 A m^{-2} until blistering occurs.

Hydrogen dosage by thermal desorption

Hydrogen trapped after permeation tests is quantified by thermal desorption. It consists in heating a sample up to 600 °C in a vacuum device (Fig. 1 and 2) in order to extract hydrogen trapped in the material. Desorbed hydrogen is stored into a

volume *V* maintained under vacuum, and hydrogen pressure is measured. Thanks to a previous calibration, it is possible to link final pressure to hydrogen content in the sample.

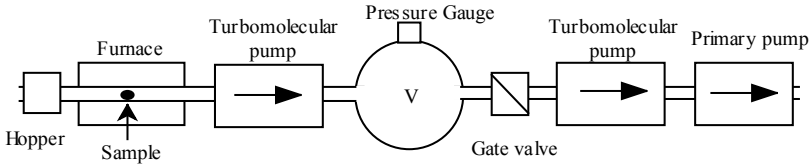


Figure 1: General diagram for hydrogen dosage by vacuum thermal desorption.

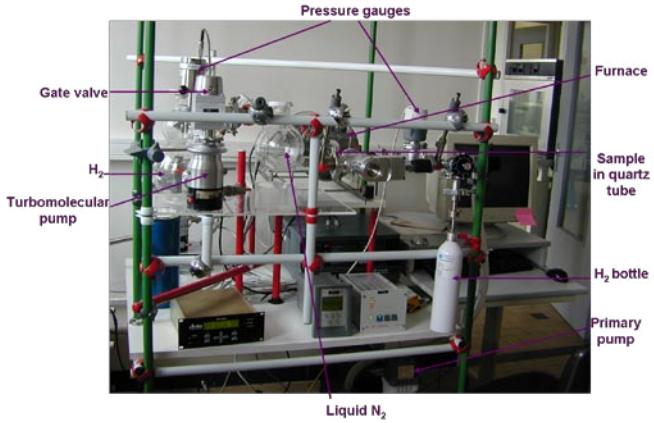


Figure 2: Photography of the hydrogen dosage by thermal desorption device

Mechanical tests

Mechanical properties (listed on Table 2) were evaluated with ordinary tensile tests performed at room temperature under the constant strain rate of 2.7 10^{-4} s^{-1} on flat samples with a 100 kN capacity Zwick /Roell machine.
Then, the same tensile test procedure is employed for samples "softly" hydrogenated (H_2SO_4 1 N, at room temperature under i = 300 A m^{-2} during 4 hours) and severely hydrogenated (solution is H_2SO_4 + 5 mg L^{-1} As_2O_3).

Table 2: Mechanical properties of VHSS; UTS=Ultimate Tensile Strength, YS= Yield Strength, HV: Vickers Hardness

Steel	UTS (MPA)	YS(MPA)	Elongation (%)	HV(Vickers)
A steel	917	596	29.5	211
B steel	1029	961	6.7	308

RESULTS AND DISCUSSION

Diffusion characteristics

For A and B steels, permeation transients have a classical shape (Fig 3). By modelling H diffusion in steel, effective diffusivity *D* and apparent solubility C_0, are evaluated from build-up transient in H_2SO_4 0.1 N solution with arsenic.
Supposing that the surface evolution is negligible during build-up transient, we can apply the usual model which assumes that hydrogen concentration at the entry side is constant. Then the beginning of a build-up transient can be written [7, 8]:

$$\frac{P(\tau)}{P_\infty} = \frac{2}{\sqrt{\pi\,\tau}} \exp\left(-\frac{1}{4\,\tau}\right) \quad \text{(eq.1)}$$

with: $P(\tau)$: hydrogen permeation rate (H at. cm^{-2} s^{-1}) at the dimensionless time $\tau = Dt/e^2$

$P_\infty = DC_0/e$: theoretical steady state permeation rate

D: diffusivity of hydrogen (cm^2 s^{-1})

e: sample thickness (cm)

C_0: diffusible hydrogen concentration at entry side (H at. cm^{-3} with 2.11 10^{19} H at. cm^{-3} = 1 ppm), named apparent solubility.

Permeation rate *P(t)* is related to the recorded current *i(t)* by:

$$P(t) = \frac{i(t)}{S\,q} \quad \text{(eq.2)}$$

where *S* is the useful area (1 cm^2), *q* = 1.6 10^{-19} C, and *i(t)* is in A.
The diffusivity evaluation method is more precisely described in [3].
Table 3 provides mean values for diffusivity D, apparent solubility C_0 and trapping.

Table 3: Hydrogen diffusion characteristics determined by electrochemical permeation and dosage by thermal desorption

steel	A steel	B steel
D ($m^2.s^{-1}$)	2.8 10^{-11}	2.2 10^{-10}
C_0 (ppm) for i_c = -200 A m^{-2}	43.53	2.65
diffusible and weakly trapped [H] (ppm)	46.73	4.51
irreversible [H] (ppm) after total desorption	0.27	0.25
[H] (ppm) in as received steel	0.28	0.21

Diffusion coefficient values suggests that hydrogen atoms diffuse easily at room temperature in these steels and thereby is susceptible to move to regions of crack tip and high stress strain in general, which may be dangerous for steel. But once hydrogen egress is complete, hydrogen content values are very low, being close to those for as received specimen while diffusible hydrogen content is very high. These

results demonstrate that hydrogen diffuses and effuses easily, without noticeable trapping. High diffusivity and low solubility are due to the very fine homogeneous microstructure with few irreversible traps.

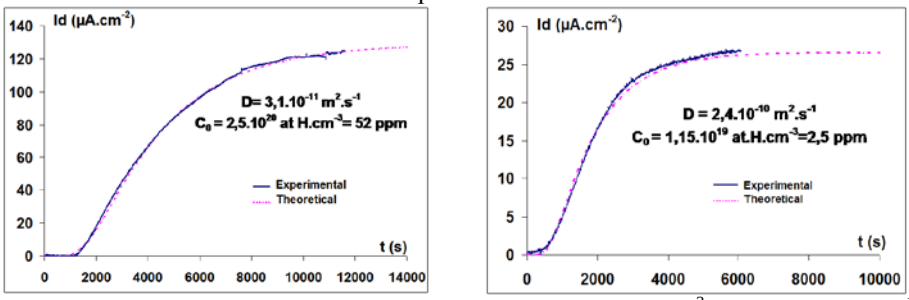


Figure 3: Permeation build-up transients, $i_{cathodic}$ = -20 mA.cm^{-2}, H_2SO_4 + 5 mg L^{-1} As_2O_3; (a) A steel (thickness = 0.095 cm), (b) B steel (thickness = 0.165 cm).

Hydrogen effects on mechanical properties

The stress strain curves of charged specimens were compared to those of as received samples (Fig. 4 and 5). Table 4 shows that elongations to fracture are lower for the severe hydrogen charged samples for both steels, which is due to a higher absorption of H. For B steel, severe charging provokes fracture in the elastic domain.

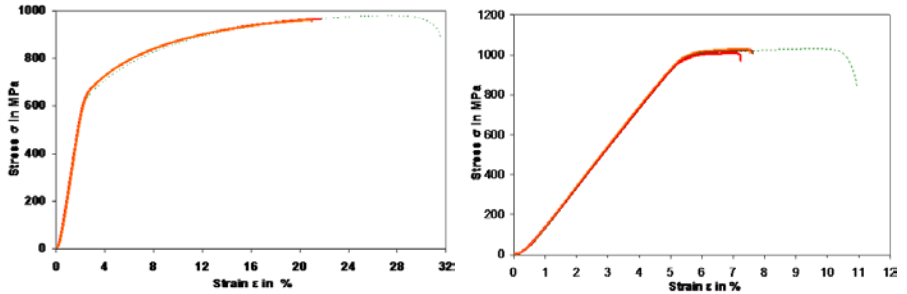


Figure 4: Stress–strain curves of steels A (a) and B (b); dashed line: as received; solid line: after hydrogen charging during 4 hours in H_2SO_4 1N at i_c = 300 A m^{-2}

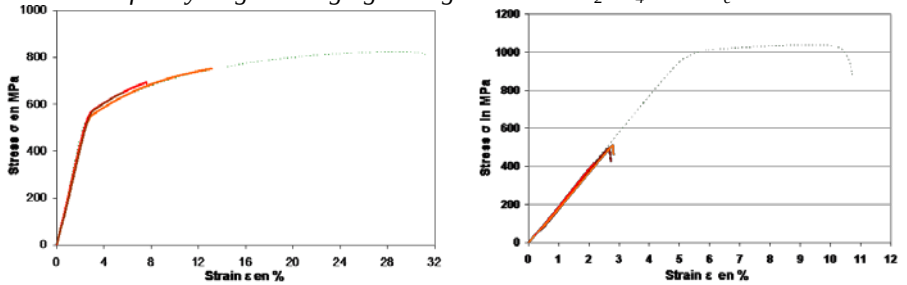


Figure 5: Same as figure. 4, for severe charging conditions (4 hours in H_2SO_4 1N + 5 mg.L^{-1} As_2O_3,i_c = 300 A .m^{-2}).

Table 4: Elongation comparison before and after hydrogenation

Steel	Elongation (%) as received	Elongation (%) after "soft" charging	Elongation (%) after severe charging
A steel	29.5	18.2	3.5
B steel	6.7	2.5	0

SEM micrographs of the fracture surfaces are shown in Fig 6 and 7. The rupture surface of softly charged specimens are mostly composed of dimples that are characteristic of a ductile fracture while brittle fracture occurs when arsenic is present in charging solution.

For B steel, intergranular secondary cracks reveal accumulation of hydrogen along grain boundaries. For A steel, SEM examinations reveal transgranular brittle cleavage fracture resulting from grain cracking through the ferritic phase. This confirms the assumption that reversible H trapping sites such as grain boundaries for B steel and second phases (austenite, martensite) for A steel trap a considerable amount of hydrogen. Thus, this diffusible hydrogen initiates the cracking in the presence of high tensile stress due to mechanical solicitation during tensile test.

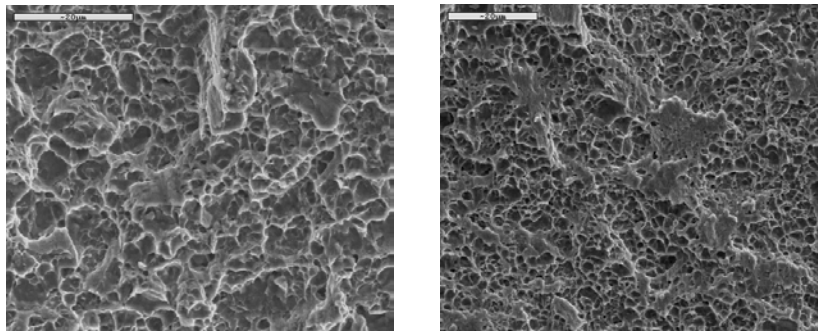


Figure 6: Scanning electron micrographs of fracture surfaces A steel (a) and B steel (b) with cathodic charging at 300 A m^{-2} during 4 hours. Both are ductile fractures.

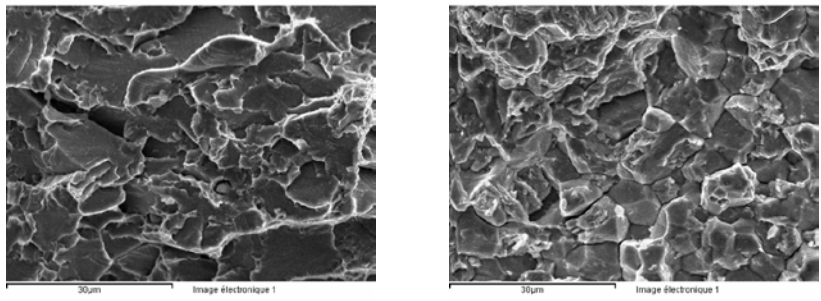


Figure 7: Same as fig. 6, for severe charging conditions (4 hours in H_2SO_4 1N + 5 mg.L^{-1} As_2O_3 ,i_c = 300 A m^{-2}).

CONCLUSIONS

The effects of hydrogen on the behavior of two very high strength steels have been investigated by means of electrochemical permeation tests, and ordinary tensile tests on specimens after severe hydrogen charging in H_2SO_4 0,1 N with an addition of 5 $mg.L^{-1}$ As_2O_3, used as hydrogenation promoter.
The results indicate that hydrogen diffuses and removes easily from these steels, due to a high diffusivity at room temperature for both steels ($2.8\ 10^{-11}$ $m^2\ s^{-1}$ and $2.2\ 10^{-10}$ $m^2\ s^{-1}$. for A and B steels, respectively). On the other hand, solubility appears to be low. Because of the lack of strong trapping sites, hydrogen residual content is also very low, and embrittlement is due to diffusible and weakly trapped H.
Mechanical tests, when achieved immediately after severe H charging, highlights important loss of plasticity. SEM examinations of the rupture surface show brittle transgranular rupture for A steel and brittle intergranular rupture for B steel.
All these results emphasis the danger of diffusible hydrogen that tend to diffuse to strained region and initiate cracking during tensile tests.

ACKNOWLEDGMENTS

The authors gratefully acknowledge financial and technical support from the company ELECTROPOLI (Z.A. Parc d'Affaires 50240 Saint James FRANCE).

REFERENCES

1. J.L.Gu, K.D.Chang,H.S.Fang and B.Z.Bai "Delayed fracture Properties of 1500 MPa Bainite/Martensite Dual-Phase High strength steel and its hydrogen traps", *Iron and Steel Institute of Japan International,* Vol 42, (2002**),** pp**.**1560-1564
2. Hojo, Tomohiko et al. " Hydrogen embrittlement of Ultra high Strength Low Alloy TRIP-aided steels", *Journal of the Iron and Steel Institute of Japan,* Vol 90, N°3(2006**),** pp.177-182
3. Ly C., Jérôme M., Guillot J-B, Sojka J., Ruscassier N., « Hydrogen embrittlement of very high strength steels and influence of the microstructure », "Proc. Eurocorr 2007", Freiburg in Bresgau, Germany, 2007, 11 p CD
4. Zhang Y., Ma Y., Kang Yanli, Hao Li ,"Mechanical properties and microstructure of TRIP steels produced using TSCR process", *Journal of university of science and technology Beijing*, Vol 13, N°5 (2006), pp 416-419
5. M.A.V. Devanathan and Z. Stachurski, "*Proceedings of the Royal Society*", London, 1962 , pp 90-102
6. P. Manolatos and M. Jérôme, "A thin palladium coating for hydrogen permeation studies" , *Electrochimica Acta,* Vol 41, N°3, (1996**)**, pp. 359-365.
7. J. McBreen, L. Nanis, W. Beck, *Journal of The Electrochemical Society,* Vol 113**, (**1966), pp 1218.
8. L. Nanis, T.K. Govindan Namboodhiri, *Journal of The Electrochemical Society*, Vol 119,(1972), pp. 69

Effects of Hydrogen on Materials
Proceedings of the 2008 International Hydrogen Conference
Brian Somerday, Petros Sofronis, Russell Jones, editors, p 308-315
Copyright © 2009 ASM International®
All rights reserved.
www.asminternational.org

STRUCTURAL MATERIALS ISSUES IN THE DEVELOPMENT OF THE HYDROGEN ENERGY INFRASTRUCTURE IN JAPAN

Yukitaka Murakami
Kyushu University and the Research Center for Hydrogen Industrial Use and Storage (HYDROGENIUS), AIST, 744 Moto-Oka, Nishi-ku, Fukuoka, 819-0395 JAPAN

1. INTRODUCTION : BACK GROUND OF HYDROGEN ENERGY TECHNOLOGY DEVELOPMENT IN JAPAN AND HYDROGENIUS PROJECT

In 2001, the Japanese government introduced the scenario of commercialization of the fuel cell vehicle (FCV) and stationary fuel cell (SFC) whereby the introduction of 50,000 FCVs is planned by 2010.

However, during the process to this technological development, the difficulty of achieving the goal such a scenario has been recognized. The reason for the difficulty has been attributed to the lack of basic research. It was pointed out that simple technological developments of FCV, SFC, and related infrastructure and its demonstration could not lead us to the complete solution. The conclusion reached out the discussion for the Fuel Cell Commercialization Conference of Japan (FCCJ) was "Return to the Basics". Following the conclusion, the Ministry of Economy, Trade and Industry (METI) started three projects; first the project for the basic research on fuel cell (FC-CUBIC) in 2005, second in 2006 the fundamental research project on advanced hydrogen science which is a 7-year project and includes the basic research on hydrogen embrittlement (HE), tribology, thermo-physical properties, and simulation (HYDROGENIUS), and third the project for hydrogen storage materials (HYDRO-STAR) in 2007.

The present overview paper introduces the new experimental results on HE recently obtained by the HYDROGENIUS research team. Two case studies for the incident of a dispenser hose of the hydrogen supply stations demonstrated in Nagoya in 2005 and for a structural integrity investigation on the 40MPa hydrogen storage cylinder demonstrated for 4 years in Tokyo will also be introduced in terms of the fatigue data obtained in HYDROGENIUS.

2. EFFECT OF HYDROGEN ON MATERIAL STRENGTH

2.1 Effect of Hydrogen on Static Strength of Steels

Figure 1 shows the results from tensile tests on a pipeline steel, JIS-SGP (0.078 C steel) [1] and the mechanism of void growth. The hydrogen-charged specimens (Fig. 1(b)) show a peculiar void growth inside the specimen in tensile test. The lateral void growth followed by coalescence (Fig. 1(c)) resulted in shallower dimple formation in hydrogen-charged specimens.

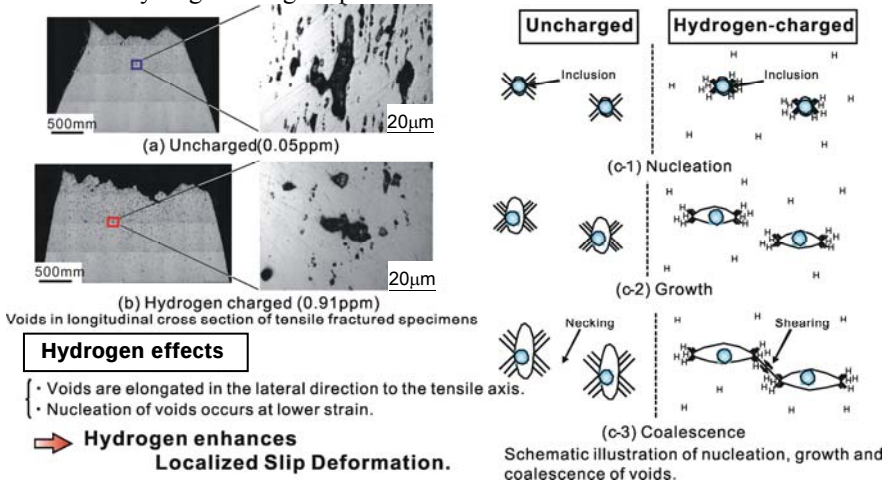


Figure 1: Development of voids in the tensile test of JIS-SGP (0.078% carbon steel)

2.2 Effect of Hydrogen on Fatigue Crack Growth

Almost all kinds of commercial steels have been investigated in terms of hydrogen embrittlement at HYDROGENIUS. In this overview, only the results for a Cr-Mo steel and two austenitic stainless steels which are currently used in hydrogen energy systems will be discussed. The chemical compositions and Vickers hardness are shown in Table 1. The fatigue test specimen having 7 mm diameter contains a small artificial hole with 100 μm diameter as a crack starter.

*Table 1 Chemical composition (w%, *wppm) and Vickers hardness HV*

	C	Si	Mn	P	S	Ni	Cr	Mo	Cu	H*	*HV*
SCM435	0.37	0.18	0.78	0.025	0.015	0.09	1.05	0.15	0.1		330
SUS304	0.06	0.36	1.09	0.030	0.023	8.19	18.66	-		2.2	176
SUS316L	0.019	0.78	1.40	0.037	0.010	12.08	17.00	2.04		2.6	157

2.2.1 Cr-Mo steel: JIS SCM435

Cr-Mo steel: JIS SCM435 is a candidate material for the hydrogen storage cylinder in hydrogen stations equipped with a 35MPa hydrogen supply system to the Fuel Cell Vehicle (FCV).

Figure 2 shows the crack growth behavior [2]. The fatigue crack growth rate da/dN in hydrogen charged specimens is much higher than in the uncharged specimens. Another important point is that da/dN increases with decreasing test frequency. Figure 3 shows the relationship between da/dN and stress intensity factor range ΔK [2] in terms of hydrogen content and test frequency f. The dotted line of Fig. 3 shows approximately 30 times acceleration of fatigue crack growth rate in the presence of hydrogen and can be considered to be the upper bound to the hydrogen effect under low frequency that should be used for the fatigue life prediction design of the hydrogen storage cylinder.

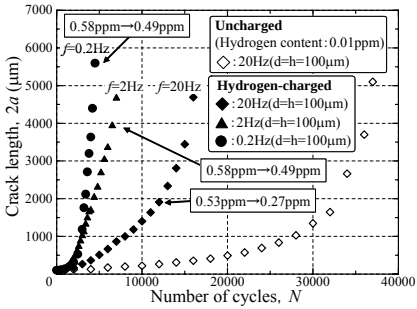


Figure 2:Relationship between crack length 2a and number of cycles N. σ_a = 600 MPa. Material:SCM435 (H. Tanaka, et al[2])

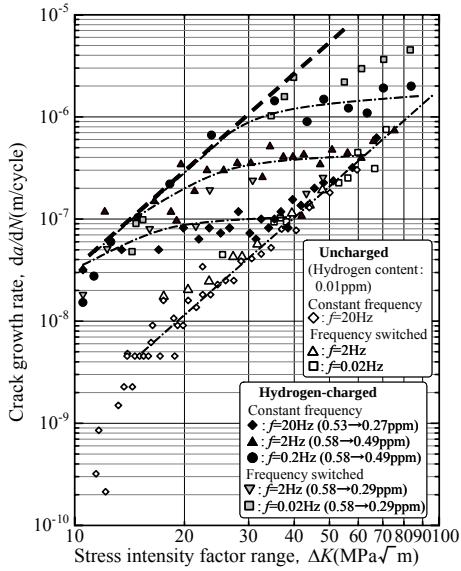


Figure 3:Relationship between da/dN and ΔK. Material:SCM435(H.Tanaka, et al[2])

2-2-2 Effect of Hydrogen on Fatigue Crack Growth Behavior of Austenitic Stainless Steels

A. Hydrogen entry into austenitic stainless steels.

Figure 4[3] shows the hydrogen desorption spectra for an uncharged Type 316L specimen (curve A), and for a hydrogen-charged specimen (curve B). The height of the peak at around 300 °C, which indicates diffusible hydrogen, shows an increase due to hydrogen charging. On the other hand, the height of the peak at around 400 °C, which indicates non-diffusible hydrogen, shows that there is no significant difference between the hydrogen-charged and uncharged specimens. It should be noted that 2.6 wppm non-diffusible hydrogen is contained even in the uncharged Type 316L.

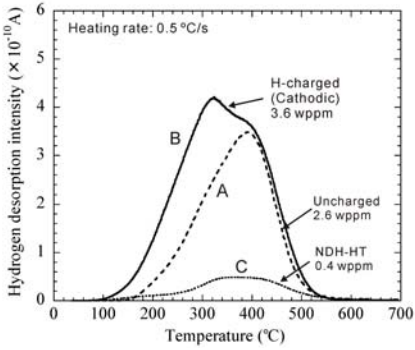
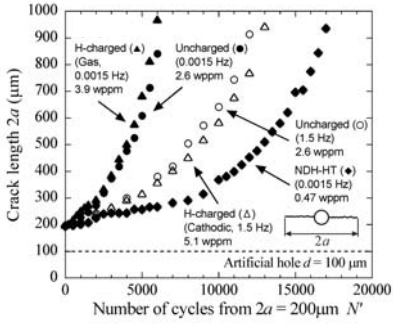


Figure 4: Hydrogen thermal desorption spectrum for Type 316L[3]

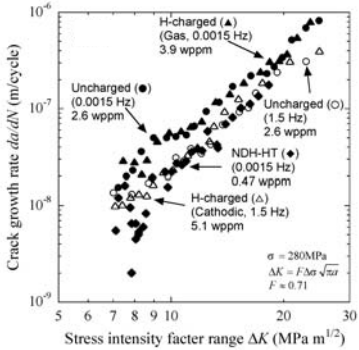
B. Effects of hydrogen and test frequency on fatigue crack growth.

Figure 5(a) [3] shows the relationship between the crack length, 2*a*, and the number of cycles, *N*, for type 304 and type 316L specimens. Figure 5(b) [3] shows the relationship between the fatigue crack growth rate, d*a*/d*N*, and the stress intensity factor range, Δ*K*, for type 316L. In type 316L tested at a frequency of 1.5 Hz, there was no pronounced difference between the hydrogen-charged specimen and the uncharged specimen. The fatigue crack growth rates of the hydrogen-charged type 316L, tested at the frequency $f = 0.0015$ Hz, were 2 to 3 times higher than those of type 316L tested at $f = 1.5$ Hz. Surprisingly, the uncharged specimen also exhibited an obviously definite crack growth rate increase as the test frequency decreased from 1.5 Hz to 0.0015 Hz.

In the range of $\Delta K < 9$ MPa·m$^{1/2}$(Fig. 12(b)), the crack growth rate is slow and it is presumed that there is sufficient time for hydrogen to concentrate in the vicinity of crack tip during one cycle at a frequency of 0.0015 Hz.



(a) Crack growth curve

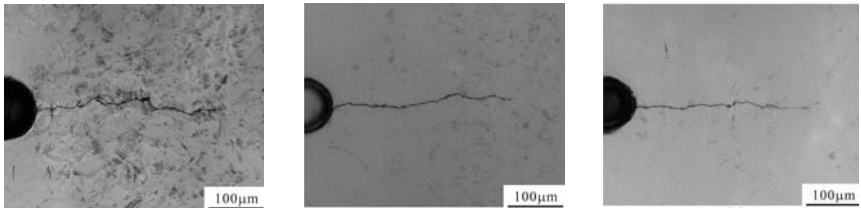


(b) Effect of H-content and *f* on d*a*/d*N*

Figure 5: Influence of hydrogen and test frequency f on crack growth from 2a = 200μm of type 316L(σ = 280MPa) [3].

Figure 6[3] shows micrographs of fatigue cracks taken by the replica method for Type 304 specimens. Slip bands in the hydrogen-charged specimen were more localized, in the vicinity of crack tips, in comparison to those in the uncharged specimen. Even for the uncharged Type 304 specimen (Fig. 6(b)), slip band localization in the crack tip vicinity was observed in the low frequency test (f = 0.0015 Hz).

Strain-induced martensitic transformation occurred on fracture surfaces at both test frequencies: $f \sim 1.5$ Hz and 0.0015 Hz. It should be noted that even in type 316L, which previously was thought extremely difficult to transform to martensite at ambient temperature, martensitic transformation took place at fatigue crack tips.

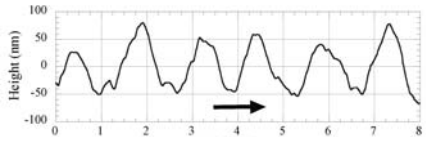


(a) uncharged (f = 1.2Hz, 2a = 782μm, N = 11000, 2.2wppm)
(b) uncharged (f = 0.0015Hz, 2a = 778μm, N = 8300, 2.2wppm)
(c) H-charged (f = 1.2Hz, 2a = 801μm, N = 5150,3.7wppm)

Figure 6: Effect of H-charge and loading frequency f on crack growth behavior (type 304, σ = 280MPa) [3].

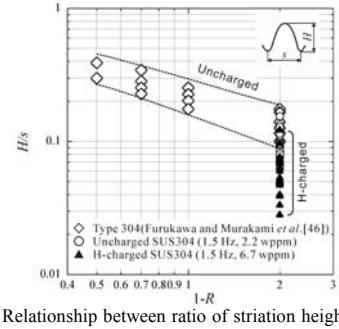
C. Effects of hydrogen on striation formation.

The topography of striations was observed in the hydrogen-charged and uncharged type 304 specimens tested under the same conditions. In the uncharged specimen each striation was regularly formed and roughly triangular in shape (Fig. 7(a)). In the hydrogen-charged specimen, on the other hand, striations were irregularly shaped, and the striation height was lower compared to that for the uncharged specimen (Fig. 7(b)). Figure 7(c) shows the striation height H and spacing ratio H/s data for type 304 in the present study, together with data from Furukawa and



(a) uncharged (σ =260MPa, f = 1.5Hz, 2.2wppm)

(b) H-charged (σ =260MPa, f = 1.5Hz, 6.7wppm)



(c) Relationship between ratio of striation height H to spacing s, H/s, and stress ratio (1-R)

Figure 7: Effect of H-charge on striation morphology

Murakami *et al*.[4]. The figure indicates that the *H*/*s* data obtained from the stereographic SEM images in this study, for the uncharged specimen tested at $f = 1.5$ Hz, had a good correlation with Furukawa and Murakami *et al*.'s data. Considering that the features of striation shape for the uncharged specimen, tested at the frequency of 0.0015 Hz, were very similar to those for the hydrogen-charged specimen (Fig. 7(b)), it follows that testing at the low frequency ($f = 0.0015$ Hz) enhances the hydrogen effect, even in the uncharged specimens which contain non-diffusible hydrogen at a level of 2 ~ 3 wppm [3].

D. What happens if non-diffusible hydrogen is removed by special heat treatment?

Even in the uncharged specimens the fatigue crack growth rate is increased by decreasing the test frequency down to 0.0015 Hz. The only possible cause of this surprising phenomenon is the effect of non-diffusible hydrogen, at the level of 2 ~ 3 wppm, which is unavoidably trapped in the material during the production process. This non-diffusible hydrogen has not been suspected, in previous hydrogen embrittlement studies, as a possible cause of hydrogen embrittlement. However, if this non-diffusible hydrogen can cause hydrogen embrittlement, it means that the hydrogen embrittlement of austenitic stainless steels can occur even in the absence of an external hydrogen environment.

In order to investigate the influence of the so-called non-diffusible hydrogen on fatigue crack growth, a special heat treatment was applied. This consists of soaking type 316L at 450 °C for 450 h, and type 304 at 300 °C for 600 h, in a vacuum of 6.0×10^{-3} Pa. We called this special heat treatment Non-Diffusible Hydrogen desorption Heat Treatment (NDH-HT)[38]. The effect of NDH-HT is clearly shown in Fig. 4, in which the hydrogen content in a conventionally heat treated type 316L is 2.6 wppm, whereas in the sample subjected to NDH-HT the content is 0.4 wppm (Curve C). Thus, NDH-HT removes the hydrogen, which is strongly trapped at the center (O-site) of an octahedron of the FCC lattice, where the potential energy is much lower than that for hydrogen trapped in the quadratic lattice of a BCC material (T-site) [5].

Figures 5(a) and (b) show the fatigue crack growth behavior of NDH-HT specimens. Fatigue tests were carried out at a frequency of 1.5 Hz until a crack had grown to 200 μm in length, including the hole diameter (100 μm), and the test frequency was then changed to 0.0015 Hz. Surprisingly, the fatigue crack growth rate of an NDH-HT specimen was substantially decreased in comparison with a hydrogen-charged specimen, and even in comparison with an uncharged specimen. Further evidence of the effect of NDH-HT was seen in the striation height-spacing ratios (*H/s*) which are shifted to higher values. The above facts are definite proof that even the non-diffusible hydrogen contained in conventionally solution treated austenitic stainless steels influences fatigue crack growth rates. From the result of this experiment we

can identify that at a very low test frequency, of the order of 0.0015 Hz, there is sufficient time for hydrogen to be transported to fatigue crack tips through lattice defects such as edge dislocations. Thus, it is vitally important to take the effect of loading frequency into consideration for the prediction of fatigue lives and the safety of infrastructures and components which, in actual service, are used in hydrogen environments.

3. CASE STUDIES

3.1 Dispenser Failure at the Hydrogen Station of EXPO 2005 in Nagoya

Figure 8 shows the schematic view of the dispenser at the hydrogen station of EXPO 2005 in Nagoya in which a hydrogen leakage incident occurred in May, 2005. The dispenser material was type 316L austenitic stainless steel. The crack growth rate in the dispenser hose was much higher than the prediction. By the failure analysis, the cause for the difference between the prediction and the actual fatigue life was identified to be the low load frequency in actual service (8 min) in the presence of hydrogen.

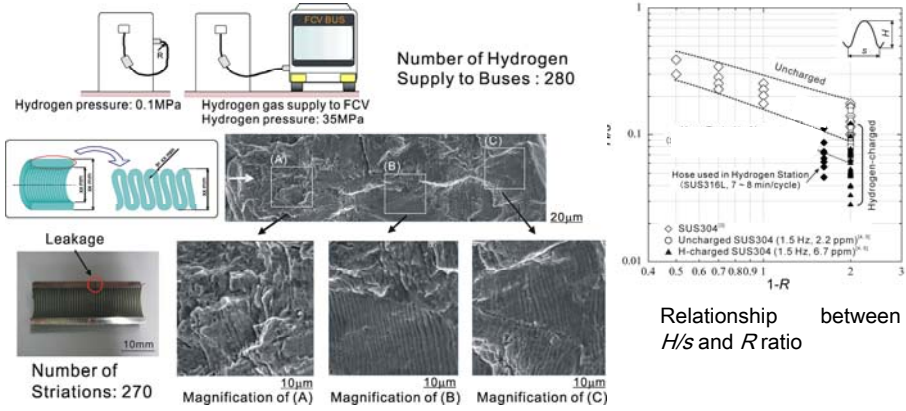


Figure 8: Dispenser failure in EXPO2005 in Nagoya [6]

3.2 Hydrogen Storage Cylinder at Kasumigaseki Hydrogen Station, Tokyo

Figure 9 shows the hydrogen storage cylinder and the process of structural integrity assessment. The material of the cylinder was the Cr-Mo steel whose fatigue data are presented in Fig. 3. The conclusion reached through failure analysis at HYDROGENIUS was that the remaining life of the hydrogen storage cylinder under the demonstration condition was at least 15 years.

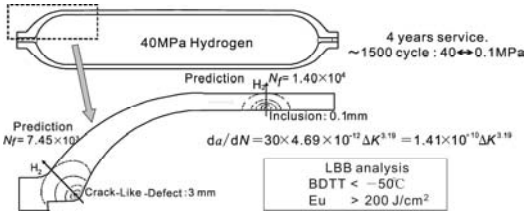


Figure 9: Case study on a hydrogen storage cylinder of Cr-Mo steel [7]

4. CONCLUSIONS

The HYDROGENIUS project, one of three basic hydrogen research projects sponsored and funded by the Japanese Government, was first described. The basic mechanism of hydrogen embrittlement in the fatigue of a Cr-Mo steel JIS SCM435 and two austenitic stainless steels, type 304 and type 316L, has been discussed in terms of the effects of hydrogen and load frequency on fatigue crack growth rates. Two case studies on the demonstrated hydrogen infrastructures in Japan were discussed to exemplify the effects of hydrogen and loading frequency in real-life applications.

ACKNOWLEGMENTS

This research has been supported by the NEDO Fundament Research Project on Advanced Hydrogen Science (2006 to 2012).

REFERENCES

1. Matsuo, T. *et al*, “Effect of Hydrogen and Prestrain on Tensile Properties of Carbon Steel SGP (0.078C-0.012Si- 0.35Mn, mass%) for 0.1 MPa Hydrogen Pipelines”, *Trans. JSME, A,* Vol. 74, No. 744 (2008), in press.
2. Tanaka, H. *et al*, “Effect of Hydrogen and Frequency on Fatigue Behavior of SCM435 Steel for Storage Cylinder of Hydrogen Station”, *Trans. JSME, A*, Vol. 73, No. 736 (2007), pp. 1358-1365.
3. Murakami, Y. *et al*, “Hydrogen Embrittlement Mechanism in Fatigue Austenitic Stainless Steels”, *Metallurgical and Materials Trans*., Vol. 39A (2008), pp.1327-1339.
4. Furukawa, K. *et al*, “A Method for Determining Stress Ratio of Fatigue Loading from the Width and Height of Striation”,*Int.J.Fatigue*,Vol.20(1998),pp.509-516.
5. Fukai, Y., The Metal-Hydrogen System: basic bulk properties, Springer (New York, 1993)
6. Murakami, Y. *et al*, “Failure Analysis of SUS316L Flexible Hose for Hydrogen Station and Fatigue Life Prediction Method”, Submitted elsewhere (2008).
7. NEDO Report on the Investigation of the Hydrogen Storage Cylinder of Kasumigaseki Hydrogen Station (2008).

Effects of Hydrogen on Materials
Proceedings of the 2008 International Hydrogen Conference
Brian Somerday, Petros Sofronis, Russell Jones, editors, p 316-323
Copyright © 2009 ASM International®
All rights reserved.
www.asminternational.org

HYDROGEN DELIVERY: INFRASTRUCTURE, CHALLENGES, AND MATERIALS NEEDS

S.J. Pawel
Oak Ridge National Laboratory, Oak Ridge, TN 37831 USA

M.R. Gardiner
U. S. Department of Energy, Washington, DC, 20585 USA

ABSTRACT

Current domestic energy policy is aimed at encouraging the development of alternative fuels such as hydrogen for use as a renewable and environmentally-friendly alternative to traditional petroleum-based fuels for transportation and stationary power. The purpose of the Hydrogen Delivery Technical Team is to provide insight and input on hydrogen delivery infrastructure research. Ongoing research has identified materials R&D challenges required to support this infrastructure. A few of these challenges are summarized with emphasis placed on materials.

INTRODUCTION

The emphasis of domestic energy policy includes four broad-based goals:

- Reduce dependence on foreign petroleum to create a more secure energy supply
- Reduce greenhouse gas emissions and other environmental impacts
- Create a more diverse, reliable, and low cost energy infrastructure to meet demand
- Improve energy efficiency and productivity to drive economic growth

The transportation sector is presently responsible for about 67% of domestic oil consumption (see Fig. 1). Of the amount devoted to transportation, two thirds is used as fuel for light duty vehicles. A viable alternative to petroleum-based fuels for cars and light trucks will likely increase energy security and have substantial environmental benefits.

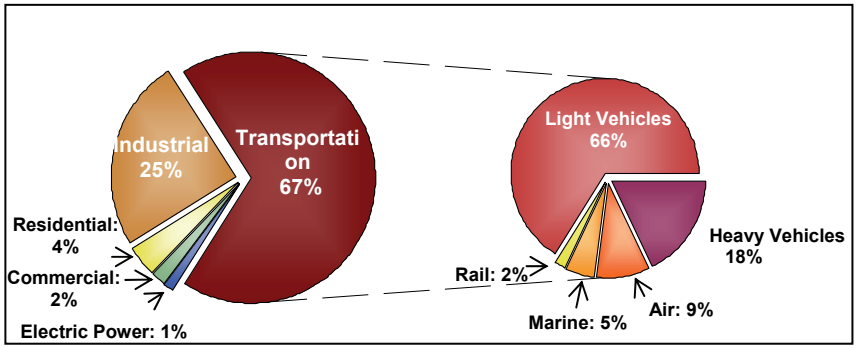


Figure 1: Domestic oil consumption statistics

The Hydrogen Fuel Initiative (beginning January 2003) committed $1.2B over five years to develop hydrogen, fuel cell, and related infrastructure technologies to enable hydrogen fuel cell vehicles, with an initial goal of "technological readiness" by 2015. This initiative, along with other Executive Orders, laws, and policy statements in the past few years, is designed to encourage partnerships with the private sector, accelerate research and development, and facilitate initial market penetration by overcoming potential barriers to deployment (and acceptance) of hydrogen as an alternative fuel. Figure 2 below presents a simplified timeline for the US DOE Hydrogen, Fuel Cells, and Infrastructure Technologies (HFCIT) Program. The Hydrogen Program calls for strong participation by Government (primarily directing and funding priority work) early in the effort, with increasing participation and leadership from Industry later in the effort to commercialize and improve/expand the required technologies. Some portions of the timeline have been extended due to funding impacts from Congressionally-directed funding (appropriations) and reprioritization of funding (including some zero-budgets) among individual technical areas.

Hydrogen Delivery Tech Team

At the behest of Department of Energy (DOE), the HFCIT Program is supported by a number of "Tech Teams." A Technical Team is led by DOE staff, often supported by a contractor, and populated primarily by senior personnel representing energy companies and/or automotive OEMs as well as a few Federal laboratory participants. The objectives of each Technical Team determine the required membership. The purpose of each Technical Team is to function as a sounding board for Federal strategy, guide R&D planning (which includes preparation of an R&D roadmap), and perform technical project reviews. Technical Teams have been established for many aspects of a potential hydrogen fuels economy, including such diverse areas as production, delivery, storage, fuel cells, codes and standards, systems integration, and analysis.

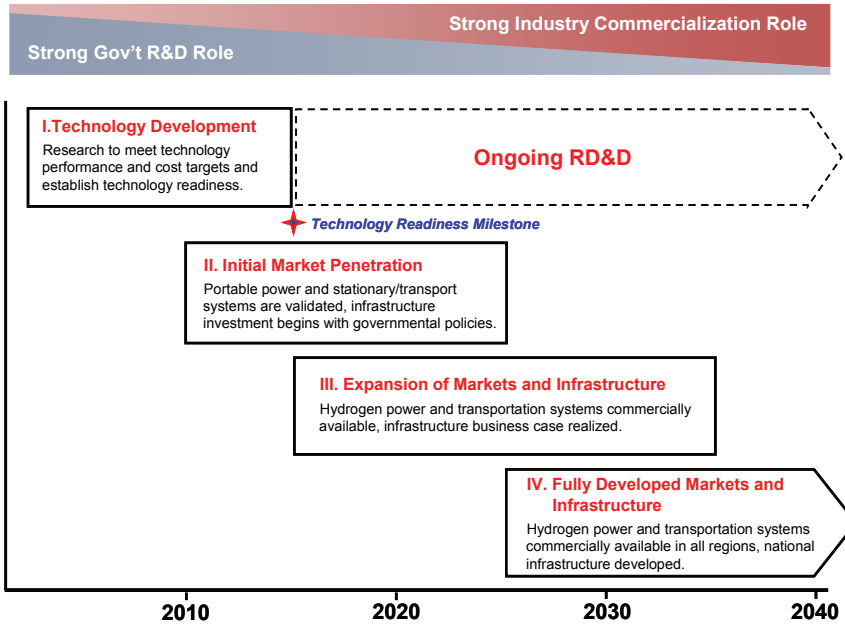


Figure 2: Schematic of HFCIT proposed timeline for technology development and market penetration of hydrogen as a transportation fuel

Delivery of hydrogen is considered to be a key component of an overall hydrogen fuel economy. The scope of the Delivery Program is considered to incorporate the movement of hydrogen from the point of centralized or distributed production through the dispenser at the refueling station to the vehicle. The overall goal of the Delivery Program is to develop hydrogen technologies that enable the introduction and long-term viability of hydrogen as an energy carrier for transportation and stationary power. As for all aspects of the HFCIT Program, the R&D and related metrics are driven by cost targets established by DOE. The current cost target goal for hydrogen delivery is $\leq$ \$1.00 per gallon of gasoline equivalent (gge, approximately 1 kg hydrogen) by the year 2017, not including production costs or taxes.

The Delivery Program is presently focused on three primary pathways for hydrogen delivery:

- gaseous delivery via truck (tube trailer) or pipeline
- liquid delivery via tank truck
- carrier delivery via tank truck or pipeline

Of course, other related pathways are possible, such as barge or rail transportation, but these are technically similar to trucks in terms of the transported container requirements while not as geographically available to a national program. Other pathways including hydrogen carriers are also under investigation.

One of the tools available to the Hydrogen Delivery Tech Team is the Hydrogen Components Model called H2A. The model includes a spreadsheet incorporating each delivery system component with associated cost and performance characteristics for each component. Most of the cost data is based on presently available equipment, labor rates, and efficiencies, etc., and the remainder is based on estimates for limited production of next-generation equipment provided by interested companies that support the Hydrogen Program. In addition, H2A includes a scenario model, which allows for virtual assembly of a hydrogen delivery infrastructure designed to serve various market supply and demand situations, with a wide variety of inputs selected/varied by the analyst (such as urban population, pathway or pathway combination, number of hydrogen vehicles, number of refueling stations as well as size/geographic distribution of stations, expected return-on-investment, etc.). It is recognized that the H2A model is perhaps not capable of absolute costs associated with any particular pathway/scenario combination, but it is widely agreed that the model can be used to estimate relative system costs and identify areas on which limited R&D resources can be focused to most substantially impact overall delivery costs in the future.

Several substantial challenges to reaching the delivery cost target have been identified via H2A analysis, which has influenced the early R&D that has been performed. The following paragraphs highlight some of the most significant findings regarding material and cost challenges for critical components of a hydrogen delivery infrastructure.

Materials Challenges and Opportunities

Pipelines

Pipelines are presently considered to be the low-cost pathway for hydrogen delivery for the long-term, when market penetration and resulting high demand require large quantities of hydrogen. However, a number of critical issues for pipelines have been identified that deserve consideration. The main barrier is the high cost of installation relative to initial hydrogen demand.

Technical challenges include many issues. For example, the grades of carbon steel used in the construction of pipelines are known to be susceptible to a phenomenon termed hydrogen embrittlement (HE). In many service environments, pipeline steels retain good ductility and toughness properties essentially identical to those of unexposed steel. However, exposure to hydrogen can cause pipeline steels – particularly those with high strength levels, susceptible microstructures, or severe loading conditions – to become brittle and subject to very unstable (catastrophically high) crack growth rates. It is a complicated process and the term “HE” itself incorporates several closely related phenomena, but in the simplest terms, hydrogen penetrates into the steel structure as a monatomic species in a process which is a strong function of surface condition, hydrogen fugacity, and electrochemical

potential. Once in the steel, some of the hydrogen accumulates at discontinuities within the structure or perhaps recombines to a diatomic species and becomes trapped at particular sites within the matrix. The accumulated hydrogen within the steel apparently alters deformation mechanisms and/or cohesive forces within the structure and thus can, under certain loading conditions, dramatically reduce ductility and toughness for some steel alloys. Of particular concern for a potential network of steel pipelines carrying hydrogen is the inevitable pressure cycling in a large system with variable demand, as there are indications that crack growth in steels may be particularly sensitive to hydrogen under fatigue loads. While there are no known hydrogen-related failures in the limited number of miles of hydrogen pipelines in service today, it is significant that the pressures involved are relatively low and relatively constant. There are, however, reports of third-party damage to hydrogen pipelines with incident rates similar to those experienced for all buried pipelines. The consequences of such incidences, especially from impact loads, may be more severe for hydrogen-saturated steel than for other service environments.

One possibility that has been discussed, in Europe as well as in the USA, is using the existing infrastructure of steel pipelines that distribute natural gas and petroleum-based fuels to distribute hydrogen. In the USA, this infrastructure is presently in use at near 100% capacity, however, and it is not apparent that demand for natural gas will drop sufficiently during the transition to more carbon-neutral fuels that sufficient transport capacity can be made available to hydrogen. In addition, of course, is the concept that the hydrogen purity required for fuel cells will be higher than can be delivered in a pipeline system that co-transports a variety of products.

Further, the existing infrastructure is quite old in some cases – it was quite possibly designed and installed to requirements less demanding (for example, acceptable grades of steel, permitted weld and inspection techniques, allowable flaw sizes, etc.) than those that may be imposed on a hydrogen delivery system. Also, during its previous service, the pipeline may have accumulated wall-thinning/deterioration from corrosion, soil shifting, or third-party damage (e.g., impacts resulting from an uninformed backhoe operator) or perhaps property changes resulting from maintenance/repair. As a result of the uncertain pipeline condition, the pressure rating of such a system may be in question.

These factors – that the existing steel pipeline infrastructure is old/degraded and in use – suggest the potential need for a new pipeline infrastructure. The potential need for new construction offers additional challenges. One is the potential cost of newly acquired right-of-way – in some urban areas it might not be available at any cost, particularly in light of the potential inaccessibility for new construction in highly populated areas for a relatively new and unknown fuel.

If it is determined that a new system of pipelines would be required to distribute fuel-cell grade hydrogen, the capital cost of new construction would be a significant issue. A recent survey of steel pipeline construction costs [1] suggested that for the years 1999-2003 – the data studied most extensively at the time of the Delivery Tech

Team formation in December 2003 – the average transmission line costs for the survey years were only a modest function of pipe diameter and were generically near $1M/mile. More recent data [2] indicates average transmission line costs for land-based projects may have swelled to $2M/mile or more for larger diameters. In order to meet the cost targets for pipeline delivery, a value closer to $0.5M/mile may be required. Interestingly, the sum of material plus labor for these construction projects is relatively constant over time at about 70% of the total pipeline costs. The other 30% includes contributions from right-of-way purchase, regulatory fees, surveying, engineering, equipment, management, and administration. The significant point here is that the latter 30% can not be substantially influenced by R&D, so that reduction of the cost/mile by ~50% (or more) requires a reduction in the materials plus labor costs by ~80% (or more). This sort of cost reduction seems unlikely, but it does suggest R&D direction for the overall program as:

- developments that increase material cost are low priority, such as development of new alloys and heat treatments or application of coatings to prevent hydrogen permeation or corrosion;

- developments that minimize pipeline labor costs are a high priority, such as dramatically increasing the lengths between welds/joints and reducing inspection/surveillance and corrosion requirements.

The latter concept, for example, suggests the development of fiber-reinforced polymer pipelines as an area for development. In principle, FRP pipelines could be spooled in extended lengths (depending on diameter, perhaps as much as a mile) for delivery to the construction location, which would drastically decrease the number of welds/joints per unit length in a pipeline, directly reducing both labor (handling, fit-up, joining) and inspection (various non-destructive examinations, leak-checking) costs. Further, FRP pipelines would likely require far less corrosion protection (e.g., cathodic protection or paint systems for buried steel). However, steel pipelines must remain an option as industry has a long and successful history with this type of construction and, as a result, they are readily accepted by various codes and regulators and could be deployed for near-term transition uses. Additional development required for steel pipelines includes more thorough understanding of manipulation of microstructure and weld procedures to minimize hydrogen embrittlement issues and to gather sufficient property data for modern pipeline steels to enable efficient design and minimization of material requirements.

Compressors

At present, standard reciprocating compressors for hydrogen exhibit poor reliability for a range of gas services. Typically, users must have essentially redundant capability to account for frequent and extensive maintenance requirements. In addition, standard centrifugal compressors are not terribly efficient for hydrogen due to the small size of the hydrogen molecule.

Development opportunities exist for high strength hydrogen-compatible materials appropriate for high speed compressors capable of high pressure service at somewhat elevated temperatures. As a part of this development, new bearing and seal materials are potentially required, and studies of wear and tribology issues in high speed/pressure compressors are needed. Current compression studies are examining novel electrochemical schemes and hydride adsorption/desorption cycles.

Storage

Storage of hydrogen appears to be a relatively expensive component of a delivery infrastructure. The daily and seasonal variability in the demand cycle and the customer expectations associated with fill time and availability impose significant demands (size, pressure) on storage requirements. For on-board storage, conformable, high pressure (high energy density) storage schemes are required. For off-board storage, materials not susceptible to fatigue loading in high pressure hydrogen and schemes to reduce the costs for large scale storage, such as use of liquid hydrogen or storage in underground caverns, which may require liners to reduce permeability or increase safety.

Another form of off-board storage is the container capability associated with tube trailers. Currently, these are very energy inefficient in that ~ 40,000 kg of truck weight is required to deliver ~ 300 kg of hydrogen. New, higher pressure storage tanks (with new materials and designs) are required to improve tube trailer capability for the transition to hydrogen fuels for transportation. Higher pressure storage is also required to reduce the space footprint required (and thus the relative costs) for storage capability at refueling stations.

Liquefaction

Liquid hydrogen has some advantages as a delivery option: quality requirements are generally not an issue, it provides small footprint stations, and is most similar to today's infrastructure. Based on high cost, liquefaction appears to be most relevant to the transition period when hydrogen makes an initial penetration into the fuel market. The costs associated with liquefaction are high primarily due to the energy of liquefaction (~25% is associated with the energetic ortho-para conversion) and the high capital cost of liquefaction equipment (there are substantial economies of scale, rendering small-scale liquefaction relatively prohibitive). Distributed liquefaction would short-cut many obstacles associated with distributing hydrogen. Opportunities for materials development include improved insulation materials and active magnetic regenerative liquefiers.

Public Safety

To increase public safety and ultimately acceptance of a new fuel, codes and standards for construction and performance of hydrogen delivery components must

be developed. Opportunities for materials research in this realm include sensor development and odorant compatibility with hydrogen for fuel cells.

CONCLUSIONS

In order to meet cost targets for a hydrogen delivery infrastructure, a number of materials and other challenges related to requirements for improved performance and/or capital costs have been identified. An aggressive research and development program – with consistent funding – is needed to address these needs and enable a cost- and energy-efficient hydrogen delivery infrastructure.

ACKNOWLEDGMENTS

The authors gratefully acknowledge the financial support of the US Department of Energy Hydrogen, Fuel Cells, and Infrastructure Technologies Program. The authors also thank J. Kegerreis and J. Simnick – other senior members of the Hydrogen Delivery Tech Team – for review of the manuscript. Reviews were also provided by Z. Feng, G. Muralidharan, and D. Stinton, all of Oak Ridge National Laboratory. Monterey Gardiner of the US DOE prepared the final manuscript.

REFERENCES

1. W. R. True, "Pipeline Economics – Special Report," *Oil and Gas Journal,* September 8, 2003, p.60-92. [In particular, see p.74.]

2. C. E. Smith, Pipeline Economics – Special Report," *Oil and Gas Journal,* September 1, 2008, p.50-69. [In particular, see p. 58-62.]

Effects of Hydrogen on Materials
Proceedings of the 2008 International Hydrogen Conference
Brian Somerday, Petros Sofronis, Russell Jones, editors, p 324-331
Copyright © 2009 ASM International®
All rights reserved.
www.asminternational.org

Recent Progress of Research and Development for Fuel Cell Vehicle Application

Koichi Kojima
Fuel Cell System Engineering Div. TOYOTA Motor Corporation,
1 Toyota-cho, Toyota, Aichi, 471-8571 Japan

ABSTRACT

Concerns surrounding the timing of peak oil for conventional fossil fuels (i.e., the point at which the maximum global production rate will be reached) and the growing need to reduce CO_2 emissions are increasing the importance of energy source diversification. For vehicles, this can be accomplished by more efficient internal combustion engines (ICE), the use of bioethanol, more widespread application of ICE-hybrid systems, and the development of technologies that use electricity and hydrogen, such as plug-in hybrid vehicles (PHV) and fuel cell hybrid vehicles (FCHV). Since Toyota started limited lease of the Toyota FCHV, the world's first market-ready fuel cell vehicle, in 2002, Toyota has steadily improved the technology, and has succeeded in significantly extending the vehicle's cruising range in actual driving conditions and enhancing its cold start capabilities. For the next step, Toyota aims to work toward the commercialization and popularization of fuel cell vehicles by focusing on reducing costs and improving durability, and by cooperating with governments and energy companies to establish hydrogen infrastructure.

1. INTRODUCTION

The recent surge in the price of oil has intensified the debate about the timing of peak oil, i.e., the point at which the maximum production rate of conventional fossil fuels will be reached and become inadequate to meet demand. Since 1980, the discovery of new oil fields has fallen below consumption, which means that the advent of peak oil in the relatively near future appears to be inevitable.

At present, over 90 percent of automotive fuel comes from petroleum. In addition, energy demand from developing countries is expected to increase substantially in the foreseeable future. For energy security, the diversification of energy sources by the use of non-conventional oil, synthetic fuel, and biofuel has been attracting attention. The ideal automotive fuel is liquid fuel with high energy density, but due to various constraints, it appears unlikely that any of the alternative liquid fuels mentioned above will be able to meet all demand. Electricity and hydrogen are therefore expected to make up the shortfall.

The most fundamental technology for the utilization of electricity is the rechargeable battery. Despite recent interest in advanced lithium-ion and other types

of rechargeable batteries, their energy density is still too low to provide electric vehicles (EVs) with a sufficient cruising range. Therefore, for the near future, lithium-ion batteries are likely to be a viable option first for hybrid vehicles (HVs) and plug-in hybrid vehicles (PHVs).

By contrast, hydrogen has a higher energy density than a battery and when used for a fuel cell vehicle (FCV), no pollutants such as CO_2, NOx, and HC are emitted when the vehicle is running. In addition, a fuel cell hybrid vehicle (FCHV) has extremely high energy efficiency. In city driving, it can achieve upwards of 50 to 60 percent energy efficiency. Therefore, hydrogen is regarded as a potentially promising power source for automobiles in the future.

Moreover, there is widening recognition that climate change is accelerating. This issue, spurred by abnormal meteorological conditions around the world, is attributable to increased emissions of greenhouse gases such as CO_2. Since the 20th century, when the consumption of fossil fuels in large quantities began, the concentration of CO_2 has increased sharply. Therefore, the transportation sector, which accounts for approximately 20 percent of the total, needs to cut its CO_2 emissions significantly.

Hydrogen can be produced from a variety of primary energy sources. If the amount of CO_2 emissions during the hydrogen production process can be minimized, the use of hydrogen holds considerable promise for the reduction of CO_2. As discussed above, hydrogen-powered FCVs have many advantages. FCVs are not exclusively dependent on fossil fuels, and should therefore prove to be an effective way of diversifying energy sources and curbing CO_2 emissions in the future. In addition, hydrogen has a higher energy density than a rechargeable battery. For these reasons, there is strong impetus toward commercialization of FCVs.

2. Details and Current Status of Technological Issues Confronting the FCHV

Figure 1 shows the technological hurdles to improving the marketability of the FCHV. As discussed below, steady progress has been achieved on some of these issues. This section primarily focuses on the current status of an improved Toyota FCHV, the latest model, the Toyota FCHV-adv, featuring substantial advances in practical cruising range and freeze start capabilities, and the issues that must be resolved in the future.

2.1. Practical Cruising Range

One of the weaknesses of hydrogen-powered FCVs is a short practical cruising range. Compared with gasoline and other types of liquid fuel, hydrogen has a low volumetric energy density, which is a disadvantage for an on-board fuel source. In fact, whereas the average gasoline vehicle has a practical cruising range of 450 to

650 km, the practical cruising range of the 2005 Toyota FCHV was approximately 220 km, which needed to be substantially improved (Fig. 2) [1].

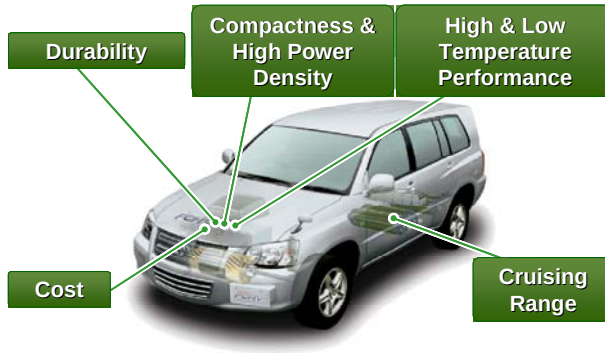


Figure 1 Technological issues of Toyota FCHV.

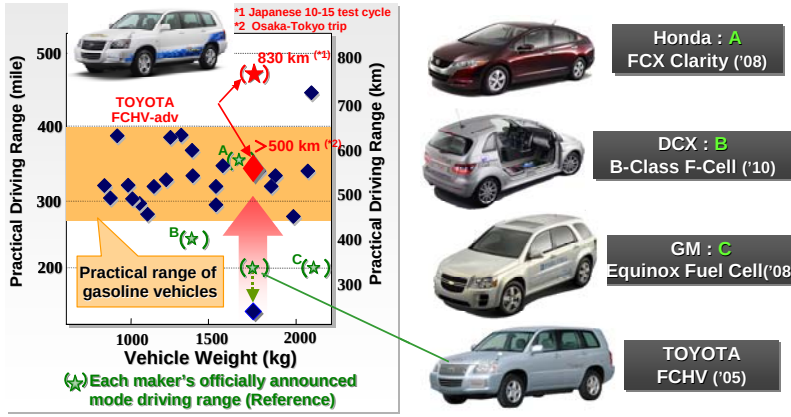


Figure 2 Practical cruising range.

Development of the Toyota FCHV-adv, progressed with the target of achieving a practical cruising range of 500 km. Extending the practical cruising range requires improving the practical fuel efficiency and increasing the amount of usable hydrogen.

Better fuel efficiency was accomplished by the accumulation of small improvements. Principally by reviewing the system, this development reduced losses occurring in the auxiliary units (such as the air compressor and the hydrogen pump) that are needed to operate the FC stack, and increased the amount of regenerative energy recovered from braking. These efforts achieved an

approximately 25 percent improvement in vehicle fuel efficiency compared with the 2005 model.

To increase the amount of usable hydrogen, the following improvements were made.

(1) The hydrogen filling pressure was increased to 70 MPa.
(2) The carbon fiber layer was made thinner to increase the inner volume of the hydrogen storage tank and reduce the tank weight.
(3) The valve size was reduced to increase the external volume of the tank and aluminum materials were applied to reduce the weight of the valve.
(4) The residual (unusable) gas was reduced.

As a result, while minimizing increases in the external volume and mass of the high-pressure hydrogen tank, the amount of usable hydrogen was increased approximately 1.9-fold compared with the 2005 model (35 MPa tanks).

Also, compared with the 2005 model, the FCHV-adv is approximately 25 percent more fuel efficient and contains approximately 1.9 times the amount of usable hydrogen. These improvements enable an approximately 2.4-fold increase in practical cruising range, to 500 km.

This shows that it is possible to extend cruising range, one of the major issues of the FCHV. However, the size of the high-pressure hydrogen tank remains more than double that of a gasoline tank, and basic material research is required for achieving a more compact and lighter hydrogen storage system (Fig. 3).

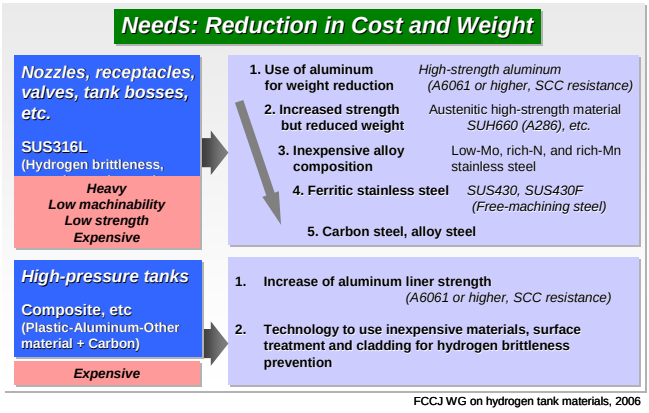


Figure 3 Future metallic materials for high-pressure hydrogen storage system.

2.2. Freeze Start Capabilities

Another issue confronting the FCHV, which only emits water as a waste product of power generation, is its freeze start capabilities. This refers to the problem of the freezing of generated water when the temperature is below zero, which impedes the power generation process. Over the past few years, several automotive companies

have reported substantial improvements in freeze start capabilities. Toyota's efforts proceeded while targeting -30ºC for the FCHV-adv, which is equivalent to current gasoline vehicles.

In order to ensure the FCHV system has adequate freeze start capabilities, the vehicle must be properly designed and controlled to preclude malfunction of the FC stack or system components caused by freezing under two possible scenarios: the vehicle being left unattended at freezing temperatures after running; and starting or driving of the vehicle at low temperatures.

To resolve these issues, the inside of a fuel cell below freezing point was visualized to investigate the phenomena and locations of freezing [2)]. Figure 4 shows the results of visualization inside a cell during operation at -10ºC. It indicates that even below freezing point, generated water exists for a while in a super-cooled state, allowing fuel cell operation to continue.

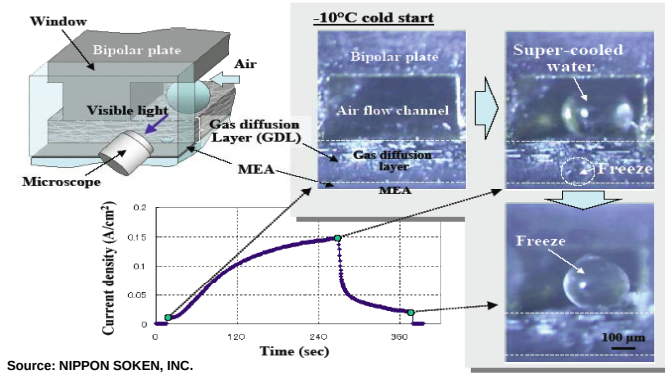


Figure 4 Visualization inside cell.

The visualization studies enabled the freeze start capabilities of the FC system to be improved by modifying the FC stack and control system. As a result, the FCHV-adv is capable of starting at a temperature of -30ºC. In evaluations conducted under actual environmental conditions, it was verified that the vehicle could start and run without problem in external temperatures as low as -37ºC.

2.3. Durability of FC Stack

As discussed above, significant improvements were made in cruising range and freeze start capabilities, which are major technological issues confronting the FCHV. To achieve further improvements and to ensure the viability of the FCHV as a commercial product, it is necessary to focus on the durability of the FC stack and reducing the cost of the FCHV system. Points to be addressed to improve the durability of the FC stack include the prevention of crossover due to fractures in the

electrolyte membrane, and performance decay as a result of catalytic electrode deterioration.

There have been significant improvements in crossover durability in the past several years. However, given that thinner electrolyte membranes will be introduced to improve performance, further technological development is needed as well as cost reduction of the membrane. In addition, the current level of performance degradation falls short of the minimum 15-year goal.

The degradation of the catalyst itself is main cause of the cell performance decay. To prevent the degradation, the catalyst particles including Pt need to be controlled at nano or atomic level. For it, understanding the properties of these nano-sized materials is essential and techniques for observing the material structures, such as an in-situ observation, are required.

Figure 5 shows the results of in-situ transmission electron microscope (TEM) observation of Pt reactions on Al_2O_3 [3]. It was observed that Pt particles started to move on the Al_2O_3 surface and coagulated with each other. To design catalyst for FCV, this technique will be useful.

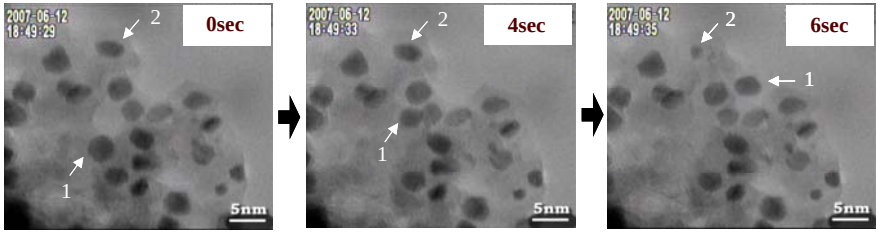


Figure 5 In-situ observation of Pt reactions using TEM (850℃, O_2 1Pa).

2.4. Cost Reduction

At present, the cost of the FCHV system remains high. To make the FCHV affordable for customers, its cost must be reduced and the remaining technological issues solved at the same time. Toyota's approach to cost reduction consists of two steps. The first step is to reduce costs to one-tenth the current level by reviewing materials and design, and the second step is to reduce costs to one-tenth again through mass production. Successful cost reduction will lead to popularization of the FCHV on a larger scale.

2.5. Summary of Current Status of Technological Issues

Figure 6 shows a summary of the current status of the technological issues confronting the Toyota FCHV-adv. In the light of the fact that some of the

technological issues are being solved on a steady basis, further efforts are required to reduce size and weight, improve durability, and lower costs.

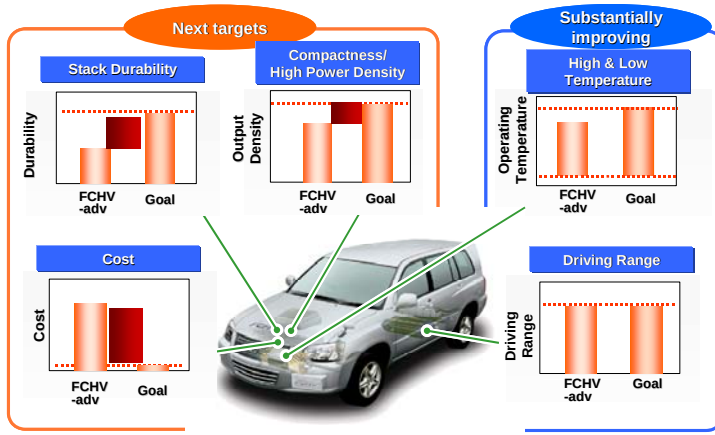


Figure 6 Latest status of technological issues confronting the Toyota FCHV-adv.

3. Issue of Hydrogen Infrastructure

The establishment of hydrogen infrastructure is essential for the popularization of FCVs. In addition to setting up hydrogen refueling stations, hydrogen production, transportation, and supply technologies must be developed in a manner that minimizes CO_2 emissions and costs. Codes and standards must also be established to ensure the safe handling of large volumes of hydrogen. It will become increasingly important to work together with government agencies and energy suppliers.

4. Prospects for Popularization of FCVs

Although it is difficult to predict the extent to which FCVs can be accepted in the market, the efforts between now and the year 2030 will have a significant impact. The introduction of the FCVs and the establishment of hydrogen infrastructure are currently entangled in a chicken and egg relationship. Energy suppliers and automobile manufacturers need to exchange views and information to promote mutual understanding. It goes without saying that national and local governments will also have an important role to play.

Replacement of the approximately 800 million vehicles currently on the road across the globe with vehicles powered by new energy sources such as FCVs will

require at least several decades, including the construction of infrastructure and the introduction of the necessary vehicles. Toyota will make efforts to develop production technology aiming toward the mass production of FC stacks and hydrogen tanks at the same time as technology for FC systems.

Toyota also intends to contribute to the building of a hydrogen energy society by working together with governments and energy suppliers.

5. Conclusion

The development and popularization of the FCVs is a pressing and critical issue for the diversification of energy sources and the reduction of CO_2 emissions. While steadily solving technological issues, the Toyota FCHV-adv has achieved a practical cruising range of over 500 km and a freeze start capability of -30ºC. In the future, basic material research is required for improving durability and reducing cost.

REFERENCES

1) S. Aso, M. Kizaki, H. Mizuno, "Development Progress of the Toyota Fuel Cell Hybrid Vehicle" *SAE 2008 World Congress*, No.2008-01-0420 (2008).
2) Y. Ishikawa, H. Hamada, M. Uehara, and M. Shiozawa, J. Power Sources, **179**, 547 (2008).
3) K. Kishita, H. Saka, K. Kuroda, A. Watabe, and T. Kamino, "In Situ Observation of Catalyst Reactions Using Transmission Electron Microscope" *SAE 2008 World Congress*, No.2008-01-1266 (2008).

Effects of Hydrogen on Materials
Proceedings of the 2008 International Hydrogen Conference
Brian Somerday, Petros Sofronis, Russell Jones, editors, p 332-340
Copyright © 2009 ASM International®
All rights reserved.
www.asminternational.org

METALLURGICAL CONSIDERATIONS FOR COMMERCIAL STEELS USED FOR HYDROGEN SERVICE

Douglas Stalheim
DGS Metallurgical Solutions, Inc.,15003 NE 10th Street,
Vancouver, WA 98684 USA

Louis Hayden
Louis Hayden Consultants,1301 Bonnie Ave
Bethlehem, PA 18017 USA

ABSTRACT

There are numerous grades of steels that are potentially commercially available for use in hydrogen service. Many of those grades are covered under societal specifications such as ASTM, API, etc. which give manufacturers of steel liberal chemistry limits to produce the desired mechanical properties. This along with different manufacturer's physical capabilities results in grades with similar mechanical properties, but differing microstructures and cleanliness. When monatomic hydrogen is able to diffuse into the steel matrix it looks for areas of high residual stress to collect. The largest source of residual stresses in a steel matrix is related to volume mismatches of microstructures. Other sources of residual stresses come from the overall cleanliness of the steel. Inclusion morphology and frequency create the overall cleanliness of these steels. Different chemical composition coupled with processing can affect microstructural and cleanliness variation that can have either beneficial or detrimental effects when exposed to monatomic hydrogen. This paper will discuss societal specifications and the influence of individual chemical composition and processing that is used in the production of commercial grade steels on microstructures and cleanliness. This discussion will include vintage and current steels used in the transportation of oil and gas. Because of these variations, the ASME B31.12 Hydrogen Piping and Pipeline Code Committee have developed two design methods that take current steel specifications and chemical compositions into consideration. Due to the variability of chemistry and the lack of statistically meaningful test data these two methods place a design or testing burden on the owner of the pipeline or piping system. Research and development that can be applied to an understanding of the desirable microstructure along with a cleanliness level that is suitable in commercial grade steels for hydrogen service is imperative.

INTRODUCTION

As a nation, we are dependent on foreign sources for the oil and natural gas necessary to drive our economy. In addition, there is increasing concern over the build-up of

greenhouse gases in the atmosphere that may lead to global warming. Various renewable energy concepts have been proposed, but only hydrogen as a fuel offers an infinite supply and leaves no objectionable by-products – only water.

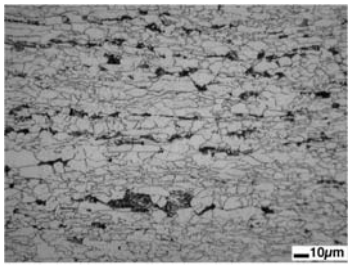
To achieve this goal we must begin a shift from our current hydrocarbon based infrastructure to a hydrogen-based infrastructure. This will require compromise in the way we fuel our vehicles and it will occur in stages. The one common thread between our current infrastructure and the new hydrogen economy is the transport, storage and delivery of the fuel to the point of use. One major concern is the public fear, and eventual acceptance, of bulk hydrogen transportation and storage. Therefore, the development and selection of materials that safely handle hydrogen in its various forms is a critical factor in the public acceptance equation.

This paper will concentrate on the pipelines to transport hydrogen fuel to support all aspects of the US transportation industry. It is the intent of this paper to discuss and analyze the materials that may be applicable for the massive infrastructure that must be developed. This discussion will center on the microstructures of carbon and high strength low alloy steels that appear to be most resistant to hydrogen embrittlement when used in hydrogen pipeline service.

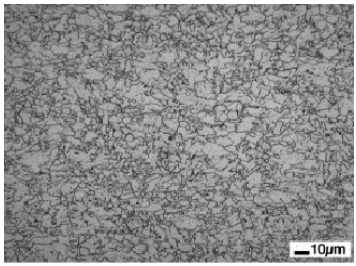
PIPELINE STEEL METALLURGY

Microstructure

The two most common microstructures that have been used in pipeline steels are ferrite/pearlite or a ferrite/bainite (acicular ferrite (a low carbon form of bainite)) [1], Fig. 1. The majority of the pipelines in the world that are currently servicing the oil and gas transmission pipeline infrastructure utilize a ferrite/pearlite microstructure. Recently, there has been a design shift from this microstructure to the ferrite/bainite (acicular ferrite) microstructure. This shift is primarily the result of the desire for higher operating pressures and fossil fuel source locations (strain based pipeline design for seismic, permafrost, etc. operating environments) which require higher strengths (API X80 and above) and toughness.



Example of Ferrite/Pearlite (<10%) Microstructure



Example of Ferrite/Bainite (acicular ferrite) Microstructure

Figure 1: Examples of typical microstructures used in pipeline steels.

Strength and Alloy Design

Pipeline steels produced and placed into service in the North American oil and gas transmission infrastructure in the 1940-60 timeframe were a simple C-Mn alloy design without any specific requirements to sulfur content or overall cleanliness. These grades were lower strength 50 (345 MPa) and 60 (414 MPa) KSI minimum yield strengths. The carbon content would be in the 0.20 wt% range with sulfur content around 0.020 wt%. These steels were processed via hot rolling and sometimes followed by normalizing. This would produce a ferrite/pearlite microstructure with a volume fraction of pearlite in the 30-50% range. As technology evolved the carbon (<0.10 wt%) and sulfur (<0.007 wt%) contents would be reduced, overall cleanliness improved and microalloy additions of niobium and vanadium would be used. These steels would be termed HSLA (high strength low alloy) steels by the industry. These HSLA steels would be processed with thermomechanical control processing (TMCP) resulting in higher strength grades of 65 – 80 KSI (440 – 550 MPa) minimum yield strength. The microstructure would continue to be a ferrite/pearlite microstructure, however due to the lower carbon content the volume fraction of pearlite would be reduced to less than 10% [2].

Since the 1990's there has been a shift toward the ferrite/bainite (acicular ferrite) microstructure. This microstructure is typically used in grades with minimum yield strengths ≥ 65 ksi (440 MPa). Grades utilizing this microstructure for pipeline transmission typically are produced using clean steel technology (for inclusion morphology control) with sulfur contents less than 0.003%. In addition, carbon contents <0.07% are routine. Other elements such as nickel and/or molybdenum must be added or higher contents of niobium or some combination that can form the bainitic microstructure through retardation of the kinetics of pearlite formation. The alloy design for this microstructure will form various volume fractions of bainite (acicular ferrite) depending on alloy design and processing.

Additionally, steels produced for sour service (hydrogen induced cracking, HIC) applications will have carbon contents <0.05% and sulfur contents less that 0.003%. This produces a very low volume fraction of pearlite, ~ less than 1%. This alloy design and resulting microstructure have demonstrated resistance to hydrogen cracking when exposed in NACE testing and service. Recently using the same low carbon approach, but creating a ferrite/acicular ferrite microstructure has also shown good HIC performance in NACE testing.

Table 1 shows typical alloy design used today in transmission pipeline steels.

Table 1: Example of Alloy Design for Various Strength Levels and Microstructure used in Transmission Pipeline Steels

API Grade	Steel Alloying Approach
X120	AF/Bainite/Martensite, C <0.10, Mn<2.0, Si<0.40, Nb<0.06, Cu, Ni, Cr, Mo, V, B, Pcm≤0.25
X100	AF/Bainite, C<0.06, Mn<2.0, Si<0.40,Nb<0.06, Cu, Ni, Cr, Mo, V, Pcm≤0.23
X80	F/AF, C≤0.06, Mn<1.70, Si<0.40, Nb≤0.10, Cu, Ni, Cr, Pcm≤0.18
	F/AF, C≤0.06, Mn<1.70, Si<0.40, Nb≤0.10, Cu, Ni, Mo, Pcm≤0.21
X70	D/t<50: F/AF, C≤0.06, Mn≤1.65, Si<0.40, Nb≤0.10 only, or Nb+Mo, Pcm≤0.18 or 0.21
	D/t>50 F/P, C≤0.10, Mn≤1.65, Si<0.40, Nb≤0.065 only, or Nb+V≤0.15, Pcm≤0.20
X65	F/P, C≤0.10, Mn≤1.65, Si<0.40, Nb≤0.065 only, or Nb+V≤0.15, Pcm≤0.23
X65 Sour Service	F/P, C≤0.05, Mn≤1.35, S≤0.003, Si<0.30, Cu+Ni+Cr ≤0.70, Nb≤0.065 only, or Nb+V≤0.15, Pcm≤0.15
X60	F/P, C≤0.10, Mn≤1.50, Si<0.40, Nb≤0.065 only, or Nb+V≤0.12, Pcm≤0.23
X60 Sour Service	F/P, C≤0.05, Mn≤1.20, S≤0.003, Si<0.30, Cu+Ni+Cr ≤0.70, Nb≤0.065 only, or Nb+V≤0.12, Pcm≤0.15
X52	F/P, C≤0.10, Mn≤1.20, Si<0.40, Nb≤0.050 only, Pcm≤0.17
X52 Sour Service	F/P, C≤0.05, Mn≤1.10, S≤0.003, Si<0.30, Cu+Ni+Cr ≤0.60, Nb≤0.050 only, or Nb+V≤0.10, Pcm≤0.13
X42	F/P, C≤0.10, Mn≤1.00, Si<0.40, Nb≤0.050 only, Pcm≤0.16
5LB	F/P, C≤0.20, Mn≤1.00, Si<0.40, Pcm≤0.16

F/P – Ferrite/Pearlite microstructure, F/AF – Ferrite/Acicular Ferrite microstructure,
Pcm – Ito-Bessyo Carbon Equivalent Formula, D/t – pipe diameter to thickness ratio

Pipeline Steel Processing

Depending on the strength requirement, alloy design and any microstructural considerations, rolling of plate or coil intended for pipeline applications can fall under four basic strategies, as shown in Fig. 2. The four basic strategies are as follows [3]:

Conventional hot rolling:

- Hot Rolled (HR) – the product finishes rolling at its prescribed final thickness with no regard to the final reduction temperature, i.e. it finishes naturally based on the mill's capability.
- Control Rolled (CR) – this involves setting a desired finish temperature and/or invoking a mild (2xfinal thickness, or 2T) intermediate hold temperature along with a desired finish temperature.

Thermo-mechanical rolling (TMCP):

- Thermo Mechanical Control Processing (TMCP) – generally involves a more substantial form of control rolling, i.e. a 3T-5T intermediate hold at 832-900 °C, along with a finish rolling temperature close to the steel's Ar_3.
- High Temperature Processing TMCP (HTP) again involves a substantial (3T-5T) intermediate hold but at 925-1020 C due to the higher Nb content, along with higher finish temperatures typically +80 °C above Ar_3.

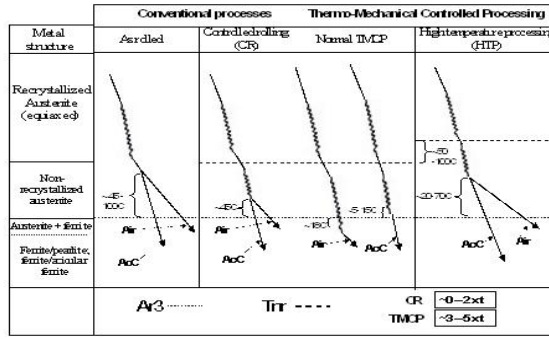


Figure 2: Schematic of four basic strategies used in the rolling pipeline steels

Mechanical property requirements (strength, toughness, etc.), chemistry being used (C, Mn, solute elements (Cu, Ni, Cr, Mo), microalloy strategy (Nb, V)), any microstructural considerations (ferrite/pearlite vs. ferrite/bainite, etc.) and a given mill's equipment capabilities will determine which strategy and the detail of the strategy that should be used.

It is this potential for various alloy designs and processing that can result in various microstructures and volume fractions of microstructures, but all with the similar final mechanical properties. Figure 3 shows how a single chemistry processed with various cooling rates can result in various volume fractions of ferrite/bainite as illustrated at cooling rate 15-20 C/s resulting in a 50% ferrite and 50% bainitic microstructure [4]. Increasing the cooling rate increases the volume fraction of bainite while decreasing the cooling rate increases the volume fraction ferrite.

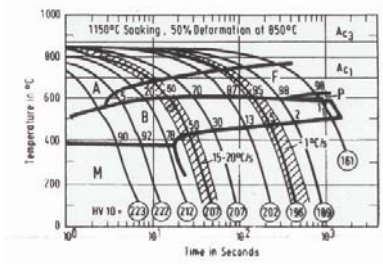
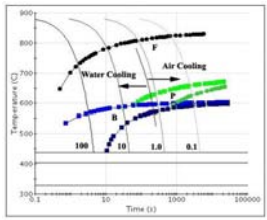
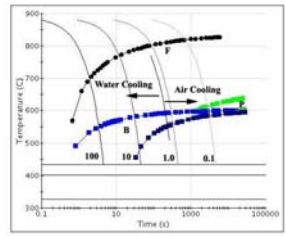


Figure 3: Illustration of cooling rate effect on volume fraction microstructure formation for a given alloy design.

Alloy design has a large influence on which microstructure can be formed. Figure 4 shows a continuous cooling transformation diagram (CCT) comparison of microstructure vs. cooling rate for C-Mn-Si-V-Nb pipeline steel vs. a C-Mn-Si-Mo-Nb pipeline steel [5]. Both can produce strength requirements for API X70.



CCT Diagram C-Mn-Si-V-Nb Pipeline Steel



CCT Diagram C-Mn-Si-Mo-Nb Pipeline Steel

Figure 4: CCT diagram showing comparison of two pipeline alloys.

Resistance to Hydrogen Induced Cracking

It has been well documented that resistance to hydrogen induced cracking in a sour service pipeline (corrosive environment) is heavily dependent on the microstructure formed and more importantly the volume fractions of a given microstructure. Hydrogen in the steel matrix collects at areas of high residual stress. Microstructural mismatches result in up to 50% of the total residual stress in a piece of steel. The most resistant microstructure to hydrogen induced cracking is a 100% tempered martensite. Key words in that statement are "tempered" (implying stress relief) and "100% martensite" (implying only one microstructure present). One of the highest areas of residual stress in a steel matrix is at the interface between two different microstructures. This is a common site for cracking to occur in a steel matrix when exposed to hydrogen. However, different microstructures and morphology ("banded vs. "islands") of the microstructure seem to create situations where residual stresses at these interfaces are low enough that hydrogen does not collect, hence making the microstructure resistant to hydrogen cracking or embrittlement. Table 2 shows four different pipeline microstructures performance in regard to their resistance to hydrogen when exposed to NACE TM0284 Solution A (low pH) test protocol [6].

Table 2: Example of four different pipeline microstructures hydrogen resistance in NACE TM0284 Solution A testing.

Structure	Crack Length Ratio (CLR)	Crack Sensitivity Ratio (CSR)	Crack Thickness Ratio (CTR)	Comment HIC Performance
Ferrite/Pearlite[1]	11.8	0	0.1	Poor
Ferrite/Acicular Ferrite[2]	0.4[2]	0	0	Good
Ferrite/Acicular Ferrite/Pearlite[3]	0	0	0	Good
Ferrite/Acicular Ferrite[4]	0	0	0	Good

1 - Pearlite approximately 7% by volume typical for chemistry design and processing
2 – Small amount of cracking not associated with microstructure, but rather inclusions
3 – Pearlite < 1% by volume related to processing of steel
4 – Steel purposely designed for HIC performance in sour service applications

Granted that the NACE testing is a corrosive type test for hydrogen embrittlement/ cracking and there may be concern that it does not represent the situation in a gaseous high pressure hydrogen environment, however it does not really matter how the hydrogen enters the steel matrix, once it is in the matrix the microstructures ability to resist embrittlement/cracking can be evaluated. This makes the NACE test a method to which an evaluation and screening of microstructures that may have potential for high pressure gaseous hydrogen service valid. Those microstructures that seem to perform poorly in a NACE test may be suitable for some applications in high pressure gaseous hydrogen. Determining the threshold to which a given microstructure and more importantly the volume fractions of given microstructural constituent that is suitable for high pressure gaseous hydrogen service is an important area that needs further research.

Specifications

As microstructures and volume fractions of microstructural constituents are identified as resistant to hydrogen induced cracking, how a producer of steel for these applications designs and processes the alloy can be critical. As was illustrated prior, there can be several different alloy designs/processing parameters that can produce the same mechanical property requirements. Today's specifications (ASTM, API, ISO 3183, etc.) for steels used in the pipeline infrastructure have fairly liberal alloy limits, Table 3 [7, 8, 9].

Table 3: Example of chemistry limits for equivalent strength steels used in pipeline service.

Major Elements (Maximum)	API 5L 43rd Edition X42 PSL 2	ASTM A53	ISO 3183 X42M
C	0.24	0.30	0.22
Mn	1.30	1.20	1.30
Si	No Limit	No Limit	0.45
P	0.025	0.05	0.025
S	0.015	0.025	0.015
Microalloy	Sum ≤ 0.15	V – 0.08 only	V&Nb – 0.05

This is not necessarily bad, but one has to understand that from this a given grade produced by two different manufacturers may have significantly different microstructures. In other words, not all API X70 necessarily has the same microstructure. This can have significance in regard to specifying the appropriate microstructure that has been found to be suitable for service in a high pressure gaseous hydrogen environment. Table 4 illustrates two alloy approaches that could be used to produce API X70 and ASTM A53 pipe and the expected microstructure that could be developed from alloy design.

Table 4: Illustration of possible alloy design and resultant microstructure for two pipeline grades of steel.

Major Element	API X70 Option 1	API X70 Option 2	ASTM A53 Gr B Option 1	ASTM A53 Gr B Option 2
C	0.07	0.04	0.08	0.18
Mn	1.55	1.55	1.10	0.80
Si	0.30	0.15	0.30	0.30
V	0.055	NA	NA	NA
Nb	0.065	0.065	NA	NA
Mo	NA	0.15	NA	NA
Estimated Microstructure	Ferrite/ Pearlite (~ 7-10%)	Ferrite/ Acicular Ferrite	Ferrite/ Pearlite (~12%)	Ferrite/Pearlite (~25%)

CONCLUSIONS

Chemistry specifications for pipeline steels are fairly liberal. This can result in manufacturers producing pipeline steels with various chemical compositions. Microstructure and more importantly a volume fraction of a particular microstructure plays a major role in a steels ability to resist hydrogen cracking/embrittlement. It has been illustrated that various grades of pipeline steels could be produced using different alloy designs resulting in various different microstructures and volume fractions of microstructural constituents. An understanding of microstructures and volume fractions of microstructures is required to properly design pipeline steels for use in high pressure gaseous hydrogen service. This research is critical to understanding if existing steel pipeline infrastructures can be used and if not what new pipeline steels should be used in a new infrastructure for transportation of high pressure gaseous hydrogen.

REFERENCES

1. Stalheim, D. *et al,* Alloy Designs for High Strength Oil and Gas Transmission Linepipe Steels, *Proceedings of Microalloyed Steels for the Oil & Gas Industry Symposium*, TMS, 2007, pp.73-108.
2. Hulka, K. Niobium Microalloyed Plate Products for Welded Constructions, Short Course Presentation, Anyang China, June 2006.
3. Hulka, K. *et al,* High Temperature Processing of Linepipe Steels, *Proceedings of the International Symposium Niobium 2001*, TMS, v. 1, p. 650 – 700, 2001.
4. Yajima et al., 'Extensive Application of TMCP-manufactured High Tensile Steel Plates to Ship Hulls and Offshore Structures', Mitsubishi Heavy Industries Technical Review, Vol 24 No. 1, February 1987.
5. Stalheim, D, *et al,* The Role of Continuous Cooling Transformation Diagrams in Material Design for High Strength Oil and Gas Transmission Pipeline Steels, *Proceedings of ASME 6th International Pipeline Conference*, Calgary, Alberta Canada, 2006.
6. Das, S, "Materials Solutions for Hydrogen Delivery in Pipelines", Presentation to the DOE Hydrogen Merit Review, Arlington, VA, June 2008.

7. API 5L, 43rd Edition Specification for Linepipe, March 2004.
8. ASTM A53/A53M-02, ASTM Standards, Volume 01.01, Steel – Piping, Tubing, Fittings, 2004.
9. ISO 3183-3 International Standard “Petroleum and Natural Gas Industries – Steel Pipe for Pipelines – Technical Delivery Conditions. ISO 3183-3, 2007.

Effects of Hydrogen on Materials
Proceedings of the 2008 International Hydrogen Conference
Brian Somerday, Petros Sofronis, Russell Jones, editors, p 341-348
Copyright © 2009 ASM International®
All rights reserved.
www.asminternational.org

SUSTAINED LOAD CRACKING OF STEELS FOR HYDROGEN STORAGE AND DELIVERY

K.A. Nibur, B.P. Somerday, D.K. Balch, C. San Marchi
Sandia National Laboratories, Livermore, CA, USA

ABSTRACT

It has become generally accepted that high strength steels (tensile strength >950 MPa) are unsuitable for use as hydrogen containment vessels due to the hydrogen-assisted fracture susceptibility of these alloys, therefore, interest has shifted to lower strength steels. Sustained load cracking experiments were conducted on four such steels following the basic procedures of a new American Society of Mechanical Engineers (ASME) design code. Resulting measurements of the threshold stress intensity factor for hydrogen-assisted fracture suggest these steels could be used reliably in high-pressure hydrogen service. Examination of the fracture surfaces and fracture profiles suggests hydrogen induced cracking occurs preferentially in ferrite grains and proceeds due to decohesion at carbide and martensite lath interfaces.

INTRODUCTION

Significant data have been generated on the fracture response of high strength, low alloy steels in hydrogen environments[1]. Because these alloys are susceptible to severe hydrogen-assisted fracture, much of this testing has been performed at relatively low hydrogen pressures. Industrial gas companies have decades of successful experience using lower strength alloys (<950 MPa) for hydrogen pressure vessels and pipelines, yet, despite this, remarkably little laboratory data exist for these lower yield strength steels. The exception is the work by Loginow and Phelps[2] who measured the sustained load cracking threshold stress intensity factor, K_{TH}, for a large variety of low to moderate strength steels (600 to 1000 MPa) in hydrogen gas in a commercially relevant pressure range (20 to 100 MPa). Their set of data showed that K_{TH} increases as either the hydrogen gas pressure or the strength of the alloy is reduced.

A new design code has recently been developed by ASME which provides a fracture mechanics based approach to the design of pressure vessels containing high pressure hydrogen[3]. The code, published as Article KD-10 in Section VIII, Division 3 of the ASME Boiler and Pressure Vessel Code, requires the measurement of K_{TH} and

fatigue crack growth rates in hydrogen gas at the design pressure. The purpose of this current study is to measure K_{TH} from several commercial alloys to assess the testing procedures dictated by KD-10, to provide benchmark data with which future data can be compared, and to study the hydrogen-assisted fracture modes in moderate strength steels.

EXPERIMENTAL PROCEDURES

Three Cr-Mo pressure vessel steels and a C-Mn linepipe steel were acquired in the form of curved panels cut from commercially produced tubular products. The three pressure vessel steels, meeting compositional specifications for DOT 3AAX, DOT 3T, and SA372 grade J, are generally consistent with AISI 41xx grade Cr-Mo steels with carbon content varying from 0.30 to 0.48. The actual compositions and yield strengths provided by the manufacturer are provided in Table 1. The fourth alloy tested was X100 line pipe steel, a micro-alloyed low carbon steel of proprietary composition with a yield strength of 786 MPa, measured in the circumferential direction.

Table 1: Composition and yield strength of the pressure vessel steels tested.

	C	Cr	Mo	Al	Mn	Si	P	S	Fe	S_Y (MPa)
SA372 grade J	0.48	0.96	0.18	0.026	0.92	0.30	0.010	0.002	Bal	717
DOT 3AAX	0.30	0.95	0.18	0.030	0.63	0.28	0.008	0.005	Bal	641
DOT 3T	0.45	0.97	0.18	0.034	0.86	0.25	0.013	0.006	Bal	896

Fracture mechanics test specimens were machined in accordance with ASTM E1681-03 modified bolt load wedge-opening-load (WOL) geometry; such that the crack plane was normal to the circumferential direction and crack propagation was parallel to the longitudinal direction of the tubular products. All of the specimens had the same in-plane geometry with width, W, equal to 56.9 mm, however the thickness was determined by the wall thickness of the tubular product. The SA372 grade J specimens were machined to 22.2mm thickness. The DOT 3AAX, DOT 3T and X100 steels were machined to utilize the full wall thickness of the starting product which was 17, 14, and 21 mm for the DOT 3AAX, DOT 3T and X100 steels, respectively. For these full-wall thickness specimens the specimen sides were curved corresponding to the outer diameter of the tubular products which was 635 mm for the DOT 3AAX, 560 mm for the DOT 3T and 1320mm for the X100. Side grooves were machined along the broad faces of the WOL specimens prior to pre-cracking to a total depth of 16% of the specimen thickness, B.

Pre-cracking was accomplished via cyclic loading in air to create starting crack lengths of 0.55 W at a final maximum stress intensity factor of 27 MPa $m^{1/2}$. Specimens were then placed into a glovebox with oxygen and moisture levels

controlled to below 2 ppm O_2 and 8 ppm H_2O to minimize surface oxides at the crack tip while load was applied to the specimens by bolt loading.

The bolt-loaded specimens were placed into a pressure vessel and the vessel was sealed while still inside the glovebox. The pressure vessel was then removed from the glovebox and, after a purging all associated gas manifolds,was filled to the test pressure with 99.9999% pure hydrogen gas. Test pressures varied from 21 to 138 MPa.

The stress intensity factor, K, was calculated using the relationship in ASTM E1681-03, such that K_{TH} is calculated based on physical measurements of the front face displacement applied to the specimen during bolt loading and the final crack length. Extensive details of the testing procedure are available in reference [4].

RESULTS

Optical micrographs from each of the four steels etched with Nital are shown in Figure 1. The DOT 3AAX, SA372 grade J and DOT 3T (Fig. 1 (a-c)) consist of a fine microstructure of ferrite (light phase), bainite and tempered martensite. The X100 (Fig. 1(d)) is composed of ferrite, acicular ferrite and bainite.

Values of K_{TH} were measured from three to six replicates of each alloy tested in 103 MPa hydrogen gas. These data are plotted as a function of yield strength in Fig. 2(a). This plot demonstrates that K_{TH} increases with decreasing strength. The effect of varying hydrogen gas pressure was demonstrated with DOT 3T and X100 specimens (Fig. 2(b)). X100 specimens were tested in hydrogen gas at pressures of 21, 103, and 138 MPa. A substantial reduction of K_{TH}, from 85 to 45 MPa $m^{1/2}$ was measured between tests performed in 21 and 103 MPa hydrogen gas; however, no further reduction of K_{TH} was measured for the test performed in 138 MPa hydrogen. Specimens from DOT 3T were tested at 41 and 103 MPa hydrogen gas pressure and a moderate reduction of K_{TH} from 45 to 35 MPa $m^{1/2}$was measured as the gas pressure increased.

The variation in values of K_{TH} measured for replicate specimens appears to be systematic in nature. As shown in a previous publication [4], K_{TH} increased as the initial applied stress intensity factor increased. This is postulated to result from residual plastic deformation on the back face of the specimen, which may affect the arrest position of cracks as they near the back face. This problem is compounded by the need to apply a large initial stress intensity factor (large displacements) to the specimens in order to initiate propagation of cracks, since crack bifurcation upon initial loading may reduce the effective stress intensity factor [4].

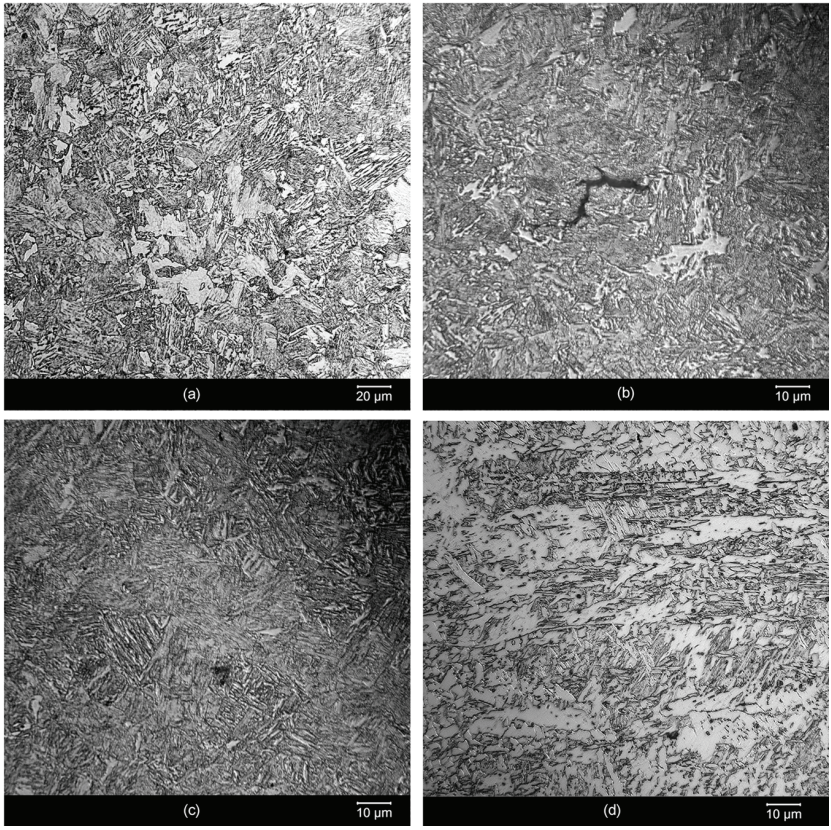


Figure 1. Optical micrographs showing polished and Nital etched microstructures of (a)DOT 3AAX, (b) SA372 grade J, (c) DOT 3T, and (d) X100. Images are oriented such that the long axis of the tube is left to right and radial direction is vertical. The crack in (b) results from the section's proximity to the fracture surface.

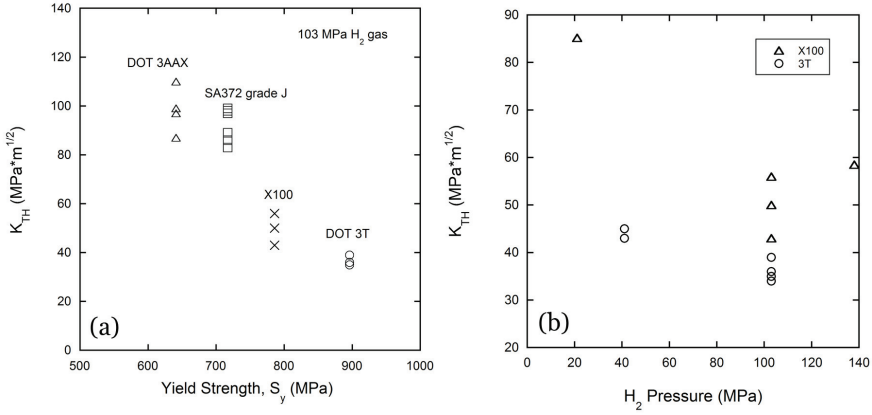


Figure 2. K_{TH} plotted as a function of (a) yield strength and (b) H_2 gas pressure.

The appearance of the fracture surfaces was similar for all of the specimens tested. Secondary electron images (SEI) of the hydrogen assisted fracture surface of a DOT 3AAX specimen and an X100 specimen are shown in Fig. 3. Fracture surfaces from DOT 3T and SA372 grade J appear similar to the DOT 3AAX with the exception that a greater density of secondary cracking was observed on the DOT 3T specimens. No indication of common fracture modes such as microvoid coalescence or intergranular fracture were found on any of the primary fracture surfaces; however, secondary cracking in the DOT 3T appears to be following grain boundaries to some extent. The dominant characteristic of the fracture surfaces is a feathery appearance. Arrows in Fig. 3 point to examples of feather-like features in the DOT 3AAX and X100. These features are much larger and are oriented with the crack propagation direction (also the rolling direction) in the X100, whereas those on the DOT 3AAX tend to be smaller and less aligned.

Examination of polished and etched cross sections of the fracture surface reveals transgranular cracking through ferrite grains (Fig. 4). The blunting of a crack in the DOT 3AAX about 50 μm below the primary fracture surface (Fig. 4(a)) demonstrates that the fracture process involves significant plasticity; however, the sharp cracks, noted by arrows, suggest that the fracture process may begin as sharp, transgranular cracks in the ferrite. Similar sharp, transgranular cracks were also observed in ferrite grains in the X100 (Fig. 4b).

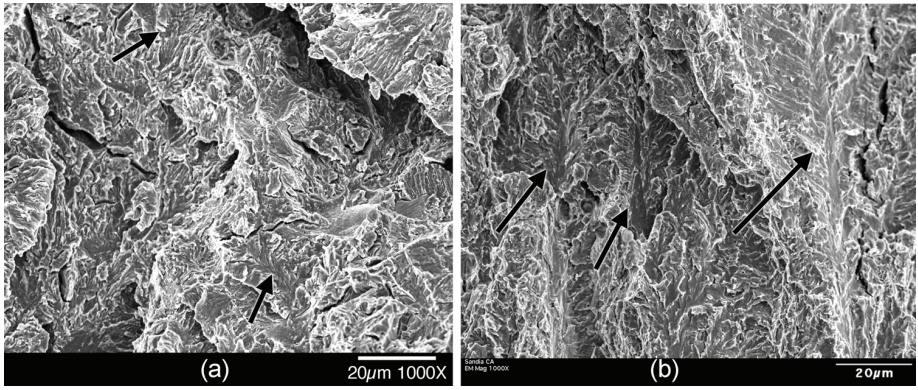


Figure 3. Fracture surface images of (a) DOT 3AAX and (b) X100. Arrows point to examples of feather-like features on the fracture surface.

DISCUSSION

K_{TH} Measurements

The data presented in Figure 2 corroborate the trends identified by Loginow and Phelps [2] that K_{TH} can be increased either by decreasing the alloy strength or by

decreasing the hydrogen gas pressure. Similar ranges of alloy composition, strength and hydrogen gas pressure were examined in both the Loginow and Phelps and the current studies and, while the nature of the trends were the same, the actual values of K_{TH} measured in the current study were as much as two times the values obtained by Loginow and Phelps for a given set of conditions [4]. One possible reason for this, as pointed out in a previous publication [4], may be that the fracture toughness in air (e.g. K_{Ic}) of modern steels has improved over those tested by Loginow and Phelps. A second, and perhaps more significant source of this difference, may be in the analytical solution used to calculate a value of K_{TH} from the position of the arrested crack. For crack lengths greater than 0.8 times the specimen width (a/W>0.8), the K-solution suggested by ASTM E1681 is as much as two times greater than the Novak and Rolfe solution [5] referenced by Loginow and Phelps [2]. The accuracy of the solution provided in ASTM E1681 has been independently verified as accurate for all crack lengths in unpublished finite element analyses by two researchers[6,7].

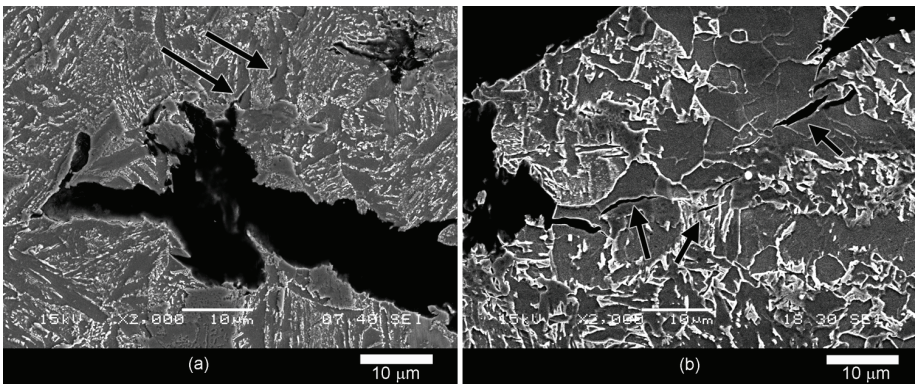


Figure 4. Fracture profiles etched with Nital showing transgranular cracks in (a) DOT 3AAX and (b) X100.

Fracture Mechanisms

The fracture surfaces of all four alloys consist of transgranular fracture surface features, but the precise fracture path relative to the microstructure is not clear. Fracture surfaces very similar to those presented here have been observed by other researchers studying hydrogen-assisted cracking in low to moderate strength steel. It has often been vaguely referred to as *quasicleavage* (e.g. [8]). Takeda and McMahon refer to fracture modes that are similar to those in Fig. 3 simply as plasticity-related hydrogen-induced cracking (PRHIC) [9]. They suggest it results from a combination of glide plane decohesion and decohesion along martensite lath interfaces.

The fracture surfaces are notable for the absence of intergranular and cleavage fracture. That said, neither of these fracture modes can be ruled out entirely due to

the fine features and complicated nature of both the microstructures and fracture surfaces of these steels. Secondary cracking in the DOT 3T, for instance, occasionally shows features resembling grain boundary triple points suggesting that some small degree of intergranular fracture may have taken place. Cross sectional views of the DOT 3AAX and X100 both show sharp, transgranular cracks in ferrite grains which are suggestive of localized cleavage fracture although slip plane fracture cannot be ruled out as a possibility.

The presence of these sharp cracks in ferrite grains suggests that ferrite may play an important role in hydrogen assisted cracking of ferritic steels. The size and orientation of ferrite grains in both the DOT 3AAX and X100, seen in the optical micrographs (Fig. 1) are consistent with the feather-like features seen on the fracture surfaces (Fig. 3). The value of examining fracture profiles, such as those presented in Fig. 4, is that they indicate the early stages of crack propagation. The transgranular ferrite cracks occurred prior to complete propagation of the primary crack. This indicates that the initial stages of crack advance involve cracking through ferrite grains. Subsequent crack growth occurs by linking of these ferrite microcracks.

It is not particularly surprising that ferrite appears to be a susceptible constituent to hydrogen induced cracking. In all steel alloy classes, ferrite has consistently been observed to be vulnerable to hydrogen assisted cracking. Cleavage of ferritic phases in stainless steel alloys (e.g. welds [10], forgings [11], and duplex alloys [12]) has been observed in hydrogen precharged test specimens. Additionally, Cialone and Holbrook [13]discovered that ferrite was far more susceptible to hydrogen-assisted fatigue crack growth than was pearlite.

The observations of this study, along with those of Takeda and McMahon [9], suggest that hydrogen-assisted crack advance in Cr-Mo and C-Mn steels is preceded by cracking of the ferrite either by cleavage or by glide plane decohesion. Further crack advance through other microstructure constituents may include hydrogen induced decohesion of carbide or lath interfaces.

CONCLUSIONS

Threshold stress intensity factors at crack arrest (K_{TH}) have been measured for three low alloy pressure vessel steels and a C-Mn line pipe steel. The highest values of K_{TH} were observed to correlate to the lowest values of yield strength and lowest hydrogen gas pressure. Values of nearly 100 MPa $m^{1/2}$ were measured for alloys with yield strength less than 750 MPa. Fracture surfaces show no significant indications of cleavage or intergranular fracture. Transgranular cracking of ferrite grains appears to represent the first step in hydrogen-assisted crack propagation.

ACKNOWLEDGMENTS

Sandia is a multiprogram laboratory operated by Sandia Corporation, a Lockheed Martin Company, for the United States Department of Energy under contract DE-AC04-94AL85000.

REFERENCES

1 Gangloff, R.P. “Hydrogen assisted cracking of high strength alloys” in *Comprehensive Structural Integrity*, Vol. 6, I. Milne, R.O. Ritchie and B. Karihaloo, Eds., Elsevier Science, New York, NY, (2003), pp. 31-101.
2 Loginow, A.W. and Phelps, E.H. “Steels for Seamless Hydrogen Pressure Vessels” *Corrosion*, Vol. 31, No. 11, November (1975), pp. 404-412.
3 ASME Section VIII, Division 3 Code, 2007 Edition, Article KD-10, “Special Requirements for Vessels in High Pressure Gaseous Hydrogen Transport and Storage service”, ASME, New York, NY
4 Nibur, K.A., Somerday, B.P., San Marchi, C., and Balch, D.K. “Measurement of sustained-load cracking thresholds for steels in hydrogen delivery and storage” Proceedings of PVP2008, 2008 ASME Pressure Vessels and Piping Division Conference, July 27-31, 2008, Chicago, Illinois. PVP2008-61298.
5 Novak, S.R. and Rolfe, S.T. “Modified WOL specimen for K_{Iscc} environmental testing” *Journal of Materials*, JMLSA, Vol. 4, (1969), pp. 701-728.
6 Sofronis, P., University of Illinois, Urbana, Ill. Private communication 2008.
7 Foulk, J.W., Sandia Natl. Labs., Livermore, CA. Private communication 2008.
8 Beachem, C.D. “A new model for hydrogen-assisted cracking (hydrogen “embrittlement”)”, *Metall. Trans*., Vol. 3, (1972), pp. 437-451.
9 Takeda, Y. and McMahon, C.J., Jr “Strain controlled vs stress controlled hydrogen induced fracture in a quenched and tempered steel” *Metallurgical Transactions A*, Vol. 12A, 1981, pp.1255-1266.
10 Somerday, B.P., Balch, D.K., Dadfarnia, M., Nibur, K.A., Cadden, C.H., and Sofronis, P., “Hydrogen-Assisted Crack Propagation in Austenitic Stainless Steel Fusion Welds” *Metallurgical and Materials Transactions A*, 2008, in review.
11 Nibur, K.A., Somerday, B.P., Balch, D.K., and San Marchi, C. “The Role of Localized Deformation in Hydrogen-Assisted Crack Propagation in 21Cr-6Ni-9Mn Stainless Steel” *Metallurgical and Materials Transactions A*, 2008, in review
12 San Marchi, C., Somerday, B.P., Zelinski, J., Tang, X., and Schiroky, G.H. “Mechanical properties of super duplex stainless steel 2507 after gas phase thermal precharging with hydrogen” *Met Trans*, Vol. 38A, (2007), pp. 2763-2775.
13 Cialone, H.J. and Holbrook, J.H. “Microstructure and fractographic features of hydrogen-accelerated fatigue crack growth in steels” in *Microstructural Science* Vol. 14, Eds. M.R. Louthan, I. LeMay, and G.F. Vander Voort, ASM, Metals Park, OH, (1987), pp. 407-422.

Effects of Hydrogen on Materials
Proceedings of the 2008 International Hydrogen Conference
Brian Somerday, Petros Sofronis, Russell Jones, editors, p 349-356
Copyright © 2009 ASM International®
All rights reserved.
www.asminternational.org

Tensile and Fracture Properties of Carbon and Low Alloy Steels in High Pressure Hydrogen

Kang Xu and Mahendra Rana

Praxair, 175 East Park Dr., Tonawanda, NY 14150

INTRODUCTION

Carbon steels and low alloy steels are widely used in handling high pressure hydrogen gas. However, because of the well known hydrogen embrittlement issues, only low to intermediate strength carbon steels and alloy steels are considered for hydrogen applications at relatively low pressures. At higher pressures, austenitic stainless steels which exhibit no property degradation in hydrogen, are commonly specified.

The strength of materials and hydrogen pressure are considered to be the most important factors in gaseous hydrogen embrittlement. The property degradation of high strength carbon and low alloy steels in hydrogen gas has been extensively studied and reported. It is well established that the fracture toughness of carbon and low alloy steels decreases with increasing alloy strength and hydrogen pressure. In welded constructions, restrictions have been applied to chemical composition to limit the carbon equivalent so that adequate toughness is guaranteed in the weld and heat affected zone (HAZ). Additionally, attempts also have been made to limit the allowable design stress as a function of alloy strength and the hydrogen pressure by ASME B31.12 Hydrogen Piping and Pipeline Committee. However, these attempts were found to be lacking in technical basis [1]. One of the reasons is that the pressure dependence of the mechanical properties of low and intermediate strength carbon or alloy steels has not been systematically documented.

Based on the service experience, ASME Boiler and Pressure Vessel Code VIII-3 (Code) defined the high pressure hydrogen and high strength steels according to pressure vessel construction method. In a welded construction, the high pressure is defined as hydrogen partial pressures higher than 17.3 MPa or 5.2 MPa when the steel tensile strength exceeds 621 MPa. In a non-welded construction, the high pressure is defined as hydrogen partial pressures higher than 41.1 MPa or 5.2 MPa when the steel tensile strength exceeds 945 MPa. The Code limits the maximum design pressure to be 100 MPa [2].

In this investigation, a low strength carbon steel (ASME SA-106 Grade B, UTS ~ 480 MPa) and an intermediate strength alloy steel (ASME SA372 Grade J Class 70, UTS ~ 830 MPa) were selected to measure tensile properties at various hydrogen pressures. The dependence of yield strength, tensile strength, tensile elongation and tensile reduction of area on hydrogen pressure was documented. The change in fracture mode was also documented.

MATERIALS AND EXPERIMENT PROCEDURES

Materials

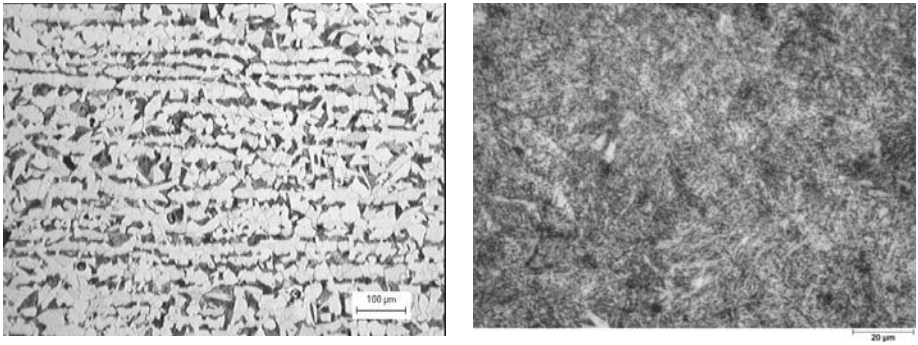
Two alloys were tested: ASME SA-106 Grade B and ASME SA-372 Grade J Class 70. SA-106 is used in piping applications and SA372 is used in the construction of ASME VIII-1 pressure vessels. The chemical composition and tensile properties are listed in Tables 1 and 2. The SA-106 is a plain carbon steel which has a ferrite and pearlite microstructure as shown in Figure 1(a). It has a much lower strength than the SA-372 as shown in Table 2. SA 372 is a Cr-Mo quench and temper alloy steel which has a tempered martensite microstructure, as shown in Figure 1(b). Both materials have been tested in hydrogen to measure fracture toughness in previous studies [2 ,3]. Both materials have been accepted in hydrogen service.

Table 1. Chemical composition of SA-106 and SA-372

Material	C	Mn	P	S	Si	Cr	Mo	Al
SA106 Gr. B	0.18	1.06	0.009	0.009	0.24	0.05	0.01	0.037
SA372 Gr. J	0.46	0.92	0.01	0.005	0.25	0.96	0.18	0.22

Table 2. Tensile properties of SA-106 and SA-372

Material	0.2% Yield (MPa)	UTS (MPa)	EL in 2" G. L. (%)	RA (%)
SA106 Gr. B	297	518	28	55
SA372 Gr. J	725	883	20	60



(a) SA-106 (b) SA-372

Figure 1. Microstructures

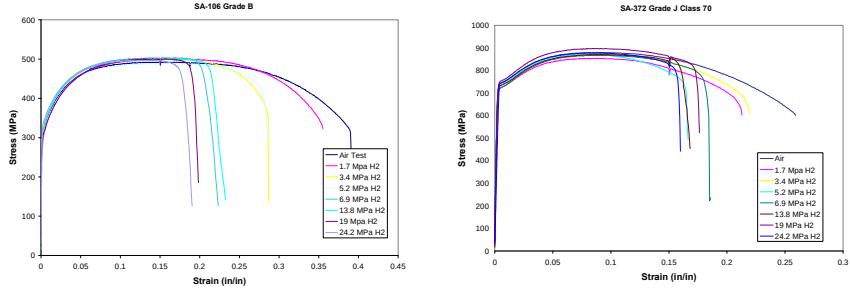
Experimental Procedures

All hydrogen tests were conducted in an autoclave mounted in a servo hydraulic testing frame. The tensile specimens had a gage length of 12.7 mm. The tests in hydrogen were conducted at pressures from 1.7 to 24.2 MPa. Since gaseous hydrogen embrittlement is sensitive to loading rate, the tensile loading rate in hydrogen tests was selected as 0.1 mm/min which is corresponding to a strain rate of $1.3x10^{-4}$ /s. The strain rate was at least one order magnitude lower than regular tensile tests. The slower loading rate would encourage hydrogen diffusion and maximize the embrittlement effect. A regular extensometer was used to measure the strain to up to 15%, beyond which the strain was converted from the displacement data because of the limit of the extensometer. The calibration of the extensometer was checked and verified in high pressure hydrogen. The impurities in hydrogen gas were monitored by analyzing the gas contents after test. It was found that the moisture level was higher than expected (20-80 ppm). The overall impurity was considered low and satisfactory.

EXPERIMENTAL RESULTS

Tensile Properties:

The tensile stress strain curves at different hydrogen pressures are shown in Figures 2(a) and (b) for SA-106 and SA-372 respectively. It is apparent that the hydrogen pressure has no influence on the yield and tensile strengths but a significant impact on the tensile ductility (elongation and reduction of area). The difference is insignificant at the initial portion of the stress strain curves tested in air and in hydrogen up to the uniform elongation. The yield strength, work hardening rate and tensile strength were essentially the same in air and in hydrogen.

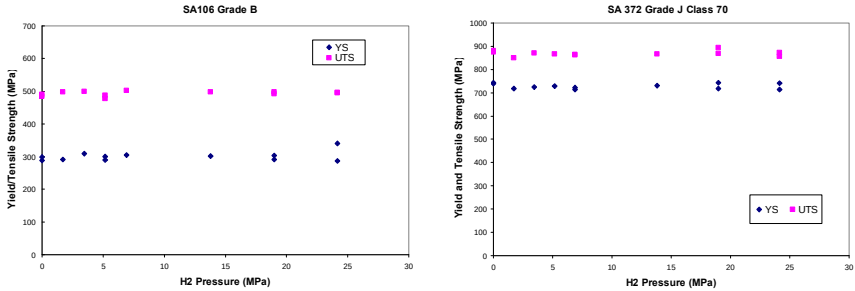


(a) SA-106 (b) SA-372

Figure 2. Stress strain curves

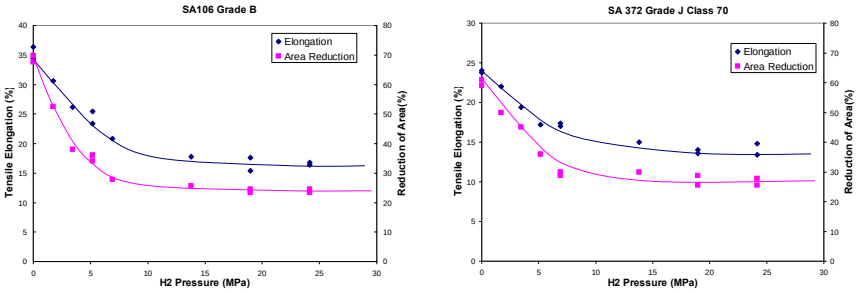
The dependence of tensile properties of SA-106 and SA-372 on hydrogen pressure is shown in Figures 3 and 4. Both materials exhibited a similar dependence on hydrogen pressure. The yield and tensile strengths were not affected by hydrogen, as shown in Figures 3(a) and 3(b). The tensile elongation and area reduction showed a gradual reduction with increasing hydrogen pressure to about 6.9 MPa, beyond

which the tensile ductility did not show further reductions as shown in Figures 4(a) and 4(b). The amount of reduction in tensile ductility for the two materials is also comparable: On average SA-106 showed 43% and 64 % reductions in elongation and reduction of area respectively; whereas SA-372 showed 37% and 58% reductions in elongation and area reduction respectively.



(a) SA-106 (b) SA-372

Figure 3. Dependence of yield/tensile strength of on hydrogen pressure

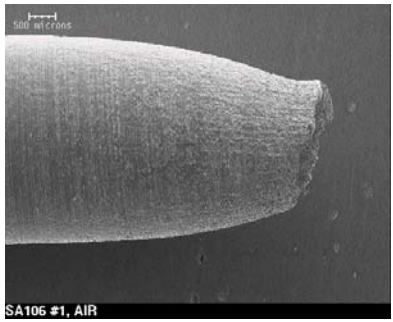


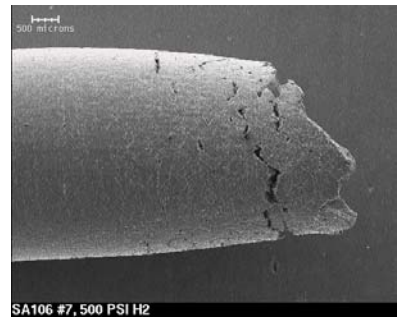
(a) SA-106 (b) SA-372

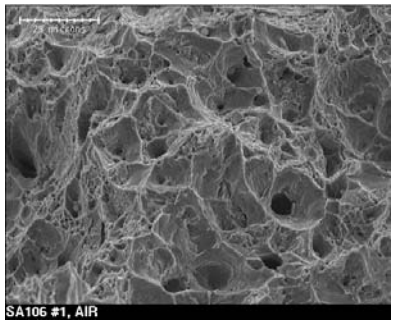
Figure 4. Dependence of tensile ductility on hydrogen pressure

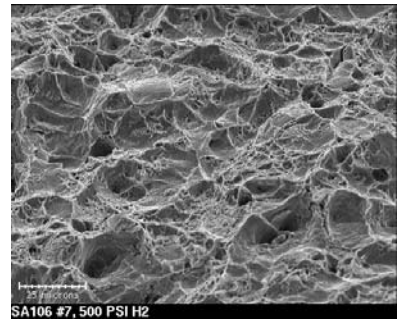
Fracture Mode:

Hydrogen had a significant effect on the fracture mode of the tension tested specimens. Figures 5(a) to 5(d) show the fracture surfaces of SA-106 observed in Scanning Electron Microscope (SEM). The specimen tested in air exhibited typical dimple ductile fracture with significant necking. At 3.5 MPa hydrogen, the material still exhibited considerable ductility. The hydrogen effect can be seen from the fissure cracks on the specimen surface. The fracture surface was still dominated by ductile dimples with the presence of brittle cleavage fracture as shown in Figure 5(b). At 6.9 MPa H2, the ductility was significantly reduced and no visible necking was noticed. The fracture surface was very flat and ductile dimples completely disappeared (Figure 5(c)). The fracture mode was 100% brittle transgranlar cleavage fracture with some tear ridges. At higher hydrogen pressures, the fracture surface remained essentially the same as the one at 6.9 MPa H2. The change in fracture mode in hydrogen closely followed the change of tensile ductility as described in the previous section. The fracture behavior of SA-372 as a function of hydrogen pressure was very similar to that of SA-106.

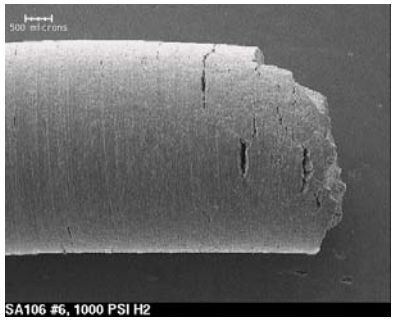


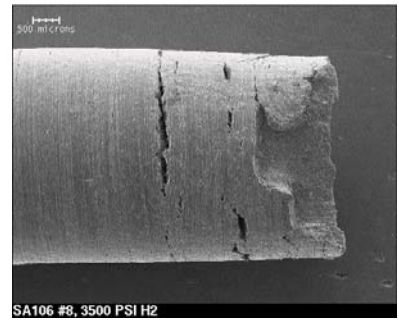


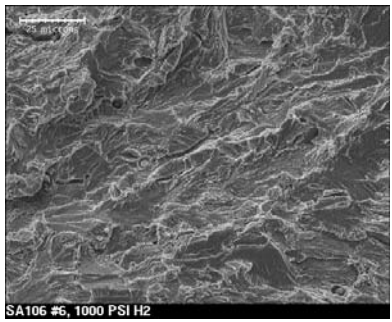


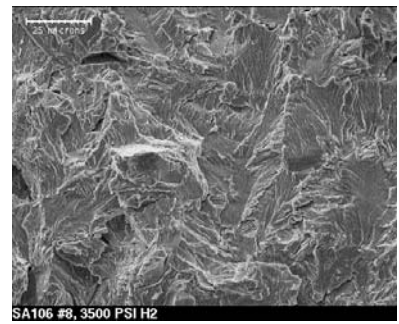


(a) Air test (b) 3.5 MPa H2









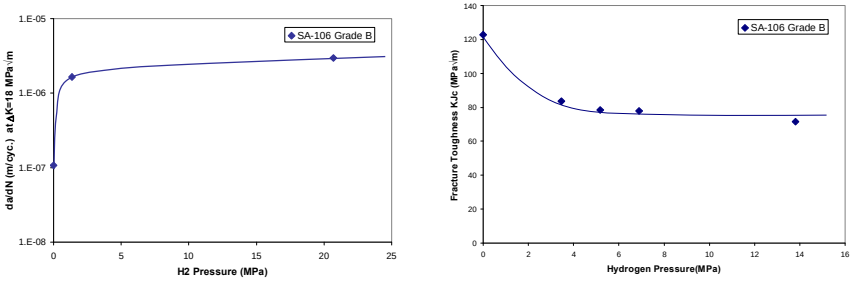
(c)6.9 MPa H2 (d) 24.2 MPa H2

Figure 5. Fracture surface of SA-106 tensile specimens: (a) air (b) 3.5 MPa H2 (c) 6.9 MPa H2 and (d) 24.2 MPa H2

DISCUSSION

The data presented above demonstrated that in the range studied, the presence of high pressure hydrogen did not affect the strength of carbon and alloy steels with tensile strength up to 880 MPa. The effect of hydrogen pressure was only observed on the tensile ductility of the steels. The tensile ductility reduced with hydrogen pressure but the reduction saturated at about 6.9 MPa and no further degradation was observed beyond that pressure. The amount of ductility reduction at saturation was about 40% and 60% for elongation and area reduction respectively. The tensile fracture mode showed a similar change with hydrogen pressure.

A similar saturation with hydrogen pressure has been observed in the fracture toughness and fatigue crack growth rate [3]. Figure 6 shows the pressure effect on the fatigue crack growth rate (da/dN) of SA-106, which increased rapidly with hydrogen pressure but saturated at about 2.5×10^{-6} m/cyc. at 3.5 MPa H2. Figure 9 shows the pressure effect on the fracture toughness of SA-106, which decreased from 120 MPa√m without hydrogen, to about 70 MPa√m at 6.9 MPa H2 and saturated at this value.



(a) da/dN (b) K_{Jc}

Figure 6. da/dN and K_{Jc} in hydrogen for SA-106[3]

The property saturation with hydrogen pressure indicated that the property degradation is controlled by the saturation of hydrogen traps. Once the material is saturated with hydrogen, no further property degradation occurs. It has been reported that quenched and tempered steels with tensile strength as low as 820 MPa exhibited sustained load cracking [4]. However, a separate study has demonstrated that even with 880MPa tensile strength, the SA 372 did not show any tendency of hydrogen cracking at pressures up to 31 MPa. For low to intermediate strength steels which do not exhibit sustained load cracking in hydrogen, a continuous plastic deformation seems to be a necessary condition for hydrogen embrittlement to occur, which suggests dislocation activities play an essential role in hydrogen embrittlement. The saturation effect on the tensile ductility, da/dN and fracture toughness can be related to the hydrogen saturation of dislocations, which limits their ability to transport hydrogen along the slip plane. The observation also suggested that the mechanism of hydrogen embrittlement of low strength steels is hydrogen enhanced localized plasticity [5].

The ASME Code allowable design stresses are established by applying a design margin to yield strength or tensile strength for pipelines and pressure vessels. Since it has been demonstrated that hydrogen has an insignificant influence on the yield and tensile strength, the current design rule appears to be adequate for H2 service. The reduced ductility in hydrogen does not affect the structural integrity of the component since the applied nominal stresses are within the linear elastic range, much lower than the yield strength. The reduced fracture toughness in hydrogen should be considered. However, the relatively high fracture toughness (K_{1c}) of the low to intermediate strength steels warrants that the failure is mostly controlled by the strength rather that by fracture toughness in hydrogen. Additionally, the ductility and fracture toughness degradation in hydrogen saturates at about 6.9 MPa and a higher hydrogen pressure does not appear to result in additional degradations. Therefore, for carbon and low alloyed steels which are not susceptible to sustained load cracking in a hydrogen environment, current ASME design rules are sufficient regardless of the hydrogen pressure. A fracture assessment [2] is necessary for higher strength alloys which exhibit a lower threshold stress intensity factor (K_{1H}) in hydrogen or for welded constructions that contain possible extra hard spots in the weld and heat affected zone (HAZ) which are susceptible to hydrogen cracking. In cyclic service, the fatigue crack growth rate (da/dN) significantly increases by the presence of hydrogen. However, hydrogen does not appear to affect fatigue crack initiation and threshold cyclic stress intensity factor (ΔK_{th}). These factors must be taken into account in the design for cyclic service.

It is also pointed out that commercial seamless carbon and low alloy steel vessels have been successfully used in hydrogen at pressures up to 42 MPa and no in-service failures have been observed due to the loss of ductility. This indicates that the reduced ductility in H2 is still high enough for satisfactory service. There has been no industrial experience with carbon and low alloy steels in hydrogen pressures beyond 100 MPa.

CONCLUSIONS

In previous studies, carbon steels exhibited moderately reduced fracture toughness and substantially increased fatigue crack growth rate in high pressure hydrogen. The degradation in both fracture toughness and fatigue crack growth rate saturated with hydrogen pressure. In this study, tensile tests were performed on SA-106 grade B and SA-372 Grade J class 70 steels at hydrogen pressures up to 24.2 MPa. The effect of hydrogen pressure on tensile properties was documented. The conclusions are summarized as follows:

1. In the range studied, the presence of high pressure hydrogen has an insignificant effect on the yield strength, tensile strength and work hardening rate. The initial portion of the stress strain curve up to the uniform elongation strain is essentially the same in air and in high pressure hydrogen.
2. Hydrogen pressure has a significant effect on the tensile ductility. The maximum reduction in tensile elongation and reduction of area was about

40% and 60% respectively in hydrogen. The reductions saturated at about 6.9 MPa H2 and no further reduction was observed at higher hydrogen pressures. The tensile fracture mode showed a similar change with hydrogen pressure.

3. The current ASME strength based design rules are sufficient for low to intermediate strength alloys which do not exhibit cracking in hydrogen under static loading conditions. Hydrogen pressure appears to be not a factor. A satisfactory industrial service experience has been noted with carbon or low alloy steels at hydrogen pressures up to 42 MPa. Fracture assessment should be performed for high strength steels that exhibit cracking tendency or in weld constructions.

REFERENCES

1. Design Guideline for B31.12 Piping and Pipeline, ASME B31.12 Hydrogen Piping and Pipeline Committee.
2. Rana, M.D., Rawls, G. B., Sims, J.R., Upitis, E. "Technical Basis And Application Of New Rules On Fracture Control Of High Pressure Hydrogen Vessel In ASME Section VIII, Division 3 Code" PVP 2007 Conference
3. R. Zawierucha, K. Xu, "Hydrogen Pipeline Steels", in Materials for Hydrogen Economy Symposium, Materials Science and Technology 2005 Conference and Exhibition, p. 79, 2005
4. A. W. Loginow and E. H. Phelps, "Steels for Seamless Hydrogen Pressure Vessels", Corrosion, Vol. 31, No. 11, p. 404-412, November, 1975.
5. S. P. Lynch, "Mechanisms of Hydrogen Assisted Cracking – a Review", Hydrogen Effects on Materials Behavior and Corrosion Deformation Interactions, Ed. N. R. Moody, A. W. Thompson, R. Ricker, G. Was and R. Jones, TMS, 2002, p. 449.

Effects of Hydrogen on Materials
Proceedings of the 2008 International Hydrogen Conference
Brian Somerday, Petros Sofronis, Russell Jones, editors, p 357-364
Copyright © 2009 ASM International®
All rights reserved.
www.asminternational.org

DAMAGE UNDER HIGH-PRESSURE HYDROGEN ENVIRONMENT OF A HIGH STRENGTH PIPELINE STEEL X80

I. Moro, L. Briottet, P. Lemoine
CEA, LITEN, DTH, F-38054 Grenoble, France.

E. Andrieu, C. Blanc, G. Odemer
CIRIMAT/ENSIACET, Toulouse, France.

J. Chêne, F. Jambon
CEA, DEN, F-91191 Saclay, France.

KEYWORDS

High strength steel, X80, Hydrogen embrittlement, Hydrogen content, Mechanical tests under high pressure H_2, Trapped / Lattice hydrogen.

INTRODUCTION

The present study deals with an assessment of the hydrogen embrittlement (HE) susceptibility of a high strength steel grade (X80). The respective influence of hydrogen location, in lattice sites or traps, and the associated mechanisms have been addressed through hydrogen concentration measurements, mechanical testing in gaseous hydrogen atmosphere at room temperature and modeling of hydrogen diffusion. The results may contribute to a better understanding of HE in such ferrito-pearlitic steels in order to establish a predictive model of rupture in high pressure hydrogen gas.

EXPERIMENTAL PROCEDURE

Materials

Two materials were considered in this study: a high strength steel grade X80 used for pipeline applications and, for comparison purpose, Armco iron (99.8% Fe) with an average grain size of 80 µm. X80 has a ferrito-pearlitic microstructure with a ferrite grain size ranging between 5 and 15 µm. Its chemical composition is given in Table 1.

Table 1: Chemical composition of X80 (weight %)

C	Mn	Si	Nb	V	Cu	P	S
0.075	1.86	0.35	0.05	<0.01	0.22	0.015	<0.003

Hydrogen content

To evaluate HE susceptibility of the materials, the hydrogen content has been measured on strained tensile specimens. Flat tensile specimens were hydrogenated during 60 min in hydrogen gas at 30 MPa and then plastically deformed at 0, 3, 6 and 12% with a strain-rate of $5x10^{-5}s^{-1}$ under 30 MPa H_2 gas. Specimens were kept in liquid nitrogen at the end of the tests. Few minutes before measuring the hydrogen content, the tensile specimens were taken from liquid nitrogen and cut to prepare small samples (≅2x3x5mm) for hydrogen concentration measurements. The samples were mechanically polished with #1200 SiC grit paper and cleaned in ethanol and acetone. The hydrogen concentration was measured using the nitrogen-carrier-fusion thermal conductivity method (JUWE H-Mat 2500 analyser), which involved melting the samples at 1500°C. For each condition at least 4 measurements were performed.

Tensile tests in hydrogen gaseous environment

Tensile tests were carried out on a MTS servo hydraulic testing system in a pressure vessel filled with gaseous hydrogen or nitrogen up to 35 MPa. Before mechanical loading the specimens were exposed to the gaseous atmosphere for 30 min for smooth axisymetric specimens and 60 min for notched axisymetric specimens. This may favor H entry in the samples during this precharging period. However it has been shown that the duration of precharging has low influence on HE. All the tests have been conducted at room temperature and a strain rate of $5x10^{-5}s^{-1}$.

RESULTS

Measure of hydrogen content versus plastic strain

A plot of the hydrogen content trapped in the dislocations C_T versus the plastic strain is presented in Figure 1. C_T has been deduced from the experimental measurements taking into account the initial H content from elaboration, the lattice H content and H in preexisting traps.
First it appears that for both materials, trapped hydrogen content increases with plastic strain. These results agree with previous ones [1,2]. However, assuming that traps are fully saturated with one hydrogen atom per trap site, our values of C_T in iron are higher than those of Kunmick *et al*. [2]. In fact, for annealed pure iron they obtained a trap density N_T of $8.5x10^{+20}$ m^{-3} and for 15 % cold-worked pure iron N_T was equal to $5.9x10^{+22}$ m^{-3}. This discrepancy may be attributed to the method which was used and to irreversible trapping. Kunmick *et al*. [2] obtained N_T by permeation transient measurements at low H_2 pressure and used each specimen for 40-60 permeation runs. They noticed that the first run may lead to results different from later runs, which can be the indication of irreversible trapping.

Moreover, the occupancy of low energy traps is very low at such H_2 pressure.
Also, it can be noticed that Kunmick found C_T nearly constant above a critical plastic strain ε_{pc}=60%. Considering X80, saturation of trapped hydrogen is obtained above 10%.

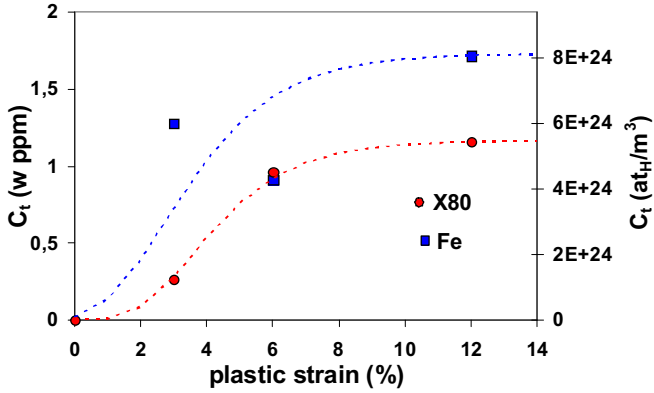


Figure 1: Evolution of C_T, with plastic strain ε_p

Second, trapped hydrogen content is found higher in iron than in X80. This result looks surprising taking into account that the interfaces between ferrite and pearlite are likely to trap hydrogen atoms. An explanation could be linked to the higher apparent diffusion coefficient in iron than in X80 inducing a deeper penetration of H in iron.
Finally, by interpolating experimental data, the evolution of C_T with ε_p can be expressed as:

$$C_T\left(at_H / m^3\right) = 10^{24.73 - 3.74\exp\left(-60.17\varepsilon_p\right)} \quad \text{for X80} \quad (1)$$

$$C_T\left(at_H / m^3\right) = 10^{24.91 - 1.86\exp\left(-53.4\varepsilon_p\right)} \quad \text{for iron} \quad (2)$$

Tensile tests on smooth axisymetric specimens in H_2 gas

We investigated the susceptibility of X80 to HE and the influence of strain rates. Tensile tests were carried out at various strain rates in 30 MPa gaseous hydrogen environments (Fig. 2).
One specimen was tested under 30 MPa of nitrogen at $5x10^{-5}$ s^{-1} for comparison. It is observed that hydrogen does not influence the yield stress nor the ultimate tensile stress. Ductility is strongly decreased by hydrogen after the onset of necking and with strain rate. This result agrees with those of previous workers [3].
The influence of hydrogen pressure has been addressed on tensile tests performed at $5x10^{-5}$ s^{-1}. Tests were carried out under three hydrogen gas pressure: 0.1, 10 and 30 MPa (Fig. 3). It is observed that HE appears above a critical hydrogen pressure. Under a hydrogen pressure of 0.1 MPa

of H_2 gas, the ductility is not decreased in significant proportion. Post mortem analysis in terms of reduction of area at fracture as well as gage length and fracture surface observations did not reveal any effect of hydrogen. By comparison at 10 MPa the loss of ductility is close to that obtained under 30 MPa. This experimental fact can be explained, using Sievert's law [4] which predicts a hydrogen solubility proportional to $\sqrt{P_{H2}}$. According to this law, the hydrogen solubilities under the explored experimental conditions are the following: $C_{L1}=2.1x10^{+22}$ at_H/m^3 at 30 MPa, $C_{L2}=1.2x10^{+22}$ at_H/m^3 at 10 MPa and $C_{L3}=1.2x10^{+21}$ at_H/m^3 at 0.1 MPa. It is then concluded that C_{L3} is too low to induce HE in the studied material providing that the solubility was reached during the experiment.

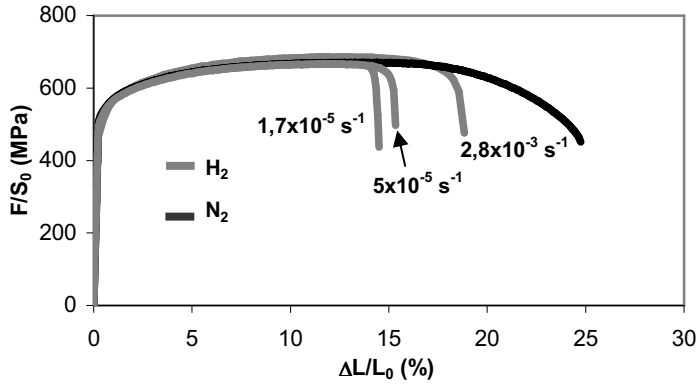


Figure 2: Tensile tests in hydrogen gas - Effect of strain rate.

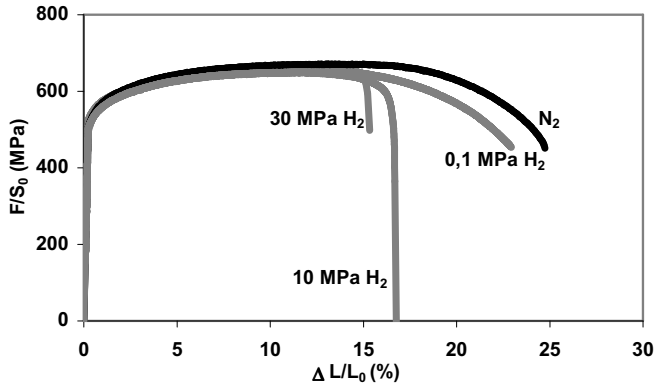


Figure 3: Tensile tests in hydrogen gas - Effect of hydrogen pressure

The fractographs of smooth axisymetric specimens (Fig 4) show the difference of ductility under nitrogen and hydrogen gas. The fracture surfaces are ductile with dimples under nitrogen and look brittle under hydrogen. Moreover, cracks parallel to the pearlite alignments of the microstructure are observed under hydrogen. A longitudinal section of a

specimen tested under hydrogen shows microcracks perpendicular to the tensile direction and mostly located through pearlite phases.

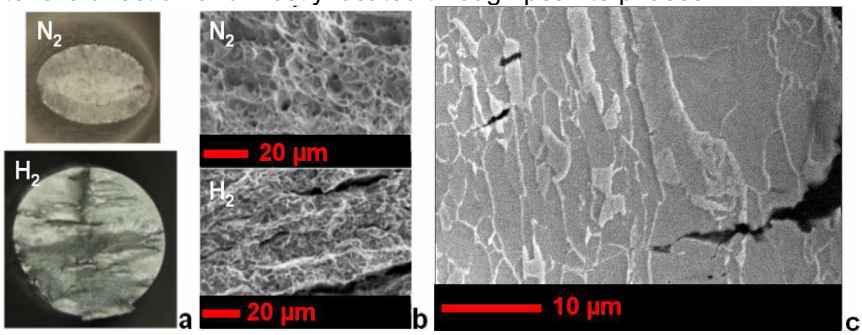


Figure 4: Surface rupture (a) SEM fractographs (b) and longitudinal section (c) of smooth specimens broken in nitrogen and hydrogen gas

Tensile tests on notched axisymetric specimens in H_2 gas

Tensile tests were carried out on notched axisymetric X80 specimen at 0.05 mm/min under 30 MPa hydrogen gas. Several notch radius were studied ranging from 0.1, 0.8, 3.4 and 10 mm (Fig. 5).

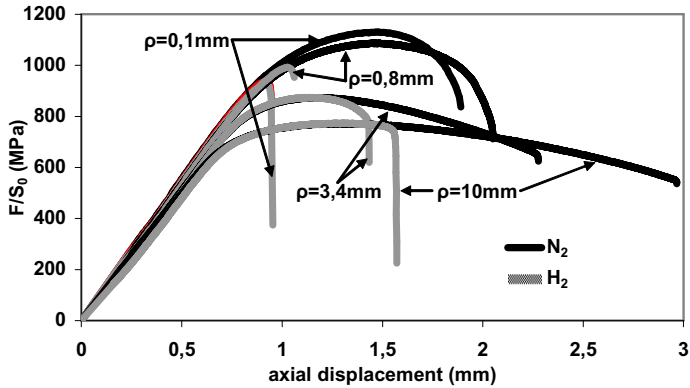


Figure 5: Tensile tests on notched axisymetric specimens.

According to Bridgman's description of the mechanical state of notched specimens, the stress triaxiality was respectively equal to 3.1, 1.4, 0.7 and 0.5. For the specimens with the lowest stress triaxialities, i.e. ρ=3.4 and10mm, the maximum stress did not depend on the type of gaseous environment (Fig. 5). However, displacements at fracture were strongly decreased under hydrogen. At the highest stress triaxialities, ie ρ= 0.1 and 0.8 mm, the maximum loads reached were significantly decreased under hydrogen testing conditions. Moreover, an embrittlement index, based on the respective reduction area under nitrogen and hydrogen gas, showed that HE strongly increased with stress triaxiality.

Simulation of hydrogen diffusion

Using the model developed by Krom *et al*. [5], assuming equilibrium between hydrogen in lattice sites and traps [6], the hydrogen diffusion, coupled with the mechanical fields, has been simulated in the tensile specimens using FEM CAST3M. The parameters used are: trap binding energy W_b=60 kJ/mol, number of lattice sites N_L=5.1x10^{+29} m^{-3}, lattice diffusion constant D_0=1.27x10^{-8} m²/s, partial molar volume of hydrogen V_H=2x10^{-6} m^3/mol. The function $N_T(\varepsilon_p)$ is given by equation (1). In Fig. 6, C_L and C_T are given along the radius of the smallest section of specimens ρ=0.1 and 10 mm at onset of rupture in hydrogen environment. The initial hydrogen concentration in the sample is 0 at$_H$/m^3, and is imposed equal to 2.13x10^{22} at$_H$/m^3 on the external surfaces.

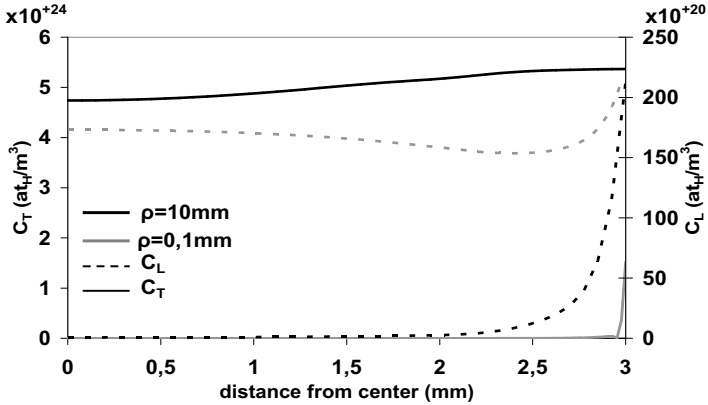


Figure 6: Evolution of C_L and C_T in the smallest section of the specimens

It can be noticed that the values of C_T given by the simulations are closely connected with experimental data. As an example, for ρ=10 mm, at the end of the simulation ε_p=26.8% and C_T=5.15x10^{+24} at$_H$/m^3. Equation (1) gives $C_T(\varepsilon_p$=26.8%)=5.37x10^{+24} at$_H$/m^3. This result tends to confirm the value chosen for Wb. Indeed, the same simulation performed with W_b=20 kJ/mol gives C_T=9.55x10^{+20} at$_H$/m^3.

Trapped hydrogen effect on HE

Interrupted tensile tests were performed on axisymetric notched specimens in X80. The tests were stopped and unloaded just beforerupture (dark cross in Fig. 7). The hydrogen pressure was then removed and replaced by 0.2 MPa in nitrogen during 3 hours. The tests were then continued until rupture in nitrogen. The dwell duration has been defined using previous simulations to allow lattice hydrogen to leave specimens while keeping the major part of trapped hydrogen. After the dwell under nitrogen, specimens with high stress triaxiality, i.e. ρ=0.1 mm, exhibit the same maximum stress as in air, unlike tests fully realized in hydrogen gas. However, for both

geometries, even if ductility after degassing specimens in nitrogen is greater than for those which were tested on hydrogen gas only, it is still lower than for specimens tested on nitrogen gas only.

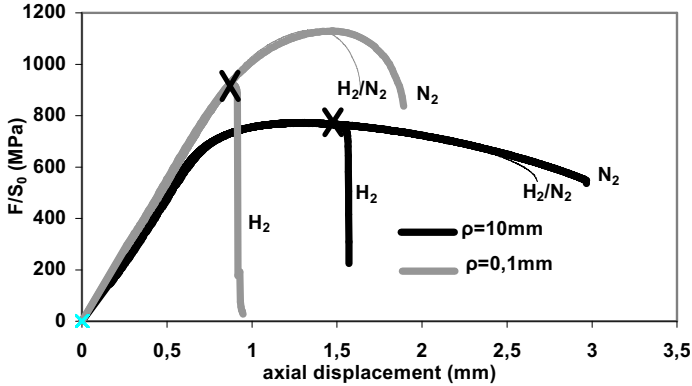


Figure 7: Interrupted tensile tests on notched axisymetric specimens.

DISCUSSION

Although it seems clear that H content is strongly influenced by plastic strain and by H transport by dislocations, numerous damage mechanisms are proposed to explain HE. Among those, Hydrogen Enhanced Plasticity (HELP) and Hydrogen Induce Decohesion (HID) [7,8] seem appropriate in our conditions. The first one expresses the fact that hydrogen atoms in metal affect dislocations behavior. The second one is based on the assumption that hydrogen decreases the atomic bonding of materials. However, part of lattice as well as weakly or strongly trapped hydrogen in these mechanisms is not clear but will influence predictive rupture models in terms of location and moment of rupture.

Studying the previous results (Fig. 2) and according to equation (1), we can assume that at the onset of rupture the specimens have similar C_T because ε_p>10%. However, the simulations show that C_L is greater in the test at$1.7x10^{-5}$ s^{-1} than at $2.8x10^{-3}$ s^{-1} because hydrogen has time to diffuse. This result shows that trapped hydrogen is not the only responsible for HE. It also explains why elongation at rupture is greater at low strain rate. Regarding tests at different hydrogen pressure (Fig. 3) and equation (1), the same conclusions can be made since at the onset of rupture C_T is similar for each test and C_L decreases with hydrogen pressure. Moreover, the interrupted tests (Fig. 7) and the associated simulations (Fig. 6) show that the remaining hydrogen (mainly trapped) leads only to low HE. Thus, rupture can not be explained by a critical value of C_T, but more probably by a critical set of C_L or $C_{tot}=C_L+C_T$, associated to a mechanical parameter such as ε_p. Furthermore, the observed localization of microcracks in the

pearlite phases implies that the microstructure should be taken into account in a predictive rupture model.

CONCLUSION

HE susceptibility of X80 was studied through hydrogen content measurements and mechanical tests in hydrogen gas. An expression of $C_T(\varepsilon_p)$ was established and used to simulate hydrogen diffusion coupled with mechanical fields. Moreover, it was shown that trapped hydrogen content increases with ε_p and seems to reach a constant value above a strain of 10%. The correlation between the simulations and the trapped hydrogen measurements is in favor of a rather high value of the trap biding energy (about 60 kJ/mol). The mechanical tests in hydrogen gas show that HE decreases with strain rate and increases with hydrogen pressure and stress triaxiality. Moreover, these tests, correlated with the simulations, bring a better understanding of the trapped and lattice hydrogen influence in HE. Even if C_T is higher than C_L, strongly trapped hydrogen can not be responsible by itself for HE. Fracture in hydrogen seems strongly dependent of the local lattice or total hydrogen concentration, associated to mechanical parameters, probably plastic strain. Finally, it was shown that microstructure has an influence on HE with microcracks mostly located through pearlite phases. This will be further investigated through SIMS analysis on deuterium charged specimens.

REFERENCES

1. M.L. Hill and E.W. Johnson, "Hydrogen in cold worked Iron-Carbon alloys and the mechanism of hydrogen embrittlement", *Transactions of the metallurgical society of AIME,* Vol. 215, pp. 717-725 (1959)
2. A.J. Kumnick and H.H. Johnson, "Deep trapping states for hydrogen in deformed iron", *Acta Metall.*, Vol. 28, pp. 33-39, (1980)
3. A.H.M. Krom *et al*., "The effect of strain rate on hydrogen distribution in round tensile specimens", *Materials Science and Engineering,* Vol. A27, pp. 22-30, (1999)
4. A.M. Brass, J. Chêne and L. Coudreuse, "Fragilisation des aciers par l'hydrogène : mécanismes", *Techniques de l'Ingénieur,* Vol. M176
5. A.H.M.Krom *et al*., "Hydrogen transport near a blunting crack tip", *JMPS*, Vol. 47, pp. 971-992, (1999)
6. R.A. Oriani, "The diffusion and trapping of hydrogen in steel", *Acta Metallurgica*, Vol.18, pp. 147-157, (1970)
7. P. Sofronis, I.M. Robertson, D.D. Johnson and B. Somerday, "Hydrogen embrittlement - Fundamentals, Modeling and experiment", DOE Hydrogen Pipeline Working Group Meeting, September 25, (2007)
8. H.K. Birnbaum, I.M. Robertson, P. Sofronis and D. Teter, "Mechanisms of hydrogen related fracture - A review", European Federation of Corrosion Publications, n°21, pp. 172-195, (1997)

Effects of Hydrogen on Materials
Proceedings of the 2008 International Hydrogen Conference
Brian Somerday, Petros Sofronis, Russell Jones, editors, p 365-372
Copyright © 2009 ASM International®
All rights reserved.
www.asminternational.org

EFFECTS OF HYDROGEN AND PRESTRAIN ON TENSILE PROPERTIES OF LOW-CARBON STEEL USED IN HYDROGEN PIPELINES

Hiroshi Nishiguchi
Graduate School of Engineering, Kyushu University, Fukuoka, Japan

Yoshihiro Fukushima and Saburo Matsuoka
Department of Mechanical Engineering Science, Kyushu University, Fukuoka, Japan and The Research Center for Hydrogen Industrial Use and Storage (HYDROGENIUS), National Institute of Advanced Industrial Science and Technology (AIST), Fukuoka, Japan

INTRODUCTION

A carbon steel pipe for pressure service, STPG370 (STPG), has been investigated for use in hydrogen pipelines. Under the exposure to a high-pressure (1 MPa) hydrogen environment, steel suffers from hydrogen embrittlement [1–3]. In addition, gas pipelines in Japan must be made earthquake-proof in order to prevent them from being affected by large cyclic strains. Three to five cycles of cyclic strain with an amplitude of 3% are experienced for Level 2 earthquakes such as the "Great Hanshin-Awaji Earthquake," and fifty to sixty cycles of cyclic strain with an amplitude of 0.5% are experienced for Level 1 earthquakes such as the "Great Kanto Earthquake." In this study, the effects of hydrogen and prestrain on the tensile properties of STPG were investigated. Furthermore, the role of pearlite in decreasing the ductility of carbon steel in the presence of hydrogen was discussed.

EXPERIMENTAL METHODS

An STPG pipe (outer diameter: 407 mm; radial thickness: 8 mm) was produced by hot rolling. Table 1 shows the chemical composition and Vickers hardness of the STPG pipe. The Vickers hardness was found to be 127 (±5%) kgf/mm^2 (indentation force: 9.8 kN; holding time: 30 s; number of measured points: 20). Figure 1 shows a microstructure (ferrite-pearlite) of the longitudinal section of the STPG pipe. Figure 2 shows the image of one of the tensile specimens, which were machined out from the STPG pipe in the axial direction. These tensile specimens were cylindrical with a diameter of 4.8 mm and length of 30 mm. All the specimens were polished with emery paper #600. Virgin and prestrained specimens were prepared. The virgin

Table 1: Chemical composition (mass%) and Vickers hardness of STPG.

C	Si	Mn	P	S	*HV*
0.19	0.21	0.56	0.012	0.010	127

samples were subjected to a total strain of 10 or 20% by tensile test to yield the prestrained specimens. For hydrogen precharging, tensile specimens with prestrains (ε_{pre}) of 0, 10, and 20% were immersed in a 20 mass% aqueous solution of ammonium thiocyanate at 313 K for 48 h. The hydrogen content was measured by a gas chromatography-type thermal desorption analyzer (TDA). The rate of temperature increase was 0.028 K/s. Tensile tests were carried out at room temperature in air. The cross-head speed was 1 mm/min. The elongation was measured by an extension meter with a gage length of 25 mm. After the tensile tests, the fracture surfaces were observed by a scanning electron microscope (SEM). After the longitudinal sections of the tensile fracture specimens were buff polished and etched using 3% nital, the sections were observed by SEM.

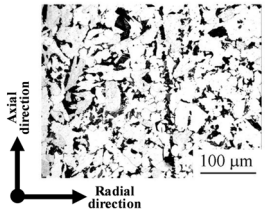


Figure 1: Microstructure of STPG.

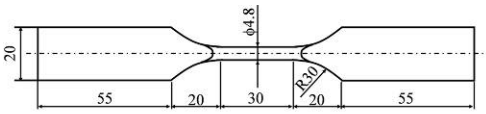


Figure 2: Dimensions of the tensile specimen (mm). Thickness: 5 mm.

RESULTS AND DISCUSSION

The hydrogen contents, C_H, of the uncharged and hydrogen-precharged specimens before the tensile tests were measured. The hydrogen contents, C_H, of the uncharged specimens were found to be 0.0 wppm both for ε_{pre} = 0% (virgin specimen) and ε_{pre} = 20%. The hydrogen contents of the hydrogen-precharged specimens were 0.2 wppm for ε_{pre} = 0%, 1.0 wppm for ε_{pre} = 10% and 2.6 wppm for ε_{pre} = 20%. Thus, the hydrogen contents of the hydrogen-precharged specimen increased with ε_{pre}. Note that the total hold time in the air from the hydrogen charge to the hydrogen measurement was about 40 min.

Figure 3 shows the nominal stress-strain curves. In this figure, C_H is the hydrogen content before the tensile test, $C_{H,R}$ is the residual hydrogen content after the tensile test, and Δt is the total hold time in the air. The $C_{H,R}$ was measured after about 45 min from the tensile test. The asterisk (*) mark in Figs. 3(b) and (c) indicates necking near the edge of the extension meter. In this case, the nominal strain measurements are not very accurate. Therefore, the reduction of area is used as a measure of ductility loss caused by hydrogen [4–6]. At ε_{pre} = 0% (Fig. 3(a)), the curves obtained before and after hydrogen precharging overlapped, and there was no significant difference in reduction of area (ϕ = 69%) between the hydrogen-precharged and uncharged specimens. This is due to the low hydrogen contents in the uncharged specimen (C_H = 0.0 wppm) and the hydrogen-precharged virgin specimen ($C_{H,R}$ = 0.1 wppm, Δt = 117 min). Figure 3(b) shows the nominal

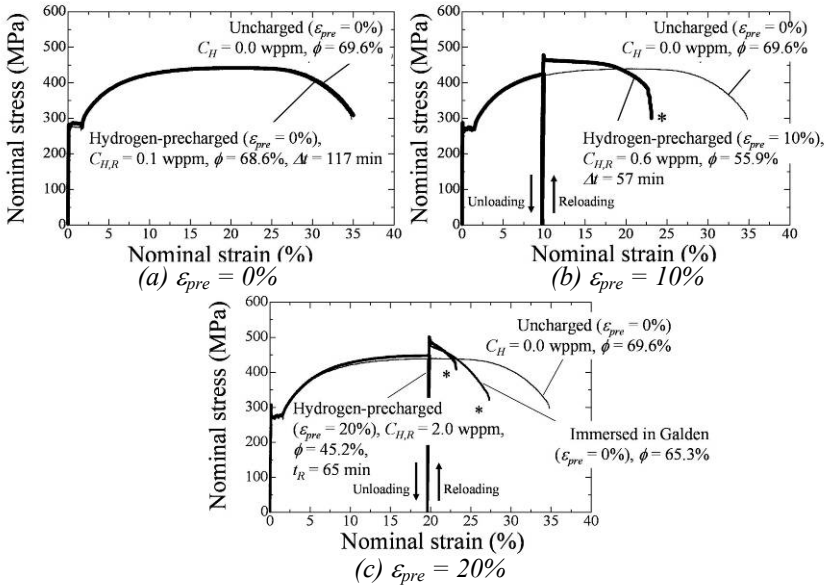
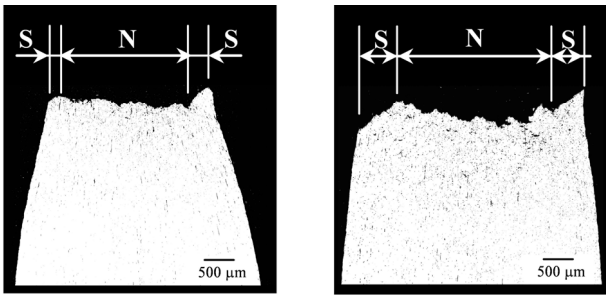


*Figure 3: Nominal stress-strain curves of hydrogen-precharged and uncharged specimens. ε_{pre}: Prestrain, C_H: Hydrogen content measured before tensile test. $C_{H,R}$: Residual hydrogen content measured after tensile test, ϕ: Reduction of area, Δt :Total hold time in the air. * : Necking near the edge of extension meter.*

stress-strain curve for the hydrogen-precharged specimen with ε_{pre} = 10%. A yield point appeared because the specimen was aged in the aqueous ammonium thiocyanate solution at 313 K for 48 h. With an increase in ε_{pre} from 0% to 10%, the residual hydrogen content, $C_{H,R}$, of the hydrogen-precharged specimens increased from 0.1 wppm to 0.6 wppm, while ϕ decreased from 69% to 55%. As shown in Fig. 3(c), the yield point also appears in the case of ε_{pre} = 20%. In this case, $C_{H,R}$ was 2.0 wppm and ϕ was 45.2%. Figure 3(c) also shows the result of an additional tensile test. A 20% prestrained specimen was immersed in Galden (a heat transfer fluid) at 313 K for 48 h. Though the temperature and time were the same as those used for the hydrogen-precharged specimen, hydrogen was not charged to the specimen. The specimen was reloaded onto the tensile machine. The yield point was also observed in the case of the specimen immersed in Galden. However, the value of ϕ for the uncharged specimen (69.6%) was found to be almost similar to that for the specimen immersed in Galden (65.3%), suggesting that ϕ is unaffected by the appearance of the definite yield point. Accordingly, it was concluded that an increase in the hydrogen content brings about a decrease in ϕ in the prestrained specimens.

Figure 4 shows the low-magnification optical microscopic images of the longitudinal cross-sections of the uncharged virgin specimen and the hydrogen-precharged specimen with ε_{pre} = 20%. All the specimens, including the two specimens shown in

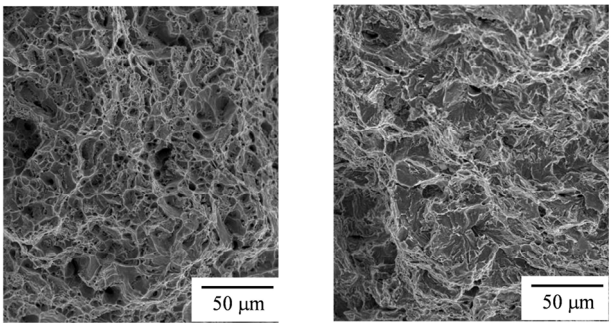
Fig. 4, are subjected to cup-and-cone fracture, which consists of a normal stress fracture and a shear stress fracture. The shear stress region in the hydrogen-precharged specimen with ε_{pre} = 20% was wider than that in the other specimens, implying that hydrogen enhances the shear stress fracture. A similar behavior was observed in Cr-Mo steel [6]. Figure 5 shows the magnified SEM images of the surfaces with normal stress fracture. The fracture surfaces of the uncharged virgin specimen and hydrogen-precharged virgin specimen were found to be covered with dimples. On the other hand, the fracture surfaces of the prestrained hydrogen-precharged specimens were covered with the quasi-cleavage like features and dimples. As will be described, the quasi-cleavage like features may be related to the crack forming along slip bands (See Fig. 9(b) and Fig. 10(b)). Figures 6 and 7 show the SEM images of the longitudinal cross-sections of the tensile fracture specimens. Pearlite cracks were found to be formed in all the specimens. The true strain (ε) at the fracture point was 1.19 for the uncharged virgin specimen (Fig. 6(a))



(a) ε_{pre} = 0% Uncharged ($C_{H,R}$ = 0.0 wppm)

(b) ε_{pre} = 20% Hydrogen-precharged ($C_{H,R}$ = 2.0 wppm)

Figure 4: Longitudinal cross-section of tensile fracture specimens. ε_{pre}: Prestrain, $C_{H,R}$: Residual hydrogen content, N: Normal stress fracture region, S: Shear stress fracture region.



(a) ε_{pre} = 0% Uncharged ($C_{H,R}$ = 0.0 wppm)

(b) ε_{pre} = 20% Hydrogen-precharged ($C_{H,R}$ = 2.0 wppm)

Figure 5: Fracture surfaces of the ruptured samples after the tensile test. ε_{pre} : Prestrain, $C_{H,R}$: Residual hydrogen content.

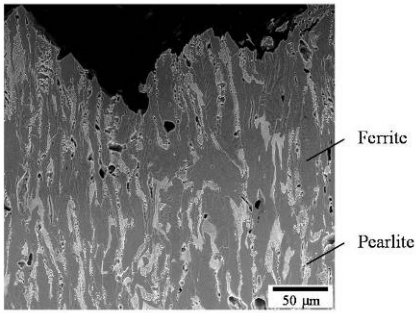
and 0.60 for the hydrogen-precharged specimen with ε_{pre} = 20% (Fig. 7). The true strain ε was calculated using the relation $\varepsilon = \ln (A_0 / A)$, where A_0 is the area of the cross-section before the tensile test, and A is the area of the cross-section at the fracture point. Figure 6(b) shows the longitudinal cross-section of the uncharged virgin specimen for $\varepsilon = 0.65$. Although the value of ε is the same in Fig. 6(b) and Fig. 7, very few pearlite cracks are observed in Fig. 6(b), while many pearlite cracks are observed in Fig. 7, thereby implying that hydrogen enhances the initiation of pearlite cracks.

Figure 8 shows the relationship between the number of pearlite cracks and ε for the uncharged virgin specimen and the hydrogen-precharged specimen with ε_{pre} = 20%. The inspected area of the specimen with pearlite cracks (S_0) was 0.24 mm^2, and pearlite cracks whose lengths were longer than 2 μm were counted. Figure 8 also implies that hydrogen enhances the initiation of pearlite cracks.

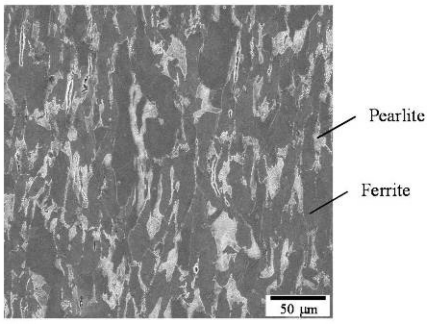
Figure 9 shows the typical pearlite cracks in the hydrogen-precharged specimen with ε_{pre} = 20%. Figures 7 and 9 show well-defined pearlite cracks that extend into the ferrite grains. On the other hand, Fig. 6(a) shows spherical cracks that are restricted to the pearlite region. Therefore, it is confirmed that hydrogen influences the growth of pearlite cracks. In addition, hydrogen influences the coalescence of the pearlite cracks. Figure 9(b) shows that the coalescence of two pearlite cracks occurs 45° to the loading direction. Since the direction of coalescence coincides with the direction of maximum shear stress, hydrogen enhances the shear stress fracture not only on a macroscopic scale (Fig. 4), but also on a microscopic scale. Figure 4 shows that the shear stress fracture region is wider in the hydrogen-precharged specimen than in the other specimens.

Murakami et al [8] investigated the effect of hydrogen on the fatigue crack growth behaviors for the austenitic stainless steels (types 304 and 316L) and found out that the fatigue crack growth rates were accelerated even by the nondiffusible hydrogen. In addition, they showed that the acceleration of fatigue crack growth was caused by the localization of slip bands at the crack tip by hydrogen.

Based on the results by Murakami *et al*. [8], the process of the pearlite crack growth is illustrated, as shown in Fig. 10. In the uncharged specimen (Fig. 10(a)), pearlite cracks are blunted by macroscopic plastic deformation and are restricted to the pearlite grains. In hydrogen-precharged specimen (Fig. 10(b)), on the other hand, hydrogen in the ferrite and pearlite concentrates at the tips of the pearlite cracks owing to stress-induced diffusion. Since this concentrated hydrogen enhances the localization of slip bands at the tip of the crack, the cracks become well-defined and extend into the ferrite grains. Since hydrogen also enhances the shear stress fracture (i.e. the shear deformation) between two pearlite cracks as shown in Fig. 9(b), the cracks easily coalesce in the hydrogen-precharged specimen. As a result, the presence of hydrogen results in a decrease in the value of ϕ in STPG.



(a) $\varepsilon = 1.19$ ($\phi = 69.6\%$)



(b) $\varepsilon = 0.65$

Figure 6: Longitudinal cross-section of uncharged virgin specimen with prestrain ε_{pre} = 0%. Residual hydrogen content $C_{H,R}$ = 0.0 wppm. ε : True strain, ϕ : Reduction in area.

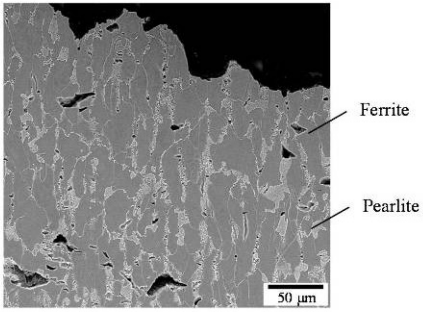


Figure 7: Longitudinal cross-section of hydrogen-precharged specimen with prestrain ε_{pre} = 20%. Residual hydrogen content $C_{H,R}$ = 2.0 wppm, True strain ε = 0.60 (Reduction in area ϕ = 45.2%).

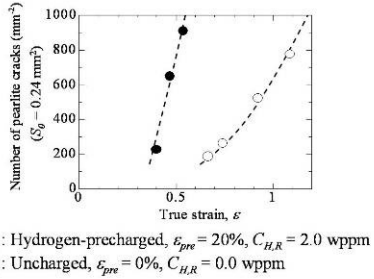
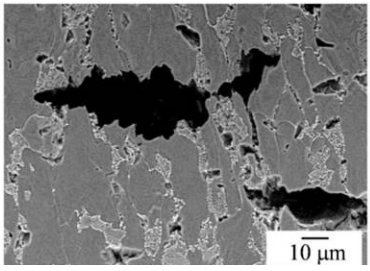
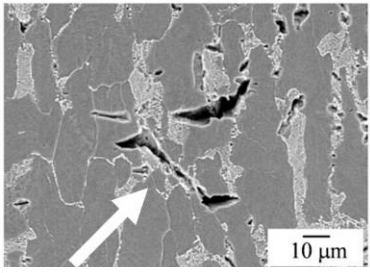


Figure 8: Relationship between true strain and number of pearlite cracks. S_0 : Inspection area, ε_{pre} : Prestrain, $C_{H,R}$: Residual hydrogen content.



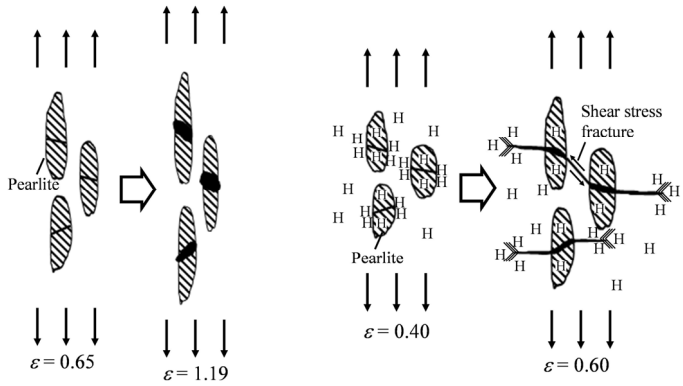
(a) Crack grew in the direction perpendicular to tensile axis



(b) Coalescence of cracks by hydrogen-enhanced shear crack

Figure 9: Magnification of typical pearlite cracks of hydrogen-precharged specimen with prestrain ε_{pre} = 20%. Residual hydrogen content $C_{H,R}$ = 2.0 wppm, True strain ε = 0.60 (Reduction in area ϕ = 45.2%).

As has been described herein, the growth and coalesce of pearlite cracks in the hydrogen-precharged specimens are due to the hydrogen-enhanced localization of slip bands at the pearlite crack tip. This means that pearlite is closely related to the hydrogen embrittlement of ferrite-pearlite carbon steel. Therefore, it is necessary to further investigate the effects of hydrogen on the tensile properties of ferrite-pearlite steel with carbon content lower than that of STPG (0.19 mass%). In Japan, STPG will be used for 1 MPa high pressure hydrogen pipelines. SGP whose carbon content is about 0.08 mass% will be used for 0.1 MPa low pressure hydrogen pipelines.



(a) Uncharged *(b) Hydrogen-precharged*

Figure 10: Schematic illustration of pearlite crack growth in uncharged and hydrogen-precharged specimens. ε : True strain.

CONCLUSION

The following conclusions can be drawn from the hydrogen content measurements, tensile tests, and SEM observations of the fracture surfaces and longitudinal cross-sections of the virgin and prestrained specimens obtained from a JIS-STPG370 carbon steel pipe, which were hydrogen-precharged by immersing them in a 20 mass% aqueous solution of ammonium thiocyanate at 313 K for 48 h.

(1) The hydrogen contents, C_H, of the uncharged specimens were found to be 0.0 wppm both for ε_{pre} = 0% (virgin specimen) and ε_{pre} = 20%. Hydrogen content, C_H, before the tensile test was low (0.2 wppm) in the hydrogen-precharged virgin specimen. On the other hand, the hydrogen content C_H increased with the prestrain in the prestrained hydrogen-precharged specimens (1.0 wppm for ε_{pre} = 10% and 2.6 wppm for ε_{pre} = 20%).

(2) There was no significant difference in the nominal stress-strain curve and reduction of area (ϕ) between the uncharged virgin (ε_{pre} = 0%) specimen and the hydrogen-precharged virgin (ε_{pre} = 0%) specimen. In this case, the hydrogen content, C_H, before the tensile test was 0.0 wppm for the uncharged specimen and the residual hydrogen content, $C_{H,R}$, was 0.1 wppm for the hydrogen-precharged

specimen. On the other hand, ϕ decreased with an increase in the residual hydrogen content in the case of the prestrained hydrogen-precharged specimens.
(3) The fracture surfaces of the uncharged virgin and hydrogen-precharged virgin specimens were covered with dimples, while the fracture surfaces of the prestrained hydrogen-precharged specimens were covered with dimples and the quasi-cleavage like features.
(4) Pearlite cracks were formed in all the specimens. The initiation of pearlite cracks occurred under the low true strain in the prestrained hydrogen-precharged specimen. In the uncharged virgin specimen and hydrogen-precharged virgin specimens, blunted pearlite cracks were formed, and these cracks were restricted to the pearlite grains. In the prestrained hydrogen-precharged specimen, on the other hand, pearlite cracks were sharp, which extended into the ferrite grains.

ACKNOWLEDGMENTS

This research has been supported by the NEDO Fundamental Research Project on Advanced Hydrogen Science (2006 to 2012).

REFERENCES

1. Troiano, A. R., "The Role of Hydrogen and Other Interstitials in the Mechanical Behavior of Metals," *Trans-ASM*, Vol. 52, (1960), pp. 54-81.
2. Beachem, C. D., "A New Model for Hydrogen-Assisted Cracking (Hydrogen "Embrittlement)," *Mech-Trans*, Vol. 3, (1972), pp.437-451.
3. Birnbaum, H. K. and Sofronis, P., "Hydrogen-Enhanced Localized Plasticity--A Mechanism for Hydrogen-Related Fracture," *Mater-Sci-Eng-A*, Vol. 176, (1994), pp191-202.
4. Safety Standard for Hydrogen and Hydrogen Systems, NASA NSS 1740, 16, (2005).
5. Yokogawa, K., Fukuyama, S., and Kudo, K., "Tensile Fracture Surfaces of Carbon Steels in High Pressure Hydrogen at Room Temperature," *J-Jpn-Inst-Metal*, Vol. 44, (1980), pp. 864-869.
6. Matsuoka, S., Homma, N., Tanaka, H., Fukushima, Y., and Murakami, Y., "Effects of Hydrogen on the Tensile Properties of 900-MPa-Class JIS-SCM435 Low-Alloy-Steel for Use in Storage Cylinder of Hydrogen Station," *J-Jpn-Inst-Metal*, Vol. 70, (2006), pp. 1002-1011.
7. Uyama, H., Nakashima, M. Morishige, K. Mine, Y., and Murakami, Y., "Effects of Hydrogen Charge on Microscopic Fatigue Behavior of Annealed Carbon Steels,", *FFEMS*, Vol. 29, (2006), pp.1066-1074.
8. Murakami, Y., Kanezaki, T., Mine, Y., Matsuoka, S., "Hydrogen Embrittlement Mechanism in Fatigue of Austenitic Stainless Steels" *Met-Mat-Trans-A*, Vol.39, (2008), pp.1327-1339.

Effects of Hydrogen on Materials
Proceedings of the 2008 International Hydrogen Conference
Brian Somerday, Petros Sofronis, Russell Jones, editors, p 373-380
Copyright © 2009 ASM International®
All rights reserved.
www.asminternational.org

THE EFFECT OF RESIDUAL HYDROGEN ON HIGH-CYCLE FATIGUE PROPERTY OF WELDED JOINTS FOR GAS PIPELINE STEEL

Tetsushi YAMAOKA
Department of Mechanical Engineering, Graduate School of Engineering, Kyushu University,744 Moto-oka, Nishi-ku, Fukuoka, 819-0395 Japan

Sergiy M. STEPANYUK, Saburo MATSUOKA
Department of Mechanical Engineering, Kyushu University, and Research Center for Hydrogen Industrial Use and Storage (HYDROGENIUS), National Institute of Advanced Industrial Science and Technology (AIST), 744 Moto-oka, Nishi-ku, Fukuoka, 819-0395 Japan

INTRODUCTION

Hydrogen is attracting attention as a source of energy, both as an alternative to fossil fuels as these become exhausted and as a means of reducing emissions of greenhouse gases and thereby curbing global warming. Pipelines will form part of the hydrogen-supply system. In general, pipelines are extended by welding. It is known that hydrogen enters into metals during welding, leading to cold cracking. It is also known that when materials are exposed to hydrogen at high pressures, the gas is absorbed and this results in the deterioration of mechanical properties of the material [1]. Therefore, to ensure the long-term safety and reliability of hydrogen pipelines, it is necessary to investigate the deterioration of mechanical properties (hydrogen embrittlement) due to the sorption of hydrogen during welding, as well as by sorption of hydrogen through exposure to high-pressure hydrogen gas. In this study, as a first step in research to ensure the safety of hydrogen pipelines, we measured the residual hydrogen in the weld metal of a pipeline, and we investigated the effects of residual hydrogen on the fatigue-crack growth properties of the weld metal.

MATERIALS AND EXPERIMENTAL METHODS

Circumferential welds in JIS-STPG370 carbon-steel pipes for pressure service (JIS code: G3454, outside diameter: 406.4 mm, thickness: 7.9 mm) were prepared. Table 1 shows the chemical composition of STPG370 and welding rods. The welds were produced by shielded metal arc welding (SMAW) on one side in a two-pass manner using a low-hydrogen-type electrode (first layer root bead, Fig. 1 C) and an ordinary ilmenite-type electrode (second layer final bead, Fig. 1 A, B). Figures 1 and 2 show the macrostructure and microstructures of the welded joint, respectively. An acicular structure is formed in the weld metal and the heat-affected zone (HAZ). The base metal has a ferrite-pearlite structure. The welded joint is nonhomogeneous in material terms: each zone (first and second layers of the weld metal, fusion line, HAZ, and base metal) has a different microstructure and grain size.

Figure 3 shows the distribution of Vickers hardness (load: 2.94 N, holding time: 30 s) of the welded joint. The Vickers hardness was measured on the cross-section surface in the welded joint at positions of $t/4$, $t/2$, and $3t/4$, where t is the thickness. The weld metal and HAZ were harder than the base metal, and the first layer was harder than the second layer.

The hydrogen contents of the weld metal, HAZ, and base metal in a welded pipe joint were measured by means of quadrupole mass spectrometer-type thermal-desorption spectrometry (TDS). The welded joint had been kept in air for more than five months. In addition, the welded-joint specimen was not charged with hydrogen. Therefore, the residual hydrogen from that originally present in the welded joint and base metal specimens was measured in this study.

Figure 4 shows the shapes and dimensions of the fatigue specimen and the small hole. Specimens were machined from the pipe in the axial direction across the welded joint that had been left in air at room temperature for about five months after welding. The centerline in the thickness direction for the specimen was coincident with that of the pipe, so that the specimen included both the first layer and second layer. The surfaces of the specimen were polished by using #2000 emery paper, followed by final buffing with 1-μm-diameter alumina. A small hole 1-mm in diameter and 1-mm deep was drilled into the surface of the first or second layer as a crack initiator. A base-metal specimen with a similar small hole was also prepared. It must be emphasized that the welded-joint specimen and base-metal specimen were not charged with hydrogen.

Fatigue tests were carried out at room temperature in laboratory air under tension-compression cyclic loading at a stress ratio of $R = -1$. Frequencies of 20, 2, and 0.2 Hz were used to investigate the effects of test frequency on the fatigue-crack behaviors for the welded joint with residual hydrogen. The replica method was used for the measurement of crack lengths.

Table 1: Chemical compositions of the base metal and weld rods.

		C	Si	Mn	P	S
Base metal		0.19	0.21	0.56	0.012	0.010
Weld rod	First layer	0.07	0.74	0.89	0.014	0.11
	Second layer	0.08	0.15	0.44	0.028	0.011

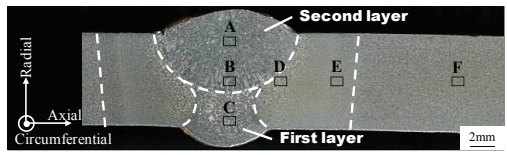


Figure 1: The macrostructure of the welded joint.

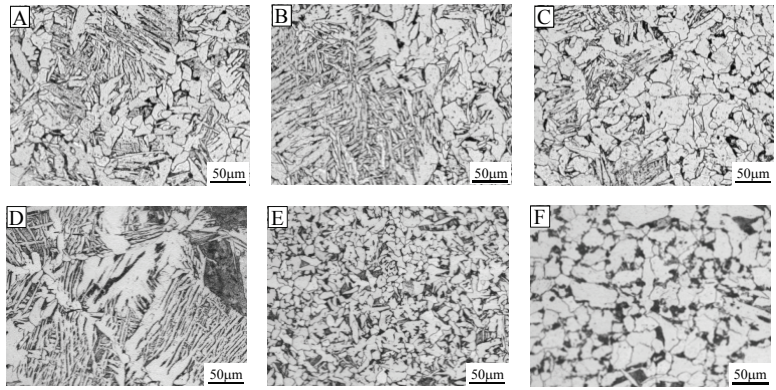


Figure 2: Microstructures of the welded joint. (A)–(F) are magnified microstructures at the locations indicated by the same letters in Fig. 1. (A) Second layer in the weld metal. (B) Second layer in the weld metal. (C) First layer in the weld metal. (D) HAZ near the fusion line. (E) HAZ near the base metal. (F) Base metal.

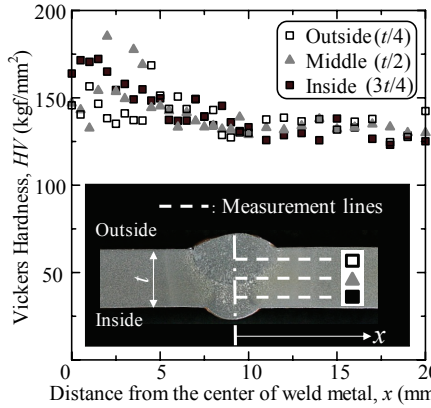


Figure 3: Distribution of the Vickers hardness of the welded joint.

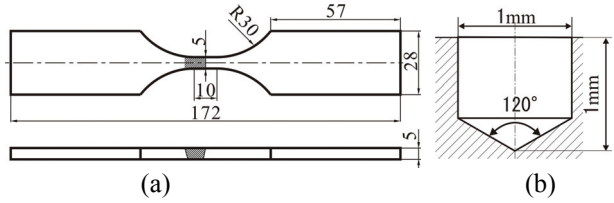


Figure 4: Shapes and dimensions of the fatigue specimen (a) and small hole (b).

RESULTS AND DISCUSSION

Hydrogen Content

Figure 5 shows the results of TDS measurements on the weld metal, HAZ, and base metal. Figure 6 shows the sampling positions of the TDS specimens from the welded joint: 5 × 5 × 0.8 mm square chips were cut from the welded joint. The chip of weld metal included portions of both the first and second layers. Little hydrogen (<0.1 wt.ppm) was desorbed from the HAZ and base metal during heating. On the other hand, large amounts of hydrogen were desorbed from the weld metal. There were three peaks (peak 1 at 100 °C and 0.2 wt.ppm; peak 2 at 200 °C and 1.0 wt.ppm; peak 3 at 350 °C and 1.7wt.ppm) in the weld metal.

Figure 7 shows the results of TDS measurements on the first and second layers of the weld metal separately. As shown in Fig. 8, two samples of the first layer (I and II) and two samples of the second layer (III and IV) were taken from the weld metal. The hydrogen contents in the second layer were much greater than those in the first layer. Table 2 summarizes the results for the hydrogen contents in the first and second layers.

The above specimens of weld metal for hydrogen measurements were sampled from the welded joint of STPG370 pipe that had been left in air at room temperature for more than five months after welding. The residual hydrogen in the weld metal is therefore considered to be nondiffusible hydrogen.

Fatigue Crack Growth

Figure 9 shows the relationship between the crack length $2a$ and the number of cycles from crack initiation N_p. A crack length of $2a$ = 1050 μm was used as the initiation crack length. Figure 9(a) shows $2a$–N_p curves for the base-metal specimen with a small hole. The fatigue properties of low-strength carbon steel depend on the test frequency [2]. A higher test frequency leads to a longer fatigue life. In Fig. 9(a), the $2a$–N_p curves at 2 and 0.2 Hz were coincident with each other, but the curve at 20 Hz showed a longer life compared with those at 2 and 0.2 Hz. Therefore, we inferred that the longer life at 20 Hz was the result of the test-frequency dependence of fatigue crack growth.

Figure 9(b) shows $2a$–N_p curves for welded joint specimens with a small hole on the surface of the first layer. In this case, the curves at 2 and 20 Hz were coincident with each other. This means that the test-frequency dependence of fatigue crack growth saturates at 20 Hz for the first layer of weld metal, whereas the dependence saturates at 2 Hz for the base metal. The saturation of fatigue life at 20 Hz occurred because the Vickers hardness was higher in the first layer of weld metal than in the base metal, as shown in Fig. 3. If we compare the curve at 0.2 Hz with the curves at 20 and 2 Hz, the curve at 0.2 Hz shows a shorter fatigue life. From these results, we

infer that the fatigue crack growth at 0.2 Hz was accelerated by residual hydrogen in the first layer of weld metal. Fig. 7 shows that the residual hydrogen content was higher in the second layer than in the first layer. This means that fatigue crack growth of second layer in the weld metal must be accelerated by residual hydrogen, too.

Figure 9(c) shows $2a$–N_p curves for the welded joint specimen with a small hole on the surface of the second layer. The fatigue crack growth rate was also accelerated at 0.2 Hz in the second layer. Accordingly, we concluded that residual hydrogen accelerates the fatigue crack growth not only in the first layer, but also in the second layer of weld metal. Murakami *et al.* [3] reported that the growth rate of a fatigue crack was accelerated at a very low frequency (0.0015 Hz) in the presence of 2–3 wt.ppm of nondiffusible hydrogen for the austenitic stainless steels SUS304 and SUS316L. Hydrogen-diffusion coefficients for carbon steels and low-alloy steels are 3–4 orders faster than those for austenitic stainless steels. Accordingly, the fatigue crack growth was accelerated at 0.2 Hz by residual hydrogen, (that is, nondiffusible hydrogen) for the weld metal of STPG370 pipe, whereas the fatigue crack growth was accelerated at 0.0015 Hz by nondiffusible hydrogen for SUS304 and SUS316L.

Fracture Surface

Figure 10 shows the fracture surfaces observed in the welded-joint specimens with a small hole in the surface of the second layer tested at 2 and 0.2 Hz. These fracture surfaces were obtained from the region near the surface of the specimen at $2a$ = 1800 μm. Flat parts, i.e. facets, were found at both 2 and 0.2 Hz. Tanaka *et al.* [4] investigated the acceleration of crack growth by hydrogen for the low-alloy steel JIS-SCM435 used in a hydrogen storage cylinder. They found that the proportion of facets increased with increasing hydrogen content. In our study, however, there was no difference in the proportion of facets at 2 Hz and at 0.2 Hz, although the crack growth rate was faster at 0.2 Hz than at 2 Hz. Figure 11 shows the magnified fracture surface of the sample shown in Fig. 10(a). Facets are clearly visible. Furthermore, there are several inclusions and blow holes. The number of inclusions and blow holes was larger in the second layer (Fig. 11) than in the first layer (Fig. 12): if inclusions and blow holes are sites for trapping of hydrogen, this explains why the hydrogen content of the second layer was greater than that of the first layer.

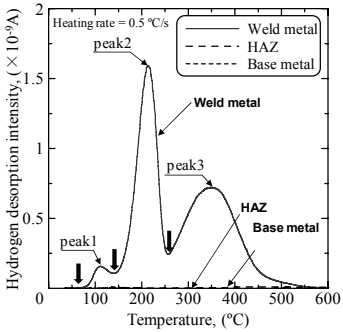


Figure 5: TDS results for the weld metal, HAZ, and base metal.

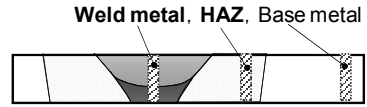


Figure 6: Sampling of TDS specimens of weld metal, HAZ, and base metal from a welded joint.

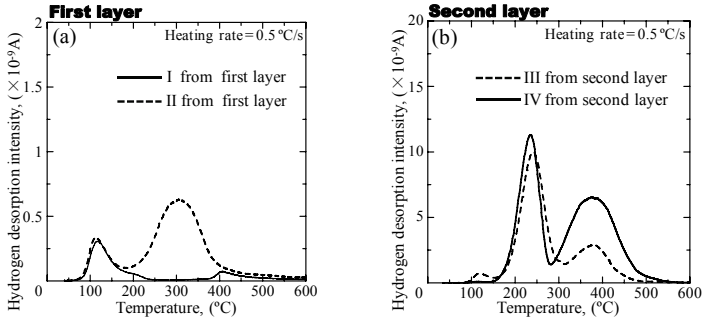


Figure 7: TDS results for the first and second layers of weld metal.(a) First layer. (b) Second layer.

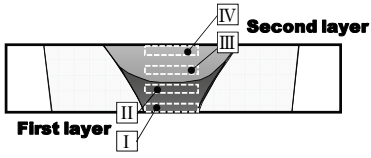


Figure 8: Sampling of TDS specimens from the first layer (I and II) and second layer (III and IV) of the welded joint.

Table 2: Hydrogen contents of the first and second layers of weld metal.

		Hydrogen content (wt.ppm)			
		peak1	peak2	peak3	Total
Weld metal	First I	0.1	0.0	0.1	0.2
	First II	0.1	0.6		0.7
	Second III	0.2	2.8	2.1	5.1
	Second IV	0.0	3.1	7.4	10.5

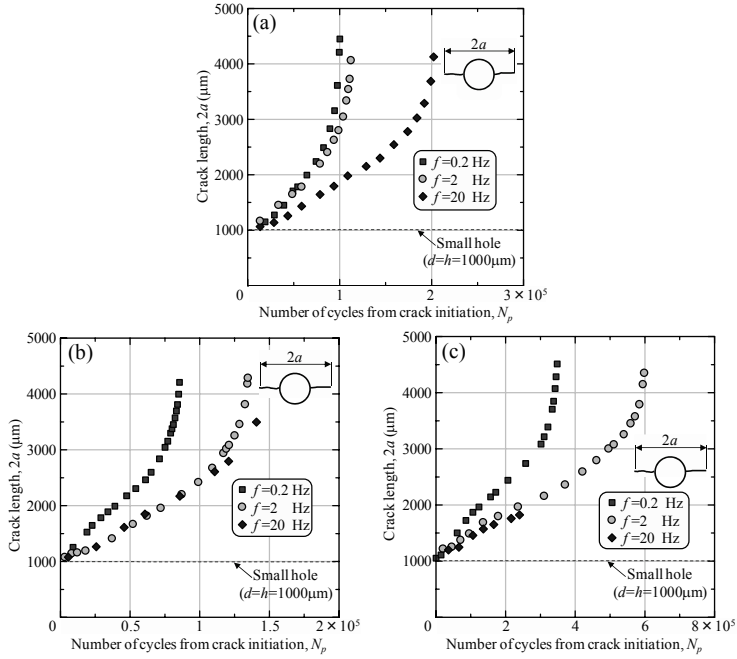


Figure 9: Crack growth curves: (a) Base metal (σ_a = 175 MPa, R = –1); (b) First layer (σ_a = 225 MPa, R = –1); (c) Second layer (σ_a = 175 MPa, R = –1).

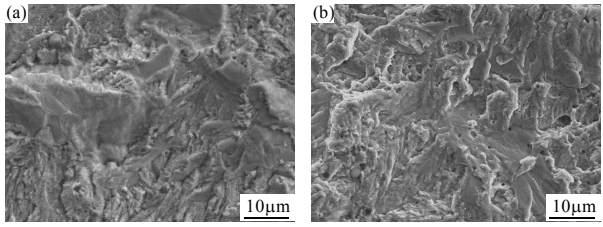


Figure 10: SEM images of the second layer: (a) f = 2 Hz. (b) f =0.2 Hz.

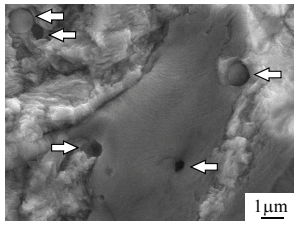


Figure 11: SEM images of the second layer showing facets, inclusions, and blowholes.

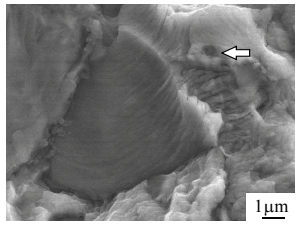


Figure 12: SEM images of the first layer. (f = 0.2 Hz).

CONCLUSIONS

The residual hydrogen contents of welded joints in STPG370 were measured by TDS without additional charging with hydrogen. The effects of residual hydrogen on fatigue crack growth were investigated at the frequencies of 20, 2, and 0.2 Hz. The results of the study can be summarized as follows.

1. The residual hydrogen content in the base metal and HAZ was very small (<0.1 wt.ppm).On the other hand, large amounts of hydrogen (2.8 wt.ppm) were desorbed from the weld metal of the uncharged welded joint. The residual hydrogen content in the second layer was much larger than that in the first layer. The STPG370 welded joints had been left in air at room temperature for more than five months after welding. The residual hydrogen in the weld metal was therefore considered to be nondiffusible hydrogen.
2. The fatigue crack was initiated by a small artificial hole introduced on the first or second layer of the weld metal. The fatigue crack growth was faster at 0.2 Hz than at 2 or 20 Hz. Accordingly we inferred that the residual nondiffusible hydrogen accelerated fatigue crack growth in the weld metal.
3. There were many inclusions and blow holes on the fracture surfaces of the weld metal. The number of inclusions and blow holes was larger in the second layer than in the first layer.

ACKNOWLEDGEMENTS

This research has been supported by the NEDO Fundamental Research Project on Advanced Hydrogen Science (2006 to 2012).

REFERENCES

1. Matsuyama, S., “Delayed Fracture” *Nikkan Kogyo Shimbun Ltd.,* (1989).
2. Tsutsumi, N., *et al,* “Effect of Test Frequency on Fatigue Strength of Low Carbon Steel,” *Trans. JSME A*, Vol. 72, No. 715 (2006), pp. 41–49.
3. Murakami, Y., *et al,* “Hydrogen Embrittlement Mechanism in Fatigue of Austenitic Stainless Steels,” *Metall. Mater. Trans. A*, Vol. 39A, No. 6 (2008), pp. 1327–1339
4. Tanaka, H., *et al,* “Effect of Hydrogen and Frequency on Fatigue Behavior of SCM435 Steel for Storage Cylinder of Hydrogen Station,” *Trans. JSME A*, Vol. 73, No. 736 (2007), pp. 1358–1365.

Effects of Hydrogen on Materials
Proceedings of the 2008 International Hydrogen Conference
Brian Somerday, Petros Sofronis, Russell Jones, editors, p 381-388
Copyright © 2009 ASM International®
All rights reserved.
www.asminternational.org

HYDROGEN EFFECTS ON FATIGUE CRACK GROWTH RATE IN HIGH STRENGTH PIPELINE STEEL*

Ph. P. Darcis, J. D. McColskey, A.N. Lasseigne and T. A. Siewert
NIST, Materials Reliability Division, 325 Broadway, Boulder, CO 80305 USA

ABSTRACT

The effect of hydrogen on fatigue crack growth rate (FCGR) in a high-strength pipeline steel was investigated. Fatigue tests were conducted in a servo-hydraulic fatigue test machine on previously hydrogen-charged API-X100 pipeline steel samples. The samples were charged in a high-pressure chamber until saturated, removed from the chamber and quickly tested in an ambient environment. Steps were taken to minimize the diffusion of hydrogen from the charged samples prior to fatigue testing. These steps were evaluated as part of this test program as well as the effects of the loading ratio and the monitoring gradient of the fatigue crack growth tests. The effects of hydrogen on FCGR are evident in the intermediate stage (stage II) of fatigue crack growth.

Keywords: Fatigue Crack Growth Rate; Hydrogen Diffusion; Hydrogen Embrittlement; Hydrogen Environment Effects.

INTRODUCTION

Hydrogen degradation has been studied for decades [1-2], however, the engineering problems associated with hydrogen are more avoided than understood. Primarily, the risk of hydrogen embrittlement is circumvented by avoiding the use of high strength materials in cases where hydrogen can be a problem. Higher-strength alloys are generally more susceptible to the effects of hydrogen. However, the economics anticipated for hydrogen fuels will likely favor high-strength steels for higher hydrogen gas operating pressures. This choice could, in turn, increase the probability of hydrogen damage in operating pipeline systems. In addition, current interests differ from past experience due to changes in the following:

- Quantity – The proposed H-economy will require a very large and diverse infrastructure of equipment for transport, storage, and distribution of hydrogen.
- Quality – The proposed infrastructure will need to be able to safely handle hydrogen from varying sources and of varying quality.
- New materials – Data currently used for pipelines and associated hardware does not cover the modern materials certain to be used in new applications.

Pipeline materials include the ferrite-pearlite steels that have been used for gas pipelines in the past, and the newer higher strength ferrite-bainite steels now favored for gas pipelines. In support of these materials, test development is needed to support a fracture mechanics approach to materials issues for the pressurized hydrogen environments of interest. Towards this goal, NIST will conduct basic research into testing methods to

* Contribution of an agency of the U.S. government, not subject to copyright

understand the influence of metallurgical factors in determining susceptibility to hydrogen embrittlement as well as into methods for the quantification of susceptibility and kinetics of hydrogen induced cracking. These considerations will assist in understanding hydrogen behavior for improved pipeline designs.

Among these considerations, a basic research for understanding the influence of hydrogen embrittlement on fatigue will be presented. This research focuses on the possibility of performing fatigue crack growth tests in air, under hydrogen influence, using a modern high-strength ferrite-bainite X100 pipeline steel. The main advantage of testing in air is to provide a low-cost test procedure using standard laboratory testing facilities, without the requirement of a pressurized hydrogen test chamber.

MATERIALS PROPERTIES

An API X100 high-strength grade pipeline steel (outside diameter 1.32 m (52 inch) and wall thickness 20.6 mm (0.81 inch)) was investigated. Table 1 contains the nominal chemical composition of this steel (weight %).

Table 1: Chemical composition of the X100 tested steel (weight %).

C	Mn	P	S	Si	Ni	Cu	Mo
0.07	1.90	0.008	0.0005	0.10	0.50	0.30	0.15

To measure the tensile properties of the pipeline material, round tensile specimens (6 mm diameter) were machined from the X100 steel. All specimens had a gauge length of 25.4 mm. Experiments were performed in a closed-loop servo-hydraulic machine of 100 kN capacity. Tests were conducted in displacement control at a rate of 0.1 mm/min. Three tests were conducted for the transverse direction and three for the longitudinal direction (axial orientation). No tests were performed in the through-thickness orientation. The X100 steel mean mechanical properties are shown in Table 2; E is the Young's modulus, $\sigma_{0.2}$ the yield stress, σ_{UTS} the ultimate strength, e_u the uniform elongation, and e_f the fracture elongation.

Table 2: X100 steel mechanical properties (mean).

Orientation	E (GPa)	$\sigma_{0.2}$ (MPa)	σ_{UTS} (MPa)	$\sigma_{0.2}/\sigma_{UTS}$	e_u (%)	e_f (%)	e_u/e_f
Longitudinal	204.1	732	806	0.91	4.6	20.3	0.23
Transverse	206.5	798	827	0.97	4.1	19.3	0.21

EXPERIMENTAL DETERMINATION OF DIFFUSION COEFFICIENT

For determination of the hydrogen diffusion coefficient in X100 pipeline steel, experiments were performed using gaseous pre-charged specimens. The hydrogen is introduced into the steel in a controlled and efficient manner using a high pressure gaseous hydrogen atmosphere. Steel pipeline specimens are hydrogen charged at a maximum pressure of 6.89 MPa (1000 psig) at 100˚C for specific time intervals to achieve hydrogen saturation in the specimen. Once the pipeline specimen is saturated

with hydrogen, the specimen is removed from the gaseous atmosphere into the air to allow the hydrogen to diffuse out of the specimen at room temperature. Experimental results of the hydrogen diffusion out of the specimen are shown in Fig. 1. The hydrogen content was determined by gas chromatography.

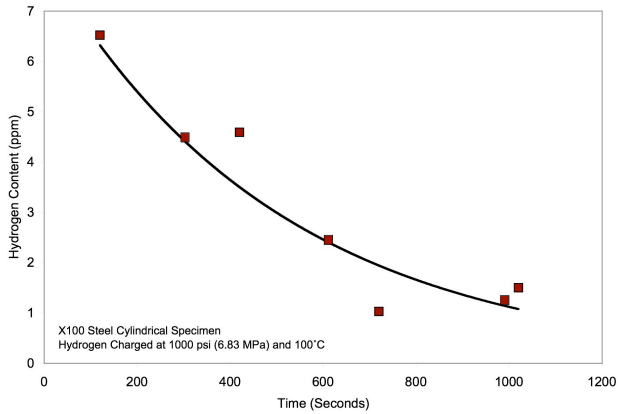


Figure 1: Hydrogen content as a function of time for hydrogen charged X100 pipeline steel specimens. Hydrogen content was determined by gas chromatography.

The diffusion coefficient of hydrogen (at room temperature) in X100 pipeline steel has been calculated to be approximately $4.75*10^{-2}$ mm^2/sec. The X100 pipeline steel saturated with hydrogen at approximately 38 ppm, but very quickly diffused out of the specimen. Note that the hydrogen content in Fig. 1 begins at approximately 7 ppm of hydrogen instead of the saturation hydrogen content of 38 ppm, which is due to the time lag (less than 10 minutes) between taking specimens out of the hydrogen reactor and setting up for synchronized diffusion experiments resulting in significant hydrogen losses. It is also important to note that the diffusion coefficient of hydrogen is based on many factors [2], which can each greatly affect the diffusion coefficient within the same material. For a given material, the diffusion coefficient can vary by orders of magnitude, dependent upon its specific conditions.

FATIGUE CRACK GROWTH EXPERIMENTAL SET-UP

A vast amount of FCGR (Fatigue Crack Growth Rate) data, in a gaseous hydrogen environment, exists in the open literature [3-4]. The most common way to estimate fatigue crack growth is to employ a linear-elastic fatigue-crack-growth model based on the "Paris Law" relationship: $da/dN = C(\Delta K)^m$, where, da/dN (mm/cycle) is the increment of crack growth per cycle, C and m are empirical constants (characteristics of the material), and ΔK ($MPa \cdot m^{1/2}$) is the stress intensity factor range.

The influence of hydrogen on fatigue crack growth in steels has been studied mostly using low cycle fatigue loading [5-6]. Based on these studies, our hydrogen-influenced

FCGR test specimens were cycled at a frequency of 1.0 Hz. The specimens, prior to charging, were fatigue cycled at 10 Hz in order to have a faster test time.

FCGR tests were conducted on compact tension specimens (C(T)), as defined in ASTM E647-05, machined from the longitudinal orientation, with the crack parallel to the pipe axis. Experiments were performed in a closed-loop servo-hydraulic machine of 100 kN capacity. Specimens were ground to 19.9 mm thickness (96 % of the original pipeline thickness) and were tested with no flattening. Specimen geometry and dimensions, as defined in ASTM E647-05, are depicted in Fig. 2a). A 3.2 mm through-thickness notch with a V-notch tip was introduced using a sharpened circular cutting blade. A Crack Mouth Opening Displacement (CMOD) gauge, for monitoring the crack length, was mounted in the specimen load line, directly across the notch opening. The test set-up is shown in Fig. 2b.

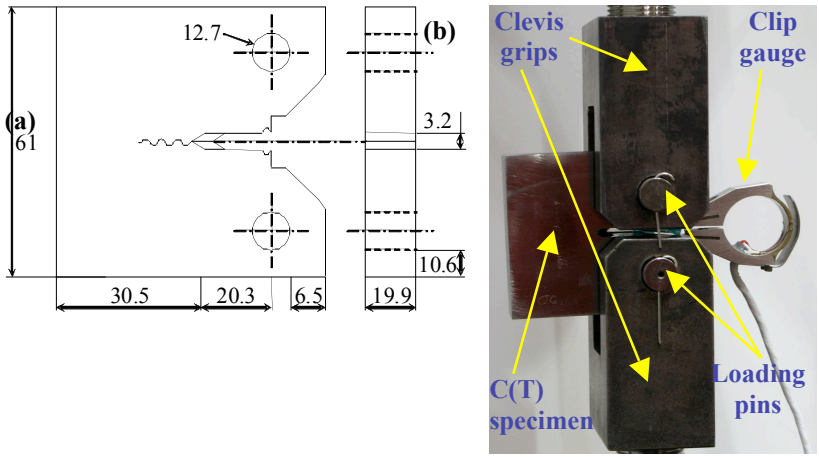


Figure 2: a) C(T) specimen dimensions (mm); b) Fatigue crack growth experimental set-up.

A stepwise increasing ΔK test was used with a normalized K gradient (C) equal to 0.05 or 0.1 (1/mm). The tests were performed in air. The specimens were initially fatigued in air until the last third of stage II of the fatigue crack growth (corresponding to the end of the stable crack growth). The specimens were then charged with hydrogen and placed in the machine and fatigue tested in air, permitting the effect of the hydrogen to be seen in the latter part of stage II, before the expected rapid diffusion rate of hydrogen occurred. This permitted the hydrogen effect to take place during the longest length of the crack propagation. Furthermore, this last third of the stage II permitted a $\Delta K > 20$ MPa.m$^{1/2}$, which corresponds to the beginning of the hydrogen effect on FCGR [6-7].

There are multiple coating and poisoning techniques used to trap hydrogen within the charged specimen. In previous experiments [8] different commonly used barrier coatings (cadmium, nickel, etc.) were compared for hydrogen charged specimens as a function of time to determine minimum hydrogen loss. Tin proved to be the most effective barrier as

a function of time. In order to keep the hydrogen from diffusing out of these test samples, some C(T) specimens were tinned after the hydrogen charging. During the specimen's transportation, from the hydrogen charging facility to the fatigue test facility, the specimens were submerged in liquid nitrogen (LN_2) to further minimize the hydrogen loss. The effects of the loading ratio, ΔK slope, the tinning and the liquid nitrogen were investigated. Test parameters are shown in Table 3.

Table 3: Test parameters for the FCGR test specimens.

Specimen	Loading ratio, R	ΔK slope (1/mm)	Hydrogen charging	Tinning
X100-1	0.1	0.05	No	No
X100-2	0.1	0.05	Yes	Yes
X100-3	0.1	0.1	No	No
X100-4	0.1	0.1	Yes	No
X100-5	0.1	0.1	Yes	Yes
X100-6	0.4	0.1	No	No
X100-7	0.4	0.1	Yes	Yes
X100-8	0.4	0.1	No*	No
X100-9	0.4	0.1	Yes	Yes

* submerged in liquid nitrogen (LN_2) before testing.

EXPERIMENTAL RESULTS AND DISCUSSION

The crack growth and FCGR curves for the tests performed at a loading ratio equal at 0.1 (specimens X100-1 through X100-5) are presented in Fig. 3, and the tests performed at a loading ratio equal at 0.4 (specimens X100-6 through X100-9) are presented in Fig. 4.

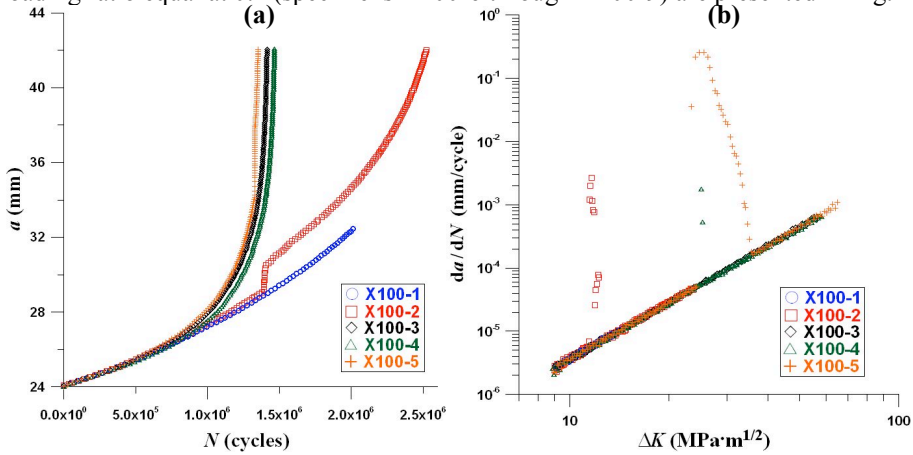


Figure 3: Influence of hydrogen on (a) crack growth and on (b) fatigue crack growth rate on various tests performed at a loading ratio equal to 0.1.

From the Fig. 3, different comments can be made:

- The results in Figure 3(b) clearly show the pronounced embrittling effect due to hydrogen charging, especially in the specimens using the tin coating technique (X100-2 and X100-5). This embrittlement effect lasted for 87 min. in specimen X100-2 and 91 min. in specimen X100-5. This period of time is longer that the diffusion of hydrogen in air (see Fig. 1). Specimen X100-4 (not tinned) shows some limited effects of the hydrogen charging before the hydrogen quickly diffused (approximately 5 minutes) from the specimen.
- In terms of the relationship between the degree of crack growth enhancement and ΔK, the results suggest that there is a peak of embrittlement in the Paris regime. This peak seems present at a value of ΔK between 20 to 40 MPa·m^{½}. This observation was seen by Mittal et al. [7] at values of ΔK between 35 to 40 MPa·m^{½}; which is considered to be quite a high level of stress intensity range.
- The variation of the stress intensity factor range test slope, between 0.05 (tests X100-1 and X100-2) and 0.1 (tests X100-3 through X100-5), has limited influence on the FCGR results. The tests performed at a ΔK slope equal to 0.1 have the advantage to run faster than the 0.05 tests (see Fig. 3a); this led us to use 0.1 for the FCGR tests performed at $R = 0.4$.
- Paris law parameter determination was carried out using the two reference tests X100-1 and X100-3. The calculated parameters, $m = 3$ and $C = 3.55 \cdot 10^{-9}$ (mm/cycle; MPa·m$^{1/2}$), agree well with previous FCGR tests performed on the same pipeline steel in air, using middle tension specimens [8].
- The diffusivity time comparison between tinned specimens, X100-2 and X100-5 (about 90 min) and the untinned specimen, X100-4, (about 5 min) clearly shows the limits of hydrogen testing in air.
-

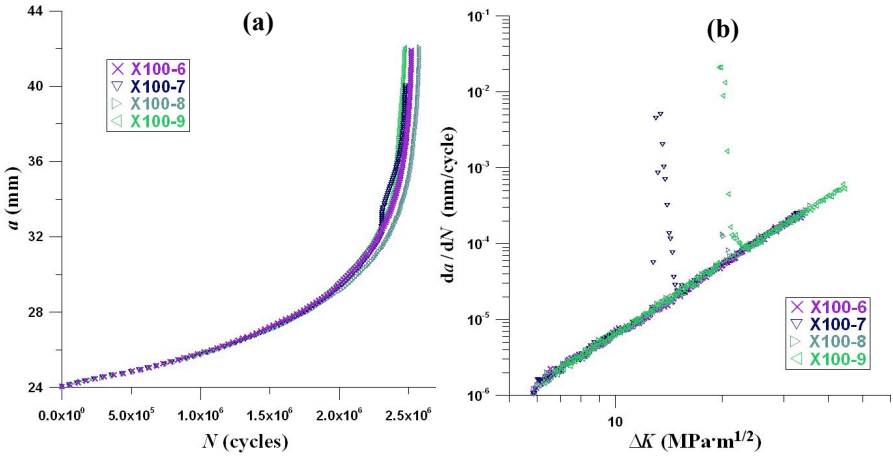


Figure 4: Influence of hydrogen on (a) crack growth and on (b) fatigue crack growth rate on various tests performed at a loading ratio equal to 0.4.

The results in Fig. 4 show the following:

- The effect of pronounced embrittlement due to hydrogen charging is confirmed with specimens X100-7 and X100-9. This embrittlement occurs for 99 min. for specimen X100-7 and 87 min. for specimen X100-9.

- In terms of the relationship between the degree of crack growth enhancement and ΔK, the results suggest that there is no peak of embrittlement in the Paris regime. This result is contradictory to our previous comments.
- Paris law parameters, $m = 3$ and $C = 6.26 \cdot 10^{-9}$ (using X100-6), agree well with previous FCGR tests performed with the same pipeline steel in air, using middle tension specimens [8]. This result, as expected, confirms the trend of higher FCGR behavior with increasing load ratio.
- The effect of liquid nitrogen on FCGR without hydrogen charging is identified using test specimen X100-8. The brief increase in FCGR, (a magnitude of 3, lasting for 15 minutes) while not significant, questions the use of LN_2 as a transportation medium for the specimens after charging.

The main observations from FCGR studies clearly demonstrate that, over a range of stress ratios from 0.1 to 0.4 and at values of ΔK between 10 and 50 MPa·m$^{1/2}$, the fatigue cracks grow faster in the presence of internal hydrogen than without it. Less effect is seen at the stress ratio $R = 0.4$ and the effect due to hydrogen is more enhanced at $R = 0.1$. Even if the tinning technique is able to increase the hydrogen embrittlement duration and increase the FCGR hydrogen embrittlement phenomenon, in comparison to FCGR tests without tin coating, this technique only limits the hydrogen diffusion in air for a relatively short period of time (approximately 90 minutes). Consequently, no reliable trend in the high strength bainite-ferrite pipeline steel FCGR behavior in a hydrogen environment can be drawn at this stage of this study. The possibility of developing a hydrogen test method in air is clearly limited. The specimen transportation in liquid nitrogen and the hydrogen diffusion during the test are two significant factors restraining the development of this method. Furthermore, the necessity of using two devices to perform hydrogen FCGR testing is problematic; the first device for hydrogen charging, and the second for fatigue testing. This requires the need for coating the specimen to minimize the diffusion of hydrogen out of the specimen between the charging and testing phases. This, in turn, eventually results in a minimal amount of data before the effect of the hydrogen is lost. A pressurized hydrogen chamber is certainly more desirable in order to obtain the full FCGR stage II crack growth curve.

CONCLUSIONS

Fatigue loading of API X100 pipeline steel, previously saturated in a hydrogen environment, significantly accelerated the FCGR relative to that observed in air. At low R values, the effects of hydrogen were more enhanced in stage II crack growth than at higher R values. Tinning of the hydrogen-charged specimens reduced the diffusivity of hydrogen out of the specimens, permitting a limited amount of FCGR data acquisition. This work clearly identifies the limitation of developing a fatigue test method in air able to evaluate the effects of hydrogen embrittlement, and directs further hydrogen-related research activities to be performed in pressurized hydrogen chambers.

REFERENCES

1. Nelson, H. G., "Testing for Hydrogen Environment Embrittlement, Primary and Secondary Influences", ASTM STP 543 (1974), pp. 152-169.
2. Lasseigne, A., "Development of Thermoelectric and Electromagnetic Techniques for Development of Interstitials in Advanced Materials", *PhD in Metallurgical and Materials Engineering*, Colorado School of Mines, 2006.
3. Chandler, W. T. *et al.*, "Cyclic-load Crack Growth in ASME SA-105 Grade II Steel in High Pressure Hydrogen at Ambient Temperature", Effect of Hydrogen on Behavior of Materials – AIME Inc. (New York, 1976), pp. 273-286.
4. Zawierucha, R. *et al.*, "Hydrogen Pipeline Steels", *Proc. Materials Science & Technology - Materials for the Hydrogen Economy*, 2005, pp. 79-90.
5. Cotterill, P. J. *et al.*, "Hydrogen Embrittlement Contributions to Fatigue Crack Growth in a Structural Steel", *Int. J. of Fatigue*, Vol. 13, No. 6 (1991), pp. 447-452.
6. Frandsen, J. D. *et al.*, "Environmentally Assisted Fatigue Crack Propagation in Steel", *Metallurgical Transactions A*, Vol. 8A, No. 2 (1977), pp. 265-272.
7. Mittal, S. C. *et al.*, "Effect of Hydrogen on Fatigue Crack Growth in Austenitic Fe-Mn-Al Steel", *Trans. of The Indian Inst. of Metals*, Vol. 49, No. 3 (1996), pp. 185-196.
8. Bussiba, A. *et al.*, "Fatigue crack growth rates in six pipeline steels", *Proc. of the 6th International Pipeline Conf*, Calgary, AL, September 2006.

Effects of Hydrogen on Materials
Proceedings of the 2008 International Hydrogen Conference
Brian Somerday, Petros Sofronis, Russell Jones, editors, p 389-396
Copyright © 2009 ASM International®
All rights reserved.
www.asminternational.org

BLISTER FRACTURE OF RUBBERS FOR O-RING EXPOSED TO HIGH PRESSURE HYDROGEN GAS

Junichiro YAMABE, and Shin NISHIMURA
Department of Mechanical Engineering Science, Kyushu University, Research Center for Hydrogen Industrial Use and Storage (HYDROGENIUS) and National Institute of Advanced Industrial Science and Technology (AIST), Fukuoka, Japan

Masatoshi NAKAO
Department of Mechanical Engineering Science, Kyushu University, Fukuoka, Japan

Hirotada FUJIWARA
Research Center for Hydrogen Industrial Use and Storage (HYDROGENIUS) and National Institute of Advanced Industrial Science and Technology (AIST), Fukuoka, Japan

INTRODUCTION

In recent years, global warming and exhaustion of fossil cells have emerged as serious environmental threats. The use of hydrogen fuel cells is an effective method for solving the abovementioned problems; several studies have been conducted on the practical use of fuel cells. Nevertheless, studies on the effect of hydrogen on the strength properties of organic materials such as plastics and rubbers have hardly been reported. In particular, the rubber used in O-ring seals has been reported to suffer from an internal fracture, which is referred as blister fracture [1], when exposed to various high-pressure gases, although there is no report on blister fractures caused by high-pressure hydrogen gas.
From this viewpoint, the objective of this study is to clarify whether hydrogen gas induces blister fractures in rubber materials and to identify the effect of fillers on the penetration properties of hydrogen and blister damages. For this purpose, EPDM (Ethylene-Propylene Rubber) and NBR (Nitrile-Butadiene Rubber) composites were exposed to hydrogen gas at a maximum pressure of 10 MPa. Further, on the basis of these results, the relationship between the penetration properties of hydrogen, the tensile properties, which are indicative of the elastic modulus and fracture strength, and the blister damage in these composites was investigated.

MATERIALS AND EXPERIMENTAL METHOD

Materials

Table 1 shows the chemical composition, density, and mechanical properties of the EPDM and NBR composites used for the measurement of the penetration properties

of hydrogen and blister tests. Carbon black (CB, average particle size: 0.03 μm, specific surface area: 65 mm^2/g) and silica (SC, average particle size: 12 μm, specific surface area: 154 mm^2/g) were used as fillers. Nine types of EPDM and NBR composites were tested in this study. CB was compounded with EPDM and NBR in the weight ratio of 100:50 to obtain EPDM-CB50 and NBR-CB50, and in the weight ratio of 100:25 obtain EPDM-CB25 and NBR-CB25. SC was compounded with EPDM and NBR in the weight ratio of 100:60 to obtain EPDM-SC60 and NBR-SC60. No fillers were added to EPDM-NF, EPDM-NFT, and NBR-NF. The volume fraction of CB in EPDM-CB50 and NBR-CB50 was the same as that of SC in EPDM-SC60 and NBR-SC60. Since EPDM-NFT was transparent, the initiation and growth of blisters occurring in the specimen could be clearly observed. The other composites were not transparent.

Table 1 Chemical composition (part by wt.), density and mechanical properties.

Items	EPDM					NBR			
	CB50	CB25	SC60	NF	NFT	CB50	CB25	SC60	NF
EPDM	100	100	100	100	100	-	-	-	-
NBR	-	-	-	-	-	100	100	100	100
Stearic acid	1.0	1.0	1.0	1.0	-	1.0	1.0	1.0	1.0
Zinc oxide	5.0	5.0	5.0	5.0	-	5.0	5.0	5.0	5.0
Sulfur	1.5	1.5	1.5	1.5	-	1.5	1.5	1.5	1.5
1,3,5-Triallyli-socyanurate	-	-	-	-	1.0	-	-	-	-
Dicumyl peroxide	-	-	-	-	2.5	-	-	-	-
Carbon Black	50	25	-	-	-	50	25	-	-
Silica	-	-	60	-	-	-	-	60	-
Hardness	A 79	A 68	A 91	A 54	A 52	A 77	A 67	A 85	A 52
Density (g/cm^3)	1.093	1.016	1.136	0.928	0.857	1.191	1.123	1.248	1.035
E (MPa)	7.9	4.3	9.3	2.1	2.0	6.3	3.3	7.5	1.7
σ_n (MPa)	19	11	13	1.3	1.0	24	14	28	2.0
λ_F	3.6	3.9	3.6	2.3	1.9	4.0	4.7	7.5	4.3

E: Elastic modulus, σ_n: Nominal fracture strength, λ_F: Fracture stretch (at room temperature).

Experimental Method

A cylindrical specimen (diameter: 13 mm; thickness: 2 mm) was used for the measurement of the penetration properties of hydrogen. The specimen was exposed to hydrogen gas at a maximum pressure of 10 MPa at 30 °C, and the hydrogen content of the specimen was measured by thermal desorption analysis (TDA). The time of exposure to hydrogen was varied from 2 to 24 h. Diffusion of hydrogen is considered to be faster in a rubber material than in a metal; a large volume of hydrogen was released from the specimen before the measurement tests. Even though the specimen was stored in liquid nitrogen or a refrigerator, the temperature was not sufficiently low to delay the hydrogen release from the specimen, in the case that its hydrogen penetrated into the specimen as a hydrogen molecule not atom. Hence, after exposure of the specimen to hydrogen, the hydrogen release profile was measured at 30 °C by TDA, and then, assuming that the hydrogen release is a

diffusion-controlled process and the size of the specimen is constant, Eq. (1) was fitted to the remaining hydrogen content of the specimen by the least-square method for estimating the unknown parameters, i.e., the equilibrium hydrogen content, C_{H0}, and diffusivity, D [2]. In other words, C_{H0} was extrapolated from the remaining hydrogen content:

$$C_{H,R}(t) = \frac{32}{\pi^2} \cdot C_{H0} \times \{ \sum_{n=0}^{\infty} \frac{\exp[-(2n+1)^2 \pi^2 Dt / \ell^2]}{(2n+1)^2} \} \times \{ \sum_{n=1}^{\infty} \frac{\exp[-D\beta_n^2 t / \rho^2]}{\beta_n^2} \} \quad (1)$$

where, $C_{H,R}(t)$ is the remaining hydrogen content at t (wt. ppm); t, the time elapsed after decompression (s); C_{H0}, the equilibrium hydrogen content (wt. ppm); D, diffusivity (m^2/s), β_n, the root of the zero-order Bessel function, ℓ, the thickness of the specimen (m), and ρ, the radius of the specimen (m), where the hydrogen content is based on the weight of a rubber composite. In this study, the measurement of the penetration properties of hydrogen was commenced within approximately 10 minutes after decompression. From the measurements, it was confirmed that the increase in the size of the specimens was equal to or less than 2% at the hydrogen pressure of ≤10 MPa.

For the blister tests, a cylindrical specimen (diameter: 29 mm; thickness: 12.5 mm) was used. The specimen was exposed to hydrogen gas at 10 MPa and 30 °C. The transparent composite, EPDM-NFT, was directly observed using an optical microscope. Specimens of the other composites were cut with a cutter, and their cross-sections were observed using an optical microscope.

RESULTS AND DISCUSSION

Hydrogen release profiles

Figure 1 shows the hydrogen release profiles of NBR-NF, SC60, and CB50 exposed to hydrogen gas at 10 MPa and 30 °C. The hydrogen contents in these specimens stabilized at the equilibrium value. The experimental data for NBR-NF and SC60 were well approximated by Eq. (1), while those for NBR-CB50 were not. These tendencies were also observed in the hydrogen release profiles of the EPDM composites, thus implying that CB traps hydrogen. McNabb et al. [3] analyzed hydrogen diffusion for a trapping system in steels, and reported that the processes of diffusion and absorption in traps become essentially uncoupled or independent of one another when a specimen is small. In this study, although the processes of diffusion and absorption in traps were not completely uncoupled, hydrogen which was not trapped by CB was released; then the hydrogen trapped by CB was released. Therefore, it is assumed that hydrogen in the CB-containing composites was released under the combined effect of two diffusion-controlled processes, one of which is fast diffusion due to the hydrogen in the polymer, and the other of which is relatively slow diffusion due to the hydrogen reversibly trapped by CB. On the basis of this idea, the experimental data shown in Fig. 1(c) could be conveniently approximated by Eq. (2):

$$C_{\mathrm{H,R}}(t) = C_{\mathrm{H,R}}^{\mathrm{Polymer}}(t) + C_{\mathrm{H,R}}^{\mathrm{Filler}}(t) \tag{2}$$

where, $C_{\mathrm{H,R}}^{\mathrm{Polymer}}(t)$ is the remaining hydrogen content in the polymer (wt. ppm), and $C_{\mathrm{H,R}}^{\mathrm{Filler}}(t)$ is the remaining hydrogen content of the hydrogen trapped by CB (wt. ppm). $C_{\mathrm{H,R}}^{\mathrm{Polymer}}(t)$ and $C_{\mathrm{H,R}}^{\mathrm{Filler}}(t)$ are expressed as follows:

$$C_{\mathrm{H,R}}^{\mathrm{i}}(t) = \frac{32}{\pi^2} \cdot C_{\mathrm{H0}}^{\mathrm{i}} \times \{ \sum_{n=0}^{\infty} \frac{\exp[-(2n+1)^2 \pi^2 D^{\mathrm{i}} t / \ell^2]}{(2n+1)^2} \} \times \{ \sum_{n=1}^{\infty} \frac{\exp[-D^{\mathrm{i}} \beta_n^2 t / \rho^2]}{\beta_n^2} \} \tag{3}$$

$\mathrm{i} = \mathrm{Polymer, Filler}$

where, $C_{\mathrm{H0}}^{\mathrm{Polymer}}$ is the equilibrium hydrogen content in the polymer (wt. ppm); $C_{\mathrm{H0}}^{\mathrm{Filler}}$, the equilibrium hydrogen content of the hydrogen trapped by CB (wt. ppm); D^{polymer}, the diffusivity of hydrogen in the polymer ($\mathrm{m^2/s}$); and D^{Filler}, the diffusivity of hydrogen trapped by CB ($\mathrm{m^2/s}$). Fig. 1(c) shows the approximation of $C_{\mathrm{H,R}}(t)$ by both Eq. (1) and Eq. (2). The remaining hydrogen content in NBR-CB50 is well approximated by Eq. (2). Therefore, the equilibrium hydrogen contents in the CB50 and CB25 composites were extrapolated by Eq. (2) in this study.

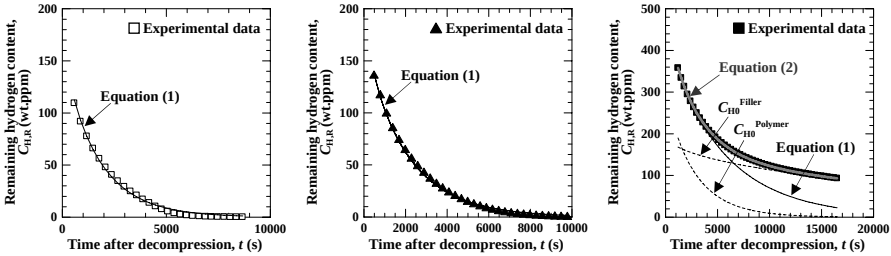


Figure 1: Relationship between remaining hydrogen content and time elapsed after decompression of NBR composites exposed to hydrogen gas (10 MPa) at 30 °C: (a) NBR-NF, (b) NBR-SC60, (c) NBR-CB50.

Relationship between equilibrium hydrogen content and hydrogen pressure

Figure 2 (a) shows the relationship between the C_{H0} values and hydrogen pressures P for all the composites. At hydrogen pressures of ≤ 10 MPa, C_{H0} of all the composites were found to be nearly proportional to the hydrogen pressures, i.e., the equilibrium hydrogen contents followed Henry's law, which is expressed as $C_{\mathrm{H0}} = SP$ (S: Solubility). This implies that hydrogen penetrates a rubber material as a hydrogen molecule.

Figure 2(b) shows the S values obtained from the extrapolation method shown in Fig. 2(a) and those obtained by a conventional permeation method [4]. This permeation test was conducted under at 30 °C at the difference pressure between 0.6 and 0 MPa. The value of S obtained by extrapolation was roughly consistent with that obtained from the conventional permeation method; therefore, the results obtained from Fig. 2(a) by the extrapolation method can be considered to be reliable.

The C_{H0} values in the CB50 and CB25 composites were found to be greater than those in the SC60 and NF composites, irrespective of the type of polymer. Trapping of hydrogen by CB is considered to be one of the reasons for the increase in C_{H0}. In order to confirm whether hydrogen molecules are trapped by CB and SC or not, these powders were exposed to hydrogen gas at 10 MPa and 30 °C for 65 h, and the hydrogen contents were subsequently measured by TDA. These measurements were commenced within approximately 3 h after exposure of these powders to hydrogen. Consequently, the remaining hydrogen contents in the CB and SC powders were 140 wt. ppm and 2 wt. ppm, respectively; therefore, trapping of hydrogen by CB was confirmed to be one of the reasons for the C_{H0} values of CB50 and CB25 composites being higher than those in the other composites.

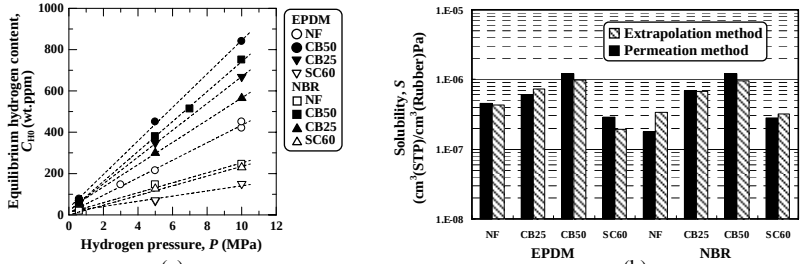


Figure 2: Measurement of hydrogen content: (a) Relationship between C_{H0} and P, (b) Comparison of S between extrapolation and permeation methods.

Blister initiation and growth behavior

Figure 3 shows the optical microscope images of EPDM-NFT after it was exposed to hydrogen gas at 10 MPa and 30 °C for 65 h. The observation was commenced within 5.5 min after decompression. A large number blisters were found to have been formed in the specimen, as can be seen from Fig. 3(a); then, these blisters grew with time after decompression. This type of crack growth is generally referred to as static crack growth since the cracks grow under static loading. The minimum blister size that could be observed in this study was of the order of a few micrometers. Similar to the case of EPDM-NFT, blisters observed on the cross-section of other composites that were cut with a cutter were also a few micrometers in size.

Figure 4 shows the blister damage in the composites exposed to hydrogen gas at 10 MPa and 30 °C for 65 h. These specimens were cut after the swelling caused by their exposure to hydrogen receded completely. The arrows shown in Fig. 4 indicate the maximum observed area of the blisters on the cross-section of the specimens. The degree of these blister damages differed with the type of composite, and the blister damages were found to be more severe in EPDM-NF and NBR-NF than in the others. This is because the elastic modulus E and fracture strength σ_n of these composites are lower than those of the other composites. In contrast, no blister formation was observed on the surfaces of EPDM-SC60 and NBR-SC60, although

their tensile properties (E and σ_T) were similar to those of the CB-containing composites. This is considered to be due to the difference in the hydrogen contents between the SC-containing and CB-containing composites. Thus, both tensile properties and hydrogen contents of the composites influence the blister damage.

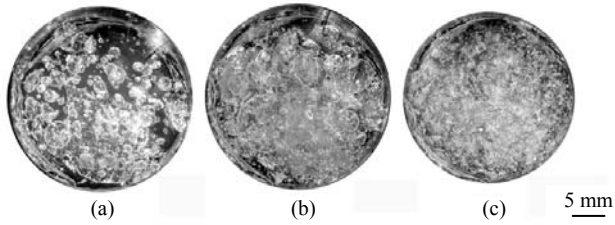


Figure 3: Initiation and growth of blisters in EPDM-NFT exposed to hydrogen gas at 10 MPa and 30 °C for 65 h; (a) 5.5 min after decompression, (b) 7 min after decompression, (c) 24 h after decompression.

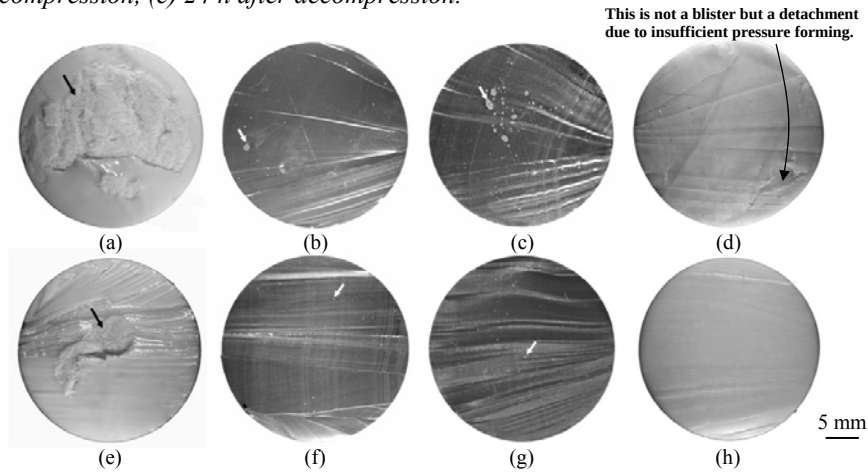


Figure 4: Blister damages in rubber composites exposed to hydrogen gas at 10 MPa and 30 °C for 65 h: (a) EPDM-NF, (b) EPDM-CB50, (c) EPDM-CB25, (d) EPDM-SC60, (e) NBR-NF, (f) NBR-CB50, (g) NBR-CB25, (h) NBR-SC60.

Relationship between blister damage, tensile properties, and hydrogen contents

It is considered that after a high-pressure hydrogen gas is decompressed, the solute hydrogen molecules in the rubber composites become supersaturated. As a result, micrometer-sized bubbles are formed in the composite, which in turn initiate crack formation. Bubbles that do not induce cracks will go out, making them unobservable.

It is considered that these bubbles will originate from defects which are initially present in the composite [5] and inhomogeneous sites. If hydrogen gas is sustained without decompression, the crack does not initiate due to external

constraints. In this study, the bubbles are regarded as spherical cavities; further, it is assumed that a crack is initiated from a rubber composite when the maximum tangential stress, $\sigma_{\theta,\max}$, around a spherical cavity subjected to an inner pressure, Π, existing in an infinite body exceeds the true fracture stress, σ_T, of the rubber composites as the first approximation. Under incompressibility, $\sigma_T = \sigma_n\lambda$. Although both $\sigma_{\theta,\max}$ and the notch size influence crack initiation, the minimum blister sizes of all the composites are roughly equal; therefore, the effect of the notch size was conventionally ignored. Moreover, by assuming that Π is proportional to C_{H0}, the relationship between the blister damage, the equilibrium hydrogen content and the tensile properties of the composites were investigated. Regarding a rubber composite as a super-elastic material [6], its strain energy density can be expressed as follows:

$$W(I_1, I_2) = C_{10}(I_1 - 3) + C_{01}(I_2 - 3) + C_{20}(I_1 - 3)^2 \tag{4}$$

where, I_1 and I_2 are invariants, and C_{ij} is the material constant. In this case, the values of Π_F and $\sigma_{\theta,\max}$ at the initiation of cracks are expressed using λ_F and C_{ij} as follows [7]:

$$\Pi_F = (5 - \frac{1}{\lambda_F^4} - \frac{4}{\lambda_F})C_{10} - 2(1 + \frac{1}{\lambda_F^2} - 2\lambda_F)C_{01} - (\frac{177}{5} + \frac{1}{\lambda_F^8} + \frac{8}{5\lambda_F^5} - \frac{6}{\lambda_F^4} + \frac{8}{\lambda_F^2} - \frac{24}{\lambda_F} - 16\lambda_F)C_{20} \tag{5}$$

$$\begin{aligned}\sigma_{\theta,\max} = {} & (-5 - \frac{1}{\lambda_F^4} + \frac{4}{\lambda_F} + 2\lambda_F^2)C_{10} + 2(1 - 2\lambda_F + \lambda_F^4)C_{01} \\ & + (\frac{177}{5} - \frac{3}{\lambda_F^8} + \frac{8}{5\lambda_F^5} + \frac{6}{\lambda_F^4} + \frac{4}{\lambda_F^2} - \frac{24}{\lambda_F} - 16\lambda_F - 12\lambda_F^2 + 8\lambda_F^4)C_{20}\end{aligned} \tag{6}$$

Figure 5 shows the relationship between Π_F and C_{H0} of the composites exposed to hydrogen gas at 10 MPa and 30 °C, where the C_{H0} values are based on not the weight of a rubber composite but that of a polymer. The Π_F values increase with an increase of E and σ_T. The result implies that the degree of blister damage can be controlled by C_{H0} and tensile properties such as E and σ_T of the composites. As observed from Fig. 5, the degree of blister damage in the composites decreases with a decrease in C_{H0} and an increase in E and σ_T.

CONCLUSIONS

In this study, EPDM and NBR composites were exposed to hydrogen gas (≤10 MPa), and the relationship between blister damages, penetration properties of hydrogen, and tensile properties of the composites were investigated. The results obtained can be summarized as follows:

1. Irrespective of the type and addition of fillers, the C_{H0} values of all the composites tested in this study followed Henry's law and were proportional to hydrogen pressures of 10 MPa or lesser. This implies that hydrogen penetrates a rubber material as a hydrogen molecule.
2. The hydrogen contents of the EPDM and NBR composites increased upon the addition of CB. Trapping of hydrogen by CB was confirmed to be one of the reasons for the increase in the hydrogen content.

3. After decompression, micrometer-sized blisters were formed in the composites, and these grew in size with the passage of time.
4. Both hydrogen contents and tensile properties such as E and σ_T of the composites influenced blister damage, and the degree of the blister damage in the composites decreased with a decrease in C_{H0} and an increase in E and σ_T.

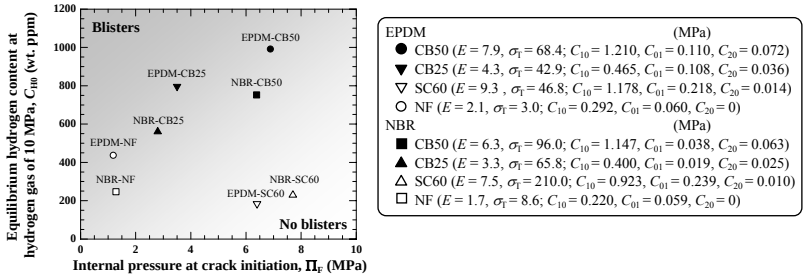


Figure 5: Relationship between Π_F and C_{H0} of the composites exposited to hydrogen gas at 10 MPa and 30 ^oC for 65 h.

ACKNOWLEDGMENTS

This research has been supported by the NEDO Fundamental Research Project on Advanced Hydrogen Science (2006 to 2012).

REFERENCES

1. Biscoe B. J. et al., “Explosive decompression failure of rubber: A review of the origins of pneumatic stress induced rupture in elastomer,” Rubber chemistry and technology, Vol. 67, No. 3 (1994), pp. 384–416.
2. Demarez A. L. et al., “Diffusion of hydrogen in mild steel,” Acta Metallurgica, Vol. 2, Mar (1954), pp. 214–223.
3. McNabb A., Foster P. K., A New Analysis of the Diffusion of Hydrogen in Iron and Ferritic Steels, Transactions of The Metallurgical Society of AIME, Vol. 227, June (1963), pp. 618–627.
4. Van Amerongen G. J., “Diffusion in elastomers,” Rubber chemistry and technology, Vol. 37, No. 5 (1964), pp.1067–1103.
5. Gent A. N., Tompkins, Nucleation and Growth of Gas Bubbles in Elastomers, Journal of Applied Physics, Vol. 40, No. 6 (1969), pp. 2520–2525.
6. Ogden R. W., “Non-linear Elastic Deformations,” John Wiley & Sons (1984).
7. Green A. E. et al., “Theoretical Elasticity,” Oxford at the Clarendon Press (1954), pp.104–108.

Effects of Hydrogen on Materials
Proceedings of the 2008 International Hydrogen Conference
Brian Somerday, Petros Sofronis, Russell Jones, editors, p 397-404
Copyright © 2009 ASM International®
All rights reserved.
www.asminternational.org

A STUDY ON BLISTER DAMAGES OF RUBBER O-RING BY HIGH PRESSURE HYDROGEN DURABILITY TESTER

Atsushi KOGA, Junichi NAKAYAMA, and Hideyuki TOKUMITSU
Corporate Technology Office, NOK CORPORATION, Kanagawa, Japan.

Masaya OTSUKA
O-rings Division, NOK CORPORATION, Kumamoto, Japan.

Junichiro YAMABE, and Shin NISHIMURA
Department of Mechanical Engineering Science, Kyushu University, Research Center for Hydrogen Industrial Use and Storage (HYDROGENIUS) and National Institute of Advanced Industrial Science and Technology (AIST), Fukuoka, Japan.

INTRODUCTION

Rubber O-rings, which are equipped to high pressure hydrogen tanks of fuel cell electric vehicles, are repeatedly exposed to high pressure hydrogen gas. Exposure of rubber O-rings to high pressure gas sometimes causes mechanical damages such as large deformation, swelling and blistering after decompression, although there are no reports on blister fracture caused by high pressure hydrogen gas [(1)]. In this study, the blister is defined as a crack or bubble initiating from the inside of a specimen after decompression. With increasing decompression rate, these mechanical damages generally tend to be more serious. In these mechanical damages, blister damage is the most important from the viewpoint of durability and sealing performance of the rubber O-ring. The degree of the blister damage is influenced by not only material properties but also test conditions such as decompression rate, maximum pressure, ambient temperature, etc. Moreover, the shape of the O-ring also influences the degree of blister damage. Figure 1 shows the schematic representations of cracks caused by decompression [(2)-(5)].

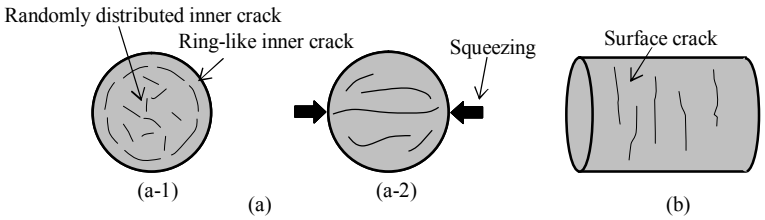


Figure 1: Schematic representations of cracks generated after decompression: (a) Inner crack, (a-1) Without squeezing, (a-2) With squeezing, (b) Surface crack at rapid decompression rate [(2)-(5)].

When a rubber exposed to high pressure hydrogen gas is not squeezed, randomly distributed cracks and ring-like cracks are formed. The former cracks are thought to be due to stress concentration of bubbles formed by super-saturated hydrogen in the rubber structure after decompression. As for the latter cracks, it has been reported that shear stress due to hydrogen concentration gradient at decompression influences the generation of this type of cracks [(4)]. When the rubber is squeezed, cracks parallel to squeezing are formed due to tensile stress generated at the center of a specimen. Moreover, surface cracks may also be formed when decompression rates are rapid, more than 1 MPa/sec. In this study, we developed a high pressure hydrogen durability tester for rubber O-rings which enables repeated exposure of the O-rings to high pressure gas (Maximum pressure: 90 MPa, Maximum decompression rate; 22.5 MPa/sec) and temperatures ranging from –60 to 100 ^{o}C. Durability tests to reproduce actual fractures occurring in O-rings used for hydrogen equipment were conducted at certain cycle conditions.

EXAMPLE OF BLISTER FRACTURE OF O-RING EXPOSED TO HIGH PRESSURE HYDROGEN GAS

The material of the O-ring shown here for sealing in high pressure hydrogen gas was acryloNitrile - Butadiene - Rubber (NBR)[(7)], which is copolymerization rubber material as for acrylonitrile and butadiene with density of 1.286 g/cm^3. Figure 2(a) shows the appearance of the O-ring. It has an inner diameter of 140 mm and cross-section diameter of 5.5 mm. Figure 2(c) shows the schematic representation of the installation of the O-ring, squeezed in the radius direction.

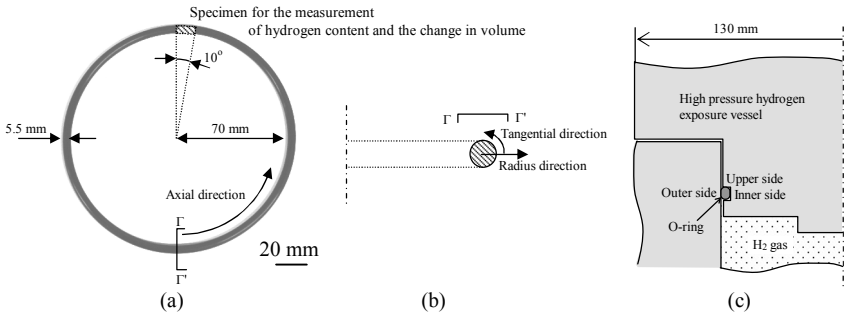


Figure 2: Appearance and installation conditions of O-ring used for high pressure hydrogen vessel: (a) Appearance of O-ring, (b) Cross section of Γ-Γ', (c) Installation of O-ring.

The squeeze ratio was 30 %, which is the upper limit since conventional squeeze ratios range from 8 to 30 %. The definition of the squeeze ratio, which is illustrated later in Fig. 6, is the ratio of un-deformed O-ring diameter to displacement of O-ring holder. The hydrogen gas enters from the lower side of the O-ring. The hydrogen vessel installing the O-ring was used in 100 MPa hydrogen gas at room temperature. The compression time from atmospheric pressure to 100 MPa, holding time at 100 MPa, and decompression time from 100 MPa to

atmospheric pressure were 30 minutes respectively. This cyclic hydrogen exposure was carried out 20 cycles.

Figure 3 shows an example of cracks formed in O-ring exposed repeatedly to 100 MPa hydrogen gas. Shown in Figs. 3(a) and (b) are an optical microscope image and SEM image of the fracture surface. A long crack measuring 20 mm can be seen on the surface. The elliptical patterns observed on the fracture surface suggest that the crack was caused by fracture. SEM observation also shows that the fracture originates from the inside of the O-ring, not the surface.
Figure 4 shows an optical microscope image of Γ–Γ' shown in Fig. 3(b). The fracture surface of the pair in Fig. 3(b) is also used to create this image. The crack grows macroscopically parallel to the squeeze direction.

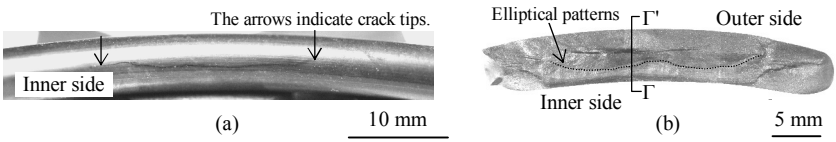


Figure 3: Example of crack formed in O-ring exposed repeatedly to 100 MPa hydrogen gas: (a) Optical microscope image, (b) SEM image of fracture surface.

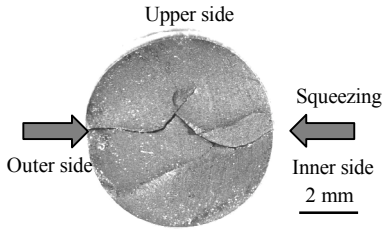


Figure 4: Optical microscope image of cross section Γ – Γ'.

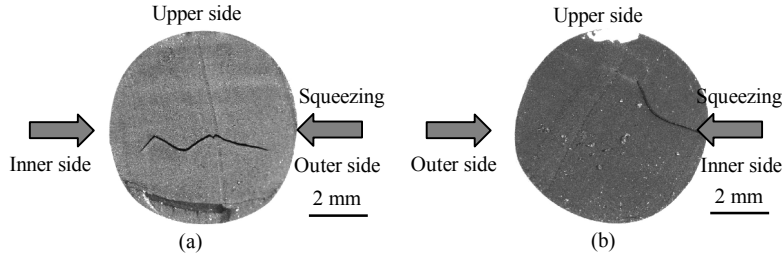


Figure 5: Optical microscope images of inner and surface cracks formed in O-ring exposed repeatedly to 100 MPa hydrogen gas.

Figure 5 shows other examples of cracks, which are inner and surface cracks formed in O-rings. The inner crack shown in Fig. 5(a) is the same as that shown in Fig. 4, i.e., the crack grows macroscopically parallel to the squeeze direction.

The surface crack shown in Fig. 5 (b) is formed at the sites near the surface, whose fracture is thought to originate from inside by SEM observation as well as the inner crack in Fig. 5(a). The surface crack shown in Fig. 5 (b) is believed to influence tensile stress generated by hydrogen concentration gradient at decompression.

EXPERIMENTAL METHOD

A blister test was conducted using Ethylene-Propylene(-DieneMonomer) (EPDM) [7]rubber composite which is conventionally used for sealing in high pressure hydrogen gas. Table 1 shows the material properties of the EPDM rubber composite. Figure 6(a) shows a schematic representation of the high pressure hydrogen durability tester developed. This tester can be operated at hydrogen pressures ranging from 6 to 90 MPa, and temperatures ranging from –60 to 100 ^{o}C using a gas compressor and temperature chamber. Durability tests were conducted at arbitrary hydrogen pressure cycles. The maximum decompression rate was 22.5 MPa/sec. The pressured hydrogen gas was repeatedly supplied to eight O-ring holders installed O-rings by using pressure control valve. Hydrogen gas leakage is detected by hydrogen concentration sensor set at lower pressure side, whose regulated limit is 2,000 ppm.

Table 1 Material properties of EPDM rubber composite.

Properties	
Durometer hardness (points)	A 71
Density (g/cm^3)	1.308
Elastic modulus, E (MPa)	4.3
Nominal tensile stress, σ_n (MPa)	7.9
Fracture stretch, λ_F	4.3

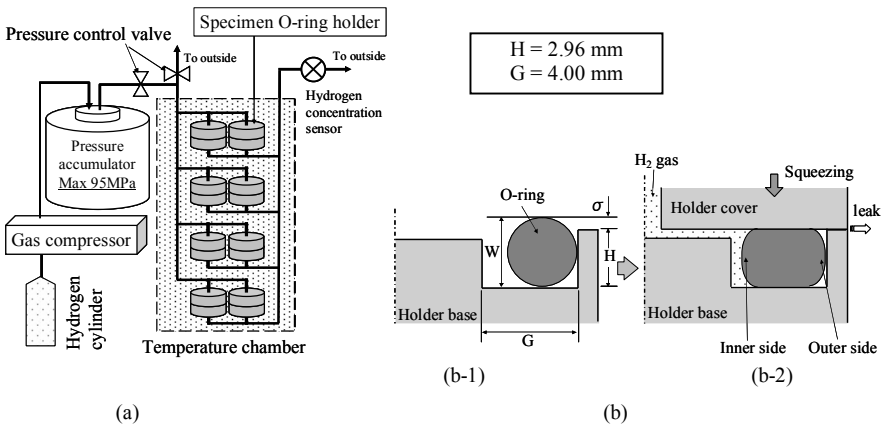


Figure 6: Schematic representation of high pressure durability tester: (a) Experimental setup, (b) Details of installation of O-ring, (b-1) Without squeezing, (b-2) With squeezing.

Figure 6 (b) shows the details of the installation of these O-rings. The squeeze ratio is generally expressed as follows:

$$\text{Squeeze ratio} = \frac{\sigma}{W} \times 100\,(\%) \tag{1}$$

where, $\sigma = W - H$, W is the cross-section diameter (mm), and H is the depth of groove (mm). During the durability test, the O-ring was deformed by squeezing as shown in Fig. 6(b-2), after which high pressure hydrogen gas was supplied from the inside from the O-ring. In this study, the two kinds of O-rings shown in Table 3 were used. The fracture of the O-rings was evaluated based on the volume of leaked hydrogen gas, which was measured by a hydrogen concentration sensor. Table 2 shows the detailed specifications of the tester.

Table 2 Detailed specifications of durability tester.

Parameters	Minimum	Maximum
Pressure upper point: P_U (MPa)	6	90
Pressure lower point: P_L (MPa)	0.1	10
Holding time at P_U: t_U (hours)	0	99
Holding time at P_L: t_L (hours)	0	99
Compression time: α_U (sec)	15 (5 to 90MPa)	
Decompression time: α_D	4 sec.	1hour
Temperature: T (°C)	-60	100

Table 3 Shapes and dimensions of O-ring used for durability tests.

Parameters	No. 1	No. 2
Cross-section diameter: W (mm)	3.53	3.30
Inner diameter: ID (mm)	11.9	12.3
Squeeze ratio (%)	16	11

RESULTS AND DISCUSSION

Figures 7(a) to (c) show the appearance and cross section of the No. 1 O-ring exposed once to 90 MPa hydrogen gas at 30 °C. Figure 7(d) shows the cycle conditions. The parting line is a line formed at the molding process of a rubber, which sometimes induce crack initiation. The leakage of hydrogen gas more than the regulated limit was not seen at this condition. No cracks are also seen from Figs. 7(a) to (c).

Figures 8(a) to (c) show the appearance and cross section of the No. 2 O-ring exposed 65 cycles to 90 MPa hydrogen gas at 30 °C. Figure 8(d) shows the cycle condition. During the cycle test, there was not the leakage of hydrogen gas more than the regulated limit. From the observation of the cross section shown in Fig. 8(c), no inner crack was observed despite cyclic exposures to high pressure hydrogen gas. Consequently, we conducted durability tests at 85 °C, since the

tensile properties of a rubber material generally decreases at high temperature. Figures 9(a) to (c) show the appearance and cross section of the No. 1 O-ring exposed eight cycles to 90 MPa hydrogen gas at 85 ^{o}C. Figure 9(d) shows the cycle condition. In this test, hydrogen gas leakage more than the regulated limit occurred after eight cycles. From the observation of the cross section, two cracks can be seen. Since the location of initiation and the growth direction of these cracks are similar to those of the cracks in Fig. 5(b), we reproduced the blister fracture of an actual O-ring by this tester.

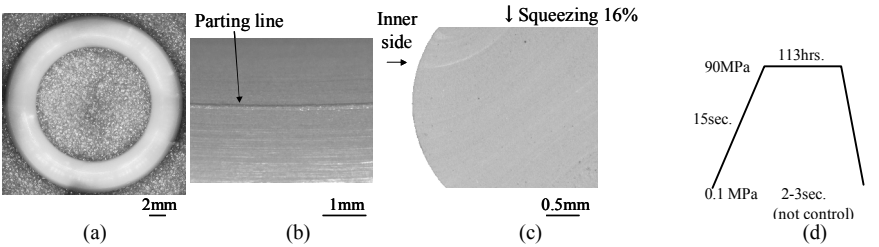


Figure 7: Appearance and cross section of No. 1 O-ring exposed once to 90 MPa hydrogen gas at 30 ^{o}C: (a) Appearance, (b) Magnification of surface, (c) Cross section, (d) Cycle condition.

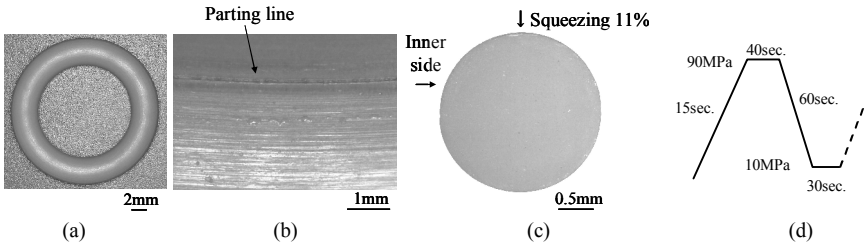


Figure 8: Appearance and cross section of No. 2 O-ring exposed 65 cycles to 90 MPa hydrogen gas at 30 ^{o}C: (a) Appearance, (b) Magnification of surface, (c) Cross section, (d) Cycle condition.

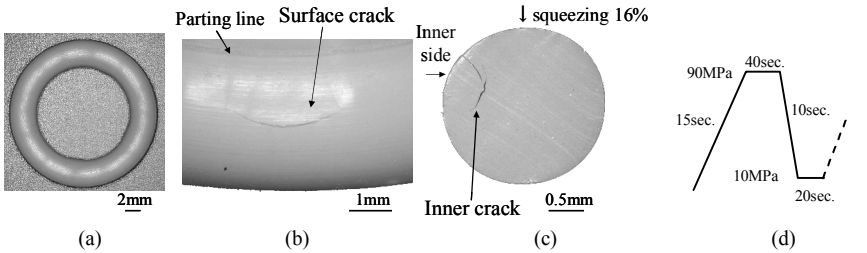


Figure 9: Appearance and cross section of No. 1 O-ring exposed eight cycles to 90 MPa hydrogen gas at 85 ^{o}C: (a) Appearance, (b) Magnification of surface, (c) Cross section, (d) Cycle condition.

One of the reasons why the crack as shown in Fig. 5(a) does not occur may be because of the difference in squeeze ratio, i.e., the squeeze ratio of the No.1 O-ring is 16 %, and considerably lower than that of the O-ring shown in Fig. 5, which is 30 %.
Figure 10 shows an example of another kind of fracture called extrusion [6]. Extrusion generally occurs when a cross section area of a rubber O-ring is expanded by a large swelling shown in Fig. 11. When exposed to high pressure hydrogen gas, extrusions caused by large swellings also influence the durability of the O-ring as well as blistering.

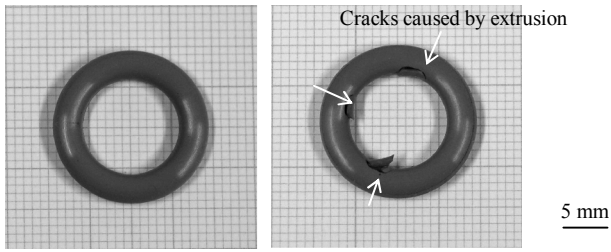


Figure 10: Appearance of No. 1 O-ring exposed a few cycles to 90 MPa hydrogen gas at 100 °C: (a) Before test, (b) After test.

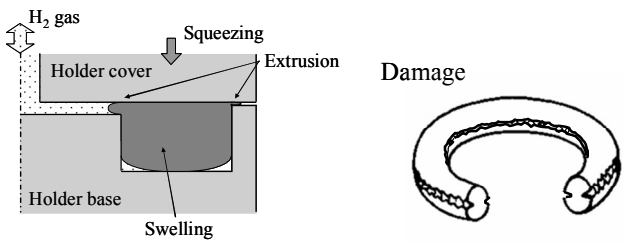


Figure 11: Schematic representation of damage by extrusion.

CONCLUSIONS

In this study, we developed a high pressure hydrogen durability tester for rubber O-rings which enables repeated exposure of the O-rings to high pressure gas (Maximum pressure: 90 MPa, Maximum decompression rate; 22.5 MPa/sec) and temperatures ranging from –60 to 100 °C. Durability tests to reproduce actual fractures occurring in O-rings used for hydrogen equipment were conducted at certain cycle conditions. The results obtained can be summarized as follows:

1. Cyclic tests were conducted at 65 cycles in exposure to 90 MPa hydrogen gas at 30 ^{o}C. No cracks due to blistering were formed on the rubber O-ring. In contrast, cracks due to blistering were formed at 9 cycles when exposed to 90 MPa hydrogen gas at 85 ^{o}C, indicating that the durability of the O-ring decreases with increasing temperature.

2. The location of initiation and the growth direction of the cracks generated in durability tests were similar to those of cracks generated from the O-ring actually used for hydrogen equipment, indicating that the actual conditions of O-rings in use were successfully reproduced by this tester.

3. Cracks caused by extrusion as well as blistering were formed in cyclic exposure to high pressure hydrogen gas. This suggests that rubber O-rings swell largely when exposed to 100 MPa hydrogen gas.

ACKNOWLEDGMENTS

This research has been supported by the NEDO Fundamental Research Project on Advanced Hydrogen Science (2006 to 2012).

REFERENCES

1. Biscoe B. J. et al., “Explosive decompression failure of rubber: A review of the origins of pneumatic stress induced rupture in elastomer”, Rubber chemistry and technology, Vol. 67, No. 3 (1994), pp. 384-416.
2. Gent A. N., “Nucleation and growth of gas bubbles in elastomers”, Journal of applied physics, Vol. 40, No. 6 (1969), pp. 2520-2525.
3. Zakaria S., “Why rubber explodes”, Chemtech, Vol. 20, No. 8 (1990), pp. 492-495.
4. Briscoe B. J., “Internal crack symmetry phenomena during gas-induced rupture of elastomers”, Rubber chemistry and technology, Vol. 65, No. 3 (1992), pp. 350 -373.
5. Embury P., “High-pressure gas testing of elastomer seals and a practical approach to designing for explosive decompression service”, Sealing technology, Vol 2004, No. 6 (2004), pp.6-11.
6. The national O-ring Engineering Manual, Seven Steps to O-Ring Design, National O-Ring Division, Federal-Mogul Corporation, Downey, California, (1975).
7. ISO 1629

Effects of Hydrogen on Materials
Proceedings of the 2008 International Hydrogen Conference
Brian Somerday, Petros Sofronis, Russell Jones, editors, p 405-412
Copyright © 2009 ASM International®
All rights reserved.
www.asminternational.org

FRICTION AND WEAR OF METALS AND COATINGS USED IN HYDROGEN

Robert Erck, George Fenske, and Osman Eryilmaz
Argonne National Laboratory, Argonne, IL USA

ABSTRACT

Mechanical components used in the production and delivery of hydrogen, such as those used in compressors for pipeline or point-of-delivery applications, can be subject to excessive wear, have poor reliability, or may require the use of lubricants that can contaminate the hydrogen. In order to understand these potential problems affecting the economics and reliability of components, experiments were undertaken to assess the friction and wear properties of candidate materials, such as stainless steel, Ti, and Ni alloys. Coatings, based on graphite, diamondlike carbon (DLC), or MoS_2 were also examined. Tribological test results are presented for high-speed sliding tests of materials in pure hydrogen, other gases and vacuum. Measured metal/metal friction coefficients fell between 0.4 and 1.4, but for coatings such as MoS_2 or DLC, the friction coefficients were between 0.05 and 0.2 and coating/metal transfer was observed. Friction coefficients varied strongly with sliding speed but were insensitive to sliding load. Some graphs of typical frictional behavior are presented and summary frictional data are tabulated.

INTRODUCTION

The study of hydrogen effects in materials is important in many technological areas such as hydrogen embrittlement in engineering materials, hydrogen separation membranes, catalysis, hydrogen fuel transport, and aqueous corrosion. For materials exposed to gaseous H_2, the degradation of mechanical properties can be a significant problem and has been studied extensively. Research has tended to focus primarily on non sliding (but perhaps cyclically loaded) systems, and hydrogen diffusion, solubility, accelerated crack propagation and hydride formation have been studied. Dynamic sliding conditions have been less studied and are less understood, due in part to the difficulty of performing tribological sliding tests in H_2 gas, especially at elevated temperatures.

Mechanical components used in gaseous H_2 service, such as compressor bearings or valves, will be subject to tribological issues arising from an environment that includes static embrittlement, reduction of oxide layers, frictional heating, and the effects of local “hot spots” that occur when microscopic asperities slide past each

other at high speed. Models of asperity heating show flash temperature increases of several hundred degrees for even modest friction coefficients. Other sources of heat input to compressor parts may be exposure to the the adiabatically heated gas itself as well as mechanical frictional heating of sliding seals or rubbing foil-bearing pad bearings.

The need for dry operation in H_2, at elevated temperatures, imposes restrictions on the lubricants allowed, and unprotected metals generally have poor tribological properties. Some well-known dry lubrication concepts are already known. MoS_2 and WS_2 derive their lubricity from their weakly bonded molecular layers and can provide low friction and durability [1]. In the absence of oxygen, such compounds can withstand high temperatures. Another solid lubricant concept is that of a non-reactive soft metal (such as Ag) which can easily shear under high pressure [2], and shows promise for Stirling engines that use H_2 as a working gas. It has been known for a long time that graphite, though a classical dry lubricant, requires the presence of water vapor to be lubricious [3], whereas other solid lubricants may benefit from pure H_2. Other high-temperature sliding systems have been studied, but many challenges still remain in terms of friction and wear [4,5]. The frictional properties in inert atmospheres [6] and vacuum and water vapor [7] are well known, but little is known about behavior in hydrogen.

EXPERIMENT

Figure 1 shows a photo of the benchtop thrust-washer configuration tribometer that was used for the tests. A 50mm-dia circular disk is spun against a 50mmx50mm square stationary flat at speeds up to 10,000 rpm at ambient gas pressure. Sliding surfaces were lapped to a mirror smoothness prior to sliding or coating. The presence of frictional heating limited the duration of the tests to several minutes. Sliding can be performed in air, N_2 (< 4 ppm O_2), 99.995% H2 (<5 ppm O_2, H_2O), N_2-5%H_2 mixture, vacuum, and water-saturated atmospheres of the same.

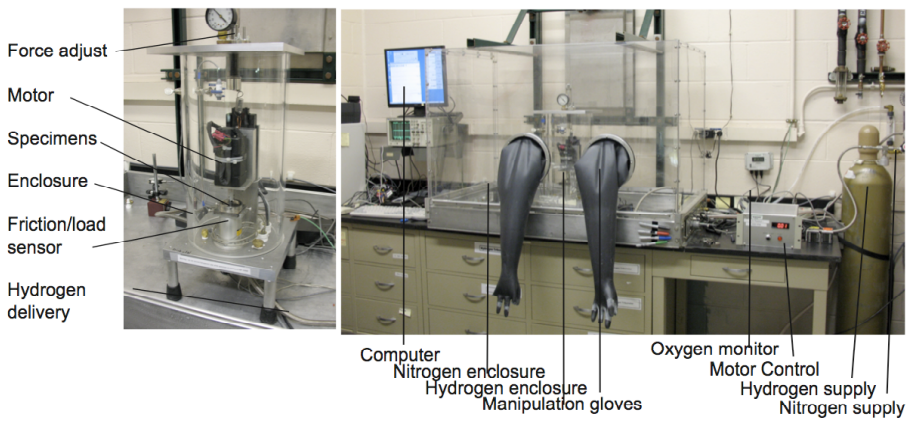


Figure 1: photograph of thrust washer tribometer (L), and the enclosure/gas delivery system (R).

Due to flammability concerns, the small tribometer that contains pure H_2 is placed inside a N_2 filled box. Friction coefficients were calculated from measured torque values. Thrust washer sliding was done on Ti-6Al-4V, 6061-T6 Al, 316 stainless steel, and X-750 Ni alloy samples uncoated, or coated with DLC, a friable MoS_2 or a bonded commercial MoS_2 coating. Although Ti alloys are not being considered for use in the production and delivery of H_2, Ti was included to serve as a model alloy that has a high reactivity with oxygen and H_2O and thus may give insight into tribochemistry that may occur at the sliding surface. Tests were performed either using rotation speed ramped up and down to assess friction as a function of sliding speed, with manually ramped load to assess friction as a function of load, or with different atmospheres to assess effect of ambient gas on friction. The DLC coating that was used was an amorphous carbon containing approximately 39% H [6].

RESULTS

Fig. 2 shows graphs of friction coefficients as a function for sliding time for Ti-6Al-4V sliding in air as a function of time for 4N load and variable speed or 6500 rpm at variable load. Because friction is often a complicated function of sliding speed and load, the graphs show not just friction coefficient, but also sliding speed, load, and torque to present a complete picture.

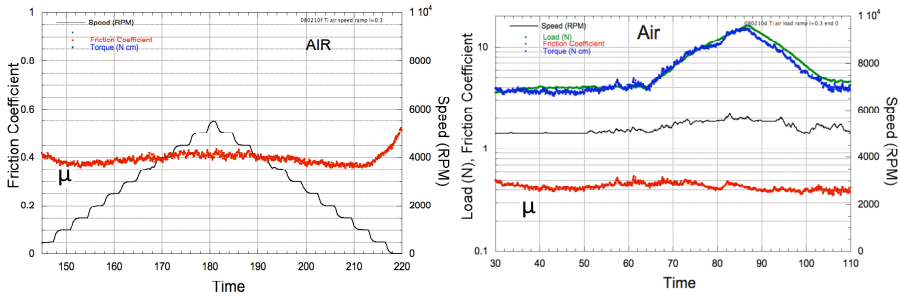


Figure 2. Graphs of friction coefficients as a function of sliding time for Ti-6Al-4V in air, for 4 N load and variable speed (L) or constant 6500 rpm and variable load (R).

The friction of this Ti alloy is remarkably steady over a range of rotation speeds, increasing somewhat at the lower speeds, and for a range of loads from 4 to 18 N at a constant sliding speed. For sliding in H_2, the friction coefficient exceeded 1.5, presumably because existing oxide layers are mechanically removed/disturbed and are unable to reform in the reducing environment. The dry sliding will deform. The measured surface roughness of the worn surfaces was 2.1 μm Sa where Sa is the surface arithmetic roughness. In contrast, strong dependence of friction coefficient on sliding speed is measured for X-750 and all other alloys slid against themselves. (Fig. 3.) In general, higher sliding speeds produced lower friction coefficients, consistent with a picture of softening of surface layers due to dynamic flash heating of surface asperities. A steady increase in friction is measured for the X-750 sliding in pure H_2, which may be due to a reduction or removal of passivating layers.

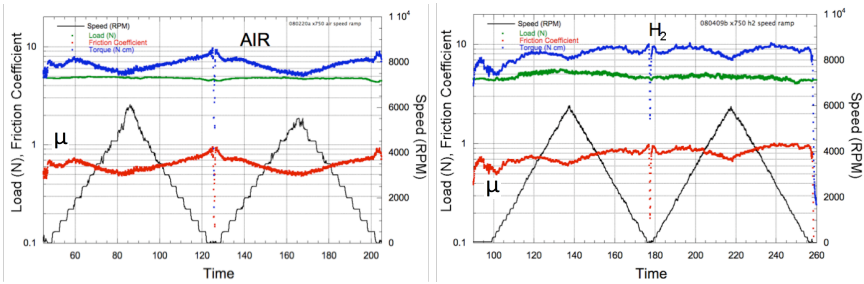


Figure 3: Graphs of friction coefficients as a function of sliding time for X-750 in air (L) and H_2 (R) for ramped sliding speeds.

Post-test examination (Fig. 4) shows wear and galling after metal/metal contact for all sliding atmospheres using optical microscopy (left) and optical interference profilometry

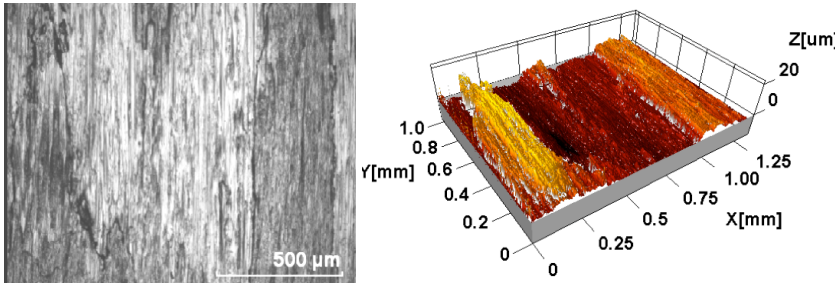


Figure 4: Optical image and pseudo color 3-D view of worn X-750.

Two MoS_2 coatings (approx 25 μm thick) were obtained from a commercial manufacturer; a rough and somewhat friable coating and one that was organically bonding. No dependence of friction on gas environment or load could be discerned for these coatings. Fig. 5 shows friction behavior for the coatings in H_2 for a test where the speed was ramped up and down twice.

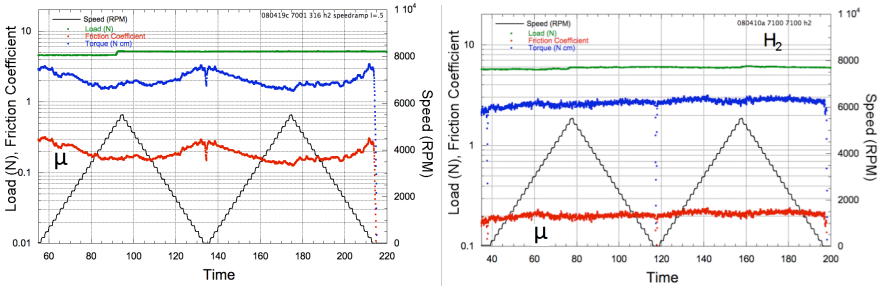


Figure 5: Friction coefficient as a function of time for the friable MoS_2 coating sliding against 316 (L) and bonded MoS_2 sliding against itself *(R).*

Friction coefficients are generally close to 0.2 although the more friable coating had lower friction at higher sliding speeds. The measured surface roughness of the worn MoS_2 and bonded MoS_2 surfaces was 0.3 µm and 0.5 µm Sa respectively. Wear debris powder was observed after these tests.

When the bonded coatings were slid against bare 316 stainless steel, material was transferred from the coated to the uncoated surface, producing a "transfer film" (Fig. 6 left). The actual sliding thus occurs between MoS2 surfaces and the friction coefficient (0.2) is essentially identical to the coated/coated sliding condition. The darkest thickest areas are about a micrometer thick as measured by optical interference profilometry.

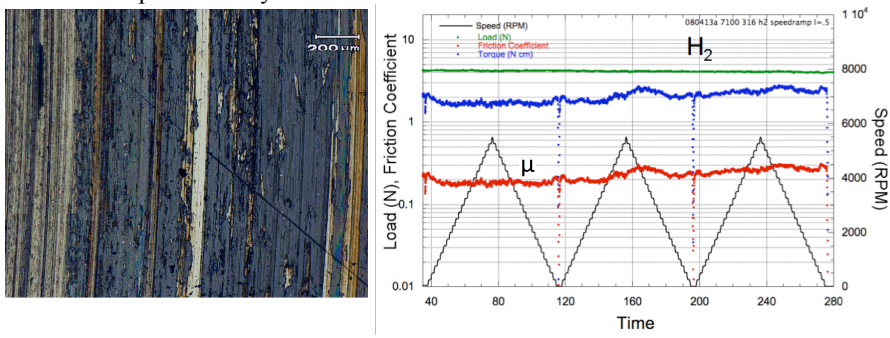


Figure 6: Optical micrograph of transfer film produced on 316 steel from MoS_2 bonded coating after 280s test cycle (L), friction coefficient as a function of time for sliding in H_2 (R)

The sliding behavior of 6061 Al was similar to that of Ti except that friction coefficients were large, and seizure occurred in dilute H_2. The roughness of the heavily deformed surface layers was 1.8 µm. Metal specimens exhibited the high wear rates typical of dry sliding with evidence of galling and material transfer between disk and flat.

The DLC coating exhibits low friction when slid against 316 stainless steel in H_2. (Figure 7).

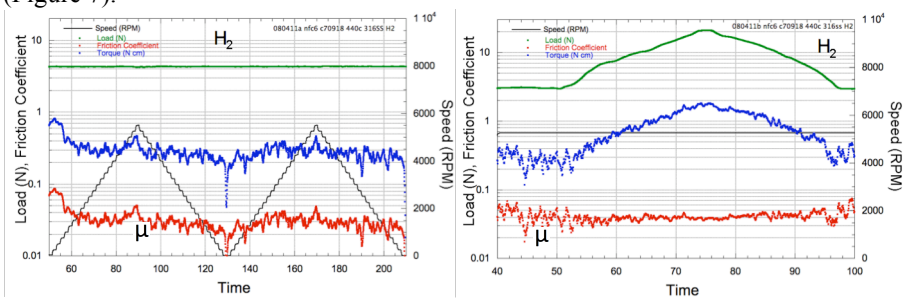


Figure 7: Graph of friction coefficient as a function of time for the DLC coating slid against bare 316 stainless steel over a range of speeds (L) and loads (R) in hydrogen.

In H_2, friction coefficients around 0.03-0.04 were measured, which seemed to decrease with continued sliding. In vacuum and pure N2 gas, the friction coefficients were almost as low, but in open air, friction coefficients were near 0.3 (not shown). To confirm that the higher friction was due to water vapor, tests were conducted in atmospheres of N_2 and H_2 that had been saturated with water vapor, and high friction was measured in each case (Figure 8), consistent with the observation that water can be strongly adsorbed to sliding surfaces, and amorphous carbon is not special in this regard.

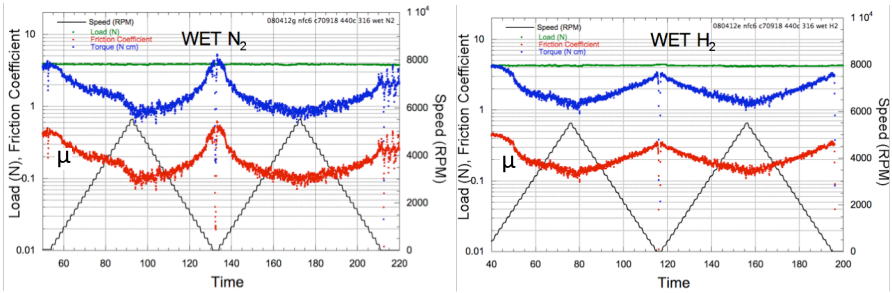


Figure 8: Graph of friction coefficient as a function of time for the DLC coating slid against bare 316 stainless in water saturated N_2 (L)and H_2 (R).

Friction of DLC sliding against 316 steel is shown in Figure 9, in which the presence of oxygen and/or water vapor degrades the frictional performance.

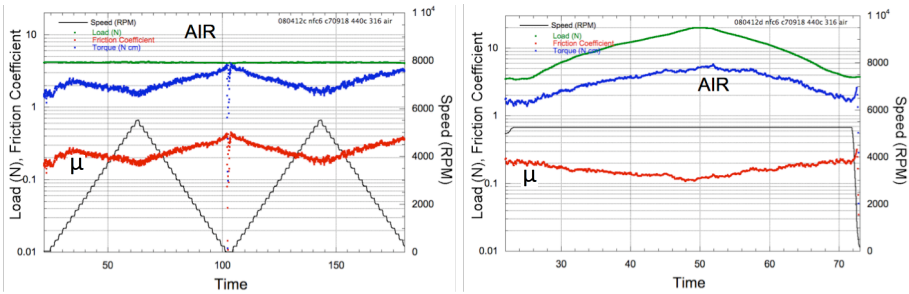


Figure 9: Graph of friction coefficient as a function of time for the DLC coating slid against bare 316 stainless steel over a range of speeds (L) and loads (R) in air.

The mechanism of DLC lubrication in H_2 is by transfer layer and subsequent sliding. As Figure 10 shows, the DLC transfer film gives a colored appearance (left), due to optical interference when on the order of a micrometer in thickness. The differences

in shading and color represent differing thicknesses. The wear track on the opposing flat (right) shows smoothing and burnishing of the uniformly-coated surface.

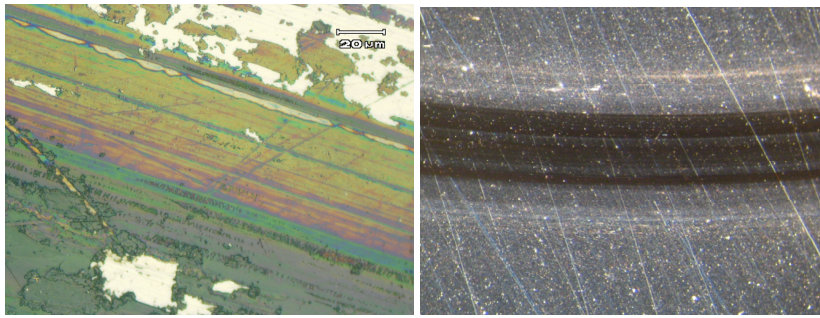


Figure 10: optical micrograph of DLC transfer layer on 316 steel (L), optical macrograph of burnished wear track area on coated flat (R).

Table I summarizes the friction coefficients obtained in the study. Where a range of friction coefficients is indicated, this reflects the variability of friction coefficient as a function of sliding speed or time.

Table 1: compilation of friction coefficients of sliding couples in indicated atmospheres for metal alloys, MoS_2 ,organically bonded MoS_2 and DLC coatings.

	Open Air	100% N_2	96%N_2/4%H_2	Vacuo	100% H_2
Ni X-750	0.5–0.9	0.5–0.9	0.6–1	0.5–0.9	0.6-0.9
Al 6061	-	1–1.5	0.5– 1	0.8–1.2	
Ti alloy	0.4	~0.5	~0.5	0.5–0.6	0.5-2
316 steel	0.4–0.9	0.6–1	0.6–1	0.5–0.8	0.6-0.9
MoS_2/ MoS_2	0.25–0.5	0.3–0.6	0.25	0.3	
MoS_2/316	0.1-0.2	0.1-0.2	-	0.1-0.3	0.1-0.2
MoS_2 OB	-	0.2–0.25	0.25	0.3	0.2
MoS_2 OB/316	0.2-0.3	0.2-0.3	-	0.3-0.5	0.2-0.3
DLC/316	0.2-0.4	0.03-0.05	-	0.03-0.05	0.03-0.04

CONCLUSIONS

For the sliding tests conducted, all metal/metal sliding contacts gave technologically unacceptably high friction and wear performance regardless of test environment. The removal of native oxides by pure H_2 combined with sliding generally produced higher friction coefficients. The friction coefficient of all the material pairs studied was largely independent of load for the load ranges used (2-20 N) but was often a strong function of sliding speed, usually smaller friction coefficient at higher sliding speeds consistent with thermal effects at high speeds. The smallest friction coefficients were obtained for the coated test samples. The diamondlike carbon gave lowest friction and wear in dry environments, but performance is degraded in any environment where substantial amounts of water vapor is present. The beneficial

effect of coatings can be realized with only one surface coated, and a beneficial transfer will form as needed on the counterface.

ACKNOWLEDGMENTS

The work was supported by the Department of Energy / Office of Energy Efficiency and Renewable Energy / Hydrogen, Fuel Cells and Infrastructure Program / Hydrogen Delivery, under Contract DE-AC02-06CH-11357

REFERENCES

1 Heshmat, H. Hryniewicz, P. Walton II, J. F., Willis, J. P. Jahanmir, S. and DellaCorte C. "Low-Fricton Wear-Resistant Coatings for High-Temperature Foil Bearings," Tribol. Intl., Vol. 38, 2005, pp. 1059-1075.

2 Sliney, H. E, DellaCorte, C., and Lukaszewics, V., "The Tribology of PS212 Coatings and PM212 Composites for the Lubrication of Titanium 6Al-4V Components of a Stirling Engine Space Power System," *Tribol. Trans*, Vol. 38, Iss. 3, 1995, pp. 497-506.

3 Savage, R. H., "Graphite Lubrication," J. Appl. Phys. Vol. 19, No. 1, 1948, pp. 1-10.

4 Gardos, M. N,, and Gabelich, S. A., "Atmospheric Effects of Friction, Friction Noise and Wear with Silicon and Diamond. Part II. SEM Tribometry of Silicon in Vacuum and Hydrogen," *Tribol. Lett*, Vol. 6, 1999. Pp. 87-102.

5 DellaCorte, C, and Steinetz, "Sliding Durability of Candidate Seal Fiber Materials in Hydrogen from 25 to 900°C" NASA 105939, March 1993.

6 Erdemir, A, Eryilmaz, O. L, and Fenske, G. R, "Synthesis of Diamondlike Carbon Films with Superlow Friction and Wear Properties," *J. Vac. Sci. Technol. A,* Vol.18, No. 4 (2000), pp. 1987-1992.

7 Andersson, J., Erck, R. A, and Erdemir, A., "Frictional Behavior of Diamondlike Carbon films in Vacuum and under Varying Water Vapor Pressure," *Surf.Coat.Technolog*., Vol. 163-164, 2003, pp. 535-540

Effects of Hydrogen on Materials
Proceedings of the 2008 International Hydrogen Conference
Brian Somerday, Petros Sofronis, Russell Jones, editors, p 413-420
Copyright © 2009 ASM International®
All rights reserved.
www.asminternational.org

Residual stress relaxation in shot-peened high strength low alloy steel and its implications for hydrogen assisted cracking

Alan Turnbull
National Physical Laboratory, Teddington, Middlesex, UK

ABSTRACT

The relaxation of compressive residual stress in shot-peened 300M high strength low alloy steel in response to applied loads has been investigated and the implication for resistance to hydrogen assisted cracking assessed by subsequent static load testing in 3.5% NaCl at stresses near the 0.2 % proof stress. Tests were conducted with notched cadmium or Al-based coated specimens at open circuit and with uncoated specimens at the most negative potential associated with these coatings. Despite significant residual stress relaxation from prior compressive loading none of the specimens showed evidence of hydrogen assisted cracking when tested at tensile stresses just below the 0.2% proof stress. This is reassuring from an engineering perspective but the performance under corrosion fatigue conditions remains to be established.

INTRODUCTION

Shot-peening, laser-peening and burnishing have been used extensively in a range of applications to introduce near surface compressive stress and minimise the risk of fatigue or environment induced cracking. On the whole this has been a successful strategy but it is not often appreciated that relaxation of this beneficial compressive residual stress may occur in response to service loading [1,2]. This is most likely where occasional high amplitude fluctuating loads are important and macroscopic or microscopic yielding ensues. Residual stress relaxation in response to mechanical loading is not a new phenomenon [3] but general awareness is often limited. As a consequence, there has been perhaps misplaced confidence in the effectiveness of induced surface compressive stresses, especially in relation to fatigue for which testing is most often based on constant amplitude loading [4]. For stress corrosion cracking and hydrogen assisted cracking, there are similar concerns about the long-term viability of residual compressive stress. A particular example is high strength low alloy (HSLA) steels for which the possibility of hydrogen assisted cracking must

be considered should a combination of coating damage, allowing hydrogen entry, and high service stress arise when the prior induced compressive stresses have been relaxed. In a previous study on a shot-peened HSLA steel, we mapped out the extent of residual stress relaxation in response to applied stress, both static and cyclic [5]. Here, we summarise the key findings from the shot-peening investigation but focus primarily on the potential consequence for hydrogen assisted cracking.

EXPERIMENTAL METHOD

The material tested was a 300M high strength low alloy steel supplied by the industry partner in heat-treated form (details are commercially restricted) with a nominal chemical composition in mass%: C: 0.38-0.46; Cr: 0.7-0.95; Mn: 0.6-0.9; Ni: 1.65-2.0; Si: 1.45-1.8; V: 0.05 min; P: 0.01 max; S: 0.01 max. Tensile testpieces with a 16 mm gauge length and diameter 8 mm were used with the specimens ground according to an industry in-house standard. The 0.2% proof stress ($\sigma_{0.2}$) in compression and tension were respectively about -1790 MPa and 1713 MPa and the proportional limit respectively about 1352 MPa (strain: 0.67%) and 1245 MPa (strain: 0.64%). After machining, a number of specimens were shot-peened according to the specification: MI 230H, 8 to 12 Almen A, and 100% coverage. The residual stress was then measured using X-ray diffraction (XRD), complemented by subsequent incremental hole-drilling [5]. The XRD measurements were made with a circular collimator of diameter 1 mm. The incremental hole drilling measurements were carried out according to the procedures outlined in NPL Good Practice Guide No 53 [6]. To assess the extent of relaxation of the residual stress in response to applied stress we undertook single-shot loading of varying magnitude (compression and tension) for one batch of specimens and determined the residual stress off-load. The effect of fatigue loading on stress relaxation is described elsewhere [5].

A separate batch of shot-peened specimens was used for the exposure tests with specimens uncoated, coated with cadmium or coated with a SermeTel® aluminium-based coating according to an in-house specification. The actual coating thickness was deduced from prior measurement of the specimen diameter and comparing that with the coated specimen. Prior to testing, a compressive load was applied to generate the required level of relaxation. A quality check was made to ensure that the relative extent of relaxation was the same as for the first batch of specimens.

In corrosion testing of coated specimens it is common to introduce local damage to the coating, usually by scribing. There is no standard for controlled scribing of coated stress corrosion specimens. Hence, the scribing was achieved using a lathe tool with a cutting tip having an angle of 60 ° as per the ASTM specification for scribing of coatings [7] and with tool tip radius of 115 µm or 65 µm. The intention was to create a controlled notch that had a depth within the surface compressive layer not greater than the peak in compressive stress (i.e. below or about 50 µm). The maximum depth was usually between 25 µm and 70 µm. The width of the notch at the mouth varied

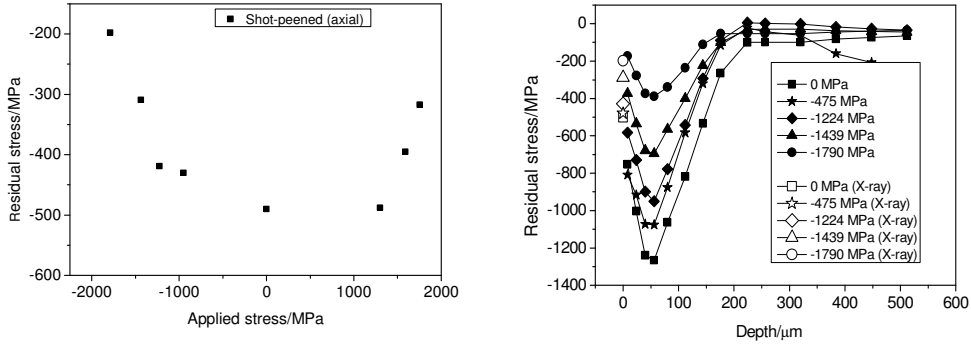
with the tool tip radius and depth but typically was of the order of 140 μm for the sharp notch and about 160 μm using the 115 μm tip tool.

The exposure tests were carried out with the cylindrical tensile specimen under constant load at 22±2 °C and contained in a polycarbonate test vessel through which 3.5% NaCl was circulated slowly from a 10 L reservoir. Tests were carried out with uncoated specimens at an applied potential associated with a particular coating or with the coated specimens at open circuit. In the absence of failure, specimens were broken open by fatigue loading after baking out any absorbed hydrogen in an oven at 100 °C for a minimum of 3 days. In one case, effort was made to mark the fracture surface by, for example, heat tinting at 600 °C for up to 2 hours to ensure clear identification of any stress corrosion crack should it exist.

RESULTS

Residual stress of shot-peened specimens

The variation of residual stress in response to an applied stress is shown for axial residual stress in Fig. 1a (XRD data). The depth variation of these stresses is shown in Fig. 1b. The hole-drilling technique becomes less reliable with increasing depth for small diameter specimens and this accounts for the apparent lack of balancing tensile stresses, which must exist, albeit small. The XRD measurements (which sample the first 10 μm from the surface) compare reasonably with the hole-drilling measurements at a depth of 8 μm, though the latter tended to suggest a smaller absolute value of the residual stress.



(a) (b)

Figure 1: Relaxation of axial residual stress in 300 M steel following single-shot loading as determined by (a) XRD and (b) hole-drilling.

A shot-peened steel will exhibit gradients of cold work, and hence deformation properties in the material, biaxial stress state, and a complex variation in stress, with

a peak in compressive stress below the surface that can be markedly greater than the near-surface residual stress. Superimposed on this will be the applied stress. Despite these complexities, relaxation tended to ensue when the combined compressive stresses at the surface (within 10 μm) exceeded the proportional limit of the unpeened steel. Although the combined compressive stress just below the surface shows a peak that would exceed the 0.2% proof stress before the proportional limit was achieved at the surface, the relaxation was not significant, perhaps reflecting elastic constraint of the adjacent material at lower combined stress levels. In relation to applied tensile stress, relaxation did not occur until the applied tensile stress was significantly above the proportional limit for the unpeened specimen. This could be explained by the relaxation being constrained by the adjacent near-surface region, which under load would be in net tension but at relative low stress levels well below the proportional limit.

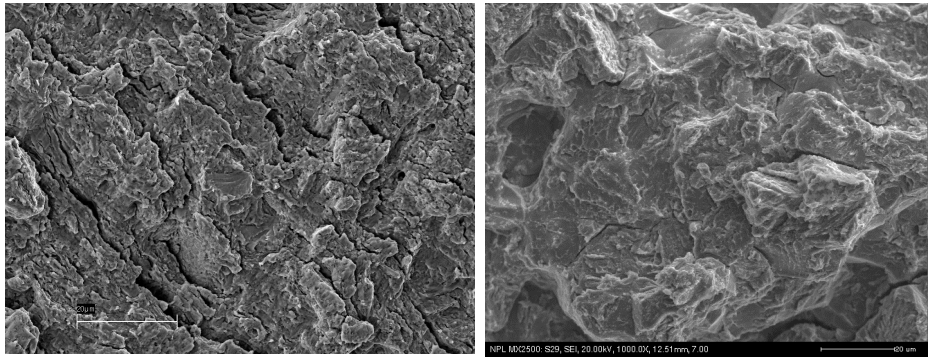
Exposure tests

Coated specimens

A cadmium-coated specimen was evaluated initially with the specimen subjected to a prior applied stress of - 1440 MPa to induce residual stress relaxation. The specimen was notched to a maximum depth of 20 μm using the tool with tip radius 115 μm (this tool was used initially before it became apparent that failure did not occur so readily). The applied tensile stress was 1440 MPa (84% of tensile $\sigma_{0.2}$) with the net stress near-surface estimated to be 1031 MPa and about 705 MPa at 50 μm depth. The corrosion potential was in the range -0.78 V SCE to –0.82 V SCE for a short period after immersion but then drifted more positive with time, attaining a value of –0.65 V SCE at test completion, 20 days. No failure was observed. The specimen was removed, washed and then held in an oven for several days at 100 °C to remove hydrogen before being fatigue-loaded to failure and the fracture surface examined by scanning electron microscopy (SEM). There was no evidence of any stress corrosion crack precursors, the fracture surface being representative of fatigue cracking in air.

These conditions were clearly not severe enough to induce stress corrosion cracking and thus there was a focus for subsequent testing on the Al-based coating, because of the more negative potential and the greater amount of hydrogen uptake expected. The first test was conducted with a scribe made by the 115 μm radius tool with maximum depth of 26 μm. Prior to scribing, residual stress relaxation was induced by an applied stress of –1440 MPa. The scribed specimen was then stressed to +1440 MPa in the 3.5% NaCl solution at open circuit. Upon immersion, the corrosion potential was –0.74 V SCE and then drifted more negative in a couple of days to –0.94 V SCE before attaining –0.9 V SCE by the end of the test; the exposure time was 13 days in this case. No failure occurred. The specimen was removed, hydrogen baked out as before, and the specimen was then fractured by fatigue. No evidence of stress corrosion cracking was apparent.

The subsequent test on the Al-based coating was made more severe by adopting a higher prior applied compressive stress of –1790 MPa (0.2 % compressive proof stress), scribing with the sharp 65 μm tool to a maximum depth of 72 μm and then applying a stress of 1530 MPa (about 89% of tensile $\sigma_{0.2}$) in the test solution. The net section stress in the near-surface region should then be about 1332 MPa and at 50 μm depth about 1142 MPa. The specimen was exposed for 14 days but without failing. The specimen was removed, treated as before, and then fatigued to failure. Given the severity of the test conditions and the expectation of hydrogen assisted cracking the fracture surface was examined in detail. However, FEG-SEM evaluation at different locations showed a fracture surface that was better explained by the fatigue cracking applied after exposure and baking out of hydrogen (Fig. 2a). For comparison, the fracture surface of the 300M steel that failed from hydrogen assisted cracking at high charging current densities is shown in Fig. 2b. It would be deduced that there appears no observable environment induced cracking mode and that the facture surface is essentially associated with the subsequent fatigue loading in air.



(a) (b)

Figure 2. Detail of fracture surface of notched 300M steel (a) with Al-based coating exposed to 3.5% NaCl and fatigued to failure in air after desorption of mobile hydrogen (b) uncoated and exposed to 3.5% NaCl at high cathodic charging current density. The micron markers are 20 μm.

Uncoated specimens

With no failure of the coated specimens it was prudent to test an uncoated specimen to encourage more general hydrogen uptake in the steel, as delocalisation could dilute the concentration at the notch [8], and to remove the uncertainty with regard to the effect of a larger area of coating damage. Again, a stress of –1790 MPa was applied to a shot-peened specimen prior to the exposure test to induce maximum stress relaxation. The specimen was then scribed with the 65 μm radius tool tip to a depth ranging round the circumference of 27 μm - 48 μm, to simulate the condition for the

Al-base coating test (albeit somewhat less deep at the maximum depth). The exposure test was conducted at –0.94 V SCE (the most negative potential for the Al-base coating) with an initial applied stress of 1530 MPa (about 89% of tensile $\sigma_{0.2}$). The net section stress in the near-surface region should then be about 1332 MPa and at 50 μm depth about 1142 MPa. The specimen was tested for 25 d. At that time, with no observable failure, the applied stress was increased to 1627 MPa (about 95% of tensile $\sigma_{0.2}$). No failure was observed after a further 4 days exposure and the test was terminated. The specimen was then treated as before to remove residual mobile hydrogen and then fatigued to failure at 5 Hz with a stress range of 800 MPa and stress ratio 0.2. The fracture surface close to the notch root (Fig. 5) was again more commensurate with fatigue following exposure than with hydrogen assisted cracking. There was some evidence of porosity in this specimen.

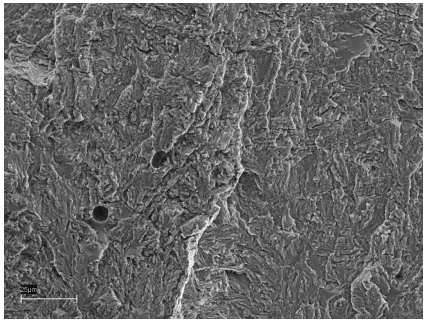


Figure 3: Fracture surface of an uncoated, notched 300M steel specimen exposed to 3.5% NaCl at –0.94 V SCE and then fatigued in air after desorption of mobile hydrogen. The micron marker is 25 μm.

DISCUSSION

The results suggest that stress relaxation will occur in service to some degree depending on the specific loading history. There is confidence in that statement in view of the range of measurements made (and in separate work on laser-peened specimens) and the repeatability of those measurements on different batches. However, uncertain knowledge about the detailed loading in service precludes a predictive capability with respect to establishing inspection intervals. Nevertheless, measurement of remanent residual stress at regular intervals should be considered.

In assessing the stress corrosion cracking likelihood in relation to residual stress relaxation definite statements are more challenging because of the complex dependence of cracking on the loading rate and the nature of coating and surface damage that might act as precursors to cracking. Also, mechanical notching inherently introduces uncertainty with respect to its effect on the local residual stress and deformation state. There is a concern too about the short-term nature of laboratory testing and whether this might lead to non-conservative conclusions.

Nevertheless, the results herein do suggest that hydrogen assisted cracking of shot-peened specimens does not occur readily despite significant relaxation of residual stress following applied compressive stress at the 0.2% proof stress. Whilst further relaxation could occur with a few more cycles of very high stress amplitude [5], this would seem an unlikely service scenario.

Does this mean that no hydrogen assisted cracking of the shot-peened steel can ensue? Clearly a deeper notch (at a depth greater than the peak in Fig. 1b) would lead to a greater stress concentration with reduced compressive stress to offset the applied stress, and failure would be more likely. Tests with deep notches are often used to promote the effectiveness of laser peening or burnishing (which induces compressive stresses to depths up to 1 mm) where stress corrosion testing with notch depths of 0.5 mm inevitably ensures that shot-peening appears inadequate [9]. A more important issue is whether the present tests are sufficiently conservative that we have confidence that relaxation can be tolerated for shallow defects.

Test duration could be an issue if it is argued that the absorbed hydrogen has to get to the region of maximum tensile stress at sufficient concentration (depths greater than 200 μm). The effective diffusivity of hydrogen in high strength steels depends on the detailed microstructure and charging conditions. Our own measurements on AISI 4340 steel at about –1.0 V SCE [10] and those of Carr and Robinson [11] suggest a value of about 2×10^{-7} cm^2s^{-1}. A value of 1×10^{-8} cm^2s^{-1} to account for additional trapping in the cold worked layer of 300M steel would seem a reasonable approximate basis for estimating the extent of hydrogen entry, though that needs to be substantiated. On that basis, near steady-state hydrogen charging at 200 μm below the surface (hence tensile region) is predicted within a test exposure time of 14 days yet no cracking ensued with uncoated specimens at –0.94 V SCE. An absence of combined strain and hydrogen localisation would seem the pertinent explanation.

These results are re-assuring from an engineering perspective in suggesting that the significance of stress relaxation for stress corrosion cracking/hydrogen assisted cracking is not as severe as first envisaged in initiating this study. However, we have not as yet tested under slow strain rate and corrosion fatigue conditions and it is possible for these case that stress relaxation would increase the risk of failure, as noted elsewhere in full-scale fatigue testing of landing gear in air [12].

CONCLUSIONS

Compressive or tensile stress applied to shot-peened 300M steel leads to relaxation of the induced compressive residual stress with the relaxation being most significant for applied compressive stress.

Using notched shot-peened specimens with prior applied compressive stresses to induce very marked relaxation of the residual compressive stress, constant load tests

in 3.5% NaCl at controlled potential or on sacrificial coated specimens indicated no evidence of hydrogen assisted cracking despite applied tensile stresses at 95% of $\sigma_{0.2}$.

The results are re-assuring for the industry but further studies under slow strain rate and corrosion fatigue conditions are required.

ACKNOWLEDGEMENTS

This work was supported by the Performance of Materials Programme of the United Kingdom Department of Trade and Industry, Airbus, the Civil Aviation Authority UK, Messier-Dowty, and Metal Improvement Company Incorporated. The constructive comments from experts in these organisations are gratefully acknowledged. Dr Shengqi Zhou conducted most of the exposure tests.

REFERENCES

1. Lohe, D. and Vohringer, O., 'Stability of Residual Stresses', in Handbook of residual stress and deformation of steel, G.Totten, M. Howes, T. Inoue (eds.) (ASM, Ohio, 2002) pp. 54-69.
2. Turnbull, A., Integrity of shot-peened high strength steel components in the context of residual stress relaxation and hydrogen uptake, NPL Report DEPC MPE 022, 2005.
3. Mordfin, L., Editor, Mechanical Relaxation of Residual Stresses, ASTM STP 993 (PA, 1988).
4. Hatamleh, O., et al., Int. J. Fatigue, Vol. 29 (2007) pp.421-434.
5. Turnbull, A, J J Pitts and J D Lord, Residual stress relaxation in shot-peened high strength low alloy steel, Mater. Sci. Tech., Vol. 24 (2008) pp. 327-334.
6. Grant, P. V., Lord, J. D., P. S. Whitehead 'The Measurement of Residual Stresses by the Incremental Hole Drilling Technique.' NPL Measurement Good Practice Guide No. 53 – Issue 2, Jan 2006.
7. ASTM D1654-05, Evaluation of painted or coated specimens subjected to corrosive environment (ASTM International, 2005).
8. Turnbull, A. and Miller, G.F. Corrosion Science, Vol. 30 (1990) pp. 293-298.
9. Prevey, P.S., et al, "Mitigation of SCC and corrosion fatigue failures in 300M landing gear steel using mechanical suppression", Proc. 6th Aircraft Corrosion Workshop, August 24-27, 2004, Solomon Island, MD.
10. Turnbull, A., "Testing and modelling for prediction of hydrogen embrittlement", *Proc. of Ageing Studies and Lifetime Extension of Materials*, Oxford, July, 1999, ed. L/G. Malinson, Kluwer Academic Press, 2001.
11. Carr, M.J. and Robinson, M.J., Trans. IMF, Vol. 73 (1995) pp. 58-64.
12. Tuegel, E.J. and Brooks, C.L., Int. J. Fatigue, 19 (1997) S245-S251

Effects of Hydrogen on Materials
Proceedings of the 2008 International Hydrogen Conference
Brian Somerday, Petros Sofronis, Russell Jones, editors, p 421-428
Copyright © 2009 ASM International®
All rights reserved.
www.asminternational.org

DETERMINATION OF STAINLESS STEELS MECHANICAL PROPERTIES IN HIGH-PRESSURE HYDROGEN

A.I.Balitskii, V.I.Vitvitskii

Department of Hydrogen Resistance of Materials Karpenko Physico-Mechanical Institute National Academy of Sciences of Ukraine, Lviv, Ukraine

ABSTRACT

The influence of high-pressure hydrogen at room temperature on the static and fatigue properties of corrosion-resistant materials based on iron and nickel is compared for different types of loads. The sequence of characteristics can be arranged in the order of increase in the influence of hydrogen as follows: fatigue limit, ultimate strength of notched specimens, relative elongation of smooth specimens, fracture pressure for a membrane under biaxial tension, percentage reduction of the area of smooth specimens, percentage reduction of the area of specimens with concentrators, and low-cycle durability. The micromechanism of hydrogen fracture is characterized by the presence of a great number of microstructural fracture sites (bulk damage) and the completeness of local plastic relaxation.

INTRODUCTION

Modern energy units construction elements have exploited in the contact with gaseous hydrogen. Note that on the forcible power plant (FPP) and nuclear power plant (NPP) there exist the hydrogen-produced apparatus (electrolyzers, freezers, separators, condensate accumulators, etc.), wide branched and long system of hydrogen pipeline, pumps, system of cleaning and drying of hydrogen. So, we can say that the problem of workability assessment of structural steels in gaseous hydrogen environments is actual for modern power engineering [1–3]. The interaction of hydrogen with structural materials is characterized by the presence of temperature extrema of embrittlement.

Specimens made of alloys based on iron, nickel, and titanium (for comparison) operate under different temperature and force conditions in structural elements of

hydrogen, fossil, nuclear power-generating equipment. As a common feature of their operation, one can mention loading at near room temperatures under high pressures of the hydrogen containing environment. The correct choice of materials must be based on the data on their hydrogen resistance obtained under comparable conditions of adequate experiments. At present, we do not have any generally accepted criterion of hydrogen resistance, the reliable relationships between the properties under loads of different types are absent, and the comparative data [4–6] are quite poor.

MATERIALS AND EXPERIMENTAL PROCEDURE

The aim of the present work is to determine the experimental conditions responsible for the maximum hydrogen degradation, perform the assessment of defects and fracture, and improve the hydrogen resistance of materials with different bases. As a result, hydrogen resistance was compared for different types of loading, the conditions of maximum influence of hydrogen were determined, the materials based on Fe, Ni, and Ti were arranged in the order of decrease in hydrogen resistance, the distinctive features of damage and fracture were determined, and some measures aimed at increasing the hydrogen resistance of materials were proposed.

The results of investigations under loads of different types comparing the coefficients of the maximum influence of hydrogen [5, 6] β_H equal to the ratios of the coefficients obtained under a pressure of hydrogen of 35 MPa and in air on special design equipments in the Department of Hydrogen Resistance of Materials Karpenko Physico-Mechanical Institute National Academy of Sciences of Ukraine. Thus the characteristics of the investigated materials under different types of loading according to their sensitivity to high-pressure hydrogen were compared by were ordered (Fig.1). The tests were performed at strain rates guaranteeing the maximum influence of the medium for each loading mode. The sequence of properties arranged in the order of increase in the influence of the medium has the form: the fatigue limit (specimens with Ø5 mm for a rotational speed of 3000 rpm on a base of $5 \cdot 10^6$ cycles), the ultimate strength of specimens containing circular notches (the diameter of the specimen under a circular concentrator is equal to 5 mm and the radius of the notch to 0.1 mm), the relative elongation of smooth specimens (Ø 5 mm), the fracture pressure under biaxial tension, the percentage reduction of the area of specimens with concentrators, and low-cycle durability (sign-preserving bending with a frequency of 0.5 Hz for smooth specimens 2–3 mm in thickness).

RESULTS AND DISCUSSION

Role of the Loading Mode

The indicated sequence of characteristics can change depending on the material of the base and the mechanism of hardening. Thus, for Fe-Ni and Ni alloys (Fig.1; alloys *b* and *c*, segments 3 and 5) hardened with disperse coherent intermetallic compounds, the relative elongation is more sensitive to hydrogen than the percentage

reduction of the area [as in the case of steels (Fig. 1; alloy *a*, segments 3 and 5)] but the highest sensitivity is observed for low-cycle durability.

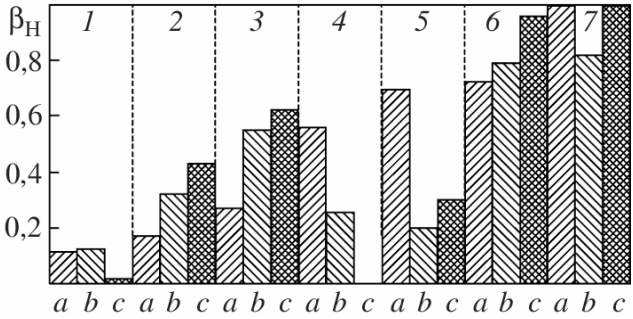


Figure1: The coefficients of the influence of hydrogen β_H on the following characteristics of 03Kh12N10MT (a), KhN55MBYu (b), and KhN65MTYu (c) steels: 1 – low-cycle fatigue durability under pulsating pure bending, ε = 1.6%; p_H = 35 MPa; 293 K; frequency of cycles – 0.5 Hz; 2 – percent reduction in area of the specimen with a circumferential notch (notch diameter, d_n = 5 mm; notch radius, r_n = 0.1 mm; p_H = 35 MPa; deformation rate v = 0.1 mm/min); 3 – the same for smooth specimens (d =5mm; v = 0.1 mm/min); 4 – failure pressure under biaxial tension of a membrane; 5 – percent elongation of smooth specimens (d = 5 mm; v = 0.1 mm/min); 6 – ultimate strength of notched specimens (d_n = 5 mm; r_n = 0.1 mm; p_H = 35 MPa; v = 0.1 mm/min); 7 – endurance limit, p_H = 35 MPa; 293 K; 50 Hz; d = 5 mm).

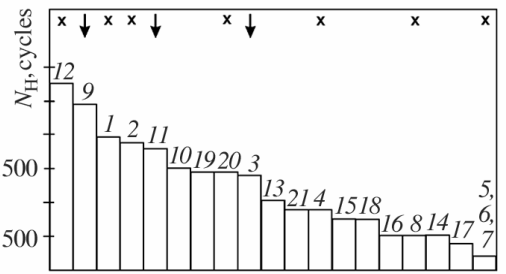


Figure 2: Descending ordering of Fe, Ni and Ti-based materials low-cycle durability in hydrogen at p_H = 35 MPa; ε = 1.6%; 0.5 Hz; 293 K. Specimens of thickness 2…3 mm. ↓ – durability decreases after preliminary hydrogenation (773 K, 2 h, 35 MPa); x – does not decrease. Numbers at columns correspond to the numbers of materials in Table 1.

Low-Cycle Hydrogen Resistance of Steels and Alloys

The resistance to the action of high-pressure hydrogen ($p_H = 35\,MPa$) under low-cycle loading at 293 K was compared for corrosion-resistant steels, iron-nickel alloys, α-, and $\alpha+\beta$-titanium alloys, and high nickel alloys (Table 1). The tests were performed in an IP-2VTD installation (equipment for low sycle fatigue tests with plane bending) [6] by the method described in [5]. The thickness of smooth specimens varied from 2 to 3 mm. The amplitude of relative strains in the outer fibers was equal to 1.6%.

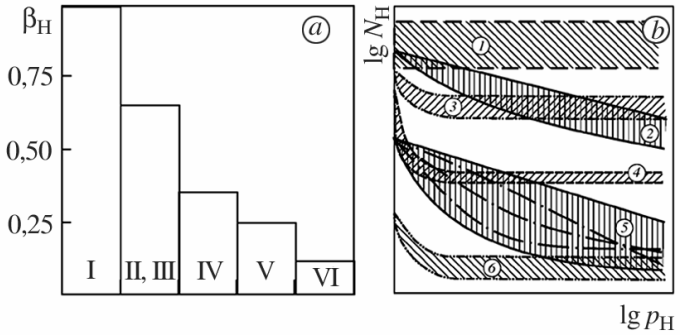


Figure 3: Effect of phase composition on coefficient, β_H, (a) and typical dependences of low-cycle durability of alloys on hydrogen pressure (b): I – homogeneous refined Fe- and Fe–Ni-based austenite – 12, 1; II – Fe–Ni-base, γ + IM – 9, 11, 10, 13; III – Fe base, γ + N in solution – 2, 3; IV – Fe base, γ + M def. – 4; V – Ni base + IM + K – 15, 18, 16, 14, 17; VI – Fe base, maraging steel M + IM + K, ferrite – 5, 6, 7. Numbers correspond to materials in Table 1.

Table 1: Investigated Materials

No.	Chemical composition, thermal treatment (TT), structure, $\sigma_{0.2}$, Mpa
	Steels
1.	00Kh20N23V2T, H, γ, 220
2.	06Kh14G20AN10M, H, γ, 510; nitrogen content = 0.34%
3.	06Kh13G20AN5, H, γ, 420; nitrogen content = 0.15%
4.	08Kh18N10T, H, γ + M, straining, 320
5.	08Kh17T, H, ferrite, 360
6.	02Kh11N11TM, st. TT, M + IM, 930
7.	20Kh14N3M2V, st. TT, M + IM + carbides, 790
8.	03Kh11N8K4M2FVD, st. TT, γ + M + IM, 1070
	Iron-Nickel Alloys
9.	04Kh11N21T2Ryu, st. TT, γ + IM, 890
10.	04Kh12N36T3Yu, st. TT, γ + IM, 820
11.	04Kh11N43M2T, st. γ + IM, 820
12.	04Kh11N43M2T, stepwise H with elevation of temperature, γ +IM min, 820
13.	04Kh11N43M2T, st. TT + aging, γ + IM, 770
	Medium and High Alloys Based on Ni
14.	Kh19N55MBYu, st. TT, γ + IM, 700
15.	Kh19N55MBYu, st. TT+ stepwise H with elevation of temp., γ + IM min, 370
16.	Kh19N55MBYu, st. TT + aging, γ + IM, 660
17.	Kh15N60K8M7YuTZV, st. TT, γ + IM + C, 800
18.	Kh20N60M9V5Yu2, st. TT, γ + IM + C, 900

	Alloys Based on Ti
19.	VT5-1kt (Ti-Al-Sn), powder [gas isostatic pressing (GIP)], α -phase, 700
20.	VT6-S (Ti-Al-V), powder (GIP), $\alpha+\beta$ - phase, 850
21.	VT6-S (Ti-Al-V), deformed, $\alpha+\beta$ -phase, 850

Comments: H – hardening, γ - austenite, M – martensite, IM – intermetallic compounds, st. TT – standard thermal treatment (H + aging), C – carbides.

The highest hydrogen resistance (*Figures 2 and 3a*) is observed for hardened austenitic materials, namely, for the refined steel 1 and Fe-Ni medium alloy 12 (the numbers of the materials correspond to their numbers in *Table 1*). After the dissolution of the excess phases, these materials exhibit the highest possible (for their properties (durability in hydrogen (1800 and 2700 cycles to failure, respectively) equal to their durability in air (*Figure 3*). The hydrogen resistance of the medium iron-nickel *alloys 11, 9, and 10* in the aged state is proportional to the content of titanium and the Ti/Al ratio [7] specifying the composition and stoichiometry of hardening precipitates [8, 9]. In the analyzed case, these factors serve as indicators of the microstructural concentration of strains at the active centers of preferable hydrogen adsorption and defects of the metal. The procedure of over aging decreases the durability of *alloy 13*.

The durability's of the homogeneous steels 2 and 3 alloyed with dissolved nitrogen are close to the durability of *steel 1*. Their serviceability increases with the content of dissolved nitrogen, which means that these materials can be regarded as promising for increasing the hydrogen resistance of structures. The VN6-C alloy was tested in the powder (20) and deformed (21) states. It is known [10] that the oxide films on Ti alloys serve as a barrier for hydrogen absorption and play the role of the main cause of the compatibility of these alloys with numerous oxygen-containing media. However, an abrupt worsening of the mechanical properties of the powder α - alloys at temperatures of about 373 K should be regarded as an argument against their application in hydrogen [8].Hydrogen much more intensely embrittles steels from the transition class and with unstable austenite (4 and 8). This means that the stability of austenite should be regarded as one of the major factors responsible for the hydrogen resistance of steels.

The *high nickel alloys 18 and 19* characterized by variations in the grain size and inhomogeneous distributions of precipitates have the lowest parameters in hydrogen as well as the Kh19N55MBYu low nickel *alloy 14* after hardening and aging. The maraging and ferritic steels (*5, 6 and 7, Table 1*) suffer catastrophic degradation in hydrogen.

Distinctive Features of Defects and Fracture in Hydrogen

For the most promising fcc materials, the micromechanisms of low-cycle fracture in hydrogen and in air are quite different. Under loading in inert media, the cracks are initiated as a result of either separation in a shear band or cleavage of large inclusions. In the zone of growth of a fatigue crack, the micropattern of the fracture

surfaces is striated. The step and direction of fatigue stripe with bends change in passing through the grain boundaries and annealing twins. The process is described by the mechanism of alternative shear proposed by Neumann [11] according to which, in metals with fcc lattices, the fatigue crack propagates in a slip plane adjacent to the crack tip in one cycle, in slip plane crossing the previous plane in the next cycle, and so on. Therefore, the striated topography sensitive to the singularities of slipping in fcc crystals (varying from one grain to another and in passing through the boundary of the twins) is predominant in the fracture surfaces. In the zone of initiation of a hydrogen crack, we often encountered intragranular cleavages, crystallographic cleavage facets, and the regions of intergranular fracture. The hydrogen crack propagates along the grain boundaries. In hydrogen, fracture is mist often initiated in the vicinity of agglomerates of large grain boundary $M_{23}C_6$ and M_6C carbides, where the relaxation of stresses by slipping is impossible.

Fracture according to the mechanism of quasicleavage occurs as a result of merging of numerous local cracks (located, as a rule, in different cleavage planes of separate grains) into a single crack [12,13]. As a result of plastic deformation and breaks of bridges between the cracks, we observe the formation of microscopic elements of the surface topography in the form of ridges, steps, etc. The presence of a disperse chaotic structure formed by the substructure, phase boundaries, etc. is a typical feature of quasicleavage. At the same time, the presence of smooth regions in the fracture surface is associated with intense shear strains typical of ductile fracture. In general, quasicleavage is regarded as a result of plastic strains localized and exhausted in thin interlayers and leading to microfracture [12-16]. This is also confirmed by the formation of a cellular pattern on the surface of hydrogen fracture in age-hardening alloys. The process of fine-pit fracture accompanied by the formation of pits on dispersed intermetallic compounds (ductile micromechanism) is caused by a flow localized in boundary microvolumes of insignificant thickness [13-16].

Thus, the fracture processes running in hydrogen are characterized by the possibility of existence of numerous simultaneously realized sources of initiation (active centers of concentration of hydrogen). Indeed, a metal which fails in air is weakened, as a rule, by an isolated defect. In Hydrogen, it is crossed by a system of dispersed microcracks. The fractographic data agree with the results of nondestructive testing. The investigations of the electric conductivity of the surfaces of specimens of 12Kh18N10T steel under low-cycle loading confirm the existence of a qualitative difference between the accumulation of fatigue defects in hydrogen (preliminary electrolytic hydrogenation) and in air. The macroscopic localization of defects in hydrogen occurs earlier and is accompanied by the formation of several cracks. The changes in the electric conductivity and magnetic permeability of the metal reveal a much higher degree of damage (*Figure 4*). Moreover, the process running in hydrogen is more intense both prior to and after the initiation of the main crack in volumes participating and not participating in the development of the macrodefect.

The integranular microscopic fracture surfaces in hydrogen are most often formed by the elements of ductile fracture. A similar situation is also observed in titanium

alloys, where the microscopic surface topography under the conditions of integranular static fracture in high-pressure hydrogen is formed by small ductile cups [8].

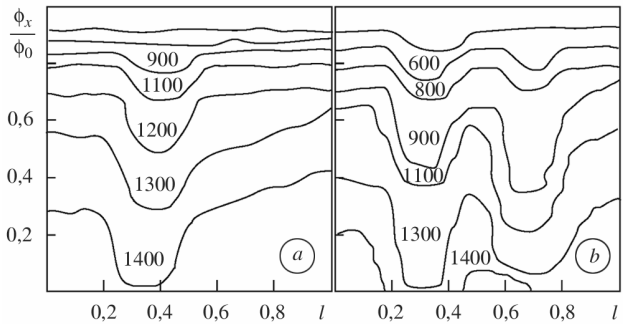


Figure 4: Relative variation of the electric conductivity gauge signal φ_x/φ_0 (φ_0 – initial value) along the 12Kh18N10T steel specimen length, l, under low-cycle loading (LCL) in air at ε = 1.37%.; a – without preliminary hydrogenation; b – hydrogenation before LCL (2 h, 1N H_2SO_4 + 5 mg/l As_2O_3 solution, cathodic polarization current 100 A/m^2, anode – platinum). Numbers indicate the number of cycles [13].

The specific features of the micromechanism affect the dependences of low-cycle hydrogen resistance on pressure (*see Figure 3*). For steels whose phase compositions are much more homogeneous than the phase compositions of age-hardening steels, the plots of the dependence of the fatigue life on the pressure of hydrogen decrease especially rapidly for pressures ≤ 6 MPa (*Figure 3, curves 3, 4, and 6*). For the minimum structural inhomogeneity (refined stable austenitic steel or hardened Fe-Ni alloys) in the state of substitutional solid solution, the γ-materials are absolutely insensitive to the medium (*Figure 3, curve 1*).

CONCLUSIONS

As a distinctive feature of the micromechanism of low-cycle fracture of austenitic steels and alloys in hydrogen, one can mention a great number of defects whose role is played by microstructural concentrators and the zones of localized plastic strains. Specifically, the hydrogen resistance of homogeneous austenitic steels increases with the stability of austenite and the amount of dissolved nitrogen as well as a result of hardening with overheating and preliminary compression (with an optimum level attained at about 20%). At the same time, the hydrogen resistance of high nickel alloys increases as a result of the dispersion of intermetallic compounds caused by the changes in the temperature of aging.

REFERENCES

1. Balits'kyi O.I. "Two Methods of investigation of the influence of hydrogen on the propagation rate of a crack and behavior o fracture of high-strength steels", *Materials Science*, vol.34, No. 4 (1998), pp. 574- 583.

2. Balits'kyi O.I., Modern Materials for Powerful Turbogenerators , National Academy of Sciences of Ukraine. Karpenko Physico-Mechanical Institute (Lviv, 1999), 284p. Library of Congress Catalog Control Card Number: 00 693623.
3. Balitskii A.I., Panasyuk V.V. "Workability Assessment of Structural Steels of Power Plant Units in Hydrogen Environments", *Problems of Strength* (2008), in press.
4. Vytvyts'kyi V.I., Tkachov V.I., and Grebenyuk S.O. "High-Cycle Fatigue of Steels in High-Pressure Hydrogen",*Fiz.-Khim. Mekh. Mater*., vol.34, No.1(1998), pp.111-112.
5. Tkachov V.I., Ivas'kevych L.M., and Vinvits'kyi V.I. "Methodical Aspects of the Evaluation of Hydrogen Resistance of Steels", *Fiz.-Khim. Mekh. Mater.,* vol.38, No. 4 (2002), pp.17-25.
6. Tkachov V.I., Kholodnyi V.I., and Levina I.N. Serviceability of Steels and Alloys in Hydrogen, Vertikal (Lvov, 1999), 256 p.
7. Vitvits'kyi V.I. "Low-Cycle Fatigue Life of Steels in High-Pressure Hydrogen", *Fiz.-Khim. Mekh. Mater*., vol.40, No. 1(2004), p.55-59.
8. Vinvits'kyi V.I., Tkachov V.I., Grebenyuk S.O., and Ivas'kevych L.M. "Mechanical Properties of Powder Titanium alloys in Hydrogen", *Fiz.-Khim. Mekh. Mater.,* vol.39, No. 3(2003), pp.117-119.
9. Pickering F.B. Physical Metallurgy and the Design of Steels, Metallurgia (Moscow, 1986).
10. Briant C.L. and Banerji S.K. (editors), Embrittlement of Engineering Alloys, Metallurgia (Moscow, 1988).
11. Broek D., Elementary Engineering Fracture Mechanics, Vysshaya Shkola (Moscow, 1980).
12. Smirnova A.V., Kokorin G.A., Polonskaya S.M., Electron Microscopy in the Science of Metals. A Handbook, Metallurgiya (Moscow, 1985).
13. Pilyushenko V.P., Vinokur B.B., Kondratyuk S.K., A Handbook of the Practical Science of Metals, Tekhnika (Kiev, 1984).
14. Pokhmurskii V. I. and Balitskii A. I. "Hydrogen Influence upon Cracking Resistance and Fracture Character of Austenitic Non-Magnetic Steel, *Hydrogen Effects on Material Behaviour: Proc. 4th Int. Conf.*, Edited by Neville R. Moody and Anthony W.Thompson, The Mineral, Metals, Materials Soc.(Warrendale, Pa: 1990), pp. 985–990.
15. Balitskii A.I., Pokhmurskii V.I., Fedorov V.V. and Voloshyn L.I. "Hydrogen Effects on the Physico-Mechanical Properties of Protective Coatings and Oxygen Films on Austenitic Steels", *Abstracts of Fifth International Conference on "Hydrogen Effect of Material Behaviour",* Jackson Lake Lodge, WY, Sept.11-15, 1994, p.14.
16. Balitskii A.I., Pokhmurskii V.I, Krokhmalny O.O. "Evaluating of Electrolytic Hydrogenation Influence on Fatigue Crack Growth Resistance of High-Strength Steels", *Abstracts of International Conference on Hydrogen Effects on Material Behaviour and Corrosion Deformation Interactions (H-CDI)* , Jackson Lake Lodge, Moran, WY, 2002, pp.65-66.

Effects of Hydrogen on Materials
Proceedings of the 2008 International Hydrogen Conference
Brian Somerday, Petros Sofronis, Russell Jones, editors, p 429-437
Copyright © 2009 ASM International®
All rights reserved.
www.asminternational.org

QUANTITATIVE ANALYSIS OF HYDROGEN ISOTOPES IN THE NEAR SURFACE REGION OF SOLIDS

Patrick Trocellier
CEA – DEN/DANS/DMN, Service de Recherche de Métallurgie Physique, Centre de Saclay, 91191 Gif sur Yvette, France

ABSTRACT

Hydrogen is not the most difficult element to analyse in the near surface region of solids besides its mobility. A lot of physico-chemical methods allow hydrogen to be determine in a quantitative way. This review first summarizes the characterization tools available for hydrogen analysis. In a second section, few applications examples will be given. In the last section, we will focus our attention on ion beam induced analytical methods which allow the quantitative determination of hydrogen isotope (^{1}H, ^{2}H, ^{3}H) depth profiles on a few micrometers beneath the surface.

INTRODUCTION

The analysis of hydrogen isotopes in the near surface region of solids must not be considered as a hard task. The main related problem is due to the relative weakness of the chemical bonds in which hydrogen atoms are engaged. Consequently, the perturbation induced within the investigated target medium by the incident probe may enhance hydrogen mobility and makes its quantitative measurement fairly difficult.
Owing to the wide range of secondary effects induced by the presence of hydrogen in any material, it is of great importance to accurately determine its elemental distribution as well at the target surface as within the volume. Hydrogen is a quite troublesome element mainly due to the fact that its electronic structure with only a single external electron makes it fairly invisible for a large number of analytical methods such as X-ray microanalysis and electron spectroscopy (Auger and XPS). Nevertheless, Physics and Chemistry offer to researchers and engineers a complete range of powerful characterization techniques.
In the first part of this paper, we will give some details about the available techniques without describing in details their basic principles. Then, we will focus our attention on a few application examples concerning hydrogen measurement in solids using some of these techniques. The third part of this paper will be devoted to ion beam induced analytical methods which offer several powerful tools for the quantitative determination of hydrogen and its isotopes.

AVAILABLE TECHNIQUES

There is a huge number of analytical tools available to perform hydrogen analysis at a solid surface in terms of nature of the incident probe as well in terms of basic

physical principles. Table 1 summarizes these characterization techniques. The methods are classified as a function of the nature of the incident probe: temperature (T), magnetic field (H), photons (hν), electrons (e-), neutrons (n), ions (i) or radioactive decay (β-). The type of spectroscopy used to record the response of the material is also detailed. Several corresponding references are also given in which the basic principles and the main advantages and drawbacks of the methods are discussed in details. To simplify the reading of Table 1, we have listed the methods by indicating only the usual acronym attached to them: TDS for thermal desorption spectrometry; NMR for nuclear magnetic resonance; FTIR for Fourier transform infra-red spectrometry; LIPS for laser induced-plasma spectroscopy; TOF-ESD for time of flight electron desorption spectroscopy; NIP for neutron imaging plate; ENAA for epithermal neutron activation analysis; NERDA for neutron elastic recoil detection analysis; SANS for small angle neutron scattering; GDOES/MS for mass spectrometry glow discharge optical emission spectroscopy; SIMS for secondary ion mass spectrometry; AMS for accelerator mass spectrometry; IBA for ion beam analysis including ERDA/ERCS (elastic recoil detection analysis/elastic recoil coincidence spectrometry) and NRA (resonant or non resonant nuclear reaction analysis); □-autoradiography used in tritium tracing experiments.
For any investigated material, it appears that the choice of the most appropriate method will depend on the nature of the information requested.

FEW APPLICATION EXAMPLES

Alkali-alumino-borosilicate glasses are considered as fully representative inactive simulated-materials for nuclear waste glasses. For safety reason, it is of primary importance to understand and model their chemical durability. Angeli and coworkers have studied the first steps of glass hydration by nuclear magnetic resonance (NMR) [4], coupling ^{1}H-^{29}Si and ^{1}H-^{27}Al cross-polarization (CP) magic angle spinning (MAS) NMR, ^{1}H double quantum (DQ) MAS NMR and ^{27}Al multiple quantum (MQ) MAS NMR measurements. Under acidic conditions, ^{29}Si CP MAS NMR data show that the repolymerized silicate networks have similar configuration.

Table 1 : Physico-chemical methods used to determine hydrogen isotopes in the near surface region of solids.

Incident probe	Usual acronym	Outgoing measurement	Reference
T	TDS	Mass spectrometry	[1 - 3]
H	NMR	Magnetic field variation	[4]
hν	FTIR	Absorption spectroscopy	[5]
hν	LIBS	Optical emission spectroscopy	[6]
e^-	TOF-ESD	Mass spectrometry	[7]
n	ENAA	Gamma-ray spectrometry	[8]
n	NIP	Neutron radiography	[9]
n	NERDA	Recoil nucleus detection	[10]

n	SANS	Small angle neutron scattering	[11]
i	GDOES/MS	Mass spectrometry	[12 - 13]
i	SIMS	Mass spectrometry	[14, 15]
i	AMS	Mass spectrometry	[16, 17]
i	NRA	Charged particle, gamma-ray or neutron emission	[14, 18 – 20]
i	ERDA	Recoil nucleus detection	[21, 22]
i	ERCS	Proton coincidence spectrometry	[23 - 25]
β-	β-autoradiography	β-decay	[26, 27]

Zirconium as a second nearest neighbour increases the ^{29}Si isotropic chemical shift. The gel porosity is influenced by the pristine glass composition, modifying the silicon-proton interactions. From ^{1}H DQ and ^{1}H-^{29}Si CP MAS NMR experiments, it was possible to discriminate between silanol groups (isolated or not) and physisorbed molecular water near $Si(Q_2)$, $Si(Q_3)$, and $Si(Q_4)$ sites, as well as to gain insight into the hydrogen-bonding interaction and the mobility of the proton species. These experiments were also carried out on heated samples (180°C) to evidence hydrogen bonds between hydroxyl groups on molecular water. Alteration in basic media resulted in a gel structure that is more dependent on the initial glass composition. ^{27}Al MQ MAS NMR data revealed an exchange of charge compensating cations of the $[AlO_4]^-$ groups during glass alteration. ^{1}H-^{27}Al CP MAS NMR data provide information about the proximities of these two nuclei and two aluminum environments have been distinguished.

The second example is extracted from a work by Cairon and co-workers on the presence of hydroxyl groups in steamed NaHY zeolites used as acid catalysts in petroleum refining and petrochemistry [5]. The presence of an unusual (OH) group located at 3700 cm^{-1} has been found by FTIR examination. This group is thermally stable and characterized by a soft acid strength. It appears that the concentration of this unusual (OH) group depends on the level of Na exchange and reaches a maximum for 34 Na per unit cell.

The study of the behaviour of hydrogen on the surface of plasma facing components in fusion devices is important for the design of the fuel recycling, plasma control, safe management of tritium inventory. Kubota and co-workers have applied the NERDA technique to polymers submitted to the plasma of the JT-60U fusion reactor in order to profile simultaneously H and D over a depth around 1 mm [10]. The hydrogen depth profile measured on the plasma facing component sample (polyethylene) covers 800 μm depth and exhibits three distinct retention contributions respectively near the surface below 200 μm (I), between 200 and 400 μm (II) and above 400 μm. The corresponding H concentration are 2.8, 0.3 and 3.3 $10^{22}/m^2$ respectively. The estimated D retention is around 3.5 $10^{21}/m^2$ giving a sensitivity of about 60 appm for D.

The precipitation of hydride in metals and alloys is often associated with failure of components made from these materials. Then our last example is related to the study

of H and D segregation at zirconium (0001) surface by coupling SIMS, Auger spectroscopy and direct observation of nuclear reaction [14]. The variation of the deuterium depth profile versus the annealing time at 150°C was determined at the Zr (0001) surface using the D(d, p)4He non resonant nuclear reaction analysis method. It proved the existence of both a temperature and a concentration threshold for the segregation process of H and D and also the existence of a solubility limit over which hydride precipitation is able to control the segregation process.

ION BEAM-BASED METHODS

We are now going to detail a specific family of analytical techniques: ion beam based methods. When a beam of light charged particles (protons, deuterons, helium-3 or helium-4 ions) produced by an electrostatic accelerator hit a target sample with a kinetic energy in the MeV range, different types of interactions are able to occur between the incident ions and the target atoms. Among them, nuclear interactions allow to probe the nuclei from the lightest elements (from Z = 1 to Z = 17) of the target in a very specific way [20]. The Coulomb interaction forces can be sufficiently efficient to make the collision
between the incident ion and the target atom remaining elastic. The motion of the two involved bodies are slightly modified; the first one is scattered and the second recoiled. This is the basis of two analytical methods called elastic recoil detection analysis (ERDA) and elastic recoil coincidence scattering (ERCS) used for hydrogen depth profiling in the near surface region of solids:
- $^{1}H(^{4}He, ^{4}He)^{1}H$ (ERDA) and $^{1}H(p, p)^{1}H$ (ERCS).
If the incident ion succeeds to cross the Coulomb barrier of the target nucleus, then nuclear forces drive the interaction process and a true nuclear reaction may occur. The incident ion is absorbed by the target nucleus and charged particles, gamma-rays and a recoil nucleus are emitted. This is the so-called nuclear reaction analysis technique (NRA) as for example: $^{27}Al(p, \gamma)^{28}Si$; $^{12}C(d, p)^{13}C$; $^{19}F(p, \alpha\gamma)^{16}O$; $^{16}O(^{3}He, p)^{18}F$; $^{14}N(\alpha, p)^{17}O$; $^{1}H(11B, \alpha)^{8}Be$.
In a very small number of cases, Physics makes the nuclear reaction much more probable than predicted by the theory. In fact, the excitation energy of the complex system formed by the absorption of the ion by the target nucleus (compound nucleus) is exactly equal to the energy value of one of the discrete energetic levels of this metastable nucleus and resonances may occur [20]. Among the most famous analytical resonances, the following reactions with ^{16}O and ^{19}F as respective compound nuclei can be outlined: $^{15}N(p, \alpha\gamma)^{12}C$ near 429 keV; $^{18}O(p, \square)^{15}N$ near 629 keV.
Recently, ion beam analysis techniques available for hydrogen measurement have become more and more attractive with the progress of elemental mapping tools offered by nuclear microprobes working with 1 μm^2 beam spots [23 - 25].

HYDROGEN MEASUREMENTS BY ION BEAM-BASED METHODS

Now, we will try to illustrate the interest of ion beam analysis techniques to determine quantitative hydrogen isotope distributions in the near surface region of solids. The first step of the corrosion process for an alkali-silicate glass corresponds to the ionic exchange between sodium (or potassium) ions from the glass network with the protons brought by the aqueous solution. The progress of this ion interdiffusion can be efficiently investigated by using the following resonant nuclear reactions: $^{1}H(^{15}N, \alpha\,\gamma)^{12}C$ and $^{23}Na(p, \alpha\,\gamma)^{20}Ne$. The comparison of H and Na depth profiles measured after 25 days of leaching at 20°C for a soda alumino-borosilicate glass at pH=7 in static mode suggests that the interdiffusion process obeys to a 1/1 ion exchange [28].

The second example deals with aging mechanisms of transition metal hydrides, more precisely titanium deutero-tritide. One single analysis based on the simultaneous observation of several non resonant nuclear reactions using a 450 keV deuteron beam allows the quantitative determination of D, T and of the decay product of T (^{3}He) without any interferences with oxygen and carbon coming from a possible oxidation/carbonatation of the titanium surface. Figure 1 gives a typical energy spectrum recorded on a $Ti(D,T)_2$ sample irradiated by 450 keV deuterons [18]. In this spectrum, a doublet and a very thin peak successively appear in the low energy region (as magnified in the insert in the center); a second narrow peak occurs in the high energy region. They correspond to the following nuclear reactions: $^{3}H(d, n)^{4}He$; $^{3}He(d, p)^{4}He$; $^{2}H(d, p)^{3}H$; $^{3}He(d, p)^{4}He$. Peaks from $^{16}O(d, p)^{17}O$ and $^{12}C(d, p)^{13}C$ nuclear reactions are not visible on this spectrum due to their very low cross-sections at 450 keV [20]. By scanning the surface sample, D, T and ^{3}He quantitative lateral distributions are derived together with depth profiles using specific ion beam analysis data processing software as summarized by Barradas in [29].

The last application example of IBA methods to hydrogen measurement we will discuss concerns the use of ERDA. It is known that polyimide electrical properties might be strongly modified by high energy heavy-ion irradiation. The nuclear microanalysis group at Saclay has studied the evolution of the hydrogen distribution in 12.5 µm thin polyimide foils after high-energy heavy ion irradiation (50 MeV ^{32}S between 2.8 10^{13} to 1.3 $10^{15}/cm^2$) using helium-4 induced ERDA in transmission geometry [30]. Figure 2 gives the reference spectra for the unirradiated sample and ion increasing fluences. The shape of the hydrogen distribution suggests the formation of deep H-enriched zones in the irradiated polymer.

Figure 1: Deuteron-induced nuclear reactions detected on a titanium deutero-tritide (after Trocellier and Le Pioufle [18]).

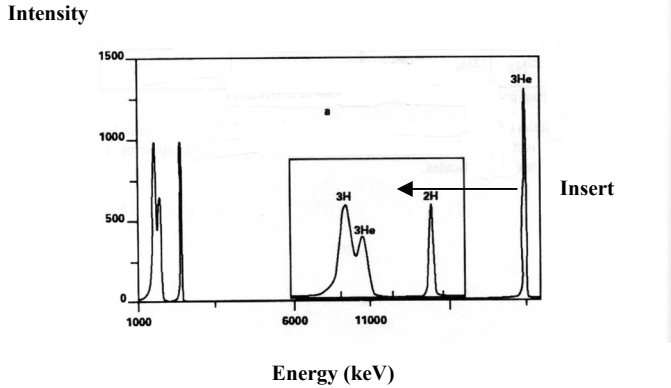
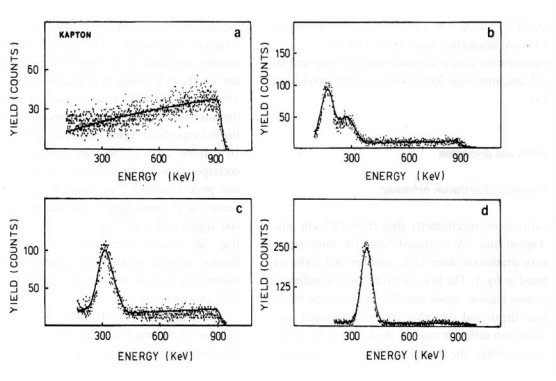


Figure 2: ERDA spectra for a 12.5 µm thin polyimide foil irradiated by 50 MeV ^{32}S ions (after Trocellier and coworkers [29]).



CONCLUSION

All the application examples discussed in this paper clearly demonstrate th powerfulness of a wide range of analytical techniques for quantitative determinatio of hydrogen isotopes ($_1H$, D or T) in the near surface region of solids. The choice o the most appropriate technique will depend on the analytical performance that mus be enhanced. To simplify, it can be argued that sensitivity could be associated wit mass spectrometry; depth resolution could be associated with glow discharge secondary ion mass spectrometry or resonant nuclear reaction; analysed depth coul be associated with ion beam analysis methods, accelerator mass spectrometry an neutron elastic recoil detection; hydrogen mapping could be associated with electro

stimulated desorption, β- autoradiography and elastic recoil detection analysis (using a microbeam); quantitative depth profiling could be associated with ion beam analysis methods; isotopic analysis could be associated with mass spectrometry or ion beam analysis methods.
Furthermore, it is often interesting to couple several analytical methods to optimize the performances of the measurements like SIMS, Auger spectroscopy and nuclear reaction analysis as in [14], SIMS and NRA as in [15] or FTIR and ERDA as in [31] for example.

REFERENCES

1. Hayashi, S., "Thermal desorption spectra of hydrogen isotopes in the monohydride phase of V-H-D and Ti-V-H-D systems", *J. Alloys Compounds,* Vol. 359, (2003), pp. 281-286.
2. Fu-Gao Wei, Tsuzaki, K., "Response of hydrogen trapping capability to microstructural change in tempered Fe-0.2C martensite", *Scripta Materialia,* Vol. 52, (2005), pp. 467-472.
3. Oya, Y., Miyauchi, H., Suda, T., Nishikawa, Y., Oda, T., Okuno, K., Tanaka, S., "Effects of helium implantation on hydrogen isotope retention behavior in SiC", *J. Nuclear Materials*, Vol. 363-365, (2007), pp. 933-937.
4. Angeli, F., Gaillard, M., Jollivet, P., Charpentier, T., "Influence of glass composition and alteration solution on leached silicate glass structure: A solidstate NMR investigation", *Geochimica Cosmochimica Acta,* Vol. 70, (2006), pp. 2577-2590.
5. Cairon, O., Loustanau, A., Gautier, M., « FTIR studies of unusual OH groups in steamed HNaY zeolites: Influence of Na insertion", *J. Phys. Chem. Sol.* Vol. 67, (2006), pp. 994_-997.
6. Pardede, M., Kurniawan, K.H., Tjung Jie Klie, Hedwig, R., Idris, N., Kobayashi, T., Maruyama, T., Yong Inn Lee, Kagawa, K., May On Tija, "Hydrogen analysis in solid samples using laser-induced helium plasma at atmospheric pressure, *J. Applied Letters,* Vol. 98, (2005), pp. 043105-1/5.
7. Ueda, K., Itoh, Y., "Two-dimensional hydrogen behaviors on solid surfaces studied by hydrogen microscope", *Surface Science*, Vol. 600, (2006), pp. 1684-1688.
8. Dóczi, R., Csikai, J., Sanami, T., Fayez-Hassan, M., "Bulk hydrogen analysis using epithermal neutrons", *J. Radioanalytical Nuclear Chemistry*, Vol. 266, (2005), pp. 11-17.
9. Yasuda, R., Nakata, M., Matsubayashi, M., Harada, K., Hatakeyama, Y., Amano, H., "Application of hydrogen analysis by neutron imaging plate method to zircaloy cladding tubes", *J. Nuclear Materials*, Vol. 320, (2003), pp. 223-230.
10. Kubota, N., Kondo, K., Ochiai, K., Nishitani, T., "Neutron elastic recoil detection for hydrogen isotope analysis in fusion materials", *J. Nuclear Materials*, Vol. 367-370, (2007), pp. 1596-1600.

11. Maxelon, M., Pundt, A., Pyckhout-Hintzen, W., Kirchheim, R., “Small angle neutron scattering of hydrogen segregation dislocations in palladium”, *Scripta Materialia*, Vol. 44, (2001), pp. 817-822.
12. Michler, J., Aeberhard, M., Velten, D., Winter, S., Payling, R., Breme, J., “Depth profiling by GDOES: Application of hydrogen and d.c. bias voltage corrections to the analysis of thin oxide films”, *Thin Solid Films*, Vol. 447-448, (2004), pp. 278-283.
13. Rout, T.K., “Nanolayered oxide on a steel surface reduces surface reactivity: Evaluation by glow discharge optical emission spectroscopy”, *Scripta Materialia*, Vol. 56, (2007), pp. 573 -576.
14. Chun-si Zhang, Flinn, B.J., Norton, P.R., “Segregation of hydrogen on zirconium (OOO1) studied by SIMS, work function, Auger electron spectroscopy and nuclear reaction analysis”, *J. Nuclear Materials*, Vol. 199, (1993), pp. 231-236.
15. Reiche, I., Castaing, J., Calligaro, Th., Salomon, J., Aucouturier, M., Reinholz, U., Weise, H.P., “Analyse of hydrogen in quartz and in sapphire using depth profiling by ERDA at atmospheric pressure: Comparison with resonant NRA and SIMS”, *Nuclear Instruments Methods Physics Research* , Vol. B249, (2006), pp. 608-611.
16. Stan-Sion, C., Behrisch, R., Coad, J.P., Kreiiig, U., Kubo, F., Lazarev, V., Lindig, S., Mayer, M., Nolte, E., Peacock, A., Rohrer, L., Roth, J., “Hydrogen isotope depth profiling in carbon samples from the erosion dominated inner vessel walls of JET”, *J. Nuclear Materials*, Vol. 290-293, (2003), pp. 491-495.
17. Sun, G.Y., Friedrich, M., Grötzschel, R., Bürger, W., Behrisch, R., Garcia-Rosales, C., “Quantitative AMS depth profiling of the hydrogen isotopes collected in graphite divertor and wall tiles of the tokamak ASDEX-Upgrade”, *J. Nuclear Materials,* Vol. 246, (1997), pp. 9-16.
18. Trocellier, P. Le Pioufle, M., « La microsonde nucléaire du centre d’études de Bruyères-le-Châtel en sciences des matériaux », *Revue Scientifique et Technique de la Défense*, Vol. 1, (1994), pp. 137- 146.
19. Trocellier, P ., Berger, P., Berthier, B., Berthoumieux, E., Gallien, J.P., Metrich, N., Moreau, C., Mosbah, M., Varela, M.E., « Nuclear microprobe and nuclear reaction spectrometry at a few square micrometer level : Myth or reality”, *Nuclear instruments Methods Physics Research* , Vol. B158, (1999), pp. 221.227.
20. Trocellier, P., Trouslard, Ph., « Spectrométrie de collisions élastiques et de réactions nucléaires » *Techniques de l’Ingénieur, Traité Analyse et Caractérisation*, Vol. P2560, 2561 et 2562, (2001).
21. Tirira, J., Serruys, Y., Trocellier, P., Forward Recoil Spectrometry, Plenum Press (New York, 1996).
22. Tirira, J., Trocellier, P., Frontier, J.P., Massiot, Ph., Costantini, J.M., “3D hydrogen profiling by elastic recoil detection analysis in transmission geometry”, *Nuclear Instruments Methods Physics Research*, Vol. B50, (1990), pp. 135-139.
23. Wegdén, M., Kristiansson, P., Pastouvic, Z., Skogby, H., Auzelyte, V., Elfman, M., Malmqvist, K.G., Nilsson, C., Pallon, J., Shariff, A., “”Hydrogen analysis by p – p scattering in geological material”, *Nuclear Instruments Methods Physics Research,* Vol. B219-220, (2004), pp. 550-554.

24. Berger, P., Gallien, J.P., Khodja, H., Daudin, L., Berger, M.H., Sayir, A., "Hydrogen incorporation into high temperature protonic conductors: Nuclear microprobe microanalysis by means of 1H(p, p)1H scattering", *Nuclear Instruments Methods Physics Research*, Vol. B249, (2006), pp. 527-531.
25. Berger, P., Gallien, J.P., Khodja, H., Daudin, L., Berger, M.H., Sayir, A., "Nuclear microprobe local hydrogen measurements in HPTC", *Solid State Ionics, Vol. 177*, (2006), pp. 1655-1658.
26. Chêne, J., Trocellier, P., "Investigation of alkali borosilicate glass durability using tritium tracing, β-autoradiography, scanning electron microscopy and ion beam analysis", *J. Non Crystalline Solids* **337**, Vol. 337, (2004), pp. 86-96.
27. Hanada, H., Otsuka, T., Nakashima, H., Sasaki, S. Hayakawa, M., Sugisaki, M., "Profiling of hydrogen accumulation in a tempered martensite microstructure by means of tritium autoradiography", *Scripta Materialia,* Vol. 53, (2003), pp. 1279-1284.
28. Trocellier, P., Engelmann, Ch., "Caractérisation des couches hydrolysées de verres altérés en milieu aqueux au moyen de techniques nucléaires d'analyse", *Rivista della Stazione Sperimentale del Vetro* , Vol. 5, (1984), pp. 145-147.
29. Barradas, N.P., Arstila, K., Battistig, G., Biancni, M., Dytlewski, N., Jeynes, C., Kótai, E., Lulli, G., Mayer, M., Rauhala, E., Szilágyi, E., Thompson, M., « Summary of IAEA intercomparison of IBA software », *Nuclear Instruments Methods Physics Research*, Vol. B266, (2008), pp. 1338-1342.
30. Trocellier, P., Tirira, J., Massiot, Ph., Gosset, J., Costantini, J.M., "Nuclear microprobe study of the composition degradation induced in polyimides by irradiation with high-energy heavy ions", *Nuclear Instruments Methods Physics Research*, Vol. B54, (1991), pp. 118-122.
31. Bureau, H., Trocellier, P., Shaw, C., Khodja, H., Bolfan-Casanova, N., Demouchy, S., "Determination of the concentration of water dissolved in glasses and minerals using nuclear microprobe", *Nuclear Instruments Methods Physics Research*, Vol. B210, (2003), pp. 449-454.

Effects of Hydrogen on Materials
Proceedings of the 2008 International Hydrogen Conference
Brian Somerday, Petros Sofronis, Russell Jones, editors, p 438-447
Copyright © 2009 ASM International®
All rights reserved.
www.asminternational.org

HYDROGEN TRAPPING MECHANISMS IN STRUCTURAL MATERIALS

Dan Eliezer[1]
[1]*Ben-Gurion University of the Negev, Beer-Sheva 84105, Israel*

Thomas Boellinghaus[2]
[2] *Federal Institute for Materials Research and Testing (BAM), Berlin, D-12205, Germany*

Keywords: hydrogen trapping, Thermal desorption spectroscopy, Activation energy, Binding energy.

ABSTRACT

Thermal desorption spectroscopy is a very sensitive and accurate technique for studying hydrogen's diffusion and trapping processes in structural materials. The technique involves accurate measurement of the desorption rate of gas atoms, saluted or trapped in the material, while heating the sample at a known rate. This paper reviews the thermal desorption spectroscopy (TDS) application in Titanium based alloys, Titanium alloy Low Cost Beta (Timetal LCB) and supermartensitic stainless steel (SMSS).

1. INTRODUCTION

Hydrogen is not homogeneously distributed within materials. It can be found either in the host lattice, or segregated into atomic and microstructural imperfections, such as vacancies, solute atoms, dislocations, grain boundaries, voids and second phase particles. In these localized regions, the mean residence time of a hydrogen atom is considerably longer than in a normal interstitial lattice site. In the extreme case, these regions act as sinks which retain the hydrogen atom, even during thermo-mechanical loading. The generic term for this phenomenon is “hydrogen trapping”, localized regions are therefore designated as hydrogen trap sites [1]. Thermal desorption spectroscopy is a very sensitive and accurate technique for studying hydrogen diffusion and trapping processes in structural materials. This technique involves accurate measurements of the desorption rate of gas atoms, saluted or trapped in the material, while heating the sample at a known rate. By using this method we can measure the density and binding energies of a series of trap sites by using one measurement. This paper reviews the thermal desorption spectroscopy (TDS) applications in quantitative studies of hydrogen trapping and release behavior in different structured materials. The paper addresses our recent TDS results, obtained from the study of hydrogen evolution from Ti-based alloys, Timetal LCB and supermartensitic stainless steels. The objective of this study is to better understand the hydrogen interaction with selected structural alloys. In this study the

thermodynamics and the kinetic nature of the interactions between different trapping sites and hydrogen will be described.

2. HYDROGEN TRAPING MECHANISMS

The strength of a trap site (i.e. the fraction of time in which a hydrogen atom resides within the trap site) depends on the binding energy (E_B) of the hydrogen atom to the trap. The energy associated with this reaction is the hydrogen–trap binding energy (E_B). Hydrogen atoms may then be considered as either released from or captured by the trap site until equilibrium is reached. This paper addresses, in detail, the model developed by Lee and Lee [2], which is based exclusively on hydrogen evolution from trap sites, and neglects the diffusion processes. When a hydrogenated sample is heated at a constant rate and the rate of hydrogen desorption is plotted versus temperature, a peak is obtained. Desorption rate initially increases since the probability for hydrogen release from a trap increases faster than the decrease in the content of hydrogen in this trap. Subsequently, desorption rate decreases to zero as a result of the low hydrogen content remaining in the trap. In general, the temperature producing maximal desorption is determined by: the activation energy of hydrogen release from the trap, the order of desorption reaction and the heating rate. The peak intensity, on the other hand, depends on the content of trapped hydrogen and on the heating rate [3].

3. HYDROGEN TRAPPING OF TI-BASED ALLOYS

3.1. Ti-based Alloys

The material used for this study was a duplex-annealed Ti–6Al–4V alloy, with a bi-modal α + β microstructure, in which, 60 vol.% consists of equiaxed primary α, and 40 vol.% transformed-β (acicular secondary α), as described in detail elsewhere [4]. Hydrogen was introduced to the alloy, by cathodic charging at room temperature, in a H_3PO_4:glycerine (1:2, volume) electrolyte, using a constant current density of 50 mA/cm^2, for different charging times.

3.2 . Electrochemically Charged Ti–6Al–4V

Typical TDS spectra for 12 and 48 h electrochemically charged specimens are shown in Fig. 1. The heating rate (temperature ramp) was kept constant at 5 °C/min.

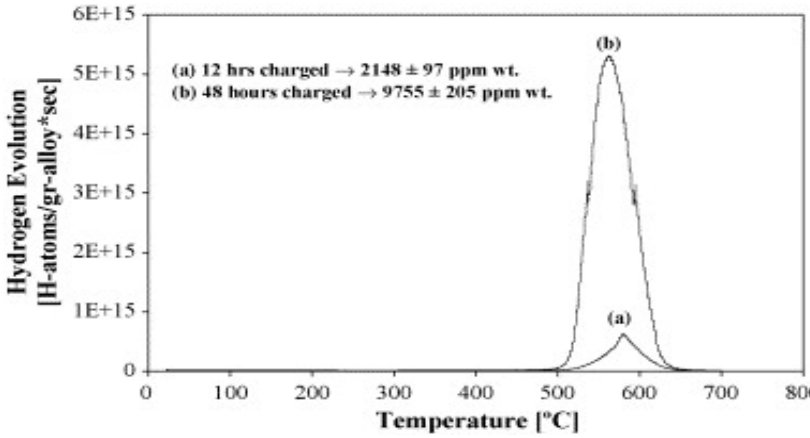


Fig. 1. TDS plots of 12 and 48 h hydrogenated Ti–6Al–4V specimens, using a constant heating rate of 5 °C/min.

When comparing the TDA spectra it can be noted that both plots are characterized by one main desorption peak between 562 and 580 °C. The intensity of desorption peaks increase when the sample is pre-charged with a higher content of hydrogen. The apparent activation energy level for hydrogen evolution was estimated from the shift of peak temperatures with the increase in the applied heating rate. The typical heating rate dependence of thermal desorption from 48 h cathodically charged specimens is described in Fig. 2 and Table 1. The activation energy level for hydrogen release is of a relatively high value, which is characteristic of irreversible trapping. The effective energy of deuterium desorption was found to be ~95 kJ/mole for the beta-annealed alloy and approximately ~64 kJ/mole for duplex-annealed material [4].

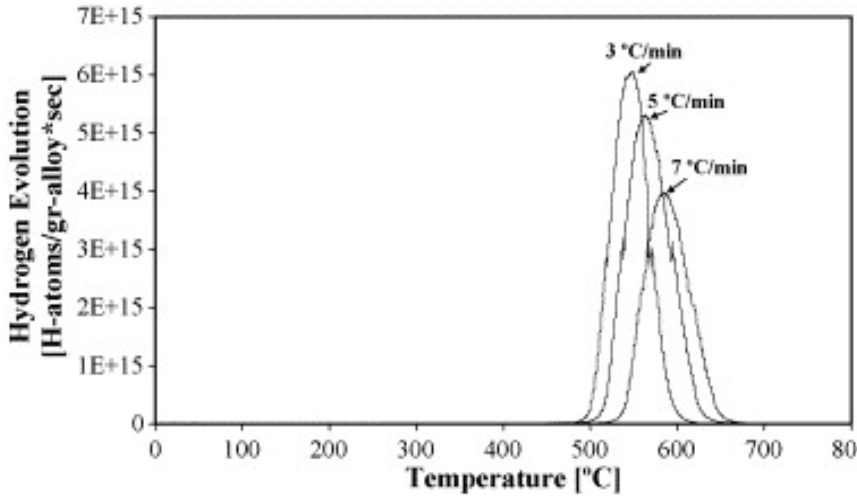


Fig. 2. TDS spectra of 48 h electrochemically hydrogenated Ti–6Al–4V alloy, at a heating rates of 3 and 5 °C/min.

Table 1. Summary of TDS calculated parameters of 48 h electrochemically hydrogenated Ti–6Al–4V alloy, at heating rates of 3, 5 and 7 °C/min

Heating rate (°C/min)	Temperature at desorption peak (°C)	Half height peak width (°C)	Maximal desorption rate ($\times 10^{15}$ H-atoms/g alloy s)
3	548	45	6.06
5	562	62.5	5.32
7	584	66	3.94

Supported by X-Ray Diffraction (XRD) data of the hydrogenated specimen, before and after TDS, hydrogen evolution might occur due to titanium hydride precipitation and its dissociation at elevated temperatures. A similar value (106 kJ/mole) of the activation energy for δ-hydride dissociation was reported by Takasaki et al. [5]. Another possible site for hydrogen accumulation, which might act as an irreversible trap, could be the α–β interface, as is noted by Young and Scully [6].

4. HYDROGEN TRAPPING IN TIMETAL LCB ALLOYS

Low Cost Beta (LCB) has been specially designed by Timet for the reduction of alloy costs through the replacement of more costly beta stabilizing elements. Timetal LCB (Ti–4.5Fe–6.8Mo–1.5Al) offers the best combination of desirable properties at an economical price. In previous studies of BCC β-Ti alloys it has been observed that hydrogen in solid solution in the β lattice, can have a significant effect on the ductile-to-brittle transition leading to a change in the fracture mode from ductile, micro-void coalescence to brittle cleavage [7] [8].

4.1. Hydrogen Desorption

The quantities of hydrogen desorbed by the employment of TDS, after cathodic charging, are described in Table 2. It can clearly be seen that the desorbed quantity of hydrogen is significantly higher for the longer charged specimen. It is noted that with an increased charging time, TDS desorption peaks of the specimens are shifted to lower temperature values, after only 24 h of charging, which indicates faster kinetics of hydrogen evolution. The typical heating rate dependence of thermal desorption from 6 to 72 h cathodically charged specimens is shown in Fig. 3 (a) and (b). It can be seen that with an increased heating rate, desorption peaks of both samples are shifted to higher temperatures. Quantifications of several desorption parameters are provided in Table 2.

Table 2. Hydrogen concentrations desorbed in as-received Ti-LCB specimens following electrochemical charging.

Charging time(h)	Desorption peak temperature [°C]	Total CH desorbed [ppm]
0	537	34.3
6	520	153
12	522	266
24	522	835
48	492	1600
72	487	2182

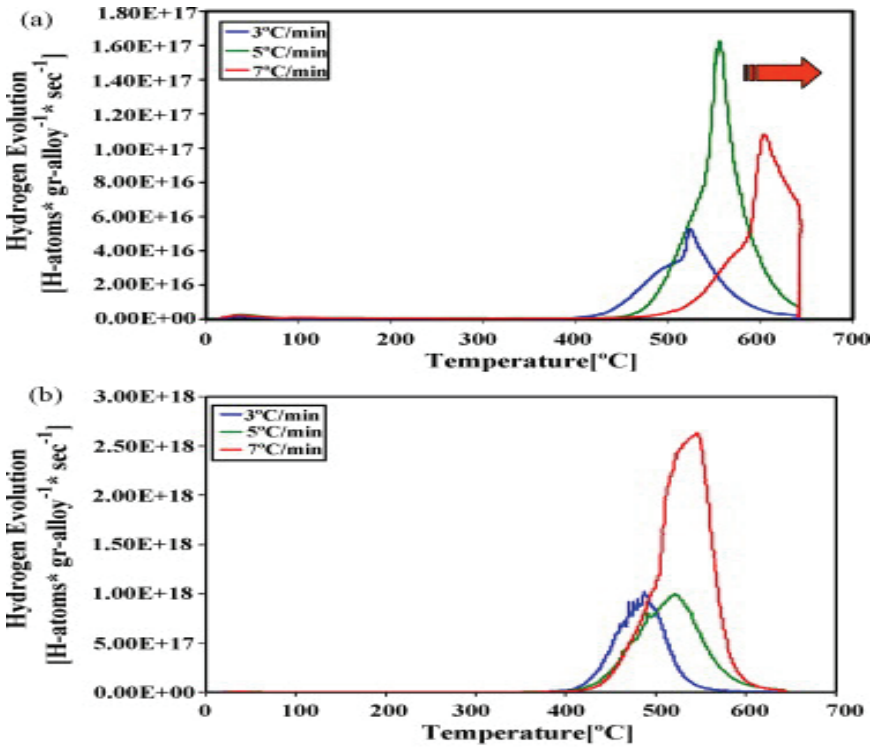


Fig. 3. Heating rate dependence of hydrogen evolution from specimens electrochemically charged for: (a) 6 h, (b) 72 h.

The calculated activation and binding energies of TDS desorption peaks for different electrochemical charging times are presented in Table 3.

Table 3.Calculated desorption and binding energies of peaks observed in the TDS plot of Ti-LCB specimens following electrochemical charging.

Charging time [h]	Activation energy (E_a) [kJ/mol]	Binding energy (E_B) [kJ/mol]
6	47.37	19.57
12	49.29	21.49
24	48.11	20.31
48	60.2	32.4
72	61.4	33.6

These results indicate that the probable traps are reversible as their binding energy values are all much lower than the upper limit value of 60 kJ/mole suggested for reversible traps in steels. The relatively low estimated values of trapping and binding energy, which point to a reversible trap site, could be related to different pre-stress condition-induced defects, i.e., dislocations, vacancies, elastic fields etc., as well as to their interaction with existing potential trap sites, such as grain boundaries and interface stress fields that are induced by particle pre-precipitation.

5. HYDROGEN TRAPPING IN SUPERMARTENSITIC STAINLESS STEEL TIG WELDS

Supermartensitic stainless steels are essentially iron-based alloys which also contain chromium, nickel and molybdenum. Supermartensitic alloys have increasingly been applied in the oil & gas industries. Welded components are subjected to sour service conditions, providing a potential risk for hydrogen uptake, degradation and cracking of supermartensitic stainless steels. The alloy was exposed to hydrogen in three different modes: electrochemical hydrogenation, gaseous-phase hydrogenation and hydrogen introduced by GTA welding via a mixed Ar + H_2 shielding gas. Hydrogen/Deuterium evolution and trapping characteristics were studied via TDS. Fig. 4 demonstrates hydrogen contents in different welding areas.

5.1 Hydrogen Desorption

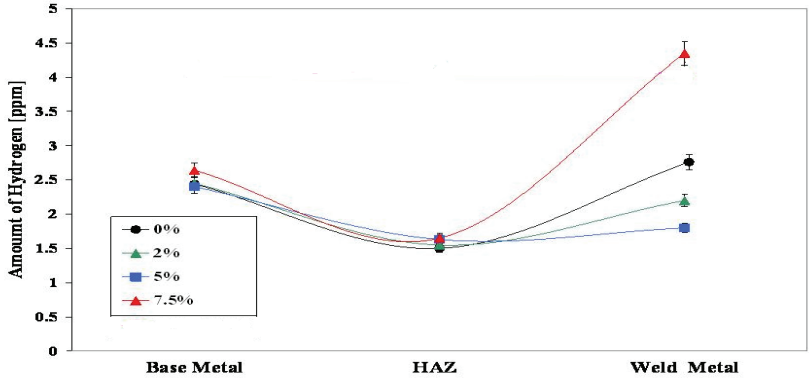


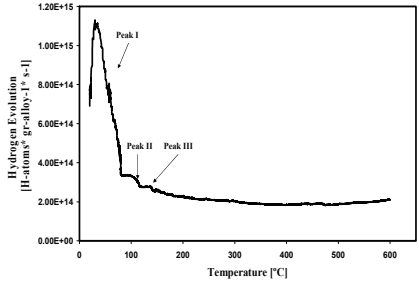
Fig 4 Hydrogen contents in different welding areas of SMSS TIG welded in gas shield atmospheres containing different hydrogen percentages

It can generally be stated that the higher the fugacity of hydrogen in the atmosphere the larger the hydrogen concentrations absorbed in the alloy. The hydrogen content absorbed in the electrochemically charged specimen is the highest, and differs from the as-received specimen by around two orders of magnitude. This result can be attributed to high hydrogen concentrations produced on the sample surface thereby suppressing most of the recombination during electrochemical charging, as reported in former studies [9]. The distribution of hydrogen in the volume is dependent on the hydrogen charging technique, i. e. if hydrogen is introduced from the surface during electrolytic or gaseous-phase charging, or if it is introduced by a welding arc and is homogenously distributed, as for instance in a weld metal. Internal hydrogen distribution is also significantly dependent on various weld microstructures, as a result of their different diffusivities and solubilities

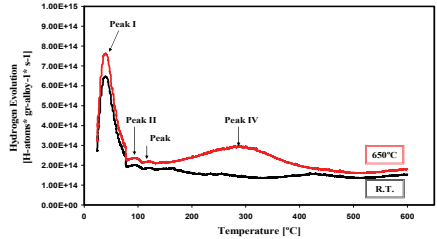
5.2 Desorption Characteristics

Characteristics of hydrogen desorption from the SMSS specimens are presented in Figures 5 and 6. All the spectra exhibited a first peak at relatively low temperatures, i. e. around room temperature, indicating a larger loss of hydrogen by the height of the peak. These peaks are probably associated with hydrogen escaping from the specimen's surface at relatively low activation energy level of approximately 4.5 kJ.

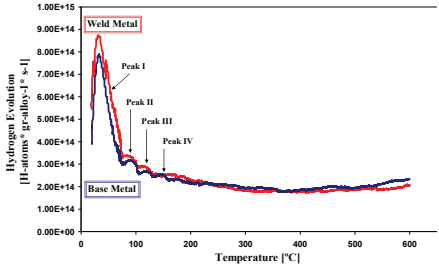
a) As received material at differing charging temperatures and at a heating rate of 3ºC/min



b) gas-phase charged (1 atm, 6.5 hours) at different charging temperatures and at a heating rate of 3ºC/min



c) Different SMSS weld microstructures of alloy, TIG welded in Ar+0 % H_2



d) Different SMSS weld microstructures of alloy, TIG welded in Ar+7.5 % H_2

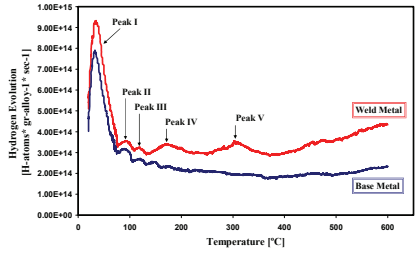
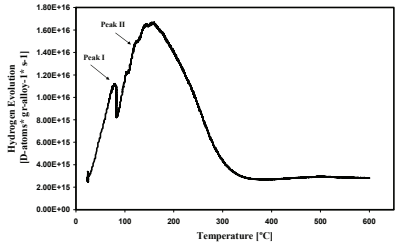


Figure 5: TDS spectrum of SMSS

a) as-received material



b) weld metal

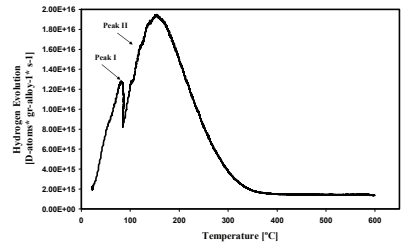


Figure 6: TDS spectra of samples electrochemically charged with deuterium for a 24 hour period, TIG welded in gas shield atmospheres containing Ar+7.5 % H_2 at a heating rate of 3ºC/min

The present results show that due to the relatively small activation energies measured, the retained austenite very much affects the transport of hydrogen in the investigated SMSS weld microstructures. However, it also has to be anticipated that the hydrogen evolution from these microstructures is diffusion controlled [8]. This means that hydrogen is not trapped irreversibly in all the supermartensitic weld microstructures, regardless of the charging process. The hydrogen evolution process was found to be dependent on the hydrogenation mode. As regards specimens that were subjected to hydrogen in the atmosphere (as received, TIG welded and gas phase hydrogenation) TDS spectrums exhibited several evolution peaks, also at higher temperatures. As regards specimens that were subjected to electrochemical hydrogenation, hydrogen evolution was observed in a large single peak that covered a wide temperature range, but was located at lower temperatures. This means that hydrogen is trapped more deeply in the investigated SMSS weld microstructures when introduced during welding rather than during cathodic charging. The hydrogen evolution spectrum appears as a large single peak because each peak is superimposed as a result of a considerable amount of hydrogen evolution.

6. CONCLUSIONS

- Thermal desorption spectroscopy is a very sensitive and accurate technique for studying hydrogen's diffusion and trapping processes in structural materials. The technique involves accurate measurement of the desorption rate of gas atoms, saluted or trapped in the material, while heating the sample at a known rate.
- In a Ti–6Al–4V alloy, hydrogen evolution plots exhibited only one main desorption peak, at elevated temperatures, with a significantly high activation energy value for hydrogen release, attributed to titanium's hydride dissociation at elevated temperatures. This is irrespective of the way hydrogen is introduced to the alloy.
- When the Ti-LCB alloy is electrochemically charged with hydrogen, based on the relatively low activation energy values for hydrogen release, it can be concluded that hydrogen evolution is related to desorption from reversible trapping states, e.g. grain boundaries, elastic fields, and vacancies.
- From the investigation of the effect of different hydrogen exposures of welded supermartensitic stainless steels it can be deduced that the amount of absorbed hydrogen is significantly dependent on the different modes of hydrogenation. During the process of electrochemical charging the absorbed hydrogen concentrations can reach much higher levels than during charging in a gaseous hydrogen atmosphere or during welding SMSS in a hydrogenated shielding gas with up to 7.5 vol.% H_2.
- The hydrogen evolution process was found to be dependent on the hydrogenation mode. The hydrogen is trapped more deeply in the weld microstructures if introduced during welding rather than by cathodic charging.

REFERENCES

[1] G.M. Pressouyre and I.M. Bernstein, *Metall. Trans A.* 12, (1981), p. 835.
[2] S.M. Lee and J.Y.L. Lee, *Appl. Phys.* 63, 9, (1988), p. 4758.
[3] E. Tal-Gutelmacher, D. Eliezer , E. Abramov, *Mater. Sci. Eng A* . 445, (2007), p. 625.
[4] E. Tal-Gutelmacher, D. Eliezer and D. Eylon, *Mater. Sci. Eng A.*. 381, 1–2, (2004), p. 230.
[5] A. Takasaki, Y. Furuya, K. Ojima and Y. Taneda, *J. Alloys Compd.* 224, (1995), p. 269.
[6] G.A. Young and J.R. Scully, *Scripta Metall. Mater.* 28 (1993), p. 507.
[7] E. Sukedai, H. Yagi, D. Yoshimitsu, H. Matsumoto, T. Ando, W.F. Xu and H. Hashimoto, *Ultramicroscopy 98* (2004), p. 209.
[8] H.K. Birnbaum and P. Sofronis, *Mater. Sci. Eng A.* 176 (1994), p.191.
[9] D. Seeger and Th. Boellinghaus "Hydrogen Permeation in Supermartensitic Stainless Steel Weld Microstructures" *Proc. of the NACE Corrosion 2004 Conf.*, New Orleans, LA, March. (2004), paper no. 04142
[10] S.-M. Lee and J.-Y. Lee, *Metall. Transactions A*. 17 (1986), p. 181.

Effects of Hydrogen on Materials
Proceedings of the 2008 International Hydrogen Conference
Brian Somerday, Petros Sofronis, Russell Jones, editors, p 448-455
Copyright © 2009 ASM International®
All rights reserved.
www.asminternational.org

NANO-PRECIPITATES DESIGN WITH HYDROGEN TRAPPING CHARACTER IN HIGH STRENGTH STEELS

Fu-Gao Wei*, Toru Hara and Kaneaki Tsuzaki
Structural Metals Center, National Institute for Materials Science
1-2-1 Sengen, Tsukuba, Ibaraki 305-0047, JAPAN
**Now at Technology Development Department, YAKIN Kawasaki Co., Ltd.*
4-2 Kojima-cho, Kawasaki-ku, Kawasaki, Kanagawa 210-8558, JAPAN

ABSTRACT

Nano-precipitates of alloy carbides TiC, NbC and VC in tempered martensite have been characterized by means of high-resolution transmission electron microscope (HRTEM) and correlated to the hydrogen trapping property. The examination of whether the amount of hydrogen absorbed by the TiC particles depends on their surface area or volume indicate that the coherent and semi-coherent TiC particles trap hydrogen at the precipitate/matrix interface at ambient temperature while the incoherent TiC particles trap hydrogen inside themselves only at high temperatures. Coherent and semi-coherent NbC and VC particles also demonstrate a surface area dependence of hydrogen trapping capacity with NbC > TiC >> VC. Contrary to TiC, incoherent NbC and VC particles are unable to trap hydrogen.

INTRODUCTION

Titanium carbide has been known to have a strong interaction with hydrogen through the electrochemical permeation method [1] and the thermal desorption spectrometry (TDS) analysis [2,3]. The activation energy for the desorption of hydrogen from TiC precipitates in steels was estimated to be as high as 95 kJ/mol [1] or 87 kJ/mol [2]. Our recent study also showed high activation energy for TiC particles [4]. However, these results only seemed to be valid for incoherent TiC particles. The coherent or semi-coherent TiC particles in the 0.42C-0.30Ti steel demonstrated a different hydrogen trapping characteristic; the activation energy is much lower than that for the incoherent particles [5]. Pressouyre and Bernstein [1, 6] pointed out earlier that the TiC particle becomes more reversible when its coherency with the matrix is increased; however, no experimental evidence has been provided. On the other hand, an autoradiography imaging of hydrogen [7] suggested that hydrogen is trapped at the precipitate/matrix interface. Thus, the first purpose of the present study is to investigate the relationship between the size and coherency of the TiC precipitate and its hydrogen trapping property. The first step is to produce a series of TiC precipitates of various interfacial characters ranging from coherent through semi-coherent to incoherent by heat treatment. The second step is to characterize these precipitates on an atomic scale; however, this was not possible due to the strong magnetism interference of low-alloy ferritic or martensitic steel. The third step is to

correlate the size and coherency of the TiC precipitate to its hydrogen trapping property with an emphasis of obtaining the answer to the two questions: (1) how does the hydrogen trapping characteristic change with a successive variation of interfacial character from coherent to incoherent, and (2) does the amount of hydrogen trapped by (semi-)coherent and incoherent TiC precipitates depend on their surface area or volume? The answer to the second question determines the trap site of hydrogen to be the precipitate/matrix interface or to be inside the precipitate. The second purpose of the study is to investigate the hydrogen trapping properties of NbC and VC precipitates which have the same crystal structure as that of TiC.

EXPERIMENTAL METHOD

Three steels containing equal molar fractions of TiC, NbC and VC, respectively, i.e. 0.05C-0.20Ti-2.0Ni, 0.05C-0.41Nb-2.0Ni and 0.05C-0.24V-2.0Ni in mass% were prepared. The major conditions which were described elsewhere [8] are: (1) quenching from 1350 ºC and tempering at 300 ~ 1000 ºC for 3 h, (2) dimension of the specimen for TDS analysis being ϕ5x40 mm, (3) cathodic charging of hydrogen in a 3 mass% NaCl aqueous solution at a current density of 1 A/m^2 for a short time of 1h to investigate the deep traps associated with TiC precipitates, (4) hydrogen analysis by TDS at a heating rate of 100 ºC/h, (5) estimation of the activation energy for hydrogen desorption from traps by fitting the experimentally measured desorption spectrum to the Kissinger's first-order reaction kinetic formula [4] (6) microstructural observation by means of HRTEM. The tempering temperature for NbC- and VC-containing steels was limited to 700 ºC and the hydrogen charging time was extended to 48 h until the saturation of hydrogen entry.

RESULTS AND DISCUSSION

Microstructural characterization of TiC precipitates on the atomic scale

Austenitization at 1350 ºC dissolved all the TiC particles in austenite. Then a fully martensitic microstructure was produced by the quenching that followed. Tempering at 300 ~ 1100 ºC after the quenching produced a series of TiC precipitates with interfacial characters changing from coherent to incoherent as expected. No precipitates other than TiC were observed. TiC began to precipitate at 500 ºC as a coherent precipitate and changed to semi-coherent particles at about 550 ºC. The semi-coherent character existed to 800 ºC beyond which it lost its coherency with the matrix. Coherent and semi-coherent TiC precipitates exhibit a disk like shape with its broad face on the {100} planes of ferrite and satisfies the Baker-Nutting orientation relationship with the ferrite, i.e. $(100)_{TiC}//(100)_{\alpha}$, $[011]_{TiC}//[001]_{\alpha}$ [9], as shown in Fig. 1. The change in the size and shape of the TiC precipitate with tempering temperature is summarized in Fig. 2. Both the diameter and the thickness of the disc-like semi-coherent TiC precipitate increase with increasing tempering temperature

with an abnormal increase at 800 ºC. Incoherent TiC precipitates formed above 800 ºC were observed to be approximately spherical.

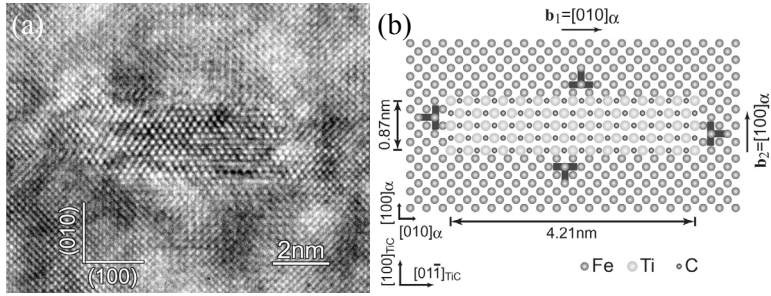


Figure 1: Semi-coherent TiC precipitate in the0.05C-0.20Ti-2.0Ni steel tempered at 600 ºC. (a) HRTEM micrograph and (b) schematic illustration of the lattice match.

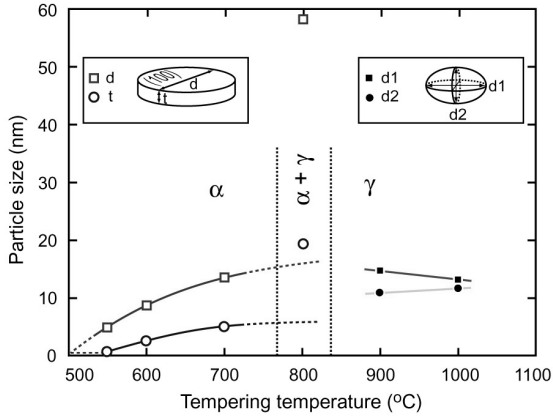


Figure 2: Change in size and shape of TiC precipitate in the 0.05C-0.20Ti-2.0Ni steel with tempering temperature.

Hydrogen trapping of TiC precipitates with interfacial characters from coherent to incoherent

The results of the TDS analysis on samples tempered at 300 to 1100 ºC are shown in Fig.3. A short hydrogen charging time of 1h was selected for detecting the deepest trap associated with the TiC precipitates. Only a small peak at about 120 °C is present for the samples that were tempered below 500 °C. However, the desorption peak becomes larger and shifts to about 230 °C when the material is tempered at 500 °C. On tempering above 550 °C, the 230 °C peak splits into two peaks; one remains at 230 °C and the other (the subsidiary peak) shifts towards a high temperature as the tempering temperature increases. The 230 °C peak becomes

smaller when the tempering temperature increases and disappears in the spectrum of the sample that was tempered at 1000 °C.

The peak located at 120 °C supposedly resulted from the hydrogen trapped by the grain boundaries and dislocations in the martensitic matrix [8]. The 230 °C desorption peak was contributed from the hydrogen that was trapped by the broad face of the disc-shaped TiC precipitate. The subsidiary peak that split from the 230 °C peak is from the side face of the precipitate. The hydrogen desorption activation energy deduced from the 230 °C peak was about 55.8 kJ/mol for the samples that were tempered from 600 to 800 °C. By dividing the hydrogen content by the total surface area of the broad faces, the hydrogen trapped by the broad faces of the disk-like semi-coherent TiC precipitate was estimated to be constant and about 1.3 atoms/nm^2 (Fig.4). These findings strongly suggest that hydrogen associated with the 230 °C peak is trapped at the same deep site on the broad face of the semi-coherent TiC precipitate. The deep site is probably the core of misfit dislocations as shown in Fig.1b. It is predicted that NbC of higher and VC of lower lattice mismatch will trap more and less hydrogen than TiC, respectively. It is also predicted that hydrogen is likely to occupy the less distorted sites other than the misfit dislocation core on the interface when more hydrogen is charged into the steels.

In contrast to the 230 °C peak, the subsidiary desorption peak that is separated from it cannot be rationalized by the constant hydrogen content per unit surface area as shown in Fig.4. The subsidiary desorption peak is interpreted to result from the hydrogen trapped at the carbon vacancy sites within the TiC precipitate beneath the side interface. Thermo-Calc calculation demonstrated that more equilibrium carbon vacancies form at higher temperature [8]. Locally higher concentration of carbon vacancies may form beneath the side face during the Ostward ripening process of TiC precipitates during which the smaller particles begin to dissolve from the side face preferentially with a faster dissolution rate of carbon than titanium [10].

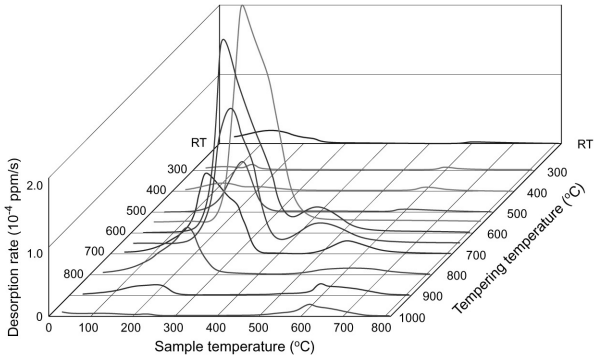


Figure 3: Evolution of the TDS spectrum of the 0.05C-0.20Ti-2.0Ni steel quenched and tempered at various temperatures. Hydrogen charging time: 1h.

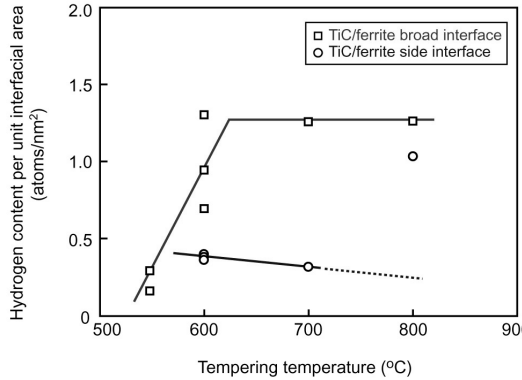


Figure 4: The hydrogen trapped by the unit area of the broad and the side faces of the semi-coherent TiC precipitate, respectively. Hydrogen charging time: 1h.

Hydrogen trapping characteristics of incoherent TiC particles

TiC particles have long been considered as a strong trap which can absorb hydrogen easily at ambient temperature. As described above, coherent and semi-coherent TiC precipitates are able to trap hydrogen easily during cathodic charging at room temperature. However, it was found that incoherent TiC particles do not trap hydrogen at all at room temperature [11] unless at high temperatures. The incoherent TiC particles as shown in Fig.5 that remained after austenitization absorb hydrogen from the environmental atmosphere. The hydrogen trapped by the incoherent TiC, which is characterized by a desorption peak at around 600 °C, depends on the amount [8] of undissolved TiC particles (Fig.6a). At room temperature, the incoherent TiC particles cannot be charged with hydrogen even with a long charging time and a high current density (Fig.6b). The inability of hydrogen trapping of incoherent TiC particles at low temperatures is explained by the trap site of carbon vacancies which requires high activation energy for both trapping and detrapping of hydrogen.

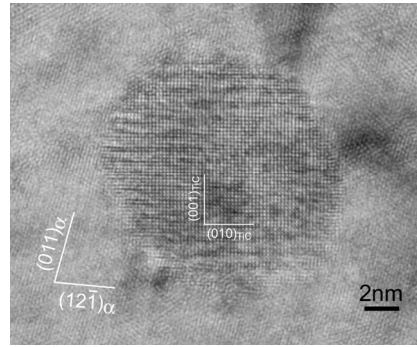


Figure 5: An incoherent particle in the 0.05C-0.20Ti-2.0Ni steel.

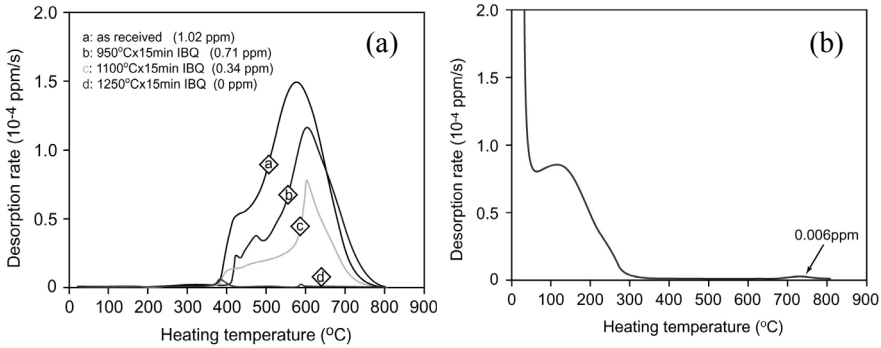


Figure 6: TDS analysis of hydrogen trapped by incoherent TiC particles in the as-received 0.05C-0.20Ti-2.0Ni steel. (a) Analysis without cathodic charging after austenitization at various temperatures, and (b) analysis after vacuum degassing at 950 °C and prolonged cathodic hydrogen charging at a high current density.

Here, the possibility of incoherent precipitate/matrix interface as a trap site cannot be excluded completely, but it must be very weak and be small in quantity and its desorption peak cannot be distinguished from those at about 120 °C from other kinds of trap sites like grain boundary and dislocation (Fig.6b).

Hydrogen trapping of NbC and VC precipitates

NbC and VC nano-precipitates show a disk-like appearance like that of TiC and maintain the Baker-Nutting orientation relationship with ferrite. However, their diameters differ noticeably compared to that of TiC although they all have almost the same thickness (Fig.7) [12]. The diameter of the disk-shaped carbide is proportional to the reciprocal of its lattice misfit (Fig.8a), which means that there is the same number of misfit dislocations on the broad face of each particle if the same misfit dislocation configuration is assumed (Fig.8b). The physical meaning for this relation in not clear now. It seems that formation of misfit dislocation on the broad face controls the growth rate of the semi-coherent particle.

Fig.9 shows the TDS spectra obtained after hydrogen charging to saturation for the three steels tempered at 700 °C containing the NbC, TiC and VC precipitates, respectively. Contrary to TiC, NbC and VC do not have a desorption peak at around 600 °C. The reason for this difference has not been clarified yet. One possibility is that the latter two carbides are also able to trap hydrogen at their carbon vacancies but trapping does not happen at the present charging condition. The precipitates contribute significantly to the desorption peaks below 350 °C. The hydrogen trapping ability of the alloy carbides varies in the descending order of NbC > TiC >> VC. This finding shows a good agreement with the above prediction based on the density of misfit dislocations on the broad face of the disk-shaped alloy carbide precipitate.

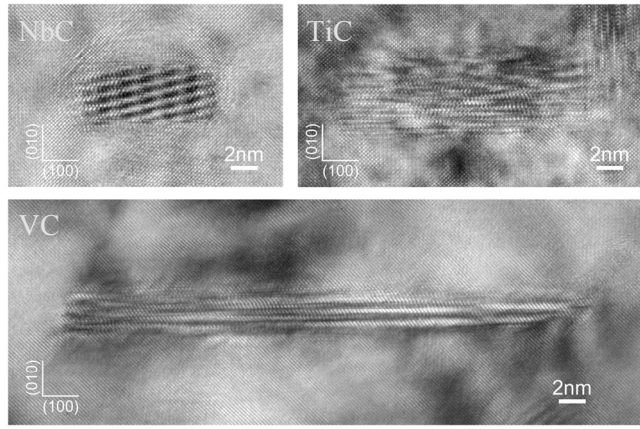


Figure 7: HRTEM micrographs of NbC, TiC and VC precipitates in the 0.05C-0.41Nb-2.0Ni, 0.05C-0.20Ti-2.0Ni and 0.05C-0.24V-2.0Ni steels quenched and tempered at 700 ºC, respectively.

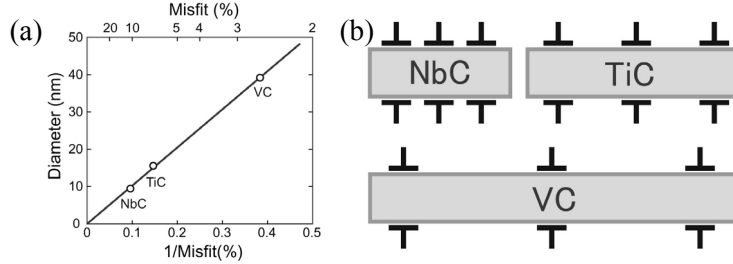


Figure 8: Size and morphology of disk-like NbC, TiC and VC in the steels tempered at 700 ºC. (a) Relationship between diameter and lattice misfit, and (b) illustration of misfit dislocations on the broad faces of the precipitates.

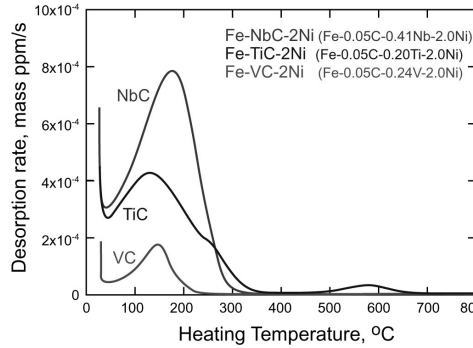


Figure 9: TDS spectra for 0.05C-0.41Nb-2.0Ni, 0.05C-0.20Ti-2.0Ni and 0.05C-0.24V-2.0Ni steels quenched and tempered at 700 ºC. Charging time: 48h.

The results obtained in this study emphasize that the hydrogen trapping property, i.e. hydrogen trapping capacity and the hydrogen-precipitate interaction energy, depends considerably on the type of alloy carbides, precipitate/ferrite interfacial character and the crystal defects within the precipitate. Composition selection and microstructural control of alloy carbides may offer a variety of options for the application of alloy carbides as hydrogen trap sites in the development of hydrogen embrittlement resistant steels.

Conclusions

1. (Semi-)coherent TiC precipitates trap hydrogen at precipitate/ferrite interfaces. The core of misfit dislocations on the broad face of the disk-shaped precipitate is supposed to act as hydrogen trap sites at a low hydrogen concentration.
2. Incoherent TiC particle is unable to trap hydrogen at ambient temperature. High temperatures are required for incoherent TiC particle to trap and detrap hydrogen. The carbon vacancies are probably the trap sites for hydrogen in incoherent TiC particles
3. The hydrogen trapping ability of (semi-)coherent alloy carbides varies in the descending order of NbC > TiC >> VC. Unlike TiC, neither NbC nor VC show any desorption peak at high temperatures around 600 °C.

REFERENCES

1. Pressouyre G.M. and Bernstein I.M., Metall. Trans. A, 9A(1978), pp.1571-1580.
2. Lee H.G. and Lee J.Y., Acta Metall., 32(1984), pp.131-136.
3. Lee S. M. and Lee J.Y., Acta Metall., 35(1987), pp.2695-2700.
4. Wei F.G., Hara T. and Tsuzaki K., Metall. Mater. Trans. B, 35B(2004), pp.587-597.
5. Wei F.G., Hara T., Tsuchida T. and Tsuzaki K., Iron Steel Inst. Jpn. Int., 43(2003), pp.539-547.
6. Pressouyre G.M. and Bernstein I.M., Metall. Trans. A, 10A(1979), pp.1571-1573.
7. Asaoka A., Lapasset G., Aucouturier M. and Lacombe P., Corrosion, 34(1978), pp.39-47.
8. Wei, F.G. and Tsuzaki K., Metall. Mater. Trans. A, 37A(2006), pp.331-353.
9. Wei F.G., Hara T. and Tsuzaki K., Phil. Mag., 84(2004), pp.1735-1751.
10. Wei F.G. and Tsuzaki K., Ferrum (Bulletin of the Iron and Steel Institute of Japan), 12(2007), pp.766-770.
11. Wei F.G. and Tsuzaki K., Metall. Mater. Trans. A, 35A(2004), pp.3155-3163.
12. Wei F.G. and Tsuzaki K., Second Place Award of International Metallographic Contest, Class 3: Electron Microscopy – Transmission and Analytical, 2008, http://www.metallography.com/ims/contest.htm.

Effects of Hydrogen on Materials
Proceedings of the 2008 International Hydrogen Conference
Brian Somerday, Petros Sofronis, Russell Jones, editors, p 456-463
Copyright © 2009 ASM International®
All rights reserved.
www.asminternational.org

HYDROGEN TRAPPING CHARACTER OF NANO-SIZED NbC PRECIPITATES IN TEMPERED MARTENSITE

Fu-Gao Wei
Structural Metals Center, National Institute for Materials Science
1-2-1 Sengen, Tsukuba, Ibaraki 305-0047, JAPAN
Now at Technology Development Department, YAKIN Kawasaki Co., Ltd.
4-2 Kojima-cho, Kawasaki-ku, Kawasaki, Kanagawa 210-8558, JAPAN

Kaneaki Tsuzaki
Structural Metals Center, National Institute for Materials Science
1-2-1 Sengen, Tsukuba, Ibaraki 305-0047, JAPAN

ABSTRACT

The hydrogen trapping character of NbC nano-particles in a 0.05C-0.41Nb-2.0Ni tempered martensitic steel was investigated by hydrogen thermal-desorption spectrometry (TDS) analysis and atomic-level microstructural observation. The steel trapped the most hydrogen after tempering at 600 ºC, and the trapped hydrogen decreased with increasing tempering temperature. The precipitation of NbC nanoparticles is responsible for the sharp increase at 600 ºC. The coarsening of precipitates reduces the amount of trapped hydrogen. The TDS analysis of the same specimen charged with various levels of hydrogen concentration indicated that the apparent activation energy for desorption from NbC precipitates is dependent on hydrogen concentration. Hydrogen trap sites are discussed in terms of the character of the NbC/matrix interface and the crystal defects present at and around the interface.

INTRODUCTION

Alloy carbides which are known for their secondary hardening effect in steels are attracting more and more attention for their additional beneficial effect on resistance to hydrogen embrittlement. Alloy carbides are believed to act as hydrogen trap sites which prevent hydrogen from moving to stress concentration regions. Yamasaki and Takahashi [1] found that the addition of vanadium reduces susceptibility to hydrogen embrittlement. They attributed the improvement to the precipitation of vanadium carbide which supposedly traps the harmful hydrogen in the steel. Recently, our group along with some other groups carried out a systematic investigation of the hydrogen trapping property of alloy carbides in steels, mainly for VC [2-4] and TiC [5]. However, little is known about NbC. Thus, the primary objective of this study is to investigate the hydrogen trapping/detrapping behavior of NbC.

A good trap requires not only the hydrogen trapping capacity but also moderate interaction energy [6]. Too weak a trap is not able to control diffusive hydrogen. On the other hand, too strong a trap is likely to absorb hydrogen irreversibly until saturation and fails to trap additional hydrogen. A trap associated with a specific kind of precipitate or other crystal defects has usually been described with a fixed characteristic interaction energy [7]; however, a previous experiment [8] suggested that the apparent activation energy for hydrogen desorption from a certain precipitate depends on the level of the amount of hydrogen, which means that a precipitate may involve a series of trap sites with different interaction energies. The distribution of the interaction energies associated with a type of crystal defect was defined as a site energy distribution by Kirchheim [9]. Therefore, this study puts an additional emphasis on the hydrogen concentration dependence of activation energy for hydrogen detrapping from the NbC precipitate. The hydrogen content was adjusted by exposing the fully charged specimen to vacuum for a period of time before thermal desorption spectrometry.

EXPERIMENTAL

A high purity 0.05C-0.41Nb-2.0Ni steel (Fe-NbC-2Ni) was used for study. This steel contains the same molar fraction of MX-type carbide as in the 0.05C-0.20Ti-2.0Ni steel (Fe-TiC-2Ni) in a previous work [5]. The ratio of Nb to C was adjusted to obey the stoichiometry of NbC without an excess of either Nb or C. The heat treatment, hydrogen charging and TDS analysis of the present steel were all the same as those for the 0.05C-0.20Ti-2.0Ni steel in the previous study. The major conditions were: (1) quenching from 1350ºC and tempering at 300 ~ 800 ºC for 3 h, (2) dimension of specimen for TDS analysis: ϕ5x40 mm, (3) cathodic charging of hydrogen in a (3 mass% NaCl + 0.3 mass% NH_4SCN) aqueous solution at a current density of 1 A/m^2 for a short time of 1h to investigate the deep traps associated with alloy carbide precipitates, (4) hydrogen analysis by TDS at a heating rate of 100 ºC/h, (5) estimation of the activation energy for hydrogen desorption from the traps by fitting the experimentally measured desorption spectrum to the Kissinger's first-order reaction kinetic formula [5], and (6) microstructural observation by means of high resolution transmission electron microscope (HRTEM).

An additional experiment was performed in the present study to evaluate the desorption kinetics of hydrogen from the hydrogen traps. First, the specimen was cathodically charged with hydrogen in the same condition described except for the charging time. The charging time was 48 h which was long enough for the specimen to be saturated with hydrogen. Next, the charged specimen was immediately moved in vacuum in the spectrometer for a series of time at room temperature. The desorption rate of hydrogen was recorded continuously. Finally, the specimen was heated to start the TDS analysis. The total hydrogen was calculated by taking the sum of the hydrogen released at room temperature before heating and that during the TDS analysis. The specimen tempered at 700 ºC was selected for this investigation.

RESULTS AND DISCUSSION

Vickers Hardness

The change in the Vickers hardness (49 N load) with tempering temperature is shown in Fig.1. The data of the TiC precipitate in the previous paper [5] is plotted for comparison. The secondary hardening peak appears at 550 ºC, which is similar to that of the TiC-precipitated steel; however, the hardness is higher than that of TiC over the entire tempering temperature range.

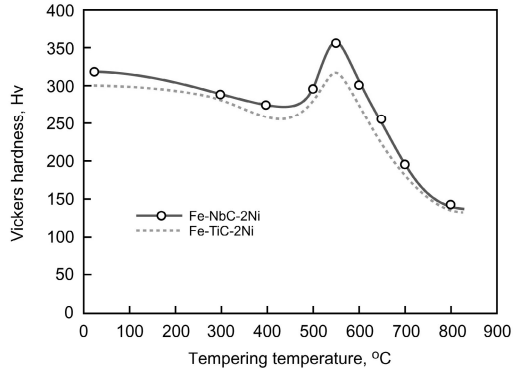


Figure 1: Change in Vickers hardness with tempering temperature.

HRTEM observation

A full lath martensitic microstructure containing 100% lath martensite was obtained after quenching from 1350 °C. Only NbC was observed to precipitate on tempering. No cementite was observed. Disc-like NbC particles that precipitated at 600 ºC and 700 ºC are shown in Fig.2 with their broad faces on the {100} ferrite planes parallel to the view direction. The NbC precipitates adopted the Baker-Nutting orientation relationship (B-N OR), i.e. $(100)_{NbC}//(100)_{\alpha}$, $[011]_{NbC}//[001]_{\alpha}$ with the ferrite matrix. Characteristic Moiré fringes usually appeared on the NbC particles. The configuration of the fringes indicated a slight deviation of several degrees from the exact B-N OR between the precipitate and its ferrite matrix [10]. This phenomenon is similar to that of the TiC precipitation. The deviation is more obvious in the coarsened NbC precipitate in the specimen tempered at 800 ºC as shown in Fig.3. The ferrite is orientated exactly to <100> while the NbC precipitate deviates by an angle that is sufficient to make the <110> lattice fringes of the precipitate almost fade out. The interface becomes curved, which is different from that of TiC, as the latter precipitate kept its disc-like shape at the same tempering temperature.

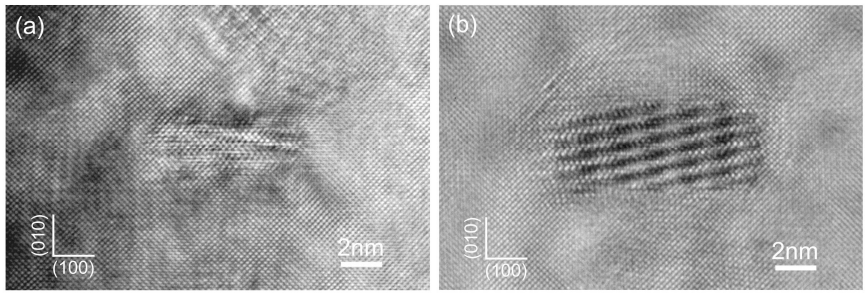


Figure 2: HRTEM micrographs of NbC precipitates in the specimens tempered at (a) 600 ºC and (b) 700ºC.

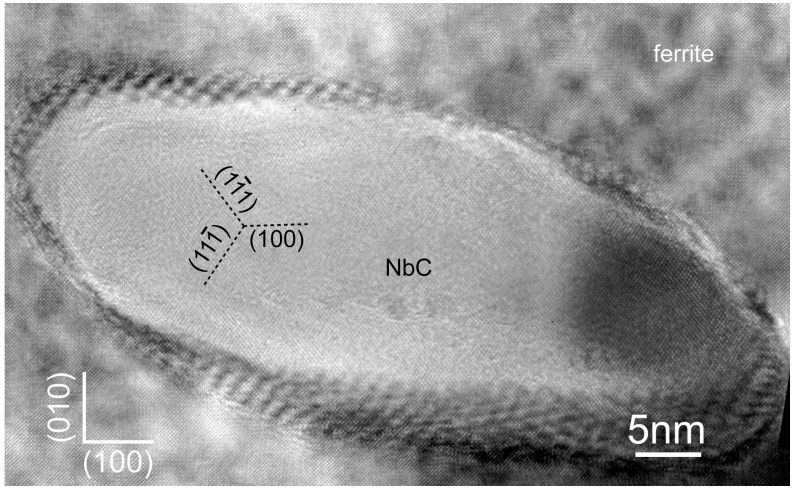


Figure 3: HRTEM micrograph of a NbC precipitate in the specimen tempered at 800ºC.

TDS analysis

Selected hydrogen desorption spectra for specimens charged with hydrogen for 1 h are shown in Fig.4. Only a small amount of hydrogen is trapped by the as-quenched specimen without any precipitates. The desorption peak is located at about 80ºC and no desorption peak is detected above 200 ºC. A sharp increase in both the hydrogen amount and the desorption peak temperature occurs on tempering at 600 ºC. The sharp increase corresponds to the precipitation of nano-sized NbC particles. Tempering at higher temperatures reduces the height of the desorption peak and shifts the desorption peak slightly to lower temperatures. One major difference between NbC and TiC with regard to the hydrogen desorption spectrum is that the desorption peak that occurs at a high temperature of around 600ºC does not appear in the case of NbC.

The amount of trapped hydrogen after a 1 h charging is plotted against tempering temperature as shown in Fig.5. The data for the 0.05C-0.20Ti-2.0Ni steel [5] is also included. The 0.05C-0.41Nb-2.0Ni steel shows a slightly higher hydrogen content over the entire tempering temperature range but shows the same trend of hydrogen trapping ability as that of the 0.05C-0.20Ti-2.0Ni steel. After showing a slight decrease on tempering at lower temperatures, both the 0.05C-0.41Nb-2.0Ni and the 0.05C-0.20Ti-2.0Ni steels begin to increase the amount of trapped hydrogen and reach a maximum value at 600 ºC. Above 600 ºC, the hydrogen content decreases with increasing tempering temperature. The variation of hydrogen content above 500 ºC can be explained by the precipitation of NbC particles. The hydrogen content starts to increase as the NbC precipitation takes place at around 500 ºC and shows the highest value at 600 ºC where the NbC precipitation is considered to be completed. Note that the peak of the hydrogen content does not coincide with that of hardness shown in Fig.1 with regard to tempering temperature. The latter is 50 ºC lower. A possible interpretation for the difference is that the size of the precipitates has different effects on hydrogen trapping and hardness. Hardness shows more effect at smaller size. The coarsening of precipitates leads to a decrease in hydrogen content like hardness. This finding clearly indicates that the amount of trapped hydrogen is basically dependent on the precipitate/matrix interface. In our previous study [5], hydrogen that was deeply trapped in the TiC semi-coherent precipitate after a 1 h charging was suggested to be located at the broad face of the disc-like TiC precipitate and more specifically at the misfit dislocation lines. As a matter of fact, our small angle neutron scattering experiment [11] using the specimen tempered at 600 ºC suggested that hydrogen may be located at the precipitate/matrix interface.

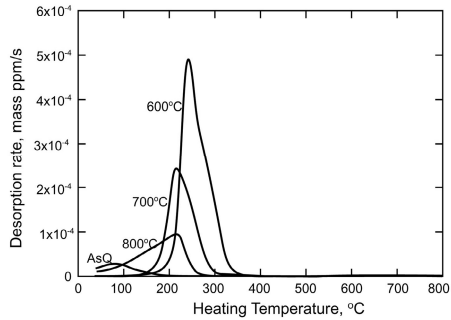


Figure 4: Selected TDS spectra for the as-quenched specimen and those tempered at 600, 700 and 800 ºC. 1 h hydrogen charging. Heating rate: 100ºC/h.

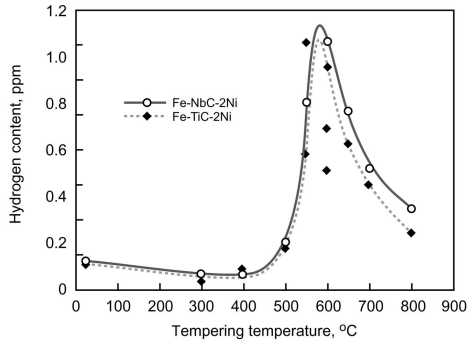


Figure 5: Change in hydrogen content with tempering temperature. 1 h hydrogen charging.

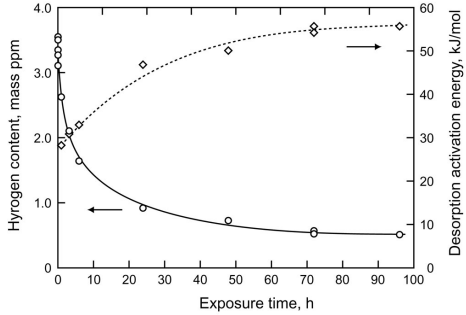


Figure 6: The content of hydrogen remaining after exposure in vacuum and the corresponding apparent desorption activation energy as a function of exposure time. Specimen tempered at 700 ºC. 48 h charging before exposure.

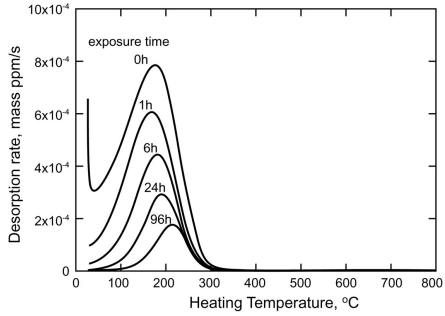


Figure 7: TDS spectra measured after exposure in vacuum for different times. Specimen tempered at 700 ºC. 48 h charging before exposure. Heating rate: 100ºC/h.

The results of the TDS analysis of hydrogen desorption in vacuum for the specimen tempered at 700 ºC are shown in Figs. 6 and 7. The specimen absorbs as much as 3.3 ppm hydrogen after a 48 h charging. The trapped hydrogen is released quickly at the early stage of exposure as shown in Fig.6.; however, the desorption rate becomes fairly slow after a 24 h exposure. Over 0.5 ppm hydrogen remains after a 96 h exposure. Typical TDS spectra obtained after exposure are shown in Fig.7. The height of the desorption peak decreases with exposure time. Asymmetrical decreasing rate with respect to the peak temperature was observed. The lower temperature part of the desorption peak decreases faster than the higher temperature part. The peak temperature is also shown to shift to higher temperature as the exposure time increases. This result suggests that the weakly trapped hydrogen is released first while the strongly trapped hydrogen remains behind. Fitting each desorption spectrum provides the apparent desorption activation energy for the corresponding exposure time. These values are shown in Fig.6. The apparent activation energy increases from 28 kJ/mol before exposure and doubles its value after a 96 h exposure.

Figure 5 shows that the major part of the trapped hydrogen in tempered martensite is known to derive from the NbC precipitates. The traps associated with the tempered martensite matrix, like the grain boundary, lath boundary and dislocation, contribute only a little fraction of the total trapped hydrogen and their interaction with hydrogen is weak compared to that of the NbC precipitates. The NbC precipitate shows a higher interaction with hydrogen; however, the interaction does not seem to be constant. Precipitation can generate various trap sites with different interaction intensities with hydrogen. These sites may be the precipitate/ferrite interface, the coherency strain region surrounding the precipitate and even the crystal defect within the precipitate. The distribution of all these sites with different interaction energies, which is also called site energy distribution [9], determines the trapping/detrapping characteristics of the NbC precipitate. During exposure in vacuum, hydrogen is released rapidly from the weak sites but sluggishly from the strong sites. For this reason, the apparent activation energy for hydrogen desorption from the NbC precipitates changes continuously with hydrogen content, i.e., the longer the exposure time, the higher the apparent activation energy.

CONCLUSION

Hydrogen absorption and desorption from tempered martensite in a 0.05C-0.41Nb-2.0Ni steel have been studied by means of thermal desorption spectrometry after a detailed microstructural observation. The following conclusions can be drawn.

1. Precipitation of NbC in tempered martensite results in a rapid increase in hydrogen trapping ability with a maximum hydrogen content at a tempering temperature of 600 ºC. The trapped hydrogen content decreases with increasing tempering temperature due to the coarsening of NbC precipitate particles.

2. Hydrogen trapping ability of NbC is slightly higher than that of the TiC precipitate.
3. The NbC precipitate consists of hydrogen trap sites of various interaction energies. For this reason, the apparent activation energy for hydrogen desorption from the NbC precipitates depends on the total amount of the hydrogen remaining trapped.

REFERENCES

1. Yamasaki S. and Takahashi T., "Evaluation method of delayed fracture property of high strength steels", Tetsu-to-Hagane, vol. 83(1997), pp.454-459.
2. Tsuchida T., Hara T. and Tsuzaki K., "Relationship between microstructure and hydrogen absorption behavior in a V-bearing high strength steel", Tetsu-to-Hagane, vol. 88(2002), pp.771-78.
3. Asahi H., Hirakami D. and Yamasaki S., "Hydrogen trapping behavior in Vanadium-added steel", ISIJ Intl., vol.43(2003), pp.527-533.
4. Yamasaki S. and Bhadeshia HKDH, "M_4C_3 precipitation in Fe-C-Mo-V steels and relationship to hydrogen trapping", Proc. R. Soc. A, vol.462(2006), pp.2315-2330.
5. Wei, F.G. and Tsuzaki K., "Quantitative analysis on hydrogen trapping of TiC particles in steel", Metall. Mater. Trans. A, vol.37A(2006), pp.331-353.
6. Wei, F.G., Hara T. and Tsuzaki K., "Design of nanosized TiC precipitates for trapping detrimental hydrogen in high strength steels", Trans. Mater. Res. Soc. Japan, vol. 29(2004), pp.3473-3476.
7. Hirth J. P., "Effects of hydrogen on the properties of iron and steel", Metall. Trans. A, vol.11A(1980), pp. 861-90.
8. Takai K., Obata T. and Nagoshi S., "Change in hydrogen trapping sites in high-strength steels during absorption and desorption of hydrogen", CAMP-ISIJ, vol.16 (2003) , pp.567-567.
9. Kirchheim R., "Hydrogen solubility and diffusivity in defective and amorphous metals", Prog. Mater. Sci., vol.32(1988), pp.261-325.
10. Wei F.G., Hara T. and Tsuzaki K., "High-resolution transmission electron microscopy study of crystallography and morphology of TiC precipitates in tempered steel", Phil. Mag., 84(2004), pp.1735-1751.
11. Ohnuma M., Suzuki J., Wei F.G. and Tsuzaki K., "Direct observation of hydrogen trapped by NbC in steel using small-angle neutron", Scr. Mater., 58(2008), pp.142-145.

Effects of Hydrogen on Materials
Proceedings of the 2008 International Hydrogen Conference
Brian Somerday, Petros Sofronis, Russell Jones, editors, p 464-468
Copyright © 2009 ASM International®
All rights reserved.
www.asminternational.org

HYDROGEN TRAPPING AT DISLOCATIONS IN PALLADIUM AT LOW TEMPERATURE: RESULTS FROM INELASTIC NEUTRON SCATTERING AND ADVANCED COMPUTATIONS

Brent J. Heuser and Hyunsu Ju
University of Illinois, Dept. Nuclear, Plasma, and Radiological Engineering, Urbana, IL USA

Dallas R. Trinkle
University of Illinois, Dept. Materials Science and Engineering, Urbana, IL USA

Terrence J. Udovic
NIST Center for Neutron Research, National Institute of Standards and Technology, Gaithersburg, MD USA

ABSTRACT

Hydrogen trapping at dislocations in deformed $PdH_{0.0008}$ has been investigated with a combination of incoherent inelastic neutron scattering (IINS) and advanced computational techniques. The results from the IINS measurements indicate the formation of the hydride phase at dislocations at 4 K. Density functional theory results of a relaxed lattice containing an edge dislocation split into partials exhibit large local volumetric dilatation associated with hydrogen in near-core interstitial sites.

INTRODUCTION

Hydrogen trapping at dislocations in Pd has been of interest for many decades [1-5] and is further investigated here with an experimental technique (IINS) that has not found wide-spread use in the study of trapped solutes. IINS has excellent sensitivity to hydrogen in metals because of the very large incoherent bound atom cross section (80.3 barns) of the proton. In addition, simple metals such as Pd that contain one atom per primitive cell do not exhibit optic phonon modes. In this case, the addition of hydrogen leads to optic modes which can be exploited for study.

Complementary information has been provided by density functional theory (DFT) results in which an edge dislocation, split into two partial dislocations has been relaxed. Insertion of one hydrogen atom into the partial dislocation core demonstrates that a large lattice dilatation occurs.

EXPERIMENTAL RESULTS

The IINS measurements were performed with the Filter-Analyzer Neutron Spectrometer (FANS) at the NIST Center for Neutron Research (NCNR) [6]. This instrument uses a neutron low-energy band-pass filter made up of Be, Bi, and graphite to preclude all neutrons above ~ 2 meV before detection. An IINS measurement with this instrument consists of scanning the incident energy on to the sample while recording the intensity passed by the filter with a bank of neutron detectors that covers 1.13 steradians. Inelastic data recorded with the FANS represent an integration over a significant wavevector transfer range, both because of the large detector solid angle and because polycrystalline samples are typically used, and are largely incoherent measurements (as opposed to coherent inelastic measurements). The intensity from IINS is proportional to the vibrational density of states (DOS) of the system, in this case interstitial hydrogen [7].

The sample consisted of 21 grams of polycrystalline Pd supplied by Alpha Aesar [8]. This material was in the form of a sheet 0.25 mm thick that was cold rolled in the as-received condition. The sample material was subsequently cycled across the hydride miscibility gap twice to generate additional dislocation defects beyond those induced by cold rolling—the sample in this state is referred to as "deformed" below. Cycling was performed at 60 ºC at a H_2 gas pressure of approximately 400 Torr. After three IINS measurements of the deformed sample, the sample material was annealed under vacuum for 4.5 hours at 900 ºC—the sample in this state is referred to as "annealed" below. In all, four IINS measurements were performed with this sample material: deformed $PdH_{0.63}$ at 4 K, deformed $PdH_{0.0008}$ at 4 K, deformed $PdH_{0.0008}$ at 295 K, and annealed $PdH_{0.015}$ at 295 K.

The two 4-K measurements are compared in Fig. 1a, while the two 295-K measurements are compared in Fig. 1b. Of key importance in these comparisons is 1) the correspondence of the primary peaks in each DOS at a given temperature and 2) the shift in peak energy of the deformed $PdH_{0.0008}$ induced by heating from 4 K to 295 K. The primary peak in the $PdH_{0.63}$ 4 K measurement corresponds to the transverse optic mode observed in the Pd hydride phonon dispersion curves. The transverse optic mode in Pd hydride has very little dispersion [9] and consequently leads to a peak in the IINS spectrum. The fact that the primary peak in the 4 K deformed $PdH_{0.0008}$ spectrum, albeit more poorly defined, occurs at the same energy is significant. This is proof that the hydrogen in this sample is in the hydride phase at 4 K. Given the very low hydrogen concentration and heavily deformed sample matrix, the deformed $PdH_{0.0008}$ spectrum represents solely that of hydrogen trapped at dislocations. Further, since the measurement was performed at 4 K, it is expected that only the strongest, near-core dislocation trap sites are occupied. Upon warming, the peak in the deformed $PdH_{0.0008}$ spectrum shifts to higher energy and closely matches that of the annealed $PdH_{0.015}$, which, at 295 K, represents the solid solution phase of Pd. This peak shift is therefore expected if the trapped hydrogen undergoes a hydride to solid solution phase transformation from 4 K to 295 K.

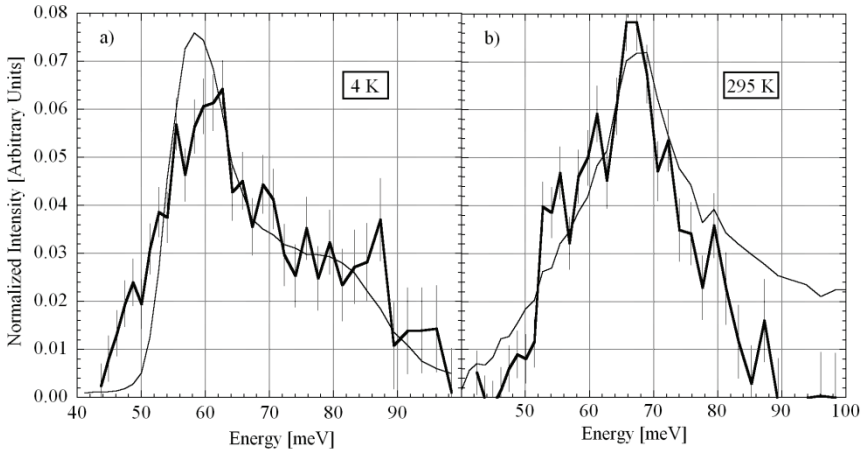


Figure 1. Comparison of the four IINS measurements presented in this work. Apart from multiple phonon background events, only hydrogen-induced optic modes occur in this energy region. The deformed $PdH_{0.63}$ (thin line) and deformed $PdH_{0.0008}$ (thick line) at 4 K are compared in a), while the annealed $PdH_{0.015}$ (thin line) and deformed $PdH_{0.0008}$ (thick line) at 295 K are compared in b).

COMPUTATIONAL RESULTS

The goal of the DFT work is to provide a computational analog to the IINS measurements. Given that the IINS measurements and corresponding vibrational DOS are of interstitial hydrogen trapped at dislocations, the DFT treatment must include both the dislocation trapping sites and interstitial hydrogen. Using the local density approximation (LDA) for the exchange correlation potential and accurate projector augmented-wave (PAW) treatment of the ion cores of Pd and H yielded lattice constant, elastic moduli, and the hydrogen-hydrogen separation distance all in good agreement with experiment for alpha-Pd, alpha-Pd with a H interstitial, and beta-$PdH_{0.625}$. The Pd phonon dispersion curves and vibrational DOS were in very good agreement as well. To account for the presence of dislocation trapping sites, a Pd simulation cell with 382 atoms containing a single edge dislocation was created and relaxed using flexible boundary condition methods that correctly treat the long-range strain field of a dislocation. During relaxation, the perfect dislocation split into two partials in the slip plane. The volumetric lattice strains—computed from changes in nearest-neighbor distances—associated with the two partial dislocations, calculated at both the Pd site and the octahedral interstitial site, are shown in Figure 2.

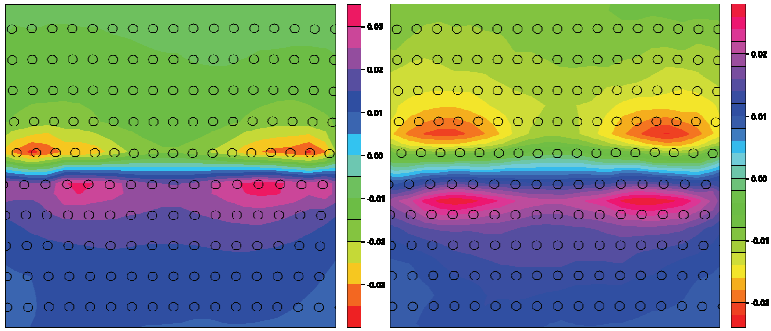


Figure 2. Calculated volumetric lattice strain at Pd atom sites (left) and octahedral sites (right) determined from ab initio relaxation. Compressive strains exist above the horizontal glide plane (plane bisecting both figures in the middle), while tensile strains exist below. The circles represent the relaxed Pd atomic positions.

Relaxation of this system with a single hydrogen atom residing at a core trapping site—chosen as the octahedral site with the largest tensile strain—is shown in Figure 3. The local volumetric dilatation associated with this single hydrogen atom is large (0.089 at the hydrogen octahedral site), as is the dilatation at the first nearest-neighbor octahedral site (0.045). These are significantly larger than the corresponding calculated values for H in an octahedral site in fcc-Pd, 0.046 and 0.025, respectively, and indicate that the near-core trapping environment is more elastically compliant. Given the large volume dilatation associated with the hydride phase ($\Delta V/V \sim 0.12$ in Pd), the compliant dislocation environment is anticipated to adequately accommodate the hydride phase formation.

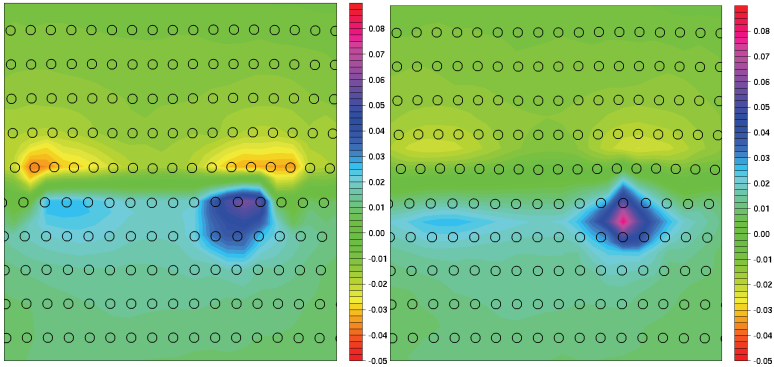


Figure 3. Calculated volumetric lattice strain at Pd atom sites (left) and octahedral sites (right) determined from ab initio relaxation of two partial edge dislocations with a single hydrogen atom placed just below the glide plane of the right-hand partial dislocation. Compressive strains exist above the glide plane, while tensile strains exist below. The large tensile strains associated with the hydrogen atom are shown as darker, then lighter contrast below the glide plane and to the right of center. The circles represent the relaxed Pd atomic positions.

CONCLUSIONS

The goal of this work was to investigate the low-temperature behavior of hydrogen trapped at dislocations in Pd. The vibrational DOS measured with IINS exhibits the signature of the hydride phase at 4 K and the solid solution phase at 295 K. Given the very low hydrogen concentration in the sample ([H]/[Pd]=0.0008), this temperature response is attributed to the trapped hydrogen undergoing a phase transformation (solid solution to Pd hydride) upon cooling to 4 K. DFT calculations support this conclusion via the large local tensile strains associated with hydrogen at near-core trapping sites.

ACKNOWLEDGMENTS

This work is supported by the NSF under Grant No. DMR-0804810.

REFERENCES

1. T.B. Flanagan, J.F. Lynch, J.D. Clewley, B. von Turkovich, J. Less-Common Met., Vol. 49, (1976), pp. 13.

2. R. Kirchheim, Scripta Metall., Vol. 44, (1980), pp. 905.

3. W.G. Wolfer and M.I. Baskes, Acta Metall., Vol. 33, (1985), pp. 2005.

4. B.J. Heuser and J.S. King, J. Alloys Compds., Vol. 261, (1997), pp.225.

5. D. Wang, H. Noh, S. Luo, T.B. Flanagan, J. Alloys Compds., Vol. 339, (2002), pp. 76.

6. T.J. Udovic, D.A. Neumann, J. Leão, and C.M. Brown, Nucl. Instrum. Methods Phys. Res. A, Vol. 517, (2004), pp. 189.

7. G.L. Squires, Introduction to the Theory of Thermal Neutron Scattering, Cambridge University Press, Cambridge, 1978.

8. Manufacturers are identified in order to provide complete identification of experimental conditions, and such identification is not intended as a recommendation or endorsement by the NIST.

9. J.M. Rowe, J.J. Rush, H.G. Smith, M. Mostoller, and H.E. Flotow, Phys. Rev. Lett., Vol. 33, (1974) pp. 1297.

Effects of Hydrogen on Materials
Proceedings of the 2008 International Hydrogen Conference
Brian Somerday, Petros Sofronis, Russell Jones, editors, p 469-476
Copyright © 2009 ASM International®
All rights reserved.
www.asminternational.org

COMPARING THERMAL DESORPTION SPECTROSCOPY WITH ELECTROCHEMICAL PERMEATION IN ORDER TO REVEAL THE HYDROGEN MANAGEMENT IN HIGH STRENGTH STEELS

***K. Verbeken*[1,2,*]**
[1]Department of Materials Science and Engineering, Faculty of Engineering, Ghent University (UGent), Technologiepark 903, B-9052 Ghent, Belgium
[2]Microstructure Physics, Max-Planck-Institut für Eisenforschung, Max-Planck-Strasse 1, 40237 Düsseldorf, Germany
**Postdoctoral fellow with the Fund for Scientific Research-Flanders (Belgium) (F.W.O. Vlaanderen)*

L. Duprez
ArcelorMittal Research Industry Gent, J.F.Kennedylaan 3, B-9060 Zelzate, Belgium

M. Verhaege
Department of Materials Science and Engineering*, Faculty of Engineering, Ghent University, Ghent, Belgium*

INTRODUCTION

High strength steels are frequently used in a wide variety of industrial applications because of their superior mechanical properties. During processing and in service, a lot of opportunities occur where the surface of the material is in contact with hydrogen, resulting in absorption of this element into the alloy. The entry of hydrogen into iron and its alloys is an undesired phenomenon because hydrogen is one of the most damaging species having a disadvantageous effect on the physical and mechanical properties of metals [1]. A tremendous amount of literature is available on the harmful effects of hydrogen in these alloys: considerable loss in mechanical properties (plasticity, ability to withstand static sustained loads and dynamic cyclic loading) and delayed hydrogen fracture such as hydrogen-induced cracking.
In general, one may distinguish the following processes in a metal/hydrogen system: (i) the entry of hydrogen from the surrounding environment into the metal, (ii) the transport (diffusion) of hydrogen inside the metal and (iii) the trapping of hydrogen at structural defects and/or formation of hydrides phases [2]. The efficiency of hydrogen entry is characterized by the concentration of hydrogen dissolved in the metal just beneath its surface. This hydrogen forms an interstitial solid solution, i.e. hydrogen atoms randomly distributed among metal atoms in the metal lattice. Since only this form of hydrogen is able to move through the metal according to the laws of

diffusion, it is called “diffusible” hydrogen. The transport of diffusible hydrogen is described by the lattice diffusion coefficient *D*. Additionally hydrogen can be “trapped” at dislocations, grain boundaries, non-metallic inclusions, etc., These forms of hydrogen are more tightly bound within the metal and they show lesser mobility. The trapped hydrogen and the trapping itself are characterized by the concentration (distribution) of hydrogen among different structural defects and phases. There are clearly two kinds of hydrogen traps, namely reversible and irreversible traps. Reversible trapping is associated with limited residence time of hydrogen at a specific temperature - generally with low interaction energy - while irreversible trapping is linked to a permanent residence of hydrogen at a specific temperature at sites with high activation energy [3].
Quantification of the hydrogen concentration in the material and assessment of trap sites interaction with hydrogen atoms are important to understand failure mechanisms of high strength steel constructions. To gather reliable information on the above processes, mainly two types of experimental techniques are used: the electrochemical permeation technique (EPT) and thermal desorption spectroscopy (TDS).
The electrochemical permeation technique is based on the pioneering work of Devanathan and Stachursky [4]. By this technique, the hydrogen content of the metal, the density of the trap sites, as well as the binding energy of the dominant reversible trap site can be measured. However, although two consecutive permeation transients allow to obtain a first indication of the amount of irreversible traps [5], it is most difficult to make a detailed distinction between the different types of traps. The thermal desorption method, involving measurements of hydrogen desorption flux under controlled temperature ramping conditions, is more beneficial since it can provide all the information derived from the method described above, including the amount and binding energies of a series of trap sites [6, 7].
Recently, ArcelorMittal installed in collaboration with Ghent University a hydrogen lab where both types of experiments can be performed. In this paper, results obtained by EPT are compared with those obtained by TDS. It is shown that both techniques contribute in a complementary way to the improvement of the understanding of hydrogen interaction with the tested high strength steels.

EXPERIMENTAL

Materials

Two materials were investigated in this study: a ferrite-martensite DP600 grade and pure iron as reference material. The chemical composition of these samples is shown in table 1, the optical microstructures are shown elsewhere [8].

Table 1: Chemical composition in wt % of the investigated materials

	C	**Mn**	**Si**	**Other**
Pure iron	0.0015	0.0003	0	< 0.002 Al, P
DP600	0.07	1.50	0.25	0.4%-0.8% Cr+Mo

TDS and EPT measurements

For the TDS experiments, samples with a diameter of 20 mm and a thickness of 0.7 mm have been electrolytically hydrogen charged using an arsenic aqueous solution (0.5g As_2O_3 – 0.25g $HgCl_2$ – 60ml H_2SO_4 / 1l H_2O). The samples were charged for 1h at room temperature, using a current density of 0.8mA/cm². After charging, the samples were cleaned with distilled water and acetone, the surface and edges were polished to remove the electrolyte and cleaned again with distilled water and acetone. After charging, the hydrogen content was determined via melt extraction with an H-MAT 2500® (Ströhlein GmbH & Co). TDS analysis of hydrogen charged samples was done by heating the samples from room temperature up to 900K at a heating rate of 400 K/h, detection of hydrogen was done using a quadruple mass spectrometer (Pfeiffer®). The tests were started when the pressure was less than $3.5x10^{-6}$ mbar. The time between the end of the charging and the start of the test was kept constant at 1h. A deconvolution of the thermal desorption spectrum was performed using the Peak Fitting Module in OriginPro. More details on sample preparation and analysis of the obtained spectra are given in [9, 10]

For the EPT experiments following procedure was used: The samples were cut as circular disks with a diameter of 20 mm from sheets of 1 mm thickness and prepared on 80 to 1200 SiC grit paper and polished with MD MOL (3 µm) and MD NAP (1 µm) in diamond polish. The resulting thickness was 0.5 mm. After cleaning the samples were stored in isopropanol. The membrane was palladinized on both sides and mounted between two electrochemical cells and operated at the detection side as described in [5]. The area exposed to the solutions was 1 cm^2.

A typical measurement cycle consists of following stages. After H-unloading of the membrane as described in ref 8, the membrane was charged at its entry side with hydrogen cathodically generated from 0.1 M NaOH at a current density i_c=2.5 mA/cm^2. After about 15 h, when the entry surface became sufficiently active and the permeation rate achieved a steady-state level, two cycles of increased loading at 6.75 mA/cm^2 (1.5 hours) followed by decreased loading at the original level (2.5 mA/cm^2 were performed. These cycles were followed by complete discharging (cathodic current switched of) and finally by a second stage of complete loading at 2.5 mA/cm^2. The successive partial decay and build-up transients were measured and analyzed to generate the desired data. All experiments were carried out at 25°C.

RESULTS AND DISCUSSION

Thermal Desorption Analysis of pure iron and DP600

Before the TDS measurements, the samples were charged. It was found elsewhere [10] that a charging time of 1h is enough to reach saturation. At saturation level, the DP steel contained about 6.8wppm hydrogen, while the pure iron contained

2.9 wppm hydrogen. Figure 1 shows the TDS curves for both materials. Between 300K and 500K, the spectrum of the DP600 grade seems to be composed of 2 subpeaks, i.e. at 334K and 374K, as indicated elsewhere in this volume [10]. Even a minor peak was observed around 559K, but this peak is discussed elsewhere together with the deconvolution of the TDS spectrum in Gaussian sub-peaks [10]. Comparing both curves, it is clear that DP600 holds, as can be expected, approximately eight times more hydrogen than pure iron. Extra results on pure Fe in various deformed (dislocation variation) and annealed (grain size variation) states indicated that the peaks in the DP600 spectrum cannot be attributed to dislocations and grain boundaries [9].

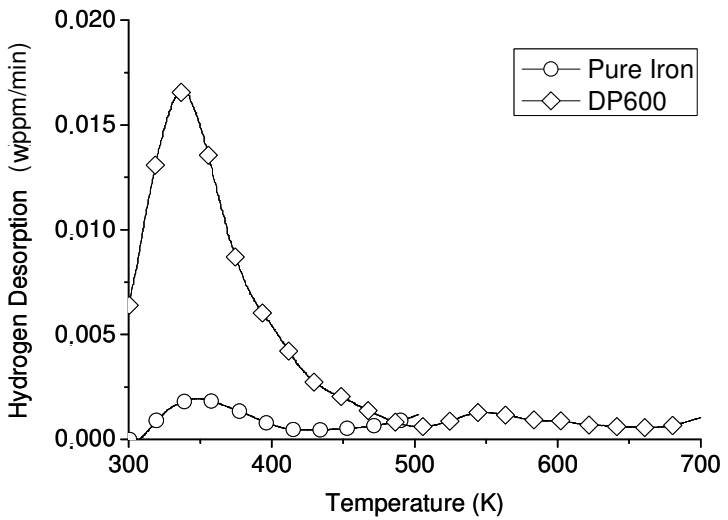


Figure 1: TDS curves for the indicated materials. Heating: from room temperature to 900 K. Heating rate: 400K/h.

Figure 2 shows the calculated H-profiles and total H-content as a function of desorption time. The calculations were done for a 1mm pure Fe sample, charged initially with a homogeneous hydrogen content of 3wppm, based on the diffusion coefficient for pure Fe. The graphs illustrate that hydrogen effusion from a ferritic steel is extremely fast. If no traps are present or only very weak traps, almost all hydrogen has left the sample after 10 minutes. Hence, when a sample is charged with hydrogen and subsequently measured by means of the TDS technique, the free and weakly trapped hydrogen signal will decrease considerably since a minimum time to achieve the necessary vacuum (1h in our case), allowing the hydrogen to effuse before. Here, the electrochemical technique comes into play, as it is very complementary to the TDS technique. Indeed, as during electrochemical permeation, the hydrogen is detected simultaneously with the charging, this technique allows to

investigate the effect of weaker traps, such as dislocations, grain boundaries, etc. In this way, the two techniques can be very complementary and allow to obtain a complete image of the H-trapping inside a steel grade.

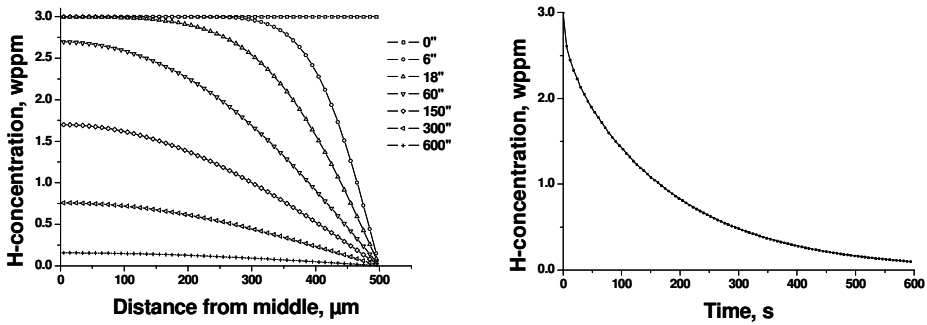


Figure 2: Calculated H-profiles and total H-content as a function of desorption time for a 1mm pure Fe sample, charged initially with a homogeneous H-content of 3wppm, based on the diffusion coefficient for pure Fe.

Electrochemical permeation tests (EPT) on pure iron and DP600

The raw data obtained for a complete EPT experiment, as mentioned above, on DP600 are shown in figure 3. As the permeation curves, corresponding to the increase of the cathodic current from 2.5mA/cm² to 6.75mA/cm² showed some unexpected variations, they are not discussed in this contribution. Emphasis is put on the transient curves corresponding to the increase of the cathodic curves from 0mA/cm² to 2.5mA/cm². As the steady state value of the curves was expected to be influenced by small variations in the quality of the Pd-coating on the entry side, the curves were normalized.

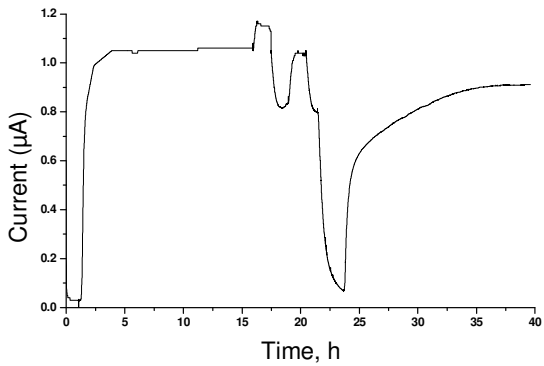


Figure 3: Evolution of exit current as a function of time for a complete EPT cycle

Figure 4 shows the first and second permeation curves for the pure Fe and the DP600 grade.
From the figure it is clear:

- The hydrogen permeation time is much higher for the DP600 (i.e. 610s) than for the pure Fe (i.e. 70s).
- The slope of the anodic current curve is much lower for the DP600 grade
- The second curve shifts to shorter times for both materials, which indicates the presence of traps that were filled with H during the first permeation.
- The shift is much more pronounced for the DP600, which again confirms the increased H trapping capacity of the DP600, as illustrated in the TDS results.
- The second part of the second permeation curve deviates, in such a way that the slope of the curve becomes much lower after some time. This makes it impossible to calculate the surface between the first and second permeation curve, which should be a quantitative indication of the amount of irreversible traps. Extra work is ongoing to explain this phenomenon.

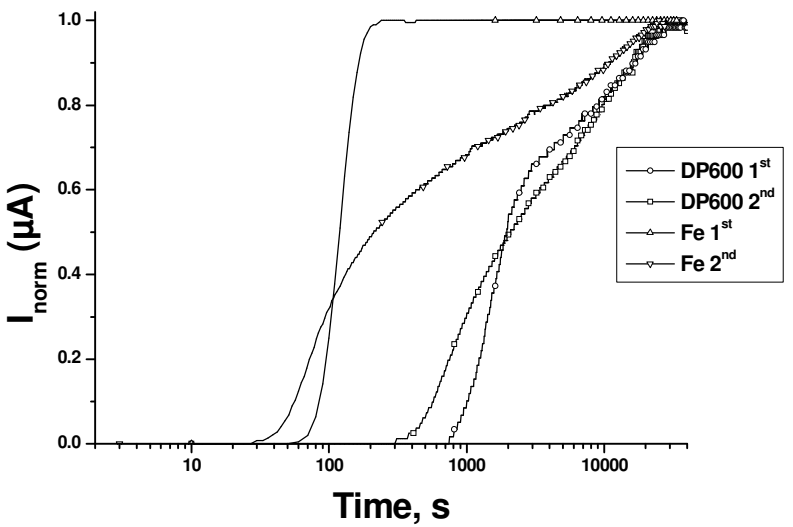


Figure 4: Normalised first and second permeation curve for the pure Fe and the DP600

Both observations confirm the higher trapping capacity of the DP600, as shown with the TDS technique. Table 2 shows the various parameters that can be calculated from the permeation curves, i.e. the permeation time, the hydrogen permeation index (H_2I),

the diffusion coefficient. From the results mentioned in this table, it is immediately clear that DP600 contains considerably more possible traps, since the values for t_p and t_{lag} are significantly higher for the DP steel. This is also illustrated by the difference in the approximate values for the diffusion coefficient, which are given in Table 2. It must be mentioned that the value for pure iron that is obtained here, i.e. 3.21 10^{-4} cm²/s is reasonably close to a value mentioned in literature, i.e. 10^{-4} cm²/s [11]. Similar values as the one we obtained were also reported by Hagi [12]. Finally, a good correlation is found between the ratios of the areas under the TDS curves for both materials and the ratio of the H_2I's for both materials. In both cases, this ratio was approximately eight. More mathematical analysis and more detailed experiments will be performed to calculate the diffusion coefficients from the shape of the transient curves and activation energies in a more detailed manner, when performing measurements at different temperatures. However, as mentioned in another contribution, data should be generated on simple, generic alloys, containing one main microstructural feature to come to a correct interpretation of the results.

Table 2: Parameters as calculated from the permeation curves of Figure 4, with D_{eff} = effective diffusion coefficient, taking into account the presence of reversible and irreversible traps, H_2I = hydrogen permeation index, d_1 = specimen thickness in cm, d_2 = specimen thickness in mm, t_p = time in min for hydrogen to reach the exit side (increase of the anodic current), t_{lag} = time to achieve a value of $J(t)/J_{ss}$=0.63 (s) [5]

	t_p [s]	t_{lag}[s]	$H_2I = t_p/d_2^2$ [min/mm²]	$D_{eff} = d_1^2 / 6t_{lag}$ [cm²/s]
Pure Fe (0.50mm)	70s = 1.17min	130s	4.64	$3.21 \cdot 10^{-4}$
DP600 (0.52mm)	610s = 10.17min	1750s	37.62	$2.58 \cdot 10^{-5}$

CONCLUSIONS

In this work, the complementarity of the thermal desorption technique and the electrochemical permeation technique was highlighted. As the thermal desorption technique requires a minimum time to start the linear heating, it is more difficult to visualize very weak H-traps as part of the hydrogen will be desorbed before the start of the measurement. The electrochemical permeation technique, performed with in-situ charging, can therefore bring extra information to the TDS results.
TDS and EPT measurements were done on pure Fe and a DP600 grade to compare the two methodologies. A nice correspondence between the results of both techniques; both methodologies confirm the much higher trapping capacity of the DP600 grade.

REFERENCES

1. Oriani, R.A., Hirth, J.P., Smialowski, M. (Eds.), Hydrogen Degradation of Ferrous Alloys, Noyes Publications, Park Ridge (NJ, 1985).
2. Zakroczymski, T., "Adaptation of the electrochemical permeation technique for studying entry, transport and trapping of hydrogen in metals," *Electrochemica Acta*, Vol. 51 (2006),pp. 2261-2266.
3. Mamani, S.C., "Study of hydrogen permeation and diffusion in steels: predictive model for determination of desorbed hydrogen," Master thesis, University of Puerto Rico, Mayagüez campus (2005).
4. Devanathan, M.A., Stachursky, Z.O.J., *Journal of the electrochemical society*, Vol 111 (1964), p. 619.
5. ASTM designation G 148-97, "Standard practice for evaluation of hydrogen uptake, permeation and transport in metals by an electrochemical technique", ASTM, 100 Barr Harbor Drive, PO Box C700, West Conshohocken, PA, USA.
6. Turnbull, A., Hutchings, R.B., Ferriss, D.H., "Modelling thermal desorption of hydrogen from metals," *Materials Science and Engineering A*, Vol 238 (1997), pp. 317-328.
7. Tal-Gutelmacher, E., Eliezer, D., Abramov, E., "Thermal desorption spectroscopy (TDS)- Application in quantitative study of hydrogen evolution and trapping in crystalline and non-crystalline materials," *Materials Science and Engineering A*, Vol 445-446 (2007), pp. 625-631.
8. Duprez, L., Verbeken, K., Verhaege, M., "Effect of Hydrogen on the Mechanical Properties of Multiphase High Strength Steels," Proceedings Hydrogen 2008, accepted.
9. Pérez Escobar, D., Duprez, L., Verbeken, K., Verhaege, M., "Identification of the hydrogen trap sites in high strength steels," Proceedings Hydrogen 2008, accepted.
10. Pérez Escobar, D., Verbeken, K., Duprez, L., Verhaege, M., "Experimental evaluation of the hydrogen distribution in steel by thermal desorption spectroscopy," Proceedings Hydrogen 2008, accepted.
11. Gehrmann, F., Einfluβ der Nitride von V, Nb und Ti auf Diffusion und Löslichkeit von Wasserstoff in Eisen, Fortschritt Berichte VDI Reihe 5: Grund- und Werkstoffe, Nr. 350, VDI-Verlag Düsseldorf, 1994.
12. Hagi, H., "Diffusion coefficient of hydrogen in iron without trapping by dislocations and impurities," *Materials Transactions*, Vol. 35, No. 2 (1994), pp. 112-117.

Effects of Hydrogen on Materials
Proceedings of the 2008 International Hydrogen Conference
Brian Somerday, Petros Sofronis, Russell Jones, editors, p 477-484
Copyright © 2009 ASM International®
All rights reserved.
www.asminternational.org

EXPERIMENTAL EVALUATION OF THE HYDROGEN DISTRIBUTION IN STEEL BY THERMAL DESORPTION SPECTROSCOPY

***Diana Perez Escobar*[1]**
[1]*Department of Metallurgy and Materials Science, Faculty of Engineering, Ghent University (UGent), Technologiepark 903, B-9052 Ghent, Belgium*

***Kim Verbeken*[1,2,*]**
[1]*Department of Metallurgy and Materials Science, Faculty of Engineering, Ghent University (UGent), Technologiepark 903, B-9052 Ghent, Belgium*
[2]*Microstructure Physics, Max-Planck-Institut für Eisenforschung, Max-Planck-Strasse 1, 40237 Düsseldorf, Germany*
**Postdoctoral fellow with the Fund for Scientific Research-Flanders (Belgium) (F.W.O. Vlaanderen)*

***Lode Duprez*[3]**
[3]*ArcelorMittal Research Industry Gent, J.F.Kennedylaan 3, B-9060 Zelzate, Belgium*

***Marc Verhaege*[1]**
[1]*Department of Metallurgy and Materials Science, Faculty of Engineering, Ghent University (UGent), Technologiepark 903, B-9052 Ghent, Belgium*

ABSTRACT

Thermal desorption spectroscopy has been described in literature as an excellent tool to study the hydrogen distribution inside metals. Moreover, this technique allows to make a distinction between the different trap sites in the material based on calculations of the activation energy, *e.g.* grain boundaries are reversible trap sites, characterized by a low activation energy, while some precipitates, such as TiC, are irreversible trap sites, characterized by a high activation energy.
In the present work, samples of four different steels were cathodically charged at a constant current density of 0.8 mA/cm^2. A meticulous charging procedure was found to be necessary. After charging, the sample was placed into the thermal desorption spectroscope. A deconvolution of the spectra obtained allowed to determine the different peak temperatures. However, it was demonstrated that a correct interpretation of TDS spectra requires the knowledge of how the TDS spectra look like for generic alloys.

INTRODUCTION

Hydrogen is an omnipresent element, which can be introduced in steel during its production or during its use. The harmful consequences of the exposure of steel to a hydrogen containing environment was first discussed by Johnson [1]. It was shown in this work that hydrogen caused a decrease in ductility leading to the phenomenon of hydrogen embrittlement. Nowadays, high strength steels are increasingly used in hydrogen containing environments, which causes the problem of hydrogen induced cracking of these steels to be very relevant. [2]

The detrimental effect of hydrogen is closely related with the solubility and diffusivity of hydrogen in the steel matrix. On the one hand, the solubility of hydrogen is known to be rather low in ferritic steels [3]. On the other hand, once the hydrogen is absorbed, it has to move trough the crystal lattice by diffusion. Hydrogen because of its small size is an interstitial element with a relatively high diffusion rate in ferritic steels, even at room temperature.

The distribution of hydrogen inside the crystal lattice is, however, not homogeneous. Lattice defects, such as vacancies, substitutional elements, dislocations, grain boundaries and precipitates, create regions where the dissolved hydrogen atom can be in a lower energy state than in the normal interstitial positions. The binding energy E_B of hydrogen at these places is higher and the consequent longer stay of the hydrogen atom at these positions lowers the effective hydrogen diffusivity. These places are called hydrogen traps and the strength of the traps is determined by the binding energy. When increasing the temperature, the activation energy E_A for hydrogen to be released from the trap is reached and hydrogen can escape from the trap.

Pressouyre [4] made a classification of the possible traps and suggested that vacancies, alloying elements, dislocations and phase boundaries are possible traps. Podgurski and Oriani [5] showed that insoluble inclusions can also increase the hydrogen concentration above the solubility limit. Wei and Tsuzaki [6] demonstrated that there is a considerable difference between (semi) coherent TiC precipitates and incoherent TiC precipitates with respect to hydrogen trapping capacity, interaction energy with hydrogen and the possibility to absorb hydrogen from the environment. It was also found that the amount of hydrogen that can be kept in incoherent particles depends on their volume which strongly indicates that hydrogen is dissolved inside these particles. Pressouyre and Bernstein [7] mentioned in their work that the binding energy of TiC traps decreases with increasing degree of coherence with the matrix. The same authors also argued that a uniform distribution of small, irreversible hydrogen traps would offer a maximal resistance against hydrogen embrittlement. Big irreversible traps would be the most harmful because they considerably raise the risk for hydrogen embrittlement. Different literature sources [6-13] give values for the activation energy of different types of hydrogen traps. In the present work, it was aimed for to use Thermal Desorption Spectroscopy (TDS) to study the presence of hydrogen at different traps in various multiphase high strength steels. The charging procedure together with the complex microstructures of these high strength steels was

found to have a profound effect on the TDS spectra obtained and to influence the interpretation of these data.

EXPERIMENTAL PROCEDURE

Materials

Four different types of steel sheets were used. The chemical composition of these steels is summarized in Table 1. DP600 is a ferritic-martensitic dual phase steel; FB450 is a ferritic-bainitic steel. S550MC contains ferrite, pearlite and Ti-Nb precipitates; TRIP700 is a multiphase steel containing ferrite, bainite and retained austenite.

Table 1: Chemical composition of the different steels used.

	C	Mn	Si	Other
FB450	0.07	1.00	0.10	0.5%-1.0% Cr
TRIP700	0.17	1.60	0.40	1%-2% Al 0.04%-0.1% P
DP600	0.07	1.50	0.25	0.4%-0.8% Cr+Mo
S550MC	0.07	0.95	0.00	0.08%-0.12% Ti+Nb

Hydrogen charging

Discs of 20mm diameter and 1mm thickness were charged cathodically in a poly-carbonate cell between two symmetric Pt anodes. The electrolyte used in the tests is an arsenic aqueous solution (0.5g As_2O_3 – 0.25g $HgCl_2$ – 60ml H_2SO_4 / 1l H_2O). The samples were charged for 1h at room temperature, using a current density of 0.8mA/cm². After charging, the samples were cleaned with distilled water and acetone, the surface and edges were polished to remove the electrolyte and cleaned again with distilled water and acetone. 60 seconds after charging, the hydrogen content was determined via melt extraction with an H-MAT 2500® (Ströhlein GmbH & Co).

Thermal desorption spectroscopy (TDS)

TDS analysis of hydrogen charged samples was done by heating the samples from room temperature up to 900K, using a quadruple mass spectrometer (Pfeiffer) to detect the hydrogen. The tests were started when the pressure was less than 3.5×10^{-6} mbar. The time between the end of the charging and the start of the test was kept constant, *i.e.* 1h.
A deconvolution of the thermal desorption spectrum was performed using the Peak Fitting Module in OriginPro 7.5, assuming that the sub-peaks had a Gaussian shape. This deconvolution provided the value of the different peak temperatures. The

deconvoluted profiles obtained by TDS were modeled by using the method developed by Lee et al. [9, 14]. The activation energy E_A was determined by plotting $\ln(\phi/T^2_P)$ as a function of $(1/T_P)$ with T_P being the peak temperature (in K) and ϕ the heating rate (in K/h)[15].

RESULTS AND DISCUSSION

Hydrogen charging

Before the TDS measurements, during cathodic charging, the samples were saturated with hydrogen. After charging, hydrogen is assumed to be present in both interstitial lattice places as well as near lattice defects, *i.e.* at hydrogen traps. Figure 1 gives an overview of the hydrogen content of the samples after different charging times. 1h was considered to be sufficient to saturate the sample with hydrogen.
It is clear from Figure 1 that the hydrogen at saturation is about 5 to 6 wppm for all steels studied, except for the TRIP700CR which has a hydrogen content of 8.8 wppm. This might be correlated with the presence of retained austenite in the TRIP steel and the higher solubility of hydrogen in a face centred cubic lattice with respect to a body centred cubic crystal structure.
After charging, the specimens were covered with a black deposit. This deposit was found to mainly consist of arsenic residues originating from the charging electrolyte. As will be shown in the TDS section, this deposition had to be removed because of its drastic influence on the TDS spectrum.

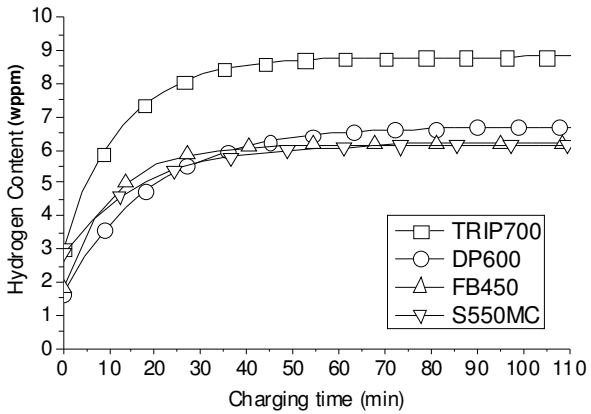


Figure 1: Hydrogen content (wppm) as a function of charging time (min).The H content was determined 60 seconds after the end of charging.

Thermal desorption spectroscopy (TDS)

Figure 2 shows two TDS spectra for the FB450 steel. The first was done on the steel as it was obtained after charging, *i.e.* covered with the black arsenic deposit. The

second spectrum corresponds with the specimen where the deposit was removed by manual grinding after charging. It is clear that the removed surface layer consisted among others of some hydrogen containing compound. Consequently, this compound influenced the spectrum obtained significantly and this clearly illustrates the necessity of a meticulous sample preparation in order to avoid that the handling of the sample will distort the results from the TDS measurement.

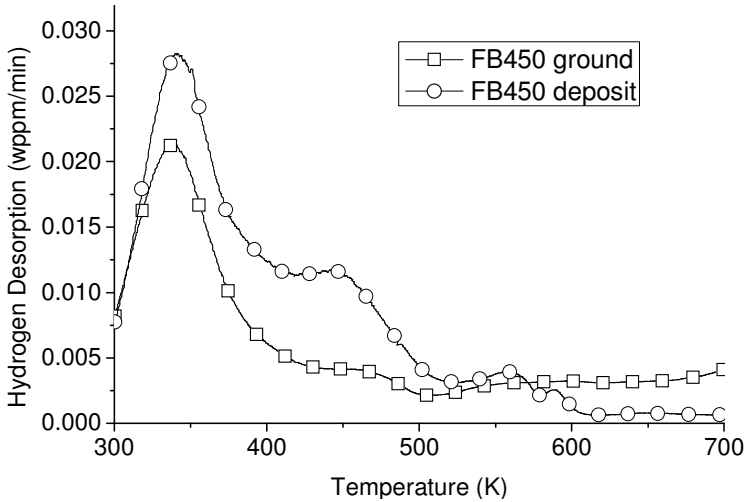


Figure 2: TDS spectrum of the FB450 steel with and without the arsenic (As) deposit obtained for a heating rate of 400K/h.

Taking into account these findings, TDS spectra were measured for the four steels, as is shown in Figure 3. Although the TRIP grade was found to contain more hydrogen immediately after the charging, the TDS curves - registered 1h after the end of the charging – show that the S550MC contained the highest TDS peak. This indicates that the desorption kinetics appear to be slower for the S550MC grade, which could be related to the huge amount of Ti- and Nb- based precipitates in this grade.

The data of one of the steels, namely the DP600, were taken from this figure in order to study it in more detail. These data, after subtracting the background are shown in Figure 4. In this figure, the result of the deconvolution in Gaussian sub-peaks is shown as well. Best fitting results ($R^2 > 0.9995$) were obtained when three peaks were assumed. The three separate peaks are also shown in Figure 4 together with the sum of these peaks (grey line). The three corresponding peak temperatures were found to be 61°C, 101°C and 286°C. As was mentioned above, there is a correlation between the peak temperature T_P and the heating rate ϕ that allows to calculate the activation energy E_A of the different hydrogen traps. After measuring TDS spectra for various heating rates, $\ln(\phi/T_P)$ can be plotted as a function of $(1/T_P)$ and the slope of the curve equals $-(E_A/R)$.

The activation energy that is associated with the peak temperature of the first peak in Figure 4 is of the same order of magnitude as the values that are reported by Choo

and Lee [9] for dislocations, i.e. 27 kJ/mol, and for vacancies, i.e. 35.15 kJ/mol. However, as is shown elsewhere [16], the presence of additional dislocations in the material as a consequence of cold deformation did not appear to influence the TDS spectra obtained. Therefore, it seems unlikely that the first peak should be without doubt attributed to the release of hydrogen trapped near dislocations.

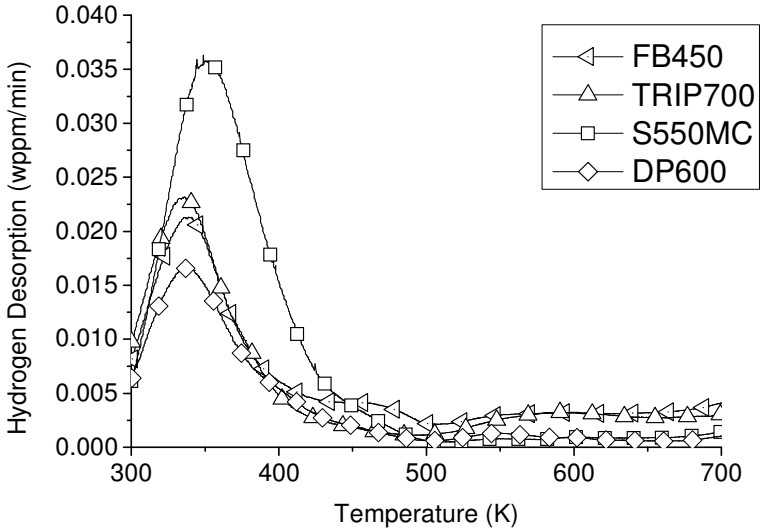


Figure 3: TDS spectrum for the four steel studied. Spectra were obtained after removing the black arsenic deposit and for a heating rate of 400K/h.

As mentioned above, scientific literature provides activation energies for several other possible hydrogen traps that are present in the microstructure of the materials studied in this work. However, the authors of this work believe that it is not possible to just calculate the activation energy associated with a certain peak and to correlate this activation energy with literature data in order to identify the peak. For example for the DP600 steel, it is known that heating this material from room temperature to about 350°C is accompanied by several changes in the microstructure. Waterschoot et al. [17] identified the segregation of carbon to lattice defects at lower temperatures, the precipitation of η and Hägg carbides at intermediate temperatures and the transformation of retained austenite and the precipitation of cementite at higher temperature. It can be assumed that these phenomena, which include the disappearance and creation of possible hydrogen traps, will influence the interactions between iron, carbon, hydrogen and other alloying elements. Consequently, they will also affect the release of hydrogen trapped in the material after charging, *i.e.* the TDS spectrum.

In addition, each mathematical deconvolution is based on some assumptions, which might endanger the correctness of the analysis. The major risk is that the

deconvolution into a number of Gaussian sub-peaks is done without a 100% clear insight of how many traps are physically present in the steel.
In order to try to uniquely define the traps that release hydrogen and their corresponding activation energy, it is the author's vision that further study on the interaction between hydrogen and high strength steels will need to focus on the study of generic alloys in which the effect of different kinds of traps can be isolated in the best possible way. A first onset of this study was already described elsewhere [16].

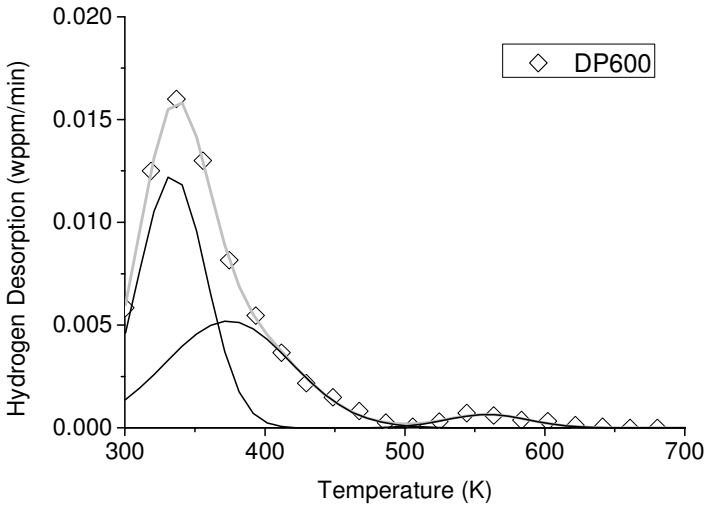


Figure 4: TDS spectrum for the DP600. Black, thin lines are the results of the deconvolution. The grey, thick line is the sum of the three deconvolution peaks.

CONCLUSION

TDS measurements were done on four multiphase high strength steels. The S550MC grade, containing a huge amount of Ti- and Nb- based precipitates, had the highest H-peak, indicating higher solubility and lower effusion kinetics. More work is ongoing to obtain a better insight.
It was also shown that the TDS technique is very sensitive requiring very accurate and reproducible experimental procedures: both when preparing the samples as well as when analyzing the data obtained.

- Sample surfaces must be prepared in an identical way before charging
- Charging must be performed in reproducible conditions
- The surface must be cleaned from all residues that may distort the spectrum obtained.
- Care must be taken when performing detailed mathematical analysis of the data: the deconvolution must be based on a correct knowledge of the H-traps that are physically present. All phenomena occurring during the heating might affect the spectrum obtained.

Therefore, it is the author's belief that correct interpretation of the spectra obtained for complex phase high strength steels requires the knowledge of basic, generic alloys containing only one trap.

REFERENCES

1. Johnson, W.H., "On Some Remarkable Changes Produced in Iron and Steel by the Action of Hydrogen and Acids," *Proceedings of the Royal Society of London*, vol. 23 (1875), p. 168.
2. Duprez L., Verbeken K., Verhaege M., "Effect of Hydrogen on the Mechanical Properties of Multiphase High Strength Steels", Proceedings Hydrogen 2008.
3. Oriani, R.A., "Fundamental Aspects Stress Corrosion Cracking," Conference, Houston, Texas, (1969), p. 32.
4. Pressouyre, G.M., "Trap Theory of Hydrogen Embrittlement," *Acta Met*., vol. 28 (1980), pp. 895 – 911.
5. Podgurski, H.H. and Oriani, R.A., "Nitrogenation of Fe-Al Alloys .3. Absorption of Hydrogen in Nitrogenated Fe-Al Alloys," *Met. Trans. A*, vol. 3 (1972), p. 2055.
6. Wei, F.G. and Tsuzaki, K., "Quantitative Analysis on Hydrogen Trapping of TiC Particles in Steel," *Met. Trans. A*, vol. 37 (2006), p. 331.
7. Pressouyre, G.M. and Bernstein, I.M., "A Quantitative Analysis of Hydrogen Trapping," *Met. Trans. A*, vol. 9 (1978), pp. 1571 – 1579.
8. Takai, K., Chiba, Y., Noguchi, K. en Nozue, A., "Visualization of the Hydrogen Desorption Process from Ferrite, Perlite and Graphite by Secondary Ion Mass Spectrometry", *Met. Trans. A*, vol. 33 (2002), pp. 2659 – 2665.
9. Choo, W.Y. and Lee, J.-Y., "Thermal-Analysis of Trapped Hydrogen in Pure Iron," *Met. Trans. A*, vol. 13 (1982), pp. 135 – 140.
10. Gibala, R. and DeMiglio, D.S., "Hydrogen Effects in Metals", TMS, 1981, p. 13.
11. Lee, J.Y., Lee, J.L. and Choo, W.Y., "Current Solutions to Hydrogen Problems in Steel," ASM (1982), p. 423.
12. Iino, M., "Evaluation of Hydrogen-Trap Binding Enthalpy," *Met. Trans. A*, vol. 18 (1987), pp. 1559 – 1564.
13. Hirth, J.P., "Effects of Hydrogen on the Properties of Iron and Steel," *Met. Trans. A*, vol. 11 (1980), pp. 861 – 890.
14. Lee, J.-Y. and Lee, J.L., *Metal Science*, vol. 17 (1962), pp. 426 – 432.
15. Ramunni, V.P., De Paiva Coelho, T. and de Miranda, P.E.V., "Interaction of hydrogen with the microstructure of low-carbon steel," *Mat. Sci. and Eng. A*, vol. 435 – 436 (2006), p. 514.
16. Perez Escobar D., Duprez L., Verbeken K., Verhaege M., "Identification of the Hydrogen Trap Sites in Multiphase High Strength Steels", Proceedings Hydrogen 2008.
17. Waterschoot T., Verbeken K., De Cooman B.C., "Tempering Kinetics of the Martensitic Phase in DP Steel", *ISIJ Int.*, Vol. 46, No. 1 (2006), pp. 138-146.

Effects of Hydrogen on Materials
Proceedings of the 2008 International Hydrogen Conference
Brian Somerday, Petros Sofronis, Russell Jones, editors, p 485-492
Copyright © 2009 ASM International®
All rights reserved.
www.asminternational.org

Identification of the hydrogen trap sites in a high strength TRIP steel by means of Thermal Desorption Spectroscopy

***D. Pérez Escobar*[1]**
[1]*Department of Materials Science and Engineering, Faculty of Engineering, Ghent University (UGent), Technologiepark 903, B-9052 Ghent, Belgium*

***L. Duprez*[2]**
[2]*ArcelorMittal Research Industry Gent, J.F.Kennedylaan 3, B-9060 Zelzate, Belgium*

***K. Verbeken*[1,3,*]**
[1]*Department of Materials Science and Engineering, Faculty of Engineering, Ghent University (UGent), Technologiepark 903, B-9052 Ghent, Belgium*
[3]*Microstructure Physics, Max-Planck-Institut für Eisenforschung, Max-Planck-Strasse 1, 40237 Düsseldorf, Germany*
**Postdoctoral fellow with the Fund for Scientific Research-Flanders (Belgium) (F.W.O. Vlaanderen)*

***M. Verhaege*[1]**
[1]*Department of Materials Science and Engineering, Faculty of Engineering, Ghent University (UGent), Technologiepark 903, B-9052 Ghent, Belgium*

ABSTRACT

In the present work, various Thermal Desorption Spectroscopy (TDS) experiments and an in-depth study of the microstructure were performed on a TRIP steel (TRIP700) in order to make a correlation between the microstructural features of this material (e.g. grain boundaries, dislocations, etc.) and the peaks that were visible during Thermal Desorption Spectroscopy (TDS). The results obtained for the TRIP grade were compared with those obtained for electrolytic pure iron, which only contained a limited amount of possible trap sites.

INTRODUCTION

The presence of hydrogen in steels is well known to be detrimental for the mechanical properties of the material in certain conditions, *i.e.* it decreases the toughness and may give rise to unpredictable failure. High strength steels turn out to be even more sensitive to this type of embrittlement. Nowadays, the use of high strength steels in hydrogen rich environments becomes increasingly more important in industry. Therefore, a detailed study of the behavior of hydrogen in these steels is necessary to be able to predict the potential damage.
Hydrogen that is absorbed in the steel is not homogenously distributed inside the material. It can be found either in the lattice in interstitial positions, or in microstructural imperfections such as vacancies, solute atoms, dislocations, grain and phase boundaries, etc [1]. These places are called hydrogen traps and the

strength of the traps is expressed by the binding energy [2]. Hydrogen has a high diffusivity in ferritic steel but it can also be trapped at various trap sites, which have a reversible or irreversible character depending on their activation energy. The binding energy E_B of hydrogen at these microstructural imperfections is higher and the consequent longer stay of the hydrogen atom at these positions lowers the effective diffusivity.
Previous work using Thermal Desorption Spectroscopy (TDS) revealed the presence of hydrogen at different traps in the material and showed that the different peaks could be related to literature data on the activation energy of different traps present.
Summarized, hydrogen is known to have a high lattice diffusivity throughout the matrix of ferritic steels, but it can also be trapped at various microstructural defects, which have a reversible or irreversible character depending on their activation energy. Thermal Desorption Spectroscopy (TDS) can help to reveal the presence of hydrogen at the different traps in the steel and allows to calculate their corresponding activation energy. In this technique, a sample, previously charged with hydrogen, is heated at a linear heating rate, following a predefined temperature profile. Simultaneously the amount of gas desorbed from the material is recorded. TDS spectra are usually composed of many desorption peaks, which can be associated with different kinetic processes [3]. When increasing the temperature, the activation energy E_A for hydrogen to be released from the trap is reached and hydrogen can escape from the trap.

The aim of this work was to investigate the distribution of hydrogen in a commercial TRIP steel using Thermal Desorption Spectroscopy (TDS) and to compare it with electrolytic pure iron. Both materials were also studied after deformation in order to increase the understanding on the effect of the dislocations on the TDS spectra.

EXPERIMENTAL

Materials

Pure iron and a TRIP steel (TRIP700), consisting of ferrite, bainite and retained austenite, were studied in this work. The chemical composition of these materials is shown in Table 1.

Table1. Chemical composition of the materials (in weight percent)

Element	C	Mn	Si	Other
Pure Iron	0.0015	0.0003	0	1%-2% Al 0.04%-0.1% P
TRIP700	0.171	1.6	0.37	0

The pure iron specimens were produced in a Pfeiffer VSG100 vacuum melting and casting unit, operated under an argon gas protective atmosphere. The pure iron was processed by hot and cold rolling to sheets of 1.8mm thickness. Subsequently, the sheets were annealed in an air furnace at 890°C for 1h. Part of the latter material was then cold deformed up to 15% by tensile testing. 20mm diameter circular TDS

samples of both, non deformed and 15% deformed pure iron, were punched and ground to 0.65mm thickness.
The TRIP steel is a commercial TRIP700 steel of around 0.7mm thickness. The material was cold deformed by tensile testing with 0%, 5%, 10%, 15% and 17% elongation and then grinded to 0.65mm thickness. X-ray analysis was used to determine retained austenite volume fractions and the carbon content of these samples. A Siemens D5000 diffractometer using Mo K_α radiation operating at 50kV and 50mA was used. The retained austenite volume fraction was determined with the direct comparison method [4] using the integrated intensity of the $(200)_\alpha$, $(112)_\alpha$, $(220)_\gamma$ and $(311)_\gamma$ peaks. The carbon content was determined according to Cullity [4].

Hydrogen Charging

The TDS samples were charged electrochemically with H by cathodic charging. The electrolyte used in the tests is an arsenic aqueous solution (0.5g As_2O_3 – 0.25g $HgCl_2$ – 60ml H_2SO_4 / 1l H_2O). The samples were charged for 1h at room temperature, using a current density of 0.8mA/cm². Figure 1 gives an overview of the hydrogen content of the samples as a function of the charging time. A charging time of 1h was considered sufficient to saturate the sample with hydrogen [2].

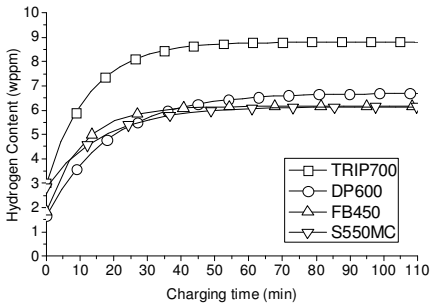


Figure 1: Hydrogen content (ppm) as a function of charging time (min).

After charging, the samples were cleaned with distilled water and acetone. Then the surface and edges were polished to remove the electrolyte residues. Finally, the samples were cleaned again with distilled water and acetone.
Preliminary tests showed that the TDS-spectra are influenced by many factors such as the surface roughness, the sample geometry as well as the state of the electrolyte used for hydrogen charging. Therefore, significant attention was paid to a meticulous sample preparation in order to guarantee reproducible results.

Thermal desorption spectroscopy

TDS was done on the hydrogen charged samples using a quadruple mass spectrometer while heating the sample from room temperature to 900K at a rate of 400K/h. The tests were started once the overall pressure in the vacuum chamber was less than 3.5×10^{-6} mbar. The time between the end of the charging and the start

of the thermal desorption test was the same for all samples, i.e. 1 hour. To make all TDS results comparable, discs of 20mm diameter and 0.65mm thickness were made for both materials.

RESULTS AND DISCUSSION

TDA analysis of the TRIP700 grade

Figure 2 shows the TDS results for the TRIP700 steel with different amounts of tensile deformation. The spectra consisted of one major peak around 340K. In addition a much smaller peak was also sometimes detected around 450K. As the latter peak was less clear, the focus of this contribution was put on the first peak. The curves indicate that the amount of hydrogen stored in the first peak increased for higher deformations. Moreover, for higher deformations, the low temperature peak appeared to shift to slightly higher temperatures.

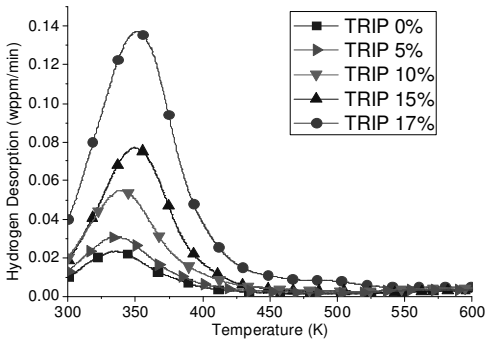


Figure 2: TDS results of TRIP700 with different deformations

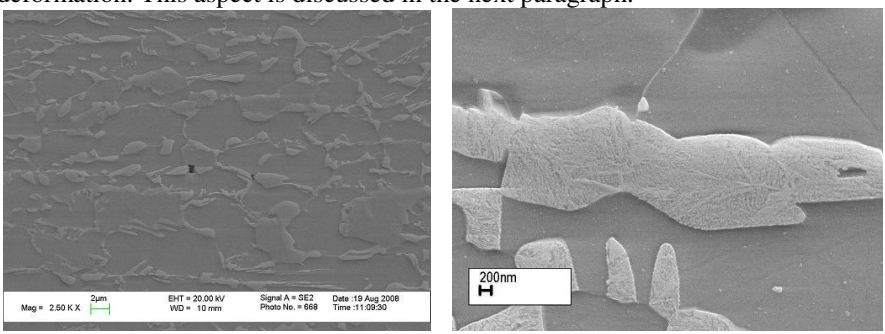
Table 2 shows the results of the retained austenite quantification from the XRD results on the TRIP700, which was 0%, 5%, 10%, 15% and 17% tensile deformed. The amount of retained austenite for TRIP samples decreased as the cold deformation increases.

Table 2. Fraction of retained austenite and carbon content in TRIP700 samples

Sample	0%	5%	10%	15%	17%
Frac. Retained austenite	9.56	5.19	3.74	1.78	1.22
Carbon Content	1.22	1.22	1.22	1.22	1.22

As austenite has a higher solubility than ferrite or martensite, the authors expected that with more deformation, *i.e.* less retained austenite, the amount of stored hydrogen in the sample would be less, and consequently the TDS peak would decrease. The results, however, show clearly the opposite.
Figure 3 shows two SEM (Scanning Electron Microscopy) micrographs of a TRIP steel that was cold deformed. The light phases are bainite and retained austenite. While the bainite has a lath structure, the retained austenite has not. The dark gray

phase is ferrite. Fig 3(a) illustrates that for higher amount of deformation, cracks started to occur between the transformed austenite islands. In Fig 3(b) one can see the martensite formation inside the retained austenite. These two phenomena might explain the increased H-peak for higher amounts of deformation, despite the decreasing volume fraction of retained austenite.
Takai and Nozue indicated that the lower-temperature TDS peak might correspond to the hydrogen desorbed from the trapping sites such as point defects, clusters and dislocations [5]. Hence, another possible explanation for the increasing H-peak with higher deformations might be the introduction of dislocations during deformation. This aspect is discussed in the next paragraph.



(a) *(b)*

Figure 3: SEM micrographs of a deformed TRIP steel illustrating crack formation (left) and retained austenite to martensite transformation (right)

Comparing the TRIP grade with pure Fe

Figure 4 shows the TDS curves of pure iron in annealed condition, pure iron 15% deformed, TRIP700 non-deformed and TRIP700 17% deformed.

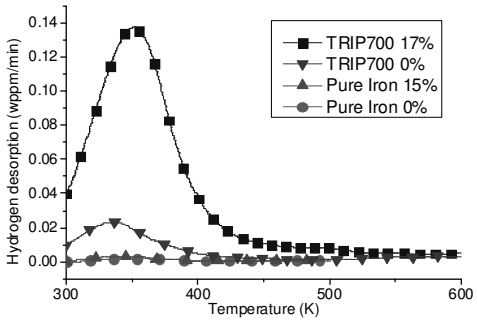


Figure 4: TDS results of pure iron, pure iron 15% deformed, TRIP700 and TRIP700 17% deformed

Comparing the results of the pure iron with the TRIP700, it can be noticed that the TRIP steel can hold much more hydrogen than the pure iron. Moreover, although deformation causes the TDS peak to increase significantly for the TRIP700, there is almost no difference between the TDS spectra of the non-deformed and

deformed pure iron samples. Only a minor increase was observed, as shown further in this work. This is most probably related to the fact that dislocations are a relatively weak trap. Consequently, during the one hour between the end of the cathodic charging and the start of the TDS measurement, the weakly trapped hydrogen was released from the sample. This effect is possibly influenced by the fact that the sample has to be put under high vacuum before the TDS measurement can start. From this, it can be concluded that the increasing H-peak, with increased deformation in the TRIP700, cannot be attributed to the increased amount of dislocations in the ferrite.

Desorption rates of the deformed pure iron and TRIP700

To differentiate the possible H-traps, TDS tests were done after different desorption times for pure iron deformed 15% in tension. For each test, a new sample was charged for 1h, and kept in vacuum during a certain time before the start of the linear heating. All measurements were performed in such a way that the initial pressures of the tests were the same (less than 3.5×10^{-6} mbar). It can be seen in Fig. 5 that a small peak is present in the spectrum of the deformed pure Fe, measured after 52 minutes (which in fact corresponds to the curve of Fig 4). It is possible to see that the peak decreases very quickly with increasing desorption times. After 131 minutes, there is almost no hydrogen left in the sample.

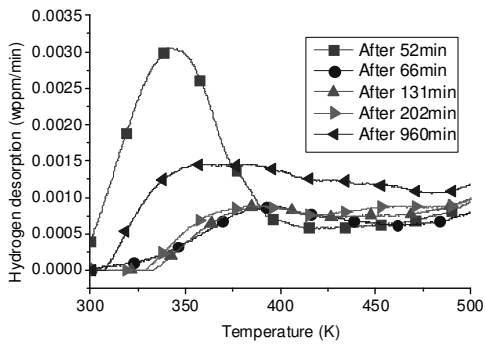


Figure 5: Pure iron TDS results after different desorption times

For the TRIP deformed 17%, TDS tests after different desorption times were done in the same conditions as for pure iron deformed 15%. The results are shown in Fig. 6. It can be seen that, again, the hydrogen effuses from the steel, resulting in a decreasing H-peak with increasing desorption times. However, after around 15h, some hydrogen is still present in the steel. Next, it can be seen that for longer desorption times, the remaining H-peak shifts to higher temperatures. This could indicate that the initial H-peak was in fact an overlay of two or more peaks, each one with different desorption kinetics. Once the first peak has disappeared, the second peak becomes more visible. Alternatively, this observed peak shift might also be related to the fact that each metallurgical trap site is characterized by a distribution of binding energies as was reported by Kirchheim [6] and by Wei and

Tsuzaki [7]. This so-called site energy distribution determines the trapping/detrapping distribution of the trap site and this concept might imply that the observed changes in the features of the peak are a consequence of the fact that the hydrogen on the lower end of the distribution is released first and so on. More measurements and data analysis are, however, needed to confirm these findings.

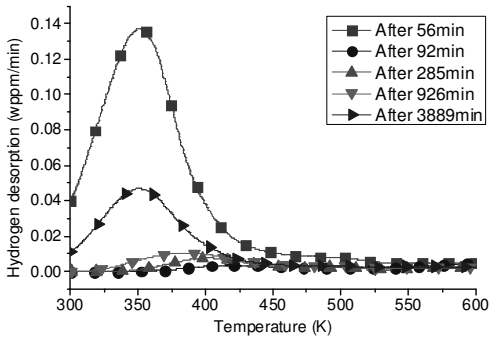
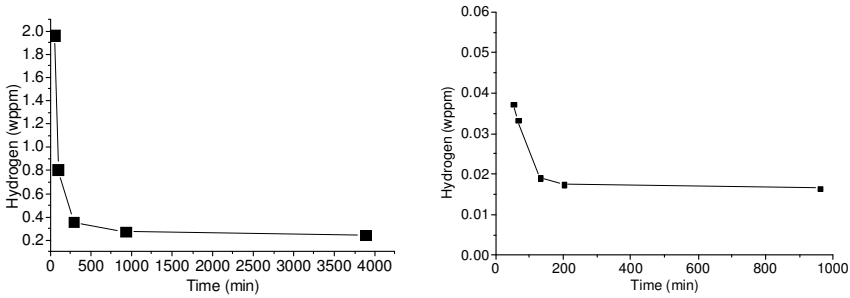


Figure 6. TRIP700 TDS results after different desorption times

Via numerical integration of the spectra, the total amount of hydrogen (ppm) that is desorbed as a function of the time was calculated. Fig. 7 shows the results for the pure iron 15% deformed and TRIP700 17% deformed.



(a) *(b)*

Figure 7. Hydrogen desorption as a function of time for (a) pure iron 15% deformed and (b) TRIP700 17% deformed

Again, it can be seen that the "low temperature peak" in the TRIP grade can store much more hydrogen than the low temperature peak in the pure iron. In addition, the hydrogen in the TRIP grade effuses at a much slower pace than in the pure iron, indicating a clearly stronger trapping behavior in the TRIP grade. More detailed mathematical analysis of the data, together with more measurements, should give more insight in the distribution of hydrogen inside complex multiphase high strength steels. One part of the future work will consist of TDS analysis on generic alloys containing mainly one microstructural feature.

CONCLUSIONS

Hydrogen thermal desorption analysis was done on pure iron and a multiphase high strength TRIP700 grade, in non-deformed and deformed state.

- The TDS spectrum of the TRIP700 grade consists mainly of one large low temperature peak, which increases with increasing amount of deformation. This evolution is opposite to what was expected based on the decreasing retained austenite content with increasing amount of deformation.
- Comparison of the TDS spectra between the TRIP700 and pure iron, in non-deformed and deformed state, indicates that the increasing H-peak (with increased deformation) in the TRIP grade can most probably not be attributed to the increased amount of dislocations. SEM images indicate that microcracks and/or martensite (formed from the retained austenite) could be possible explanations. However, more experimental work is needed to confirm this.
- TDS measurements after different desorption times might allow to visualize the different traps that might be hidden behind one apparent hydrogen TDS peak.

REFERENCES

1. E. Tal-Gutelmacher, D. Eliezer, E. Abramov. Thermal desorption spectroscopy (TDS) – Application in quantitative study of hydrogen evolution and trapping in crystalline and non-crystalline materials. Materials Science and Engineering A 445-446 (2007), pp. 625-631.
2. D. Pérez Escobar, K. Verbeken, L. Duprez, M. Verhaege. Experimental Evolution of the Hydrogen distribution in steel by Thermal Desorption Spectroscopy. Proceedings Hydrogen 2008 conference. Wyoming – USA.
3. F.J. Castro, G. Meyer. Thermal desorption spectroscopy (TDS) method for hydrogen desorption characterization (I): theoretical aspects. Journal of alloys and Compounds, 2002, Vol.330, pp.59-63
4. B.D. Cullity and S.R. Stock: Elements of X-ray Diffraction 3rd ed., Prentice Hall, NY, 2001, pp.215-242.
5. Kenichi Takai and Akira Nozue. Hydrogen Permeation and Trapping Characteristics of Cold-Drawn Pure Iron and Eutectoid Steel Evaluated by Thermal Desorption Spectrometry. Corrosion 2000. Nace International, Houston, Texas, March 2000, PA, 2000, pp. 1-10.
6. R. Kirchheim. Hydrogen solubility and diffusivity in defective and amorphous metals. Progress in Materials Science, 1988, Vol.32, pp.261-325.
7. F.G. Wei, K. Tsuzaki. Hydrogen trapping character of nano-sized NbC precipitates in tempered martensite. Proceedings Hydrogen 2008 conference. Wyoming – USA.

Effects of Hydrogen on Materials
Proceedings of the 2008 International Hydrogen Conference
Brian Somerday, Petros Sofronis, Russell Jones, editors, p 493-500
Copyright © 2009 ASM International®
All rights reserved.
www.asminternational.org

DETERMINATION OF DIFFUSIBLE HYDROGEN CONTENT IN COATED HIGH-STRENGTH STEELS

C. Georges
Surface Engineering Department, Centre for Research in Metallurgy, Liege, Belgium

T. Sturel
ArcelorMittal Research, Maizières-les-Metz, France

ABSTRACT

Within the framework of very high strength steels development, delayed fracture due to hydrogen may be encountered if uncontrolled hydrogen charging is reached, especially for coated products. In order to optimize coating processes and produce safe materials, it is therefore essential to address hydrogen pick-up or release with relevant measurements. Thermal desorption analysis (TDA) is a highly sensitive and well-known method to study hydrogen desorption from steel products. It allows to get diffusible hydrogen content, which is known to be the relevant quantity to measure when dealing with delayed fracture. Moreover TDA gives information on how hydrogen is trapped inside the steel structure. In this communication, application of TDA to coated products is reported. TDA has been applied to laboratory electrogalvanized high strength steels in order to study hydrogen distribution and coating effect. Special attention was devoted to sample storage and preparation in order to avoid hydrogen desorption by uncoated edges. Two main contributions were detected: diffusible hydrogen (weakly trapped) and interface/coating hydrogen.

Key words: Thermal desorption analysis, diffusible hydrogen, coated high-strength steel.

INTRODUCTION

In order to reduce the weight of the vehicles and therefore the vehicle fuel consumption, high strength steels are largely integrated within the body of modern cars. As it is well known that tensile strength increase leads roughly to a higher hydrogen embrittlement susceptibility, uncontrolled hydrogen charging must be avoided [1-3], especially when a coating hinders hydrogen to escape from the steel [4-5]. Moreover, in the case of electroplated products, a proportion of the current passed during coating deposition results in the generation of hydrogen, which could diffuse into the steel after incorporation in the deposit and increase the hydrogen level into the steel [6-8].

The susceptibility to hydrogen embrittlement is strongly affected by the interaction of hydrogen with traps. The reversible traps (low binding energy) often induce a high susceptibility to hydrogen embrittlement [1-2,9]. The characterization of microstructural trapping of hydrogen in steels is therefore essential in order to optimize coating processes and produce safe coated materials. Thermal desorption analysis (TDA) (also named thermal desorption spectroscopy (TDS)) has been applied for the study of hydrogen trapping in iron and steels [10-13]. In most cases, the desorption-rate peak appears at around 100°C to 200°C. Since the majority of hydrogen composing the peak diffuses out readily at room temperature, this peak is often termed as diffusible hydrogen [3], *i.e.*, hydrogen weakly trapped. Due to the fast diffusion of hydrogen at room temperature and the low hydrogen contents involved (typically from 0.1 to several mass ppm), special care must be accorded to sample storage in order to avoid hydrogen degassing before measurement. Moreover, oxidation, condensation or contamination during preparation could alter the sample surface. Non identified peaks attributed to surface preparation by experimenters using thermal desorption are sometimes reported [14]. Finally, concerning coated products analysed by TDA, hardly anything is reported.

In the present article, a method to determine diffusible hydrogen from coated high strength steels with TDA has been set up. Special attention has been devoted to sample storage and preparation in order to avoid hydrogen desorption by uncoated edges.

EXPERIMENTAL PROCEDURE

Material

The material investigated is a dual phase steel of 980MPa minimum tensile strength (DP980). Its microstructure (after a sodium disulfite etching) is presented in the Fig. 1. Chemical composition in C, Mn and Si elements is respectively 0.15, 1.9 and 0,2 in weight percent.

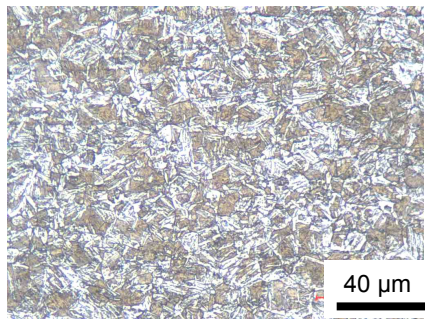


Figure 1: Optical micrograph of studied sample after a sodium disulfite etching.

Thermal Desorption Analysis

The TDA set-up consists of a heating room in which the flat samples are heated by an I-R furnace at varying heating rates under a flow of pure nitrogen up to 900°C. The temperature is followed by a thermocouple spot welded on the sample. Hydrogen released is carried by nitrogen and detected by mass spectrometry. The sample dimensions are 25 x 80 mm². The thickness can vary from 0.8 mm to 2 mm. Filters are included in order to avoid a spectrometer contamination. A key parameter in order to realize sensefull measurements remains the calibration. In this study, calibration is performed by a certified gas mixture of 50 ppm (+/- 0.7 ppm) hydrogen in nitrogen. In order to avoid hydrogen desorption before measurement, the samples are stored in liquid nitrogen after being electro galvanized. Desorption curves will always depict the desorption rate (mass ppm/min) as a function of the temperature (°C).

Charging and electro galvanizing

A soft charging method was used [15] in order to avoid any damage to the microstructure. The samples are electrically charged in an electrolyte of 3% NaCl solution with an addition of ammonium thiocyanate (NH4SCN) at room temperature. This solution is approximately neutral so that corrosion can be avoided. The cathodic charging current density was fixed to 0.1 mA/cm². After charging, samples were immediately dipped into liquid nitrogen in order to prevent hydrogen escape before electro galvanizing. The electro-galvanizing was performed after alkaline cleaning (50gr/l concentrate, 10 seconds at 80°C) and pickling (a few seconds in HCl 4:7). The electrolyte consists of 109 gr/l of KCl and 167 gr/l of $ZnCl_2$. Deposing time was adapted in order to obtain 7-8µ of Zn thickness.

X-Ray Diffraction

The evolution of the coating nature during the TDA test has been studied by X-ray diffraction measurements on samples from interrupted TDA tests. The heating rate was 100°C/hour to allow a better peak deconvolution. X-Ray diffraction patterns were measured on a classical θ - 2θ diffractometer using *Co* $K\alpha$ radiation and a solid-state detector.

RESULTS AND DISCUSSION

Figure 2 presents desorption curves as a function of charging time for uncoated samples. Two peaks can be observed at 150-160°C and 450-500°C. The first peak will be named diffusible hydrogen in what follows. Figure 3 depicts the evolution of H contained in the first peak as a function of the charging time. A plateau at 1.2-1.4 ppm is observed. A charging time

of 1 hour has been chosen in order to obtain about 0.5 ppm within first peak.

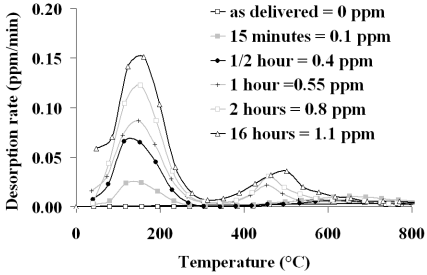


Figure 2: Desorption curves as a function of the charging time (heating rate = 20°C/min).

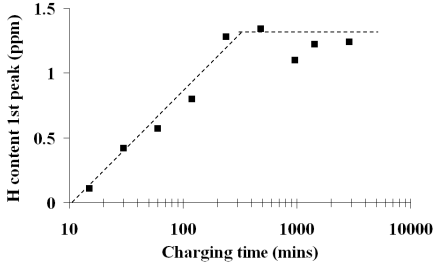


Figure 3: Evolution of the hydrogen extracted from the first peak as a function of the charging time.

Results about coated samples will be presented in present section. As Zn coating presents a tight layer to hydrogen desorption, the removal of the coating before the measurement by TDA must be tackled. In order to be sure that the entire Zn coating is removed (but not steel), a chemical removal consisting of a pickling with HCl (1:1) and 5 g/l of Hexamethylentetramine has been performed. The heating rate applied was 20°C/min as for uncoated samples.

Figure 4 depicts desorption curves of coated samples before and after chemical removal of the coating. Hydrogen values represents the integration of desorption curve until the end of the peak. In the coated sample, three main contributions, corresponding to peaks at 300°C, 365°C and 570°C, can be observed. The peak temperatures are higher than those observed for uncoated samples [10-13] due to diffusion. The amount of H desorbed after the first peak is 0.55 ppm and is equal to 1.15 ppm at 900°C. A better deconvolution of the peaks will be obtained as explained further (Fig. 5).

After the coating removal, only two peaks can be distinguished. It is worth noting that the intensity of the peaks is largely influenced by the coating removal. Only 0.15 ppm of H are measured for the first peak and 0.35 ppm of H are detected at 900°C. An additive curve presenting the effect of one week room temperature holding (sample 25*80 mm²) is also added. The first peak disappears completely, indicating the diffusible character of hydrogen trapped. The second peak is supposed to be related to hydrogen trapped in the coating and/or at the steel-coating interface as it fully disappears after coating removal. The last peak is related to hydrogen deeply trapped and will be not discussed here. As the coating removal induces degassing of H, further tests have been performed by keeping coating.

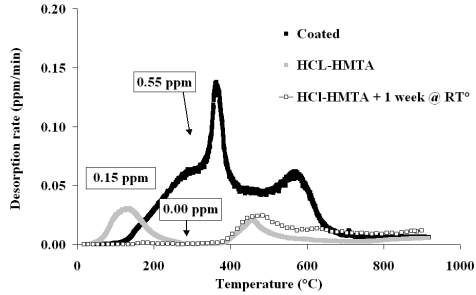
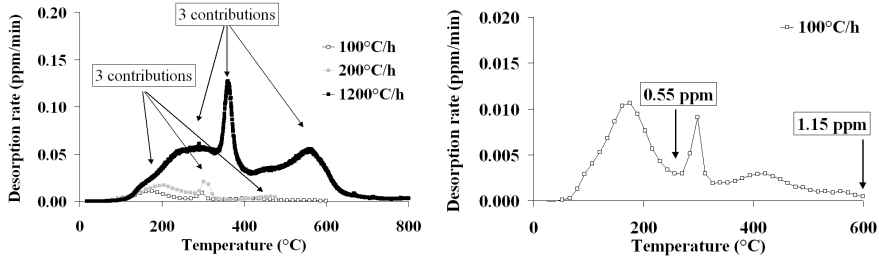


Figure 4: Desorption curves after charging, lab electro galvanizing and chemical removal of coating. (heating rate = 20°C/min)

In order to allow a better peak deconvolution, varying heating rates have been tested (Fig. 5). The slowest one (100°C/h) leads to the best peak deconvolution and has been chosen for further experiments. In this case, the first and second peaks are located at 200°C and 300°C, respectively. As desorption rate is expressed in ppm/min, slower heating rates will induce lower peaks, but the total amount of hydrogen desorbed is similar for both heating rates.



(a) (b)

Figure 5: Desorption curves of samples reheated at varying heating rates (a) and focus of measurement at 100°C/h (b).

A rapid desorption of H at room temperature is observed for uncoated samples (Fig. 4). However, a similar observation is noticed for coated samples. Figure 6 presents the effect of room temperature holding of samples (25*80 mm²). A large decrease in the height of the first peak (~0.25 ppm) is observed after one month, the second peak remaining at nearly similar level. This is the reason why samples have been stored in liquid nitrogen until hydrogen measurement. In this case, no hydrogen desorption is measured (even for small samples) as it can be observed in Fig. 7 which presents desorption curves of charged and lab-electrogalvanized samples (25*80 mm²) after varying hold times in liquid nitrogen. No desorption is observed after 4 months holding.

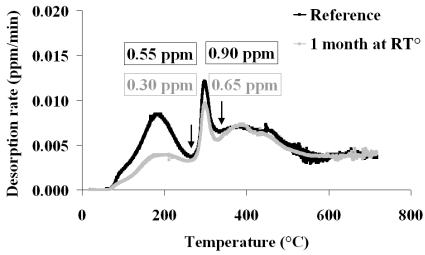


*Figure 6: Desorption curves of samples (25*80) before and after 1 month of isothermal holding at room temperature (heating rate = 100°C/hour).*

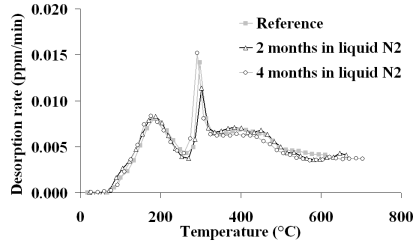


Figure 7: Desorption curves for samples cathodically charged and lab electrogalvanized after holding in liquid nitrogen (heating rate = 100°C/hour).

The shapes of first and second peak are quite different. The first peak is broad as it is supposed to result from hydrogen desorption by the bare edges. The coating is supposed to remain tight until 300°C. In this case, determination of the activation energy from the approach of Choo and Lee [11,14,16] can not be performed due to diffusion. However, it can be supposed that traps involved for such microstructures are dislocations and martensite lath boundaries [1,3].

In contrast, the second peak is sharper and concerns hydrogen trapped in the coating. Interrupted heatings were performed in order to study the coating evolution during TDA measurement. Figures 8 and 9 present the X-ray diffraction patterns for sample before and after reheating at 100°C/hour to 330°C. Before reheating, only Zn and iron phases are detected, but once the second peak appears the Zeta phase appears too. It is supposed that the zeta phase allows rapid diffusion of hydrogen, while hydrogen diffusion in the Zn phase is very slow. In presence of the Zeta phase, all hydrogen trapped in the coating would be released simultaneously. Optical micrographs of interrupted heating samples (300°C and 330°C) are presented in Fig. 10. At 300°C the thickness of the Zeta phase is about 3 µm, while all the coating is transformed into Zeta at 330°C.

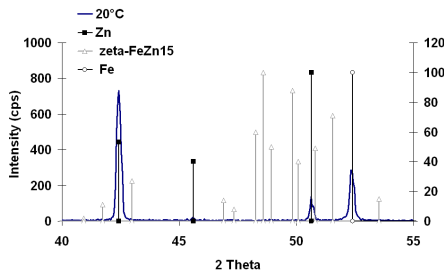


Figure 8: X-ray diffraction pattern

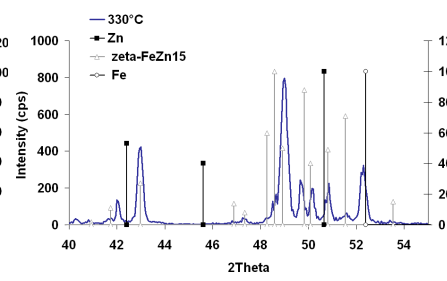
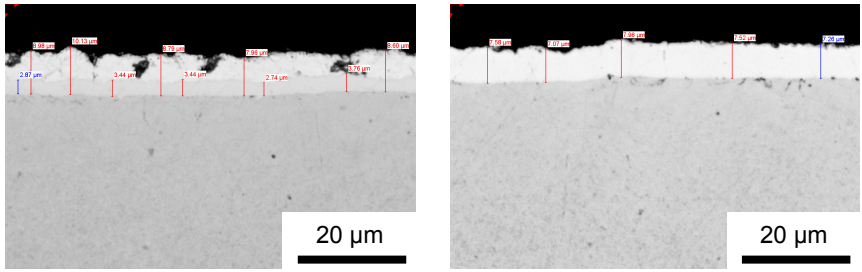


Figure 9: X-ray diffraction pattern

for sample before reheating. *for sample after reheating up to 330°C.*



(a) (b)

Figure 10: Optical micrograph of samples after interrupted TDA test at 300°C (a) and 330°C (b) (heating rate = 100°C/hour).

CONCLUSION

Hydrogen extracted from cathodically charged and electrogalvanized high strength steels was quantified by thermal desorption analysis (TDA). It is demonstrated that a slow heating rate (100°C/h) is required to allow a better peak deconvolution and that storage in liquid nitrogen retains all hydrogen.

Measurements were performed with and without Zn coating removal. Reliable measurement of diffusible hydrogen, after Zn coating removal, is nearly impossible as an uncontrolled part of this quantity escapes very rapidly from free surfaces. Therefore, it is recommended to perform measurements with coating even if it is much more difficult to manage than the coating removal method.

The peak ending at 300°C (heating rate 20°C/min) was considered as diffusible hydrogen escaping by the bare edges, while the peak at 365°C deals with hydrogen trapped in the coating whose desorption is allowed after appearance of the Zeta phase.

REFERENCES

1. Gu, J. L. *et al*, “Delayed Fracture Properties of 1500 MPa Bainite-Martensite Dual-phase High Strength Steel and Its Hydrogen Traps”, ISIJ International, Vol. 42, No.12 (2002), pp. 1560-1564.
2. Hilditch, T. B. *et al*, “Response to Hydrogen Charging in High Strength Automotive Sheet Steel Products”, SAE SP, No. 1764 (2003), pp. 47-56.
3. Nagumo, M., “Function of Hydrogen in Embrittlement of High-strength Steels”, ISIJ International, Vol. 41, No. 6 (2001), pp. 590-598.

4. Casanova, T. *et al*, “Hydrogen Absorption during Zinc Plating on Steel”, Corrosion Science, Vol. 39, No. 3 (1997), pp. 529-537.
5. Townsend, H. E., “Effects of Zinc Coatings on the Stress Corrosion Cracking and Hydrogen Embrittlement of Low-Alloy Steel” Metallurgical Transactions A, Vol. 6A (1975), pp. 877-883.
6. Carr, M. J. and Robinson, M. J., “The Effects of Zinc Alloy Electroplating on the Hydrogen Embrittlement of High Strength Steels”, Trans. I.M.F., Vol. 73, No. 2 (1995), pp. 58-64.
7. Hiller, E. M. K. and Robinson, M. J., “Hydrogen Embrittlement of High Strength Steel Electroplated with Zinc-Cobalt Alloys”, Corrosion Science, Vol. 46 (2004), pp. 715-727.
8. Hiller, E. M. K. and Robinson, M. J., “Permeation Measurements to Study Hydrogen Uptake by Steels Electroplated with Zinc-Cobalt Alloys, Corrosion Science, Vol. 48 (2006), pp. 1019-1035.
9. Pressouyre, G. M. and Bernstein, I. M., “A Quantitative Analysis of Hydrogen Trapping”, Metallurgical Transactions A, Vol. 9A (1978), pp. 1571-1580.
10. Katano, G. *et al*, “Observation of Hydrogen Distribution in High-Strength Steel", Journal of Materials Science, Vol. 36 (2001), pp. 2277-2286.
11. Choo, W. Y. and Lee, J. Y., “Hydrogen Trapping Phenomena in Carbon Steel”, Journal of Materials Science, Vol. 17 (1982), pp. 1930-1938.
12. Nagumo, M. *et al*, “Nature of Hydrogen Trapping Sites in Steels Induced by Plastic Deformation”, Journal of Alloys and Compounds, Vols. 293-295 (1999), pp. 310-316.
13. Nagumo, M. *et al*, “Hydrogen Thermal Desorption Relevant to Delayed-Fracture Susceptibility of High-Strength Steels”, Metallurgical and Materials Transactions A, Vol. 32A (2001), pp. 339-347.
14. Wei, F. G. *et al*, “ Precise Determination of the Activation Energy for Desorption of Hydrogen in Two Ti-Added Steels by a Single Thermal Desorption Spectrum”, Metallurgical and Materials Transactions B, Vol. 35B, (2004), pp. 587-597.
15. Hayashi, K., “Evaluation of Hydrogen Embrittlement Susceptibility for Sheet Steels”, Proc. JSAE annual congress, May 2004, Vol. 18, No. 4 (2004), pp. 5-8.
16. Choo, W. Y. and Lee, J. Y., “Thermal Analysis of Trapped Hydrogen in Pure Iron”, Metallurgical Transactions A, Vol. 13A (1982), pp. 135-140.

Effects of Hydrogen on Materials
Proceedings of the 2008 International Hydrogen Conference
Brian Somerday, Petros Sofronis, Russell Jones, editors, p 501-507
Copyright © 2009 ASM International®
All rights reserved.
www.asminternational.org

HYDROGEN DISTRIBUTION IN STRESSED SUPER ALLOYS - A TRITIUM AUTORADIOGRAPHY INVESTIGATION

Ming Au
Savannah River National Laboratory
Aiken, SC, USA

ABSTRACT

The hydrogen distribution in Ni base super alloys was investigated by tritium autoradiography. It was found that hydrogen concentrates along the grain boundaries and interface of carbides – matrix and inclusion-matrix in annealed alloys. Under mechanical stress, the twisted and rotated boundaries, twin transformation and slipped plains surrounded them trapped significant hydrogen due to high stress and strain in these locations. It suggests that the deformation and displacement of grain boundaries may be most responsible for hydrogen embrittlement.

INTRODUCTION

Understanding hydrogen distribution in the materials microstructure is fundamentally important to prevent and mitigate hydrogen embrittlement [1-3]. Tritium autoradiography has been used to investigate hydrogen distribution, therefore to predict hydrogen behavior at macroscopic scale [4-7]. It is known that the stress plays critical role in hydrogen induced stress corrosion and cracking because the local stress influences hydrogen mobility and concentration. However, the vast majority of autoradiography studies have been performed on non-stressed samples at ambient temperature. In this work, the stressed Ni base super alloy specimens have been investigated by high temperature autoradiography. The experimental results and discussions are presented in this paper.

EXPERIMENTAL DETAILS

Materials

Two Ni base super alloys, Inconel 600 and X750, have been investigated in this work. Table 1 shows their chemical compositions and heat treatment state.

Table 1 Compositions and treatment of the super alloys

Materials	Composition (wt%)							Heat treatment
	Ni	Cr	Fe	Ti	Al	Nb	C	
Inconel 600	78	16	6				<0.03	1065°C/1h/air cool
Inconel x750	74	15	7	2.5	0.6	0.8	<0.03	1065°C/1h/air cool 704°C/20h/air cool

Specimen preparation

The notched specimens were loaded with stress by tightening the bolt (Fig.1) and then were charged by tritium in an electrochemical cell. After charging, they were cut from region in front of the notch tip (as dot line indicated in Fig.1) to the size of 15 x 5 x 10 mm that covers whole thickness of the notched specimen (10 mm). Then, they were polished by normal metallographic procedure. For comparison, a stress-free specimen of the annealed 600 superalloy was also prepared.

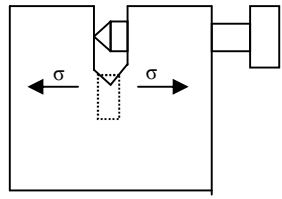


Fig. 1 The schematic of the bolt-loaded and notched specimen for tritium charge. The autoradiography sample was cut from the charged specimen as dot line show.

Tritium charge

Tritium charge was conducted in the radioactive proof glove box (Fig.2). Tritium was introduced into the specimens by cathodic charging in a tritiated molten salt solution. The initial amount of tritium was 10 C_i (Curie) and a specific activity of 5 C_i/cm^3 was used. The eutectic salt was made by mixing 57 wt% $NaHSO_4$ and 43 wt% $KHSO_4$. 1500 g eutectic salt and 50 ml tritiated water (0.2 C_i/ml) were heated and molten at 150^oC. The tritium concentration of salt bath was 12.7 mC_i/ml. Cathodic charging took 3 hours under a constant potential of 0.85 V Ag/Ag^+ at 150^oC. After charging, the specimens were removed from cell and rinsed with distilled water. The tritiated surface layer generated by tritium absorption was then removed by hand-grinding with 600 grit strip. The specimens remained in the radioactive proof glove box for 24 hours to allow out-gassing of the diffusible tritium.

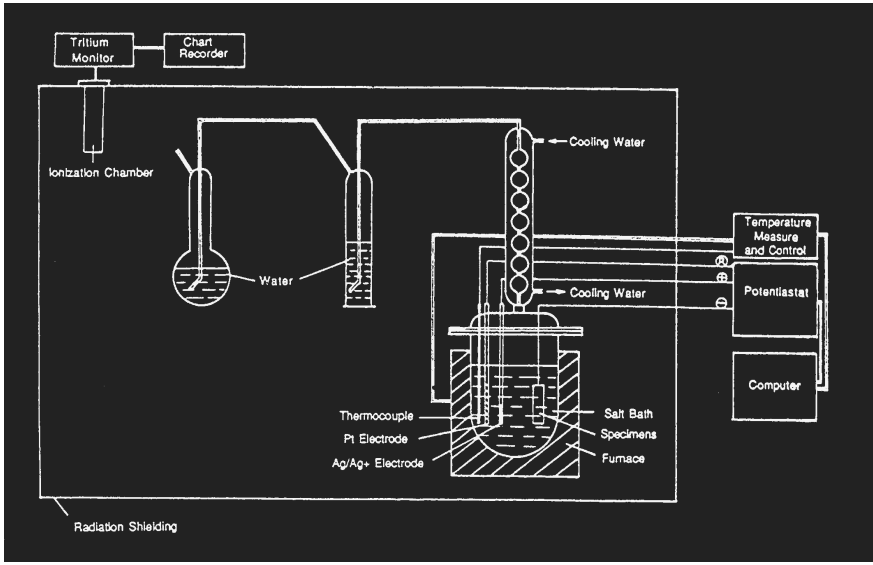


Fig.2 Schematic of electrochemical tritium charging apparatus

Specimen surface polishing

The charged specimens were polished step by step with 9μ, 6μ and 1μ diamond paste under fume hood and then etched by 3% Br-methanol solution. The etched surface was coated by carbon to prevent possible chemical reaction with radioactive photo emulsion and reduce the static charge of SEM (Scanning Electron Microscope).

Radiation sensitive film coating and process

The L.4 type ILFORD radiation sensitive emulsion with 140 nm average crystal diameter of silver bromide was coated to the surface of specimens. A thin film with close-packed monogranular arrangement of silver bromide grains was obtained carefully using well-controlled technique. The film was processed with Kodak D-19 film developer.

SEM Observation

The specimens were then directly observed with SEM. The silver grains resulting from the development of activated silver bromide grains appeared in SEM image as white dots (average diameter of silver grains is about 1500 Å) superimposed on the etched microstructure (Fig.3). The low energy β-emission from tritium (E_{max} = 18 KeV) that reaches the AgBr layer comes from a very thin layer under the surface (about 2000 Å). This fact companioning with small AgBr grain size (1500 Å) leads to very good resolving power for the method [8, 9].

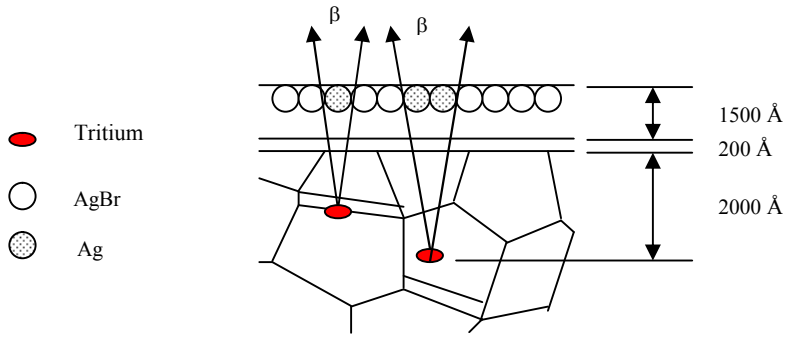


Fig.3 Schematic of the depth of β-emission source and surface emulsion coating layer

RESULTS AND DISCUSSION

Hydrogen distribution in the annealed 600 superalloy

The autoradiography of the annealed 600 superalloy shows that the hydrogen was trapped in certain microstructure. In the order of decrease of hydrogen intensity, these locations are (1) interface of inclusions and matrix (A in Fig.4); (2) the interface of primary carbides and matrix (B in Fig.4) and the grain boundaries on which carbides precipitated (C in Fig.4). It is believed that the disordered interface area has more interstitial sites with low potential energy to attract and hold the hydrogen atoms.

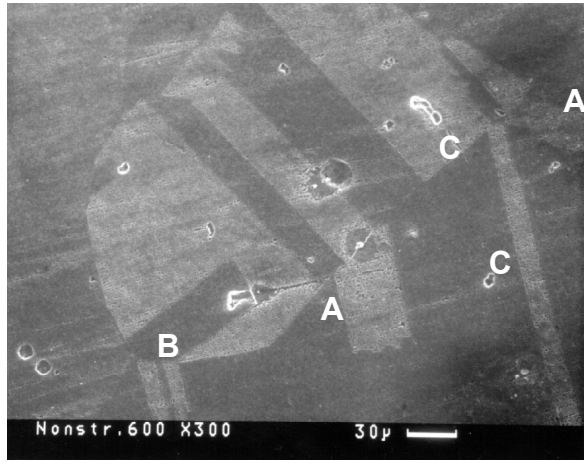


Fig.4 Autoradiography microstructure of the stress-free 600 superalloy. Hydrogen is trapped on the interface of inclusions and matrix (A); interface of carbides and matrix (B) and grain boundaries (C). X300

Hydrogen distribution in the stressed 600 and X750 super alloys

In these stressed specimens, the intensity orders of hydrogen traps obviously differ from non-stressed ones because the stress forces the plains to slip and rotate resulting in severe plastic deformation around the grain boundaries. Hydrogen was trapped in order of decrease of its intensity on (1) the deformed grain boundaries of the slipping plains (A in Fig.5 and C in Fig.6); (2) the interface of carbides and matrix (B in Fig.5 and A in Fig.6); (3) Some carbides that are rich in Ti and Nb elements (B in Fig.6). The elements such as Ti, Nb and Ta possess a strong chemical affinity to bind with hydrogen through possible chemical adsorption. The reactions $Nb+0.2H_2 = NbH_{0.42}$ and $Ta + 0.13\ H_2 = TaH_{0.26}$ will take place only under 0.1 MPa of hydrogen pressure and at -48^oC and 10^oC respectively [10]. It is possible that the carbides that contain Ti, Nb and Ta become hydrogen traps by themselves in addition of the interfaces of carbides and matrix [11-13]. It is noted that some grain boundaries are heavily etched due to more hydrogen presented such as "A" area in the Fig.5. It implies the possible correlation of severe corrosion and hydrogen traps.

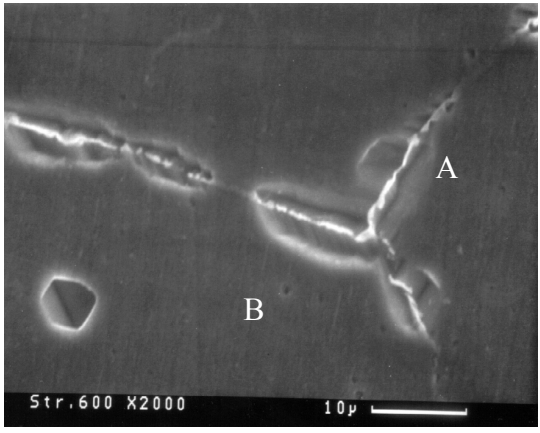


Fig.5 Hydrogen is trapped on the slipped grain boundaries and interface of carbides-matrix in stressed 600 super alloy (X2000)

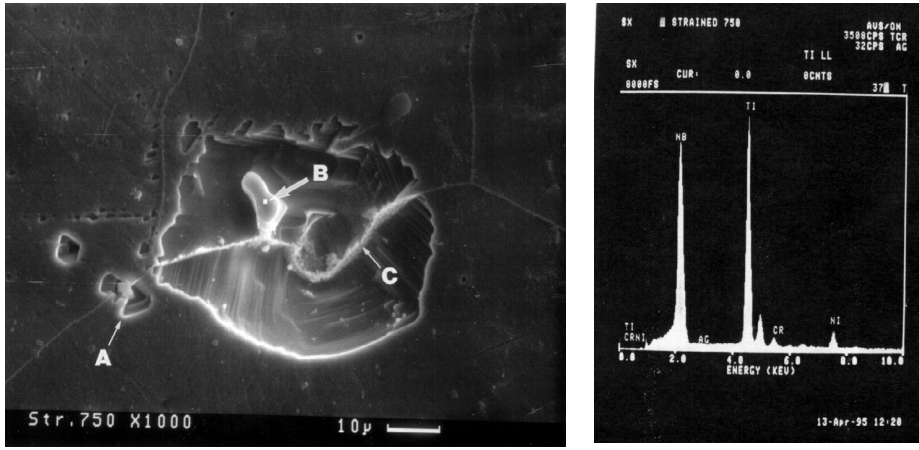


Fig.6 Hydrogen is trapped on twisted grain boundaries (C), carbides (B) and interface of carbides-matrix (A) in stressed X750 super alloy. EDX of the carbide (B) detected Ti, Nb, Ta, Ni Cr elements (X1,000)

Hydrogen concentrated around deformed and rotated grain boundaries

Under high stress, some grain boundaries twisted, slipped and even rotated. The displacement of the grain boundaries absorb most mechanical stress applied to the specimens and generate potential wells for hydrogen migrating and settling to. The twisted grain boundaries and the slipping plains surround them trapped hydrogen (arrows in Fig.7). The severe rotated grain boundaries attracted significant hydrogen and even triggered twin transformation (arrows in Fig.8).

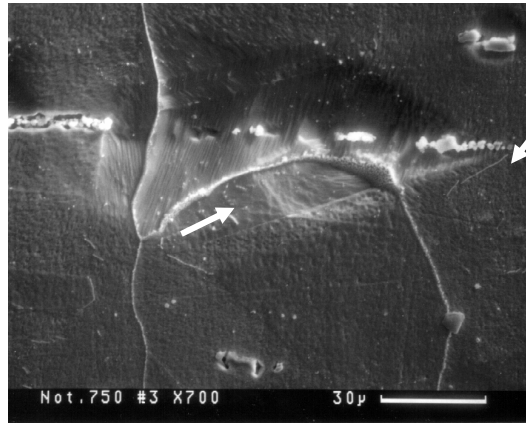


Fig.7 Under stress, the grain boundaries twist and slip trapping hydrogen (X700)

CONCLUSIONS

Tritium autoradiography is the powerful tool to reveal hydrogen distribution visually in the microstructure of materials. Hydrogen is concentrated around the grain boundaries, inclusion and carbides. Under mechanical stress, the deformation and displacement of grain boundaries create local wells of potential energy for hydrogen migration and settlement. The twisted and rotated grain boundaries and the slipping plains surround them trapped significant hydrogen. The deformed and displaced grain boundaries may be the most favorable area for initiation of stress induced stress corrosion and cracking.

ACKNOWLEDGEMENTS

This work has been done in author's previous employment with Carnegie Mellon University.

REFERENCES

[1] Y. Shen, P. G. Shewmon, Corrosion (1991) 712-718
[2] D. M. Symons, PhD. Thesis, Carnegie Mellon University, 1990
[3] W. S. Walston, PhD. Thesis, Carnegie Mellon University, 1990
[4] B. A. Wilcox, G. C. Smith, Acta. Met. V12 (1964) 371-376
[5] G. M. Pressouyre, Acta. Met. V28 (1980) 895-911
[6] A. T. Festschrift, in: R. Gibala, R. F. Hehemann (Eds.)
Hydrogen Embrittlement and Stress Corrosion Cracking, ASM, 1984
[7] M. I. Baskes, C. F. Melius, Z. Phys. Chem. Neue Folge 116 (1979) 289-299
[8] J. P. Laurent, G. Lapasset, Int. J. Appl. Isot. V24 (1978) 213
[9] G. V. Prabhu Gaunkar, A. M. Huntz, P. Lacombe, Int. J. Appl. Rad. Isot. V30 (1979) 761
[10] T. Massalski, Binary Alloy Phase Diagrams, ASM, 1993
[11] R. L. Zanowick, W. E. Wallace, J. Chem. Phys. 36 (1962) 2059
[12] W. E. Wallace, P. Kofstad et al, Pure Appl. Chem. 2 (1961) 281
[13] G. G. Lobowitz, The Solid-State Chemistry of Binary metal Hydrides, W. A. Benjamin Inc. New York, 1965, pp. 23 - 49 and 91 - 113

Effects of Hydrogen on Materials
Proceedings of the 2008 International Hydrogen Conference
Brian Somerday, Petros Sofronis, Russell Jones, editors, p 508-515
Copyright © 2009 ASM International®
All rights reserved.
www.asminternational.org

HYDROGEN DIFFUSION IN 9Cr STEEL: EFFECT OF MICROSTRUCTURE

Carolina Hurtado Noreña
Universidad de San Martín, Instituto de Tecnología Jorge Sabato, San Martín, provincia de Buenos Aires, Argentina.

Pablo Bruzzoni
Comisión Nacional de Energía Atómica, Buenos Aires, Argentina.

ABSTRACT

9Cr steels such as T9 are mainly used in tubes of steam generator for conventional thermal power plants. This material would not suffer hydrogen damage in normal operation. However, it could be susceptible to hydrogen embrittlement as it is cooled to room temperature during plant stops.
From the academic point of view, 9Cr steels are interesting because they are expected to present conventional trapping ascribed to microstructural defects (dislocations, carbides, etc) as well as a possible effect of Chromium as a minority component of the metallic matrix.
In this work we have studied the diffusion and trapping of hydrogen in T9 steel membranes with thickness of 0.15 to 0.30 mm. The hydrogen permeation method with gas phase charging and electrochemical detection has been used, at temperatures ranging from 30°C to 70°C. The steel was studied in three different metallurgical conditions: as received (quenched + tempered), annealed (775°C, 4 h), and quenched (970°C, 40 min, air cooling). The microstructure of these conditions has been assessed by means of optical microscopy and scanning electron microscopy.
The permeation transients (rising and decreasing) have been normalized with respect to the membrane thickness, permeation coefficients, apparent hydrogen diffusion coefficients and average trapping energies have been determined. The nature of the hydrogen traps is discussed.

KEY WORDS: Permeation, diffusion, microstructure, hydrogen, 9Cr steels.

INTRODUCTION

The ferritic-martensitic 9% Cr steels and other with similar Chromium contents find important applications in high temperature components in thermoelectrical power plants. These applications are possible due to a good

corrosion resistance and excellent mechanical properties at high temperature, easy microstructure control, good thermal conductivity and low thermal expansion coefficient. The excellent high temperature properties are due to a particular microstructure which contains submicroscopical carbide particles [1]. These materials may present failures during service as a result of microstructural changes that may occur after prolonged times at elevated temperatures and aggressive media, or by excessive local heating of the component, leading to the degradation of the corrosion resistance and the mechanical properties. Also, this material may be subjected to hydrogen damage during plant stops, i. e. at temperature much lower than the service temperature [2].

It has been reported that the microstructure plays an important role in the behaviour of the material in the presence of hydrogen [3, 4], due to the presence of traps that delay the diffusion process and increase the hydrogen solubility. These traps i.e. are locations in the metal lattice that retain hydrogen and decrease the apparent diffusion coefficient of hydrogen, are generally related with lattice defects and precipitate particles.

In this work the behaviour of T91 steel with different microstructural states in the presence of hydrogen is studied by mean of the hydrogen permeation technique. The permeation tests were performed at temperatures which are lower than the normal service temperatures of the components fabricated with this material. From the dependence of the apparent hydrogen diffusion coefficient on the different steel microstructure, some considerations can be made on the hydrogen trapping in this material.

EXPERIMENTAL

Permeation membranes

The material for used in this work is a Tenaris T91 (9Cr 1Mo) steel whose composition is shown in Table 1.

Table 1: Chemical composition of the 9%Cr-1%Mo steel

Element	**C**	**Mn**	**Si**	**Ni**	**Cr**	**Mo**	**Cu**	**V**	**Nb**
weight %	0,11	0,36	0,26	0,15	8,21	0,90	0,15	0,21	0,09

The material in the as received state (AR) had been subjected to a normalising treatment at 1060ºC followed by a temper treatment at 780ºC during 40 minutes, as reported by the manufacturer. From this material, disk shaped membranes of 35 mm diameter and a thickness ranging from 150 µm to 300 µm were cut. The permeation membranes were then subjected to different thermal treatments and subsequently to the permeation tests.

The different thermal treatments applied to the permeation membranes in order to obtain different microstructures are listed in Table 2.

Table 2: Details of the thermal treatments

Thermal Treatment	Identification
970ºC/40 min + 775ºC/4 h – furnace cooling	FC
970ºC/40 min – air cooling	AC

The as received (AR) membranes as well as the thermally treated membranes (FC and AC) were polished with SiC paper up to Nº600 grit. Then, they were electropolished in $HClO_4$ 10% in Butyl Cellosolve, at a temperature lower than 5°C during 15 minutes, with the objective of eliminating all the deformation introduced during mechanical polishing, which could affect the results of the permeation tests.

Prior to the permeation tests, the membrane was covered on both entry and exit surfaces with a nano Pd film. To accomplish this, the membranes were pickled in HCl 1:1 during 5 seconds, then rinsed with water and immersed in a solution deaereated with nitrogen which contained 2,5 mg of Pd in the form of $Na_2[Pd(NO_2)_4]$ and 150 ml of 0.1 M NaOH. The electrodeposition took place at a constant current density of 100 µA cm^{-2} during 2600 seg. The Pd film is applied on the input surface in order to allow the hydrogen entry from the gas phase. At the exit surface, it is applied and to avoid the surface impedance due to formation the iron oxide passive film and ensure a complete oxidation of the emerging hydrogen.

Hydrogen permeation tests

The permeation tests were carried out according to the electrochemical permeation technique introduced by Devanathan and Stachurski. The permeation membrane was mounted in the middle of a double cell, thus separating two glass chambers, the charging chamber and the detection chamber. Gas phase charging was achieved by circulating Hydrogen gas through the permeation chamber.

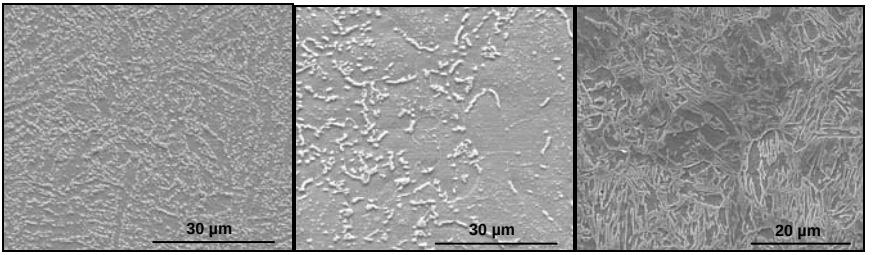
The hydrogen emerging at the exit surface was detected electrochemically. The electrolyte was a 0.1M NaOH aqueous solution which was deaereated though a constant bubbling of nitrogen. A Pt counterelectrode and a Pd/H reference electrode completed the detection cell. The electrochemical potential at the detection cell was fixed at +0,200 V *vs.* the Standard Hydrogen Electrode with the help of a potentiostat. The hydrogen current density i_H was obtained after subtracting a low background current; this current is the faradaic equivalent of the hydrogen flux J_H across the exit side of the membrane, according to $J_H = i_H F$ where F is the Faraday constant. Prior to the tests, a degassing stage at 70°C/16h was performed in the permeation cell. Then, four sequences of raising-decay transients were

recorded at 30°C. The decay transient was initiated by displacing the H_2 in the charging chamber with nitrogen.

RESULTS AND DISCUSSION

Material characterisation

A microstructural analysis has been performed on each of the different samples studied, corresponding to the different thermal treatments FC and AC, and on the as received (AR) material. Optical Microscopy and Scanning Electron Microscopy were used. The results show the ability of this material to developed different microstructures depending on the treatment temperature and the cooling rate. In Fig. 1 the microstructures corresponding to the different thermal treatments are shown.



a) T91 Steel As received b) T91 Steel FC c) T91 Steel AC

Fig. 1: Microstructures obtained for T91 Steel alter each thermal treatment

In Fig. 1a it can observed that the as received material had a ferritic matrix with precipitated carbides resulting from the quenching and tempering treatments carried out by the steel manufacturer. The carbide particles are aligned, following the pattern of parent martensite phase. The microstructure resulting from the FC treatment is shown in Fig. 1b. This treatment consisted in an austenization stage at 970°C followed by a second stage carried out in the ferrite + carbide region of the phase diagram just below the eutectoid temperature, aimed at achieving a large ferritic grain size. The resulting microstructure was a ferritic matrix with ferrite grains 5 to 30 µm in size and carbide particles which precipitated mainly at ferrite grain boundaries. Figure 1c shows the martensitic microstructure which was the result of the AC treatment.

Hydrogen permeation

Two samples of each metallurgical condition were tested. The recorded permeation transients (i_H vs. time) were normalised with respect to the membrane thickness L. For the three metallurgical conditions it is observed that when the temperature increases the steady state flux increases and the

transient develops faster. This is illustrated in Fig. 2. for one specimen of the FC condition.

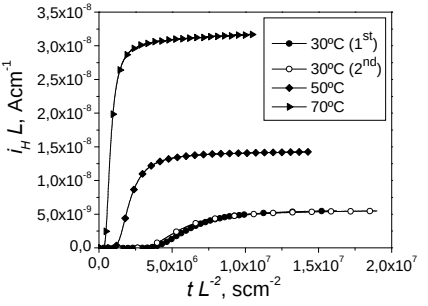


Fig.2: Permeation rising transients of the FC condition at different temperatures

The permeation transients were used to calculate the apparent hydrogen diffusion coefficient by four different methods: tangent time t_{tan} and lag time t_{lag} from the rising or permeation transients ($D_{tang\ p}$; $D_{lag,p}$) and from the decay transients ($D_{tang,d}$; $D_{lag,d}$), according to $D_{tan} = L^2/(2\ \pi^2\ t_{tan})$ and $D_{lag} = L^2/(6\ t_{lag})$ [5]. The results of individual samples are presented in table 3 together with the normalised steady state hydrogen flux $J_{H,ss}\ L$. The values of this latter parameter indicate that the permeation coefficient is one order of magnitude lower than that of pure iron [6].

In Fig. 3 a logarithmic plot of the apparent diffusion coefficient D_{ap} *vs.* the inverse of the absolute temperature for the FC metallurgical condition is presented. It is observed that, independently of the calculation method, D_{ap} increases with increasing test temperature. Also, it can be seen that the diffusion coefficient calculated by the tangent time method from the decay transient yields the higher value, while the tangent time in the rising transient yields the lower one. The time lag method yields intermediate values. This suggests that moderate energy traps with high occupation fraction play an important role in the diffusion process. As the test temperature increases, the D_{ap} values seem to converge to a single value, which is consistent which the assumption of the high trap occupation.

Figure 4 is an Arrhenius type plot where the dependence of the apparent diffusion coefficient (in this case that one obtained from the lag time of the rising transient) with the metallurgical state on the microstructural state of the material is shown. Here it can be observed that the AC samples consisting of as quenched martensite present the highest value of D_{ap}. From the slope of the plot it can be seen that the trap energy is lowest for this AC condition. The values of the activation energy for diffusion were: E_D = 43.7 kJ mol^{-1} for the As Received sample, E_D = 41.4 kJ mol^{-1} for the FC sample, and E_D = 35.1 kJmol^{-1} for the AC sample. The as received material which is tempered martensite presents the lowest values of D_{ap}. The FC condition

consisting in a ferrite matrix with precipitated carbides presents values of D_{ap} nearly as high as those of the AC condition.

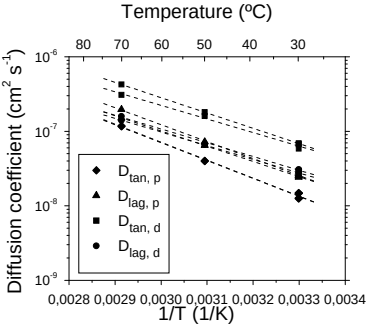


Fig. 3: Arrhenius type graph of the apparent hydrogen diffusion coefficient obtained from the FC samples, calculated by 4 different methods.

Table 3: Normalised steady state hydrogen flux and hydrogen apparent diffusion coefficient calculated by the 4 methods described in the text, for the different metallurgical states of the 9Cr steel: AR, FC and AC

	T ºC	$J_{H,ss}\,L$ mol cm^{-1}s^{-1}	$D_{tan,\,p}$ cm^2 s^{-1}	$D_{lag,\,p}$ cm^2 s^{-1}	$D_{lag,\,d}$ cm^2 s^{-1}	$D_{tan,\,d}$ cm^2 s^{-1}
AR	30 (1st)	3,5E-14	4,6E-09	9,9E-09	8,5E-09	1,9E-08
		6,7E-14	4,3E-09	8,3E-09	9,3E-09	2,3E-08
	30 (2nd)	3,5E-14	4,9E-09	1,1E-08	8,1E-09	1,5E-08
		6,7E-14	4,8E-09	9,0E-09	1,2E-08	2,2E-08
	50	9,1E-14	1,5E-08	2,7E-08	2,8E-08	5,8E-08
		1,7E-13	1,5E-08	2,6E-08	2,8E-08	6,1E-08
	70	2,1E-13	4,4E-08	7,9E-08	6,2E-08	1,2E-07
		3,7E-13	4,3E-08	6,7E-08	6,0E-08	1,4E-07
FC	30 (1st)	4,4E-14	1,3E-08	2,6E-08	2,8E-08	5,8E-08
		5,9E-14	1,3E-08	2,4E-08	3,0E-08	6,9E-08
	30 (2nd)	4,3E-14	1,5E-08	2,6E-08	2,8E-08	6,7E-08
		5,8E-14	1,5E-08	2,5E-08	3,1E-08	6,8E-08
	50	1,1E-13	4,0E-08	7,2E-08	6,6E-08	1,6E-07
		1,5E-13	4,0E-08	6,5E-08	6,8E-08	1,8E-07
	70	2,3E-13	1,2E-07	2,0E-07	1,4E-07	3,1E-07
		3,3E-13	1,2E-07	1,5E-07	1,6E-07	4,2E-07
AC	30 (1st)	2,9E-14	1,6E-08	3,2E-08	3,7E-08	5,2E-08
		2,6E-14	2,2E-08	3,7E-08	4,0E-08	5,7E-08
	30 (2nd)	2,9E-14	1,6E-08	3,3E-08	3,9E-08	4,6E-08
		2,5E-14	2,2E-08	3,8E-08	4,2E-08	6,0E-08
	50	7,2E-14	4,6E-08	9,0E-08	9,6E-08	1,3E-07
		6,5E-14	5,8E-08	9,6E-08	8,6E-08	1,5E-07
	70	1,6E-13	1,2E-07	1,7E-07	2,1E-07	2,9E-07
		1,6E-13	1,3E-07	1,8E-07	1,7E-07	3,3E-07

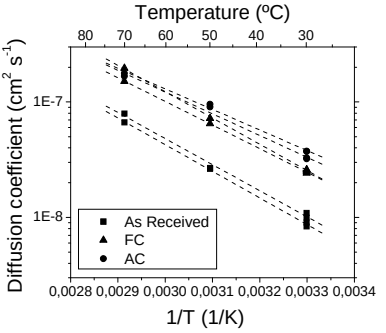


Fig. 4: Arrhenius type graph showing the variation of the hydrogen diffusion coefficient $D_{lag,p}$ with the test temperature for the different microstructural states of the 9Cr steel.

The present results show that the temper treatment at 780°C of the as quenched material causes a marked decrease of D_{ap}. Parvathavarthini ***et al*** [2], measured D_{ap} in 9Cr1Mo steel with different metallurgical conditions. In the air cooled condition they obtained $D_{ap} = 1.30\times10^{-8}$ cm^2 s^{-1}. After a temper treatment at 750ºC, D_{ap} increases to $4{,}54\times10^{8}$ cm^2 s^{-1}, and finally with an austenizing treatment at 950°C followed by furnace cooling, they observe $D_{ap} = 3\text{x}10^{-8}$ cm^{2}s^{-1}. The results of Parvathavarthini ***et al*** [2] show a minimum value of the diffusion coefficient for the AC condition, contrary to the present results. However, it must be taken into account that the steel used in [2] contains neither V nor Nb in its composition, and that the hydrogen activity in [2] is two orders of magnitude higher than in the present work. The behaviour of D_{ap} found in the present work is different from that one found in low alloy steels, in which the quenching treatment produces a martensite with a high dislocation density and consequently a high trap density. The subsequent tempering treatment of low alloy steels causes an increase of the apparent diffusion coefficient [7].

The decrease of D_{ap} after tempering has been observed in type 403 12 Cr conventional steel [8] and in a 13Cr modified steel [7]. In this latter case, the decrease has been attributed to the appearance of the austenite phase; however, in the case of [8] and the present work, the temper treatment does not give rise to the formation of austenite. This fact suggest that the tempering treatment performed on the T91 steel causes some microstructural changes related to the presence of Cr in the bcc lattice, which are more important, regarding interaction with hydrogen, than the well known effect of annihilating the dislocations of the as quenched martensite in low alloy steels.

From other point of view, when comparing the present results with those of [2] it appears that the presence of Nb and V could have an important effect on the creation of traps in the quenched + tempered state. This should be investigated in future work.

The three conditions AR, FC and AC show no differences between the first and second permeation transients performed at 30°C. This indicates that the amount of traps that remain occupied after the first transient is negligible.

CONCLUSIONS

1. The microstructural corresponding to the different thermal treatments of the T91 steel were: tempered martensite (AR), ferrite (FC) and as quenched martensite (AC).
2. The steady state permeation flux of the T91 steel is on order of magnitude lower than that of pure, annealed iron. It is slightly lower in the AC state than in the FC or AR states.
3. The apparent hydrogen diffusion coefficient in the T91 steel is markedly lower in the AR state than in the AC state, which is observed in 12% and 13% Cr steels but not in low alloy steels.

REFERENCES

1. Bush, D.R., *Valve magazine*, Vol. 13, No. 1 (2001), pp. 1-8.
2. Parvathavarthini, N., Saroja, S. and Dayal, R.K., *Journal of nuclear materials*, No. 264 (1999), pp. 35-47.
3. Parvathavarthini, N., Dayal R.K., and Gnanamoorthy, J.B., *Corrosion science*, Vol. 52, No. 7 (1996), pp. 540-551.
4. Saroja, S., Vijayalakshmi M. and Raghunathan V.S., *Materials Transactions, JIM*, Vol. 34, No. 10 (1993), pp. 901-906.
5. Boes, N. and Züchner H., *Journal of the less-common metals*, No. 49 (1976), pp. 223-240.
6. Chaudhary, R.S. and Riecke, E., *Werkstoffe und Korrosion* Vol. 32, (1981), pp.66-72.
7. Gesnouin, C., Hazarabedian, A., Bruzzoni, P., Ovejero García, J., Bilmes, P. and Llorente, C., *Corrosion science*, Vol. 46 (2004) pp. 1633-1647.
8. Sakamoto, Y. and Hanada U., *Materials Transactions, JIM*, Vol. 18 (1977), pp. 466-470.
9. Bruzzoni, P., Domizzi, G., Luppo, M. I., Zalcman, D., and Ovejero-García, J., “Hydrogen Effects on Materials”. A. W. Thompson and N. R. Moody. The Minerals and Metals Society, Warrendale, Pennsylvania (1996), pp. 1001-1009.

Effects of Hydrogen on Materials
Proceedings of the 2008 International Hydrogen Conference
Brian Somerday, Petros Sofronis, Russell Jones, editors, p 516-523
Copyright © 2009 ASM International®
All rights reserved.
www.asminternational.org

SURFACE EFFECTS DURING HYDROGEN PERMEATION IN PD-PLATED AND NI-PLATED IRON MEMBRANES

Pablo Bruzzoni, Juan R. Collet Lacoste and Ricardo M. Carranza
Comisión Nacional de Energía Atómica, Buenos Aires, Argentina

ABSTRACT

In this work we studied the interaction of hydrogen with Pd and Ni thin (10 nm to 10 μm) films which were electrodeposited on an iron permeation membrane of known properties. The hydrogen permeation technique with electrochemical detection and either gas phase or cathodic charging was used. After reaching steady state permeation in such a system, a sinusoidal perturbation was imposed to the hydrogen activity at the entry surface, frequency response analysis was performed and a transfer function was obtained. To evaluate the results, a theoretical transfer function of hydrogen permeation through a bilayer with a finite hydrogen transfer rate across the hydrogenating medium/electrodeposited metal interface, was developed. The corresponding hydrogen transfer coefficients have been determined.

INTRODUCTION

Hydrogen diffusion in steels at room temperature (0-90°C) is usually studied by the hydrogen permeation technique. This technique is aimed at obtaining the diffusion parameters of the bulk metal, but may be affected by surface effects which could render misleading results.

In this paper we do not concentrate on spurious films that could be present on the surfaces of the permeation membrane, such as a passive oxide film, or deformed layers resulting from mechanical polishing. We concentrate instead on the hydrogen transfer rate across the hydrogenating environment/metal interface.

When the hydrogen permeation transient is evaluated [1], the assumed boundary condition at the input side of the permeation membrane is either constant concentration [2] or constant flux [3]. In fact, these two boundary conditions represent extreme cases for the rate limiting step in the permeation process:

- Constant concentration implies local equilibrium at the input interface, i.e. fast transfer rate across the interface and permeation rate limited by the bulk metal.
- Constant flux implies that the transfer across the interface is the limiting step.

Crespo *et al* [4] suggest that there is no reason to choose only these extreme cases. They propose instead a phenomenological model which assumes that hydrogen flux has two components which follow either constant concentration or constant flow boundary conditions. The participation of each component in the overall process is quantified by a parameter which is obtained by fitting this model to the experimental data.

In this paper we attempt to describe the transport process that takes place at the input interface. A literature review [5] on the hydrogen transfer rate across the H_2/Pd interface shows that the transfer rate depends on many factors, among which the most important are: the hydrogen pressure (or hydrogen activity) at the gas phase; the presence of contaminant atoms or molecules (S, O, CO, etc) on the metal surface, and the surface activation, i.e. the ratio effective area : geometrical area. The most relevant facts are:

1. At very low pressures the transfer rate across very clean surfaces is very high and proportional to the hydrogen pressure, which shows that the dissociative chemisorption reaction $H_2 \rightarrow 2H$ (adsorbed) is the rate limiting step.
2. At moderate to high pressures the transfer rate is proportional to the square root of the hydrogen pressure, which means that the passage from adsorbed hydrogen to absorbed (interstitial) hydrogen –"*ad-ab* transition"– is rate limiting.
3. The contamination of the surface drastically reduces the transfer rate.
4. The activation of the surface (for example a Pd black deposit) increases the transfer rate referred to the geometrical area.

Additionally, the characterisation of the surface by different methods suggests that during contact of the metal with hydrogen, a thin (*ca.* 1 nm thickness) subsurface, H- rich layer forms, which seems to have great influence on the hydrogen transfer rate [6, 7].

The literature review on hydrogen transfer across the H_2-Ni interface [5] shows similar qualitative results. However, there is not as much quantitative data on this system as on the H_2/Pd system.

According to these literature reviews, for a typical hydrogen permeation experiment (moderate to high pressures and possible presence of surface contaminants), we expect that the transfer rate across the input interface will be limited by the *ad-ab* transition, i.e. the transfer rate will be proportional to

the square root of the hydrogen pressure. Hence we propose the following kinetic equation:

$$J_H = \Phi_{H_2,Me}\left(a_1 - a_2\right) \qquad \text{(Equation 1)}$$

where J_H is the transfer rate across the interface [mole H m^{-2} s^{-1}], $\Phi_{H_2,Me}$ is the hydrogen transfer coefficient, a_1 is the hydrogen activity at the gas phase (equal to the square root of the hydrogen partial pressure by definition), $a_2 = c_H / S_{Me}$ is the hydrogen activity at the bulk metal close to the interface, c_H is the hydrogen concentration at this location and S_{Me} is the Sieverts' constant of the metal *Me*.

To determine the hydrogen transfer coefficient we carried out hydrogen permeation experiments with either gas phase charging or cathodic charging and electrochemical detection. The permeation membranes were made of iron with an electrodeposited film of either Pd or Ni at the input surface. We used the frequency response analysis technique, in which a perturbation signal is superimposed to a steady state value of an input variable, and a response signal of an output variable is recorded. The input variable was the hydrogen pressure (gas phase charging) or the electrochemical potential (cathodic charging). The output variable was the hydrogen flux at the exit surface of the permeation membrane. We obtained an experimental complex permeation transfer function $H(\omega)$ and we compared it with a theoretical one, thus obtaining the parameters for the best fit, among them the hydrogen transfer coefficient. The mathematical expressions of the theoretical permeation transfer functions and also for the complex impedance at the input interface (which has been measured in the cathodic charging experiments) have been presented elsewhere [5] for an "RDD" system, i.e. a system which consists of two diffusing flat plates in series with a finite transfer rate at the input interface.

EXPERIMENTAL

Permeation membranes were pure iron plates (Goodfellow 99.5%, 100 to 900 µm thick) which were annealed (900°C for 1 h), electropolished and covered with an electrodeposited, ca. 10 nm thick Pd film at the exit surface in order to avoid surface impedances and to ensure quantitative detection of emerging hydrogen [3, 8, 9]. On the input side Pd (3 to 1000 nm thick) or Ni (10 nm to 10 µm thick) films were electrodeposited. The film thickness *L* of the thinner films (L < 1 µm) was assessed by processing X-ray electron probe microanalysis data with the GMR film software [10]

The frequency response analysis was carried out with a Solartron 1254 frequency response analyser (FRA). At the input surface either cathodic charging or gas phase charging was performed. The temperatures for both types of test ranged from 25°C to 70°C.

Gas phase charging was carried out by putting the input side in contact with pure hydrogen gas at a steady state pressure of *ca*. 1.2 bar. The pressure fluctuation was achieved with an electromechanical system composed of a piston, and electrical motor, a pressure transducer and a feedback amplifier, which followed the generator voltage signal of the FRA .The maximum frequency achieved by this system was 1 Hz. The fluctuating current at the exit side was introduced into one analyser channel of the FRA and the transfer function $H_{i_s,p}$, which relates the fluctuating hydrogen pressure at the input side with the fluctuating hydrogen current density at the exit side, was obtained.

Cathodic charging was carried out in 0.1M NaOH aqueous solution with a potentiostat in the potentiostatic mode, where a fluctuating potential signal was superimposed to the steady state potential. By using the four analyser channels, both the complex impedance at the input side and the permeation transfer function H_{i_s,i_e} which relates the fluctuating charging current density at the entry side with the fluctuating hydrogen current density at the exit side were recorded. Cathodic charging was performed only on the Ni/Fe system.

RESULTS AND DISCUSSION

The theoretical transfer functions were fitted to the measured ones by a non linear least squares fitting program based on the Marquardt method [11]. The fitting procedure yielded a list of parameters. The results concerning one of these parameters (the hydrogen transfer coefficient across the input interface) will be presented and discussed here.

Plated Pd input surfaces

The permeation transfer function of the RDD model contains 8 parameters, which are the Sieverts' constant, the diffusion coefficient and the thickness of each diffusing medium, the hydrogen transfer coefficient at the input interface $\Phi_{H_2/Pd}$ and a correction factor for the effective membrane area f_A. In order to carry out the fitting procedure, a number of parameters of the RDD model were fixed according to literature data or to direct independent measurement. Particularly, the Pd film thickness was assessed through X-ray electron probe microanalysis and Pd solubility data was that of the α' ($PdH_{0.7}$) phase which is the stable one at ~1 bar hydrogen pressure and the test temperatures [12]. The adjusted parameters were: 1) the diffusion coefficient of Hydrogen in the iron substrate, which usually yielded a value of *ca*. 7×10^{-5} cm^2 s^{-1} at 25°C; 2) f_A; and 3) $\Phi_{H_2/Pd}$. Fig. 1 is a plot of this latter parameter at 25°C, which shows an unexpected dependence on the

exposure time to the hydrogen environment. Other important fact is the marked dependence of $\Phi_{H_2/Pd}$ on the surface activation treatment. Measurements at other temperatures up to 70°C, not shown here, [5] show little dependence of $\Phi_{H_2/Pd}$ on temperature. The scatter of the results for similar Pd films is rather high, up to one order of magnitude, which should be attributed to uncontrolled state and/or contamination of the surface. The tendency of $\Phi_{H_2/Pd}$ to decrease with increasing exposure time to hydrogen might be explained by the gradual accumulation of subsurface hydrogen [7] at the first atomic layers of the Pd film.

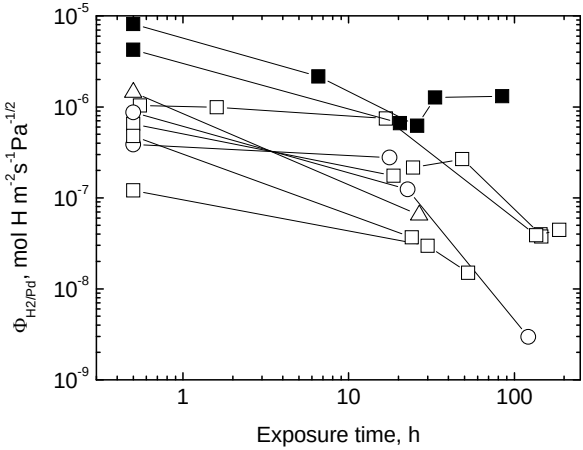


Figure 1: Hydrogen transfer coefficient at the input (H_2/Pd) interface of the H_2/Pd/Fe/Pd/0.1N NaOH system vs. exposure time to hydrogen at 25°C. Nature of the Pd deposit at the input interface: a) electrodeposited bright film with thickness of 10 nm (□), 100 nm (○) and 1000 nm (△); b) electrodeposited Pd black with equivalent thickness of ca. 140 nm (■)

In order to assess the influence of this surface effect on the results of the permeation technique, a critical parameter to be considered is the response time of the Pd film: for smaller response times, less important surface effects are expected. This response time is proportional both to $1/\Phi_{H_2/Pd}$ and to the capacity of the film to accumulate hydrogen. In this context, the Pd black deposit with a high $\Phi_{H_2/Pd}$ presents the disadvantage of requiring a considerable thickness, *ca*. 140 nm minimum equivalent thickness, which increases the hydrogen absorption capacity.

Ni plated input surfaces

The thickness of the electrodeposited Ni films ranged from 10 nm to 10 µm. The frequency response technique was in this case useful to perform a precise determination of the Sieverts' constant S_{Ni} and the diffusion coefficient D_{Ni} of the electrodeposited Ni film. Literature [13] reports that S_{Ni} and D_{Ni} in electrodeposited Ni films are quite different from S_{Ni} and D_{Ni} in bulk Ni. Therefore S_{Ni} and D_{Ni} were not taken from literature but fitted to the experimental permeation transfer functions together with $\Phi_{H_2/Ni}$ and f_A.

In the case of cathodic charging, both the complex impedance at the input surface and the permeation transfer function were used in the fitting procedure. The theoretical permeation transfer function and the impedance include as additional parameters: the kinetic constants of the hydrogen evolution reactions, namely k_V (Volmer), k_T (Tafel) and k_H (Heyrovsky), the equilibrium constant for the adsorption reaction K_{ad}, the diffusion coefficient of molecular hydrogen in the electrolyte D_{aq} and the thickness of the electrolyte boundary layer adjacent to the input surface L_{aq}. The energy shift coefficients α_V and α_H for the Volmer and Heyrovsky proton discharge reactions were assumed to be 0.5. At low overpotentials it was found that the molecular hydrogen was taken away from the electrode surface by diffusion to the bulk electrolyte rather than by bubble formation. The fitted parameters were: k_V, k_T, k_H, $\Phi_{H_2/Ni}$, D_{Ni} and S_{Ni}.

Contrary to the Pd plated input surface, in this case the transfer coefficient $\Phi_{H_2/Ni}$ is low enough to reduce the steady state hydrogen flow across the permeation membrane. Therefore, $\Phi_{H_2/Ni}$ can also be determined from the measurement of the steady state hydrogen flow. Fig. 2a shows the hydrogen transfer coefficient $\Phi_{H_2/Ni}$ (gas phase charging tests) as a function of the exposure time to hydrogen at four different temperatures. $\Phi_{H_2/Ni}$ increases slightly with temperature and decreases slightly with increasing exposure time to the hydrogenating environment. The influence of the exposure time is not as important as in the H_2/Pd system. The initial value of $\Phi_{H_2/Ni}$ is 1 to 2 orders of magnitude lower than the initial value of $\Phi_{H_2/Pd}$. The independence of $\Phi_{H_2/Ni}$ on the Ni film thickness suggests that the phenomenon studied here is a true interface process which involves a few atomic layers of the Ni film.

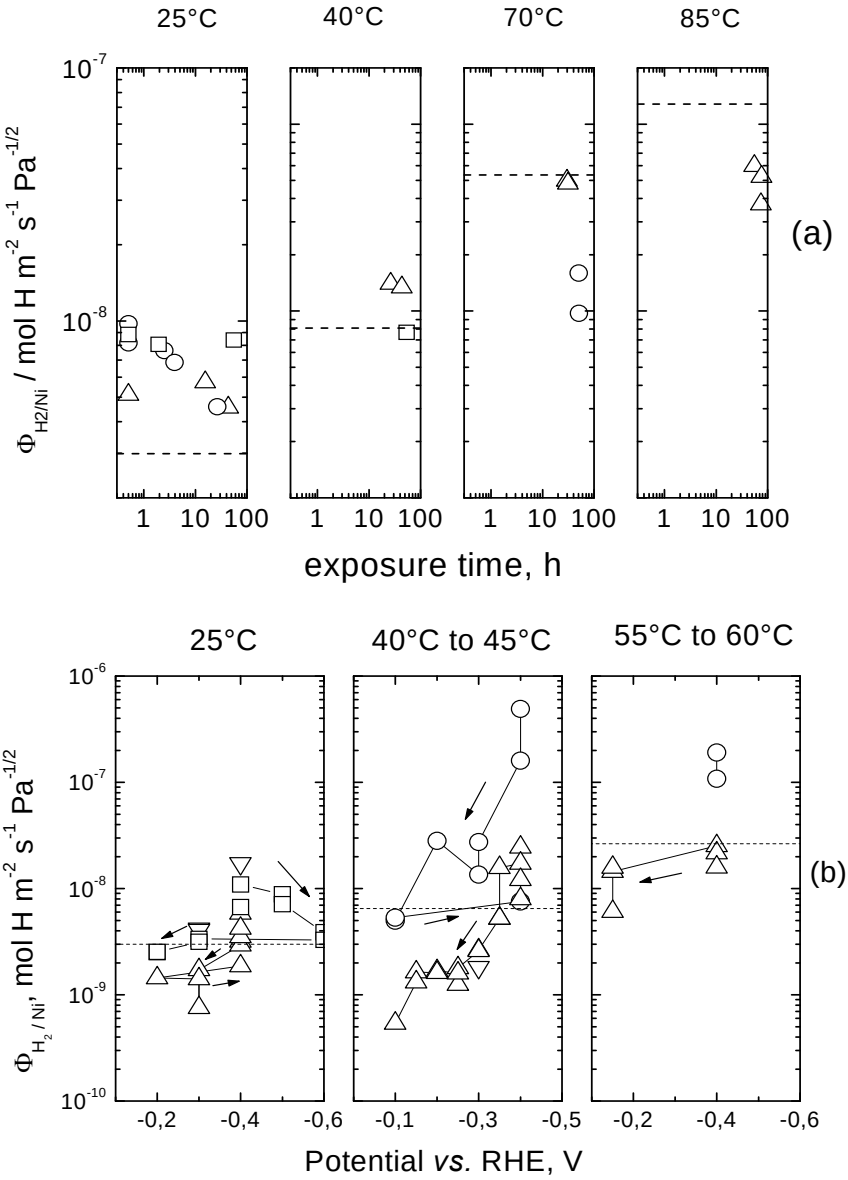


Fig. 2. Hydrogen transfer coefficient at the input (H_2/Ni) interface of the systems: H_2/Ni/Fe/Pd/0.1M NaOH (a) and 0.1M NaOH/Ni/Fe/Pd/0.1M NaOH (b). Bright Ni electrodeposit with thickness of 10 nm (□), 100 nm (○), 1 μm (△), and 10 μm (▽). Dashed lines indicate the hydrogen transfer coefficient calculated from steady state data of the H_2/Ni/Fe/Pd/0.1M NaOH system.

Similar values of $\Phi_{H_2/Ni}$ were obtained in the tests with cathodic charging (Fig. 2b). In this case, $\Phi_{H_2/Ni}$ is plotted vs. the applied potential referred to the reversible hydrogen electrode scale. This shows that the transfer process is not dependent on the hydrogenating medium, which gives support to the present assumption regarding the transfer law, eq. 1. In the case of cathodic charging there is no definite influence of the exposure time, as shown by the arrows on the graphs

CONCLUSION

Hydrogen transfer coefficients across the H_2/Pd, H_2Ni (gas phase charging) and NaOH/Ni (cathodic charging) interfaces have been determined for Ni and Pd electrodeposited films. These values, together with the hydrogen absorption capacity of the film, determine a response time constant which is useful to quantify surface effects in hydrogen permeation experiments.

ACKNOWLEDGMENTS

We thank the support of Comisión Nacional de Energía Atómica, Argentina.

REFERENCES

1. N. Boes and H. Züchner, J. Less-Common Metals, Vol. 49 (1976) 223.
2. E. Riecke and K. Bohnenkamp, Z. Metallkde., Vol. 75 (1984) 76.
3. Su-Il Pyun and R. A. Oriani, Corrosion Science, Vol. 29, (1989) 485.
4. P. Bruzzoni, R.M. Carranza, J.R. Collet Lacoste and E.A. Crespo, Electrochimica Acta, Vol.44 (1999) 2693.
5. P. Bruzzoni, Ph. D. Thesis. Universidad de Buenos Aires (2003).
6. H. Conrad, G.Ertl and E.E. Latta, Surface Science, Vol. 41 (1974) 435.
7. G.L. Powell, J.R. Kirkpatrick and J.W. Conant, J. Less-Common Metals, Vol. 172-174 (1991) 867.
8. P. Manolatos, M. Jerome and J. Galland, Electrochimica Acta, Vol. 40 (1995) 867.
9. P. Bruzzoni and G. Garavaglia, Corrosion Science, Vol. 33 (1992) 1797.
10. R.A Waldo. An iteration procedure to calculate film compositions and thicknesses in electron-probe microanalysis. Microbeam Analysis-1988 (23rd conference). San Francisco Press (1988) p. 310-314.
11. M.J.D. Powell, Computer Journal, Vol. 7, No. 2 (1964)
12. J.C. Hamilton and W.A. Swansiger, in “Hydrogen Effects on Materials”. A.W. Thompson and N.R. Moody, eds. The Minerals, Metals and Materials Society. Warrendale, Pennsylvania (1996) p. 271.
13. T.M. Harris and R.M. Latanision, Met. Trans. Vol. 22A (1991) 351-355.

Effects of Hydrogen on Materials
Proceedings of the 2008 International Hydrogen Conference
Brian Somerday, Petros Sofronis, Russell Jones, editors, p 524-531
Copyright © 2009 ASM International®
All rights reserved.
www.asminternational.org

NON-DESTRUCTIVE DETERMINATION OF THE DIFFUSION COEFFICIENT OF HYDROGEN IN STEEL

Angelique N. Lasseigne, J.D. McColskey, T.A. Siewert
National Institute of Standards and Technology, Boulder, CO, USA

K. Koenig, Joshua E. Jackson, David L. Olson, B. Mishra
Colorado School of Mines, Golden, CO, USA

ABSTRACT

Electronic tools are being developed to guarantee steel integrity by relating quantitative hydrogen content measurements in steel to its physical properties. Electronic tools can provide an increased sensitivity in hydrogen measurements compared to traditional analytical hydrogen techniques because the tools are a function of the electron concentration, effective mass, and dominating scattering mechanisms. Two non-destructive electronic sensors based on thermoelectric power and low frequency impedance have been developed to quickly and cost-effectively assess hydrogen content as a function of time in steel and its weldments. Monitoring of hydrogen content as a function of time with the non-destructive electronic tools allows for correlation of electronic measurements to the diffusion coefficient of hydrogen through the use of Fick's 2nd law and the Slope method. Examples of the use of both non-destructive electronic tools for hydrogen content determination as a function of time are presented and discussed in this paper.

INTRODUCTION

This paper introduces the use of non-destructive electronic tools for the assessment of diffusible hydrogen content in steels and steel weldments. Non-destructive electronic tools, such as thermoelectric power, offer increased sensitivity for assessment of hydrogen in steel compared to traditional analytical techniques because the electronic tools are a function of the electron concentration, the effective mass, and any scattering parameters. Interstitial hydrogen atoms either donate or accept electrons to/from the host metal electron conduction bands, so the addition of a hydrogen atom results in a change to both electron concentration and the Fermi energy level, which both change the electronic effective mass. The effective mass is a measure of the curvature of the electronic bands at the Fermi energy level, and the thermoelectric power coefficient is extremely sensitive to changes in the electron concentration and Fermi energy level (e.g. interstitial additions). Hydrogen additions similarly affect magnetic properties of metals because magnetic properties are sensitive to changes in atomic volume and chemical binding (donation of electrons to the host metal electron bands) during filling of the

interstitial sites. Electronic and magnetic techniques are complementary techniques for measuring interstitial contents in materials. Electromagnetic techniques such as low frequency impedance measurements can also be utilized for hydrogen content assessment. Impedance measurements are very similar to thermoelectric power measurements in that impedance is also very sensitive to changes in the electron conduction bands of the steel because the addition of hydrogen changes the material resistivity. Both thermoelectric power and low frequency impedance have been used to provide diffusible hydrogen content measurements as a function of time, which can be used to calculate the diffusion coefficient of hydrogen using Fick's 2nd Law.

Thermoelectric Power

The thermoelectric power coefficient (also referred to as the Seebeck coefficient) is a temperature-dependent electronic material property that can be described as the entropy of the free electrons in the alloy. In metallic alloys, the value and the sign of the thermoelectric power coefficient are dependent upon the electronic features in the vicinity of the Fermi energy level, the effective mass tensor, the density of electronic states, and the dominating scattering mechanism.[1] In turn, the Fermi energy value (Fermi energy surface in the k-space) changes with electronic filling in the conduction band due to the electron donation by hydrogen atoms. For example, with the high degeneracy of the free electron gas, the resulting thermoelectric power coefficient, Z, is related to electronic theory through the following expression:

$$Z = \left(\pm\frac{\bar{k}}{e}\right)(27.1)\left(r+\frac{3}{2}\right)\left(\frac{m_e}{h^2}\right)\left(\bar{k}Tn^{\left(-\frac{2}{3}\right)}\right) \qquad [1]$$

where r is the scattering parameter determined by the dominating scattering mechanism, and h is Planck's constant, $\bar{k}$ is Boltzmann's constant, n is the electron concentration, and m_e is the effective mass. From the free electron model, the electron concentration is directly related to the Fermi energy. The electronic effective mass defines the rate of Fermi energy change with increasing electron concentration.[1] The effective mass can be described as:

$$m_e = \hbar^2\left(\frac{d^2E}{dk^2}\right)^{-1} \qquad [2]$$

where k is the wave number. The effective mass, m_e, describes the shape of the s, p, and d bands that are in contact with the Fermi energy level. The shape of the bands at the contact position offers a characteristic indication that can be measured with changes in the Fermi energy level due to electron donation from the hydrogen addition.

To gauge the magnitude of the thermoelectric power effect, the thermoelectric power coefficient, Γ, is defined as the potential difference developed, dV, per unit temperature difference, dT:

$$\Gamma = \frac{dV}{dT} \qquad [3]$$

Two copper probes maintained at a constant temperature difference (controlled through internal heating cartridges and thermocouples), are placed on the material and then gives rise to a potential, V, between the copper probe and the material being investigated. The thermoelectric power coefficient of the Γ_a, is then calculated as:

$$\Gamma_a = \frac{V}{\Delta T} - \Gamma_{Cu} \qquad [4]$$

where Γ_{Cu} is the thermoelectric power coefficient of the reference copper probe. The temperature difference applied utilizing the thermoelectric power probes is very small (10˚C) to minimize the temperature-induced microstructural or mechanical changes ensuring a true property assessment.

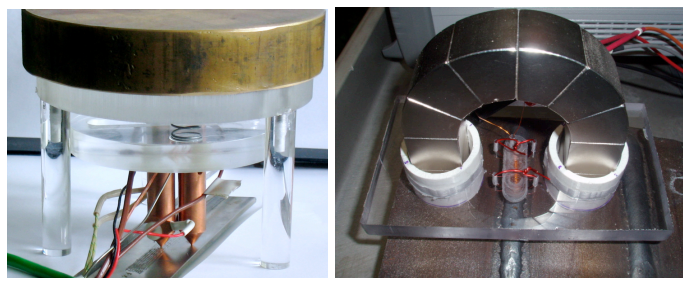


Figure 1: (a) Thermoelectric power surface contact probes and (b) low frequency impedance measurement probe for half inch thick steel specimens.

Low Frequency Impedance

Low frequency impedance measurements can provide an alternate nondestructive, non-contact method for monitoring diffusible hydrogen content in steel and weldments through coatings or lift-off. Previous research has found that low frequency impedance measurements are extremely sensitive to variations in hydrogen content in high strength steel specimens.[2]

In eddy current testing for hydrogen determination, a low frequency electromagnetic (EM) field is generated in a conductor by an alternating current. When placed in close proximity of the steel, the generated EM field induces currents (eddy currents) within the inspected material. In response, the eddy currents induced in the inspected material generates a magnetic field. The EM fields from the induction coil and the inspected

material must be detected either by electromagnetic induction in a coil. When an AC current is applied, the coil possesses both resistance and reactance. Along with resistance, there is a changing flux in the coil, which exhibits inductance.[3] The impedance, Z, may then be expressed as:

$$Z = \sqrt{(\omega L - \frac{1}{\omega C})^2 + R^2} \quad [5]$$

where ω is angular frequency, L is inductance, C is capacitance, and R is resistance. Impedance is a measurement of resistance, but with depth capabilities provided by the angular frequency.

To understand the effect of hydrogen on impedance, it is best to examine the resistance term of the impedance, which is where the actual change in hydrogen is being measured. At low induction frequencies, the inductance and capacitance terms are negligible. Therefore, impedance is approximately equal to resistance.[4] The resistance is given as:

$$R = \frac{\rho l}{A} \quad [6]$$

where ρ is resistivity, l is the length of the specimen, and A is the area of the specimen. The net resistivity is expressed by Matthiessen's rule, which states that independent scattering processes are additive:

$$\rho_{net} = \rho_{lattice} + \rho_{thermal} + \rho_{Hydrogen}[H] \quad [7]$$

where $\rho_{lattice}$ is scattering due to grain boundaries, defects, and other phenomena in the lattice, $\rho_{thermal}$ is thermal scattering due to temperature, and $\rho_{hydrogen}$ is the change in resistivity due to the addition of hydrogen atoms. When diffusible hydrogen enters into the metal, it also acts as a source of scattering, which arises from a departure from regularity in the ion lattice. The scattering due to the hydrogen atoms is independent of thermal scattering.

Accounting for the net resistivity and the angular frequency, the resistance can be re-written as:

$$R = \frac{(\rho_l + \rho_t + \rho_H[H])l(\omega + 1)^{1/2}}{A_o} \quad [8]$$

EXAMPLES OF THE USE OF THERMOELECTRIC POWER AND LOW FREQUENCY IMPEDANCE FOR DIFFUSIBLE HYDROGEN CONTENT DETERMINATION

Thermoelectric power and low frequency impedance measurements can both be utilized to provide hydrogen content measurements as a function of time to be correlated to material properties such as diffusion coefficient of hydrogen in a specific material or region. To run such a test, steel specimens have been charged with high- pressure gaseous hydrogen at temperature for extended periods of time. The goal is to achieve saturation and/or homogenization of hydrogen in the particular steel specimen, which includes that all hydrogen traps, both reversible and irreversible, are completely saturated. The saturated condition also gives a better indication of the likely condition of in-service pipeline steel in ten years as compared to brand new pipeline steel.

For a finite system with complete homogenization, it is assumed that solutions to Fick's laws exist, which are the product of a function of time T(t) and distance X(x). It is assumed that the concentration C is:

$$C(x,t) = X(x)T(t) \qquad [9]$$

The boundary conditions for diffusion of hydrogen out of a finite steel specimen are given as:

$$C(x,0) = C_o,\ 0 < x < h \qquad [10]$$

$$C(h,t) = 0 \text{ and } x = 0 \text{ at } t > 0 \qquad [11]$$

The solution to Fick's 2nd law is:

$$C(x,t) = \frac{4C_o}{\pi}\sum_{j=0}^{\infty}\frac{1}{(2j+1)}\sin\frac{(2j+1)\pi x}{h}\exp\left[\left(\frac{(2j+1)\pi}{h}\right)^2 Dt\right] \qquad [12]$$

For the situation of hydrogen gas removal, it is difficult to determine the hydrogen concentration at various depths, but what can be determined is the quantity of hydrogen that has been given off or the quantity of hydrogen remaining in the metal. For this purpose the average concentration is given as:

$$\bar{c} = \frac{1}{h}\int_0^h C(x,t)dx = \frac{8C_o}{\pi^2}\sum_{j=0}^{\infty}\frac{1}{(2j+1)^2}\exp\left[\left(\frac{(2j+1)\pi}{h}\right)^2 Dt\right] \quad [13]$$

Differentiating Equation 14 with respect to time gives:

$$\frac{\partial C}{\partial t} = \frac{nD^2t}{r^4}\exp\left(\frac{2\pi^2Dt}{r^2}\right)\left(1-\frac{\pi^2D}{r^2}\right) \quad [15]$$

which is important because it allows the Slope Method from ASTM Standard G-148-97 to be utilized to determine the diffusion coefficient of hydrogen for the specific conditions. It is important to note that all non-destructive tools must be initially calibrated using an alternate technique such as gas chromatography to quantify the hydrogen content as a function of time.

Comparison of Seebeck Effect and Low Frequency Impedance on X65 Pipeline Steel

Figures 2 (a) and (b) provide thermoelectric power coefficient and low frequency impedance measurements plotted as a function of time for hydrogen charged X65 grade steel specimen. The X65 steel specimen was deoxidized and then hydrogen charged at 1000 psi for 912 hours at 100˚C. Trying to synchronize three different tests resulted in large hydrogen losses, so that the initial hydrogen content in Figures 2 (a) and (b) are undetectable by gas chromatography because it is near one plus/minus a half of a part per million. The reason this data is important is that is shows the sensitivity in non-destructive electronic tools to measure hydrogen at levels lower than one part per million. The data between the two different electronic tools also correlate to one another showing that hydrogen has finally reached equilibrium in the steel.

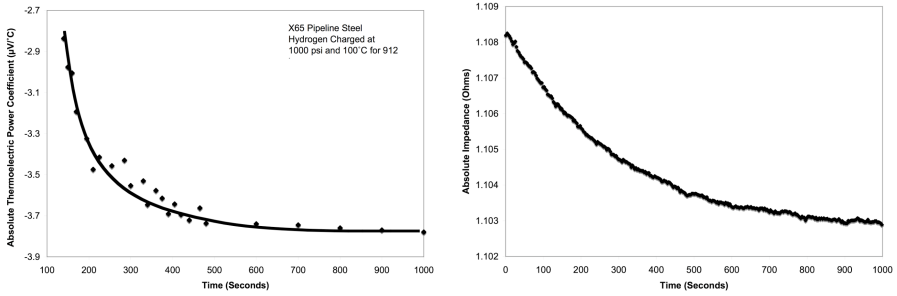


Figure 2 – (a) Thermoelectric power coefficient as a function of time (as hydrogen diffuses out) and (b) low frequency impedance as a function of time (as hydrogen diffuses out) for a gaseous hydrogen pre-charged X65 steel pipeline specimen.

Figures 3 (a) and (b) compare thermoelectric power coefficient measurements between ferritic-bainitic steel and an austenitic stainless steel as hydrogen diffuses out of the specimens. Austenite is known to have a high hydrogen solubility and low hydrogen diffusivity, while ferrite has low hydrogen solubility and high hydrogen diffusivity.

Figure 3 (a) indicates a much a quicker diffusion coefficient of hydrogen than in Figure 3 (b) agreeing with the common rule of thumb. The y-axes cannot be compared between materials because the electronic tools are calibrated to a standard. Figures 3 (a) and (b) are calibrated to different standards and can only be compared in terms of the rate of hydrogen coming out of the specimens. This data is important to show differentiation between materials with very different hydrogen diffusion rates.

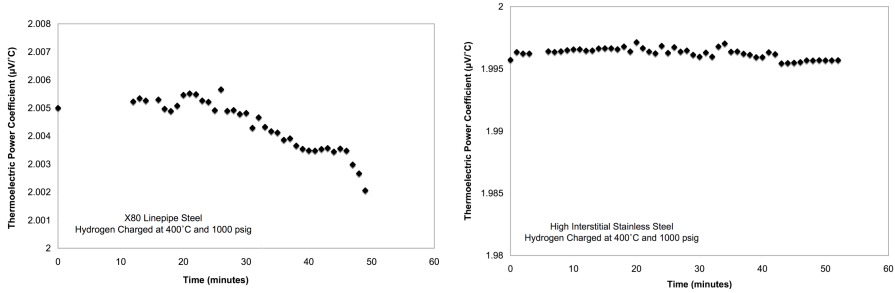


Figure 3: (a) Thermoelectric power as a function of time (as hydrogen diffuses out) for a gaseous hydrogen pre-charged X80 steel pipeline specimen and (b) thermoelectric power as a function of time (as hydrogen diffuses out) for a gaseous hydrogen pre-charged X80 pipeline steel specimen.

The last example presented here is the use of low frequency impedance measurements to monitor hydrogen content immediately following welding. Researchers have shown that up to eight hours after welding, hydrogen is still dynamic in the weldment and heat-affected zone.[5] To vary the hydrogen content in the weldments, different levels of hydrogen were introduced into the weld shielding gas while holding all other welding parameters constant. Figure 4 shows impedance as a function of time as hydrogen diffuses out of the weld bead for three different weld beads with three different shielding gases. The data starts approximately four and a half minutes after welding to allow for heat corrections from the weld metal. A thermocouple is also attached to measure the temperature of the weld for calibration of the sensor.

The low frequency impedance decreases as the hydrogen content in the shielding gas increases. This phenomenon is different than what has been seen previously on homogenous laboratory steel specimens where low frequency impedance increases with increasing hydrogen content. The effect of hydrogen on the shielding gas and on the weld-cooling rate is represented in this data. Higher hydrogen contents in the shielding gas results in a weld bead with a very high cooling rate, while shielding gas without hydrogen has a weld bead with a very slow cooling rate. The effect of hydrogen on cooling rates and hydrogen evolution out of the weld pool are being separated by holding the welding plate at a constant temperature to watch only hydrogen diffusion. The results are currently being reproduced and expanded upon.

Stress gradients must also be considered when trying to obtain accurate diffusion measurements. This is especially important for fatigue testing with crack tips because hydrogen will try to accumulate in the region around the crack tip as opposed to homogeneously distributing itself in the metal lattice. The flux of hydrogen in the system

is product of the concentration, mobility, and driving force. The stress in the lattice is a new driving force. This effect of the stress gradient on the diffusion coefficient of hydrogen in steel is under investigation.

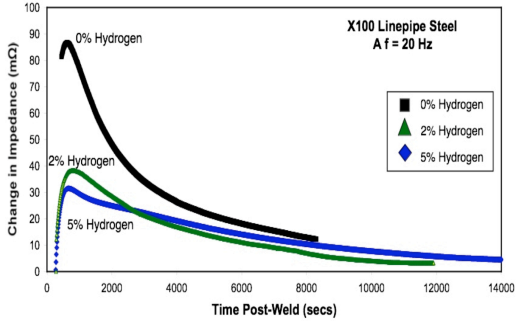


Figure 4: Change in low frequency impedance as a function of time (as hydrogen diffuses out) for X100 steel pipeline weld specimens.[2]

CONCLUSIONS

With proper calibration, both thermoelectric power and low frequency impedance can be used to monitor hydrogen content as a function of time to provide valuable material property information.

ACKNOWLEDGMENTS

The authors would like to thank and acknowledge the support of DOT-PHMSA.

REFERENCES

1. Park, Y.D., Lasseigne, A.N., Kaydanov, V.I., Olson, D.L., 10th CF/DRDC Meeting on Naval Applications of Materials Technology, "Thermoelectric Diagnostics for Non-Destructive Evaluation of Materials", CRDC, Dartmouth, NS, Canada, May13-15, (2003), pp. 648-666.
2. Lasseigne, A.N., Koenig, K., Olson, D.L., Jackson, J.E., Mishra, B., and McColskey, J.D., "Real-Time Low Frequency Impedance Measurements for Determination of Hydrogen Content in Pipeline Steel", QNDE 2008, Chicago, Illinois, AIP, (July, 2008), In press.
3. Bray, D.E. and Stanley, R.K., *Non-Destructive Evaluation: A Tool in Design, Manufacturing, and Service*, Rev. Ed., CRC Press, Inc., Boca Raton, FL,(1997).
4. Lasseigne, A.N., Anton, J.M., Siewert, T.A., Olson, D.L., Mishra, B., and Jackson, J.E., "Advanced Non-Destructive Measurement Scheme to Actively Monitor Hydrogen Content in Steel Pipelines", QNDE 2007, Golden, Colorado, AIP, (July, 2007), In press.
5. Yurioka, N., and Suzuki, H., "Hydrogen-Assisted Cracking in C-Mn and Lo-Alloy Steel Weldments", Int. Mater. Rev. 35(4), (1990), pp. 217-249.

Effects of Hydrogen on Materials
Proceedings of the 2008 International Hydrogen Conference
Brian Somerday, Petros Sofronis, Russell Jones, editors, p 532-539
Copyright © 2009 ASM International®
All rights reserved.
www.asminternational.org

HYDROGEN PENETRATION BEHAVIOR OF HIGH STRENGTH LOW ALLOY STEEL WITH PLASTIC DEFORMATION IN GASEOUS HYDROGEN

Koichi TAKASAWA, Yoru WADA, Ryoji ISHIGAKI and Yasuhiko TANAKA
The Japan Steel Works, Ltd., Muroran Research Laboratory, 4, Chatsu-machi, Muroran, Hokkaido, Japan

ABSTRACT

In order to investigate the behavior of hydrogen penetration in high strength low alloy steel caused by the tensile deformation in hydrogen atmosphere, the thermal desorption analysis for the tensile specimens deformed in hydrogen atmosphere was performed. The test material was the high yield strength steel plate for welded structure (JIS G 3128, SHY685NS). The tensile tests were carried out in 0.5MPa hydrogen atmosphere using the specially designed miniature tensile apparatus, and the hydrogen contents were measured by thermal desorption analysis (TDA) using a quadrupole mass spectrometer (QMS) in the temperature range from room temperature to 600ºC. Hydrogen penetration of the order of 10^{-3} mass ppm into the specimen was observed after tensile test in hydrogen atmosphere. Hydrogen penetrated into the specimens has also been measured even after the exposure to the air up to 6 hours in room temperature. The activation energy for hydrogen desorption was approximately calculated to be $27\pm1 kJ \cdot mol^{-1}$. This value is coincident with the binding energy between hydrogen and dislocation.

KEY WORDS

hydrogen environment embrittlement, high strength low alloy steel, thermal desorption analysis, plastic deformation, hydrogen penetration, dislocation

INTRODUCTION

The mechanism of hydrogen environment embrittlement in high strength steel has been strongly desired to be clarified systematically for designing and manufacturing the hydrogen gas equipment, such as a storage tank for high pressure hydrogen gas. Hydrogen transportation by dislocations has been considered as a very important elementary step of hydrogen embrittlement. So far, numerous studies have been done, for example, concerning the hydrogen effects on the dislocation mobility [1,2] and hydrogen accelerated transportation by dislocations [3,4]. However, hydrogen penetration behavior from the gaseous environment caused by deformation has not been well known. Numerical data like trap energy has been required to be accumulated to approach the problem. The objective of this study is the quantitative characterization of the hydrogen penetration caused by tensile deformation in the gaseous hydrogen environment in high strength steel.

EXPERIMENTAL PROCEDURE

Material and Specimens

The material was the high yield strength steel plate for welded structure, specified as JIS G 3128 SHY685NS. The chemical composition was shown in Table 1. The material was heat-treated at 920°C for 2h and water-quenched, then, to adjust proper strength, it was tempered 620°C for 3h. After heat treatment, the material was machined to rectangular, plate-type tension test specimens of 19mm (0.741inch) in overall length (parallel part: 8mm), 4mm (0.156inch) wide (parallel part: 3mm) and 1mm (0.039inch) in thickness. The configuration of specimens is shown in Fig.1. The surfaces of all specimens were polished by abrasive paper of #800 along the tensile direction. All specimens were cleaned in acetone for a few minutes using an ultrasonic cleaner, and then were weighed by electric balance.

Table 1 Chemical composition (mass%)
(Lower: specification value of JIS G 3128, Min./Max.)

C	Si	Mn	P	S	Ni	Cr	Mo	V	Cu	B
0.10	0.23	0.97	0.006	0.0006	1.45	0.50	0.51	0.04	0.23	0.0009
Max. 0.14	Max. 0.55	Max. 1.50	Max. 0.015	Max. 0.015	0.30/ 1.50	Max. 0.80	Max. 0.60	Max. 0.05	Max. 0.50	Max. 0.005

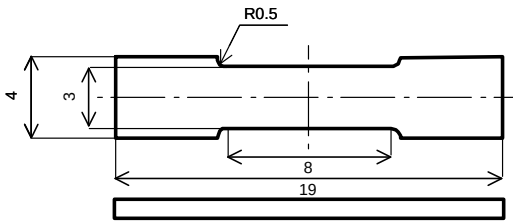


Fig.1 Specimen configuration

Tensile Test and Determination of Hydrogen Content

The tensile tests were carried out in 0.5MPa pure hydrogen gas environment using the specially designed miniature tensile test apparatus. The load capacity is 5kN, and the stroke rate can be varied from 0.01mm/min to 10mm/min. The cross-head displacement of the apparatus was calibrated and converted to strain using the strain gauge. The purity of hydrogen gas was higher than 99.99999%, especially the content of oxygen was suppressed below 1ppm.

As a distinguishing property of this apparatus, the dedicated vessel for transporting the specimen from tensile test apparatus to the QMS without exposure to the air is equipped. After a tensile test in hydrogen gas atmosphere, the specimen was quickly detached from the gripping device and put in the vessel, and then transported to QMS. Using this vessel, the hydrogen desorption analysis could be started within 10 minutes after finishing the tensile test.

The amount of hydrogen that penetrates into a specimen was expected to be very small. So, prior to the tensile test, the specimens were heated up to 600°C in a QMS to remove the hydrogen initially contained in the specimens. Then, the hydrogen content of the specimens was measured again to confirm that the initial hydrogen was desorbed.

Tensile tests were conducted on the following conditions; loaded up to 70%~86% of 0.2% proof stress (0.2% P.S.), loaded up to the tensile strength (T.S.). Stain rates were varied in the range between $1.1\times10^{-6}s^{-1}$ and $1.1\times10^{-4}s^{-1}$. Some specimens were exposed to the air for a few periods ranging from 0 to 6 hours after finishing the tensile test in 0.5MPa hydrogen gas at room temperature, and then their hydrogen content were quantified.

TDA of hydrogen contents were performed by a QMS. The temperature range measuring hydrogen content was from room temperature to 600°C. The heating rate was varied in the range between 50°C/h and 1800°C/h. Hydrogen contents of each specimen were determined by integration the desorption profiles in the temperature range from 50°C to 300°C.

RESULTS

Figure 2 shows the stress-displacement curves. Fig.3 (a) is the profile of the specimen only exposed to 0.5MPa hydrogen for 0.5h. The heating rate of each profile is 1800°C/h. Fig.3 (b) and (c) are the profile of the specimens that were unloaded below 0.2% P.S. In every profiles of Fig.3, numbers (1), (2) and (3) mean the following; TDA profile of the hydrogen initially contained in a specimen, TDA profile before tensile test and TDA profile after a tensile test, respectively. Comparing Fig.3 (a) to other profiles, peaks can be observed around 100°C~200°C of the profiles of (3). This indicates that hydrogen has penetrated into the specimen from the hydrogen gas environment during tensile deformation.

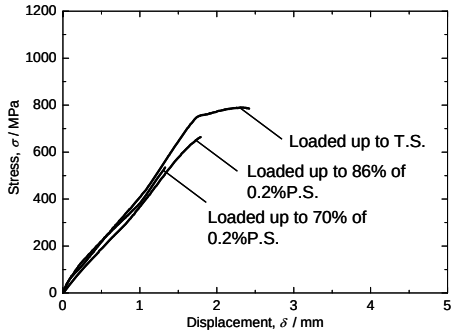


Fig. 2 Stress-displacement curves

Figure 4 shows the profiles of the specimens loaded up to T.S., and then exposed to the air for various periods. The heating rate of each profile is 1800°C/h. As seen the profiles in Fig.4, the peaks around 100°C~200°C have been observed regardless of increasing exposure time, showing that the hydrogen introduced from gas environment by tensile deformation are hard to escape from the specimen, even if it is exposed to the air for several hours. On the other hand, the peak heights of the profiles in Fig.4 around 150°C have been gradually decreased with increasing exposure time. This implies that detrapping of hydrogen caused by a microstructual

change in a specimen, for example, the annihilation of the unstable defects, has been occurred.

Figure 5 shows the hydrogen content of the specimens after tensile tests. Before loads have reached to the 0.2% P.S., hydrogen contents have increased with increasing load. When loads have reached up to T.S., hydrogen contents have increased moreover. However, the contents are very small, and approximately one tenth of the initial. The hydrogen contents have not varied according to the exposure time in air. The content was roughly a constant value of $6\sim8\times10^{-3}$ mass ppm.

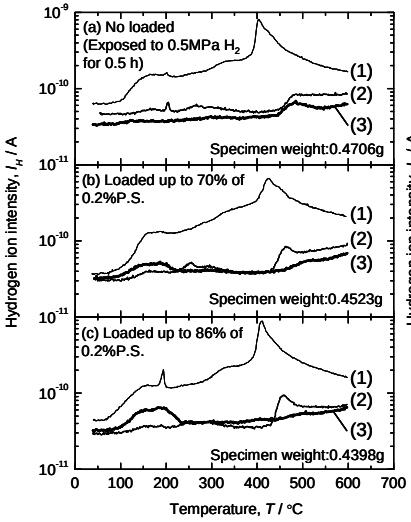


Fig.3 Hydrogen desorption profiles

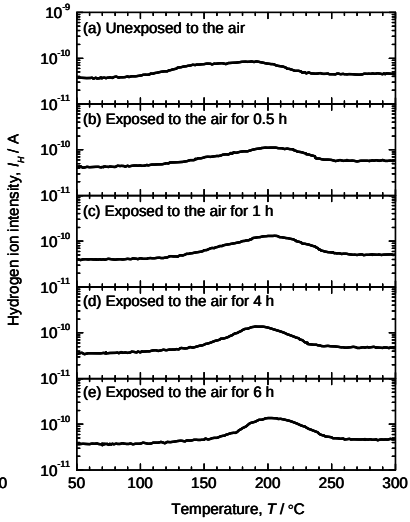


Fig.4 Hydrogen desorption profiles

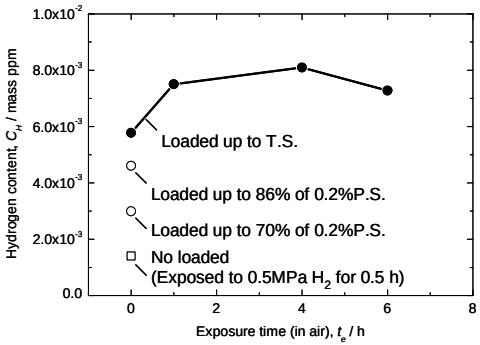


Fig.5 Relationship between hydrogen content and exposure time to the air

Figure 6 shows the hydrogen desorption profiles with various heating rate. The specimens were loaded up to T.S. in the strain rate of $1.1\times10^{-5}s^{-1}$.Two peaks have

been observed in each profile. The peak of lower temperature has been named T_{p1}, and that of higher temperature has been named T_{p2}. Both peaks have shifted to lower temperature with decreasing heating rate. The relationship between specimen weight and peak temperatures is shown in Fig.7. No specimen weight dependence of peak temperature has been observed.

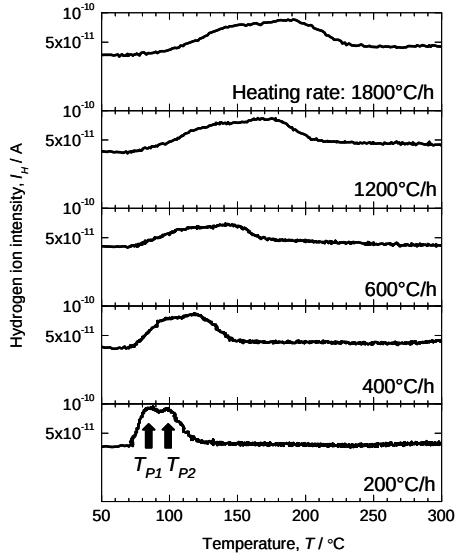


Fig.6 Hydrogen desorption profiles with various heating rate

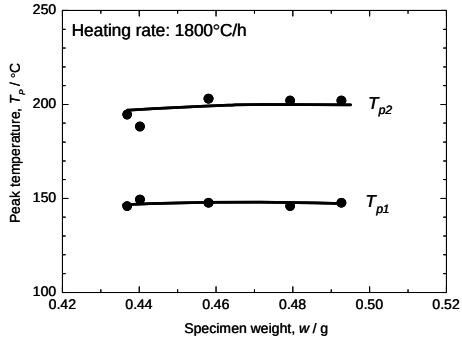


Fig. 7 Specimen weight dependence of peak temperature

The peak temperature T_p and heating rate ϕ have been related with the following equation [5];

$$\frac{E_a \phi}{\mathrm{R}T_p^{\,2}} = \mathrm{A}\exp\left(-\frac{E_a}{\mathrm{R}T_p}\right) \tag{1}$$

where E_a is the activation energy of desorption, ϕ is the heating rate, T_p is the peak temperature, A is the constant and R is the gas constant. Fig.8 shows the relationship between the values of ϕ / T_p^2 and inverse peak temperature $1 / T_p$. Both plots for T_{p1} and T_{p2} have shown the linearity. The activation energy E_{a1} and E_{a2} corresponding to T_{p1} and T_{p2} were 33±2kJ·mol^{-1} and 27±1kJ·mol^{-1}, respectively.

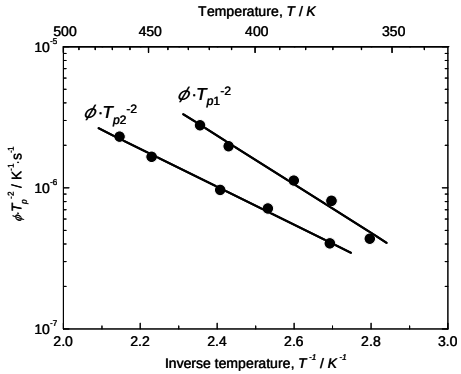


Fig.8 Peak temperature dependence of the values of ϕ / T_p^2

Figure 9 describes the strain dependence of the hydrogen content in the specimen. The open symbols show the hydrogen content obtained through the following way; to strain the specimen by the same amount as solid symbols in 0.1MPa nitrogen, then expose the specimens to 0.5MPa hydrogen at room temperature. The solid line is the stress-strain curve measured by use of strain gauge. Before specimens have yielded, hydrogen content has increased with increasing strain. However, after yielding, hydrogen content has slightly decreased. The strain rate dependence of the hydrogen content in the specimen is shown in Fig.10. No strong dependence has been observed.

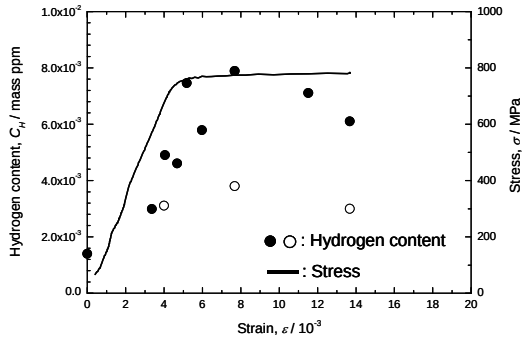


Fig.9 Relationship between hydrogen content and strain

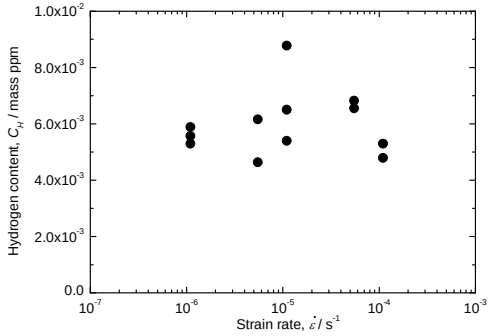


Fig.10 Relationship between hydrogen content and strain rate

DISCUSSION

The hydrogen desorption profiles shown in Fig.3 indicate that hydrogen can also penetrate into a steel before yielding. The specimen of this work contains large amount of dislocations because of its bainitic microstructure. So, hydrogen penetration observed before yielding is considered to be caused by the mobile dislocations, which can move even when the load is below the yield point.

The activation energy of the hydrogen desorption E_{a2} is nearly equal to the binding energy between hydrogen dislocation ever reported [5,6,7,8]. Conceivably, one of the trap sites generated by tensile deformation is dislocation. However, the other activation energy of this study E_{a1} is slight larger than E_{a2}, while the peak temperature T_{p1} is lower than T_{p2}. As seen in Fig.4, the peak heights of T_{p1} have been decreased with increasing exposure time. The energy of E_{a1} may be related the binding energy between hydrogen and unstable trap site, such as a small gap like vacancy resulted in cutting the dislocations. Decreasing of the peak height may have shown the hydrogen release behavior due to the annihilation of such unstable defects.

Donovan has researched as to the strain dependence of hydrogen release rate in 304L stainless steel, showing that the hydrogen release rate rapidly increased at the proportional limit or yield point, and then it decreased with increasing strain after yielding [9]. In this work, a remarkable increase of hydrogen content has not been observed at yield point, but observed a gradual increase of hydrogen content before yielding. This may have been attributed to bainitic structure comparatively contained much of a mobile dislocation.

CONCLUSIONS

Quantitative data on the hydrogen penetration behavior in steel have been obtained. Hydrogen penetration has been confirmed even when the specimen has not yielded. One of the trap sites generated due to tensile deformation has been clarified to dislocation.

ACKNOWLEDGMENTS

This work has been sponsored by the following organization in Japan; New Energy and Industrial Technology Development Organization (NEDO) and Petroleum Energy Center (PEC).

REFERENCES

1. Sofronis, P. and Birnbaum, H. K., "Mechanics of the hydrogen-dislocation-impurity interactions-I. Increasing shear modulus," *J. Mech. Phys. Solids,* Vol. 43, No. 1 (1995), pp. 49-90.
2. Delafosse, D., Chateau, J-P., Chambreuil, A. and Magnin, T., "Dislocation-hydrogen interactions during stress corrosion cracking in FCC metals: experiments on single crystals and numerical simulations," *Mater. Sci. Eng. A,* Vol. A 234-236, (1995), pp. 889-892.
3. Tien, J. K., Thompson, A. W., Bernstein, I. M. and Richards, R. J., "Hydrogen transport by dislocations," *Metall. Trans. A,* Vol. 7, No.6 (1976), pp. 821-829.
4. Hashimoto, M. and Latanision, R. M., "Theoretical study of hydrogen transport during plastic deformation in iron," *Acta. Metall.,* Vol. 36, No.7 (1988), pp. 1837-1854.
5. Choo, W. Y. and Lee, J. Y., "Thermal analysis of trapped hydrogen in pure iron," *Metall. Trans. A,* Vol. 13, No.1 (1982), pp. 135-140.
6. Hagi, H. and Hayashi, Y., "Dislocation trapping in hydrogen and deuterium diffusion in iron," *J. Jpn. Inst. Met.,* Vol. 49, No.5 (1985), pp. 327-331.
7. Choo, W. Y. and Lee, J. Y., "Effect of cold working on the hydrogen trapping phenomena in pure iron," *Metall. Trans. A,* Vol. 14, No.7 (1982), pp. 1299-1305.
8. Asano, S., Hara, K., Nakai, Y. and Ohtani, N., "The trapping effect of dislocations on hydrogen diffusion in mild steel," *J. Jpn. Inst. Met.,* Vol. 38, No.7 (1974), pp. 626-632.
9. Donovan, J. A., "Accelerated evolution of hydrogen from metals during plastic deformation," *Metall. Trans. A,* Vol. 7, No.11 (1976), pp. 1677-1683.

Effects of Hydrogen on Materials
Proceedings of the 2008 International Hydrogen Conference
Brian Somerday, Petros Sofronis, Russell Jones, editors, p 540-547
Copyright © 2009 ASM International®
All rights reserved.
www.asminternational.org

MAGNETOCORROSION OF PIPELINE STEEL

Joshua E. Jackson, David L. Olson, B. Mishra, A.J. Roubidoux
Colorado School of Mines, Golden, CO, USA

Angelique N. Lasseigne
National Institute of Standards and Technology, Boulder, CO, USA

ABSTRACT

The effects of magnetocorrosion, altered corrosion behavior in the presence of magnetic fields, are described for pipeline steels. Changes in corrosion behavior, including pitting, cracking, and hydrogen ingress, were assessed with and without an applied magnetic field. Electrochemical charging of pipeline steel specimens in the presence of a magnetic field led to significant increases in observed magnetocorrosion. Correlation of the observed corrosion with microstructure, mechanical properties, and magnetic properties was utilized to determine the important factors in magnetocorrosion. Electrochemical impedance spectroscopy testing indicated a significant impedance shift in the presence of a magnetic field.

INTRODUCTION

Stress-corrosion and hydrogen-assisted cracking have been attributed to a wide variety of failures, coated and uncoated pipelines, including those with cathodic protection systems. Hydrogen content surveys of pipeline steels have indicated (as compared with the as-installed state) increases of sixfold after one to two years of operation and more than tenfold after more than ten years in operation [1]. Many pipelines designed for expected operational lifetimes of 25-40 years are well beyond their initial designed operating life. For new construction, the pipeline industry increasingly utilizes higher strength grades of steel, thinner wall dimensions, and larger pipe diameters, along with increasingly negative potentials being used for cathodic protection. A review of pipeline fracture statistics found that as the average diameter has increased from 820 to 1020 mm, the length of pipeline ruptures increased from 29 to 50 m and the average operating time of the pipeline decreased from 21 to 13.7 years [2]. These changes are likely to significantly increase the number of stress-corrosion and hydrogen-assisted failures [3]. Numerous factors that influence the apparent hydrogen solubility of pipeline steels have been described, including non-metallic inclusions and cold work, both of which increase the number of hydrogen trapping sites [4]. Pipelines have many contributions to high-stress regions, such as weldments, grain boundaries, voids, crack tips, and hoop stresses,

the last of which is the largest. Hydrogen-induced cracks, fatigue cracks, cracks in the weld heat-affected zone, and stress corrosion cracks are the most common types of cracking in pipelines. Additional factors change the hydrogen absorption rate and saturation concentration, such as exposure to acidic environments or disturbance of the Helmholtz double layer (HDL) and/or the Gouy-Chapman layer (GCL).

Remanent magnetic fields are established in pipeline steel from numerous sources, including welding, nondestructive testing, magnetic clamps, magnetic lifts, and others. Similarly, electric fields are commonly present from cathodic protection currents that are constantly maintained to provide corrosion protection. Magnetocorrosion has been observed during electrochemical corrosion testing of pipeline steels at varied magnetization levels; previous and current research indicate increased hydrogen content, pitting, and cracking of pipeline steels during electrochemical charging in the presence of a magnetic field as compared to charging with no magnetic field. Cold work was shown to further increase magnetocorrosion effects [5]. Thermodynamic and kinetic modeling of the influence of magnetic and electric fields on pipeline steel corrosion were previously described [6].

EXPERIMENTAL WORK

The experimental work included the assessment of the microstructure, mechanical properties, and magnetic properties of pipeline steel grades X52, X65, X70, X80, and X100 to determine any correlations of properties with observed magnetocorrosion, electrochemical impedance spectroscopy, and other behaviors including as the observed characteristics of bubble nucleation during electrochemical charging. The directional orientation of the microstructures increased with increasing strength, while the yield strengths were all within fifteen to thirty percent above the minimum requirement of the API 5L specification for the X52 through X100 steel grades.

Assessment of Magnetic Properties

During in-line inspection of pipelines with magnetic flux leakage tools, saturating magnetic fields are applied and areas of magnetic flux leakage indicate potential areas of defects. Magnetic fields on the order of 1.4 to 1.8 T and 3.5 to 20 Oe are commonly utilized during magnetic flux leakage to ensure complete magnetic saturation. Following passage of the inspection tool, remanent magnetic fields from 0.3 to 1.5 T remain in the pipeline steel (the value of which is dependent upon a number of variables including material composition, stress state, dislocation density, and other factors) [7]. Magnetic property measurements were made using a Vibrating Sample Magnetometer (VSM) for X70 and X80 grade steels. For approximate observation of magnetic properties, this technique is sufficient, but for accurate correlation of magnetic properties to observed magnetocorrosion, improved magnetic properties assessment techniques (a hysteresisgraph with a single strip tester) were employed. The large magnetic saturation values that were measured were consistent with other CSM-NIST measurements [5] and values measured from 36 linepipe

steels [8]. Figure 1 indicates the measured magnetic remanence calculated from magnetic hysteresis loops measured at 30 Hz as a function of maximum applied magnetic field for longitudinal (L) and radial (R) samples of X52 (X52L and X52R), X65 (X65L), X70 (X70L and X70R), and from two X100 type steels (X100A L, X100A R, X100B L, and X100B R). Increased directionality (due to processing) of higher-strength steel samples results in greater disparity between magnetic properties in the longitudinal and radial directions.

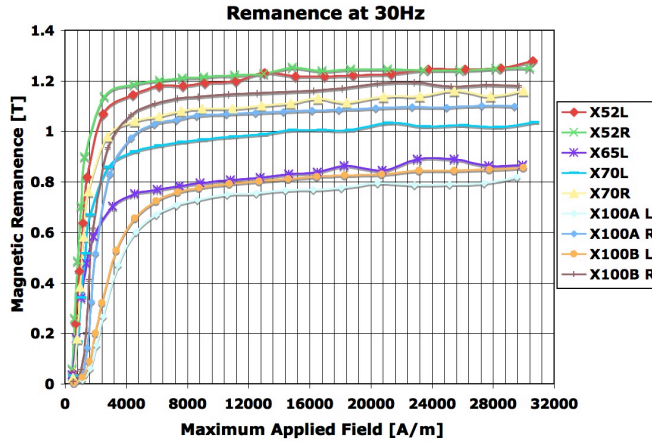


Figure 1 - Magnetic remanence as a function of maximum applied field was measured in a single strip tester at 30 Hz for longitudinal (L) and radial (R) samples of X52, X65, X70, X100A, and X100B pipeline steels.

Assessment by Electrochemical Impedance Spectroscopy

Electrochemical impedance spectroscopy (EIS) is a common technique utilized to assess the impedance of an electrode system. EIS utilizes a relatively small AC field superimposed on a cathodic or anodic current of choice and is useful for assessment of process dynamics and surface characteristics. The AC voltage variation typically has little or no effect on the phenomena being studied, particularly when a much larger constant applied voltage is being utilized. The electrochemical kinetics of magnetocorrosion were modeled [9] and tested with EIS to assess the corroding surface behavior. A significant shift in the electrochemical impedance is observed in the presence of magnetic fields of maximum strength of approximately 0.6 T. Models of the surface electron interactions were introduced to evaluate the increase in impedance [9]. The potentiodynamic curves for each steel type allow determination of the cathodic voltage region of the working electrode (specimen). Varying of the applied AC field frequency allows assessment of a wide variety of chemical and physical properties, because impedance is a function of the resistivity (a measure of the exchange current density), capacitance (a measure of the influence of the HDL), and inductance (a measure of the influence of the GCL).
Thirty-minute cathodic charging steps at a given voltage were followed by impedance sweeps at the same voltage with varied levels of DC voltage, AC voltage,

and finally a potentiodynamic polarization sweep. For the selected steels, the change from anode to cathode occurs between -500 and -550 mV, and therefore the analysis of electrochemical impedance was performed at voltages from -550 mV to -1500 mV. Frequency sweeps from 0.1 to 100,000 Hz were performed to measure electrochemical impedance at these voltages with and without an applied magnetic field with an approximate maximum value of 0.6 T for X52, X65, X70, X80, and X100 grade pipeline steels. Direct current voltages of -0.55, -0.65, -0.75, -0.85, -0.95, -1.05, -1.25, and -1.50 V relative to the open circuit potential were applied, and a substantial shift in the impedance across all frequencies was observed in the presence of a magnetic field, as well as significant spread in the low-frequency range. The measured impedance data, shown for X52, X65, and X70 (A and B) pipeline steels at -0.55 V in Figure 2, suggest that the resistivity, capacitance, and inductance are all altered by an applied magnetic field. The change in low-frequency data (below approximately 1000 Hz) suggests the effect of stirring of the Helmholtz double layer is decreasing the capacitance when the magnetic field is applied, resulting in an increase in the measured impedance. The small change of impedance in the high-frequency range suggests a limited disturbance of the Gouy-Chapman layer. The current was set at a minimum of 100 mA, but was not included in the measured EIS data. However, current measurements during the cathodic charging step (prior to each EIS sweep) were consistent with the measured impedances, assuming a constant voltage and the relationship of V=IZ (in the non-magnetic cases, lower impedance resulted in decreased current during cathodic charging and vice versa). Ongoing experimentation is being performed (with varied magnetic field strength, voltage, and other parameters) to determine the nature of the observed magnetocorrosion and impedance shifts in the presence of a magnetic field and the relationship between laboratory testing and *in-situ* effects on full-scale pipelines.

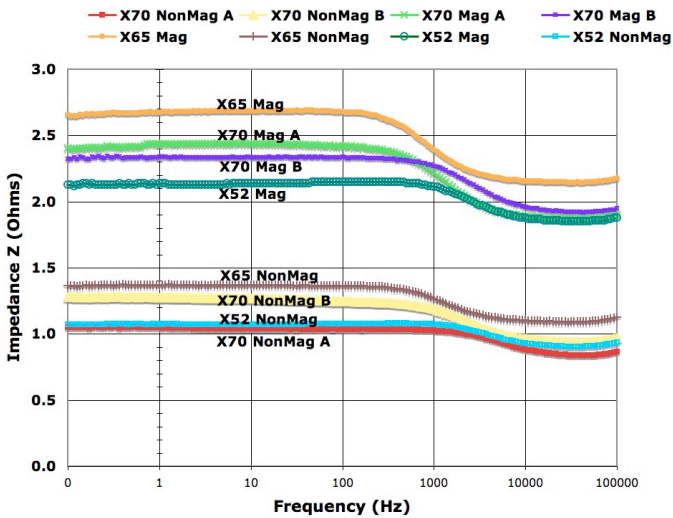


Figure 2- Impedance as a function of frequency (from 100,000 to 0.1 Hz) of a 50 mV AC perturbation field for X52, X65, and X70 grade steel with applied DC field of -550 mV and approximate maximum magnetic fields of 0 (NM) and 0.6 (M) T.

Magnetocorrosion Assessment

Electrochemical hydrogen charging and impedance spectroscopy measurements were performed to confirm the previous work [5] and extend the data by varying the strength of the magnetic field, temperature, and other variables. A consistent testing regimen was established to minimize variations in the measured hydrogen content due to losses from the sample until combustion in the Leco hydrogen analyzer commenced. Electrochemical charging and impedance measurement experiments were performed in a 1N sulfuric acid solution with and without a (maximum) applied magnetic field of 0.6 T. The results obtained (with an applied DC voltage of -0.55 V) from the current hydrogen charging experiments (dark points - Roubidoux) are in good agreement with the preliminary experimental results (hollow points - Sanchez) as shown in Figure 3 [5].

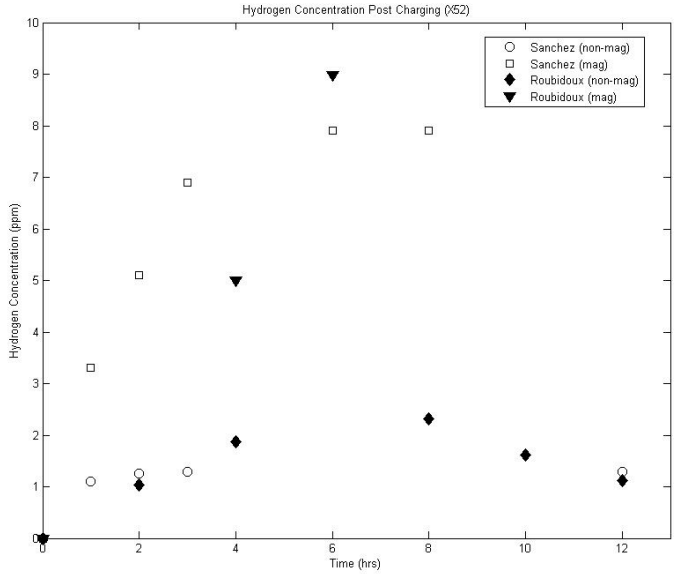
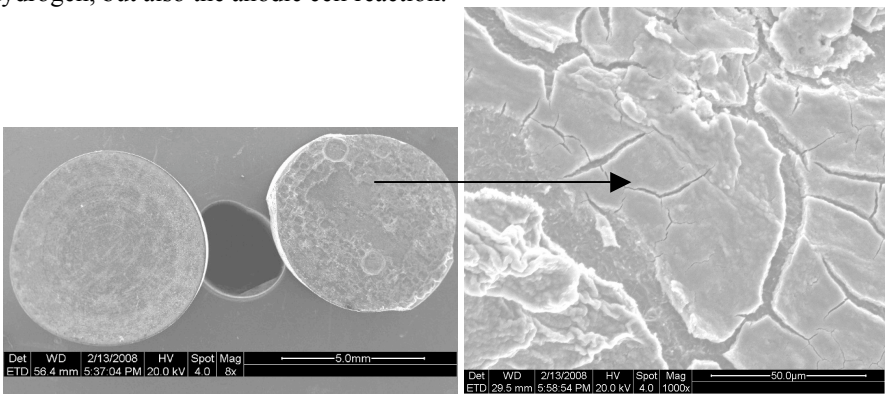


Figure 3 - Comparison of hydrogen concentration as a function of electrochemical charging time at -0.55 V (dark points) with previous data (hollow) [5].

The hydrogen concentration, as a function of charging time, confirmed that a magnetic field has a significant effect on absorbed hydrogen pipeline steel. At the surface of each magnet mount, the magnetic field was approximately 1.0 T, but with a separation distance of 12.7 mm (0.5 inches) between the magnet faces (the minimum required for specimen insertion), the maximum measured magnetic field strength was approximately 1.0 T. Figure 4 includes SEM images of specimens of X100 type steel (a) significant pitting visible at 8X magnification after charging for eight hours in (left) no magnetic field and (right) an approximate maximum 1.0 T field and (b) widespread cracking observed at 1000X magnification. These data clearly indicated severe corrosion of the magnetized specimen, with extensive pitting

and cracking, and only very minor corrosion of the unmagnetized specimen. Increased nucleation and propagation of cracks in a magnetic field, as described in Table 1, suggests the threshold level for hydrogen damage was more easily reached in a magnetic field. The observed pitting was an anodic behavior that suggests magnetization not only increases the cathodic cell reaction, the generation of hydrogen, but also the anodic cell reaction.



(A) (B)

Figure 4 - SEM image of X100 type steel specimen after electrochemical charging for eight hours in (a) at 8X in (left) no magnetic field and (right and B) in approximately (maximum) 1.0 T magnetic field, and (B) 1000X in an approximately maximum 1.0 T magnetic field.

Table 1 - Pitting and cracking analysis of X52, X65, X70, X80, and X100 type pipeline steels.

8 Hours	**Pitting**	**Pitting**	**Cracking**	**Cracking**
Steel	***Non-mag***	***Magnet***	***Non-mag***	***Magnet***
X52	**No**	**Yes**	**No**	**Yes**
X65	**No**	**Moderate**	**No**	**Moderate**
X70	**Minor**	**Yes**	**No**	**Yes**
X80	**Minor**	**Yes**	**No**	**Yes**
X100	**No**	**Heavy**	**No**	**Heavy**

The accelerated corrosion observed in the laboratory hydrogen charging setup is proposed to be an effective simulation of corrosion in a pipeline, in which the sources of hydrogen, electric current, and magnetic field are numerous and corrosion occurs over long periods. Longer-term test with less severe operating parameters and variables should be performed to assess this theory. Proposed thermodynamic models including the effects of spin alignment, magnetostriction, and solute-strain have been developed. A possible kinetic model for enhanced hydrogen pickup and corrosion, based on surface effects associated with the Gouy-Chapman layer and the Helmholtz double layer, was examined. Disturbance of these layers acts to limit

hydrogen transport from the environment into the steel and the transport of anodic product ions to the surface. The combination of large magnetic fields and cathodic protection currents returning in the pipe simultaneously may disturb these surface layers. Alteration of these layers may result in hydrogen super-saturation of the steel by directly altering the system kinetics. Each of these effects on the hydrogen content in magnetized steel was mechanistically described [9]. The predicted mechanism of corrosion based on this assessment suggests magnetocorrosion is most likely to occur late in the operational life of the pipeline coating, when the return currents from cathodic protection increase. As this occurs, the stirring mechanism may increase and lead to increased corrosion. Electrochemical impedance spectroscopy measurements suggest that the exchange current density may be modified when stirring alters the Helmholtz double layer, leading to the observed increases in hydrogen content, pitting, and cracking.

Bubble Formation and Flow

Bubble nucleation and flow was observed to differ in the presence of a magnetic field. During electrochemical charging with no magnetic field, bubbles nucleated and flowed directly up the side of the sample to the surface of the charging solution. When a magnetic field was introduced, the size of nucleated bubbles decreased and a complex helical flow pattern was observed in which bubbles flowed up and around the specimens. Bubble nucleation follows the classical theories of nucleation, such that a critical radius of atoms are required to nucleate so that nucleation and growth processes may proceed. Ongoing measurements are being performed to assess this observed magnetohydrodynamic behavior [10]. These measurements will determine if increased stirring from magnetohydrodynamics makes it harder for a critical radius of atoms to nucleate, thus reducing the size and amount of nucleated bubbles [9].

CONCLUSIONS

A significant increase in laboratory measurements of corrosion (magnetocorrosion), including hydrogen content, pitting and cracking occurs in the presence of a magnetic field. Significant magnetic remanence exists in pipeline steel, even following the application of magnetic fields at moderate levels. Sensitive measurements with electrochemical impedance spectroscopy of the corroding surface indicate a substantial change inr the presence of a magnetic field. The magnetic, mechanical, and magnetocorrosion behavior of pipeline steels have been measured, and only an apparent correlation between magnetic properties and magnetocorrosion exists but requires further assessment. This work corresponds with literature (magnetization and hydrogen cracking), anecdotal evidence, and experience in similar applications (magnetoelectrodeposition). There is a need to determine field strength effects (rate equation, acceptable limits) on pipeline integrity. Collaborations to continue field observations of corrosion and magnetization behavior in pipeline steels are ongoing. The described results indicate electromagnetic enhanced corrosion can be a concern in situations in which

significant electromagnetic fields are experienced. Based on these laboratory tests, sources of significant magnetic remanence appear likely to actively raise the hydrogen content and likelihood of hydrogen-related damage, particularly in older cathodic protected coated pipelines. Thermodynamic and kinetic models were introduced to assist in explaining the observed data.

ACKNOWLEDGMENTS

Kind thanks are offered to the U.S. Mineral Management Service and the U.S. Office of Pipeline Safety for their ongoing support and guidance, and to Dr. Ron Goldfarb of the National Institute of Standards and Technology – Magnetic Division for technical assistance.

REFERENCES

1. Mazel A.G., "On stress corrosion cracking of gas pipelines. Reliability and safety of gas pipelines subject to stress corrosion cracking", STP 2–4, Moscow: RAO Gazprom, (1993) pp. 11–22.
2. Polyakov, V.N. and Kharionovsky, V.V., "Statistics of transmission pipeline fractures" In: Rossmanith, H.P., editor, Structural failure product liability and technical insurance, London: E & FN Spon, (1996) pp. 353–61.
3. Shipilov, A.S., and May, I.L., "Structural Integrity of Aging Buried Pipelines Having Cathodic Protection", Engineering Failure Analysis, Vol. 13, Elsevier Science, (2006) pp. 1159-1176.
4. Maroef, I. S., Olson, D. L., Eberhart, M., and Edwards, G.R., "Hydrogen Trapping in Ferritic Steel Weld Metal", *Int. Mat. Rev.,* Vol. 47, No. 4, (2002) pp. 191-223.
5. Sanchez, F.J., Mishra, B., and Olson, D.L. "Magnetization Effect on Hydrogen Absorption in High-strength Steels and its Implications", *Scripta Mat.*, Vol. 53, No. 12, (2005) pp. 1443-1448.
6. Jackson, J.E., Olson, D.L., Lasseigne-Jackson, A.N., Mishra, B., and Siewert, T.A., "Correlating The Influence of Magnetic Field on Solute Content in Metals Using the Thermodynamic Auxiliary Work Functions", Proceedings of the Sixteenth Symposium on Thermophysical Properties, July 30- August 4, (2006), Boulder, CO, USA.
7. Bray, D.E. and Stanley, R.K., Nondestructive Evaluation, a Tool in Design, Manufacturing, and Service, Revised Edition, CRC Press, (1997).
8. Nestleroth, J.B. and Crouch, A.E. "Variations of Magnetic Properties in Pipeline Steels", Prepared for U.S. Dept. of Transportation DTRS56-96-C-0010 Washington, D.C. (1997).
9. Jackson, J.E., Roubidoux, J.A, Lasseigne, A.N., Mishra, B., and Olson, D.L., "Assessment of Magnetocorrosion by Magnetic and Impedance Measurements", Proceedings of QNDE 2008, Chicago, IL, American Institute of Physics, Melville, N. Y. (2008).
10. Fahidy, T.Z., "Magnetoelectrolysis", *J Appl. Electrochem.*, Vol. 13, (1983) pg. 553.

Effects of Hydrogen on Materials
Proceedings of the 2008 International Hydrogen Conference
Brian Somerday, Petros Sofronis, Russell Jones, editors, p 548-555
Copyright © 2009 ASM International®
All rights reserved.
www.asminternational.org

HYDROGEN INTERACTIONS WITH TITANIUM THIN FILMS

E. Tal-Gutelmacher, R. Gemma, A. Pundt and R. Kirchheim
Institute for Materials Physics, Georg-August University of Goettingen,
Friedrich-Hundt-Platz 1, 37077 Goettingen, Germany

ABSTRACT

Nanocrystalline titanium films were prepared on sapphire substrates in an UHV chamber, by means of ion beam sputter deposition under Ar-atmosphere at the pressure of $1{,}5 \cdot 10^{-4}$ mbar, with a deposition rate of 2,1 nm/min. The crystal structure was investigated by means of X-Ray diffraction. For electrochemical hydrogen charging, the films were covered by a 30 nm thick layer of Pd in order to prevent oxidation and facilitate hydrogen absorption. The samples were step-by-step charged with hydrogen by electrochemical charging. An Ag/AgCl (sat.) and Pt wires were used as the reference and the counter electrode, respectively. XRD measurements were performed before and after hydrogenation in order to investigate the effect of hydrogen on the microstructure. The main characteristics of hydrogen's absorption behaviour, as well as the thermodynamics and phase boundaries of titanium-hydrogen thin films are discussed in detail with specific emphasis on the comparison to titanium-hydrogen bulk system. Shifted phase boundaries and narrowed miscibility gaps were observed in Ti-H nanocrystalline film system. Large compressive stresses built up in these films during hydrogen absorption. In low hydrogen concentration range, α-phase region, the films behaved linear elastically, whereas with further hydrogenation, plastic deformation processes occur. Ti-hydride phase is quite stable, indicating an insignificant hydrogen loss in Ti-films.

INTRODUCTION

Titanium and its conventional alloys reveal a high affinity for hydrogen, being capable to absorb up to 60 at.% hydrogen at 600ºC, and even higher contents can be alloyed at lower temperatures. The hydrogen interaction with titanium takes the form of a simple eutectoid transformation with the α + hydride phases forming directly from the β phase [1, 2]. The strong stabilizing effect of hydrogen on the beta phase field results in a decrease of the alpha to beta transformation temperature from 882ºC to an eutectoid temperature of 300ºC. At this eutectoid temperature, the concentrations of hydrogen in the alpha, beta and delta (hydride) phases are 6.72 at%, 39 at% and 51.9 at%, respectively. The terminal hydrogen solubility in the beta phase (without the formation of a hydride phase) can reach as high as 50 at% at elevated temperatures above 600ºC. On the other hand, in the alpha phase, the

terminal hydrogen solubility is only approximately 7 at% at 300ºC and decreases rapidly with decreasing temperature. At room temperature, the terminal hydrogen solubility in alpha titanium is quite negligible (~0.04 at%) [3, 4]. Since in the group IV transition metals hydrogen tends to occupy tetrahedral interstitial sites [5], the higher solubility, as well as the rapid diffusion (especially at elevated temperatures) of hydrogen in the beta titanium results from the relatively open body centered cubic (bcc) structure, which consists of 12 tetrahedral and 6 octahedral interstices. In comparison, the hexagonal closed packed (hcp) lattice of alpha titanium exhibits only 4 tetrahedral and 2 octahedral interstitial sites.

As the forementioned hydrogen behavior within bulk titanium has been well-established and reviewed [1-6], this is not the case with titanium thin films. By reducing the system size to the nanometer-scale, the surface-to-volume atom ratio, and for nanocrystalline materials, the interface-to-volume atom ratio, becomes large. Therefore, surface and interface contributions become more relevant and are expected to change the system properties compared to bulk. Thin films are usually deposited onto substrates that are either single crystals, polycrystals or amorphous. The deposition conditions, e.g. technique, temperature, pressure, kinetic energy of the atoms, and the lattice misfit between film and substrate affect the films microstructure and the intrinsic stress of the as-grown thin film. The microstructure of thin films can be rather different and contain numerous microstructural defects. Films' grains can be of all sizes, ranging between that of nanocrystals with a high density of grain boundaries, to single crystals for epitaxial films. The mean grain size can also change in the vertical direction. Even when the grain size is maximized by epitaxial film growth, dislocations are generated during the film's growth process to adjust for the lattice mismatch between the film and the substrate. In the vicinity of these defects the hydrogen solubility is altered compared to conventional interstitial lattice sites [7, 8]. Furthermore, the interpretation of results in metal-hydrogen nanosized systems is complicated because the exact determination of the hydrogen concentration is difficult [9]. However, using electrochemical hydrogen charging technique under the proper conditions, the hydrogen concentration can be accurately determined via Faraday's law [8-10].

In this study the thermodynamics of ion beam sputtered titanium films during hydrogen absorption are investigated by electromotive force (EMF) measurements. The phase boundaries obtained from the EMF-Pressure-Concentration curves are confirmed by X-Ray diffraction (XRD) measurements. In-situ stress measurements reveal that high compressive stresses develop in Ti-films during hydrogen absorption. The change in the stress increase with hydrogen concentration is in good agreement with the observed phase boundaries.

EXPERIMENTAL PROCEDURE

Titanium films of 220 nm thickness were prepared on 0.2 mm thick, (001) oriented sapphire (Al_2O_3) substrates, in an UHV chamber by ion beam sputter deposition, at room temperature. The base pressure in the chamber was $3 \cdot 10^{-8}$ mbar, whereas the

deposition took place under Argon atmosphere at the pressure of $1.5 \cdot 10^{-4}$ mbar. The deposition rate was 2.1 nm/min. The sputtering parameters are described in Table 1.

Table 1: Sputtering parameters of Ti-films.

Cathode	Discharge		Beam		Accelerator		Neutralizer	
Current (A)	Current (A)	Voltage (V)	Current (mA)	Voltage (V)	Current (A)	Voltage (V)	Heater (A)	Emission (mA)
2.70	0.15	55	12	599	0	200	2.57	15

In order to prevent oxidation and facilitate the electrochemical hydrogen charging, Ti-films were covered with a 30 nm thick Pd cap layer, which was also deposited at room temperature, under the same aforementioned conditions. The film's thickness was measured by profilometry. The crystal structure of the as-sputtered films was investigated by X-Ray diffraction using a Phillips X-Pert diffractometer with a Co-Kα radiation. Step by step hydrogen charging [9] was performed electrochemically in a 1:2 (vol.) H_3PO_4 : Glycerine electrolyte, at room temperature. An Ag/AgCl (sat.) and Pt wires were used as the reference and the counter electrode. The current density was 0.05 mA during each loading step. The electrolyte was carefully cleaned from oxygen by prior Argon gas bubbling, so that no hydrogen losses due to H2O formation occurred. The hydrogen concentration in the films was calculated from the measured electric charge by using Faraday's law. Neither buckling, nor detachment of the film from the substrate, was observed after hydrogen loading, indicating good adhesion between the Ti-films and the sapphire substrates. XRD measurements were conducted after each charging step in order to study the microstructural changes induced by hydrogen absorption and correlate them to the phase boundaries obtained from the EMF curves. The stresses developing in the film during hydrogen loading were in-situ determined by measuring the deflection of the substrate using the set-up described elsewhere [11], calculating its radius of curvature and inserting it to Stoney's equation [12].

$$\sigma = \frac{-E_s}{6(1-\nu_s)} \cdot \frac{t_s^{\,2}}{t_f R} \qquad (1)$$

where E_s and ν_s are the Young's Modulus and the Poisson's ratio of the substrate, t_s and t_f are respectively the thicknesses of the substrate and the film, and R is the substrate's radius of curvature

RESULTS AND DISCUSSION

Under the present sputtering conditions, the Ti-film grew as a nanocrystalline layer on the basal plane of the sapphire substrate. Besides the peaks of the substrate and

the Pd-cap, the only diffraction signal from the Ti-film was a broad peak around 43.3º, which in principle might be attributed to the (0002) hexagonal α-Ti. The XRD 2θ-θ scans of 220 nm Ti-films (Fig. 1) show a preferred basal plane orientation (0002), i.e. most grains are oriented so that the {000l} planes are parallel with the substrate.

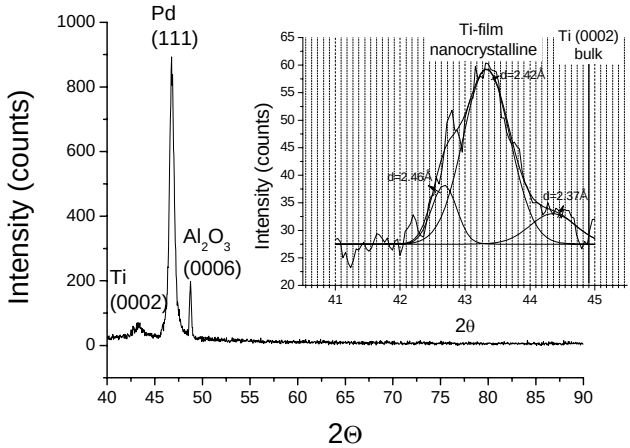


Figure 1: XRD pattern of 220 nm Ti-film sputtered at RT on (0001) Al_2O_3 substrate. Enlargement of the broad Ti-peak is shown in the inset.

The asymmetric shape of the diffraction pattern indicates that it is a superposition of three contributions from the Ti layer with different inter-planar spacing. It should be mentioned that the corresponding inter-planar spacing in bulk Ti is $d_{(0002)}$ = 2.3413Å [13] (the black solid line in the inset of Fig. 1). Thus, it is clear that the out-of-plane $d_{(0002)}$ lattice spacing in Ti-film is significantly larger than in bulk Ti, but this could result from residual strain of growth (intrinsic) origin [14], such as in-plane compressive stresses, caused by film clamping to sapphire substrate. A similar observation was reported for nanocrystalline Nb-films sputtered at room temperature on polished (100) Si-substrates [15]. From Full Width at Half Maxima (FWHM) of the Ti-peak, the calculated out-of-plane grain size (diameter) using Debye-Scherrer formula was found to be 13 nm.

The results of EMF measurements during hydrogen charging of 220 nm Ti-films, carried out at 294 K, are shown in Fig. 2. All the results shown below are those of the first charging. In comparison to Ti-H bulk system, Ti-H films exhibit significant changes. The plateau pressure of the sample is elevated compared to that of Ti–H bulk system. A plateau pressure of 10^{-11} Pa for bulk Ti at room temperature was extrapolated from [16]. The phase boundaries are shifted, α-phase limit is increased and the miscibility gap (two phase region) is narrowed, as summarized in Table 2.

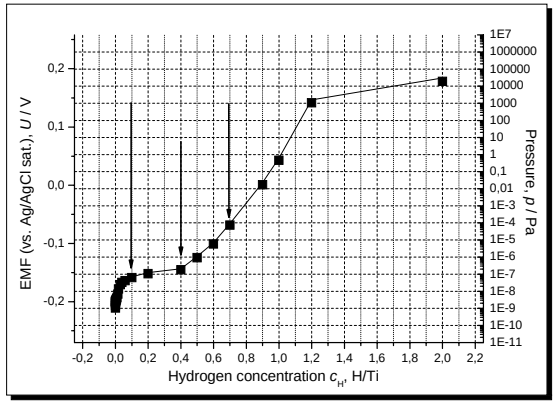


Figure 2: EMF-Pressure-Concentration curves of 220 nm Ti-film sputtered at RT on (0001) Al_2O_3 substrate. The arrows present the hydrogen concentrations where microstructural changes were observed by XRD.

Table 2: *Hydrogen solubility at room temperature in Ti-H systems.*

Ti-H systems	α-phase limit, [H/Ti, (at.%)]	Miscibility gap, [H/Ti, (at.%)]	Hydride's precipitation [H/Ti, (at.%)]	Remarks
Ti-bulk	4E-4 (0,04)	4E-4-1,5 (0,04-60)	1,5 (60)	As found in [1, 2]
Ti-film	0,1 (9)	0,1-0,7 (9-41)	0.7 (41)	Experimentally determined by EMF, XRD and stress measurements

The results of in-situ stress measurements and hydrogen cvharging, i.e. EMF measurements, are plotted in Fig. 3. In the α-phase region (for low concentrations below H/Ti = 0.1), the linear increase of compressive stress with a slope of −1.95 GPa/c_H was confirmed. Since the films are clamped to elastically hard substrates, the elastic volume expansion due to hydrogen absorption can take place only in out-of-plane direction z at low H concentrations. Remarkable slope changes in the stress curve are observed at hydrogen concentrations of 0.1, 0.7 and 1.2 H/Ti. These concentrations correspond to the phase boundaries obtained from the EMF and XRD measurements as will be described in the following section. At hydrogen concentrations between 0.1 – 0.7 H/Ti indicating the two-phase region, the curve bents towards a smaller stress increase. The deviation from elastic behaviour with the increase in hydrogen concentration can be explained by plastic deformation processes, which are attributed to the presence of misfit dislocations near the interface and to the emission of extrinsic dislocation loops during phase

transformation/hydride precipitation [17]. Between 0.7 – 1.2 H/Ti, the hydride phase region, the slope of the curve is quite similar to the slope observed for the α-phase. The slope change indicating further slow increase of the compressive stress above 1.2 H/Ti could be related to the charging of the Pd-capping layer, similar to the reports on Y-films [18]. The total hydrogen related stress for these nanocrystalline Ti-films is -2.0 GPa.

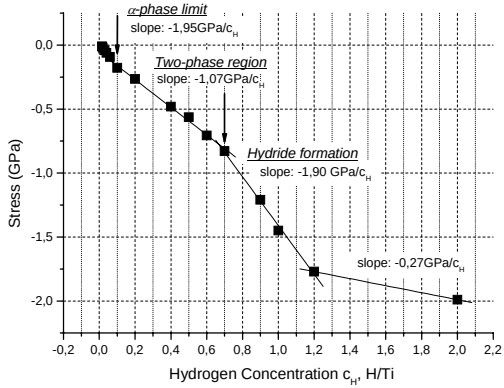


Figure 3: Stress curves of 220 nm Ti-film during hydrogen absorption, simultaneously obtained with EMF measurement. Slope variations occur at phase boundaries.

XRD results after each H-loading step are presented in Fig. 4. Hydrogen absorption up to 0.1 H/Ti leads to expansion of the α-Ti phase, as indicated by the shift of the broad (0002) peak to lower diffraction angles (Fig. 4.c.). However, the lattice parameter is not linearly increased. At 0.4 H/Ti a second peak appears at 40.8º in additional to the shifted Ti-peak, indicating the presence of the two-phase region. At 0.7 H/Ti, the α-phase peak disappears and the XRD pattern consists only of the hydride peak, which shifts to lower angles with further hydrogen absorption. From the broad, sole XRD peak it cannot be excluded whether the hydride structure is tetragonal or face-centered cubic. Reports on hydride precipitation in vapor deposited Ti thin films [19] revealed that two different hydrides formed on epitaxially electron-beam deposited Ti films, the face-centered tetragonal ($c/a > 1$) γ-hydride, and fcc δ-hydride. Nevertheless, the transformation of Ti to Ti-hydride results in a change of the film symmetry from hcp to either fcc or fct, which is accompanied by a volume increase that causes a release of a total compressive stress of -2,0 GPa. The brittle hydrides formed in the Ti-film are believed to cause decohesion from the sapphire substrate in these highly stressed regions [19]. However, no detachment, buckling or spalling was observed in these loaded films.

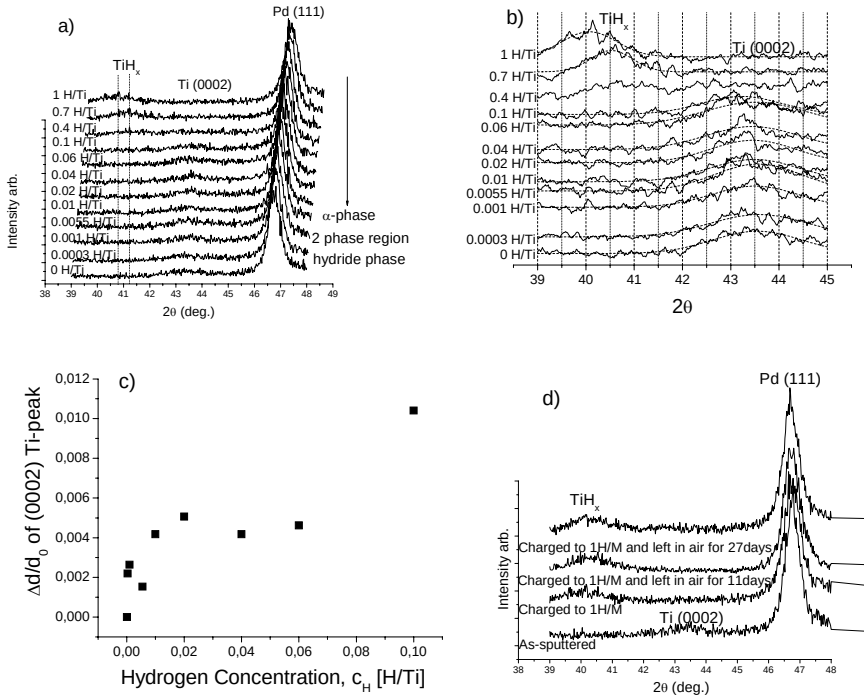


Figure 4: XRD pattern of 220 nm Ti-film sputtered at RT on (0001) Al_2O_3 substrate; Enlargement of the broad Ti-peak is shown in (b); (c) Relative expansion of inter-planar spacing, d, with hydrogen absorption in Ti α-phase; (d) XRD patterns of as-sputtered, H-charged up to c_H=1 H/M and left in air for different times

The hydride phase is quite stable, as indicated by XRD patterns in Fig. 4.d. Even after 27 days that the film was left in air, the diffraction pattern consists only of the hydride peak, which is slightly shifted to higher angles. Therefore, hydrogen loss is rather insignificant in these Ti-films.

CONCLUSIONS

In this study the main characteristics of hydrogen's absorption behaviour, the thermodynamics and phase boundaries of titanium-hydrogen thin films were investigated, with specific emphasis on the comparison to titanium-hydrogen bulk system. Hydrogen behavior in nanocrystalline Ti-thin films revealed significant changes in comparison to bulk material. Shifted phase boundaries and narrowed miscibility gaps appeared, as confirmed by simultaneously EMF, XRD and stress measurements. These changes can be attributed to both nano-structural (defects, i.e.

grain boundaries) and stress contributions. Large compressive stresses built up in Ti-films during hydrogen absorption. In low hydrogen concentration range, α-phase region, the films behaved linear elastically, whereas with further hydrogenation, plastic deformation processes occur. Ti-hydride phase is quite stable, indicating an insignificant hydrogen loss in these nanocrystalline Ti-films.

ACKNOWLEDGMENTS

The financial support of Alexander von Humboldt foundation is highly acknowledged.

REFERENCES

1. H. Numakura and M. Coiwa: Acta Metall. 32 (1984) p. 1799.
2. G.C. Woo, C.E. Weatherly, C.E. Coleman and R. W. Gillbert: Acta Metall. 33 (1985) p. 1897.
3. N.E. Paton and J.C. Williams, in: Effect of Hydrogen on Behavior of Materials, edited by: A.W. Thompson and I. M. Bernstein, AIME, New York, NY, (1976) p. 409.
4. H.G. Nelson, in: Hydrogen Effects in Metals, edited by: A.W. Thompson and N.R. Moody, TMS, Warrendale, PA, (1996) p. 699.
5. H. Wipf, B. Kappesser and R. Werner: J. Alloys and Comp. 310 (2000) p. 190.
6. E. Tal-Gutelmacher and D. Eliezer: JOM 57(9) (2005) p. 46.
7. A. Pundt: Adv. Eng. Mat. 6 (2004) p. 11.
8. A. Pundt and R. Kirchheim: Annu. Rev. Mater. Res. 36 (2006) p. 555.
9. R. Kirchheim: Prog. Mater. Sci. 32 (1988) p. 261.
10. H. Zuchner: Z. Naturforschung A. 25 (1970) p. 1490.
11. A. Pundt, E. Nikitin, P. Pekarski and R. Kirchheim: Acta Mat. 52 (2004) p. 1579.
12. G.G. Stoney: Proc. R. Soc. London, Ser. A, 82 (1909) 172.
13. ICDD – International Centre for Diffraction Data, Newtown Square, PA 19073-3273.
14. R. Checchetto and P. Scardi: J. Mater. Res. 14 (1999) p. 1969.
15. J. Cizek et. al.: J. Alloys and Comp. 446-447 (2007) p. 484.
16. E. Fromm and E. Gebhardt: Gase und Kohlenstoff in Metallen (Springer-Verlag, Berlin Heidelberg 1976).
17. U. Laudahn, A. Pundt, M. Bicker, U.v. Hulsen, U. Geyer, T. Wagner and R. Kirchheim: J. Alloys and Comp. 293-295 (1999) p. 490.
18. M. Dornheim, A. Pundt, R. Kirchheim, S.J. Molen, E.S. Kooji, J. Kerssemakers, R. Griessen, H. Harms and U. Geyer: J. Appl. Phys. 93 (2003) p. 8958.
19. S.R. Peddada, I.M. Robertson and H.K. Birnbaum: J. Mater. Res. 8 (1993) p. 291.

Effects of Hydrogen on Materials
Proceedings of the 2008 International Hydrogen Conference
Brian Somerday, Petros Sofronis, Russell Jones, editors, p 556-561
Copyright © 2009 ASM International®
All rights reserved.
www.asminternational.org

Corrosion of Uranium by Hydrogen at Low Hydrogen Pressures

G. Louis Powell
Y-12 National Security Complex, Oak Ridge, Tennessee, United States

Roland K. Schulze
Los Alamos National Laboratory, Los Alamos, New Mexico, United States

Wigbert J. Siekhaus
Lawrence Livermore National Laboratory, Livermore, California, United States

KEY WORDS

hydrogen absorbing materials, corrosion, catalyst, kinetics, gas-solid reactions

INTRODUCTION

The corrosion of uranium by hydrogen has been studied extensively and is characterized by pitting corrosion following an initiation time. Variability and unpredictability of the initiation time and the pitting characteristics are the salient features of this corrosion, and in the case of typically-machined engineering-grade uranium metal having a coherent oxide film, conditions eliminating this initiation time have never been achieved. Recent work by Teeter, et al.[1] (and a host of references therein) indicates that, at ambient temperature in the limit of low pressures, the initiation time appears to approach infinity. Ultra-high vacuum (UHV) baking (200^oC – 300^oC) of the uranium followed by exposure to very pure H_2 yields a much more predictable corrosion process with shorter initiation times[2-4], but the initiation time has never been eliminated for uranium having an oxide film. The coherent uranium oxide film plays a salient role in this process probably as both a physical and a chemical barrier, as does the residual work in the uranium metal, impurities in the gas phase, and the chemical and physical nature of the oxide. Recent observations by Bingert et al.[5] of "blisters" forming underneath the uranium oxide film prior to pit formation adds an additional process to the mechanisms of hydriding initiation. In order to gain more insight into this process, experiments have been carried out independently at the Y-12 National Security Complex (Y-12), Los Alamos National Laboratory (LANL), and Lawrence Livermore National Laboratory (LLNL) to further explore the implications of results reported by Teeter et al.[1] and Bingert et al[5]. These results, though preliminary, have been pooled in this report to form a basis for formulating a testable model for uranium hydride initiation.

*Managed by B&W Y-12, L. L. C. for the U. S. DEPARTMENT OF ENERGY under contract DE-AC05-00OR22800

EXPERIMENTAL

Experiments at Y-12 were directed towards measuring the initiation kinetics at low pressures and at ambient temperature to determine if hydriding would initiate at hydrogen pressures in the 100 Pa (1 Torr, an order of magnitude below that reported by Teeter[1]) range using ultrapure (Air Liquide six-9's pure UH_3 powder filtered) H_2 (UPH_2) to corrode uranium specimens aged or thermally activated under UHV conditions. Additional experimental control over the variables in this corrosion process was achieved by choosing the U substrate to be a spherical uranium powder (<100 μm) produced by sizing the product of the reduction of uranium oxide powder. Compared to a typical uranium corrosion coupon, this material has a high specific surface area with no corners or back-sides, the uranium metal was well annealed due to slow cooling from the melt during the reduction process, and the spherical uranium particles are coated with a coherent oxide film resulting from water exposure during a leaching process. The initiation of hydriding by H_2 pressure decrease was observed for this U powder (100 mg), aged at ambient temperature (20°C +/- 5°C) for ~600 Ms in a static argon environment followed by aging for 32 Ms in an UHV system (~2 L, 8 Ls^{-1} ion pump), by exposing the specimen to 1038.6 mL of UPH_2 at 128.22 Pa and 19°C via a <1 s expansion into a static volume using an MKS Type 690A01TRB pressure sensor and an Omega DP116 type K thermocouple temperature sensor, both monitored by a Nicolet 4094 digital oscilloscope at 1 s, 20 s, 200 s time intervals with 15 bit precision. The resulting reaction as pressure decrease (a la Teeter, et al.[1]) is given in Fig. 1. Figure 2 gives the results of a similar experiment that differed in that the UHV aging time was ~2.5 Ms followed by a 65 ks UHV bake at 300°C before exposing the specimen to 133.11 Pa UPH_2 in 1039.1 mL at 19°C. A pressure drop of 1 Pa represents a reaction extent of 8.55 X 10^{-7} mol H or 0.068 mol % conversion of the specimen to UH_3.

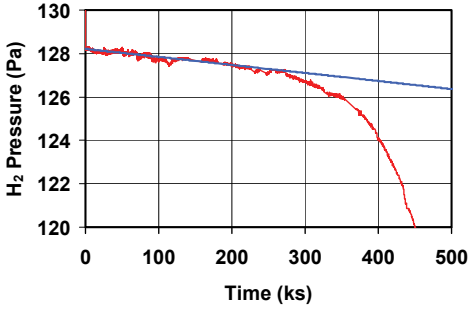


Figure 1. The initiation of the hydriding reaction of U powder at 19°C after extensive aging at ambient temperature. The straight line represents a linear fit of the data for the first 250 ks.

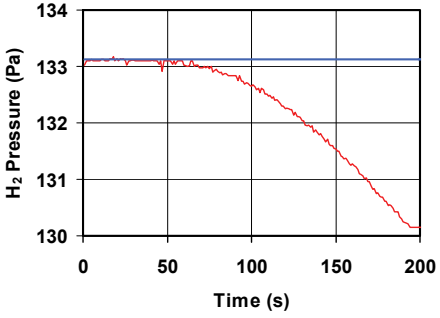


Figure 2. The initiation of the hydriding reaction of U powder at 19°C after thermal activation at 300°C. The straight line represents the linear pressure drop from the ambient aging only experiment, Fig. 1.

Experiments at LANL were directed towards observing blister formation on an engineering grade U disc 32 mm in diameter by 5 mm thick with rounded edges. Surface preparation was a wet grind using 600 grit sandpaper followed by a water rinse. The disc were then placed in UHV, gold-plated, minimal volume cells, evacuated for 864 ks at 70°C, and then exposed to ~400 Pa static H_2 for 570 ks during which time some pressure drop indicated initiation of the hydriding reaction. Examination of the disc by scanning Electron Microscopy (SEM) demonstrated that blisters of the type reported by Bingert were abundant (~300 per square centimeter >20 μm), had a common linear orientation, and each blister could be associated with an obvious defect (i.e., an inclusion, grain boundary, etc.). Typical SEM images of these blisters are shown in Fig. 3. No blisters were observed on a similar U disc that displayed pitting corrosion.

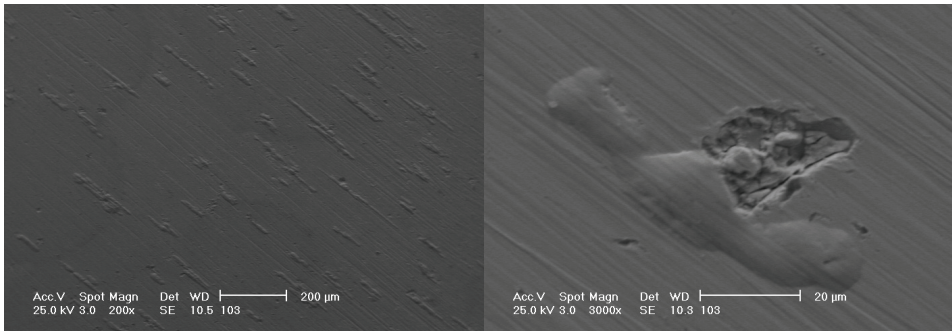


Figure 3. SEM blister formation images observed for the early stages of hydriding of U disc exposed to H_2 at 70°C.

Experiments at LLNL were directed towards observing the transition between blister formation and pit formation on engineering grade U that was mechanically polished (1μm diamond) and within minutes introduced into a UHV system. In the UHV system, the specimen was exposed to pure H_2 at 760 Torr and ambient temperature. The H_2 was removed as soon as a few hydride spots were visible by optical microscopy (~100X). Thereafter the U specimen was heated in vacuum to 200°C for ~30 ks to decompose UH_3 and to reduce its pyrophoric tendencies. The specimen was then transferred in air into a focused ion beam (FIB)/SEM system. Figure 4 shows a circular blister 4 μm in diameter with an inclusion located in the upper center part of the blister and cracks in the surface indicating that this blister may be on its way to become a pit. Figure 5 shows a pit 12 μm in diameter with a grain boundary extending from it into the lower left corner of the micrograph. Along that grain boundary are a number of small blisters. A surface film is rolling up with the "eruption" indicating that (1) forces are pushing on the surface from underneath and (2) this surface film, which is about 1 μm thick, is ductile and mostly uranium metal. Given the brief exposure to air for this sample, the oxide film on this surface is likely to be less than 20 nm. The flat spot in the middle of this pit is the surface of the metal and close inspection disclosed scratch marks from the polishing. Figure 6 shows a 60° FIB section through the center of the pit shown in Fig. 5. The penetration of the UH_3 into the U metal is non spherical and appears to be following a

grain boundary into the metal. The porosity in the pit subsurface region is due to shrinkage resulting from the conversion of UH_3 to U.

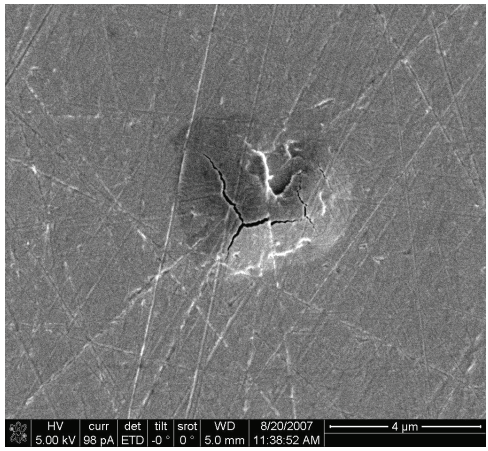


Figure 4. A circular blister with cracks indicating that it is about to become a pit.

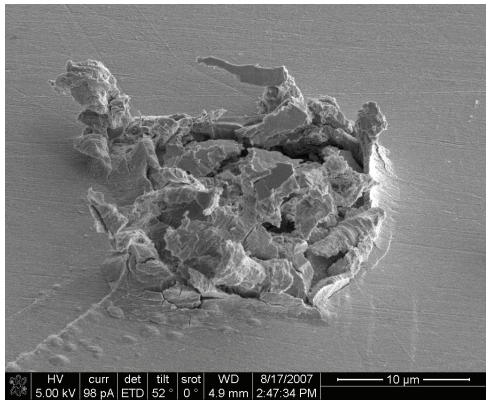


Figure 5. A corrosion pit with adjacent grain boundary, blisters, and surface film rollups.

DISCUSSION

Pure H_2 reacts with bare U by first dissolving in the U and subsequently precipitating as UH_3 as has been very effectively measured and modeled by Condon, Larson, and Kirkpatrick[2,3,6,7] to describe the reaction of hydrogen with pure U powders and the linear hydriding rate once corrosion pits have grown to completely eliminate the oxide film on U. They also demonstrated that oxidizing species in the gas phase and on the solid retard hydriding by suppressing the solubility of hydrogen in U, and that mechanical work in the U metal retards hydriding by opposing the large volume expansion required to nucleate UH_3 inside U. Once pitting has initiated, the same process drives pit growth and the eventual complete elimination of the uranium oxide film. The model for blister formation is based on these concepts. First assume that the coherent oxide on uranium typically tens of nanometers thick is an excellent physical barrier to hydrogen, except where there are physical defects such as inclusions and grain boundaries. This protective film is made thicker by the surface phase at the oxide-metal interface that suppresses the hydrogen solubility in the metal adjacent to the oxide. Mechanical work introduced near the surface by machining and polishing adds to the resistance of the region just underneath the oxide film to UH_3 nucleation. This work shows by electron microscopy of nascent hydride sites of micron dimensions that hydrogen transport below the mechanically deformed layer and the oxide layer occurs first at inclusions and grain boundaries and leads to the formation of blisters. With increasing hydrogen exposure these blisters break open and lead to what is usually called pitting corrosion. Thus the hydrogen can dissolve in the U only in small regions underneath the resisting surface film. The UH_3 mass grows slowly under great compression. The interface between the growing UH_3 mass and the U metal is the same mix of U metal and UH_3 precipitate as described in the Condon-Kirkpatrick Model[3] except the process is very slow because of the low cross-section for supplying hydrogen

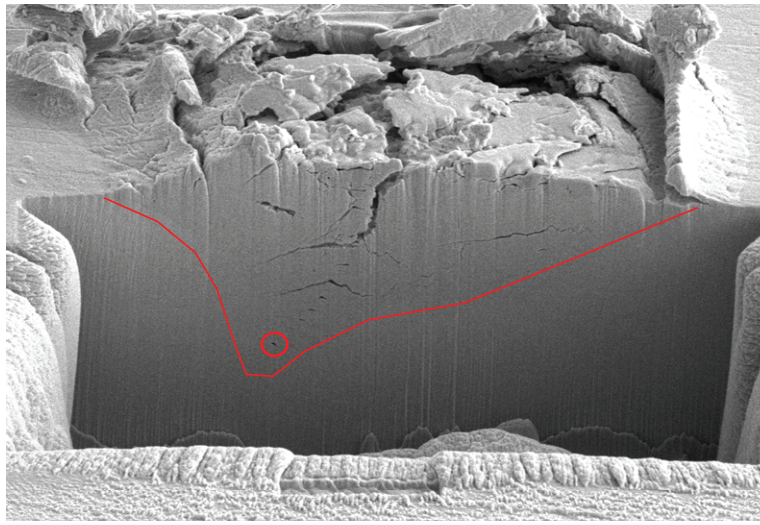


Figure 6. An SEM of a 60° FIB section through the center of the pit shown in Fig. 5 showing the penetration pattern of the UH_3 in the pit.

and the tortuous path for hydrogen through the compressed UH_3 product. Once breakthrough hydride sites (Fig. 4) occur, these sites have a tremendous increase in H_2 supply and the process converts to pit growth rather than blister formation.

CONCLUSIONS

For U having an oxide film, the initiation of hydriding is very slow under the best of conditions because the UH_3 must first form as a subsurface compressed mass that receives hydrogen through a very limited access region. Once a blister ruptures (a breakaway hydride site), the reaction can accelerate with the growing exposure of U unprotected by an oxide film. The Y-12 work demonstrates that slow initiation exists under the best conditions of aging and gas purity. The LANL work demonstrates that blisters are commonplace and occur in abundance. The LLNL work demonstrates that blisters erupt into pits. Optical observation of hydride pits does not reveal blistering, since the blisters have already disintegrated once they have reached a size where optical observation is typically applied. Further correlation of the results from each laboratory was not done since the Y-12 work had no microscopic results and the LANL and LLNL work was less quantitative in the measurement of hydriding extent. If the quantitative hydriding rate experimental capabilities can be closely coupled with the FIB/SEM measurements without exposure to air (Ideally, real time imaging of the surface during quantitative hydriding), then characterization of surface conditions that limit hydride initiation would be observed.

ACKNOWLEDGEMENTS

The authors gratefully acknowledge the support of LANL workers M. A. Hill, S. Gleiman, C. Necker, and D. Teeter.

REFERENCES

1. D. R. Teeter, R. J. Hanrahan, Jr., C. J. Wetteland, “Uranium Hydride Nucleation Kinetics, Effects of Oxide Thickiness and Vacuum Outgassing,” in “Hydrogen Effects on Material Behavior and Corrosion Deformation Interactions,” N. R. Moody. W. Thompson, R. E. Ricker, G. W. Was, and R. H. Jones,., eds. **TMS**, (2003).
2. G. L. Powell, W. L. Harper, and J. R. Kirkpatrick, "The Kinetics of the Hydriding of Uranium Metal," *J. Less Common Metals 172-174*, 116-123 (1991)
3. G. L. Powell, R. N. Ceo, W. L. Harper, and J. R. Kirkpatrick, "The Kinetics of the Hydriding of Uranium Metal II", *Z. Phys. Chem. NF, 181*, 275-282 (1993).
4. G. L. Powell, “Reaction of Oxygen with Uranium Hydride,” in “Advanced Materials for Energy Conversion II,” D. Chandra, R. G. Bautista, and L. Schlapbach, eds., TMS, (2004).
5. J. D. Bingert, R. J. Hanrahan Jr., R.D. Field, and P.O. Dickerson , “Texture Effects on the Nucleation of Uranium Hydride on α-Uranium”, *J. Alloys and Compounds*, 365, 138-48 (2004).
6. G. L. Powell, “Hydrogen in Uranium”, *Proceedings of the Depleted Uranium Conference, Y/DZ-2797*, MRC (Oak Ridge) May 2007.
7. J. B. Condon and E. A. Larson, “Kinetics of the Uranium-Hydrogen System”, *J. Chem. Phys., 59*, 1973, 855-865.
8 J. B. Condon, “Calculated vs. Experimental Hydrogen Reaction Rates with Uranium”, *J. Phys. Chem. 79*, 392-396 (1975).

Effects of Hydrogen on Materials
Proceedings of the 2008 International Hydrogen Conference
Brian Somerday, Petros Sofronis, Russell Jones, editors, p 562-569
Copyright © 2009 ASM International®
All rights reserved.
www.asminternational.org

CRACK-TIP HYDROGEN ACCUMULATION IN METALS UNDER TRANSIENT LOADING

J. Toribio and V. Kharin
Department of Materials Engineering, University of Salamanca
Campus Viriato, Avda. Requejo 33, 49022 Zamora, Spain
E-mail: toribio@usal.es; vikharin@gmail.com

INTRODUCTION

The basic idea about hydrogen assisted cracking (HAC) in metals states that fracture events near the crack tip are determined by a critical combination of hydrogen concentration C and responsible components of stress and plastic strain tensors $\underline{\underline{\boldsymbol{\sigma}}}$ and $\underline{\underline{\boldsymbol{\varepsilon}}}^p$ [1-3]. This may be expressed in terms of the critical concentration C_{cr} as a function of the stress-strain state parameters, *e.g.*, the maximal principal stress σ_1 and the equivalent plastic strain ε_{eq}^p, for definiteness [2,3]: $C_{cr} = C_{cr}(\sigma_1, \varepsilon_{eq}^p)$. Near-tip rupture event occurs at time t in a material unit at a certain location $\boldsymbol{x} = \boldsymbol{x}_c$, when

$$C(\mathbf{x}_c, t) = C_{cr}(\mathbf{x}_c, t) \equiv C_{cr}\left(\sigma_1(\mathbf{x}_c, t), \varepsilon_{eq}^p(\mathbf{x}_c, t)\right). \quad (1)$$

This way, HAC is controlled by the near-tip hydrogen accumulation. Stress-strain assisted hydrogen diffusion has been substantiated as the transport mode ruling HAC under ample range of conditions [1-5]. It has received various model treatments [1-6]. All of them take into account the effects of mechanical variables on hydrogen solubility K_S and diffusivity D in metals, but handle them in different terms, either relating strain-effects on solubility and diffusivity explicitly with the role of traps [4,5], or treating them phenomenologically, i.e., taking effective (apparent) strain-dependent solubility and diffusivity, $K_{S\varepsilon} = K_{S\varepsilon}(\varepsilon_{eq}^p)$ and $D = D(\varepsilon_{eq}^p)$, "as they are" [2,3,6]. The stress-dependent term $K_{S\sigma}$ of the overall hydrogen solubility $K_S = K_{S\sigma}K_{S\varepsilon}$ is commonly taken in the classical form $K_{S\sigma} = \exp(V_H\sigma/RT)$, where V_H is the partial molar volume of hydrogen in metal, R the universal gas constant, T the absolute temperature, and σ the hydrostatic stress.

Analysis of the near-tip hydrogen diffusion has received much attention [1-5], offering thorough data for sustained load case. Scarce data has been generated regarding the effects of non-steady loading history, such as cyclic (pre-)loading, and rising load dynamics. This paper outlines the attempts to fill-in some deficiencies on this matter bringing insight into the factors which can promote HAC in service.

MODELLING OUTLINE

Hydrogen Diffusion Model [2,3,6]

Phenomenological treatment of hydrogen diffusion attending the facts of stress and strain effects on hydrogen solubility and diffusivity renders its flux as follows:

$$\boldsymbol{J} = -D(\varepsilon_{eq}^{p})\left[\nabla C - C\left(\frac{V_{\mathrm{H}}}{RT}\nabla\sigma + \frac{\nabla K_{S\varepsilon}(\varepsilon_{eq}^{p})}{K_{S\varepsilon}(\varepsilon_{eq}^{p})}\right)\right], \qquad (2)$$

through which the diffusion equation in terms of concentration is derived readily, $\partial C/\partial t = \nabla\cdot\boldsymbol{J}$. The entry conditions for hydrogen into the metal often correspond to the equilibrium on the material-environment interface Γ:

$$C(\Gamma,t) = C_0 K_S\left(\sigma(\Gamma,t),\varepsilon_{eq}^{p}(\Gamma,t)\right) \equiv C_0 \exp\left(\frac{V_{\mathrm{H}}}{RT}\sigma(\Gamma,t)\right) K_{S\varepsilon}\left(\varepsilon_{eq}^{p}(\Gamma,t)\right), \qquad (3)$$

where the equilibrium concentration in the stress-strain free metal C_0 is associated with the thermodynamical hydrogen activity in the environment.

Basic Model Approach

A plane-strain mode I crack was analysed under small scale yielding (SSY), so that the stress intensity factor (SIF) K could be the controlling variable. Since every cracked solid has a fatigue pre-cracking history, it was considered worthwhile to involve load cycling in simulations of the near-tip metal hydrogenation not only as transient loading *per se*, but as a prelude for HAC at rising load. Simulated loading cases consisted of zero-to-tension load cycling with maximal SIF $K_{\max}$ followed by monotonic loading at constant SIF rate $dK/dt = \dot{K}$. To analyse near-tip hydrogenation, large deformation modelling is necessary since this affects not only the near-tip stress-strain states, but also diffusion distances.

Extensive mechanical input data for the near-tip diffusion were generated [7-12] *via* finite element (FE) analyses of the crack-tip mechanics using a model approach which was substantiated elsewhere [7] taking a special care to ensure the K-dominated SSY under cyclic loading. Double-edge-cracked panel, where undeformed crack had parallel faces and semicircular tip of the width b_0, was analysed under remote traction. Conventional rate-independent J_2-elastoplasticity theory was used with material behaviour described by the power-law relation for equivalent stress $\sigma_{eq} \propto (\varepsilon_{eq}^{p})^{n}$, and the set of the material characteristics included the Young modulus E, the yield stress σ_0, the Poisson coefficient ν, and the hardening exponent n. To account for Bauschinger effect which might be important under reversed stress-history, combined isotropic-kinematic hardening rules were explored. Stress-strain data were generated for a range of model parameters typical for medium- to high-strength steels: σ_0/E = 0.003 to 0.008, ν = 0.3, n between 0 and 0.2, and b_0 = 5 μm, with K_{max} from 30 to 60 MPa·m$^{1/2}$ [7-12]. In particular, these

values correspond to steel subjected to various grades of cold-drawing, a prototype material for which ample experimental studies of HAC have been performed [13]. Hydrogen-related characteristics were typical for steels [1-5,7,8,14]: $V_H = 2 \cdot 10^{-6}$ m^3/mol and $D = 10^{-13}$ m^2/s at ambient temperature T = 293 K. This D was taken from the lower band of values from 10^{-15} to 10^{-8} m^2/s proper to prototype steels [14] owing to an expectedly high density of traps. Note, that modelling results can be adjusted to whichever magnitude of D by means of proper scaling of a conveniently chosen characteristic distance L and time t (i.e., the loading rate) using the similitude criterion for diffusion equation – dimensionless time $\tau = Dt/L^2$ [12]. The coupled problem of nonlinear solid mechanics and stress-strain assisted diffusion was solved with the use of non-linear FE procedure described elsewhere [7,8,12].

RESULTS

Relevant Aspects of the Near-Tip Mechanical Fields

All generated near-tip stress-strain fields [7-12] were quite similar concerning their main features revealed at coarser visualisation, whereas differences dependent on the constitutive behaviour were detected at finer resolution, which involved strain localizations forming spiral-like shear-bands, see examples in Fig. 1. The patterns along the depth x beyond the tip of mechanical variables, σ_1 with σ from one side and ε_{eq}^{p} from another, manifest separation of their maxima situated at $x_{c\sigma}$ and $x_{c\varepsilon}$, respectively (Fig. 1).

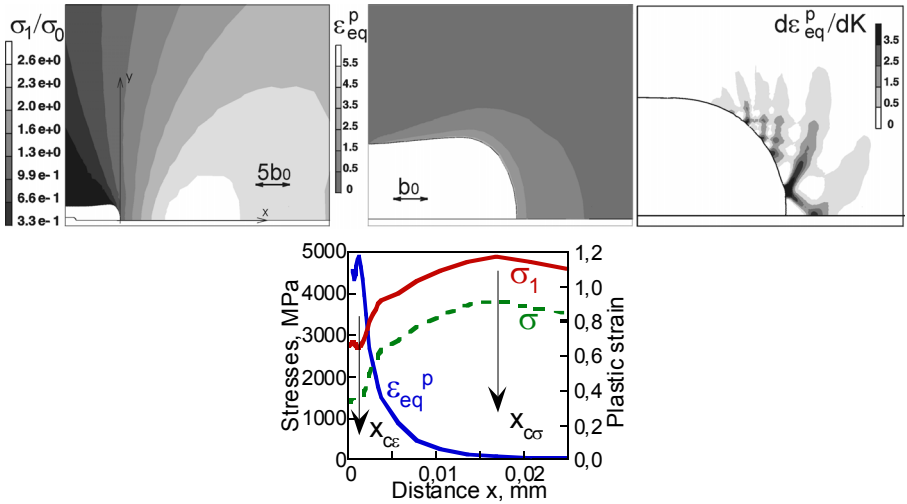


Figure 1: Typical near-tip fields at $K \approx K_{max}$ during rising load after fatigue pre-cracking(E = 195 GPa, σ_0 = 1500 MPa, n = 0.06): coarse views of the axial stress and plastic strain, and shear banding at fine resolution (at the top), and the patterns of stress-strain characteristics in the crack plane beyond the tip (at the bottom).

This implies two potential microfracture loci near the crack tip. The first one is associated with large plastic strain around $x_{c\varepsilon}$ (Fig. 1), where strain-controlled microfracture mode can operate. The other potential site of microfracture dominated by the maximal stress σ_1 is at $x_{c\sigma}$. The depth $x_{c\varepsilon}$ remains rather constant when loading goes on, whereas $x_{c\sigma}$ increases rapidly with load, $x_{c\sigma} \propto K^2$ [7,8,10,11]. The extremum of stress σ, which pulls hydrogen towards prospective fracture sites, has fairly the same location $x_{c\sigma}$. As a result, depending on the material, stress-strain state, and on the distribution of hydrogen, microscopic fracture mode and respective fracture criterion (1) may become either stress- or strain-controlled. Then, transient inhomogeneous hydrogen distributions with transitory over-hydrogenation in one potential rupture site comparing with another may be decisive in switching between stress- and strain-controlled rupture events and respective loci during HAC. This adds uncetainty to the definition of the critical distance x_c in HAC. Since x_c is also the required hydrogen penetration depth, this must have consequences for the interrelations between stress-strain evolutions, hydrogen transport, and HAC kinetics under transient loadings.

Near-Tip Hydrogen Accumulation Under Rising Load

To exemplify the modelling results corresponding to prototype experiments [13], the case of pre-cracking under K_{max} = 50 MPa·m$^{1/2}$ and posterior hydrogenation under rising load at $\dot{K}$ = 0.15 and 1.5 MPa·m$^{1/2}$/min towards a reference SIF value K_R = 1.3K_{max} is outlined. The evolutions of the near-tip stress-strain field and hydrogen distribution resulting from stress-assisted diffusion under boundary condition (3) and zero initial hydrogen content in metal, $C|_{t=0}$ = 0, are presented in Fig. 2. The equilibrium distributions of hydrogen for given instantaneous mechanical fields, being for this case $C_{eq}(x) = C_0\exp(V_H\sigma(x;K)/RT)$, are also shown there for comparison. The results are rather similar for both $\dot{K}$ values, although at the slower one the concentration $C(x,t)$ lagged closer behind the equilibrium distribution corresponding to the instantaneous stress field, which is $C_{eq}(\sigma(x;K = \dot{K}t))$.

The peculiarity of the dynamic loading in comparison with the sustained one is that the position $x_{c\sigma}$ of the maximal tensile stresses (both σ and σ_1) is not stationary, but passes through the high-strain zone and moves deeper into the metal as load increases. When load rises not too fast, so that equilibrium hydrogenation can be approached at corresponding diffusion depths, as it occurs at the rates $\dot{K}$ chosen in simulations, the stress peak is able to build up and drag the accompanying peak of hydrogen concentration (cf. plots in Fig. 2). This peak passes the locus $x_{c\varepsilon}$ of the potential strain-controlled fracture causing there transient over-hydrogenation, which later relaxes towards the equilibrium level (Fig. 3, left). On the other hand, the position of maximal stress $x_{c\sigma}$ moves acceleratingly into the depth, $x_{c\sigma} \propto K^2 = (\dot{K}t)^2$, so that over-equilibrium hydrogenation can never occur there, but hydrogen accumulation remains more or less far behind the equilibrium saturation $C_{eq}(x;K)$, Fig. 3, right. This over-hydrogenation at the strain concentration site $x_{c\varepsilon}$ commences at still low SIF levels on the background of already elevated near-tip strains, and it

persists during substantial part of load rising and augmentation of plastic strain and tensile stress. This brings a possibility for the criterion of hydrogen assisted rupture (1) to be met there at lower SIF than it could occur at sustained load, when over-equlibrium hydrogenation has no place. This way, load dynamics may act as a promoter of HAC, which has been noted in some experiments, see review [15].

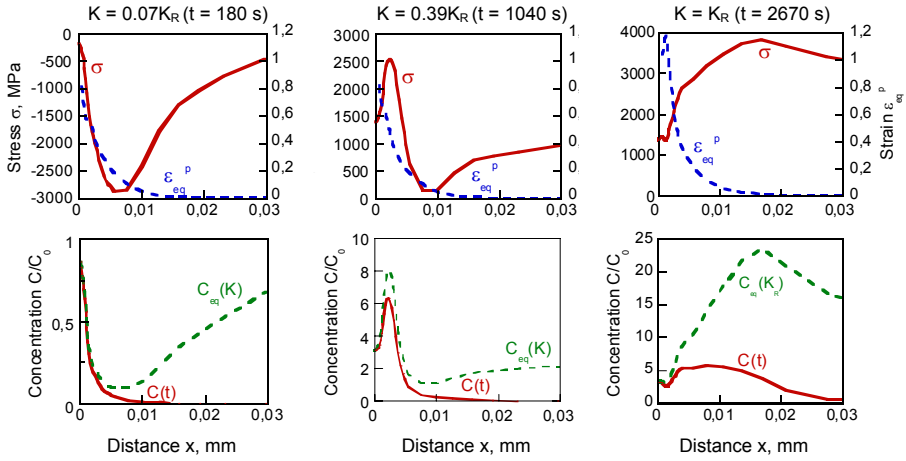


Figure 2: Near-tip stress, strain (top row, solid and dotted curves, respectively) and hydrogen concentration (bottom row, solid curve) in a cyclically pre-loaded specimen (E = 195 GPa, σ_0 = 1500 MPa, n = 0.06) at indicated instants during rising load HAC test at $\dot{K}$ = 1.5 MPa·m$^{1/2}$/min; for reference the equilibrium concentration for the instantaneous load levels, $C_{eq}(\sigma(K))$, is depicted by dotted line.

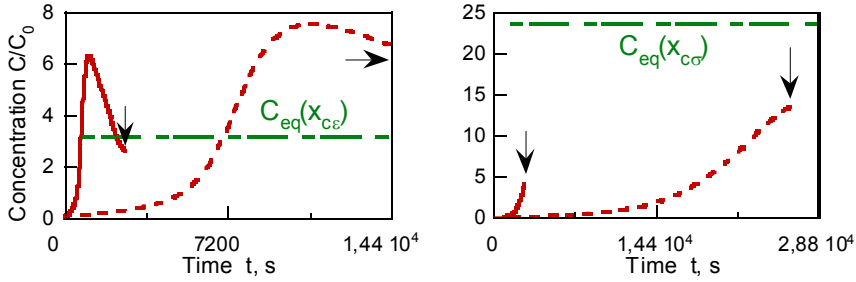


Fig. 3. Concentration evolutions in possible strain- and stress-dominated fracture loci, respectively, $x_{c\varepsilon}$ (left-hand picture) and $x_{c\sigma}$ (right-hand graph), during dynamic HAC tests at $\dot{K}$ = 1.5 and 0.15 MPa·m$^{1/2}$/min (solid and dashed curves). Arrows indicate the moments of attainment of a reference load K = K_R. The dash-dot lines indicate the equilibrium concentration levels in respective locations under sustained load at K = K_R at which HAC initiates.

Cyclic Load Effects on the Near-Tip Hydrogen Accumulation

Generated data [7-12] manifested that, under sine-waveform zero-to-tension load cycling, the very-near-tip stress patterns do not repeat the applied load waveform, but acquire Π-like shapes displaying sharp stress rising and stabilisation at some tensile magnitudes during nearly the whole forward loading period, and then jumping down to rather stable compressive levels maintained during the whole unloading (Fig. 4). Correspondingly, the stress-controlled component of the diffusion driving force changes the sign at every load reversal in a manner that it pulls hydrogen into the metal nearly as long as the forward loading phase of a cycle lasts, and pushes it out during the period of unloading. Thus, alteration of the applied load cycle symmetry changes the durations of these hydrogen pull and push phases within a cycle of loading (Fig. 4, right-hand plot), which must have consequences for hydrogen accumulation near the crack tip during fatigue in a way that extended pull phase – longer forward loading – favours near-tip hydrogen accumulation and *vice versa*. These observations open the way to develop a rationale concerning loading waveform effects on hydrogen assisted fatigue: positive sawtooth waveform gives faster cracking rates than symmetrical sine, triangular or Π-like shapes, and the negative one acts *vice versa* [16,17].

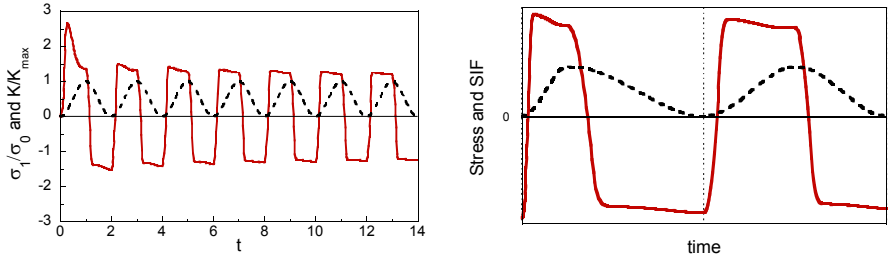


Figure 4: The patterns of stress evolution in the close near-tip vicinity (solid line) under remote cyclic loading (broken line): calculated stress trajectory under symmetrical sine waveform (to the left) and the effect of the applied waveform distortion on the time under tension near the crack tip (to the right).

Modelling of the near-tip hydrogen accumulation by diffusion under sine-waveform loading with frequency 0.05 Hz gave the results shown in Fig. 5. The concentration $C(x,t)$ of hydrogen supplied by an environment always lags behind the evolution of the equilibrium hydrogen absorbtion capacity of stressed-strained material $C_{eq}(x;K)$, which oscillates as the stress-strain state rules, but the delay gaps between them are greater with longer diffusion depths. Corresponding divergence of concentrations $\Delta C = C - C_{eq}$ is accumulated from cycle to cycle in additive-like manner providing concentration increase as long as loading goes on. Since the relative divergence $\Delta C/C$ is greater at longer diffusion distances, this increase turns out to be relatively

steeper there, whereas at rather short distances, where the equilibrium can be quickly achieved, hydrogen is effectively pushed and pulled within every cycle leaving small residual discrepancy with respect to equilibrium concentration. Then, a nearly constant-amplitude oscillation of concentration occurs in the band somewhere between the levels of equilibrium saturation corresponding to the maximal compressive and tensile cyclic near-tip stresses. Near-tip hydrogenation under cyclic loading remains substantially lower than the concentration $C_{max.load}(t)$ which would be under sustained load at $K = K_{max}$, in terms of total time under loading, and even in terms of cumulated time of permanence of the near-tip region under tensile local stresses during load cycling. Deeper from the tip, hydrogen accumulation manifests a clear increase. It can even proceed faster than under sustained load at $K = K_{max}$ in terms of cumulative time during which near-tip stresses remain tensile.

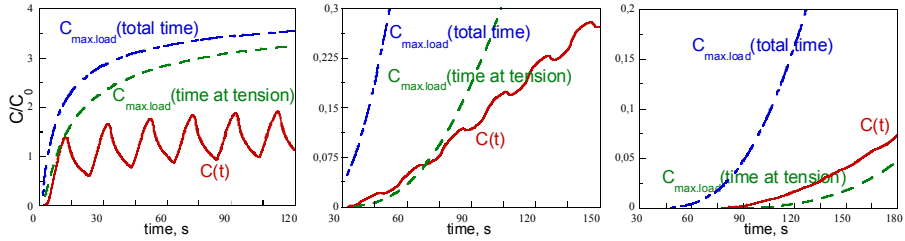


Figure 5: Near-tip hydrogen accumulation under sine waveform cyclic loading (solid lines) and under sustained load $K = K_{max}$ during the total time of loading (dash-dot lines) and the accumulated time of permanence of tensile near-tip stresses (broken line); left to right: from the close to the tip locations to the farer ones.

CONCLUSIONS

Exhaustive data on the near-tip mechanics under variable loading conditions were generated, which opened the way to interpret certain aspects of hydrogen assisted cracking (HAC) associated with transient stress-strain fields generated by monotonic and cyclic loading, such as the effect of the loading rate, waveform or frequency.

From the comparison of the conditions for HAC initiation from the point of view of hydrogen accumulation in the fracture process zone, we conclude that load dynamics may act as a promoter of HAC when localised plastic strain at relatively short depths beyond the tip is controlling in the microstructural modes of fracture assisted by hydrogen.

With regard to cyclic loading, revealed near-tip stress fields pointed to the causes of the waveform dependence of hydrogen assisted fatigue cracking. Modelling of the near-tip hydrogen diffusion pointed out that, as well as under monotonic loading, hydrogenation at every instant goes behind the equilibrium hydrogen distribution C_{eq}

corresponding to instantaneous stress-strain state, but the manner of approaching this C_{eq}, either from downward or from upward (in a given material point) depends on the interplay between corresponding diffusion path, available diffusion time, and hydrogen mobility.

ACKNOWLEDGEMENTS

The authors gratefully acknowledge the financial support received from different institutions: MCYT (Grant MAT2002-01831), MEC (Grant BIA2005-08965) and JCyL (Grants SA078/04, SA067A05 and SA111A07).

REFERENCES

1. Van Leeuwen, H.-P., *Eng. Fract. Mech.*, Vol. 6 (1974), pp. 141-161.
2. Toribio, J., Kharin, V., *Fatigue Fract. Eng. Mater. Struct.*, Vol. 20 (1997), pp. 729-745.
3. Toribio, J., Kharin, V., *Nucl. Eng. and Des.*, Vol. 182 (1998), pp. 149-163.
4. Sofronis, P., McMeeking, R., *J. Mech. Phys. Solids*, Vol. 37 (1989), pp. 317-350.
5. Krom, A.H.M. *et al*, *J. Mech. Phys. Solids*, Vol. 47 (1999), pp. 971-992.
6. Toribio, J., Kharin, V., *Fusion Eng. and Des*., Vol. 51-52 (2000), pp. 213-218.
7. Toribio, J., Kharin, V., Advances in Fatigue Crack Closure Measurement and Analysis: Second Volume, ASTM STP 1343 (1999), pp. 440-458.
8. Toribio, J., Kharin, V., Environmentally Assisted Cracking: Predictive Methods for Risk Assessment and Evaluation of Materials, Equipment, and Structures, ASTM STP 1401 (2000), pp. 329-342.
9. Toribio, J., Kharin, V., *Mater. Sci. and Eng*., Vol. A319-321 (2000), pp. 535-539.
10. Toribio, J., Kharin, V., *Int. J. Fracture*, 139 (2006), pp. 333-340.
11. Toribio, J., Kharin, V., *Int. J. Fracture*, 140 (2006), pp. 285-292.
12. Toribio, J., Kharin, V., *Materials Sci*., Vol. 38 (2002), pp. 514-525.
13. Toribio J., Lancha A.M., *Mater. and Struct.*, Vol. 26 (1993), pp. 30-37.
14. Hirth, J.P., *Met. Trans*., Vol. A11 (1980), pp. 861-890.
15. Toribio, J., Kharin, V., *Materials Sci.*, Vol. 34 (1998), pp. 476-489.
16. Wang, Z. F. *et al*, *Corrosion Sci*., Vol. 37 (1995), pp. 1551-1565.
17. Achilles, R. D., Bulloch, J. H., *Int. J. Press. Ves. Pip*., Vol. 30 (1987), pp. 375-389.

Effects of Hydrogen on Materials
Proceedings of the 2008 International Hydrogen Conference
Brian Somerday, Petros Sofronis, Russell Jones, editors, p 570-579
Copyright © 2009 ASM International®
All rights reserved.
www.asminternational.org

SENSITIVITY TO TEMPERATURE AND MATERIAL PROPERTIES OF HYDROGEN CONCENTRATION AT A CRACK TIP IN AUSTENITIC STAINLESS STEEL

Philip Schembri
Los Alamos National Laboratory, Los Alamos, NM, USA

ABSTRACT

The focus of the current work is quantification of the effect of material properties (structural and diffusion) and temperature on the stress and hydrogen concentration at the tip of a crack. A coupled finite element model of a compact tension specimen is used in which the effect of stress and trapping on the hydrogen diffusion is accounted for. Results show that, within the ranges of inputs considered, increasing yield stress and decreasing temperature have similar effects on the maximum stress. Also, yield stress and temperature are shown to have comparable effects on the lattice hydrogen concentration. Trap site density has a much larger effect on trap concentration than does trap binding energy since traps saturate quickly within the ranges of inputs considered.

KEYWORDS

Crack-tip fields, finite element analysis, sensitivity analysis

INTRODUCTION

Hydrogen assisted cracking is a well known phenomenon [1, 2] and affects many industries, including the nuclear power industry and the emerging hydrogen economy. Obtaining fracture toughness data that is useful for structural assessment is a difficult task, partly due to the logistical challenges faced in performing such tests and partly due to the difficulty in ensuring that crack tip conditions are representative of those at a postulated crack tip in the component (i.e. that the data is *transferable*). The latter issue can be addressed by modeling the test specimen and the component to compare the stress and hydrogen concentration in each.

Models for calculating crack tip fields, such as those used by Sofronis and McMeeking [3], Ellyin and Wu [4], Toribio et al. [5], and Mao and Li [6], are based

on the phenomenon that diffusing hydrogen is attracted to lattice sites that are volumetrically stretched. These models tend to be quite complicated, involving numerous input parameters, many of which are not known precisely. Uncertainty in the inputs naturally leads to uncertainty in the results. This uncertainty can be better understood if the sensitivity of the model outputs to the various input parameters is known. The objective of this paper is to estimate these sensitivities for a specific material system – protium dissolved in worked austenitic stainless steel (e.g. forged 316L or 21Cr-6Ni-9Mn), in the temperature and hydrogen pressure ranges of -60C to 70C and 1000psi to 20,000psi, respectively. It should be noted that this study does not aim to quantify the uncertainty in the results of the model (indeed, no statistical distributions are assumed for the inputs), but merely to quantify the sensitivity of the outputs to each input.

MODEL DESCRIPTION

The physical processes considered in the present model are the following

- Elastic-plastic material response with isotropic strain hardening
- Migration of hydrogen to regions of high hydrostatic tensile stress
- Trapping of hydrogen at a single type of trap site of uniform density

Note that in this model there is no mechanism by which hydrogen affects the stress state, so a simultaneous solution of the momentum and mass conservation equations is not required. This is a reasonable approximation since, in the temperature and pressure range under consideration, large concentrations of hydrogen typically do not dissolve in austenitic stainless steels [7]. Also, hydrogen enhanced plasticity is assumed for this investigation not to play a large role. Note that the commercial FE software ABAQUS [8] was used to perform the necessary calculations, with user subroutines where necessary (e.g. to include trapped hydrogen concentrations in transient calculations).

The equations typically used to describe the above processes have been discussed in detail by other researchers (see, for example, [3] for the discussion most relevant to the present calculations, and [9] or [10] for similar work), so only a summary is given here. Also, the updated Lagrangian formulation of the linear momentum conservation equation is described in the ABAQUS documentation [8] and will not be discussed further. The hydrogen concentration is found by solving the weak form (e.g. [11]) of the mass conservation equation, modified to include the effect of the hydrostatic stress on the hydrogen flux and balancing trapped and lattice hydrogen consistent with Oriani's formulation [12]:

$$\left([M]+\left[\hat{M}\right]\right)\{\dot{C}_L\}+[K]\{C_L\}=\{F\}, \qquad (1)$$

where:

$$[M]_{ij}=\int_V \psi_i\psi_j\,dV\,,$$

$$\left[\hat{M}\right]_{ij} = \int_V \left[\frac{C_T}{C_L}\left(1-\theta_T\right)\right]\psi_i\psi_j dV,$$

$$\left[K\right]_{ij} = \int_V D\left(\nabla\psi_i\cdot\nabla\psi_j - \frac{V_H}{RT}\psi_j\nabla\psi_i\cdot\nabla\sigma_h\right)dV,$$

$$\left\{F\right\}_i = \int_S \psi_i\eta\, dS,$$

where C_L and C_T are, respectively, the lattice and trapped hydrogen concentrations; θ_T is the fraction of total trap sites, N_T, that are filled; V_M is the martial molar volume of hydrogen in iron; R is the gas constant; T is temperature; σ_h is the hydrostatic stress; η is the hydrogen flux through the boundary, S, of the body, V; $D = D_0\exp\left(-H_D/RT\right)$ is the diffusivity; ψ_i (i=1,2,…,N) are the finite element approximation functions and N is the number of nodes. The total (C=C_L+C_T) and lattice concentrations are related through

$$C = C_L\left(1+\frac{N_T K_T}{N_L + C_L K_T}\right) \tag{2}$$

where $K_T = \exp\left(-E_T/RT\right)$ is an equilibrium constant that depends on the strength of the trap expressed in terms of the trap binding energy, E_T.

Equation (1) is integrated using a backward difference scheme, with the Newton-Raphson method used to estimate the solution to the nonlinear system at each time increment. A user element was written for use in ABAQUS to accomplish these tasks. Notice that the equilibrium form of this equation ($\left\{\dot{C}_L\right\}=0$) is linear and that the equilibrium lattice concentration does not depend on the trapped concentration.

A half-symmetry model of a compact tension (CT) specimen, as might be used in a crack arrest test [13], is chosen to be modeled. The specimen size is W=1.5", where W is the distance from the load line (the center of the loading hole) to the back face, and plane strain is assumed. Small scale yielding conditions are maintained, so that the resulting stress distribution is similar to that obtained using a boundary layer model. The mesh consists of 9439 isoparametric 4-node (bilinear) quadrilateral elements. The crack tip is modeled following the methods of McMeeking [14]. The tip is initially blunt, with a radius of 0.025μm, and load is applied such that the crack tip opening displacement (CTOD) is about 5 times the initial diameter.

The initial condition for the above mass balance equation is that of a uniform lattice concentration, C_L^*, and the boundary condition is a prescribed concentration, $C_L^{surface} = C_L^*$, on all free surfaces with zero hydrogen flux prescribed on the symmetry plane. These conditions are intended to simulate a pre-charged (see, for example, [15]) threshold arrest test [13, 16].

The surface concentration is related to the pressure and temperature of the hydrogen gas by

$$C_L^{surface} = S\sqrt{f}\,, \tag{3}$$

Where S is the solubility,

$$S = S_0 \exp\left(-H_S/RT\right), \tag{4}$$

and f is the hydrogen fugacity

$$f = \exp\left(\frac{Pb}{RT}\right), \tag{5}$$

with $b \approx 15.84$ cm^{3}mol^{-1}, which represents the finite volume of the hydrogen molecules in an Able-Noble equation of state:

$$V_m = \frac{RT}{P} + b \tag{6}$$

S_0 and H_S are material constants typically determined by thermal desorption or permeability experiments. The conditions necessary for these relations to be good approximations are discussed by San Marchi et al. [7].

SENSITIVITY ANALYSIS

In order to estimate the sensitivity of the model's outputs to changes in input parameters the model's response surface (the output as a function of the inputs) is sampled at many points and a simple polynomial surface is fit to the results. Assuming the regressed surface adequately fits the response surface, it can be analyzed to determine how heavily each input parameter influences the result.

Table 1 lists the input parameters varied in the sensitivity study, a typical value for each, and the range of values over which each was varied. The yield strength (YS) was expected to have a large effect on the stress and hydrogen concentrations, as was the hardening. However, the hardening was not included explicitly in the parameters to be varied since it was observed that, at room temperature, the hardening for alloys of most interest (21-6-9, 316L, 304L) was very similar. On the other hand, both the yield stress and hardening have been observed to vary with temperature. Thus, to keep track of the effects of yield stress, hardening and temperature, the *room temperature* yield strength (YS_{RT}) was chosen as an input to vary, along with the temperature. Consistent with the observations, "room temperature hardening" remained constant, while the actual hardening was allowed to vary with temperature.

To calculate (approximately) yield strength and hardening as a function of temperature, the following empirical relations were determined based on tensile test data of 21-6-9, 316L, and 304L forged stainless steels:

$$\begin{aligned} YS &= g(T)YS_{RT} \\ g(T) &= 3.5\left(T-163\right)^{-0.35} + 0.35 \quad (T \text{ in K}) \end{aligned} \tag{7}$$

and

$$\begin{aligned} \alpha = &-3.67E-13(T-273)^2 + 1.44E-10\left(T-273\right), \\ &+1.46E-8 \quad (T \text{ in K}) \end{aligned} \tag{8}$$

where α characterizes the hardening in a representation of the material hardening curve composed of two stitched Ramberg-Osgood curves:

$$\varepsilon_p = \begin{cases} 0.002\left(\dfrac{\sigma}{YS}\right)^n & \text{for } \sigma \le YS \\ \dfrac{\sigma - YS}{E_{0.2}} + \alpha\left(\sigma - YS\right)^m + \varepsilon_{0.2} - \dfrac{\sigma}{E} & \text{for } \sigma > YS \end{cases}, \tag{9}$$

where σ is the yield stress as a function of plastic strain, ε_p and E is the Young's modulus. The point (YS, $\varepsilon_{0.2}$) is where the two curves join, and n and m are hardening exponents. In order that the slope be continuous, we have that

$$E_{0.2} = \frac{E}{1 + 0.002n\left(E/YS\right)} \tag{10}$$

A similar method for fitting stainless steel hardening curves was used by Rasmussen [17]. For the materials of interest, it was found that n=13.4 and m=1.5 provided a good fit over the range of YS_{RT} and temperatures considered. The only parameter in equation (9) required to change with temperature is α. Thus, specifying YS_{RT} and T completely determines the material hardening curve.

Table 1: Input parameters varied in the sensitivity analysis, their typical values, and the range over which each was varied.

i	**Parameter**	**Typical value**	**Range**
1	Yield strength (YS_{RT})	80 ksi	55 to 105 ksi
2	Partial molar volume (V_H)	2 cc/mol	1.6l to 2.6 cc/mol
3	Pressure (P)	10 ksi	1 to 20 ksi
4	Solubility coefficient (S_0)	222 mol/m^3-MPa$^{1/2}$	100 to 500 mol/m^3-MPa$^{1/2}$
5	Solubility enthalpy (H_S)	5.9 kJ/mol	5.9 to 8.65 kJ/mol
6	Diffusivity coefficient (D_0)	5.4E-7 m^2/s	2.01E-7 to 6.6E-7 m^2/s
7	Diffusivity enthalpy (H_D)	53.9 kJ/mol	49.3 to 54 kJ/mol
8	Trap binding energy (E_T)	1 eV	0.1 to 1 eV
9	Number of traps (N_T)	10^{15} sites/mm^3	10^{13} to 10^{20} sites/ mm^3
10	Temperature (T)	22 C	-60 to 70 C

The ranges of solubility and diffusivity parameters were chosen based on the range of measured values compiled by San Marchi et al. [7]. The pressure range reflects the broad range of pressures used in hydrogen storage applications. The range of V_H was chosen based on the measured ranges compiled by Hirth [1]. The ranges of trap density and binding energy were chosen based on the values given by Hirth [1] and Thomas [18]. Also considered were the measured density and binding energy of helium bubbles precipitated in tritium-exposed stainless steel. This is motivated by nuclear energy applications. Binding energies for helium bubbles were estimated by Wilson et al. [19] to be on the order of 1 eV, while the density of bubbles was estimated to be about 10^{13} bubbles/mm^3 (providing an estimated trap site density of

10^{13}-10^{15} traps/mm^3) by counting the bubbles visible in the TEM work of Tosten and Morgan [20].

50 different combinations of input parameters within the ranges shown in Table 1 were created using a Latin Hypercube space filling design algorithm [21]. This algorithm attempts to maximize the minimum distance between points in the input parameter space while requiring that the levels of each input be spaced evenly. The commercial software JMP [22] was used to perform these calculations as well as to fit the surface to the resulting output.

The output variables studied were the maximum hydrostatic stress ahead of the crack tip (σ^{max}), the maximum equilibrium lattice hydrogen concentration ($C_L^{\max}$), the maximum equilibrium trapped hydrogen concentration ($C_T^{\max}$), and the time taken to reach 90% of the equilibrium concentration (t^{eq}). Note that, unlike the other outputs, t^{eq} *is* sensitive to the actual applied CTOD.

Based on the results of the 50 sample points discussed above, a surface was fit to each of the four model outputs. Designating the output variables as Y_i (i=1,2,3,4) and the input parameters as X_j (j=1,2,…,10), the ith response has the general form

$$Y_i(X_1, X_2, ..., X_{10}) = \sum_{k=1}^{10} A_k^i X_k + \sum_{p=1}^{10}\sum_{q=1}^{10} B_{pq}^i \left(X_p - X_p^{mid}\right)\left(X_q - X_q^{mid}\right) \qquad (11)$$

In other words, the surface is an incomplete quadratic polynomial, with the coefficients A_k^i and B_{pq}^i obtained through least squares fitting to the sample points. X_p^{mid} is the midpoint of the range of the pth input. Based on the assumptions of the model, some of the dependencies can be eliminated a priori. Also, since the range of both $C_T^{\max}$ and t^{eq} span several orders of magnitude, the response surfaces are fit to the logarithm of these results. Similarly, the logarithm of N_T was used as the input parameter varied in (11) since it also spans several orders of magnitude.

RESULTS AND DISCUSSION

As Saltelli suggests [23], an appropriate estimate of the sensitivity of a model to an input is the amount by which the input changes the output, scaled by the range of the input (the scaling is necessary so that the sensitivity does not depend on the units chosen for the input parameter). Thus, the sensitivities are estimated by the scaled polynomial coefficients A_k^i and B_{pq}^i, which gives the first order effects and first order interactions, respectively. Note that the resulting sensitivities will depend on how wide a range was chosen for each input.

The R^2 for each of the regressed surfaces was greater than 99%, so they were judged to be reasonably good fits of the model response surfaces. Fig. 1 shows the scaled

polynomial coefficients A_k^i, normalized by the largest coefficient. We see that σ^{max} is affected by YS_{RT} only slightly more than it is affected by T, and that (intuitively) increasing temperature causes σ^{max} to decrease.

$C_L^{\max}$ is a strong function of P, S_0 and H_S, although care must be taken in interpreting this result since, unlike S_0 and H_0, the pressure was varied over an order of magnitude. $C_L^{\max}$ depends to a lesser degree on YS_{RT}, V_H, and T. Thus, we would expect a material that has been forged to have a larger hydrogen concentration than a material with the same chemistry that has an annealed microstructure. The small effect of T (compared to P and the solubility parameters) on $C_L^{\max}$ may be because, although the solubility increases with temperature (tending to increase $C_L^{\max}$), the yield strength and hardening decrease (tending to decrease $C_L^{\max}$). Note that the result of this reduced effect of T is that T and YS_{RT} have comparable effects on the crack tip lattice hydrogen concentration.

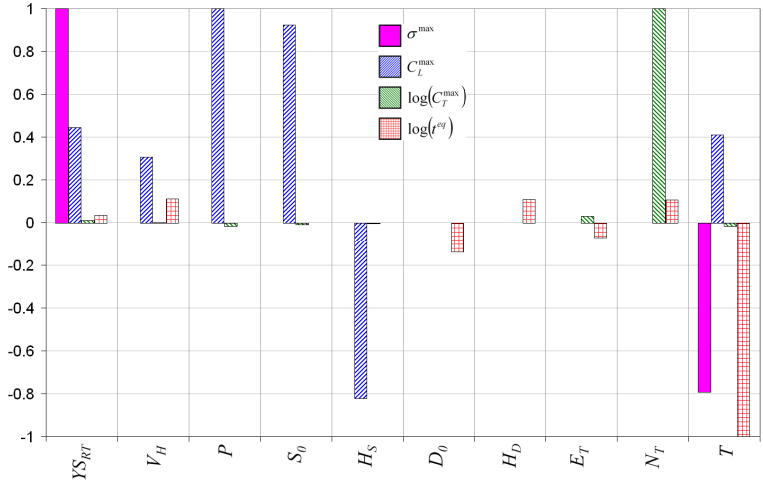


Figure 1: Main effects (scaled polynomial coefficients, normalized by the maximum respective output value) of inputs on the four output variables.

$C_T^{\max}$ depends almost exclusively on N_T, although there is a small effect due to E_T. This may be a result of the relatively high range chosen for E_T relative to the saturation binding energy range. Thus, a majority of sample points showed saturated trapped concentrations, biasing the sensitivity in favor of N_T. Of course, this is a realistic result in the case where traps (like helium bubbles) do have high binding energies.

Predictably, t^{eq} depends mostly on temperature, decreasing as temperature increases. However, it also depends on V_H, D_0, H_D, E_T and N_T. The dependence on V_H is explained by recalling that this parameter controls the amount by which the stress

affects the diffusion, and thus the amount of "extra" hydrogen that the lattice must absorb before equilibrium can be reached. The dependence on N_T and E_T is explained by the effective reduction in diffusivity that occurs while hydrogen traps are filling [12]. This effect would likely have appeared stronger if the range of E_T were lower since the relatively high range used here ensured that traps were saturated (i.e. no longer filling) for many of the sample points. Note that although it is interesting that the effect of V_H is similar to that of the diffusivity parameters, these effects are still quite small compared to the effect of temperature.

CONCLUSIONS

A coupled stress/diffusion model with trapping was implemented using finite elements, and the sensitivities of the outputs to each of the inputs were estimated by fitting a polynomial surface to the true response surface, sampled at 50 points. The main effects show the following, *valid for the range of inputs considered*:

- Peak stress increases with room temperature yield stress (i.e. with the amount of working in the material) and decreases with temperature. The effects of working and temperature are of similar magnitudes.
- Trap site density has a much larger effect on trap concentration than does trap binding energy since traps tend to saturate quickly.
- The time needed for the system to reach equilibrium is a strong function of temperature. The effect of trap parameters and stress coupling is of the same order as the effect of the diffusion coefficients.
- The peak lattice concentration is a strong function of hydrogen pressure and solubility parameters but is also a moderate function of room-temperature yield stress, partial molar volume of hydrogen, and temperature.
- Yield stress and temperature have comparable effects on the lattice hydrogen concentration

ACKNOWLEDGMENTS

The author would like to thank Ryan Melcher, Dorian Balch, Brian Somerday, and Petros Sofronis for the many enlightening discussions that helped to motivate and refine this study. This work was performed at Los Alamos National Laboratory under DOE Contract No. E-7405-ENG-36.

REFERENCES

1. Hirth, J.P., "Effects of Hydrogen on the Properties of Iron and Steel," *Met. Trans.*, Vol. 11A (1980), pp. 861-890.
2. Gangloff, R.P., "Hydrogen Assisted Cracking" in: *Comprehensive Structural Integrity*, Vol 6, Milne, I., Ritchie, R.O., and Karihaloo, B., Eds., Elsevier Science (New York, 2003) pp. 31-101.

3. Sofronis, P. and McMeeking, R.M., "Numerical Analysis of Hydrogen Transport Near a Blunting Crack Tip," *J. Mech. Phys. Solids*, Vol 37, No 3 (1989), pp. 317-350.
4. Ellyin, F. and Wu, J., "Effect of Hydride Precipitation on the Elastoplastic Stress Field Near a Crack Tip," *Acta Met.*, Vol 42 No 8 (1994), pp. 2709-2717.
5. Toribio, J., Valiente, A., Cortes, R., and Caballero, L., "Modelling Hydrogen Embrittlement in 316L Austenitic Stainless Steel for the First Wall of the Next European Torus," *Fusion Eng. Design*, Vol 29 (1995), pp. 442-447.
6. Mao, S.X. and Li, M., "Mechanics and Thermodynamics on the Stress and Hydrogen Interaction in Crack Tip Stress Corrosion: Experiment and Theory," J. Mech. Phys. Solids, Vol 46, No 6 (1998), pp. 1125-1137.
7. San Marchi, C., Somerday, B.P., and Robinson, S.L., "Permeability, Solubility and Diffusivity of Hydrogen Isotopes in Stainless Steels and High Gas Pressures," Int. J. Hydrogen Energy, Vol 32 (2007), pp. 100-116.
8. ABAQUS Theory Manual, Ver 6.75, (2007), ABAQUS Inc, Pawtucket, RI.
9. Girrens, S.P. and Smith, F.W., "Finite Element Analysis fof Coupled Constituent Diffusion in Thermoelastic Solids," Applied Mechanics and Engineering, Vol 62, No 2 (1987), pp. 209-223.
10. Varias, A.G. and Massih, A.R., "Simulation of Hydrogen Embrittlement in Zirconium Alloys Under Stress and Temperature Gradients," J. Nucl. Mater., Vol279, No2-3 (2000), pp. 273-285.
11. Reddy, J.N., An Introduction to the Finite Element Method, McGraw Hill, Inc (New York, 1993), pp. 28-33.
12. Oriani, R.A., "The Diffusion and Trapping of Hydrogen in Steel," Acta Met., Vol 18 (1970), pp.147-157.
13. ASTM E1681, Determining Threshold Stress Intensity Factors for Environmentally-Assisted Cracking of Metallic Materials, Vol. 3.01 (2003), ASTM.
14. McMeeking, R.M., "Finite Deformation Analysis of Crack-Tip Opening in Elastic-Plastic Materials and Implications for Fracture," J. Mech. Phys. Solids, Vol 25 (1977), pp. 357-381.
15. Moody, N.R., Perra, M.W., and Robinson, S.L., "Hydrogen-Induced Cracking in a Iron-Based Superalloy" in: Hydrogen Effects on Material Behavior, Moody N.R. and Thompson A.W., Eds, The Minerals, Metals, and Materials Society, Warrendale PA (1990), pp. 625-635.
16. Perra, M.W., "Sustained-Load Cracking of Austenitic Steels in Gaseous Hydrogen" in: Environmental Degradation of Engineering Materials in Hydrogen, Louthan, M.R., MvNitt, R.P., and Sisson, R.D., Eds, Blacksburg VA: Laboratory for the Study of Environmental Degradation of Engineering Materials, Virginia Polytechnic Institute (1981), pp.321-333.
17. Rasmussen, K.J.R., "Full-Range Stress-Strain Curves for Stainless Steel Alloys," J. Constr. Steel. Res., Vol 59 (2003), pp. 47-61.
18. Thomas, G.J., "Hydrogen Trapping in FCC Metals" in: Hydrogen Effects in Metals, Bernstein, I.M. and Thompson A.W., Eds, The Metallurgical Society of AIME, Warrendale PA (1981), pp. 77-85.

19. Wilson, K.L., Pontau, A.E., Haggmark, L.G., and Baskes, M.I., "Trapping of Deuterium in Helium-Damaged Steels: He+ Fluence Dependence," J. Nucl. Mater., Vol 103-104 (1981), pp.493-498.
20. Tosten, M.H. and Morgan M.J., "The Effects of Helium Bubble Microstructure on Ductility in Annealed and HERF 21Cr-6Ni-9Mn Stainless Steel," WSRC-RP-92-551, Westinghouse Savannah River Company (1998).
21. McKay, M.D. and Beckman, R.J., "A Comparison of Three Methods for Selecting Values of Input Variables in the Analysis of Output from a Computer Code," Technimetrics, Vol 21, No 2 (1979), pp.239-245.
22. User Guide JMP 7, (2007), SAS Institute Inc, Cary NC.
23. Saltelli, A., "Global Sensitivity Analysis: An Introduction" in: Sensitivity Analysis of Model Output, Hanson, K.M. and Hemez, F.M., Eds, Los Alamos National Laboratory, Los Alamos NM (2005), pp. 27-43.

Effects of Hydrogen on Materials
Proceedings of the 2008 International Hydrogen Conference
Brian Somerday, Petros Sofronis, Russell Jones, editors, p 580-587
Copyright © 2009 ASM International®
All rights reserved.
www.asminternational.org

Finite Element Analysis of Hydrogen Diffusion in Materials

Hiroshi KANAYAMA,
Department of Mechanical Engineering, Kyushu University,
Nishi-Ku, Fukuoka, 819-0395, Japan
Stephane NDONG-MEFANE,
Graduate School of Engineering, Kyushu University,
Nishi-Ku, Fukuoka, 819-0395, Japan
Masao OGINO,
Department of Mechanical Engineering, Kyushu University,
Nishi-Ku, Fukuoka, 819-0395, Japan

INTRODUCTION

In previous studies [1], Krom et al.'s work [2] on hydrogen diffusion has been successfully reproduced, using a non-symmetric coefficient matrix for each time step. Some numerical instabilities occurring for high values of the Peclet number have been corrected by using the work of Franca et al. [3] and a way to choose a valid stabilization parameter was established [4]. Using the stabilized scheme previously established, the results obtained for different versions of the stabilized scheme are examined in order to establish the best one.

THE HYDROGEN TRANSPORT EQUATION

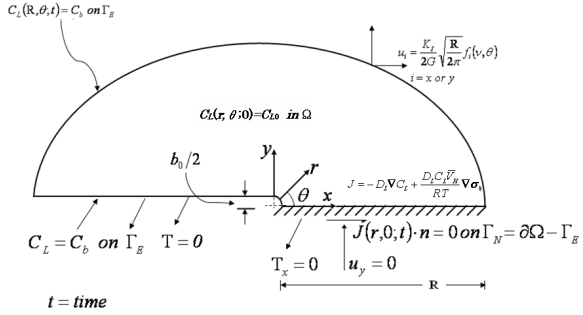


Fig. 1 Description of the boundary and initial conditions for the one side coupled diffusion and elasto-plastic problem under small scale yielding conditions [5].

Using the model presented in Fig. 1, a body with a volume Ω and a surface $\partial\Omega=\Gamma$ is considered. In the previous work [1], the hydrogen transport equation mainly based on Krom et al. [2], which is itself based on Sofronis and McMeeking's work [5] has been introduced. The time-implicit scheme for the advection diffusion equation presented in the previous work [1] is

$$\left(\left[1+\frac{N_L K_T N_T(\varepsilon_p^n)}{\left(K_T C_L^n + N_L\right)^2}\right]\left(\frac{C_L^{n+1}-C_L^n}{\Delta t}\right), C_L^*\right)_\Omega + \left(D_L \nabla C_L^{n+1}, \nabla C_L^*\right)_\Omega \tag{1}$$

$$-\left(\frac{C_L^{n+1} D_L \overline{V}_H}{RT}\nabla\sigma_h^n, \nabla C_L^*\right)_\Omega + \left(C_L^{n+1}\frac{K_T}{K_T C_L^n + N_L} 29.508 N_T(\varepsilon_p^n) e^{-5.5\varepsilon_p^n}\frac{\varepsilon_p^{n+1}-\varepsilon_p^n}{\Delta t}, C_L^*\right)_\Omega = 0.$$

In Eq. (1), $(A,B)_\Omega = \int_\Omega A \cdot B d\Omega$. C_L^{n+1} is the number of hydrogen atoms per unit volume in lattice sites at the time step $(n+1)\Delta t$. R is the gas constant, K_T is the equilibrium constant such that $K_T = e^{-\Delta E_T/RT}$ with ΔE_T as the trap binding energy, T is the absolute temperature, and σ_h is defined as the hydrostatic stress such that $\sigma_h = \frac{1}{3}\sum_{i=1}^{3}\sigma_{ii}$ where the component σ_{ij} is the stress tensor component. The subscripts *i* and *j* are usually denoted x, y, z instead of 1, 2, 3. $\overline{V}_H$ is the partial molar volume of hydrogen, ε_P is the plastic strain, N_L and N_T are the lattice site and the trap site densities, and D_L is the diffusion constant. More details about these expressions can be found in the previous paper [1].

OVERVIEW OF PREVIOUS RESULTS

The model is a half disc with a radius of $1.5\times10^{-1} m$ and a thickness of 8.25×10^{-4} *m*. The crack can be considered as a horizontal band going from the center to the left until the circumference of the half disc with an initial crack tip opening of 1.0×10^{-5} *m*. The mesh consists of 10,656 nodes and 3,706 10-node tetrahedral elements, and is refined near the crack tip [6]. A recapitulation of the constant values can be found in Table 1.

Table 1 Constant values.

Diffusion constant	D_L	$1.27\times10^{-8} m^2\cdot s^{-1}$
Gas constant	R	$8.3144 J\cdot mol^{-1}\cdot K^{-1}$
Temperature	T	$300 K$
Initial hydrogen concentration	C_{L0}	$2.08\times10^{21} m^{-3}$
Partial molar volume of hydrogen	$\overline{V}_H$	$2.0\times10^{-6} m^3\cdot mol^{-1}$
Lattice sites per unit volume	N_L	$5.10\times10^{29} m^{-3}$
Trap binding energy	ΔE_T	$-60\times10^3 J\cdot mol^{-1}$
Poisson ratio	ν	0.3
Young modulus	E	$207 GPa$
Yield stress	σ_y	$250 MPa$

The hydrogen distribution in lattice sites at 130 s has been compared with Krom et al. results in Fig. 2. The results with the strain rate factor and without the strain rate factor are computed for a loading time of 130 s. C_{L0} is the initial hydrogen concentration throughout the entire domain. Effects of the strain rate factor can be observed in both results.

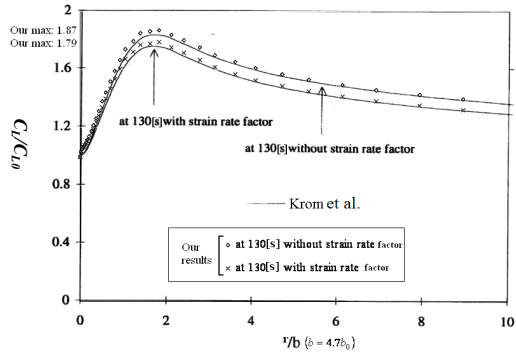


Fig. 2 $\left(C_L/C_{L0}\right)$ *ahead of the crack tip by our scheme and by Krom et al. scheme at 130 s (end of loading).*

AN INSTABILITY PROBLEM

The Peclet number is a dimensionless number relating the rate of advection of a flow to its rate of diffusion and defined as $\frac{Velocity \times Chareacteristic\ Length}{Diffusion\ Constant}$. Considering the crack opening b_0 as the characteristic length and the term $\left(\frac{D_L \overline{V}_H}{RT}\right)\nabla\sigma_h^n$ as the velocity, a Peclet number of the order 10 is computed. In actual cases, the gradient of hydrostatic stress may be increased, for example through a sharper crack. In this paper, for simplicity the Peclet number has been increased artificially by increasing the partial molar volume $\overline{V}_H$, to observe the effects of a higher Peclet number on the hydrogen distribution. Of course, the relevance of the resulting Peclet number values to diffusion in real-life materials needs to be further investigated. The appearance of small instabilities manifested by negative values of hydrogen concentration is observed after increasing the Peclet number thirty times through the increase of the partial molar volume $\overline{V}_H$.

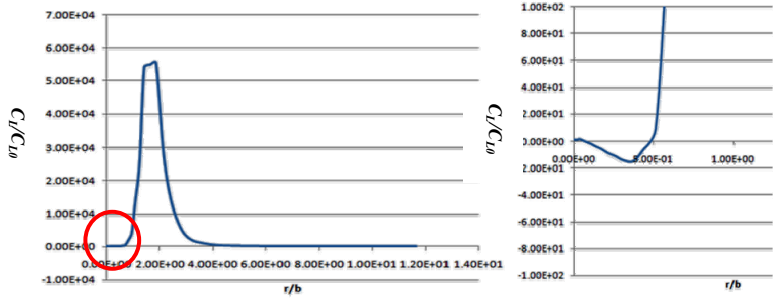


Fig. 3 Hydrogen distribution near the crack tip after a loading time of 130 s for a high value of the Peclet number (30 times higher).

It appears in Fig. 3 that the maximum normalized concentration of hydrogen is very high. This is probably due to the choice of increasing the Peclet number through the partial molar volume. In a next study, for more accuracy in the results, the choice of

increasing the hydrostatic stress gradient instead of the partial molar volume should be adopted.

A STABILIZED SCHEME

In order to solve the instability problem presented above, a stabilization method is applied to the non-symmetric scheme related to Eq. (1). The work of Franca et al. on stabilized schemes for advection diffusion equations [3] has been used. Applying the same principle used in their paper on the considered advection diffusion equation, the following stabilized equation is gotten

$$\left(\left[1+\frac{N_L K_T N_T(\varepsilon_p^n)}{\left(K_T C_{L_h}^n + N_L\right)^2}\right]\left(\frac{C_{L_h}^{n+1}-C_{L_h}^n}{\Delta t}\right), C_{L_h}^*\right)_\Omega - \left(C_{L_h}^{n+1}\frac{D_L \overline{V}_H}{RT}\nabla\sigma_h^n, \nabla C_{L_h}^*\right)_\Omega$$

$$+\left(D_L \nabla C_{L_h}^{n+1}, \nabla C_{L_h}^*\right)_\Omega + \left(C_{L_h}^{n+1}\frac{K_T}{K_T C_{L_h}^n + N_L} 29.508\, N_T(\varepsilon_p^n) e^{-5.5\varepsilon_p^n}\frac{\varepsilon_p^{n+1}-\varepsilon_p^n}{\Delta t}, C_{L_h}^*\right)_\Omega$$

$$+\sum_{K\in\Im_h}\tau^n \left(\begin{array}{l} \left[1+\dfrac{N_L K_T N_T(\varepsilon_p^n)}{\left(K_T C_{L_h}^n + N_L\right)^2}\right]\left(\dfrac{C_{L_h}^{n+1}-C_{L_h}^n}{\Delta t}\right) + \nabla\cdot\left(C_{L_h}^{n+1}\dfrac{D_L\overline{V}_H}{RT}\nabla\sigma_h^n\right) \\ -\nabla\cdot\left(D_L\nabla C_{L_h}^{n+1}\right) \\ +C_{L_h}^{n+1}\dfrac{K_T}{K_T C_{L_h}^n + N_L} 29.508\, N_T(\varepsilon_p^n) e^{-5.5\varepsilon_p^n}\dfrac{\varepsilon_p^{n+1}-\varepsilon_p^n}{\Delta t}, \\ \nabla\cdot\left(C_{L_h}^*\dfrac{D_L\overline{V}_H}{RT}\nabla\sigma_h^n\right) - \nabla\cdot\left(D_L\nabla C_{L_h}^*\right) \end{array}\right)_K = 0. \tag{2}$$

It is important to notice that in the present study, the conservative advection diffusion equation is the base of our model. On the other hand, Franca et al. use in their paper [3] the non-conservative advection diffusion equation. The stabilization parameter is first defined by considering the non-stationary case and using a previous work conducted by Tabata and Suzuki [7] as

$$\tau^n = \min\left\{\frac{\Delta t}{2}, \frac{h_k}{2\left|\dfrac{D_L\left(\overline{V}_H\right)_\tau}{RT}\nabla\sigma_h^n\right|}, \frac{h_k^2}{12 D_L}\right\}, \tag{3}$$

and we also set

$$a = \tau^n \nabla\cdot\left(D_L \nabla C_{L_h}^*\right), \tag{4}$$

where $C_{L_h}^{n+1}$ is the finite element approximation of C_L^{n+1}, $C_{L_h}^*$ is the test function, and h_k is the maximum length of the tetrahedral element. It is noted that $\nabla\sigma_h^n$ is computed by the linear interpolation based on vertex nodal values over the quadratic tetrahedral element. It will later be shown that the value of τ^n needs to be adjusted.

It is very important at this stage to mention that besides the fact that the present equation is based on an advection diffusion equation, it gives several differences with the equations solved by Franca et al. [3] and Tabata and Suzuki [7], which solve problems different from the present one. Thus, an experimental adjustement of the stabilization parameter might be necessary, because it should be determined depending on the problem and its mathematically rigorous justification is very difficult.

RESULTS

In our previous study [4], the necessity to readjust the stabilization parameter and to use a new parameter τ^* instead of the original τ^n in order to obtain valid results in both cases of $a^*=0$ and $a^*\neq 0$ has been explained. A way to choose the stabilization parameter has also been explained in the paper, and in the case of $a^* = \tau^* \nabla \cdot \left(D_L \nabla C_{L_h}^*\right) = 0$, the best stabilization parameter is the one with the value of average concentration closest to zero and corresponds to $\tau^*=9.0 \times 10^{-4}\tau^n = 1.77 \times 10^{-7}$. In this paper, we still set $a^*=0$.

Once the stabilization parameter has been determined, it is used in high Peclet number conditions without any further change. Thus, the partial molar volume in the stabilization parameter remains at $\left(\overline{V}_H\right)_\tau = 2\times10^{-6} m^3 \cdot mol^{-1}$ in Eq. (3), while $\overline{V}_H$ is increased in the rest of the equation i.e. Eq. (2), to create high values of the Peclet number. The results are presented for different values of the Peclet number and compared with results where $\left(\overline{V}_H\right)_\tau = \overline{V}_H$.

The highest Peclet number calculated in the original Galerkin's result is Pe=24.2. Results can be observed in Table 2 (the results in Table 2 are computed with $\left(\overline{V}_H\right)_\tau \neq \overline{V}_H$). The results obtained in this table are not only close to the Galerkin-stable results (Case 1) but also are well-improved in Case 2 and Case 3.

Table 2 Results for different values of the Peclet number with the stabilization parameter $\tau^* = 1.0 \times 10^{-3} \tau^n$. ×: *The computation gives negative results or stops,* ○: *results without negative values,* □: *Improved results with some negative values.*

	Peclet number	Galerkin	Stabilization term $a^* = 0$
Case 1	24.2	○	○
Case 2	726	×	○
Case 3	1,210	×	○
Case 4	2,420	×	□

In Fig. 4, the stabilization term reduces the oscillations and removes all the negative values appearing in the Galerkin method. One can also notice that the maximum concentration is decreased. In Fig. 5 however, some negative values remain. Fig 6 shows the higher efficiency of the stabilization parameter set as $\left(\overline{V}_H\right)_\tau \neq \overline{V}_H$, compared with $\left(\overline{V}_H\right)_\tau = \overline{V}_H$.

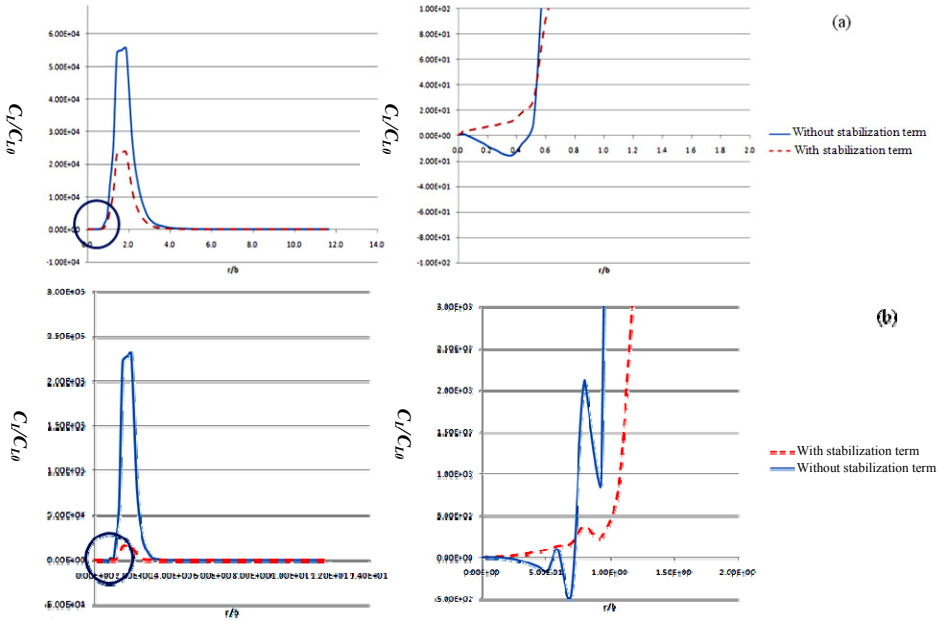


Fig. 4 Results of hydrogen distribution near the crack tip after a loading time of 130 s with a stabilization parameter of $\tau^* = 1.0 \times 10^{-3} \tau^n$ *and* $\left(\overline{V}_H\right)_\tau \neq \overline{V}_H$. *(a): Case 2, (b): Case 3.*

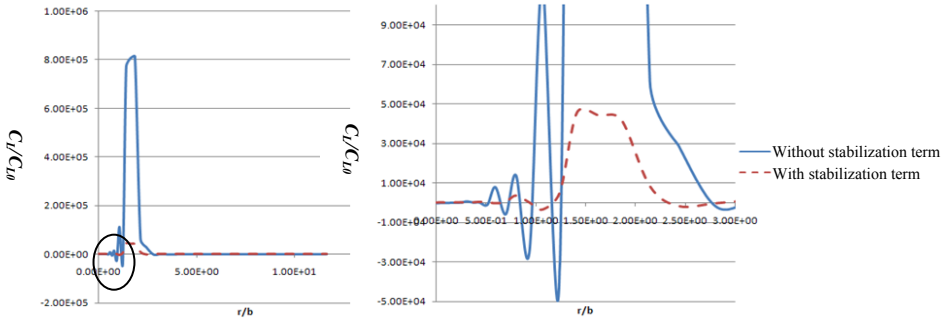


Fig. 5 Results of hydrogen distribution near the crack tip after a loading time of 130 s with a stabilization parameter of $\tau^*=1.0\times 10^{-3}\tau^n$ *in Case 4* $\left(\left(\overline{V}_H\right)_\tau \neq \overline{V}_H\right)$.

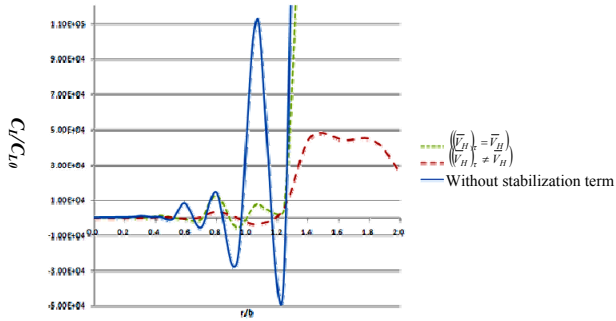


Fig. 6 Comparison of hydrogen distribution near the crack tip after a loading time of 130 s for different settings of the stabilization parameter in Case 4, with $\tau^*=1.0\times 10^{-3}\tau^n$.

CONCLUSIONS

The best stabilized results seem to appear for the case of $a^* = 0$. The present results have been improved for the previous work conducted on this subject [4]. However some modifications are still necessary, such as increasing the hydrostatic stress gradient instead of the partial molar volume and also using steel with a higher yield stress. In this paper, a 30 times higher Pechlet number is used to show negative hydrogen concentration. In real situation where the hydrostatic stress gradient is higher, it should clearly be shown whether such a high value of the Pechlet number really happens or not. Unfortunately, for the present authors, this work is not so easy one, because their main concern is numerical analysis and preparation of suitable input data for the real situation takes a time. So we want to show this crucial point in our forthcoming paper. Also, we have one private information [8] that under high strength steel, negative hydrogen concentration really happens with the Galerkin approach. We hope that these matters will clearly be shown in near future and the present numerical results will have some meaning to understand the phenomena of high hydrostatic stress gradient.

ACKNOWLEDGMENTS

This research has been conducted as part of “Fundamental Research Project on Advanced Hydrogen Science” funded by New Energy and Industrial Technology Development Organization (NEDO). The authors would also like to say sincere thanks to referees for their severe and encouraging comments.

REFERENCES

[1] H. Kanayama, T. Shingoh, S. Ndong-Mefane, M. Ogino, R. Shioya, H. Kawai, Numerical analysis of hydrogen diffusion problems using the finite element method, *Theoretical and Applied Mechanics*, Vol. 56 (2008), pp. 389-400.

[2] A.H.M. Krom, R.W.J Koers, A. Bakker, Hydrogen transport near a blunting crack, *Journal of the Mechanics and Physics of Solids,* Vol. 47 (1999), pp. 971-992.

[3] L.P. Franca, S. L. Frey, T.J.R. Hughes, Stabilized finite element methods: I. Application to the advective-diffusive model, *Computer Methods in Applied Mechanics and Engineering*, Vol. 95 (1992), pp. 253-276.

[4] S. Ndong-Mefane, H. Kanayama, M. Ogino, M. F. El-Amin, A stabilization method for the hydrogen diffusion model in materials, *Journal of Computational Science and Technology,* Vol.2, No. 4 (2008), pp. 447-458.

[5] P. Sofronis, R. M. McMeeking, Numerical analysis of hydrogen transport near a blunting crack tip, *Journal of the Mechanics and Physics*, Vol. 37 (1989), pp. 317-350.

[6] R. Miresmaeili, M. Ogino, R.Shioya, H. Kawai, H. Kanayama, Modeling of the hydrostatic stress and equivalent plastic strain distributions around the blunting crack tip in impure iron, *Memoirs of the Faculty of Engineering, Kyushu University,* Vol. 68, No. 4 (2008), pp. 151-161 .

[7] M. Tabata, A. Suzuki, A stabilized finite element method for the Rayleigh-Benard equations with finite Prandtl number in a spherical shell, *Computer Methods in Applied Mechanics and Engineering*, Vol. 190 (2000), pp. 387-402.

[8] T. Kanezaki, Private communication.

Effects of Hydrogen on Materials
Proceedings of the 2008 International Hydrogen Conference
Brian Somerday, Petros Sofronis, Russell Jones, editors, p 588-595
Copyright © 2009 ASM International®
All rights reserved.
www.asminternational.org

Modeling of Hydrogen Assisted Cold Cracking in High Strength Steel Welds

Th. Boellinghaus
Federal Institute for Materials Research and Testing (BAM), Berlin, Germany

P. Wongpanya
Suranaree University of Technology, Nakhon Ratchasima, Thailand

ABSTRACT

Integrity assessments of welded steel components considering hydrogen assisted cracking (HAC) predominantly focus on hydrogen assisted stress corrosion cracking (HASCC) during service. But, already during fabrication welding steel components might fail by hydrogen assisted cold cracking (HACC) and within the recent years, such phenomena are increasingly gaining importance again by the industrial demands for weldable extra high strength structural steels with yield strengths of up to 1300 MPa, as for instance in mobile crane production. Avoidance of HACC associated failures requires a decent understanding of the appearance in the weld microstructures of these materials to identify sufficient hydrogen removal heat treatments. For this purpose, thermal, structural and hydrogen diffusion finite element analyses have been coupled into a numerical model accounting for crack initiation as well as for crack propagation. The model considers the exceeding of the critical hydrogen strain combination for the local microstructure as failure criterion, since hydrogen predominantly degrades the deformation capabilities and less affects the strength of such microstructures. The two dimensional simulations of a root pass and a multi layer S 1100 QL steel weld at typical shrinkage restraints exhibited significant dependence of the crack appearance on the hydrogen concentration level introduced into the weld metal via the arc. For avoidance of HACC in such welds and as a first step towards improvement of existing guidelines and standards, hydrogen removal heat treatment procedures have additionally been determined by modeling of the respective hydrogen diffusion and effusion process.

INTRODUCTION

Due to their large strength spectrum between 235 and 1100 MPa, fine grained structural steels are very frequently applied to welded steel components in numerous industrial branches. Introduction of ferritic-pearlitic materials with lower yield

strengths of up to 460 MPa more than 20 years ago has been associated with severe failures by HACC during fabrication welding and subsequent cooling, as for instance in offshore industry. After extensive testing and respective specification of welding as well as HACC prevention heat treatment procedures, such production drawbacks seemed to be avoidable. But, the number of HACC based weld failures is again increasing within the recent years which is particularly associated with welding of water-quenched and tempered structural steels having yield strengths above 700 MPa, sometimes resulting in engineering catastrophes, like the failure of a S 890 downhill tubular for a hydro power plant [1]. Aside the fact that that the metallurgical mechanisms of HACC have not yet been fully understood, as one reason it has to be considered that the base materials change with increasing design yield strength from a ferritic-pearlitic into a bainitic and finally into a martensitic microstructure. The ductility of the high strength steel types is extensively tuned during production and thus, it becomes extremely difficult to match the base material microstructures and properties in the weld metal and the heat affected zone (HAZ) during fabrication welding. With increasing design yield strength the weld microstructures become thus more prone to degradation by hydrogen introduced via the welding arc. As illustrated by Fig. 1, the critical hydrogen concentration for zero ductility, i. e. coincident 0.2 proof stress and tensile strength, is drastically reduced with increasing the base material design yield strength. The S 1100 base material, representing the upper limit of the currently available types, also appears to be very sensitive to hydrogen. As a further reason, the recommended heat treatment procedures have been evaluated by homogeneously heated small scale test specimens at undefined shrinkage restraints. But, frequently specified preheating and interpass temperature procedures increase the transverse residual stresses in restrained butt joints at realistic shrinkage restraints (Fig. 2), do not provide long enough higher temperatures during the cooling cycle for sufficient hydrogen evolution from the weld metal and might even cause undesired hydrogen accumulations in the HAZ [2]. Consequently, the currently recommended HACC avoidance procedures [3] have to be re-considered with respect to hydrogen degradation of extra high strength weld microstructures and inhomogeneous heat treatments interacting with the stresses and strains developing during welding and subsequent cooling of real components.

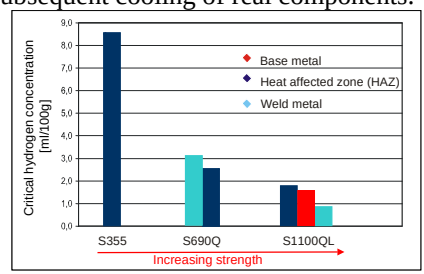


Figure 1: Critical hydrogen concentration dependent on the design strength level of structural steels

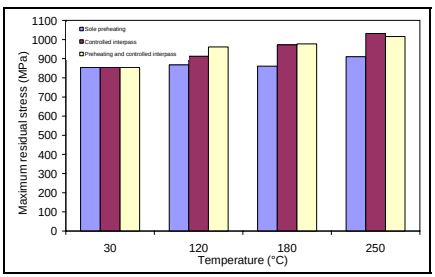
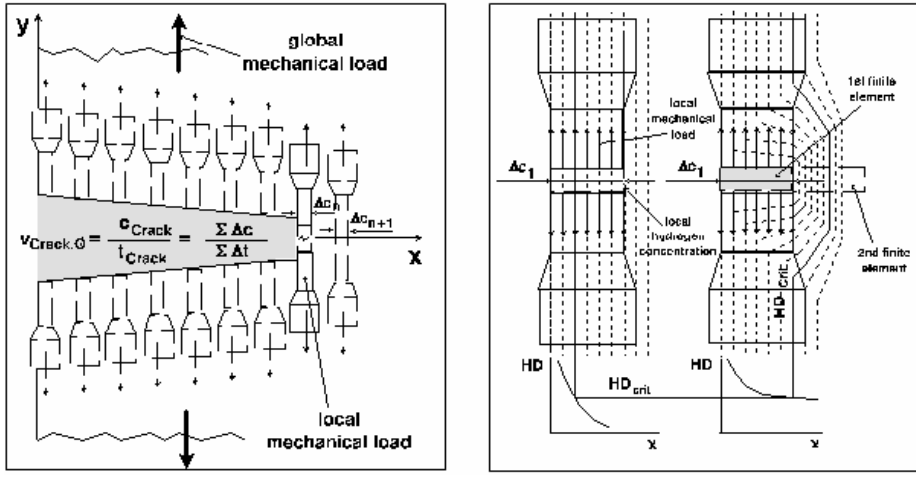


Figure 2: Increasing transverse residual stresses in a S 1100 weld with preheating and interpass temperature

NUMERICAL APPROACH

To gain more insight into the appearance of HACC in high strength structural steel welds, a numerical model to simulate HASCC initiation and propagation has been modified [2]. The model has been designed as an engineering approach on the macro-scale and is primarily focused on the interaction of the local mechanical load with the respective hydrogen concentration in the specific local weld microstructures [4, 5], but provides also a framework to incorporate quantified micro-scale effects on cracking. The approach is based on the assumption of a sequence of fictitious tensile specimens alongside a predefined crack path (Fig. 3) and consequently, each tensile specimen is represented by a respective finite element in the numerical model. Since hydrogen degrades more the ductility than the strength of steel microstructures, fracture of a specimen (element) is assumed, if the actual mechanical load – here, in terms of the true fracture strain – exceeds the experimentally determined local hydrogen concentration dependent limit for the specific weld microstructure. Vice versa, exceeding the limit of the hydrogen concentration in the local microstructure for the respective local mechanical load might be applied as crack criterion. Crack initiation and propagation is thus simply modeled by the failure of the elements ahead of the crack tip for which the critical hydrogen concentration and true fracture strain combination is exceeded. As illustrated in Fig. 4, such HACC modeling has been realized by indirect coupling of time-step based thermal, elastic-plastic structural and hydrogen diffusion finite element analyses (FEA). Coupling of the various FEA types, comparison of crack criteria and deletion of elements for crack propagation has been realized by external files [2].



a) Crack propagation as a sequence of ruptured fictitious tensile specimens

b) Hydrogen redistribution caused by crack propagation at the first specimen

Figure 3: Illustration of the crack modeling concept by fictive tensile specimens [4]

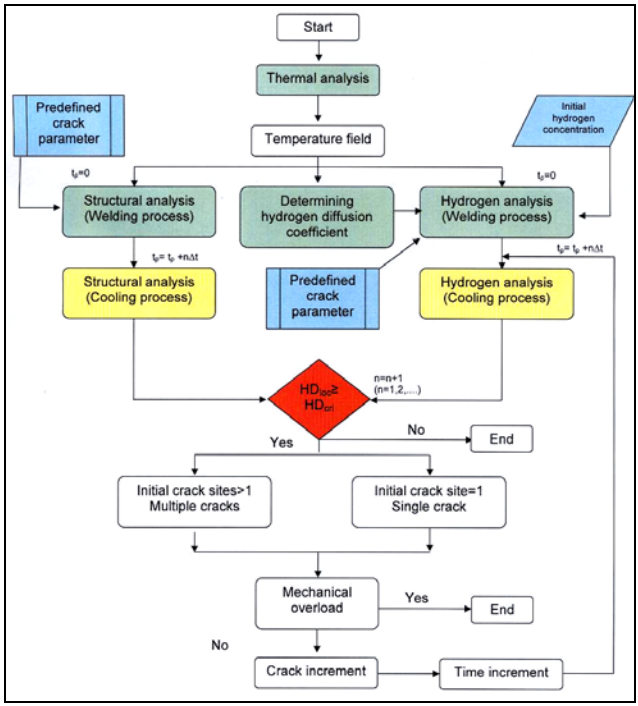


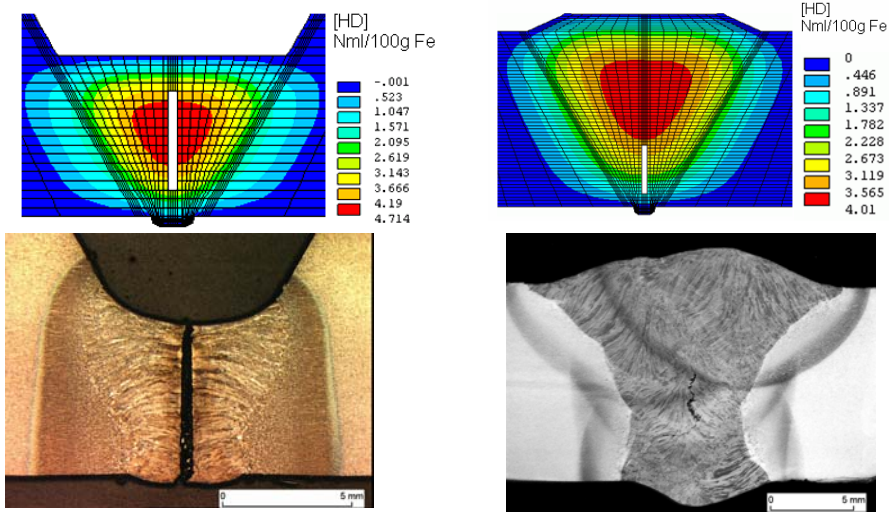
Figure 4: Flow chart for modeling HACC by coupled time-step based thermal, elastic-plastic structural and hydrogen diffusion finite element analyses

As a first application, HACC in a root and a multi-layer weld of a 60° butt joint of a S 1100 steel has been simulated, corresponding to respective Instrumented Restraint Cracking (IRC) Tests [6] with 12 and 20 mm thick plates at a restraint length of 55 mm, under the following assumptions and boundary conditions:

Hydrogen introduced by the welding arc is usually homogeneously distributed in the liquid pool and has thus been modeled as initial concentrations at the nodes representing the weld metal. As verified by respective experiments, no irreversible trapping occurs in the S 1100 weld microstructures and the temperature dependent effective diffusion coefficients range within a previously determined scatterband for micro alloyed low carbon structural steels [5]. Considering the lower boundary curve, the time, temperature and microstructure dependent hydrogen diffusion calculations have thus been carried out based on Fick´s Laws. In all analyses, the joints have been divided into four different material zones corresponding to the S 1100 QL weld microstructures, i. e. weld metal (WM), coarse grained heat affected zone (CGHAZ), fine grained heat affected zone (FGHAZ) and the base material (BM). The material properties for such microstructures have very carefully been selected corresponding to values for steels with similar chemical compositions. The mesh density, particularly alongside the predefined crack paths, accounts to the steep concentration and strain gradients to be expected during welding. As crack criterion, the true fracture strain curve dependent on the hydrogen concentration has been determined with hydrogen-saturated small tensile specimens for all four microstructures.

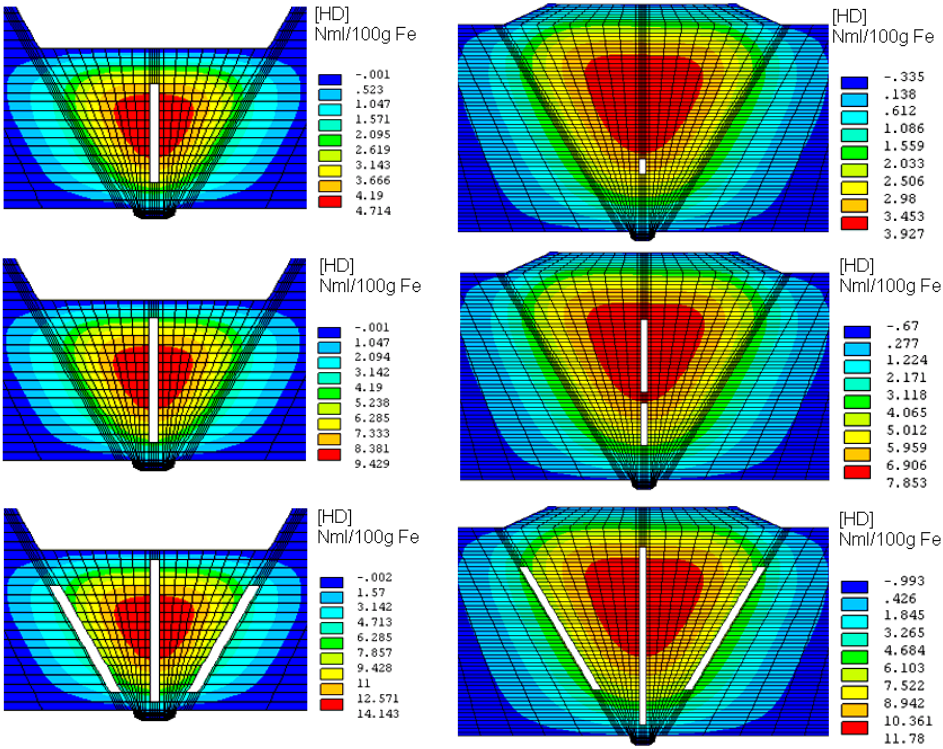
HACC LOCATION

Welding of earlier developed structural steels with higher Carbon contents usually revealed hard microstructures in the HAZ which in the weld metal was avoided by special filler materials. The high strength levels of newer thermo-mechanically processed and/or water-quenched and tempered base materials are usually matched by rapid cooling after welding revealing respectively hard weld metals. The most HACC susceptible region of fine grained structural steel joints has thus been shifted from the HAZ into the weld metal. This particularly applies to welding of the new S 1100 and S 1300 types for which the currently produced fillers can not even match the base material strength which provides an additional cracking risk regardless if hydrogen has been introduced. As illustrated in Fig. 5, the HACC location at the weld metal centerline of the root and multi layer S 1100 steel weld corresponds to these considerations and agrees well with respective experiments. The simulations revealed that cracking in the root weld is initiated in the weld metal centre and within fractions of a second proceeds in both directions (Fig. 5a). In the five layer weld, the crack starts in the lower third at the weld centerline and then expands very fast towards the bottom. The hair line crack evolving from the main crack (Fig. 5b) apparently corresponds to such behavior. The longer crack in the single pass also indicates that the root weld represents the most susceptible part of the joint.
Increasing initial hydrogen concentrations in the weld metal cause additional cracking in the HAZ close to the fusionline in both butt welds (Fig. 6). A comparison of Fig. 6b to Fig. 7 elucidates that after cooling to room temperature the locations of the maximum hydrogen concentrations and the maximum strains in the welds are different and thus, might not necessarily be relevant to the appearance of



a) Root weld (HD_0 = 5 Nml/100g) b) Five layer weld (HD_0 = 5 Nml/100g)

Figure 5: Modeled and experimentally determined crack locations in S 1100 welds

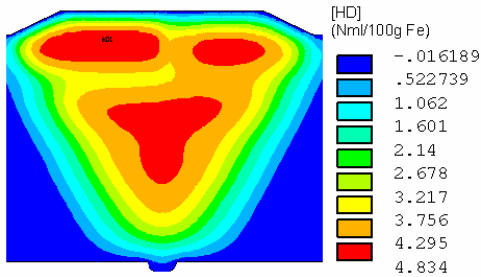


a) Root weld b) Five layer weld

Figure 6: Crack appearance with increasing initial hydrogen concentrations

cracking. While the maximum concentrations occur in the centre of the weld and in the two top layers (Fig. 7a), the maximum strains are located in the lower third at the weld centerline and at the bottom side along the fusionline (Fig. 7b). But at a lower initial level of 5 Nml/100 g, cracking (Fig. 6b) appears above the location with the maximum strains and below the region with the maximum hydrogen concentration.

a)



b)

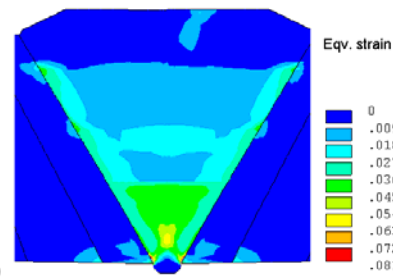
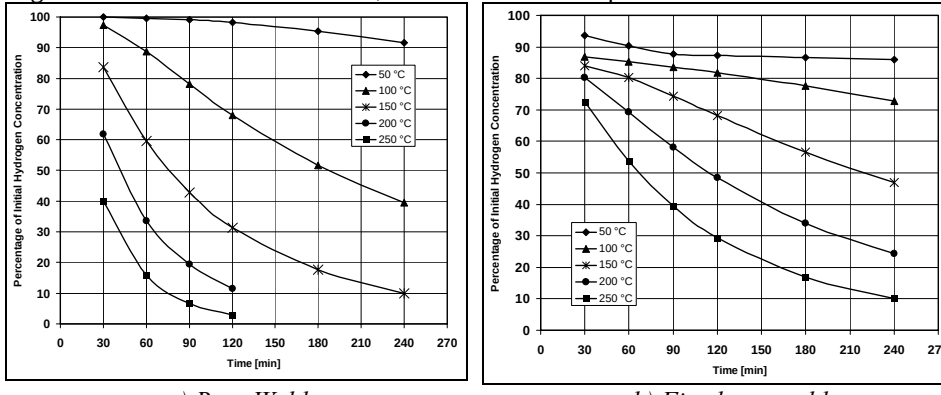


Figure 7: Hydrogen concentrations (a) and strains (b) after cooling of the five layer weld

At an initial concentration of 10 Nml/100g two cracks start at the weld centerline and finally merge (Fig. 6b). Respectively more hydrogen is diffusing into the HAZ at a high initial concentration of 15 Nml/100g and crack critical levels are reached for the high strains (Fig. 7b) at the fusion line. This generally means that only those regions are relevant for crack initiation and propagation where a critical hydrogen concentration-strain combination is exceeded.

HACC AVOIDANCE

Previous modeling of the hydrogen diffusion and effusion process already confirmed that HACC during welding of high strength structural steels cannot simply be avoided by preheating or controlled interpass temperatures [7] and that postheating at temperatures of up to 250 °C and sufficiently long times represents a much more appropriate procedure to combat HACC [2]. As a contribution to practical welding of structural steels, so-called hydrogen removal heat treatment (HRHT) diagrams have been developed. In such diagrams, as shown in Fig. 8 for the root and five layer weld of the S 1100 steel, the maximum hydrogen concentration in the weld after completion of the HRHT process and cooling to room temperature related to the initial concentration is plotted versus the postheating time for the various temperatures. Postheating procedures required for crack safe welding can then very simply be drawn from such diagrams, if the crack critical limit for the hydrogen concentration in the various microstructures is known. For instance, assuming 1 ml/100g as crack critical limit in all S 1100 weld microstructures (Fig. 1) and an initial concentration in the weld metal of 5 ml/100g, the required HRHT procedures can be evaluated alongside the 20 % line. Postheating at 250 °C for 60 min would be sufficient for the root weld and 180 min for the five layer weld, respectively. The much longer times required for the five layer weld can be explained by the larger total hydrogen amount and respectively longer diffusion and effusion distances. However, the curves are oriented at the maximum hydrogen concentrations regardless of the location and thus, the obtained HRHT procedures are conservative.



a) Root Weld *b) Five layer weld*

Figure 8: HRHT diagrams for a S 1100 60° V butt joint

Conclusions

From the first applications of modeling hydrogen assisted cold cracking in extra high strength structural steel welds, the following conclusions can be drawn:
1. The present model based on critical combinations of hydrogen concentration and mechanical load in terms of true fracture strain allows precise simulation of HACC initiation and propagation in steel welds and correctly reflects real crack locations.
2. The distribution of the local hydrogen concentration and mechanical load in the specific weld microstructures is significantly dependent on the weld geometry which has accurately to be modeled to identify crack critical regions.
3. Although HACC in high strength structural steel welds occurs predominantly in the weld metal, multiple cracking at various locations and also in the HAZ has to be considered, if the initial concentration in the weld metal exceeds a specific limit.
4. In contrast to preheating and a controlled interpass temperature, HACC in high strength structural steel joints can be avoided by postheating. The developed HRHT diagrams provide a fast and practical tool to determine HACC avoidance procedures in welded high strength structural steel microstructures.
Future modeling of hydrogen diffusion and cracking will be targeted at investigations of the influence of various material compositions, joint configurations, preparation type and number of layers on HACC in welds. The model might be developed further by incorporation of quantified micro-scaled mechanisms and by utilizing re-meshing features for crack propagation.

References

1. Cerjak, H., Dimmler, G., Enzinger, N., “Steel S 890 for Pressurized Shaft CD: Review of Metallurgical Investigations”, *Intern. Conf. Proc. High Strength Steels for Hydropower Plants,* Technical University Graz, 2005
2. Wongpanya, P., Boellinghaus, Th., Lothongkum, G., Hoffmeister, H., “Numerical Modelling of Cold Cracking Initiation and Propagation in S 1100 Root Welds”, *Welding in the World*, Vol. 53 (2009), No. 3-4, in print
3. N. N.: “Welding Recommendations for Welding of Metallic Materials – Part 2: Arc Welding of Ferritic Materials”, EN 1011-2, 2001
4. Boellinghaus, Th., Hoffmeister, H., “Numerical Model for Hydrogen Assisted Cracking”, *Corrosion*, Vol. 56, No. 6 (2000), pp. 611-622
5. Boellinghaus, Th., Hoffmeister, H., Dangeleit, A., “A Scatterband for Hydrogen Diffusion Coefficients in Micro Alloyed Low Carbon Structural Steels”, *Welding in the World*, Vol. 35, No.2 (1995), pp. 83-96
6. Hoffmeister, H., “Concept and Procedure of the IRC-Test for Assessing Hydrogen Assisted Weld Cracking”, *Steel Research*, Vol. 57, No.7 (1987), pp. 344-347
7. Wongpanya, P., Boellinghaus, Th., Lothongkum, G., “Effects of Hydrogen Removal Heat Treatments on Residual Stresses in High Strength Structural Steel Welds”, *Welding in the World*, Vol. 50 (2006), pp. 96-103

Effects of Hydrogen on Materials
Proceedings of the 2008 International Hydrogen Conference
Brian Somerday, Petros Sofronis, Russell Jones, editors, p 596-603
Copyright © 2009 ASM International®
All rights reserved.
www.asminternational.org

INFLUENCE OF DRAWING-INDUCED RESIDUAL STRESSES AND STRAINS ON HYDROGEN EMBRITTLEMENT OF COLD DRAWN WIRES

J. Toribio, M. Lorenzo and V. Kharin
Department of Materials Engineering, University of Salamanca
Campus Viriato, Avda. Requejo 33, 49022 Zamora, Spain

ABSTRACT

Hydrogen embrittlement (HE) plays a relevant role in the performance of cold-drawn prestressing steel wires in harsh environments. To this end, the knowledge of residual stresses and plastic strains in wires due to cold-drawing, as well as of wires hydrogenation from harsh environments are the keys to successful predictions of wire lives. This paper advances previous analyses of HE in cold-drawn prestressing wires via numerical modelling, first, of *the whole* cold-drawing process (all the stages of cold drawing) to gain the distributions of residual stresses and plastic strains, and next, of the stress-strain assisted hydrogen diffusion in wires towards creation of the conditions for HE nucleation. Generated results prove the relevant role of residual stress-and-strain field in hydrogen accumulation in the wires, as well as their possible consequences for HE.

1. INTRODUCTION

Steel wires are used for concrete structures prestressing, which is a powerful civil engineering technique aiming to introduce desirable stresses and counterbalance undesirable ones so that the combination of prestressing and service loading produces stresses within specified limits [1]. Prestressing steel wires are usually made of eutectoid pearlitic steel heavily cold drawn to create elevated tensile properties. These wires, once subjected to high service stresses, remain such forever, usually in hostile environments, e.g., due to atmospheric humidity. All that makes them susceptible to surface cracking, in particular of the stress corrosion origin. Environmentally assisted fracture of prestressing steels has been the subject of extensive studies which substantiated the importance of hydrogen embrittlement (HE) in deterioration of structures [2].

The importance of HE in the performance of cold-drawn pearlitic wires is so high that the former International Federation for Prestressing (FIP) –now the International

Federation for Concrete (FIB)– proposed the Ammonium Thiocyanate Test (ATT) which is considered well suited for steel control and acceptance [3]. However, despite being in use as a standard test method, it reveals neither how HE goes on in prestressing wires nor the roles of various manufacturing and service factors. With regard to manufacturing factors affecting the strength and life of prestressing wires, apart of the properties of material *per se*, the issue of residual stresses is the essential one [4,5].

The pioneering paper [6] established an important milestone by establishing a *quantitative* relationship between the level of near-surface residual stresses, which were represented by hypothetical stress distributions, and HE of prestressing steel wires. In [6] the combined effect of the applied tensile stress modified by a residual one, as a mechanical crack-driving factor from one side, and of the hydrostatic stress gradient, as the driving force for hydrogen diffusion and pre-requisite for HE from the other side, both were taken into account.

This paper goes further in the research, and the earlier developed model [6] is advanced with regard to the analysis of the influence of the residual stress-*and*-strain profiles on hydrogenation of cold-drawn prestressing steel wires. To this end, certain aspects of the earlier proposed model [6] are advanced here, and applied to analyse, in particular, the influence of residual stress-strain profiles induced by *progressive* (*multi-step*) cold drawing on the hydrogen-affected behaviour of the prestressing steel wires.

2. RESIDUAL STRESSES AND PLASTIC STRAINS DUE TO PROGRESSIVE COLD DRAWING

To proceed with the implementation of the presented model to describe HE of prestressing wires, the first step is to determine the residual stresses and plastic strains in wires generated by cold drawing. To this end, this analysis is divided into two parts: firstly, the mechanical analysis, by the finite element method, of the stress-strain fields during cold drawing; secondly, the chemical analysis, by a Galerkin-type weighted-residual method, of hydrogen diffusion assisted by both stress and strain, where the stress-strain fields obtained in the mechanical analysis act as input data for the posterior chemical analysis.

In this work, a real (commercial) cold drawing process in several passes (i steps or stages) was modelled. The base material at the beginning of the manufacturing chain was a hot-rolled pearlitic steel (0.74% C, 0.70% Mn, 0.20% Si, 0.015% P, 0.023% S) whose Young modulus is E =199 GPa and whose 0.2%-offset yield strength is σ_Y = 710 MPa. For this steel FEM simulations of wire drawing process were performed in order to obtain the residual stress and strains fields. In these simulations the constitutive material model was an elastoplastic solid with von Mises yield surface, associated flow rule, and isotropic strain-hardening.

Cold drawing consists of the passing of the steel wire through a hard die, as shown in Fig. 1. The die was modelled with an inlet angle $\alpha = 7.6º$, and the material of the die (tungsten carbide) was considered to be rigid due to its very high Young modulus in relation to that of the wire. Friction between the wire and the die was not considered in the numerical modelling. Initial dimensions of the wire were $d_0 = 12$mm (initial diameter) and $L_0 = 60$mm (initial length). In the case of the commercial cold-drawn pearlitic wire used in this analysis, the progressive (or repetitive) cold drawing process is divided into six passes, so as to produce a cold-drawn wire (commercial prestressing steel, six steps of cold drawing) from a hot rolled bar (base material which is not cold drawn yet).

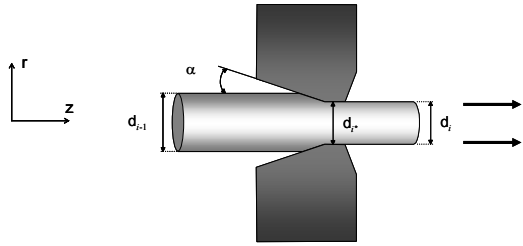


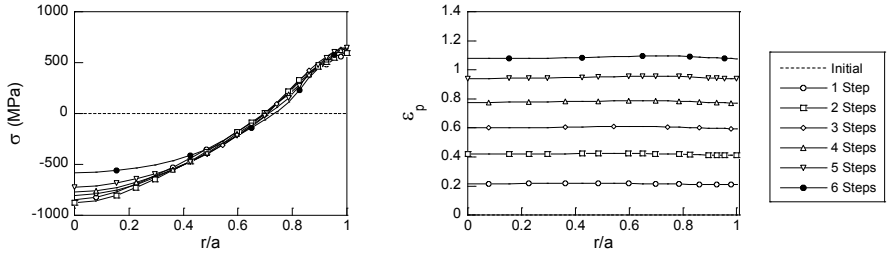
Figure 1: Schematic of the cold drawing process: passing of the steel through the die (one pass of cold drawing).

The axisymmetric formulation is suitable for simulations. Corresponding finite element model was created to model the drawing process in cylindrical coordinates (r,z) shown in Fig. 1. The boundary condition of the prescribed axial displacement was imposed on the front extreme of the rod. Elastoplastic large deformation – large strain calculations were performed using a general-purpose finite element code with updated lagrangian formulation. Several finite element meshes formed by four-node quadrilaterals were tried until the acceptable mesh-convergence of the result was ensured. Mesh was refined in the area next to the contact surface between the two bodies (the wire and the die).

3. DISTRIBUTION OF RESIDUAL STRESS AND STRAIN

Figure 2a shows the evolution of hydrostatic stress and Fig. 2b equivalent plastic strains during the different stages of cold drawing as a function of the radial coordinate in dimensionless form (r/a), being a the outer wire radius, $a = d/2$. It is seen in Fig. 2a that, after each drawing pass, the level of residual hydrostatic stress increases and the diameter decreases progressively. This is a very dangerous situation, since the pioneering paper [6] (until now, the only one establishing a *quantitative* relationship between the level of near-surface residual stresses and the HE susceptibility of prestressing steels) undoubtedly demonstrate by quantitative

modelling the deleterious effect of near-surface tensile residual stresses on the HE performance of cold-drawn prestressing steel wires.



(a) (b)

Figure 2: Evolution of hydrostatic stress (a) and plastic strain (b) at different stages of cold drawing as a function of the dimensionless radial coordinate r/a.

It is important to notice that numerical results exhibit a kind of self-similitude with regard to the coordinate dependence, since Fig. 2a shows that all results fit into the same band when represented as a function of the dimensionless coordinate (r/a), which allows a prediction of the stress field in the wire for any stage of cold drawing on the basis of the numerical results from a previous drawing pass. Fig. 2b shows the evolution with cold drawing of the equivalent plastic strain ε_p affecting the strain dependent component of the solubility [7, 8], and this variable, ε_p, could be properly called residual plastic strain. The plots in Fig. 2b indicate a progressive accumulation of plastic strain with cold drawing.

4. HYDROGEN ACCUMULATION IN THE COLD DRAWN STEEL WIRE

The hydrogen diffusion model used in this paper is that proposed in previous works by the authors [7,8] (cf. these papers for details of the meaning of the variables). To discriminate the contributions of stress and plastic strain on hydrogenation of wire, three hydrogen diffusion cases were considered: (a) stress-and-strain assisted diffusion; (b) stress-only assisted diffusion, with $\nabla K_S(\varepsilon_p) = 0$; (c) conventional diffusion with no stress assistance. The respective equations are:

$$\mathbf{J} = -D(\varepsilon_p)\left\{\nabla C - C\left[\Omega\nabla\sigma + \frac{\nabla K_{S\varepsilon}(\varepsilon_p)}{K_{S\varepsilon}(\varepsilon_p)}\right]\right\}, \tag{1a}$$

$$\mathbf{J} = -D(\varepsilon_p)\left\{\nabla C - C\left[\Omega\nabla\sigma\right]\right\}, \tag{1b}$$

$$\mathbf{J} = -D(\varepsilon_p)\nabla C, \tag{1c}$$

The results of the computations for stress-strain assisted diffusion (1a), stress-only assisted diffusion (1b) and conventional diffusion (1c) are presented as concentration distributions in Fig. 3 (spatial distributions for different times) and Fig. 4 (time distributions for different space locations) in terms of dimensionless concentration C(r,t)/C* where the reference concentration C* represents the hydrogenating capacity of environment modified by applied stress σ_{app}, *i.e.*, the equilibrium hydrogen concentration in stressed virgin material, which within elasticity limits is $C^* = C^0_{eq} \exp(\sigma_{app}/3)$.

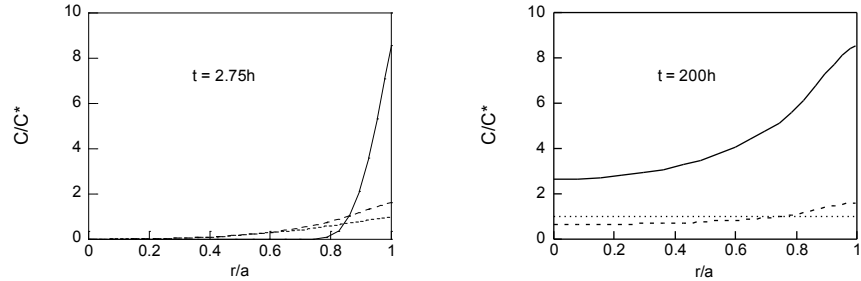


Figure 3: Distributions of relative concentrations of hydrogen (C/C) as a function of the dimensionless radial coordinate r/a, at two different diffusion times of 2.75 hours (a) and 200 hours (b), for the three modelling schemes used in this work: stress-and-strain assisted diffusion (full line), stress-only assisted diffusion (dashed line) and conventional diffusion with no stress or strain assistance (dotted line).*

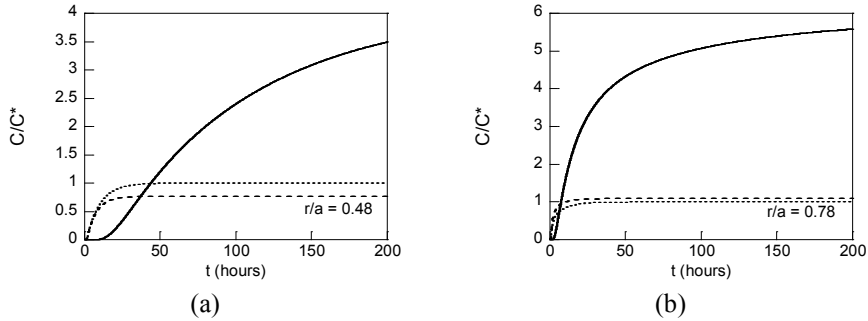


Figure 4: Time evolution of relative concentrations of hydrogen (C/C) at a point placed at r/a = 0.48 (a) and r/a = 0.78 (b), for the three modelling schemes used in this work: stress-and-strain assisted diffusion (full line), stress-only assisted diffusion (dashed line) and conventional diffusion with no stress or strain assistance (dotted line).*

From presented results, it follows that the effects of residual stress and strain on hydrogenation results in a local increase of hydrogen concentration in the highly

stressed areas of the wire, *i.e.*, near the wire surface where hydrostatic residual stresses are tensile and plastic strains are high enough after the whole drawing process. This is clearly observed in Fig. 3 where the concentration distributions at the wire skin (*i.e.* at r/a = 1) and its vicinity, especially for short diffusion times (Fig. 3a) for which there is no time to supply hydrogen to more internal areas. These numerical results confirm the danger of tensile residual stresses near the wire surface in the matter of HE susceptibility of prestressing steels (as pointed out in the pioneering work [6]) but emphasize, in original manner, the key role of plastic strain.

Figure 4 indicates that time evolution of hydrogen concentrations at different locations increase with time in such a manner that the trend approaches a steady state associated with saturation. The approach to this steady state is faster in the case of stress-only assisted diffusion (dashed lines of Fig. 4) than in the case of stress-strain assisted diffusion (full line of Fig. 4), whereas the conventional diffusion (dotted lines of Fig. 4) behaves in a similar manner as the stress-only assisted diffusion. With regard to the differences between distinct locations, the approach to the steady stated situation is faster in points located closer to the wire surface (r/a = 0.78) than at deeper points (r/a = 0.48).

To analyze the two afore-said effects, Fig. 3 is the key item. It shows that relative over-hydrogenation occurs at the wire surface r = a and its vicinity (critical area where a hydrogen–induced crack could appear). In terms of the hydrogenation of a wire skin of definite thickness, where critical events of HE can be expected to occur (cf., [6]), residual strain field dramatically increases the amount of hydrogen accumulated in this skin at short diffusion times (t = 2.75 h; Fig. 3a), and increases even more this amount at long exposure times (t = 200h; Fig. 3b), thus enhancing the hydrogenation of prestressing steel wires. Therefore, in highly strained materials as cold drawn steels the increase of hydrogen solubility due to accumulated plastic strain predominates over the decrease of hydrogen diffusivity (mobility) in plastically strained material.

Considering a given material element in the wire skin where HE initiates, *i.e.*, a specific location or fracture nucleation site of depth x_c, this depth represents the dimension of the critical surface (subsurface) crack, as suggested in the pioneering work [6], and could be estimated as 450 μm, *i.e.*, $r = a - x_c \approx 0.9a$. Fig. 3 shows that, at this critical location, the stress-strain assisted diffusion model predicts a much higher amount of hydrogen in the critical area than the stress-only assisted diffusion or the conventional diffusion models (the ratio is about 4.8). Therefore, plastic strain fields must be taken into account in hydrogen diffusion models in cold drawn wires because the consideration of stress-only assisted diffusion leads to dramatic (and non conservative) underestimation of the hydrogen content in the critical region.

5. CONCLUSIONS

Numerical modelling of the entire drawing process in several passes was performed to know the whole distributions of inhomogeneous plastic strains and triaxial residual stresses generated in the wires throughout the process. The magnitudes and gradients of such variables are the key factors in metal hydrogenation assisted by stress and strain fields within the wires. The following conclusions may be drawn from the mechanical (stress-strain) simulation:

i. The radial distributions of residual stresses after each drawing pass exhibit a sort of self-similitude with regard to the coordinate dependence, since they fit into a unique band when plotted against the dimensionless radial coordinate, and this happens in all drawing passes for hydrostatic stresses, which allows a prediction of the stress field in the wire for any stage of cold drawing on the basis of the numerical results from a previous drawing pass.

ii. Residual stress distributions are of tensile nature in the wire skin and its vicinity, with a maximum just at the surface. This is very dangerous from the point of view of the HE susceptibility of the cold drawn wires, considering the deleterious effect of such tensile near-surface residual stresses on the performance of the prestressing steel wires, since tensile stresses are driving forces for hydrogen entry and diffusion.

iii. There is a progressive accumulation of equivalent plastic strain with cold drawing, and this can affect hydrogen diffusion assisted by stress and strain in two ways: firstly, by raising hydrogen solubility due to accumulated plastic strain, thereby resulting in greater hydrogen absorption; secondly, by lowering hydrogen diffusivity (and thus mobility) in plastically strained material, thus delaying hydrogen accumulation in the wires.

Numerical modelling of the hydrogen diffusion was performed using three models: diffusion assisted by the stress and strain fields, diffusion assisted only by the stress field and conventional diffusion according to a Fick type law, so as to evaluate the relative roles of the stress and strain fields on hydrogen diffusion within the cold drawn prestressing steel wires. The following conclusions may be drawn from the chemical (hydrogen diffusion) simulation on the basis of the mechanical (stress-strain) results:

i. The maximum values of hydrogen concentration are achieved at the wire skin and its vicinity, the place where a potential HE crack could appear to promote failure of the prestressing steel wires. This is valid for both short and long times for diffusion, although in the case of long exposures to hydrogen the penetration distances are higher, but even with this deeper penetration the maximum of concentration remains just at the wire surface.

ii. Time evolution of hydrogen concentration indicates that a steady state situation is asymptotically approached for $t \rightarrow \infty$. The approach to the steady state concentration is slower in the case of stress-and-strain assisted diffusion and faster in the two cases of stress-only assisted diffusion and conventional diffusion in the Fick's sense. In the two latter at least 200 hours are necessary to reach an almost horizontal slope in the C(t) curve at most locations.

iii. In the critical (fracture) region associated with HE, hydrogen concentration distributions for stress-and-strain diffusion are quite higher ($\approx$ 4.8 times) than those for stress-only and conventional diffusion. Therefore, plastic strain fields must be taken into account in hydrogen diffusion models in cold drawn wires because the consideration of stress-only assisted diffusion leads to dramatic (and non conservative) underestimation of the hydrogen content in the critical region.

ACKNOWLEDGMENTS

The authors gratefully acknowledge the financial support received from different institutions: MCYT (Grant MAT2002-01831), MEC (Grant BIA2005-08965), JCyL (Grants SA078/04, SA067A05 and SA111A07).

REFERENCES

1. Valiente, A., Elices M. "Premature failure of prestressed steel bars". *Engng. Failure Analysis*, Vol. 5, (1998), pp. 219-227.
2. Bergsma, F., Boon, J.W., Etienne, C.F. "Détermination de la sensibilité des aciers précontrains à la fragilisation par l'hydrogène". *Rev. Métallurgie*, Vol. 75, (1978), pp. 153-164.
3. FIP-78. Stress Corrosion Test. Stress Corrosion Cracking Resistance for Prestressing Tendons. Techn. Rep. No. 5. FIP, (Wexham Springs, Slough., 1981) p
4. Katagiri K., Sato T., Kasaba K., Sasaki S., Tashiro H. "Effects of post-drawing treatments on the fatigue strength of eutectoid steel wires". *Fatigue Fract. Engng. Mater. Struct.*, Vol. 22, (1999), pp. 753-760.
5. Elices M. "Influence of residual stresses in the performance of cold drawn pearlitic wires". *J. Mater. Sci.*, Vol. 39, (2004), pp.3889-3899.
6. Toribio J., Elices M. "Influence of residual stresses on hydrogen embrittlement susceptibility of prestressing steels". *Int. J. Solids and Struct.*, Vol. 28, (1991), pp. 791-803.
7. Toribio J., Kharin V. "K-dominance condition in hydrogen assisted cracking: the role of the far field". *Fatigue Fract. Engng. Mater. Struct.*, Vol. 20, (1997), pp. 729-745.
8. Toribio J., Kharin V. "A hydrogen diffusion model for applications in fusion nuclear technology". *Fusion Engng. Design*, Vol. 51-52, (2000), pp. 213-218.

Effects of Hydrogen on Materials
Proceedings of the 2008 International Hydrogen Conference
Brian Somerday, Petros Sofronis, Russell Jones, editors, p 604-612
Copyright © 2009 ASM International®
All rights reserved.
www.asminternational.org

COHESIVE ZONE MODEL FOR HYDROGEN EMBRITTLEMENT OF GRAIN BOUNDARIES IN AL 5xxx ALLOYS

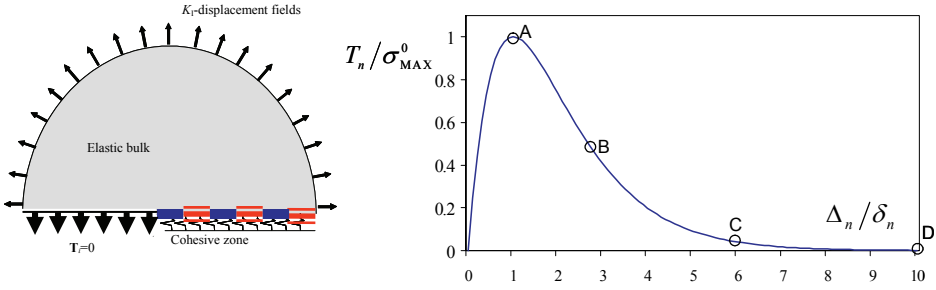
F. El-Houdaigui, N. Benali, R. Estevez
Université de Lyon, INSA Lyon, MATEIS UMR CNRS 5510
20 avenue Albert Einstein, F-69621 Villeurbanne cedex

D. Tanguy
Ecole Nationale Supérieure de Mines de St Etienne, Centre SMS,
158 cours Fauriel, F-42023, St Etienne

INTRODUCTION

The aluminium alloys of the 5xxx series can be susceptible to stress corrosion cracking (SCC) when immersed in an aqueous environment. Crack propagation involves the anodic dissolution of the Al_3Mg_2 compounds along the grain boundaries and also the embrittlement of the interface between these precipitates and the matrix [1], ahead of the crack tip, due to H trapping. Hydrogen is produced within the crack by the anodic dissolution. The susceptibility to SCC and H embrittlement exhibits a strong dependence with the size and distribution of the intergranular precipitates. The peak sensitivity is obtained when the precipitation is so called 'continuous'. In fact, the apparent 'continuity' stems from the observation of densely distributed lens shaped precipitates (50 nm long / 80 angstroms wide), in TEM. It appears that 5xxx alloys are very resistant to crack initiation after a solution heat treatment or when the precipitates are globulized when overaged. The role of H in the failure of grain boundaries has been studied in depth in the 7xxx series where trapping of H at the Mg rich intergranular precipitates, more precisely at the matrix-precipitates interface, has been directly observed [1]. However, the grain boundary in between these tiny precipitates is expected to be a weak trap for H. How does the failure take place along such heterogeneous interface and how the precipitates size effect arise remain to be clarified.

The purpose of the present study is to gain insight on the micromechanics of the failure process by comparing a precipitate free interface with heterogeneous interfaces of various sizes of precipitates. We examine how a heterogeneous hydrogen embrittlement of the magnesium precipitates could weaken the grain boundary. To the end, we analyse the conditions for crack propagation along a heterogeneous interface inserted in between two elastic bulks, where a crack emerges. The heterogeneous interface for the grain boundary consists in safe domains and others where hydrogen can be trapped resulting in a progressive reduction of the cohesive strength. We investigate the resulting strength variation of the grain boundary and how this could assist failure.



(a) (b)

Figure 1: (a) the small scale yielding problem with a linear elastic, isotropic bulk and a cohesive zone interface along the crack symmetry plane. (b) The variation of the traction-opening cohesive zone adopted in the description. Different σ_{max}^0 are considered for a heterogeneous interface, plain-blue and line-red domains in (a).

MODELLING INTERGRANULAR DECOHESION

The problem formulation is depicted in Fig. 1a. We assume that the bulk material is isotropic linear elastic, as a first step, in order to focus on the details of the failure process along the interface. We analyse a mode I fracture process under plane strain conditions. Small scale yielding is assumed and a boundary layer approach is adopted that results in prescribing the displacement K_I-fields along the outer circle. A natural crack is considered with a traction free face. Cohesive zones are laid down along the crack symmetry plane, along the location of the maximum principal stress. In the case of a homogeneous problem, the cohesive zone properties are uniform along the interface with the traction-opening displacement reported in Fig. 1b, borrowed from Needleman [2,3]. The variation of the traction-opening cohesive surface shows a maximum (see Fig. 1b) for (A) $T_n = \sigma_{max}^0$, followed by progressive debonding with $T_n = \sigma_{max}^0/2$ at (B) up to the onset of crack propagation at (C). The area under the T_n-Δ_n plot corresponds to the work of separation $\Phi_{SEP} = \exp(1).\ \sigma_{max}^0\delta_n$, with σ_{max}^0 and δ_n being material parameters related to the properties of the interface.

For the case of a homogeneous interface representative of an unbrittled, hydrogen free, interface we have considered σ_{max}^0= 1GPa and δ_n=1nm resulting in Φ_{SEP}=2.7J/m^2. These values correspond to an energy of separation within 1-10J/m^2 which represents that for interatomic debonding by cleavage in a single crystal and also the surface energy between a metal-ceramic interface. Adjusting the opening at the onset of debonding δ_n to 1nm results in an opening about 6nm for complete decohesion and cease of the cohesive forces. Such value of δ_n involves a maximum traction σ_{max}^0 of 1GPa, which is thought representative for most metal based interfaces as discussed in [2]. By taking the Young's modulus E=70 GPa and Poisson's ratio ν=0.3, the theoretical toughness is $K_I^{CR} \approx 0.46\text{MPa}\sqrt{\text{m}}$. In Fig. 2.1,

we have reported the resistance curve versus the crack advance and the corresponding load level in terms of $K_I(\Delta a)$, with the crack extension Δa normalised

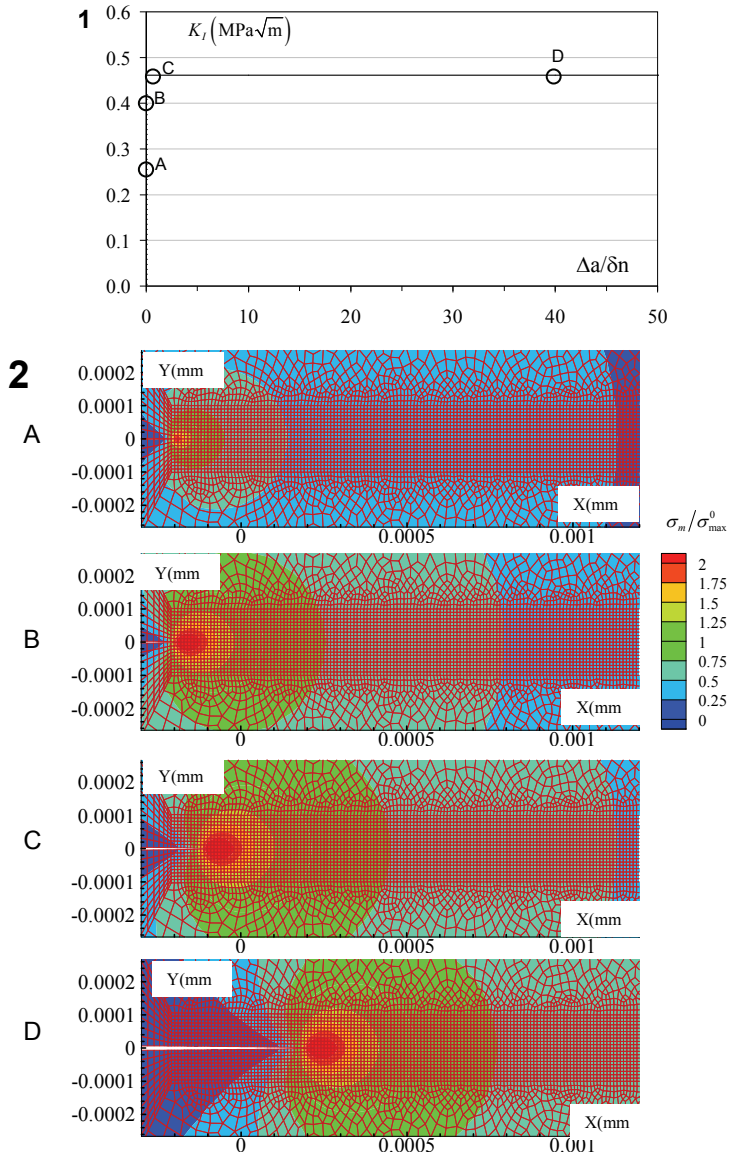


Figure 2 : for the homogeneous unbrittled interface, (1) resistance curve with the variation of the applied load in terms of K_I with the crack advance, (2) contour of the mean stress normalized with $\sigma_{max}{}^0$ at stages A, B, C (onset of crack advance) and D (during the crack advance) marked in the plot (1b).

with δ_n for the stages A-B-C-D of Fig. 1b. The corresponding distribution of the mean stress, normalised with σ_{max}^0, for those stages are reported in Figs. 2.2.
The initial natural crack tip emerges at the left of the refined zones in Fig. 2.2. For the stages A-B-C of the traction-opening (see Fig. 1b) of the first cohesive element at the crack tip, the maximum in the mean stress distribution indicates the position of the tip of the cohesive zone ahead the crack tip. At the onset of debonding (A), this maximum is very close to the location of the crack tip. The extension of the cohesive process zone can be evaluated from the abscissa of the maximum in A and C, which is approximately 200nm.
Crack propagation results in a further progression of the stress concentration and **related process zone** along the crack symmetry plane as shown for stage D.
The extension of the cohesive process zone observed in Fig.2.2C appears to be about 200nm. This is actually consistent with the analytical estimate [4], which provides an intrinsic length scale into the problem, as $\Lambda^{CZ} = 9\pi/32 \times (K_I^{CR}/\sigma_{max}^0)^2 \approx 190\,\text{nm}$. It is worth noting that the length Λ^{CZ} of this process zone coincides with the range for which precipitates size effects are reported for the alloys under consideration.
We now consider the case of a heterogeneous interface as depicted in Fig. 1a with equally long non-brittle and embrittled ligaments, the latter representing the damaged interface between the precipitates and the grains. The embrittlement is incorporated with a dependence of σ_{max} with the neighbouring concentration of hydrogen. Recent studies [5,6] which focused on the influence of a concentration of hydrogen atoms covering atomic plane of a single structure of Al or α-Fe provide some insight of how much the reduction in σ_{max}^0 can be. Albeit the embrittlement along the precipitates involves a mechanism different from those addressed in [5,6], we assume that the reduction in the traction at decohesion is of similar order of magnitude. By considering the situation with a material pre-charged with hydrogen, we consider that the reduction in the bonding properties of the precipitate-grain interface results in a decrease in $\sigma_{max}=\sigma_{max}^0/5$, this corresponding to the minimum value reported in [5] for Al.

INFLUENCE OF A HETEROGENEOUS GRAIN BOUNDARY ON FAILURE AND RELATED EMBRITTLEMENT

By accounting for a heterogeneous interface of various zone lengths, we analyse the condition for crack propagation for non-brittle and embrittled ligaments of which size varies from 50nm to 200nm, the two zones being equally long. Their maximum traction at debonding is σ_{max}^0=1GPa and σ_{max}=0.2GPa, while the characteristic length at decohesion δ_n=1nm is kept constant. In all cases analysed, the cohesive zone at the crack tip corresponds to a non-brittle ligament and is followed by an embrittled one (see Fig. 1a). Thus, the onset of crack propagation for the cohesive ligament at the crack tip corresponds to the toughness of the heterogeneous interface.

In Figs. 3, we have reported the mean stress distribution normalised by σ_{max}^{0} for the stages A,B,C of Fig.1b of the non-brittle cohesive element at the crack tip.

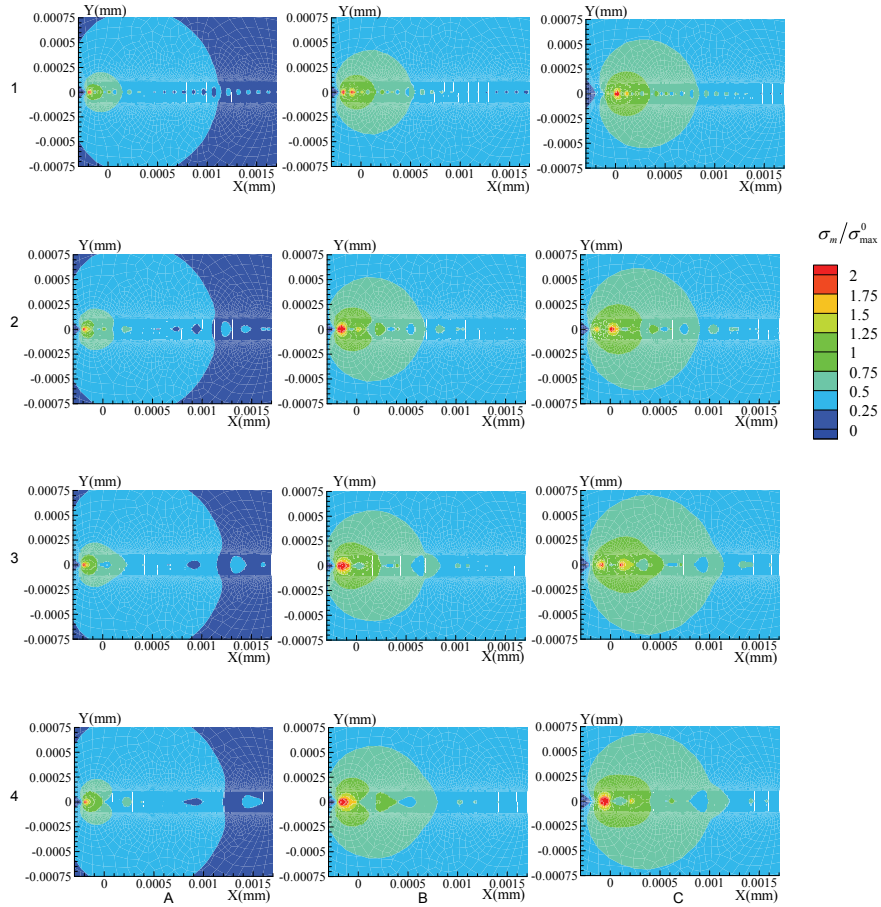


Figure 3: contours of the mean stress normalized with σ_{max}^{0} peak stress of the unbrittled cohesive zone at stage A, B, C of the cohesive ligament at the crack tip. These distributions correspond to ligaments of (1) 50nm, (2) 100nm, (3) 150 nm and (4) 200nm.

The references 1,2,3,4 correspond to lengths of ligaments of 50nm, 100nm, 150nm and 200nm respectively. The cases 1, 2 and also 3 show a similar failure process and for these three cases, the process zone for the non-brittle ligament is weakened at the locations of the precipitates zones. In the case 1 with ligaments 50nm long, the contour 1A in Fig. 3 indicates the location of the crack tip. We observe in 1B that during the debonding of the first non-brittle ligament, the stress concentration is shifted toward the second non-brittle cohesive zone, ahead of the crack tip. At the

onset of crack propagation (1C in Fig. 3), this second non-brittle cohesive zone has already started to debond. This case, and similarly case 2 for a ligament 100nm long

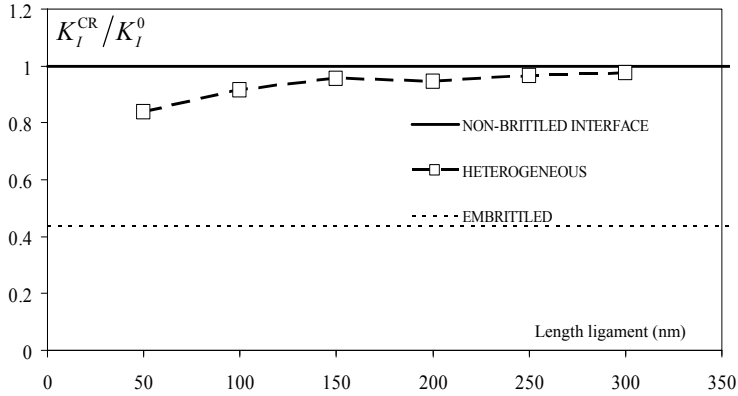


Figure 4: Variation of the toughness with a heterogeneous interface, the length of the ligaments varies from 50nm to 300nm, by intervals of 50nm. The toughness K_I^{CR} for the onset of crack propagation is normalized with K_I^0 corresponding to the homogeneous, unbrittled ligament.

(see Fig. 3), illustrates the assistance of the weakened ligament in the failure process. This is also observed for the 150nm long ligaments in case 3 but this is no longer the case with for those that are 200nm long.

For the case 4 in Fig. 3 with 200nm long ligaments, the failure process is similar to that reported in Fig. 2 for the homogeneous non-brittle interface: the stress concentration remains located within the cohesive zone at the crack tip and no transfer of the stress concentration towards the second cohesive zone ahead of the crack tip is observed. In this case and for longer ligaments, no effective assistance from the weakened cohesive zone to the failure process is observed.

In Fig. 4, we have reported the variation of the toughness at the onset of crack propagation normalized with that of the homogeneous unbrittled cohesive zone with the length of the un-brittle/weakened ligaments of the heterogeneous interface. We observed that the major embrittlement effect takes place for the interface containing the smallest brittled regions, some influence is also seen for the 100nm long weakened cohesive zone. For longer unbrittled/brittled ligaments, the influence on the failure is modest or negligible.

DISCUSSION AND CONCLUSION

In Fig. 4, it is seen that the toughness of the heterogeneous interface remains at a level closer to that of the non-brittle one than to that of the homogenous weakened ligament. The major embrittlement effect is observed for an interface in which the heterogeneous zone is the smaller, in the present work this corresponds to 50nm long ligaments. In this case, the interface toughness is reduced by 17% when compared to

that of the homogeneous unbrittled one, and by 9% for the 100nm long ligaments. For ligaments of length equal or longer than 150nm, no noticeable effect on the toughness is observed. In the case of a heterogeneous interface, the results reported in Fig. 4 indicate that the account for the reduction of the cohesive properties of the weakened interface does not provide enough information on the embritlement process. In the present analysis, we point out that the extension of the brittled region and its interaction with the unbrittled one govern the amount of toughness reduction related to a partial H embrittlement along the precipitates. The reduction of the toughness of the heterogeneous ligament remains much smaller to that observed for a homogeneous weakened region.

It is worth noting that a reduction of the toughness by 17% implies a weakening of the energy of separation by approximately 30%. From the results reported in Fig.4, one can somehow homogenized the cohesive properties from the measurement of the toughness and related energy for separation. If we adopt a homogenized cohesive zone identical to that presented in Fig. 1, we have $\Phi_{SEP} = K_{CR}^2 / E' = \exp(1).\sigma_{MAX}^{EFF}.\delta_n$, in which δ_n remains unchanged while the reduction of the traction at separation $\sigma_{MAX}^{EFF} \approx 0.7\sigma_{MAX}^0$ for the shortest ligaments of 50nm. This points out that the largest reduction in the cohesive properties for the cases investigated here are modest compared to that of the weakened region, those affected by the H embrittlement, for which $\sigma_{max} = 0.2\ \sigma_{max}^0$.

The analysis of the cohesive properties of the weakened region as performed in [5,6] focus on the reduction of the stress at which the debonding is triggered and also on the related energy for separation. Such analyses are necessary to estimate the magnitude of the embrittlement and similar analyses will have to be developed to gain insight on the failure process along the Al_3Mg_2 interface with the Al grains. However, those investigations are necessary but these are not sufficient when a heterogeneous interface has to be considered, as in the case of the grain boundaries in the AA5xxx alloys. Because the extent of the cohesive process zone appears to be of the order of 0.2 to 1 micron depending of the traction at debonding and the energy of separation, the toughness of such heterogeneous interface results from the interaction and related stress distribution between non-brittle and weakened zones. The analysis of such interaction is shown tractable by a finite element analysis as presented here, with account of the cohesive properties of the interface with a cohesive surface methodology. The present work has focused on this aspect and for the sake of simplicity but also to point out this feature, the bulk has been considered elastic only. The analysis of the relative length ratio between the non-brittle and brittled ligaments on the failure properties is under progress. This probably influences the magnitude of the toughness reduction of the heterogeneous interface but this is expected to remain within the range reported here.

In a forthcoming study, the influence of the kinetics related to H-diffusion from the crack tip into the bulk and along the interface on the debonding process will be considered. If elasticity only is considered, the present results will be affected only by the kinetics related to H-diffusion, the region over which H progresses is

expected to extend over the 200nm where heterogeneous effects are shown important here. However, this will have to be confirmed by additional calculations. Future work will focus on the interaction between debonding along the heterogeneous interface local plasticity and H-diffusion and trapping. The development of plasticity affect the local distribution of the mean stress due to incompatibility and through H-trapping, is expected to modify its distribution and related decoesion process. This effect will be analysed within the above formulation with a standard and high order description of bulk plasticity coupled to H-diffusion similarly to Sofronis and McMecking seminal article [7], with account for a maximum traction of the H-concentration. While the microstructure certainly plays a role on the local stress distribution, crack propagation is thought largely dependent on the embrittlement of ligaments along the grain boundaries. Those which do not exhibit Al_3Mg_2 precipitates are probably affected as well by traces of Mg segregation which can result in a similar weakening effect, the magnitude of which remains to be estimated, with atomistic calculations for instance. The analysis of the influence of the embrittlement with a homogenized cohesive zone derived from the results reported in Fig. 4 will be embedded along the grain boundaries in a 2D polycrystal. The aim is at investigating whether the presence of initial stresses issued for the forming process could promote failure assisted by the environment. This will be the purpose of a forthcoming work. However, the size effect on the corrosion of Al 5xxx alloys is shown to originate from the interaction of the length of cohesive process zone and that of the interface precipitates.

ACKNOWLEDGMENTS

The authors gratefully acknowledge the Agence Nationale pour la Recherche under the program 'HINTER' and the 'cluster de recherche MACODEV' of the Région Rhone Alpes, France for their financial support.

REFERENCES

1. Christodoulou L, Flower H M, "Hydrogen embrittlement and trapping in Al-6%Zn-3%Mg.", Acta Metall., Vol. 28 (1980), pp. 481-487.
2. Needleman A., "Continuum model for void nucleation by decohesion debonding", J. Appl. Mech., Vol. 54 (1987), pp. 525-531.
3. Xu X.-P., Needleman A., "Numerical Simulations of fast crack growth in brittle solids", J. Mech. Phys. Sol., Vol. 42 (1994), pp. 1397-1434.
4. Rice R.Y. "The mechanics of earthquake rupture", in: Dziewonski AM, Boschi E (eds) Physics of the earth's interior, Italian Physical Society and North-Holland, Amsterdam,The Netherlands, p 555, 1980.
5. Van der Ven A., Ceder G., "The thermodynamics of decohesion", Acta Mater., Vol. 52 (2004), pp. 1223-1235.
6. Serebrinsky S., Carter E.A., Ortiz M., "A quantum-mechanically informed continuum model of hydrogen embrittlement", J. Mech. Phys. Sol., Vol. 52, (2004), pp. 2403-2430.

7. Sofronis P., McMeeking R.M., “Numerical analysis of hydrogen transport near a blunting crack tip”, J. Mech. Phys. Sol., Vol. 37, (1989), pp. 317-350.

Effects of Hydrogen on Materials
Proceedings of the 2008 International Hydrogen Conference
Brian Somerday, Petros Sofronis, Russell Jones, editors, p 613-621
Copyright © 2009 ASM International®
All rights reserved.
www.asminternational.org

MODELING ISSUES ON HYDROGEN-INDUCED INTERGRANULAR CRACKING UNDER SUSTAINED LOAD

M. Dadfarnia, P. Sofronis
Department of Mechanical Science and Engineering, University of Illinois at Urbana-Champaign, Urbana, Illinois, USA

B. P. Somerday
Sandia National Laboratories, Livermore, California, USA

J. B. Liu, D. D. Johnson, I. M. Robertson
Department of Material Science and Engineering, University of Illinois at Urbana-Champaign, Urbana, Illinois, USA

ABSTRACT

The study of hydrogen embrittlement of materials has not as of yet led to methods that can be used to design safe and reliable hydrogen containment components in which hydrogen-induced degradation is associated with subcritical crack growth. For example, current design guidelines for pipelines only tacitly address subcritical cracking by applying arbitrary, conservative safety factors on the applied stress. In an effort to understand the mechanics of sustained-load cracking in a gaseous hydrogen environment, we investigate crack propagation in the Fe-Ni-Co superalloy IN903 for which experiments by Moody *et al*. [1] suggest that hydrogen promotes failure by intergranular cracking at pressures greater than 100MPa. In the present work, we model the hydrogen effect on grain boundary cohesion through the thermodynamic theory of Mishin *et al*. [2] which addresses transient separation accounting for the rate of hydrogen diffusion into the separating interface. We calibrate the parameters of the theory through first-principles calculations and information from the experiments and we simulate crack propagation by cohesive finite element methodology. The results reveal a number of issues related to the complexity of the failure mechanism and the robustness of the cohesive element methodology.

INTRODUCTION

Sustained-load cracking experiments are an effective means to quantify the resistance of materials to hydrogen-induced fracture. The associated threshold stress intensity factor [3] is used for the safe and reliable design of structures and components operating in the presence of hydrogen gas.

Using the wedge opening loading (WOL) IN903 specimens, Moody *et al*. [1]

observed intergranular cracking when the sample was first bolt-loaded to a stress intensity factor K_I^0=57.8MPa√m and then exposed to 207MPa hydrogen pressure associated with an equilibrium concentration on the crack surface of 6135 appm. After about 20 days of slow growth, the crack stopped and the corresponding threshold stress intensity factor was 33.5MPa√m. We attempt to simulate this experiment by modeling the hydrogen/deformation interactions upon crack propagation through a cohesive element methodology and first-principles calculation results for the grain boundary cohesion. The purpose is to identify and understand critical issues and parameters that underlie the mechanistic prediction of the threshold stress intensity in high strength systems. We note that at smaller hydrogen gas pressures the mode of failure of alloy IN903 exhibits ductile characteristics. At 20.7MPa, fracture occurred by slip banding whereas at 44.8MPa the fracture mode was mixed consisting of slip band and intergranular features. The ductile form of failure of IN903 was investigated by Dadfarnia *et al*. [4].

A large number of investigators used the cohesive element approach to study interfacial separation [5] or ductile crack propagation [6]. A brief review of the numerical analysis of crack propagation methods and their relevance to hydrogen-induced crack growth is presented by Ahn *et al*. [7] who simulated ductile crack propagation in A533B pressure vessel steel promoted by void growth and coalescence. In general, simulation of crack propagation by cohesive elements requires a traction-separation law characterized by the cohesive energy (area under the curve), maximum cohesive stress, and maximum separation distance. From these three parameters, only two are independent. Frequently, these parameters are calibrated by fitting the simulated crack propagation response to experimental data [8].

In the present work, we analyze brittle crack propagation along the grain boundaries concurrently with hydrogen diffusion in the material through both bulk lattice sites and the separating interface (grain boundary). The model allows for hydrogen solute exchange between the bulk and the interface regardless of the rate at which the interface opens up. In other words, the thermodynamic model describes the cohesive properties of the grain boundary while the interfacial solute population changes dynamically during separation. Liang and Sofronis [9] simulated decohesion assuming that the interface opens up at constant solute chemical potential.

MODEL FORMULATION

Thermodynamics of Interfacial Decohesion

We first review the thermodynamic model of Mishin *et al*. [2] for interfacial decohesion. Consider a plane interface experiencing a uniform separation δ under a normal tensile stress σ_{int} while hydrogen atoms diffuse in the created open space. The state of the interface can be characterized by the hydrogen coverage (H atom per

metal atom) $c_{\text{int}} = \theta_{\text{int}}\,\beta_{\text{int}} = C_{\text{int}} / N_{\text{int}}$, where N_{int} denotes the number of metal atoms per unit area, β_{int} the available interfacial sites per host atom, θ_{int} the occupancy of the interfacial sites, and C_{int} H atoms per area. Following Mishin *et al*. [2], the Helmholtz free energy for the interface (energy per metal atom) can be written as

$$df = \sigma / N_{\text{int}}\, d\delta + \mu_{\text{int}} dc_{\text{int}}\,, \tag{1}$$

where the chemical potential of a hydrogen atom μ_{int} in the interface is given by

$$\mu_{\text{int}} = \left(\partial f / \partial c_{\text{int}}\right)_{\delta} \tag{2}$$

and the opening stress by

$$\sigma_{\text{int}} = N_{\text{int}} \left(\partial f / \partial \delta\right)_{c_{\text{int}}}\,. \tag{3}$$

A convenient form for the free energy is

$$f(c_{\text{int}}, \delta) = \varepsilon(c_{\text{int}}) + \varphi(c_{\text{int}}, \delta) + \beta_{\text{int}} k\Theta[\theta_{\text{int}} \ln \theta_{\text{int}} + (1-\theta_{\text{int}}) \ln(1-\theta_{\text{int}})] \tag{4}$$

where $\varepsilon(c_{\text{int}})$ denotes the surface energy (completely separated interface), $\varphi(c_{\text{int}}, \delta)$ represents the cohesive energy of the interface, $k = R/N_A$ is Boltzmann's constant with R = 8.314 J/mol K being the universal gas constant and $N_A = 6.0232\times10^{23}$ atoms/mol Avogadro's number, and Θ is the absolute temperature. As a first approximation, we assume linear interpolations for the forms $\varepsilon(c_{\text{int}})$ and $\varphi(c_{\text{int}}, \delta)$, that is,

$$\varepsilon(c_{\text{int}}) = (1 - c_{\text{int}} / c_c)\varepsilon_A + (c_{\text{int}} / c_c)\varepsilon_B \tag{5}$$

$$\varphi(c_{\text{int}}, \delta) = (1 - c_{\text{int}} / c_c)\varphi_A(\delta) + (c_{\text{int}} / c_c)\varphi_B(\delta) \tag{6}$$

where $\varphi_A(\delta)$ and ε_A are respectively the cohesive energy and twice the surface energy of the pure interface (no hydrogen atoms), and $\varphi_B(\delta)$ and ε_B are the corresponding terms when the interface is fully saturated with hydrogen (θ_{int} =1) at concentration c_c. Assuming zero equilibrium separation in the absence of stress, we approximate the cohesive energies by the following quadratic functions

$$\varphi_A(\delta) = \varphi_A^0\left[4(1-q)^3 - 3(1-q)^4\right] \text{ and } \varphi_B(\delta) = \varphi_B^0\left[4(1-q)^3 - 3(1-q)^4\right], \tag{7}$$

where $q = \delta / \delta_c$ is normalized separation, δ_c is the critical separation at which the interface loses cohesion and splits into two non-interacting free surfaces, and φ_A^0 and φ_B^0 are respectively the cohesive energies of the interface with no hydrogen and fully saturated interface in the absence of stress. Substitution of Eqs. (4) through (7) into (2) and (3) yields respectively the forms for the chemical potential and the interfacial stress

$$\mu_{\text{int}} = N_A(\varepsilon_B - \varepsilon_A)/c_c + \frac{N_A\left(\varphi_B^0 - \varphi_A^0\right)}{c_c}\left[4(1-q)^3 - 3(1-q)^4\right] + R\Theta \ln \frac{c_{\text{int}}}{\beta_{\text{int}} - c_{\text{int}}}\,, \tag{8}$$

$$\sigma_{\text{int}}(c_{\text{int}}, \delta) = -\frac{12 N_{\text{int}}}{\delta_c}\left[(1 - c_{\text{int}} / c_c)\varphi_A^0 + (c_{\text{int}} / c_c)\varphi_B^0\right] q(1-q)^2\,. \tag{9}$$

In the absence of hydrogen ($c_{\text{int}} = 0$), the interfacial stress is given by

$$\sigma_{\text{int}} = -\frac{12 N_{\text{int}} \varphi_A^0}{\delta_c} q(1-q)^2 \tag{10}$$

and the reversible work of separation by

$$(2\gamma_{\text{int}})_0 = \int_0^{\delta_c} \sigma_{\text{int}}(\delta) d\,\delta = \delta_c \int_0^1 \sigma_{\text{int}}(q) dq = -N_{\text{int}} \varphi_A^0 \,. \tag{11}$$

According to the present model, the interfacial stress σ_{int} in the absence of hydrogen attains its maximum $\sigma_{\max}$, which we term *interfacial cohesive stress*, at $q = 1/3$ or $\delta = \delta_c/3$ and is given by

$$\sigma_{\max} = -\frac{16 N_{\text{int}} \varphi_A^0}{9\delta_c} = \frac{16(2\gamma_{\text{int}})_0}{9\delta_c} \,. \tag{12}$$

Introducing $\kappa = \varphi_B^0 / \varphi_A^0$ to denote the ratio of the cohesive energy of the interface in the absence of hydrogen to that under full hydrogen coverage, we may recast Eq. (9) for the interfacial stress as

$$\sigma_{\text{int}}(c_{\text{int}}, q) = \frac{27}{4} \sigma_{\max} \left[1 + (\kappa - 1) c_{\text{int}} / c_c\right] q (1-q)^2 \,. \tag{13}$$

Equation (13) for the interfacial stress provides the traction-separation law that we use to characterize the mechanical response of the interface at given hydrogen coverage c_{int}. The critical separation δ_c is calculated from (12) once the cohesive stress $\sigma_{\max}$ and reversible work of separation $(2\gamma_{\text{int}})_0$ in the absence of hydrogen are known. For the calculation of the ratio $\kappa = \varphi_B^0 / \varphi_A^0$ the cohesive energy φ_B^0 for a fully saturated interface is needed since φ_A^0 can be calculated from $(2\gamma_{\text{int}})_0$ through Eq. (11). In the following we use first-principles calculations to ascertain the magnitude of the parameters φ_A^0 and κ.

First-principles Calculations

We use first-principles calculations to determine the nature of the hydrogen effect on the cohesive property parameters. We use a model $\Sigma 3[1\,\bar{1}\,0](111)$ grain boundary in a BCC iron lattice; $N_{\text{int}} = 5.116\times10^{18}$ atoms/m^2 and $\beta_{\text{int}} = 1$. Cell calculations in the absence of hydrogen provide the formation energy per unit area of a free surface, $2\gamma_s$, and a grain boundary, γ_{gb}, relative to the perfect lattice. We then calculate the reversible work of separation in the absence of hydrogen as $(2\gamma_{\text{int}})_0 = 2\gamma_s - \gamma_{gb} = 2.598$ J/m^2 and we determine through Eq. (11) the associated interfacial cohesive energy $\varphi_A^0 = -5.078\times10^{-19}$ J/atom. Next, we calculate the changes $\Delta(2\gamma_s)$ and $\Delta\gamma_{gb}$ induced by hydrogen respectively to the surface and grain boundary energies at given hydrogen coverage c_{int}. The difference $\Delta E = \Delta(2\gamma_s) - \Delta\gamma_{gb}$ is also equal to the difference $\left(2\gamma_{\text{int}}\right)_{c_{\text{int}}} - \left(2\gamma_{\text{int}}\right)_0$, where by virtue of Eq. (13) the reversible work of separation $\left(2\gamma_{\text{int}}\right)_{c_{\text{int}}}$ at coverage c_{int} can be expressed as

$$\left(2\gamma_{\text{int}}\right)_{c_{\text{int}}} = \left(2\gamma_{\text{int}}\right)_0 \left[1 + (\kappa - 1) c_{\text{int}} / c_c\right]. \tag{14}$$

Having calculated ΔE at various values of the interfacial hydrogen coverage and using Eq. (14), we calculate the parameter $\kappa = \varphi_B^0 / \varphi_A^0$ as a function of hydrogen coverage. The results are shown in Table 1 from which we deduce that κ is approximately constant and equal to 0.87. This validates the assumption made in the

previous subsection that for small and moderate values of hydrogen coverage the interfacial cohesive energy varies almost linearly with hydrogen coverage c_{int}. Calculations show that without relaxation the behavior is clearly linear, whereas there is actually an increased decohesion effect due to the internal relaxations related to charge-density rearrangements. At large solute coverage (~1.0), the linear approximation is a ~20% low estimate.

Table 1: Ab-initio calculation of $\kappa = \varphi_B^0 / \varphi_A^0$ *for various values of the hydrogen solute coverage* θ_{int} *of a BCC* $\Sigma 3[1\,\bar{1}0](111)$ *grain boundary.*

θ_{int}	0.25	0.5	1.0
$\kappa = 1 + \dfrac{\Delta E}{\left(2\gamma_{\text{int}}\right)_{c_{\text{int}}}} \dfrac{1}{c_{\text{int}} / c_c}$	0.874	0.870	0.856

Hydrogen Transport

We consider hydrogen transport by stress-driven diffusion through normal interstitial lattice sites (NILS) in the bulk material accounting for trapping at microstructural defects. Diffusion through NILS is motivated by gradients in the chemical potential of hydrogen $\mu = \mu_0 + R\Theta \ln \theta_L - \sigma_{kk} V_H / 3$ in the host metal lattice, where μ_0 is the chemical potential in the standard state. We also consider concurrent hydrogen diffusion along the separating interface that simulates intergranular crack propagation. This mode of 1-D transport along the interface is motivated by the chemical potential μ_{int} as given by Eq. (8). As hydrogen diffuses through the separating interface and the NILS sites in the bulk, there is a continuous exchange of hydrogen atoms between the interface and the adjacent bulk NILS such that continuity of the chemical potential of hydrogen across the interface is maintained. This yields a relationship between the interfacial coverage and the NILS occupancy in the form $\theta_{\text{int}} / (1-\theta_{\text{int}}) = S_m S_q \theta_L$ where $S_m = \exp\{[\mu_0 - N_A(\varepsilon_B - \varepsilon_A)/c_c - N_A \varphi_A^0 (\kappa - 1)/c_c] / R\Theta\}$ and $S_q = \exp\{(-N_A \varphi_A^0 (\kappa - 1)/c_c\, [4(1-q)^3 - 3(1-q)^4 - 1] - \sigma_{kk} V_H / 3)/R\Theta\}$. For a non-separating interface ($q = 0$) in a stress free material $S_q = 1$, and hence reduces to $\theta_{\text{int}} / (1-\theta_{\text{int}}) = S_m \theta_L$. Thus, the parameter S_m is an equilibrium constant that can be rephrased as $S_m = \exp(W_{BI} / R\Theta)$, where $W_{BI} = 11.6$ kJ/mol [10] is the binding energy of the hydrogen solutes to the interface (grain boundary in the present case).

We solve the coupled bulk-diffusion and interfacial diffusion problems under the side constraint of chemical potential continuity across the interface as in the work of Liang and Sofronis [9]. In addition, we obtain the solution to the hydrogen transport by considering its coupling with the material deformation both in the bulk and in the form of hydrogen-induced crack propagation.

RESULTS

The material parameters used in the simulations are reported in the work of Moody *et al*. [1] and Dadfarnia *et al*. [4]. In the absence of hydrogen, the fracture toughness of IN903 is K_{IC} = 90 MPa√m. Thus for the reversible work of separation, we assume $(2\gamma_{\text{int}})_0 = K_{Ic}^2(1-\nu^2)/E$. We note that this value of 51.9kJ/m^2 is 5 orders of magnitude larger than the value furnished by the atomistic calculations for the model grain boundary. Setting the cohesive stress $\sigma_{\max} = 3.5\sigma_0$, we determine from Eq. (12) the critical interfacial separation δ_c = 24.4μm. In the simulations, we observed no crack growth when, as dictated by ab-initio simulations, we use κ = 0.87 in the traction separation law (13) along with $\varphi_A^0 = -5.078\times10^{-19}$ J/atom in the chemical potential of hydrogen (8) in the interface. Thus we determine the value of κ from Eq. (14) in which we use $(2\gamma_{\text{int}})_{c_c} = K_{th}^2(1-\nu^2)/E$ under the assumption that the interface is saturated ($c_{\text{int}} = c_c$) when the crack stops at threshold stress intensity. Thus unless otherwise specified, we use $\kappa = (33.5/90)^2 = 0.138$ in Eq. (13) to calculate the interfacial stress. In Eq. (8) for the calculation of the chemical potential of hydrogen at the interface we use $\varphi_A^0 = -5.078\times10^{-19}$ J/atom and κ = 0.138. We note that we observed no crack growth for $\kappa \geq 0.40$.

Figure 1 shows the simulation of slow crack growth for different values of the hydrogen diffusion D_{int} along the interface and $D = 1.66\times10^{-15}$ m^2/s through NILS. Independently of the value of D_{int} used in the simulations, the crack stopped at threshold stress intensity K_{th} calculated [3] about equal to 40MPa√m

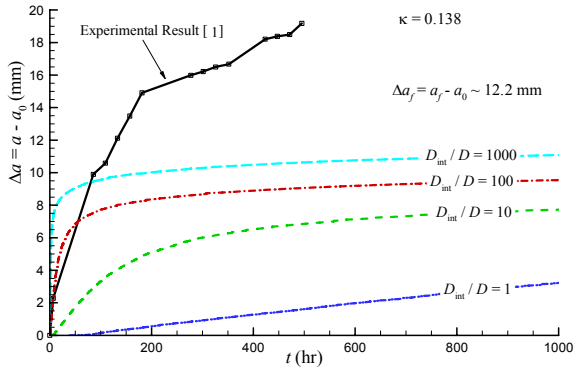


Figure 1. Crack length vs time as a function of the interfacial diffusion coefficient. The parameters a_0 and a_f are initial and final crack length and κ=0.138 denotes the ratio of cohesive energy of hydrogen-saturated interface to cohesive energy of hydrogen-free interface.

CONCLUDING DISCUSSION

Sustained-load crack propagation in the WOL specimen loaded initially at K_I^0=57.8MPa√m is taking place in the presence of a hydrogen saturated plateau ahead of the crack tip (see Fig. 2). The size of this plateau depends on the magnitude of the parameter κ and the applied load and is equal to 0.37, 0.4, 0.44, and 0.53 mm respectively for κ = 0.1, 0.138, 0.2, 0.3 at the onset of growth. This plateau can be viewed as a characteristic distance (~10 grains at the onset) of saturated hydrogen coverage for continued crack growth. Whereas it can be said that the simulations predicted the threshold stress intensity 40MPa (experimental value of 33.5MPa√m), they did not predict the associated amount of the crack growth (simulated 12.2μm vs experimental 19.17μm). Certainly this relates to the reduced sensitivity of the stress intensity factor on the crack length close to threshold. The assumed magnitude of the diffusion coefficient along the interface D_{int} affected the time at which the crack was arrested but it had no effect on the distance the crack travelled. Calculations with a different initial stress intensity factor, i.e. K_I^0=50MPa√m, yielded the same threshold value of 40MPa√m. The binding energy of the interface W_{BI} was assumed 11.6kJ/mol as calculated by Lassila and Birnbaum [10]. Simulations show that a higher value of the binding energy, e.g. 20.5kJ/mol [11], results in longer crack growth Δa (13.9μm) due to larger segregations of hydrogen in the interface.

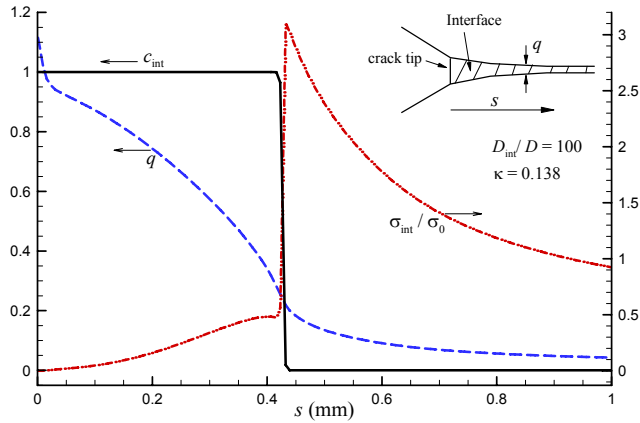


Figure 2. Profile of interfacial hydrogen concentration c_{int}, normalized separation q, and normalized stress $\sigma_{\text{int}}/\sigma_0$ upon the onset of crack propagation at time t=2600sec.

In cohesive element calculations of crack propagation, onset of crack advance occurs when the energy release rate is equal to the work of separation calculated from the traction separation law [6]. Therefore, in the IN903 system, for the crack to start at K_I = 90 MPa√m (fracture toughness of hydrogen-free material) and arrest at K_{th} = 33.5 MPa√m (in high pressure hydrogen gas) the work of separation for the cohesive elements should be reduced by hydrogen by as much as 85%, a fact not warranted by atomistic simulations under pure brittle decohesion of grain boundaries.

The magnitude of the cohesive energy of the hydrogen-free interface

$\varphi_A^0 = -(2\gamma_{\text{int}})_0 / N_{\text{int}}$ affects the diffusion of hydrogen along the interface (cf. Eq. (8)). A stronger interface is associated with a steeper transition in the interfacial hydrogen profile from the saturated plateau (Fig. 2). More importantly, the use of a different work of separation for the evaluation of the chemical potential from that used in calibrating the traction-separation law for the mechanical response needs to be resolved.

ACKNOWLEDGMENTS

Support from the U.S. Department of Energy under Grant GO15045 and the National Science Foundation under Grant DMR 0302470 is gratefully acknowledged.

REFERENCES

1. Moody, N. R., Perra, M. W. and Robinson, S. L., "Hydrogen Pressure and Crack Tip Stress Effects on Slow Crack Growth Thresholds in an Iron-Based Supperalloy," *Scr Metall*, Vol. 22, No. 8 (1988) pp. 1261-1266.
2. Mishin, Y., Sofronis, P. and Bassani, J. L., "Thermodynamic and Kinetic Aspects of Interfacial Decohesion," *Acta Mater*, Vol. 50, No. 14 (2002) pp. 3609-3622.
3. *Annual Book of ASTM Standards*, Standard Test Method for Determining Threshold Stress Intensity Factor for Environmentally-Assisted Cracking of Metallic Materials, ASTM E 1681-03, ASTM International, West Conshohocken, (2007) PA 19328.
4. Dadfarnia, M., Somerday, B. P., Sofronis, P. and Moody, N. R., "A Combined Materials Science/Applied Mechanics Approach Toward Understanding the Role of Microstructure in Hydrogen Embrittlement of Materials," in *Int Hydrogen Energy Development Forum*, Fukuoka, Japan, (2007) pp. 58-67.
5. Needleman, A., "A Continuum Model for Void Nucleation by Inclusion Debonding," *J Appl Mech*, Vol. 54, No. 3 (1987) pp. 525-531.
6. Tvergaard, V. and Hutchinson, J. W., "The Relation Between Crack Growth Resistance and Fracture Process Parameters in Elasto-Plastic Solids," *J Mech Phys Solids*, Vol. 40, No. 6 (1992) pp. 1377-1397.
7. Ahn, D. C., Sofronis, P. and Dodds, R., "Modeling of Hydrogen-Assisted Ductile Crack Propagation in Metals and Alloys," *Int J Fract*, Vol. 145, No. 2 (2007) pp. 135-157.
8. Scheider, I., Pfuff, M., and Dietzel, W., "Simulation of Hydrogen Aassisted Stress Corrosion Cracking Using the Cohesive Model," *Eng Fract Mech*, Vol. 75, No. 15 (2008), pp. 4283-4291.
9. Liang, Y. and Sofronis, P., "Micromechanics and Numerical Modeling of the Hydrogen-Particle-Matrix Interactions in Nickel-Base Alloys," *Model Simul Mater Sci Eng*, Vol. 11, No. 4 (2003) pp. 523-551.

10. Lassila, D. H. and Birnbaum, H. K., “The Effect of Diffusive Segregation on the Fracture of Hydrogen Charged Nickel,” *Acta Metall*, Vol. 36, No. 10 (1988) pp. 2821-2825.
11. Lee, S-M. and Lee, J-Y., “The Trapping and Transport Phenomena of Hydrogen in Nickel,” *Metall Trans A*, Vol. 17, No. 2 (1986) pp. 181-187.

Effects of Hydrogen on Materials
Proceedings of the 2008 International Hydrogen Conference
Brian Somerday, Petros Sofronis, Russell Jones, editors, p 622-631
Copyright © 2009 ASM International®
All rights reserved.
www.asminternational.org

HYDROGEN INDUCED STRESS CRACKING IN 25% CR DUPLEX STAINLESS STEEL SIMULATED BY COHESIVE ZONE MODELLING

Vigdis Olden, Erling Østby
SINTEF, Dept. of Applied Mechanics and Corrosion, Trondheim, Norway
Christian Thaulow, Roy Johnsen
NTNU, Dept. of Engineering Design and Materials, Trondheim, Norway

INTRODUCTION

Hydrogen embrittlement, in short HE is the most general term used for cracking influenced by hydrogen. The traditional definition of HE is that it requires the presence of hydrogen, stress and a sensitive microstructure to occur. This is the case also for HISC. However the HISC term is more frequently applied within the oil and gas community on hydrogen induced failures occurring subsea.

One of the main challenges is to link the micromechanical and diffusion processes present in the fracture process zone, with the global behavior of the component or structure. The two best established micromechanical models describing hydrogen embrittlement are the hydrogen enhanced decohesion HEDE [1-3] and the hydrogen enhanced local plasticity HELP [4 - 6] models. HEDE is based on the hypothesis that interstitial hydrogen lowers the cohesive strength by dilatation of the atomic lattice and thereby lowering the fracture energy. This implies that hydrogen decreases the energy barrier for either grain boundary or cleavage plane decohesion. HELP is characterized by atomic hydrogen that enhances the mobility of dislocations through an elastic shielding effect in preferred crystallographic planes at the crack tip causing locally reduced shear strength.

In recent years the cohesive zone modelling (CZM) approach has gained interest in finite element modelling of hydrogen induced fracture. The relevant constitutive "material" response is a traction-separation description; an evaluation which gives the amount of energy required to create new surfaces. A traction separation law (TSL) is a function described by the cohesive stress (σ) and separation (δ). The area below the curve represents the critical separation energy, Γ_c. A frequently used TSL is the polynomial function proposed for fracture in ductile materials first introduced by Needleman in 1987 [7] and further developed by Tvergaard [8]:

$$\sigma(\delta) = \frac{27}{4}\sigma_c \frac{\delta}{\delta_c}\left(1-\frac{\delta}{\delta_c}\right)^2 \quad for\ \delta < \delta_c,\ otherwise\ \ 0 \tag{1}$$

σ_c denotes the critical cohesive stress, δ_c the critical opening of the cohesive element. The separation energy for the polynomial description is calculated from

$\Gamma_c = \frac{9}{16}\sigma_c \delta_c$. The stress intensity factor K_I can be calculated by $K_I = \left[\frac{E \cdot \Gamma_c}{1-\nu^2}\right]^{1/2}$,

where E is the Young's modulus and ν is Poisson's rate. The stress intensity factor is strictly valid for a linear elastic material only, which implies that for an elastic plastic material K_I only can account for the separation energy and not for any plastic work. Note also that the present work considers the mode I plain strain opening case and that the influence of variations in stress triaxiality around the crack tip is not evaluated. K_{HISC} is the threshold value below which HISC induced cracking will not occur or be sub critically slow.

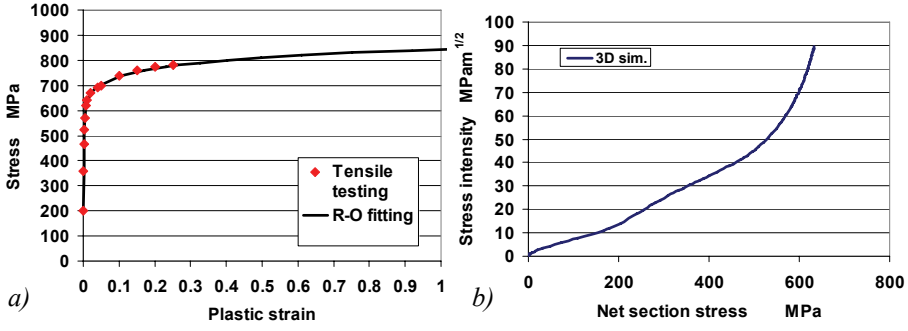
DESCRIPTION OF THE MODEL

The applied model consists of a three step FE simulation procedure including elastic-plastic stress analysis, diffusion analysis and finally elastic-plastic stress analysis with hydrogen influenced cohesive elements implemented in the crack path. The applied FE code is ABAQUS Standard 6.5 [10].

Elastic plastic stress analyses

2D elastic plastic stress analysis is performed using the standard Mises material model with a material specific stress-strain curve for the duplex stainless steel. A Ramberg-Osgood power law fitting to the tensile test results gave best fit for a hardening exponent of n=17. Fig. 1a and Table 1 give the mechanical properties and input parameters for the FE analyses.

Fig. *1*b show the applied stress intensity as a function of net section stress retrieved by a 3D FE analyses of a SENT[1] specimen using this material description. The resulting stress field at each applied stress level is given as an initial condition to the diffusion analysis.



[1] Single Edge Notch Tesile

Fig. 1 Material properties and applied stress intensity a) Tensile test results and R-O fitted stress strain curve b) Stress intensity as a function of applied net section stress.

Table 1 Material properties and input for the elastic plastic stress analyses

Yield stress, σ_y MPa	Young's mod. E MPa	Poisson's rate, ν	Applied stress MPa
600	200 000	0.3	400 – 540

Diffusion analysis

Stress driven diffusion given in ABAQUS is represented by a modified Fick's law with respect to the hydrostatic stress. The applied diffusion coefficient is $3.7 \cdot 10^{-12}$ m^2/s based on data from diffusion measurements on duplex stainless steel reported by Zackroczymski and Owczarek [12]. According to Sofronis and McMeeking [13] and Krom and Bakker [14] there is a competition for the hydrogen between the hydrostatic stress field and the highly strained area at the notch tip. Their models are based on the principle by Oriani [2] that populations of hydrogen in trapping sites and in lattice always are in equilibrium. Fick's law including both the effect of hydrostatic pressure, p, and trapping due to plastic strain ε_p is given as:

$$\frac{C_L + C_T(1-\theta_T)}{C_L}\frac{\partial C_L}{\partial t} = \nabla \cdot (D_L \nabla C_L) - \nabla \cdot \left(\frac{D_L C_L V_H}{R\left(T - T^Z\right)} \nabla p \right) - \theta_T \frac{dN_T}{d\varepsilon_p}\frac{\partial \varepsilon_p}{\partial t} \qquad (2)$$

C_L and C_T is the hydrogen concentration in lattice and traps, D is the diffusion coefficient, $\overline{V}_H$ is the partial molar volume of hydrogen in iron-based alloys, R the gas constant (8.3142 J/mol K), N_T is the number of trapping sites, T the actual and T^Z the absolute zero temperature.

In the present work an approach based on the work by Taha & Sofronis [15] is used. Their work revealed shape similarity between the plastic strain distribution and the hydrogen concentration profile in traps in front of a crack tip when exposed to surface hydrogen. Based on [15] we propose a linear correlation between the trapped hydrogen concentration and the plastic strain:

$$C_T = (49.0 \cdot \varepsilon_p + 0.1) \cdot C_L \qquad (3)$$

The relation implies that when the plastic strain is larger than ~ 2%, trapping will yield the dominating influence on the hydrogen concentration. The correlation is implemented in a user defined cohesive element subroutine adding the plastic strain (trapped) hydrogen contribution to the lattice concentration. By reading the plastic strain in the neighbouring continuum elements C_T is calculated and added to C_L for each increment and node before giving the total hydrogen concentration C to the

TSL. Fig. 2 shows the simulated hydrogen distribution in front of the crack tip after 200 and 5000 hours with and without the influence of trapping due to plastic strain at an applied stress of 400 MPa. Trapping due to plastic strain is the main "driving force" acting on the hydrogen concentration close to the crack tip at all stress levels included in this study.

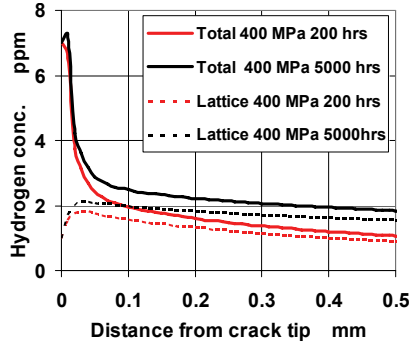


Fig. 2 Distribution of hydrogen concentration in front of the crack tip after 200 and 5000 hours at 400 MPa. Continuous lines are the total H conc., C_T; dotted lines are the lattice H conc., C_L , without the influence of trapping due to plastic strain,.

Hydrogen influenced traction separation law

A polynomial TSL is chosen based on previous research [11]. A relation for the coupling between hydrogen coverage, θ, and the local critical hydrogen dependent cohesive stress, σ_c (θ) for bcc Fe proposed by Serebrinsky et al. [9] is applied:

$$\frac{\sigma_c(\theta)}{\sigma_c(0)} = 1 - 1.0467\theta + 0.1687\theta^2 \qquad (4)$$

where $\sigma_c(0)$ is the local critical cohesive stress without hydrogen influence. The relation is based on a fitting of surface energy values reported in [16]. The applied cohesive stress of $\sigma_c(0) = 3.7 \cdot \sigma_y$ is in line with suggestions in [19] using $4 \cdot \sigma_y$ as the critical cohesive stress in a polynomial TSL without hydrogen influence. A plot of the cohesive law with hydrogen influence according to Eq. 4 is shown in Fig. 3.

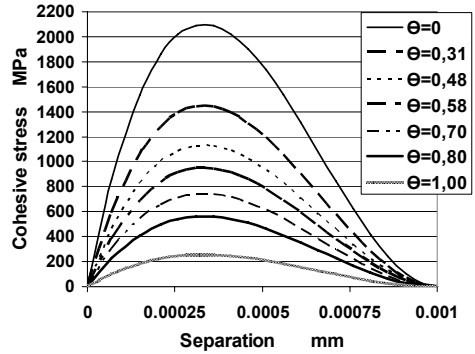


Fig. 3 Hydrogen influenced cohesive law.

Hydrogen coverage is defined as a function of the hydrogen concentration and the Gibbs free energy difference Δg_b^0 between the interface and the surrounding material as expressed in the Langmuir-McLean isotherm [17]. Crack initiation is defined as zero cohesive stress and critical opening (δ_c) in the first cohesive element. The continuum elements are a four node bilinear plain strain type. Due to symmetry only half of the sample is modelled. The element size along the symmetry axis, which also is the crack path, is 10 µm. A sharp notch represents the fatigue crack tip. Note that the critical event in the simulations is collapse of the first cohesive element. The user defined cohesive elements are implemented in ABAQUS Standard using a FORTRAN sub-routine [18]. Fig. 4 a-b gives an overview and a detail view of the elements in the notch tip area.

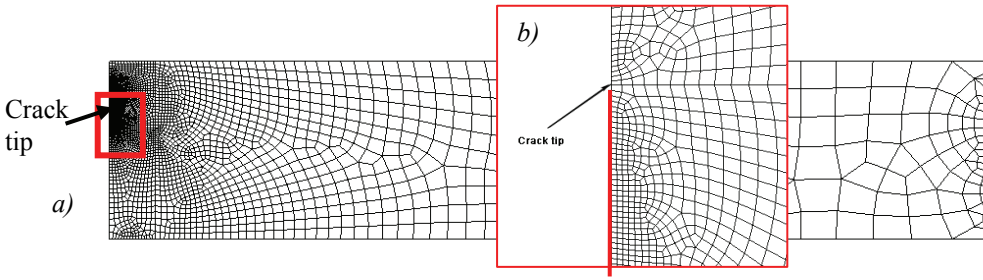


Fig. 4 FE model a) overview b) close up of the crack tip area. The location of the cohesive elements along the symmetry axis is indicated with a red line.

EXPERIMENTS

The material is a forged 25% Cr duplex stainless steel pipe with an outer diameter of 273 mm and a wall thickness of 21.44 mm. Chemical composition in weight % is C: 0.016, Si: 0.23, Mn: 0.79, P: 0.021, S: 0.001, Cr: 25.0, Ni: 6.98, Mo: 3.82, Cu: 0.32. Ferrite content according to ASTM E562 is 46% and the average austenite spacing is 13µm. Rectangular 9 mm x12 mm SENT specimens were machined

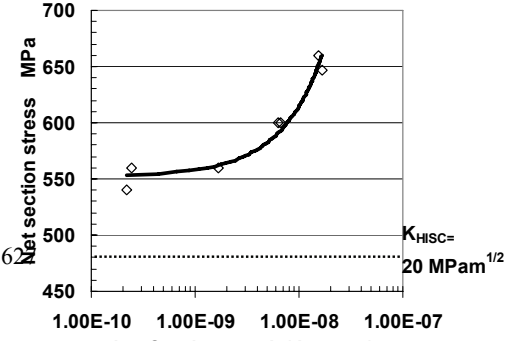
parallel with the length axis of the pipe. A 2 mm deep notch was prepared by a combination of spark erosion (1 mm) and fatigue cracking (1mm). The specimens were submerged in circulating artificial sea water at 4°C with a cathodic protection potential of -1050 mV_{SCE} and applied net section constant load tensile stresses between 540 and 660 MPa. Net section stress and CMOD[2] were recorded. A sharp rise in CMOD marked the onset of final unstable fracture (stage III crack growth). Duration of stable crack growth (stage II) was taken as the linear part of the CMOD curve. Two samples were unloaded during stage II crack growth and taken out of the test rig.

Comparison with laboratory experiments

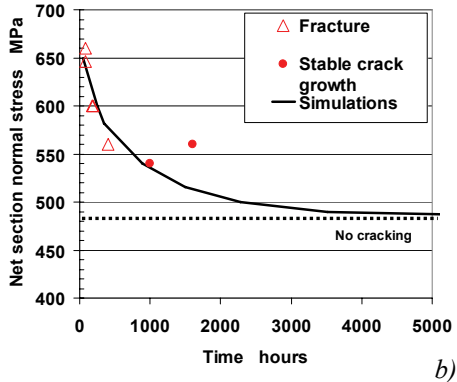
In the cohesive FE analysis best fit to the laboratory results was obtained for the cohesive parameters: $\sigma_c(0)$= 2200 MPa (~3.7 times the yield strength) and δ_c=0.005 mm, see line in Fig. 5 a. Red triangles represent the laboratory results (duration of crack initiation + stage II crack growth); filled circles denote samples unloaded during stage II crack growth. The suggested cohesive parameters are a result of a fitting procedure varying the maximum stress between 3.5 and 4 times the yield strength [19]. The suggested critical separation value was obtained by varying δ_c between 0.1 – 0.5 times the cohesive element size, Δ. Also according to [19], the value of 0.1 times Δ was chosen as the starting point for the procedure.

Without the effect of hydrogen the applied cohesive parameters yield a threshold stress intensity factor of K_0 = 117 MPa$\sqrt{m}$. Maximum hydrogen concentration at a net section stress of 480 MPa is 7 ppm representing a hydrogen coverage of θ= 0.76, which according to Eq. 4 gives a critical hydrogen influenced cohesive stress of 660 MPa and hence a K_{HISC} value of 20 MPa$\sqrt{m}$. The simulated results indicate that fracture will not occur below a net section stress level of 480 MPa (80% of the yield stress).

As previously reported [11] the simulated fracture initiates in the surface element and not at the location of the maximum stress, which is consistent with the high hydrogen content close to the surface. The total cohesive fracture process zone r is roughly 0.25mm. The ratio between the fracture process zone and the element size r/Δ gives an indication of how well the mesh resolves the stresses and strains. In our model r/Δ = 25, which according to [19, 21] gives a satisfactory resolution of the local stress and strain field.



[2] Crack Mouth Opening Displacement



a) b)

Fig. 5 Results a) SENT test results compared with FE simulations. b) Crack propagation rate plotted as a function of net section stress.

The dominating fracture mode in the stable crack propagation area is trans-granular cleavage in ferrite with ductile tearing of austenite, which is typical HISC fracture topography in duplex stainless steel. The lengths of the stage II cracks were measured with an optical microscope. Hydrogen induced crack lengths, measured at the mid section of the samples, ranged from 0.8 mm to 3.9 mm. By dividing the crack length with the stage II crack propagation time, crack propagation rates da/dt between ~$2.2 \cdot 10^{-10}$ m/s to $1.5 \cdot 10^{-8}$ m/s were obtained; see Fig 5 b.

DISCUSSION

The applied cohesive stress of $\sigma_c(0) = 3.7 \cdot \sigma_y$ is in line with suggestions by Tvergaard and Hutchinson [19] using $4 \cdot \sigma_y$ as the critical cohesive stress in polynomial TSL without hydrogen influence. Later Serebrinsky et al. [9] applied the same level of critical stress in linear hydrogen influenced TSL's and found good agreement with fracture threshold stresses for high strength steel in aqueous solutions.

According to the simulations the stress intensity for the 25%Cr duplex stainless steel below which cracking will not occur is $K_{HISC} = 20$ MPa$\sqrt{m}$ at a net section stress of 480 MPa. Lee and Gangloff [21] reported a threshold stress value of 9.3 MPa$\sqrt{m}$ in high strength steel. This was martensitic steel with yield strength above 1700 MPa, which implies higher sensitivity to HISC than in our duplex steel. A threshold value of about 25 MPa$\sqrt{m}$ for steel with 1600 MPa yield strength is reported in [9].

Crack rates in these experiments vary from about $2.2 \cdot 10^{-10}$ m/s for the lowest stress up to $1.5 \cdot 10^{-8}$ m/s for the highest stresses. Lee and Gangloff [21] suggested a subcritical crack growth rate of $2.5 \cdot 10^{-10}$ m/s for martensitic stainless steel, which is in fact very similar to the slowest crack growth rate in the present study. For hydrogen assisted cracking there is a close relationship between the hydrogen diffusion rate and the crack propagation rate. A diffusion coefficient of $3.7 \cdot 10^{-12}$

m^2/s as applied in the FE analyses represents a lattice diffusion rate of about of $1 \cdot 10^{-9}$ m/s as calculated by Crank's thick plate solution [22], which is within the range of the measured crack growth rates.

The proposed cohesive parameters in this work are not meant to reproduce the actual micro-mechanisms but rather to be a representation of the onset of failure at the different stress levels and the presence of H. Reading off the total H concentration as a function of stress and plastic strain into the TSL, represents a simplified procedure of taking the effect of trapping into account. To be able to reproduce discontinuous HISC cracking in the cohesive elements an iterative coupling between both the stress and strain field surrounding the cohesive zone and the diffusion analyses is required.

CONCLUSIONS

Constant load SENT testing at applied stresses of 450-550 MPa of not precharged 25%Cr duplex stainless steel in 3.5% NaCl at 4°C and a corrosion protection potential of -1050 mV_{SCE} revealed hydrogen induced stress cracking prior to final fracture.

The stable crack growth rates ranged from $2.2 \cdot 10^{-10}$ m/s to $1.5 \cdot 10^{-8}$ m/s which is consistent with the hydrogen diffusion rate.

For prediction of crack initiation a finite element simulation procedure with hydrogen dependant cohesive elements in the crack path was carried out. Best fit to experimental results was obtained for an initial critical cohesive stress of 2200 MPa ($\sigma_c = 3.7 \cdot \sigma_y$) and a separation ($\delta_C$) of 0.005 mm. The simulations indicate a lower bound applied net section stress of 480 MPa giving a threshold stress intensity factor (K_{HISC}) of 20 MPa$\sqrt{m}$.

In the simulations both lattice and trapped hydrogen contributes to a lowering of the stress necessary for the onset of fracture. A direct relation between plastic strain and trapped hydrogen concentration is implemented. The relation implies that compared to stress driven lattice diffusion plastic strain is the main contributor to the simulated hydrogen concentration and crack initiation in the fracture process zone.

REFERENCES

1. Troiano, A.R., The role of hydrogen and other interstitials in the mechanical behaviour of metals , Transactions of the ASM, Vol. 52, 1960, p. 54-80
2. Oriani, R.A., The diffusion and trapping of hydrogen in steel, Acta Metall. 18, 1970, p. 147-157.

3. Gerberich, W.W et al., Hydrogen induced cracking mechanism-are there critical experiments? , Hydrogen Effects in Materials, The Minerals, Metals & Materials Society, 1996, p. 539-551
4. Birnbaum, H.K., Sofronis, P., Hydrogen-enhanced localized plasticity-a mechanism for hydrogen-related fracture, Mater. Sci. and Eng., A176, 1994, p. 191-202
5. Delafosse, D. and Magnin, T.: Hydrogen induced plasticity in stress corrosion cracking of engineering systems, Engng Fracture Mech. 68, 2001, p. 693-729.
6. Robertson, I.M.: The effect of hydrogen on dislocation dynamics , Engng Fracture Mech. 68, 2001, p. 671-692
7. Needleman, A., A Continuum Model for Void Nucleation by Inclusion Debonding, Jrnl of Applied Mech., Vol. 54, 1987, p. 525-531.
8. Tvergaard, V., Effect of fiber debonding in a whisker-reinforced metal, Mater. Sci. and Engng A, Vol. 125 (2), 1990, p. 203-213
9. Serebrinsky et. al., A quantum-mechanically informed continuum model of hydrogen embrittlement, Jrnl of the Mech. and Phys. of Solids, 52, 2004, p. 2403-2430
10. ABAQUS, Version 6.5, Users' manual, ABAQUS Inc. 2004
11. Olden, V. et al.: Application of hydrogen influenced cohesive laws in the prediction of hydrogen induced stress cracking in 25%Cr duplex stainless steel , Engng Fracture Mech., 75 (8), 2008, p. 2333-2351
12. Zakroczymski, T., Owzcarek, E., Electrochemical investigation of hydrogen absorption in a duplex stainless steel , Acta Materialia, 50, 2002, p. 2701-2713
13. Sofronis, P., McMeeking, R. M., Numerical analysis of hydrogen transport near a blunting crack tip, Jrnl of the Mech. and Phys. of Solids 37 (3), 1989, p. 317-350
14. Krom, A.H.M. , Koers, R.W.J., Bakker, A., Hydrogen transport near a blunting crack tip , Jrnl of the Mech. and Phys. of Solids, 47, 1999, p. 971-992
15. Taha, A., Sofronis, P., A micromechanics approach to the study of hydrogen transport and embrittlement , Engng Fracture Mech. 68, 2001, p. 803-837
16. Jiang , D.E., Carter, E.A., First principles assessment of ideal fracture energies of materials with mobile impurities: implications for hydrogen embrittlement of metals , Acta Materialia 52, 2004, p. 4801-4807
17. Hondros, E. D., Seah, M. P. , The theory of Grain Boundary Segregation in Terms of Surface Adsorption Analogues, Metallurgical Trans. A, Vol 8A, 1977, p. 1363-1371
18. Scheider, I., Cohesive model for crack propagation analyses of structures with elastic-plastic material behaviour, GKSS internal report no WMS/2000/19.
19. Tvergaard, V., Hutchinson, J.W., The relation between crack growth resistance and fracture process parameters in elastic-plastic solids , Jrnl of Mech. Phys. and Solids, 40 (6), 1992, p. 1377-1397
20. Camacho, G.T., Ortiz, M., Computational modelling of impact damage in brittle materials, Intern. Jrnl of Solids and Structures, 33, 20-22, 1996, p. 2899-2938

21. Lee, Y., Gangloff, R.P., Measurement and Modelling of Hydrogen Environment-Assisted Cracking of Ultra-High-Strength Steel, Metallurg. and Mater. Trans. A, 38A, 2007, p. 2174-2190
22. Crank, J., The Mathematics of Diffusion, 2nd Ed., Oxford University Press, 1975

Effects of Hydrogen on Materials
Proceedings of the 2008 International Hydrogen Conference
Brian Somerday, Petros Sofronis, Russell Jones, editors, p 632-639
Copyright © 2009 ASM International®
All rights reserved.
www.asminternational.org

FIRST-PRINCIPLES PREDICTION OF HYDRIDE PHASE STABILITY AND THE THERMODYNAMICS OF DECOHESION

Anton Van der Ven, Qingchuan Xu, Jishnu Bhattacharya
Department of Materials Science and Engineering
The University of Michigan,
Ann Arbor, MI, 48109

ABSTRACT
Unlike most impurities, hydrogen atoms exhibit high mobilities in the solid state, allowing a stressed solid to equilibrate rapidly. This can dramatically affect mechanical properties at the atomic scale, including the traction curve for cleavage along crystallographic planes. Here, factors that affect hydride phase stability at finite temperature and anisotropic stress states are described, with a focus on the Ti-H system. Furthermore, a thermodynamic formalism is reviewed that enables a first-principles prediction of traction curves for decohesion at constant hydrogen chemical potential, reflecting conditions in which hydrogen locally equilibrates along the decohesion zone.

INTRODUCTION
The coupling between mechanics and chemistry in the solid state is probably most pronounced in the presence of hydrogen. As an interstitial element in crystalline solids, dissolved hydrogen has a high mobility, allowing it to rapidly redistribute in response to changes in mechanical loading. The accumulation of hydrogen at, grain boundaries, internal defects or regions of high stress intensity can lead to important modifications in local mechanical properties. Furthermore, many metals and alloys are susceptible to hydride formation, resulting in qualitative changes in mechanical properties. Anisotropic states of stress commonly encountered in the solid state, either due to external loading or during solid-state hydride nucleation and growth, will in turn alter chemical equilibrium. First-principles electronic structure methods based on density functional theory (DFT) [1] have proven invaluable in elucidating and predicting a wide variety of fundamental properties of crystalline solids containing hydrogen, including electronic structure [2,3],relative stability [4,5,6,7], mechanical properties [8,9,10] as well as energy barriers for interstitial diffusion [11,12,13]. However, the output of DFT calculations correspond to zero Kelvin predictions. Hydride formation and hydrogen embrittlement occur at finite temperature where thermal excitations and entropy play a crucial role. It is here that statistical mechanics must be invoked to link first-principles total energy calculations with macroscopic thermodynamic potentials. The Helmholtz free energy F of a solid is formally related to the partition function Q according to $F=-k_BT\ln Q$ (k_B is Boltzmann's constant) with

$$Q = \sum_s \exp\left(\frac{-E_s}{k_B T}\right) \quad (1)$$

The sum extends over all excited states, s, of the solid having energy E_s. The energies E_s are quantities that can be calculated from first principles. For solids containing hydrogen, the excited states, s, that contribute most to the free energy include (i) configurational excitations associated with different arrangements of hydrogen atoms and (ii) vibrational excitations. Electronic excitations contribute as well, but are usually of less importance.

Here we give an overview of how hydride phase stability can be predicted from first principles at finite temperature and under different loading conditions. We also describe a thermodynamic formalism to predict traction curves for decohesion accounting for variable hydrogen concentration between decohering planes as a function of separation at constant hydrogen chemical potential [9,10].

METHODOLOGY

Density functional theory within its common approximations (e.g. local density approximation, LDA, or generalized gradient approximation, GGA) provides a computationally tractable approach to calculate the total energy of any arrangement of atoms from first principles. These methods can be used to predict mechanical properties at constant composition, including traction curves for decohesion and elastic moduli, as these are first and second derivatives respectively of the total energy with respect to dimensional changes of the crystal. Figure 1(a) for example illustrates the energy calculated with DFT as an hcp Ti crystal is rigidly separated across a pair of close-packed (0001) planes (the energies were calculated with *VASP* using the projector augmented wave method [14,15,16]). The traction curve for decohesion is then simply the derivative of the energy versus separation and is plotted in Fig. 1(b). (Traction curves can also be extracted from DFT calculations that incorporate full atomic relaxation as explained in ref [9]) DFT methods allow us to predict the energies, E_s, of vibrational and configurational excitations appearing in the partition function Eq. 1. Due to computational limitations, though, it is not possible to

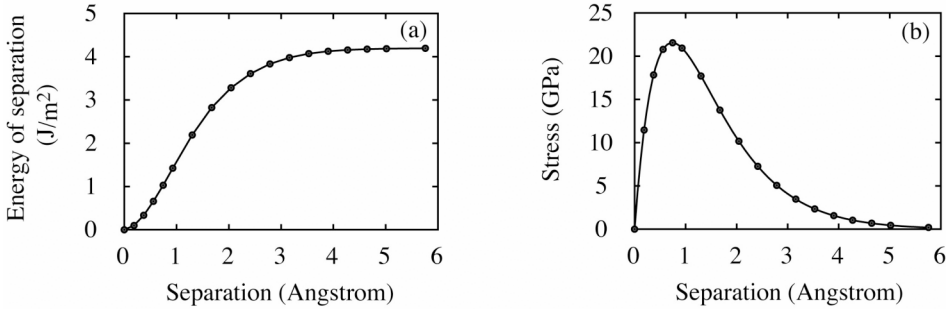


Figure 1: (a) The energy as a function of distance as two rigid slabs of Ti are separated across close packed (0001) atomic planes. (b) The traction curve for decohesion obtained as the derivative of the plot in figure (a).

calculate the energy of all excited states with DFT, as there are simply too many. Hence it is necessary to use effective Hamiltonians that are parameterized with a limited number of DFT calculations but that can accurately extrapolate the energy to all other relevant excitations. We can distinguish between two well-established effective Hamiltonians, (i) the cluster expansion to account for configurational degrees of freedom [17] and (ii) lattice dynamical Hamiltonians to describe vibrational excitations [18,6]. Solids that dissolve hydrogen interstitially exhibit configurational degrees of freedom associated with all possible ways of distributing hydrogen atoms over the interstitial sites of the crystal. A mathematical representation of a particular hydrogen arrangement over the interstitial sites of a crystal is possible with the introduction of occupation variables σ_i assigned to each interstitial site *i*, which is +1 if hydrogen occupies the site and -1 if the site is vacant. A vector of occupation variables $\vec{\sigma} = \{\sigma_1,...,\sigma_i,...,\sigma_N\}$ then uniquely characterizes the arrangement of hydrogen over *N* interstitial sites. Furthermore, it is possible to expand the dependence of the configurational energy as a sum of polynomials of the occupation variables according to [17].

$$E(\vec{\sigma}) = V_o + \sum_i V_i \sigma_i + \sum_{i,j} V_{ij} \sigma_i \sigma_j + \sum_{i,j,k} V_{ijk} \sigma_i \sigma_j \sigma_k + ... \qquad (2)$$

where the indices *i,j,k*, correspond to collections of interstitial sites that form point, pair, triplet etc. clusters, while the coefficients V_o, V_{ij}, and V_{ijk} are constants determined by fitting the energy expression Eq. (2) to explicit DFT calculations of a subset of hydrogen configurations over the interstitial sites of the solid. A cluster expansion is ideal to be used in Monte Carlo simulations to calculate thermodynamic properties of the solid at finite temperature [5].

While vibrational degrees of freedom are often neglected in first-principles studies of phase stability, they become important in hydrogen containing solids, as hydrogen atoms are very light. The vibrational free energy can be determined with first-principles predictions of the phonon density of states [19]. When anharmonic contributions are important, as they typically are to rationalize structural phase transformations, it is necessary to resort to Monte Carlo simulations applied to effective Hamiltonians expressed in terms of relevant vibrational degrees of freedom [18,6].

HYDRIDE PHASE STABILITY: THE TI-H SYSTEM

As an example we consider the Ti-H system, which exhibits a variety of stable hydrides with some degree of off-stoichiometry [20] and in the case of TiH_2, a susceptibility to a structural phase transformation from cubic symmetry at high temperature to tetragonal symmetry at low temperature [21]. Pure Ti is stable in the hcp crystal structure (α-Ti) below 1150 K. However, the hydrogen atoms in $\gamma-TiH$ and $\delta-TiH_2$ order over the tetrahedral interstitial sites of an fcc Ti sublattice. An analysis of low temperature hydride phase stability in Ti-H, therefore, requires a consideration of hcp and fcc Ti with interstitial hydrogen occupancy [5].

Figure 2(a) illustrates free energies at 300K as a function of hydrogen concentration. The free energies of fcc Ti and the fcc-based hydrides, γ and δ, were calculated with Monte Carlo simulations applied to a cluster expansion of the configurational energy of hydrogen over interstitial sites of fcc Ti while the free energy of α–Ti (hcp) was calculated within a mean field approximation [5]. Consistent with experiment, Fig. 2(a) shows that α–Ti has a lower free energy than fcc Ti for dilute hydrogen concentrations. For higher hydrogen concentrations, Fig. 2(a) shows that δ–TiH_2 is thermodynamically stable over a large hydrogen concentration interval: the hydride can tolerate a large concentration of vacancies over the tetrahedral sites, introducing an important degree of configurational entropy. As is evident from Fig. 2(a), an intermediate hydride, γ–TiH, is predicted to be metastable [22,5].

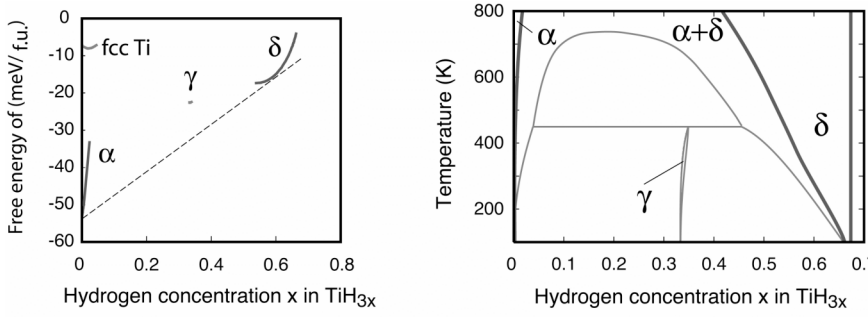


Figure 2: (a) Calculated free energies at 300 K as a function of hydrogen concentration in Ti. (b) Calculated stable (thick lines) and metastable (thin lines, only fcc based phases) phase diagram in the Ti-H system.

Free energy curves as illustrated in Fig. 2(a) allow us to construct an equilibrium phase diagram that maps stable phases as a function of temperature and hydrogen concentration. This is illustrated in Fig. 2(b) for the Ti-H system, where the solid thick lines represent the equilibrium phase diagram and the thin lines denote metastable phase stability by considering only fcc-Ti and its hydrides γ-TiH and δ-TiH_2. Bcc Ti, which forms at high temperature, was not considered in the construction of this phase diagram. The Monte Carlo simulations also provide insight about site occupancy, showing that hydrogen prefers octahedral sites at dilute concentrations and tetrahedral sites at high hydrogen concentrations [5].

The δ–TiH_2 phase not only exhibits configurational disorder due to hydrogen vacancies, but also undergoes a structural phase transition to a tetragonal distortion upon cooling [21]. While this transformation could have its origin in electronic structure changes with temperature, as explored in ref [3,4], a recent study [6] showed that it can also be explained in terms of the excitation of anharmonic vibrational degrees of freedom. First-principles total energy calculations with DFT predict that cubic TiH_2 is mechanically unstable with respect to tetragonal distortions, raising fundamental questions about the true nature of the high temperature cubic

form of TiH_2. Monte Carlo simulations applied to an anharmonic lattice dynamical Hamiltonian of TiH_2, parameterized by DFT calculations, predict a tetragonal to cubic phase transformation upon heating, as illustrated in Fig. 3, where the high temperature cubic phase is in fact only cubic on average, undergoing anharmonic local fluctuations [6].

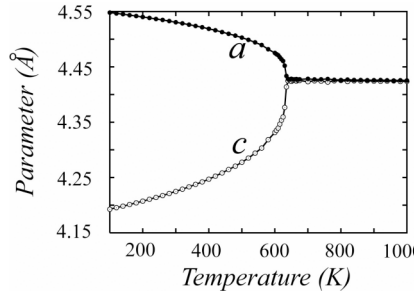


Figure 3: Predicted *a* and *c* lattice parameters as a function of temperature for TiH_2.

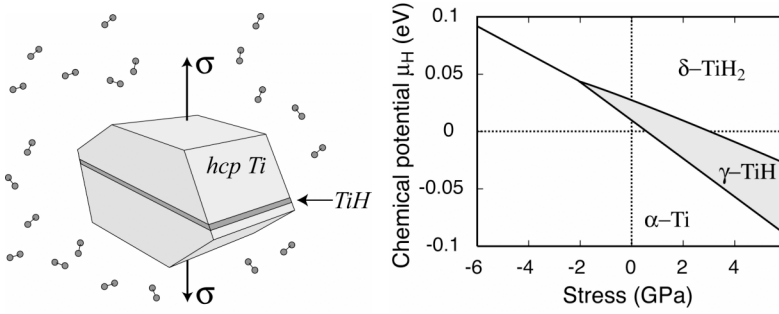
While γ–TiH is predicted to be metastable in Fig. 2(a), it is nevertheless observed experimentally during early stages of hydride nucleation in α–Ti [20]. The appearance of γ–TiH during the early stages of hydride formation can be explained by an increase of its thermodynamic stability relative to α–Ti and δ–TiH_2 under an anisotropic state of stress that emerges during hydride nucleation. Phase stability depicted in Fig. 2(b) was calculated assuming hydrostatic pressure. However, during solid-state phase transformations, nucleating phases often form coherently within the matrix phase, which due to anisotropic transformation strains can be accompanied by large and anisotropic states of stress across the nucleating phase. The γ–TiH precipitates are experimentally observed to form coherently as thin plates within α–Ti with $(1\bar{1}0)$ planes of the fcc Ti-sublattice of γ–TiH parallel to the $(0\bar{1}10)$ hcp planes of α–Ti. During the early stage of plate nucleation, the dimensions in the $(1\bar{1}0)$ plane of γ–TiH are fixed by the equilibrium dimensions of the α–Ti host in the $(0\bar{1}10)$ plane. Perpendicular to the interface between γ–TiH and α–Ti, the precipitate and matrix are free to relax, with γ–TiH likely under compressive stress as its nucleation is accompanied by a volume expansion.

The analysis of phase stability under an anisotropic stress state requires the minimization of an appropriate thermodynamic potential consistent with the thermodynamic boundary conditions that exist at the early stages of hydride formation. Often hydride formation in metals occurs in a hydrogen rich environment characterized by a constant hydrogen partial pressure P_H, which determines the hydrogen chemical potential μ_H. Furthermore, for the experimentally observed plate-like precipitates, the lateral dimensions of the hydride in the $(1\bar{1}0)$ plane of the Ti fcc sublattice and those of the hcp matrix of α-Ti in the $(0\bar{1}10)$ plane are fixed. On the other hand, the dimension perpendicular to the precipitate-matrix interface is not fixed, rather its conjugate stress, σ, is an experimentally controlled variable. For these boundary conditions, the relevant characteristic potential to be minimized is a grand force potentia

$$\Phi = E - TS - \mu_H N_H - \sigma V_o \varepsilon \qquad (3)$$

where S is the entropy, ε is the strain perpendicular to the hydride-matrix interface and V_o is a reference volume (same for each phase) relative to which the stress, σ, and the strain, ε, are defined.

Fig. 4(b) illustrates a calculated phase diagram by minimizing the grand force potential, Φ, assuming the above thermodynamic boundary conditions [5]. As is clear, coherency strains that are present during early hydride formation render γ–TiH stable relative to α–Ti and δ–TiH_2 at intermediate hydrogen chemical potentials, even under compressive stresses, which are likely to prevail during hydride formation. The reference state for μ_H in Fig. 4(b) corresponds to the equilibrium $\alpha \rightarrow \delta$ transformation chemical potential under hydrostatic pressure. The phase diagram of Fig. 4(b) was calculated at zero Kelvin and the phase bounds will shift at finite temperature. Nevertheless, the diagram illustrates how varying boundary conditions in the solid state can alter relative phase stability to select out phases that are not stable under hydrostatic pressure.



(a) (b)

Figure 4: (a) δ–TiH hydrides are observed to form as coherent plates within hcp Ti grains at constant hydrogen partial pressure (which fixes μ_H). (b) Coherent phase diagram as a function of hydrogen chemical potential and stress.

TRACTION CURVES AND HYDROGEN

The presence of hydrogen in a solid will locally modify mechanical properties, reducing for example its resistance to decohesion [22]. The concentration of a deforming solid is not always locally constant, especially when mobile species such as hydrogen are present. The binding energy for hydrogen atoms to interstitial sites of a decohering region changes as the interstitial site is deformed. This leads to a different equilibrium hydrogen concentration in regions that are deformed. If decohesion occurs slowly, the hydrogen concentration between decohering planes can equilibrate, leading to a uniform hydrogen chemical potential, μ_H, throughout the solid. The relevant thermodynamic boundary condition to be imposed on a cohesive zone, defined loosely as the region between decohering atomic planes, is a constant hydrogen chemical potential as opposed to a constant hydrogen concentration.

DFT calculations of traction curves for decohesion are performed at constant concentration. A statistical mechanical treatment is therefore necessary to predict traction curves at constant temperature and hydrogen chemical potential [9,10]. Here

again a cluster expansion can be used to describe the energy of the cohesive zone as a function of hydrogen arrangement between separating atomic planes. However, since the hydrogen binding energy to those sites and the interactions among hydrogen atoms depend on the distance between separating atomic planes, δ, the coefficients of the cluster expansion, V_{ijk}, are also a function of δ. By implementing the cluster expansion in Monte Carlo or a mean field approximation, it is possible to calculate thermodynamic potentials, such as a grand force potential for the cohesive zone, Eq. (3), from which phase stability during decohesion, traction curves and hydrogen concentrations can be derived [9,10].

As an example, Fig. 5(a) illustrates the hydrogen concentration at constant hydrogen chemical potential μ_H in the tetrahedral sites between decohering (111) planes of fcc Al as a function of the degree of separation δ. For small separations, δ, the hydrogen concentration is negligible, but increases rapidly in a narrow interval of intermediate separation and then saturates. The rapid change in hydrogen concentration between separating planes at constant μ_H affects the traction curve for decohesion considerably. Fig. 5(b) illustrates the traction curve at constant μ_H superimposed on constant composition traction curves. At constant μ_H, the maximum stress for decohesion is reduced slightly. However, above a critical hydrogen chemical potential, the shape of the traction curve changes due to a stress induced phase transformation

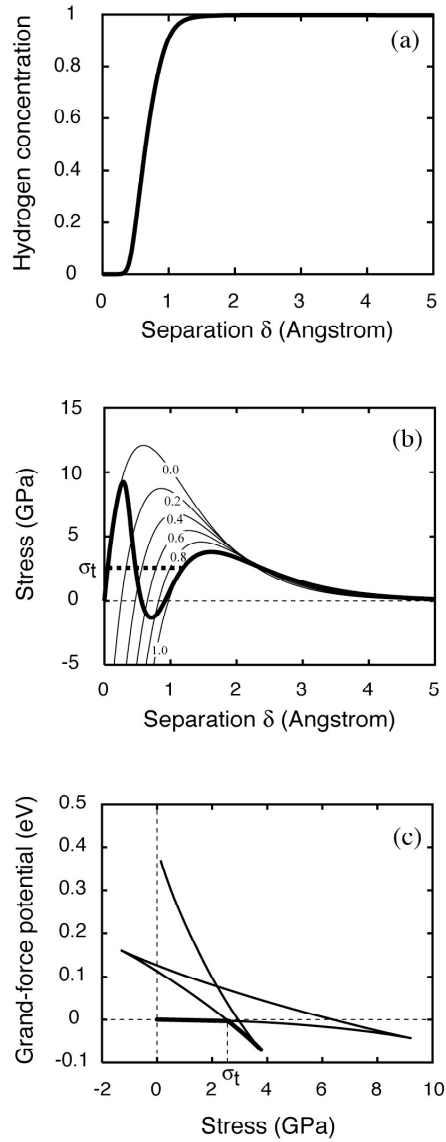


Figure 5: (a) Hydrogen concentration between docohering (111) planes of fcc Al at constant μ_H. (b) Traction curves at different hydrogen concentrations (thin lines) and at constant μ_H (think line). (c) Grand force potential as a function of stress. A first order phase transformation occurs at stress σ_t.

[10]. The equilibrium state at constant σ and μ_H is determined by a minimum of the grand force potential, illustrated in Fig. 5(c) as a function of σ. The crossing of two branches of the grand-force potential at the stress σ_t indicates a phase transition. On a traction curve plot, this phase transformation corresponds to a discontinuous jump in separation δ (accompanied by a discontinuous jump in hydrogen concentration) at constant stress σ_t, as illustrated by the dashed line in Fig. 5(c). The phase transformation at σ_t allows the cohesive zone to bypass the first branch of the constant μ_H traction curve with a high stress for decohesion by transforming to a fully saturated state characterized by a low stress for decohesion [9,10].

CONCLUSIONS

We have described how finite temperature phase stability and traction curves for decohesion of solids in the presence of hydrogen can be calculated by combining first-principles DFT calculations with statistical mechanics methods.

REFERENCES

1. R. G. Parr, W. T. Yang, "Density-Functional Theory of Atoms and Molecules", Oxford University Press, (1989).
2. H. Smithson, D. Morgan, C. Marianetti, A. Van der Ven, A. Predith, G. Ceder, Phys. Rev. B 66, 144107 (2002).
3. M. Gupta, Solid State Communications, 29, 47 (1979).
4. A. Van der Ven, D. Morgan, Y. S. Meng, G. Ceder, J. Electrochem. Soc., 153, A210 (2006).
5. Qingchuan Xu, A. Van der Ven, Phys. Rev. B 76, 064207 (2007).
6. J. Bhattacharya, A. Van der Ven, Acta Materialia, 56, 4226-4232 (2008).
7. V. Ozolins, E. H. Majzoub, C. Wolverton, Phys. Rev. Lett. **100**, 135501 (2008).
8. G. Lu, Q. Zhang, N. Kioussis, E. Kaxiras, Phys. Rev. Lett. **87**, 096601 (2001).
9. A. Van der Ven, G. Ceder, Acta Materialia, 52(5),1223 (2004).
10. A. Van der Ven, G. Ceder, Phys. Rev. B, Rapid communications 67,060101 (2003).
11. D. E. Jiang, E. A. Carter, Phys. Rev. B **70**, 064102 (2004).
12. C. Wolverton, V. Ozolins, M. Asta, Phys. Rev. B **69**, 144109 (2004).
13. A. Van der Ven, J. C. Thomas, Q. C. Xu, B. Swoboda, D. Morgan, Phys. Rev. B 78, 104306 (2008).
14. G. Kresse, J. Furthmuller, Phys. Rev. B **54**, 11169 (1996).
15. P. E. Blochl, Phys. Rev. B **50**, 17953 (1994).
16. G. Kresse, D. Joubert, Phys. Rev. B **59**, 1758 (1999).
17. J. M. Sanchez, F. Ducastelle, D. Gratias, Physica A, **128**, 334 (1984).
18. W. Zhong, D. Vanderbilt, K. M. Rabe, Phys. Rev. Lett. **73**, 1861 (1994).
19. A. van de Walle, G. Ceder, Rev. Mod. Phys. **74**, 11 (2002).
20. H. Numakura, M. Koiwa, Acta Metal. **32**, 1799 (1984).
21. H. L. Yakel, Acta Crystallographica, 11, 46 (1958).
22. J. R. Rice, J. S. Wang, Materials Science and Engineering A, **107**, 23 (1989).

Effects of Hydrogen on Materials
Proceedings of the 2008 International Hydrogen Conference
Brian Somerday, Petros Sofronis, Russell Jones, editors, p 640-646
Copyright © 2009 ASM International®
All rights reserved.
www.asminternational.org

MODELING THE PLASTIC ZONE AHEAD OF A CRACK BY TWO DIMENSIONAL DISCRETE DISLOCATION DYNAMICS

D. Tanguy, D. Delafosse and M. Razafindrazaka
CNRS, UMR 5146, Ecole des Mines,
158 cours Fauriel, 42023 Saint-Etienne (France)

ABSTRACT

We present a detailed analysis of the kinetic of the formation of a plastic zone ahead of a crack tip, modeled by discrete dislocation dynamics (in two dimensions). The effect of crack tip emission is emphasized by comparing the average shielding (local stress intensity factor) and the microstructure obtained with and without a dislocation source aligned with the crack tip. The results are averaged over multiple runs in order to obtain significant differences which overcome the dependence on source distribution. It is found that crack tip emission creates a pile up which major role is to shield more efficiently the tip. We conclude on the necessity to consider emission from the tip when simulating ductile solids like fcc crystals.

INTRODUCTION

Modeling crack propagation, assisted by environmental effects (hydrogen embrittlement, oxidation, liquid metal embrittlement or irradiation induced segregations), in ductile crystals like fcc relies on two aspects: the loss of cohesion of the structure at or ahead of the crack tip, and the modeling of the plastic zone which tends to shield the crack from the external load. The first task requires a detailed representation of the atomic arrangement of the atoms (metals and impurity solutes) in the vicinity of the crack tip and can be, in a first approach, treated like a theoretical brittle problem , i.e. by intentionally forbidding any plastic activity during the fracture simulation [1]. The second task can be treated within the framework of discrete dislocation dynamics [2,3], at the scale of the first grain ahead of the tip. This paper is devoted to the second aspect, with a special attention in analyzing which ingredients should be considered in the model to obtain the best ductility (shielding), as fcc crystals are of primary interest. More specifically, the influence of dislocation emission from the tip on the microstructure is quantified. The paper is organized as follows: first the simulation set up is briefly reviewed; second, two representative simulations are detailed: with and without emission from the tip. We will show the crucial role played by the pile up formed ahead of the crack, in the case

of a ductile orientation. Third, the results are summarized and future developments are presented.

SIMULATION SET UP

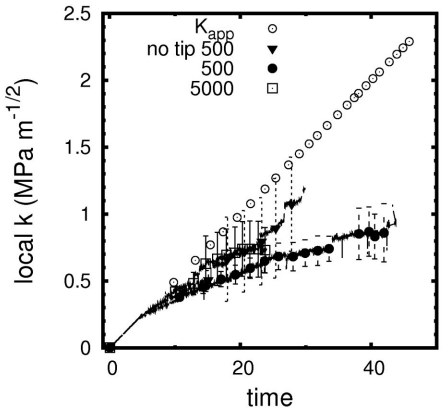


Figure 1: Time evolution of the applied stress intensity factor K_{app}, the local stress intensity factor k_{local} with and without emission from the tip. The error bars represent the dispersion on results due to the sensitivity to the distribution of sources in the system.

The computation domain is a disc of 10 µm radius (Fig. 2 and 3) which borders are impenetrable to dislocations (dislocations are stored at the boundaries). An impenetrable interface lies along the X axis (Fig. 2 i). The crack tip is at (0,0). The crack is semi infinite, coming from X<0. The vector of the plastic deformation are dislocation loops which are represented, in this 2D model, by edge dislocation dipoles. Franck-Read sources are modeled by point sources, which emit a dipole if the resolved shear stress exceeds a critical value, for a sufficient long time. The Peach and Koehler (P&K) forces are computed on each dislocation via the stress tensor obtained by Lin and Thomson [4] by the method of complex potentials, for a semi-infinite crack. These stresses incorporate: the external, applied, load characterized by the stress intensity factor K_{app}, the ``image forces" due to the crack dislocation interactions and the interactions between dislocations. These are moved according to the law $dx/dt = \alpha f$, where x is the position of the dislocation along the glide plane and f is the projection of the P&K force. No cross slip is allowed. A set of local rules are added to take into account some dislocation reactions: the interaction with obstacles and the formation of junctions [5]. Annihilation is allowed. Prior to testing this model to investigate crack tip plasticity, it was tested in traction without cracks. The stress/strain curve and the dislocation microstructure were monitored [5]. The density of sources and obstacles are adjusted to obtain a

homogeneous distribution of dislocations and a plastic hardening on the traction curve.

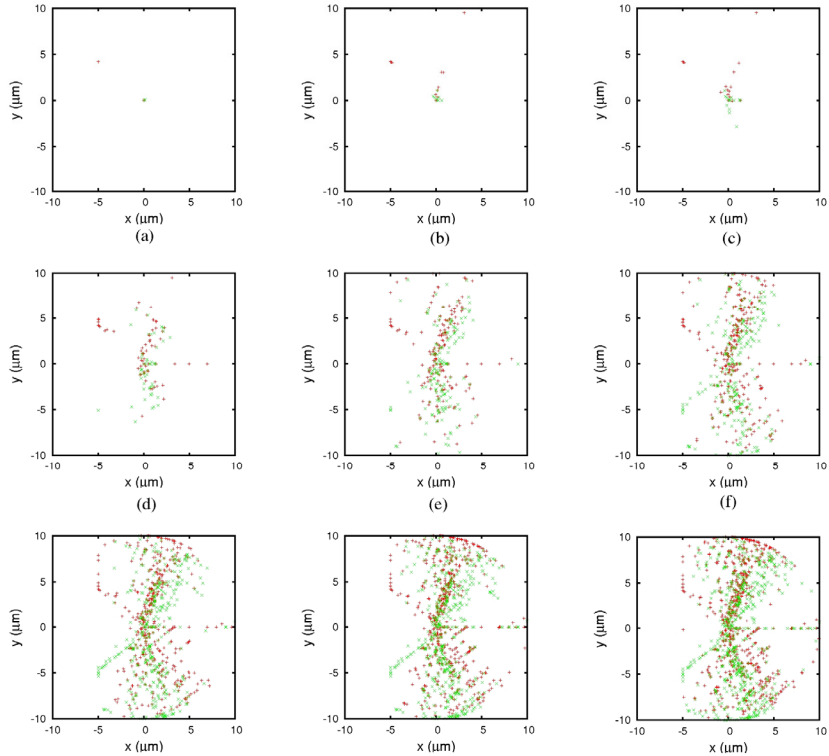


Figure 2: Dislocation configurations obtained without emission from the tip, for load levels: (a) 0.25MPa $m^{1/2}$ (b) (c) (d) 0.65MPa $m^{1/2}$ (e) 0.9MPa $m^{1/2}$ (f) 1.MPa $m^{1/2}$ (g) 1.2MPa $m^{1/2}$ (h) 1.3MPa $m^{1/2}$ (i) 1.5MPa $m^{1/2}$.

In the case of the crack, the central quantity is the local stress intensity factor [4,6]. The theory of crack-dislocation interaction shows that a dislocation induces a stress singularity at the tip, of the same shape as the one induced by the external load. By superposition, the stress intensity factor in the presence of a collection of dislocations is $k=K_{app}-\sum_i k_i$, where the sum is over all dislocations in the system.

When k_i is positive (resp. negative), the dislocation is said to be of shielding character (resp. anti-shielding) in the sense that it decreases (resp. increases) the load on the crack tip. As a first approach, we consider that a semi-brittle crack starts propagating when the local k reaches the critical value given by the Griffith criterion [1].

In the following, we measure k as the applied load is increased and the plastic zone develops. The focus is on the influence of crack tip emission.

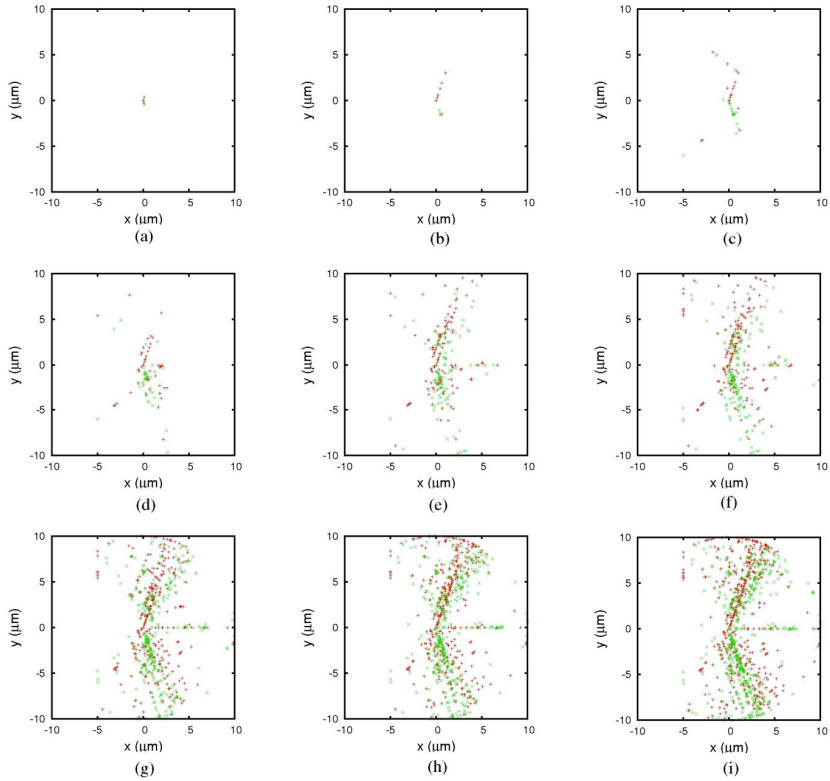


Figure 3: Dislocation configurations obtained with emission ``from the tip'', for load levels: (a) 0.25MPa $m^{1/2}$, (b) 0.4MPa $m^{1/2}$, (c) 0.48MPa $m^{1/2}$, (d) 0.6MPa $m^{1/2}$, (e) 0.75MPa $m^{1/2}$, (f) 0.9MPa $m^{1/2}$, (g) 1MPa $m^{1/2}$, (h) 1.2MPa $m^{1/2}$, (i) 1.3MPa $m^{1/2}$.

COMPARING SHIELDING AND MICROSTRUCTURES WITH AND WITHOUT CRACK TIP EMISSION

Figure 1 shows the time evolution of the applied K (K_{app}) and the local k when no emission from the tip is allowed (label ``no tip 500'') and when it is allowed (label ``500''). The numbers 500 and 5000 refer to different obstacle densities (5000 being 10 times denser than 500), but this effect will not be discussed here. Crack tip emission is modeled , as a first approach, by putting a dislocation source at 100nm

from the tip on the glide plane which intersects the tip. This gives a low critical load for dislocation emission, of the order of 0.25MPa $m^{1/2} \approx 0.2\ k_{IG}$ (k_{IG} is the critical Griffith load for theoretical brittle fracture. In the material chosen here, 316L stainless steel, $k_{IG} \approx 0.9$MPa $m^{1/2}$). This is a very crude model, especially because it imposes a large dislocation free zone, of 200nm, which is certainly overestimated, with the consequence that the brittle character of the model is emphasized. From Fig. 1, the shielding is significantly less efficient when no tip emission is allowed. In the following, we present snapshots taken from two characteristic simulations. From them, we will analyze the reason why the shielding is less efficient and why the dispersion (error bars on Fig. 1) is so large.

In both cases, the orientation of the glide planes is θ=70.75. We can show, by considering the elastic field of the crack tip, that this orientation is the one where the resolved shear stress in the glide plane intersecting the tip is the highest: meaning that the projection of the stress along this direction is high and the location of the highest shear stress in the simulation domain is close to the line θ=70.75 which intersects the tip. On both cases (Fig. 2i and Fig. 3i), the dislocation density shows two wide bands at $\approx$ +/- 70, which is coherent with the analysis above, based on elasticity (no dislocations). The main difference in microstructure is the presence of a dense pile up (Fig. 3 b and i) at θ=+70.75. No pile ups form in the case where dislocation emission from the tip is not forced. The importance of the pile up is quantified in Fig. 4. The two top graphs (Fig. 4a and b) show k_{local} as a function of a radius r. For each value of r, only the contribution from the dislocations closer than r from the tip are accounted for in the calculation of k(r). The two bottom graphs show the same information but only taking into account the dislocations of the shear bands. A ``band'' is the region of the domain which includes the tip, is oriented at θ=70.75 and has a width of 500nm when dislocation emission is forbidden. The width is only 50nm otherwise, i.e. only the contribution of the dislocations in the pile up is considered (Fig. 4d). The different curves on the same graph correspond to the snapshots in Fig. 2 and Fig. 3. It is striking to see, by comparing Fig. 4c and d, that almost no net shielding is obtained from the shear band when no pile up is present. Comparing Fig. 4b and d, we can conclude that the pile up is responsible for 1/3 of the total shielding, which is a large proportion (100 dislocations are contained in the pile up, when more than 1000 in total are contained is the system).

In most of the curves in Fig. 4a and b, there is a discontinuity at $r=0^+$. It arises from the dislocations (shielding or anti-shielding) stored at the interface, ahead of the tip. Those closer to the tip have a strong influence on the shielding because $k_i \propto r_i^{-1/2}$ where r_i is the distance from dislocation i to the tip. For example, the upper curve on Fig. 4b corresponds to $K_{app}=k(0)=1.3$MPa $m^{1/2}$, whereas the value at r=50nm is 1.5MPa $m^{1/2}$. This is due to anti-shielding dislocations storage at the interface, close to the tip. We have performed multiple runs and found that there is no preferential localization of secondary slip, i.e. dislocations are stored homogeneously along the interface, on average. On a single run, as those of Fig. 2 and 3, dislocations are always localized in a few slip planes. This involves large fluctuations in k(r) from

one run to the other (obstacle and source distribution are changed, keeping the densities constants). This effect is more pronounced when no pile up forms ahead of the tip, which leads to large error bars on Fig. 1. Nevertheless, it has to be stressed again that the sequences of configurations that we present in this paper a representative of the differences observed between simulations with and without emission from the tip.

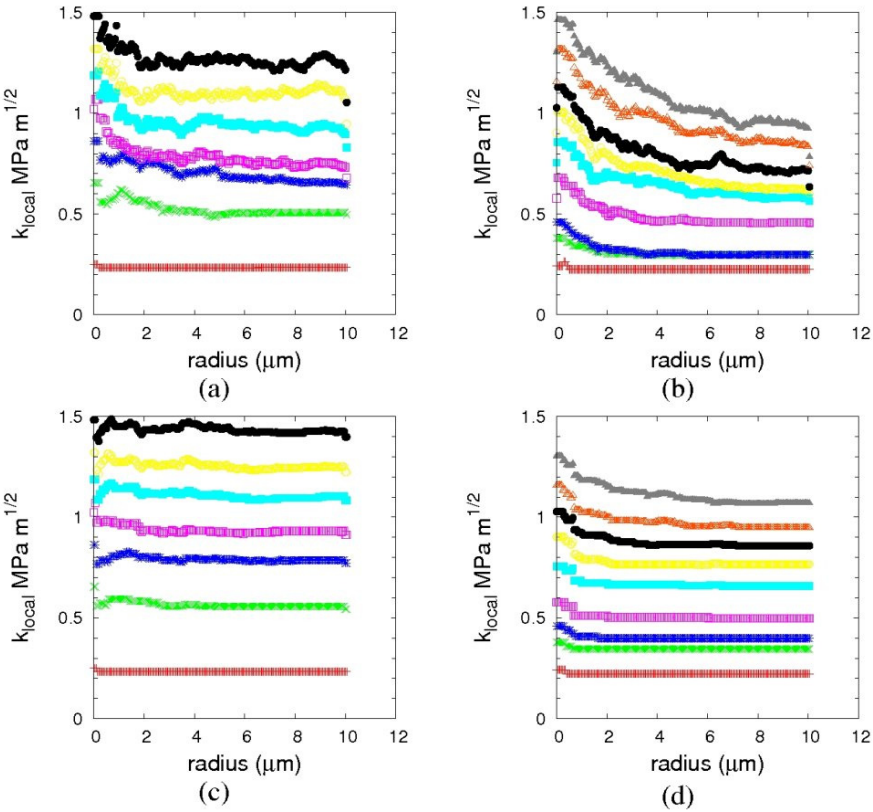


Figure 4: Shielding produced by the configurations shown on Fig. 2 (a: local k, c: local k produced by the dislocations in a band 500nm wide centered on the glide plane intersecting the tip) for a typical simulation without emission ``from the tip'' and Fig. 3 (b: local k, d: local k produced by the dislocations of the pile up, i.e. only the dislocations belonging to the glide intersecting the tip are considered), with emission ``from the tip''.

CONCLUSION

We have shown quantitatively that crack tip dislocation emission is an essential feature of the simulation of ductile crack orientations, like {111}<112> in fcc. Improvements of the emission model, in particular in the definition of a realistic dislocation free zone are currently being investigated by atomistic simuulations, in the continuity of the work presented in [6].

[1] D. Tanguy, in Hydrogen 2008 proceedings.
[2] S. G. Roberts, in Multiscale Phenomena in Plasticity, edited by J. Lépinoux, D. Mazière, V. Pontikis, and G. Saada (Kluwer Academic Press, Netherlands, 2000), p. 349.
[3] V. Deshpande, A. Needleman, and E. V. D. Giessen, acta mater. 51, 1 (2003).
[4] I. H. Lin and R. Thomson, Acta Metall. 34, 187 (1986).
[5] M. Razafindrazaka, D. Tanguy, and D. Delafosse, submitted to Mat. Sci. Eng. A (2009).
[6] D. Tanguy, M. Razafindrazaka, and D. Delafosse, acta mater. 56, 2441 (2008).

Effects of Hydrogen on Materials
Proceedings of the 2008 International Hydrogen Conference
Brian Somerday, Petros Sofronis, Russell Jones, editors, p 647-654
Copyright © 2009 ASM International®
All rights reserved.
www.asminternational.org

MULTI-SCALE SIMULATION OF CRACK TIP SHIELDING: CONSTRAINED MOLECULAR DYNAMICS AND ELASTIC CALCULATIONS

D. Tanguy
CNRS, UMR 5146, Ecole des Mines de Saint-Etienne, 158 cours Fauriel, Fr-42023 Saint-Etienne, France

ABSTRACT

This paper presents, in a synthetic way, a first approach to a multi-scale simulation of semi-brittle crack propagation in crystalline solids. It involves the derivation of new equations of motion for molecular dynamics (MD) which provide a precise control over dislocation activity (nucleation and mobility) at the atomic scale. The transfer of the fracture information from atomistics towards mesoscopic models of fracture, which include the plastic zone, is made by a single scalar k which characterizes the mechanical load ``felt'' by the crack. By monitoring the events occurring at the tip in a series of quenched molecular dynamics simulations at increasing levels of k, critical k values can be found: $k_{Ic}$ for cleavage propagation, $k_{Ie}$ for dislocation emission and $k_{Iv}$ for ``vacancy injection''. As the procedure used to measure k is made coherent with continuum elasticity, the critical k can be injected in simulations at a higher scale, in particular in discrete dislocation dynamics simulations (DDD). To demonstrate this, we study the simple case of a sharp crack in a single crystal. Two twin problems are treated in parallel: a nanoscale flaw in an MD box and a semi-infinite crack in an infinite elastic continuous medium, both in the presence of a shielding dislocation, in 2D, and loaded at the same k. An excellent agreement is obtained once a full dislocation is emitted from the tip, whereas a large discrepancy is observed when only the first partial is emitted. As a consequence, the concept of ``local k'' i.e. an effective stress intensity factor which incorporates the influence of the dislocation configuration, is valid and can be used as a boundary condition in the atomistic calculation that do not need to incorporate explicitly dislocations. Finally, the ingredients of DDD are recalled to show, in practice, how the critical k values from MD can be used.

INTRODUCTION

Crack propagation does not occur in ductile crystals (austenitic stainless steels, aluminum and nickel based alloys...) under tensile load. They fail, after a large, irreversible, deformation by coalescence of voids and intense, localized, plastic shear. On the contrary, when degradation from the environment occurs (irradiation, H embrittlement, liquid metal embrittlement...), a crack might nucleate at the

surface and propagate through the crystal, either because of embrittlement by adsorption at the tip or by absorption and segregation at defects ahead of the tip, like interfaces . Another important class of solids is those which exhibit a brittle to ductile transition (BDT), like body centered cubic crystals (ferritic steels, β titanium...) or silicon. In this case, the response of the material to an external load is largely dominated either by dislocation mobility or multiplication. At low temperature, thermal activation is not efficient enough to enable dislocation movement and the system relaxes its elastic energy by propagating a crack. At high temperature, dislocations are emitted and arrange in such a way as to release the elastic energy. The transition between these two behaviors is usually not sharp [1], at a definite temperature (T_c), when the system contains enough built in dislocations that can act as sources. It means that within a temperature window around T_c, these materials could also develop brittle cracks in a noticeably ductile matrix. Therefore, both problems (environment degradation, including H embrittlement, and BDT) rely on the same basic situation: a loaded crack tip in interaction with a collection of dislocations.

Our approach of the simulation of this situation is somewhat ``radical'' in the sense that we believe that crack-dislocation interactions should be modeled at a mesoscale, using elasticity theory (and, if possible, discrete dislocations), whereas crack tip phenomena should be treated at the atomic scale by MD. It means that dislocation nucleation during crack propagation should be forbidden in MD simulations (blunting can be taken into account), except when dealing the specific problem of emission from the tip. This is because MD box are not large enough and the time scales are too short to handle the formation of a dislocation microstructure. To achieve this decoupling, we derive equations of motion which incorporate a constraint in order to control dislocation activity (nucleation and mobility) in MD simulations. These are used only to measure some quantities characteristic of the fracture process at the tip that can be transferred to higher scales, as shown below.

The connection between atomistics and the mesoscale (from the nm to 10 μm, in 2D) relies on the powerful results of the continuum theory of cracks. Linear elasticity and complex analysis provide analytical solutions for the stress fields valid in all space, in the presence of dislocations [2] (in 2D). The first major result is the universal shape of the asymptotic fields close to the tip:

$$\sigma_{zz} = \frac{k}{\sqrt{2\pi r}} f(\theta) \qquad (1)$$

where the dependence on the remote load, boundary shapes, crack length are all included in the single scalar k called the stress intensity factor. For example, for a flaw of length 2a, in an infinite medium, loaded by a stress τ: $k = \sigma\sqrt{\pi a}$. When dislocations are present, k depends on the configuration i.e. on the set of dislocation positions, but Eq. 1 is still valid. In this case, k is referred to as the ``local k'' and the applied load as $K_{applied}$ [2]. $K_{applied}$ is the stress intensity factor that the crack would undergo from the remote load if there were no dislocations. The crack is said to be ``shielded'' if $k<K_{applied}$. The second important result is the connection with the

elastic energy release rate G (the variation of the stored elastic energy with the crack length): $G=k^2/E'$, where E' is an elastic constant. For a perfect brittle crack propagation, where the shape of the crack remains self-similar, the Griffith energy balance provides a fracture criterion: $2\gamma_S=G=k^2/E'$, where $2\gamma_S$ is the excess energy of the newly created surfaces. In the same spirit, we perform intensive quenched molecular dynamics simulations at increasing levels of load, measure k and detect the critical k values for the elementary processes at the tip: k_{Ic} for cleavage, k_{Ie} for dislocation emission, k_{Iv} for nucleation of vacancies... If the ``local k'' concept holds, these values could be incorporated in mesoscale simulations.

In this paper, we recall the derivation of the equations for constrained molecular dynamics (CMD) and apply them: first in a system containing a crack alone, getting access to numerical values for k_{Ic}, k_{Ie} and k_{Iv}; second, in the case where a single dislocation interacts with a crack. The constraints are applied at increasing distances from the crack tip where the dislocation is pinned. The stress calculation at the atomic scale shows how much shielding is provided by the dislocation as a function of its distance to the tip, which, compared to the elastic solution, provides a test of the local k concept. Finally, we briefly expose the principle of a discrete dislocation dynamics (DDD) simulation, just to give a first example of how the critical k can be used at the mesoscale. All the details concerning the different methods can be found in [3-5]. Here, the emphasis is on making the link between them.

CONSTRAINED MOLECULAR DYNAMICS

In order to control the dislocation activity, the local shear (the non elastic perturbation of the environment left along the glide plane by the displacement of the defect) has to be measured by an order parameter. We use a centrosymmetry parameter CS_i, inspired by [6]:

$$CS_i = \sum_j \vec{q}_j - \vec{q}_i + \vec{q}_{j+6} - \vec{q}_i \cdot \vec{b} \qquad (2)$$

where i is the label of the particle where the local shear is evaluated and j is the label of its first neighbors, in the undeformed structure. The vectors $\vec{q}$ are the positions of the particles. The labels j and j+6 refer to a pair of opposite first neighbors in the undeformed structure of a centrosymmetric crystal, like fcc. Finally, the vectorial sum over all the pairs is projected on the glide direction $\vec{b}$. $\vec{b}$ is known a priori, from crystallography (for example, the 12 Shockley partial orientations in fcc). This order parameter is very close to zero when the structure is only elastically deformed and takes a large value, close to mb^2 when a dislocation of Burgers vector b has sheared its local environment. m is the number of first neighbor pairs which are sheared by the dislocation. For example, m=3 for a glide along a {111} plane in fcc.

Then, the constraint is:

$$CS_i < CS \qquad (3)$$

where CS is a constant threshold, higher that the variations of CS_i due to the elastic deformations alone. If n particles are constrained, Eq.3 form a set of coupled equations which depend only on positions: holonomic constraints. Following [7, 8], equations of motions are derived [3] which incorporate these constraints by means of Lagrange multipliers. The additional term they contain is a configurational force aligned along the glide direction specified by $\vec{b}$ in Eq.2. We recall that holonomic constraints don't produce any work. This property is interesting, as shown in the next paragraph, when the method is used to constrain crack tips in order to study purely brittle crack propagation.

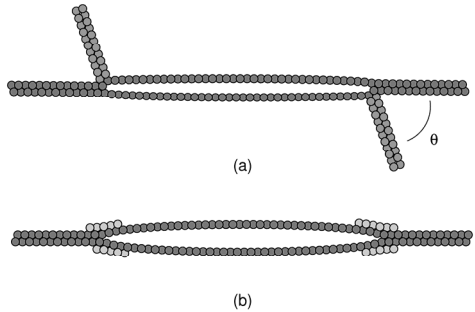


Figure 1 : (a) An intrinsically ductile crack, loaded just above k_{Ie}, emits a Shockley partial dislocation. The crack lies along a {111} plane in fcc with a crack front along <110>. The interatomic potential is the phenomenological Al from [11]. (b) A brittle crack, loaded just above k_{IG}, propagates. The light gray particles are constrained. The potential is the same as in (a).

A first application is the quantification of the intrinsic ductility versus brittleness of a material. Consider a crack (Fig. 1), in an fcc single crystal, lying along a {111} plane, with a crack front lying along <110>, loaded in traction (mode I). In this orientation, most fcc crystals are intrinsically ductile (except pathological cases like Iridium) which means that a dislocation is spontaneously emitted from the crack tip at a critical load. It is not possible to explore the brittle configurations in that case, which are clearly not physical, but nevertheless interesting if one wants to know how much the cohesion should be decreased (by impurity segregation for example) in order to get a transition from intrinsic ductility to brittleness [9]. By constraining the particles in the vicinity of the crack tip (light gray particles on Fig. 1b), such brittle configurations can be explored. In the calculations of Fig. 1, the traction is applied by a rigid displacement at the border of the box. This is not an efficient way to characterize the load at the crack tip. As explained in the introduction, it is more convenient to use the stress intensity factor. Following [10], we measure k at the tip by fitting the virial stress profile on the Inglis solution. With the interatomic potential given in [11], we observe dislocation emission at $k_{Ie} \approx 0.64\ k_{IG}$, brittle crack propagation at $k_{Ic} \approx k_{IG}$ and also an original mechanism, where vacancies form

just ahead of the crack tip, at $k_{Iv} \approx k_{IG}$. This last result is obtained on a blunted crack tip constrained one plane further away than the crack presented on Fig. 1.

CRACK TIP SHIELDING

Table 1 : Distances where the dislocations are pinned, along the slip plane inclined at θ=70° (zero is the tip). See figure 1 for the orientation of the slip plane. The numbers represent different configurations and are consistent through all the figures and text. Configurations beyond (resp. below) 4 contain a perfect dislocation (resp. a partial dislocation and a stacking fault, as in Fig. 1 a).

Frame number	0	1	2	3	4	6	10
Distance (a_0)	0	3.7	7.4	11	14.7	22.1	36.8

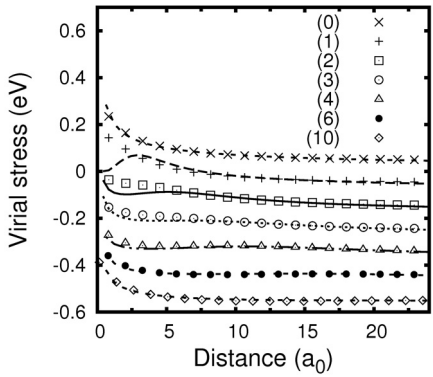


Figure 2 : Comparison of the stress profiles (traction) obtained by CMD (symbols) and elastic calculations (lines). The positions of the dislocation are given in table 1. The frames are shifted downward by steps of 0.1eV for clarity. Multiply the stress values by 9.8 to have GPa.

We now turn to the basic concept underlying the multi-scale simulation of semi-brittle cracking: the local k felt by the crack tip in the presence of a dislocation. Two twin problems are treated in parallel. The first calculation, done by CMD, concerns a nanometer scale flaw, of length $2a=16a_0$. The second is a semi-infinite crack in an infinite isotropic medium treated by the elastic theory [2]. To introduce a dislocation in the atomistic box, the load is increased slightly above k_{Ie} and a small mode III is added to force the emission of the second partial, whose Burgers vector is not in the plane of the figure because of the crystallographic orientation. The crucial point is to obtain static stress fields which are the one that can be compared to elasticity. As the dislocation is perfect, it is not tied to the crack tip by the stacking fault ribbon. Therefore, it should cross the box and get stuck at the border. CMD can efficiently pin the dislocation: instead of constraining particles at the immediate vicinity of the crack tip, they can be constrained at some chosen positions, further away, along the

glide plane [4]. A set of positions is shown in table 1. The stress profiles computed by both methods, for these configurations, are presented in Fig. 2.

On the curves (1) to (3), the agreement is bad between CMD and elasticity. The configurations correspond to the emission of the first Shockley partial with a stacking fault ribbon joining the tip. Curves (4) to (10), where the agreement is remarkable, correspond to a fully formed, perfect, dislocation. Curve (0), in Fig. 2, represents the load in the absence of dislocation and the stress singularity is characterized by $K_{applied}$. As the dislocation is emitted, the stress singularity is indeed decreased and the good agreement with elasticity allows the use of the analytical formulas for the computation of k. The concept of local k is therefore valid, provided the dislocation is perfect. Note that elasticity breaks down, not because of nonlinearity (the stress levels are still in the range where the potential is reasonably linear), but because of the presence of the stacking fault. The surprise is the quite large distance that must separate the crack from the dislocation in order for the analytical formulas to be valid: of the order of $10a_0$ (Table 1), 4nm, with respect to the Burgers vector dimension ($0.7a_0$).

DISCRETE DISLOCATION DYNAMICS

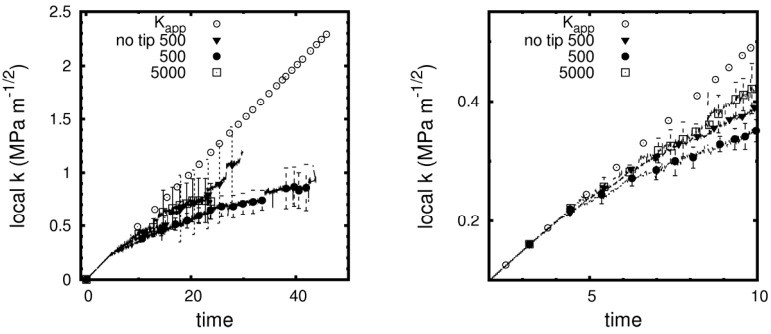


Figure 3 : (a) Time variation of k and $K_{applied}$ obtained by discrete dislocation dynamics, (b) zoom of (a).

The basic ingredients of the simulation are recalled. A trace of the crystalline structure is included in this continuum elasticity based simulation by fixing the orientation of the glide planes. The entire space is covered by parallel slip planes, with a spacing of the order of 80b, where b is the Burgers vector of the dislocations considered. Dislocation sources are randomly distributed on these slip planes. Time t is discretized. From the value of $K_{applied}$ at time t, the stress field can be computed at any point in space using analytical stress formulas. When the stress on a source is higher than a critical value for nucleation τ_{nuc}, the source is activated and a dislocation dipole is emitted which, in this simple 2D model, represents the trace of a

dislocation loop. Once a dislocation is emitted, it is displaced according to a velocity law:

$$\vec{v}=B\vec{f} \qquad (4)$$

where $\vec{f}$ is the Peach and Koelher force obtained from $\vec{f}=\overline{\overline{\sigma}}\vec{b}\wedge\vec{\xi}$ where $\vec{\xi}$ is the line vector. B is a constant. $\overline{\overline{\sigma}}$ is the stress tensor computed from the complex potentials in [2] which included the contribution of the crack and all the dislocations. It was used previously by Chateau [12] for treating the problem of H segregation at a pile up ahead of a crack. Phenomenological rules are also applied to describe the pinning at obstacles, the line tension effect, annihilation and junction formation [13]. A dislocation structure develops in front of the crack tip, with formation of intense slip bands due to crack tip emission and activation of sources in region of high resolved shear (primary and secondary slip) [5, 14]. Figure 3 shows the time evolution of the local k which includes the contribution of the whole dislocation structure. At early times, the local k and the applied K are the same, until emission is activated (first from the tip and then from many other sources). Emission ``from the tip" occurs at $k_{Ie}\approx 0.25MPa\sqrt{m}$. The criterion is such that a new dislocation can not be emitted until the preceding has moved away, the speed of which depends on the density of obstacles and the dislocation configuration, in particular the formation of junctions. Therefore, in between two dislocation emissions, K and k increase and k becomes higher than k_{Ie}. The critical load for brittle propagation is $k_{Ic}\approx 0.9MPa\sqrt{m}$, which should be reached, by extrapolation, for $K\approx 3MPa\sqrt{m}$. Then, in principle, the crack should be advanced by an infinitesimal amount and the local k recomputed.

CONCLUSION

We have seen that constrained molecular dynamics (CMD) can be used to calculate the response of a crack tip loaded by a stress intensity factor, “local k”, that can represent the effective load felt by the crack in the presence of a plastic zone. The issue is to determine how close to the tip the dislocations can be in order that $k=k_{critical}$ remains a valid fracture criterion. Indeed, local k is related to the elastic energy release rate, only if the dislocation free zone is big enough. Although we have not yet answered to this question, we have shown, on the school case of the perfect crack in a single crystal, what the different steps should be to model semi-brittle fracture: calculate k_{Ic} and k_{Ie} at the atomic scale; perform a continuum mechanics based calculation of the local k (here discrete dislocation dynamics is used); when $k=k_{Ic}$, check by using k as a boundary condition in CMD that the crack propagates, by eventually including the dislocations closest to the tip in the CMD calculation.

So far we have only discussed a generic semi-brittle calculation. In relation to H embrittlement, the CMD calculations should be performed on a box containing a

grain boundary with different H content (segregated). It should also be kept in mind that the plastic part of the calculation, which can be performed independently, should also be improved, at least in the case of 2D discrete dislocation dynamics, because these models do not provide enough shielding. The coupling between the atomic and the plastic part resides in the applicability of the fracture criterion, i.e. on the behavior of the tip in the presence of dislocations very close to it. One of the purpose of the present paper is to show that CMD provides the flexibility to handle such calculations, with pinned dislocations, close to the tip, with equilibrium stress fields consistent with continuum.

ACKNOWLEDGMENTS

This work is supported by the French Agence Nationale de la Recherche under project H-inter (number ANR-06-BLAN60231).

[1] S. G. Roberts, in Multiscale Phenomena in Plasticity, edited by J. Lépinoux, D. Mazière, V. Pontikis, and G. Saada (Kluwer Academic Press, Netherlands, 2000), p. 349.
[2] I. H. Lin and R. Thomson, Acta Metall. **34**, 187 (1986).
[3] D. Tanguy, Phys. Rev. B **76**, 144115 (2007).
[4] D. Tanguy, M. Razafindrazaka, and D. Delafosse, Acta Mater. **56**, 2441 (2008).
[5] D. Tanguy, D. Delafosse, and M. Razafindrazaka, submitted to Acta Mater. (2008).
[6] C. L. Kelchner, S. J. Plimpton, and J. C. Hamilton, Phys. Rev. B **58**, 11085 (1998).
[7] J. P. Ryckaert, G. Ciccotti, and H. J. C. Berendsen, J. Comp. Phys. **23**, 327 (1977).
[8] H. Goldstein, Classical Mechanics, 2nd edition (Addisson-Wesley, Reading, Mass., 1980).
[9] J. R. Rice and R. Thomson, Philos. Mag. **29**, 73 (1974).
[10] A. Mattoni, L. Colombo, and F. Cleri, Phys. Rev. B **70**, 094108 (2004).
[11] A. Aslanides and V. Pontikis, Phil. Mag. Lett. **78**, 377 (1998).
[12] J. P. Chateau, D. Delafosse, and T. Magnin, Acta Mater. **50**, 1523 (2002).
[13] M. Razafindrazaka, D. Tanguy, and D. Delafosse, submitted to Mat. Sci. Eng. A (2008).
[14] D. Tanguy, D. Delafosse, and M. Razafindrazaka, in H2008 proceedings (2008).
Email: tanguy@emse.fr

Effects of Hydrogen on Materials
Proceedings of the 2008 International Hydrogen Conference
Brian Somerday, Petros Sofronis, Russell Jones, editors, p 655-662
Copyright © 2009 ASM International®
All rights reserved.
www.asminternational.org

ATOMISTIC STUDY OF HYDROGEN DIFFUSION AROUND DISLOCATIONS IN ALPHA IRON

Shinya Taketomi, Ryosuke Matsumoto and Noriyuki Miyazaki
Department of Mechanical Engineering and Science, Kyoto University, Sakyo-ku, Kyoto, Japan
National Institute of Advanced Industrial Science and Technology, Japan

INTRODUCTION

Hydrogen embrittlement is a well-known phenomenon in which hydrogen lowers the strength of materials. Despite extensive investigations, the role of hydrogen in materials remains unclear. A well-known effect of hydrogen on mechanical properties is a reduction in ductility [1]. Hence, the interactions between dislocations and hydrogen atoms have been considered important in understanding the hydrogen embrittlement process [2-5].

To clarify the fundamental effects of hydrogen on dislocation activity, it is necessary to obtain precise estimates of the local distribution and the concentration of hydrogen around dislocations [6,7]. In our previous study [6], hydrogen-trap energy distribution around the {112}<111> edge dislocation in alpha iron was investigated, based on an atomistic model, and the characteristic hydrogen distribution was derived. However no calculations were made on other dislocations.

The edge dislocation core is commonly known as a rapid diffusion path for solute atoms in the dislocation line direction (pipe diffusion). An edge dislocation core usually has large spaces, thus the solute atom is considered to diffuse easily. However the hydrogen atom is extremely small compared to other solute atoms, therefore the hydrogen diffusion behavior is thought to be different [8]. Detailed analysis of hydrogen pipe diffusion within the dislocation core has not been conducted.

In this paper, the hydrogen-trap energy distribution around the edge dislocation core was investigated and the occurrence of pipe diffusion discussed. Since hydrogen diffusion within the dislocation core is rarely observed in the time scale of molecular dynamics simulation [6], the occurrence of pipe diffusion is investigated using the nudged elastic band (NEB) method to estimate the activation energy for hydrogen diffusion along the dislocation line. The material chosen for this study is alpha iron, because pure iron has been reported to be sensitive to hydrogen [9], and its alloys (such as carbon steel and stainless steels) are expected to serve as hydrogen storage and piping components, due to their low costs.

ANALYISIS METHODS

Analysis Model

In general, alpha iron has {110}<111> and {112}<111> main slip systems. In this study, we deal with those two kinds of edge dislocations. The crystallographic orientations are shown in Fig. 1. The slip occurs on the {112} and {110} planes, and the slip direction <111> was set along the *x* axis. Periodic boundary conditions were applied along the *x* and *z* axes. Iron atoms within the dark shaded region in Fig. 1 were removed to introduce an edge dislocation, and then the relaxation of the atomic structure was performed by conjugate gradient (CG) method. During the structural relaxation process, the movement of atoms along the *y* axis was fixed and compression was applied along the *x* axis, to fill the removed plane. After that, the unit cell size and the atomic positions were relaxed until the *x* axis stress (σ_{xx}) decreased sufficiently. The {112}<111> and {110}<111> analysis systems contain 49,878 and 51,030 iron atoms, respectively. The dimensions of the {112}<111> edge dislocation unit cell are 9.93, 8.26, and 7.30 nm, and the {110}<111> edge dislocation are 9.93, 8.62, and 7.02 nm, along the *x*, *y* and *z* axes, respectively. Three atomic layers at the top and bottom of the unit cell were considered as boundary layers, and their displacements were fixed. The embedded atom method (EAM) potential, developed by Wen et al. [10], was adopted as the interatomic potential.

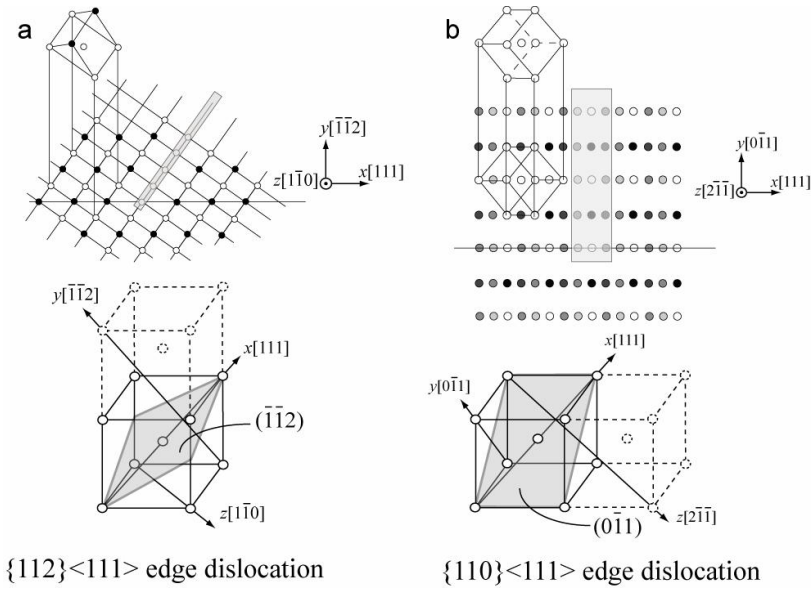


Fig. 1 Simulation models and coordinate systems. Fe atoms within the dark shaded regions in the upper figures are removed to introduce an edge dislocation.

Hydrogen Occupation Sites in Alpha Iron

There are two types of hydrogen occupation sites within the un-deformed bcc lattice, as shown in Fig. 2. One is the tetrahedral site (T site) and the other is the octahedral site (O site). The T site is the more stable occupation site for a hydrogen atom in most bcc metals [11], however, it has been reported that the O site becomes more stable under a deformed condition, for bcc-structured metal [12]. Here we are dealing with the disordered crystalline region near the dislocation core, and therefore, hydrogen atom in both T and O sites are taken into consideration. Here, T sites within the perfect bcc lattice correspond to the vertices of a Voronoi polyhedron, as shown in Fig. 2. Moreover, the O sites are located at the center of the square on the polyhedron surfaces. Using these rules, hydrogen occupation sites were estimated under lattice distortion conditions. Although, these sites do not exactly correspond to the T and O sites in a significantly distorted lattice, for convenience, we will hereafter refer to these sites as T and O sites, respectively.

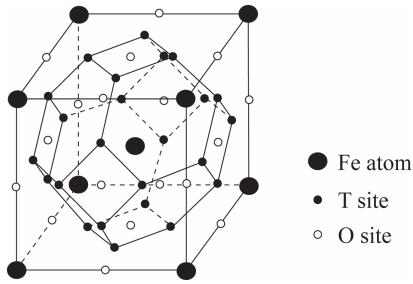


Fig. 2 Hydrogen occupation sites within the un-deformed bcc lattice and Voronoi polyhedron.

RESULTS AND DISCUSSIONS

Atomistic Structure of Dislocation

The atomic configurations and structures around the dislocation core after relaxation are shown in Fig. 3. The crystalline structure was detected using common neighbor analysis (CNA) [13]. In this figure, bcc-structured atoms are shown as white, and the others as black spheres. The initial position of the dislocation core is shown by the dislocation symbol ($\perp$). We hereafter consider the crystalline disordered region, denoted by the black dotted circle in Fig. 3, as the dislocation core. The sizes of the dislocation core for each dislocation are almost equal.

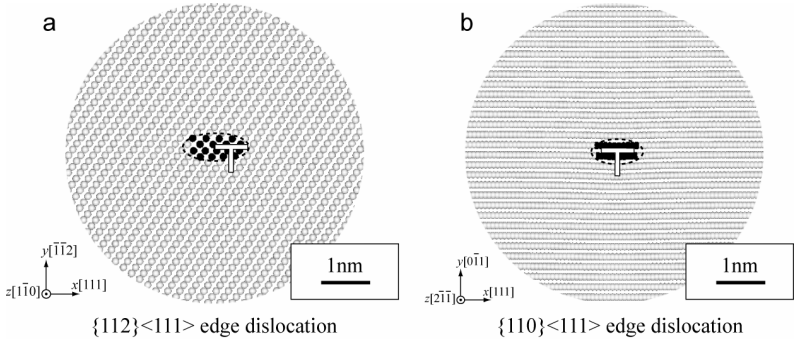


Fig. 3 Atomistic structure of edge dislocations detected by common neighbor analysis (CNA). White spheres correspond to bcc structures and black to non-bcc structures.

Distribution of Hydrogen-Trap Energy around the Dislocation Core

A hydrogen atom was introduced into each T and O site detected by Voronoi tessellation. The positions of the Fe and H atoms were then relaxed by the CG method to minimize the total potential energy. Then the hydrogen-trap energy, $\Delta E_d(\boldsymbol{r})$, at the hydrogen occupation site $\boldsymbol{r}$, was calculated using the equation:

$$\Delta E_d(\boldsymbol{r}) = -\left[\left\{\Phi_{d,H}(\boldsymbol{r}) - \left(\Phi_d + \frac{1}{2}\Phi_{H2}\right)\right\} - H^T\right], \quad (1)$$

where, $\Phi_{d,H}(\boldsymbol{r})$ is the potential energy of the system with a hydrogen atom at a trap site located at $\boldsymbol{r}$. Φ_d is the potential energy of the system without hydrogen, Φ_{H2} is the potential energy of the hydrogen molecule, and H^T is the heat of solution of the hydrogen atom on the T site in the alpha iron lattice, with a value equal to 4.5×10^{-20} J. Both edge dislocations have the strongest hydrogen-trap sites within the dislocation core. The distributions of hydrogen-trap sites around the {112}<111> and {110}<111> edge dislocation cores are shown in Figs. 4(a) and (b), respectively. The position of the initial dislocation core (⊤) and the dislocation core region (the dotted line in Fig. 3) are also shown in the figure. Blue spheres correspond to the typical hydrogen trap sites with strong trap-energy after structural relaxation; the other spheres are Fe atoms. Here, black and white Fe atoms are the upper and lower layers of the dislocation core, respectively. Hydrogen-trap energies at each site are shown in Table 1. Trap sites (b) and (h)/(o) are the strongest trap sites for the {112}<111> and {110}<111> edge dislocations, respectively. The maximum hydrogen-trap energy in the dislocation core is about 7.8×10^{-20} and 7.9×10^{-20} J. These values agree with the range of experimental estimations (3.19×10^{-20} [14] and 9.95×10^{-20} J [15]). Here, the {110}<111> edge dislocation shows a symmetrical distribution of Fe atoms and hydrogen-trap sites, as shown in Fig. 4(b) and Table 1.

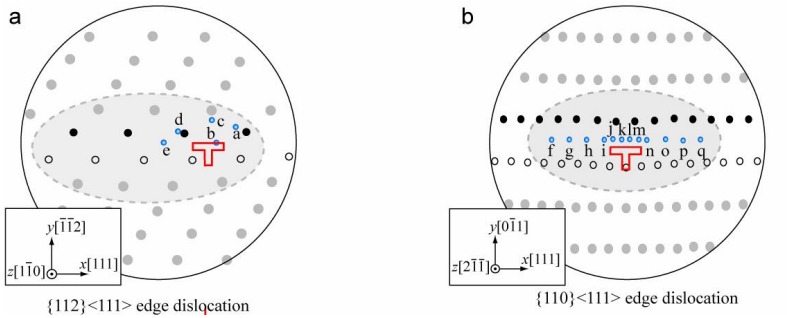


Fig. 4 Hydrogen-trap site distribution around the dislocation core. (a) Hydrogen trap sites around the {112}<111> edge dislocation core. The initial dislocation core is indicated by the red dislocation symbol. The dislocation core estimated in Fig. 3 is shown in the shaded region. (b) Hydrogen trap sites around the {110}<111> edge dislocation core.

Table 1 Hydrogen-trap energies ($\Delta E_d(\boldsymbol{r})$) for each trap site within the edge dislocation core.

{112}<111>	a	b	c	d	e	
$\Delta E_d(\boldsymbol{r})$ ($\times 10^{-20}$ J)	2.11	7.79	6.82	4.88	6.64	
{110}<111>	f, q	g, p	h, o	i, n	j, m	k, l
$\Delta E_d(\boldsymbol{r})$ ($\times 10^{-20}$ J)	7.60	7.75	7.89	7.86	7.47	7.73

Activation Energy for Hydrogen Pipe Diffusion

In this section, we investigate the occurrence of hydrogen pipe diffusion in alpha iron. The nudged elastic band (NEB) method was adopted to estimate the activation energy for hydrogen diffusion in alpha iron. The NEB method is a transition state theory and enables us to obtain the minimum energy path (MEP) and the minimum energy barrier for the reaction. Although, quantum diffusion also contributes to hydrogen diffusion, it is difficult to deal the quantum diffusion. In this paper, only the classical thermal activation process was taken into consideration. First, we investigate the activation energy for hydrogen diffusion between neighboring T sites within a non-deformed lattice. The activation energy is calculated as $\Delta E_{bulk} = 0.54\times10^{-20}$ J $= 0.034$ eV, and is in good agreement with the experimental results ($\Delta E_{bulk} = 0.035$ eV [16]), even the quantum diffusion was not taken into consideration.

A hydrogen atom is assumed to be trapped at the strongest trap site ((b) and (h)/(o)) for each dislocation. Then, all the diffusion paths within the dislocation core are investigated. As a result, the diffusion path with a lower energy barrier along the dislocation line direction (i.e., the diffusion path for hydrogen pipe diffusion) was determined. The atomistic structure of the slip plane and the hydrogen occupation sites are shown in Fig. 5. For the {112}<111> edge dislocation, the diffusion path is b1-a1-a2-b2-b3..., as shown by the pink line in Fig. 5(a). The activation energy is shown in Table 2. The maximum activation energy for diffusing along this path $\Delta E_{\{112\}\text{core}}$ is 6.16×10^{-20} J. For the {110}<111> edge dislocation, the diffusion path is h1-i1-j1-...-o1-..., as shown in Fig. 5(b). The activation energy is shown in Table 2. The maximum activation energy to diffuse along this path $\Delta E_{\{110\}\text{core}}$ is 5.41×10^{-20} J. Here, the probability of a hydrogen jump (thermal activation process) in the dislocation core is given by $P_{\text{core}} = \exp(-\Delta E_{\text{core}}/k_{\text{B}}T)$, where k_{B} is Boltzmann's constant and T is the absolute temperature. Therefore, one order difference in the activation energy between ΔE_{core} and ΔE_{bulk} results in a further difference in hydrogen diffusivity. These results indicate that the edge dislocation core in alpha iron could not be a rapid hydrogen diffusion path within this analytical model. This result is the opposite of that for other interstitial solute atoms (e.g., carbon, nitrogen) in alpha iron. We attribute this to the size of hydrogen atom. Since hydrogen atoms are extremely small, they can be strongly trapped in the space of the dislocation core and

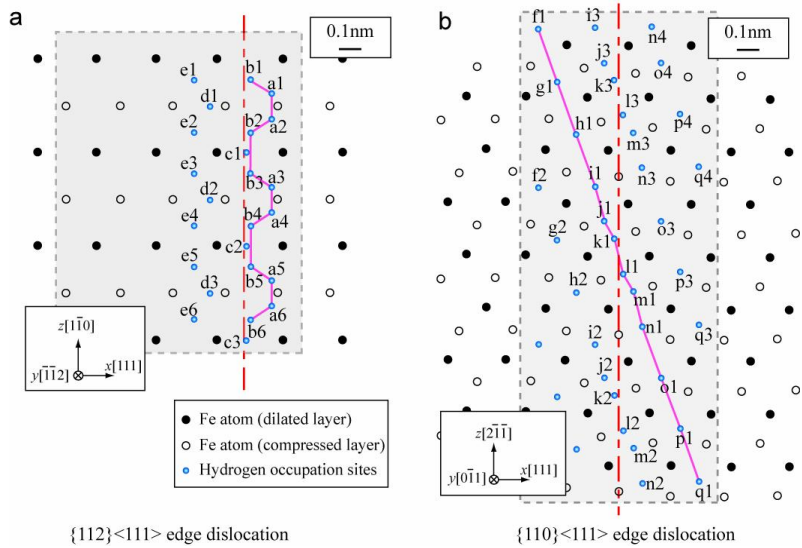


Fig. 5 Hydrogen diffusion path along the dislocation line within the dislocation core. (a) Hydrogen trap site distribution on the {112} plane. Hydrogen diffusion path along the dislocation line (pipe diffusion) is shown by the pink line, and the initial dislocation line is shown by the dashed red line. (b) Hydrogen trap site distribution on the {110} plane.

fall into a deep potential valley. This increases the activation energy required for diffusion. These results were obtained by the classical thermal activation model and the quantum diffusion was not taken into consideration. Here, the occurrence of quantum diffusion is very sensitive to the distances between the trap sites. Distances between hydrogen trap sites within the dislocation core are much longer (≈ 0.2 nm) compared to that in bcc lattice (≈ 0.1 nm). Therefore we consider the quantum effect for hydrogen diffusion within dislocation core becomes smaller.

Table 2 Activation energy (ΔE_{core}) for hydrogen pipe diffusion.

a	{112}<111>	b1-a1	a1-a2	a2-b2	b2-b3		
	$\Delta E_{\{112\}\mathrm{core}}$ ($\times 10^{-20}$ J)	6.16	1.35	0.48	2.28		
b	{110}<111>	f1-g1	g1-h1	h1-i1	i1-j1	j1-k1	k1-l1
	$\Delta E_{\{110\}\mathrm{core}}$ ($\times 10^{-20}$ J)	5.26	4.76	3.81	1.79	2.28	1.83
	{110}<111>	l1-m1	m1-n1	n1-o1	o1-p1	p1-q1	
	$\Delta E_{\{110\}\mathrm{core}}$ ($\times 10^{-20}$ J)	2.54	1.40	3.77	4.90	5.41	

CONCLUSIONS

Hydrogen-trap energy within the edge dislocation core in alpha iron was investigated, based on an atomistic model. The {112}<111> and {110}<111> edge dislocations show almost the same maximum hydrogen-trap energies ($\Delta E_{\mathrm{d}}(\boldsymbol{r}) = 7.8\times10^{-20}$ and $\Delta E_{\mathrm{d}}(\boldsymbol{r}) = 7.9\times10^{-20}$ J) within their cores. Taking these trap sites into consideration, the activation energies for hydrogen pipe diffusion were estimated using the NEB method, and the activation energy for pipe diffusion ($\Delta E_{\{112\}\mathrm{core}} = 6.16\times10^{-20}$ J and $\Delta E_{\{110\}\mathrm{core}} = 5.41\times10^{-20}$ J) was higher than for bulk diffusion ($\Delta E_{\mathrm{bulk}} = 0.54\times10^{-20}$ J), with one order difference. This result indicates that hydrogen pipe diffusion under these conditions would be difficult.

ACKNOWLEDGMENTS

This research was partially supported by the Fundamental Research Project on Advanced Hydrogen Science funded by the New Energy Development Organization (NEDO).

REFERENCES

1. Han, G., He, J., Fukuyama, S. and Yokogawa, K., “Effect of Strain-induced Martensite on Hydrogen Environment Embrittlement of Sensitized Austentic

Stainless Steels at Low Temperature," *Acta Materialia*, Vol. 46 (1998), pp. 4559-4570.
2. Beachem, C. D., "New Model for Hydrogen-assisted Cracking (Hydrogen Embrittlement)," *Metallurgical Transaction*, Vol. 3, No. 2 (1972), pp. 437-451.
3. Ferreira, P. J., Robertson, I. M. and Birnbaum, H. K., "Hydrogen Effects on the Chacacter of Dislocations in High-Purity Aluminum," *Acta Materialia*, Vol. 47, No. 10 (1999), pp. 2991-2998.
4. Taketomi, S., Matsumoto, R. and Miyazaki, N., "Atomistic Simulation of the Effects of Hydrogen on the Mobility of Edge Dislocation in Alpha Iron," *Journal of Materials Science*, Vol. 43, No. 3 (2008), pp. 1166-1169.
5. Sofronis, P., Birnbaum, H. K., "Mechanics of the Hydrogen-Dislocation-Impurity interactions I. Increasing Shear Modulus," *Journal of the Mechanics and Physics of Solids*, Vol. 43, No. 1 (1995), pp. 49-90.
6. Taketomi, S., Matsumoto, R. and Miyazaki, N., "Atomistic Study of Hydrogen Distribution and Diffusion Around a {112}<111> Edge Dislocation in Alpha Iron," *Acta Materialia*, Vol. 56, No. 15 (2008), pp. 3761-3769.
7. Matsumoto, R., Inoue, Y., Taketomi, S. and Miyazaki, N., "Influence of shear strain on the hydrogen trapped in bcc-Fe: A first-principles-based study," Scripta Mater, (2009).(in press)
8. Fukai, Y., Tanaka,K., Uchida, H., Hydrogen and Metal, Uchida-Rokakuho (1998) [in Japanese] p.117
9. Kimura, A., Matsui, H. and Kimura, H., "The Work-hardening Behavior of Hydrogen-charged High Purity Iron Single Crystals at Temperatures between 296 and 200K," *Materials Science and Engineering*, Vol. 58 (1983), pp. 211-222.
10. Wen, M., Xu, X. J., Fukuyama, S. and Yokogawa, K., "Embedded-atom-method Functions for the Body-centered-cubic Iron and Hydrogen," *Journal of Materials Research*, Vol. 16, No. 12 (2001), pp. 3496-3502.
11. Yagi, E., Kobayashi, T., Nakamura H., Fukai, Y. and Watanabe, K., "Stress-induced Site Change of H in V observed by Channeling Experiments", *Physical Review B*, Vol. 31, No. 3 (1985), pp. 1640-1642.
12. Fukai, Y., "Site Preference of Interstitial Hydrogen in Metals", *Journal of the Less-Common Metals,* Vol. 101 (1984), pp. 1-16.
13. Honeycutt, J. D. and Andersen H. C., "Molecular Dynamics Study of Melting and Freezing of Small Lennard-Jones Clusters," *Journal of Physical Chemistry*, Vol. 91, No. 19 (1987), pp. 4950-4963.
14. Choo, W. Y. and Lee, L. Y., "Thermal Analysis of Trapped Hydrogen in Pure Iron," *Metallurgical Transactions. A,* Vol. 13, No. 1 (1982), pp. 135-140.
15. Kumnick, A. J. and Johnson, H. H., "Deep Trapping States for Hydrogen in Deformed Iron," *Acta Metallurgica,* Vol. 28, (1980), pp.33-39.
16. Wipf, H., Hydrogen in Metals III: Topics in applied physics, Vol. 73 Springer-Verlag (Berlin, 1997) p. 51.

Effects of Hydrogen on Materials
Proceedings of the 2008 International Hydrogen Conference
Brian Somerday, Petros Sofronis, Russell Jones, editors, p 663-670
Copyright © 2009 ASM International®
All rights reserved.
www.asminternational.org

ESTIMATION OF HYDROGEN DISTRIBUTION AROUND DISLOCATIONS BASED ON FIRST PRINCIPLES CALCULATIONS

Ryosuke Matsumoto, Shinya Taketomi and Noriyuki Miyazaki
Department of Mechanical Engineering and Science, Kyoto University, Sakyo-ku, Kyoto 606-8501, Japan
National Institute of Advanced Industrial Science and Technology, Japan

Yoshinori Inoue
Graduate School of Engineering, Kyoto University, Japan

INTRODUCTION

Despite extensive investigations into hydrogen related fractures, the specific mechanisms remain the subject of debate. The difficulties are attributed in part to complicated interactions between hydrogen and various lattice defects [1-7]. Although the average hydrogen concentration is very low in steel, typically on the order of ppm, the local hydrogen concentration around lattice defects is usually much higher. Further, hydrogen accompanying lattice defects strongly influences the behavior of the defects, i.e., hydrogen stabilizes the vacancies [1, 2], and changes the mobility of dislocations [3-7]. Furthermore, hydrogen causes intergranular fractures in high-strength steel [8].

Knowing the hydrogen trap state in materials, i.e., the number of lattice defect traps, and the strength of each trap, is important for understanding the nature of hydrogen related fractures and also for the development of materials and their engineering applications. Thermal desorption approaches have been used to categorize the trapped hydrogen and to analyze its effect on the mechanical properties. However, each lattice defect does not have a single trap energy; dislocations have a strong trap site at the dislocation center [9, 10] and many weaker, but not negligible, trap sites around it [11]. Thus, the contributions of the various lattice defects overlap, and understanding the details of the hydrogen trap state is difficult.

In this study, we first estimate the distributions of hydrogen trap energy around the edge and screw dislocations in bcc-Fe, using the elastic solution of the strain field and the dependency of the heat of solution on elastic strain, which is preliminarily obtained by the embedded atom method (EAM) potential, developed by Wen et al. (EAM(Wen) potential) [12]. We also demonstrate the validity of our estimation method by comparing the results with those obtained by direct estimation using molecular statics simulations [11]. Finally, we show the distributions of hydrogen trap energy around the edge and screw dislocations in Al, following an estimation of

the strain effect on the heat of solution of hydrogen, using density functional theory (DFT).

ANALYTICAL PROCEEDURE

Hydrogen Occupation Sites

There are two types of interstices in fcc, bcc, and hcp lattices: a tetrahedral (t)-site and an octahedral (o)-site. The occupation site of hydrogen may change, depending on the elastic strain applied to the lattice. In fact, although hydrogen in an undeformed bcc lattice prefers to occupy a t-site rather than an o-site, it has been reported that o-site occupation becomes more stable under monoaxial tensile conditions for bcc metals [13]. Therefore, both occupation sites possibly influence the hydrogen distribution around a stress singular point. In this study, we consider both occupation sites.

Although the spatial configurations of t- and o-site in fcc lattice are isotropic in *x*-, *y*-, and *z*-axes, those in bcc and hcp lattices are anisotropic. We call the t- and o-sites that are symmetric only in the *y*- and *z*-axes the t_x- and o_x-sites, respectively; the other occupation sites are notated similarly [14-16].

Estimation of Trap Energy Yielded by Elastic Strain

We introduced a hydrogen atom into a t- or o-site in a strained lattice, and calculated the energy of the system $E_{\mathrm{MH}}(\varepsilon_{ij})$ (ground-state energy for DFT calculations and total potential energy for estimations using an interatomic potential). According to the symmetrical property of the occupation sites, we apply two different tensile strains (ε_x and ε_y (= ε_z)) and two different shear strains (ε_{xy} and ε_{yz} (= ε_{zx})) for t_x- and o_x-site occupations. The relationship for an occupation site (t_y-, t_z-, o_y-, or o_z-site) is easily obtained by changing indexes.

In this paper, we define the strain using the lattice size for the case without hydrogen, and the strain effects are estimated in the range of $|\varepsilon_{ij}| \le 0.05$—almost equal to the elastic strain around the dislocation core. All atomic positions are relaxed under fixed lattice conditions. The heat of solution for incorporation of hydrogen into the strained lattice is estimated by

$$E^{\mathrm{HOS}}(\varepsilon_{ij}) = E_{\mathrm{MH}}(\varepsilon_{ij}) - \left(n \times e_{\mathrm{M}}(\varepsilon_{ij}) + \frac{1}{2} E_{\mathrm{H2}} \right), \qquad (1)$$

where $e_{\mathrm{M}}(\varepsilon_{ij})$ is the energy of one atom in the unit lattice under strain ε_{ij}, n is the number of lattice-site atoms in the calculation model, and E_{H2} is the energy of a hydrogen molecule. $E^{\mathrm{HOS}}(\varepsilon_{ij})$ includes the influences of the nonlinear elasticity and chemical interactions. The contribution to the trap energy of strain ε_{ij} is expressed as

$$\Delta E^{\mathrm{Trap\_ij}}\left(\varepsilon_{ij}\right) = -\left(H^{\mathrm{HOS}}\left(\varepsilon_{ij}\right) - H^{\mathrm{HOS}}(0)\right). \quad (2)$$

The strain effect on the hydrogen trap can be approximated using the amount of lattice dilatation caused by hydrogen. However, for hydrogen, the stable occupation site changes depending on the strain, and in some cases, different kinds of occupation sites combine into one or certain occupation sites disappear [11, 13, 16]. Thus, the actual estimation of the relation is important.

Superimposing Procedure on Elastic Strain Fields

We estimate the trap energy yielded by elastic strain $\boldsymbol{\varepsilon}'$ at the occupation site positioned at $\boldsymbol{x}'$ by (1) using the rotation tensor, the strain tensor $\boldsymbol{\varepsilon}'$ and the coordinates of the hydrogen occupation site $\boldsymbol{x}'$ are transformed to the reference coordinate system, where contributions of the elastic strain on the hydrogen trap energy were preliminarily estimated by DFT or the interatomic potential as a function of ε_{ij}; (2) the occupation site is classified as a t_x-, t_y-, or t_z-site (or o_x-, o_y-, or o_z-site); (3) the contribution to trap energy from each strain element ε_{ij} is calculated using $\Delta E^{\mathrm{Trap\_ij}}$; (4) the absolute contribution to trap energy from all strain components $\Delta E^{\mathrm{Trap\_T}}(\boldsymbol{\varepsilon})$ is estimated as the linear sum of each strain contribution $\Delta E^{\mathrm{Trap\_ij}}(\varepsilon_{ij})$; and, (5) finally, the trap energy $E^{\mathrm{Trap}}(\boldsymbol{\varepsilon})$ is estimated by considering the difference in the heat of solution between t- and o-sites at an undeformed state (e.g., for o-site occupations in bcc-Fe; $E^{\mathrm{Trap}}(\boldsymbol{\varepsilon}) = \Delta E^{\mathrm{Trap\_T}}(\boldsymbol{\varepsilon}) + (H^{\mathrm{HOS\_t\text{-}site}} - H^{\mathrm{HOS\_o\text{-}site}})$).

We use the elastic solutions for isotropic medium for the simplicity. To include the effect of the width of the dislocation core, we used the Peierls–Nabarro model [17] for the elastic solution of the edge dislocation. This superimposing method does not take into account hydrogen–hydrogen interactions and hydrogen effect on the elastic constants. We consider that these influences are small unless the atomic percent of hydrogen approaches tens of percent.

RESULTS

Distributions of Hydrogen Trap Energy around Dislocations in bcc-Fe

Estimating the dependency of the heat of solution on strain using DFT calculations is computationally expensive for a sufficiently large bcc-Fe lattice. Here we use the EAM(Wen) potential [12], as its accuracy has been carefully verified using DFT calculations [16]. We obtained the relationship using the EAM(Wen) potential for a sufficiently large lattice ($10 \times 10 \times 10$ lattices ($n = 2000$)).

Figure 1(a) and (b) shows the distribution of hydrogen trap energy around the {112}<111> edge dislocation and {112}<111> screw dislocation, respectively.

Strong trap sites are distributed both under the edge dislocation (region A in Fig. 1(a)) where intensive volumetric strain arises and on the slip plane of the edge dislocation (region B in Fig. 1(a)), and even around the screw dislocation that does not have a volumetric strain component. It is widely thought that the interaction between the strain field of a screw dislocation and hydrogen is negligible. However, comparing the distributions around the edge (Fig. 1(a)) and screw (Fig. 1(b)) dislocations (and also Fig. 2(a) and Fig. 2(b)), confirmed that the elastic interaction between hydrogen and screw dislocation is not negligibly small.

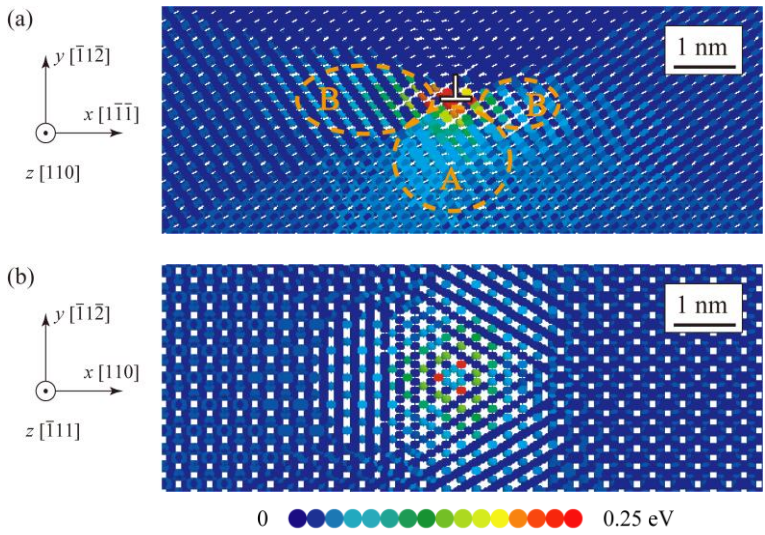


Figure 1: (Color CD-ROM version) Distribution of the hydrogen trap energy around dislocations in bcc-Fe: The dislocation line is oriented along the z-axis and the slip plane is located on the xz-plane. (a) and (b) show the distributions around the {112}<111> edge and {112}<111> screw dislocations, respectively.

Figure 2(a) and (b) presents the distribution of hydrogen trap energy around the {112}<111> edge [11] and {112}<111> screw dislocations, obtained by direct estimation using molecular statics simulations, respectively. The dislocation cores, detected as the non-crystalline region, are shown by dashed circles. Figs. 1 and 2 confirmed good agreement between the direct calculation and the superimposing method, except inside and in the vicinity of the dislocation core. Considering the change in crystalline structure in the dislocation core and the applicability limit of the elastic solution, the disagreements are a natural consequence and the error is small.

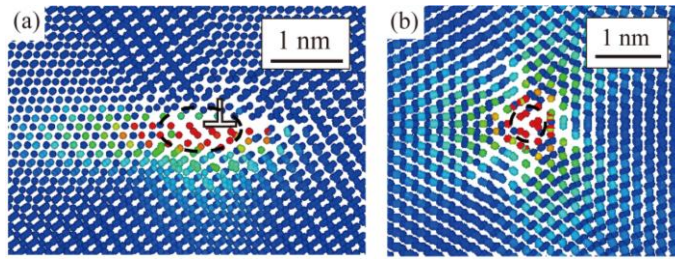


Figure 2: (Color CD-ROM version) Distribution of hydrogen trap energy around dislocation in bcc-Fe, obtained by molecular statics simulation: The crystal orientations and color bar are the same as Fig. 1. (a) and (b) show the distributions around the {112}<111> edge and {112}<111> screw dislocations, respectively.

Distributions of Hydrogen Trap Energy around Dislocations in Al

We obtained the relationship between the heat of solution and elastic strain using DFT calculations for 3 × 3 × 3 lattices (n = 108). We performed DFT calculations within the generalized gradient approximation (GGA) [18] for electron exchange and correlation, using the Vienna Ab-initio Simulation Package (VASP) [19-21]. The interactions between the ions and electrons are described by ultrasoft pseudopotential [22], and the Monkhorst–Pack scheme [23] is used to define the k points. Zero-point energy corrections, calculated from the Hessian matrix, were considered in all calculations. We used 12 × 12 × 12 k-points and a 400 eV cut-off energy per unit lattice. This calculation condition gives $H^{\mathrm{HOS\_t\text{-}site}}$ = 0.70 eV and $H^{\mathrm{HOS\_o\text{-}site}}$ = 0.78 eV, and these values agree well with previous report [24]. The calculated elastic strain effects on the heat of solution are shown in Fig. 3. Here we used E_{H2} = −6.79 eV as the ground-state energy of a hydrogen molecule.

Figure 4 (a) and (b) shows the distribution of hydrogen trap energy around the {111}<110> edge and {111}<110> screw dislocation, respectively. The elastic interaction between hydrogen and edge dislocation in Al is much weaker compare to that in bcc-Fe. Hydrogen atoms yield only isotropic dilatation in an fcc lattice, and thus, the trap energy yielded by elastic strain field around the screw dislocation is very small.

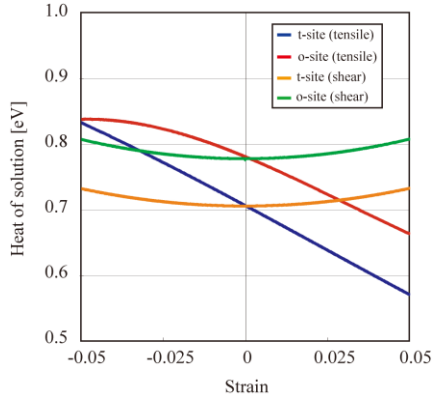


Figure 3: (Color CD-ROM version) Influence of tensile strain on the heat of solution of hydrogen incorporated into Al, estimated by DFT calculations.

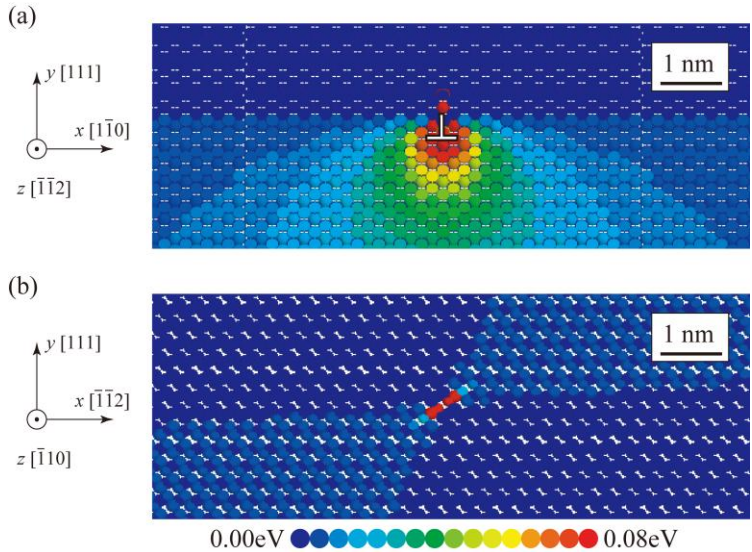


Figure 4: (Color CD-ROM version) Distribution of hydrogen trap energy around dislocations in Al: (a) and (b) show the {111}<110> edge and {111}<110> screw dislocations, respectively.

CONCLUSIONS

We estimated the distributions of hydrogen trap energy around the edge and screw dislocations in bcc-Fe and Al, using the elastic strain fields and the dependence of

the heat of solution on strain. The hydrogen in bcc-Fe showed a strong interaction with strain fields around both edge and screw dislocations. We also confirmed the validity of our method by comparing the distributions around edge and screw dislocations in bcc-Fe with those obtained by direct calculations, using molecular statics simulations. The elastic interaction between hydrogen and edge dislocation in Al is much weaker compare to that in bcc-Fe. The simple superimposing method used here is applicable for estimating the distribution of hydrogen trap energy around various stress singular points in many kinds of materials.

ACKNOWLEDGMENTS

Part of this research was supported by the "Fundamental Research Project on Advanced Hydrogen Science" funded by the New Energy and Industrial Technology Development Organization (NEDO).

REFERENCES

1. Nagumo, M., Nakamura, M. and Takai, K., "Hydrogen thermal desorption relevant to delayed-fracture susceptibility of high-strength steels," *Metall. Mater. Trans. A*, Vol. 32, No. 2 (2001), pp. 339-347.
2. Tateyama, Y. and Ohno, T., "Stability and clusterization of hydrogen- vacancy complexes in α-Fe: An ab initio study," *Phys. Rev. B* ,Vol. 67, No. 17 (2003), 174105.
3. Sofronis, P. and Birnbaum, H.K., "Mechanics of the hydrogen-dislocation-impurity interactions 1. Increasing shear modulus," *Journal of the Mechanics and Physics in Solids*, Vol. 54, No. 29 (1995), pp. 49-90.
4. Ferreira, P.J., Robertson, I.M. and Birnbaum, H.K., "Hydrogen effects on the character of dislocations in high-purity aluminum," *Acta Mater.*, Vol. 47, No. 10 (1999), pp. 2991-2998.
5. Lu, G., Zhang, Q., Kioussis, N. and Kaxiras, E., "Hydrogen-enhanced local plasticity in aluminum: an ab initio study," *Phys. Rev. Let.*, Vol. 87, No. 9 (2001), 095501.
6. Wen, M., Fukuyama, S. and Yokogawa, K., "Atomistic simulations of effect of hydrogen on kink-pair energetics of screw dislocations in bcc iron," *Acta Mater.*, Vol. 51, No. 6 (2003), pp. 1767-1773.
7. Taketomi, S., Matsumoto, R. and Miyazaki, N., "Atomistic simulation of the effects of hydrogen on the mobility of edge dislocation in alpha iron," *J. Mater. Sci.*, Vol. 43, No. 3 (2008), pp. 1166-1169.
8. Hinotani, S., Terasaki, F. and Takahashi, K., "Hydrogen Embrittlement of High Strength Steels in High Pressure Hydrogen Gas at Ambient Temperature," *Tetsu-to-Hagane*, Vol. 64, No. 7 (1978), pp. 899-905. (in Japanese)

9. Juan, A., Irigoyen, B. and Gesari, S., "Electronic structure and bonding of hydrogen in a screw dislocated bcc Fe," *Applied Surface Science*, Vol. 172, No. 1-2 (2001), pp. 8-17.
10. Gesari, S., Irigoyen, B. and Juan, A., "The location of atomic hydrogen in an edge-dislocated bcc Fe," *Journal of Physics D-Applied Physics*, Vol. 31, No. 17 (1998), pp. 2179-2183.
11. Taketomi, S., Matsumoto, R. and Miyazaki, N., "Atomistic study of hydrogen distribution and diffusion around a {112}<111> edge dislocation in alpha iron," *Acta Materialia*, Vol. 56, No. 15 (2008), pp. 3761-3769.
12. Wen, M., Xu, X.J., Fukuyama, S. and Yokogawa, K.,"Embedded-atom-method functions for the body-centered-cubic iron and hydrogen,", *J. Mater. Res.*, Vol. 16, No. 12 (2001), pp. 3496-3502.
13. Fukai, Y., "Site preference of interstitial hydrogen in metals," *J. Less-Common Met.*, Vol. 101, No. 8 (1984), pp. 1-16.
14. Cochardt, A.W., Schoek, G. and Wiedersich, H., "Interaction between dislocations and interstitial atoms in body-centered cubic metals," *Acta Metal.*, Vol. 3, No. 6 (1955), pp. 533-537.
15. Clouet, E., Garruchet, S., Nguyen, H., Perez, M. and Becquart, C.S., "Dislocation interaction with C in α-Fe: A comparison between atomic simulations and elasticity theory," *Acta Mater.*, Vol. 56, No. 14 (2008), pp. 3450-3460.
16. Matsumoto, R., Inoue, Y., Taketomi, S. and Miyazaki, N., "Influence of shear strain on the hydrogen trapped in bcc-Fe: A first-principles-based study," *Scripta Mater*, (2008), doi:10.1016/j.scriptamat.2008.12.009.
17. Hirth, J.P. and Lothe, J., Theory of Dislocations, Krieger Publishing Company (Florida, 1982), p. 218.
18. Perdew, J.P. and Wang, Y., "Accurate and simple analytic representation of the electron-gas correlation-energy," *Phys. Rev. B*, Vol. 45, No.23 (1992), pp. 13244-13249.
19. Kresse, G. and Hafner, J., "Ab-initio molecular-dynamics for open-shell transition-metals," *Phys. Rev. B*, Vol. 48, No. 17 (1993), pp. 13115-13118.
20. Kresse, G. and Furthmüller, J., "Efficient iterative schemes for ab initio total-energy calculations using a plane-wave basis set," *Phys. Rev. B*, Vol. 54, No. 16 (1996), pp. 11169-11186.
21. Kresse, G. and Furthmüller, J., "Efficiency of ab-initio total energy calculations for metals and semiconductors using a plane-wave basis set," *Comput. Mater. Sci.*, Vol. 6, No. 1 (1996), pp. 15-50.
22. Vanderbilt, D., "Soft self-consistent pseudopotentials in a generalized eigenvalue formalism," *Phys. Rev. B*, Vol. 41, No. 11 (1990), pp. 7892-7895
23. Monkhorst, H.J. and Pack, J.D., "Special points for Brillouin-zone integrations," *Phys. Rev. B* ,Vol. 13, No. 12 (1976), pp. 5188-5192.
24. Wolverton, C., Ozoliņš, V. and Asta, M., "Hydrogen in aluminum: First-principles calculations of structure and thermodynamics," *Phys. Rev. B*, Vol. 69, No. 14 (2004), 144109.

Effects of Hydrogen on Materials
Proceedings of the 2008 International Hydrogen Conference
Brian Somerday, Petros Sofronis, Russell Jones, editors, p 671-677
Copyright © 2009 ASM International®
All rights reserved.
www.asminternational.org

MONTE CARLO SIMULATION OF VACANCIES AT AL-Σ=33(554)[1-10]: TOWARDS INTERGRANULAR SUPERABUNDANT VACANCIES

E. Vamvakopoulos
Centre Européen de Calcul Atomique et Moléculaire,
Ecole Normale Supérieure de Lyon, 46 allée d'Italie, Fr-69007 Lyon (France).

D. Tanguy
CNRS, UMR 5146, Ecole des Mines de Saint-Etienne
158 cours Fauriel, Fr-42023, Saint-Etienne (France)

ABSTRACT

We report a detailed analysis of vacancy localization at high temperature in the Σ=33(554)[1-10] symmetrical tilt boundary, modelled by an EAM potential for Al (Ercolessi). The good localization, on average, of the vacancies allows to extend the use of our Monte Carlo simulation to this grain boundary and compute statistics of vacancy occupations, single vacancies and vacancy chains, in the Grand Canonical ensemble. These results establish the reliability of our method, an essential step on the way to modelling intergranular Superabundant Vacancies.

INTRODUCTION

The final goal of this simulation work is to model the formation of Superabundant Vacancies (SaV) and their impact on mechanical properties, at the atomic scale. In a previous work, equilibrium SaV in a perfect bulk have been simulated. In this paper, a necessary intermediate step is presented: the simulation of thermal vacancies at a grain boundary.

Superabundant vacancies are vacancy hydrogen clusters which form in large quantities because the trapping of interstitial hydrogen atoms inside a vacancy is so energetically favourable (of the order of 0.4 eV per H atom) that it can compensates the cost of the formation of the vacancy. Negative formation energies are possible in case of multiple occupancy. Experimentally, they have been observed by Fukai in a wide variety of metals [1]. For example, in Ni, at high temperature and high hydrogen pressure, VH_6 clusters (one vacancy, occupied by 6 H atoms) are formed and order in the $L1_2$ structure, giving vacancy concentrations higher than 25% at.. In less extreme conditions, like Al electrochemically charged at room temperature [2],

VH_1 can also form, but their slow diffusion kinetic limits their influence to the first micron below the surface [3].
On the theoretical side, recent ab initio calculations have predicted the stability (at low temperature) of these objects [4, 5]. Their slow formation and diffusion kinetics is also a challenge for atomistic simulations. But, if one is only interested in testing their impact on cohesion, an alternative route exists. Instead of simulating the time evolution of the system, in a realistic but infinitely long way with Molecular Dynamics (MD), the equilibrium of the system, in a well chosen statistical ensemble, can be found. We choose the ensemble which most closely resembles the situation ahead of the crack tip: (μ_M,C_H,V,T), constant chemical potential of the metal, imposed concentration of hydrogen, volume and temperature. The choice of a constant hydrogen concentration, instead of chemical potential, is made to simulate diffusion controlled embrittlement. The chemical potential of the metal is imposed to let the crystal reorganize, without being limited by the slow nucleation process of the vacancies. V is constant because at least one extensive variable must be fixed to define the thermodynamical state. It does not mean that the pressure has to be zero in the system. Stretched initial configurations can be studied. To put the orders of magnitude clear, a typical experimental case could be: the formation of SaV at a precipitate/matrix interface, one micron ahead of the crack tip, where the time scale for hydrogen diffusion from the tip is of the order of several minutes, while the reorganization of the interface, in the presence of hydrogen could be of the order of a few micro seconds, which is short with respect to diffusion time, but still very long compared to the vibrational period of the atoms (pico seconds), which is the time scale of classical MD (femto second integration time step).

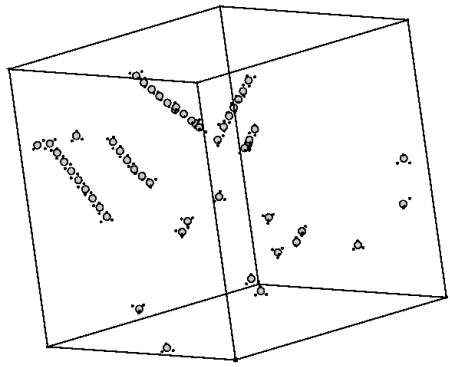


Figure 1: A snapshot of a Monte Carlo simulation at T=300K, C_H=1% at. and μ=-3.37 eV (bulk Al) [6]. Only the vacancies (large circles) and the hydrogen particles (small circles) are presented. Under these conditions, the vacancy-hydrogen clusters tend to align along dense <110> orientations of the fcc crystal.

We are especially interested in the clustering of SaV at the grain boundaries. By varying the parameters which fix equilibrium (μ_M,C_H,V,T), especially C_H, we could obtain realistic microstructures (which respect Boltzmann statistics, i.e. probable microstructures), which strength could then be characterized by MD simulations (the time scales in fracture is also an issue). To achieve this goal, we have developed a Monte Carlo method [6] which incorporates many recent developments (biased insertions, cluster moves and in some sense inherits from cavity biased methods for Grand Canonical simulations in dense systems [7-9]). It is a challenging task because the dimension of phase space is huge: three chemical species are considered (metal, hydrogen and vacancies), on two lattices (fcc and interstitial lattices), with continuous position variables (to capture the relaxations from the vacancies and from the grain boundary). In a previous paper, we have shown how this method, using Embedded Atom Method potentials for the Al-H interaction, can produce reasonably well converged SaV configurations in the bulk (Fig. 1). We now turn to the delicate task of extending the calculations to grain boundaries (GBs). Defining vacancies in a GB is not straightforward: there could be pre-melting or self diffusion, which trigger some local core rearrangements that induce the delocalization of the vacancy, i.e. the redistribution of the free volume associated to the vacancy among the surrounding atoms. This, in turn, can help collective movements of particles and eventually the re-localization of the vacancy at a position several sites away from its initial position [10]. One has to define the proper reference structure for the GB, which, if it exists, will be used to identify missing particles. In other words, the reference structure defines lattice sites, and occupation numbers attached to them. The problem is to check if this reference structure can capture, on average, the position of the particles surrounding the vacancies. This is the principal reason why we study equilibrium vacancies, in the pure metal, before moving to SaVs.

The paper is organized as follows: first, the grain boundary structure is presented; second, the reference structure is built and its efficiency in characterizing the microstates of the system is tested by MD. The Monte Carlo (MC) method is also briefly presented. Finally, the results of MC simulations at 700K are presented. We report single vacancy concentrations and statistics of vacancy clusters along the tilt axis.

GRAIN BOUNDARY STRUCTURE AT T=0

The grain boundary (GB) chosen is the Σ=33(554)[1-10] symmetrical tilt boundary. It has a large Coincidence Site Lattice unit cell (CSL): Σ=33 (Fig. 2). Each CSL is composed of 4 structural units: 2 E units and 2 D units (Fig. 2). D units are twins and therefore are composed of lattice sites very much like bulk sites. On the contrary, E units are very heterogeneous. They are the preferential host sites for vacancies, especially the E_1 site where the vacancy formation energy at T=0 is E_f^v=0.47 eV (bulk value 0.69 eV). A nice feature of this boundary is that its structural units enter in the composition of a whole family of tilt boundaries of axis [1-10]. By changing the misorientation angle, the proportion of E units can be increased and so the

density of hosts sites for defects. This opens the possibility to investigate structure controlled embrittlement sensitivity.

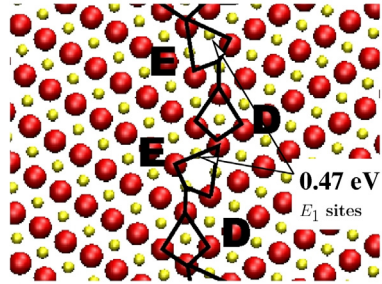


Figure 2: Symmetrical tilt boundary Σ=33(554)[1-10] at T=0. It is composed of two structural units, labelled E and D. The lowest vacancy formation energy is obtained on sites E_1: E_f^v =0.43 eV at T=0 (E_f^v=0.69 eV on a bulk site).

MONTE CARLO SIMULATIONS IN THE GRAND CANONICAL ENSEMBLE

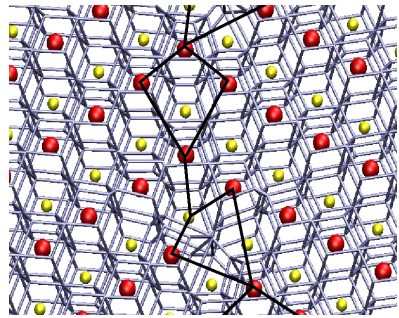


Figure 3: A Voronoï decomposition of space is used in the Monte Carlo simulation. The nodes are the relaxed positions of the particles at T=0. Occupation numbers are affected to these nodes. When a node is occupied, the particle performs a random walk inside the cell defined by the Voronoï construction around the node. Meanwhile, spin flips (changes of occupation numbers) are proposed to equilibrate the vacancy concentration.

Monte Carlo (MC) simulations generate a (Markov) chain of microstates, which, if the chain is long enough, give a statistical representation of the equilibrium of the system. The macroscopic (or mesoscopic) equilibrium is defined by the set of

thermodynamic variables (μ_M,V,T), where we have dropped C_H since we are going to discuss only vacancies in pure metal. On can view this chain as a series of snapshots of the system, each snapshot showing how many particles are in the volume V and the position of each particle. μ is fixed, so the total number of particles fluctuates. Imagine the chain is infinite, then the number of times a microstate appears should be proportional to its Boltzmann weigth. It is not interesting to know all this information in detail. The qualities relevant at the meso/macro scale are averages, more specifically average vacancy concentrations on the sites of the GB. These are the probabilities of finding a vacancy at a specific location. These averages are simply made over the snapshots in the chain.

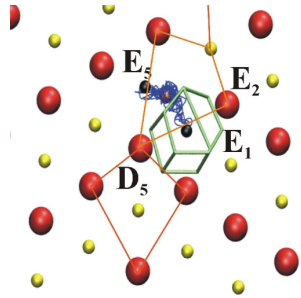


Figure 4: Schematic representation of an MD trajectory (in blue) of the first neighbor (E_5) of a vacancy on an E_1 site. In black are the nodes positions.

The critical point is the definition of the microstates, since we have to identify the vacancies. We use the following procedure: the GB structure is relaxed at T=0 by quenched MD; the relaxed positions are used to define a rigid lattice which will be the reference structure for the MC simulations at finite temperature. These fixed positions are called nodes. The nodes are used to define a Voronoï decomposition of the volume V (Fig. 3) i.e. each node is surrounded by an elementary volume V_n (where n is the index of the node) which contains all the points closer to this node than to any other one. This volume is referred to as the ``cell''. To each node are attached two quantities: the occupancy number p_n, which is 0 if the cell does not contain any particle and 1 otherwise; and, if p_n=1, a vector $\vec{u}_n$ which is the displacement of the particle from the node. Each cell is occupied by no more than one particle (self interstitials are forbidden). If the volume V is decomposed in M cells, microstate is defined by $\left(\{p_n\}^M,\{\vec{u}_n\}^N\right)$ where N is the number of particles, M-N is the number of vacancies. $\langle p_n \rangle$ is the average occupancy of node n i.e. the probability to find a particle on that site. $1-\langle p_n \rangle$ is the concentration of vacancies on that site. The averages are taken over the snapshots which constitute the chain.

The chain is constructed by the Metropolis algorithm. Starting from a microstate A, several moves are proposed: particle displacements (to $\vec{u}_n$ is added a random

increment, but in such a way that the particle stays in its cell), ``spin flips" (a p_n value is switched), particle exchanges (an empty and a filled cell are exchanged). The transition to a new microstate is accepted with a probability based on the ratio of the Boltzmann weights of the two states.

This model breaks down if the nodes do not correspond, within some reasonable distortions, to the equilibrium position of the particles. When vacancies are considered, the neighbors experience large relaxations and might be stabilized at new equilibrium positions. We have performed intensive MD simulations to study the dynamics of the neighbors of the vacancies sitting on sites E_1. Figure 4 presents the most important findings. Site E_1 is the one which has the highest probability to host a vacancy. When a vacancy is placed anywhere in the GB, it diffuses until it gets trapped at an E_1 site. MD simulations at T=700K are therefore performed with a starting configuration where E_1 hosts a vacancy. The most affected neighbor is the particle originally sitting on site E_5. It becomes ``delocalized", i.e. its vibrational amplitude is greatly enhanced as it visits both sites E_1 and E_5. On average, it spends more time inside the E_5 cell, with a new equilibrium position shifted towards E_1 (orange sphere on Fig. 4), but still inside cell E_5. Therefore, no new equilibrium positions are created which require the refinement of the grid. The occupancy numbers are truly representative of the localization of the particles and the vacancies in the system. MC simulations based on this representation o the microstates can be run safely.

We have also shown that forbidding boundary crossings between empty and filled cells leads to errors of 7% of the formation free energy of the vacancy. As this value cumulates when vacancy clusters are considered, it can lead to serious errors. Therefore, boundary crossings are important features of the Monte Carlo method.

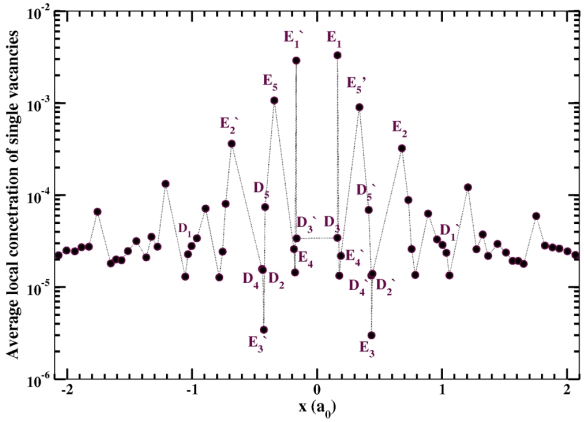


Figure 5: Profile of the average thermal vacancy concentrations obtained by Monte Carlo simulation at T=700K, μ=-3.54 eV (Al) [11]. The volume is constant and adjusted to have zero stress perpendicular to the grain boundary.

EQUILIBRIUM VACANCY CONCENTRATIONS

Figure 5 shows the vacancy concentration profiles perpendicular to the GB obtained at T=700K and μ=-3.54 eV. Each point represents one GB site, but also the plane composed by all the equivalent sites in the different CSL (the system has a periodicity along the tilt axis and perpendicular to it). The computational cost is heavy because the occupations and the positions are sampled at the same time, but these results show that it is possible to reach good statistics. We have also run the simulations long enough to obtain converged vacancy cluster concentrations. Up to five vacancies have been found to align along the tilt axis, on E_1 sites. More results and details can be found in [11], together with a lattice model and free formation energies which confirm that the calculations have converged.

CONCLUSION

We have extended our Monte Carlo simulation method to treat the problem of computing realistic vacancy concentrations at the core of grain boundaries. The next step is to add hydrogen particles and quantify how they boost the vacancy concentrations at low temperature (T=300K). The main focus will be in varying the H concentration and monitor the degree of SaV saturation in the GB. We believe this is a key element in the understanding of the loss of mechanical strength of the grain boundaries in fcc crystals.

ACKNOWLEDGMENTS

This work is supported by the French Agence Nationale de la Recherche under project H-inter (number ANR-06-BLAN60231), CECAM (Centre Européen de Calcul Atomique et Moléculaire, Prof. Mareschal) and Région Rhône-Alpes.

[1] Y. Fukai, The Metal Hydrogen system, 2nd edition (Springer, 2005).
[2] H. K. Birnbaum, C. Buckley, F. Zeides, E. Sirois, P. Rozenak, S. Spooner, and J. S. Lin, J. Alloys Comp. 253-254, 260 (1997).
[3] R. P. Gangloff, in Cracking of Metals (EICM-2), edited by S. Shipilov (Elsevier Science, Oxford, UK, 2005).
[4] Y. Tateyama and T. Ohno, Phys. Rev. B 67, 174105 (2003).
[5] G. Lu and E. Kaxiras, Phys. Rev. Lett. 94, 155501 (2005).
[6] D. Tanguy and M. Mareschal, Phys. Rev. B 72, 174116 (2005).
[7] W. C. Swope and H. C. Andersen, Phys. Rev. A 46, 4539 (1992).
[8] K. Bagchi, H. C. Andersen, and W. C. Swope, Phys. Rev. Lett. 76, 255 (1996).
[9] W. C. Swope and H. C. Andersen, J. Chem. Phys. 102, 2851 (1995).
[10] M. R. Sørensen, Y. Mishin, and A. F. Voter, Phys. Rev. B 62, 003658 (2000).
[11] E. Vamvakopoulos and D. Tanguy, Phys. Rev. B (accepted).
Email: evamvak@yahoo.com, (E. Vamvakopoulos now at Univ. Ioanina, Greece)
Email: tanguy@emse.fr

Effects of Hydrogen on Materials
Proceedings of the 2008 International Hydrogen Conference
Brian Somerday, Petros Sofronis, Russell Jones, editors, p 678-685
Copyright © 2009 ASM International®
All rights reserved.
www.asminternational.org

EFFECTS OF THE DENSITY OF STATES ON THE STACKING FAULT ENERGY AND HYDROGEN EMBRITTLEMENT OF TRANSITION METALS AND ALLOYS

Jonathan A. Lee

NASA-Marshall Space Flight Center
Materials & Processes Laboratory
Mail Code EM30
Huntsville, AL 35812

ABSTRACT

Previously, a quantitative correlation was proposed between the density of states at the Fermi energy level N (E_f) and the hydrogen (H) embrittlement for several transitional metals, binary alloys, and complex alloys. The correlation was based on the d-band electron filling and charge transfer between H electron and metals, which are characterized by the electron-to-atom (e/a) ratio. This paper expands the scope of this theory by reviewing the effects of N (E_f) on the Stacking Fault Energy (SFE), and the correlation between the SFE and H embrittlement for Fe-Ni, Fe-Co, Ni-Co, Ni-W, Cu-Ni and Pd-Ag binary alloys. The paper presents a concept which is contrary to the hydrogen-dislocation transport (HDT) model. According to the HDT model, increasing susceptibility to H embrittlement would occur with decreasing SFE since increased slip planarity would optimize H transport by dislocations to the fracture sites. In this paper, the argument is that metals with low SFE may increase the slip planarity, but it may not necessarily result in increasing susceptibility to H embrittlement. Experimentally, it is found that maximum in H embrittlement does not often coincide with the minimum SFE values for several binary alloy systems. It is proposed that H embrittlement is likely to increase if the value for N (E_f) from the metal is high due to the presence of the unfilled d-states. It is also proposed that the introduction of H electrons into the d-band metals will result in a reduction of high N (E_f) values, thereby, decreasing SFE for metals that are susceptible to H embrittlement.

INTRODUCTION

This paper expands the scope of a hydrogen (H) embrittlement theory presented previously in 1994 at this conference-series on H effects on materials [1]. This work is based on the concept that H embrittlement is related to a quantum property called the electron density of states at the Fermi energy level N (E_f). In recent years, the relationship between electronic structure and mechanical properties of materials has received considerable attention, with the development of atomistic models of fracture mechanics [2, 3]. However, the atomistic modeling of mechanical behaviors has limited practicality, or lacks computational capabilities in order to provide accurate information or prediction for mechanical properties. In the case of predicting H embrittlement, the atomistic models have yet to provide satisfactory predictions for many engineering alloy systems. On the other hand, despite great progress on the understanding of mechanical properties based on the treatment of dislocation-movements and interaction with the crystal lattices [4, 5], the quantitative prediction of H embrittlement behaviors are not satisfactory within the frame work of classical dislocation theory, which usually neglects to address the reduction of metal's bonding strength (cohesive energy) based on the complex electronic charge transfer (electrochemical interaction) between the H electrons and the host metal's electrons.

The proposed theory is a semi-empirical model to allow successful H embrittlement prediction for many transition metals and alloys. The basis of the theory is summarized as follows: since the cohesive strength of a transition metal is governed by the bonding energy of the d-electrons [6] occupied near the Fermi energy level (E_f), the theory proposes that H embrittlement effect is a reduction of the bonding energy of the metal atoms by the introduction of the H electrons into the d-band of the host metal. In general, the N (E_f) value describes the number of electron states that are available to be occupied. If there is limited number of states available for the H electrons to occupy the host metal's electron band at the Fermi level, then H embrittlement is expected to be minimal. In other words, H embrittlement is likely to increase if the value of the N (E_f) from the host metal is increased. It has been shown that H solubility in transition metals could be correlated with the N (E_f) values, according to M. R. Louthan [7], who showed that H solubility increases with increasing electron density of states at the Fermi level. Louthan also suggested that susceptibility to H embrittlement is at least partially dependent on the solubility of H atoms in the host metal, which is a worthy notion to partially support the basis of this theory based on the concept of N (E_f).

RESULTS

Relationship between H Embrittlement and N (Ef)

According to the Debye theory on the specific heat of metals at low temperatures [8], the N (E_f) values for certain metals can be estimated from experimental data for the electronic specific heat coefficients (ESHC). It was shown in the previous paper [1] that a semi-empirical method, which was derived by A. R. Miedema [9], could be used to calculate the ESHC values for binary alloys, based on the d-band electron filling, work function, charge transfer, and the change in the electron-per-atom (e/a) ratio, which takes place upon alloying. It is noteworthy that the plot of ESHC versus e/a, as derived from Miedema, is not the same from the classical "rigid band" model. Nevertheless, using these values for ESHC, the validity of this H theory presented in [1] is good, with excellent H embrittlement predictions for several transition elements, binary and ternary alloys. It was found that the H embrittlement property can vary systematically in going from one element to the next as arranged in the periodic table as 3d, 4d and 5d electron band for transition metals. If we know the position of a transition element, arranged in the periodic table as the atomic number (Z_i), and have a rough idea of how the ESHC values vary across a row or down a group, we can make a fair guess for the H embrittlement of another element positioned near by this Z_i value. This observed trend seems to echo the visual representation of the periodic table law, which states that certain properties of the elements repeat periodically when arranged by the order of increasing atomic number [10].

While the role of e/a ratio and charge transfer are well recognized in the study of phase stability of solid solutions, intermetallic compound formation, and liquidus temperatures in metals and alloys [11], we propose that H embrittlement property can also be characterized by the e/a ratio. Figure 1 shows the predicted H embrittlement index (right vertical axis) as a function of e/a ratio, for transition elements and their adjacent binary alloys, based on the values for ESHC (left vertical axis) as suggested by Miedema. In this paper, the H embrittlement index, originally calculated in terms of percent reduction of ductility or notch tensile strength ratio test in H and in an inert environment at high pressures [1], has been simplified into five categories: negligible, small, moderate, severe, and extreme. With the addition of the "moderate" category, the practicality of this proposed H embrittlement classification is actually not a new idea. It is based on a well-known H embrittlement database with practical classification guide as published by the ASTM and AIAA sourcebook [12, 13].

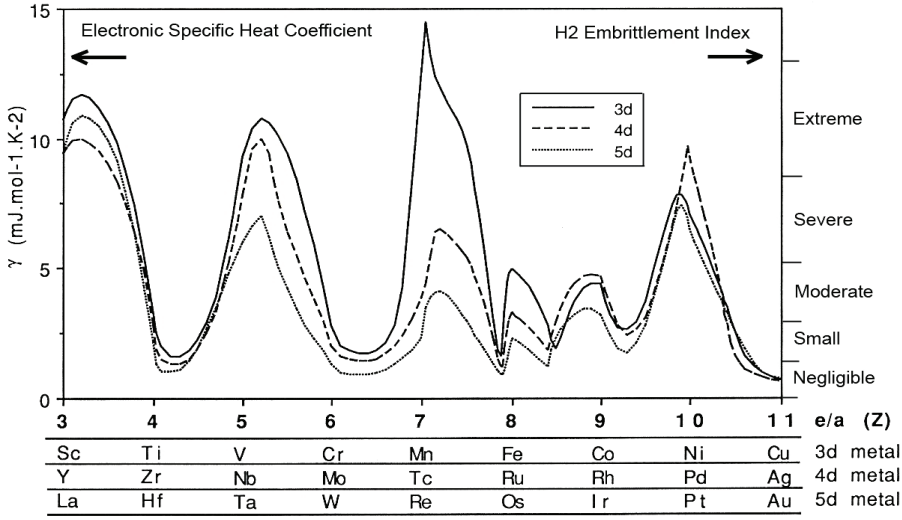


Figure 1: Predicted H embrittlement index (right vertical axis) as a function of e/a ratio, for all transition elements and their adjacent binary alloys, based on the curves for ESHC as suggested A.R. Miedema (left vertical axis).

Relationship between N (Ef) and Stacking Fault Energy (SFE)

Having shown the correlation between N (E_f) and H embrittlement from previous work [1], this paper now expands the scope of the theory by briefly discussing the N (E_f) effects on the Stacking Fault Energy (SFE), in an attempt to present some correlations between SFE and H embrittlement. Since SFE influences the mechanical properties, the subject of SFE and the effects of H embrittlement have been reported by several researchers with some contradicting results. Furthermore, the hydrogen-dislocation transport (HDT) model has been used to some extend by many researchers in order to explain the influence of SFE upon the H embrittlement effects of metals. This paper proposes a concept that is contrary to the HDT model, and one of its goals is to show that metals with low SFE may increase the slip planarity, as suggested by the HDT model, but it may not necessarily result in increasing susceptibility to H embrittlement.

According to I. R. Harris [14] the influence of d-electron band structure for transition metals and binary alloys on the SFE has been proposed, and the correlations between SFE and the e/a ratio for copper and silver binary alloys have been shown by P.C. Gallagher [15]. There is a strong agreement amongst researchers that a correlation between N (E_f) and SFE does exist. However, the exact relationship between N (E_f) and SFE could be contradictory based on experimental data for some systems. For example, N. I. Noskova [16] and A. A. Ogwu [17] proposed that SFE is inversely proportional to N (E_f) for pure transition metals and intermetallics; while other workers have showed that it is directly proportional to N (E_f) for binary alloys [14,18,19]. The discrepancy amongst these studies could be the fact that experimental values for SFE are difficult to measure accurately and can vary by an order in magnitude for some metals. For example, it has reported that SFE for pure nickel [20] can vary from 79 mJ/m^2 to 415 mJ/m^2, and for tungsten [16, 21] from 50 mJ/m^2 to more than 300 mJ/m^2. Large discrepancy in SFE values could also come from different experimental techniques that have been used by various researchers with different levels of sensitivity, temperatures, material purities and processes [22, 23]. Perhaps, the large variation in the SFE values could be a result from the increased in complexity of charge transfers from the 4s- and 3d electrons near the Fermi level for certain alloy systems.

For complex alloys with chemical compositions derived from several transitions metals, it would be useful to see whether a correlation between N (E_f) and SFE would exist. Recently, two studies on the effects of nitrogen content on austenitic steels have reported that a correlation between N (E_f) and SFE for complex alloys does exist. According to V. Gavriljuk [24], the N (E_f) has been found to be directly proportional to the SFE for Cr18Ni16Mn10 steel and inversely proportional to the SFE for Cr15Mn17 steel as shown in Figure 2. This direct correlation for Cr18Ni16Mn10 has also been confirmed by Y. Petrov [25], who shows that a direct correlation between SFE and the number of free electron concentration (e_f/a). This has a similar representation to the N (E_f) as shown in Figure 3A. It is still unclear as to why the N (E_f) is inversely proportional to SFE for Cr15Mn17 steel, yet it was found to directly proportional to the number of plasma electron concentration (e/a) as shown by Y. Petrov in Figure 3B. Additional work is necessary in order to understand the mechanism of this relationship for austenitic steels. Nevertheless, one can wonder if there would be an inverse or direct correlation between SFE and H embrittlement, at least for simple binary alloys.

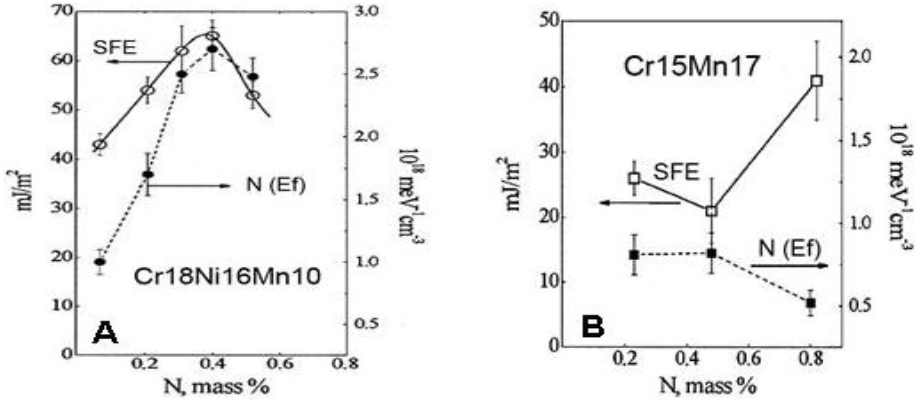


Figure 2: Direct and inverse correlation between N (E_f) and the SFE on the nitrogen content in austenitic steels for Cr18Ni16Mn10 and Cr15Mn17. [Data from Ref. 24].

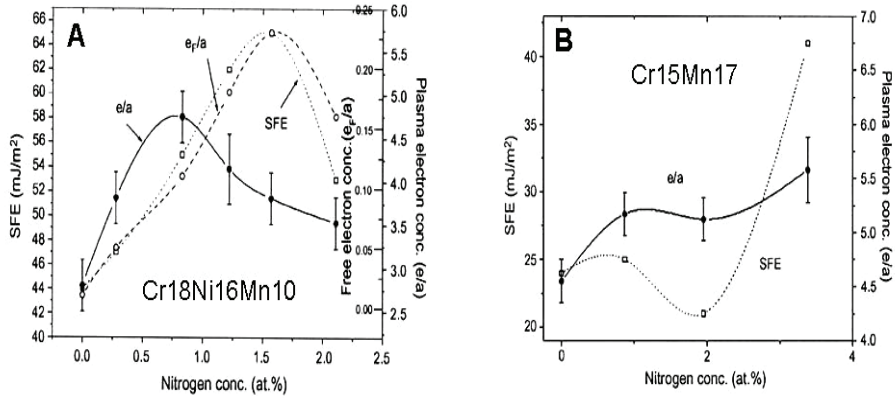


Figure 3: Correlation for free electron and plasma electron concentrations versus SFE on the nitrogen content in austenitic steels for Cr18Ni16Mn10 and Cr15Mn17. [Data from Ref. 25]

Correlation between SFE and H Embrittlement

Cu-Ni and Pd-Ag binary alloys have been selected for this study because they form a complete range of single-phase solid solution, and they are also positioned on the periodic table as adjacent transition elements in the 3d and 4d band metals, respectively. Positioned next to Cu and Ag in the periodic table, the SFE values for Ni and Pd metals are high, but for Cu and Ag the SFE values are low. It is important to recognize that the N (E_f) values for Pd and Ni are high because their 3d and 4d electron bands are partially filled, and Cu and Ag have low N (E_f) values because the d-electron bands are completely filled [14]. Experimental data for Cu-Ni alloy are taken from [1, 26], and the data for Pd-Ag alloy from [27, 28]. Figure 4 shows that a direct correlation between SFE and H embrittlement is observed for both Cu-Ni and Pd-Ag. It is also found that the H embrittlement effects would become negligible when SFE falls below an approximate value of ~40 mJ/m^2. For both Cu-Ni and Pd-Ag alloys, the on-set value for negligible H embrittlement effects occurs when either the Cu or Ag content in their binary alloy is approximately >60 wt.%. The significance of this 60 wt.% value for Cu and Ag will be explained further in this paper based on the d-band filling by H electrons.

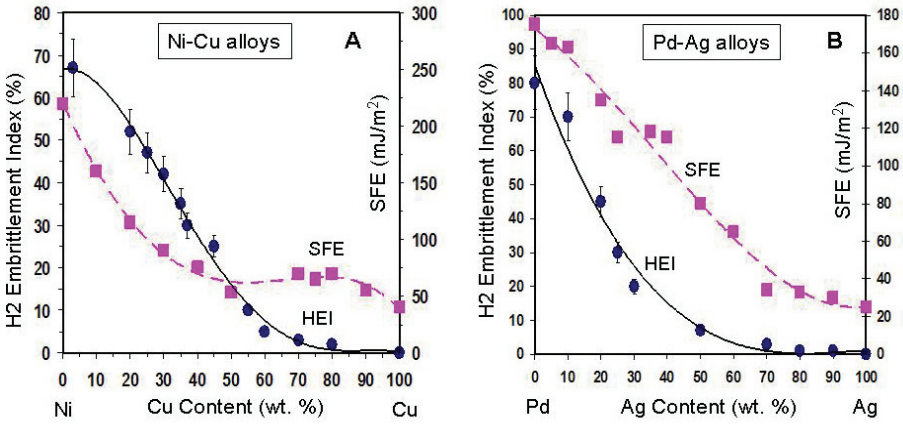


Figure 4: Direct correlation between SFE and H embrittlement for Ni-Cu and Pd-Ag alloys.

Co-Ni has been selected for this study because it also forms a continuous range of solid solution, and the Co and Ni element are also positioned adjacent to each other on the periodic table. Fe-Ni has been selected because H embrittlement and N (E_f) data are available based on Miedema calculation scheme as shown in a previous study [1]. Experimental data for Co-Ni alloy are taken from [1, 29, 30, 31], and the data for Fe-Ni alloy are from [1, 32, 33]. Figure 5 shows a direct correlation between SFE and H embrittlement for both Co-Ni and Fe-Ni alloy. In these systems, the correlation is similar to the Cu-Ni and Pd-Ag systems: it is found that H embrittlement effects increase proportionally to the increasing values of SFE. For Co-Ni alloys, H embrittlement effects would become negligible when SFE falls below an approximate value ~40 mJ/m^2, and the embrittlement effects appear to be minimal when Ni is kept approximately 20 wt.%. A similar trend is observed for Fe-Ni alloys with H embrittlement appear to be minimal, when SFE falls below 40 mJ/m^2, corresponding to a Ni content of approximately 40 wt.%.

Using available SFE data measured for Fe-Co alloy from T. Tisone [34], with compositions ranging from 6 to 12 atomic % Fe, when comparing the SFE values against the experimental HEI data taken from [1], it is found that H embrittlement effects increase proportionally to the increasing values of SFE. Similarly, from limited SFE data for Ni-W alloy by T. Tiearney [35], with compositions ranging from 0 to 12 % atomic tungsten, it is found that SFE also vary directly with H embrittlement data from previous experimental work at NASA (unpublished data).

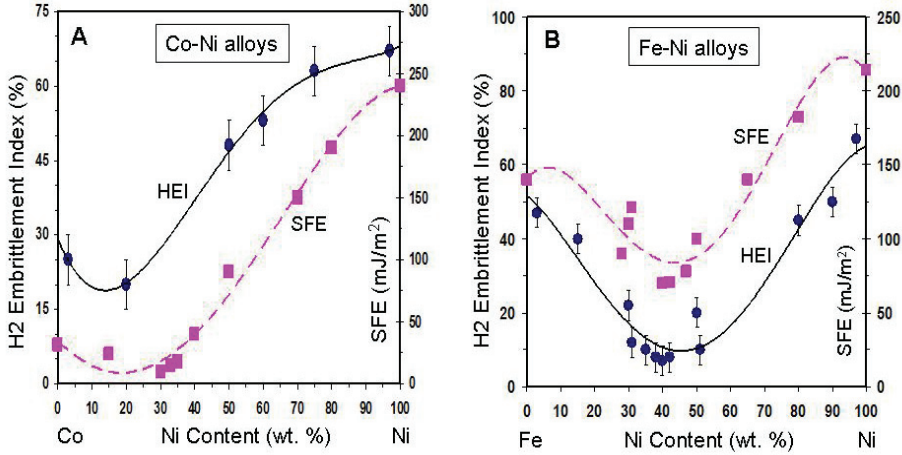


Figure 5: Direct correlation between SFE and H embrittlement for Co-Ni and Fe-Ni alloys.

The behaviors as observed in Figs. 4 and 5 can be interpreted as follows: according to I.R. Harris [14], the presence of the unfilled d-states results in high values of N (E_f) and SFE for Ni and Pd, which have approximately 0.55 and 0.60 electron holes per atom, respectively. From Fig. 4, the values for SFE seem to reach their minimal points at roughly 55 wt. % Ni and 60% wt. Ag for Cu-Ni and Pd-Ag alloy, respectively. This behavior can be interpreted in terms of filling up of the electron holes in the d band of Ni and Pd with available electrons from Cu and Ag atoms. The result is that a filled d-state will lead to lower values for the N (E_f) and SFE in comparison to the unfilled d-states. Since the cohesive strength is related to the bonding energy of the d-electrons [6], this paper proposes that H embrittlement is a reduction of the cohesive strength by the introduction of the H electrons to the unfilled d-bands. When the d-band is nearly full by alloying at certain compositional ranges, the H embrittlement effect is expected to be minimal. Indeed, it was found that the H embrittlement effect is minimal at roughly 55 wt. % Ni and 60% wt. Ag for Cu-Ni and Pd-Ag alloy, respectively.

Similar explanation, based on the presence of unfilled d-states, is suggested for the H embrittlement for many binary alloys investigated previously in [1]. Interestingly, it is observed that H embrittlement effects would appear to be minimal when SFE falls below an approximate value of ~40 mJ/m^2. However, this minimum value may not be universal based on the brief discussion from the previous section concerning austenitic stainless steels and the inaccuracy of measuring SFE values. For example, experimental data from the literature for the SFE of austenitic AISI 310 steel alone can vary significantly from 40 mJ/m^2 to 104 mJ/m^2 [36].

DISCUSSION

This paper presents a collection of a data on a large set of binary alloys. The evolution of the SFE and H embrittlement index, as a function of the alloy composition, shows some similar trend. In these systems, it seems that a low value of SFE is correlated to a low susceptibility to H embrittlement. This finding is not in agreement with the HDT model as known in [37-39]. According to the HDT model, increasing susceptibility to H embrittlement would occur with decreasing SFE, since increased slip planarity would optimize H transport by dislocations to the fracture sites. A. W. Thompson suggested that such enriched regions of H at fracture sites could somehow assist the fracture process that leads to H embrittlement through enhanced void nucleation [40]. This notion of H enhanced void nucleation by HDT has been disputed by C. E.

Price [41]. In another case, D. M Symons [38] used the HDT model to explain the H embrittlement mechanism of Fe-Cr-Ni alloys, yet he also recognized in his study that enhanced slip planarity, due to low SFE, did not affect the fracture behavior of the H uncharged specimens. In reference to the SFE study on Co-Ni alloy, Tang and Thompson [37] questioned the effectiveness of the HDT model by stating that their "result certainly demonstrates that a correlation among (high) SFE and H-induced ductility losses can not be general". In this paper, the argument is that metals with low SFE may increase the slip planarity, but it may not necessarily result in increasing susceptibility to H embrittlement. Indeed, experimental data presented in this paper have shown that the maximum H embrittlement does not always coincide with the minimum SFE values.

It is proposed that H embrittlement is likely to increase for metals with relatively high N (E_f) value. In most cases, presence of a large unfilled d-state is believed to result in a large increase of N (E_f) and subsequently an increase in SFE value. However, because of the complex charge transfer between the free and plasma electron concentrations as explained in [25], the increase in N (E_f) values may not necessarily lead to an increase in SFE values for some complex metal systems. For example, the N (E_f) is inversely proportional to SFE for Fe-15Cr-17Mn but directly proportional to Fe-18Cr-16Ni-10Mn austenitic steels [24]. It is proposed that the introduction of H electrons into the metals could reduce the N (E_f) values, thereby; result in a decreasing SFE for materials that are susceptible to H embrittlement. This behavior can be interpreted in terms of filling up of the electron holes in the d band with available electrons from H, similar to alloying effects. Indeed, the H effects of decreasing the N (E_f) and SFE of metals have been confirmed by several researchers [42- 45].

The relevancy of plotting SFE against some mechanical properties has been questioned by P. Coulomb [46] and A. King [47], who suggested that experimental values for some SFE are very difficult to measure accurately, and the exact definition and role of SFE for B.C.C and H.C.P metals are not so well understood. Therefore, it has been suggested that some SFE values should be regarded as merely qualitative parameters rather than quantitative when plotting against another mechanical property for certain metals. Moreover, the direct or inverse relationship between N (E_f) and SFE is still unclear for some complex alloys such as austenitic steels. Nevertheless, experimental data for SFE as presented in this paper appear to correlate well with N (E_f) for Fe-Ni, Fe-Co, Ni-Co, Ni-W, Cu-Ni and Pd-Ag alloys, possibly because the effects of N (E_f) on the SFE are well understood based on the d-electron band filling scheme for these specific binary alloys. Therefore, this paper suggests that N (E_f) as derived by A. R. Miedema should be used primarily, in conjunction with certain SFE data as a secondary source, to strengthen the predicting capabilities for H embrittlement.

CONCLUSION

1. It is proposed that H embrittlement is a reduction of the bonding strength of the metal atoms by the introduction of H electrons into the d-band. H embrittlement is likely to increase if the value for N (E_f) is high due to the presence of the unfilled d-states. It is also proposed that the introduction of H into the metals will likely reduce the high N (E_f) values, thereby, decreasing high SFE values for metals that are susceptible to H2 embrittlement.

2. According to the HDT model, increasing susceptibility to H embrittlement would occur with decreasing SFE since increased slip planarity would optimize H transport by dislocations to the fracture sites. The argument presented here is that metals with low SFE may increase the slip planarity, but it may not necessarily result in increasing susceptibility to H embrittlement. Evidently, it is found that maximum H embrittlement does not often coincide with the minimum SFE values. Applicable to the binary alloy systems presented here, it is observed that H embrittlement would appear to be minimal when SFE falls below an approximate value of ~40 mJ/m^2.

REFERENCES

1. J.A. Lee, "A Theory for Hydrogen Embrittlement of Transition Metals & Their Alloys," Hydrogen Effects in Materials, A. W. Thompson & N. R. Moody, eds., TMS, 1996.
2. R. Ninomiya, et al., Journ. Alloys & Compounds, **215** (1994), pp. 315-323.
3. J.M. MacLaren, et al., Phys. Rev. Lett., **63** (1989), No. 23, pp. 2586-2589.
4. C.D. Gelatt, et al., Phys. Rev. B, **15** (1977), pp. 1613.
5. F.R.N. Nabarro, Theory of Crystal Dislocations, Clarendon Press, Oxford, 1967.
6. J.P. Hirth, J. Lothe, Theory of dislocations, McGraw-Hill, New York, 1968.
7. M.R. Louthan, et al., Mat. Sci. Eng., **10** (1972), pp. 357-368.
8. F. Heiniger, et al., Phys. Kondens. Mat., **5** (1966), pp. 243-286.
9. A.R. Miedema, J. Phys. F: Metal Phys., **3** (1973), pp.1803-1818.
10. J. Sienko, et al., Chemistry Principles & Applications, McGraw-Hill, NY, 1979.
11. G.P. Tiwari, R.V. Ramanujan, Journ. Mat. Sci., **36** (2001), pp. 271-283.
12. Guide to Safety of Hydrogen & Hydrogen Systems, ANSI/AIAA, G-095-2004.
13. W.T. Chandler, R.J. Walter, "Testing to Determine the Effect of High-Pressure Hydrogen Environments on the Mechanical Properties of Metals", Hydrogen Embrittlement Testing, ASTM STP 543 (1974), pp.170-197.
14. I.R. Harris, et al., Phil. Mag., **14** (1966), pp. 325-333.
15. P.C. Gallagher, Metal. Trans., **1** (1970), pp. 2429-2461.
16. N.I. Noskova, et al., Fiz. Metal. Metall., **20**, no. 6 (1966), pp. 920-924.
17. A.A. Ogwu, T.J. Davies, Journ. Mat. Sci., **28** (1993), pp. 847-852.
18. J.M. MacLaren, "Electronic Structure of Stacking Faults in Pd-Cu, Pd-Ag, and Ag-Au Alloys", Stability of Materials, A. Gonis et al., eds., Plenum Press, NY (1966), pp. 407-412.
19. I.L. Dillamore, Metal. Trans. **1** (1970), pp. 2463-2470.
20. C.B. Carter, S.M. Holmes, Phil. Mag., **35**, no. 5 (1977), pp. 1161-1172.
21. D.A. Smith, K.M. Bowkett, Phil. Mag., **18**, (1968), pp. 1219-1233.
22. M. Ahlers, Metall. Trans., **1** (1970), pp. 2415-2427.
23. R.P. Reed, R.E. Schramm, J. Appl. Phys., **45** (1974), pp. 4705-4711.
24. V. Gavriljuk, Y. Petrov, B. Shanina, Scripta Mat., **55** (2006), pp. 537-540.
25. Y.N. Petrov, Scripta Mat., **53** (2005), pp. 1201-1206.
26. I.R. Harris, et al., Phil. Mag., **14** (1966), pp. 325-333.
27. T. Maruno, et al., J. Japan Inst. Metals, **47**, No. 9 (1983), pp. 768-775.
28. L. Dillamore, Metal. Trans., **1** (1970), pp. 2463-2470.
29. T. Ericsson, Acta Metall., **14** (1966), pp. 853-865.
30. C.M. Wan, J.G. Byrne, Int. Journ. Fracture, **11**, (1975), pp. 251-255.
31. C.K.L. Davies, et al., Acta Metall., **21** (1966). pp. 1343-1348.
32. R.E. Schramm, R.P. Reed, Metall. Trans. A, **7A**, (1976), pp. 359-363.
33. E.D. Butakova, et al, Fiz. Metal. Metall., **35**, no. 3 (1973), pp. 662-664.
34. T.C. Tisone, Acta Metall., **21** (1973), pp. 229-236.
35. T.C. Tiearney, N.J. Grant, Metall. Trans. A, **13A** (1982), pp. 1827-1836.
36. C. G. Rhodes, A.W. Thompson, Metall. Trans., **8A** (1977), pp.1901-1906.
37. X. Tang, A.W. Thompson, Mat. Sci. Eng., **A186** (1994), pp. 113-119.
38. D.M. Symons, Metall. Mat. Trans., **28A** (1997), pp. 655-663.
39. R.E. Stoltz, J.B. Sande, Metall. Trans., **11A** (1980), pp. 1033-1037.
40. A.W. Thompson, Scripta Met., **16** (1982), pp. 1189-1192.
41. C.E. Price, L.B. Traylor, Scripta Met., **17** (1983), pp. 901-904.
42. M.B. Whiteman, A.R. Troiano, Phys. Sta. Sol., **7** (1964), pp. K109-K110.
43. A.E. Pontini, J.D. Hermida, Scripta Mater., **37** (1997). pp. 1831-1840.
44. A. Juan, et al., Inter. Journ. Hydrogen Energy, **27** (2002), pp. 333-338.
45. M. Gupta, Journ. Alloys & Compounds, **293-295** (1999), pp. 190-201
46. P. Coulomb, Scripta Metall., **15** (1981), pp. 769-770.
47. A.H. King, Scripta Metall., **16** (1982), pp. 1181-1182.

Effects of Hydrogen on Materials
Proceedings of the 2008 International Hydrogen Conference
Brian Somerday, Petros Sofronis, Russell Jones, editors, p 686-693
Copyright © 2009 ASM International®
All rights reserved.
www.asminternational.org

PHYSICS OF HE PLATELETS IN METAL TRITIDES

Donald F. Cowgill
Sandia National Laboratories, Livermore, CA USA

ABSTRACT

Thin He-filled platelets bounded by an attached dislocation dipole are shown to be stable structures in fcc metals with low surface energy and high shear modulus. They can form from Griffith-like nano-cracks, grow by radial expansion of the dipole, and transition to spherical bubbles if the dislocations become detached. Formulations of gas pressures within these precipitates are tested by lattice dilation data and changes in their dimensions with age.

INTRODUCTION

Evolution of the helium bubbles and retention of He within aging palladium tritide has been described previously [1]. This model follows bubble nucleation and growth, including the effects of bubble interactions. It establishes a condition for ligament material fracture between spherical bubbles and percolates [2] this condition to widespread inter-bubble fracture and the onset of rapid He release. The model successfully accounts for the observed early He release fraction, bubble and material characteristics including bubble pressures, material swelling, and tritide plateau pressure shifts with age. Observed lognormal distributions of bubble spacing and size follow from the bubble self-nucleation process.

Application of the model to erbium tritide requires some modifications, most notably those due to differences in bubble shape and the strong reactivity of the metal with its environment. Using transmission electron microscopy (TEM), Thomas and Mintz [4] and others [5] observed spherical bubbles in Pd tritide, whereas Gelles *et al* [6] found the bubbles in Er tritide to be thin platelets. It will be shown that the shape of these He bubbles is determined by the mechanical properties of the metal hydride lattice. Platelet growth with age will be described by a multi-stage model, which begins with the opening of He-filled nano-cracks that transition to platelets. These platelets are predicted to further transition to spherical bubbles in some materials. Percolation of inter-platelet fracture and resulting rapid release of He from platelets and the effects of the surface reactivity will be described in future publications.

THE PLATELET SHAPE

High helium pressures within the spherical bubbles in fcc Pd tritide cause the bubbles to grow by the punching of prismatic dislocation loops as depicted in Fig. 1.

This is a deliberate process in which He added at each step maintains the bubble pressure. Dislocation loops are initiated at the edge of the bubble and proceed around, eventually detaching from the sphere. The bubble grows by adding a

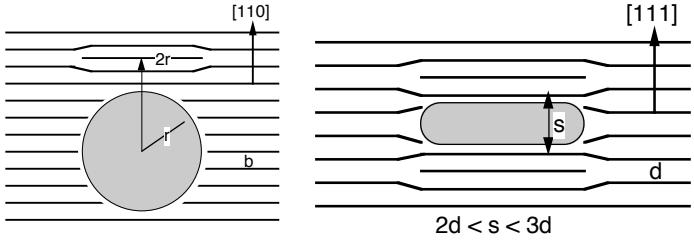


Figure 1. Dislocation loop punching from a spherical bubble and side view of a platelet surrounded by a dislocation dipole.

cylindrical segment of length b between the two hemispheres. Orientation of the segment alternates between Burgers directions of the fcc lattice, maintaining the general spherical shape. As a result of this slow process, abrupt changes in bubble pressure or lattice stress are absent; and the pressure required for a volume expansion dV has simple components due to the bubble surface energy and lattice strain energy. For a spherical bubble of radius r, at equilibrium pressure p_e

$$p_e\, dV = \gamma\, dA \quad \text{(surface energy)}, \tag{1}$$
$$p_e\, \pi r^2\, b = \gamma\, 2\pi r\, b. \tag{2}$$

Here γ is the surface energy of the material and b is its Burgers' vector in the direction of growth. To punch the loop, the bubble pressure (stress) must produce a lattice strain of b/2 in the b direction over a dislocation of length $2\pi r$. Thus, from

$$\text{stress} = \mu\ \text{strain} \tag{3}$$
$$p_s\, \pi r^2 = \mu\, [(b/2)/d]\, 2\pi r d, \tag{4}$$

where μ is the shear modulus in the b direction. Summing p_e and p_s gives Trinkaus' pressure [7] for growth by dislocation loop punching (LP)

$$p_{LP} = 2\gamma/r + \mu b/r. \tag{5}$$

Other more complicated expressions for loop punching that contain pressure change effects do not appear to fit the available aging data on Pd tritide [1].

Imagine now a thin He-filled platelet located between the relatively open (111) planes of an fcc lattice as shown in Fig. 1, where d is the planar spacing. If the adjacent (111) planes are each displaced by more than d/2 but less than d, dislocation loops will be created, but not escape. They will remain trapped within the strain field of the platelet, adding a dislocation dipole to the structure. The addition of He

causes the platelet structure to grow radially by adding metal atoms to the dislocation in a spiral fashion, provided its plane-to-plane thickness s remains less than 3d. Using an annular volume expansion in Eq. (1) gives

$$p_e \pi[(r+b)^2 - r^2]\, s = \gamma\, 2\pi[(r+b)^2 - r^2 + (r+b)s - rs] \quad (6)$$
$$p_e = (2\gamma/s)\,[(2r+b+s)/(2r+b)]. \quad (7)$$

Similarly, the strain equation Eq. (3) becomes

$$p_s \pi[(r+b)^2 - r^2] = \mu\,[(d/2)/b]\, 2\pi[(r+b) - r]\, b \quad (8)$$
$$p_s = \mu d/(2r+b). \quad (9)$$

Combining Eqs. (7) and (9) gives the pressure for growth by dislocation dipole expansion (DE)

$$p_{DE} = (2\gamma/s)\,[(2r+b+s)/(2r+b)] + \mu d/(2r+b) \quad (10)$$
$$\approx 2\gamma/s + \mu d/2r,$$

where the approximation holds at large values of r/s.

The first terms in Eqs. (5) and (10) result from the surface energy and the second from the strain energy. For materials with a high surface energy, minimization of the total energy favors a spherical shape; whereas for materials with a high shear modulus, platelets are preferred. Material parameters for the two tritides mentioned above, Pd and Er, are given in Table 1. It appears that the platelet-shaped bubbles in Er tritide are caused by a low $\gamma/\mu b$, the ratio of surface energy to strain energy.

Table 1. Surface and strain energy parameters of Pd [1] and Er [8,9] tritides. (Surface energies are approximated by those of the metals.)

Tritide	γ(GPa-nm)	μ(GPa)	b(nm)	ν	$\gamma/\mu b$
Pd	1.54	33.6	.2852	.381	0.16
Er	0.637	57.4	.3623	.238	0.03

Bubble pressures corresponding to loop punching from spheres, Eq. (5), and dipole expansion for platelets, Eq. (10), in the two materials are plotted in Fig. 2a, as a function of precipitate major radius r. For Pd tritide, p_{LP} is lower than p_{DE} over much of this range of r. Thus these bubbles grow by loop punching and are spherical. For Er tritide, the opposite is true, p_{DE} is lower than p_{LP}, and platelets are the preferred shape. At large r, the situation appears to change for the Er system; however, an examination of the projected platelet area shows that such large platelets should interconnect before this radius is reached. Interestingly, the plot also indicates platelets should be initially preferred in Pd tritide when r<2.5 nm.

It may be argued that the bubbles in fcc materials should all evolve from He-filled nano-cracks. He atoms should accumulate in the relatively open space between

(111) planes in planar-coordinated adjacent octahedral sites. This He will spread the metal planes elastically to form Griffith-like nano-cracks (NC) with internal pressure given by [10]

$$p_{NC} = 4\gamma/s \quad (11)$$
$$s = 4[\gamma(1-\nu)r/\pi\mu]^{1/2}. \quad (12)$$

Here, s is the full crack width and ν is Poisson's ratio. After s opens to 2d, the addition of more He will cause dislocations to be generated at the crack tips. A high resolution TEM image of such a structure during its formation appears to have been captured by Thiebaut *et al* [5] in Pd tritide after 3 months of aging. Careful examination of the lattice planes in Thiebaut's figure 3 shows a dislocation forming at one end of a 2 nm long planar interstitial defect but not yet at the other end.

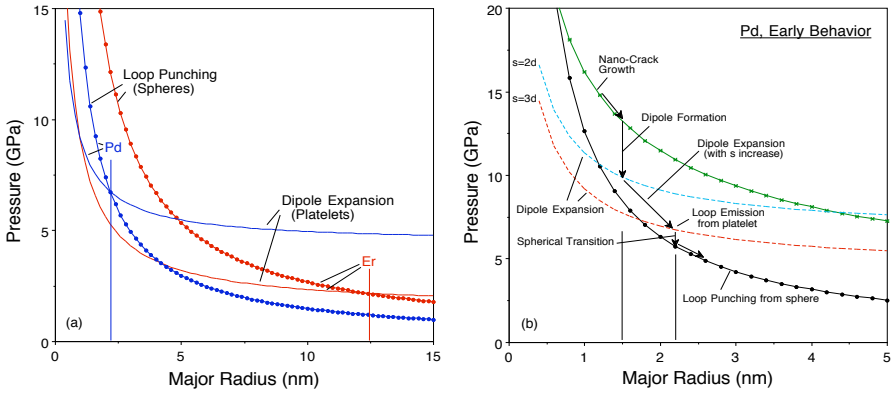


Figure 2. (a) He bubble pressures in Pd and Er tritides as determined by dislocation loop punching (•), Eq. (5) and dipole expansion (-), Eq. (10) processes. (b) Early stages of bubble growth in Pd tritide showing transition from nano-cracks to platelets to spherical bubbles.

Thus the early growth of bubbles in Pd tritide should involve multiple shapes, as described in Fig. 2b. The active shape and growth mechanism is determined by the lowest energy, provided this shape is accessible. Helium first collects between (111) planes opening nano-cracks described by Eqs. (11) and (12). As He is added, the crack radius r and thickness s increase. When s=2d, a lower-pressure (lower-energy) dislocation dipole configuration forms and the precipitate pressure decreases to that required for dipole expansion, given by Eq. (10). With additional He, the dipole expands and s continues to slowly increase. Equation (12) continues to remain valid as long as the dislocations and their strain fields remain attached to the precipitate. When s=3d, the dipole escapes. At this loop emission point, transition to the spherical shape begins and

$$p_{LE} = (2\gamma/s)[(2r+b+s)/(2r+b)] + (\mu b/r)(b/d). \quad (13)$$

That is, the He pressure is composed of the surface energy of a platelet and the strain energy for loop-punching increased by $b/d = (3/2)^{1/2}$, a factor resulting from the fact that loops are punched along [110] Burgers directions rather than normal to the platelet. Additional loops continue to be punched along Burgers directions increasing the precipitate thickness and dropping its pressure until it becomes a sphere, after which, the pressure is given by Eq. (5). Transition points between stages are given by the intersections of the curves in the figure.

LATTICE DILATION

Testing of the precipitate pressure formulations for the various shapes and their transitions is provided by lattice dilation data on aging tritides. Tensile stress created by the precipitates produces a positive da/a. For spherical bubbles at the loop-punching pressure, this hydrostatic tensile stress balances the excess bubble pressure $p_{LP}'=p_{LP}-2\gamma/r$, or

$$p_{LP}' (dV/V) = B^* (3\ da/a)_{LP.} \tag{14}$$

Here, $dV/V = (4/3)\pi r^3 n_B$ is the material's bubble volume fraction, n_B is the bubble density, and B* is the effective bulk modulus of aged material [11]. For platelets growing by dipole expansion, the [111] tensile stress balances the excess platelet pressure $p_{DE}'=p_{DE}-(2\gamma/s)[(2r+b+s)/(2r+b)]$, or

$$p_{DE}' (dA/A)\ 4/3^{1/2} = E^* (da/a)_{DE,} \tag{15}$$

where $dA/A = \pi r^2 (n_B/4)^{2/3}$ and E* is the Young's modulus of aged material [11]. Here there are four sets of platelets in the four (111) planes, each with material area fraction dA/A producing a projected stress of $1/3^{1/2}$ along each of the [100] axes.

From Eqs. (14) and (15), the lattice dilations produced by the two bubble shapes are given by

$$(da/a)_{LP} = (1/3\ B^*)\ p_{LP}'\ (dV/V) \tag{16}$$
$$(da/a)_{DE} = (4/3^{1/2}\ E^*)\ p_{DE}'\ (dA/A). \tag{17}$$

Numerical evaluation of these two expressions shows that the first factor in Eq. (17) is about 5 times that in Eq. (16), while $dA/A \approx 3\ dV/V$ for r=1 nm bubbles at the typical $n_B=10^{24}$ bubbles/m^3. Thus $(da/a)_{DE} \approx 15\ (da/a)_{LP}$; i.e., the platelet shape produces a much greater lattice dilation.

The observed lattice parameter change in Pd tritide [12] is shown in Fig. 3a. Also shown are the dilations calculated using Eqs. (16) and (17) with $n_B=5\times10^{23}$ bubbles/m^3. The rapid initial dilation does not fit loop-punching behavior for spherical bubbles. Rather, it is much more closely described by high pressure Griffith crack growth and platelet expansion. During this initial phase, no lattice defects are created, other than those attached to the platelets, since no dislocation loops are emitted. Around .005 He/M concentration, the dilation rate slows

considerably. This He/M corresponds to a platelet radius of about 2.2 nm, in good agreement with the beginning of the shape transition region in Fig. 2b. Bubble volumes increase about 8-fold during the transition from platelets to spheres, while r is relatively constant. The calculated He concentration for spherical bubbles with radius r=2.2 nm is .04 He/M, in good agreement with the end of the transition region. At higher He/M, the dilation appears follow that produced by loop punching. It is noted that the lattice strain created by platelets is not relaxed by this transition. It appears the dislocation loops emitted during the transition are retained within the material and maintain the high stress level. It is also be noted that a distribution of bubble sizes and spacings will cause this transition to occur gradually over a range of He/M and that the calculation given above is for the average bubble.

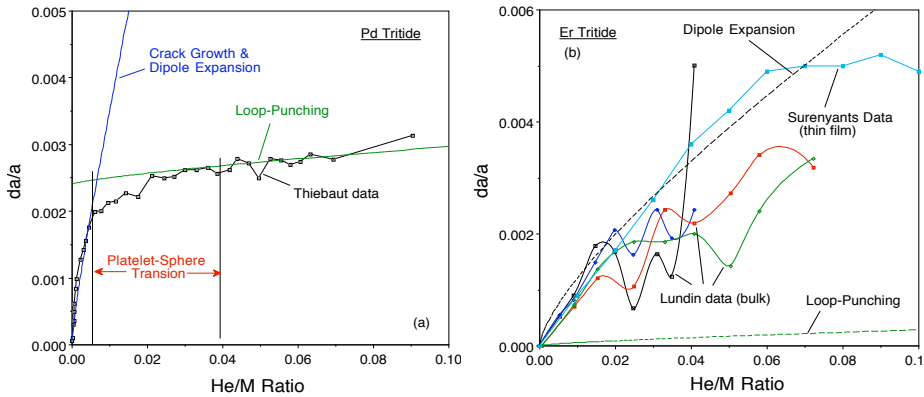


Figure 3. Lattice dilation of Pd and Er tritides as a function of age (He/M ratio).

The situation is similar for Er tritide as shown in Fig. 3b. However, here lattice dilation continues at the rapid rate described by dipole expansion to a much higher He/M concentration than for Pd tritide. Data from Er thin films [13] shows an unpredicted leveling off around .06 He/M, well before the average platelet interactions should become significant. This may be due to interactions between large platelets or preferred platelet orientations relative to film plane. The rapid gyrations observed for bulk material [14] likely reflect stress relaxations resulting from such interactions or with lattice defects created during the hydriding process.

PLATELET DIMENSIONS

The model accounts for the platelet dimensions measured in Er tritide films by Bond *et al* [15]. Figure 4a shows the observed platelet diameter 2r as a function of age. The solid curve is the platelet size calculated using Eq. (10), along with expressions for the conservation of He and the He equation of state as given in [1], and a density of 5×10^{23} platelets/m^3. The initial part of the curve presents precipitate growth as nano-cracks, while the latter part is platelets. The constant diameter region from .14 to .18 He/M corresponds to dipole formation.

Figure 4b shows a comparison of the calculated and TEM-measured precipitate thickness. Here, the Er (111) plane spacing is determined by adding twice the Er plane half-spacing (d) to the calculated He precipitate thickness. The model appears to slightly underestimate the platelet thickness. This may be due to differences between the properties of Er metal and Er hydride. Indeed, it is proposed that accurate measurement of the precipitate thickness may provide a reliable determination of the surface energy through Eq. (12).

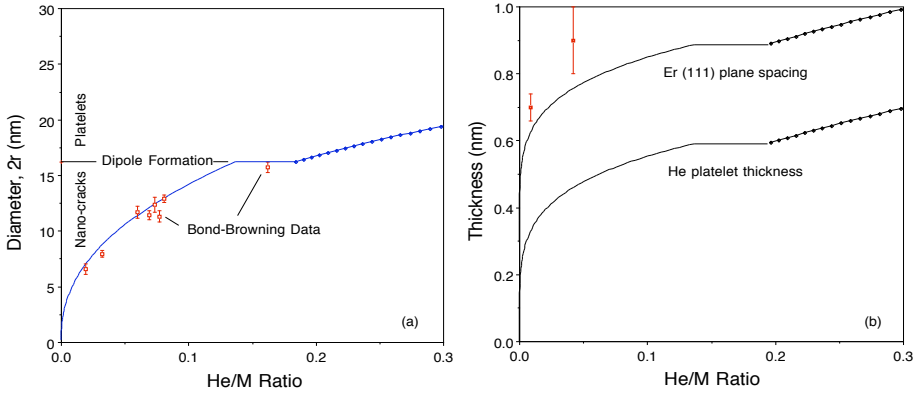


Figure 4. Dimensions of the platelets in Er tritide.

PRECIPITATE SHAPES IN OTHER MATERIALS

The relationship between surface energy and strain energy controlling He bubble shape is also tested by insoluble gas precipitates observed in other metals. Table 2 lists various fcc, hcp, and bcc metals and metal tritides in which gas precipitates have been documented, along with the precipitate shapes and estimates of the ratio $2\gamma/\mu b$. Platelets appear to be preferred shape in all materials with low $2\gamma/\mu b$, particularly at small r where $s/2r > 2\gamma/\mu b$. Indeed, this condition seems to hold for all three lattice structures.

Table 2. Surface/strain energy ratio and precipitate shape in various materials.

fcc						hcp		bcc		
ErT_2	ScT_2	TiT_2	Ni	ZrT_2	PdT	Be	Ti-α	W	V-α	Nb-α
.061	.104	.117	.180	.258	.322	.051	.238	.103	.312	.350
Platelets		Spheres				Plat.	Sph.	Plat.	Spheres	

SUMMARY AND CONCLUSIONS

Thin He-filled platelets bounded by an attached dislocation dipole are preferred structures in fcc metals with low surface energy and high shear modulus. They grow by radial expansion of the dipole with an internal pressure lower than that required

for dislocation loop punching. The slow thickness increase during this growth will cause them to transition to spherical bubbles if the dislocations become detached. Formulations of the gas pressures within these precipitates agree with observed lattice dilation data and changes in their dimensions with age. Precipitate shapes within hcp and bcc metals also appear to follow this behavior.

ACKNOWLEDGMENTS

Many thanks to Clark Snow and Jim Browning of Sandia for their informative discussions on Er tritide and Gillian Bond of New Mexico Institute of Mining and Technology for use of her TEM data on aging Er tritide films. This work was supported by the US Department of Energy under contract DE-AC04-94AL85000.

REFERENCES

1. Cowgill, D.F., "Helium Nano-Bubble Evolution in Aging Metal Tritides," Sandia National Laboratories Report, SAND2004-1739; Fusion Sci. and Tech. **48** (2005) 539.
2. Cowgill, D.F., "Helium Bubble Linkage and the Transition to Rapid He Release in Aging Pd Tritide," Sandia National Laboratories Report, SAND2006-7779.
3. Wilson, W.D. *et al*, "Self-Trapping of He in Metals," Phys. Rev. B **24** (1981) 5616.
4. Thomas, G.J. and Mintz, J.M., "Helium Bubbles in Palladium Tritide," J. Nucl. Mater. **116** (1983) 336.
5. Thiebaut, S. et al, "TEM Study of the Aging of Palladium-Based Alloys During Tritium Storage," J. Nucl. Mater. **277**, (2000) 217.
6. Gelles, D.S. et al, "Microstructural Features in Aged Erbium Tritide Foils," 23rd ASTM International Symp. on Eff. of Radiat. on Materials, San Jose, CA, 2006.
7. Trinkaus, H., "Energetics and Formation Kinetics of Helium Bubbles in Metals," Radiat. Eff. **78** (1983) 189.
8. Gschneidner, K.A., in Handbook of Chemistry and Physics, 88th Ed, CRC Press (Boca Raton, FL, 2007-8), p. 4-124.
9. Knapp, J., and Browning, J.F., "Nanoindentation Characterization of ErT_2 Thin Films," J. Nucl. Mater. **350** (2005) 147.
10. Chen, J. et al, "Evolution of Helium Platelets and Associated Dislocation Loops in α-SiC," Phys. Rev. Letters **82** (1999) 2709.
11. Wolfer, W.G., "The Elastic Properties of Aged Palladium Tritides," Sandia National Laboratories Report, SAND90-8253.
12. Thiebaut, S. et al, "Structural changes in Pd (Rh, Pt) solid solutions due to ^{3}He formation during tritium storage," Phys Rev. B **57** (1998) 10379.
13. Surenyants, V.V. *et al*, "Development of Tritium Targets," VNIIA, Moscow, RU, ISTC Report No. 323, 1999.
14. Lundin, C.E. and Sullivan, R.L., "X-ray Structural Analysis of Metal-Hydrogen Systems," Univ. of Denver, Denver Res. Institute Rept., DRI #2573, June 1971.
15. Bond, G.M. *et al*, "TEM Study of Helium Bubble Evolution in Erbium Ditritide," *Hydrogen and Helium Isotopes in Materials Conf*, Albuquerque, NM, Feb. 6, 2007.

Effects of Hydrogen on Materials
Proceedings of the 2008 International Hydrogen Conference
Brian Somerday, Petros Sofronis, Russell Jones, editors, p 694-701
Copyright © 2009 ASM International®
All rights reserved.
www.asminternational.org

TRANSMISSION ELECTRON MICROSCOPY STUDY OF HELIUM-BEARING FUSION WELDS

M. H. Tosten and M. J. Morgan
Savannah River National Laboratory
Aiken, SC 29808 USA

ABSTRACT

A transmission electron microscopy (TEM) study was conducted to characterize the helium bubble distributions in tritium-charged-and-aged 304L and 21Cr-6Ni-9Mn stainless steel fusion welds containing approximately 150 appm helium-3. TEM foils were prepared from C-shaped fracture toughness test specimens containing delta (δ) ferrite levels ranging from 4 to 33 volume percent. The weld microstructures in the low ferrite welds consisted mostly of austenite and discontinuous, skeletal δ ferrite. In welds with higher levels of δ ferrite, the ferrite was more continuous and, in some areas of the 33 volume percent sample, was the matrix/majority phase. The helium bubble microstructures observed were similar in all samples. Bubbles were found in the austenite but not in the δ ferrite. In the austenite, bubbles had nucleated homogeneously in the grain interiors and heterogeneously on dislocations. Bubbles were not found on any austenite/austenite grain boundaries or at the austenite/δ ferrite interphase interfaces. Bubbles were not observed in the δ ferrite because of the combined effects of the low solubility and rapid diffusion of tritium through the δ ferrite which limited the amount of helium present to form visible bubbles.

INTRODUCTION

Research studies at the Savannah River Site (SRS) have focused on the effects of tritium and its decay product, helium-3, on the mechanical properties of austenitic stainless steels used to contain tritium gas [e.g., 1-3]. These studies have shown that the presence of tritium and helium-3 have a detrimental effect on the fracture toughness properties of these materials. Until recently, studies have focused mainly on the mechanical property variations that occur in the austenitic base materials. However, little work has been done to understand how tritium and helium-3 affect the mechanical properties of the fusion welds that are inherent to the design of some tritium storage vessels.

Typical fusion welds contain austenite (fcc phase) and a smaller amount of δ ferrite (bcc phase). The δ ferrite phase is needed to prevent solidification and

liquation cracking when welding austenitic stainless steels. A recent study of tritium-free material showed that the microstructures that developed in multi-pass fusion welds are very complex and become increasingly so as the δ ferrite content increases [4]. Of prime interest in tritium/helium-containing welds is the role that δ ferrite plays in the deformation/fracture process and how the presence of this phase affects the helium bubble microstructure in the fusion zones.

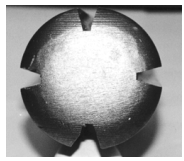
The purpose of this study was to document the helium bubble distribution that existed in fusion welds made on 304L and 21Cr-6Ni-9Mn stainless steels. This study provided a foundation for understanding the influence of weld microstructure on the helium bubble distribution (size and location) in both the heat-affected zones (HAZs) and fusion zones of these welds.

EXPERIMENTAL PROCEDURE

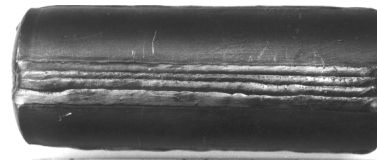
A series of tritium-charged-and-aged fusion welds, with a range of δ ferrite contents, were prepared using 304L and 21Cr-6Ni-9Mn stainless steel base materials in combination with electron beam and gas tungsten arc welding using a variety of stainless steel filler wires. The base materials were a 304L weld critical plate, a 304L cylindrical forging and a 21Cr-6Ni-9Mn cylindrical forging. The 304L forging was prepared using a high-energy-rate-forging (HERF) process while the 21Cr-6Ni-9Mn forging was made by a conventional forging process. Ferrite levels in the welds varied from about 4 to 33 vol.%. The higher ferrite welds were made using Type 308L, 309L MOD (modified for higher ferrite content), and 312 MOD stainless steel filler wires.

Once welded, the base materials (plate and forgings) were sectioned into C-shaped fracture toughness specimens (Fig. 1). These specimens were exposed to tritium gas at a temperature of 623K and a pressure of about 34 MPa for 3 weeks. The conditions of the charging were designed to saturate the samples with tritium without changing the starting microstructure. After charging, samples were aged for 8 months at 250K to produce a helium content of ~150 appm. Measured helium concentrations in the base metals agreed well with the calculated, target helium concentrations; however, weldments had 33-50% less helium than expected.

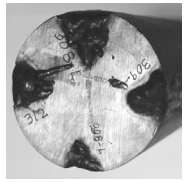
Specimens for TEM analysis were prepared from C-shaped specimens after fracture toughness testing. Figure 2 is a schematic illustration of the sample sectioning procedure. Several thin slices were cut from each test specimen beginning immediately adjacent to the fracture surface (plastically deformed region) and continuing into the weld HAZ and base metal. Two 3 mm diameter disks were punched from each slice. Thin foils were prepared from each disk using a twin jet electropolisher and a solution of 57% methanol, 39% butyl cellosolve, and 4% perchloric acid at 35Vdc and 243K. All TEM was performed using a JEOL 2010 operating at 200 kV.



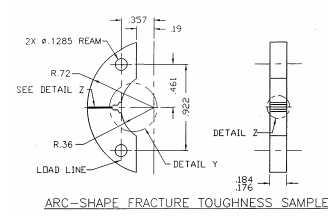
a.



c.



b.



d.

Figure 1. HERF 304L forging showing (a) V-grooves prior to welding, (b) a cross-section of forging after welding, (c) one multi-pass weld along the 8" length of the same forging, and (d) a schematic of a fracture toughness specimen machined from the forgings and weld critical plate. Specimens were machined so the notch would be located at the weld center line.

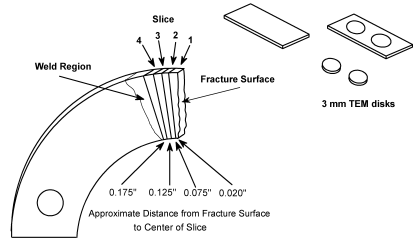


Figure 2. Schematic diagram illustrating the sectioning procedure used to generate TEM disks from the fusion weld region of a fracture toughness specimen.

RESULTS: General Microstructure

Welds with a range of δ ferrite contents of 4 to 33 vol.% were examined in this study. Images shown in Figs. 3a-d illustrate the variety of microstructures observed in the weld fusion zones. Figures 3a-c show the morphological differences in the δ ferrite phase as the volume fraction and Cr_{eq}/Ni_{eq} ratios in the weldments increased. Figure 3d is an image from a low δ ferrite-containing weld that was located close to the fracture surface of a C-shaped

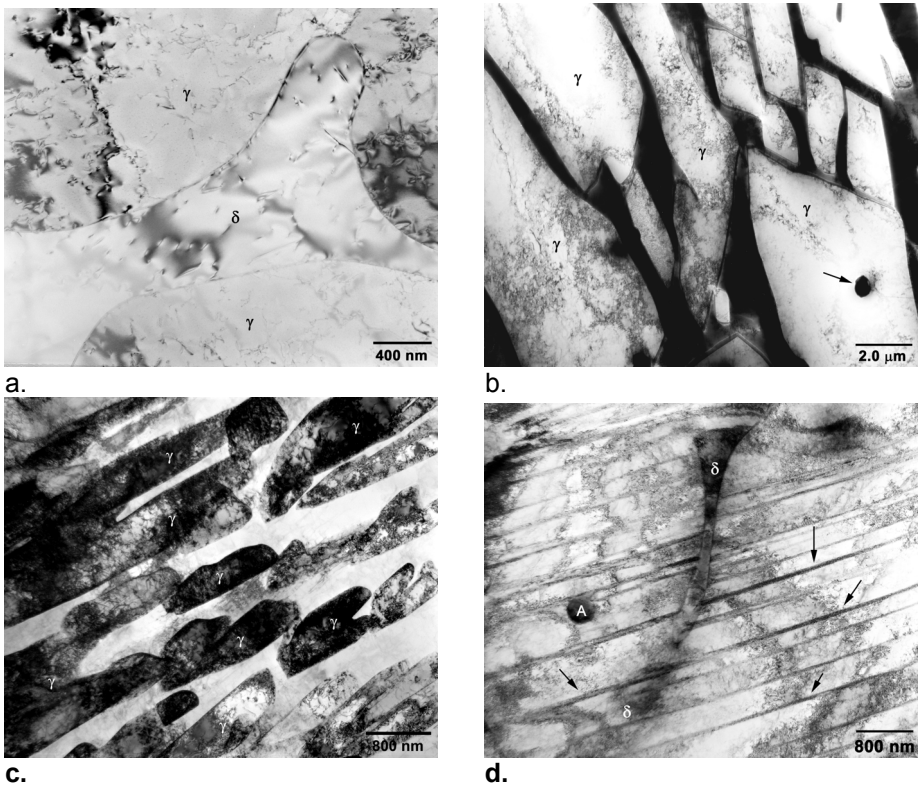


Figure 3. Images of weld microstructures observed in an (a) 8 vol.% δ ferrite weld, (b) a 12 vol.% δ ferrite weld, and (c) a 33 vol.% δ ferrite weld. (d) Deformation twinning in the plastically deformed region of a 5 vol.% δ ferrite weld. Oxide inclusions are located at the arrow in (b) and at "A" in (d).

test specimen. This image shows a microstructure that is mostly austenite with some skeletal ferrite. The more distinctive features in this image, however, are the deformation twins (e.g., marked with arrows) in the austenite. Plastic deformation by way of twinning was observed in all welds in regions closest to the fracture surfaces of the test specimens. Delta ferrite appeared to provide some resistance to deformation, particularly in specimens with higher Cr_{eq}/Ni_{eq} ratios.

RESULTS: Helium-Bearing Welds

The helium bubble distribution in all welds was very similar. Specifically, helium bubbles were observed in the austenite but not in the δ ferrite. Figure 4 is an image from a weld made on the 21Cr-6Ni-9Mn conventional forging using 308L filler wire. This image shows a δ ferrite "grain" in an austenite matrix. The small black "dots" visible in the austenite matrix arise from strain

contrast associated with the presence of helium bubbles. As evidenced in Fig. 4, black "dots" (bubbles) are not present in the δ ferrite. Careful examination of many ferrite regions under a variety of tilt/contrast conditions failed to locate any bubbles in the δ ferrite phase in any of the welds.

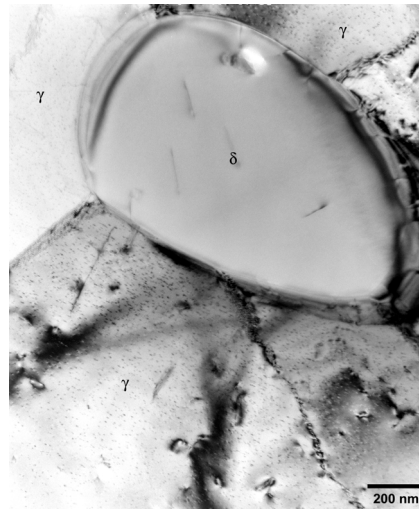
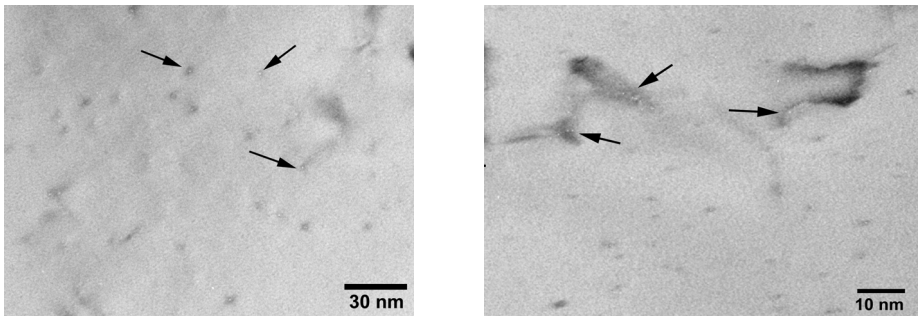


Figure 4. Image from a 5 vol.% δ ferrite weld showing a δ ferrite grain in an austenitic "matrix". The black "dots" in the austenite arise from strain contrast from helium bubbles. No black "dots" are visible in the δ ferrite.

The distribution of helium bubbles in the austenite in all of the weldments closely matched the helium bubble microstructure observed in the weld HAZs. That is, helium bubbles were observed within the grain interiors and not on the grain boundaries. The helium bubble distribution in the austenite is illustrated in Figure 5. These images are from austenite regions in a mixed wire weld on the 304L plate. Figure 5a is a high magnification image showing bubbles that nucleated in the interior of an austenite grain. The imaging conditions were such that many 2-3 nm sized bubbles (appearing as small "white" dots in this under-focused image) were visible. These bubbles likely formed by "homogeneous" nucleation at vacancies or vacancy clusters which are strong traps for helium in the matrix. In other austenite grains, helium bubbles were observed on dislocations (Fig. 5b). Dislocations are known to be potent heterogeneous nucleation sites for bubbles [5,6].

Interfaces play an important role in the fracture processes in tritium/helium-containing materials, so the austenite/austenite and austenite/ferrite boundaries in the weldments were investigated carefully. An interphase boundary is imaged in Fig. 6. Close examination of this and many other interfaces failed to detect bubbles in these areas. As mentioned above, the black "dots" in the austenite grain indicate the locations of helium bubbles.



a. b.

Figure 5. Helium bubbles in the austenite phase. Bubbles have formed in the matrix (a) and on dislocations in (b).

Again, there are no black "dots" in the δ ferrite region in this image. Examination of the near-boundary region in this image also revealed a narrow region extending along the boundary region that is devoid of bubbles. Regions like this are termed bubble-free zones (BFZs) and were observed previously in another study [7]. BFZ formation is believed related to the reduction in the vacancy concentration in the near-boundary region which reduces the amount of trapped helium available to form bubbles.

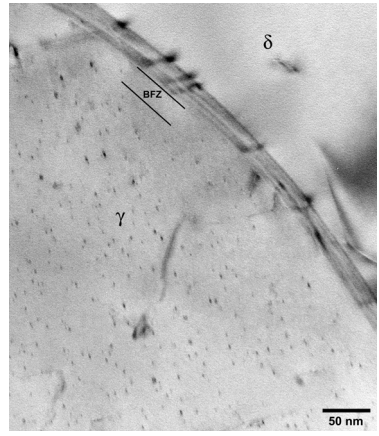


Figure 6. An image of an interface between the austenite and δ ferrite. Bubbles were not observed on these type boundaries. A bubble-free zone (BFZ) exists in the near boundary region.

DISCUSSION

The helium bubble distributions observed in the austenite phase were consistent with those observed in other studies at SRNL [1,3-5,7]. In these

studies, helium bubbles were observed commonly in the grain interiors, on dislocations, and sometimes on carbide/matrix interfaces and austenite/austenite grain boundaries. In the present study, helium bubbles were not observed in the δ ferrite phase. There are at least two possible reasons for this.

Firstly, it may simply be that there is less helium present in the δ ferrite to form bubbles. Unlike the fcc austenite phase (high hydrogen/tritium solubility and low diffusivity), the bcc ferrite phase is characterized by low tritium solubility and the rapid diffusion of tritium through the metal lattice. Therefore, the ferrite lattice tends to reject tritium and what is there diffuses out more rapidly before it decays to helium-3. Calculations show that pure α ferrite (also bcc) charged and aged using the sample conditions employed in the current study would contain about 13 appm helium [8]. This value is about 10 times less than the measured helium concentrations in the fully austenitic base materials. (Diffusivity/solubility differences may also explain the variability in the measured helium content of the welds as well as the drop-off in helium content in those welds containing high levels of ferrite.) As a result, the helium in the ferrite may be more widely dispersed over a large number of trap sites thus reducing the available helium in any one area to form a stable cluster or, at least, a cluster large enough to see in the TEM.

The second reason for not seeing helium bubbles in the δ ferrite may be related to the technique used to image them. Nanometer-sized helium bubbles are imaged in the TEM using an under/over-focusing technique [9]. In the under-focused condition bubbles appear brighter than the background, i.e., they look like voids, and in the over-focused condition bubbles appear as black dots and are darker imaging than the background. The imaging technique, however, is limited to resolving bubbles greater than about 0.7 nm in diameter. Below this size bubbles cannot be discerned from the background contrast in the image. Therefore, as alluded to above, bubbles (or maybe in fact, clusters of helium atoms) could have been present in the δ ferrite but were too small to be resolved with the TEM.

SUMMARY

The helium bubble distributions in fusion welds containing 4 to 33 volume percent δ ferrite and approximately 150 appm helium-3 were characterized. In the low δ ferrite welds, the microstructure was primarily austenite and discontinuous, skeletal δ ferrite. In welds with higher levels of δ ferrite the ferrite was more continuous and the austenite/ferrite interfaces more planar. In some areas of the highest δ ferrite weld, the ferrite was the matrix phase. Helium bubbles were observed in the austenite phase and not in the δ ferrite. The failure to observe bubbles in the δ ferrite was probably related to the limited solubility and the rapid diffusion of tritium in that phase resulting in a reduced amount of helium available to form bubbles of sufficient size to view

in the TEM. Bubbles in the austenite nucleated homogeneously in the grain interiors and on matrix dislocations. These results were consistent with previous studies of helium bubbles in austenitic stainless steels. Bubbles were not observed on the austenite/austenite or austenite/ferrite boundaries.

ACKNOWLEDGEMENTS

This document was prepared in conjunction with work accomplished under Contract No. DE-AC09-08SR22470 with the U.S. Department of Energy.

REFERENCES

1. Morgan, M. J. and Tosten, M. H., "Microstructure and Yield Strengths Effects on Hydrogen and Tritium-Exposed HERF Stainless Steels", Proc. 4th Int. Conf. on the Effects of Hydrogen on the Behavior of Materials, Moran, WY, 1990, pp. 447-58.

2. Morgan, M. J. and Lohmeier, D. A., "Threshold Stress Intensities and Crack Growth in Tritium-Exposed HERF Stainless Steels", Proc. 4th Int. Conf. on the Effects of Hydrogen on the Behavior of Materials, Moran WY, 1990, pp. 459-68.

3. Morgan M. J. and Tosten, M. H., "Tritium and Decay Helium Effects on the Fracture Toughness Properties of Types 316L, 304L, 21Cr-6Ni-9Mn Stainless Steels", Proc. 5th Int. Conf. on the Effects of Hydrogen on the Behavior of Materials, Moran, WY, 1996, pp. 873-82.

4. Tosten, M. H. and Morgan, M. J., "Microstructural Study of Fusion Welds in 304L and 21Cr-6Ni-9Mn Stainless Steels", WSRC-TR-2004-00456, WSRC, Aiken, SC.

5. Tosten, M. H and Morgan, M. J., "The Effects of Helium Bubble Microstructure on Ductility in Annealed and HERF 21Cr-6Ni-9Mn Stainless Steel", WSRC-RP-92-551, WSRC, Aiken, SC.

6. Robinson S. L., "Tritium and Helium Effects on Plastic Deformation in AISI 316 Stainless Steel", Mater. Sci. Eng., vol. 96, 1987, pp. 7-16.

7. Tosten, M. H. and Kestin, P. A., "Helium Bubble Distributions in Reactor Tank Repair Specimens - Part I.", WSRC-TR-91-141, WSRC, Aiken, SC.

8. Clark, E. A., WSRC, Unpublished research, 2005.

9. Rhüle, M. F., "Transmission Electron Microscopy of Radiation-Induced Defects", Proc. Int. Conf. on Radiation-Induced Voids in Metals, Albany, NY, 1972, pp. 255-91.

Effects of Hydrogen on Materials
Proceedings of the 2008 International Hydrogen Conference
Brian Somerday, Petros Sofronis, Russell Jones, editors, p 702-709
Copyright © 2009 ASM International®
All rights reserved.
www.asminternational.org

SYNERGISTIC EFFECTS BETWEEN HYDROGEN AND/OR HELIUM ACCUMULATION AND ION IRRADIATION DAMAGE IN NUCLEAR RELATED MATERIALS

Patrick Trocellier
CEA – DEN/DANS/DMN, Service de Recherche de Métallurgie Physique, Centre de Saclay, 91191 Gif sur Yvette, France

ABSTRACT

It is well known that sequential or simultaneous ion-irradiations of metals and alloys did not modify their microstructure and mechanical properties in the same way. This paper tends to make a brief review of this particular problem in the field of nuclear related materials by discussing some examples available in the opened literature.

INTRODUCTION

The pioneering works from Brimhall [1], Farrell [2] and Lévy [3] have shown that sequential or simultaneous ion-irradiations of metals and alloys did not modify their microstructure and mechanical properties in the same way. The interest on the synergistic effects between irradiation damage and gas accumulation strongly increases in parallel with the development of the research devoted to materials for Generation IV nuclear reactors and fusion applications. It concerns metals and alloys as well as oxide, carbide or nitride ceramics.

In this paper, we are going to successively review the impact of simultaneous irradiation damage/gas accumulation on the microstructure, the atomic transport mechanisms and the mechanical and physico-chemical properties of materials for future nuclear applications.

MICROSTRUCTURAL IMPACT

Silicon carbide composites are now being developed as structural materials for fusion power reactors in part due to their high temperature strength and low-residual radioactivity following neutron irradiation. Fusion irradiation conditions imply both a high irradiation fluence up to 150 – 200 dpa and high gas concentration, typically 130 appm/dpa for He and 40 appm/dpa for H [4].

In a recent paper Keng and co-workers have investigated the microstructural evolution of Tyranno-SA SiCf/SiC composite irradiated at 1073 K and 1273 K by transmission electron microscopy [5]. Table 1 summarizes their dual- (6 MeV Si^{3+} and 1.13 MeV He^{+} or 800 keV He^{+} and 280 keV H^{+}) and triple-beam (6 MeV Si^{3+}, 800 keV He^{+} and 280 keV H^{+}) experimental configurations.

Table 1: Dual- and triple-beam configuration adopted by Keng for Tyranno-SA SiCf/SiC composite irradiation [5].

	Si^{3+}	He^{+}	H^{+}
Energy	6 MeV	800 keV	280 keV
Projected range (µm)	2.40	1.56	1.56
Dose	10 dpa at 1073 K 100 dpa at 1273 K		
Dose rate (dpa/s)	4×10^{-4}		
Concentration (appm)		15 000	6 000

The main observations resulting from TEM examinations of the irradiated samples are summarized in Table 2.

Table 2: Main results on cavity size (nm) and number density ($1 \times 10^{22}/m^3$) of Tyranno-SA/SiC irradiated at 1073 and 1273 K (after H.T. Keng [5]).

Conditions	Size		Density	
	Matrix	Fiber	Matrix	Fiber
Dual-beam Si/He, 10 dpa, 1073 K	1.2	X	0.85	X
Triple-beam Si/He/H, 10 dpa, 1073 K	1	0.85	1.2	3
Dual-beam Si/He, 100 dpa, 1073 K	9	5	0.26	0.45
Dual-beam Si/He, 10 dpa, 1273 K	37	15	0.14	0.27
Dual-beam He/H, $1.5 10^4/6\ 10^3$, 1073 K	2	1	3.4	5.6
Dual-beam He/H, $1.5 10^4/6\ 10^3$, 1273 K	10	2	0.9	2.7
Single-beam He, 10^4 appm, 1473 K	3	X	N	X

X = no cavity, N = not investigated.

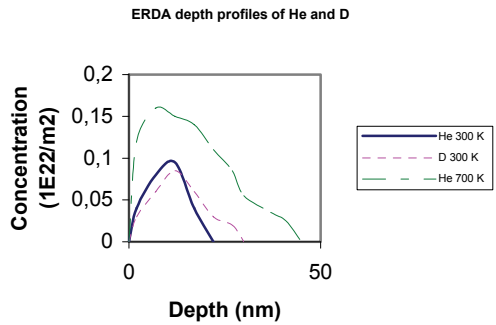
Cavities were found mainly on the grain boundaries of SiCf/SiC composite, and cavity coarsening was observed after higher temperature (1273 K) irradiation. It is clear that H atoms enhance cavity nucleation due to their high diffusivity in SiC. The cavity density is higher in the TSA fiber than in the matrix due to its smaller grain size offering more possible cavity nucleation sites.

EFFECTS ON ATOMIC TRANSPORT

Due to its good thermal properties (high melting point and good thermal conductivity) as well as a low sputtering yield for minimizing impurity generation, tungsten is a primary candidate for the high flux, low-energy region of the divertor in ITER. Under plasma burning conditions, tungsten will be irradiated simultaneously by T and T hydrogen fuel and He. He is considered as highly insoluble in all metals due to its closed electronic shell structure. Thus, the blistering process is one of the most relevant effects of helium accumulation inducing a strong degradation of the mechanical properties of the metal.

Lee and co-workers have recently studied the trapping of hydrogen and helium in polycrystalline tungsten irradiated with 500 eV He^+, H^+ and D^+ ions individually or sequentially at 300 or 700 K [6]. Figure 1 displays the implanted hydrogen and helium depth profiles measured by elastic recoil detection analysis for sequential 500 eV He^+ - D^+ irradiations at 300 and 700 K.

Figure 1: Hydrogen and helium depth profiles measured by elastic recoil detection analysis for sequential 500 eV He^+ - D^+ irradiations at 300 and 700 K (curves redrawn after data published by Lee [6]).



No D was observed at 700 K. The detrapping of helium and hydrogen in tungsten was measured by thermal desorption spectrometry (TDS). He is thought to form He vacancy complexes or bubbles. Increasing the sample temperature to 700 K does not significantly affect the trapping behavior of He.
The main TDS observations can be summarized as follow:

- for single He^+ irradiation, 3 TDS peaks appear respectively at 500, 1000 and 1200 K ;
- for sequential He^+ - D^+ irradiation conducted at 300 K, there is no He release for T > 800 K but a significative release of He and D between 400 and 800 K associated to interstitial He and D near surface desorption ;

- for sequential He^+ - D^+ irradiation conducted at 700 K, the intensity of the 1000 K TDS He peak strongly decreases coupled with a low release at 800 K. No D trapping is found ;
- the sequential D^+ - He^+ irradiation conducted at 300 K results in He trapping as in the case of the single He^+ irradiation with a significative decrease of D release from the near surface ;
- for sequential D^+ - He^+ irradiation conducted at 700 K, no D effect on trapping behavior of He is shown.

EFFECTS ON PHYSICO-CHEMICAL AND MECHANICAL PROPERTIES

Ferritic/martensitic steels are one of the candidate materials for the vessel of the spallation target and first priority materials of structure for fusion power reactors. These systems need to operate at relatively high temperature and He atom accumulation may affect both their ductile to brittle transition temperature as well as their swelling behavior or irradiation hardening.

Wakai and co-workers have performed triple beam irradiation experiments to study the effects of gas atoms and displacement damage on mechanical properties and microstructure of the reduced activation ferritic/martensitic (RAFM) alloy F82H [7], whose chemical composition is: 89.71Fe - 7.82Cr – 1.98W – 0.19V – 0.1Mn – 0.09C – 0.07Si - 0.04Ta (in wt. %). Table 3 summarizes the irradiation conditions adopted by Wakai.

Table 3: Triple beam irradiation conditions adopted by Wakai to study the behavior of RAFM alloy F82H [7].

	Fe^{3+}	He^+	H^+
Energy	10.5 MeV	1.05 MeV	380 keV
Temperature/dose	543 K/20 dpa 633 K/50 dpa		
Concentration (appm/dpa)		10	40

The hardness of F82H alloy is increased by triple beam, dual beam and single beam irradiation and the increment of hardness is higher at 633 K than at 543 K as it is shown on Figure 2.

Figure 2: Micro-hardness evolution of F82H alloy versus displacement damage (curves redrawn after data published by Wakai [7]).

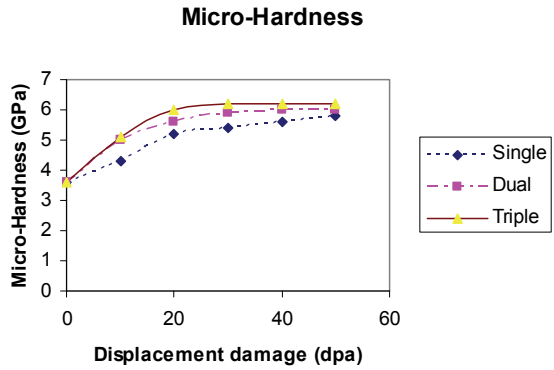
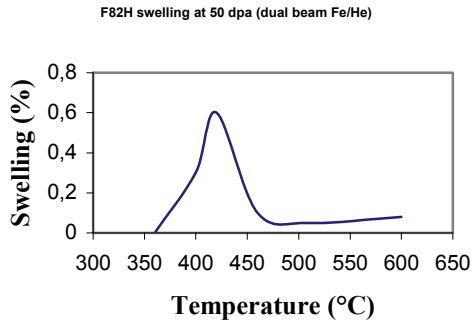


Figure 3 shows the variation of the swelling versus temperature for a dual beam irradiation (Fe/He) at 50 dpa [7]. A peak is observed near 703 K and the corresponding swelling value is about 0.6 %. Small punch testing of F82H at 873 and 973K showed that implantation of 84 appm He at 393K increased strength with no degradation in ductility Fracture toughness testing at 573K showed that implantation of 84 appm He decreased toughness significantly compared to the toughness of samples with no helium production beyond a maximum strength in the ductile temperature regime. This behavior can be related with the occurrence of sub-boundaries (lath, pack or cracking induced by He migration).

Figure 3: Swelling variation of F82H alloy in function of temperature for a dual beam irradiation (Fe/He) at 50 dpa (curve redrawn after data published by Wakai [7]).



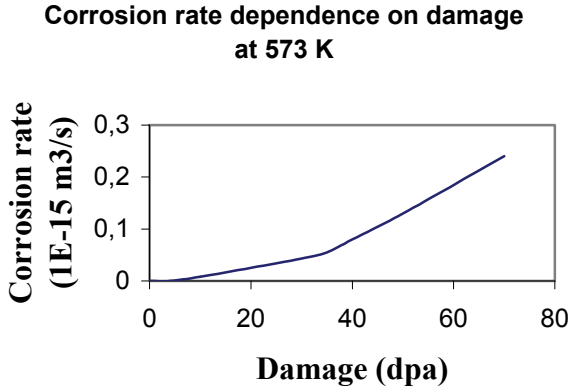
Austenitic steels are good candidate structural materials for spallation targets. Nemoto and co-workers have studied the evolution of the corrosion behavior of a Fe-18Ni-12Cr steel in mercury after dual beam irradiation (Ni/He or Ni/H) [8]. The irradiation configuration is summarized in Table 4. The corrosion rate values are determined using atomic force microscopy imaging technique.

Table 4 : Dual beam irradiation conditions adopted by Nemoto and co-workers [8].

	Ni^{3+}	He^{2+}	H^{+}
Energy	12 MeV	900 keV	340 keV
Dose	up to 35 dpa		
Concentration (appm/dpa)		500	500
Temperature	473 – 773 K		

Figure 4 shows the variation of the corrosion rate of a Fe-18Ni-12Cr austenitic steel in mercury versus the irradiation damage cumulated at 573 K.

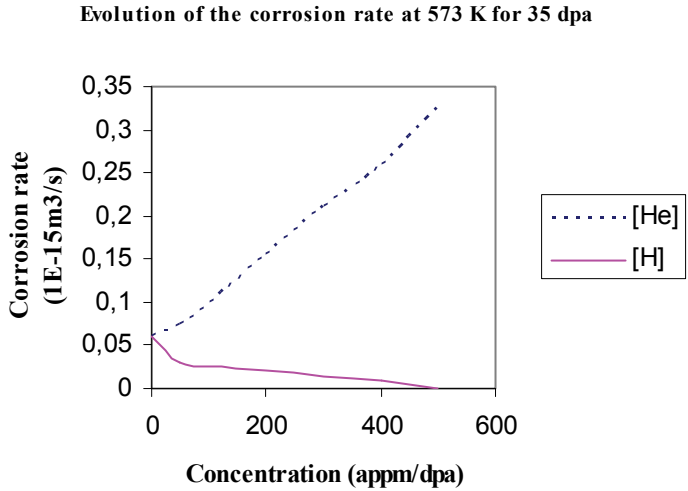
Figure 4: Variation of the corrosion rate of the austenitic steel in mercury versus the irradiation damage cumulated at 573 K (curve redrawn after data published by Nemoto [8]).



No effect was observed below 5 dpa. Then, the corrosion rate seems to exhibit two different linear regimes: between 5 and 35 dpa and above 35 dpa. When irradiation dose increases the corrosion rate increases and when irradiation T increases the corrosion rate increases. It is classically considered that the increase of vacancy diffusion with temperature and dose leads to an increase of Cr depletion on grain boundaries causing corrosion enhancement.

Figure 5 displays the variation of the corrosion rate versus hydrogen and helium concentrations. The relationship corrosion rate/[H] appears to be nearly linear, when [H] increases the corrosion rate increases due to the interactions between H and vacancies that may enhance Cr segregation. In contrast, when [He] increases the corrosion rate decreases. This last result can be explained by the formation of stable He-vacancy pairs that may inhibit the Cr depletion mentioned above.

Figure 5: Variation of the corrosion rate of the austenitic steel in mercury versus hydrogen and helium concentration at 573 K for 35 dpa (curves redrawn after data published by Nemoto [8]).



CONCLUSION

Multi ion beam irradiation facilities are becoming very efficient tools to study the synergistic effects between hydrogen and/or helium accumulation and ion irradiation damage in nuclear materials for fusion and Generation IV reactor applications. Positive or negative consequences have been already observed as well in terms of microstructure evolution or physical/mechanical/chemical property modifications as in terms of atomic transport mechanisms for both metallic alloys and ceramics. The main driving force consists in the level of interactions between H (He) atoms with point defects or defect clusters.

REFERENCES

1. Brimhall, J.L., Simonen, E.P., “Effect of helium on void formation in nickel”, *J. Nuclear Materials,* Vol. 68, (1977), pp. 235-243.

2. Farrell, K., Packan, N.H., “Damage structure in nimonic PE16 alloy ion bombarded to high doses and gas levels”, *J. Nuclear Materials*, Vol. 103&104, (1981), pp. 1059-1062.
3. Lévy, V., Gilbon, D., Rivera, C., “Influence of helium on swelling of steels”, *ASTM STP*, Vol. 870, (1985), pp. 317-329.
4. Taguchi, T. Igawa, N., Miwa, S., Wakai, E., Jitsukawa, S., Snead,L.L., Hasegawa, A., “Synergistic effects of implanted helium and hydrogen and the effect of irradiation temperature on the microstructure of SiC/SiC composites”, *J. Nuclear Materials*, Vol. 335, (2004), pp. 508-514.
5. Keng, H.T., Li, S.W., Wu, S.W., Ji-Jung Kai, Fu-Rong Chen, Katoh, Y., Kohyama, A., “Cavity formation in Tyranno-SA SiCf/SiC composite irradiated with multiple-ion beam at elevated temperatures”, *J. Nuclear Materials*, Vol. 367-370, (2007), pp. 753-757.
6. Lee, H.T., Haasz, A.A., Davis, J.W., Macaulay-Newcombe, R.G., “Hydrogen and helium trapping in tungsten under single and sequential irradiations”, *J. Nuclear Materials*, Vol. 360(2007), pp. 196-207.
7. Wakai, E., Ando, M., Sawai, T., Kikuchi, K., Furuya, K., Sato, M., Oka, K., Ohnuki, S., Tomita, H., Tomita, T., Kato, Y., Takada, F., “Effect of gas atoms and displacement damage on mechanical properties and microstructures of F82H”, *J. Nuclear Materials,* Vol. 356, (2006), pp. 95-104.
8. Nemoto, Y., Miwa, Y., Kaji, Y., Tsukada, T., “Effect of ion irradiation and implantation of H and He on the corrosion behavior of austenitic stainless steel”, J. Nuclear Materials, Vol. 343, (2005), pp. 313-317.

Effects of Hydrogen on Materials
Proceedings of the 2008 International Hydrogen Conference
Brian Somerday, Petros Sofronis, Russell Jones, editors, p 710-717
Copyright © 2009 ASM International®
All rights reserved.
www.asminternational.org

ADHESION AND FRACTURE OF SCANDIUM DEUTERIDE FILMS

M. S. Kennedy
Clemson University, Clemson, SC USA

N. R. Moody, M. Clift
Sandia National Laboratories, Livermore, CA USA

D. P. Adams, L. Espada, D. R. Kammler, E. D. Reedy Jr
Sandia National Laboratories, Albuquerque, NM USA

D. F. Bahr
Washington State University, Pullman, WA USA

ABSTRACT

Performance and reliability of thin film devices are governed by the composition and structure of the films and their interfaces. These are particularly important issues for scandium and scandium deuteride films used in neutron tube applications, where the interaction between the microstructure, high residual stresses and hydrogen diffusion can lead to premature failure. This study combines small-volume mechanical property and interfacial fracture tests to define the effects of ageing on properties of 150 nm thick scandium and scandium deuteride films. Film aging was simulated by rapid thermal annealing. During this treatment, the film's structure and composition were altered, resulting in mechanical property and fracture energy changes. The interfacial fracture energy decreased from over 3 J m^{-2} to less than 1 J m^{-2} after accelerated aging by rapid thermal annealing.

INTRODUCTION

Neutron generators are used in a variety of fields that include material analysis, medical research, explosives detection and homeland security operations [1]. Neutron generation can occur using three primary methods: accelerator-based neutron tubes, radioisotopes and nuclear reactors [2]. Of these, accelerator-based neutron tubes are the most popular because the formation of neutrons may be started and stopped, and they are compact [1, 2]. Several companies produce neutron tubes, including Thermo Electron, Sodern EADS, Halliburton Co, Baker Hughes, Inc., and Sclumberger Ltd [2] in addition to those developed at national laboratories [1].

Neutron targets typically consist of a metal-hydride (either -deuteride or -tritide) film on a copper [3] or molybdenum [4] substrate. Neutrons are generated when the target is bombarded with a beam of deuterons according to the D-D reaction [3]

$$ {}_{1}^{2}H + {}_{1}^{2}H \rightarrow {}_{0}^{1}n + {}_{2}^{4}He + Q \qquad (2) $$

for a metal-deuteride target, and the D-T reaction [3]

$$ {}_{1}^{2}H + {}_{1}^{3}H \rightarrow {}_{0}^{4}n + {}_{2}^{4}He + Q, \qquad (1) $$

for a metal-tritide target (where Q is the heat of formation).

Preparation of the target material impacts the consistency of generated neutrons. The metal selection impacts neutron emission yield and also the mechanical stability of the target [3]. Neutron emission yield is related to the density of hydrogen being stored. For metal-hydrides the approximate closest distance between H atoms is 0.2 nm [5]. This distance has recently been shortened in alloyed systems to approximately 0.15 nm [5]. Previous work on scandium films has shown that film thickness does not significantly alter diffusion of the deuterium through the film when temperatures range from 12 °C to 250 °C [6].

Mechanical stability is a concern, because mechanical properties change drastically with increasing hydrogen content [2]. The hydrogen can form a metal-hydride phase that has significantly smaller elastic moduli than the parent metal, or hydrogen interstitials can enhance dislocation mobility along slip planes [7] which is the cause of hydrogen embrittlement. For example, hydrides have been shown to form in pure titanium when exposed to hydrogen at high temperature. The formation of hydrides in Ti decreased the elongation to failure and caused brittle fracture [8]. Particular to this work, interactions between the microstructure, high residual stresses and hydrogen diffusion may then lead to premature failure of the hydride films [9]. The formation of hydrides may generate large film stresses, as shown in Figure 1 [1]. This is a clear driving force for failure and a cause for reliability concerns.

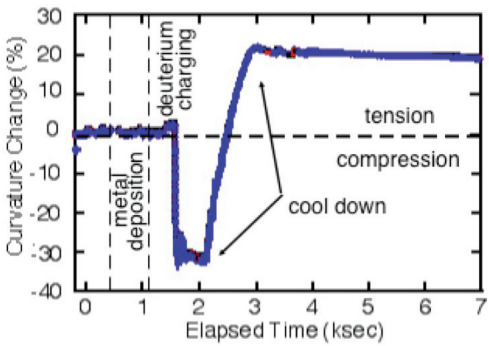


Figure 1: Stress evolution during deuterium charging and cooling. This shows a large growth of stresses [1].

This study focuses on the reliability of rare earth metals used for neutron targets; specifically, the reliability of Sc and ScD_2 films under initial deposition conditions and after accelerated aging. Many reports have outlined how the formation of metal-hydrides (deuterides) can be made by exposing rare earth metals, including

scandium, to hydrogen (deuterium). Although ScD_2 has a relatively low neutron emission rate, it has the advantages of reaching steady-state yield quickly, good thermal stability and does not exhibit crater formation on the target surface like titanium [3]. This study looks at the mechanical and chemical properties, before and after accelerated ageing, of Sc/SiO_2 and ScD_2/SiO_2 using Auger analysis, adhesion testing, and instrumented indentation (nanoindentation). These tests will allow for a better understanding of the aging mechanisms in ScD_2 target systems and their impact on mechanical reliability.

EXPERIMENT DESIGN

Test samples were fabricated following a two-step production procedure using deuterium to facilitate testing. 150 nm Sc films were sputtered onto four inch diameter, thermally oxidized silicon wafers. Some of the Sc films were then thermally charged with deuterium to form ScD_2. Accelerated ageing was performed by rapid thermal annealing (RTA) at 650˚C for 25 seconds to simulate the effect of partial aging during neutron generation. Grain size and orientation were measured before and after deuterium charging.

Changes in film and interface composition were explored using scanning Auger microscopy, by sputtering through the film thickness. The mechanical properties of both the as-deposited and aged films were then determined by nanoindentation with the Nanoindenter XP using a Berkovich tip and the continuous stiffness method. Continuous stiffness measurements were made at a frequency of 45 Hz and amplitude of 2 nm. The analysis and calculations to extract mechanical properties has been described in other work [10].

The four-point bending test method was chosen to measure the interfacial fracture resistance of the Sc/SiO_2 and ScD_2/SiO_2 interfaces. This method is advantageous because the film thickness does not need to be known, and the residual stresses of the films do not affect the measured adhesion energy values [12, 13]. This, then, will allow us to determine whether deadhesion of ScD_2 is due primarily to the effect of increasing film stress, or by progressive weakening of the interface. 3.8 mm wide beams were diced from Si {100} wafers with and without films. Notches were sawn into the backside of beams with Sc films. Si beams were then bonded to the beams with film using a low-temperature epoxy (Allied High Tech EpoxyBond 100) and cured at 150 °C for 45 minutes. This was a longer cure time than recommended by the makers to ensure complete curing. After bonding, all the Si surfaces on the sandwich specimens were chemically polished with HNA (1:3:8 $HF:HNO_3:HAc$). The inner and outer spans used for four-point bending experiments were 25 mm and 40 mm, and the loading rate was 1 $\mu m\ s^{-1}$.

CHEMICAL AND MECHANICAL PROPERTIES

Film atomic compositions were measured through the thickness in the as-deposited and aged states by scanning Auger microscopy, and grain size and orientation were measured by scanning electron microscopy. Auger scans revealed that a strong reaction occurred between the Sc and ScD_2 films and oxidized silicon substrates during deposition as shown in Figure 2(a) and Figure 2(b). This is indicated by the relative shifts of the Sc and O peaks. This is possibly due to a high density of reactive oxygen in the oxide after the wet oxidation process. After accelerated aging, the silicon dioxide appeared to dissociate at a faster rate than the as deposited systems, as shown in Figure 2(c). The structures of the Sc and ScD_2 films, hexagonal and FCC respectively, did not change after accelerated aging. There was also no clear change in grain size. There was a strong change in chemical composition, which led to alterations in the mechanical properties after accelerated aging.

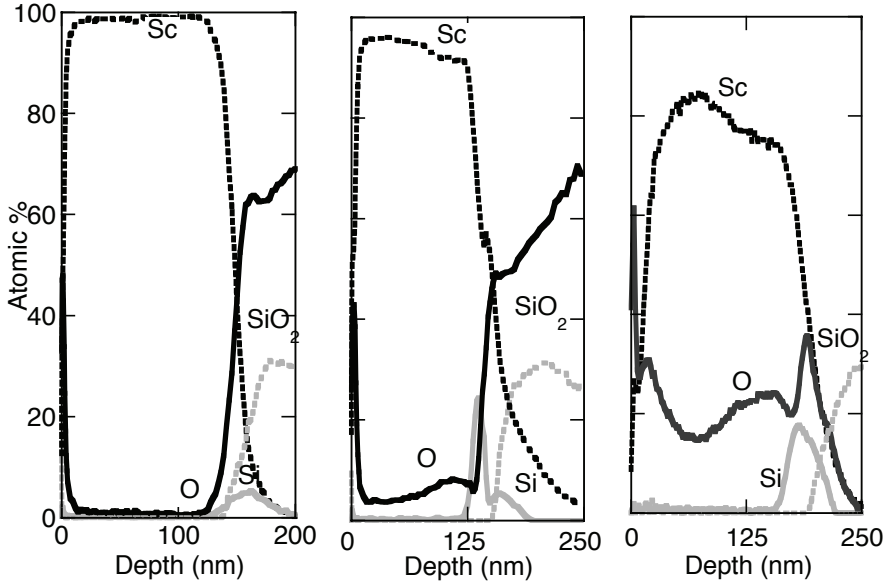
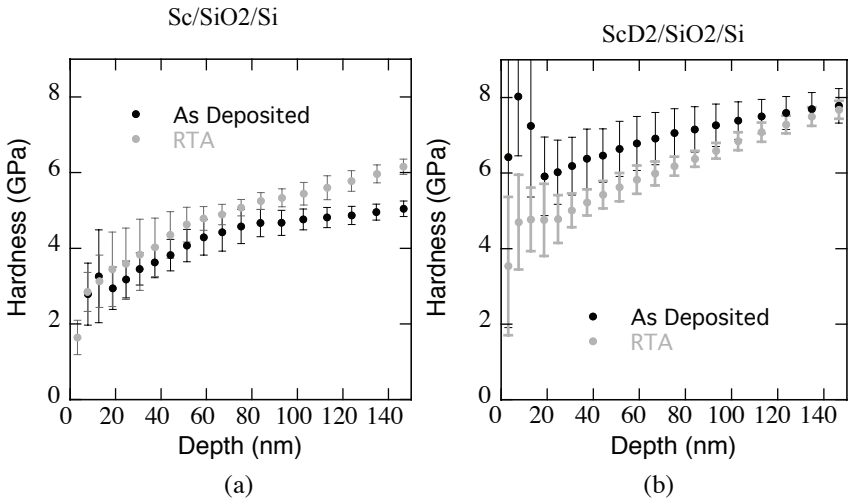


Figure 2. Silicon dioxide dissociation during deposition markedly changes composition along the interface and into the Sc (a) and ScD_2 (b) films. The changes accelerate with brief exposures to elevated temperatures as shown in (c) for films given a 650 ˚C rapid thermal anneal for 25 seconds.

As these films were annealed, their hardness evolved. The as-deposited films show that the hardness of the ScD_2 films were significantly higher than the Sc films, Figure 3(a). After aging, Figure 3(b), the ScD_2 and Sc films had similar hardness values. This was due to significant softening of the ScD_2.



(a) (b)

Figure 3. Hardness values of (a) $Sc/SiO_2/Si$ and (b) $ScD_2/SiO_2/Si$ film systems before and after aging. This shows that ScD undergoes a softening process.

INTERFACIAL FRACTURE ENERGY MEASUREMENT

Fracture energies were measured using four point bend tests [12, 13]. Eight samples of each type were tested; two to eight samples failed at the interfaces of interest (the Sc/SiO_2 or ScD_2/SiO_2 interface) for each system. In a four-point bend adhesion test, the interfacial fracture energy is calculated from substrate dimensions and elastic properties, as well as the applied load at which a "plateau" is observed in a load-displacement trace. A plateau load is indicative of neutral fracture geometry; that is, the crack neither accelerates nor stabilizes at fixed applied force. Typical load-displacement curves for ScD_2 with and without aging are shown in Figure 4. The initial plateau loads were first averaged over 20 μm for each individual sample and then the average of two samples was used to used to calculate the interfacial fracture energy. The fracture energy was the converted to a mode I energy using the empirically derived relationship by Hutchinson [14]. The measured values of interfacial fracture energy are shown in Figure 5. This figure indicates that both the Sc and ScD_2 film systems have a large decrease in interfacial fracture energy after aging. During aging, the compositions change (Figure 2) and the interface roughness increases. The drop in fracture energy is due to the change in film compositions seen composition during the RTA process. Although the Sc appears to have a higher interfacial fracture energy than the ScD_2 film, further testing is needed due to the small number of samples that failed along the interface.

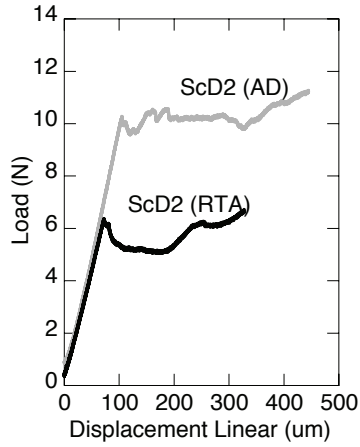


Figure 4: Load-displacement curves from four point bend tests of ScD_2 film systems in the as-deposited (AD) and aged (RTA) conditions.

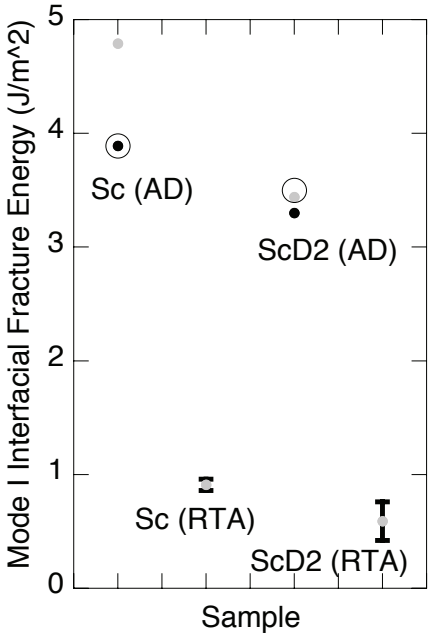


Figure 5: Calculations from the load plateaus show that the Sc and ScD_2 film systems have a large decrease in adhesion energy with aging (RTA) when compared to the as-deposited condition.

CONCLUSIONS

Accelerated aging of films for neutron generation were shown to have strong effects on the chemical composition, mechanical properties and fracture energies of the Sc and ScD_2 film systems. The ScD_2 films were much harder than the Sc films when initially deposited, but showed significant softening after accelerated aging. The interfacial fracture resistance testing also altered with aging - both the Sc and ScD_2 systems from over 3 J m^{-2} to less than 1 J m^{-2}.

ACKNOWLEDGMENTS

The authors thank Kim Archuleta from Sandia National Laboratories in Albuquerque, NM for her technical assistance in fabricating the films for this study. The authors also thank Sandia National Laboratories, a Lockheed Martin Company for the United States Department of Energy's National Nuclear Security Administration for support under Contract DE-AC04 94AL85000.

REFERENCES

1. Reijonen J. Compact neutron generators for medical, home land security, and planetary exploration. vol. 2005. Knoxville, TN, United States: Institute of Electrical and Electronics Engineers Inc., Piscataway, NJ 08855-1331, United States, 2005. p.49.
2. Chichester DL, Simpson JD. Compact accelerator neutron generators. Industrial Physicist 2003;9:22.
3. Monnin C, Ballanger A, Sciora E, Steinbrunn A, Alexandre P, Pelcot G. Characterization of deuteride titanium targets used in neutron generators. Nuclear Instruments and Methods in Physics Research, Section A: Accelerators, Spectrometers, Detectors and Associated Equipment 2000;453:493.
4. Walko RJ, Rochau GE. High Output Neuton Tube Using an Occuled Gas Ion Source. IEEE Transactions on Nuclear Science 1980;NS-28:1531.
5. Yartys VA, Riabov AB, Denys RV, Sato M, Delaplane RG. Novel intermetallic hydrides. Journal of Alloys and Compounds 2006;408-412:273.
6. Cowgill DF. Dynamic ion beam method for measuring deuterium diffusion in films. IEEE Transactions on Nuclear Science 1980;NS-28:1851.
7. Nibur KA, Bahr DF, Somerday BP. Hydrogen effects on dislocation activity in austenitic stainless steel. Acta Materialia 2006;54:267
8. Briant CL, Wang ZF, Chollocoop N. Hydrogen embrittlement of commercial purity titanium. Corrosion Science 2002;44:1875.
9. Adams DP, Rodriguez MA, Moody N, Floro JA, Romero JA. Structure and properties of reactively-deposited erbium hydride thin films. Moran, WY, United States: Minerals, Metals and Materials Society, Warrendale, PA 15086, United States, 2003. p.363.

10. Li X, Bhushan B. A review of nanoindentation continuous stiffness measurement technique and its applications. Materials Characterization 2002;48:11.
11. Kriese MD, Gerberich WW, Moody NR. Quantitative adhesion measures of multilayer films: Part I. Indentation mechanics. Journal of Materials Research 1999;14:300
12. Litteken CS, Strohband S, Dauskardt RH. Residual stress effects on plastic deformation and interfacial fracture in thin-film structures. Acta Materialia 2005;53:1955.
13. Ma Q, Bumgarner J, Fujimoto H, Lane M, Dauskardt RH. Adhesion measurement of interfaces in multilayer interconnect structures. Materials Reliability in Microelectronics VII. Symposium 1997:3.
14. Hutchinson JW, Suo Z. Mixed mode cracking in layer materials. Advances in Applied Mechanics, Vol 29 1992;29:63.
15. Cordill MJ, Moody NR, Bahr DF. The effects of plasticity on adhesion of hard films on ductile interlayers. Acta Materialia 2005;53:2555.

Effects of Hydrogen on Materials
Proceedings of the 2008 International Hydrogen Conference
Brian Somerday, Petros Sofronis, Russell Jones, editors, p 718-725
Copyright © 2009 ASM International®
All rights reserved.
www.asminternational.org

D LOSS AS A FUNCTION OF TEMPERATURE IN ERD_2 FILMS ON KOVAR WITH AND WITHOUT AN INTERMEDIATE MO DIFFUSION BARRIER

Daniel R. Kammler, William R. Wampler, Stuart B. Van Deusen Saskia H. King, Ralph G. Tissot, Luke N. Brewer, Loren I. Espada, Ronald S. Goeke

Sandia National Laboratories, Albuquerque, NM 87185 United States

ABSTRACT

The mechanisms governing D loss in ErD_2 films with and without a Mo diffusion barrier on kovar substrates were studied between 200 and 600 °C via in-situ Ion Beam Analysis (IBA). Significant intermixing between kovar and Er was observed above 450°C and between kovar and ErD_2 above 500 °C. The D loss mechanism in ErD_2 films was found to change from intermixing between kovar and ErD_2 at low temperatures (< 500 °C) to thermal decomposition at higher temperatures (> 500 °C). Diffusion between kovar and ErD_2 was measured isothermally at 500 and 550 °C. An activation energy of 2.1 eV and a pre-exponential factor of 0.071 cm^2/s were determined. Diffusion between the kovar components and ErD_2 film was inhibited by depositing a 200 nm Mo diffusion barrier between the kovar substrate and the ErD_2 film. The processing of the Mo diffusion barrier was shown to impact its performance. Intermixing between the kovar / Mo / ErD_2 stack becomes significant between 500 and 550 °C with a sputter deposited Mo diffusion barrier and between 550 and 600 °C for an electron-beam evaporated Mo diffusion barrier.

KEYWORDS: Diffusion, Erbium Deuteride, Hydrogen Storage

INTRODUCTION

Hydrogen isotopes useful in the production of neutrons can be stored in a metal occluder material such as Er. The stable temperature range of the hydrided occluder material is governed by a combination of thermodynamic[1] and kinetic[2] factors. In the case of a thin film occluder an important consideration is the time and temperature required to produce a reaction between the film and the substrate that will drive out the stored hydrogen isotopes. In some cases the stable temperature range can be significantly decreased by this interaction. Insertion of a suitable diffusion barrier between the occluder material and the substrate can help inhibit this effect. The results of an ion beam analysis (IBA) study to understand the extent to which Mo can serve as a diffusion barrier to prevent a reaction between an ErD_2 film and its kovar substrate are reported here.

In the IBA experiments described in this paper, both Rutherford Backscattering (RBS) and Nuclear Reaction Analysis (NRA) techniques were performed in-situ as a sample was heated to and held at temperatures between 200 °C and 600°C. The RBS data set provided information about the intermixing and/or reaction between the Er, Mo, and the components of the kovar. The NRA data yielded a quantitative picture of the Er/D ratio vs. depth in the ErD_2/kovar and ErD_2/Mo/kovar specimens.

EXPERIMENTAL

Table 1 below summarizes how each sample was processed and characterized.

Table 1. Summary of process conditions and subsequent characterization of samples

Sample ID	Mo deposition method (temperature)	Er deposition temperature	Sample Hydrided with D_2 ?	Characterization summary
1	No Mo	450 °C	No	20 min Isochronal (200-600 °C) RBS
2	No Mo	450 °C	Yes	20 min Isochronal (200-600 °C) RBS
3	No Mo	450 °C	Yes	Isothermal (500°C) RBS & NRA
4	No Mo	450 °C	Yes	Isothermal (550°C) RBS & NRA
5	Sputtered Mo (ambient)	450 °C	Yes	20 min Isochronal (200-600 °C) RBS & NRA
6	E-beam Mo (450 °C)	450 °C	Yes	20 min Isochronal (200-600 °C) RBS & NRA

Substrates for these experiments were 0.75 inch diameter kovar coupons that were degreased and chemically etched, wet hydrogen fired, and vacuum fired. The kovar alloy was comprised of 53 wt. % Fe, 29 wt% Ni, 17 wt.% Co, 0.35 wt.% Mn. The degrease and etch operation involved cleaning the as-received coupons with a 10% aqueous Brulin solution, pickling them in a boiling DI H_2O (45%) and HCl (55%) solution for 30 s, and etching in a solution of CH_3COOH (83%), HNO_3 (16.5%), and HCl (0.5 %) heated between 50 and 60 °C for 60 s (all percentages by volume of the concentrated acids). Immediately after the etch process the coupons were thoroughly rinsed in DI H_2O and denatured ethanol and blown dry with N_2. The wet hydrogen fire process consisted of a 30 min 800 °C anneal to remove residual metal oxides and organic contaminants.[3] The vacuum fire process involved a 30 min anneal at 600°C to remove dissolved gases and residual metal oxides.[3]

Mo was deposited by either DC magnetron sputtering or electron-beam evaporation. DC magnetron sputtering was performed in an Ar ambient at 10 mTorr at a rate of .54 nm/s using an 8 inch diameter target and 1 kW of power. Sputter deposition took place at ambient temperature. The base pressure prior to sputtering was 8.2 x 10^{-7} torr. During electron-beam evaporation substrates were heated to 450 °C. A base pressure of 8.3 x 10^{-7} torr was achieved prior to evaporation at a rate 1 nm/s. The target thickness of Mo films was 200 nm.

Er was deposited by electron-beam evaporation in 3 separate runs with base pressures below 1.5 x 10^{-6} torr. Substrates were kept at 450 °C and the Er deposition rate was 1 nm/s. The thickness for Er films was 500 nm. Following Mo and Er depositions a subset of the film stacks in this study were hydrided as noted in Table 1 using D_2 in a custom Sievert's apparatus.

In between each film deposition step and after final hydriding all specimens were sealed (using a bag sealer) in plastic bags where they remained until being processed further and/or being characterized. These bags were sealed with ambient air present.

Ion beam analysis was used to monitor changes in the films during annealing. Rutherford backscattering (RBS) with 2 MeV ^{4}He and D(^{3}He, p)^{4}He nuclear reaction analysis (NRA) with 800 keV ^{3}He were used to monitor changes in Er and deuterium concentrations versus depth. In both cases energy spectra were recorded using silicon charged particle detectors and conventional data acquisition systems for particle energy spectroscopy. During the annealing experiments, the samples were clamped to a resistively heated stage under vacuum in the ion-beam analysis target chamber. The sample temperature was measured by chromel-alumel thermocouples spot welded to the samples. Ion beam analysis was done with the samples near room temperature after each anneal. Heat-up and cool-down rates were typically about 50 °C per minute. This insured that heat-up and cool-down times were short compared to anneal times. Vacuum in the analysis chamber was 10^{-7} torr. A liquid N_2 cold trap was used to reduce sample oxidation from residual water vapor during annealing.

RESULTS AND DISCUSSION

Isochronal anneals of Er/Kovar and ErD_2/kovar

Figures 1 and 2 show RBS data from samples 1 and 2 in Table 1 collected during an isochronal annealing sequence with 20 minute anneal periods at successively higher temperatures from 200 to 600 °C in 50 °C increments. The horizontal axis is proportional to the energy of the scattered He ion. Counts near channel 460 are due to He scattered from Er at the surface. He ions scattered from Er beneath the surface reach the detector with less energy due to energy lost passing through the material. The scattering yield depends on the local Er concentration. The step in scattering yield near channel 360 indicates the back edge of the Er film at the interface with the kovar substrate. The step in counts just below channel 300 is from He scattered from kovar at the interface with the Er film.

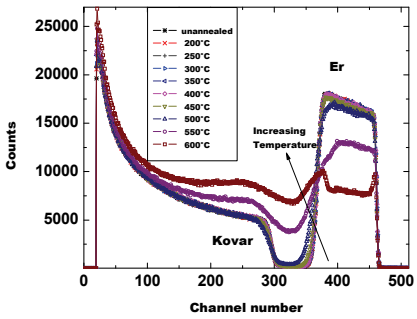


Fig. 1 RBS data from Sample 1: Er/kovar

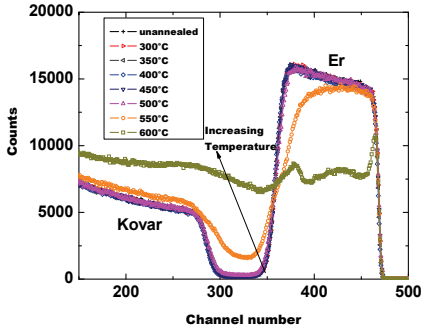


Fig. 2 RBS data from Sample 2: ErD_2 /kovar

Annealing causes broadening of the back edge of the Er peak due to mixing between the Er and kovar. Similar broadening is seen in the scattering from the kovar edge. The decrease in the height of the Er peak (with increasing temperature) indicates a decrease in the average local Er concentration at the corresponding depth. The decrease (with increasing temperature) is greatest at the Er back edge and smallest at the Er front edge. This is consistent with a diffusion driven gradient of Fe, Co, and Ni from the Er/kovar interface to the surface. These changes begin between 400 and 450°C and increase rapidly above 450 °C.

Figure 2 shows RBS data collected from sample 2 which was an ErD_2/kovar specimen annealed isochronally between 300°C and 600 °C in 50 °C increments for 20 minute intervals. Between 450-500°C changes become evident in the RBS spectra that indicate mixing between the elements of the kovar (Fe, Ni, and Co) and the ErD_2 film on top. These changes are more rapid above 500°C.

Isothermal anneals of ErD_2/Kovar

Figures 3 and 4 show RBS and NRA data collected from sample 3 which was an ErD_2/kovar specimen annealed isothermally for varying times at 500 °C. Mixing between the ErD_2/kovar is evident between 35 and 75 minutes of total annealing time. The NRA data show a change in the D/Er ratio between 35 and 75 minutes as well. D loss occurs predominantly from the ErD_2/kovar interface (rather than the ErD_2/vacuum interface). Figures 5 and 6 are similar to 3 and 4. They show RBS and NRA data collected from sample 4 which was an ErD_2/kovar specimen heated isothermally for varying times at 550 °C. At this higher temperature, mixing between the elements of the kovar (Fe, Ni, Co) and the ErD_2 film is more rapid and is already evident after only 5 minutes time. The NRA data show D loss after 5 minutes as well. Again, the D loss is predominantly from the ErD_2/kovar interface. Quantitative information related to the extent of intermixing can be obtained from the data in Figs. 3 and 5 which can then be used to extract an activation energy for diffusion of Er into kovar.

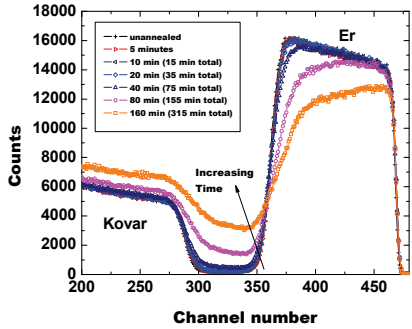


Fig. 3 RBS data from sample 3: ErD_2/kovar annealed at 500 °C

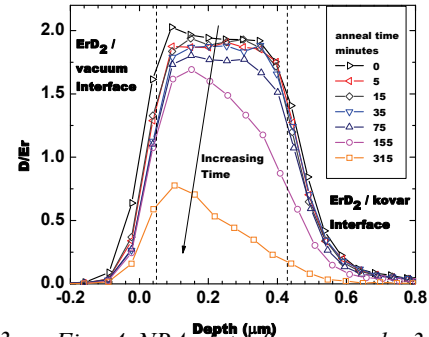


Fig. 4 NRA data from sample 3: ErD_2/kovar annealed at 500 °C

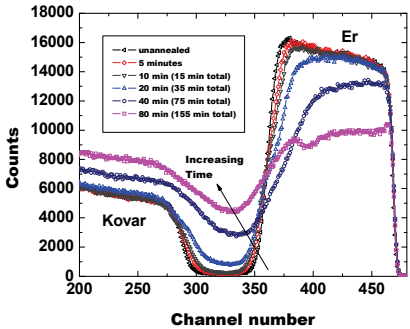


Fig. 5 RBS data from sample 4: ErD_2/kovar annealed at 550 °C

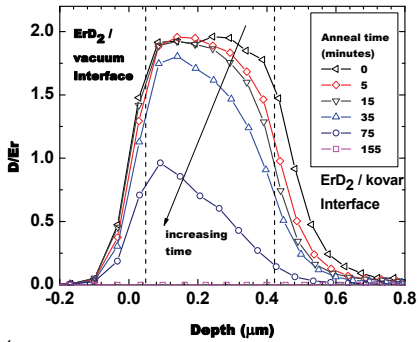


Fig. 6 NRA data from sample 4: ErD_2/kovar annealed at 550 °C

The solution to the diffusion equation in one dimension for a diffusion couple between Er and kovar is shown below[4]:

$$\frac{c}{c_0} = \frac{1}{2}\left[1 - erf\left(\frac{x}{2\sqrt{Dt}}\right)\right] \quad \textbf{(1)}$$

$$D = D_0 e^{-\frac{Q}{kT}} \quad \textbf{(2)}$$

Here c is [Er] as function of time (t) and position (x), c_0 is the concentration at time zero, D is the diffusion coefficient in equation 2. D_0 is the pre-exponential factor, Q is an activation energy, T is temperature, and k is Boltzmann's constant. While this solution fits with the initial boundary condition of the Er concentration profile we realize that we are making numerous other assumptions. We do not consider formation of intermetallic phases or the impact of concentration gradients on diffusion coefficients. We assume that Er diffuses out of the ErD_2 film into a kovar "solvent". Several factors contribute to broadening of the back edge of the Er peak in the RBS spectra in Figs. 3 and 5, including finite energy resolution of the detector, energy straggling of the ions, roughness of the interface between ErD_2 and kovar, variations in thickness of the ErD_2 film, and broadening of the interface due to

diffusion. In analyzing the RBS spectra we have used the SIMNRA simulation package.[5] Detector resolution is determined from the width of the Er front edge. Energy straggling effects are known and included in the simulation. Broadening of the back edge of the Er peak due to interface roughness, film thickness variations and mixing are collectively simulated by assuming a Gaussian distribution of ErD_2 film thicknesses, characterized by a FWHM (full width half max) Γ. Since RBS measures Er concentration vs. depth averaged over the area of analysis (1x1 mm), the influence of a graded interface from mixing is similar to the effect of a distribution of film thicknesses, so the two effects can be treated in a similar way. The width of this Gaussian distribution, is determined by fitting the spectrum simulated by SIMNRA to the data. The width Γ_0 for the as-deposited film prior to annealing characterizes the contributions from interface roughness, film thickness variations and initial mixing during deposition and loading of the film. The increased broadening observed after annealing Γ_D results from mixing by diffusion, and is related to the diffusion length $(Dt)^{1/2}$, since the derivative of equation 1 (dc/dx) is a Gaussian with $\Gamma_D = 3.33\ (Dt)^{1/2}$. The thickness distribution after annealing has the combined width $\Gamma=(\Gamma_0^2 + \Gamma_D^2)^{1/2}$.

A diffusion length is thus determined from the fit to each of the RBS data sets in Figs. 3 and 5 and is plotted against $\sqrt{t}$ in Fig. 7. Values for the diffusion coefficient at 500 and 550 °C are obtained from the slopes of least squares fits (lines in Fig. 7) to the diffusion length versus $\sqrt{t}$.

With values for the diffusion coefficient at two temperatures, an activation energy, Q, for diffusion and a pre-exponential factor D_0 can be obtained from equation 2. Doing this yields an activation energy of 2.1 eV and a pre-exponential D_0 of 0.071 cm^2/s. These parameters can then be used to generate the erbium concentration profiles for different times and temperatures. Figure 8 shows [Er] profiles at 550 °C.

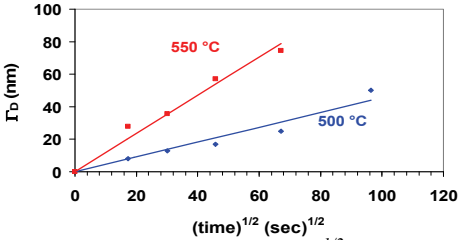


Fig. 7 Plot of Γ_D vs. $Time^{1/2}$

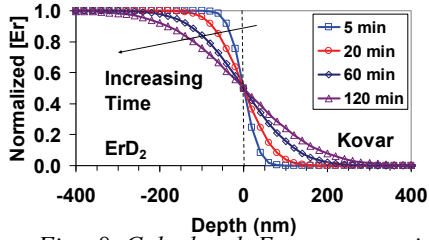


Fig. 8 Calculated Er concentration profile at 550 °C

ErD_2/Mo/Kovar RBS and NRA Studies

Figures 9 and 10 show RBS and NRA data collected from sample 5 which was an ErD_2(500 nm)/Mo(200 nm sputtered)/kovar specimen heated isochronally (20 minute increments) at temperatures between 300 °C and 600 °C. In these RBS spectra there is an additional peak between the Er back edge and the kovar front

edge, from the Mo layer between the kovar and ErD_2. Between 500 °C and 550 °C intermixing between the kovar, Mo diffusion barrier, and ErD_2 film begins.

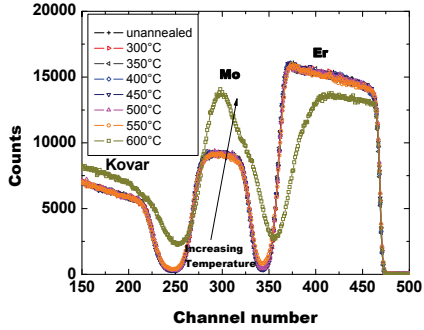


Fig. 9 RBS data from sample 5: ErD_2/Mo(sputtered)/kovar

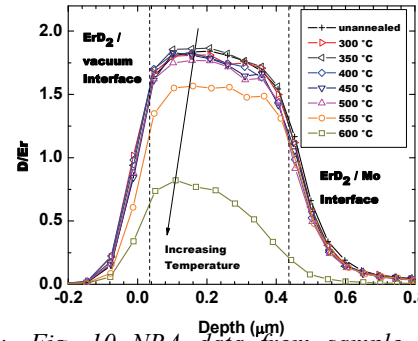


Fig. 10 NRA data from sample 5: ErD_2/Mo(sputtered)/kovar

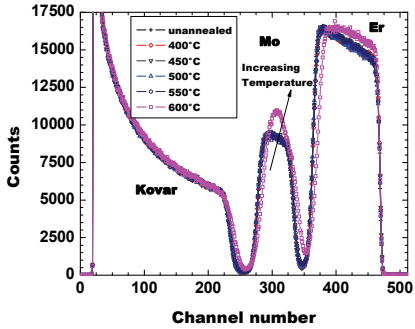


Fig. 11 RBS data from sample 6: ErD_2/Mo(evap)/kovar

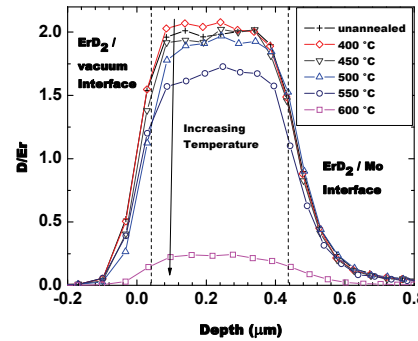


Fig. 12 NRA data from sample 6: ErD_2/Mo(evap)/kovar

Above 550 °C intermixing becomes significant. D loss begins between 500 and 550 °C as shown in Fig. 10. The loss appears to be more uniform (compared to Figs. 4 and 6) throughout the ErD_2 film, although there does appear to be slightly higher loss near the ErD_2/Mo interface at 600°C. Figures 11 and 12 show RBS and NRA data collected from sample 6 which was an ErD_2(500 nm)/Mo(200 nm electron-beam evaporated)/kovar specimen heated isochronally (20 minute increments) at temperatures between 300 °C and 600 °C. No evidence of intermixing appears until the sample exceeds 550°C. D loss begins between 500 and 550 °C and is uniform throughout the ErD_2 film. Figures 10 and 12 show significant D loss prior to the onset of intermixing. In these cases ErD_2 decomposition is probably limited by surface release and therefore may depend on surface conditions, e.g. oxide.

The data in Figs. 9 and 11 indicate that Mo produced using the electron-beam process is a marginally better diffusion barrier than that produced using the sputtered Mo process. Scanning Transmission Electron Microscopy (STEM) data collected during a previous study suggest this may be a consequence of the different film microstructures produced by the different processing techniques. Compositional

information collected from cross-sections of film stacks (prepared in a manner identical to those in Figs. 9 and 11) that had been subjected to a 2 hr. 564 °C high vacuum anneal revealed that the sputtered Mo had substantial quantities of Er along the grain boundaries.[6] This was consistent with the observation that the sputtered Mo also had a columnar grain structure with a significantly higher aspect ratio and more grain boundary area than the electron-beam evaporated Mo.[6]

SUMMARY AND CONCLUSIONS

The intermixing between a kovar substrate and Er or ErD_2 films with and without the presence of an intermediate Mo diffusion barrier was investigated for different times and temperatures using a combination of IBA techniques. Substantial intermixing begins between 400 and 450°C for Er/kovar and 450 to 500 °C for ErD_2/kovar. Release of deuterium from the ErD_2 films in this study was found to be driven both by intermixing with components of the kovar substrate (< 500 °C) and thermal decomposition (> 500 °C). RBS data collected isothermally at 500 and 550 °C have yielded an activation energy of 2.1 eV and a pre-exponential factor of 0.071 cm^2/s for diffusion of Er into kovar from ErD_2. The presence of a Mo diffusion barrier was shown to help reduce intermixing between the ErD_2 film and kovar substrate. Differences in the effectiveness of the electron-beam evaporated Mo diffusion barrier (which showed evidence of intermixing between 550-600 °C) and the sputtered Mo diffusion barrier (which showed evidence of intermixing between 500-550 °C) may be a consequence of their different microstructures.

ACKNOWLEDGMENTS

Special thanks to Cathy Sobczak for sputtering deposition, Firouzeh Jalali for evaporation, and Kathleen Hatch for D loading. Sandia is a multiprogram laboratory operated by Sandia Corporation, a Lockheed Martin Company, for the United States Department of Energy under contract DE-AC04-94AL85000.

REFERENCES

1.W. M. Mueller, J. P. Blackledge and G. G. Libowitz, Metal Hydrides, Academic Press (New York, 1968), pp. 51-89.
2.P. S. Rudman, "Hydriding and Dehydriding Kinetics," *Journal of Less-Common Metals*, Vol. 89, No. (1983), pp. 93-110.
3.L. Beavis, private communication, Sandia National Laboratories, (2005).
4.A. G. Guy and J. J. Hren, Elements of Physical Metallurgy, Addison-Wesley (Menlo Park, CA, 1974), p. 382.
5.M. Mayer, "SIMNRA User's Guide," Max-Planck-Institut für Plasmaphysik, Report IPP 9/113 (1997)
6.D. R. Kammler et al. "Evaluation of Diffusion Barrier Materials to Inhibit mixing between Kovar and Erbium Hydride," Sandia National Laboratories, SAND2006-5864 (2006).

Effects of Hydrogen on Materials
Proceedings of the 2008 International Hydrogen Conference
Brian Somerday, Petros Sofronis, Russell Jones, editors, p 726-734
Copyright © 2009 ASM International®
All rights reserved.
www.asminternational.org

TRITIUM EFFECTS ON DYNAMIC MECHANICAL PROPERTIES OF POLYMERIC MATERIALS

Elliot A. Clark
Savannah River National Laboratory, Aiken, South Carolina USA

ABSTRACT

Dynamic mechanical analysis has been used to characterize the effects of tritium gas (initially 1 atm. pressure, ambient temperature) exposure over times up to 2.3 years on several thermoplastics- ultrahigh molecular weight polyethylene (UHMW-PE), polytetrafluoroethylene (PTFE), and Vespel® polyimide, and on several formulations of elastomers based on ethylene propylene diene monomer (EPDM). Tritium exposure stiffened the elastic modulus of UHMW-PE up to about 1 year and then softened it, and reduced the viscous response monotonically with time. PTFE initially stiffened, however the samples became too weak to handle after nine months exposure. The dynamic properties of Vespel® were not affected. The glass transition temperature of the EPDM formulations increased approximately 4° C. following three months tritium exposure.

INTRODUCTION

There are three known isotopes of hydrogen: "protium" (^{1}H), deuterium (^{2}H), and tritium (^{3}H). Tritium is radioactive, decaying by the beta decay mechanism with a Half-life of 12.3 years; the average decay energy is 5.7 KeV, and the maximum decay energy is 18.6 KeV [1]. Hydrogen molecules dissolve in and permeate polymeric materials [2], and so if tritium gas contacts structural polymers, tritium will likewise permeate the polymers. The radioactive decay of tritium results in a beta particle having a penetration depth of about 6 microns in matter of unit density and about 6 mm in air [3]. If solid polymers are exposed to tritium gas, the beta particles will impinge on the surface (directly from the gas) and also the bulk of the polymer will be exposed to beta radiation from decaying dissolved tritium molecules.

Polymers degrade when exposed to ionizing radiation [4, 5, 6]. The amount of degradation depends on many factors including polymer type, specific formulation, total dose, dose rate, and presence of oxygen. When polymers are exposed to ionizing radiation (gamma rays, alpha particles, or beta particles from tritium decay), highly reactive "free radical" groups form when the energy of the ionizing photon or particle is absorbed. These free radical groups continue to react in turn, in many complicated ways, and the initial overall response of any given polymer can be thought of as being either cross-linking or degradation by chain-scission. Materials

that cross-link initially become stiffer, stronger and less pliable and those that degrade initially become weaker and then finally decompose to a form that has no mechanical strength, such as a powder or a liquid. Some polymers undergo one dominant mode of degradation, while others exhibit a mixed mode of both cross-linking and chain-scission.

Many commercially available gas processing components (valves, seals, pumps, etc.) contain polymers; polymers are especially useful for reproducible seals such as valve stem tips and O-rings. Avoiding all polymers in tritium handling systems is thus economically impractical. There is a fairly large scientific literature about the relative resistance of polymers to gamma radiation in air, and to select polymers for tritium service it is assumed that the relative resistance of polymers to tritium is the same as that of the same polymers to gamma radiation in air. However, the service lifetime of a given polymeric component in a specific application currently can only be determined by monitoring the performance of the component.

To help understand the performance of polymers in tritium processing, a program is underway at the Savannah River Site to study effects of tritium gas exposure on the properties of several thermoplastics and elastomers. Materials used currently or historically at the Savannah River Site tritium facilities are chosen for study: three thermoplastics i) ultrahigh molecular weight polyethylene (UHMW-PE), ii) polytetrafluoroethylene (PTFE), and iii) Vespel® polyimide and four types of the elastomer ethylene propylene diene monomer (EPDM). Dynamic Mechanical Analysis (DMA) was used to evaluate the mechanical properties of the exposed polymer.

MATERIALS AND EXPOSURE CONDITIONS

UHMW-PE, PTFE, and Vespel® samples were cut from nominally 1.6 mm (1/16") thick sheet, to a size of about 30 mm by 10 mm. The PTFE was "virgin" unfilled, and the Vespel® was the SP-1 unfilled grade. The EPDM samples were obtained from Los Alamos National Laboratory (LANL): sheets of Nordel™ 1440 and Royalene® 580H, both standard graphite filled sheets from vendors and formulations synthesized without graphite at LANL were provided. The filled Nordel™ 1440 had a nominal thickness of 1.94 mm, the filled Royalene® 580 0.85 mm, the unfilled Nordel™ 0.7 mm and the unfilled Royalene® 0.65 mm. The filled polymers appeared black, and the unfilled versions appeared light grey. Rectangular slab-shaped samples having nominal lengths of 33 mm and nominal width of 9 mm were cut from the sheets.

The samples were exposed in closed stainless steel containers to what initially was 101 kPa (1 atmosphere) of pure tritium gas at ambient (room) temperature for various times, and the effects of tritium on the polymer samples was characterized by DMA.

DYNAMIC MECHANICAL ANALYSIS

A TA Instruments model 2980 dynamic mechanical analyzer was used for this study. This device applies a sinusoidal force at specified frequencies, and the resulting phase angle δ between the load and displacement is measured. From the measured load, displacement amplitude, phase angle and knowing the specimen geometry (rectangular slab used in this study) and sample holder type, the system calculates the various quantities that describe the elastic and viscoelastic properties. The modulus is represented as a complex number: the real part or "storage modulus" is a measure of the elastic deformation of the polymer, and the imaginary part or "loss modulus" measures the time-dependent viscoelastic deformation. Tan δ is the loss modulus divided by the storage modulus.

The sample configuration was the three-point bend configuration for the thermoplastics (ultrahigh molecular weight polyethylene (UHMW-PE), polytetrafluoroethylene (PTFE), and Vespel® polyimide) and single cantilever for the elastomer EPDM samples. The DMA controls the sinusoidal displacement amplitude, which is chosen to be within the region of linear viscoelasticity as determined in preliminary experiments that varied the amplitude. The force required to achieve the chosen amplitude and the phase angle between the applied force and the displacement of the sample, is measured continuously while the sample temperature is increased with time at 1° C/minute, and the device calculates the storage and loss moduli and tan δ for the chosen frequencies (1, 3, 10, 30 Hz) and temperature.

RESULTS

UHMW-PE

The loss modulus of unexposed UHMW-PE exhibits a pronounced maximum at 50° C. at 1 Hz (Fig. 1) that is reduced significantly after tritium exposure (Fig. 2). The tan delta of unexposed UHMW-PE increases significantly starting at room temperature to the softening point (Fig. 1), and this increase is eliminated from the tritium exposed material (Fig. 2).

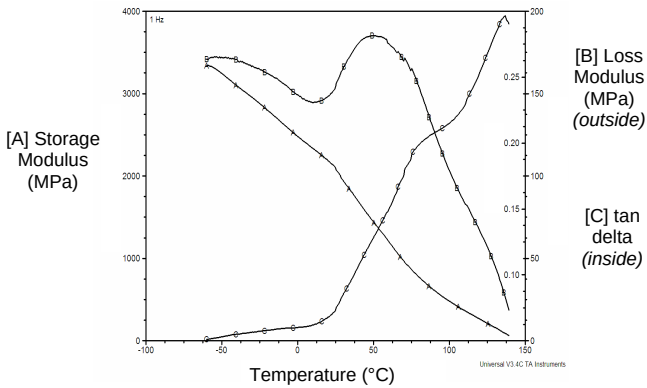


Figure 1: Storage modulus [A], loss modulus [B] and tan delta [C] of unexposed UHMW-PE. 1 Hz. test frequency, temperature initially at -60° C. and increased at 1° C./min. [7]

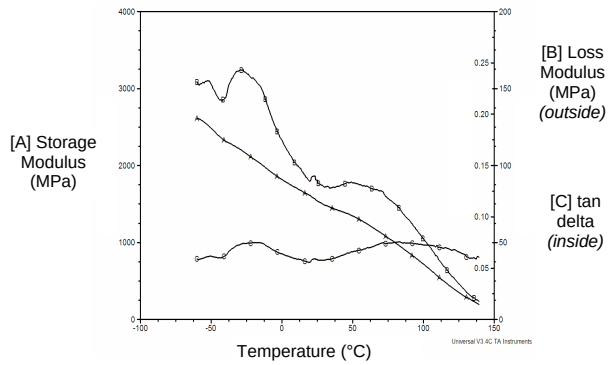


Figure 2: Storage modulus [A], loss modulus [B] and tan delta [C] of UHMW-PE after 2.3 years tritium exposure. 1 Hz. Temperature set at -60° C. and increased at 1° C./min. [7].

The storage modulus of UHMW-PE initially increases with the length of tritium exposure, and then decreases (Fig. 3). This observation is in accord with the classical concept of initial stiffening by radiation induced cross-linking, followed by a net degradation of properties.

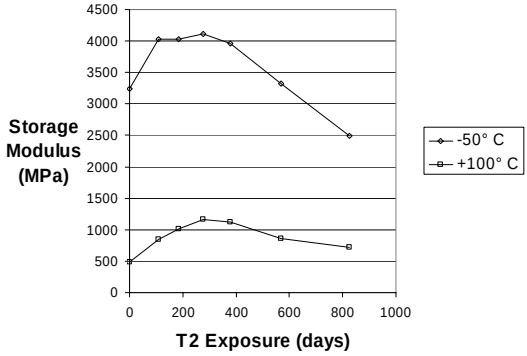


Figure 3. Variation of storage modulus of UHMW-PE with exposure time, at -50° and +100° C. as indicated. 1Hz [7].

At 100° C. there is a significant increase in the storage modulus with test frequency of unexposed UHMW-PE, and tritium exposure decreases this significantly (Fig. 4).

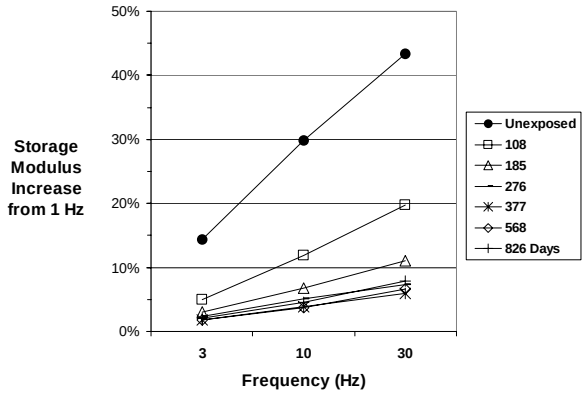


Figure 4: Storage modulus of UHMW-PE at 3, 10 and 30 Hz divided by that at 1 Hz, for various lengths of tritium exposure (0-826 days as indicated)[7]. Temperature 100° C.

PTFE

The storage modulus, loss modulus, and tan delta of PTFE reveal a crystallographic phase transition at about 30° C. (Fig. 5) [8]. This feature is independent of test frequency (1, 3, 10, 30 Hz).

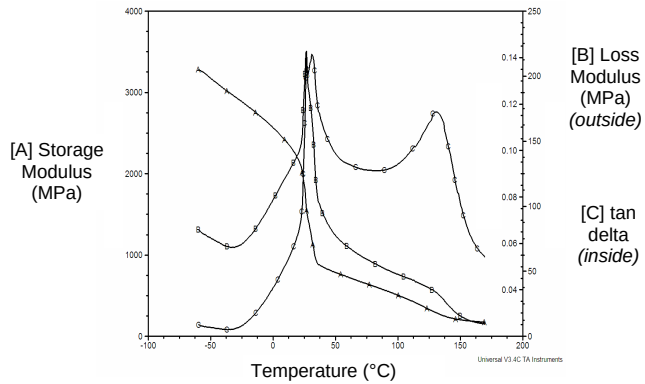


Figure 5. Storage modulus [A], loss modulus [B], and tan delta [C] of unexposed PTFE. 1 Hz applied load, 1° C./min temperature rise. [7]

The crystallographic phase transition does not change with tritium exposure; however the tan delta peak between 100-160° C. is reduced similarly to UHMW-PE (Fig. 6).

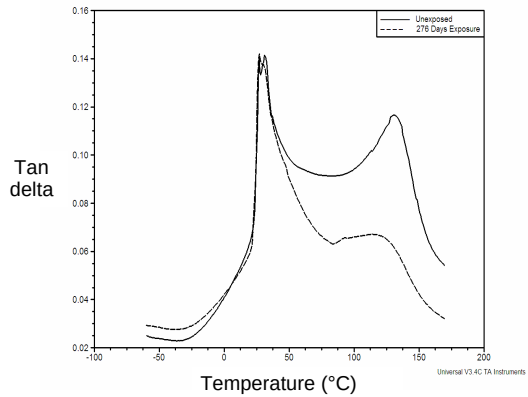


Figure 6. Tan delta versus temperature for PTFE, unexposed (solid line) and 276 days exposure to tritium gas (dotted line)[7]

PTFE samples exposed to tritium for longer than 276 days were too weak to handle without breaking. Up to 276 days exposure, the storage modulus increased and the frequency dependence of the storage modulus decreased similar to UHMW-PE.

Vespel® polyimide

The viscoelastic response of Vespel® SP-1 polyimide (Fig. 7) was unaffected by tritium exposure of up to 2.3 years.

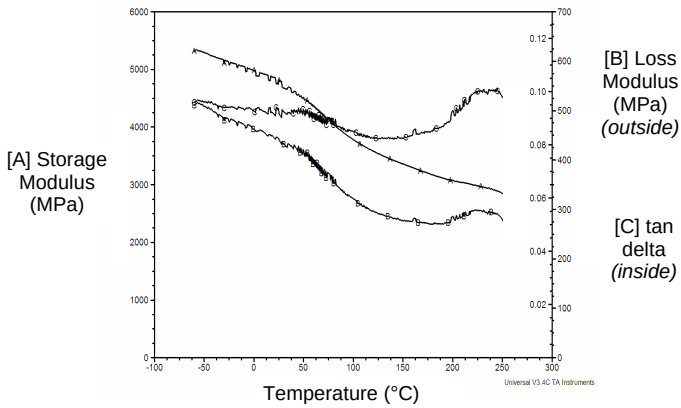


Figure 7. Storage modulus (A), loss modulus (B), tan delta (C) of unexposed Vespel® SP-1 polyimide. 1 Hz applied load, 1° C./min temperature rise.[7]

EPDM

ASTM E 1640 "Standard Test Method for Assignment of the Glass Transition Temperature by Dynamic Mechanical Analysis" uses the intersection of two tangents of the storage modulus versus temperature curve: the tangent of data below Tg and the tangent at the inflection point of the modulus in the middle of the glass transition (Fig. 8). The temperature of the tangents intersection is regarded as being Tg. The standard requires an applied frequency of 1 Hz and a temperature increase rate of 1 °C/minute, which were used for these tests. Another method for determining Tg is the peak temperature of the loss modulus (Fig. 8).

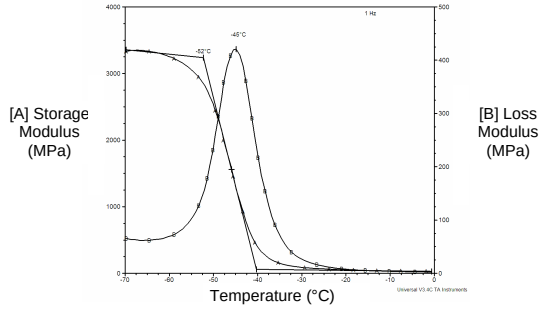


Figure 8. Storage Modulus (A) and Loss Modulus (B) of one-week exposed filled Nordel® 1440 at 1 Hz, temperature increasing 1° C./min. Tangent intercept method of ASTM E-1640 giving Tg= -52° C. and loss modulus peak temperature Tg = -45° C. is shown.

A plot of the measured glass transition temperatures reveals that three months of tritium exposure results in about a 3° C. increase in Tg (Fig. 9) for all four resins tested. There was no difference comparing the filled versus unfilled material, and the

Royalene® resins had a uniformly lower Tg than that for the comparable Nordel® resins (Fig. 9)

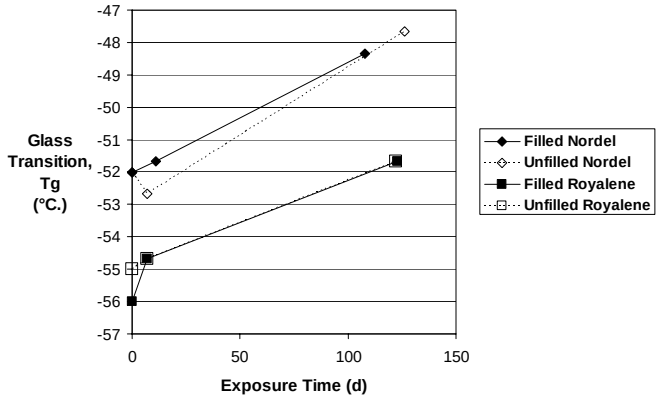


Figure 9. Glass transition temperature (Tg ° C.) versus tritium exposure time. (Tg determined using the ASTM E-1640 tangent intercept method.

CONCLUSIONS

Tritium gas exposure reduces the viscoelastic response of UHMW-PE and PTFE. The exposure initially increases the storage modulus for both, and for UHMW-PE eventually the storage modulus decreases. This behavior is consistent with the degradation of polymers by other types of ionizing radiation. The glass transition temperature of several EPDM formulations increases with tritium gas exposure.

ACKNOWLEDGMENTS

The efforts of K. Shanahan, G. Staack, W. Britt, G.M. Thomas, K. Neikirk, and D. Pilgrim of Savannah River National Laboratory and M. Smith, formerly of Los Alamos National Laboratory, is gratefully acknowledged.

REFERENCES

1. DOE Handbook: Tritium Handling and Safe Storage. US Department of Energy Handbook, Appendix A, DOE-HDBK 1129-2007 (2007). URL: http://www.hss.energy.gov/NuclearSafety/techstds/standard/hdbk1129/hdbk1129-07.pdf

2. S. Pauly, "Permeability and Diffusion Data", chapter in J. Brandrup, E.H. Immergut, E.A. Grulke, eds. Polymer Handbook (Fourth Edition). Wiley-Interscience (New York 1999), pp. 543-569.

3. E.A. Evans, Tritium and its Compounds. D. Van Nostrand (Princeton, New Jersey USA 1966), p. 2.

4. D.C. Phillips. “Effects of Radiation on Polymers”. *Materials Science and Technology*, Vol. 4 (January 1988), pp 85-91.

5. A. Chapiro. Radiation Chemistry of Polymeric Systems. Vol. XV of series High Polymers, Wiley-Interscience (New York 1962), Chapter IX.

6. W.W. Parkinson, O. Sisman. “The Use of Plastics and Elastomers in Nuclear Radiation”. *Nuclear Engineering and Design*, vol. 17 (1971), pp 247-280.

7. E.A. Clark, K. L. Shanahan, “Effects of Tritium on UHMW-PE, PTFE, and Vespel® polyimide”, *Fusion Science and Technology*, 52 (2007), pp 1007-1011.

8. P. J. Rae, E. N. Brown, “The Properties of Poly(tetrafluoroethylene) (PTFE) in Tension”. *Polymer*, 46 (2005), p. 8128.

Effects of Hydrogen on Materials
Proceedings of the 2008 International Hydrogen Conference
Brian Somerday, Petros Sofronis, Russell Jones, editors, p 735-742
Copyright © 2009 ASM International®
All rights reserved.
www.asminternational.org

STUDIES OF HYDROGEN ISOTOPES SUPERPERMEATION THROUGH MEMBRANES OF GROUP V METALS ON "PROMETHEUS" SETUP

R.K. Musyaev, A.A. Yukhimchuk, B.S. Lebedev
Russian Federal Nuclear Center-All–Russian Research Institute of Experimental Physics (RFNC-VNIIEF), Sarov, Nizhny Novgorod Region, Russia

A.O. Busnyuk, M.E. Notkin, A.A. Samartsev, A.I. Livshits
St.Peterburg State University of Telecommunications (SUT), St.Peterburg, Russia

ABSTRACT

To develop the membrane pumping technology and to simulate tritium recirculation by means of superpermeable membranes at Russian Federal Nuclear Center -VNIIEF in the "Prometheus" setup, the experiments on superpermeation of hydrogen isotopes through membranes of Group V metals were carried out. The superpermeability phenomenon was suggested to use in fusion machines to separate the fuel mixture from helium ashes, to arrange in-vessel fuel recirculation contours and effective evacuation of fuel mixture out of machine exhaust.

The experimental results on superpermeation of thermal atoms of hydrogen isotopes including tritium through a cylindrical niobium and vanadium membranes are presented. The possibility of effective pumping, separation of hydrogen isotopes from helium and residual gas, compression and recuperation of hydrogen isotopes by means of superpermeable membrane was demonstrated. The evaluation of membrane pumping rates and asymmetry degree of niobium and vanadium membranes was given. It follows from results that the separation of D/T from He with employment of the techniques of superpermeable membranes might reduce the total amount of tritium in fuel cycle and substantially enhance the resource of cryogenic pumps evacuating helium.

INTRODUCTION

The term "superpermeability" taken in this paper implies that metallic membranes of a macroscopic thickness may be virtually "transparent" to suprathermal (≥ 1 eV) hydrogen particles, comparable an opening of the same area. Virtually the whole

flux of gas being implanted in metal lattice, or even just sticking to metal surface, passes through the membrane, irrespective of its temperature and thickness.
Selective pumping and recycling techniques based on superpermeability can be employed in fusion reactor fuel cycle and periphery systems [1,2]. The authors suggest that a major part of D/T (e.g. 99%, or even more) should be extracted from the reactor exhaust and put back into fuel cycle before it reaches the cryopumps, which are designed for evacuating virtually only helium and gas impurities. The fuel mixture is to be isolated by means of superpermeable membranes placed on the path between the core plasma and cryopumps; such membranes are capable of selectively letting through hydrogen (D/T) – continuously, with a very high speed, and with an automatic orders-of-magnitude compression of the permeating gas.
The materials most suitable to obtain superpermeability are the Group 5 metals: V, Nb and Ta. Vanadium is likely to be the best of them for fusion applications due to its uniquely low induced radioactivity. The studies of the superpermeability phenomenon with all three hydrogen isotopes through niobium and vanadium membranes are shown in this paper.

EXPERIMENTAL

Experimental studies of the superpermeability phenomenon have been performed with a cell (Fig.1) of the "Prometheus" setup [3, 4]. The cell comprises a cylindrical membrane of group V metals (100 mm diameter, 180 mm height, and 0.1 mm thickness) and thermal atomizer. The membrane is positioned vertically to divide the cell into an inlet and an outlet chambers. The inlet and outlet chambers are continually pumped with ion pumps through ducts with conductivities for H_2 of 18 l/s and 15 l/s, respectively.

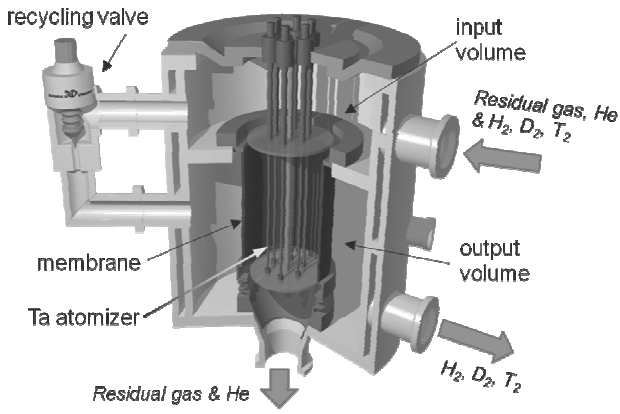


Figure 1: The cell of "Prometheus" setup for study of superpermeation of hydrogen isotopes.

The thermal atomizer placed inside the membrane consists of three separate tantalum ribbons that can be ohmically heated up to a temperature of 2300 K. Their total surface area amounts to 120 cm^2 (about 20% of the membrane area). Due to the atomizer operation the membrane is heated by radiation. Membrane temperature is measured with pyrometers. The cylindrical membrane ends are screened by two quartz disks to prevent the losses of atoms produced by the atomizer inside the membrane hollow, and also to partly protect other device elements from the influence of atomic hydrogen.

Membrane Pumping and demonstration of Compression and Tritium recirculation

At first a constant flux of hydrogen flowed through the continuously pumped inlet chamber at pressure of 10^{-7} to 10^{-4} mbar. In order to prevent embrittlement of the atomizer ribbons because of hydrogen absorption, their temperature was kept in the range of 500K to 700K. Heating of the atomizer ribbons to temperature from 1300K to 2100K results in drastic rise of dissociation rate (atomization) of hydrogen molecules at the atomizer surface. Produced atoms are getting at the membrane inlet surface, stick at it, get dissolved in the metal, permeate to the membrane outlet side, and are released from the outlet surface as molecules. The essential part of produced atoms permeated through the membrane in our experimental conditions. As a result we obtain a typical pattern of superpermeability phenomenon: the pressure in the inlet chamber is decreased steeply, while the pressure of hydrogen in the outlet chamber is rising until a steady state permeation flux is established (Fig. 2). After reduction of atomizer temperature to initial value ("switching off" of the atomizer) the inlet and outlet pressures return to their initial levels.

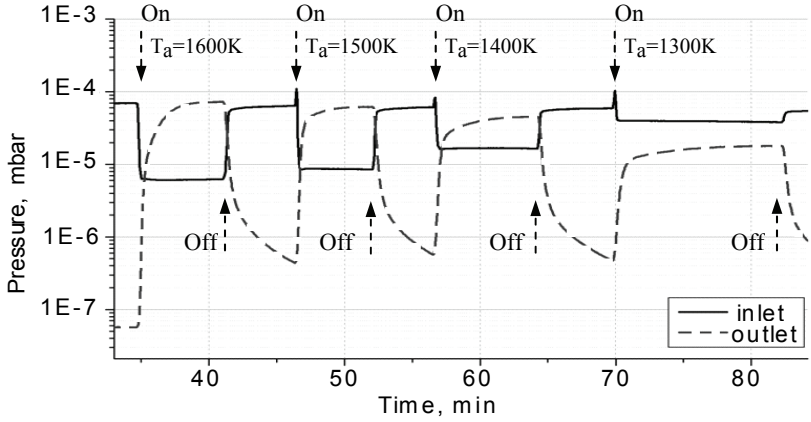


Figure 2: A typical pattern of hydrogen isotopes pressures at inlet and outlet sides of the membrane by "switching on" the atomizer to different temperature.

A special experiment has been carried out to demonstrate a possibility of compression and recirculation of permeating hydrogen. The pumping of outlet chamber with the external pump was ceased after permeating flux reached the steady state level. As a result, the outlet pressure got rising (see Fig. 3) due to the accumulation of permeating hydrogen in the outlet chamber (compression mode). That was accompanied with an inlet pressure rise because of an enhanced molecular driven permeation through the membrane back from the outlet to the inlet side. Comparison of the pressure increment at the input and output sides was used to calculate such an important membrane parameter as maximum compression (ratio of outlet to inlet pressures). As one can see in Fig.3, the compression value exceeds three orders of magnitude.

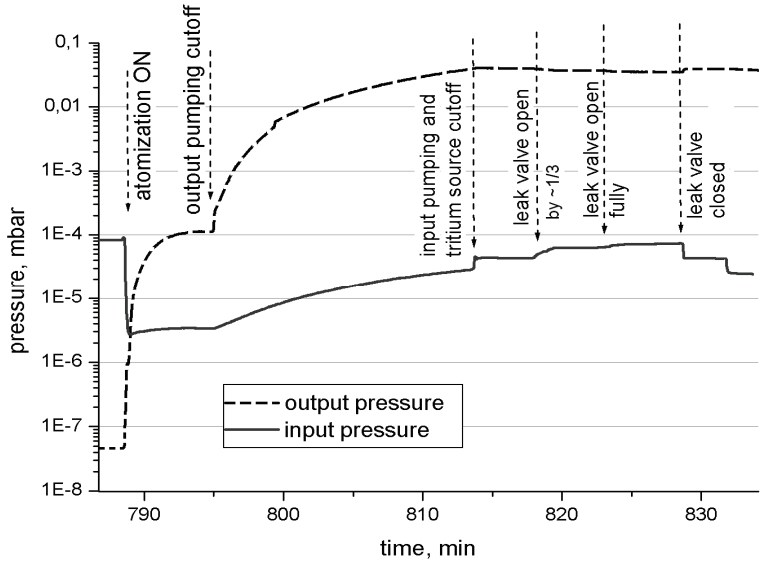


Figure 3: Demonstration of compression and tritium recirculation by means of superpermeable membrane.

It was also revealed from the obtained data that the membrane behaves strongly asymmetric – a major part of atomic hydrogen absorbed by membrane at the inlet side is released to outlet side. Comparison of the pressure increment at the input and output side was used to calculate the degree of the membrane asymmetry (relation between the inlet permeating flow and the outlet flow), which depend on the sticking coefficients (experimental value: $\alpha_{inlet}=2\cdot10^{-5}\div5\cdot10^{-5}$ and α_{outlet} $\sim2\cdot10^{-4}$). Probable cause of the asymmetry is deposition of tantalum onto the inlet membrane surface from atomizer.

A membrane pumping system based on superpermeability permits an effective separation of helium and evacuation of the fuel mixture from the fuel machine exhaust. Since the membrane is able to compress the gas permeating through it, one

also can arrange a direct recirculation of the hydrogen evacuated by the membrane and its return into the fuel cycle.

In order to demonstrate the possibility of recirculation a leak valve ("recycling valve" in Fig. 1) connecting the outlet and inlet chambers was opened to let part of tritium gas accumulated in the outlet chamber back into the inlet chamber. Before the valve was opened (Fig.3) both the inlet chamber pumping by the ion pump and tritium admittance from tritium source were ceased. The varying of the vacuum conductivity of the leak valve allows changing the influx so that the inlet pressure can be adjusted to any value in the operation range. As a result, a closed tritium circuit was formed.

The membrane pumping rate of hydrogen isotopes was determined at different temperatures of atomizer by comparing it with the duct conductance σ_{in} of the inlet chamber:

$$S = \left(\frac{p_1}{p_2} - 1 \right) \cdot \sigma_{in}$$

where p_1 is an initial partial pressure in the inlet chamber before initiation of the atomizer, and p_2 is a steady state inlet partial pressure with the atomizer operating. As it was shown in our previous papers [3], selective pumping rate of superpermeable membrane is inversely proportional to square root of isotopic mass as a first approximation. Experimental data on the membrane pumping rate of protium, deuterium and tritium as a function of inlet gas pressure are shown in Fig.4.

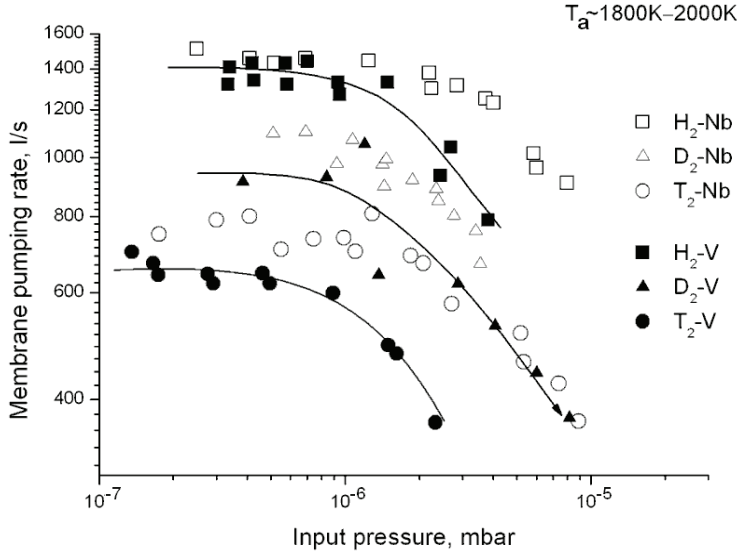


Figure 4: Comparison of the membrane pumping rates for protium, deuterium and tritium

Tritium and helium mixture experiment

The obvious separation of D/T mixtures from He is one of proposals put forward on superpermeable membranes applications in fusion [2]. A special experiment was staged to demonstrate this separation possibility of mixture. Experimental curves on time dependence of partial pressure obtained by mass-spectrometers for atomic mass 4 m/e and 6 m/e are shown in Fig.5. The experiment is initiated with the establishment of a constant gas mixture flux. After the atomizer had been switched (point of time t_1) and a permeation flux had been established, the helium flux to inlet chamber was ceased (point of time t_2). Then the atomizer was switched off (point of time t_3) and on again (point of time t_4). After second switching on, the helium flux was opened into inlet chamber again (point of time t_5). As can be seen from picture the outlet pressure doesn't respond to change of inlet pressure that means of selective possibility of superpermeable membranes for hydrogen isotopes.

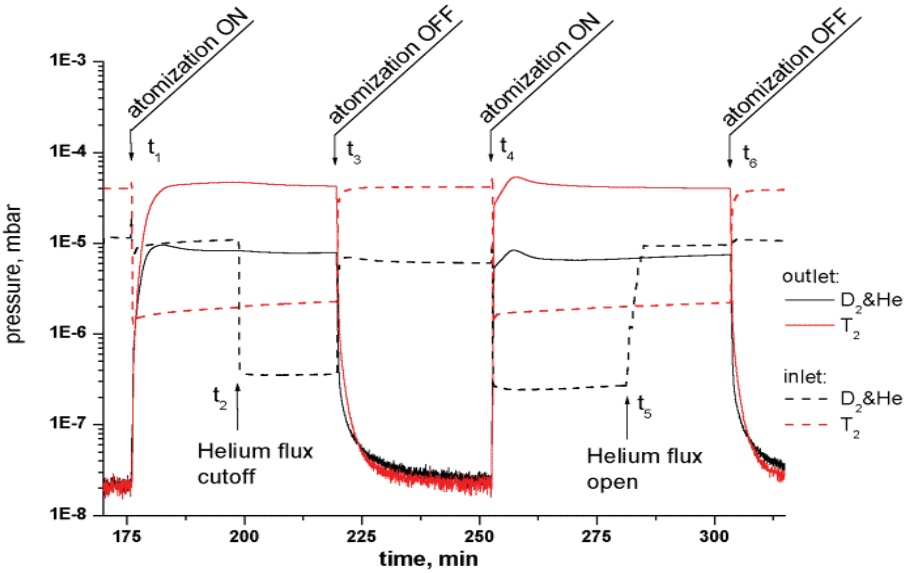


Figure 5: Time dependence of partial pressure at the inlet and outlet sides of the membrane that occurs under change of helium flux.

Tritium inventory

To estimate the tritium inventory in the membrane bulk the shaded area in Fig.6 was calculated for different temperatures of membrane under same initial flux. Temperature dependence of tritium retention under experimental upstream flux equals ~10^{16} T/sec during continual evacuation of outlet chamber is presented in

Fig.7. This retention means a quantity of tritium per cubic cm of metal membrane. This result is in accord with calculated evaluation value from work [5] that point to a possible way to decrease the tritium inventory in the membrane by means of operation at higher temperature, where superpermeable regime still exists [6].

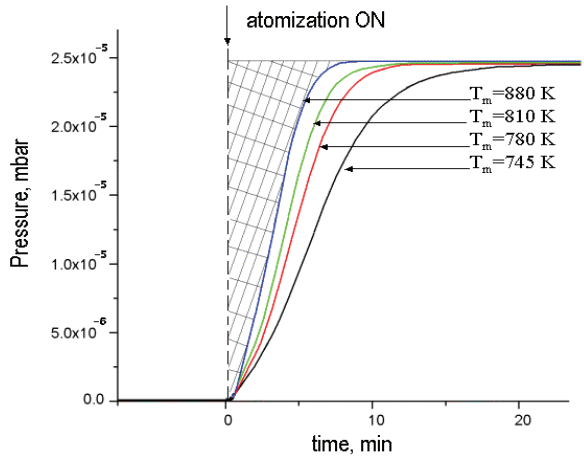


Figure 6: Time dependence of tritium pressure at the outlet side of the membrane for different membrane temperatures.

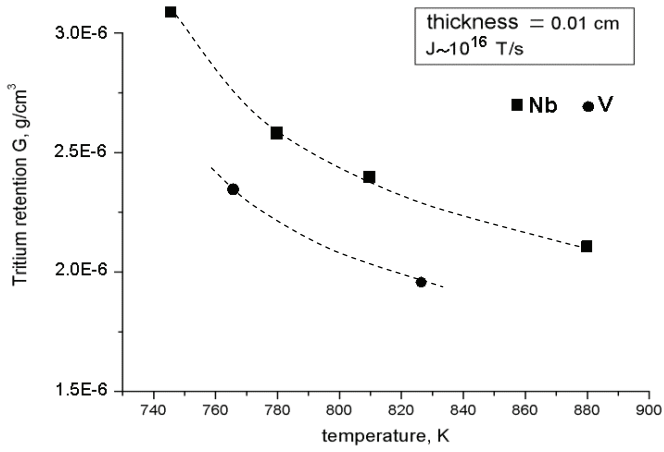


Figure 7: Temperature dependence of tritium inventory to volume unit of membrane.

CONCLUSION

The superpermeation of hydrogen isotopes, including tritium, through vanadium and niobium membranes was experimentally observed. The membrane pumping rate was found to be inversely proportional to square root of isotopic mass. The maximum membrane pumping rate amounts to 2.5-2.3 l/(cm^2sec) for protium, 1.8-1.5 l/(cm^2sec) for deuterium and 1.4-1.2 l/(cm^2sec) for tritium.
The possibility of effective pumping, separation from helium and residual gas, compression and recirculation of hydrogen isotopes by means of superpermeable membranes of the Group V metals as well as tritium inventory decrease under temperature increasing were demonstrated.

ACKNOWLEDGMENT

This work was supported by ISTC under Project #2854.

REFERENCES

1. A.I. Livshits, M.E. Notkin and A.A. Samartsev, “Physico-chemical origin of superpermebaility – large-scale effects of surface chemistry on “hot” hydrogen permeation and absorption in metals,” *J.Nucl.Mater*., No. 170 (1990), pp.79–94.
2. A. I. Livshits et al., ”Superpermeability: Critical points for Applications in Fusion”, *J.Nucl.Mater*., 220-222 (1995), p.259.
3. R.K.Musyaev et al., “Tritium superpermeability: experimental investigation and simulation of tritium recirculation in “Prometheus” setup”, *Fusion Science and Technology*, Vol.48 (2005), pp.35-38.
4. A.A.Yukhimchuk et al., “Device for investigations of tritium retention in and permeation through metals and structural materials,”. *Hydrogen Recycling at Plasma Facing Materials, NATO Science Series, II Mathematics, Physics and Chemistry*, No.1 (2000), pp.339-348.
5. A.I. Livshits, Y. Hatano and K Watanabe, “Superpermeability in the fusion technology: tritium accumulation and compression”, *J.Fusion Science and Technology*, Vol.41 (2002), pp.882-886.
6. A.I. Livshits, “Superpermeability of solid membranes and gas evacuation. Part I. Theory”, *Vacuum*, No.29 (1979), p.103.

AUTHOR INDEX

A
Adams, D.P. 710
Aguilar, A. 267
Akiyama, E. 54
Al-Faqeer, F.M. 284
Andrieu, E. 357
Andronova, E. 123
Atrens, A. 259
Au, M. 501
Aubert, I. 78

B
Bahr, D.F. 179, 710
Balch, D.K. 88, 341
Balitskii, A.I. 421
Barannikova, S. 97
Barnoush, A. 187
Battacharya, J. 632
Benal, N. 604
Berberich, W.W. 38
Birbilis, N. 243
Blanc, C. 357
Boellinghaus, T. 438, 588
Braun, R. 251
Brewer, L.N. 718
Briottet, L. 357
Bruzzoni, P. 508, 516
Busnyuk, A.O. 735

C
Campillo, B. 267, 275
Carranza, R.M. 516
Chêne, J. 357
Christ, H.-J. 227
Clark, E.A. 726
Clift, M. 710
Colín, J. 275
Collet Lacoste, J.R. 516
Cowgill, D.F. 686
Creus, J. 292
Cruz-Hernández, F. 275

D
Dadfarnia, M. 613
Darcis, Ph.P. 381
Delafosse, D. 78, 640
Dietzel, W. 259
Duprez, L. 62, 469, 477, 485

E
El Alami, H. 292
El-Huodaigui, F. 604
Eliezer, D. 438
Erck, R. 405
Eryilmaz, O. 405
Escobar, D.P. 477, 485
Espada, L. 710, 718
Estevez, R. 604

F
Feaugas, X. 78, 292
Fenske, G. 405
Ferreira, P.J. 22
Flores, O. 267
Fragiel, A. 275
Fujiwara, H. 389
Fukushima, Y. 365

G
Gangloff, R.P. 1
Gardiner, M.R. 316
Gavriljuk, V.G. 163
Gemma, R. 548
Georges, C. 493
Goeke, R.S. 718
Guillot, J.-B. 300

H
Hänninen, H. 97, 123
Hara, T. 448
Hayden, L. 332
Heuser, B.J. 464
Higashida, K. 203

I
Inoue, Y. 663
Ishigaki, R. 532

J
Jackson, J.E. 524, 540
Jambon, F. 357
Jérome, M. 300
Johnsen, R. 622
Johnson, D.D. 613
Ju, H. 464

K
Kainer, K.U. 259
Kameda, J. 46
Kammler, D.R. 710, 718
Kanayama, H. 580
Kanezaki, T. 131
Kennedy, M.S. 710
Kharin, V. 562, 596
King, S.H. 718
Kirchheim, R. 548
Knight, S.P. 243
Kobayashi, T. 211
Koenig, K. 524
Koga, A. 397
Kojima, K. 324

L
Lam, P.-S., ... 171
Lasseigne, A.N. 381, 524, 540
Lebedev, B.S. 735
Lee, J.A. 678
Leisk, G. 139
Lemoine, P. 357
Li, S. 54
Lillig, D. 22
Liu, J.B. 613
Liu, X. 46
Livshits, A.I. 735
López, H.F. 267
Lorenzo, M. 596
Ly, C. 300
Lynch, S.P. 243

M
Martinez, L. 267
Matson, D. 139
Matsukado, K. 54
Matsumoto, R. 655, 663
Matsuo, T. 105
Matsuoka, S. 105, 131, 365, 373
McColskey, J.D. 381, 524
McMahon, C.J. 46
Melcher, R.J. 113
Michler, T. 88
Miné, Y. 131
Mishra, B. 524, 540
Miyazaki, N. 655, 663
Moody, N.R. 710
Morgan, M.J. 46, 171, 694
Moro, I. 357
Muddle, B.C. 243
Murakami, Y. 105, 131, 308
Musyaev, R.K. 735

N
Nakao, M. 389
Nakayama, J. 397
Ndong-Mefane, S. 580
Nibur, K.A. 88, 179, 211, 341
Nishiguchi, H. 365
Nishimura, S. 389, 397
Noguchi, H. 203
Noreña, C.H. 508
Notkin, M.E. 735

O
Odemer, G. 357
Ogino, M. 580
Olden, V. 622
Olive, J.M. 78
Olson, D.L. 524, 540
Østby, E. 622
Otsuka, M. 397
Ovejero, E. 70
Overman, N.R. 179

P
Pawel, S.J. 316
Pickering, H.W. 284
Pitchure, D.J. 219
Powell, G.L. 556
Pundt, A. 548

R
Rana, M. 349
Razafindrazaka, M. 640
Reedy, E.D. 710
Ricker, R.E. 219
Rissanen, L. 123
Robertson, I.M. 22, 613
Roubidoux, A.J. 540
Ruscassier, N. 300

S
Saigal, A. 139
Saintier, N. 78
Samartsev, A.A. 735
San Marchi, C. 88, 139, 147, 179, 211, 341
Saukkonen T. 97, 123
Schembri, P.E. 113, 570
Schmidt, P. 227
Schulze, R.K. 556
Serna, S. 275
Shiroky, G.H. 88, 147
Shoda, H. 195
Shyvanyuk, V.N. 163
Siekhaus, W.J. 556
Siewert, T.A. 381, 524
Skipper, C. 139
Sofronis, P. 38, 613
Sojka, J. 300
Somerday, B.P. 88, 147, 211, 341, 613
Stalheim, D. 332
Stauffer, D.D. 38
Stepanyuk, S.M. 373
Sturel, T. 493
Sun, D.L. 235
Świątnicki, W. 155

T
Takahashi, Y. 203
Takai, K. 195
Takasawa, K. 532
Taketomi, S. 655, 663
Tal-Gutelmacher, E. 548
Tanaka, M. 203
Tanaka, Y. 532
Tang, X. 88, 147
Tanguy, D. 604, 640, 647, 671
Teus, S.M. 163
Thaulow, C. 622
Tissot, R.G. 718
Tokumitsu, H. 397
Toribio, J. 70, 562, 596
Torres-Islas, A. 275
Tosten, M.H. 694
Trinkle, D.R. 464
Trocellier, P. 429, 702
Tsuzaki, K. 54, 448, 456
Tuomisto, F. 97
Turnbull, A. 413

U
Udovic, T.J. 464

V
Vamvakopoulos, E. 671
Van der Ven, A. 632
Van Deusen, S.B. 718
Vehoff, H. 187
Verbeken, K. 62, 469, 477, 485
Verhaege, M. 62, 469, 477, 485
Vitvitskii, V.I. 421

W
Wada, Y. 532
Wampler, W.R. 718
Wang, M. 54
Wang, Q. 235
Wei, F.-G. 448, 456
Wheeler, D.A. 171
Winzer, N. 259
Wongpanya, P. 588

X
Xu, K. 349
Xu, Q. 632

Y
Yagodzinskyy, Y. 97, 123
Yamabe, J. 105, 389, 397
Yamaoka, T. 373
Yukhimchuk, A.A. 735

Z
Zagal, J.M. 267
Zhang, B. 54
Zhang, Z. 54
Zuev, L. 97

SUBJECT INDEX

25% Cr duplex stainless steel, 622–631
  experiments, 626–628
    laboratory experiments, 627–628
    SENT test results, 628 (F)
  model description, 623–626
    applied stress intensity, 623–624 (F)
    diffusion analysis, 624–625
    elastic plastic stress analyses, 623–624, 624 (T)
    FE model, 626 (F)
    hydrogen concentration, 625 (F)
    hydrogen influenced cohesive law, 626 (F)
    material properties, 623–624 (F)
    traction separation law, 625–626
9Cr steel, 508–515
  apparent hydrogen diffusion coefficient, 513 (F)
  experimental, 509–511
    9%Cr-1%Mo steel, 509 (T)
    hydrogen permeation tests, 510–511
    permeation membranes, 509–510
    thermal treatments, 510 (T)
  hydrogen apparent diffusion coefficient, 513 (T)
  hydrogen permeation, 511–515
  material characterization, 511
  microstructural states, 514 (F)
  normalised steady state hydrogen flux, 513 (T)
  permeation rising transients, 512 (F)
  T91 Steel, 511 (F)

A

AISI 316 austenitic stainless steel (welded)
  hydrogen-assisted fracture, 147–154
    alloy composition, 149 (T)
    experimental, 149
    fracture mode, 151–153
    fusion zone, 148 (F)
    hydrogen-precharged welds, 152 (F)
    notched tensile properties, 150–151, 151 (T)
    smooth tensile properties, 150, 150 (T)
    welded smooth tensile specimens, 152 (F)
Al 5xxx alloys
  cohesive zone model, 604–612
    heterogeneous grain boundary, 607–609
    homogeneous unbrittled interface, 606 (F)
    intergranular decohesion, modelling, 605–607
    mean stress, contours of, 608 (F)
    small scale yielding problem, 605 (F)
    toughness, variation of, 609 (F)
    traction-opening cohesive zone, 605 (F)
alloy 600
  crack growth rates, 271 (T)
  crack tips, 271 (F)
  exhibited crack paths, 271 (F)
  exhibited Inconel alloy precipitates, 272 (F)
  exhibited microstructures, 270 (F)
  experimental, 268–269
    exposed M-WOL sample, 269 (F)
    setup, 269 (F)
  fatigue testing results, 273 (T)
  Inconel 600
    chemical composition, 268 (T)
    mechanical properties, 269 (T)
alloy 7050-T7451 plate
  stress corrosion cracking
    brittle transgranular fracture, 256 (F)
    cleavage-like fracture, 256 (F)
    crack arrest markings, 257 (F)
    cycles-to-failure vs. frequency, 255 (F)
    cyclic loading tests, 254 (T)
    experimental, 252
    secondary cracks, 257 (F)
    stress corrosion cracking, 251–258
    striations on cleavage-like facets, 256 (F)
    time-to-failure data, 253 (F), 254 (T)
    time-to-failure vs. displacement rate, 255 (F)
    transgranular stress corrosion cracking, 253 (F), 257 (F)
alpha iron
  hydrogen diffusion, atomistic study of, 655–662
    activation energy, 659–661, 661 (T)
    analysis methods, 656–657
    analysis model, 656
    common neighbor analysis (CNA), 658 (F)
    coordinate systems, 656 (F)
    dislocation, atomistic structure of, 657–658
    dislocation core, 658–659
    edge dislocations, 658 (F)
    hydrogen diffusion path, 660 (F)
    hydrogen pipe diffusion, 659–661, 661 (T)
    hydrogen-trap energy, 658–659
    hydrogen-trap site distribution, 659 (F)
    simulation models, 656 (F)
  hydrogen occupation sites, 657, 657 (F)
  Voronoi polyhedron, 657 (F)
Al-Zn-Mg-Cu alloys
  SCC, mechanism of, 249

Al-Zn-Mg-Cu alloys *(continued)*
crack-arrest markings, 249 (F)
GBPs, 249 (F)
intergranular-fracture surface, 249 (F)
stress-corrosion cracking of, 243–250
7075 alloy, 247 (F)
7079 (T/2 alloy), 247 (F)
7079 (T/6) alloy, 247 (F)
alloys, composition of, 244 (T)
electrochemical measurements, 247–248
experimental, 244
grain boundary microstructures, 247 (F)
OA 7079 (T/6 and T/2) and 7075, microstructural comparisons, 246–247
OCP, 248 (F)
overaged 7075 alloy, 248 (F)
overaged 7079 (T/2) alloy, 248 (F)
overaged 7079 (T/6) alloy, 248 (F)
PA and OA 7079 (T/6 position), microstructural comparisons, 246, 246 (F), 246 (T)
rate-controlling processes, 248–249
SCC plateau velocity vs. ageing time, 245 (F)
SCC velocity at high K, 245 (F)
SCC velocity data, 244–245
T651 alloys, overaged, 247 (T)
aqueous chloride-nitrate solution
alloy 7050-T7451 plate, 251–258
brittle transgranular fracture, 256 (F)
cleavage-like fracture, 256 (F)
crack arrest markings, 257 (F)
cycles-to-failure vs. frequency, 255 (F)
cyclic loading tests, 254 (T)
experimental, 252
secondary cracks, 257 (F)
stress corrosion cracking, 251–258
striations on cleavage-like facets, 256 (F)
time-to-failure data, 253 (F), 254 (T)
time-to-failure vs. displacement rate, 255 (F)
transgranular stress corrosion cracking, 253 (F), 257 (F)
arsenic, 300–307
atomistic study
alpha iron, 655–662
activation energy, 659–661, 661 (T)
analysis methods, 656–657
analysis model, 656
common neighbor analysis (CNA), 658 (F)
coordinate systems, 656 (F)
dislocation, atomistic structure of, 657–658
dislocation core, 658–659
edge dislocations, 658 (F)
hydrogen diffusion path, 660 (F)
hydrogen pipe diffusion, 659–661, 661 (T)
hydrogen-trap energy, 658–659
hydrogen-trap site distribution, 659 (F)
simulation models, 656 (F)
austenitic alloys, 78–87
crystal plasticity modeling, 84–85
numerical calculation, 85 (F)
SBH^g, 86 (F)
elementary plasticity mechanisms, 79–81
dislocation, 80 (F)
line tension, 80 (F)
self-energy per unit length, 80 (F)
nickel single crystals, 81–83
dislocation structures, 83 (F)
"single glide" plane, 83 (F)
true stress-strain curves, 82 (F)
plasticity, 81–83
polycrystalline 316L, 83–86
optical images, 84 (F)
slip-shears, 84 (F)
slip-steps, 84 (F)
topographical AFM image, 84 (F)
slip localization, 83–86
austenitic stainless steel
crack tip, 570–579
inputs on the four outputs, effects of, 576 (F)
model description, 571–573
sensitivity analysis, 573–575, 574 (T)
hydrogen-assisted fracture, 88–96
microstructural boundaries, 91
microvoid coalescence, 89–90
super duplex 2507 stainless steel, 96 (F)
tensile fracture surfaces, 94 (F), 95 (F)
two-phase microstructures, 91–92
type 316 austenitic stainless steel, 94 (F), 95 (F), 96 (F)
hydrogen-induced fatigue crack growth acceleration, 131–138
acceleration rate, 137 (F)
drilled hole, 132 (F)
fatigue crack growth, 132–133
fatigue crack growth curves, 132 (F)
fatigue crack tip, 136–138
fatigue test specimen, 132 (F)
fatigue tests, 132
hydrogen migration, 137 (F)
martensitic transformation, 133–136
material, 131–132
specimen, 131–132
martensitic transformation, 133–136
fatigue fracture surface, 134 (F)
martensitic transformation, 135 (F)
slip bands, 135 (F)
transformed martensite, 134 (F)
plastic strain localization, single crystals, 97–104
electron backscatter diffraction (EBSD) images, 101 (F)
experimental, 98–99

hydrogen charging procedure, 98–99
materials, 98
methods, 99
PAS parameters, 103 (F)
slip line structure, 101 (F)
slip lines, 101 (F)
specimens, 98
stress-strain curves, 99 (F)
techniques, 99
type 316L (*see* type 316L austenitic stainless steel)
austenitic steels
embrittlement, 163–170
charging conditions, 164 (T)
chemical compositions, 164 (T)
Cr18Ni10N0.2, 165 (T)
ε_H-martensite, 166 (T)
ε-martensite fraction, 168 (F)
experimental, 164–165
experimental conditions, 164 (T)
hydrogen-charged (denominator) steels, 167 (T)
hydrogen-charged single crystals, 165 (F)
hydrogen-charged steel Cr25Ni25, 166 (F)
hydrogen-free (numerator) steels, 167 (T)
hydrogen-free single crystals, 165 (F)
hydrogen-free steels, 167 (F)
methods, 164 (T)
stress-elongation curves, 168 (F)
austenitic-ferritic steel
embrittlement, 155–162
AFM image, 159 (F)
area at fracture, 157 (F)
dark (magnetic) laths of martensite, 159 (F)
dislocations, 159 (F)
DSS samples, 160 (T)
duplex steel, stress-strain curves, 157 (F)
fatigue crack propagation, 158–159
fatigue rate propagation rate, 158 (F)
hydrogen charging, 159
hydrogen embrittlement, 156–158, 160–161
investigated steel samples, 156 (T)
secondary cracks, 158 (F)
slow strain rate tests, 156–158
stacking faults, 159 (F)
steel fracture surface, 157 (F)

B

blister damages. *See* high pressure hydrogen durability tester
blister fracture, 389–396, 398–400
bubble free zone (BFZ), 699 (F)

C

carbon steels, 349–356
experimental procedures, 351
experimental results
da/dn in hydrogen (SA-106), 354 (F)
fracture mode, 352–353
fracture surface (SA-106 tensile specimens), 353 (F)
stress strain curves, 351 (F)
tensile ductility, 352 (F)
tensile properties, 351–352
yield/tensile strength, 352 (F)
materials, 350
SA-106, chemical composition, 350 (T)
SA-106, tensile properties, 350 (T)
SA-372, chemical composition, 350 (T)
SA-372, tensile properties, 350 (T)
microstructures, 350 (F)
cathodic hydrogen charging
analytical methods for studying, 284–291
i_o values, 288 (F)
iodide ion concentrations, 290 (F)
IPZA analysis, 284–287
k values, 289 (F)
k_1 values, 288 (F)
θ_{i-}, comparison of, 288 (F)
θ_H, values of, 290 (F)
recombination rate constants, 290 (F)
cathodic hydrogenation, 300–307
diffusion characteristics, 304–305
experimental procedures
electrochemical permeation tests, 302, 304 (T)
thermal desorption, 302–303
hydrogen diffusion characteristics, 304 (T)
hydrogen dosage, 302–303
materials, 301–302
chemical composition, 301 (T)
mechanical properties, hydrogen effects on, 305–306
elongation comparison, 306 (T)
fracture surfaces, 306 (F)
stress-strain curves, 305 (F)
mechanical tests, 303
permeation build-up transients, 305 (F)
thermal desorption, 302–303, 304 (T)
vacuum thermal desorption, 303 (F)
VHSS, 303 (T)
coatings used in hydrogen, 405–412
DLC coating, 409–410 (F), 410 (F)
DLC transfer layer, 411 (F)0
enclosure/gas delivery system, 406 (F)
experiment, 406–407
friable MoS_2 coating, 408 (F)
friction coefficients, 407 (F), 408 (F), 411 (T)
sliding couples, 411 (T)
thrust washer tribometer, 406 (F)
Ti-6Al-4V, 407 (F)
transfer film, 409 (F)
worn X-750, 408 (F)
X-750, 408 (F)

cohesive zone model
Al 5xxx alloys, 604–612
heterogeneous grain boundary, 607–609
homogeneous unbrittled interface, 606 (F)
intergranular decohesion, 605–607
mean stress, 608 (F)
small scale yielding problem, 605 (F)
toughness, 609 (F)
traction-opening cohesive zone, 605 (F)
cohesive zone modelling, 622–631
experiments, 626–628
laboratory experiments, 627–628
SENT test results, 628 (F)
model description, 623–626
applied stress intensity, 623–624 (F)
diffusion analysis, 624–625
elastic plastic stress analyses, 623–624, 624 (T)
FE model, 626 (F)
hydrogen concentration, 625 (F)
hydrogen influenced cohesive law, 626 (F)
material properties, 623–624 (F)
traction separation law, 625–626
cold drawn wires, 596–603
cold drawing process, 598 (F)
hydrogen accumulation, 599–601
hydrostatic stress, 599 (F)
plastic strain, 599 (F)
plastic strains, 597–598
progressive cold drawing, 597–598
relative concentrations of hydrogen (C/C*), 600 (F)
residual strains, 598–599
residual stress, 598–599
residual stresses, 597–598
commercial steels, 332–340
pipeline steel metallurgy, 333–339
alloy design, 334–335
alloy design and resultant microstructure, 339 (T)
CCT diagram (two pipeline alloys), 337 (F)
chemistry limits, 338 (T)
cooling rate effect, 336 (F)
hot rolling, 335
hydrogen induced cracking, 337–338
microstructure, 333
microstructures, typical, 333 (F)
NACE TM0284 Solution A testing, 337 (T)
processing, 335
rolling pipeline steels, 336 (F)
specifications, 338
strength design, 334–335
thermo-mechanical rolling (TMCP), 335–336
transmission pipeline steels, 335 (T)
volume fraction microstructure formation, 336 (F)
common neighbor analysis (CNA), 658 (F)
compressors, 321–322
constrained molecular dynamics, 649–651
crack tip shielding
multi-scale simulation, 647–654
brittle crack, 650 (F)
constrained molecular dynamics, 649–651
crack tip shielding, 651–652
discrete dislocation dynamics, 652–653
distances where the dislocations are pinned, 651 (T)
elastic calculations, 651 (F)
intrinsically ductile crack, 650 (F)
K and $K_{applied}$, 652 (F)
stress profiles, 651 (F)
time variation of K and $K_{applied}$, 652 (F)
crack-tip hydrogen accumulation, 562–569
axial stress, 564 (F)
calculated stress trajectory, 567 (F)
concentration evolutions, 566 (F)
crack plane, 564 (F)
cyclic load effects, 567–568
hydrogen concentration, 566 (F)
modelling outline
basic model approach, 563–564
hydrogen diffusion model, 563
near-tip hydrogen accumulation, 565–566, 567–568, 568 (F)
near-tip mechanical fields, 564–565
near-tip strain, 566 (F)
near-tip stress, 566 (F)
plastic strain, 564 (F)
remote cyclic loading, 567 (F)
shear banding, 564 (F)
stress evolution, 567 (F)
typical near-tip fields, 564 (F)
waveform distortion, 567 (F)
crack-tip hydrogen profiles, 113–122
Cross Sectional Plot (XSP), 213 (F)
crystals, 38–45
Stage I, HELP, 39
21-6-9 stainless steel, 40 (F)
aluminides, 41 (F), 42 (F)
applied shear stress, 42 (F)
dislocation nucleation effects (singularities), 40–42
dislocation velocity effects, 39
load displacement curves, 40 (F)
low density dislocation populations, 39 (F)
nanoindentation, 40 (F)
normalized activation volumes, 41 (F)
steels, 42 (F)
Ti-30Mo, 40 (F)

Stage II, HELP and HEDE, 42
crystals, 43 (F)
Fe-3% Si, 43 (F)
hydrogen enhanced cleavage, 42–44
hydrogen-induced slow crack growth, 43 (F)
slip bands, 43 (F)

D

D loss, 718–725
degradation susceptibility (DS), 200 (F)
density of states
SFE and H embrittlement, 682–683, 682 (F), 683 (F)
transition metals and alloys, 678–685
Co-Ni alloy, 683 (F)
Cr15Mn17, 681 (F)
Cr18Ni16Mn10, 681 (F)
Fe-Ni alloy, 683 (F)
H embrittlement and N (Ef), 679–680
N (Ef) and stacking fault energy (SFE), 680–681
Ni-Cu alloy, 682 (F)
nitrogen content, 681 (F)
Pd-Ag alloy, 682 (F)
predicted H embrittlement index, 680 (F)
SFE and H embrittlement, 682–683
diffusible hydrogen content, 493–500
coated high-strength steels
charging, 495
desorption curves, 496 (F), 497 (F), 498 (F)
electro galvanizing, 495
experimental procedure, 494–495
first peak, 496 (F)
interrupted TDA test, 499 (F)0
material, 494
sodium disulfite etching, 494 (F)
thermal desorption analysis, 495
x-ray diffraction, 495
x-ray diffraction pattern, 498 (F)
dimple formation, 108–111
dislocation slip bands, 43 (F)
dislocations
Al, 667–668, 668 (F)
analytical procedure, 664–665
bcc-Fe, 665–667, 666 (F)
edge dislocations, 668 (F)
elastic strain, 664–665
elastic strain fields, 665
hydrogen occupation sites, 664
hydrogen trap energy, 665–667, 666 (F), 667–668, 667 (F)
screw dislocations, 668 (F)
superimposing procedure, 665
trap energy, 664–665
drawing-induced residual stresses and strains, 596–603

E

electrochemical impedance spectroscopy (EIS), 542–543
electrochemical permeation tests (EPT), 473–475
DP600, 473–475
exit current, 473 (F)
normalised first permeation curve, 474 (F)
normalised second permeation curve, 474 (F)
permeation curves, 475 (T)
pure iron, 473–475
electron backscatter diffraction (EBSD), 101 (F)
embrittled fracture toughness, 113–122
21Cr-6Ni-9Mn forging, 115 (T)
calculated crack-tip hydrogen profile, 119–120
hydrostatic stress and plastic strain, 119 (F)
crack-tip hydrogen concentration profiles, 117 (F)
diffusion modeling, 116
experiment description, 114–116
fracture toughness testing, 116
hydrogen exposure, 115–116
J-$_{IC}$, 117
J-R curve, 117
material, 114–115
mechanics modeling, 116
optical microscopy, 118–119
crack-tip hydrogen concentration profile effects, 119 (F)
visible tearing onset, 118 (F)
specimen definitions, 114–115
environmental hydrogen entry
cyclic corrosion test, 56, 59–60
cyclic corrosion test chamber, 59 (F)
diffusible hydrogen concentration, 59 (F)
fracture stress, 59 (F)
fracture stress and diffusible hydrogen concentration, 60 (F)
heat treatment conditions, 56 (T)
hydrogen charging, 56
hydrogen-charged specimens, 57–59
maximum principal stress, 58 (F)
stress concentration factor, 58 (F)
materials, 55–56
Slow Strain Rate Test (SSRT), 56, 59–60
specimens, 55–56
thermal desorption analysis, 57
EPDM, 732–733
ERD_2 films, 718–725
ErD_2/kovar, isochronal anneals, 720–721
RBS data, 721 (F)
ErD_2/kovar, isothermal anneals, 721–723

ERD_2 films *(continued)*
Calculated Er concentration profile, 723 (F)
NRA data, 722 (F)
Plot of Γ_D vs. $Time^{1/2}$, 723 (F)
RBS data, 722 (F)
ErD_2/kovar NRA studies, 723–725
NRA data, 724 (F)
ErD_2/kovar RBS studies, 723–725
RBS data, 724 (F)
Er/kovar, isochronal anneals, 720–721
RBS data, 721 (F)
experimental, 719–720
process conditions, 719 (T)
samples, 719 (T)

F

fatigue crack growth rate, 381–388
crack growth, 385 (F), 386 (F)
diffusion coefficient, 382–383
hydrogen charged X100, 383 (F)
experimental set-up, 383–385
C(T) specimen dimensions, 384 (F)
fatigue crack growth, 384 (F)
FCGR test specimens, 385 (T)
fatigue crack growth rate, 385 (F), 386 (F)
materials properties, 382
X100 steel, 382 (T)
FCC nickel alloys, 78–87
crystal plasticity modeling, 84–85
numerical calculation, 85 (F)
SBH^g, 86 (F)
elementary plasticity mechanisms, 79–81
dislocation, 80 (F)
line tension, 80 (F)
self-energy per unit length, 80 (F)
nickel single crystals, 81–83
dislocation structures, 83 (F)
"single glide" plane, 83 (F)
true stress-strain curves, 82 (F)
plasticity, 81–83
polycrystalline 316L, 83–86
optical images, 84 (F)
slip-shears, 84 (F)
slip-steps, 84 (F)
topographical AFM image, 84 (F)
slip localization, 83–86
finite element analysis
hydrogen diffusion, 580–587
constant values, 581 (T)
crack tip, 585 (F), 586 (F)
elasto-plastic problem, 580 (F)
hydrogen distribution, 582 (F)
hydrogen transport equation, 580–581
instability problem, 582–583
lattice sites, 582 (F)
one side coupled diffusion, 580 (F)
Peclet number, 582 (F), 585 (T)
stabilized scheme, 583–584
first-principles
calculations, 663–670
hydride phase stability, 632–639
fracture surface topography analysis (FRASTA), 211–218
conjugate surface spacing, 217 (F)
Cross Sectional Plot (XSP), 213 (F)
cross-sectional plots, 216 (F)
Fractured Area Projection Plot (FAPP), 213 (F), 215 (F)
operation, 213 (F)
procedure, 212–213
SA372 Grade J specimen, 214 (F)
specimen analyzed, 213–214
Fractured Area Projection Plot (FAPP), 213 (F), 215 (F)
fuel cell vehicle application, 324–331
cruising range, 325–326
FC stack, 328–329
FCVs, 330–331
freeze start capabilities, 327–328
high-pressure hydrogen storage system, 327 (F)
inside cell, 328 (F)
metallic materials, future, 327 (F)
Pt reactions, 329 (F)
technological issues, 325–330, 330 (F)
Toyota FCHV
practical cruising range, 326 (F)
technological issues, 326 (F)
Toyota FCHV-adv, 330 (F)

G

gas pipeline steel. *See* welded joints
Grand Canonical ensemble, 674–676
Group V metals. *See* hydrogen isotopes superpermeation

H

He platelets, 686–693
dimensions, 691–692, 692 (F)
lattice dilation, 690–691, 691 (F)
other materials, 692
precipitate shape, 692 (T)
surface/strain energy ratio, 692 (T)
shape, 686–690
bubble growth, 689 (F)
dipole expansion, 689 (F)
dislocation dipole, 687 (F)
dislocation loop, 687 (F)
dislocation loop punching, 689 (F)
He bubble pressures, 689 (F)
spherical bubbles, 689 (F)
strain energy parameters, 688 (T)
surface energy parameters, 688 (T)
HEAC
data base, 4–10

mechanism-based modeling, 10–18
HEDE. *See* HELP
helium-bearing fusion welds
helium-bearing welds
austenitic "matrix", 698 (F)
bubble free zone (BFZ), 699 (F)
δ ferrite grain, 698 (F)
helium bubbles, 699 (F)
transmission electron microscopy (TEM) study of, 694–701
deformation twinning, 697 (F)
experimental procedure, 695–696
fusion weld region, 696 (F)
general microstructure, 696–697
HERF 304L forging, 696 (F)
oxide inclusions, 697 (F)
sectioning procedure, 696 (F)
weld microstructures, 697 (F)
HELP
Stage I, HELP, 39
21-6-9 stainless steel, 40 (F)
aluminides, 41 (F), 42 (F)
applied shear stress, 42 (F)
dislocation nucleation effects (singularities), 40–42
dislocation velocity effects, 39
load displacement curves, 40 (F)
low density dislocation populations, 39 (F)
nanoindentation, 40 (F)
normalized activation volumes, 41 (F)
steels, 42 (F)
Ti-30Mo, 40 (F)
Stage II, HELP and HEDE, 42
crystals, 43 (F)
Fe-3% Si, 43 (F)
hydrogen enhanced cleavage, 42–44
hydrogen-induced slow crack growth, 43 (F)
slip bands, 43 (F)
high pressure hydrogen durability tester, 397–404
blister fracture, example, 398–400
crack (example), 399 (F)
cracks generated after decompression, 397 (F)
cross section, optical microscope image, 399 (F)
experimental method, 400–401
durability tester, 401 (T)
durability tests, 401 (T)
EPDM rubber composite, 400 (T)
high pressure durability tester, 400 (F)
extrusion, damage by, 403 (F)1
high pressure hydrogen vessel, 398 (F)
inner cracks, 399 (F)
No. 1 O-ring, 402 (F), 403 (F)
No. 2 O-ring, 402 (F)
O-ring, 398 (F), 401 (T)
surface cracks, 399 (F)
high pressure hydrogen gas, 389–396, 398–400
high strength low alloy steel
plastic deformation, 532–539
chemical composition, 533 (T)
experimental procedure, 532–534
hydrogen content, 533–534
hydrogen content and exposure time to the air, 533 (F)
hydrogen content and strain, 537 (F)
hydrogen content and strain rate, 538 (F)
hydrogen desorption profiles, 535 (F), 536 (F)
material, 533
peak temperature, 536 (F)
peak temperature dependence, 537 (F)
specimen configuration, 533 (F)
specimen weight dependence, 536 (F)
stress-displacement curves, 534 (F)
tensile test, 533–534
high strength pipeline steel, damage under high-pressure hydrogen environment, 357–364
C_L, 362 (F)
C_T, 359 (F), 362 (F)
experimental procedure
hydrogen content, 358
materials, 357
tensile tests (hydrogen gaseous environment), 358
X80, 357 (T)
hydrogen content vs. plastic strain, 358–359
hydrogen diffusion, 362
hydrogen pressure, 360 (F)
interrupted tensile tests, 363 (F)
notched axisymetric specimens, 361, 361 (F), 363 (F)
smooth axisymetric specimens in H_2 gas, 359–360
strain rate, 360 (F)
surface rupture, 361 (F)
tensile tests, 360 (F)
trapped hydrogen effect, 362–363
high strength pipeline steel, fatigue crack growth rate, 381–388
crack growth, 385 (F), 386 (F)
diffusion coefficient, 382–383
hydrogen charged X100, 383 (F)
experimental set-up, 383–385
C(T) specimen dimensions, 384 (F)
fatigue crack growth, 384 (F)
FCGR test specimens, 385 (T)
fatigue crack growth rate on, 385 (F), 386 (F)
materials properties, 382
X100 steel, 382 (T)
high strength steel welds
hydrogen assisted cold cracking, 588–595
coupled time-step based thermal finite element analyses, 591 (F)
crack appearance, 593 (F)
crack modeling concept, 590 (F)

high strength steel welds *(continued)*
critical hydrogen concentration, 589 (F)
elastic-plastic structural finite element analyses, 591 (F)
five layer weld, 593 (F)
HACC, flow chart for modeling, 591 (F)
HACC avoidance, 594
HACC location, 592–594
HRHT diagrams, 594 (F)
hydrogen concentrations desorbed, 593 (F)
hydrogen diffusion finite element analyses, 591 (F)
increasing transverse residual stresses, 589 (F)
numerical approach, 590–591
S 1100 60° V butt joint, 594 (F)
S 1100 welds, 592 (F)
high strength steels
electrochemical permeation tests (EPT), 473–475
DP600, 473–475
exit current, 473 (F)
normalised first permeation curve, 474 (F)
normalised second permeation curve, 474 (F)
permeation curves, 475 (T)
pure iron, 473–475
hydrogen management in, 469–476
EPT measurements, 471
experimental, 470–471
materials, 470, 470 (T)
TDS measurements, 471
nano-precipitates design
0.05C-0.20Ti-2.0Ni steel, 451 (F), 454 (F)
0.05C-0.24V-2.0Ni steel, 454 (F)
0.05C-0.41Nb-2.0Ni steel, 454 (F)
disk-like NbC, 454 (F)
disk-like TiC, 454 (F)
disk-like VC, 454 (F)
experimental method, 449
incoherent particle, 452 (F)
incoherent TiC particles, 452–453, 453 (F)
NbC precipitate, 453–455, 454 (F)
semi-coherent TiC precipitate, 450 (F), 452 (F)
TiC precipitates, 449–450, 450–452, 450 (F), 454 (F)
VC precipitate, 453–455, 454 (F)
thermal desorption analysis, 471–473
calculated H-profiles, 473 (F)
DP600, 471–473
pure iron, 471–473
TDS curves, 472 (F)
total H-content, 473 (F)
high strength TRIP steel, 485–492
hydrogen trap sites
deformed TRIP steel, 489 (F)
experimental, 486–488
hydrogen charging, 487
hydrogen content (ppm), 487 (F)
hydrogen desorption, 491 (F)
materials, 486–487, 487 (T)
pure Fe deformed, 490–491
pure iron TDS results, 490 (F)
thermal desorption spectroscopy (TDS), 487–488
TRIP grade with pure Fe, 489–490, 489 (F)
TRIP700 deformed, 490–491
TRIP700 grade, 488–489, 488 (F)
TRIP700 samples, 488 (T)
TRIP700 TDS results, 491 (F)
high-cycle fatigue, 373–380
base metal, 374 (T)
crack growth curves, 379 (F)
experimental methods, 374–375
fatigue crack growth, 376–377
fatigue specimen, 375 (F)
first layer, 379 (F)2
fracture surface, 377, 379
hydrogen content, 376
materials, 373–374
second layer, 379 (F)
small hole, 375 (F)
TDS results, 378 (F)
TDS specimens, 378 (F)
weld metal, 378 (T)
weld rods, 374 (T)
welded joint
macrostructure, 374 (F)
microstructures, 374 (F)
Vickers hardness, 375 (F)
high-pressure hydrogen, 421–428
alloys, 423–425
coefficient, $\square_H$, 424 (F)
defects in hydrogen, 425–427
electric conductivity gauge signal, 427 (F)
experimental procedure, 422
fracture in hydrogen, 425–427
investigated materials, 424–425 (T)
loading mode, role of, 422–423
03Kh12N10MT steel, 423 (F)
KhN55MBYu steel, 423 (F)
KhN65MTYu steel, 423 (F)
low-cycle durability, 423 (F)
materials, 422
steels, 423–425
high-strength carbon steels
constant load tests, 126–127
fractography, 128 (F)
time to fracture, 125 (F)
experimental methods, 125
experimental techniques, 125
hydrogen charging procedure, 125
hydrogen thermal desorption, 127–129
hydrogen partial pressure, 129 (F)

temperature dependencies, 129 (F)
SSRT tensile tests, 125–126
stress-strain curves (austenitic and duplex stainless steels), 126 (F)
high-strength steels, coated, 493–500
diffusible hydrogen content
charging, 495
desorption curves, 496 (F), 497 (F), 498 (F)
electro galvanizing, 495
experimental procedure, 494–495
first peak, 496 (F)
interrupted TDA test, 499 (F)0
material, 494
sodium disulfite etching, 494 (F)
thermal desorption analysis, 495
x-ray diffraction, 495
x-ray diffraction pattern, 498 (F)
high-strength steels, hydrogen embrittlement of, 54–61
cyclic corrosion test, 56, 59–60
cyclic corrosion test chamber, 59 (F)
diffusible hydrogen concentration, 59 (F)
fracture stress, 59 (F)
fracture stress and diffusible hydrogen concentration, 60 (F)
heat treatment conditions, 56 (T)
hydrogen charging, 56
hydrogen-charged specimens, 57–59
maximum principal stress, 58 (F)
stress concentration factor, 58 (F)
materials, 55–56
Slow Strain Rate Test (SSRT), 56, 59–60
specimens, 55–56
thermal desorption analysis, 57
high-strength steels, hydrogen-induced cracking of, 46–53
4340-type steel, 47 (F), 48 (F)
5% nickel steel, 48–52
5% NiCrMoV Steel, 51 (T)
aging time, 50 (F)
ductile to brittle behavior, 51 (F)
high-purity 5% Ni steel, 52 (F)
high-purity modified HY130-type steel, 50 (T)
"ideally pure" 4340-type steel, 49 (F)
impurity segregation, 50 (F)
threshold stress intensity, 50 (F)
HY130-type steel, 47 (F)
IG fracture, 47 (F)
TG fracture, 47 (F)
threshold stress intensity, 48 (F)
ultra-high-strength steel, 47–48
H-trap binding energy, 12 (T)
hydride phase stability, 623–639
hydrogen, 637–639
grand force potential, 638 (F)
hydrogen concentration, 638 (F)
traction curves, 638 (F)
methodology, 633–634
energy as a function of distance, 633 (F)
traction curve for decohesion, 633 (F)
Ti-H system, 634–637
a and c lattice parameters, 636 (F)
calculated free energies, 635 (F)
calculated metastable phase diagram, 635 (F)
calculated stable phase diagram, 635 (F)
coherent phase diagram, 637 (F)
δ–TiH hydrides, 637 (F)
traction curves, 637–639
hydrogen assisted cold cracking (HACC), 588–595
hydrogen assisted cracking, 413–420
hydrogen delivery, 316–323
compressors, 321–322
domestic oil consumption statistics, 317 (F)
HFCIT proposed timeline, 318 (F)
liquefaction, 322
materials challenges, 319–321
opportunities, 319–321
pipelines, 319–321
public safety, 322–323
tech team, 317–319
transportation fuel, 318 (F)
hydrogen diffusion
9Cr steel (*see* 9Cr steel)
atomistic study (*see* atomistic study)
finite element analysis (*see* finite element analysis)
hydrogen diffusion model, 563
hydrogen embrittlement, 22–37
310S stainless steel, 25 (F)
Al, 28 (F)
Al 5xxx alloys, grain boundaries, 604–612
heterogeneous grain boundary, 607–609
homogeneous unbrittled interface, 606 (F)
intergranular decohesion, 605–607
mean stress, 608 (F)
small scale yielding problem, 605 (F)
toughness, 609 (F)
traction-opening cohesive zone, 605 (F)
cold drawn wires, 596–603
cold drawing process, 598 (F)
hydrogen accumulation, 599–601
hydrostatic stress, 599 (F)
plastic strain, 599 (F)
plastic strains, 597–598
progressive cold drawing, 597–598
relative concentrations of hydrogen (C/C*), 600 (F)
residual strains, 598–599
residual stress, 598–599
residual stresses, 597–598
crack advance, 26 (F)
cracking mode, 32 (F)

hydrogen embrittlement *(continued)*
cross-slip, 28 (F)
deformation mode, 32 (F)
deuterium distribution, 30 (F)
dislocation motion, 26 (F)
dislocations, 25 (F)
drop-cast material, 32 (F)
forged boron-free material, 32 (F)
hydrogen-induced transition, 29 (F)
IN903, 26 (F)
misorientation angles, 32 (F)
misorientation map, 32 (F)
Ni L_3 peak, 31 (F)
Ni_3Al, 30 (F), 32 (F)
Ni_3Al (boron free), 32 (F)
Ni-S alloy, 29 (F)
partial dislocations, 25 (F)
pile-up, 27 (F)
separation distance, 27 (F)
SIMS sulfur distribution, 30 (F)
transition metals and alloys, 678–685
Co-Ni alloy, 683 (F)
Cr15Mn17, 681 (F)
Cr18Ni16Mn10, 681 (F)
Fe-Ni alloy, 683 (F)
H embrittlement and N (Ef), 679–680
N (Ef) and stacking fault energy (SFE), 680–681
Ni-Cu alloy, 682 (F)
nitrogen content, 681 (F)
Pd-Ag alloy, 682 (F)
predicted H embrittlement index, 680 (F)
SFE and H embrittlement, 682–683, 682 (F), 683 (T)
hydrogen induced stress cracking, 622–631
experiments, 626–628
laboratory experiments, 627–628
SENT test results, 628 (F)
model description, 623–626
applied stress intensity, 623–624 (F)
diffusion analysis, 624–625
elastic plastic stress analyses, 623–624, 624 (T)
FE model, 626 (F)
hydrogen concentration, 625 (F)
hydrogen influenced cohesive law, 626 (F)
material properties, 623–624 (F)
traction separation law, 625–626
hydrogen isotopes, 429–437
application examples, 430–432
available techniques, 429–430
deuteron-induced nuclear reactions, 434 (F)
ERDA spectra, 434 (F)
ion beam-based methods, 432, 433–434
physico-chemical methods, 430–431 (T)
titanium deuterotritide, 434 (F)
hydrogen isotopes superpermeation, 735–742
compression, 737–739, 738 (F)
deuterium, 739 (F)
experimental, 736–737
hydrogen isotopes pressures, 737 (F)
membrane pumping, 737–739
membrane pumping rates, 739 (F)
“Prometheus” setup, 736 (F)
protium, 739 (F)
superpermeable membrane, 738 (F)
tritium, 739 (F)
tritium and helium mixture experiment, 740
helium flux, 740 (F)
partial pressure, 740 (F)
time dependence, 740 (F)
tritium inventory, 740–741
temperature dependence, 741 (F)
time dependence, 741 (F)
tritium pressure, 741 (F)
tritium recirculation, 737–739, 738 (F)
hydrogen pipelines, 365–372
experimental methods, 365–366
hydrogen-precharged specimen, 370 (F), 371–372
nominal stress-strain curves, 367 (F)
pearlite crack growth, 371 (F)
pearlite cracks, 370 (F)
ruptured samples, 368 (F)
STPG
chemical composition, 365 (T)
microstructure, 366 (F)
tensile specimen, 366 (F)
tensile fracture specimens, 368 (F)
true strain and pearlite cracks, 370 (F)
uncharged virgin specimen, 370 (F)
hydrogen precharged stainless steels. *See* nanoindentation
hydrogen trap sites, 485–492
hydrogen trapping character
high strength steels, 448–455
nano-sized NbC precipitates, 456–463
hydrogen trapping mechanisms, 438–447
hydrogen trapping (palladium), 464–468
hydrogen-assisted fracture
AISI 316 austenitic stainless steel (welded), 147–154
alloy composition, 149 (T)
experimental, 149
fracture mode, 151–153
fusion zone, 148 (F)
hydrogen-precharged welds, 152 (F)
notched tensile properties, 150–151, 151 (T)
smooth tensile properties, 150, 150 (T)
welded smooth tensile specimens, 152 (F)
austenitic stainless steels, 88–96
microstructural boundaries, 91
microvoid coalescence, 89–90
super duplex 2507 stainless steel, 96 (F)
tensile fracture surfaces, 94 (F), 95 (F)

two-phase microstructures, 91–92
type 316 austenitic stainless steel, 94 (F), 95 (F), 96 (F)
hydrogen-assisted fracture mechanism. *See* fracture surface topography analysis (FRASTA)
hydrogen-induced cracking, 46–53
4340-type steel, 47 (F), 48 (F)
5% nickel steel, 48–52
5% NiCrMoV Steel, 51 (T)
aging time, 50 (F)
ductile to brittle behavior, 51 (F)
high-purity 5% Ni steel, 52 (F)
high-purity modified HY130-type steel, 50 (T)
"ideally pure" 4340-type steel, 49 (F)
impurity segregation, 50 (F)
threshold stress intensity, 50 (F)
HY130-type steel, 47 (F)
IG fracture, 47 (F)
TG fracture, 47 (F)
threshold stress intensity, 48 (F)
ultra-high-strength steel, 47–48
hydrogen-induced fatigue crack growth acceleration
austenitic stainless steel, 131–138
acceleration rate, 137 (F)
drilled hole, 132 (F)
fatigue crack growth, 132–133
fatigue crack growth curves, 132 (F)
fatigue crack tip, 136–138
fatigue test specimen, 132 (F)
fatigue tests, 132
hydrogen migration, 137 (F)
martensitic transformation, 133–136
material, 131–132
specimen, 131–132
hydrogen-induced intergranular cracking, 613–621
model formulation, 614–617
ab-initio calculation, 617 (T)
first-principles calculations, 616–617
hydrogen transport, 617
interfacial decohesion, 614–616
interfacial diffusion coefficient, 618 (F)
interfacial hydrogen concentration, 619 (F)
normalized separation, 619 (F)
normalized stress, 619 (F)
hydrogen-induced transition, 29 (F)

I

IG fracture, 47 (F)
impurity segregation, 50 (F)
in situ electrochemical nanoindentation, 187–194
experimental procedure, 188
free energy curves, 191 (F)
free energy curves of HDN, 191 (T)
H effect, 192 (T)
L-D curves, 189 (F)
material constants, 191 (T)
mean pop-in load, 189 (T)
pop-in load, 189 (F)
sample preparation, 188 (T)
sample testing, 188 (T)
samples studied, 188 (T)
inelastic neutron scattering, 464–468
interfacial decohesion, 614–616
intergranular Superabundant Vacancies, 671–677
IPZA analysis, 284–287

J

Japan, hydrogen energy infrastructure, 308–315
austenitic stainless steels
crack growth, 311 (F)
crack growth behavior, 312 (F)
fatigue crack growth, 311–312
H-charge, 312 (F)
hydrogen entry, 310
hydrogen thermal desorption spectrum, 311 (F)
loading frequency, 312 (F)
non-diffusible hydrogen, 313–314
special heat treatment, 313–314
striation formation, 312–313
striation morphology, 312 (F)
type 316L, 311 (F)
case studies
dispenser failure, 314, 314 (F)
hydrogen station, EXPO 2005 (Nagoya), 314
hydrogen storage cylinder, 314–315
hydrogen storage cylinder of Cr-Mo steel, 315 (F)
Kasumigaseki Hydrogen Station, Tokyo, 314–315
material strength, 308–314
chemical composition, 309 (T)
crack length and number of cycles, 310 (F)
Cr-Mo steel: JIS SCM435, 309–310
fatigue crack growth, 309
steels, 308–309
voids, 309 (F)

L

lattice defect formation and degradation, 195–202
acceleration of, 197–198
experimental, 196–197
hydrogen and strain, 197 (F)
hydrogen charging, 196
hydrogen degradation, 198–201
hydrogen degradation evaluation, 197
Inconel 625
degradation susceptibility (DS), 200 (F)
hydrogen content, 200 (F)
stress-strain curves, 200 (F)
TDA profiles, 199 (F)
materials, 196

lattice defect formation and degradation pure iron *(continued)*
DS values, 201 (F)
hydrogen content, 198 (F), 201 (F)
lattice defect, 199 (F)
stress-strain curves, 201 (F)
TDA profiles, 198 (F)
TDA, 197
liquefaction, 322
low alloy steels, 349–356
experimental procedures, 351
experimental results
da/dn in hydrogen (SA-106), 357–364
fracture mode, 352–353
fracture surface (SA-106 tensile specimens), 353 (F)
stress strain curves, 351 (F)
tensile ductility, 352 (F)
tensile properties, 351–352
yield/tensile strength, 352 (F)
materials, 350
SA-106, 350 (T)
SA-372, 350 (T)
microstructures, 350 (F)
low carbon steel, 365–372
experimental methods, 365–366
hydrogen-precharged specimen, 370 (F)
nominal stress-strain curves, 367 (F)
pearlite crack growth, 371 (F)0
pearlite cracks, 370 (F)
ruptured samples, 368 (F)
STPG
chemical composition, 365 (T)
microstructure, 366 (F)
tensile specimen, 366 (F)
tensile fracture specimens, 368 (F)
true strain and pearlite cracks, 370 (F)
true strain and pearlite cracks, relationship between, 370 (F)
uncharged virgin specimen, 370 (F)

M

magnetocorrosion, 540–547
pipeline steel
bubble flow, 546
bubble formation, 546
cracking analysis, 545 (T)
electrochemical impedance spectroscopy (EIS), 542–543
hydrogen concentration, 544 (F)
impedance, 543 (F)
magnetic remanence, 542 (F)
magnetocorrosion assessment, 544–546
pitting analysis, 545 (T)
X100 type steel specimen, 545 (F)
martensitic transformation, 133–136
metal tritides, 686–693
lattice dilation, 690–691, 691 (F)
other materials, 692
precipitate shape, 692 (T)
surface/strain energy ratio, 692 (T)
platelet dimensions, 691–692, 692 (F)
platelet shape, 686–690
bubble growth, 689 (F)
dipole expansion, 689 (F)
dislocation dipole, 687 (F)
dislocation loop, 687 (F)
dislocation loop punching, 689 (F)
He bubble pressures, 689 (F)
spherical bubbles, 689 (F)
strain energy parameters, 688 (T)
surface energy parameters, 688 (T)
metals used in hydrogen, 405–412
DLC coating, 409–410 (F), 410 (F)
DLC transfer layer, 411 (F)0
enclosure/gas delivery system, 406 (F)
experiment, 406–407
friable MoS_2 coating, 408 (F)
friction coefficients, 407 (F), 408 (F), 411 (T)
sliding couples, 411 (T)
thrust washer tribometer, 406 (F)
Ti-6Al-4V, 407 (F)
transfer film, 409 (F)
worn X-750, 408 (F)
X-750, 408 (F)
metastable austenitic stainless steels, 123–130
average grain size, 124 (T)
constant load tests, 126–127
fractography, 128 (F)
time to fracture, 125 (F)
experimental
methods, 125
techniques, 125
hydrogen charging procedure, 125
hydrogen thermal desorption, 127–129
hydrogen partial pressure in TDS apparatus, 129 (F)
temperature dependencies, 129 (F)
materials, 124–125
mechanical properties, 124 (T)
phase structure, 124 (T)
specimens, 124–125
SSRT tensile tests, 125–126
stress-strain curves, 126 (F)
metastable beta titanium alloys
thermohydrogen processing (THP), 227–234, 229 (F)
4-step-sTHP concept, 232 (F)
beta-stabilizing hydrogen effect, 232 (F)
composition, 229 (T)
dehydrogenation, 233 (F)
hydrogen uptake, 231 (F)
near-beta titanium alloy Ti 10-2-3, 232 (F)
normalized hydrogen concentration profiles, 231 (F)

Mg-Al alloys
fracture surface (AM30), 262 (F)
fracture surface (AZ31), 262 (F)
fracture surface morphology (AZ91), 262 (F)
SCC fracture surface (AZ91)
fine parallel markings, 261 (F)
parallel facets, 261 (F)
parallel markings, 262 (F)
SCC surface fracture (AM30), 263 (F)
SCC surface fracture (AZ31), 263 (F)
secondary crack (AZ91), 261 (F)
stress corrosion cracking, 259–266
stress vs. apparent strain curves
AM30, 260 (F)
AZ31, 260 (F)
AZ91, 260 (F)
microalloyed pipeline steels
hydrogen sour environments conditions for cracking, 275–283
corrosion rates, 278 (F)
crack growth rates, 280 (F)
experimental, 276–277
free corrosion potentials, 278 (F)
K_{Ith} values, 280 (F)
steels chemical composition, 277 (T)
steels crack growths, 281 (T)
mixed-mode hydrogen assisted cracking, 70–77
experimental programme, 70–71
experimental results, 71–75
fracture surfaces, 72 (F)
fractographic analysis, 71–74
microscopic modes of fracture (steel), 73 (F), 74 (F)
materials science approach, 75
macroscopic crack parameters, 75 (F)
microstructural orientation angles, 75 (F)
Mo diffusion barrier, 718–725
Monte Carlo simulation, 671–677
equilibrium vacancy concentrations, 677
grain boundary structure at T=0, 673–674
symmetrical tilt boundary □=33(554) [1-10] at T=0, 674 (F)
Grand Canonical ensemble, 674–676
average thermal vacancy concentrations, 676 (F)
MD trajectory, 675 (F)
Voronoï decomposition of space, 674 (F)
snapshot of, 672 (F)
multiphase high strength steels, 62–69
A80 value, evolution of, 66 (F)
H-charged samples, 64–65
DP600 grade, 65 (F)
H-charging, 64
cathodic hydrogen charging, 64 (F)
H-charging time, 67 (F)
H-content, 65 (F)
hydrogen thermal desorption curve (DP600 grade), 68–69 (F)
materials, 63
DP600 grade, 63 (F)
FB450 grade, 63 (F)
S550MC grade, 63 (F)
TRIP700 grade, 63 (F)
Re, evolution of, 67 (F)
tensile curves, TRIP700 grade, 66 (F)
tensile testing, 64–65
thermal desorption analysis, 65

N

nanoindentation, 179–186
constants, 183 (T)
EBSD results, 181 (F)
elastic modulus, 184 (T)
experiment design, 180–181
alloys, 180 (T)
tensile testing data, 180 (T)
indentation pattern, 181 (F)
typical load – displacement curves, 182 (F)
nano-precipitates design, 448–455
nano-sized NbC precipitates, 456–463
near surface region of solids, 429–437
nickel
plastic strain localization, single crystals, 97–104
electron backscatter diffraction (EBSD) images, 101 (F)
experimental, 98–99
experimental methods, 99
experimental techniques, 99
hydrogen charging procedure, 98–99
materials, 98
PAS parameters, 103 (F)
slip line structure, 101 (F)
slip lines, 101 (F)
specimens, 98
stress-strain curves, 99 (F)
nickel metal in sulphuric acid
hydrogen evolution reaction, 292–299
cathodic polarization curves, 296 (F)
dislocation patterns issues, 294 (T)
dislocations distributions, 297 (F)
experimental setup, 293–294
thermo-kinetic analyze, 294–295
Ni-plated iron membranes
hydrogen permeation, 516–523
experimental, 518–519
input (H_2/Ni) interface, 522 (F)
input (H_2/Pd) interface, 520 (F)
Ni plated input surfaces, 521–523
plated Pd input surfaces, 519–520
nuclear related materials
hydrogen and/or helium accumulation and ion irradiation damage, 702–709
atomic transport, 704–705
austenitic steel in mercury, corrosion rate, 707 (F), 708 (F)

nuclear related materials *(continued)*
cavity size, 703 (T)
dual- and triple-beam configuration, 703 (T)
dual beam irradiation conditions, 707 (T)
dual beam irradiation (Fe/He), 706 (F)
F82H alloy, 706 (F)
hydrogen and helium concentration at 573 K, 708 (F)
hydrogen and helium depth profiles, 704 (F)
irradiation damage cumulated at 573 K, 707 (F)
mechanical properties, 705–708
microstructural impact, 702–703
number density, 703 (T)
physico-chemical properties, 705–708
RAFM alloy F82H, 705 (T)
triple beam irradiation conditions, 705 (T)
Tyranno-SA SiCf/SiC composite irradiation, 703 (T)
Tyranno-SA/SiC, 703 (T)

O

O-ring. *See* rubbers for O-ring

P

palladium
hydrogen trapping at dislocations, 464–468
calculated volumetric lattice strain, 467 (F)
computational results, 466–467
experimental results, 465–466
four IINS measurements, 466 (F)
octahedral sites, 467 (F)
Pd atom sites, 467 (F)
Pd-plated iron membranes
hydrogen permeation, 516–523
experimental, 518–519
input (H_2/Ni) interface, 522 (F)
input (H_2/Pd) interface, 520 (F)
Ni plated input surfaces, 521–523
plated Pd input surfaces, 519–520
pearlitic steels, progressively drawn, 70–77
experimental programme, 70–71
experimental results, 71–75
fracture surfaces, 72 (F)
fractographic analysis, 71–74
microscopic modes of fracture (steel), 73 (F), 74 (F)
materials science approach, 75
macroscopic crack parameters, 75 (F)
microstructural orientation angles, 75 (F)
pipeline steel
magnetocorrosion, 540–547
bubble flow, 546
bubble formation, 546
cracking analysis, 545 (T)
electrochemical impedance spectroscopy (EIS), 542–543
experimental work, 541–546
hydrogen concentration, 544 (F)
impedance, 543 (F)
magnetic properties, 541–542
magnetic remanence, 542 (F)
magnetocorrosion assessment, 544–546
pitting analysis, 545 (T)
X100 type steel specimen, 545 (F)
pipeline steel metallurgy, 333–339
alloy design, 334–335
alloy design and resultant microstructure, 339 (T)
CCT diagram (two pipeline alloys), 337 (F)
chemistry limits, 338 (T)
cooling rate effect, 336 (F)
hot rolling, 335
hydrogen induced cracking, 337–338
microstructure, 333
microstructures, typical, 333 (F)
NACE TM0284 Solution A testing, 337 (T)
processing, 335
rolling pipeline steels, 336 (F)
specifications, 338
strength design, 334–335
thermo-mechanical rolling (TMCP), 335–336
transmission pipeline steels, 335 (T)
volume fraction microstructure formation, 336 (F)
pipelines, 319–321
plastic zone, modeling, 640–646
crack tip emission, 643–645
shielding, 645 (F)
shielding and microstructures, 643–645
simulation set up, 641–643
applied stress intensity factor, 641 (F)
dislocations configurations, 642 (F), 643 (F)
polymeric materials, 726–734
dynamic mechanical analysis, 728
EPDM, 732–733
glass transitions temperature (Tg ° C.), 733 (F)
loss modulus, 732 (F)
storage modulus, 732 (F)
tan delta, 732 (F)
tritium exposure time, 733 (F)
exposure conditions, 727
materials, 727
PTFE, 730–731
tan delta vs. temperature, 731 (F)
UHMW-PE, 728–730
storage modulus, 730 (F)
UHMW-PE (2.3 years) tritium exposure
loss modulus, 729 (F)
storage modulus, 729 (F)
tan delta, 729 (F)
unexposed PTFE
loss modulus, 731 (F)

storage modulus, 731 (F)
tan delta, 731 (F)
unexposed UHMW-PE
loss modulus, 729 (F)
storage modulus, 729 (F)
tan delta, 729 (F)
unexposed Vespel® SP-1 polyimide
loss modulus, 732 (F)
storage modulus, 732 (F)
tan delta, 732 (F)
Vespel® polyimide, 731–732
prestrain
hydrogen pipelines, 365–372
low carbon steel, 365–372
type 316L austenitic stainless steel, 105–112
"Prometheus" setup. *See* hydrogen isotopes superpermeation
PTFE, 730–731
pure iron (cold worked)
elastic modulus and anelastic response of, 219–226
anelastic relaxations, 224 (F)
diatomic potential energy vs. separation curves, 220 (F)
displacements, 222 (F)
elastic displacement, 223 (T)
experimental, 221–222
Ferrovac E iron alloy, 221 (T)
square wave load, 222 (F)

R

residual hydrogen. *See* welded joints
residual stress relaxation, 413–420
rubber O-ring, 397–404
blister fracture, example, 398–400
crack, example, 399 (F)
cracks generated after decompression, 397 (F)
cross section, 399 (F)
experimental method, 400–401
durability tester, 401 (T)
durability tests, 401 (T)
EPDM rubber composite, 400 (T)
high pressure durability tester, 400 (F)
extrusion, 403 (F)1
high pressure hydrogen vessel, 398 (F)
inner cracks, 399 (F)
No. 1 O-ring, 402 (F), 403 (F)
No. 2 O-ring, 402 (F)
surface cracks, 399 (F)
rubbers for O-ring, 389–396
blister damage, tensile properties, and hydrogen contents, 394–395
blister growth, 394 (F)
blister initiation, 393–394, 394 (F)
composites exposited to hydrogen gas, 396 (F)
decompression of NBR composites, 392 (F)
equilibrium hydrogen content and hydrogen pressure, 392–393
experimental method, 390–391
growth behavior, 393–394
hydrogen content, 393 (F)
hydrogen release profiles, 391–392
materials, 389–390
chemical composition, 390 (T)
$\Pi_F$and C_{HO}, 396 (F)
rubber composites, 394 (F)

S

scandium deuteride films, 710–717
chemical properties, 713–714
experiment design, 712
hardness values
$ScD_2/SiO_2/Si$ film system, 714 (F)
$Sc/SiO_2/Si$ film system, 714 (F)
interfacial fracture energy measurement, 714–715
adhesion energy, 715 (F)
four point bend tests of ScD_2 film systems, 715 (F)
load-displacement curves, 715 (F)
mechanical properties, 713–714
silicon dioxide dissociation, 713 (F)
stress evolution, 711 (F)
science-based prognosis
alloy steels, 5 (F)
C-Mn steels, 5 (F), 17 (F)
cold worked 304 austenitic stainless steel, 8 (F)
Fe-superalloy, 9 (F), 13 (F)
HEAC data base, 4–10
crack arrest, 7 (F)
fatigue crack propagation rate, 8 (F)
high strength alloys, 5 (F)
high strength martensitic steels, 10 (F)
hydrocarbon inhibition, 10 (F)
low PH_2 environment enhanced fatigue propagation, 10 (F)
low strength ferrite-pearlite A516(70) steel, 6 (F)
threshold stress intensity, 5 (F), 9 (F)
HEAC growth rate, 14–15
HRR hydrostatic stress distributions, 15 (F)
quasi-static loading, 14–15
SGB hydrostatic stress distributions, 15 (F)
HEAC mechanism-based modeling, 10–18
adjustable parameters, 14 (T)
blunting, 15 (F)
C-Mn steels, 17 (F)
crack tip fracture process zone, 11–12
crack tip localization, 12 (T)
cyclic loading, 15–18
decohesion-based model of K_{TH}, 14 (T)
frequency, 17 (F)

science-based prognosis *(continued)*
H-trap binding energy, 12 (T)
hydrogen localization, 11–12
hydrostatic stress, 12 (T)
key length-scales, 15 (F)
measured and model predicted K_{TH} vs. H concentration, 13 (F)
quasi-static loading, 12–14
threshold stress intensity, 12–14
time dependence, 15–18
high strength alloys, 5 (F)
high strength martensitic steels, 10 (F)0
high strength steel (R_C 36), 10 (F)
hydrogen environment cracking, 1–4
H_2 damage evolution, 3 (F)
HEAC, 2 (F)
low strength ferrite-pearlite A516(70) steel, 6 (F)
Ni-superalloy, 9 (F), 13 (F)
SA-105 C-Mn steel, 8 (F)
shot-peened high strength low alloy steel, 413–420
300 M steel, 415 (F)
experimental method, 414–415
exposure tests
coated specimens, 416–417
notched 300M steel, 417 (F)
uncoated specimens, 417–418
uncoated/notched 300M steel, 418 (F)
shot-peened specimens, 415–416
slip bands, 43 (F)
Slow Strain Rate Test (SSRT), 56, 59–60
Stacking Fault Energy (SFE), 680–681
Stage II fatigue crack tip, 203–210
crack propagation rate, 205 (F)
crack wake, 209 (F)
experimental method, 203–204
crystallographic orientation of, 204 (F)
specimen, 204 (F)
fracture surface, 206 (F)
neat-tip region, 207–208 (F)
stress intensity factor range, 205 (F)
steel
diffusion coefficient of hydrogen, 524–531
diffusible hydrogen content determination, 528–531
gaseous hydrogen pre-charged X65 steel pipeline specimen, 529 (F)
gaseous hydrogen pre-charged X80 steel pipeline specimen, 530 (F)
low frequency impedance, 526–527
low frequency impedance measurement probe, 526 (F)
Seebeck effect and low frequency impedance, 529–531
thermoelectric power, 525–526
thermoelectric power surface contact probes, 526 (F)
X100 steel pipeline weld specimens, 531 (F)
X65 pipeline steel, 529–531
hydrogen distribution in, 477–484
DP600, 482 (F)
experimental procedure, 479–480
FB450 steel, 481 (F)
four studied steels, 482 (F)
hydrogen charging, 479, 480
hydrogen content (wppm), 480 (F)
materials, 479, 479 (T)
thermal desorption spectroscopy (TDS), 479–480, 480–483
steels, sustained load cracking of, 341–348
DOT 3AAX, 344 (F), 345 (F), 346 (F)
DOT 3T, 344 (F)
experimental procedures, 342–343
fracture mechanisms, 346–347
fracture surface images, 345 (F)
K_{TH} measurements, 345–346
K_{TH} plotted as function of H_2 gas pressure, 344 (F)
K_{TH} plotted as function of yield strength, 344 (F)
pressure vessel steels tested
composition, 342 (T)
yield strength, 342 (T)
SA372 grade J, 344 (F)
transgranular cracks, 346 (F)
X100, 344 (F), 345 (F), 346 (F)
stress corrosion cracking
alloy 600, 267–274
alloy 7050-T7451 plate, 251–258
Al-Zn-Mg-Cu alloys, 243–250
Mg-Al alloys, 259–266
structural alloy performance
alloy steels, 5 (F)
C-Mn steels, 5 (F), 17 (F)
cold worked 304 austenitic stainless steel, 8 (F)
Fe-superalloy, 9 (F), 13 (F)
HEAC data base, 4–10
crack arrest, 7 (F)
fatigue crack propagation rate, 8 (F)
high strength alloys, 5 (F)
high strength martensitic steels, 10 (F)
hydrocarbon inhibition, 10 (F)
low PH_2 environment enhanced fatigue propagation, 10 (F)
low strength ferrite-pearlite A516(70) steel, 6 (F)
threshold stress intensity, 5 (F), 9 (F)
HEAC growth rate, 14–15
HRR hydrostatic stress distributions, 15 (F)
quasi-static loading, 14–15
SGB hydrostatic stress distributions, 15 (F)

HEAC mechanism-based modeling, 10–18
adjustable parameters, 14 (T)
blunting, 15 (F)
C-Mn steels, 17 (F)
crack tip fracture process zone, 11–12
crack tip localization, 12 (T)
cyclic loading, 15–18
decohesion-based model of K_{TH}, 14 (T)
frequency, 17 (F)
H-trap binding energy, 12 (T)
hydrogen localization, 11–12
hydrostatic stress, 12 (T)
key length-scales, 15 (F)
measured and model predicted K_{TH} vs. H concentration, 13 (F)
quasi-static loading, 12–14
threshold stress intensity, 12–14
time dependence, 15–18
high strength alloys, 5 (F)
high strength martensitic steels, 10 (F)0
high strength steel (R_C 36), 10 (F)
hydrogen environment cracking, 1–4
H_2 damage evolution, 3 (F)
HEAC, 2 (F)
low strength ferrite-pearlite A516(70) steel, 6 (F)
Ni-superalloy, 9 (F), 13 (F)
SA-105 C-Mn steel, 8 (F)
structural materials, 438–447
hydrogen trapping mechanisms, 439
supermartensitic stainless steel TIG welds, 443–446
desorption characteristics, 444–446
hydrogen contents, 444 (F)
hydrogen desorption, 444
samples electrochemically charged with deuterium, 445 (F)
TDS spectrum of SMSS, 445 (F)
Ti-based alloys, 439–441
electrochemically hydrogenated Ti–6Al–4V alloy, 440–441 (F), 441 (T)
electronically charged Ti-6Al-4V, 439–441
hydrogenated Ti–6Al–4V specimens, 440 (F)
Ti-based alloys, 439
Timetal LCB alloys, 441–443
hydrogen concentrations desorbed, 442 (T)
hydrogen desorption, 441–443
hydrogen evolution, 442 (F)
TDS plot of Ti-LCB specimens, 443 (T)
super alloys
tritium autoradiography investigation, 501–507
annealed 600 superalloy, 504
β-emission source, depth of, 504 (F)
bolt-loaded specimen, 502 (F)
deformed grain boundaries, 506
electrochemical tritium charging apparatus, 503 (F)
experimental details, 501–504
grain boundaries, under stress, 506 (F)
materials, 501, 501 (T)
notched specimen, 502 (F)
radiation sensitive film coating, 503
radiation sensitive film process, 503
rotated grain boundaries, 506
SEM observation, 503–504
specimen preparation, 502
specimen surface polishing, 503
stressed 600 super alloy, 505–506
stressed 600 super alloy (X2000), 505 (F)
stressed X750 super alloy, 505–506, 506 (F)
stress-free 600 superalloy, 504 (F)
surface emulsion coating layer, 504 (F)
tritium charge, 502
supermartensitic stainless steel TIG welds, 443–446

T

tempered martensite, 456–463
experimental, 457
HRTEM
micrographs, 459 (F)
observation, 458–459
TDS analysis, 459–462
hydrogen content, 461 (F)
TDS spectra, 460 (F), 461 (F)
Vickers hardness, 458, 458 (F)
TG fracture, 47 (F)
thermal desorption spectroscopy (TDS), 469–476, 485–492
hydrogen trap sites, high strength steel, 485–492
pure iron 15% deformed, 489 (F)
pure iron TDS results, 489 (F), 490 (F)
TRIP700, TDS results, 489 (F)
TRIP700 17% deformed, 489 (F)
TRIP700 TDS results, 488 (F), 491 (F)
steel, hydrogen distribution in, 477–484
DP600, TDS spectrum for, 482 (F)
experimental procedure, 479–480
FB450 steel, TDS spectrum of, 481 (F)
four studied steels, TDS spectrum for, 482 (F)
hydrogen charging, 479, 480
hydrogen content (wppm), 480 (F)
materials, 479, 479 (T)
thermal desorption spectroscopy (TDS), 479–480, 480–483
thermal desorption analysis, 471–473
calculated H-profiles, 473 (F)
DP600, 471–473
pure iron, 471–473

thermal desorption spectroscopy (TDS) *(continued)*
TDS curves, 472 (F)
total H-content, 473 (F)
Thermo Mechanical Control Processing (TMCP), 335–336
thermodynamics of decohesion
hydrogen, 637–639
grand force potential, 638 (F)
hydrogen concentration, 638 (F)
traction curves, 638 (F)
Ti-H system
a and c lattice parameters, predicted, 636 (F)
calculated metastable phase diagram, 635 (F)
calculated stable phase diagram, 635 (F)
coherent phase diagram, 637 (F)
δ–TiH hydrides, 637 (F)
traction curves, 637–639
thermoelectric power, 525–526
thermohydrogen processing (THP)
metastable beta titanium alloys, 227–234, 229 (F)
4-step-sTHP concept, 232 (F)
alloys, composition of, 229 (T)
beta-stabilizing hydrogen effect, 232 (F)
dehydrogenation, 233 (F)
hydrogen uptake, 231 (F)
near-beta titanium alloy Ti 10-2-3, 232 (F)
normalized hydrogen concentration profiles, 231 (F)
Ti-6Al-4V alloy, 235–242
experimental, 236
mechanical properties by hydrogenation, 240–241
fracture morphologies, 241 (F)
mechanical properties, 240 (T)
microstructure, 236–240, 238 (F)
hydrogenating, 237 (F)
solid solution and aging, after, 239 (F)
Ti-H system, 634–637
Timetal LCB alloys, 441–443
hydrogen concentrations desorbed, 442 (T)
hydrogen desorption, 441–443
hydrogen evolution, 442 (F)
TDS plot of Ti-LCB specimens, 443 (T)
titanium thin films, 548–555
220 nm Ti-film
broad Ti-peak, 551 (F), 554 (F)
EMF measurement, 553 (F)
EMF-Pressure-Concentration curves, 551 (F)
stress curves, 553 (F)
XRD pattern, 551 (F), 554 (F)
experimental procedure, 549–550
hydrogen solubility, 552 (T)
sputtering parameters, 550 (T)
Ti-H systems, 552 (T)
transient loading, 562–569
transition metals and alloys
density of states, 678–685
Co-Ni alloy, 683 (F)
Cr15Mn17, 681 (F)
Cr18Ni16Mn10, 681 (F)
Fe-Ni alloy, 683 (F)
H embrittlement and N (Ef), 679–680
N (Ef) and stacking fault energy (SFE), 680–681
Ni-Cu alloy, 682 (F)
nitrogen content, 681 (F)
Pd-Ag alloy, 682 (F)
predicted H embrittlement index, 680 (F)
SFE and H embrittlement, 682–683, 682 (F), 683 (F)
transmission electron microscopy (TEM) study
helium-bearing fusion welds, 694–701
austenitic "matrix", 698 (F)
bubble free zone (BFZ), 699 (F)
δ ferrite grain, 698 (F)
deformation twinning, 697 (F)
experimental procedure, 695–696
fusion weld region, 696 (F)
general microstructure, 696–697
helium bubbles, 699 (F)
HERF 304L forging, 696 (F)
oxide inclusions, 697 (F)
sectioning procedure, 696 (F)
weld microstructures, 697 (F)
tritium autoradiography investigation, 501–507
annealed 600 superalloy, 504
β-emission source, depth of, 504 (F)
bolt-loaded specimen, 502 (F)
deformed grain boundaries, 506
electrochemical tritium charging apparatus, 503 (F)
experimental details, 501–504
grain boundaries, under stress, 506 (F)
materials, 501, 501 (T)
notched specimen, 502 (F)
radiation sensitive film coating, 503
radiation sensitive film process, 503
rotated grain boundaries, 506
SEM observation, 503–504
specimen preparation, 502
specimen surface polishing, 503
stressed 600 super alloy, 505–506
stressed 600 super alloy (X2000), 505 (F)
stressed X750 super alloy, 505–506, 506 (F)
stress-free 600 superalloy, 504 (F)
surface emulsion coating layer, 504 (F)
tritium charge, 502
tritium effects. *See* polymeric materials
two dimensional discrete dislocation dynamics, 640–646

crack tip emission, 643–645
shielding, 645 (F)
shielding and microstructures, comparing, 643–645
simulation set up, 641–643
applied stress intensity factor, 641 (F)
dislocations configurations, 642 (F), 643 (F)
type 304L stainless steel
strain-induced martensite formation, 171–178
experimental procedure, 172
fractured tensile specimens, 173 (F)
hydrogen-charged sample fracture features, 176 (F)
hydrogen-charged samples, 177 (F)
stainless steel forgings, 172 (T)
tensile behavior, 173 (F)
tensile specimens, 173 (F), 174 (F), 175 (F)
tensile test, 174 (F)
type 316 stainless steel
internal hydrogen, effect on fatigue strength, 139–146
alloy H, 142 (F), 143 (F), 144 (F)
alloy I, 144 (F)
compositions, 141 (T)
fatigue life, 142–143
fatigue testing, 141
hydrogen content, 143
hydrogen precharging, 140–141
materials, 140–141d
mechanical properties, 142 (T)
representative tensile flow curves, 142 (F)
S-N curve, 144 (F)
tensile properties, 141–142
tensile testing, 141
type 316L austenitic stainless steel, 105–112
chemical composition, 106 (T)
dimple formation, 108–111
shear stress-fracture region, 111 (F)
tensile fracture surfaces, 110 (F)
experimental method, 106
hydrogen absorption properties, 107
hydrogen exposed disc-shaped specimens, 107 (F)
tensile-fracture specimens, 107 (F)
material, 106
tensile properties, 107–108
argon- and hydrogen-exposed specimens, 108 (F)
reduction of area against prestrain, 108 (F)

U

UHMW-PE, 728–730
uranium, corrosion by hydrogen, 556–561
60° FIB section, SEM of, 560 (F)
blisters, 559 (F)
circular blister, 559 (F)
corrosion pit, 559 (F)
experimental, 557–559
grain boundary, 559 (F)
hydriding reaction of U powder, 557 (F)
SEM blister formation images, 558 (F)
surface film rollups, 559 (F)

V

very high strength steels, 300–307
diffusion characteristics, 304–305
experimental procedures
electrochemical permeation tests, 302, 304 (T)
thermal desorption, 302–303
hydrogen diffusion characteristics, 304 (T)
hydrogen dosage, 302–303
materials, 301–302
chemical composition, 301 (T)
mechanical properties, 305–306
elongation comparison, 306 (T)
fracture surfaces, 306 (F)
stress-strain curves, 305 (F)
mechanical tests, 303
permeation build-up transients, 305 (F)
thermal desorption, 302–303, 304 (T)
vacuum thermal desorption, 303 (F)
VHSS, 303 (T)
Vespel® polyimide, 731–732
Vickers hardness, 458, 458 (F)
Voronoï decomposition of space, 674 (F)

W

welded joints, 373–380
base metal, chemical composition, 374 (T)
crack growth curves, 379 (F)
experimental methods, 374–375
fatigue crack growth, 376–377
fatigue specimen, 375 (F)
first layer, 379 (F)2
fracture surface, 377, 379
hydrogen content, 376
materials, 373–374
second layer, 379 (F)
small hole, 375 (F)
TDS results, 378 (F)
TDS specimens, 378 (F)
weld metal, 378 (T)
weld rods, 374 (T)
welded joint
macrostructure, 374 (F)
microstructures, 374 (F)
Vickers hardness, 375 (F)